

Lecture Notes in Mechanical Engineering

Harshit K. Dave
Uday Shanker Dixit
Dumitru Nedelcu *Editors*


Recent Advances in Manufacturing Processes and Systems

Select Proceedings of RAM 2021

 Springer


Lecture Notes in Mechanical Engineering

Series Editors

Francisco Cavas-Martínez , Departamento de Estructuras, Universidad Politécnica de Cartagena, Cartagena, Murcia, Spain

Fakher Chaari, National School of Engineers, University of Sfax, Sfax, Tunisia

Francesca di Mare, Institute of Energy Technology, Ruhr-Universität Bochum, Bochum, Nordrhein-Westfalen, Germany

Francesco Gherardini , Dipartimento di Ingegneria, Università di Modena e Reggio Emilia, Modena, Italy

Mohamed Haddar, National School of Engineers of Sfax (ENIS), Sfax, Tunisia

Vitalii Ivanov, Department of Manufacturing Engineering, Machines and Tools, Sumy State University, Sumy, Ukraine

Young W. Kwon, Department of Manufacturing Engineering and Aerospace Engineering, Graduate School of Engineering and Applied Science, Monterey, CA, USA

Justyna Trojanowska, Poznan University of Technology, Poznan, Poland

Lecture Notes in Mechanical Engineering (LNME) publishes the latest developments in Mechanical Engineering—quickly, informally and with high quality. Original research reported in proceedings and post-proceedings represents the core of LNME. Volumes published in LNME embrace all aspects, subfields and new challenges of mechanical engineering. Topics in the series include:

- Engineering Design
- Machinery and Machine Elements
- Mechanical Structures and Stress Analysis
- Automotive Engineering
- Engine Technology
- Aerospace Technology and Astronautics
- Nanotechnology and Microengineering
- Control, Robotics, Mechatronics
- MEMS
- Theoretical and Applied Mechanics
- Dynamical Systems, Control
- Fluid Mechanics
- Engineering Thermodynamics, Heat and Mass Transfer
- Manufacturing
- Precision Engineering, Instrumentation, Measurement
- Materials Engineering
- Tribology and Surface Technology

To submit a proposal or request further information, please contact the Springer Editor of your location:

China: Ms. Ella Zhang at ella.zhang@springer.com

India: Priya Vyas at priya.vyas@springer.com

Rest of Asia, Australia, New Zealand: Swati Meherishi at swati.meherishi@springer.com

All other countries: Dr. Leontina Di Cecco at Leontina.dicecco@springer.com

To submit a proposal for a monograph, please check our Springer Tracts in Mechanical Engineering at <https://link.springer.com/bookseries/11693> or contact Leontina.dicecco@springer.com

Indexed by SCOPUS. All books published in the series are submitted for consideration in Web of Science.

More information about this series at <https://link.springer.com/bookseries/11236>

Harshit K. Dave · Uday Shanker Dixit ·
Dumitru Nedelcu
Editors

Recent Advances in Manufacturing Processes and Systems

Select Proceedings of RAM 2021

 Springer

Editors

Harshit K. Dave
Department of Mechanical Engineering
S. V. National Institute of Technology
Surat, Gujarat, India

Uday Shanker Dixit
Department of Mechanical Engineering
Indian Institute of Technology Guwahati
Guwahati, Assam, India

Dumitru Nedelcu
Gheorghe Asachi Technical
University of Iasi
Iasi, Romania

ISSN 2195-4356

ISSN 2195-4364 (electronic)

Lecture Notes in Mechanical Engineering

ISBN 978-981-16-7786-1

ISBN 978-981-16-7787-8 (eBook)

<https://doi.org/10.1007/978-981-16-7787-8>

© The Editor(s) (if applicable) and The Author(s), under exclusive license to Springer Nature Singapore Pte Ltd. 2022

This work is subject to copyright. All rights are solely and exclusively licensed by the Publisher, whether the whole or part of the material is concerned, specifically the rights of translation, reprinting, reuse of illustrations, recitation, broadcasting, reproduction on microfilms or in any other physical way, and transmission or information storage and retrieval, electronic adaptation, computer software, or by similar or dissimilar methodology now known or hereafter developed.

The use of general descriptive names, registered names, trademarks, service marks, etc. in this publication does not imply, even in the absence of a specific statement, that such names are exempt from the relevant protective laws and regulations and therefore free for general use.

The publisher, the authors and the editors are safe to assume that the advice and information in this book are believed to be true and accurate at the date of publication. Neither the publisher nor the authors or the editors give a warranty, expressed or implied, with respect to the material contained herein or for any errors or omissions that may have been made. The publisher remains neutral with regard to jurisdictional claims in published maps and institutional affiliations.

This Springer imprint is published by the registered company Springer Nature Singapore Pte Ltd.

The registered company address is: 152 Beach Road, #21-01/04 Gateway East, Singapore 189721, Singapore

Preface

Since 2010, Department of Mechanical Engineering at Sardar Vallabhbhai National Institute of Technology, Surat, has been organizing series of conferences on “Recent Advances in Manufacturing.” In order to enable the sharing of knowledge in the areas of manufacturing technologies, we have organized six national conferences on “Recent Advances in Manufacturing” since 2010, and the first international conference on Recent Advances in Manufacturing (RAM-2020) was organized in July 2020. The conference is organized to bring the academicians, researchers and practicing engineers for sharing their experiences in the field of advance manufacturing. RAM-2021 aims to provide the opportunity for networking among participant institutes/organizations/industries to systematically confront the challenges in mutual areas of interest to advance manufacturing technology in these areas.

The proceedings volumes are published in the Springer series *Lecture Notes in Mechanical Engineering* in two volumes, viz. Volume 1—*Recent Advances in Manufacturing: Processes and Systems* and Volume 2—*Recent Advances in Manufacturing: Modeling and Optimization*. We also acknowledge the academic support from Prof. Dumitru Nedelcu, Prof. U. S. Dixit, Prof. J. Ramkumar and Prof. Panagiotis Kyratsis while editing both the volumes. In this volume, a total of 80 papers have been included in the domain of conventional and unconventional material removal processes, material forming processes, welding and joining processes, casting processes, additive manufacturing processes and characterization of composite materials.

As the entire world is facing the threat from corona pandemic, the international as well as interstate travel is restricted. However, we have tried our best to carve out a comprehensive schedule, keynote speakers, oral presentations in both online and offline mode, all of which will facilitate stimulating insightful discussions within the research community. In spite of such a pandemic situation, 181 participants have presented their findings and exchanged ideas related to manufacturing domain.

We are thankful to the conference organizing committee members, the advisory committee members, the reviewers, session chairs and the volunteers, without whose generous contributions this conference would not have been successfully conducted.

Most of all, we thank the participants for enriching the international conference with their active participation.

Surat, India

Dr. Shailendra Kumar
Organizing Secretary

Dr. Harshit K. Dave
Organizing Secretary, RAM-2021

Contents

A Study on Residual Stress Distribution in Welded Joint of P91 and SS304H Steel Plate	1
Sachin Sirohi, P. K. Taraphdar, Prakash Kumar, and Chandan Pandey	
A Methodology for Data-Driven Estimation of Forging Load	11
Kaustabh Chatterjee, Uday S. Dixit, Jian Zhang, and Pavel A. Petrov	
A Preliminary Investigation on Different Tool Wears in Sustainable Electrical Discharge Machining of Ti-6Al-4V	23
Shaik M. Basha, Harshit K. Dave, and Himanshu V. Patel	
A Review on Microstructure and Mechanical Properties of L-PBF 17-4PH and 15-5PH SS	37
I. Kartikeya Sarma, N. Selvraj, and A. Kumar	
A Review on Twin Wire Arc Additive Manufacturing of Metals and Alloys: Microstructure and Mechanical Properties	55
Poonam S. Deshmukh and Dan Sathiaraj	
A State of the Art Review of Additively Manufactured Auxetic Structures	69
Shailendra Kumar, Swapnil Vyavahare, Soham Teraiya, Jyothi Kootikuppala, and Harika Bogala	
ABS-Fly Ash Composite Filaments for Fused Deposition Modeling	85
Abdullah Alduais, Feyza Kazanç, Göknur Bayram, and Sezer Özerinç	
A Comparative Study and Optimization of Parameters of Turning UD-GFRP in Dry, Wet and Cryogenic Condition by Using PCD Tool with Taguchi Method	97
Hazari Naresh and Padhy Chinmaya Prasad	

An Experimental Investigation on Effect of Process Parameters on Microstructure and Mechanical Properties of Spheroidal Graphite Cast Iron	115
Harshit P. Modi, Jay R. Raval, Deep S. Patel, and Vipul P. Patel	
An Insight of Compacted Graphite Iron (CGI) Characteristics and Its Production: A Review	131
Mamta Patel and Komal Dave	
An Overview on Metallic and Ceramic Biomaterials	149
Soham V. Kulkarni, Amit C. Nemade, and Puskaraj D. Sonawwanay	
Analysis of Deep Drawing Process on Composite Sheet	167
Preyashi B. Manjrawala and Dhyey R. Savaliya	
Anatomy of a Fused Filament Fabrication (FFF) 3D Printing System for High-Grade Polymers (HGPs)—An Overview	179
Chinmaya Prasad Padhy, S. Suryakumar, and N. Raghunath Reddy	
Appropriateness Investigation on Three Different Layers Fashion of Specially Treated Banana/Epoxy/Fiberglass Hybrid Composite for Bio-medical Appliances	197
T. Malyadri, Afreen Begum, Nagasrisaihari Sunkara, and M. S. Srinivasa Rao	
Automation Advancements in Wind Turbine Blade Production: A Review	209
K. P. Desai, D. Binu, A. V. V. D. Pavan, and A. P. Kamath	
Characterization of Damage Behavior During Hot Forging	223
Ahmed A. M. Okasha, Hussein M. A. Hussein, Mostafa Shazly, and Osama M. Dawood	
Cutting Force Assessment in HSM of Inconel 718 Aided with Water Vapour as an Eco-Friendly Cutting Fluid	243
Ganesh S. Kadam and Raju S. Pawade	
“Design and Development of S Band Radio Frequency (RF) Cavity Filter Using Carbon Fibre Reinforcement Polymer (CFRP) Material for Communication Satellites”	253
Dipak Chopda, Vijay Kumar, Komal Dave, Prempal Kumar, Prashant Kumar, Nitin Kumar, and Hemendra Kansara	
Design and Manufacturing of a Test Rig for Experimental Studies on Misalignment Effect Between Rotors	265
Mili Hota and V. D. Dhiman	

Design, Modeling, and Simulation of Low-Cost Magnetorheological Fluid-Based Prosthetic Leg 281
 Ganapati Shastry, Ashish Toby, Seung Bok Choi, Vikram G. Kamble, and T. Jagadeesha

Development and Comparison of Natural Fiber Composite Boards Made Using Water Hyacinth Fiber 295
 Tony Varghese, Muhzin Ibnu, Mathews K. Tom, Mathew Joseph, and Rony Sebastian

Development of Al₂O₃ Nanoparticulates AA6061-T6 Aluminium Alloy Functionally Graded Composites via Friction Stir Processing: Effect of Tool Pin Profile on Mechanical and Tribological Properties 305
 M. D. Sameer, B. Archith Reddy, Ch. Sai Kumar, N. Saiteja, and J. Dhanush

Development of Part Build Orientation Algorithm for FDM 3D Printing 317
 Rushikesh P. Urunkar and Sachin Mastud

Development of Twin Fin Extension Liquefier Design for FFF 3D Printers Through Finite Element Analysis 329
 Ashish Agrawal, Mansingh Armo, Deepak Kumar, Siddharth Singh, Krishnanand, and Mohammad Taufik

Effect of Corrosion Behaviour of Microplasma Arc Welded Stainless Steel 316L Thin Sheet 339
 Dipankar Saha, Abhradip Pal, Chandan Das, and Sukhomay Pal

Effect of Electrode Vibration Welding on Impact and Tensile Strength of 1018 Mild Steel Weld Joints 347
 Bade Venkata Suresh, Y. Shireesha, and P. Srinivasa Rao

Effect of Low Temperature Treatments on the Stabilization of Transition Class Steel Used in Satellite Launch Vehicles 361
 Tony Varghese, K. Sreekumar, K. Thomas Tharian, and Saju Sebastian

Effect of Nozzle Geometry on Melt Flow of Eutectic Sn–Bi Low-Melting Point Alloy in Fused Deposition Modeling 369
 Alok Kumar Trivedi, P. S. Robi, and Sukhomay Pal

Effect of the Rolling Direction on the Mechanical and Microstructural Properties of AISI 316L Stainless Steel Welded Joint 381
 Vivekananda Haldar and Sukhomay Pal

Effect of Tool Movement in Electro-Discharge Machining Process—A Review 391
 Sudhanshu Kumar and Dilip Sen

Enhancement of Mechanical Properties Alkali-Treatment and Polylactic Acid Coated Woven Jute Fiber Reinforced Composites	403
P. Naresh Sagar, Naveen Reddy CH, and T. Malyadri	
Designing and Developing of a Renewable Agrobot to Enhance Harvest Productivity and Reduce Water Consumption	415
Arafa S. Sobh, Hussein M. A. Hussien, and Ali Abd El-Aty	
Estimation of Mechanical Properties of Kenaf Fiber Reinforced Polyester Composites	427
Shilpa S. Bhambure and Addanki S. Rao	
Evaluating Torsional Properties of FDM Components for Various Layer Heights	437
Prasad A. Hatwalne and S. B. Thakare	
Experimental Investigation in Wire Cut EDM of Inconel 718 Superalloy	445
Ayanesh Y. Joshi, Vaishal J. Banker, Kenil K. Patel, Kashyap S. Patel, Devarsh M. Joshi, and Madhav R. Purohit	
Experimental Investigation of Average Surface Roughness and Chip Morphology in End Milling of Aluminium Alloy 6151 Using Uncoated and TiAlN-Coated HSS Tools	457
I. Suresh Kannan	
Experimental Investigation of Mechanical Properties of AA 7075-T6 by Friction Stir Processing	465
A. D. Wable and S. B. Patil	
Experimental Investigation on Mechanical Properties of Friction Stir Dissimilar Welded Joints of Al AA6063 and SS 304 Alloys	479
Debashis Mishra and Anil Kumar Das	
Experimental Investigations to Enhance the Rheological Properties of Vegetable Oils Blending with Mineral Oil	487
Santhosh Kumar Kamarapu, M. Amarnath, and B. Suresha	
Experimental Study on Tensile Behavior of Tri-axial Hybrid Fiber Composites	493
Yegireddi Shireesha and Govind Nandipati	
Forming Simulation of Bump Foils Used in Complaint Gas Foil Bearings	503
Rakesh K. Sahoo, Debabrata Mohapatra, and Suraj K. Behera	
Friction Stir Welding of Heat-Treated Inconel 718 Alloy, and Its Mechanical and Microstructural Analysis	523
Sanjay Raj and Pankaj Biswas	

Heat Transfer Model of Coil in a Bell Annealing Furnace 533
 Deepoo Kumar, Nurni N. Viswanathan, and Partha Sarathi Sarkar

Hybridized Nanotubes and Graphene Oxide in CFRP Development for Space Use 545
 J. D. Solanki, D. A. Vartak, Y. S. Ghotekar, N. A. Deshpande, N. Kumar, B. Satyanarayana, A. K. Lal, and P. M. Bhatt

Investigation on Effect of Different Tool Configurations on Heat Generation During Friction Stir Welding (FSW) of AA 6061 T6 555
 Nisarg Patel, Shalin Marathe, and Harit Raval

Investigation on Mechanical Properties of 3D Printed PETG Material 571
 T. Malyadri, Nagasrisaihari Sunkara, and M. S. Srinivasa Rao

Mechanical Behavior of Inconel 625 and 17-4 PH Stainless Steel Processed by Atomic Diffusion Additive Manufacturing 583
 Balaji M. Jagtap, Ganesh M. Kakandikar, and Samidha A. Jawade

Mechanical Behavior of Nylon Load Bearing Structures Fabricated by Fused Deposition Modeling 595
 Sanket S. Jagtap, Ganesh P. Borikar, and Snehal B. Kolekar

Mechanical Characterization of Composite Material Fabricated by Friction Stir Processing Technique 609
 V. Pradeep, Anil Kumar Bodukuri, and Madeeha Zoufeen

Mechanical Characterisation of Nano Hybrid Composites 623
 A. Vinay, T. Malyadri, and Lanka Sandeep Raj

Mechanical Properties of 3D-Printed ABS with Combinations of Two Fillers: Graphene Nanoplatelets, TiO₂, ATO Nanocomposites, and Zinc Oxide Micro (ZnOm) 635
 N. Vidakis, M. Petousis, E. Velidakis, and A. Maniadi

Mechanical Testing and Optimization of Bamboo and Tamarind Fiber Composites 647
 Gowdagiri Venkatesha Prasanna, Achyutuni Venkata Naga Sri Harsha, Vemula Sunil Kumar, and Rapolu Srilekha

Mechanical, Degradation, and Flammable Behavior of VALOX_{100-x}—X Wt.% Polycarbonates Composite Materials for Electrical Plugs, Sockets, and Extension Applications 659
 Khalid Algadah, Subbarayan Sivasankaran, and Abdulaziz S. Alaboodi

Methods and Parameter Optimization of Manufacturing Process Using Alginate-Based Hydrogel Bioinks	673
M. B. Łabowska, P. Szymczyk-Ziółkowska, I. Michalak, and J. Detyna	
Microstructural and Mechanical Properties Analysis of Fibre Laser Welding of Dissimilar AA6061 and AA2024 Aluminium Alloy	681
Pradyumn Kumar Arya, Vivek Kumar, Dan Sathiaraj, I. A. Palani, and Neelesh Kumar Jain	
Modelling Factors Influencing Company Decision on Distribution Structure Using Interpretive Structure Modelling (ISM)	689
Mudit Kumar Rawat and Rajiv Kumar Sharma	
Modern Processes Improvements and Capability Analysis of Friction Stir Welded Dissimilar Nonferrous Materials—A Review	701
Rajnish Singh and Yogesh Kumar	
Novel Hybrid Bio Composites of PLA with Waste Bio Fillers	717
D. V. Lohar, A. M. Nikalje, and P. G. Damle	
Investigation on Formability of Tailor Welded Blanks (TWBs) During Single Point Incremental Forming (SPIF) Process	731
Gireesh Sripathireddy, Shalin Marathe, and Harit Raval	
Optimization of Design Parameters Under Compression and Shear Loading of FDM Fabricated Re-Entrant Auxetic Structure Using Failure Mode Map	747
Shailendra Kumar, Swapnil Vyavahare, and Kokani Nirmal	
Parametric Influences on Powder Mixed Dielectric in Wire EDM for Processing Ti6Al4V	761
Sadananda Chakraborty, Souren Mitra, and Dipankar Bose	
Performance of a Single Point Cutting Tool with Textured Surfaces: A Comparative Study of Different Textured Patterns	777
Manoj Nikam, Anurag Karulkar, Aveek Chowdhury, Hasan Khalfay, and Darshan Rathod	
Post Processing 3D Printed UAV Wing Enabling Trailing Edge Morphing Technology	791
Krunalkumar N. Patel, Anirudh Manoj, Mohammed Shams H. Sayed, K. Shah Kaushal, Swayam J. Shah, and Harshit K. Dave	
Preliminary Investigations of Low Plasticity Burnishing Process on Mechanical Properties of Aluminum Alloy	803
S. R. Thorat and A. G. Thakur	

Recent Advancements in Hybrid Investment Casting Process—A Review 817
 C. V. Morsiya and S. N. Pandya

Recent Advancements in TIG Cladding Process on Non-ferrous Alloys: A Review 833
 Sujeet Kumar and Anil Kumar Das

Reinforced Composites from Natural Fiber: A Review 847
 Sagar Singh, Chitranjan Agarwal, M. S. Khidiya, and M. A. Saloda

Research Progress in Gas Tungsten Arc Cladding on Steel: A Critical Review 859
 Md Sarfaraz Alam and Anil Kumar Das

Review of Enhancement of Polymer for Material Extrusion Process by Combining with Filler Material 869
 Mizab Ahmed E. A. Bardi, Shubham A. Bokade, Sushant L. Gunjal, Omkar R. Bedade, and Shreeprasad S. Manohar

Review on Friction-Based Additive Manufacturing Processes: Types, Defects, and Applications 885
 Bhumi K. Patel, Falak P. Patel, and Vishvesh J. Badheka

Selection of Optimal EDM Process Parameters for Machining Maraging Steel Using Grey-Fuzzy Relational analysis—An Experimental Approach 905
 M. D. Sameer, B. Sai Kartheek Reddy, N. Amrutha, K. Srishma, and K. Samantha

Shore Hardness Characterization of FDM Printed PLA/Epoxy/MGFs Composite Material Structure 919
 Ammar Mustafa, Bandar Aloyaydi, Subbarayan Sivasankaran, and Fahad A. Al-Mufadi

Study on Impact Properties of Hybrid Composites Fabricated by VARTM Process for Structural Applications 927
 Prasanth Kumar Kottapalli, Sai Kumar Balla, Himanshu V. Patel, and Harshit K. Dave

Study on Influence of Process Parameters on Feature Quality and Depth of Features Produced by Heat-Assisted Incremental Forming 935
 Vishal John Mathai, Joseph Babu, Noel Peter, Leo Mathew, and Sobin Siby

Study the Characterization of Hydroxyapatite and Silver Doped Hydroxyapatite Using Pin-on-Disc 947
 L. B. Mulla, G. G. Mujawar, P. B. Gavali, and Y. N. Dhulugade

Synthesis of Bulk Consolidated Ti-46Al-1B (at%) Alloy via Powder Metallurgy Route Using Induction Sintering Technique 957
Mrigesh N. Verma and Vijay N. Nadakuduru

The Development of Cemented Carbide with Cobalt Composition Gradient by Powder Metallurgy Method 969
Rityuj Singh Parihar and Neha Verma

Utilizing Generative Design for Additive Manufacturing 977
Ioannis Ntintakis, Georgios E. Stavroulakis, Georgios Sfakianakis, and Nikolaos Fiotodimitrakis

Vision-Based Object Classification Using Deep Learning for Mixed Palletizing Operation in an Automated Warehouse Environment 991
Anubhav Dinesh Patel and Abhra Roy Chowdhury

Welding Processes for Additive Manufacturing—Processes, Materials, and Defects 1013
Falak P. Patel, Bhumi K. Patel, and Vishvesh J. Badheka

About the Editors

Dr. Harshit K. Dave is currently working as an Associate Professor at the Department of Mechanical Engineering, S. V. National Institute of Technology, Surat. He obtained his B.E. (Mechanical) from Saurashtra University, Rajkot, and M.E. (Production) from M. S. University, Vadodara, and Ph.D. from SVNIT, Surat. His major areas of research interests include unconventional machining processes, micro-machining processes, machining of advanced materials, additive manufacturing processes, and modeling & optimization of machining processes, composite fabrication. He has published more than 50 papers in reputed international journals. Dr. Harshit Dave has carried out several research projects funded by DST, MHRD, and GUGCOST etc.

Dr. Uday Shanker Dixit is currently working as a Professor at Indian Institute of Technology, Guwahati. He earned his B.E. (Mechanical) from University of Roorkee in 1987 and M.Tech. (Mechanical) from IIT Kanpur, in 1993, and Ph.D. from IIT Kanpur in 1998. His current research interest is finite element method and soft computing applications in a wide variety of problems in manufacturing and design. He is also working in the domain of mechatronics. He holds 130 publications in reputed journals, 16 books and 38 book chapters. Dr. Uday Shanker has completed several sponsored projects and consultancy work sanctioned by various funding agencies.

Dr. Dumitru Nedelcu is currently working as a Professor at the Department of Machine Manufacturing Technology, Technical University of Iasi (TUIASI). He obtained his graduation in mechanical engineering from Polytechnic Institute of Iasi, Romania and Ph.D. from Technical University of Iasi, Romania. His major areas of research interests include fine mechanics technologies and technologies to obtain and process composite materials. Dr. Nedelcu Dumitru holds four patents and is the author of 60 refereed publications and 15 books. Over the years he got 17 national/international awards.

A Study on Residual Stress Distribution in Welded Joint of P91 and SS304H Steel Plate



Sachin Sirohi, P. K. Taraphdar, Prakash Kumar, and Chandan Pandey

Abstract The experimental study has been done to investigate the through thickness residual stress variation in P91/SS304H welds joint. The gas tungsten arc welding (GTAW) has been performed for joining of the dissimilar metal using the Ni-based ERNiCrMo-3 filler. The residual stress measurement was performed in the weld metal, SS304H HAZ and P92 HAZ. The results showed a considerable deviation in residual stresses along the thickness and in the transverse direction of the weldments. The PWHT showed a significant effect on magnitude and nature of the transverse and longitudinal residual stress for both weld metal and HAZ.

Keywords P91 · SS304H · IN625 · Residual stress · Welding

1 Introduction

The 9–12% Cr steel is used in boiler and turbine components to operate at higher temperature (600–650 °C) due to its attractive creep resistance at higher temperature [1, 2]. However, 9–12% Cr steels show the degradation in oxidation resistance at temperature more than 650 °C [1]. Hence, boiler components like reheater and superheater tubes with operating temperatures more than 650 °C are generally made

S. Sirohi (✉)

Department Mechanical Engineering, SRM IST NCR Campus, Modinagar 201204, India

P. K. Taraphdar

School of Mechanical Sciences, Indian Institute of Technology Bhubaneswar, Bhubaneswar 752050, India

P. Kumar

Department of Production Engineering, National Institute of Technology Tiruchirappalli, Tiruchirappalli 620015, India

e-mail: prakashkumar@nitt.edu

C. Pandey

Department of Mechanical Engineering, Indian Institute of Technology Jodhpur, Jodhpur 342037, India

e-mail: jscpandey@iitj.ac.in

of austenitic grade SS304L, SS304H steel, or Ni-based superalloy IN617, IN718 [3, 4]. Joining of these two steels requires to reduce the total operating cost of the power plant. The frequently used 9–12% Cr steel are P91, P911, and P92, which derived their strength by tempered martensite and carbide precipitates of type $M_{23}C_6$ and MX [5, 6]. In austenitic grade steel, the SS304L and SS304H are more commonly employed in power plants because of its high oxidation and corrosion resistance [7, 8]. Both P91 steel and SS304H steel shows the difference in thermo-physical and mechanical properties and chemical composition. The variation in coefficient of thermal expansion and thermal conductivity of these two steels creates the major problem during the joining and a high amount of residual stress is obtained along the welded joint [9, 10]. The high heat input and variation in composition and mechanical properties of these two steels results in poor structural integrity, as presented by the researchers [11–22]. The high amount of residual stresses and difference in mechanical properties along the welded joint leads to premature failure of the weld component. The diffusion of the elements along the weld metal and heat-affected zone (HAZ) interface was also observed during dissimilar welding of SS304H and P91 steel. The dissimilar joining is mainly concerned with the application of the heat input and filler metal. The welding of these two steel using the matching P91 filler has reported poor impact toughness due to the development of the fresh martensite in weld metal [10, 13]. For stainless steel grade filler, solidification cracking is reported as the major issue [23]. For joining the SS304H and P91 steel, Ni-based filler such as IN82, IN617, and IN625 has been reported as the best choice due to attractive creep properties at high-temperature [24, 25]. The other reasons behind the selection of the Ni-based filler are their thermal conductivity and thermal expansion coefficient, which lies in between SS304H and P91 steel and it also helps to stop the diffusion of the elements. Numerous research articles have been published on the use of Ni-based filler to join the P91 and SS304H steel. However, residual stress along the welded joint still exists, which can be minimized either by minimizing the heat input or performing the post-weld heat treatment (PWHT). However, a study related to the residual stress analysis of P91 and SS304H welded joint for Ni-based filler has not been found. The objective of this work is to examine the residual stress variation along the welded joint for the Ni-based IN625 filler. The effect of the PWHT on residual stress variation has also been studied and results obtained after PWHT, compared with the as-welded condition.

2 Work Material and Testing

The P91 and SS304H plate of thickness 8.5 mm were welded using the gas tungsten arc welding technique with the IN625 filler. After the welding, PWHT was employed at 760 °C for 2 h. The detail about the welding process parameters and groove design has been given into previously published work [26]. The design of groove, groove machined plate, and top and back side of the welded plate is revealed in Fig. 1a–c [26].

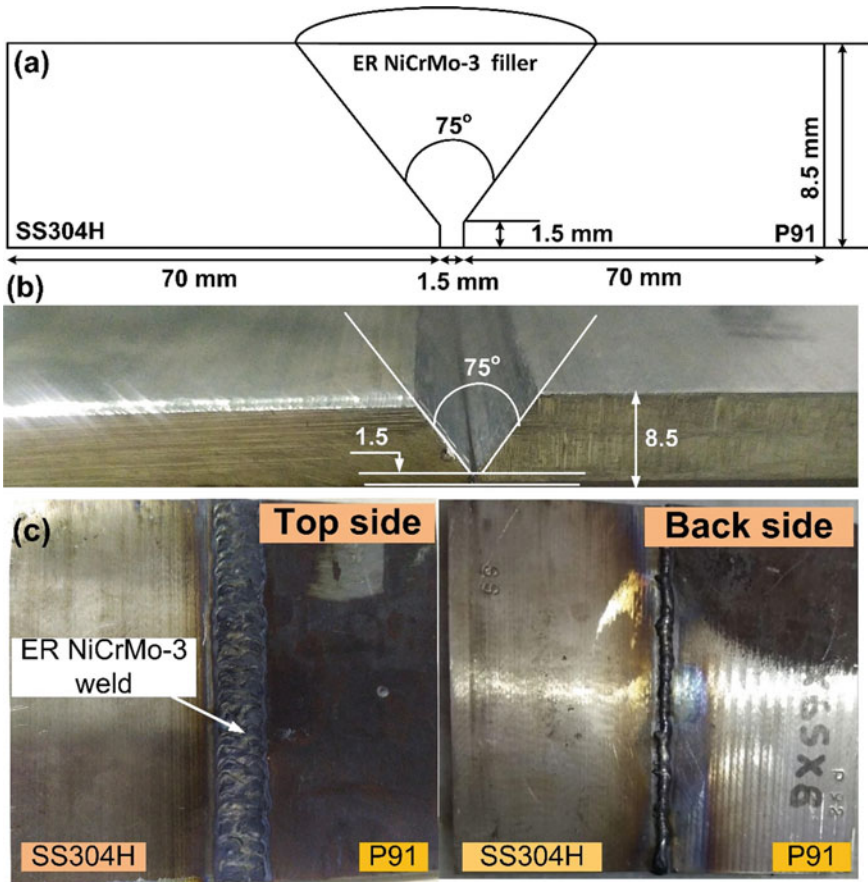


Fig. 1 a Groove details, b plate after machining the groove, c top and back side of the welded plate

After joining and PWHT, through-hole thickness measurement was performed. For the measurement of residual stress distribution in the weld zone and the HAZ, deep hole drilling (DHD) method was used. Four essential steps are followed in the DHD technique, which is revealed in Fig. 2. In first step, a through thickness hole of diameter 3 mm was drilled at desired position, i.e., weld metal or HAZ. In the second, the measurement of reference hole diameter ($d(\theta)$) was conducted with an air probe in 1 mm depth intervals across the thickness in the transverse and longitudinal directions. In third step, trepanning was done for reference hole by using the electro-discharge machining to relax the present locked-in stresses surrounding the reference hole. Subsequently, in the final step, remeasurement of the reference hole diameter ($d'(\theta)$) was performed with the air probe at the previous locations through the thickness following similar directions as before. In-plane residual stress magnitude was estimated with the help of the variation in reference hole diameter ($\Delta d(\theta) = d'(\theta) - d(\theta)$). The normalized strain $\varepsilon(\theta)$ is given below,

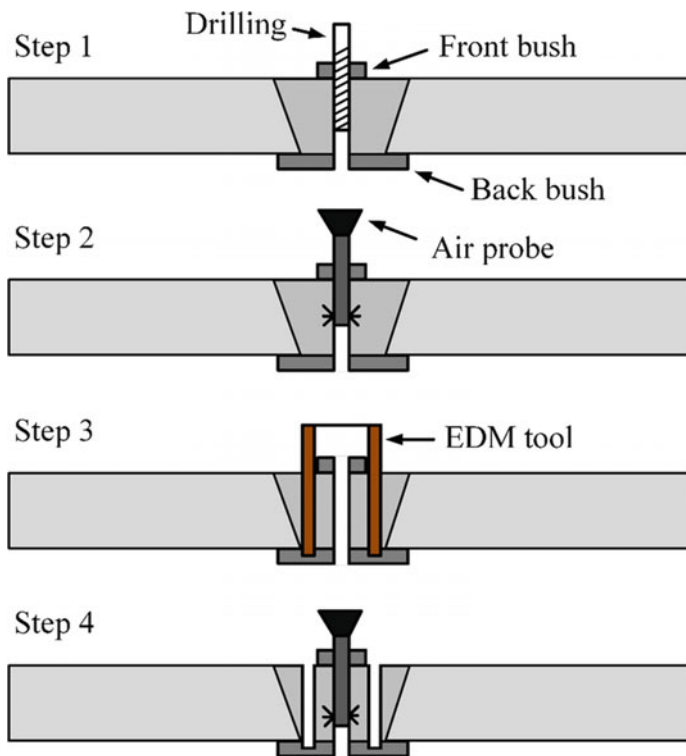


Fig. 2 Steps used in deep hole drilling method [30]

$$\varepsilon(\theta) = \frac{\Delta d(\theta)}{d(\theta)} = -\frac{1}{E} [\sigma_x p(\theta) + \sigma_y q(\theta) + \sigma_{xy} r(\theta) - \mu \sigma_z] \quad (1)$$

$$\varepsilon_z = -\frac{1}{E} [-\sigma_z - \mu(\sigma_y + \sigma_x)] \quad (2)$$

where $p(\theta) = 1 + 2\cos 2\theta$, $q(\theta) = 1 - 2\cos 2\theta$, $r(\theta) = 4\sin 2\theta$ and ε_z is the measured axial strain derived during the trepanning process. The plane stress condition is followed while determining residual stresses using the DHD technique, resulting in the conversion of the σ_z to zero. Measurements of reference hole were performed at n angles ($\theta = \theta_1, \dots, \theta_i, \dots, \theta_N$) around the hole. Thus, Eq. 1 can be rewritten as,

$$\varepsilon(\theta) = \frac{\Delta d(\theta)}{d(\theta)} = -\frac{1}{E} [\sigma_x p(\theta) + \sigma_y q(\theta) + \sigma_{xy} r(\theta)] \quad (3)$$

Here, the x -direction meets with the angular direction $\theta = 0^\circ$. Equation 3 can be reframed in a matrix format as shown below,

$$\bar{\varepsilon} = -\frac{1}{E} \mathbf{M} \times \sigma \quad (4)$$

where

$$\bar{\varepsilon} = \begin{bmatrix} \bar{\varepsilon}(\theta_1) \\ \vdots \\ \bar{\varepsilon}(\theta_i) \\ \vdots \\ \bar{\varepsilon}(\theta_N) \end{bmatrix}, \quad \mathbf{M} = \begin{bmatrix} p(\theta_1) & q(\theta_1) & r(\theta_1) \\ \vdots & \vdots & \vdots \\ p(\theta_i) & q(\theta_i) & r(\theta_i) \\ \vdots & \vdots & \vdots \\ p(\theta_N) & q(\theta_N) & r(\theta_N) \end{bmatrix} \quad \text{and } \sigma = \begin{bmatrix} \sigma_x \\ \sigma_y \\ \sigma_{xy} \end{bmatrix} \quad (5)$$

Finally, using Eq. 6, the residual stresses magnitude can be determined.

$$\hat{\sigma} = -E\mathbf{M}^* \times \bar{\mathbf{u}} \quad (6)$$

where

$$\mathbf{M}^* = (\mathbf{M}^T \times \mathbf{M})^{-1} \times \mathbf{M}^T \quad (7)$$

Here, $\hat{\sigma}$ = favorable stress vector; \mathbf{M}^* = pseudo inverse of matrix \mathbf{M} [27].

Furthermore, Mahapatra and his co-workers made the above-mentioned calculation simpler [28, 29].

The longitudinal (ε_x) and transverse (ε_y) strain is calculated by simply placing $\theta = 0^\circ$ and $\theta = 90^\circ$, respectively, in Eq. 3, as shown in Eqs. 8 and 9.

$$\varepsilon_x = \frac{\Delta d_x}{d_x} = -\frac{1}{E} [3\sigma_x - \sigma_y] \quad (8)$$

$$\varepsilon_y = \frac{\Delta d_y}{d_y} = -\frac{1}{E} [3\sigma_y - \sigma_x] \quad (9)$$

For uniaxial stress, σ_y will be zero in Eq. 8,

$$\varepsilon_x = \frac{\Delta d_x}{d_x} = -\frac{1}{E} [3\sigma_x] \quad (10)$$

Equations 8 and 9 were used to quantify the in-plane bi-axial longitudinal and transverse residual stress fields.

3 Results and Discussion

The distribution of residual stress along the thickness for a different region of the weldments is shown in Fig. 3. In the weld metal, the maximum value of the longitudinal residual stress was obtained at a depth of 6 mm from the upper surface, and it was almost constant up to a depth of 5 mm. For weld metal, the maximum value of the longitudinal residual stress in as-welded condition approached 250 MPa, which was higher than the maximum value of the transverse residual stresses of 165 MPa (Fig. 3a). After conducting the PWHT, it was found that the tensile residual stress fields transformed into compressive stresses through the thickness. The induced compressive residual stress levels were found to be comparatively higher when IN625 was used as the filler material. The maximum compressive transverse and longitudinal residual stress magnitudes in the weld zone (IN625) after PWHT were found to be -123 and -295 MPa at a depth of 5 mm from the upper surface of the weld,

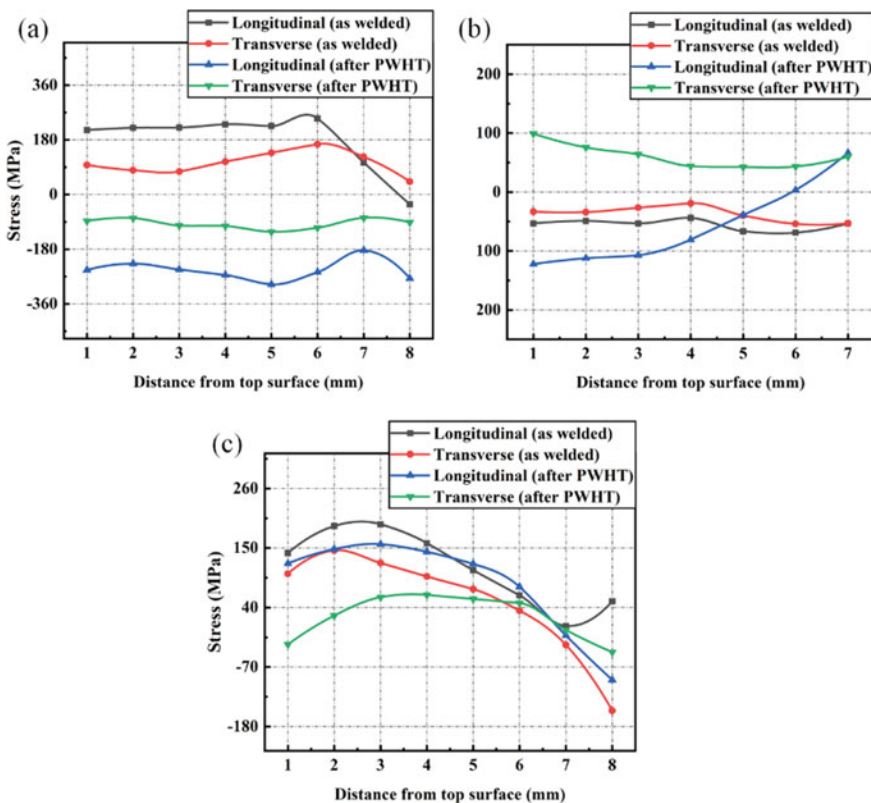


Fig. 3 Through thickness residual stress distribution in the weldment having IN625 as the filler material **a** weld zone, **b** P92 HAZ, **c** SS304H HAZ

respectively. Similar to the weld sample of IN617, the weldment of IN625 also exhibited compressive residual stresses in the HAZ of the P92 steel within a range of -19 to -70 MPa, Fig. 3b. However, following PWHT, the transverse residual stress trend moved into the tensile region, while the longitudinal residual stress trend dropped deeper into the compressive zone at the top surface, eventually becoming tensile at the bottom of the plate. The maximum longitudinal stress level of 193 MPa and maximum transverse residual stress level of 145 MPa were measured in the SS304H HAZ, as presented in Fig. 3c. The maximum value of transverse and longitudinal residual stresses in the SS304H HAZ decreased by 83 and 18%, respectively, after the PWHT, Fig. 3c.

In a comparison of the weld samples of IN617 and IN625, it was observed that the weld sample of IN625 exhibited a higher residual stress level in the weld zone, and consequently, after PWHT, it also produced a higher magnitude of compressive residual stresses in the weld zone. Both the weld samples had similar residual stress levels with marginal differences in the HAZ of P92 steel in the as-welded condition [31]. Noticeably, after PWHT, the transverse residual stress trend of the IN625 weld sample was found as tensile in nature, whereas in the IN617 weld sample, the transverse residual stress trend further moved deeper into the compressive zone after PWHT. In both cases, the longitudinal residual stress levels in the P92 HAZ increased in the compressive mode at the top surface. It was observed that the IN625 weld sample exhibited higher residual stress magnitudes in the HAZ of SS304H than the IN617 weld sample in both the longitudinal and transverse directions [31]. These residual stress levels in SS304H HAZ decreased by a certain amount after PWHT, with the transverse residual stress greatly reduced in both weld samples by an average of 80%. The differences in the thermal expansion coefficient and metallurgical properties of the corresponding dissimilar metals are directly responsible for the variations in the distribution of residual stress in these weld samples across the weld cross section.

4 Conclusion

1. The results showed a considerable deviation in residual stresses in transverse direction of the joint and along the thickness.
2. The maximum value of the longitudinal residual stress in weld metal was 250 MPa while the transverse residual stress was 165 MPa, for as-welded conditions and showed a substantial decrease in magnitude and nature after the PWHT.
3. For P91 HAZ, the compressive nature of the residual stresses was obtained throughout the depth in as-welded conditions. After the PWHT, longitudinal residual stress was measured in the root of the weld metal with a maximum magnitude of 67 MPa, which was tensile in nature. A tensile transverse residual stress was measured after the PWHT with a maximum value of 99 MPa at the top of the plate.

4. The maximum longitudinal and transverse residual stress levels in the SS304H HAZ were measured about 193 and 145 MPa, respectively, while a compressive nature of the transverse stress was measured in the root portion with a magnitude of 150 MPa. After the PWHT, a reduction was measured in residual stresses, and maximum longitudinal and transverse residual stress levels were 157 and 63 MPa, respectively.

References

Journal Article

1. Akram J, Kalvala PR, Misra M, Charit I (2017) Creep behavior of dissimilar metal weld joints between P91 and AISI 304. *Mater Sci Eng A* 688:396–406
2. Kumar S, Pandey C, Goyal A (2021) Microstructure and mechanical behavior of P91 steel dissimilar welded joints made with IN718 filler. *Int J Press Vessels Pip* 190: 104290
3. Dak G, Pandey C (2020) A critical review on dissimilar welds joint between martensitic and austenitic steel for power plant application. *J Manuf Process* 58:377–406
4. Abe F (2015) Research and development of heat-resistant materials for advanced USC power plants with steam temperatures of 700 °C and above. *Engineering* 1(2):211–224
5. Pandey C, Mahapatra MM, Kumar P, Saini N (2018) Some studies on P91 steel and their weldments. *J Alloy Compd* 743:332–364
6. Klueh RL (2005) Elevated temperature ferritic and martensitic steels and their application to future nuclear reactors. *Int Mater Rev* 50:287–310
7. Pandey C (2020) Mechanical and metallurgical characterization of dissimilar P92/SS304 L welded joints under varying heat treatment regimes. *Metall Mater Trans A* 51:2126–2142
8. Khodakov VD, Khodakov DV (2016) Structure and mechanism of formation of dissimilar welded joints in nuclear power plant made of austenitic and pearlitic steels. *Weld Int* 30(12):935–940
9. Williams JA (1984) Residual stresses in austenitic/ferritic transition joints fabricated with austenitic weld metal. *High Temp Technol* 2(3):135–140
10. Thakare JG, Pandey C, Mahapatra MM, Mulik RS (2019) An assessment for mechanical and microstructure behavior of dissimilar material welded joint between nuclear grade martensitic P91 and austenitic SS304 L steel. *J Manuf Process* 48:249–259
11. Pandey C, Mahapatra MM, Kumar P, Saini N (2018) Homogenization of P91 weldments using varying normalizing and tempering treatment. *Mater Sci Eng, A* 710:86–101
12. Shuo W, Limin W, Yi C, Shuping T (2018) Post-weld heat treatment and groove angles affect the mechanical properties of T92/Super 304H dissimilar steel weld joints. *High Temp Mater Processes (Lond)* 37(7):649–654
13. Falat L, Kopic J, Ciripova L, Sevc P, Dlouhy I (2016) The effects of postweld heat treatment and isothermal aging on T92 steel heat-affected zone mechanical properties of T92/TP316H dissimilar weldments. *J Mater Res* 31:1532–1543
14. Chen G, Song Y, Wang J, Liu J, Yu X, Hua J, Bai X, Zhang T, Zhang J, Tang W (2012) High-temperature short-term tensile test and creep rupture strength prediction of the T92/TP347H dissimilar steel weld joints. *Eng Fail Anal* 26:220–229
15. Pandey C, Mahapatra MM, Kumar P, Saini N (2018) Comparative study of autogenous tungsten inert gas welding and tungsten arc welding with filler wire for dissimilar P91 and P92 steel weld joint. *Mater Sci Eng A* 712:720–737

16. Deng J, Liang Z, Hui S, Zhao Q (2015) Aging treatment on the microstructures and mechanical properties of new groove T92/super 304H dissimilar steel joints. *High Temp Mater Processes (Lond)* 34(5):425–433
17. Vidyarthi RS, Kulkarni A, Dwivedi DK (2017) study of microstructure and mechanical property relationships of A-TIG welded P91–316L dissimilar steel joint. *Mater Sci Eng A* 695:249–257
18. Karthick K, Malarvizhi S, Balasubramanian V, Rao G (2018) Tensile properties variation across the dissimilar metal weld joint between modified 9Cr–1Mo ferritic steel and 316LN stainless steel at RT and 550 °C. *Metallogr Microstruct Anal* 7:209–221
19. Jula M, Dehmlaei R, Alavi Zaree SR (2018) The comparative evaluation of AISI 316/A387-Gr.91 steels dissimilar weld metal produced by CCGTAW and PCGTAW processes. *J Manuf Process* 36:272–280
20. Pańcikiewicz K, Świerczyńska A, Hućko P, Tumidajewicz M (2020) Laser dissimilar welding of AISI 430F and AISI 304 stainless steels. *Materials* 13(20):4540
21. Sirohi S., Pandey C, Goyal A (2020) Role of heat-treatment and filler on structure-property relationship of dissimilar welded joint of P22 and F69 steel. *Fusion Eng Des* 159: 111935
22. Sun Z, Moio T (1993) Laser beam welding of austenitic/ferritic dissimilar steel joints using nickel based filler wire. *Mater Sci Technol* 9(7):603–608
23. Mortezaie A, Shamanian M (2014) An assessment of microstructure, mechanical properties and corrosion resistance of dissimilar welds between Inconel 718 and 310S austenitic stainless steel. *Int J Press Vessels Pip* 116:37–46
24. Zhang Y, Fan M, Ding K, Zhao B, Zhang Y, He Y, Wang Y, Wu G, Wei T, Gao Y (2020) Formation and control of the residual δ -ferrite in 9% Cr-HAZ of Alloy 617/9% Cr dissimilar welded joint. *Sci Technol Weld Joining* 25(5):398–406
25. Mittal R, Sidhu BS (2015) Microstructures and mechanical properties of dissimilar T91/347H steel weldments. *J Mater Process Technol* 220:76–86
26. Sirohi S, Pandey C, Goyal A (2021) Role of the Ni-based filler (IN625) and heat-treatment on the mechanical performance of the GTA welded dissimilar joint of P91 and SS304H steel. *J Manuf Process* 65:174–189

Book Chapter

27. Taraphdar PK, Mahapatra MM, Pradhan AK, Singh PK, Sharma K, Kumar S (2021) Measurement of through-thickness residual stresses under restrained condition in pressure vessel steel weld. In: Saran VH, Misra RK (eds) *Advances in systems engineering. lecture notes in mechanical engineering*. Springer, Singapore pp 119–125

Journal Article

28. Das Banik S, Kumar S, Singh PK, Bhattacharya S, Mahapatra MM (2021) Distortion and residual stresses in thick plate weld joint of austenitic stainless steel: experiments and analysis. *J Mater Process Technol* 289: 116944

Journal Article by DOI (Before Issue Publication with Page Numbers)

29. Taraphdar PK, Kumar R, Pandey C, Mahapatra MM (2021) Significance of finite element models and solid-state phase transformation on the evaluation of weld induced residual stresses. *Met Mater Int.* <https://doi.org/10.1007/s12540-020-00921-4>

Journal Article

30. Taraphdar PK, Mahapatra MM, Pradhan, AK, Singh PK, Sharma K, Kumar S (2021) Effects of groove configuration and buttering layer on the through-thickness residual stress distribution in dissimilar welds. *Int J Press Vessels Pip* 192:104392
31. Dak G, Pandey C (2021) Experimental investigation on microstructure, mechanical properties, and residual stresses of dissimilar welded joint of martensitic P92 and AISI 304L austenitic stainless steel. *Int J Press Vessels Pip* 194:104536

A Methodology for Data-Driven Estimation of Forging Load



Kaustabh Chatterjee, Uday S. Dixit, Jian Zhang, and Pavel A. Petrov

Abstract Metal forming industry often requires to estimate forging load. Analytical and numerical techniques are not sufficient to provide an accurate estimation of the forging load. Interestingly, a large amount of shop floor forging data exists that are yet to be effectively utilised. Modelling using data-driven techniques can take care of the uncertainty associated with flow stress and friction condition. This article proposes a methodology that uses the existing information of axisymmetric forged products for the estimation of forging load by suggesting a proper value of complexity factor. Appropriate complexity factor is essential for empirically estimating the forging load in open as well as closed die forging. Estimation of forging load for open die forging is carried out for four different materials of cylindrical shape. In case of closed die forging, estimation of forging load is carried out for two different products. Forging load estimation is carried out for different sizes and for different friction conditions. The proposed methodology of using the existing data provides reasonable accuracy in the prediction of forging load.

Keywords Forging load · Complexity factor · Friction · Open die forging · Closed die forging · Axisymmetric product

K. Chatterjee (✉) · U. S. Dixit

Department of Mechanical Engineering, Indian Institute of Technology Guwahati, Guwahati 781039, India

e-mail: kaustabh@iitg.ac.in

U. S. Dixit

e-mail: uday@iitg.ac.in

J. Zhang

Shantou Institute of Light Industrial Equipment Research, Shantou University, Shantou-515063, China

e-mail: jianzhang@stu.edu.cn

P. A. Petrov

Department of Material Forming and Additive Technologies, Moscow Polytechnic University, str. B. Semenovskaya 38, 107023 Moscow, Russia

1 Introduction

Forging is one of the most popular manufacturing processes. It is a bulk metal forming process that is subjected to three-dimensional compressive stresses. Estimation and control of metal forging process are of utmost importance, particularly in this era of global competition. Researchers have been carrying out estimation of forging load, mostly using analytical, numerical and empirical methods. Such efforts are still continuing [1–3]. The deformation mechanics of forging is extremely complex. Additionally, the material flow is non-steady and non-uniform. However, with time, there has been sufficient progress in the field of analytical modelling that can accurately estimate the forging load. The main challenges in using analytical models are that they require the exact knowledge of the material behaviour during deformation and Coulomb's coefficient of friction. Assumptions such as homogenous deformation, temperature distribution due to different factors within and close to the deformation zone, and loading axes coinciding with the principal axes may be far away from reality. These drawbacks of analytical models were taken care by numerical models. With the advancement of processing power of computers, numerical models such as finite element method (FEM) provided quick estimation of forging load without the need to carry out expensive experiments [4]. However, FEM simulations are computationally expensive and can take up several hours for simulating the forging of three-dimensional products with complicated geometry. Empirical models require a lot of data for accurate estimation of forging load. To overcome these problems, researchers have started to develop intelligent databases for estimating forging load. The advancement in automation and information technology provided a golden opportunity for the manufacturing industries to store and access large amount of data. Effective utilization of such large amount of data directly from the shop floor can be used for reliable prediction of forging load.

Manufacturing industries are trying to incorporate cloud computing, big data, mobile Internet, cyber-physical system (CPS) and Internet of things (IOT) in their systems [5]. This has created interest among the researchers across the globe towards data-driven smart manufacturing [6]. Effective utilisation of manufacturing data for accurate performance prediction reduces the unnecessary downtime. Reduction of downtime improves the existing revenue of the organisation. Recently, Chatterjee et al. [7] proposed a framework for the acquisition of manufacturing data with efficient storage and performance prediction.

There are a few attempts in the past that proposes the usage of expert system for timely and effective utilisation of the accumulated data in forging. One of the initial works in expert system was carried out by Osakada and Yang [8]. They used backpropagation neural network aided expert system for determining the forming method, number of forming steps and prediction of die fracture with die defect. Katayama et al. [9] developed an expert system for the process design of a cold forging process. Expert system was also applied for determining the sequence of steps in manufacturing a part through axisymmetric cold forging [10]. Considering the uncertainty in forging process, fuzzy logic was applied. Fuzzy logic was used for

the estimation of the dimensional errors occurring during actual forging operation [11]. Gangopadhyay et al. [12] incorporated fuzzy logic in their expert system for the prediction of forging load and axial stress. Gronostajski et al. [13] used an expert system for determining the various wear mechanisms that degrade the forging tools during hot forging. Recently, deep learning techniques are also used in cold forging for condition monitoring of the machines [14]. Thus, researchers are trying hard to effectively utilise data-driven technologies in forging.

In estimating the forging load, there are two uncertain parameters: flow stress and friction condition. Flow stress significantly influences the material flow in forging operation. Flow stress is generally modelled in the form of mathematical equation, whose parameters are determined from compression tests. However, modelling of friction is itself a challenging task [15]. A thorough knowledge and a lot of skill is required for the estimation of forging load using the existing analytical and numerical models. Data-driven techniques can be effective in taking care of the various uncertainties associated with forging such as friction condition and flow stress. With time and usage, data-driven models get updated and provide more accurate results based on the feedback received from the shop floor.

In this paper, the idea is to build a robust procedure that can be used for the estimation of load in an axisymmetric forging. The methodology uses the existing information after applying the suitable correction factor depending on the situation. In order to demonstrate the methodology, simulations are carried out in place of shop floor data for axisymmetric forging of open and closed die products. In a sense, FEM simulations provide a virtual factory environment for testing the methodology.

2 Methodology

It is observed that a lot of forging data exist within an organisation and the same is not effectively utilised. The present work proposes to use such existing data for building a database such that it can be used for the estimation of forging load. For demonstrating the proposed methodology, forging is simulated using a commercial finite element package, ABAQUS. The feedback of the forging load obtained from simulations are assumed to represent the data obtained from the shop floor. The scheme adopted for estimating the forging load in open and closed die forging is shown in Fig. 1 and is discussed in details. The computational scheme could be repeated several times, while the accuracy of the computation would be enhanced.

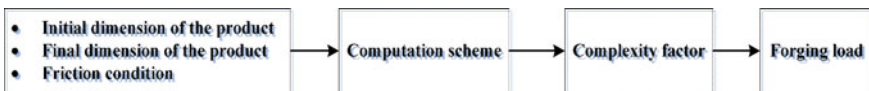


Fig. 1 Scheme for estimating forging load

2.1 Forging Load in Open Die Forging

The slab method analysis in upsetting an axisymmetric disk using Coulomb's model gives the following die pressure p at any radial coordinate r as [16]:

$$p = \sigma_o \exp\left\{\frac{2\mu}{H}(R - r)\right\}, \quad (1)$$

where σ_o is the flow stress, μ is the coefficient of friction, H is the height, R is the final radius of the disk and r is the radial coordinate. Total forging load P is obtained by integrating the die pressure p over the whole contact area of the disk with the platen and is expressed as

$$P = \frac{\sigma_o \pi H}{\mu} \left[\frac{H}{2\mu} \left\{ \exp\left(\frac{2\mu R}{H}\right) - 1 \right\} - R \right]. \quad (2)$$

An empirical relation for the estimation of forging load was given long back [17] as

$$P = C_p \sigma_o A_p, \quad (3)$$

where C_p is the complexity factor and A_p is the plan area of the forging including flash. The aim of this article is to suggest a suitable value of C_p such that it can be used for any forging case. Equating Eqs. 2 and 3, the shape complexity can be computed as

$$C_p = \frac{H}{\mu R^2} \left[\frac{H}{2\mu} \left\{ \exp\left(\frac{2\mu R}{H}\right) - 1 \right\} - R \right]. \quad (4)$$

On substituting Eqs. 4 in 3, the forging load is estimated. The suggested value of the complexity factor is applicable for any sizes and for any friction condition.

2.2 Forging Load in Closed Die Forging

For closed die forging also, estimation of forging load is carried out using Eq. 3. However, it is difficult to ascertain an exact value of the C_p for an accurate load estimation. In general, the value of C_p is determined by intuition or experience. As already highlighted, the main aim of this article is to suggest a suitable value of C_p based on relevant product information. The idea is to effectively use the existing product information related to size and friction condition for predicting the forging load with reasonable accuracy.

2.2.1 Forging Load Estimation for Different Sizes of Workpieces

Assume that there are two models of similar shape but of different sizes. One model is having smaller radius (of projected circle) than the other. Assume that the existing information of the forging load is available for the smaller model under lubricated condition. It is required to estimate the forging load of a model having larger radius. However, height and friction condition are unchanged. Using Eq. 3, the forging load P for the large model is estimated as

$$P_{\text{large}} = \left(\frac{R_{\text{large}}}{R_{\text{small}}} \right)^2 \times P_{\text{small}}. \quad (5)$$

where R is the radius of the closed die product. In this case, the smaller model is considered as the base model, as prediction is carried out based on the information available of the smaller model. Similar methodology is adopted when information of larger model exists and estimation is required for smaller model by considering larger model as the base. On obtaining the actual load, the value of the complexity factor C_p is preserved. Such C_p is used for the estimation of forging load for a completely new product with different geometry. The value of C_p is again updated and preserved based on the feedback of the actual load.

2.2.2 Forging Load Estimation for Different Friction Condition

It is assumed that there are two models of similar shape and size. However, the information of lubricated condition exists. It is required to estimate the forging load under non-lubricated condition. In order to include the effect of friction in Eq. 4, a rough idea of the complexity factor C_p is required. The value of C_p for open die forging is approximately expressed by Eq. 4. Hence, C_p for closed die forging of non-lubricated case is obtained as

$$\begin{aligned} & (C_p)_{\text{closed-nonlubricated}} \\ &= \frac{C_p \text{ from Eq. 4 for } \mu \text{ of non-lubricated case}}{C_p \text{ from Eq. 4 for } \mu \text{ of lubricated case}} \\ & \times (C_p)_{\text{closed-lubricated}} \end{aligned} \quad (6)$$

In this case, the lubricated model is considered as the base model, as prediction is carried out on the basis of the information of the lubricated model. Similar methodology is adopted to estimate the forging load for lubricated condition when data of non-lubricated condition is available. On obtaining the actual load, the value of the complexity factor C_p is preserved for the specified friction condition for further use. It is observed that estimating forging load considering the geometrically closest shape as the base model provide better accuracy in the prediction. A detailed insight is provided in the next section.

3 Results and Discussion

In this section, the efficacy of the proposed methodology for the estimation of forging load is presented. FEM simulations are carried out and the information of the forging load obtained are assumed to be analogous to the feedback obtained from the shop floor. Prediction of forging load for geometrically similar shapes are carried out using the already existing information pertaining to size and friction condition. Results are discussed for open as well as closed die forging of axisymmetric shapes.

3.1 Estimation of Forging Load in Open Die Forging

The detailed procedure for estimating the forging load in open die forging is explained in Sect. 2.1. The value of the complexity factor is computed using Eq. 4 and the forging load is ultimately estimated using Eq. 4 for four different materials. They are JIS S25C steel [18], AISI 1015 steel [19], AI 1100 aluminium [20] and commercially pure aluminium [21]. The corresponding material properties and the hardening parameters are used for the FEM simulation and for the estimation of σ_o . Results are presented for low aspect ratio and high aspect ratio.

3.1.1 Estimation of Forging Load for Low Aspect Ratio (R/H)

In this case, the forging load is estimated for four materials, viz., JIS S25C steel, AISI 1015 steel, AI 1100 aluminium and commercially pure aluminium. The workpiece is of size 10 mm radius and 20 mm height, i.e., an aspect ratio of 0.5 is considered. Analysis is carried out for 10% as well as 40% reduction of the height. Forging takes place under lubricated as well as under non-lubricated condition. A value of μ as 0.1 may represent lubricated condition, and a value of μ as 0.25 may represent non-lubricated condition. In cold forging, the Coulomb's coefficient of friction generally varies between 0.05 and 0.15; hence, $\mu = 0.25$ can be considered as an extreme case. Simulations are carried out accordingly. The complexity factor for open die forging is estimated using Eq. 4 and is substituted in Eq. 3 for the estimation of forging load under both lubricated and non-lubricated condition as shown in Figs. 2 and 3. The obtained results show that there is good accuracy in the estimation of forging load for low aspect ratio. It is to be mentioned that for forging under lubricated as well as under non-lubricated condition, an error of less than 3% is achieved in all the cases.

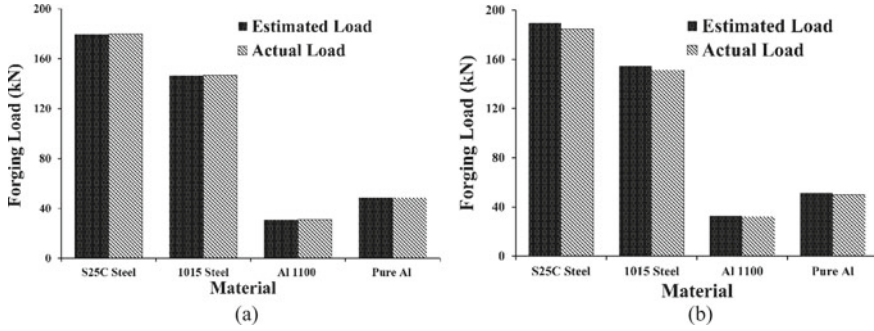


Fig. 2 Estimation of forging load for 10% reduction ($R = 10$ mm and $H = 20$ mm) **a** lubricated condition, **b** non-lubricated condition

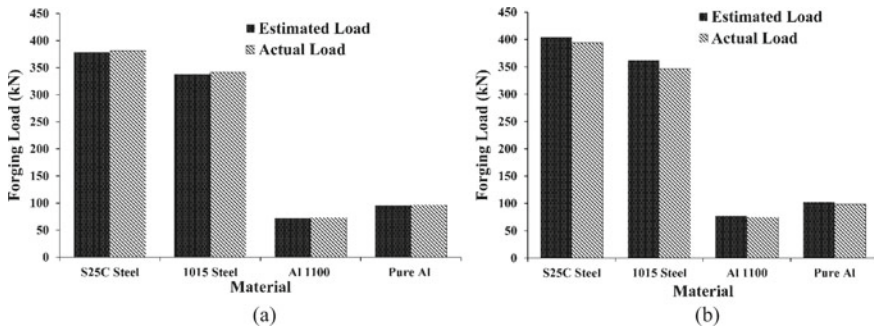


Fig. 3 Estimation of forging load for 40% reduction ($R = 10$ mm and $H = 20$ mm) **a** lubricated condition, **b** non-lubricated condition

3.1.2 Estimation of Forging Load for High Aspect Ratio (R/H)

In this case also, forging load estimation is carried out for the four materials, viz., JIS S25C steel, AISI 1015 steel, AI 1100 aluminium and commercially pure aluminium. However, the workpiece is of size 40 mm radius and 10 mm height, i.e., an aspect ratio of 4 is considered. Analysis is carried out for 10% reduction in height. Forging takes place under lubricated as well as under non-lubricated condition. Forging load is estimated using Eq. 3, and the value of C_p is computed using Eq. 4. The estimated load is validated with the actual results obtained from simulation as shown in Fig. 3. It can be seen from Fig. 4 that the estimated forging load matches well with the actual forging even at high aspect ratio. The maximum percentage error is observed to be around 3%.

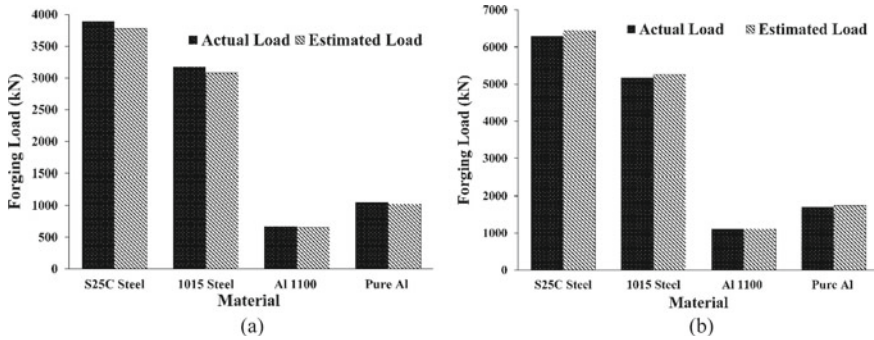


Fig. 4 Estimation of forging load for 10% reduction ($R = 40$ mm and $H = 10$ mm) **a** lubricated condition, **b** non-lubricated condition

3.2 Estimation of Forging Load in Closed Die Forging

For illustration of the methodology, two closed die products of lead are considered [2]. The corresponding material properties and the hardening parameters are used. Forging is carried out under lubricated and as well as under non-lubricated condition. The effect of size and the effect of friction are considered for the estimation of forging load.

3.2.1 Forging Load Estimation for Different Sizes

To demonstrate the effect of size on the estimation of forging load, the models shown in Fig. 5 are considered. The initial workpiece is of size 18 mm radius and 32 mm height for model 1. For model 2, the workpiece is of size 19.75 mm radius and 32 mm height. For model 3, the workpiece is of size 21.25 mm radius and 32 mm height. Further, forging is simulated for two similar models of product 1 with larger sizes as shown in Fig. 5b, c. The aim is to use the information of the forging load of model 1 to predict the forging load in model 2 and model 3.

Initially, the FEM simulated value of model 1 under lubricated condition is acquired, and the value of the complexity factor is preserved using Eq. 3. The actual

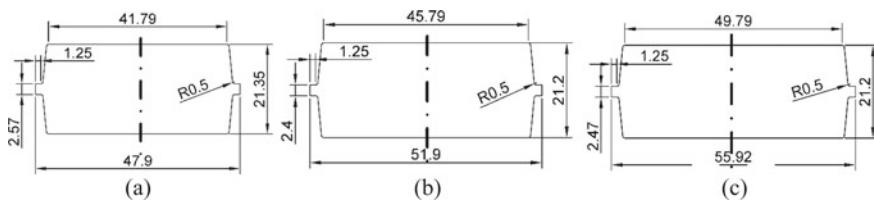


Fig. 5 Closed die forged product 1: **a** model 1, **b** model 2 and **c** model 3

Table 1 Estimation of forging load for various sizes of product 1

Model No.	Actual load (kN)	Estimated load (kN)	Error (%)	Base model
2	419.3	361.1	13.9	1
3	466.5	418.9	10.2	1
3	466.5	486.7	4.3	2

(virtually simulated) forging load for model 1 is 307.6 kN and the value of C_p is computed as 3.02. This information is used for further prediction of forging load of geometrically similar products.

Forging load estimation of model 2 is carried out under lubricated condition using the existing information of model 1. It is observed that the radius of the model 2 is 1.08 times more than that of model 1. From Eq. 3, the estimated forging load is expressed as

$$\text{Estimated Load} = (1.08)^2 \times 307.6 \text{ kN.} \tag{7}$$

The forging load is computed to be 361.1 kN, and the actual load is 419.3 kN. An error of 13.9% is observed. Similar methodology is adopted for estimating the forging load of model 3. In this case, the information of both model 1 and model 2 are available. The estimated load observed while using model 1 as the base is 418.9 kN and while using model 2 as the base, the estimated load is 486.7 kN. The actual load required is 466.5 kN. An error of 10.2% is observed while considering model 1 as the base and an error of 4.3% is observed while considering model 2 as the base. The results are given in Table 1 for product 1.

One more product is considered to demonstrate the effect of size for the estimation of forging load. The models shown in Fig. 6 are considered. The workpiece is of size 17 mm radius and 32 mm height for model 1. For model 2, the workpiece is of size 18.25 mm radius and 32 mm height. For model 3, the workpiece is of size 19.5 mm radius and 32 mm height. Further, forging is simulated under lubricated condition for two similar products with larger diameters as shown in Fig. 6b, c. The aim is to use the already existing information of product 1 in estimating the forging load of all the models of product 2.

The value of the complexity factor that is obtained in model 1 of product 1 is used for the estimation of the forging load in model 1 of product 2. On substituting

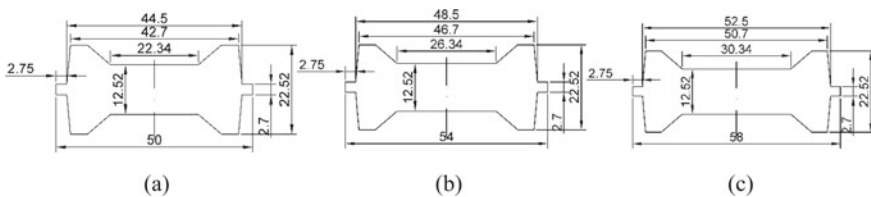


Fig. 6 Closed die forged product 2: **a** model 1, **b** model 2 and **c** model 3

Table 2 Estimation of forging load for various models of product 2

Model No.	Actual load (kN)	Estimated load (kN)	Error (%)	Base model	Base product
1	347.5	363.7	4.6	1	1
2	363.6	405.3	11.5	1	2
3	422.1	467.6	10.7	1	2
3	422.1	419.5	0.6	2	2

the value of C_p as 3.02 in Eq. 3, the forging load is estimated to be 363.7 kN. The actual load required is 347.5 kN. An error of 4.6% is obtained on using the existing information.

Forging load estimation of model 2 is carried out under lubricated condition using the existing information of model 1. Both the models belong to product 2. Based on the ratio of the radius of model 2 and model 1, the forging load is estimated as 405.3 kN. The actual load required is 363.6 kN. An error of 11.5% is attained. Similarly, model 3 of product 2 is estimated using the existing information of model 1 and model 2. Forging load estimation using model 1 gives 467.6 kN, and forging load estimation using model 2 gives 419.5 kN. The actual load required is 422.1 kN. An error of 10.7% is observed while considering model 1 as the base and an error of less than 2% is observed while considering model 2 as the base. The results are given in Table 2 for product 2. It is observed from Tables 1 and 2 that estimation of forging load using the geometrically closest shape provides better accuracy in the estimation.

3.2.2 Estimation of Forging Load for Different Friction Condition

To demonstrate the effect of friction on the estimation of forging load, model 1 of product 1 is considered. Forging load is required to be estimated under non-lubricated condition. The existing C_p for the lubricated condition ($\mu = 0.1$) is approximately estimated using Eq. 6, and the same is estimated for the non-lubricated condition ($\mu = 0.25$). The forging load is estimated for the non-lubricated condition of product 1, model 1 using the information of the forging load obtained under lubricated condition as shown in Eq. 6. The estimated forging load is 323.3 kN. The actual load required is 347.5 kN. An error of 7% is obtained. Nevertheless, based on the actual load, the value of C_p is updated and is preserved for further use.

In order to understand the combined effect of size as well as friction. It is assumed that the forging load information of product 2, model 1 exist under lubricated condition. It is required to estimate the forging load of product 2 model 3 under non-lubricated condition. Based on the ratio of the radius between the desired and the existing product, forging load is estimated under lubricated condition. The load is estimated to be 467.6 kN. The estimated load is further substituted in Eq. 6 to get the final estimated load under non-lubricated condition. The final estimated load is 495.3 kN. The actual load required to forge is 503.1 kN. An error of less than 2%

Table 3 Estimation of forging load for two friction conditions of product 1 and product 2

Product No.	Model No.	Friction condition	Actual load (kN)	Estimated load (kN)	Error (%)	Base model	Base product	Friction condition
1	1	Non-lubricated	347.5	323.3	7	–	–	Lubricated
2	3	Non-lubricated	503.1	495.3	10.2	1	2	Lubricated

is estimated while considering both size as well as friction. The results for various friction conditions are given in Table 3.

4 Conclusion

With the emergence of the fourth industrialisation, there has been an increase in the use of data-driven technologies. The trend to use existing data has increased manifolds. The present research work also utilises such existing forging data for the estimation of forging load. The following are the major outcomes from the research article:

- A robust procedure is presented for suggesting a suitable correction factor for the estimation of forging load in axisymmetric products. The shape correction factor is influenced by size and friction condition.
- Estimation of forging load in open die forging is carried out for different sizes and different friction condition for four different materials. The overall maximum error percentage obtained in the estimation is around 3%.
- Estimation of forging load in closed die forging is also carried out for different sizes and different friction condition. For demonstration purpose, two products with three models of each product are considered. Prediction of forging load is achieved with a reasonable accuracy.
- The accuracy achieved in closed die forging depends on the geometric similarity of the base model. Prediction is better if the information of geometrically closest model is utilized.

In future, the framework for developing a big database will be developed.

Acknowledgements This work is a part of a joint Indo-Russian Project entitled “Experimental and numerical research on contact friction in the process of plastic deformation by means of compression with torsion”. It is funded by Russian Foundation for Basic Research (RFBR) and Department of Science and Technology (DST) according to the Research Project № 19-58-45020 and Grant INT/RUS/RFBR/388, respectively. Dr. U.S. Dixit and Dr. P.A. Petrov gratefully acknowledge the support of the funding agencies.

References

1. Moshksar MM, Ebrahimi R (1998) An analytical approach for backward-extrusion forging of regular polygonal hollow components. *Int J Mech Sci* 40(12):1247–1263
2. Fereshteh-Saniee F, Jaafari M (2002) Analytical, numerical and experimental analyses of the closed-die forging. *J Mater Process Technol* 125:334–340
3. Hartley P, Pillinger I (2006) Numerical simulation of the forging process. *Comput Methods Appl Mech Eng* 195(48–49):6676–6690
4. Ward MJ, Miller BC, Davey K (1998) Simulation of a multi-stage railway wheel and tyre forming process. *J Mater Process Technol* 80:206–212
5. Tao F, Qi Q (2017) New IT driven service-oriented smart manufacturing: framework and characteristics. *IEEE Trans Syst Man Cybern Syst* 49(1):81–91
6. Tao F, Qi Q, Liu A, Kusiak A (2018) Data-driven smart manufacturing. *J Manuf Syst* 48:157–169
7. Chatterjee K, Zhang J, Dixit US (2020) Data-driven framework for the prediction of cutting force in turning. *IET Collab Intell Manuf* 2(2):87–95
8. Osakada K, Yang GB, Nakamura T, Mori K (1990) Expert system for cold-forging process based on FEM simulation. *CIRP Ann* 39(1):249–252
9. Katayama T, Akamatsu M, Tanaka Y (2004) Construction of PC-based expert system for cold forging process design. *J Mater Process Technol* 155:1583–1589
10. Kim C, Park CW (2006) Development of an expert system for cold forging of axisymmetric product. *Int J Adv Manuf Technol* 29(5–6):459–474
11. Park KS, Kim BJ, Moon YH (2007) Application of fuzzy expert system to estimate dimensional errors of forging products having complicated shape. *J Mater Process Technol* 187:720–724
12. Gangopadhyay T, Pratihari DK, Basak I (2011) Expert system to predict forging load and axial stress. *Appl Soft Comput* 11(1):744–753
13. Gronostajski Z, Hawryluk M, Kaszuba M, Marciniak M, Niechajowicz A, Polak S, Zwierzchowski M, Adrian A, Mrzygłód B, Durak J (2016) The expert system supporting the assessment of the durability of forging tools. *Int J Adv Manuf Technol* 82(9–12):1973–1991
14. Glaeser A, Selvaraj V, Lee S, Hwang Y, Lee K, Lee N, Lee S, Min S (2021) Applications of deep learning for fault detection in industrial cold forging. *Int J Prod Res.* <https://doi.org/10.1080/00207543.2021.1891318>
15. Dixit US, Yadav V, Pandey PM, Roy A, Silberschmidt VV (2020) Modeling of friction in manufacturing processes. In: Silberschmidt VV (ed) *Mechanics of materials in modern manufacturing methods and processing techniques*. Elsevier, Amsterdam, pp 415–444
16. Ghosh A, Mallik AK (2010) *Manufacturing science*, 2nd edn. Affiliated East West Press, New Delhi
17. Altan T, Fiorentino RJ (1971) Prediction of loads and stresses in closed-die forging. *J Manuf Sci Eng* 93(2):477–484
18. Shima S, Mori K (1979) Analysis of metal forming by the rigid-plastic finite element method based on plasticity theory for porous metals. In: Lippmann H (ed) *Metal forming plasticity*. Springer, Berlin, pp 305–317
19. Dadras P, Thomas JF Jr (1983) Analysis of axisymmetric upsetting based on flow pattern observations. *Int J Mech Sci* 25(6):421–427
20. Park JJ, Kobayashi S (1984) Three-dimensional finite element analysis of block compression. *Int J Mech Sci* 26(3):165–176
21. Hartley P, Sturgess CEN, Rowe GW (1980) Influence of friction on the prediction of forces, pressure distributions and properties in upset forging. *Int J Mech Sci* 22(12):743–753

A Preliminary Investigation on Different Tool Wears in Sustainable Electrical Discharge Machining of Ti-6Al-4V



Shaik M. Basha, Harshit K. Dave, and Himanshu V. Patel

Abstract Electrical discharge machining is a mechanical energy-based non-traditional machining process where material removal occurs by melting and vaporizing the workpiece material due to continuous recurring electrical discharges between the tool electrode and workpiece. Irrespective of the physical and mechanical properties of the workpiece material, this process can able machine any electrically conductive material. Tool electrode wear is unavoidable in this process, where the change in tool shape is directly replicated on the created feature. In this study, different wears associated with tool electrode such as end wear, side wear, and corner radius is examined while machining Ti-6Al-4V. To make the electrical discharge machining process sustainable, indigenously prepared biodiesel is used as dielectric fluid for investigation. Taguchi experimental plan (L16 orthogonal array) is executed to know the best levels for each process parameter. Analysis of variance is performed to find out the contribution of each process parameter toward the different tool wears. From the analysis of variance, it is found that irrespective of the wear associated with the tool electrode, the current is the most contributing parameter, followed by pulse-off-time, pulse-on-time, and voltage.

Keywords Jatropha · Biodiesel · EDM · Titanium · Biodegradable · Taguchi

1 Introduction

Ti-6Al-4V, which is also known as TC4, Ti64, and Grade 5 titanium alpha–beta alloy, is a material that is extensively used in the aerospace industry and for biomedical applications. Low density and high specific strength of this material make it a good

S. M. Basha (✉)

Department of Mechanical Engineering, Indian Institute of Technology Tirupati, Tirupati, Andhra Pradesh, India

e-mail: me19d507@iittp.ac.in

H. K. Dave · H. V. Patel

Department of Mechanical Engineering, Sardar Vallabhbhai National Institute of Technology, Surat, Gujrat, India

© The Author(s), under exclusive license to Springer Nature Singapore Pte Ltd. 2022

23

H. K. Dave et al. (eds.), *Recent Advances in Manufacturing Processes and Systems*,

Lecture Notes in Mechanical Engineering,

https://doi.org/10.1007/978-981-16-7787-8_3

choice for aerospace industries, where reduction in the weight of components even in grams saves several thousand dollars. Low Young's modulus, biocompatibility, and high corrosion resistance make this material best suitable for the fabrication of biomedical implants than the conventionally employed material like stainless steel and cobalt-based alloys. However, this material is poorly machinable with traditional machining processes like milling, turning, and grinding because of its high hardness and lower thermal conductivities. On the other hand, electrical discharge machining (EDM) is an advanced machining process where the material removal occurs by frequent electric discharges between the tool and workpiece. The gap between the tool electrode and workpiece is known as the inter-electrode gap (IEG), and both electrodes are immersed in a dielectric medium. Depending on the dielectric liquid properties and the process parameters, the electrical discharges melt and evaporate the workpiece and tool electrode material and produce the opposite shape of the tool electrode on the workpiece. The tool electrode wear can be classified into three different wear, namely end wear (EW), side wear (SW), and corner radius (CR). The schematic representing all these wears on the tool electrode is shown in Fig. 1.

The end wear represents the reduced length of the tool electrode upon machining. In the EDM process, a servo controller is generally used to monitor the tool electrode position. Due to this end wear, the cavity produced generally does not have the predetermined depth of cut. This portion of wear could be happening because of the electrical discharges that are taking place in the IEG. The side wear of the tool is generally caused by lateral discharges. Whenever the pulse-off-time duration is not adequate, the flushing technique may not flush the debris completely from the IEG [1]. The unflushed debris contaminates the dielectric fluid and reduces the dielectric strength or insulating property of the fluid [2]. Because of this contamination, the debris particles may also be present in the gap between the tool peripheral surface and sidewall of the created feature and responsible for the lateral discharges. These lateral discharges ultimately cause the side wear of the tool and overcut of the workpiece as shown in Fig. 1. The consequence of machining with side worn tool is the tapering of the machined cavity/feature. The formed debris is also accumulated at the corners of the tool and workpiece and results in the rounding of the sharp edges of the tool electrode due to both primary as well as secondary discharges. It is evident from Fig. 1 that these rounded cutting edges produce a fillet in the created feature instead of sharp edges.

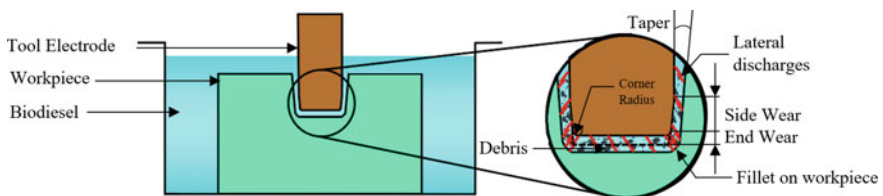


Fig. 1 Schematic of electrical discharge machining and different wears associated with tool electrode

Hydrocarbon-based dielectric fluids (Kerosene and Grade 30 EDM oil) are most commonly employed as a dielectric medium in the EDM process [3–5]. These commercial dielectric fluids emit carcinogenic fumes that are hazardous to the machine operator as well as to the environment. To overcome this problem, many of the researchers investigated the machining of Ti-6Al-4V with EDM process in the presence of tap water [6], deionized water, a combination of tap water with deionized water [7], graphite powder mixed deionized water [8] and drinking water [9], blended commercial EDM oil with paraffin oil [10], bio-oils (sunflower oil, canola oil, and Jatropha oil) [11], and biodiesel [12, 13]. In the previous studies, the researchers concentrated only on the tool wear rates, i.e., erosion of the tool electrode with respect to time. To the best of the author's knowledge, no work has been reported relating to the different wears associated with the tool electrode. The process parameters responsible for each wear associated with the tool electrode are still an unexplored area. Therefore, it is aimed to investigate the EW, SW, and CR in the presence of indigenously prepared Jatropha biodiesel from Jatropha Curcus bio-oil.

2 Biodiesel Preparation

In this section, the need for alternate dielectric fluids required for the EDM process and the methodology of preparing biodiesel from Jatropha Curcus bio-oil are discussed in detail. The basic properties required to employ the prepared biodiesel as a dielectric medium are measured from the available resources at SVNIT, Surat.

2.1 *Need for Alternate Dielectric Fluids*

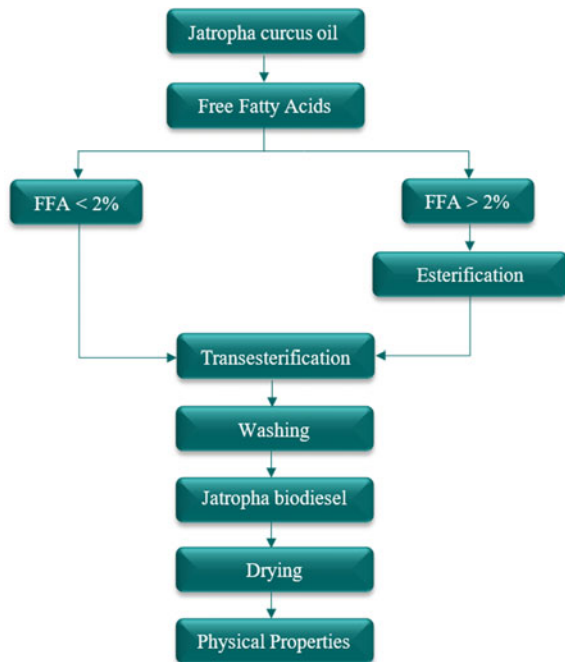
EDM process is generally carried under the presence of hydrocarbon oils, which are derivatives of petroleum [3–5]. When these oils are employed for the EDM process, upon decomposition, these oils release a tremendous amount of carbon dioxide, carbon monoxide, metallic vapors, etc., into the environment. These emissions are generally responsible for air pollution, a health hazard to the operator, and leads to Global Warming [14]. When water is used instead of hydrocarbon oils, it releases aerosol particles, carbon monoxide, etc., which are responsible for Global Dimming [15]. Biodiesel derived from non-edible plant oils, waste vegetable oils, and animal fats is usually known as “carbon-neutral fuel” which means that they release the same amount of carbon to the atmosphere that they have consumed from photosynthesis [16, 17]. Hence, the net addition of carbon to the environment is zero. In this work, biodiesel is prepared from Jatropha bio-oil to examine its performance as the dielectric fluid. Other vegetable oils can also be used for investigation (like karanja, canola, coconut, soybeans, olive, etc.), but Jatropha bio-oil is chosen because it is

non-edible. Hence, it does not pose any problem to humans in food chain competition. Biodiesel makes the EDM process sustainable in operational safety, personal health, and less pollution [18].

2.2 Methodology

The base-catalyzed transesterification process is the most economical out of different routes available for producing biodiesel from bio-oil or fats. This process requires low temperature and pressures and can produce a conversion yield of up to 98% [19]. The flowchart for preparing biodiesel from any bio-oil is shown in Fig. 2. It is inevitable to measure the free fatty acids content before performing the transesterification or the esterification processes. If the free fatty acids content is less than 2%, then the transesterification process can be directly performed without going for the esterification process. Acid value (AV) or acid number (AN) is a common parameter used to estimate the free fatty acid content in an oil or fat. It is defined as the weight of potassium hydroxide (KOH) (in milligrams) required to neutralize the organic substances present in one gram of oil or fat. The acid test is performed to measure the AV of the *Jatropha* bio-oil. To accomplish this test, 40 ml of acetone is taken in a beaker and added 1 g of *Jatropha* bio-oil along with 1–2 drops of phenolphthalein. Out of this solution, 10 ml is taken in a burette. A total of 50 ml of methanol is taken

Fig. 2 Flowchart for *Jatropha* biodiesel preparation



in a conical flask and then added 2.143 g of KOH pellets. Titration is performed until the color of the methanol mixture changes to dark pink. Noted down the consumed volume in the burette and substitute it into the following formulas to get the acid value and free fatty acid content of *Jatropha* bio-oil.

$$\text{Acid value (AV)} = \frac{(V - B) \times N \times 56.1}{W} \quad (1)$$

$$\text{Acid value (AV)} = 1.99 \times \text{Free Fatty Acids (in \%)} \quad (2)$$

where the titrant volume (V), volume in the blank (B), normality of the KOH solution (N), and weight of the sample (W) are 3.5, 3 ml, 0.1 gm/ml, and 1 gm, respectively. Substituting the above values in Eq. (1) results in the AV of 2.59 mg of KOH/g. Again substituting the AV value in Eq. (2) results in the free fatty acids content, and it is found to be 1.3%. From Fig. 2, as the free fatty acid value is less than 2%, it is not required to perform the esterification process. Hence, *Jatropha* bio-oil can be directly used for the transesterification process.

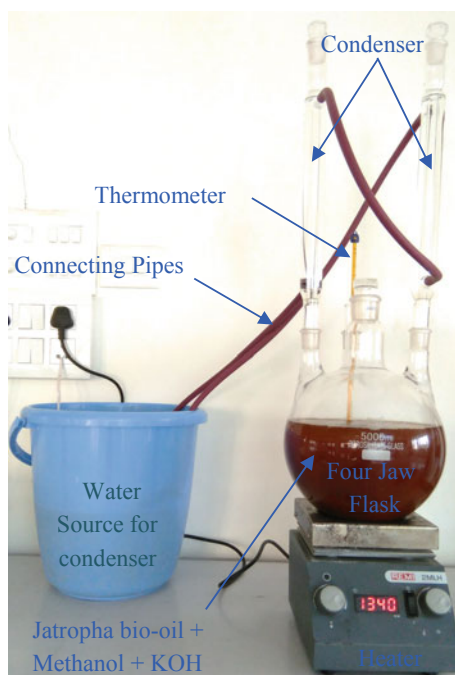
2.3 *Transesterification Process*

The best way to produce biodiesel is the transesterification of bio-oils or vegetable oils with alcohol. Transesterification is the process of exchanging the organic group of an ester with the other organic group of alcohol [20]. This transesterification process can be performed with or without the aid of a catalyst. Different catalysts can be used to increase the rate of reaction and yield of biodiesel. In this work, potassium hydroxide (KOH) is used as a catalyst, and methanol is used as alcohol. The transesterification reaction is reversible, and excess alcohol shifts the equilibrium to the product side. Apart from methanol, other alcohols such as ethanol, propanol, and butanol can also be used.

The step by step procedure for the preparation of biodiesel is as follows

- i. Fifteen grams of KOH pellets are added to 350 ml methanol in a beaker and stirred briskly until a homogenous solution is achieved.
- ii. One liter of *Jatropha* bio-oil is poured into a four-jaw flask, and the homogeneous solution of methanol is added to it. Graham condensers and thermometer are placed in the three openings provided in the flask, whereas the remaining one is simply closed, as shown in Fig. 3.
- iii. The above mixture is heated up to 70 °C and maintained at this temperature for 3–4 h. Graham condenser is used to condense the vaporized methanol back to the flask.
- iv. After the specified duration, this solution is poured into a separating flask and left it to settle down overnight. A definite two separating liquid phases

Fig. 3 Setup of biodiesel preparation



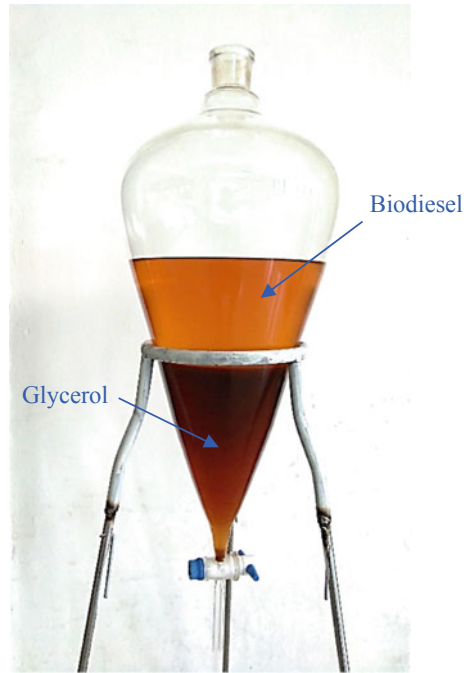
(Jatropha fatty acid methyl ester and glycerol) would be seen in the separating flask, as shown in Fig. 4.

- v. Glycerol is separated from the separating flask, and whatever Jatropha fatty acid methyl ester (Biodiesel) is left in the flask is impure because of the minute traces of glycerol. To remove these impurities, a water wash is performed.
- vi. Water is heated up to 40 °C and added to the impure biodiesel. Because of the density differences, the biodiesel settles at the top of the flask, and the water being denser compared to biodiesel settles at the bottom.
- vii. Because of the traces of glycerol (soap) in the biodiesel, the settled downed water color changes to milky white. This milky water is discarded, and freshly heated water is mixed with biodiesel. This process is performed until clear transparent water results from the mixing process.
- viii. The resulted biodiesel is taken in a beaker and heated to 100 °C and maintained at this temperature for 1.5 h. This heating process helps to vapor the water droplets present in biodiesel, if any, and thus results in pure Jatropha biodiesel.

2.4 Physical Properties

The dielectric fluid in the EDM process should have lower viscosity, moderate break-down voltage, higher flash and fire points, and extremely low electrical conductivity.

Fig. 4 Separation of biodiesel and glycerol



The former two are important properties to improve the machining efficiency, and the latter three properties are important to reduce fire and electric shock hazards in the machining zone [12]. The lower the viscosity of the dielectric fluid, the better the flushing ability and results in minimum overcut and taper [2]. Breakdown voltage is directly related to the discharge spark intensity, and it is also a measure of the insulating property of the dielectric fluid. The conventional hydrocarbon oils result in a lot of smoke in the machining region and easily catch fire, which is a severe hazard to the operator. Biodiesel generally has higher flash and fire points when compared to hydrocarbon oils, and the chances of catching fire are comparably less. The operator often comes in contact with dielectric fluid while machining is being performed. Hence, to reduce the chances of getting electric shocks, the electrical conductivity of the dielectric fluid should be as low as possible. All these properties are measured for prepared biodiesel, and the same is shown in Table 1.

Table 1 Properties of Jatropha biodiesel

S. No.	Property	Units	Measured value
1	Fire point	°C	300 ± 5
2	Flashpoint	°C	170 ± 5
3	Viscosity @ 40 °C	cSt	7 ± 0.5
4	Breakdown voltage	KV/2.5 mm	10 ± 0.4
5	Electrical conductivity	μS/cm	0.01

3 Experimentation

3.1 Machine Setup and Materials

All the experimental runs are performed on JOEMARS made EDM setup available in the Advance Manufacturing Laboratory at SVNIT, Surat, Gujrat. The tool electrode and the workpiece are firmly held in the chuck and precision vice, respectively, as shown in Fig. 5b. Both the tool electrode and workpiece are immersed in biodiesel, and side jet flushing is used for flushing. Proper precautions are taken to prevent the mixing of biodiesel with the hydrocarbon oil that is present in the sump. Electrolytic copper is considered 99.9% of pure copper and is employed as tool electrode material in the EDM process. Tool electrodes of diameter 8 ± 0.2 mm are used to create a blind hole in Ti-6Al-4V. Because of the poor electrical and thermal properties of

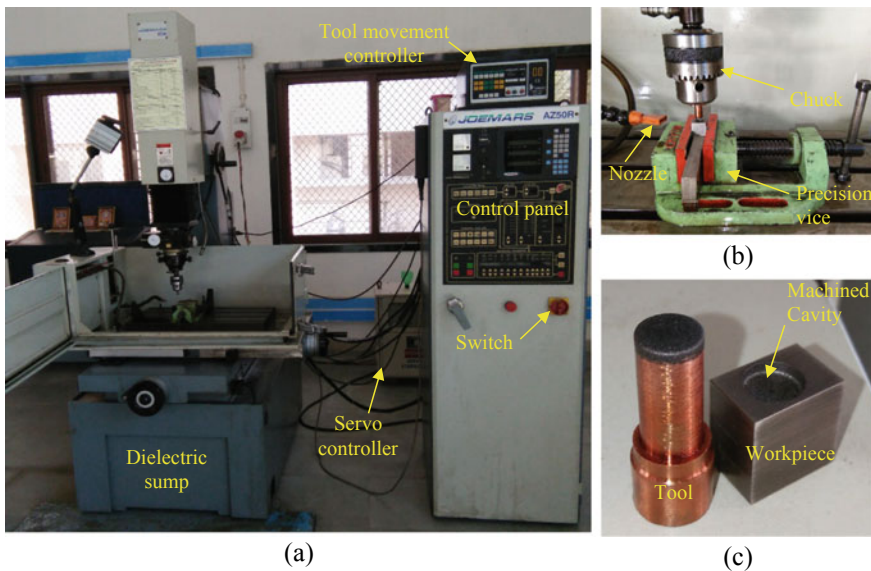


Fig. 5 a Experimental setup; b tool and workpiece settings; c tool and workpiece after machining

Ti-6Al-4V, it generally results in lower material removal rates [20]. In the EDM process, tool wear is inevitable, and it alters the dimensional tolerances of the cavity or hole being produced. Hence, it is aimed to investigate the tool electrode wear while machining one of the difficult-to-cut materials, i.e., Ti-6Al-4V.

3.2 Parametric Selection and Evaluation

Out of many other controlled parameters in the EDM process, current, voltage, pulse-on-time, and pulse-off-time are the generally used process parameters. The levels for each process parameter are selected based on literature and the range available in the EDM setup. The process parameters and their levels with S/N ratios resulted from each wear associated with the tool are given in Table 2.

All the tool electrode wear is measured by using Sipcon made vision measuring system SDM-TRZ 5300, and the setup is shown in Fig. 6. This system has a maximum resolution of 225X and can do the measure with 1 μm accuracy. The tool is fixed firmly in the precision vice, and it is exposed to white light. From the collar created on the tool, as shown in Fig. 5c, the length of the tool before and after the machining is measured, and the difference gives the EW of the tool. SW is measured from a

Table 2 S/N ratios of EW, SW, and CR

Exp. No.	L16 Taguchi orthogonal array				S/N ratio (dB)		
	Current (I)	Voltage (V)	Pulse-on-time (T _{on})	Pulse-off-time (T _{off})	EW	SW	CR
1	9	40	315	168	21.713	11.6249	10.529
2	9	55	360	240	21.884	11.0204	8.925
3	9	70	410	315	20.962	13.0116	11.807
4	9	85	475	385	23.593	12.3578	11.95
5	13	40	360	315	17.755	10.7231	12.769
6	13	55	315	385	18.165	10.2984	9.963
7	13	70	475	168	26.967	9.0418	7.313
8	13	85	410	240	19.898	9.2495	9.026
9	17	40	410	385	16.367	8.1173	6.256
10	17	55	475	315	19.371	8.8257	7.077
11	17	70	315	240	17.888	6.8108	7.23
12	17	85	360	168	20.347	5.8950	5.594
13	21	40	475	240	17.265	5.3982	4.244
14	21	55	410	168	19.824	5.3541	5.021
15	21	70	360	385	16.081	5.8526	6.035
16	21	85	315	315	17.72	6.6541	6.99

Fig. 6 Sipcon made vision measuring system



point on the tool periphery where the diameter is started decreasing till the end of the tool. An approximate circle is constructed at the rounded edge by taking multiple points on the side, and the radius of the circle is considered as the CR.

3.3 Design of Experiments

Taguchi L16 orthogonal array design is used to carry out the experimental runs. Each run is replicated two times to remove the bias in the experimental trials. It is desirable to have lower wear of the tool; therefore, the smaller-the-better Taguchi quality parameter is used to calculate the signal-to-noise (S/N) ratio. The S/N ratios for EW, SW, and CR are given in Table 2. The formula used to calculate the S/N ratios is shown below.

$$\text{Smaller the better: } \eta = -10 \log_{10} \left(\frac{1}{n} \sum_{j=1}^n y_{ij}^2 \right) \quad (3)$$

where n is the number of replication of experimental run and y_{ij} is the response of the i th quality characteristic at j th number of replication.

4 Results and Discussions

The main effects plot for EW, SW, and CR with respect to each process parameter is shown in Fig. 7. From Fig. 7, it can be inferred that lower current (9A) results in the lower erosion of the tool electrode in terms of EW, SW, and CR. This could be because of the lower energy density of the recurring electric discharges in the IEG. These lower energy discharges are responsible for minimizing erosion of the tool electrode and subsequently results in the lower EW. The lower SW and CR are mainly attributed to the secondary discharges caused by the debris generated in the IEG. In the EDM process, the IEG is generally controlled by the voltage between the tool electrode and the workpiece [2]. Higher the voltage, the higher the IEG, and vice versa. This higher IEG also reduces the energy density of each electric discharge. From Fig. 7, it can be inferred that higher voltage (85 V) leads to lower EW and CR. This could be ascribed to the increase in IEG, which results in a higher gap between the two electrodes to flush the debris and reduce the secondary discharges at the flat surface and corner of the tool electrode. However, higher voltage (85 V) resulted in larger SW, which can be attributed to the rigorous secondary discharges that happened at the periphery of the tool and wall of the workpiece. When the dielectric fluid is made to pass through the machining zone, the debris present at the peripheral gap between tool and workpiece is relatively higher to cause more secondary discharges and leads to a higher SW.

The radius of the plasma channels in the EDM process is a function of pulse-on-time [21, 22]. It has been observed that higher pulse-on-time resulted in lower discharge energy density because of the expansion of the plasma channel. The optimum pulse-on-time for lower EW and SW is observed to be at 475 μ s, whereas for

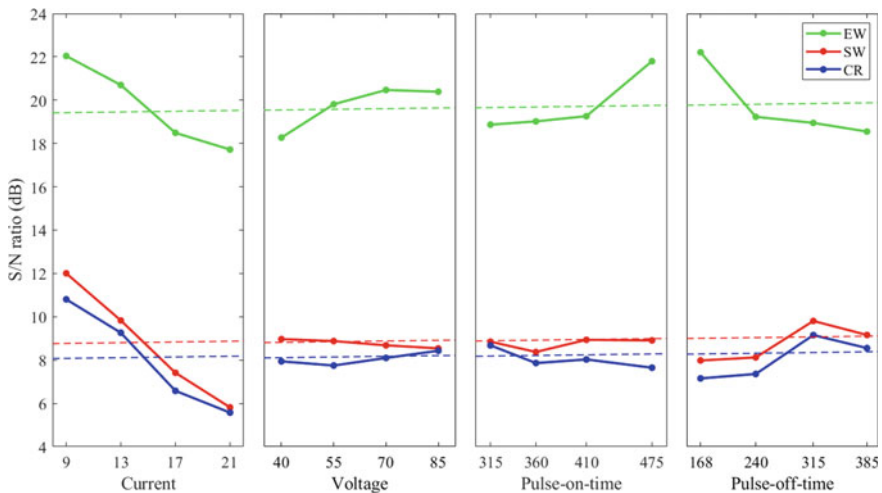


Fig. 7 Main effect plots of EW, SW, and CR with each process parameter

lower CR, it is at 315 μ s. As the pulse-on-time increases, the formed debris is forced toward the corners of the created feature, thus causing secondary discharges. These secondary discharges are most contributing to the rounding of the sharp edges of the tool electrode. The increase in the pulse-off-time lowers the generation of debris in the IEG because of the reduction in the material removal from the workpiece and tool electrode. The optimum pulse-off-time for lower SW and CR is observed to 315 μ s, whereas for lower EW, it is 168 μ s. The higher SW and CR observed could be attributed to the improper flushing, flushing method employed and dielectric fluid properties like density and viscosity.

The results obtained after performing ANOVA on EW, SW, and CR are given in Table 3. Irrespective of the wear associated with the tool electrode, current is the most contributing parameter, followed by pulse-off-time, pulse-on-time, and voltage. The combined contribution of pulse-on-time and voltage is much higher in EW, followed by CR and SW. As discussed earlier, current is responsible for the formation of debris, and pulse-off time is responsible for flushing the debris from IEG, without which the secondary discharges caused to increase the EW, SW, and CR.

Table 3 ANOVA of EW, SW, and CR

Source	DF	Seq SS	Adj SS	Adj MS	F-value	Contribution (%)
<i>End wear</i>						
Current	3	47.282	47.282	15.761	7.76	38.62
Voltage	3	12.454	12.454	4.151	2.04	10.17
Pulse-on-time	3	22.976	22.976	7.659	3.77	18.77
Pulse-off-time	3	33.620	33.620	11.207	5.52	27.46
Error	3	6.090	6.090	2.030		
Total	15	122.422				
<i>Side wear</i>						
Current	3	88.6122	88.6122	29.5374	659.92	89.43
Voltage	3	0.4431	0.4431	0.1477	3.30	0.45
Pulse-on-time	3	0.8347	0.8347	0.2782	6.22	0.84
Pulse-off-time	3	9.0653	9.0653	3.0218	67.51	9.15
Error	3	0.1343	0.1343	0.0448		
Total	15	99.0895				
<i>Corner radius</i>						
Current	3	69.3902	69.3902	23.1301	18.19	79.22
Voltage	3	0.9959	0.9959	0.3320	0.26	1.14
Pulse-on-time	3	2.3752	2.3752	0.7917	0.62	2.71
Pulse-off-time	3	11.0103	11.0103	3.6701	2.89	12.57
Error	3	3.8149	3.8149	1.2716		
Total	15	87.5864				

5 Conclusions

In this work, an attempt is made to investigate different wear: end wear, side wear, and corner radius associated with the tool electrode in the EDM process. To make the EDM process more sustainable from carcinogenic emissions, indigenously developed *Jatropha Biodiesel* was employed for investigation. From this investigation, the following conclusions are derived.

- Secondary discharges are mainly responsible for the side wear of the tool electrode and responsible for the tapering of the created feature
- Debris accumulated at the corners of the created feature is more responsible for the loss of corner edge sharpness and produces a fillet on the feature being created
- Because of the accumulation of debris at the corners of created feature, higher corner wear is observed along with lower end wear as well as side wear at 475 μ s of pulse-on-time
- Lower end wear occurs at a pulse-off-time of 168 μ s, whereas it is at 315 μ s for side wear and corner radius
- From ANOVA, it is observed that irrespective of the type of wear, the current is the most contributing parameter, followed by pulse-off-time, pulse-on-time, and voltage.
- The combined contribution of current and pulse-off-time is more than 90% in the case of side wear and corner radius.

References

1. Singh R, Dvivedi A, Kumar P (2020) EDM of high aspect ratio micro-holes on Ti-6Al-4V alloy by synchronizing energy interactions. *Mater Manuf Processes* 35(11):1188–1203
2. Basha SM, Basha MM, Raj GVP, Venkaiah N, Sankar MR (2020) Past and current trends in electric discharge based machining of Silicon Carbide. *Mater Today Proc* 26:542–548
3. Verma V, Sajeevan R (2015) Multi process parameter optimization of diesinking EDM on titanium alloy (Ti6Al4 V) using Taguchi approach. *Mater Today Proc* 2(4–5):2581–2587
4. Kao JY, Tsao CC, Wang SS, Hsu CY (2010) Optimization of the EDM parameters on machining Ti-6Al-4V with multiple quality characteristics. *Int J Adv Manuf Technol* 47(1–4):395–402
5. Balraj US, Krishna AG (2014) Multi-objective optimization of EDM process parameters using Taguchi method principal component analysis and grey relational analysis. *Int J Manuf Mater Mech Eng* 4(2):29–46
6. Tang L, Du YT (2014) Multi-objective optimization of green electrical discharge machining Ti-6Al-4V in tap water via Grey-Taguchi method. *Mater Manuf Processes* 29(5):507–513
7. Gugulothu B (2020) Optimization of process parameters on EDM of titanium alloy. *Mater Today Proc* 27:257–262
8. Rouniyar AK, Shandilya P (2018) Multi-objective optimization using Taguchi and grey relational analysis on machining of Ti-6Al-4V alloy by powder mixed EDM process. *Mater Today Proc* 5(11):23779–23788
9. Gugulothu B, Rao GKM, Rao DH, Kumsa DK, Kassa MB (2020) Experimental results on EDM of Ti-6Al-4V in drinking water with Graphite powder concentration. *Mater Today Proc*. <https://doi.org/10.1016/j.matpr.2020.07.616>

10. Priyadarshini M, Pal K (2015) Grey-Taguchi based optimization of EDM process for titanium alloy. *Mater Today Proc* 2(4–5):2472–2481
11. Singaravel B, Shekar KC, Reddy GG, Prasad SD (2020) Experimental investigation of vegetable oil as dielectric fluid in electric discharge machining of Ti-6Al-4V. *Ain Shams Eng J* 11(1):143–147
12. Basha SM, Dave HK, Patel HV (2021) Experimental investigation of jatropha curcas bio-oil and biodiesel in electric discharge machining of Ti-6Al-4V. *Mater Today Proc* 38:2102–2109
13. Basha SM, Dave HK, Patel HV (2021) Experimental investigation on the quality of electric discharge machined Ti-6Al-4V using bio-oil and biodiesel. *Mater Today Proc* 38:2249–2255
14. Lashof DA, Ahuja DR (1990) Relative contributions of greenhouse gas emissions to global warming. *Nature* 344(6266):529–531
15. Haywood JM, Bellouin N, Jones A, Boucher O, Wild M, Shine KP (2011) The roles of aerosol water vapor and cloud in future global dimming/brightening. *J Geophys Res Atmos* 116(D20)
16. Pandey VC, Singh K, Singh JS, Kumar A, Singh B, Singh RP (2012) *Jatropha curcas*: a potential biofuel plant for sustainable environmental development. *Renew Sustain Energy Rev* 16(5):2870–2883
17. Koh MY, Ghazi TIM (2011) A review of biodiesel production from *Jatropha curcas* L. oil. *Renew Sustain Energy Rev* 15(5): 2240–2251
18. Shaik MB, Patel H (2017) A review on dielectric fluids used for sustainable electro discharge machining. *Indian J Sci Res* 17(2):40–46
19. Yusoff NRB, bin Hj Hasan S, binti Abdullah NH (2013) Process to produce biodiesel using *Jatropha Curcas* Oil (JCO). *Int J Mater Sci Eng* 1:100–103
20. Otera J (1993) Transesterification. *Chem Rev* 93(4):1449–1470
21. Kojima A, Natsu W, Kunieda M (2008) Spectroscopic measurement of arc plasma diameter in EDM. *CIRP Ann* 57(1):203–207
22. Natsu W, Shimoyamada M, Kunieda M (2006) Study on expansion process of EDM arc plasma. *JSME Int J, Ser C* 49(2):600–605

A Review on Microstructure and Mechanical Properties of L-PBF 17-4PH and 15-5PH SS



I. Kartikeya Sarma, N. Selvraj, and A. Kumar

Abstract Additive manufacturing made a revolution in the Manufacturing area by producing parts with less lead time and highest complexity. It creates parts in layer by layer manner using engineering design. Metallic components in all fields can be produced by Additive manufacturing because of its near net shape production and high quality production. Many Steels can be processed using Additive manufacturing methods. 17-4PH and 15-5 PH Stainless Steels are the precipitated hardened steels which exhibits better mechanical properties after Heat treatment. Even though so many Additive manufacturing Processes are there, Selective Laser Melting gives fully dense and quality parts. In this review paper, we have given an over view on the Microstructure, mechanical, corrosion properties and fatigue properties of 17-4 PH SS and 15-5 PH SS produced by SLM and comparison with conventional parts.

Keywords Precipitation hardening · Solution annealing · Aging

1 Introduction

Additive manufacturing involves manufacturing of parts in a layer by layer manner which is generated from 3D CAD data. The main advantages of Additive manufacturing is that it produces near net shapes with extreme complexity and less lead time compared to conventional manufacturing processes. This made Additive manufacturing parts to use for medical implants, aerospace components, chemical and petrochemical applications, surgical instruments and general metal working applications [1–50]. The material that is commonly used in this application is 17-4 PH SS.

Among additive manufacturing, selective laser melting (SLM) is one of the processes to produce metal parts. Each layer is deposited by repeated melting and fusion of thin layer of the powder with previously deposited and fused layer with the

I. Kartikeya Sarma (✉) · N. Selvraj · A. Kumar
MED, NIT Warangal, Warangal 506370, India
e-mail: ikartik@student.nitw.ac.in

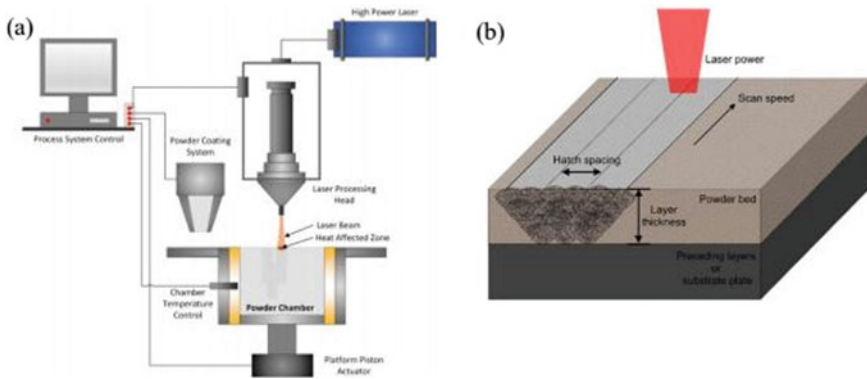


Fig. 1 a Operating procedure of LPB process, b close view of LPB process [38]

help of High Power Laser to build entire part. Selective Laser Melting Process gives high density and quality parts when compared to other processes [1–20] (Fig. 1).

1.1 About 17-4 PH SS

The considerable amount of price and good processability of steels are the reasons for them to use in Additive Manufacturing. Among the various stainless steel precipitated hardened steels has drawn attention. Among precipitated steels, 17-4 Precipitation Hardened Stainless Steel has drawn most attention because of its good mechanical and corrosion properties. It has high tensile strength, fracture toughness, impact toughness and corrosion potential up to 300 °C. Martensite phase is dominant in this kind of steel so it is used in applications in the fields of power plants, powder injection moulding industries, Marine environment. 17-4 PH SS applications in defense and aerospace industries are engine stator parts, Compressor impeller, Fasteners and Fitting gears because of its combined high hardness and strength. It also high corrosion resistance so it is used in oil and gas industry [1–23].

After solution heat treatment and quenching, martensite phase appears when we see microstructure. After aging for a temperature of 480–620 °C the strengthening occurs due to more copper precipitates in the martensite matrix and this precipitates hinders dislocation motion [18]. This steel is susceptible to hydrogen embrittlement [16]. They are promising to Production of AM parts because of its good weldability [26].

17-4PH Stainless Steel consists of chromium with a range of 15–17.5%, Ni and Cu each of 3–5% [25]. Nickel is the austenitic stabilizer. Both higher chromium content and nickel helps to have higher corrosion Potential. Due to Cu rich precipitates Precipitation Hardening occurs, which nucleate and grow during aging heat treatment (Table 1).

Table 1 Commercial chemical composition of 17-4 precipitation hardened SS

Chemical composition	Iron (Fe)	Cr	Ni	Cu	Si	Mn	Ni
% balance	Bal	17.5–15	5–3	5–3	<1.0	<1.0	0.45–0.15

1.2 Applications of 17-4 PH SS

The Applications of 17-4 Precipitation Hardened Stainless Steel are there in so many fields [1–17, 21–38] like

- Structural parts in aerospace applications
- Hand tools in Biomedical Applications
- Gate Valves
- Food Process Equipment
- Chemical Processing
- Mechanical Components
- Nuclear Waste Processing
- Storage -dry cask
- Foils, Helicopter Deck Platforms, etc. in oil and gas industry
- Paper Mill Equipment in Paper and Pulp industry
- Marine-Process Piping, seawater piping, and Heat Exchangers.

1.3 Scope of This Review Paper and Organization of This Article

In this review article, our focus is to present the review of microstructure, mechanical, fatigue and corrosion Properties of Stainless steel type of L-PBF 17-4 PH. Within this article there are subsections where effect of Heat Treatments like Solution Annealing, Aging on microstructure, Hardness, Energy Density, Wear properties, Corrosion Properties and Fatigue Properties are discussed.

In this review article 15-5 PH's Microstructure, Mechanical, Wear, Corrosion and Fatigue properties are also discussed after discussion of 17-4 PH SS within one section. Within that subsection the precipitation Hardening Principle and the 15-5 PH material Properties are discussed.

2 Methods and Discussion of Stainless Steel Type of 17-4 Precipitation Hardened

2.1 Microstructure and Texture of Stainless Steel Type of 17-4 Precipitation Hardened

Extensive studies have been performed on the SLM 17-4 PH SS to understand influence of atomizing media, scan strategy, Different Process Variables like Defocus Distance, Scan speed, Laser Power, Hatch Distance on density, microstructure and surface roughness was investigated [1–17, 21–23, 40–47].

This materials wrought alloy has fully martensite structure [26]. Martensitic structure for this alloy is slightly above the room temperature. Retained austenite also possible due to Ni as austenitic stabilizer.

Rashid et al. [2] reported that martensite and austenite both present in the fabricated samples while Paolo Leo et al. has reported grains are mixed and equiaxed. They have seen rich nano sized spherical inclusions in Mn, Si and O which are about 33 nm [8] while Luiz carneiroa et al. have reported that there are pores due to entrapment of gas.

The XRD patterns of both Water Atomized parts and Gas Atomized parts are having solely martensite and mixture of martensite and austenite phases. The grain size also decreased as the energy density decreased except for gas atomized parts [44].

Adeyami [48] reported the influence of Laser Power on LMD 17-4 PH using 316L substrate. He studied by depositing the samples by laser tracks. He varied Laser power between 1.0 and 2.6 KW with fixed Scan Speed at 1.2 m/s, fixed rate of powder flow 5 g/min and fixed rate of gas flow 2 l/min. The microstructure was dendritic and less δ -ferrite at less laser power while coarser and high δ -ferrite seen at high laser power.

From all these studies, we can conclude that the microstructure of the as- fabricated samples consists of austenite and martensite while some pores resulted because of entrapment of gas.

2.2 Microstructure and Texture of Stainless Steel Type 17-4 Precipitation Hardened After Heat Treatment

Rashid et al. [2] reported that retained austenite and martensite after heat treatment some studies has shown that martensite percentage changed after solution annealing and aging.

Sun et al. [6] reported that after solution annealing there is no change in microstructure but after aging (H 900 condition) martensite block size changed to 2.9 μm , average grain size and FCC volume fraction was also abruptly changed. For the

wrought alloy also there is no change in microstructure after solution annealing and aging.

Both TEM and EBSD analysis indicated that with oxide inclusions grain boundary migration happened after Heat treatment in SLM sample, which results in more refined grains structure than solution Heat treated wrought sample [6]. The lath size is up to 30 μm with martensite block sizes around 8 μm in As built Sample Compared to Wrought alloy.

Sun et al. [22] reported the influence of Heat Treatment on the mechanical properties and microstructure of SLM 17-4 precipitation Hardened steel and wrought alloy. He reported the effect of solution annealing Heat Treatment for 4 h 1038 °C and quenching, the martensitic structure was obtained. The samples have solutionized and aged, then the apparent microstructure obtained in AM has no differences in wrought samples. The initial microstructure also does not has any impact on Cu rich precipitation during aging Heat Treatment.

Cheruvatur [47] reported the effect of stress relieving on the wrought and AM 17-4 PH SS. He found that stress relieving for 1 h has no impact on microstructure. Even for wrought material it is insufficient to alleviate the segregation of microstructure.

From all these studies, we can conclude that the martensite and retained austenite was obtained after completion of Heat treatment some studies has shown that martensite percentage changed after solution annealing and aging.

2.3 Effect of Fabrication Environment and Atomizing Media on 17-4 PH SS Properties

Some authors investigated influence of Atomizing media on the mechanical properties and powder characteristics of 17-4 Precipitation Hardened SS [3, 9, 27–29, 45]. The atomizing media is either water atomized or gas atomized and fabrication atmosphere is either argon or nitrogen atmosphere. The microstructure is martensitic in case of argon atmosphere and austenitic in nitrogen atmosphere and 6% martensitic. The thermal conductivity of nitrogen is more so the phase content difference is 40% which helps in faster cooling rates.

The fabrication atmosphere also has impact on phases of 17-4 PH SS microstructure. In nitrogen atmosphere the retained austenite was 50–75% and in case of argon atmosphere the austenite was 8%.

At energy density 104 J/mm³ and post processed at 1315C and aged at 482C the tensile strength has improved and comparable with gas atomized UTS and YS and wrought alloy. Hardness increased as the energy density improved [3].

Heat treatment at 1315 °C and aging at 482 °C for gas atomized powder given small (30–40 nm) and large (>100 nm) enriched Cu- precipitates. The water atomized powder parts revealed fine (30 nm) enriched Cu rich precipitates distributed uniformly in BCC martensitic structure [3].

Irrinki [44] reported about the Mechanical properties of As- Fabricated Water Atomized parts are higher than As Fabricated Gas Atomized parts and conventional 17-4PH SS parts.

From all the studies, we can conclude that the fabrication atmosphere also has impact on phases of 17-4 PH SS microstructure.

2.4 Porosity and Density

The effect of defocus distance on porosity was less at medium defocus distance [1]. Rashid et al. investigated the density of sample is almost 100% and compared fabricated sample with the 3D CAD model by 3D CT Scan.

Hu [19] and Spierings [50, 51] reported the influence of scan speed and some more process variables on Density and porosity. He found that the medium scan speed giving higher denser sample because of complete melting of the sample and zero pores in the sample. As scan velocity increases the pore size will be more, the insufficient melting and balling phenomenon occur.

Somayeah pasebhani et al. reported that carbon composition is less in Gas Atomized Powder than Water Atomized Powder [3]. Paolo Leo et al. reported the defects arise due to voids resulted from aluminum oxide and unfused powder. The shape of these defects is irregular and average diameter is greater than 20microns. Fractional Area of the defects is <0.52% [5].

Irrinki [44] investigated that the Density is almost same for both water and gas atomized 17-4 PH SS L-PBF parts in as fabricated condition.

All the studies conclude that the medium scan speed giving higher denser sample because of complete melting of the sample and zero pores in the sample.

2.5 Effect of Powder Reuse

Zapico [39] investigated the morphology, chemical characteristics and microstructure of the 17-4 PH Stainless Steel after 10 and 20 manufacturing reuses. He found that EDS analysis of the powder showed that with the reuse the chemical composition was changed and higher oxide concentrations were appeared about 15 m. Moreover the XRD analysis showed increase of austenite phase with the reuse of powder which depends on the fabrication chamber atmosphere. From all the studies, we can conclude that by reusing powder, the powder properties influence the density and surface roughness of the produced part.

2.6 The Influence of Spatter Particles on Mechanical Properties

Usman [45] reported about formation of oversized (185 μm) and undersized (125 μm) spatter particles during L-PBF. The crystallographic phases, size, morphology, chemical composition and microstructure of the spatter particles also studied. The influence of the spatter particles on density, surface roughness and tensile strength of L-PBF samples were also studied. The size of undersized and oversized particles are higher than original powder. Original powder and US particles are dominated by spherical particles and oversized are dominated by spherical agglomerates.

The fusion, partially sintered spatter and satellite particles are the types of OS spatter particles. The original powder and under sized spatter particles showed equiaxed Microstructure but oversized spatter particles showed finer equiaxed Microstructure. The cause is potential nucleation sites increase resulted from adhesion of semisolid particles from oversized Spatter Particles.

Surface Roughness increased in Spatter rich parts and non spatter rich parts to 28 and 15% for cylindrical and tensile parts. The curved surface of cylindrical parts has made increase in surface roughness to 60% than flat tensile parts. Spatter rich parts have higher porosity than the non spatter rich parts. Spatter rich parts have higher porosity than the non spatter rich parts.

2.7 Effect of HT on Properties of 17-4 PH SS

2.7.1 Effect of Heat Treatment on Micro- hardness

Ponnusamy et al. [1] reported that at medium defocus distance the micro hardness was higher due to higher density and defect free component of as fabricated samples. He also reported good surface finish for the medium defocus distance samples.

Rashid et al. had reported that double scan strategy giving highest Hardness compared to single scan strategy as the laser remelts the deposited sample [2].

Most of the researchers reported that by Aging Heat Treatment, the Hardness was higher and samples are isotropic due to martensite and precipitation of Cu rich particles [4–18]. Stress relieving also reported that the Hardness was increased slightly when compared to as fabricated sample [4].

The porosity increased with energy density for PBF steels. The Vickers Hardness obtained was highest at 53.3 GJ/mm^3 and residual stresses are higher than casting steel for PBF steels.

Stress relieving for 1 h improved the hardness for SLM 17-4 Precipitation Hardened SS material [47].

From the above studies, we can conclude that the medium defocus distance and double scan Strategy gives the Highest Hardness. By Aging Heat Treatment, the

Hardness was higher and samples are isotropic due to martensite and precipitation of Cu rich particles. Stress relieving also reported that the Hardness was increased slightly when compared to as fabricated sample.

2.7.2 Effect of Heat Treatment on Elongation and Yield Strength

Heat treatment samples have lower elongation and higher yield strength compared to as built samples. It is because of change in composition, quantity and size of precipitation strengthening phases. The Heat treated and as built samples having ductile rupture [8, 9] while tensile strength is independent of part location on the build plate and also on powder reuse [11].

The Yield Strength increased and elongation decreased for the as built samples after completion of Heat treatment. This is because of change in chemical composition, quantity and size of precipitation strengthening phases. The fracture surfaces correspond to ductile fracture and tensile strength does not depend on type of build plate and powder usage after re manufacturing.

Yadallohi reported that elongation is less in vertical direction compared to horizontal direction. Plastic strains are also less compared to elastic strains for both Heat treated and as fabricated samples.

Michela et al. [16] reported about tension tests performed in air with temperature maintained at room temperature for both notched and smooth specimens for both SLM and wrought steels and aging for 4 h at 580 °C. The elongation is around 21–26% for smooth specimens for both wrought and SLM steels. The strength of SLM ferritic steel is 100 MPa lesser than wrought martensitic steel.

Flippo nalli reported the calibration of three ductile damage models of EBM Ti6Al4V and SLM 17-4 PH SS. He made a series of samples for performing mechanical characterization in static mode. He made round smooth specimens, notched specimens, testing under plane strain condition and torsion test specimens. Stress rate at critical pints are seen by FEM simulation and data collected by hybrid Experimentation and compared with damaged models.

From all the studies, we can conclude Heat treatment samples have lower elongation and higher yield strength compared to as built samples. It is because of change in composition, quantity and size of precipitation strengthening phases. The Heat treated and as built samples having ductile rupture.

2.7.3 Effect of Heat Treatment on Wear Strength of 17-4 PH SS

KC [14] investigated the wear rate is less for LP-PBF 17-4PH SS samples than Conventionally 17-4 PH SS in lubricated condition because of difference in surface roughness. As hardness is high for LP-PBF Parts so less wear rate will be there because of difference in surface roughness in these samples. The dominant wear mechanism is Adhesion during dry testing condition. The wear mechanisms surface

fatigue and abrasion are dominant in lubricated condition for both SLM and Wrought Samples.

Shibata et al. [15] investigated the wear and friction properties under oil lubrication of laser PBF stainless steels in oil lubrication in 5 different conditions by changing the scan speed and laser power for Casting Steel. The friction coefficient increased gradually from initial stage and then become constant for both SLM and wrought material. Wear rate increases with coefficient of friction for entire period.

Friction coefficient increased with normal load from initial stage. Then it is gradually increased. The mean friction coefficient and specific wear rates increases with normal loading. The PBF steels wear rates are lesser than wrought steels.

The specific wear rates also increased with mean friction coefficient during entire period. The mean friction coefficient and specific wear rates of PBF Steels are lesser than Casting steel for all the conditions.

From all the above studies, we can conclude that Wear rate is less for L-PBF 17-4 Precipitation Hardened Stainless Steel samples than Conventionally 17-4 PH SS in lubricated condition because of higher Surface Roughness.

2.7.4 Influence of Heat Treatment on Corrosion Properties of 17-4 Precipitation Hardened Stainless Steel

Michela et al. [16] reported the influence of hydrogen embrittlement is less when solution annealed than peak aging but the susceptibility decreases as the solution annealed temperature increases. Both SLM and wrought steels are influenced to Hydrogen Embrittlement with slower displacement rates. Fracture elongation was decreased with uncharged steels. SLM steels exhibit higher Hydrogen Embrittlement compared to Wrought Steels because of grain size and crack propagation and initiation was more easy in SLM ferritic steel than wrought martensitic steel.

Michella [17] reported the corrosion resistance and microstructure of SLM and wrought 17-4 PH Stainless steel. SLM as built Steel samples consists of ferrite only. After Reausteniting martensite was observed. The corrosion resistance of both as built and reasustenized samples have same corrosion resistance which is related to chemical composition. The martensitic reasustenized samples have more corrosion resistance than martensitic wrought samples because of MnS inclusions. The microstructure difference has little impact on corrosion resistance. The grain boundary and density pitting potential of As built sample greater than reasustenized parts.

From other corrosion studies also [27, 30] we can conclude that the corrosion potential of AM (even for both gas and water atomized parts) is better than the wrought parts. Better corrosion resistance for AM parts is due to its refined microstructure, inclusions, increased stability of passive film in case of nitrogen content when parts are fabricated in nitrogen atmosphere.

From all the studies, we can conclude that Corrosion potential of 17-4 Precipitation Hardened Stainless Steel (even for both gas and water atomized parts) is better than the wrought parts.

2.7.5 Effect of Heat Treatment on Fatigue Properties of 17-4 PH SS

Several studies were there on the fatigue behavior of 17-4 Precipitation Hardened Stainless Steel [9–13, 29, 46] and there are studies about fatigue crack growth behavior in both parallel and perpendicular direction. Those samples tested in parallel orientation have shorter fatigue life compared to perpendicular direction because of internal defects. The internal defects become large defect area compared to gage area, they become crack initiation sites.

Both the heat treatments solution annealing and aging did not improve the fatigue potential of 17-4 Precipitation Hardened Stainless Steel [13] while Yadollahi et al. [9] reported that the effect of HT to fatigue cracking growth was not there but the build direction of the sample showed much impact on fatigue behavior of LP-PBF samples. Large delamination observed in cracking growth direction of specimens with transverse cracking in both as fabricated and HT specimens.

He [10] also reported from fatigue test results, HT is beneficial for low cycle fatigue and but not for high cycle fatigue. Stress concentration is more in vertical direction as more area is exposed to loading. Cracks were there near surface of specimens from smaller voids due to unmelted regions in long life testing. Multiple Crack initiations were found near the surface in short life testing due to smaller voids.

Soltani-Tehrani [11] investigated the impact of re use of powder and part location on the fatigue properties. The fatigue behavior for LP-PBF metal parts with influence of powder reuse and part location on the build plate was insensitive. But the fatigue behavior of the metal parts in machined surface state was dependent on build plates part location and effect is decreasing.

Mower [46] investigated the mechanical behavior of SLM AlSi10Mg, DMLS Ti6Al4V, DMLS 17-4 PH and 316L. The fatigue strength of SLM AlSi10Mg, DMLS Ti6Al4V is inferior as that of conventional material. This is due to multiple cracks developed during cyclic loading at defects region. While fatigue strength of DMLS 17-4 PH and 316L is almost same as that of conventional material. Fatigue fractures developed prematurely before the loading.

From all the above studies, we can conclude that Samples tested in parallel direction have shorter fatigue life compared to perpendicular direction because of internal defects. Fatigue test results showed that the heat treatment will only benefit low cycle fatigue but not high cycle fatigue. The fatigue properties of 17-4 PH parts with the with the variation of part location on build plate and reuse of powder was insensitive in as fabricated condition.

Table 2 Chemical composition of 15-5 PH SS

Composition of 15-5 PH SS	Fe	Cr	Ni	Cu	Nb	Mn	Si
% balance	75	15	5	4	<0.1	<0.1	0.15–0.45

3 AM of 15-5 PH Stainless Steel

3.1 About 15-5 PH SS

Because of high strength, ductility and mechanical properties 15-5 PH is used in aerospace industries. This martensitic precipitation hardened steel mechanical properties and corrosion potential is improved by Heat treatment and by adding alloys.

Transformation of BCC ferrite Phase to FCC austenite phase when we heat above A3 temperature. To transform austenite back to Ferrite by cooling back and by carbon dissolving in FCC structure will form Cementite. When this steel is rapidly cooled, carbon atoms diffuse from the FCC phase of austenite to BCC but it does not happen. Highly strained BCT crystal forms which is known as martensite. Cooling rapidly makes carbon atoms to diffuse from austenite FCC phase to BCC but it does not happen and highly strained BCT martensite phase forms.

Shear Deformation formed by dislocations of carbon atoms makes the strength improved. Without heat treatment the ductility and strength are good but the strength increases by Heat Treatment.

15-5 PH Stainless Steel consists of Cu, Ni, Cr, Fe. Addition of Mn, Nb and Si giving benefit [39] (Table 2).

By quenching the both ductility and strength improved but it is lesser for usable value and helps for machining addition of 4% Cu after quenching makes Cu to trap in crystal structure and over saturates. Over saturating is removed by steel heating to an medium temperature then Cu becomes precipitated. It is known as Precipitation Hardening.

Increasing the temperature of steel makes Cu traps in crystal structure and produce fine particles, dislocations and improvement of strength.

3.2 Methods and Discussion of 15-5 PH SS

Several studies [18–20, 31–37, 49] reported the production of Laser PBF SLM 15-5 PH stainless steel. The influence of build direction on basic mechanical and fatigue properties were investigated and properties of AM 15-5 PH SS compared with wrought Stainless Steel. Influence of Solution Annealing and Aging on this particular steel and wrought alloy were also discussed [18–20].

Roberts [37] given that the high temperature tensile strength of AM Samples are about 30% more than wrought parts and Vickers Hardness of AM samples are 50% more than its wrought parts. Stress Rupture Tests at 211 MPa and 593 °C had shown that AM parts have 30% more rupture life than conventional parts.

Jun et al. [18] reported the influence of process variables on thermal gradient which directly affects the mechanical properties and microstructure. He also given the influence of build direction and heat treatment on the mechanical properties and microstructure. The mechanical properties and microstructure of as fabricated, solution annealing and aging, aging, solution annealing and conventionally manufactured parts were investigated. The micro structure has ferrite, martensite plus austenite. Both Solidification and Heat gradient made the formation of retained austenite and rapid cooling rates giving precipitation hardening by aging with solution HT. Hardness in horizontal direction had given high hardness than vertical except for aging. Anisotropy is common. Solution annealing parts have less hardness than other (as fabricated, aging, CM and S and A). Hardness of SLM parts are higher than CM because of rapid cooling in AM parts.

Nath et al. [19] reported on the influence of HT on microstructure, corrosion, wear and mechanical properties of 15-5PH SS parts made by SLM process. The influence of microstructure on corrosion and mechanical properties were analyzed. H900 Aging made increase in Hardness, yield strength and corrosion resistance through Cu rich Precipitates. Brittle nature made wear rate increase and decrease of impact energy. (H1150) made the specimen ductile, lesser yield strength, Low Hardness and wear and high impact energy. Solution annealing reduced anisotropy by microstructure Homogenization. Aging at high temperature and long soaking time made an impact on mechanical properties and decrease corrosion properties. Solution Annealing before Aging gives Homogenized microstructure.

Wang et al. [20] investigated the microstructural optimization for Heat treated SLM 15-5PH Stainless Steel to enhance corrosion resistance was investigated. The results showed that after aging treatment, Cu rich nanoparticles (about 10 nm) diffusely precipitated, and approximately 18–25% austenite was distributed near the molten pool boundary. The surface potential of the austenite was approximately 15 mV higher than that of martensite by scanning Kelvin probe force microscopy. However, the austenite phase disappeared and the new NbC-(Mn, Si) O duplex particles precipitated after Aging and Solution Annealing, which decreased the pitting Corrosion Potential and passive stability of film for the SLM 15-5PH stainless steel.

Nong et al. [41] reported the mechanical Properties and microstructure of the SLM15-5 PH SS and wrought SS. He found that the YS and UTS were higher compared to wrought alloy while elongation was less compared to wrought alloy. The as built sample has large volume of austenite. The austenite after retained was greatly reduced by Heat treatment and completely transformed into martensite which leads into improvement of mechanical properties. Strength and micro hardness was improved by fine grain microstructure and concentration of dislocations.

Alafaghani [49] reported the Mechanical properties and Microstructure of SLM IN 718 and SLM 15-5 PH. He made the tensile testing at three different temperatures (RT, 200 °C, 450 °C) and three different directions X, Y, Z. The microstructure

was observed by using Fry’s agent and observed with help of SEM and OM. SEM images was seen for checking powder particle size and porosity. There was no permanent change in microstructure but there was change in microstructure in different directions. Reduction in tensile properties was there with increase in temperature. Anisotropy reduced with increase in temperature.

From all the above studies, we can conclude that High temperature tensile strength of 15-4 PH SS AM Samples are about 30% more than wrought parts and Vickers Hardness of AM samples are 50% more than its wrought parts. Solution Annealing parts have less hardness than other heat treatment processes (As Fabricated, Aging and Solution annealing and Aging).Hardness of 15-5 PH SS AM parts are higher than CM because of rapid cooling in AM parts.

Aging done after completion of Solution Annealing is recommended for the homogeneity in microstructure for 15-5 PH SS AM parts. Wear and Corrosion Potential of Additive Manufactured Parts are more than Conventional Parts.

4 Summary

In this paper previous study of 17-4 PH SS and 15-5 PH SS made by laser-PBF were reviewed. The influence of heat treatment on mechanical properties like Hardness, Tensile behavior, yielding, Elongation, Wear strength, Corrosion Resistance, Fatigue properties and microstructure of both 17-4 PH SS and 15-5 PH SS made by Laser-PBF were discussed. The effect of powder reuse and Spatter Particles on the Mechanical Properties was also discussed.

Despite so many advantages of L-PBF there are some disadvantages like re melting, solidification and rapid melting of the powder during production of parts, complex microstructure. These disadvantages hamper wide applications. In future so many heat treatment procedures needed to be applied to understand the microstructure. To meet the industrial demands the influence of Heat Treatment on Wear, Corrosion, Fatigue Properties and Complex Microstructure to be studied more deeply.

Summary Table

S. No.	Material	Type of study	Conclusion
01	17-4 PH SS	Microstructure and texture before heat treatment	Microstructure of the as- fabricated samples consists of austenite and martensite while some pores resulted because of entrapment of gas
02	17-4 PH SS	Microstructure and texture after heat treatment	Martensite and retained austenite was obtained after completion of Heat Treatment some studies has shown that martensite percentage changed after solution annealing and aging

(continued)

(continued)

S. No.	Material	Type of study	Conclusion
03	17-4 PH SS	Effect of fabrication environment and atomizing media	Fabrication atmosphere also has impact on phases of 17-4 PH SS microstructure
04	17-4 PH SS	Effect of porosity and density	Medium scan speed giving higher denser sample because of complete melting of the sample and zero pores in the sample
05	17-4 PH SS	Effect of powder reuse	By reusing powder, the powder properties influence the density and surface roughness of the produced part
06	17-4 PH SS	Effect of heat treatment on micro hardness	By aging heat treatment, the hardness was higher and samples are isotropic due to martensite and precipitation of Cu rich particles. Stress relieving also reported that the Hardness was increased slightly when compared to as fabricated sample
07	17-4 PH SS	Effect of heat treatment on yield strength and elongation	Heat treatment samples have lower elongation and higher yield strength compared to as built samples
08	17-4 PH SS	Effect of heat treatment on wear strength	Wear rate is less for L-PBF 17-4 precipitation hardened stainless steel samples than conventionally 17-4 PH SS in lubricated condition because of higher surface roughness
09	17-4 PH SS	Influence of heat treatment on corrosion properties	Corrosion potential of 17-4 precipitation hardened stainless steel (even for both gas and water atomized parts) is better than the wrought parts
10	17-4 PH SS	Effect of heat treatment on fatigue properties	Heat treatment will only benefit low cycle fatigue but not high cycle fatigue. The fatigue properties of 17-4 PH parts with the with the variation of part location on build plate and reuse of powder was insensitive in as fabricated condition
11	15-5 PH SS	Effect of heat treatment on all properties of 15-5 PH SS SLM	Aging done after completion of solution annealing is recommended for the homogeneity in microstructure for 15-5 PH SS AM parts. Wear and corrosion potential of additive manufactured parts are more than conventional parts

References

1. Ponnusamy P, Masood SH, Palanisamy S, Rahman Rashid RA, Ruan D (2017) Characterization of 17-4PH alloy processed by selective laser melting. *Mater Today Proc* 4:8498–8506
2. Rashid R, Masood SH, Ruan D, Palanisamy S, Rahman Rashid RA, Brandt M, Effect of scan strategy on density and metallurgical properties of 17-4PH parts printed by selective laser melting (SLM). *J Mater Process Technol*
3. Pasebani S, Ghayoor M, Badwe S, Irrinki H, Atre SV (2010) Effect of atomizing media and post processing on mechanical properties of 17-4 PH stainless steel manufactured via selective laser melting, additive manufacturing
4. Giganto S, Zapicoa P, Ángeles Castro-Sastre M, Martínez-Pellitero S, Leo P, Perulli P (2019) Influence of the scanning strategy parameters upon the quality of the SLM parts. *Procedia Manuf* 41:698–705
5. Leo P, D'Ostuni S, Perulli P, Sastre MAC, Fernández-Abia AI, Barreiro J (2019) Analysis of microstructure and defects in 17-4 PH stainless steel sample manufactured by selective laser melting. *Procedia Manuf* 41:66–73
6. Sun Y, Hebert RJ, Aindow M (2018) Effect of heat treatments on microstructural evolution of additively manufactured and wrought 17-4PH stainless steel. *J Mater Des*
7. McWilliams B, Pramanik B, Kudzal A, Taggart-Scarff J (2018) High strain rate compressive deformation behavior of an additively manufactured stainless steel. *Additive Manuf*
8. Hu Z, Zhu H, Zhang H, Zeng X (2017) Experimental investigation on selective laser melting of 17-4PH stainless steel. *Opt Laser Technol* 87:17–25
9. Yadollahi A, Shamsaei N, Thompson SM, Elwany A, Bian L (2016) Effects of building orientation and heat treatment on fatigue behavior of selective laser melted 17-4 PH stainless steel. *Int J Fatigue* 0142–1123
10. Yadollahi A, Mahmoudi M, Elwany A, Doude H, Bian L, Newman JC Jr (2020) Effects of crack orientation and heat treatment on fatigue-crack-growth behavior of AM 17-4 PH stainless steel. *Eng Fract Mech*
11. Soltani-Tehrani A, Pegues J, Shamsaei N (2020) Fatigue behavior of additively manufactured 17-4 PH stainless steel: the effects of part location and powder re-use, additive manufacturing
12. Nezhadfar PD, Burford E, Anderson-Wedge K, Zhang B, Shao S, Daniewicz SR, Shamsaei N (2019) Fatigue crack growth behavior of additively manufactured 17-4 PH stainless steel: effects of build orientation and microstructure. *Int J Fatigue* 0168–179
13. Carneiro L, Jalalahmadib B, Ashtekarb A, Jiang Y (2019) Cyclic deformation and fatigue behavior of additively manufactured 17–4 PH stainless steel. *Int J Fatigue* 123:22–30
14. KC S, Nezhadfar PD, Phillips C, Kennedy MS, Shamsaei N, Jackson RL (2019) Tribological behavior of 17–4PH stainless steel fabricated by traditional manufacturing and laser-based additive manufacturing methods. *Wear*
15. Shibata K, Ishigaki W, Koike T, Umetsu T, Yamaguchi T, Hokkirigaw K (2016) Friction and wear behavior of stainless steel fabricated by powder bed fusion process under oil lubrication. *Tribol Int* 104:183–190
16. Alnajjar M, Christien F, Bosch C, Wolski K (2020) A comparative study of microstructure and hydrogen embrittlement of selective laser melted and wrought 17–4 PH stainless steel. *Mater Sci Eng A* 258
17. Michella A, Frédéric C, Vincent B, Cédric B, Krzysztof W, Dominic Fortes A, Telling M, Influence of microstructure and manganese sulfides on corrosion resistance of selective laser melted 17-4 PH stainless steel in acidic chloride medium
18. Leea J-R, Leea M-S, Chaeb H, Yeol Leeb S, Nac T, Kimd W-S, Jun T-S (2020) Effects of building direction and heat treatment on the local mechanical properties of direct metal laser sintered 15-5 PH stainless steel. *Mater Charact*
19. Sarkar S, Mukherjee S, Kumar CS, Nath AK (2020) Effects of heat treatment on microstructure, mechanical and corrosion properties of 15-5 PH stainless steel parts built by selective laser melting process. *J Manuf Processes* 50

20. Wang L, Dong C, Man C, Kong D, Xiao K, Li X (2019) Enhancing the corrosion resistance of selective laser melted 15-5PH martensite stainless steel via heat treatment, corrosion science
21. Meredith SD, Zuback JS, Keist JS, Palmer TA (2018) Impact of composition on the heat treatment response of additively manufactured 17-4 PH grade stainless steel. *Mater Sci Eng, A* 738:44–56. <https://doi.org/10.1016/J.MSEA.2018.09.066>
22. Sun Y, Hebert RJ, Aindow M (2020) Effect of laser scan length on the microstructure of additively manufactured 17-4PH stainless steel thin-walled parts. *Addit Manuf*
23. Sun Y, Hebert RJ, Aindow M (2017) Non-metallic inclusions in 17-4PH stainless steel parts produced by selective laser melting. *Mater Des*
24. Bajaj P, Hariharan A, Kini A, Kürnsteiner P, Raabe D, Jäggle EA (2019) Steels in additive manufacturing: a review of their microstructure and properties. *Mater Sci Eng A*
25. 3DSystems (2020) LaserForm 17-4PH (B) for ProX DMP 100, 200 and 300 direct metal printers
26. Hsiao CN, Chiou CS, Yang JR (2002) Aging reactions in a 17-4 PH stainless steel. *Mater Chem Phys* 74:134–142. [https://doi.org/10.1016/S0254-0584\(01\)00460-6](https://doi.org/10.1016/S0254-0584(01)00460-6)
27. Irrinki H, Harper T, Badwe S, Stitzel J, Gulsoy O, Gupta G, Atre SV (2018) Effects of powder characteristics and processing conditions on the corrosion performance of 17-4 PH stainless steel fabricated by laser-powder bed fusion. *Prog Addit Manuf* 3:39–49. <https://doi.org/10.1007/s40964-018-0048-0>
28. Sun Y, Hebert RJ, Aindow M (2018) Effect of heat treatments on microstructural evolution of additively manufactured and wrought 17-4PH stainless steel. *Mater Des* 156:429–440. <https://doi.org/10.1016/J.MATDES.2018.07.015>
29. Nezhadfar PD, Shrestha R, Phan N, Shamsaei N (2019) Fatigue behavior of additively manufactured 17-4 PH stainless steel: synergistic effects of surface roughness and heat treatment. *Int J Fatigue* 124:188–204. <https://doi.org/10.1016/J.IJFATIGUE.2019.02.039>
30. Stoudt MR, Ricker RE, Lass EA, Levine LE (2017) Influence of postbuild microstructure on the electrochemical behavior of additively manufactured 17-4 PH stainless steel. *JOM* 69:506–515. <https://doi.org/10.1007/s11837-016-2237-y>
31. Spierings AB, Starr TL, Wegener K (2013) Fatigue performance of additive manufactured metallic parts. *Rapid Prototyp J* 19:88–94. <https://doi.org/10.1108/13552541311302932>
32. Pal S, Tiyyagura HR, Drstvenšek I, Kumar CS (2016) The effect of post-processing and machining process parameters on properties of stainless steel PH1 product produced by direct metal laser sintering. *Procedia Eng* 149:359–365. <https://doi.org/10.1016/J.PROENG.2016.06.679>
33. Lum E, Palazotto AN, Dempsey A (2017) Analysis of the effects of additive manufacturing on the material properties of 15-5PH stainless steel. In: 58th AIAA/ASCE/AHS/ASC structure dynamics materials conference, American Institute of Aeronautics and Astronautics, Reston, Virginia, 46. <https://doi.org/10.2514/6.2017-1142>
34. López-Castro JD, Marchal A, González L, Botana J (2017) Topological optimization and manufacturing by direct metal laser sintering of an aeronautical part in 15-5PH stainless steel. *Procedia Manuf* 13:818–824. <https://doi.org/10.1016/J.PROMFG.2017.09.121>
35. Rafi HK, Starr TL, Stucker BE (2013) A comparison of the tensile, fatigue, and fracture behavior of Ti-6Al-4V and 15-5 PH stainless steel parts made by selective laser melting. *Int J Adv Manuf Technol* 69:1299–1309. <https://doi.org/10.1007/s00170-013-5106-7>
36. Alafaghani A, Qattawi A, Castañón MAG (2018) Effect of manufacturing parameters on the microstructure and mechanical properties of metal laser sintering parts of precipitate hardenable metals. *Int J Adv Manuf Technol* 99:2491–2507. <https://doi.org/10.1007/s00170-018-2586-5>
37. Roberts D, Zhang Y, Charit I, Zhang J (2018) A comparative study of microstructure and high temperature mechanical properties of 15-5 PH stainless steel processed via additive manufacturing and traditional manufacturing. *Prog Addit Manuf* 3:183–190. <https://doi.org/10.1007/s40964-018-0051-5>
38. Krauss H, Zeugner T, Zaeh MF (2014) Layerwise monitoring of the selective laser melting process by thermography. In: 8th international conference laser assistive net shape engineering LANE 2014. 56, 64–71. <https://doi.org/10.1016/j.phpro.2014.08.097>

39. Zapico P, Giganto S, Barreiro J, Martínez-Pellitero S (2020) Characterisation of 17-4PH metallic powder recycling to optimise the performance of the selective laser melting process. *J Mater Res Technol* 1273–1285
40. Zhukov A, Barakhtin B, Kuznetsov P (2017) Study of strength characteristics of steel specimens after selective laser melting of powder materials 17–4 PH,316L,324. *Phys Procedia* 89:179–186
41. Nonga XD, Zhoua XL, Li JH, Wanga YD, Zhao YF, Brochu M (2020) Selective laser melting and heat treatment of precipitation hardening stainless steel with a refined microstructure and excellent mechanical properties. *Scripta Mater*
42. Mahmoudi M, Elwany A, Yadollahi A, Thompson SM, Bian L, Shamsaei N (2017) Mechanical properties and microstructural characterization of selective laser melted 17–4 PH stainless steel. *Rapid Prototyping J* 23(2):280–294
43. Nalli F, D’Onofrio A, Broggiato GB, Cortese L (2019) Calibration and prediction assessment of different ductile damage models on Ti6Al4V and 17-4PH additive manufactured alloy. In: *AIAS 2019 international conference on stress analysis*
44. Irrinki H, Samuel Dilip Jangam J, Pasebani S, Badwe S, Stitzel J, Kate K, Gulsoy O, Atre SV (2018) Effects of particle characteristics on the microstructure and mechanical properties of 17-4 PH stainless steel fabricated by laser-powder bed fusion. *Powder Technol* 192–203
45. Ali U, Esmailizadeh R, Ahmed F, Sarker D, Muhammad W, Keshavarzkermani A, Mahmoodkhani Y, Marzbanrad E, Toyserkani E (2019) Identification and characterization of spatter particles and their effect on surface roughness, density and mechanical response of 17–4 PH stainless steel laser powder-bed fusion parts. *Mater Sci Eng, A* 756:98–107
46. Mower TM, Long MJ (2016) Mechanical behavior of additive manufactured, powder-bed laser-fused materials. *Mater Sci Eng A* 651:198–213
47. Cheruvathur S, Lass EA, Campbell CE (2015) Additive manufacturing of 17-4 PH stainless steel: post-processing heat treatment to achieve uniform reproducible microstructure. 2015 *The Minerals, Metals & Materials Society*
48. Adeyemi AA, Akinlabi ET, Mahamood RM, Sanusi KO, Pityan S, Tlotleng M (2017) Influence of laser power on microstructure of laser metal deposited 17-4 ph stainless steel. *IOP Conf Ser Mater Sci Eng* 225:012028. <https://doi.org/10.1088/1757-899X/225/1/012028>
49. Alafaghani A, Qattawi A, Alberto Garza Castañón M (2018) Effect of manufacturing parameters on the microstructure and mechanical properties of metal laser sintering parts of precipitate hardenable metals. *Int J Adv Manuf Technol*
50. Spierings AB, Schoepf M, Kiesel R, Wegener K (2014) Optimization of SLM productivity by aligning 17–4PH material properties on part requirements. *Rapid Prototyping J* 20(6):444–448
51. Spierings AB, Herres N, Levy G (2011) Influence of the particle size distribution on surface quality and mechanical properties in AM steel parts. *Rapid Prototyping J* 17(3):195–202
52. Zai L, Zhang C, Wang Y, Guo W, Wellmann D, Tian XTY (2020) Laser powder bed fusion of precipitation-hardened martensitic stainless steels. *Rev Metals* 10:255. <https://doi.org/10.3390/met10020255>

A Review on Twin Wire Arc Additive Manufacturing of Metals and Alloys: Microstructure and Mechanical Properties



Poonam S. Deshmukh and Dan Sathiaraj

Abstract Wire Arc Additive Manufacturing (WAAM) has been considered one of the promising Additive Manufacturing (AM) techniques for fabricating medium to large-sized metallic components, even with complex geometry. WAAM offers numerous advantages, such as high deposition rate, lower material utilization, and non-hazardous properties compared to powder-based processes. With the use of multiple feed wires, WAAM achieves an advantage of in-situ alloying. This technique allows the use of various multiple feed wires to form complex components with good mechanical properties. The use of multiple feed wires fixes the problem of limited availability of some metal wires that are difficult to form due to particular metal properties like brittleness and increases the deposition rate. In recent years, Twin Wire Arc Additive Manufacturing (T-WAAM) has become popular for fabricating functionally graded materials (FGMs), intermetallic alloys, and other multi-element alloys. This article reviews the various studies related to the T-WAAM technique for fabricating structures of different alloys. Besides, microstructure studies and mechanical properties of the fabricated structures along with the process feasibility are discussed. In-situ alloying offers a cost-effective method for producing various alloys and composites with desired compositions and directional properties. However, it would be appealing to develop a WAAM system combined with other secondary machining processes to fabricate finished components with minimal or no need for post-processing.

Keywords Twin wire arc additive manufacturing · In-situ alloying · Functionally graded materials · Intermetallic alloys

P. S. Deshmukh · D. Sathiaraj (✉)
Department of Mechanical Engineering, IIT Indore, Indore, India
e-mail: dansathiaraj@iiti.ac.in

P. S. Deshmukh
e-mail: phd2001103001@iiti.ac.in

1 Introduction

1.1 Additive Manufacturing

Additive Manufacturing (AM) is becoming a widely accepted technology in many manufacturing industries and academia. AM is highly popular for its ability to fabricate complex geometries in less processing time and process almost any kind of material such as metal, alloys, ceramics, and polymers. It eliminates the need for special tooling and fixtures and produces single-part components that eliminate the need for assembly. Thus, reducing overall production cost and processing time. Powder bed fusion and directed energy deposition are the most commonly used AM techniques for metals and alloys. DED can use powder feedstock or wire feedstock as per application [1]. Powder-based AM processes mainly use a high energy laser beam or electron beam as a heat source. In this case, the deposition has carried out in a sealed chamber because of safety concerns with the fine powders. The shielding gas like-argon can be used to avoid oxidation due to the reactivity of the molten pool. The use of a sealing chamber makes the process limited for producing small to medium-sized components only. Powder-based AM processes offer comparatively low deposition rates, and the cost of powders is also higher than the wires [2, 3].

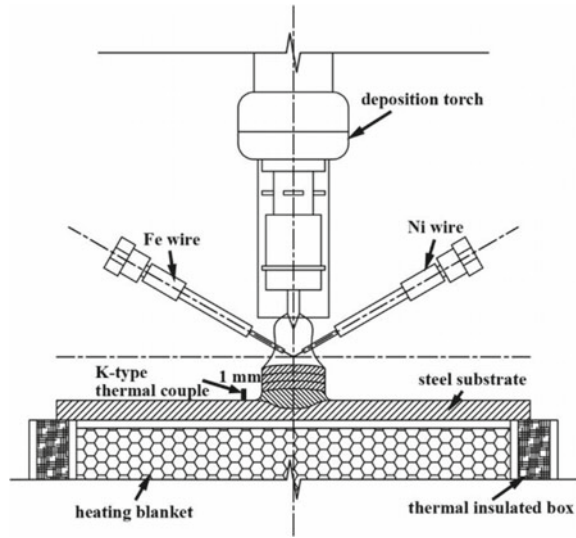
1.2 Wire Arc Additive Manufacturing (WAAM)

In current decades, WAAM has been considered a promising and hopeful technology to fabricate metallic parts due to its exceptional advantages like high deposition rate, lower capital investment, high material utilization, and non-hazardous, unlike powder-based processes. An electric arc is used as a heat source, and the welding process used may be Gas Metal Arc welding (GMAW), Gas Tungsten Arc Welding (GTAW), or Plasma Arc Welding (PAW). GMAW-based process gives a high deposition rate, but the surface finish of the sidewall is very poor. These limitations can be overcome by adapting Cold Metal Transfer (CMT) with the conventional GMAW. CMT process reduces spatters and produces good quality parts with considerably less heat input. On the other hand, GTAW-based WAAM offers better process stability and quality of the deposit. The PAW-based process provides advantages of good quality deposit with the least distortion and highest deposition rate. However, the process requires very high energy and high capital investment [2–4].

2 Twin Wire Arc Additive Manufacturing

The T-WAAM technique employs two feed wires of any metal depending on the user requirement. Thus, the technique offers an opportunity for in-situ alloying, and alloy

Fig. 1 Schematic diagram of T-WAAM process [11]



of required composition can be synthesized [5, 6]. However, some metals are difficult to form into wire because of specific properties like brittleness [7, 8]. T-WAAM rectifies this problem, and parts of desired alloy composition can be fabricated using two different wires as a feedstock and feed rate to achieve particular composition. Figure 1 represents the typical schematic diagram of the T-WAAM setup. Each wire feeder is provided with separate power sources to manipulate process parameters independently. Thus, the different alloy compositions can be obtained in-situ [5, 9].

Many researchers deployed this technique to fabricate functionally graded materials, intermetallic alloys, and some multi-element alloys [6–24].

3 Fabrication of FGMs Using T-WAAM

Marinelli et al. [10] successfully deployed T-WAAM to deposit two gradient structures of tantalum (Ta) to molybdenum (Mo) to tungsten (W) with Ta plate used as a substrate for deposition. Microstructure studies revealed that the large columnar grains in the Mo-rich regions whereas fine equiaxed grains in the W-rich regions, as shown in Fig. 2. EDS mapping confirmed cracks at the Ta–Mo interface. This might be attributed to the development of intense stress fields at the interface and dissimilar thermal expansion coefficients of Ta and Mo. However, no cracks were observed at the Mo–W interface due to the similarity of coefficient of thermal expansion. The microhardness studies revealed a constant average hardness of $\sim 95\text{HV}$ along the entire Ta substrate thickness. Ta and Mo interface showed a constant increase in hardness to 550–600 HV. Further, in Mo-rich regions, hardness decreased continuously and then became stable $\sim 240\text{HV}$. In the FGS among Mo and W, a gradual increase in

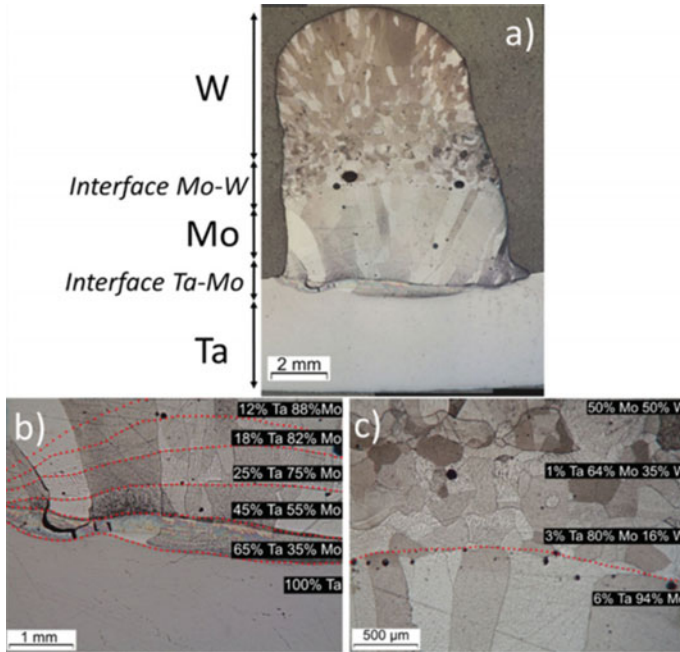
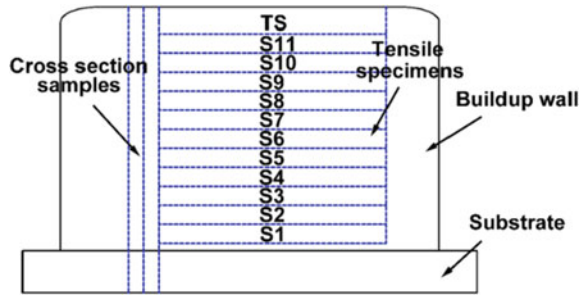


Fig. 2 Microstructure of **a** the entire functionally graded structure, **b** Ta to Mo interface, **c** Mo to W interface [10]

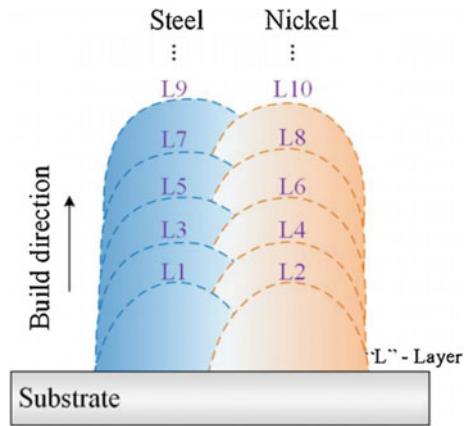
the hardness was noticed and the top W-rich region possessed ~ 400 HV. Variation in hardness with composition was observed in the FGS with Mo and W, which was attributed to formed non-homogeneous alloy due to the different melting points of two metals and rapid heating and solidification [10]. Shen et al. [9] built graded structure of Fe-FeAl using T-WAAM technique with the graded composition of 0% Al to 50% Al from bottom to top. The macrostructural studies revealed Fe-rich large columnar grains and equiaxed grains at the bottom and top, respectively. Whereas the very top region contained Al-rich lump-shaped grains. XRD studies showed Al_2O_3 peaks in sample S2 and samples S9–S11, suggesting a deficiency of inert gas while processing. Variation in microhardness was observed along build direction due to phase variations resulting from the compositional gradients. The obvious increase in hardness was observed with increasing Al-content. Figure 3 shows the extraction positions of the tensile samples. Except samples S10 and S11, all the fracture surfaces showed brittle transgranular lamellar fractures with stream patterns and without any dimples. Sample S10 and S11 contained Al content $>50\%$, and thus no stream patterns were observed. Sample S5 with 36.1 at. % Al possessed the highest strength and elongation [9]. Shen et al. [11] used T-WAAM to build Fe-Fe₃Ni structure, followed by homogenization heat treatment. The as-built sample comprised of columnar and cellular crystal in the top and bottom region, respectively. In high Ni-region and low Ni-region, the homogenization heat treatment prompted columnar

Fig. 3 Extraction positions for samples [9]



grain growth and transformation of the initial cellular structures into fully bainite and austenite. The phase volume fractions were in-situ extracted using neutron diffraction. The results revealed that the as-built FGM was composed of both the fcc-Fe₃Ni and bcc- α -Fe. Further, bcc- α dissolved into Fe₃Ni matrix after homogenization heat treatment leading to lower hardness. Microhardness studies revealed a considerable increase in hardness at the interface of a layer with 20% Ni and steel substrate owing to the generation of bcc- α -Fe. With further increase in Ni content to 25%, hardness gradually decreases due to the formation of the fcc-Fe₃Ni phase. Afterward, hardness decreases significantly above 25 at. % Ni due to attainment of binary alloy in Fe₃Ni phase region and α -Fe got vanished. However, hardness continuously increased with a further increase in Ni content. It was observed that hardness decreased after the heat treatment, and it supported the results obtained from the phase volume fraction studies [11]. Wang et al. [12] successfully deployed T-WAAM technique deposit functionally graded structure with the gradient composition ranging from 0 at. % Al to 50 at. % Al. The variation in phase composition observed increased Al content from the bottom to the top of the deposit. Microstructure and XRD studies confirmed sequential changes in structure from bottom to top as- α - β duplex \rightarrow α - α 2 lamellar \rightarrow large α 2 grains \rightarrow α 2- γ duplex lamellar \rightarrow γ -interdendrities. This trend was ascribed to the collective consequence of different phase fractions and grain size. Microhardness and tensile strength increased to peak value with increasing Al content and then decreased. The single α 2 phase region with 30–33% Al content possessed the highest tensile strength and hardness. However, the top region showed maximum ductility owing to the γ -prominent region [12]. As shown in Fig. 4, the steel-nickel interweaving structure was fabricated by Wu et al. [13] using the T-WAAM process. Cellular ferrite grains and dendritic grains were observed on the steel and nickel side, respectively. The interface showed that interlocking microstructure resulted in a strong bond. This favored improvement in mechanical properties at the interface. The interface strength improved due to solid solution strengthening due to Fe and Ni's intermixing. The research paved the way for fabricating structures of dissimilar materials as per functional requirements [13].

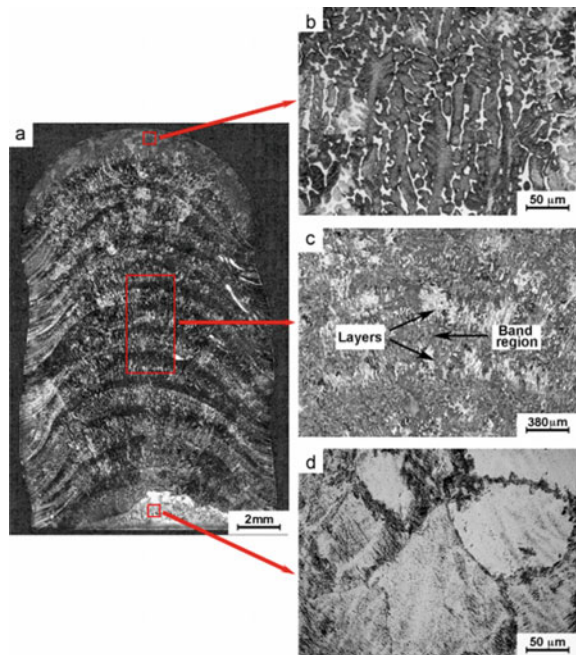
Fig. 4 Deposition path patterns [13]



4 Fabrication of Intermetallic Using T-WAAM

Ma et al. [14] built a full density γ -TiAl alloy structure using GTAW-based T-WAAM technique with Ti and Al wires as a feedstock. Microstructure, phase analysis, and mechanical properties were investigated as a function of the location in building direction. Figure 5 shows the morphology and microstructure of the cross-section along the building direction. Microstructure studies revealed that columnar grains were grown

Fig. 5 Morphology and microstructure in cross-section ($X-Z$ plane) of γ -TiAl structure fabricated using T-WAAM: **a** morphology, **b** microstructure of the top region, **c** layer bands morphology and **d** Microstructure of the near-substrate region [14]



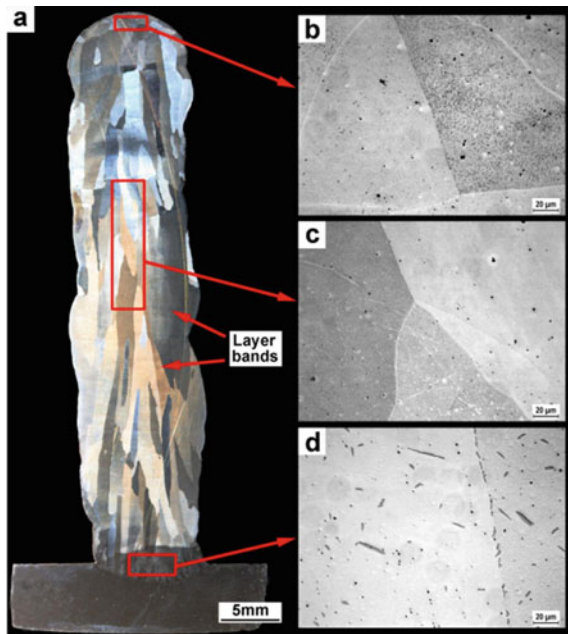
epitaxially across layer bands in the build direction. The XRD analysis confirmed that the microstructure of the deposit from bottom to top comprised sequential arrangement of large α_2 grains \rightarrow lamellar colonies of α_2 and γ lamellae + interdendritic γ phase \rightarrow fine dendrites + interdendritic γ phase. Microhardness studies confirmed the homogenous distribution of hardness along deposition direction. Conversely, there were variations in the hardness and strength along building direction attributed to varied Al. The near-substrate region possessed a significant increase in hardness but lower UTS and YS on account of low Al content and a higher fraction of α_2 as a result of relatively faster cooling than that of middle and upper layers. Also, it could be ascribed to very fine γ lamellae [14]. The same group of researchers (Ma et al., [15]) extended their research to investigate the dependence of phase transformation of T-WAAM built parts on the inter-pass temperature. XRD analysis confirmed that due to a lower cooling rate, α_2 phase fraction decreased with an increase in inter-pass temperature from 100 to 400 °C. However, no considerable changes were observed in microstructure and composition as well. The microhardness value decreased with increasing inter-pass temperature as α_2 phase fraction is also reducing. However, there was no significant decrease in the α_2 phase with an increase in temperature beyond 400 °C and so to microhardness. Thus, the study suggested that 400 °C is the most appropriate inter-pass temperature [15]. Another group of researchers [[7] fabricated TiAl structures of three different compositions using GTAW-based T-WAAM technique. XRD studies confirmed that Ti-35% Al and Ti-55% Al compositions composed of single α_2 -Ti₃Al and γ -TiAl phases, respectively. The γ -TiAl and α_2 -Ti₃Al phases were obtained with Ti-45% Al composition. Microstructure studies revealed that Ti-35% Al, Ti-45% Al, and Ti-55% Al composition composed of irregular crystal structure with grains containing α_2 plates inside grains, equiaxed crystals containing lamellar α_2 + γ laths and γ dendritic structures, respectively. Microhardness studies showed that hardness dropped considerably with high Al content. The hardness, UTS, and YS showed an increasing trend with increasing volume fraction of the α_2 phase. Nevertheless, dual α_2 + γ phases possessed higher ductility than that of single phases [7]. Another group of researchers [16] carried this work to dynamically in-situ introduce ternary elements in the TiAl intermetallic and successfully produced structures of Ti₄₅Al_{2.2}V using T-WAAM. The wires of Ti₆Al₄V and Al were used as a feedstock for deposition. XRD phase analysis confirmed that the addition of V from Ti₆Al₄V did not influence the flat features of lamellar interface and phase composition of resulting TiAl alloy. The top region of as-built Ti₄₅Al_{2.2}V alloy composed of lamellar colonies and γ -interdendrities. The band zone and layer zone, respectively, composed of fully laminar structure and equiaxed α_2 with grain boundaries containing precipitated fine laths. The introduction of the V caused interdendritic γ phase to disappear and thereby increase in tensile properties of the alloy. This phenomenon was called as V-ductilization effect. The colony size increased, and the average lamellar spacing increased with increasing heat treatment temperature. Samples exhibited lower strength and higher ductility at lower heat treatment temperatures while considerably lower strengths and ductility at higher temperatures [16]. Cai et al. [6] also performed experiments on the deposition of TiAl alloy using Al wire and Ti₆Al₄V wire feedstock. The Al wire and Ti-6Al-4V wire was fed in

TOP-TIG welding mode and conventional mode, respectively, to melt both the wires synchronously over a wide range of wire feed rates, regardless of the dissimilar melting points of both wires.

The XRD studies confirmed the increase in volume fraction of the α_2 phase from top to bottom due to different cooling rates. Microstructure studies revealed that bottom and top region composed of lamellar α_2/γ structures and coarse equiaxed α_2 grains with γ laths, respectively. In contrast, the middle zone was composed of a stripping zone with equiaxed α_2 grains with γ laths and strips-intermediate zone with fully lamellar structure. The top section possessed greater hardness than the bottom section. The hardness increased with increasing Al content, and samples with 50% Al content showed the highest compressive strength [6]. Full density Al-30% iron aluminide was deposited by Shen et al. [17] using GTAW-based T-WAAM process, and location dependence of microstructure, phases and mechanical properties were studied. All the peaks in XRD analysis performed on different regions in the deposition direction showed Fe_3Al phase.

However, the dilution affected region in the bottom section contained few acicular $\text{Fe}_3\text{AlC}_{0.5}$ precipitates. The bottom dilution affected section of the structure contained few acicular $\text{Fe}_3\text{AlC}_{0.5}$ precipitates. Figure 6 shows the macrostructural morphology and microstructure of the deposit along the building direction. Microstructure studies showed the large columnar grains grown epitaxially with smaller columnar grains in the bottom region than in the middle region, while equiaxed grains at the top region. The EDS results confirmed homogenous content of

Fig. 6 a Morphology of Al-30% iron aluminide along X-Z plane. Microstructure of: b top region, c middle region, d dilution affected zone [17]



Al above the dilution affected zone. However, distinct cooling rates of the deposited layers caused some hardness variations along building direction. Also, the tensile properties were anisotropic because of the epitaxially grown large columnar grains. The study suggested the need for grain refinement to obtain better mechanical properties [17]. Dong et al. [18] deployed GTAW-based T-WAAM to fabricate Cu-rich Cu-Al alloy and performed homogenization heat treatments to obtain homogenous material properties. Very high thermal conductivity of Cu caused difficulty in opening the melt pool in the first few layers. Thus, macrostructure studies revealed comparatively less effective wall thickness in the first few layers. The top, middle, and bottom regions' microstructure consisted of equiaxed grains, large epitaxial columnar grains, and relatively small columnar grains, respectively. The XRD characterization confirmed CuAl_2 and Cu_9Al_4 intermetallic phases in the as-fabricated deposit. After homogenization annealing treatment, Cu_9Al_4 was eliminated, and the content of CuAl_2 weakened significantly. With the decrease in precipitate phases, both the strength and ductility showed a gradual increase without considerable changes in microstructure. The significant improvement in hardness, strength and ductility of Cu-Al alloy was observed due to homogenization annealing treatment. Improvement in mechanical properties was observed to be more evident at higher annealing temperatures [18]. Wang et al. [19] explored the feasibility of the T-WAAM technique to fabricate Ni-rich NiTi alloy and investigated the microstructure and mechanical properties along deposition direction. The deposited alloy possessed different anisotropic microstructure from the bottom to the top region with increased content of Ni_4Ti_3 and decreased content of Ni_3Ti . Finally resulted in decreased transformation temperature, increased tensile strength with reduction in ductility and increased hardness. Ni_3Ti_3 precipitates induced considerable strengthening and increased brittleness with reduced ductility than Ni_4Ti_3 and Ni_3Ti_2 precipitates [19].

5 Fabrication of Multicomponent Alloys Using T-WAAM

Feng et al. [20] fabricated Cr-Ni stainless steel wall structures using single and two wire Plasma Arc Welding (PAW) based WAAM technique and investigated the microstructure and mechanical properties. The deposition rate with two wires was observed to be 1.06 times more than with a single wire. T-WAAM processed samples composed of completely grown equiaxed ferrite grains at the interface region of two successive layers, while single-WAAM processed samples composed of incomplete grown equiaxed ferrite grains in the same region. Grain size in both cases was reduced with increasing deposition speeds. Attributable to finish developed equiaxed and refined grains, T-WAAM processed samples had higher strength and extension than single-WAAM processed samples. The study postulated that the PAW-based WAAM process could provide higher processing speeds, fine microstructure, and superior mechanical properties [20]. Martensitic stainless steel 17-4 PH was fabricated using pulse GMAW-based T-WAAM by Filomoneo et al. [21] to investigate the feasibility

of the process to obtain a high production rate. The non-homogeneous grain orientation with progressive increase in grain size was observed with the increase in the heat input. Nevertheless, the restricted grain growth to an extreme extent was ascribed to combined result of high heat input and slow cooling. A complete martensitic phase with negligible austenite and without any metallic inclusion was observed in the as-built sample. The strength and hardness decreased as the grain size increased with increased wire feed rate [21]. Gu et al. [22] deployed a tandem arrangement of twin wire feedstock to fabricate Al-Cu-Mg using GMAW-based WAAM with the objective of crack minimization. Microstructure studies revealed inter-granular solidification macro and micro-cracks in the deposit. The contour maps of cracking susceptibility indicated that the alloy with Cu and Mg content in the respective range of 4.2–6.3% and 0.8–1.5% was less susceptible to cracking. The contour maps of thermal effects revealed that heat input increased with higher wire feed rate but deposited lower density alloys with a considerable increase in solidification cracks. The study suggested that cracking susceptibility decreases with an increase in hardness because refined grains and significant second phases in hard materials suppress the cracks [22]. The microstructure of Al-3.6Cu-2.2 Mg and Al-4Cu-1.8 Mg alloys are composed of non-dendritic grains at inner layers and equiaxed dendritic grains at the interlayer region. The microstructure of Al-4.4Cu-1.5 Mg alloys is composed of equiaxed dendritic grains and dendritic grains with a few non-dendritic grains at the interlayer region. The hardness increased with an increase in Cu/Mg ratio. Mechanical properties are near isotropic with a tiny difference of values in deposition and build direction. With higher Cu and lower Mg content, the strength showed an increasing trend and elongation showed decreasing trend. The fractography of fracture surfaces revealed typical brittle fractures [23]. Ke et al. [24] fabricated SS 308L using the T-WAAM process and compared microstructure and mechanical properties of deposit with that structure fabricated using single-WAAM. T-WAAM exhibited more refined grains than the middle region of the deposit was composed of cellular grains, whereas that of single-WAAM was composed of columnar grains. The XRD analysis showed that both the structures were composed of ferrite and austenite phases; however, the former contained higher ferrite content due to higher cooling rates.

Also, T-WAAM built structures possessed high hardness and strength than single-WAAM built structures. However, the fracture surfaces showed typical ductile fracture [24]. Ti and Al wires as a feedstock with Nb foil for in-situ alloying were used with the T-WAAM technique by Yang et al. [8] to fabricate Ti-6Al-7Nb biomedical alloy. The deposited alloy was composed of a basketweave Widmanstätten structure without any microvoids and cracks. The HAZ band was composed of nano-scaled Nb-rich lath β -phase, which was more refined than non-HAZ due to thermal rapid heating and cooling cycles. Although properties were observed to be anisotropic, there was a significant increase in Tensile strength and elongation by adding Nb in the Ti-6Al alloy. It was attributed to the grain refinement and the formation of nano-scaled Nb-rich lath β -phase. Fracture surfaces of Ti-6Al-7Nb alloy showed ductile-like fracture with dimples. However, TiAl alloy exhibited brittle fracture [8].

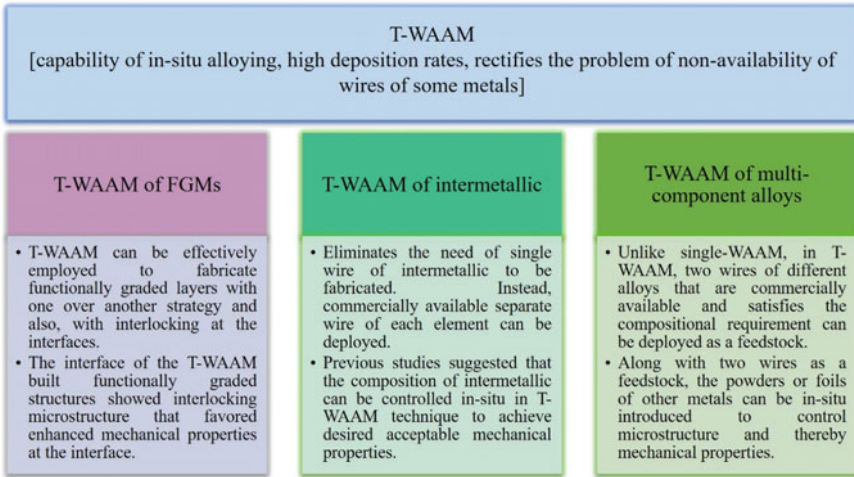


Fig. 7 Summary of the T-WAAM processing of different materials

6 Summary

Figure 7 presents the brief summary of advantages of T-WAAM along with T-WAAM processing of different materials.

7 Conclusions and Future Scope

T-WAAM is a versatile manufacturing technique that can fulfill the increasing demands of the manufacturing sector concerning processing advanced metals and alloys, processing time, and economic considerations. This technique offers an opportunity to fabricate any complex geometry of almost any material with theoretically no dimension limits at a lower overall cost and higher production rate than other subtractive and powder-based AM techniques. Previous studies showed that this technique successfully fabricates functionally graded materials, intermetallic alloys, and multi-component alloys with desired mechanical properties. However, some properties like corrosion resistance, strength at elevated temperature should be studied according to the need of the application. Further, studies may be carried out to design the process to obtain a good surface finish to reduce post-processing. Also, the numerical simulation could prove helpful to reduce the time and material wastage in process parameter optimization and predict the possible results like microstructure and residual stresses.

References

1. Paul CP, Jinoop AN, Bindra KS (2018) Metal additive manufacturing using lasers. In: Singh R, Paulo Davim J (eds) Additive manufacturing: applications and innovations. CRC Press, Florida, pp 37–94
2. Derekar KS (2018) A review of wire arc additive manufacturing and advances in wire arc additive manufacturing of aluminium. *Mater Sci Technol* 34(8):895–916. <https://doi.org/10.1080/02670836.2018.1455012>
3. Jin W, Zhang C, Jin S, Tian Y, Wellmann D, Liu W (2020) Wire arc additive manufacturing of stainless steels: a review. *Appl Sci* 10(5):1563. <https://doi.org/10.3390/app10051563>
4. Cunningham CR, Flynn JM, Shokrani A, Dhokia V, Newman ST (2018) Invited review article: strategies and processes for high quality wire arc additive manufacturing. *Addit Manuf* 22:672–686. <https://doi.org/10.1016/j.addma.2018.06.020>
5. Somashekara MA, Suryakumar S (2017) Studies on dissimilar twin-wire weld-deposition for additive manufacturing applications. *Trans Indian Inst Met* 70(8):2123–2135. <https://doi.org/10.1007/s12666-016>
6. Cai X, Dong B, Yin X, Lin S, Fan C, Yang C (2020) Wire arc additive manufacturing of titanium aluminide alloys using two-wire TOP-TIG welding: processing, microstructures, and mechanical properties. *Addit Manuf* 35:101344. <https://doi.org/10.1016/j.addma.2020.101344>
7. Wang J, Pan Z, Cuiuri D, Li H (2019) Phase constituent control and correlated properties of titanium aluminide intermetallic alloys through dual-wire arc additive manufacturing. *Mater Lett* 242:111–114. <https://doi.org/10.1016/j.matlet.2019.01.112>
8. Yang Z, Liu Q, Wang Y, Ma Z, Liu Y (2020) Fabrication of multi-element alloys by twin wire arc additive manufacturing combined with in-situ alloying. *Mater Res Lett* 8(12):477–482. <https://doi.org/10.1080/21663831.2020.1809543>
9. Shen C, Pan Z, Cuiuri D, Roberts J, Li H (2016) Fabrication of Fe-FeAl functionally graded material using the wire-arc additive manufacturing process. *Metall Mater Trans B* 47(1):763–772. <https://doi.org/10.1007/s11663-015-0509-5>
10. Marinelli G, Martina F, Lewtas H, Hancock D, Ganguly S, Williams S (2019) Functionally graded structures of refractory metals by wire arc additive manufacturing. *Sci Technol Weld Joining* 24(5):495–503. <https://doi.org/10.1080/13621718.2019.1586162>
11. Shen C, Hua X, Reid M, Liss KD, Mou G, Pan Z, Li H (2020) Thermal induced phase evolution of Fe-Fe₃Ni functionally graded material fabricated using the wire-arc additive manufacturing process: an in-situ neutron diffraction study. *J Alloy Compd* 826:154097. <https://doi.org/10.1016/j.jallcom.2020.154097>
12. Wang J, Pan Z, Ma Y, Lu Y, Shen C, Cuiuri D, Li H (2018) Characterization of wire arc additively manufactured titanium aluminide functionally graded material: microstructure, mechanical properties and oxidation behaviour. *Mater Sci Eng A* 734:110–119. <https://doi.org/10.1016/j.msea.2018.07.097>
13. Wu B, Qiu Z, Pan Z, Carpenter K, Wang T, Ding D, Li H (2020) Enhanced interface strength in steel-nickel bimetallic component fabricated using wire arc additive manufacturing with interweaving deposition strategy. *J Mater Sci Technol* 52:226–234. <https://doi.org/10.1016/j.jmst.2020.04.019>
14. Ma Y, Cuiuri D, Shen C, Li H, Pan Z (2015) Effect of interpass temperature on in-situ alloying and additive manufacturing of titanium aluminides using gas tungsten arc welding. *Addit Manuf* 8:71–77. <https://doi.org/10.1016/j.addma.2015.08.001>
15. Ma Y, Cuiuri D, Hoye N, Li H, Pan Z (2015) The effect of location on the microstructure and mechanical properties of titanium aluminides produced by additive layer manufacturing using in-situ alloying and gas tungsten arc welding. *Mater Sci Eng A* 631:230–240. <https://doi.org/10.1016/j.msea.2015.02.051>
16. Wang J, Pan Z, Wei L, He S, Cuiuri D, Li H (2019) Introduction of ternary alloying element in wire arc additive manufacturing of titanium aluminide intermetallic. *Addit Manuf* 27:236–245. <https://doi.org/10.1016/j.addma.2019.03.014>

17. Shen C, Pan Z, Cuiuri D, Dong B, Li H (2016) In-depth study of the mechanical properties for Fe3Al based iron aluminide fabricated using the wire-arc additive manufacturing process. *Mater Sci Eng A* 669:118–126. <https://doi.org/10.1007/s11663-015-0509-5>
18. Dong B, Pan Z, Shen C, Ma Y, Li H (2017) Fabrication of copper-rich Cu-Al alloy using the wire-arc additive manufacturing process. *Metall Mater Trans B* 48(6):3143–3151. <https://doi.org/10.1007/s11663-017-1071-0>
19. Wang J, Pan Z, Yang G, Han J, Chen X, Li H (2019) Location dependence of microstructure, phase transformation temperature and mechanical properties on Ni-rich NiTi alloy fabricated by wire arc additive manufacturing. *Mater Sci Eng A* 749:218–222. <https://doi.org/10.1016/j.msea.2019.02.029>
20. Feng Y, Zhan B, He J, Wang K (2018) The double-wire feed and plasma arc additive manufacturing process for deposition in Cr-Ni stainless steel. *J Mater Process Technol* 259:206–215. <https://doi.org/10.1016/j.jmatprotec.2018.04.040>
21. Martina F, Ding J, Williams S, Caballero A, Pardal G, Quintino L (2019) Tandem metal inert gas process for high productivity wire arc additive manufacturing in stainless steel. *Addit Manuf* 25:545–550. <https://doi.org/10.1016/j.addma.2018.11.022>
22. Gu J, Bai J, Ding J, Williams S, Wang L, Liu K (2018) Design and cracking susceptibility of additively manufactured Al-Cu-Mg alloys with tandem wires and pulsed arc. *J Mater Process Technol* 262:210–220. <https://doi.org/10.1016/j.jmatprotec.2018.06.030>
23. Qi Z, Cong B, Qi B, Sun H, Zhao G, Ding J (2018) Microstructure and mechanical properties of double-wire+ arc additively manufactured Al-Cu-Mg alloys. *J Mater Process Technol* 255:347–353. <https://doi.org/10.1016/j.jmatprotec.2017.12.019>
24. Ke Y, Xiong J (2020) Microstructure and mechanical properties of double-wire feed GTA additive manufactured 308L stainless steel. *Rapid Prototyping J* 5–2546. <https://doi.org/10.1108/RPJ-09-2019-0238>

A State of the Art Review of Additively Manufactured Auxetic Structures



Shailendra Kumar, Swapnil Vyavahare, Soham Teraiya,
Jyothi Kootikuppala, and Harika Bogala

Abstract Auxetic structures are negative Poisson's ratio (NPR) structures that expand under tension and contract under compression. These structures are extensively used in various applications including automotive, biomedical, sports, aerospace, and architecture. These structures have unique mechanical characteristics such as high shear modulus, energy absorption, indentation resistance, and vibro-acoustic properties. In the previous few years, these structures have been widely manufactured by various additive manufacturing (AM) technologies. In this paper, state of the art review on mechanical properties of auxetic structures namely re-entrant, chiral, arrowhead, star-shaped, missing rib, and rigid rotating structures are discussed. Further, based on the critical review the scope of future research work in this domain is identified.

Keywords Auxetic structures · Negative Poisson's ratio · Re-entrant · Chiral · Arrowhead · Missing rib · Rigid rotating structures

1 Introduction

Cellular structures are extensively employed in number of applications because of their high strength to weight ratio and high energy absorption [1]. Recently, these structures are developed with the negative Poisson's ratio (NPR). These structures are also called an auxetic structure which is based on Greek word, 'auxetikos' (means 'that may be increased') [2]. Auxetic structures are extensively utilized in various applications including aerospace, sports, biomedical, automotive, and architecture. These structures expand under tensions and contract under compression [3]. These structures have unique properties such as good shear resistance, high energy absorption, indentation resistance, and vibro-acoustic properties. Various auxetic structures are re-entrant, chiral, arrowhead, star-shaped, square grid, lozenge grid, and rigid rotating structures [4]. Figure 1 shows the geometrical arrangement of the unit

S. Kumar (✉) · S. Vyavahare · S. Teraiya · J. Kootikuppala · H. Bogala
Department of Mechanical Engineering, S.V. National Institute of Technology, Surat, India

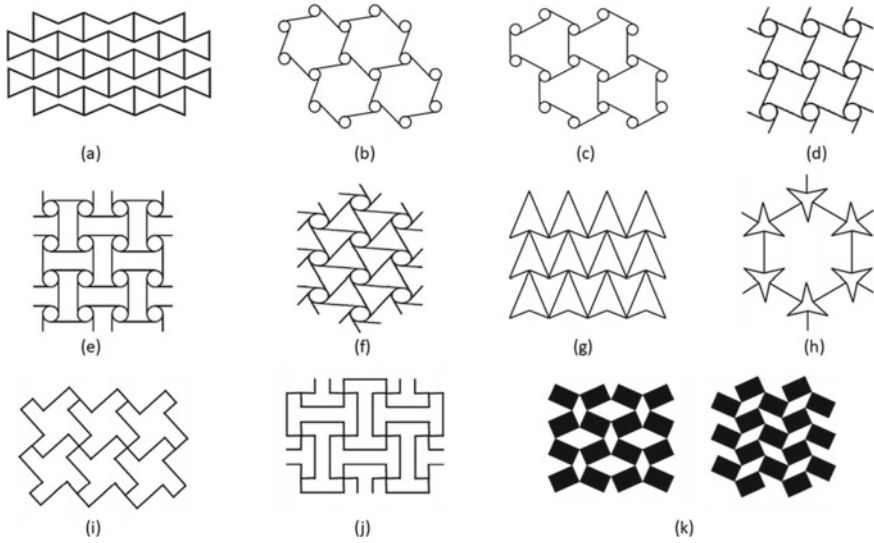


Fig. 1 Auxetic structures **a** re-entrant, **b** trichiral, **c** anti-trichiral, **d** tetrachiral, **e** anti-tetrachiral, **f** hexachiral, **g** arrowhead, **h** star-shape, **i** Lozenge grid, **j** square grid, **k** rigid rotating structures

cell of each auxetic structure. In the next section, a detailed discussion on mechanical characteristics and applications of each type of auxetic structure is discussed. Manufacturing of these structures using traditional manufacturing such as casting, welding, etc. is complicated, time consuming, and expensive. Therefore, additive manufacturing (AM) techniques emerge as convenient alternatives for manufacturing of these structures. According to American Society for Testing and Materials (ASTM) F2792-12a standard, Standard Terminology for AM Technologies, AM techniques are classified according to seven categories depending upon material, machine, and process involved in the fabrication route. These are binder jetting (BJ), directed energy deposition (DED), material extrusion (ME), material jetting (MJ), powder bed fusion (PBF), vat polymerization (VP), and sheet lamination (SL). The present paper describes the literature review related to additively manufactured auxetic structures.

2 Literature Review

Various researchers have investigated mechanical characteristics of auxetic structures using analytical, numerical, and experimental methods. Review of available literature related to mechanical properties of various auxetic structures is discussed as under.

2.1 Re-entrant Structures

A re-entrant auxetic structure is developed from the hexagonal honeycombs by changing the internal angles of the unit cell from positive to negative values. A typical re-entrant structure is shown in Fig. 1a. These structures are highly anisotropic and have higher energy absorption capacity than hexagonal honeycomb structures [5]. Doyoyo and Hu [6] studied plastic failure of auxetic lattice under uniaxial and transverse load. It is found that shear failure is due to global plastic yielding. Joshi et al. [7] conducted an experimental investigation on polycarbonate hexagonal and auxetic honeycombs fabricated using ME technique for in-plane shear loading. It is found that cell wall thickness changes failure mechanism from buckling to fracture by crack propagation as its value increases. Scarpa and Tomlin [8] determined transverse shear modulus of in-plane negative Poisson's ratio (NPR) honeycombs numerically and suggested formula for its prediction. It is found that transverse shear modulus depends on relative density and gauge thickness ratio. Ju et al. [9] explored elastic limits of various cell geometries under shear loading. They concluded that due to high bending length for shear loading, re-entrant design should be preferred over triangular or square design. Ju et al. [10] developed formulations of strain energy for shear deformation of hexagonal and re-entrant structures. Bending of vertical cell wall (h) is recognized as primary deformation mode. Zhang and Yang [11] found that when cell angle and wall thickness remain constant, strength of the structure is scale-dependent. Zorzetto et al. [12] investigated the effect of single re-entrant inclusion (SRI) into a non-re-entrant lattice using analytical and experimental methods. They manufactured specimens using polyjet printing technique of ME. They found that SRI exhibited NPR effect even when it is accompanied by regular non-re-entrant joints. Ingrole et al. [13] established a hybrid structure as amalgamation of hexagonal and re-entrant structure; which has improved mechanical characteristics than original structures. Wagner et al. [14] proposed an active auxetic structure manufactured by polyjet printing of ME technique. These structures were printed using verowhite material and subjected to 3-point bending test. These structures were able to recover their original shape when temperature stimulus is applied. Li and Wang [15] examined bending behaviour of re-entrant honeycomb topology made of verowhite polymer by polyjet AM which showed excellent energy absorption capability compared to truss and conventional honeycomb. Wang et al. [16] proved that load–displacement curve of cylindrical NPR jounce bumper is smoother and better than traditional jounce bumper. Wang et al. [17] used homogenization technique for analysis of structure in principle directions. They validated analytical and numerical results with experimental results by fabricating structures using ME technique. They found that re-entrant structure achieves stiffer properties in Y -direction for less value of angle of re-entrance. Xue et al. [18] fabricated aluminum based auxetic structures using combined manufacturing technique involving VP and investment casting; and studied their compressive behaviour. Zhang et al. [19] studied post yield behaviour of auxetic honeycomb structures. Specimens were made from stainless

steel and polymer using PBF and VP respectively. Chen et al. [20] studied compressive properties of hierarchical structures fabricated by polyjet printing of ME. They improved stiffness and energy absorption capacity by applying thermal treatment to the structure. Yang et al. [21] observed that shock absorbing properties of ME fabricated re-entrant structure is better than hexagonal honeycomb. Sarvestani et al. [22] performed flexural test on ME fabricated structures made of different core topologies such as auxetic, isomax, octet and cubic. Fang et al. [23] conducted optimization to design degraded NPR honeycomb structure for minimum weight, maximum strength and maximum stiffness. Cheng et al. [24] investigated shear stiffness of auxetic foams. They found that auxetic foams have shear stiffness value 7% lower than traditional specimens, but greater shear stress at large deformation and smoother strain hardening response compared to beam with traditional thinner core. Araújo et al. [25] evaluated effect of core geometry on flexural properties of cellular structure. Raeisi et al. [26] compared mechanical properties of ME fabricated regular, auxetic and hybrid structures by keeping their relative densities constant. They designed a hybrid structure by combining hexagonal and re-entrant structures and concluded that it exhibited best performance than original structures. Xu et al. [27] developed association of mechanical characteristics along various loading directions of AuxHex structures fabricated using selective laser sintering (SLS) technique of PBF. They found that specific energy absorption (SEA) was increased by 38% using steady failure of cells. Li et al. [28] investigated compressive properties of VP fabricated structures. They found that auxetic lattices had improved characteristics than non-auxetic lattices. Alomarah et al. [29] compared compressive properties of re-entrant chiral (RCA) and re-entrant structure fabricated using multi jet fusion technique of PBF and found that RCA structure outperformed re-entrant structure.

2.2 Chiral Structures

Chiral structures as shown in Fig. 1b–f are formed by the cylinders with tangentially connected ligaments. Various types of chiral structures are trichiral, anti-trichiral, tetrachiral, anti-tetrachiral and hexachiral. Chiral structures are widely used in various applications such as wing boxes, biomedical stents, shape memory structures, tyres and other energy absorbing structures [30]. Lakes [31] reported that the eight elastic constants are derived from the constrained compression testing of the chiral structures. Bornengo et al. [32] performed numerical investigation on in-plane mechanical properties of ME fabricated hexachiral structures used in wing boxes. They found that the structure can provide adaptive capabilities to the wing according to the change in the distribution of pressure over the airfoil. Spadoni et al. [33] performed analytical and numerical investigations to measure the buckling strength of hexachiral structure. They reported that the geometric parameters significantly influence the flat-wise performance of these structures. Spadoni et al. [34] investigated the dynamic properties of hexachiral structure used in airfoil using simulation and experimental methods. They reported that chiral truss assemblies are

useful in the airfoil because of design flexibility and multifunctionality. Scarpa et al. [35] studied the tensile properties of shape memory alloy based hexachiral structure fabricated using ME and VP techniques. They found that these structures are suitable for deployable antennas. Hassan et al. [36] developed a novel smart cellular solid by combining chiral structure with shape memory alloys. They found that such structures can be used in deployable antenna reflectors and packaging. Bettini et al. [37] used composite hexachiral structure for airfoil morphing. Miller et al. [38] used ASTM 393 and ASTM 365 standards for experimental testing of PBF manufactured tetrachiral and hexachiral structures. They reported that the chirality significantly influences the buckling strength of the structures. Abramovitch et al. [39] developed prototype for structural health monitoring using tetrachiral core structures. They found that the prototype can efficiently detect the signals from the mechanical loading and serve the purpose of carrying load. Chen et al. [40] studied influence of dimensional parameters on NPR and modulus of ME fabricated anti-tetrachiral structures. They observed that ligament length is influential for mechanical characteristics of the structure. Bacigalupo et al. [41] used analytical and numerical approaches for static and dynamic characterization of composite anti-tetrachiral structures. They observed that ratio of ligament length and node radius significantly influences the NPR and Young's modulus. Airoidi et al. [42] used numerical and experimental approaches to develop hexachiral structures for morphing. They concluded that the developed morphing components used in aircraft can be fabricated using chiral structural topology. Kepeng et al. [43] performed a shape and size optimization to keep the NPR and modulus constant at large deformation of hexachiral structure. They found that elastic properties depend on the dimensional factors of the structure. Mizzi et al. [44] studied the influence of translational disorder on auxeticity and modulus of the structure. They found that modulus increases with increase in the disorder of the structure. Huang et al. [45] demonstrated the relationships among the auxeticity, elasticity and geometrical factors of MJ fabricated anti-tetrachiral structure. The proposed design rules for the structure in order to achieve desired mechanical properties. Jiang and Li [46] studied the novel hybrid chiral structure manufactured using MJ by combining the chiral structures in hierarchical order. They observed that the geometrical parameters significantly influence mechanical properties of the structure. Ebrahimi et al. [47] developed the three-dimensional (3D) MJ fabricated anti-tetrachiral structure with planer topology using oblique load-bearing ligaments. They observed that the structure displays auxeticity in both in-plane and out-of-plane directions due to oblique ligament connections between the planes. Günaydin et al. [48] investigated the dynamics behaviour of aluminum anti-tetrachiral honeycomb structure. They reported that higher relative density increases reaction forces within the structure. Li et al. [49] investigated the characteristics of the hybrid tetra and anti-tetrachiral structure using strain energy analysis. They found that the mechanical properties are influenced by ratio of ligament length-node radius and thickness-node radius. Wu et al. [50] proposed the novel hierarchical anti-tetrachiral meta-structure having NPR. They found that the in-plane mechanical properties of the structure greatly enhanced due to combination of geometrical parameters and hierarchical levels. Wu et al. [51] compared the compressive properties of various chiral and

anti-chiral structures fabricated by SLS technique of PBF. Fu et al. [52] developed VP manufactured three-dimensional tetrachiral structure with oblique planar ligament connection. They found that the change in the direction of the oblique ligament causes the development of new 3D structure with positive Poisson's ratio in two directions and NPR in another direction. Farrugia et al. [53] investigated the influence of geometric parameters on Poisson's ratio and elastic modulus of VP manufactured anti-tetrachiral structures. They found that ligament length and thickness significantly influence the NPR in all directions of the structure. Ma et al. [54] investigated the mechanical properties of PBF manufactured cylindrical tetrachiral and anti-tetrachiral structures. They concluded that chiral cylindrical cells showed best mechanical properties among all structures. Novak et al. [55] conducted experimental investigation on mechanical properties of PBF fabricated Ti-6Al-4V chiral auxetic structures produced by selective electron beam method under blast loading. They found that SEA increases with decrease in thickness of the plates. Ruan et al. [56] developed hybrid intravascular stents using combination of anti-trichiral and re-entrant structures manufactured using VP technique. They observed that the deformation pattern and mechanical properties vary with the change in the arrangement of circular nodes. Su et al. [57] studied the effect of geometric factors on characteristics of trichiral structures. They found that as the ratio of ligament length to node radius increases, modulus decreases and Poisson's ratio increases. Attard et al. [58] designed a new class of hexachiral named starchiral by replacing the nodes with short intersecting ligaments. They further assessed the mechanical properties of the structure made by material extrusion and found that Poisson's ratio of the structures depends on relative thickness of the ligament. Lu et al. [59] proposed the concept of effective Poisson's ratio for tetrachiral structures. They found that shearing and stretching of the ligaments in the structure causes variation in the calculation of Poisson's ratio. Novak et al. [60] investigated the influence of strain rate on strength and SEA of the PBF fabricated chiral structure. The experimental and computational results suggested that the plateau stress increases with increase in loading rate.

2.3 Arrowhead Structures

Arrowhead structure was first introduced by Larsen et al. [61] by topological optimization of re-entrant auxetic structures (Fig. 1g). Qiao et al. [62] generated a model to study the effect of the design parameters of the structure on compressive strength under quasi-static, high velocity and low velocity loadings. They found that SEA proportionally varies with the square of impact velocity. Lim et al. [63] designed a 3D double arrowhead (DAH) linkage auxetic structure by intersecting 2D structures. They further developed theoretical models to study the NPR in all directions by varying the geometry of the structures. Wang et al. [64] developed jounce bumper using DAH structures using numerical and experimental investigation. They fabricated bumper using VP technique using polyamide as stuffer and polyurethane as tendon material. They reported that the novel jounce bumper can efficiently perform

its function under various loading conditions. Ma et al. [65] investigated the damping properties of VP fabricated DAH auxetic structure. They showed that required stiffness and damping capacity can be achieved by optimal inclined angles and stacking layer thickness. Zhao et al. [66] have derived an empirical formula to characterize different modes of deformations for critical impact velocity. They confirmed that dynamic crushing strength depends only on relative density and impact velocity. Gao et al. [67] studied the effect of geometrical parameters on elastic modulus and NPR of a 3D DAH using FEA. It is found that the angles of the DAH significantly influence the mechanical performance of the structure. Wang et al. [68] proved that the structure becomes stiffer with increase in compressive strain. Gao et al. [69] investigated the effect of geometrical factors on crushing strength of the 3D DAH structure. They observed that crashworthiness of DAH structure is significantly sensitive to angles and thickness of beams. Gao et al. [70] analyzed dynamic properties namely crushing strength and SEA of structure by FEA. They observed an increase in crushing strength with increase in relative density. Chen et al. [71] designed a large scale 2D DAH metallic structure to characterize energy dissipation and deformation mechanisms under air blasts. They showed that the responses mainly depend on web thickness of cells and number of layers in a structure rather than angles and length of the structure. Gu et al. [72] studied the effect of geometrical parameters of ME fabricated structures on strength under various loading conditions. They observed that short beam angle significantly influences the auxetic effect compared to long beam angle.

2.4 *Star-Shaped Structures*

Star-shaped structures are also developed by topological optimization of standard re-entrant structures. Various types of star-shaped structures are shown in Fig. 1h. Grima et al. [73] assessed star-shaped auxetic structures using a force-field based method. They showed that 4 and 6-noded structures have better auxeticity than 3-noded star-shaped structures. Carton and Ganter [74] presented a novel method of procedural modelling and 2D object patterned ME fabrication for functionally graded star-shaped, re-entrant and DAH structures. They proved the capability of the AM technologies to print and test various auxetic structures with design flexibility. Logakannan et al. [75] performed compression testing of a PBF manufactured re-entrant diamond auxetic structure. They concluded that large diamond angle and small length ratio are required for high compression strength. Further, they found that SEA of the proposed structure is better than re-entrant structure. Wei et al. [76] investigated in-plane compressive properties of PBF fabricated tristar-shaped honeycombs. They observed that inclined angle significantly influences the elastic modulus and NPR of the structure. Xu et al. [77] proposed novel 2D star-shaped ME fabricated structures using numerical and experimental approaches. They showed that proposed structures are able to effectively regulate NPR and Young's modulus while ensuring lightweight requirement.

2.5 *Missing Rib Structures*

The structures in which the auxeticity is generated by removing some of the ribs periodically are known as missing rib auxetic structures as shown in Fig. 1i, j. There are mainly two types of missing rib structures namely, square grid and lozenge grid. Elipe et al. [78] developed novel structure by modifying the geometry of the lozenge grid structures. They found that the change in geometry of basic structure influences the final mechanical properties of the structure. Bhullar et al. [79] developed lozenge grid structure that can be used to treat esophageal cancer and prevent the difficulty in swallowing. Magalhaes et al. [80] developed lozenge grid structural design using textile fibres reinforced braided structures. Lim et al. [81] proposed the analogies between the deformation pattern of the tetrachiral and lozenge grid structures. In both structures, the ligaments and nodes rotate in same direction under compression loading. Wu et al. [82] developed biomedical stents using hierarchical missing rib structures. They observed that stents can maintain axial stability along with radial expansion. Bartlomiej [83] conducted analytical investigation to study the dynamic properties of lozenge grid structures. They concluded that the optimized structures have better damping characteristics. Wang et al. [84] investigated Poisson's ratio and Young's modulus of the lozenge grid structures. Attard et al. [85] suggested that the deformation pattern of the missing rib lozenge grid is similar to tetrachiral structure based on their geometrical arrangements. Smith et al. [86] found that square grid structures can achieve and maintain NPR even at higher strain values. Liu et al. [87] developed novel auxetic structure by removing some ligaments from each cell of the square and lozenge grid structures. They concluded that the novel structure can attain better auxeticity compared to the conventional structures. Lim et al. [81] established the analogies between square grid and anti-tetrachiral structures. They observed that both the structures synchronously deform under compression and tensile loading. Farrugia et al. [88] conducted investigation on Poisson's ratio of ME manufactured square grid structures. They found that higher auxeticity can be attained by varying the geometrical parameters of the structure. Meena et al. [89] observed that the geometrical parameters significantly influence the auxeticity of the square grid structures. Further, they found that the synclastic behaviour of the structures is suitable for use in aircraft nose cones. Zhang et al. [90] developed and analyzed hybrid auxetic structures by combining the square grid and re-entrant structures using numerical and experimental methods. They fabricated these structures using ME technique. They reported that the in-plane mechanical properties of the structure are significantly influenced by cell wall aspect ratio, re-entrant angle and ratio of internal-external rib thickness.

2.6 Rigid Rotating Structures

The rigid rotating structures as shown in Fig. 1k include rigid squares, which rotate under loading. Square, triangles, rectangles, rhombus and parallelograms are used for developing the rigid structures with NPR. Grima et al. [91] considered rotating rectangles model which consists of rigid rectangles hinged along their corners. From the analytical modelling, it is found that NPR depends upon the variation in geometry of the structure. Grima et al. [92] studied rectangular rigid structures with different arrangements formed by leaving the empty spaces between the rectangles as rhombi and parallelogram. They found that aspect ratio and angles between the rectangles significantly influences the NPR of the structure along with direction of loading. Attard and Grima [93] proposed a novel 3D rotating structure by connecting the edges/sides of cuboids. They observed that when the cuboids are connected along the edges these structures have auxetic behaviour simultaneously in its three major planes. Rotating structures are used in making the base of the fabric and forming a continuous network of void spaces thereby providing the best fit to the customer [94]. Because of its diverse auxetic effects rotating rigid structures are used in the form of an oesophageal stent. The rotational movement of the arrangement causes lateral expansion of the stent and serves the biomedical application. In this study, the moulds of titanium alloy are prepared using electron beam melting of PBF technique and a master mould of ABS material is prepared using ME technique [95]. By altering the size, shape, linkage and geometry of the rotating rigid structures various sizes of pores are obtained. Due to this wide range of pore sizes, they can be used for filtration purposes [96]. Slann et al. [97] made use of rectangular and rhombic centre symmetric perforations on a plate to obtain rotating rigid structure effect. They fabricated structures using ABS-M30 by ME technique. The tensile tests showed that strains are significant at failure for lower parametric configurations and higher aspect ratios. Rotating rigid structures are most often employed in the soles of the footwear. When the sole of the shoe hits the ground, tensile force is applied so that rotation of these hinged polygons takes place. This results in expansion of material in both longitudinal and lateral direction providing upward as well as forward movement during running [98]. Li et al. [99] developed programmable hierarchical rigid rotating auxetic structures using numerical and experimental investigation under compression loading. They reported that the mechanical properties of the structure can be controlled by constraining the angle of the developed structure.

3 Comments on Literature Review

From the extensive literature review of auxetic structures, it is observed that these structures are widely used in biomedical, airfoil, smart materials and automotive parts. Initially, the auxetic structures were produced by traditional manufacturing techniques such as glueing, perforating and forming. Because of design flexibility of

AM, nowadays all the auxetic structures are easily fabricated and tested with experimentation. Due to development in the AM technologies, the design constraints have vanished and novel structures with application specific tailored properties can be developed. Summary of the major research work done and scope of further work in the field of auxetic structures is given in Table 1. Majority of the researcher has investigated the mechanical characteristics of the NPR structures using numerical and analytical modelling. The main focus of researchers is investigation of geometrical parameters on Young's modulus and Poisson's ratio. Further, the experimental investigation on other mechanical properties such as strength and SEA is very limited. Moreover, the orientation of the structures significantly influences the characteristics of the structures. So, the auxetic structures can further be experimentally investigated under in-plane and out-of-plane orientations at various strain rates.

4 Conclusion

In this article, research papers published from 1987 to 2021 in the domain of additively manufactured auxetic structures have been reviewed. The literature review is sorted into six sections depending upon class of auxetic structure, i.e. re-entrant, chiral, arrowhead, star-shaped, missing rib, and rigid rotating structures. After the review, major work is summarized in tabular form to identify scope of future scope. Considerable study has been done for evaluation of mechanical properties of AM fabricated re-entrant and chiral structures. Also, majority of researchers have investigated the mechanical properties of hexachiral and tetrachiral structures, but there is limited study on trichiral, anti-trichiral and anti-tetrachiral auxetic structures. It is found that there is limited experimental investigation on arrowhead, star-shaped, missing rib, and rigid rotating structures. Further research in the area of mechanical property evaluation of these structures is required by varying the geometrical parameters, orientations, and strain rates under various loading conditions namely shear, flexural, compression and impact. Due to recent developments in AM technologies, there is a huge scope of future research in the application domains of various types of auxetic structures in automotive, aerospace, sports and biomedical sectors.

Table 1 Major investigations in the area of characterization of auxetic structures

Researcher (s) and year	Research work done	Scope of further work
Wang et al. [16]	Analysis of uniaxial compression performance of NPR jounce bumper made of double arrowhead polyamide structures	The performance of the jounce bumper can further be compared using other auxetic structures
Wang et al. [17]	Theoretically and numerically assessed the novel structure that was designed by combination of re-entrant and star-shaped honeycomb	Structure can be produced by various AM processes and tested for further improvement
Xue et al. [18]	Study of compressive behaviour aluminum re-entrant structures made by stereolithography patterns	Structure should be further investigated using other loading conditions
Alomora et al. [29]	Performed numerical and experimental study on a novel RCA structure	Other mechanical properties, such as shear, flexural or torsional strength can be assessed
Xu et al. [77]	Proposed and investigated the novel 2D star-shaped honeycombs numerically and experimentally for Poisson's ratio and Young's modulus	Further, strength and SEA can be experimentally investigated under shear and flexural loading
Wang et al. [84]	Used numerical and computational approaches to study Young's modulus and Poisson's ratio of the lozenge grid structures	Experimental investigation is required under other loading conditions
Farrugia et al. [88]	Conducted numerical investigation on auxeticity of square grid structures	Further experimental investigation is required
Slann et al. [97]	Performed tensile testing on newly developed perforated rigid rotating structures	Structure can be further experimentally tested under other loading conditions such as compression, shear and flexural
Alderson et al. [100]	Investigated the mechanical properties of chiral structures using analytical, numerical and experimental approaches	Further, shear modulus can be studied using experimental approach
Gatt et al. [101]	Performed numerical and theoretical investigation on mechanical properties of chiral structures	Results of the study can be validated using experimental investigation

References

1. Gibson L, Ashby M (1997) Cellular solids: structure and properties (Cambridge Solid State Science Series). Cambridge University Press, Cambridge. 101017/CBO9781139878326
2. Evans K (1991) Auxetic polymers: a new range of materials. *Endeavour* 15:170–174. 101016/0160–9327 (91)90123-S
3. Lakes R (1987) Foam structures with a negative Poisson's ratio. *Science* 235:1038–1041
4. Kolken HM, Zadpoor AA (2017) Auxetic mechanical metamaterials. *RSC Adv* 7(9):5111–5129
5. Smith FC, Scarpa FL, Burriesci G (2002) Simultaneous optimization of the electromagnetic and mechanical properties of honeycomb materials. In: SPIE's 9th annual international symposium on smart structures and materials, International Society for Optics and Photonics 582–591s
6. Doyoyo M, Hu JW (2006) Plastic failure analysis of an auxetic foam or inverted strut lattice under longitudinal and shear loads. *J Mech Phys Solids* 54(7):1479–1492
7. Joshi S, Ju J, Berglund L, Rusly R, Summers JD and DesJardins JD (2010) January experimental damage characterization of hexagonal honeycombs subjected to in-plane shear loading. In: ASME 2010 international design engineering technical conferences and computers and information in engineering conference. American Society of Mechanical Engineers Digital Collection, pp 35–41
8. Scarpa F, Tomlin PJ (2000) On the transverse shear modulus of negative Poisson's ratio honeycomb structures. *Fatigue Fract Eng Mater Struct* 23(8):717–720
9. Ju J, Summers JD (2011) Compliant hexagonal periodic lattice structures having both high shear strength and high shear strain. *Mater Des* 32(2):512–524
10. Ju J, Summers JD (2011) Hyperelastic constitutive modeling of hexagonal honeycombs subjected to in-plane shear loading. *J Eng Mater Technol* 133(1):011005
11. Zhang X, Yang D (2016) Mechanical properties of auxetic cellular material consisting of re-entrant hexagonal honeycombs. *Materials* 9(11):900
12. Zorzetto L, Ruffoni D (2017) Re-entrant inclusions in cellular solids: from defects to reinforcements. *Compos Struct* 176:195–204
13. Ingrole A, Hao A, Liang R (2017) Design and modeling of auxetic and hybrid honeycomb structures for in-plane property enhancement. *Mater Des* 117:72–83
14. Wagner M, Chen T, Shea K (2017) Large shape transforming 4D auxetic structures. *3D Printing Additive Manuf* 4(3):133–142
15. Li T, Wang L (2017) Bending behavior of sandwich composite structures with tunable 3D-printed core materials. *Compos Struct* 175:46–57
16. Wang Y, Zhao W, Zhou G, Gao Q, Wang C (2018) Suspension mechanical performance and vehicle ride comfort applying a novel jounce bumper based on negative Poisson's ratio structure. *Adv Eng Softw* 122:1–12
17. Wang T, Wang L, Ma Z, Hulbert GM (2018) Elastic analysis of auxetic cellular structure consisting of re-entrant hexagonal cells using a strain-based expansion homogenization method. *Mater Des* 160:284–293
18. Xue Y, Wang X, Wang W, Zhong X, Han F (2018) Compressive property of Al-based auxetic lattice structures fabricated by 3-D printing combined with investment casting. *Mater Sci Eng A* 722:255–262
19. Zhang J, Lu G, Wang Z, Ruan D, Alomarah A, Durandet Y (2018) Large deformation of an auxetic structure in tension: experiments and finite element analysis. *Compos Struct* 184:92–101
20. Chen Y, Li T, Jia Z, Scarpa F, Yao CW, Wang L (2018) 3D printed hierarchical honeycombs with shape integrity under large compressive deformations. *Mater Des* 137:226–234
21. Yang C, Vora HD, Chang Y (2018) Behavior of auxetic structures under compression and impact forces. *Smart Mater Struct* 27(2) p025012

22. Sarvestani HY, Akbarzadeh AH, Niknam H, Hermenean K (2018) 3D printed architected polymeric sandwich panels: energy absorption and structural performance. *Compos Struct* 200:886–909
23. Fang G, Yuan S, Meng S, Liang J (2018) Graded negative Poisson's ratio honeycomb structure design and application. *J Sandwich Struct Mater* 21(7):2527–2547
24. Cheng L, Zhang P, Biyikli E, Bai J, Robbins J, To A (2017) Efficient design optimization of variable-density cellular structures for additive manufacturing: theory and experimental validation. *Rapid Prototyping J* 23(4):660–677
25. Araújo H, Leite M, Ribeiro AR, Deus AM, Reis L, Vaz MF (2019) The effect of geometry on the flexural properties of cellular core structures. *Proc Inst Mech Eng Part L J Mater Des Appl* 233(3):338–347
26. Raesi S, Tapkir P, Ansari F, Tovar A (2019) Design of a hybrid honeycomb unit cell with enhanced in-plane mechanical properties (No 2019-01-0710) SAE technical paper
27. Xu M, Xu Z, Zhang Z, Lei H, Bai Y, Fang D (2019) Mechanical properties and energy absorption capability of AuxHex structure under in-plane compression: theoretical and experimental studies. *Int J Mech Sci* 159:43–57
28. Li X, Wang Q, Yang Z, Lu Z (2019) Novel auxetic structures with enhanced mechanical properties. *Extreme Mech Lett* 27:59–65
29. Alomarah A, Masood SH, Sbarski I, Faisal B, Gao Z, Ruan D (2019) Compressive properties of 3D printed auxetic structures: experimental and numerical studies. *Virtual Phys Prototyping* 15(1):1–21
30. Wu, W, Hu W, Qian G, Liao H, Xu X, Berto F (2019) Mechanical design and multifunctional applications of chiral mechanical metamaterials: a review. *Mater Des* 180:107950
31. Lakes R (2001) Elastic and viscoelastic behavior of chiral materials. *Int J Mech Sci* 43(7):579–1589
32. Bornengo D, Scarpa F, Remillat CDLR (2005) Evaluation of hexagonal chiral structure for morphing airfoil concept. *Proc Inst Mech Eng Part G J Aerosp Eng* 219(3):185–192
33. Spadoni A, Ruzzene M, Scarpa F (2005) Global and local linear buckling behavior of a chiral cellular structure. *Phys Status Solidi (b)* 242(3):695–709
34. Spadoni A, Ruzzene M, Scarpa F (2006) Dynamic response of chiral truss-core assemblies. *J Intell Mater Syst Struct* 17(11):941–952
35. Scarpa F, Hassan MR, Ruzzene M (2006) Modeling and testing of shape memory alloy chiral honeycomb structures. In: *Smart structures and materials 2006: active materials: behavior and mechanics*, vol 6170, p 61700W. International Society for Optics and Photonics
36. Hassan MR, Scarpa F, Ruzzene M, Mohammed NA (2008) Smart shape memory alloy chiral honeycomb. *Mater Sci Eng A* 481:654–657
37. Bettini P, Airoldi A, Sala G, Landro L, Ruzzene M, Spadoni A (2010) Composite chiral structures for morphing airfoils: numerical analyses and development of a manufacturing process. *Compos B Eng* 41(2):133–147
38. Miller W, Smith CW, Scarpa F, Evans KE (2010) Flatwise buckling optimization of hexachiral and tetrachiral honeycombs. *Compos Sci Technol* 70(7):1049–1056
39. Abramovitch H, Burgard M, Edery-Azulay L, Evans KE, Hoffmeister M, Miller W, Scarpa F, Smith CW, Tee KF (2010) Smart tetrachiral and hexachiral honeycomb: Sensing and impact detection. *Compos Sci Technol* 70(7):1072–1079. <https://doi.org/101016/j.compscitech200907017>
40. Chen YJ, Scarpa F, Liu YJ, Leng JS (2013) Elasticity of anti-tetrachiral anisotropic lattices. *Int J Solids Struct* 50(6):996–1004 <https://doi.org/101016/j.ijsolstr201212004>
41. Bacigalupo A, De Bellis ML (2015) Auxetic anti-tetrachiral materials: equivalent elastic properties and frequency band-gaps. *Compos Struct* 131:530–544
42. Airoldi A, Bettini P, Panichelli P, Oktem MF, Sala G (2015) Chiral topologies for composite morphing structures—part I: development of a chiral rib for deformable airfoils. *Phys Status Solidi (b)* 252(7):1435–1445
43. Kepeng Q, Ruoyao W, Jihong Z, Zhang W (2020) Optimization design of chiral hexagonal honeycombs with prescribed elastic properties under large deformation. *Chin J Aeronaut* 33(3):902–909

44. Mizzi L, Attard D, Gatt R, Pozniak AA, Wojciechowski KW, Grima JN (2015) Influence of translational disorder on the mechanical properties of hexachiral honeycomb systems. *Compos B Eng* 80:84–91
45. Huang HH, Wong BL, Chou YC (2016) Design and properties of 3D-printed chiral auxetic metamaterials by reconfigurable connections. *Phys Status Solidi (b)* 253(8):1557–1564
46. Jiang Y, Li Y (2018) Novel 3D-printed hybrid auxetic mechanical metamaterial with chirality-induced sequential cell opening mechanisms. *Adv Eng Mater* 20(2):1700744
47. Ebrahimi H, Mousanezhad D, Nayeb-Hashemi H, Norato J, Vaziri A (2018) 3D cellular metamaterials with planar anti-chiral topology. *Mater Des* 145:226–231
48. Günaydın K, Eren Z, Türkmen H S, Kazancı Z, Scarpa F (2017) Axial low velocity impact response of anisotropic anti-tetrachiral filling lattices. In: 7th international conference on mechanics and materials in design (No June: 1053-1060)
49. Li H, Ma Y, Wen W, Wu W, Lei H, Fang D (2017) In plane mechanical properties of tetrachiral and antitetrachiral hybrid metastructures. *J Appl Mech* 84(8)
50. Wu W, Tao Y, Xia Y, Chen J, Lei H, Sun L, Fang D (2017) Mechanical properties of hierarchical anti-tetrachiral metastructures. *Extreme Mech Lett* 16:18–32
51. Wu W, Song X, Liang J, Xia R, Qian G, Fang D (2018) Mechanical properties of anti-tetrachiral auxetic stents. *Compos Struct* 185:381–392
52. Fu M, Liu F, Hu L (2018) A novel category of 3D chiral material with negative Poisson's ratio. *Compos Sci Technol* 160:11–118
53. Farrugia PS, Gatt R, Grima JN (2019) A novel three-dimensional anti-tetrachiral honeycomb. *Phys Status Solidi (b)* 256(1):1800473
54. Ma C, Lei H, Liang J, Wu W, Wang T, Fang D (2018) Macroscopic mechanical response of chiral-type cylindrical metastructures under axial compression loading. *Mater Des* 158:198–212
55. Novak N, Starčević L, Vesenjāk M, Ren Z (2019) Blast response study of the sandwich composite panels with 3D chiral auxetic core. *Compos Struct* 210:167–178
56. Ruan XL, Li JJ, Song XK, Zhou HJ, Yuan WX, Wu WW, Xia R (2018) Mechanical design of antichiral-reentrant hybrid intravascular stent. *Int J Appl Mech* 10(10):1850105
57. Su XW, Zhu DM, Zheng C, Tomovic MM (2019) Mechanical properties of 65Mn chiral structure with three ligaments. *Acta Mech Sin* 35(1):88–98
58. Attard D, Farrugia PS, Gatt R, Grima JN (2020) Starchirals—a novel class of auxetic hierarchal structures. *Int J Mech Sci* 179:105631
59. Lu X, Tan VBC, Tay TE (2020) Auxeticity of monoclinic tetrachiral honeycombs. *Compos Struct* 241:112067
60. Novak N, Vesenjāk M, Tanaka S, Hokamoto K, Ren Z (2020) Compressive behaviour of chiral auxetic cellular structures at different strain rates. *Int J Impact Eng* 141:103566
61. Larsen UD, Sigmund O, Bouwstra S (1997) Design and fabrication of compliant micromechanisms and structures with negative Poisson's ratio. *Microelectromech Syst* 6(2):99–106
62. Qiao J, Chen CQ (2015) Analyses on the in-plane impact resistance of auxetic double arrowhead honeycombs. *J Appl Mech Trans ASME* 82(5):1–9. <https://doi.org/10.1115/1.403007>
63. Lim TC (2016) A 3D auxetic material based on intersecting double arrowheads. *Phys Status Solidi (b)* 253(7):1252–1260
64. Wang Y, Wang L, Ma ZD, Wang T (2017) Finite element analysis of a jounce bumper with negative Poisson's ratio structure. *Proc Inst Mech Eng Part C J Mech Eng Sci* 231(23):4374–4387. <https://doi.org/10.1177/0954406216665415>
65. Ma L, Chen YL, Yang JS, Wang XT, Ma GL, Schmidt R, Schröder KU (2018) Modal characteristics and damping enhancement of carbon fiber composite auxetic double-arrow corrugated sandwich panels. *Compos Struct* 203:539–550. <https://doi.org/10.1016/j.compstruct.2018.07.006>
66. Zhao X, Gao Q, Wang L, Yu Q, Ma Z D (2018) Dynamic crushing of double-arrowed auxetic structure under impact loading. *Mater Des* 160:527–537. <https://doi.org/10.1016/j.matdes.2018.09.041>

67. Gao Q, Wang L, Zhou Z, Ma ZD, Wang C, Wang Y (2018) Theoretical, numerical, and experimental analysis of three-dimensional double-V honeycomb. *Mater Des* 139:380–391. <https://doi.org/101016/jmatdes201711024>
68. Wang XT, Wang B, Wen ZH, Ma L (2018) Fabrication and mechanical properties of CFRP composite three-dimensional double arrowhead auxetic structures. *Compos Sci Technol* 164:92–102. <https://doi.org/101016/jcompscitech201805014>
69. Gao Q, Ge C, Zhuang W, Wang L, Ma Z (2019) Crashworthiness analysis of double-arrowed auxetic structure under axial impact loading. *Mater Des* 161:22–34. <https://doi.org/101016/jmatdes201811013>
70. Gao Q, Liao WH, Wang L (2020) On the low-velocity impact responses of auxetic double arrowed honeycomb. *Aerosp Sci Technol* 98:105698. <https://doi.org/101016/jast2020105698>
71. Chen G, Cheng Y (2020) Design and modelling of auxetic double arrowhead honeycomb core sandwich panels for performance improvement under air blast loading. *J Sandwich Struct Mater* 1099636220935563. <https://doi.org/101177/1099636220935563>
72. Gu L, Xu Q, Zheng D, Zou H, Liu Z, Du Z (2020) Analysis of the mechanical properties of double arrowhead auxetic metamaterials under tension. *Textile Res J* 90(21–22):2411–2427. <https://doi.org/101177/0040517520924850>
73. Grima JN, Gatt R, Alderson A, Evans KE (2005) On the potential of connected stars as auxetic systems. *Mol Simul* 31(13):925–935
74. Carton MA, Ganter M (2019) Fast and simple printing of graded auxetic structures solid. *Freeform fabrication symposium—an additive manufacturing conference*: 2270–2279
75. Logakannan KP, Ramachandran V, Rengaswamy J, Gao Z, Ruan D (2020) Quasi-static and dynamic compression behaviors of a novel auxetic structure. *Compos Struct* 254:112853
76. Wei L, Zhao X, Yu Q, Zhu G (2021) Quasi-static axial compressive properties and energy absorption of star-triangular auxetic honeycomb. *Compos Struct* 267:113850
77. Xu N, Liu HT, An MR, Wang L (2021) Novel 2D star-shaped honeycombs with enhanced effective Young's modulus and negative Poisson's ratio. *Extreme Mech Lett* 43:101164
78. Elipe JCA, Lantada AD (2012) Comparative study of auxetic geometries by means of computer-aided design and engineering. *Smart Mater Struct* 21(10):105004
79. Bhullar SK, Hewage AM, Alderson A, Alderson K, Jun MB (2013) Influence of negative Poisson's ratio on stent applications. *Adv Mater* 2(3):42–47. <https://doi.org/1011648/jam2013020314>
80. Magalhaes R, Subramani P, Lisner T, Rana S, Ghiassi B, Fangueiro R, Lourenco PB (2016) Development, characterization and analysis of auxetic structures from braided composites and study the influence of material and structural parameters. *Compos Part A Appl Sci Manuf* 87:86–97. <https://doi.org/101016/jcompositesa201604020>
81. Lim TC (2017) Analogies across auxetic models based on deformation mechanism. *Phys Status Solidi—Rapid Res Lett* 11(6). <https://doi.org/101002/pssr201600440>
82. Wu W, Song X, Liang J, Xia R, Qian G, Fang D (2018) Mechanical properties of anti-tetrachiral auxetic stents. *Compos Struct* 185:381–392. <https://doi.org/101016/jcompstruct201711048>
83. Bartłomiej B (2019) Dynamic properties of optimized auxetic structures. In: *International conference on multifunctional cellular materials—book of abstracts*: 64
84. Wang S, Li Z, Zhou KF, Tan QW (2019) The equivalent elastic parameters: a lozenge grid structure with negative Poisson's ratio. *IOP Conf Ser Mater Sci Eng* 629(1). <https://doi.org/101088/1757-899X/629/1/012037>
85. Attard D, Farrugia PS, Gatt R, Grima JN (2020) Starchirals—a novel class of auxetic hierarchical structures. *Int J Mech Sci* 179 <https://doi.org/101016/jijmecsci2020105631>
86. Smith CW, Grima JN, Evans KE (2000) Novel mechanism for generating auxetic behaviour in reticulated foams: Missing rib foam model. *Acta Mater* 48(17) 4349–4356. [https://doi.org/101016/S1359-6454\(00\)00269-X](https://doi.org/101016/S1359-6454(00)00269-X)
87. Liu Y, Hu H (2010) A review on auxetic structures and polymeric materials. *Sci Res Essays* 5(10):1052–1063
88. Farrugia PS, Gatt R, Zammit Lonardelli E, Grima JN, Evans KE (2019) Different deformation mechanisms leading to auxetic behavior exhibited by missing rib square grid structures. *Phys Status Solidi (B) Basic Res* 256(1):1–7. <https://doi.org/101002/pssb201800186>

89. Meena K, Calius EP, Singamneni S (2019) An enhanced square-grid structure for additive manufacturing and improved auxetic responses *Int J Mech Mater Des* 15(2) 413–426. <https://doi.org/101007/s10999-018-9423-8>
90. Zhang W, Zhao S, Scarpa F, Wang J, Sun R (2021) In-plane mechanical behavior of novel auxetic hybrid metamaterials. *Thin-Walled Struct* 159:107191. <https://doi.org/101016/jtws2020107191>
91. Grima JN, Alderson A, Evans KE (2004) Negative Poisson's ratios from rotating rectangles. *Comput Methods Sci Technol* 10(2):137–145. <https://doi.org/1012921/cmst20041002137-145>
92. Grima JN, Farrugia PS, Gatt R, Attard D (2008) On the auxetic properties of rotating rhombi and parallelograms: a preliminary investigation. *Phys Status Solidi (B) Basic Res* 245(3):521–529. <https://doi.org/101002/pssb200777705>
93. Attard D, Grima JN (2012) A three-dimensional rotating rigid units network exhibiting negative Poisson's ratios. *Phys Status Solidi (B) Basic Res* 249(7):1330–1338. <https://doi.org/101002/pssb201084223>
94. Blakely KS, Toronjo A (2013) Articles of apparel with auxetic fabric. US Patent Active 1,413,725, 0, 20
95. Ali MN, Busfield JJC, Rehman IU (2014) Auxetic oesophageal stents: structure and mechanical properties. *J Mater Sci Mater Med* 25(2) 527–553. <https://doi.org/101007/s10856-013-5067-2>
96. Attard D, Casha AR, Grima JN (2018) Filtration properties of auxetics with rotating rigid units. *Materials* 11(5) 21–26. <https://doi.org/103390/ma11050725>
97. Slann A, White W, Scarpa F, Boba K, Farrow I (2015) Cellular plates with auxetic rectangular perforations. *Phys Status Solidi (B) Basic Res* 252(7) 1533–1539. <https://doi.org/101002/pssb201451740>
98. Stojmanovski MLA, Formosa C, Grima JN, Chockalingam N, Gatt R, Gatt A (2017) On the use of auxetics in footwear: investigating the effect of padding and padding material on forefoot pressure in high heels. *Phys Status Solidi (b)* 254(12) 1700528
99. Li X, Fan R, Fan Z, Lu Y (2021) Programmable mechanical metamaterials based on hierarchical rotating structures. *Int J Solids Struct* 216:145–155
100. Alderson A, Alderson KL, Attard D, Evans KE, Gatt R, Grima JN, Miller W, Ravirala N, Smith CW, Zied K (2010) Elastic constants of 3-, 4- and 6-connected chiral and anti-chiral honeycombs subject to uniaxial in-plane loading. *Compos Sci Technol* 70(7):1042–1048
101. Gatt R, Attard D, Farrugia PS, Azzopardi KM, Mizzi L, Brincat JP, Grima JN (2013) A realistic generic model for anti-tetrachiral systems. *Phys Status Solidi (b)* 250(10):2012–2019

ABS-Fly Ash Composite Filaments for Fused Deposition Modeling



Abdullah Alduais, Feyza Kazanç, Gökür Bayram, and Sezer Özerinç

Abstract Fused deposition modeling (FDM) is one of the most widely used additive manufacturing techniques for the fabrication of polymeric parts. Earlier applications of FDM mostly utilized pure polymers such as polylactic acid (PLA) and acrylonitrile butadiene styrene (ABS). However, there has recently been an increasing demand for composite FDM filaments to obtain superior mechanical and physical properties. Fly ash (FA), a waste of coal power plants, is a promising alternative as a filler material for developing composite filaments. Due to the massive amounts of FA generated worldwide and associated environmental concerns, there has been an increasing trend in the utilization of FA particles in the polymer industry, providing a new route for FA recycling towards reducing FA's impact on the environment. However, there has been no study to date to investigate the same route for FDM use. In this study, we incorporated 2 wt% FA into an ABS matrix using a twin-screw extruder and produced composite filaments for FDM. The specimens printed with the composite filament were tested for their microstructural, mechanical, and thermal properties through X-ray diffraction (XRD), tensile testing, differential scanning calorimetry (DSC), and thermogravimetric analysis (TGA). Overall, the properties of the composite specimens are not drastically different from those made of pure ABS, except for the decrease in the elongation at break. The results demonstrate the feasibility of using ABS-FA composites in FDM as a coloring agent that contributes to the recycling of waste material at the same time.

A. Alduais · F. Kazanç · S. Özerinç (✉)

Department of Mechanical Engineering, Middle East Technical University, Ankara, Turkey
e-mail: ozeric@metu.edu.tr

A. Alduais

e-mail: abdullah.alduais@metu.edu.tr

F. Kazanç · S. Özerinç

Department of Micro and Nanotechnology, Middle East Technical University, Ankara, Turkey

G. Bayram

Department of Chemical Engineering, Middle East Technical University, Ankara, Turkey
e-mail: gbayram@metu.edu.tr

Keywords Fused deposition modeling · Acrylonitrile butadiene styrene · Polymer-matrix composites · Fly ash · Mechanical properties

1 Introduction

Fused deposition modeling (FDM) is a technology for the additive manufacturing of polymeric materials. FDM offers the versatility and capabilities of most other additive manufacturing techniques through lower equipment and operational costs. As a result, FDM has recently become a very popular technique for the manufacturing of prototypes and the production of load-bearing components in various applications.

Figure 1 shows a schematic view of the FDM process. FDM technique employs melting and extruding a polymeric filament through a nozzle. The nozzle moves in the XY plane in the desired trajectory set by the so-called G-code. When the deposition of a layer is completed, the stage incrementally moves down in z -direction, and the process repeats. The bonding between the adjacent lines of print is achieved by the partial melting of the existing lines upon contact with the incoming hot polymer. This quality of fusion is critical for obtaining a sufficient level of structural rigidity and mechanical strength in printed parts [1].

The most commonly used filament materials for FDM are polylactic acid (PLA) and acrylonitrile butadiene styrene (ABS). Among these two alternatives, ABS is an amorphous thermoplastic polymer that has been formed by condensation polymerization of three different materials, namely, acrylonitrile, butadiene, and styrene [2]. The main advantages of ABS for FDM use include its low melting temperature, desirable rheological characteristics for extrusion, and high mechanical strength. Table 1 lists a summary of the properties of the bulk ABS.

While earlier applications of FDM have been mostly limited to conventional polymers such as ABS and PLA, recently, there has been an increasing interest in developing composite filaments [4]. Similar to the polymer-matrix composites produced

Fig. 1 Schematic view of the fused deposition modeling (FDM) process

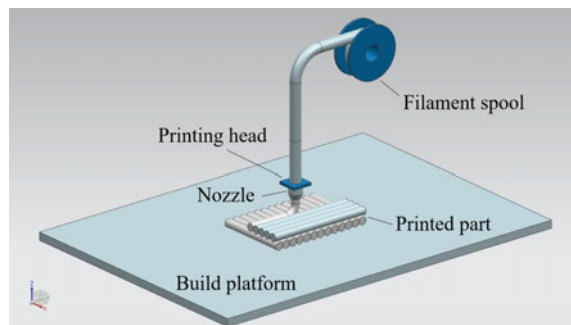


Table 1 Some physical and mechanical properties of bulk ABS [3]

Property	Unit	Value
Density	g/cm ³	1.03–1.09
Elastic modulus	GPa	1.9–2.7
Yield strength	MPa	35–58
Tensile strength	MPa	25–65
Elongation at break	%	8–20

by conventional routes, composite filaments aim at improving the mechanical, physical, or thermal properties of pure polymers. Most polymer-matrix composite filaments for FDM employ a harder secondary phase such as metallic or ceramic particles, carbon or glass fibers, and wood [4].

A promising route in this field is the utilization of waste material as the secondary phase. This approach has the primary advantages of reducing the cost of the filament and providing a new route for recycling the waste material. Among numerous alternatives, fly ash—a byproduct of pulverized coal-based power plants is promising. Fly ash (FA) is the lighter part of the coal ash, which is the non-combustible mineral-based component of the coal. More than 700 million tons of FA are generated every year [5], and utilization and recycling of this waste are still significant concerns. Only about 25% of the produced FA particles are utilized in cement factories, structural fills, and mining applications [6, 7]. The remaining FA is usually stored in dedicated landfills, causing damage to the environment [8, 9].

One classification of FA is based on the density and the size of its particles. Cenosphere-hollow particles, less than 1 g/cm³ in density, are used to produce ultra-light composites. In contrast, precipitator-spherical particles with a density between 2 and 2.5 g/cm³ [10] are usually used to improve the mechanical properties of polymer-FA composites, such as stiffness, wear resistance, and strength [11].

FA mainly consists of silicon dioxide (SiO₂), aluminum oxide (Al₂O₃), iron oxide (Fe₂O₃), and other alkali metal oxides. Table 2 summarizes some general characteristics of FA. It should be noted that the exact microstructure, chemical characteristics, and associated properties of the FA can vary considerably based on the origin and the type of coal as well as burning parameters [12].

There have been several previous studies on the employment of FA as an additive to polymers such as PLA, ABS, high-density polyethylene (HDPE), polypropylene (PP), and epoxy resin [15–19]. Table 3 shows an overview of the studies on FA-polymer composites and summarizes the key results. The addition of 5 μm-sized FA

Table 2 Some physical properties of fly ash (FA) [13, 14]

Property	Unit	Value
Particle size	μm	1–1000
Specific surface area	m ² /kg	170–1000
Color	–	Gray
Density	g/cm ³	1–2.5

Table 3 An overview of the literature on FA-polymer composites

Polymer matrix	FA size (μm)	FA loading (wt%)	Key results	References
ABS	9	10–50	Elastic modulus increased by 30%, and yield strength decreased by 17% at 30 wt% FA	[15]
PLA	5	10–50	Yield strength increased by 80% at 20 wt% FA. Using surface-modified FA particles increased the improvement to 160%	[16]
HDPE	106	10–40	Yield strength increased by 40% at 20 wt% for surface-modified FA & 10 wt% compatibilizer agent (HDPE-g-dibutyl maleate). Elongation at break decreased drastically in the meantime	[17]
PP	110	0–60	Elastic modulus improved by a factor of 3.7 at 60 wt% surface-modified FA loading. Yield strength decreased by 15%	[18]

particles to PLA at 20 wt% improved the yield and impact strengths of compression-molded specimens by 80 and 40%, respectively. When the FA was surface treated, these enhancements rose to 160 and 140%, respectively. Similarly, improvements in yield strength and elastic modulus reaching 40% was observed for injection-molded HDPE-FA composite specimens with FA loading in the range of 10–40 wt%.

On the other hand, these enhancements bring a significant reduction to elongation at break. This embrittlement increases with FA loading, and a weak interfacial adhesion between the particles and the polymer matrix also contributes to the problem.

Despite the extensive studies on polymer-based FA composites, there is no study to date that investigated the same for polymeric FDM filaments to our knowledge. This study, therefore, aims to investigate the route of utilizing ABS-FA composite filaments for FDM-based production of polymer-matrix composites. For this purpose, we produced ABS and ABS-FA composite filaments by twin-screw extrusion, and the specimens printed using these filaments were tested for their mechanical and thermal behavior.

2 Experimental Details

FA particles were obtained from a commercial coal power plant in Turkey. The FA was sieved by a 75 μm mesh to eliminate the larger particles. The sieved FA was dried in an oven at 70 °C for 3 h before mixing. Novodur HD M203FC ABS pellets were purchased from Ineos Styrolution (Germany) and were dried at 60 °C for 4 h before mixing.

A Thermoprism TSE-16-TC twin-screw extruder (L/D = 24) with a co-rotating screw configuration mixed ABS with the FA particles and produced the filaments with 2 wt% FA. The screw speed was 30 rpm, and the five-stage temperature profile from hopper to die was 190–230–230–235–240 °C, respectively. The extruded filament was cut into small pieces and extruded again to obtain better homogeneity and a more accurate filament diameter. Several measurements over the length of the filament yielded an average diameter of 1.75 ± 0.15 mm. The same conditions were used for extruding the pure ABS filament.

A Flashforge Creator Pro FDM-type 3D printer printed the dog bone-shaped tensile specimens according to ASTM D638-14 Standard Test Method for Tensile Properties of Plastics (see Fig. 2a). Table 4 summarizes the printing parameters that are common to all specimens of this study. For both pure ABS and ABS-FA composite, five identical specimens were printed and tested to verify the repeatability

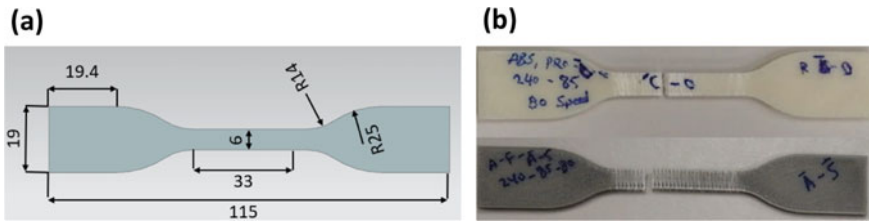


Fig. 2 a Dimensions of the tensile specimen in mm. The specimen thickness is 3.2 mm. b Photographs of tested specimens of the pure ABS (white) and the ABS-FA (grey)

Table 4 The printing parameters common to all specimens of this study

Parameter	Unit	Value
Layer thickness	mm	0.2
Printing speed	mm/s	80
Infill density	%	100
Raster pattern	–	Linear
Raster orientation	°	±45
Nozzle diameter	mm	0.4
Nozzle temperature	°C	240
Bed temperature	°C	80

of the results. A Zwick/Roell Z250 (Germany) universal testing machine performed the tensile tests at room temperature at a 20 mm/min displacement rate.

The distribution of FA in ABS and the fracture morphology of the tested specimens were investigated using an FEI QUANTA 400F field-emission SEM (Hillsboro, Oregon). The specimens were coated with 10 nm Au–Pd before imaging. X-ray Diffraction (XRD) analysis was performed using a Rigaku Ultima Diffractometer (Japan) over the 2θ range of 5° – 40° , at a scanning speed of $2^\circ/\text{min}$. Thermogravimetric analysis (TGA) was carried out using a Perkin Elmer Pyris I (MA, USA). The TGA measurements employed a heating rate of $10^\circ\text{C}/\text{min}$ in the range of 25 – 750°C under a pure nitrogen atmosphere. A TA Instruments DSC 250 (USA) was used to perform differential scanning calorimetry (DSC). The samples were heated at $10^\circ\text{C}/\text{min}$ in the range of 50 – 250°C under a pure nitrogen atmosphere.

3 Results and Discussion

Figure 3a shows the SEM image of the FA particles, and Fig. 3b illustrates the size distribution of the particles.

Figure 4 shows the XRD results of ABS and ABS-FA samples. Pure ABS has a broad peak at $2\theta = 19.5^\circ$. This peak and the shoulder at around 13.5° are in agreement with the previous measurements on ABS samples [20]. The large full width at half maximum is indicative of the amorphous structure of ABS. The ABS-FA sample shows an almost identical XRD spectrum, indicating that FA particles are well dispersed, and the low FA loading does not influence the amorphous character of the polymer. The data do not exhibit any reflections from the crystal phases of the FA either. We attribute this to the low volume fraction of FA and the detection limit of XRD measurements.

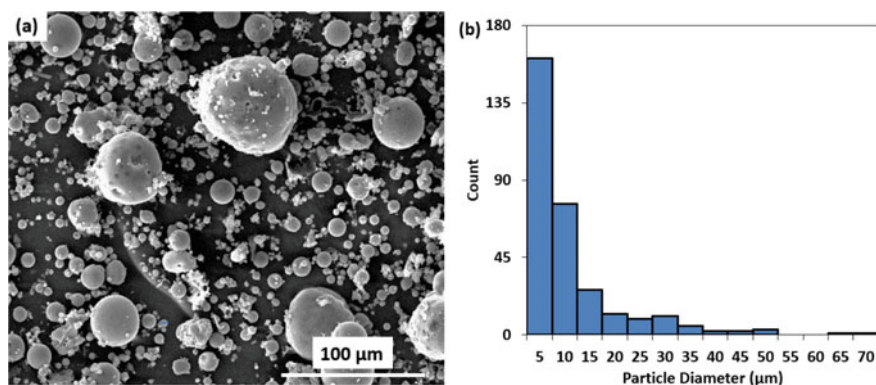


Fig. 3 a SEM image of the FA particles used in this study. b Particle size distribution

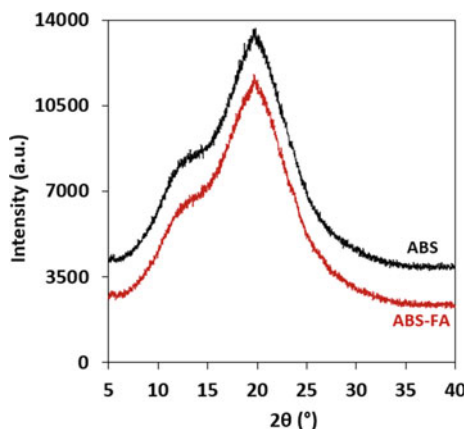


Fig. 4 XRD spectra of pure ABS and ABS-FA

Figure 5a shows the DSC results of ABS and ABS-FA specimens. For pure ABS, the results indicate a glass transition temperature (T_g) of 100 °C and a broad endothermic peak around 200 °C. These results are in agreement with the literature, reporting T_g values and broad endothermic transition values around 103–107 °C, and 210–260 °C, respectively [3, 21, 22]. Being an amorphous polymer, ABS does not exhibit a melting temperature. Therefore, the endotherm present at around 200 °C is indicative of the melting or transformation of some constituents of ABS [21].

The addition of FA particles has no significant effect on the DSC response, apart from a slight shift in the glass temperature to 104 °C. This shift might be due to the reduced chain mobility of the polymer, delaying the transition [21].

Figure 5b shows the TGA results of ABS-FA. The results for ABS and ABS-FA are virtually the same; therefore, the data of pure ABS is omitted for clarity. Pyrolysis takes place at ~500 °C with a loss of 99% of the weight. The derivative of the TGA

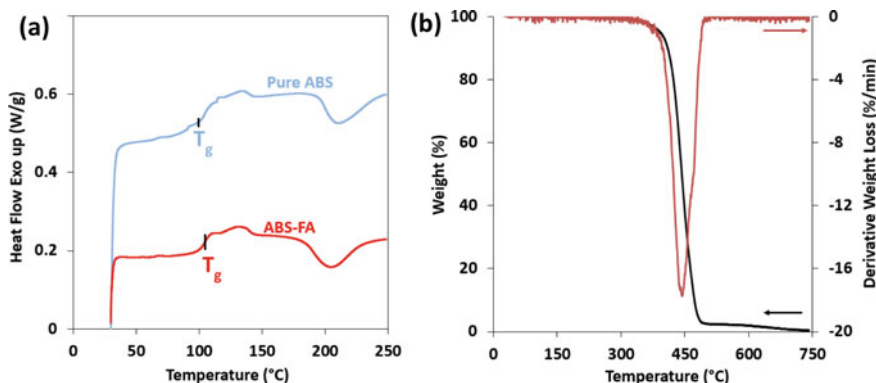


Fig. 5 a DSC data of ABS and ABS-FA. b TGA data of ABS-FA

Fig. 6 The stress–strain curves for the ABS (red) and ABS-FA (blue) specimens

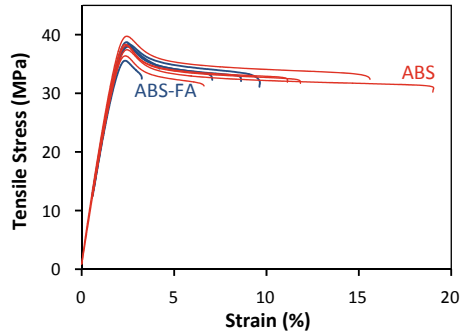


Table 5 Summary of the mechanical properties of ABS and ABS-FA specimens

Specimen	Elastic modulus (GPa)	Yield strength (MPa)	Yield strain (%)	Fracture strength (MPa)	Fracture strain (%)
ABS	2.0 ± 0.1	37.9 ± 1.1	2.4 ± 0.1	31.8 ± 0.8	12.8 ± 4.6
ABS-FA	2.0 ± 0.1	37.7 ± 1.2	2.4 ± 0.0	32.7 ± 0.8	6.5 ± 2.7

curve indicates an inflection point of 454 °C for both specimens. Previous studies showed that higher FA loadings could improve the thermal stability of the composite [15]. The almost identical results for ABS and ABS-FA in our case are attributed to the low volume fraction of the FA.

Figure 6 shows the stress–strain response of ABS and ABS-FA specimens. The results are consistent, demonstrating the repeatability of the printing and the testing procedures. Table 5 shows a summary of the results. ABS exhibits a fracture strength of about 32 MPa and an elastic modulus of 2 GPa.

Previous measurements on FDM-produced ABS specimens indicate strength and modulus values in a wide range of 26–53 MPa, and 1.5–2.2 GPa, respectively [1, 23, 24], showing that our findings are in general agreement with previous data. The wide range of values in the literature is due to the strong effect of process parameters such as nozzle temperature, raster orientation, and built orientation on the mechanical properties, a phenomenon also observed for other filament materials such as PLA and PET [25, 26]. The alternating raster angle of ±45° employed in this study is one of the most effective raster patterns that provide a relatively isotropic and strong structure. Nevertheless, the strength of the specimens of this study is lower than that of ABS produced by injection molding, exhibiting values in the range of 40–50 MPa [27, 28].

The addition of FA to ABS does not alter the mechanical properties significantly, with the exception of elongation at break. There exists an approximately 50% relative reduction in elongation at break values with the addition of the FA particles. The primary reason for the reduction in ductility is the restricted chain mobility of the polymer by the presence of the second phase. Previous work shows that surface-modified FA particles can minimize this effect; a ductility reduction of only 24%

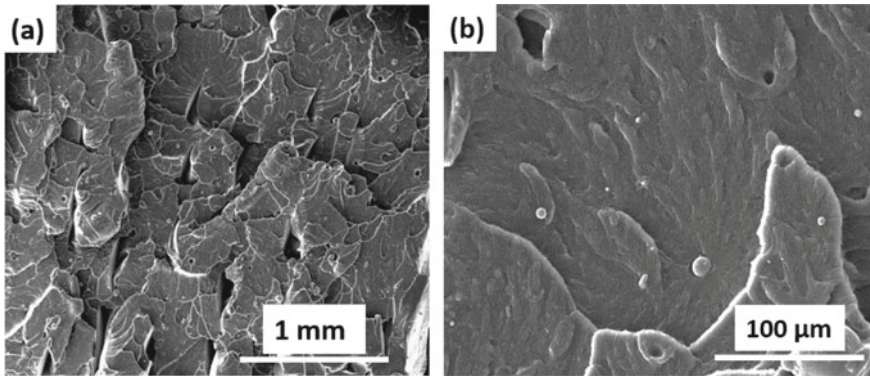


Fig. 7 SEM images of the fracture surfaces of the ABS-FA specimen. **a** and **b** show two different regions of the same surface at different magnifications

was reported at an FA loading of 30 wt% [15]. Surface-modified FA provides this improvement by generating a better interfacial adhesion between the ABS matrix and the FA particles [15]. This results in a more efficient stress and strain compatibility between the two phases and reduces the stress concentrations due to the shearing at the interface.

The analysis results show that there is a need to increase the weight fraction of FA to obtain more significant improvements in the mechanical properties. In our case, increasing the fraction of FA resulted in very brittle filaments causing frequent clogging of the printing head. A possible solution to this problem is the use of plasticizers to improve the rheological characteristics of the filament.

Figure 7 shows SEM images of the fracture surfaces of an ABS-FA specimen. Figure 7a exhibits micron-sized gaps in the polymer matrix. These defects, attributed to the relatively poor rheological characteristics of the filament, act as stress concentration sites leading to premature failure. The close-up view in Fig. 7b shows several FA particles, demonstrating the relatively weak bonding between the FA particles and the ABS matrix, which constitutes another reason for the poor ductility.

4 Conclusions

This study investigated the structural, thermal, and mechanical properties of FDM-produced ABS and ABS-FA specimens. The thermal and mechanical properties of the composite did not change significantly by the addition of 2 wt% FA. The only exception was a drastic decrease in ductility by a factor of two upon FA additions. The maintained properties of ABS-FA can be considered as an indication of the feasibility of FA additions to ABS filament, especially for coloring applications. On the other hand, for achieving any improvement in the mechanical properties through the same route, we propose the following steps for future work:

- Using surface-modified FA particles can enhance the structural integrity of the composite. Silane coupling agent compatible with the polymer matrix can be a good choice for this purpose, effectively improving the interfacial adhesion between the FA and the polymer matrix.
- Increasing the FA loading to beyond 10 wt% and utilizing a suitable plasticizer can provide strengthening and defect-free printed structures at the same time.

Acknowledgements The authors thank Dr. Çağla Meral Akgül for providing the fly ash, thank Dr. Berrak Erkmen and İrem Öztürk for their assistance with the twin-screw extrusion of the pure ABS and ABS-FA filaments, and thank Şener Akin for his help with the FA processing.

References

1. Bakır AA, Atik R, Özeriç S (2021) Mechanical properties of thermoplastic parts produced by fused deposition modeling: a review. *Rapid Prototyping J* 27:537–561
2. Moore JD (1973) Acrylonitrile-butadiene-styrene (ABS)—a review. *Composites* 14:118–130
3. Wypych G (2016) *Handbook of polymers*, 2nd edn. ChemTec Publishing, Toronto
4. Penumakala PK, Santo J, Thomas A (2020) A critical review on the fused deposition modeling of thermoplastic polymer composites. *Compos B Eng* 201:108–336
5. Ondova M, Stevulova N, Estokova A (2012) The study of the properties of fly ash based concrete composites with various chemical admixtures. Paper presented at the 20th international congress of chemical and process engineering CHISA 2012–29 August 2012
6. Yao ZT, Ji XS, Sarker PK, Tang JH, Ge LQ, Xia MS, Xi YQ (2015) A comprehensive review on the applications of coal fly ash. *Earth Sci Rev* 141:105–121
7. Bhattacharjee U, Kandpal TC (2002) Potential of fly ash utilisation in India. *Energy* 27:151–166
8. Blissett RS, Rowson NA (2012) A review of the multi-component utilisation of coal fly ash. *Fuel* 97:1–23
9. Chou M-IM (2012) Fly ash. *Encyclopedia of sustainability science and technology*. Springer, New York
10. Matsunaga T, Kim JK, Hardcastle S, Rohatgi PK (2002) Crystallinity and selected properties of fly ash particles. *Mater Sci Eng A* 325:333–343
11. Singla M, Chawla V (2010) Mechanical properties of epoxy resin—fly ash composite. *J Miner Mater Charact Eng* 09(3):199–210
12. Akın SŞ, Magalhães D, Kazanç F (2020) A study on the effects of various combustion parameters on the mineral composition of Tunçbilek fly ash. *Fuel* 275:117881
13. Ahmaruzzaman M (2010) A review on the utilization of fly ash. *Prog Energy Combust Sci* 36:327–363
14. ACIPRC-232.2-18 (2002) Report on the use of fly ash in concrete. American Concrete Institute, USA
15. Bonda S, Mohanty S, Nayak SK (2012) Viscoelastic, mechanical, and thermal characterization of fly ash-filled ABS composites and comparison of fly ash surface treatments. *Polym Compos* 33:22–34
16. Xue B, Bao J, Zhang J (2016) Ultrafine fly ash as a reinforcing filler in poly(lactic acid) matrix. *J Appl Polym Sci* 133
17. Deepthi MV, Sharma M, Sailaja RRN, Anantha P, Sampathkumaran P, Seetharamu S (2010) Mechanical and thermal characteristics of high density polyethylene-fly ash Cenospheres composites. *Mater Des* 31:2051–2060

18. Pardo SG, Bernal C, Ares A, Abad MJ, Cano J (2010) Rheological, thermal, and mechanical characterization of fly ash-thermoplastic composites with different coupling agents. *Polym Compos* 31:1722–1730
19. Kishore KSM, Sunil D, Sharathchandra S (2002) Effect of surface treatment on the impact behaviour of fly-ash filled polymer composites. *Polym Int* 51:1378–1384
20. Wang Z, Wang J, Li M, Sun K, Liu C (2014) Three-dimensional printed acrylonitrile butadiene styrene framework coated with Cu-BTC metal-organic frameworks for the removal of methylene blue. *Sci Rep* 4:1–7
21. Billah KMM, Lorenzana FAR, Martinez NL, Wicker RB, Espalin D (2020) Thermomechanical characterization of short carbon fiber and short glass fiber-reinforced ABS used in large format additive manufacturing. *Additive Manuf* 35:101299
22. Oral MA, Ersoy OG, Serhatli E (2018) Effect of acrylonitrile–butadiene–styrene/polyethylene terephthalate blends on dimensional stability, morphological, physical and mechanical properties and after aging at elevated temperature. *J Plast Film Sheeting* 34:394–417
23. Ahn SH, Montero M, Odell D, Roundy S, Wright PK (2002) Anisotropic material properties of fused deposition modeling ABS. *Rapid Prototyping J* 8:248–257
24. Banjanin B, Vladić G, Pál M, Baloš S, Dramićanin M, Rackov M, Knežević I (2018) Consistency analysis of mechanical properties of elements produced by FDM additive manufacturing technology. *Rev Mater* 23(4)
25. Kaygusuz B, Özerinç S (2019) Improving the ductility of polylactic acid parts produced by fused deposition modeling through polyhydroxyalkanoate additions. *J Appl Polym Sci* 136:48154
26. Bakır AA, Atik R, Özerinç S (2021) Effect of fused deposition modeling process parameters on the mechanical properties of recycled polyethylene terephthalate parts. *J Appl Polym Sci* 138:49709
27. Rahimi M, Esfahanian M, Moradi M (2014) Effect of reprocessing on shrinkage and mechanical properties of ABS and investigating the proper blend of virgin and recycled ABS in injection molding. *J Mater Process Technol* 214:2359–2365
28. Chen CS, Chen TJ, Der CR, Chen SC (2007) Investigation on the weldline strength of thin-wall injection molded ABS parts. *Int Commun Heat Mass Transf* 34:448–455

A Comparative Study and Optimization of Parameters of Turning UD-GFRP in Dry, Wet and Cryogenic Condition by Using PCD Tool with Taguchi Method



Hazari Naresh and Padhy Chinmaya Prasad

Abstract Major applications of composites are lightweight in aerospace applications and modern fasteners for reducing the weight purpose, in this concern composites are very difficult for machines due to non-homogeneous and anisotropic environment and it requires unique cutting tools. This work is going to investigate a comparative study of various conditions like Dry condition, Wet condition, and Cryogenic condition machining (turning) of UD-GFRP composite round with Polycrystalline diamond tool in the Lathe. The responses which measure the machining quality are: the tool wear, quality of the surface, and forces generated at various stages of inputs given to the machining of UD-GFRP composite. The optimization technique, i.e., Taguchi L9 orthogonal array is used for examinations and finding out the targeted values. The design includes three independent variables at three levels, the proposed process control independent variables are: rate of feed of tool, spindle speed or velocity of cutting, and operation depth tool in the work. The investigation aims to establish the process control by studying the relationship between Dry, wet, and Cryogenic machining condition level of inputs and degree of responses to identify the optimal level of process inputs for acceptable surface quality with minimal tool wear and cutting force condition.

Keywords UD-GFRP · Dry wet and cryogenic machining environment · L9 Taguchi optimization technique surface roughness · Polycrystalline diamond (PCD) tool

1 Introduction

As the composite plays a wide role in many applications, the machinability investigation is indispensable in particularly the UD-GFRP composite round bars. The material nature of inhomogeneous as well as anisotropic classifies it as low machinability category. Though the composite name is unique its properties could not be

H. Naresh · P. C. Prasad (✉)

Department of Mechanical Engineering, School of Technology, GITAM University, Hyderabad, India

unique due to the above-said reason. Many researchers reported the machinability investigation on synthesized on their own. The uniformity can be achieved synthesize under mass production with automation for commercial purposes. The investigation of commercial UD-GFRP composites is most beneficial. The following outcomes either support or justify the research gap appropriately [1]. Reported that though many input parameters considered for machining of composite the tool feed rate is a most influencing factor on surface roughness of machined surfaces than nose radius, cutting speed, and cutting depth. They used a conventional lathe machine and utilized PCA for optimization [2]. Recommended the carbide inserts to cut such low machinability composites, this research adopted such recommendations [3]. The enhanced coolant of water miscible with soluble Castrol in the ratio of 6: 1 outperformed in such composite machining [4]. The philosophy of conventional machining is harder tools work better than soft tools. Based on the workpieces harness the selection of appropriate tools is prime factor to meet the expected outcomes. They investigated three harder tools viz Cubic boron nitride insert, single and polycrystal diamond inserts, and reported that single crystal diamond tool outperformed [5]. Agreed in his review that the machinability of either glass or carbon fiber reinforced polymer composites are under the class of low machinability material sufficient effort must be made to machining them [6]. Recommended the Multiple regression analysis for understanding the machinability with milling operation. But this study focuses on CNC turning [7]. Published some interesting fact that machinability of composite requires more specific investigations to expand its application. The length of fiber is changed the composite properties [8]. Investigated contribution tool in precision machining of glass fiber reinforced plastics. But this study focused on the coolant and CNC turning center to improve machinability for mass production with high accuracy. Though many investigations were found in the literature related to this research interest this piece of research is most unique by considering the CNC turning center for repeatability for mass production and accurate observation of machining effects, best performed the carbide tool insert and conventional eco-friendly coolant usage.

2 Methodology

The examination considered responses like quality of machining by surface roughness, tool wear, and cutting forces, the considered input variable and constant parameters furnished in Tables 1 and 2. The 20 mm diameter GFRP rods were produced by pultrusion process. The fabricated GFRP composite rods are cut into small segments

Table 1 Levels of CNC turning process parameters

Process variable (in range) →	Low	Medium	High
Spindle speed (rpm)	1000	1200	1500
Feed of the tool (mm/ rev)	0.05	0.1	0.15
Depth of cut (mm)	0.5	1.0	1.5

Table 2 The independent and fixed process parameters

Independent process variables (in range) →	Low	Medium	High
Cutting environment	Dry, wet, and cryogenic condition	Dry, wet, and cryogenic condition	Dry, wet, and cryogenic condition
Tool material	PCD	PCD	PCD
Tool rake angle (in degree)	6	6	6

of length 150 mm and machined in the CNC machine by changing the independent process variables like feed, speed, and depth of cut, the responses like cutting forces are estimated by the dynamometer setup. After each trial, the wear of the tool is estimated by using the tool maker's microscope. The composite rods are then taken into the surface roughness tester to find out surface roughness values. These resultant parameters are assessed by using the Taguchi and Minitab programming to find economical values with respect to given input values.

The MIXMAX ST 2020 lubricating oil is employed as coolant in flood cooling form. Hence the cutting condition is wet machining. The fixed parameters are tool material, tool type (PCD)

Coolant for Wet Machining

Cutting fluid is mix-up with Water-soluble in different ratios depending on the machining operation. Cutting fluids are supplied with the help of electric motor. The storage capacity of the fluid tank is 100 liter. The cutting fluid is supplied at const rate of 0.2 liters/s. Castrol water miscible soluble coolant is utilized in this investigation and with 1:6 concentrations by volume fraction.

Coolant for Cryogenic Condition Machining

Cryogenics is clearly known as branch of physics that deals with the creation of very low temperatures and its effect on substances, this will address the aspects of getting least temperatures that do not in nature occur in the world and utilizing them for learning of nature or the human industry. Liquid nitrogen—which is colorless, odorless and tasteless, and eco-friendly to environment and used for machining of hard metal and ceramics composites for better surface finishing. For machining of composite under cryogenic condition, liquid nitrogen is used as coolant maintained at $-196\text{ }^{\circ}\text{C}$ [$-320\text{ }^{\circ}\text{F}$] temperature and used for machining to examine the various output parameters.

3 Experimentation

Here the glass fiber reinforced composite rod in turning was done with the different machinability trials. The cutting tool used is PCD inserts and its description furnished

in Table 3. The GFRP bar of 20 mm diameter and 150 mm long jobs prepared and experimented in SUPER JOBBER 500 CNC (SIEMENS 802 D SL) turning center (refer Fig. 1). The UD-GFRP composite rod specifications furnished in Table 4. All the experiment was conducted by Dry, Wet and Cryogenic conditions and recorded values, these values are analyzed by MINItab software. The individually recorded values are compared for research analysis.

The wear property of the tool was investigated with tool maker’s microscope Fig. 2. The Mitutoyo make tester employed for measuring surface roughness of machined work pieces, the surface roughness tester shown in the Fig. 3. The Fig. 4 exhibits the CNC lathe dynamometer setup facility which employed for measuring force generated while turning experimentations. The dry, wet and cryogenic machining are considered for comparative evaluation, the sample machining coolant setup are shown in the Figs. 5 and 6. The cutting tool PCD insert shows in Fig. 7. The cryogenic liquid nitrogen container cylinder is used for experimentation which shows in Fig. 8. The wet machining environment helps in extends tool life and save the UD-GFRP composite from damages. The flow rate maintained at 2 liters per minute. The machined components are shown in Fig. 9.

Table 3 Specification of PCD tool [1]

Properties of PCD tool	
Clearance angle	6°
Grade	M10
Density	3.80–4.50 g/cm ³
Hardness	1600 Vickers kg/mm ²
Young’s modulus	800–900 GPa
Thermal conductivity	150–550 W/m K
Compressive strength	7000–8000 N/mm ²
<i>Cutting edge inclination</i>	
Angle top	6°
Tool rake angle	6°

Fig. 1 CNC SUPER JOBBER 500 CNC



Table 4 Properties of prepared composite bar [1]

Sr. No.	Description of composite	Quantity/specification
1	Composite's strength on compression	600 N/mm ²
2	Youngs modulus of composite	320 N/mm ²
3	Absorption moisture/water absorption	7 × 10 ⁻² %
4	Fiber orientation	Unidirectional
5	Epoxy resin content (by weight)	25 ± 5%
6	wt% of glass fiber contribution	75 ± 5%
7	Composite's strength on tensile	650 N/mm ²
8	Composite's strength on shear	255 N/mm ²
9	Agent of reinforcement	Roving: E- glass

Fig. 2 Tool maker's microscope



Fig. 3 The facility of surface roughness



Fig. 4 CNC lathe dynamometer setup while turning of UD-GFRP



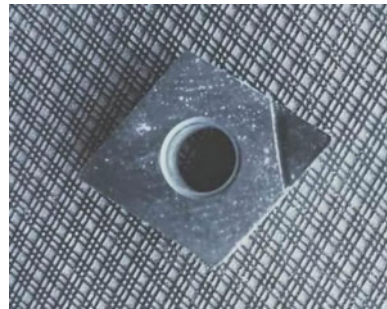
Fig. 5 CNC green turning of UN-GFRP composite rod



Fig. 6 Coolant supply setup in machine



Fig. 7 The polycrystalline diamond tool insert



4 Results and Discussion

The observed outcomes conducted experiments statistically analyzed and presented. The statistical examination is done by utilizing Minitab programming. The impressions and collaborations of Tool feed, spindle speed and, depth of cut offered average roughness on surface, wear of tool, and forces encountered while CNC turning on tool have been created utilizing multiple regression model. The analysis of variance (ANOVA) Taguchi L9 orthogonal array applied as shown in Table 5, which help to analyze the contribution of individual process parameters on responses like required

Fig. 8 Liquid nitrogen container**Fig. 9** Machined components**Table 5** Orthogonal array (L9) of Taguchi along with assigned value

Expt No	Speed (rpm)	Feed of tool (mm/rev)	Depth of cut (mm)	Insert type	Machining environment	Rake angle of tool
1	1000	0.05	0.5	PCD	Dry/wet/cryogenic	6
2	1000	0.1	1	PCD	Dry/wet/cryogenic	6
3	1000	0.15	1.5	PCD	Dry/wet/cryogenic	6
4	1200	0.05	1	PCD	Dry/wet/cryogenic	6
5	1200	0.1	1.5	PCD	Dry/wet/cryogenic	6
6	1200	0.15	0.5	PCD	Dry/wet/cryogenic	6
7	1500	0.05	1.5	PCD	Dry/wet/cryogenic	6
8	1500	0.1	0.5	PCD	Dry/wet/cryogenic	6
9	1500	0.15	1	PCD	Dry/wet/cryogenic	6

cutting forces, roughness on machined surfaces, induced hardness on surface due thermal effects, etc.

Taguchi Analysis: Tool wears response versus Speed, Feed, and Dept of cut

From experimental Tables 6, 7, and 8 explain the main effecting parameter of tool wear response, that is contribution of Tool feed, spindle speed and, depth of cut effect of tool wear response. The optimization criteria were smaller the better for tool wear response is preferable. When all the experiments are conducted and outcome of the research is found that as compared to Dry, Wet and Cryogenic environment gives better tool wear response vales and with decreasing graph as shown in Fig. 10 represent the tool wear response values graph. The cryogenic environment produces less heat while removing power type chips. The powder chips are adhesive properties while using this environment. This research shows that the cryogenic environment is best suitable while machining operation.

Tool wear response versus Speed, Feed, Dept of cut, explains the main effecting parameter of Tool wear response are 0.15 mm/rev, 1000 rpm, and 1.0 mm respectively, gives economical tool wear response meanwhile it will be followed by speed 1500 rpm, feed 0.1 and depth of cut 0.5 gives moderate tool wear and speed 1200, feed 0.05 mm and depth of cut 1.5 gives very high tool wear.

From the above comparison as the Trial 1 to 9 have mare arrangement of TAGUCHI L9 orthogonal array, according to the same, in each trial, the tool wear values are decreasing rate, i.e., in each graph indicate minimum is better one. Moreover, the tool wear factor affects the quality surface, which means when speed increases tool wears increases, but in cryogenic condition even less sped also getting less tool wear. This is the statement of quality of tool wear factor by cryogenic condition. Tool wear model formula

$$\frac{S}{7.1645} \quad \frac{R-Sq}{80.78\%} \quad \frac{R-Sq(adj)}{23.14\%}$$

Taguchi Analysis: Surface Roughness Response (μm) Versus Speed, Feed, Dept of Cut

From above experimental Tables 6, 7, and 8 explains the main effecting parameter of surface roughness, that is contribution of Tool feed, spindle speed and, depth of cut effect of surface roughness. The optimization criteria were smaller the better for surface roughness. Less value is better for tool wear and low cutting force is preferable. When all the experiments are conducted and outcome of the research is found that as compared to Dry and Wet cryogenic environment gives better surface roughness values and with decreasing graph as shown in Fig. 11 represent the surface roughness values. The cryogenic environment produces less heat while removing power type chips. The powder chips are adhesive properties while using this environment. This research shows that the cryogenic environment is best suitable while machining operation.

Figure 11 explains the main effecting parameter of surface roughness, the optimization criteria were smaller the better for surface roughness. Hence the optimal

Table 6 Experimental observations under dry machining condition

Exp. No.	Tool wear response			Surface response			Cutting force N					
	Vb1	Vb2	Vb3	Average Vb (Avg) mm	Ra1	Ra2	Ra3	Average in $\mu\text{m Ra}$	F1	F2	F3	Average in F Avg
1	0.14	0.163	0.16	0.155	4.96	5.07	5.19	5.074	16	14	15	15
2	0.09	0.125	0.1	0.105	5.42	5.96	5.68	5.692	15	16	15	15
3	0.2	0.175	0.19	0.185	5.21	5.43	5.35	5.328	17	15	16	16
4	0.07	0.09	0.04	0.066	5.7	5.83	5.73	5.751	16	18	17	17
5	0.3	0.148	0.17	0.205	5.05	4.9	4.93	4.958	19	17	18	18
6	0.59	0.41	0.58	0.526	6.12	6.82	6.36	6.436	19	18	20	19
7	0.05	0.051	0.06	0.052	5.05	5.12	5.16	5.11	20	21	19	20
8	0.2	0.234	0.22	0.215	4.56	4.69	4.49	4.58	21	21	20	21
9	1.12	0.09	1.87	1.025	6.2	6.38	6.27	6.286	20	22	21	21

Table 7 Experimental observations under wet machining condition

Exp. No.	Tool wear response			Surface response					Cutting Force(N)			
	Vb1	Vb2	V b3	Average Vb (Avg) mm	Ra1	Ra2	Ra3	Average In μm Ra	F1	F2	F3	Average in F Avg
1	0.115	0.179	0.119	0.138	3.956	5.219	5.698	4.958	15	13	15	14
2	1.022	1.08	0.842	0.981	4.991	5.359	5.458	5.269	13	14	15	14
3	0.161	0.152	0.181	0.165	5.435	5.021	4.922	5.126	15	17	14	15
4	0.065	0.051	0.053	0.056	4.951	5.942	5.644	5.512	16	15	17	16
5	0.189	0.194	0.201	0.195	4.696	4.224	5.024	4.648	18	15	17	17
6	0.688	0.359	0.356	0.468	4.949	6.25	6.651	5.950	17	19	18	18
7	0.059	0.037	0.035	0.044	4.825	5.234	5.245	5.101	19	18	20	19
8	0.277	0.198	0.109	0.195	3.454	4.352	4.988	4.265	19	20	22	20
9	0.895	1.095	0.968	0.986	5.318	5.854	6.532	5.901	18	22	20	20

Table 8 Experimental observations under cryogenic machining condition

Exp. No	Tool wear response			Surface response			Cutting force N					
	Vb1	Vb2	Vb3	Average Vb (Avg) mm	Ra1	Ra2	Ra3	Average In μm Ra	F1	F2	F3	Average in F Avg
1	0.115	0.154	0.108	0.126	3.786	3.872	4.298	3.985	14	13	15	14
2	1.005	1.024	0.742	0.924	3.851	4.529	4.258	4.213	13	14	15	14
3	0.111	0.142	0.172	0.142	3.729	4.321	4.322	4.124	15	14	14	14
4	0.055	0.041	0.043	0.046	4.584	3.993	4.289	4.289	16	15	17	16
5	0.169	0.179	0.124	0.157	3.896	4.285	4.114	4.098	16	16	17	16
6	0.598	0.365	0.316	0.426	4.306	4.275	4.194	4.258	17	18	17	17
7	0.055	0.029	0.032	0.039	3.843	4.176	4.235	4.085	19	18	18	18
8	0.227	0.138	0.098	0.154	3.836	3.852	4.088	3.925	19	20	19	19
9	0.805	1.012	0.775	0.864	3.761	3.684	4.032	3.826	18	20	20	19

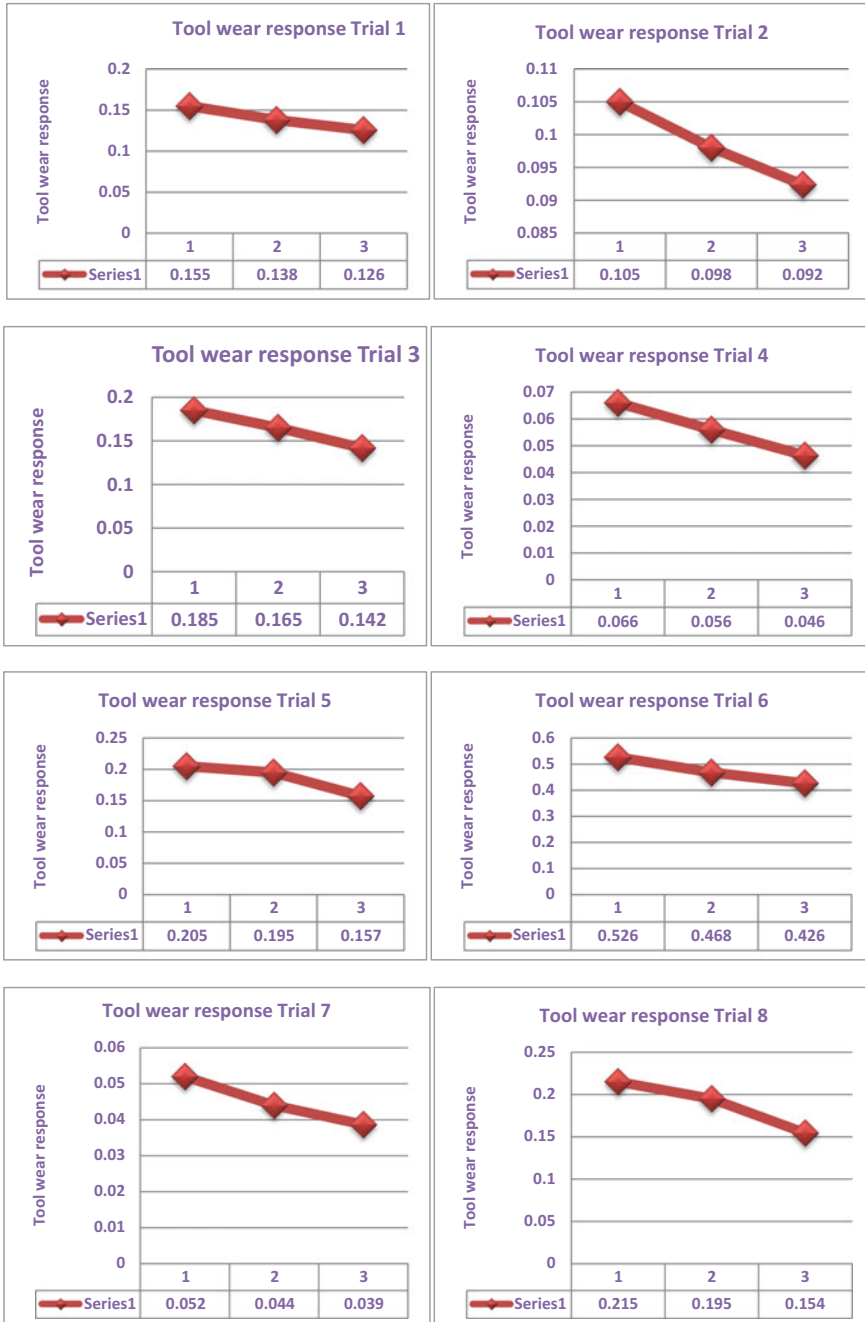
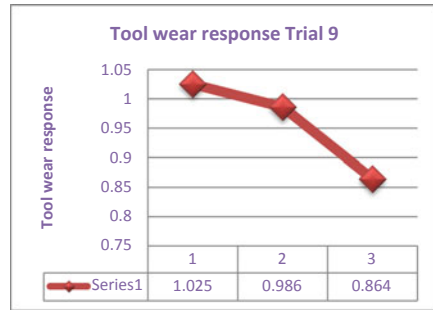


Fig. 10 Tool wears under dry wet and cryogenic condition in 9 trials

Fig. 10 (continued)



cutting parameters are: Tool feed 0.15 mm/rev, spindle speed of 1200 rpm and, depth of cut 1.0 mm.

From the above comparison as the Trial 1 to 9 have more arrangement of TAGUCHI L9 orthogonal array, according to the same, in each trial, the surface roughness values are increasing rate, i.e., in each graph indicate minimum is better one. Moreover, the source roughness factor affects the quality of surface it means when speed increases surface roughness increases, but in cryogenic conditions even less speed also get good surface quality this is the statement of quality of roughness factor by cryogenic condition.

Taguchi analysis for Cutting Force (N) versus Speed, Feed, Dept of cut

From above experimental Tables 6,7 and 8 explains the main effecting parameter of cutting force, that is contribution of Tool feed, spindle speed and, depth of cut effect of cutting force. When all the experiments are conducted and outcome of the research is found that as compared to Dry and Wet cryogenic environment gives better values and with decreasing graph as shown in Fig. 12 represent the surface roughness values. This research shows that the cryogenic environment is best suitable while machining operation The response of cutting force (N) versus Tool feed, spindle speed and, depth of cut, the main effecting parameter of cutting force (N) response for different Tool feed, spindle speed and, depth of cut are 0.15mm/ rev, 1500 rpm, and 1.5mm respectively gives economical cutting force response.

From the above comparison as the Trial 1 to 9 have more arrangement of TAGUCHI L9 orthogonal array, in each trial, the values of the cutting forces are decreasing rate, i.e., in each graph indicate minimum is better one. Moreover, the cutting forces factor is effect the tool wear it means when speed cutting forces rate is decreased, but in cryogenic condition even less speed also get the less forces this is the statement of quality cutting forces by cryogenic condition.

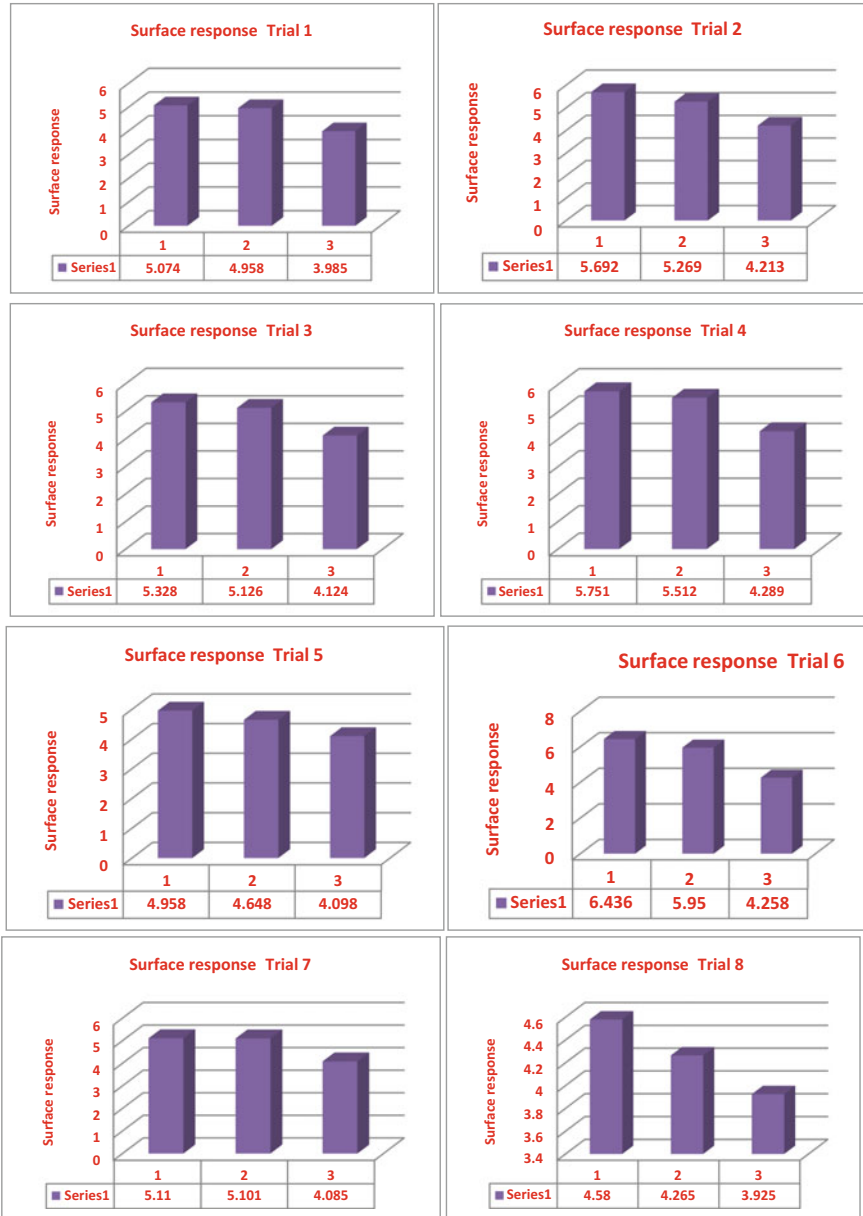
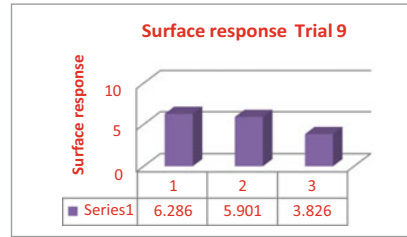


Fig. 11 Surface roughness under dry wet and cryogenic condition in 9 trials

Fig. 11 (continued)



5 Conclusion

The machinability improvement with use of polycrystalline diamond tool (PCD) as cutting tool presented in this paper. This experimental investigation optimized parameters under dry, wet and cryogenic turning based on cutting force requirements, roughness on machined surfaces, and wear of tool. The following conclusions are drawn within the range of parameters selected.

Tool wear parameter

- The main effective parameter for getting less tool wear according to Tauguchi L9 orthogonal array is Speed for 1000 rpm, feed 0.15 mm and depth of cut 1.0 mm gives economical tool wear.
- The Tool wear is highly influenced by Feed rate and it got rank 1 and 2nd depth of cut and 3rd speed parameters response.
- The main comparison in each trial gets less tool wear by using cryogenic conditions of turning.

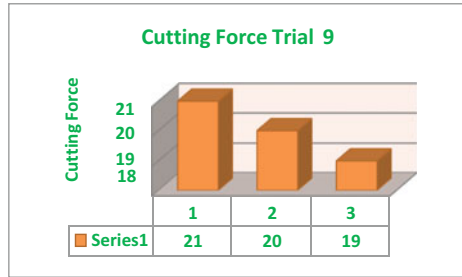
Response of surface roughness on Machined surfaces,

- The economical surface roughness is got when Speed for 1000 rpm, feed 0.15 mm and depth of cut 1.0 mm.
- The surface roughness on machined composite (UG-GFRP) rod is severally prejudiced by Tool feed rate (Rank 1), depth of cut (Rank 2) spindle speed (Rank 3).
- As a comparison good surface roughness by using cryogenic condition of turning.
- The less cutting force according to Tauguchi L9 orthogonal array is Speed for 1500 rpm, feed 0.15 mm and depth of cut 1.5 mm gives economical cutting force response.



Fig. 12 Cutting force under dry wet and cryogenic condition in 9 trials

Fig. 12 (continued)



- The cutting forces are produced high rate when the depth of cut 1.0 mm, spindle speed 1000rpm, feed 0.05 mm/rev, and require maximum cutting force.
- The main comparison in each trial gets less cutting force by using cryogenic condition of turning.

References

1. Gupta M, Kumar S (2015) Investigation of surface roughness and MRR for turning of UD-GFRP using PCA and Taguchi method. *Eng Sci Technol Int J* 18:70–81
2. Kumar S, Meenu, Satsangi PS (2013) Multiple-response optimization of turning machining by the Taguchi method and the utility concept using uni-directional glass fiber- reinforced plastic composite and carbide (k10) cutting tool. *J Mech Sci Technol* 27(9):2829–2837
3. Lee E-S (2001) Precision machining of glass fibre reinforced plastics with respect to tool characteristic. *Int J Adv Manuf Technol* 17:791–798. Springer, London Limited
4. Henerichs M, Voß R, Kuster F, Wegener K (2015) Machining of carbon fiber reinforced plastics: influence of tool geometry and fiber orientation on the machining forces. *CIRP J Manuf Sci Technol* 9:136–145
5. Karatas MA, Gokkaya H (2018) A review on machinability of carbon fiber reinforced polymer (CFRP) and glass fiber reinforced polymer (GFRP) composite materials. *Defense technology*
6. Paulo Davim J, Reis P (2004) Multiple regression analysis (MRA) in modeling milling of glass fibre reinforced plastics (GFRP). *Int J Manuf Technol Manage* 6(1/2):85–197
7. Paulo Davim J (2009) *Machining composite materials*. Wiley-ISTE
8. Lee ES (2001) Precision machining of glass fiber reinforced plastics with respect to tool characteristics. *Int J Adv Manuf Technol* 17:791–798

An Experimental Investigation on Effect of Process Parameters on Microstructure and Mechanical Properties of Spheroidal Graphite Cast Iron



Harshit P. Modi, Jay R. Raval, Deep S. Patel, and Vipul P. Patel

Abstract According to some researches, changes in process parameters, such as melting of base iron material, nodularisation procedure, percentages of nodulariser, magnesium treatment, inoculation process, form of inoculant, percentages of inoculant, and pouring methods, among others, can enhance the mechanical properties of SG cast iron. Tensile strength, hardness test, wear test, nodularity count and microstructure analysis were used to assess the accuracy of the casting. In addition, an accumulation of hard carbide occurs in the microstructure of SG iron. There are certain mechanical properties that are affected by this hard carbide construction, such as a decrease in ductility and machinability. The key goal of this paper is to present the experimental results of different process parameters on mechanical and microstructural properties of spheroidal graphite cast irons, such as the percentage of ferro silicon barium (inoculant) and the percentage of nodulariser.

Keywords Ferro silicon barium · Hardness · Inoculant · Mechanical properties · Microstructure analysis · Nodularity · Nodule count · Nodulisation · Process parameters · SG cast iron · Tensile strength

1 Introduction

Ductile iron, also known as spheroidal graphite cast irons, has seen a rise in popularity over the last two decades due to its superior strength and durability as compared to other forms of cast irons. Graphite can be found in a small spherical shape. As a result, the concentration of internal stresses can be minimised, and the mechanical properties can be greatly enhanced. Spheroids made of graphite have mechanical properties such as high tensile strength, yield strength, wear resistance and elongation. Changes in chemical composition can also affect the hardness of SGI cast iron.

Higher mechanical properties and wear resistance capability are caused by the microstructure of SG iron spheroids. In comparison, the carbon proportion in ductile

H. P. Modi (✉) · J. R. Raval · D. S. Patel · V. P. Patel

Department of Mechanical Engineering, U.V. Patel College of Engineering, Ganpat University, Mehsana, Gujarat, India

and graphite cast iron is the same. Spheroids form in the microstructure as alloying elements such as magnesium and cerium are added. These alloying elements will aid in uniformly improving the dimensions in all directions. The graphitisation rate will increase when silicon is added in excess of 2%. The rate of graphitisation increases when more than 2% silicon is added to the SG iron microstructure [1].

1.1 Nodulisation

Nodulisation is a process for converting flex to nodules of graphite present in metal. To remove sulphur and oxygen which is still present in liquid alloy, magnesium is added and it provides a residual 0.05% of magnesium; this results in the growth of spheroidal graphite, probably the interfacial energy has a high value to have a 180° this implies that the wetting of graphite does not occur. This treatment with magnesium desulphuriser iron to less than 0.02%. In nodulisation process, ferro silicon magnesium (Fe–Si–Mg) is used as nodulariser for SG cast iron. For SG cast iron, nodulariser is added to ladle at time of pouring or tapping. Magnesium treatment is another term for the nodulisation process [1].

1.2 Inoculation

Inoculation is a method in which the amount of nucleation sites required for the growth of graphite nodules or spheroids in ductile irons is increased, resulting in improved microstructure and mechanical properties. For molten SG iron, inoculation process is the most important parameter and it is done during pouring of molten metal. Inoculant is a material that is used for improvement in grain structure of SG cast iron. It also helps to improve cooling of molten metal and gives significant effect on microstructure of SG cast iron. Nowadays, there are many types of inoculants are available in industries like ferro silicon barium, ferro silicon zirconium, ferro silicon manganese, ferro silicon bismuth. Most of inoculants for cast iron are based on ferrosilicon and containing small number of active elements like calcium (Ca), aluminium (Al), barium (Ba), zirconium (Zr), strontium (Sr) and rhenium (rare earth metals) [1].

2 Literature Review

Biraje and Jadhav [2] there was a lot of space for research into the process parameters and casting materials of SG cast iron. The following findings were derived from their three trials. Different mechanical and microstructural properties were obtained by

varying the per cent of Fe-Si-Mg and the per cent of inoculant with a given chemical composition and temperature.

Patel et al. [3] Microstructural analysis revealed that the generation of pearlite in SG600 cast iron without inoculation was significantly lower than that in SG600 cast iron with Fe-Si-Ba-based inoculant. The results revealed that increasing the pearlite content of SG iron and increasing the ferrite content of grey cast iron increased the ferrite content. In addition, the grain size will be increased. As a consequence, grain size influences hardness, tensile strength and elongation.

Godbole and Jayashree [4] Image processing technique is used to do a microstructural examination of SG iron. It can be used to decide the most effective and productive SG iron casting parameters, such as nodule count, nodularity, nodule size, and ferrite and pearlite percent. Such consistency parameters affect the tensile strength and hardness of the spheroidal graphite iron casting. They used an inverted microscope to obtain test specimen photographs of SG iron casting, which were then segmented.

Waghulde [5] Any casting foundry can improve their product consistency and choose effective parameters for quality materials by using an advanced thermal analysis method. Furthermore, even modest changes, such as a decrease in casted part rejection rate, would have a major effect on profitability and other costing metrics, since the improvements would affect total poured tonnage. It may help minimise metallurgical rejection, mechanical property variations, yield, and the number of inoculants and Mg-alloys used, as well as reduce the number of inoculants and Mg-alloys used (magnesium treatment).

Madtha et al. [6] Melting process, inoculation procedure, inoculant, heat treatment and other influences affected the microstructure and mechanical properties of ductile cast iron (DCI). Because of its exceptional mechanical properties, such as high strength and good ductility, good wear resistance and good fatigue property, ductile cast iron has been used in a wide range of applications in the tubing, pump machinery, automotive, rail and heavy engineering industries.

Thacker et al. [7] Chemical composition, microstructure and mechanical properties such as percentages of perlite, ferrite, carbide, percentage of elongation, tensile strength and stiffness all affect the consistency of ductile iron pipes. During the casting process, this can be changed by analysing and optimising process parameters. By using Taguchi method L16 orthogonal array was generated in MINITAB 17 and results were analysed by experimental work at different levels of factors.

Stefanescu [8] Without using a post-inoculant, master alloys containing barium or cerium will attain a high nodule count. Since they do not show a substantial improvement in nodule count, cerium-based post-inoculants are not recommended for ductile irons. They just cannot get rid of the rough carbide in the structure. When a Ni-Mg master alloy is used for magnesium therapy; however, post-inoculation with a cerium-based inoculant will yield curious results.

Dugic and Svenson [9] The best inoculant, containing silicon, aluminium and zirconium, was chosen from an earlier experiment. Experiments were carried out on a casting of various quantities of inoculants. There is a direct connection between a limited volume of inoculant and castings that are not penetrated. Too much inoculant and a sub-optimal composition are used in industrial casting. On the castings, there

were no penetrations, bulb formations or shrinkage defects. This analysis does not involve recent inoculants, but it does include valuable knowledge about inoculation parameters and temperature.

3 Problem Formulation

In today's industry, spheroidal graphite iron casting is in high demand. Making SG iron is also a crucial and difficult job in the foundry. Many researchers used mechanical properties or microstructure analysis to study SG iron. Many researchers used a digital microscope and a digital image analyser to examine microstructure.

As per as input process parameter concern, most of researcher used either chemical properties of SG iron, temperature, percentage of inoculation and heat treatment but effect of percentage of ferro silicon barium (Fe–Si–Ba) with variation in percentage of inoculant and change in percentage of nodulariser Fe–Si–Mg not yet to be diagnosed. In microstructure of SG iron, extra amount of hard carbide generates. Due to this hard carbide structure, there are some of mechanical properties that are affected like reduction in ductility and machinability.

4 Selection of Various Process Parameters

Selected SG iron of grade IS 1865 Grade 400/12 (suitable for Impellers, valves, hollow cylinder) as per industry daily usage (Table 1).

4.1 Raw Material

Cold-rolled coil (CRC) scrap (loose), sheet scrap, pig iron scrap were used as raw material (Fig. 1).

Table 1 Composition of grade SG-400/12

Chemical element	C	Si	Mn	P	S	Mg	Fe
% weight	3.50–3.78	2.80–2.85	0.20–0.50	0.03–0.06	0.02–0.04	0.02–0.06	Balanced



Fig. 1 CRC scrap

4.2 Charging and Melting

Electrotherm makes induction furnace with 85 KW capacity of power and with 100 kg capacity crucible with lid were used to melt the base materials. Also, this induction furnace has temperature measuring instrument which can able to measure 1800 °C. CRC scrap was added after preheating the furnace crucible. After melting of previously added scrap material, some extra amount of scrap was added. At 800 °C, alloying elements like silicon, carbon and ferro silicon magnesium (nodulariser) were added to charge. After adding alloying elements, impurities were coming at the surface of the charge. Impurities were removed by a straight rod from the molten metal. At 1100 °C, a small cup of molten metal was taken from a charge and was tested on CE metre for basic information like percentage of carbon and silicon and percentage of magnesium. After testing and verifying composition, fluxing material was added to molten metal to improve melting efficiency and it was also helpful in the removal of the buildup in the melt operation (Fig. 2).

At 1300 °C, temperature melting process was done in induction furnace and charge was superheated to 1590 °C. At the same temperature, slag and flux material was removed from molten metal surface. Then after molten metal was poured into magnesium-treated ladle cover with ferro magnesium alloy powder (Fig. 3).

4.3 Size of Ladle

Ladle was used for mixing of inoculant and magnesium in molten metal with capacity of 100 kg.



Fig. 2 Electrotherm makes induction furnace



Fig. 3 Ferro silicon magnesium (nodulariser)

4.4 Selection Inoculation Method

Ladle inoculation method was used. In ladle inoculation, there are three types of inoculation method, which are gravity feeding, air-assisted injection and wire injection. From these methods, air-assisted injection method is selected as inoculation method (Fig. 4).

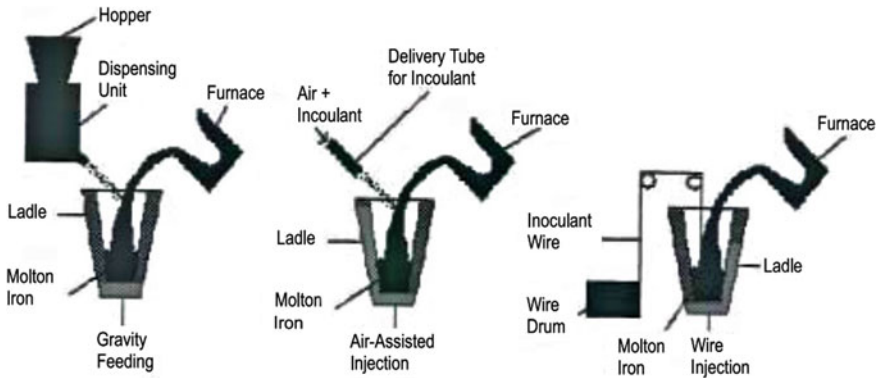


Fig. 4 Ladle inoculation methods

4.5 Selection of Inoculant

Ferro silicon barium was chosen from among the different inoculant selection parameters, as well as for SG cast iron casting InoK-SB2 (Series of cast inoculant). Ferro silicon barium is an iron-silicon alloy with regulated barium and calcium adds. Both grey and SG iron react well to this inoculant (Fig. 5).



Fig. 5 Ferro silicon barium (Fe-Si-Ba)

4.6 Moulding Sand

Sand and clay are mixed with water and occasionally horse dung to make loam sand. The aim of using horse dung in the mould is to make it permeable so that gas (such as steam) can escape during the casting process. For mixing sand and binders, sand mixing machine was used.

4.7 Pouring

For pouring purpose, 35 and 5 kg ladle was used. Gravity pouring method was used for pouring of molten metal into mould.

4.8 Casted Specimens

See Fig. 6 and Table 2.

5 Experimentation Results and Discussion

Test samples of IS 1865 Grade SGI 400/12 were prepared to determine the properties and to analyse optical microstructure to understand the behaviour of % of



Fig. 6 SGI specimens

Table 2 Specimens with selected % of inoculant

	Specimen-1	Specimen-2	Specimen-3	Specimen-4	Specimen-4
Inoculant	Ferro silicon Barium (Fe-Si-Ba)	Ferro silicon Barium (Fe-Si-Ba)	Ferro silicon Barium (Fe-Si-Ba)	Ferro silicon Barium (Fe-Si-Ba)	Ferro silicon Barium (Fe-Si-Ba)
Percentage of inoculant (%)	0.2	0.25	0.3	0.4	0.5

Table 3 Chemical composition of respected samples

Chemical elements (%)	Specimen-1	Specimen-2	Specimen-3	Specimen-4	Specimen-5
Carbon	3.42	3.47	3.50	3.58	3.64
Silicon	2.20	2.28	2.31	2.35	2.42
Sulphur	0.012	0.013	0.013	0.015	0.017
Phosphorus	0.025	0.024	0.025	0.027	0.027
Manganese	0.230	0.235	0.238	0.239	0.24
Chromium	0.010	0.010	0.010	0.010	0.010
Molybdenum	<0.001	<0.001	<0.001	<0.001	<0.001
Magnesium	0.045	0.047	0.049	0.050	0.051

Fe-Si-Mg & % of Fe-Si-Ba (inoculant), and hence, specimens were examined by spectroscopy test, hardness test, tensile test, grain size, nodularity and microscopic observation.

5.1 Spectroscopy Test

The purpose of spectroscopy test is to determine chemical composition of the IS 1865 Grade SGI 400/12. Following are the results of spectroscopic test: (Table 3).

5.2 Tensile Test

The specimen is grasped or clamped on one end of the machine’s frame, and the other end is gripped or clamped on the movable cross head. The specimen is exposed to a gradually rising load. In most cases, a hydraulic load is applied. The load measurement device determines the magnitude of the load. Elongation is measured by adding an extensometer or scale to the specimen. Equipment used for testing is MCS 400KN UTM (DMSPL/07/O2).

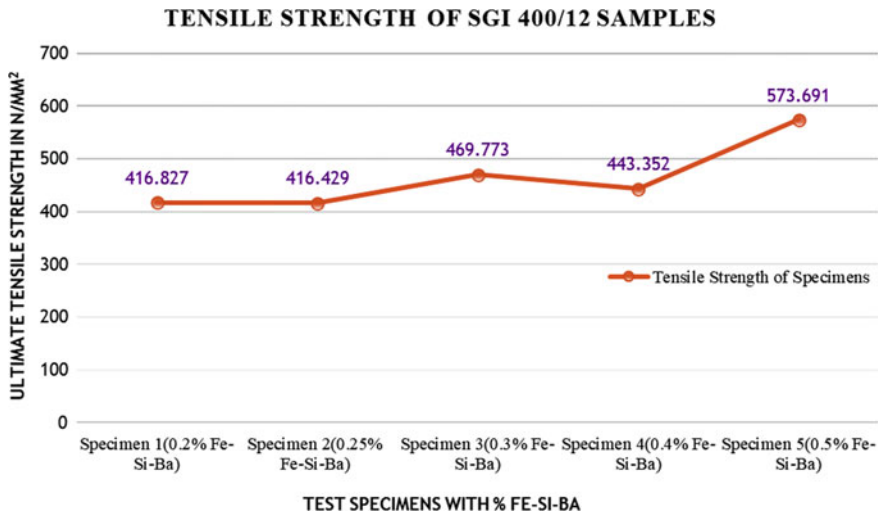


Fig. 7 Ultimate tensile strength in n/mm^2 versus test specimens with % Fe–Si–Ba

Following are the results of tensile test:

5.2.1 Observation-1

It has been observed from Fig. 7 that with change in percentages of ferro silico barium (Fe–Si–Ba) increases, the UTS for specimens with 0.2, 0.25 and 0.3% Fe–Si–Ba was 416.827, 416.249, 469.773 N/mm^2 . But for the specimen with 0.4% Fe–Si–Ba UTS was decrease to 443.352 N/mm^2 and for specimen with 0.5% Fe–Si–Ba UTS was significantly increase which was 573.691 N/mm^2 .

5.2.2 Observation-2

It can be observed from Fig. 8 that with change in percentages of ferro silico barium (Fe–Si–Ba) increases the yield strength for the 0.25% of Fe–Si–Ba to 317.606 N/mm^2 but for the 0.3 and 0.4% Fe–Si–Ba, the yield strength decreases to 292.549 and 276.422 N/mm^2 , respectively. For the 0.5% of Fe–Si–Ba, the yield strength increases significantly to 384.838 N/mm^2 .

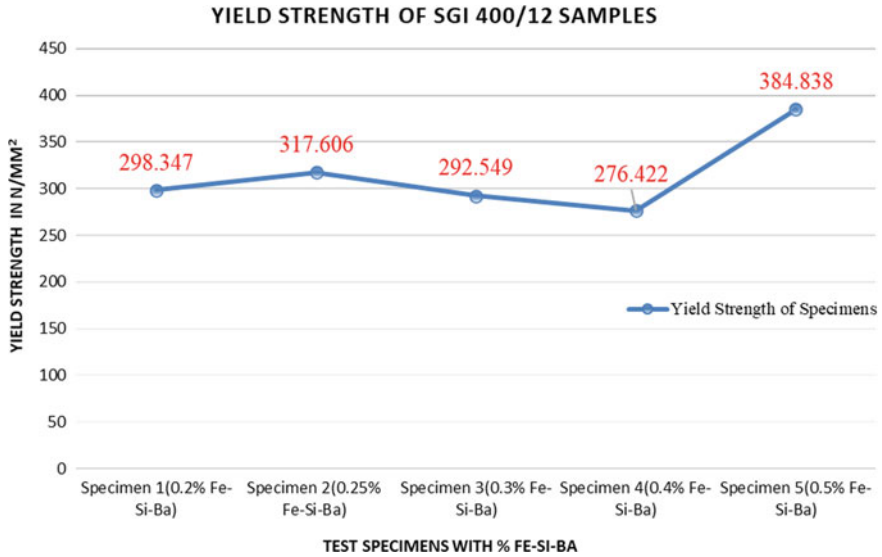


Fig. 8 Yield strength in n/mm² versus test specimens with % Fe-Si-Ba

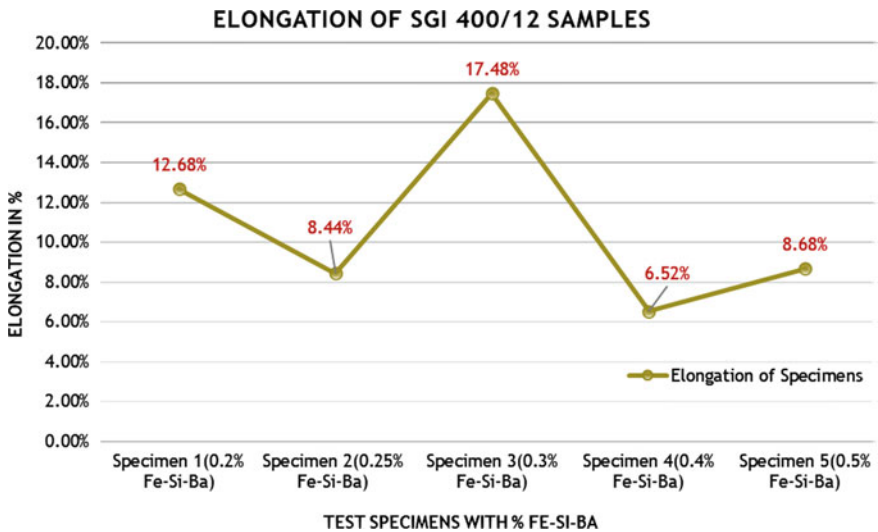


Fig. 9 Elongation in % versus test specimens with % Fe-Si-Ba

5.2.3 Observation-3

It can be observed from Fig. 9 that with change in percentages of ferro silico barium (Fe–Si–Ba) at 0.2% Fe–Si–Ba elongation was 12.68% and then decreases % of elongation to 8.44% for 0.25% Fe–Si–Ba. But for 0.3% Fe–Si–Ba, the % of elongation increases massively which was 17.48%, and for 0.4% Fe–Si–Ba, the % of elongation decreases again to 6.52% and then again it increases 8.68% for 0.5% Fe–Si–Ba.

5.3 Hardness Test

See Table 4.

5.3.1 Observation-4

It can be observed from Fig. 10 that with change in percentages of ferro silico barium (Fe–Si–Ba) at 0.2% Fe–Si–Ba hardness was 163 BHN and then it decreases to 162

Table 4 Results of hardness test

	Specimen-1	Specimen-2	Specimen-3	Specimen-4	Specimen-5
Hardness in BHN (Brinell)	163	162	177	179	205

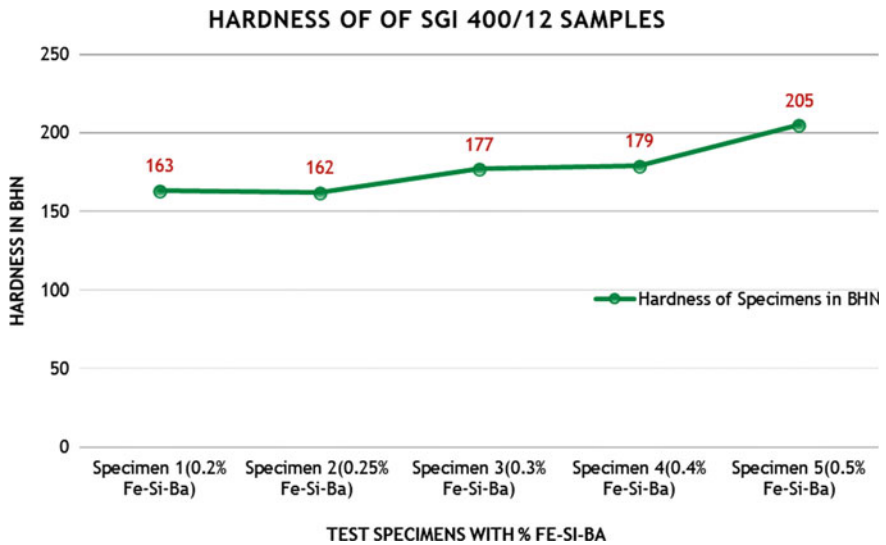


Fig. 10 Hardness in BHN versus test specimens with % Fe–Si–Ba

Table 5 Results of nodularity and nodule count

Parameters	Specimen-1	Specimen-2	Specimen-3	Specimen-4	Specimen-5
Graphite Nodules type	V, VI	V, VI	V, VI	V, VI	V, VI
Nodules size	5–6	6–7	6–7	6–7	6–7
Nodularity (%)	86	88	90	91	94
Nodule count	150 Particles/mm ²	171 Particles/mm ²	240 Particles/mm ²	303 Particles/mm ²	388 Particles/mm ²

BHN for the 0.25% Fe–Si–Ba. For 0.3% Fe–Si–Ba, hardness increases to 177 BHN, and for 0.4% Fe–Si–Ba, it also increases to 179 BHN. For the last sample with 0.5% Fe–Si–Ba, hardness increases to 205 BHN.

5.4 Nodularity and Nodule Count Test

Along with the microstructure, nodularity and nodule count were also carried out by a microscope at 100X magnification. The following are the results of nodularity and nodule counts: (Table 5).

5.5 Analysis of Microstructure

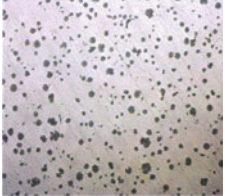
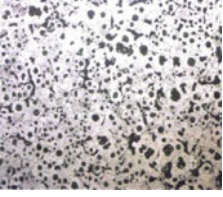

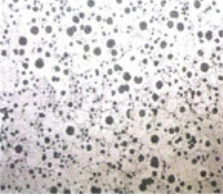
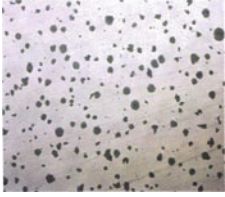


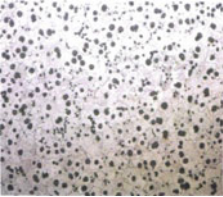

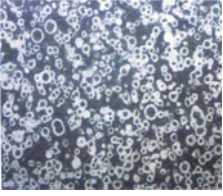
See Table 6.

6 Conclusion

From the results obtained, it can be concluded that the properties of spheroidal graphite cast iron can be enhanced and altered according to service condition and application requirement.

Earlier limitations on the usage of ductile iron due to limited knowledge of property enhancement processes can now be overcome by changing various process parameters such as melting of base iron material, nodularisation procedure, percentages of nodulariser, magnesium treatment, inoculation process, form of inoculant, percentages of inoculant, and pouring methods, among others can enhance the mechanical properties of SG cast iron. It has been found that by changing percentages of inoculant and type of inoculant, their brittle behaviour can be transformed to ductile behaviour applicable in various applications.

Table 6 Results of microstructure

No. of specimen	Inspection result at 100X (Polished)	Inspection result at 100X (Etched)	Observations
Specimen-1 (0.2% Fe–Si–Ba)			A microstructure shows graphite nodules in ferritic matrix along with the presence of pearlite Graphite nodules type is V, VI and size of nodules is 5–6 mm
Specimen-2 (0.25% Fe–Si–Ba)			A microstructure shows graphite nodules in ferritic matrix Graphite nodules type is V, VI and size of nodules is 6–7 mm
Specimen-3 (0.3% Fe–Si–Ba)			A microstructure shows graphite nodules surrounded by ferrite in the matrix of petalite Graphite nodules type is V, VI and size of nodules is 6–7 mm
Specimen-4 (0.4% Fe–Si–Ba)			A microstructure shows graphite nodules with some ferritic matrix Graphite nodules type is V, VI and size of nodules is 6–7 mm
Specimen-5 (0.5% Fe–Si–Ba)			A microstructure shows graphite nodules surrounded by ferrite in the matrix of pearlite Graphite nodules type is V, VI and size of nodules is 6–7 mm

From the experimentation on five specimens, the following results are obtained:

- At 1% Fe–Si–Mg & 0.2% Fe–Si–Ba (inoculant), Tensile strength is 416.827 N/mm² and Hardness is 163 BHN & Nodularity 86% & Nodule count is 150 Particles/mm².
- At 1% Fe–Si–Mg & 0.25% Fe–Si–Ba (inoculant), Tensile strength is 416.429 N/mm² and Hardness is 162 BHN & Nodularity 88% and Nodule count is 171 Particles/mm².
- At 1% Fe–Si–Mg & 0.3% Fe–Si–Ba (inoculant), Tensile strength is 469.773 N/mm² and Hardness is 177 BHN & Nodularity 90% & Nodule count is 240 Particles/mm².
- At 1% Fe–Si–Mg & 0.4% Fe–Si–Ba (inoculant), Tensile strength is 443.352 N/mm² and Hardness is 179 BHN & Nodularity 91% and Nodule count is 303 Particles/mm².
- At 1.5% Fe–Si–Mg & 0.5% Fe–Si–Ba (inoculant), Tensile strength is 573.691 N/mm² & Hardness is 205 BHN & Nodularity 94% and Nodule count is 388 Particles/mm².

The above experimentation can conclude that the change in percentages of Fe–Si–Mg and percentages of Fe–Si–Ba (inoculant) with variation in process parameters gives different and improved mechanical properties as well as microstructural properties.

Also, it can conclude that with combination of process parameters as 1.5% Fe–Si–Mg & 0.5% Fe–Si–Ba (inoculant) gives the better results which are tensile strength is 573.691 N/mm² & Hardness is 205 BHN & Nodularity 94% & Nodule count is 388 Particles/mm².

References

1. Modi HP, Raval JR, Patel DS, Patel VP (2021) A review on effect of process parameters on microstructure and mechanical properties of spheroidal graphite (SG) cast iron. *Int J Res Appl Sci Eng Technol (IJRASET)* 9(II):445–448
2. Biraje GS, Jadhav DM (2016) Study and observation of process parameters for spheroidal graphite (SG) iron casting. *IJSTE Int J Sci Technol Eng* 3(01):382–382
3. Patel D, Nanavati PK, Chug CM (2011) Effect of Ca and Ba containing ferrosilicon inoculants on microstructure and tensile properties of IS-210 and IS-1862 cast irons. In: National conference on emerging trends in engineering technology & management, pp 1–8
4. Godbole S (Mrs.), Jayashree V (2014) Microstructure analysis of spheroidal graphite iron (SGI) using hybrid image processing approach. *Int J Adv Res Comput Eng Technol (IJARCET)* 3(7):2268–2273
5. Waghulde S (2006) Predicting microstructure and mechanical properties of GCI and SGI by thermal analysis. The Institute of Indian Foundry men 54th Indian Foundry congress, pp 1–5
6. Madtha LS, Narendra Babu BR (2013) Experimental behavioural study of ductile cast iron microstructure and its mechanical properties. *Int J Eng Res Appl (IJERA)* 3(3):1470–1475. ISSN: 2248-9622 www.ijera.com
7. Thacker K, Joshi H, Patel NJ (2015) Analysis and optimization of parameters for casting ductile iron pipes. *Int J Eng Res Gener Sci (IJERGS)* 3(3), Part-2:382–385

8. Stefanescu DM (1973) Inoculation of ductile iron with Barium and Cerium Alloys. AFS Cast Metal J, pp 8–13
9. Dugic I, Svenson IL (1998) The effect of inoculant amount and casting temperature on metal expansion penetration in grey cast iron. Division of Component Technology Jönköping University, pp 1–10

An Insight of Compacted Graphite Iron (CGI) Characteristics and Its Production: A Review



Mamta Patel and Komal Dave

Abstract Compacted graphite iron (CGI) is one among the highly unrated material which has the potential to bridge the application gap persist using Flake graphite iron (FGI) and Spheroidal graphite iron (SGI); especially for high pressure and greater thermal loading boundary conditions. CGI microstructure comprises dense and interconnected worm/vermicular shaped graphite morphology which forms during the graphite transition from flake to sphere form or vice versa while the development of FGI and SGI. Such distinct microstructure offers intermittent mechanical and physical properties as compared to FGI & SGI, which makes CGI a unique proposition to address the industrial challenges for reliable product designing at minimal cost implication for automobile application. However, there are certain known challenges for CGI mass production due to worm graphite morphology sensitivity to foundry recipe and production approach. The worm graphite transformation stabilizes during the narrow window of flake to sphere graphite transition using the shape controlling elements so that it needs highly controlled foundry processes to bring the success for reliable mass production. Hereby, it is attempted to bring insight regarding CGI material microstructure, chemical composition, characteristics, and its technology evolution for mass production.

Keywords CGI · CG iron · Compacted graphite iron · Vermicular graphite iron

1 Introduction

The CGI was accidentally created in 1948; because of inadequate Mg, Ce, and La [1] treatment in the molten metal, intended to produce SGI. CGI contains the iron morphology where graphite particles are in form of shorter, thicker, stubby

M. Patel (✉)

Gujarat Technological University, Ahmedabad, Gujarat, India

K. Dave

Mechanical Engineering Department, L. D. College of Engineering, Ahmedabad, Gujarat, India

e-mail: dave_komal123@ldce.ac.in

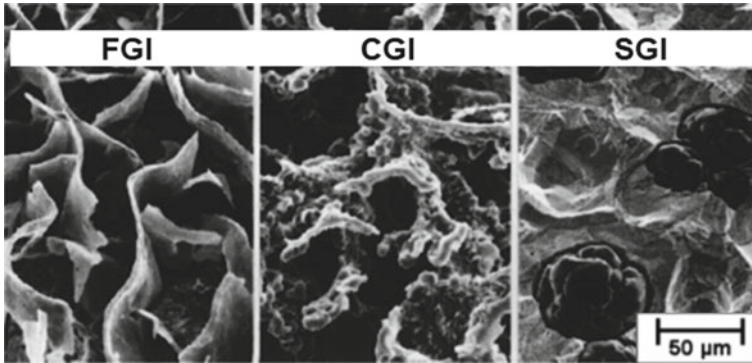


Fig. 1 3D graphite shapes using deep-etched scanning electron micrographs [5]

with rounded edges of worm shape compacted or vermicular graphite as shown in Fig. 1. Vermicular graphite depends on the roundness of flakes. Stefanescu [2] concluded that raising the degree of compactness improves the ductility, corrosion, and impact resistance, but simultaneously worsens machinability, thermal conductivity, and dampening capacity. Because of intermittent graphite shape morphology, CGI exhibits intermediate mechanical properties of FGI and SGI but better thermal conductivity than SGI; which makes it a distinct material for cumulative loading of heavy-duty and thermal applications. It outclasses FGI by 10–20% lighter weight along with superior strength and stiffness. These mechanical properties are primarily dominated by the CGI matrix—which can be controlled by many of the treatment variables such as charge material, graphite shape governing elements, chemical composition, cooling rate, pouring temperature, and holding temperature, etc.

The CGI mechanical strength varies mainly because of ferrite to pearlite transition for 300–500 MPa so with reference to it, most international standards classified its grades accordingly. Each grade exhibits distinct mechanical and thermal characteristics; ideal to fit for a wide range of automobile components applications [3] like., cylinder block, head, hydraulic housings, flywheels, bearing caps, and heavy castings, etc.

Despite the long history of ferrous material formation in the foundry, the graphite transition characteristics from flakes to compacted to spheroidal or vice versa; remains a mystery and is open to the potential scope of further research [1]. This paper narrates the insights of CGI characteristics and known production challenges, along with the recent developments.

1.1 Proposition Using CGI

As compared to FGI.

- Design and cost optimization through superior strength
- Ability to use fracture-splitting [4]
- Better strain energy absorption against impact
- Better life expectancy due to improved wear resistance
- Improved design reliability through consistent as-cast properties.

As compared to SGI.

- Improved thermal conductivity and heat transfer rate
- Reduced manufacturing cost through better machinability
- Better castability so favors for complex geometry.

2 Microstructure

The cast irons are classified as FGI, CGI, and SGI with reference to their graphite morphology consist in form of longer flakes, worms, and spheres respectively, along with the nodularity content in the range of <5%, <20% & >25% respectively. Graphite shapes and their matrix are more visible through 3D deep-etched scanning electron micrographs shown in Fig. 1 [5]. Compacted graphite interlock into the iron matrix, as a result, it furnishes strong bonding with iron whereas round edges resist the crack formation so overall we can observe the superior strength in CGI as compared to FGI.

According to ISO 16112 standard [3], CGI graphite particles are predominant in the vermicular form (equivalently type IV per ASTM A247 or form III per ISO 945-1). The spheroidal graphite content is referred in % of nodularity detected by image analysis per the criteria mentioned in the SinterCast nodularity rating chart [6] which depends on the roundness shape factor to quantify each particle between compacted or nodular, if their roundness shape factor is <0.525 or >0.625 respectively.

Matrix of ferrite and graphite forms while the austenite decomposes during the eutectoid transformation [7]. This process requires carbon reallocation, which is accomplished by carbon diffusion to graphite from austenite. This graphite morphology is critical for ferrite growth to determine the number of prism planes in the structure. Microstructure formation is sensitive to various melt treatment elements, alloys, and process parameters which are extensively discussed later hereby. Stefanescu et al. [8] studied the compacted graphite growth while solidification and observed the graphite platelets grown in the a-direction and stack in the c-direction which coarser than FGI.

3 Chemical Composition

3.1 *Melting Treatment Elements*

The graphite morphology transformation from flake to compacted form is accomplished through base metal treatment with the addition of graphite shape formation elements such as Rare Earth, Magnesium, Titanium, Aluminum, and Calcium. The quantity and combination of elements are the functions of the liquid treatment method and many other parameters discussed in the melting process section of “Foundry Practice for Cast Irons” [9]. The optimized sulfur S range for CGI production is correlated with reference of Ce, Ti, Al addition along with Mg by Nechtelberger et al. [10].

3.2 *Alloying Elements*

The tin, molybdenum, copper, and aluminum alloys can be used for CGI as-cast morphology change from ferrite to pearlite. Its typical quantities are 0.48% Cu or 0.033% Sn [11], 0.5–1% Mo [12], and up to 4.55% Al [13, 14]. As Martinez et al. [15] studied the effect of nickel, copper, and tin on composition matrix ranging from CGI to FGI and subsequently observed that although such alloys are great promoters of pearlite, those are minimally effective for CGI where Mg contains in the range of 0.04–0.15% [15] except Ti, whose impact is evident for 95% pearlite generation. Saito et al. [16] studied Mg influence on effect of tellurium for graphite spheroidizing inhibition and found that Mg samples of 0.020 mass%, the spheroidal nodule shape deteriorating with excessive tellurium content because it consumes Mg which is a spheroidizing element in treatment metal.

3.3 *Carbon Equivalent*

Compacted graphite irons characteristics are stated, from hypoeutectic carbon equivalence of 3.7 to hypereutectic carbon equivalence of 4.7 along with silicon of 1.7–3.0% and 3.1–4.0% of carbon content [14, 17, 18].

For a given section size, the reciprocal behavior of carbon and silicon influences the casting properties. Hence, it is essential to define balanced carbon and silicon content as proposed by Cornell et al. [19]. Eutectic composition is favorable to achieve the optimum casting properties for the specimen of 10–40 mm of thickness.

3.4 Sulfur Content

Typically, CGI is being produced with sulfur within the range of 0.07–0.12% [20]. With such a higher sulfur content, it needs more alloys for metal treatment to balance the residual sulfur in the range of 0.01–0.02%, after the treatment [14].

4 Mechanical Properties

The FGI, CGI, and SGI mechanical and physical properties are primarily varied by their graphite morphology. Compacted graphite is interconnected, thicker, and shorter with rounded ends in contrast to longer and sharp-ended FGI flake graphite. The CGI graphite morphology elongates more than that of FGI underrated loads. The Dawson et al. [21] performed various mechanical tests using many of the ASTM grades of FGI and SGI which later compared in Table 1 of “Compacted Graphite Iron: Cast Iron Makes a Comeback” [21], with the SinterCast CGI (0–15% nodularity without flakes and addition of titanium) properties.

SinterCast CGI properties are tabulated in Table 1, which are intermediate mechanical and thermal properties as compared to FGI & SGI. The metallic material’s mechanical properties are not only substantiated by its mechanical strength but corresponding strain or elongation capacity also matters. FGI materials break around 1% of elongation under uniaxial tensile load so it’s not preferred for high-pressurized product application. Although CGI exhibits the intermediary strength, its ductility and thermal capacity is close to SGI. This makes it an ideal choice for the application where mechanical and thermal loads act simultaneously, such as IC engine components. At room and elevated temperatures, mechanical properties are sensitive to composition, nodularity, matrix structure, and section size. As described earlier, nodularity and matrix structures are also primarily influenced by many of the operational and chemical parameters.

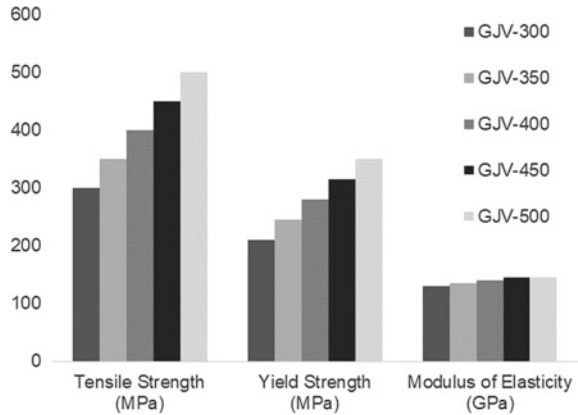
4.1 Tensile Strength

Cast irons’ tensile strengths are primarily dominated by pearlite, nodularity, and graphite morphology. The superior strength of CGI compared to FGI is because of

Table 1 SinterCast CGI mechanical properties [21]

Iron type	Matrix structure	Tensile (MPa)	Modulus (GPa)	Fatigue (MPa)	Hardness (Brinell)
CGI	Ferritic	330–400	135–145	155–185	140–180
	Pearlitic	410–580	140–150	195–225	200–250

Fig. 2 CGI minimum strengths accordance to ISO 16112 [3]



its worm-shaped graphite rather sharp graphite edges which are prone to abrupt crack propagation. As experimented by Shao et al. [22], the 0.2% yield strength negligibly improves but the ultimate tensile strength significantly rises for predominant pearlitic cast irons with the increment of nodularity content. However, 20–25% of sudden drop evident for strengths in the presence of even small fraction (1–5%) of flake graphites.

The flake graphite morphology behavior reveals that tensile strength deteriorates by 10% upon an increment of every 0.1% of carbon equivalent for FGI class-30 [23]. As shown in Fig. 2, according to ISO 16112 [3], CGI GJV-300 to GJV-500 grades minimum mechanical strengths gradually increase such as ultimate strength for 300–500 MPa, yield strength for 210–350 MPa. It has been studied that the tensile properties of CGI are not much sensitive with variation in CE than for FGI [18] but it is evident that strength increases with silicon addition.

4.2 Modulus of Elasticity

The pearlitic and ferritic matrices of CGI exhibit a modulus of elasticity for 130–160 GPa [3, 10] which is slightly lower than SGI. This can be justified through shaper and wormed graphite morphology of CGI than that of SGI spheroidal graphite. As shown in Fig. 2, according to ISO 16112 [3], the modulus of elasticity The CGI & SGI elastic modulus remains linear while initial loading because of their ductility but the same behavior does not observe for FGI because of its poor ductility.

Modulus of elasticity (Elastic modulus) gains gradually for predominate pearlite along with nodularity content until 50% but then after there is negligible gain in it as studied by Dawson et al. [24]. Similar to strength deterioration, elastic modulus also drastically falls in presence of flake graphite.

4.3 Compressive Strength

Nechtelberger et al. [25], studied the tensile-compressive strengths behavior of 179HB ferritic CGI and later compared it with SGI. The study revealed that CGI 0.1 and 0.2% compression proof strength are higher than that of tensile strengths but such differences are minimal in SGI.

Shao et al. [22], conducted the experiments to determine the compressive properties of CGI with a variation of pearlite content and found that unalloyed pearlite CGI compressive yield strength is approximately 20% higher than FGI (GG 30).

4.4 Impact Strength

Pearlite content in the iron is one of the critical constituents to define impact strength. It has been observed that at low pearlite (<10%) components pose great toughness which drastically reduces with the increment of pearlite so higher pearlitic CGI offers impact strength close to SGI. Charpy impact energy measurement highlights that CGI which is developed from the base iron of SGI has better impact energy absorption than that developed from FGI [14].

Crack initiation under impact loading proceeded in ferritic graphite fracture at its interface through trans-granular cleavage. The graphite fracture predominately occurs along the boundaries of graphite crystallites [26]. Gregorutti et al. [27] experimented that ferritic structure absorbs the highest energy (33.3 J) followed by austempered (17.2–28.4 J) structure over pearlite (14.3 J), which ultimately defines their toughness capacity.

4.5 Fatigue Strength

The fatigue behavior underlying repetitive and reversal tension–compression loadings, which prompts for premature failure of the substance. The wormed graphite shape of CGI shows prominence against notch sensitivity than flakes graphite. As a result, CGI reveals better fatigue strength than FGI. The pearlitic CGI fatigue limit at room temperature is close to 200 MPa, which degrades further to 155 MPa at 400 °C. Such a limit is almost double that of class30 FGI. As CGI has an excellent thermal capacity, it helps to gain the thermal fatigue strength too to improve the fatigue life, which is 200–400% higher than FGI [28]. These virtues make CGI for preferred choice for engine cylinder block manufacturing.

Superior fatigue strength is evident in un-notched pearlitic structures [29] which are compared with notched structures which are relatively 25% better than ferritic CGI. The fatigue endurance ratio studied to 0.44–0.46 for a ferritic to a pearlitic higher-nodularity CGI [30]. CGI & SGI are equally notched sensitive to fatigue notch

factors of >1.71 , whereas FGI is minimally notched sensitive for a notch factor <1.5 [25]. The fatigue behavior performance of pearlitic CGI is close to ferritic ductile iron. Whereas, ferritic CGI torsional fatigue limit under fully reversed loading matches SGI and has a good correlation with the bending loading behavior [31].

4.6 Hardness

During the solidification of CGI, ferritic matrices formation happens rather than pearlite; due to graphite growth and diffusion. So promoting pearlite formation, some of the stabilizing elements like copper and tin have to add in base iron which gains 10–15% superior hardness than FGI. The hardness increment rate is linear to the rate of change of pearlite structure with the presence of chromium, manganese, titanium, along other trace elements in the raw materials [22]. The Brinell hardness remains constant until 90% of nodularity.

5 Physical Properties

5.1 Thermal Conductivity and Expansion

Graphite morphology in cast iron enhances the thermal conductivity because of graphite's metallographic constituents [10]. The thermal conductivity is influenced by graphite orientation. It is up to four times higher for the graphite orientation parallel to the basal plane than perpendicular [32]. Apart from graphite morphology, nodularity is also influencing the thermal conductivity [33].

Thermal conductivity of steel and influence of alloying elements can be calculated by Eq. 1. [25],

$$\lambda = \lambda_o - \ln \Sigma C \quad (1)$$

where,

λ = Alloyed steel thermal conductivity

λ_o = Unalloyed steel thermal conductivity

ΣC = Sum of alloying elements in %

5.2 *Machinability*

As we studied earlier, CGI offers superior strength over FGI due to its graphite morphology but simultaneously it also increases its hardness and machinability. CGI machinability is widely influenced by (i) graphite shape, (ii) pearlite content, (iii) chemical elements (Mn, Si, Ti, S, Sb, Cr) and (iv) various inclusions [34]. FGI's excellent machinability is caused because of the tight graphite flakes interconnection, which reduces the mechanical strength and increases the fracture crack propagation intensity; which helps ease chip formation. Machinability worsens while graphite transformation from flakes to spheroidal and nodularity gaining for CGI & SGI constituents [34, 35]. Therefore, chip formation behavior is intermediate between FGI & SGI [36].

The study shows that upon pearlite increment, mechanical strength and hardness increase proportionately so fully pearlitic CGI is quite difficult to machine as compared to fully pearlitic FGI. But, the study reveals [34] that still CGI machinability favors slower (150 m/min) cutting and feeding speed. In FGI, manganese sulfide (MnS) is formed by the sulfur reaction which lubricates the cutting surface whereas, CGI forms the MgS by reaction of sulfur with faded Mg in molten metal. Such MgS content gains superior hardness over MnS. As a result, the machinability worsens in CGI than FGI [37]. Moreover, Titanium (0.1–0.2%) is added in CGI as a graphite stabilizer which forms hard cubic of titanium carbonatite, and tool wearing [21] increases subsequently. Titanium content increases the drilling thrust by 50% relatively for non-titanium bearing [38].

5.3 *Damping Capacity*

The damping capacity is the inherent material capacity to absorb the energy of the vibratory body upon impacting force. This is one of the critical properties to expedite its industry-wide application relevance to the noise, vibration, and harshness domain.

Damping capacity is primarily reliant on graphite shape, nodularity and forms of microstructures. The dense graphite presence in FGI acts as a damper against vibration and continuously reflects off in flakes. Once flakes graphite transforms to patch, the damping capacity decreases rapidly for CGI and SGI [22]. Relative damping capacities are 1.0:0.35:0.14 for FGI:CGI:SGI. Damping capacity also relies on elastic modulus [39] but it's not influenced by carbon and pearlite content [22]. However, this can vary within 5–10% with a change in graphite size and its density [18].

6 Castability

6.1 *The Fluidity*

The molten cast iron fluidity widely depends on the carbon, silicon contents and instantaneous temperature. However, the morphology of structure also matters on top of these variables. Flake graphite iron has superior fluidity as compared to spheroidal graphite iron. CGI can be easily poured for thin sections with higher carbon equivalent.

6.2 *Shrinkage Characteristics*

CGI casting offers better shrinkage and eliminates the porosity as compared to SGI because of mold wall movement tendency. The shrinkage volume is 4.1% for FGI, 4.8% for CGI, and 7.0% for SGI for eutectic cast irons. Solidification expansion is 4.4 for SGI, 1.0–1.8 for CGI with reference to 1.0 of FGI [40]. CGI has a greater casting yield because of the riserless gating system.

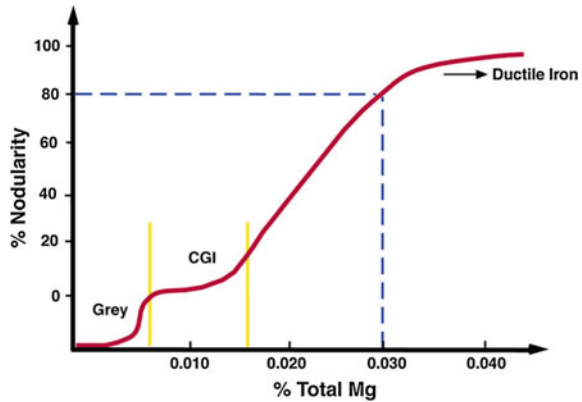
6.3 *Chilling Tendency*

The cooling zone develops at the interfacing of the super-heated metal and cold mold wall. Metal is rapidly solidifying near the cooling zone. There is a broader opinion that CGI has an intermediate chilling tendency but it has the highest chilling tendency because its effect intensifies for 6–64% of nodularity [41].

7 Production of Compacted Graphite Iron Castings

CGI microstructures stabilization range is too narrow, so it poses a substantial challenge to maintain the consistent microstructure for mass production in the foundry. A commercial CGI grade has been specified for 10–20% of nodular graphite particles with no graphite flakes [21, 24, 42]. However, mostly the stable range is found approximately for 0.008% Mg as shown in Fig. 3 [43], But in reality, Mg content is even low because active Mg fades at a rate of 0.001% per every five minutes. Apart from accurate chemical composition to produce consistent CGI, there are uncertain variables like foundry process control and workmanship that play a crucial role. Hence, it is not advisable to rely on the sandwich method for Mg fading, a one-step base metal treatment process. Moreover, the active oxygen and/or sulfur content consume the active Mg which moves Mg. stable range to the higher side.

Fig. 3 Nodularity sensitivity as a function of Mg% for cast irons [43]



Hence, it is preferred to adopt a measure-and-control kind of two-step controlled treatment approach to mitigate the risk poses by defined uncertainty. In this process, molten metal solidification behavior is measured once the base treatment process is over because by this time all the variables’ dominance exhaust. The residual nodular controlling elements are being added to gain the desired solidification behavior if it is measured to do so. Ultimately, this two-step treatment helps to counter the chances of the flake’s graphite formation efficiently. It’s difficult for traditional foundries to adopt the two-step approach because it needs a state-of-the-art control technology set up to accomplish the aim.

7.1 Variables Sensitivity Study

7.1.1 Spheroidizing (Mg) Element

There are approaches for CGI production either to use spheroidizing element Mg using FGI as a base iron or use anti-spheroidizing element Ti in SGI—to develop the intermittent CGI microstructure. As Dawson [44] studied, by addition of 0.001% Mg in base metal, the flake patch structure can be transformed into a fully compacted microstructure, which enhances ultimate tensile strength to 450 MPa from 320 MPa by conversion of fully pearlitic from flake patch microstructure.

Residual Mg% promotes nodularity in the thinner section, but in the thicker section, the solidification rate deteriorates, which fades residual Mg% effectiveness for nodularity. Following Eq. 2, the empirical formula is derived to estimate the nodularity in the produced alloys of 10–50 mm of section thickness [45]

$$\text{Nodularity}\% = 3091.4 \cdot \text{Mg}\% + 50 \cdot \text{Mg}\%(x - 30) - 9.5 \tag{2}$$

$$\text{For } 0 < \text{Mg}\% < 0.03$$

where,

$$\text{Mg \%} = \text{Residual Mg content}$$

$$x = \text{Casting thickness in mm}$$

7.1.2 Anti-spheroidizing (Ti) Element

The Titanium Ti acts as an anti-spheroidizing element to promote compacted graphite shape along with pearlite content. Ti is potent to form carbide; as a result, pearlite content also gains simultaneously. It is studied that 0.15 wt% of Ti addition improves 10% of the compacted graphite content while 5–10% of pearlite content [46]. However, pearlite content reduces with specimen thickness increment. Moreover, Ti addition helps to widen the CGI stable range for Mg for successful CGI production.

Although the anti-spheroidizing element is a reliable approach for CGI development, it has limited exposure for certain precision manufacturing applications because Ti tends to form carbide and nitro-carbide, which makes the metal very hard, which affects the machinability and tool life. Alonso et al. [47] studied how the graphite nucleation is influenced by the addition of Ti in CGI formation by restricting the growth of Mg–Ca sulfide.

7.1.3 Inoculant

The inoculant helps to promote graphite precipitation and growth, along with iron solidification. Hence, for reliable CGI production, it is essential to control inoculants simultaneously along with the controlling of graphite shape forming elements (magnesium, sulfur, lanthanum, calcium, cerium, oxygen). Regordosa et al. [48] studied the impact of inoculation and other chemical composition on CGI microstructure change while solidification.

7.1.4 The Method of Adding the Nodulizer

There are primarily sandwich and injection treatment methods are practiced for Mg addition in the molten metal. The sandwich method is quite reliable over the injection method because it helps to prevent the evaporation of Mg to intact its influence for nodule formation.

7.1.5 Porosity and Shrinkage

As we studied earlier, CGI has better castability than SGI due to lower Mg content so that the chances of having casting defects such as cold shuts, misruns, and any defects pertinent to shrinkage and porosity are significantly reduced. However, porous defects are desirable for some of the special applications where is a need for high strength and greater energy absorption capacity at a lightweight. Dawson et al. [49] proposed a method to develop porous CGI castings. The shrinkage sensitivity is quite progressive, with increments of nodular and Mg content for FGI to SGI transformation [50].

7.1.6 Holding Time on Nodularity

Re-melting of the base material is having high nodularity (around 96%) and a high residual percentage of Mg ($\approx 0.065\%$). With residual Mg control, the nodules transit to CGI with increased holding time. Vermicular graphite follows linear development along with holding time [43].

7.2 Process Control

To establish the quantitative and qualitative CGI production process, foundries need to focus on the two aspects, (i) Appropriate base metal treatment approach, and (ii) Base metal treatment monitoring and control.

7.2.1 Base Metal Treatment Approaches

However, it is not always commercially viable to produce the CGI using state-of-the-art control systems if their production volume is not high enough to yield the breakeven. Traditionally, it is practiced to produce stable CGI by Ti addition [51] for lower precision and low-volume production. Ti addition prevents nodule formation which widens the stable CGI plateau range. As researched by Schelling [52], 0.2% Ti addition stabilizes CGI formation for 50% nodular content. This method is fair where limited machining is required because Ti reacts with carbide which reduces the machinability and tool's life.

To overcome the challenges of Ti addition, the researchers [10, 40, 53] have also explored the alternative approach to develop CGI using the addition of Rare Earth (RE) metals instead of Mg. Many salient advantages are using RE metals. Like, (i) those are not aggressive to promote spheroidal graphite formation, (ii) Reduces fade rate [42] through its more stable oxides and sulfides and, (iii) Makes molten metal highly reproducible rather volatile Mg added metal. However, RE raw metal prices

are costlier than that of Mg. also these are prone for carbides formation especially for rapid cooling.

7.2.2 Treatment Process Monitoring and Control

The continuous monitoring of molten metal chemical composition is crucial to control the desired microstructure formation. Traditional foundries are lively monitoring molten metal composition using a spectrometer and controlling the recipe. However, the spectrometer shows the weightage% of each respective chemical; but it has limitations either to extract the information regarding chemical compounds prevailing for graphite morphology formation or to determine the influence of active oxygen and sulfur content over resultant behavior of metal with the production process and raw material mixture variation. Conversely, thermal analysis is primarily based on the feedback of the solidification behavior of 200 g (7Oz) of a batch iron sample. For precision and high-volume casting production, the chemical analysis technique is not favorable due to defined limitations. Hence, thermal analysis techniques have been widely adopted [44, 54].

This technique works on thermal analysis measurement of molten metal after the addition of inoculant and modifying (Mg, RE, Ti) elements. Upon feedback of thermal analysis, magnesium and/or inoculant are added in form of cored wire as

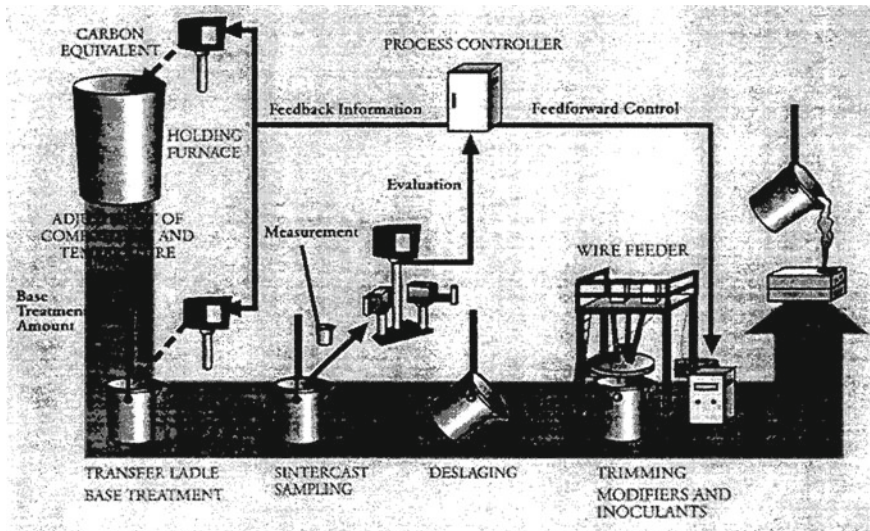


Fig. 4 Online SinterCast process control system for CGI production [56]

a corrective action, before going for pouring. The SinterCast has innovated a state-of-the-art thermal analysis control system that works on tightly integrated feedback-enabled process flow as shown in Fig. 4. In this process; the microstructure is correlated with reference of graphite growth and latent heat released by solidifying samples in the bespoke container. The SinterCast thermal analysis sample is got by immersing the steel-walled sampling device into the molten metal after the base treatment [55].

Stefanescu [57] explained the conventional cooling curve-based direct thermal analysis technique using a sand cup. Unlike sand cup, metallic cup device helps to avoid oxidation during iron pour in and lead for precise measurement of undercooling. A reactive material is layered on the inner surface of a sampler to enable Mg fading measurement. The sampling device is built with a couple of reusable thermocouples which are placed at the bottom and thermal center. The thermocouples placed at the bottom predict the iron behavior after 0.003% of Mg fading whereas the central one determines the treated base iron. In the etched cross-section of SinterCast samples, undercooled D-type flake graphite formation took place because of the loss of active magnesium [55]. The flake graphite content affects the thermal analysis cooling curve, which is referred to by the bottom thermocouple. This brings uncertainty to outline the abrupt transition between CGI and FGI.

8 Literature Gap and Future Direction

It is observed that there is a great consensus among the researchers about the CGI microstructure, chemical composition, and production process sensitivity. However, limited efforts are made to overcome the known production challenges. During such a research study, it is attempted to survey the feedback from many of the reputed foundries and foundry experts for CGI casting development. During this exercise, it is noticed the confidence level deficiency for reliable CGI production. This may be because of limited exposure and uncertain process control. Still, some of the market players only could succeed to establish thermal analysis feedback-based process control technology and their very limited information is available to the public about intrinsic working philosophy. Apart from this technique, there is no credible alternative process is innovated so far. Such production limitations restrict the industry's enthusiasm to expand the CGI application base.

Hence, a great opportunity exists to conduct extensive study to bring insight into existing process control technology. This process knowledge may help further to innovate a viable CGI production process and its control philosophy, which can be afforded by traditional metal foundries across the globe.

9 Conclusion

The narrated information shows the CGI as a prominent material to bridge the gap between FGI and SGI application need. However, it is critical to address the known CGI production challenges simultaneously to make it feasible for cost-effective product development.

References

1. Alonso G, Stefanescu DM, Larrañaga P, Suarez R (2016) Understanding compacted graphite iron solidification through interrupted solidification experiments. *Int J Cast Met Res* 29:2–11. <https://doi.org/10.1179/1743133615Y.0000000020>
2. Riposan I (2018) Modification and inoculation of cast iron, cast iron science and technology 1:160–176. <https://doi.org/10.31399/asm.hb.v01a.a0006315>
3. Compacted (Vermicular) Graphite cast iron—classification. International Standards Organization (2016)
4. Hahnel M, Wisniewski H (n.d.) Method and device for fracture-splitting a workpiece
5. Grzesik W (2017) Advanced machining processes of metallic materials
6. SinterCast Nodularity Rating Charts (1997)
7. Ko M, König M (2010) Literature review of microstructure formation in compacted graphite iron. *Int J Cast Met Res* 23:185–193. <https://doi.org/10.1179/136404609X12535244328378>
8. Stefanescu DM, Alonso G, Larran P, Suarez R (2018) A comparative study of graphite growth in cast iron and in analogous systems. *Int J Metalcast*. <https://doi.org/10.1007/s40962-017-0204-1>
9. Davis JR (1996) ASM specialty handbook cast irons—9.2 melting practice. *ASM Int*, 147–149
10. Nechtelberger E, Pühr H, von Nesselrode JB, Nakayasu A (1982) Cast iron with vermicular/compacted graphite—state of the art development, production, properties, applications. In: 49th international foundry congress, Chicago
11. Fowler J, Stefanescu DM, Prucha T (1984) Production of ferritic and pearlitic grades of compacted graphite cast iron by the in-mold process. *Trans AFS* 92:361
12. Ziegler KR, Wallace JF (1984) The effect of matrix structure and alloying on the properties of compacted graphite iron. *Trans AFS* 92:735
13. Nechtelberger E, Hummer R, Thury W (1970) Aluminum-alloyed cast iron with vermicular graphite. *Giesserei Prax* 24:387
14. Cooper KP, Loper CR Jr (1978) A critical evaluation of the production of compacted graphite cast iron. *Trans AFS* 86:267
15. Martinez F, Stefanescu DM (1983) Properties of compacted/vermicular graphite cast irons in the Fe-C-Al system produced by ladle and in-mold treatment. *Trans AFS* 91:593
16. Saito R, Maruyama T, Nakamura T, Yanagitani H, Sakai T, Nakamoto K (2018) Influence of tellurium addition to spheroidal graphite cast iron on the number of graphite particles. *Int J Metalcast*. <https://doi.org/10.1007/s40962-018-00292-y>
17. Evans ER, Dawson JV, Lalich MJ (1976) Compacted graphite cast irons and their production by a single alloy addition. *Trans AFS*. 84:215
18. Sergeant GF, Evans ER (1978) The production and properties of compacted graphite irons. *Br Foundryman* 71:115
19. Cornell HH, Loper CR Jr (1985) Variables involved in the production of compacted graphite cast iron using rare earth-containing alloys. *Trans AFS* 93:435
20. Ruff GF, Vert TC (1979) Investigation of compacted graphite iron using a high sulfur gray iron base. *Trans AFS* 87:459

21. Dawson S (1994) Compacted graphite iron : cast iron makes a comeback
22. Shao S, Dawson S, Lampic M (1998) The mechanical and physical properties of compacted graphite iron 397–411
23. Walton CF, Opar TJ (1981) Iron castings handbook. Iron Castings Society
24. Dawson S (1999) Compacted graphite iron: mechanical and physical properties for engine design. VDI Berichte 85–105.
25. Nechtelberger E (1980) The properties of cast iron up to 500°C. In: English, Technicopy Ltd., England
26. Heiber AF (1979) AFS Trans 87:569
27. Gregorutti RW, Grau JE (2014) Mechanical properties of compacted graphite cast iron with different microstructures. *Int J Cast Met Res* 27:275–281. <https://doi.org/10.1179/1743133614Y.0000000118>
28. Park YJ, Gundlach RB, Janowak JF (1987) Effects of molybdenum on thermal fatigue resistance of ductile and compacted graphite irons. *AFS Transactions*. 87–90:267–272
29. Shikida M, Kanayama Y, Nakayama H (1986) Strength and crack growth behaviors of compacted graphite vermicular cast iron in rotating bending. In: 29th Japan congress on materials research, pp 23–28
30. Loper CR, Lalich MJ, Park HK, Gyarmaty AM (1980) The relationship of microstructure to mechanical properties in compacted graphite irons. *AFS Trans* 80–160:313–330
31. Sumimoto H, Nakamura K, Umeda Y (n.d.) Relationship between graphite morphology and fatigue limit in compacted vermicular and ductile cast iron. Kinki University research report, 22
32. Mayer-Rassler E (1967) *Giesserei Prax* 54:348
33. Monroe RW, Bates CE (1985) *Trans AFS* 93:615
34. Dawson S, Hollinger I, Robbins M, Daeth J, Reuter U, Schulz H (1999) The effect of metallurgical variables on the machinability of compacted graphite iron. Design and machining workshop—CGI
35. Cohen PH, Voigt RC, Marwanga RO (2000) Influence of graphite morphology and matrix structure on chip formation during machining of ductile irons. *AFS casting congress, Pittsburg*
36. Reuter U (1999) Wear mechanisms in high-speed machining of compacted graphite iron. Design e machining workshop—CGI
37. Ulrich R (2000) The wear process of CGI cutting and machining developments, compacted graphite iron—machining Workshop. Darmstadt, Germany
38. Murthy VS, Seshan S (1984) Characteristics of compacted graphite cast iron. *AFS Trans* 84–76:373–380
39. Kurikuma T, Makimura Y, Tada M, Kobayashi T (1998) Effects of graphite morphology and matrix microstructure on damping capacity, tensile strength and Young’s modulus of casting irons, *Jpn Eng. Soc* 68:876–882
40. Stefanescu DM, Dinescu I, Craciun S, Popescu M (1979) Production of vermicular graphite cast irons by operative control and correction of graphite shape. 46th International Foundry Congress. Spain), Madrid
41. Stefanescu DM, Martinez F, Chen IG (1983) Solidification behavior of hypoeutectic and eutectic compacted graphite cast irons—chilling tendency and eutectic cells. *Trans AFS* 91:205
42. Skaland T (n.d.) High rare earth treatment of compacted graphite iron. *AFS congress*, panel 02-173
43. Hernando JC (n.d.) New Experimental technique for nodularity and Mg fading control in compacted graphite iron production on laboratory scale. <https://doi.org/10.1007/s11661-017-4315-3>
44. Dawson S (2002) Process control for the production of compacted graphite iron
45. Kim S, Cockcroft SL, Omran AM (2009) Optimization of the process parameters affecting the microstructures and properties of compacted graphite iron. *J Alloy Compd* 476:728–732. <https://doi.org/10.1016/j.jallcom.2008.09.082>
46. Shy Y, Hsu C, Lee S, Hou C (2000) Effects of titanium addition and section size on microstructure and mechanical properties of compacted graphite cast iron. *Mater Sci Eng, A* 278:54–60

47. Alonso G, Larran P, Stefanescu DM, Suarez R (2020) Graphite nucleation in compacted graphite cast iron. *Int J Metalcast*. <https://doi.org/10.1007/s40962-020-00441-2>
48. Regordosa A, De Torre U, Loizaga A, Sertucha J, Lacaze J (2019) Microstructure changes during solidification of cast irons: effect of chemical composition and inoculation on competitive spheroidal and compacted graphite growth. *Int J Metalcast*. <https://doi.org/10.1007/s40962-019-00389-y>
49. AK SD, SS MN (2009) New method for the development of porous gray cast iron castings. *Int J Metalcasting*, 43–52
50. Dawson S (2009) Controlling compacted graphite iron microstructures—what’s important, In: *The Carl Loper cast iron symposium*, pp 27–29
51. Renfang W, Yuanheng P, Manji C (1994) Research on and experience in the mass production of compacted graphite iron exhaust manifolds. BCIRA conference
52. Schelling RD (1969) Cast iron with at least 50% of the graphite in vermicular form and a process for making same. U.S. Patent 3421886
53. Qiu H-q, Chen Z-d (2007) The forty years of vermicular graphite cast iron development in China. *China Foundry* 4:91–98
54. Anjos V, Baumgart W, Kloetzen O, Ribeiro CAS, Cunha J (2009) The modern thermal analysis route to the compact graphite iron production. In: *The Carl Loper cast iron symposium* (Madison, WI)
55. Guesser W, Fundiões T, Catarina S, Schroeder T, Dawson S (2001) Production experience with compacted graphite iron automotive components 071, 1–11
56. Tholl M, Magata A, Dawson S (1996) Practical experience with passenger car engine blocks produced in high quality compacted graphite iron. *SAE Tech Pap*. <https://doi.org/10.4271/960297>
57. Stefanescu DM (2015) Thermal analysis—theory and applications in metalcasting. *Int J Metalcast* 9:7–22

An Overview on Metallic and Ceramic Biomaterials



Soham V. Kulkarni, Amit C. Nemade, and Puskaraj D. Sonawwanay 

Abstract Biomaterials used in implants or clinical instrumentation are commonly used for the re-alignment, replacement, and treatment of deteriorated tissues, broken structures, or other injuries. The study of biomaterials is primarily involved in the chemical and biology field collectively known as biochemistry, biology, tissue engineering, and material science. Appropriate material selection and their characterization is crucial consideration while manufacturing medical implants. The biomaterial used for different medical implants should possess desirable properties, mechanical strength, biostability, good corrosion resistance, and biocompatibility to get acquainted in the physiologic environments. However, many important researches in biomaterial science have come focusing on improving the physical, mechanical and chemical properties regarding the material of implant and thereby improvising the implant strength. This overview examines metallic and ceramics biomaterials which are commonly used biomaterials used in medical implants while primarily focusing on the composition, mechanical properties, advantages, limitations, and applications of the materials.

Keywords Biomaterials · Biomedical · Titanium · Stainless steel · Cobalt alloys · Ceramics · Zirconia (ZrO_2) · Alumina (Al_2O_3) · Calcium phosphate · Glass ceramics · Bioglass · Bioceramics

1 Introduction

Generally, the biomedical is the branch of science which deals with biology, medical science, and particular part of engineering as it relates with the several extents of engineering. Numerous natural body movements of humans or any living tissue or

S. V. Kulkarni · A. C. Nemade · P. D. Sonawwanay (✉)
School of Mechanical Engineering, Dr. Vishwanath Karad MIT World Peace University, Pune,
India

© The Author(s), under exclusive license to Springer Nature Singapore Pte Ltd. 2022
H. K. Dave et al. (eds.), *Recent Advances in Manufacturing Processes and Systems*,
Lecture Notes in Mechanical Engineering,
https://doi.org/10.1007/978-981-16-7787-8_11

149

any organism can be related to mechanical joints like flight of the birds, swimming of the fish in water, bone joints, diving of dolphin, wings of butterfly [1]. So, this can be anticipated that biomedical science can be directly related to engineering applications.

The materials which are capable of performing human body actions are required motions they are known as the biocompatible materials the part of a living organism that can be replaced by hybrid or original conventional material that is best substitute for a living tissue called as biocompatible materials [2]. The biomaterials have ability to interact, perform, compensate and augment the same principle working like that of living organisms [3]. Biomaterials are mostly composed of ceramic, metals, or synthetic polymers. As proceeding studies in biomaterials focus on the materials having ability to heal themselves after the destruction or any damage and materials with sound foundation and rigid utilization to adapt restoring property in itself are termed as advanced bio-inspired materials [4].

Operation and infertility practices are using biomaterials with legal connect. Previously implants such as wood, rubber, glass, and metals such as iron and gold were used as biomaterials, but due to the compatibility parameter and the compensation factor of the living tissue with the material also movement hesitation in all degrees of freedom these biomaterials got fade off over the decades after the preceding years there has been a huge amount of progression in biocompatibility and biomaterials further segregates materials in chronological classes namely class 1, class 2 and class 3 biomaterials.

The class one materials are having a direct interaction with body tissues, class two materials are erratically interacted with body tissue or for the least time period interaction, class three materials are consistently augmented and interact with living tissue. The class III materials are further bifurcated in implants of bioinert type, implants of bioactive type also implant of biodegradable type. Implants of bioinert category are indirectly performing immunological reactions. Bioactive materials are related to imitating tissue operations biodegradable implants are capable of regeneration and recycling completely decomposable [5].

The human body tissues that include the upper body tissues, lower body tissues, bone tissues, cardiovascular tissues for all mentioned parts superlative substitute functions the particular required motion, action and interaction are formulated as 'Biomaterials'. Advance encapsulation of biomaterials is 'Materials originated from synthetic and natural intact with blood, tissues, biological fluids, intended for use for prosthetic, diagnostic, therapeutic, and storage application without harmfully affecting the living tissue and its constituents [6].

Biocompatible materials have versatile areas of effective utilization in joint replacements, Bone substitutes, Bone filling materials, Hybrid muscle or ligament, Dental implants, Cardiovascular implants, Cochlear replacements.

2 Biomaterials

2.1 *Metallic Alloys*

Due to the desired chemical and mechanical properties, metal and their compositions are being used in medical field for a long time. Medical implants such as screws, fixation plates, dental implants, spinal rods are usually made up of metal and alloys of Titanium and its alloys (Ti6Al4V). Additionally, other metals including Stainless Steel (317L), aluminum alloys, tungsten alloys, and cobalt chromium alloys (Co Cr) have created rapid growth to develop other medical implantation products such as medical devices, bone fixation devices, surgeon equipment, and orthodontic instruments. The other precious metals having good mechanical properties such as gold, platinum, and the alloys of these metals are often utilized in dental applications [7]. The selection of the metal or alloy for a specific medical application primarily depends upon the factors such as its mechanical properties, chemical properties, resistance to corrosion, biocompatibility, biostability, and effective low cost [8].

The main criteria for selection of biomaterial are based on the application of the implant, its function, and the biological environment. The chemical and mechanical properties of metal or alloys have immense importance while designing orthopaedic, dental, and cardiovascular implants. While designing medical implants for orthopaedic and dental applications where bearing load comes into action, mechanical properties of the metal such as high fatigue limit and tensile strength have vital importance. Metallic implants have good load carrying capacity than implants made of polymeric and ceramic biomaterials. However, metallic implants have lower elastic modulus and lower strength in contrast to polymeric and ceramic materials [9] may affect its durability, biocompatibility, and implant life. This property to resist corrosion can be significantly reduced by using appropriate composition of metal and by avoiding the unnecessary crevices, pits, and notches in the implant [10].

2.1.1 **Titanium**

Because of Titanium's important physical, chemical, and mechanical properties and its excellent resistance to corrosion and biocompatibility Titanium has evolved as excellent material for biomedical applications in dental, cardiovascular, and orthopaedics applications. Titanium as firstly discovered by Wilhelm Gregor, initially utilized for applications in aerospace and defense industries. Because of its lightweight and high load carrying capacity, composition of Titanium, i.e., Ti alloys were then introduced in dental implants [11].

Titanium usually offers highest specific strength as compared to other alloys but has low metal density of 4.8 gm/cm^3 . Because of its insufficient fatigue strength, pure form of Titanium can be used in very limited applications. Improvement in the mechanical and overall strength of titanium is effectively attained by composition alteration with alloying constituents such as Mo, Zr, Nb, Al, V, etc. Among the titanium

Table 1 Mechanical properties of pure Titanium and TC4, Ti64 alloy [12]

Material	Ultimate tensile strength (MPa)	Yield strength (MPa)	Fatigue strength in air (MPa)	Fatigue strength in PBS	Hardness value
Ti pure	241–560	172–480	120–275	100–200	70–100 BHR
Ti–6Al–4V (TC4, Ti64)	896	827	250–300	250	30–39 HRC

alloys including TC4, Ti64, Titanium grade 7 alloy with zinc 30, Ti–15V, and Ti–20Cu, Ti6Al4V is mainly used as dental implants because of its sound mechanical and chemical properties (see Table 1) [12].

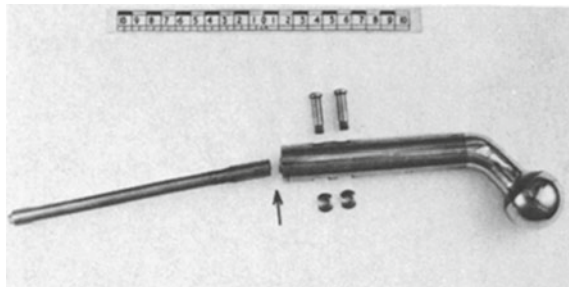
The ability of resistance to corrosion of TiO_2 surface layer separate the titanium surface from electrolyte thereby providing high resistance to corrosion. However, mechanical stress and exposure to oxygen may corrode titanium like many other base metals. The clinical research suggested that Titanium provides high resistance to corrosion when used with human tissues. It is however it should be noted that galvanic coating over titanium surface use with other metallic restorative materials main result in corrosive environment [13, 14].

Titanium exhibits excellent biocompatibility and tissue response when alloyed with appropriate alloying elements. It is important to note that aluminum and vanadium result in allergic effects on the surrounding tissues. Therefore, it is proposed to practice Ti alloys like Ti5Al2.5Fe, Ti15Zr4Nb2Ta, and Ti6Al7Nb manufactured by alloying elements Mo, Ta, and Zr replacing Al and V [12].

Ti has a comparatively low strength of 500 MPa but has a significantly high specific strength 288 N m/kg with a relatively low modulus of elasticity of 80 GPa. Table 1 illustrates the specific mechanical properties of Titanium and its alloy TC4, Ti64. Titanium alloy has same fatigue strength in air as in PPS approx. 250 MPa, which signifies that Ti-alloy exhibited no significant change in fatigue behavior in PBS [12].

Additionally, Titanium has poor shear strength and low tensile ductility which makes Titanium alloys unsustainable for bone screw and articulating surface applications as can be seen in Fig. 1 showing fatigue fracture of Titanium THR implant. Strength and elastic modulus of the material of the vital considerations by selecting

Fig. 1 Fracture of titanium THR implant due to fretting fatigue [15]



implant material. Therefore, implants made up of Titanium should have fatigue strength and high surface quality [15].

2.1.2 Stainless Steel

The SS alloy is a composition of Si, Cu, Ni, Mo, Cr, carbon, and Mn. Stainless steel is usually known for its superior resistance to corrosion. This is due to the coat of chromium on the external surface which cut off the oxygen contact, enabling the restriction to oxidation. Many clinical research and developments are carried out over the past years to augment the mechanical also chemical characteristics of SS alloys by adding different alloying elements.

Another development found that adding Ni in the composition can improve the ability of alloy to resist corrosion and thereby 317 Stainless Steel was introduced. Also, it was suggested that decreasing the carbon content in the composition effectively improves alloy's property to resist corrosion. This result in finding of another important SS alloy, 317L SS [10, 15]. The chemical composition of 317L Stainless steel comprises Cr—17.0 to 18.0%, Ni—10.0 to 14.0%, S—0.03%, C—0.03% Si—1.0%, P—0.045% and Fe in balanced form.

As shown in Fig. 2, 317L SS has been used in implants for knee replacement and ankle replacement.

Due to the desirable properties such as biocompatibility, high durability, excellent mechanical properties, and low cost required for implant manufacturing, 317L SS has been most commonly used implant material over the last few years [18–20].

After the implantation of 317L SS, further studies showed the biocorrosion of the implant resulted in Nickel (Ni) ions discharge in human physique by means of tissues surrounding the implant. This release of Ni ions may cause adverse effects on the connecting tissues, organs, and human health. Since, Nickel (Ni) is an important alloying element in the composition of 317L SS, austenitic type of characteristic microstructure was preferred over the martensitic SS) [20].

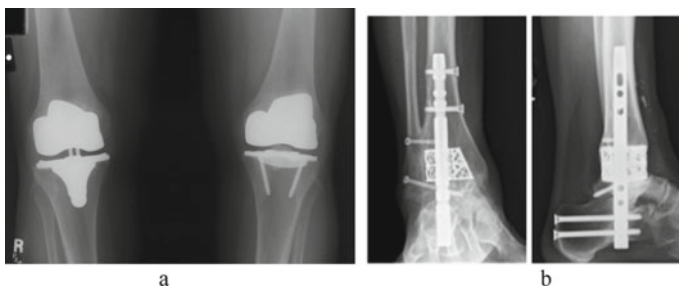


Fig. 2 Use of 317L (ASMT F138) stainless steel in **a** knee replacement, **b** ankle replacement implants [16, 17]

Martensitic SS is usually preferred in surgical instruments and dental implants while austenitic type of Stainless steel is used in large number of non-implantable medical devices as well as in total hip replacements [21]. The resulting implant made of 317L SS (austenitic) alloy was later found to have poor durability and high corrosion over its life thereby limiting its applications in the field of medical implants.

The new development in 317L SS alloy was made by introducing high concentrated nitrogen replacing Ni in the composition. The composition with high concentrated nitrogen, ASTM F2229 is tabulated in Table 2. The Ni-free SS was found to have excellent wear and corrosion resistance, high fatigue strength in contrast to the previously developed 317L SS [8, 21].

The formation of chromium carbide element in the SS composition causes corrosion and pitting of the metal at its grain boundaries. This results in the fatigue failure of the implant at the most corrosive surface. The introduced Nickel free, highly concentrated steel with grade F2229 according to American Society of Testing and Measures (ASTM) found to be more resistant and exhibited high durability in fatigue failure [22, 23]. Table 3 shows the mechanical properties of 317L SS of grade F138 in ASTM and Nickel free high concentration SS (ASTM F2229).

It is also important to note that, the stainless steel alloys are not much effective against pitting corrosive prevention also poor results in fatigue failure reduce the life of the implant. However, Nickel free, highly concentrated ASTM F2229 showed effective corrosive prevention, wear, and fatigue as no Ni ions were released to the human body [12, 24].

2.1.3 Cobalt Alloys

The CoCrMo alloy comprises Cobalt as the pure metal and C, Mo, W, Ni, and Cr as alloying metals in the composition. The role of chromium in the composition is to increase the wear resistance and ability of the alloy to resist corrosion through the oxide surface whereas Nickel, Carbon, and Molybdenum are added to enhance the resistance to corrosion, increase strength and enhance alloy's castability. It is required to control the content of carbon in the composition to maintain the mechanical properties of the alloy even at high temperatures. W was included in the base alloy to significantly increase strength, enhance corrosion resistance but decrease strength of corrosion fatigue. Concentration of all these elements in the composition is critical for fabrication technologies and controlled casting. The CoCrMo alloy exhibited excellent wear and corrosion resistance properties and provided effective mechanical properties like high modulus of elasticity (E) and great capacity to withstand fatigue failure [15].

After understanding the desirable properties of alloy, the alloy was then utilized to manufacture dental and orthopedic implants. The high strength and corrosive resistance of the alloys made further development in the joint implants such as knee-hip replacement implants and other medical devices [25, 26]. Metals including Co, Cr, and Ni are usually found to be toxic in nature and may harm the human tissue which further affects the human body. But, the composition of these elements along

Table 2 Composition of 317L stainless steel and Nickel free high concentration SS [12]

Stainless steel type	Ni	Si	Cu	N	S	Cr	Mn	C	Mo	P
316L SS (ASTM F138)	13.00–15.00	0.75	0.5	0.1	0.01	17.00–19.00	2.00	0.03	2.25–3.00	0.025
ASTM F2229	0.10	0.75	0.25	>0.90	0.01	19.00–23.00	0.50–1.50	0.08	21.00–24.00	0.03

Table 3 Mechanical properties regarding the 317L SS and Nickel free ASTM F2229 [12]

Type of stainless steel	UTS (MPa)	Yield strength (MPa)	Fatigue strength in air	Fatigue strength in PBS	Hardness (HRC)
316L SS (ASTM F138)	490–1350	190–690	220–600	220–600	25–39
ASTM F2229	931–1731	586–1551	650	500	43–50

with Mo and other alloying metals developed an alloy CoCrMo possessing high biocompatibility and also limits the release of toxic ions [27, 28]. Cobalt-based alloys are commonly utilized in annealed and casted conditions which allows the custom fabrication of the medical implant [29].

Although SS alloys exhibited excellent mechanical characteristics hence act as best substitute against Cobalt-based alloys for clinical implants and medical devices because of its. However, implantation of Co-based alloys for a long term released Co and Cr ions in the tissues and human body caused unadorned adversative effects [28].

Co-alloys usually possess great mechanical strength amounting to 960 MPa. Even when notched, these alloys have excellent resistance to fatigue failure (fatigue strength) at 10⁷ cycles of 610 Mega Pa which further can be increased with the help of further treatments. Additionally, they have high surface quality which minimizes the pitting and improves its resistance to corrosion. CoCrMo alloy has superior mechanical properties. However, the main limitations of Cobalt-based alloys are poor fatigue strength, poor ductility, high cost, and may release toxic ions in the human build and destructs the tissue cells. Another disadvantage regarding Cobalt alloyed compounds is that it fractures due to fretting fatigue and needs high-cost fabrication for implant manufacturing. Still, Co-alloy has wide range of applications in medical implants such as hip, knee joints, and joint replacements [15].

2.2 Ceramics

Use of ceramics in surgical medical devices is due to their ability to form into desirable shapes and porosities. Ceramics were familiarized in medical applications after the discovery of their excellent wear characteristics, high compressive strength, high physical characteristics, and good strength. Inherent brittleness and low ductility of the material add limitations in its use, care needs to be taken while replacing and handling ceramics [30].

The use of ceramics in medical applications is limited due to its poor tensile strength and brittleness. Although ceramics are utilized because of their excellent Veri characteristics and ability to shape into different medical devices, polymers or metals are preferred over ceramics. The most common applications of ceramics in

medical devices are bone grafts, dental implants, orthopedic medical devices, hip prostheses, and artificial knees [31].

Apatites perform a vital role in the use of ceramics in biomaterial implants. Most of the applications include fracture treatment, joint replacement, transdermic devices, cranio-maxillofacial reconstruction, periodontal treatment, fracture treatment, bone treatment, dental implants, spinal implants, and almost all applications utilize calcium phosphate-based biomaterial. Also, phosphate being the material most similar to bones possess high biocompatibility and integration, thereby preferred as ideal bioceramics in wide range of applications [31].

Other materials such as hydroxyapatite are used in dental and alloy-based orthopedic implants to provide layer of coating over the implant material, i.e., titanium or Stainless Steel, this improves the bonding of the implant surface with the human tissues. However, delamination of the coating of ceramic over the metal or alloy may adversely affect the implant and may result in its failure. Also, hydroxyapatite is preferred as filler material for the treatment of defective bones [32].

The ceramics being the nonmetallic, nonpolymeric, nonorganic used in medical industry are Zirconia (ZrO_2), Titanium, Alumina (Al_2O_3), Alumina (Al_2O_3), Biodegradable Ceramics, Pyrolytic Carbon, Bioceramics and Calcium Phosphate ceramics. The properties, advantages, disadvantages are as discussed below.

2.2.1 Zirconia (ZrO_2) and Alumina (Al_2O_3)

Zirconium oxide has been utilized in medical implants because of its excellent durability and high mechanical strength while Aluminum oxide (Al_2O_3) has excellent biocompatibility, high wear, and corrosion resistance as a result of which it has been used in wide applications in hip prosthesis and dental implants. These combined mechanical properties primarily high strength in fatigue result in development of special design and shape requirements. The surface smoothness and surface energy and of Alumina ceramic led it to have excellent mechanical properties, biocompatibility, and exceptional tribological behavior [33].

Although few ceramics having good mechanical properties are utilized in implants, Zirconia ceramics are preferred because of its superior mechanical properties providing exceptional advantages over other ceramic materials including Alumina (Al_2O_3).

Advantages

1. Zirconium oxide and Aluminum oxide ceramic material are light greys and smooth in color which is preferable in dental applications as well as in anterior rooted devices.
2. These ceramic materials provide excellent biocompatibility provides better care and protection to the implants.
3. Ceramics exhibited direct bonding with bones and tissues in orthopedic and dental applications similar to titanium implants.

4. The other benefits of Al_2O_3 and ZrO_2 ceramics over the over synthetic biomaterials include its electrical and thermal conductivity and reaction with surrounding tissues and bone environment.
5. The external bodily and mechanical characteristics of the ceramics may be possibly varied to enhance its biocompatibility.

Disadvantages

1. The exposure of ceramic material to steam team decontamination may affect the strength and durability of the ceramics.
2. Some ceramics and prostheses may provide poor resistance to corrosion [34].
3. The rough surface of ceramics may cause degradation of the bonding material which affects the surrounding bones and tissues.
4. Rough surfaces, notches, and grazes may initialize cracks in the material which ultimately may lead to failure of the implant.

2.2.2 Ceramics Based on Calcium Phosphate

Depending upon the bioactive material, various forms of CaPO_4 ceramics are used in medical implants but HA form of CaPO_4 ha been used as augmentation material for surface coating on metallic implants. Calcium Phosphate (CaPO_4) ceramics are widely used in wide range of implants and clinical surgeries preferably in dental applications [35]. The clinical results exhibited Calcium Phosphate has high fatigue strength and durability under moderately high load carrying applications thereby the ceramic has been extensively used in medical devices like blocks, cones, and rods.

The Calcium Phosphate being porous in form represents its key characteristics while CaPO_4 with similar porosity identical to spongy bone is considered to be ideal for clinical use. Because of its advantageous properties, CaPO_4 ceramics has evolved as one of the most commonly used and successful biomaterials in the past two decades, particularly HA form of the ceramic has been used expansively for hard tissue implants and in many device applications. HA ceramics have proved to be the most biocompatible material providing a strong bond to the bones and surrounding tissues. Thus, continuous investigation in HA ceramic directed to an improvement in tissue replacement and enhanced development of dental, bone implants, and many hard tissue applications [36].

Advantages

1. Color of Calcium Phosphate ceramic is similar to dental and bones.
2. The elements in the composition of CaPO_4 including phosphorous, calcium, hydrogen, and oxygen are similar to the normal biologic tissue and found to be highly pure in nature.
3. Calcium Phosphate has excellent biocompatibility.
4. For load bearing implants, CaPO_4 ceramic has identical elastic modulus to bone over any other form of material.
5. Provides the ability to restrict the flow of chemical and physical metallic ions, and exhibits negligible electrical and thermal conductivity.

2.2.3 Glass Ceramics and Bioglass

Bioactive glass that composited amounts of CaO , P_2O_5 , and SiO_2 established good bonding with bones. Modification of the surface, porosity is the key characteristic of bioglass ceramic which is advantageous for bioactivity and resorption. Bioglass and glass ceramic are most commonly used for filling defects of bones. Because of the favorable composition consisting similar proportion of phosphate and calcium salt which is identical to bones and teeth, glass ceramic biomaterial is preferred in dental and orthopedic applications [37].

When bioglass is interfaced with living tissues, it forms layer of carbonated HA which results in good bonding of the ceramic with the bone. This makes bioglass an auspicious biomaterial in the field of medical applications.

2.2.4 Tricalcium Phosphate Bioceramics

Two most broadly used types of calcium phosphates, i.e., Tricalcium Phosphate and HA have been experimentally investigated as the preferable material for bone implant. From the investigation of prior experiments, Tricalcium Phosphate ceramics could be used as bioresorbable material whereas porous or dense variety of HA ceramic could be effectively utilized for numerous long-term bone implant applications [38–42].

HA material was found to be similar to Tricalcium Phosphate in terms of bone and tissue bonding, and biocompatibility but an exhibition of expectable bio resorption rates with satisfactory physical and mechanical properties was found to be difficult with Tricalcium Phosphate ceramics.

3 Literature Gap/Future Scope

The utilization of the biomedical implants in the living organism body tissue in refined way within confined area with modulated design and maximum compatibility with organism ultimately eliminates the direct surgical solution [38, 39]. $\text{Ti}_6\text{Al}_4\text{V}$ alloyed material possesses poisonous aluminum and vanadium which are undesirable for living organisms also may anticipate detrimental glitches. For getting rid of the poisoned vanadium is substituted with Niobium and Ferrous that aids in the formation of new composites $\text{Ti}_6\text{Al}_7\text{Nb}$ also $\text{Ti}_5\text{Al}_2.5\text{Fe}$ [43, 44].

Sufficient reviews have currently illustrated that the young's elastic constant of category α , category α , and β titanium composite anticipates tremendous withstand capacity against load application [45, 46], eliminating the shielding of stress impact [47]. Hence less elastic constant category β Titanium based composite is comprehensively utilized [48, 49] for the assuage shielding stress impact [44] similarly Titanium composites with molybdenum, zirconia, niobium, ferrous, tantalum elements are utilized [50, 51].

Plastic processing techniques have aided refined particles of Titanium composite incorporates increased withstand against scratching, withstand against yielding, withstand against fatigue failure in 2CP Titanium [52].

Ceramic possesses best withstand against corrosion also anticipates the fragility, results in cracking of implant at the time of utilization hence It cannot be modified into honeycombed structure correspondingly honeycombed polymer possess least capacity to withstand an endurance against load and impact load application. So for effective fitment of the bio-implant with living tissues honeycombed implants are utilized. Hence honeycombed Titanium composites are evolving briskly as an effective bio-implant solution, it anticipates great withstand capacity against load application also least young's elasticity constant however it enables better fitment over the conventional honeycombed bio-implants [53, 54].

Several procedures of formulating honeycombed Titanium composites have been evaluated lately containing investment casting method [55], loose sintering of titanium powder, the easiest manufacturing method aimed at building honeycombed titanium also its composites are accompanied with fractional sintering of precipitate. Binder of polymerized nature is not essential in this method also henceforward abate likely adulteration in elimination of binder [56]. Sintering of slurry, manufacturing honeycombed titanium via slurry developing process consuming hydrogen and oxygen covalent bonds as developing elements [57].

The subsequent honeycombed titanium with porosity of 58% having hole size as 465 μm the ability to withstand against compression with young's elastic constant 0.19 GPa and 4150 MPa, correspondingly allows better fitment substitute for human bones [58, 59]. Sintering a blend of titanium powder also space holder technique, Space holder method, explicitly powder metallurgy practice consuming space holder resources emanates in association with its advantages like modifiable permeability amount, pore profile, and pore dimensional spreading [60, 61] which depend on the profile, proportions and bulk fraction of space holder used for blending porous titanium and its alloys.

4 Summary and Conclusion

Biomaterial	Composites	Advantages	Limitations	Applications
Metallic alloys	Titanium	Excellent biocompatibility Excellent tissue response High resistance to corrosion Highest specific strength as compared to other alloys	Low metal density of 4.8 gm/cm ³ Low strength of 500 MPa Poor shear strength Low tensile ductility	Dental implants THR implant Pedicle screw in spinal implant Surgical devices
	Stainless steel	Superior resistance corrosion High biocompatibility High durability Excellent mechanical properties Low cost	Released Ni ions may cause adverse effects on human health 317L SS (austenitic) type of alloy has poor durability Not much effective against pitting corrosive prevention Fatigue failure reduces the life of the implant	Non-implantable medical devices Total hip replacements Knee joint implant
	Cobalt alloys (CoCrMo)	Excellent wear and corrosion resistance properties Effective mechanical properties Capability to withstand fatigue failure Superior wear resistant properties	Poor fatigue strength Poor ductility Fractures due to fretting fatigue Need high-cost fabrication for implant manufacturing High cost	Clinical implants Surgical devices Medical implants such as hip, knee joints, and joint replacements

(continued)

(continued)

Biomaterial	Composites	Advantages	Limitations	Applications
Ceramics	Zirconia (ZrO ₂)	Excellent durability High mechanical strength, Exceptional tribological behavior Exhibits electrical and thermal conductivity	Exposure to steam team decontamination may affect its strength and durability Rough surface of ceramics may cause degradation of the bonding material Poor resistance to corrosion	Orthopedic implants Dental implants
	Alumina (Al ₂ O ₃)	Excellent biocompatibility High wear and corrosion resistance Exhibit direct bonding with bones and tissues	Rough surfaces, notches, and grazes may initialize crack in the material Poor wear and corrosion resistance	Hip prosthesis Dental implants
	Calcium phosphate (CaPO ₄)	High fatigue strength Superior durability Porosity identical to spongy bone is advantageous for clinical use Ability to restrict the flow of chemical and physical metallic ions	Moderately low load carrying applications	Clinical surgery instruments Medical devices like blocks, cones, and rods
	Glass ceramics and bioglass	Excellent bonding with bones and tissues Excellent biocompatibility Nontoxic in nature	Degradation of ceramic may cause loss of integrity Poor in ductility and fatigue Brittle in nature and poor bending strength	Filling defects of bones Tooth implant products Dental and orthopedic implants
	Tricalcium phosphate	Preferable material for bone implant Good bone and tissue bonding	Poor physical and mechanical properties	Bone implants

For the effective utilization of biomaterials in medical implants, the material should offer good physical and mechanical properties, biocompatibility, biostability, high strength, and good corrosion resistance. Over the past few years, varieties of biomaterial have been introduced in the field of medical implants.

Ti-alloy, Stainless Steel alloyed compounds also CoCrMo alloyed compounds are widely used biomaterials for orthopedic, dental, and cardiovascular applications. Ti based alloys have superior strength, high biocorrosion resistance, excellent pitting resistance, good biocompatibility as compared to SS alloys and CoCrMo alloys. However, Titanium alloys have major disadvantages including less bending stress withstand capacity, weak against wear stress, poor forge ability, and high cost enables its limited application in load sustaining implants.

SS alloys are relatively cheap in cost and have good mechanical properties. From the study, it was found that CoCrMo alloys have proved to be an excellent biomaterial because of its superior external bodily and mechanical characteristics, effective withstand against corrosion also better withstand against wear failure. Therefore, it has been extensively used in hip, knee joint implants.

Other than metallic biomaterials, ceramics offers excellent strength, biocompatibility, good corrosion and wear resistance, non-toxicity, and superior bioactivity.

Studies reported Bioglass and HA are the most widely used bioceramics in medical applications. However, brittleness, poor ductility, poor mechanical properties, and poor fatigue toughness limit its applications. Therefore, metallic biomaterials are used in bearing load implants instead of metallic biomaterials.

References

1. Inspired by biology, from molecules to materials to machines (Committee on biomolecular materials and processes, National Research Council of the National Academies) (2008) The National Academies Press, Washington, DC
2. Sharma CP (2005) Biomaterials and artificial organs: few challenging areas. *Trends Biomater Artif Organs* 18(2):1–7
3. Black J (1982) The education of the biomaterialist: report of a survey. *J Biomed Mater Res* 17:159–177
4. Peppas NA, Langer RL (1994) New challenges in biomaterials. *Science* 263(5154):1715–1720
5. Albertsson A-C, Varma IK (2002) Aliphatic polyesters: synthesis, properties and applications, degradable aliphatic polyesters. *Adv Polym Sci* 157(2000):1–40
6. Bronzino JD (2000) *The biomedical engineering handbook*, vol 2, 2nd edn
7. Yoruc ABH, Sener BC (2012) Biomaterials. In: Prof. Kara S (ed). *A roadmap of biomedical engineers and milestones*. ISBN: 978-953-51-0609.
8. Niinomi M (2002) Recent metallic materials for biomedical applications. *Metal Mater Trans A* 33(3):477–86
9. Silver FH, Christiansen DL (2005) *Biomaterials science and biocompatibility*
10. *Metallic Implant Materials*, in *Biomaterials* (2007). Springer New York, 99–137
11. Tschernitschek, et al (2005) Non-alloyed titanium as a bioinert metal—a review. *Quintessence Int* 36:523–530
12. Niinomi M (2002) Recent metallic materials for biomedical applications. *Metal Mater Trans A* 33(3):477–486

13. Koike M, Fujii H (2001) In vitro assessment of corrosive properties of titanium as a biomaterial. *J Oral Rehabil* 28:540–548
14. Grosogeat B, Reclaru L, Lissac M, Dalard F (1999) Measurement and evaluation of galvanic corrosion between titanium/Ti6Al4V implants and dental alloys by electrochemical techniques and auger spectrometry. *Biomaterials* 20:933–941
15. Dobbs HS (1982) Fracture of titanium orthopaedic implants. *J Mater Sci* 17:2398–2404
16. Pritchett JW (2020) Bicruciate total knee replacement. In: Rivière C, Vendittoli PA (eds) *Personalized hip and knee joint replacement*. Springer, Cham
17. Najefi A, Malhotra K, Chan O et al (2019) The Bologna-Oxford ankle replacement: a case series of clinical and radiological outcomes. *Int Orthop (SICOT)* 43:2333–2339
18. Galván JC, Larrea MT, Bracerás I, Multigner M, González-Carrasco JL (2017) In vitro corrosion behaviour of surgical 317LVM stainless steel modified by Si⁺ ion implantation—an electrochemical impedance spectroscopy study. *J Alloys Compd* 676:414–427
19. Mansur MR, Wang J, Berndt CC (2013) Microstructure, composition and hardness of laser assisted hydroxyapatite and Ti-6Al-4V composite coatings. *Surf Coat Technol* 232:482–488
20. Metallic materials. In: Davies JR (ed) (2003) *Handbook of materials for medical devices*. ASM International Materials Park, Ohio, 21–50
21. Muley SV, Vidvans AN, Chaudhari GP, Udainiya S (2017) An assessment of ultra fine grained 317L stainless steel for implant applications. *Acta Biomater* 30:408–419
22. Zhang P, Liu Z (2017) Physical-mechanical and electrochemical corrosion behaviors of additively manufactured Cr-Ni-based stainless steel formed by laser cladding. *Mater Des* 100:254–262
23. Hermawan H, Ramdan D, Djuansjah JRP (2009) Metals for biomedical applications
24. Plecko M et al (2012) Osseointegration and biocompatibility of different metal implants—a comparative experimental investigation in sheep. *BMC Musculoskelet Disord* 13(1):32
25. Pramanik S, Agarwal AK, Rai KN (2005) Chronology of total hip joint replacement and materials development, 19:115–26
26. Yamamoto RH, Sumita M (1998) Cytotoxicity evaluation of 43 metal salts using murine fibroblasts and osteoblastic cells. *J Biomed Mater Res* 39(2):331–340
27. Evans EJ, Thomas IT (1986) The in vitro toxicity of cobalt-chrome-molybdenum alloy and its constituent metals. *Biomaterials* 7(1):25–29
28. Natiella JR, Armitage JE, Greene GW Jr, Meenaghan MA (1972) Current evaluations of dental implants. *J Am Dent Assoc* 84:1358–1361
29. Haubenreich JE, Robinson FG, West KP, Frazer RQ (2005) Did we push dental ceramics too far? A brief history of ceramic dental implants. *J Long Term Eff Med Implants* 15(6):617–628
30. Vallet-Regí M (2001) Ceramics for medical applications. *J Chem Soc Dalton Trans* 2:97–108
31. Bermejo R, Danzer R (2010) High failure resistance layered ceramics using crack bifurcation and interface delamination as reinforcement mechanisms. *Eng Fract Mech* 77(11):2126–2135
32. Hench LL (1991) Bioceramics: from concept to clinic. *J Am Ceram Soc* 74(7):1487–1510
33. Lantada AD (2000) *Handbook of active materials for medical devices: advances and applications*. Pan Stanford Publishing Pte. Ltd. 978-981-4303-36-1
34. Jarcho M (1986) Biomaterial aspects of calcium phosphates: properties and applications. *Dent Clin North Am* 30(1):25–47
35. Muddugangadhar B, Shamanna A, Tripathi S, Dikshit S, Divya MS (2011) Biomaterials for dental implants: an overview. *Int J Oral Implantol Clin Res* 2:13–24
36. Bosetti M, Verne E, Ferraris M, Ravaglioli A, Cannas M (2001) In vitro characterization of zirconia coated by bioactive glass. *Biomaterials* 22(9):987–994
37. Schrooten J, Helsen JA (2000) Adhesion of bioactive glass coating to Ti6Al4V oral implant. *Biomaterials* 21(14):1461–1469
38. Renner AM (2001) The versatile use of titanium in implant prosthodontics. *Quintessence Dent Techno*:188–97
39. Ibrahim MZ, Sarhan AAD, Farazila Yusuf M, Hamdi, (2017) Biomedical materials and techniques to improve the tribological, mechanical and biomedical properties of orthopaedic implants—a review article. *J Alloy Compd* 714:636–667

40. Cicci'u M, Cervino G, Herford A et al (2018) Facial bone reconstruction using both marine or non-marine bone substitutes: evaluation of current outcomes in a systematic literature review. *Mar Drugs* 17(1):27
41. Herford AS, Cicci'u M, Efimie LF et al (2017) rhBMP-2 applied as support of distraction osteogenesis: a split-mouth histological study over nonhuman primates mandibles. *Int J Clin Exp Med* 9(9):17187–17194
42. Long M, Rack HJ (1998) Titanium alloys in total joint replacement—a materials science perspective. *Biomaterials* 19:1721–1739
43. Niinomi M (2002) Recent metallic materials for biomedical applications. *Metall Mater Trans A* 33:477–486
44. Evans FG (1976) Mechanical properties and histology of cortical bone from younger and older men. *Anat Rec* 185:1–11
45. Dingô M, Dalstra M, Danielsen CC, Kabel J, Hvid I, Linde F (1997) Age variations in the properties of human tibial trabecular bone. *J Bone J Surg* 79:995–1002
46. Gross S, Abel EW (2001) A finite element analysis of hollow stemmed hip prostheses as a means of reducing stress shielding of the femur. *J Biomech* 34:995–1003
47. Kuroda D, Niinomi M, Morinaga M, Kato Y, Yashiro T (1998) Design and mechanical properties of new β type titanium alloys for implant materials. *Mater Sci Eng A* 243:244–249
48. Sakaguchi N, Niinomi M, Akahori T, Takeda J, Toda H (2005) Relationship between tensile deformation behavior and microstructure in Ti-Nb-Ta-Zr. *Mater Sci Eng C* 25:363–369
49. Niinomi M, Akahori T, Katsura S, Yamauchi K, Ogawa M (2007) Mechanical characteristics and microstructure of drawn wire of Ti-29Nb-13Ta-4.6Zr for biomedical applications. *Mater Sci Eng C* 27:154–171
50. Nag S, Banerjee R, Fraser HL (2005) Microstructural evolution and strengthening mechanisms in Ti-Nb-Zr-Ta, Ti-Mo-Zr-Fe and Ti-15Mo biocompatible alloys. *Mater Sci Eng C* 25:357–362
51. Rack HJ, Qazi JI (2006) Titanium alloys for biomedical applications. *Mater Sci Eng C* 26:1269–1277
52. Wen CE, Yamada Y, Shimojima K, Sakaguchi Y, Chino Y, Hosokawa H, Mabuchi M (2002) Novel titanium foam for bone tissue engineering. *J Mater Res* 17:2633–2639
53. Lopez-Heredia MA, Sohiera J, Gaillard C, Quillard S, Dorget M, Layrolle P (2008) Rapid prototyped porous titanium coated with calcium phosphate as a scaffold for bone tissue engineering. *Biomaterials* 29:2608–2615
54. Yamada Y, Shimojima K, Sagaguchi Y, Mabuchi M, Nakamura M, Asahina T, Mukai T, Kanahashi H, Higashi K (2000) Processing of cellular magnesium materials. *Adv Eng Mater* 2:184–187
55. Oh IH, Nomura N, Masahashi N, Hanada S (2003) Mechanical properties of porous titanium compacts prepared by powder sintering. *Scr Mater* 49:1197–1202
56. Li H, Yu QF, Zhang B, Wang H, Fan HS, Zhang XD (2006) Fabrication and characterization of bioactive porous titanium. *Rare Met Mater Eng* 35:154–157
57. Li JP, Li SH, van-Blitterswijk CA, de-Groot KA (2005) Novel porous Ti6Al4V: characterization and cell attachment. *J Biomed Mater Res* 73A:223–233
58. Hench LL (1991) Bioceramics: from concept to clinic. *J Am Ceram Soc* 74:1487–1510
59. Wen CE, Mabuchi M, Yamada Y, Shimojima K, Chino Y, Asahina T (2001) Processing of biocompatible porous Ti and Mg. *Scr Mater* 45:1147–1153
60. Esen Z, Bor S (2007) Processing of titanium foams using magnesium spacer particles. *Scr Mater* 56:341–344
61. Laptev A, Vyal O, Bram M, Buchkremer HP, Stover D (2005) Green strength of powder compacts provided for production of highly porous titanium parts. *Powder Metall* 48:358–364

Analysis of Deep Drawing Process on Composite Sheet



Preyashi B. Manjrawala  and Dhyey R. Savaliya 

Abstract Deep drawing is a process, commonly used in industry for sheet metal operations. Components of the deep drawing process include the punch, die, blank holder, and blank. In order to take advantage of different material properties in the same component, layered composites consisting of Al and Cu clad together are used. For the experiment, four different parameters were taken, viz. sheet material, thickness, blank holder force, and lubrication. The Al–Cu composition was taken 80:20. The aim of this project was that, to deal with the different strain behaviour of Al and Cu, to compare the experimental and software results with minimum deviation in results and to study the deviations if they are occurring. The main objective was that to work with the properties of both the materials at the same time. Altair Hyperworks software was used for checking the simulation results and to see whether the desired results are achieved or not. It helps to engineer and optimize all aspects of the stamped product development cycle from concept design to finished part for metals and composites. The results checked were percentage thinning, thickness variation, strain and stress concentration. Forming limit diagram is also shown. FLD plot helped to see whether the material is safe or there is some failure. All these conditions were calculated and done in this project. After the various steps of the process, desired drawn part is produced. The output of this project is explained further in this research paper.

Keywords Deep drawing · Layered composites (Al–Cu composite) · Altair hyperworks · Forming limit diagram (FLD)

P. B. Manjrawala (✉)

Department of Mechanical Engineering, Ahmedabad University, Ahmedabad 380009, India

D. R. Savaliya

Department of Automobile Engineering, Uka Tarsadia University, Surat 394350, India

1 Introduction

Deep drawing comes under forming process. Two different metals used in this project were aluminium and copper cladded together to form one sheet of required blank diameter. They are relatively cheaper. Advantage of aluminium is low density and low cost, in the same way copper has an advantage of high electrical conductivity. Both has good ductility, so can be drawn in to desired shape. In this forming process, plastic modification of blank has been done with keeping its mass and material sticking together. Shape of blank is modified in this experiment with controlling its geometry. In this process, bimetal sheets come under combined tensile and compressive conditions. A flat blank sheet is formed into the cup-shaped component by forcing the punch against the centre portion of a blank which rests on the die ring. An entire setup includes punch, blank holder (ring), blank, and die. The blank holder is required to hold the blank in its place by some kind of blank holder force, the punch with the help of punch holder force pushes the blank down to set it in the die, and thus, the component gets the shape of the die [1]. For controlling various types of defects, it was necessary to control various physical and geometrical parameters. During the process, there were different type of defects occurred, i.e., wrinkle, fracture, tearing, orange peel, and many more. It was essential to reduce them in order to reduce production cost. Various affecting parameters are blank holding force, punch force, material property, sheet thickness, velocity of punch, etc. The software used was Altair Hyperworks for comparing its results with the experiment one. Hyperworks is simulation software used in stamping and tooling industries. It helps to engineer and optimize all aspects of stamped product development cycle from concept design to finished part for metals and composites. While carrying out this experiment, different challenges were occurred to reduce the defects in the final drawn part (Figs. 1 and 2).

In the process of deep drawing, the very first step is that the blank holder holds the blank in place which the punch is directed towards the blank. Then blank moves radially downward by the action of the punch. After that friction tries to restrict the blank to draw further. The depth portion experiences the thinning, but at the same time the flange experiences thickening. And in the last step, component is ready [2].

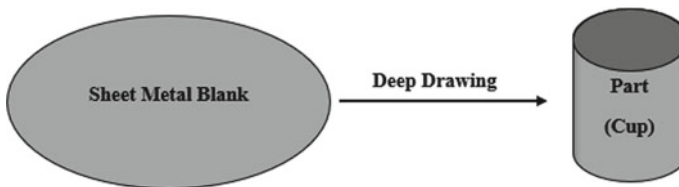


Fig. 1 Deep drawing process

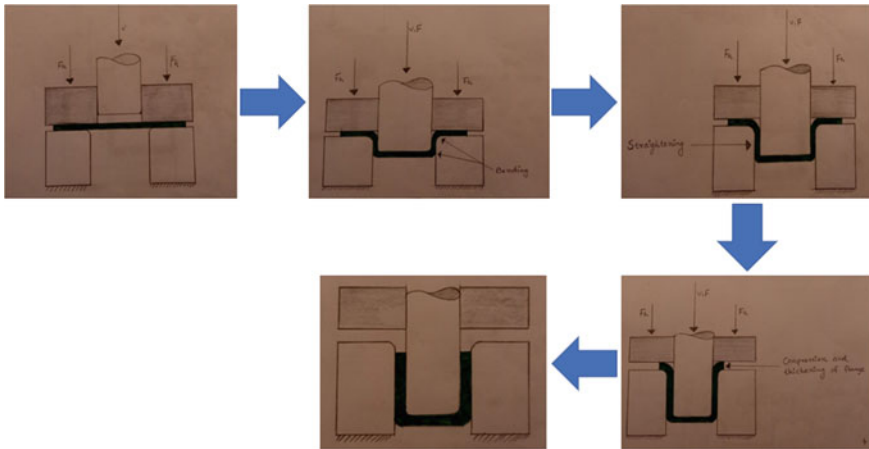


Fig. 2 Process sequence

2 Literature Review

Two relevant studies helped to understand deep drawing process. Compared to this project, it was illustrated in the literature study that analysis of deep drawing of Al–Cu was done by simulation as well as by experiment. To gain more drawability of material, Al–Cu composite used in the literature study was heated at 400 °C. In this study, micro-rolling process was done on Al–Cu laminated sheet in order to match the specification of die set in micro-forming process. Compared to this literature study, in this research, it was conducted only forming process rather than micro-deep drawing process. The final product in the literature study shows fewer defects. Also, the results of simulation agree the experiment data related to drawability, punch force, and defects [3]. In the second literature study, various parameters were selected like stacking sequence, thickness, lubrication, and blank holding force. These parameters are responsible for the deep drawing process. Also, it is shown that the copper is needed to be kept less than the aluminium portion in the blank thickness ratio. The reason is that aluminium draws more, so it needs to be thicker [3]. It was studied those different types of defects can occur if the experiment is not conducted using the proper selection of the parameters [4]. Blank holding force should be selected carefully, so that wrinkles do not occur. Lubrication is very much necessary without which the material cannot be drawn. Different type of stress acts at different portion of the cup. Top portion of the flange gets increased in the thickness as the material is added at the flange while the bottom of the cup gets reduced in the thickness. Thus, the percentage thinning comes out as positive and negative both.

All these understandings helped in carrying the experiment and to select the proper parameters to study the deep drawing process. Study drawability of the composite material, different type of defects in the deep drawing process, main objective of this work is to see whether simulation results agrees to the experiment result.

3 Experimental

The setup used in experiment for the deep drawing procedure is mechanical press. Although the hydraulic press is also available but as component needed to be drawn is small so used mechanical press. Figure 3 shows stress–strain curve for Cu and Al [5]. During the process, different values of blank holding force noted and further given into the simulation software. For making process more efficient and to increase drawability of material, lubricant was used. By changing the parameters given in Table 1, different results are obtained. Material has been confirmed the standard requirement and has been checked and inspected, which can be seen in Table 2. From Table 4, it is clearly seen that there are six samples, which are with and without defects. Table Table 5 Mechanical properties of Al–Cu compositeMaterialYield tensile strength (MPa)Modulus of elasticity (GPa)Ultimate tensile strength (MPa)Elongation (%)Poisson ratioShear modulus (GPa)Copper120117350500.3547.7Aluminium556872300.33263 shows different values of blank holding force, which is obtained by varying the blank holder pressure. From the experiment, it can be seen that at blank holding pressure 30 bar, the outcome of final product is without any defects and turn out to be safe product. On the other hand, when blank holding pressure is increased to 70 bar, product deformation cannot be taking place, because the given holding pressure was too high than the required holding pressure. By adjusting the value of blank holding pressure, behaviour of material deformation was observed (Table 5).

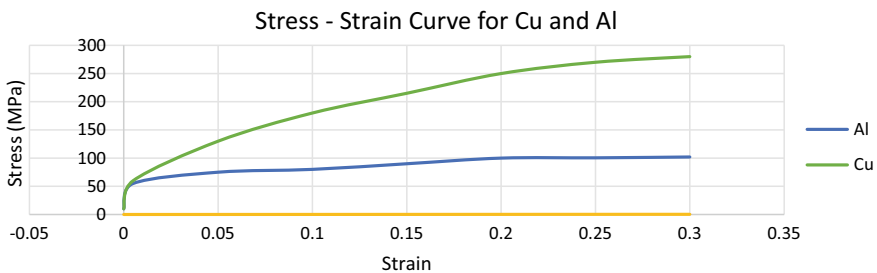


Fig. 3 Stress–strain curve for Cu and Al

Table 1 Process parameters

Stacking sequence	Thickness (mm)	Blank holding force (kN)	Lubrication
AC/CA	1, 1.5	5.37, 10.74, 32.22, 75.189	With and without lubrication

Table 2 Test result of materials

No.	Inspection item	Standard requirement	Test result
1	Shock resistance	>50 kg cm	>50 kg cm
2	Hot water resistance	Normal	Normal

Table 3 Experiment data


Forces	Thickness of blank (mm)	Pressure (bar)	Result (kN)
Maximum punch force	1	–	35.89
	1.5	–	53.84
Actual punch force	–	30 bar	6.7
Maximum tensile force	1	–	33.31
	1.5	–	49.96
Blank holding force	–	70 bar	75.189
	–	30 bar	32.22
	–	10 bar	10.74
	–	5 bar	5.37

4 Simulation

By knowing the hardening exponent and thickness of material, the FLD plot for Aluminium–copper sheet is in simulation software Altair Hyperworks as per Fig. 3 plotted. Die, punch, and blank holder design as per Figs. 3, 4, and 5 has been done for doing software simulation. All the parameters used to do simulation were the same as used in experiment. The mechanical properties of Al–Cu bimetal sheet is given in Table 4. After doing multiple numbers of simulation, the actual adjustment on the die design and other parameters are done. When the value of blank holding force 32,220 N to Al–Cu blank is given, FLD of the product shows positive result. And for the same force, value of %Thinning is varying between 18.21% and – 31.579% due to straightening of the blank, where more material is added at upper part. Thickness of final product 0.654 mm is achieved. This FLD plot of material clearly demonstrate amount of yielding, necking, and compression in the area of the product. Before manufacturing the product, helped the FLD plot to see whether the product is safe or failure. Also, it helps to make process faster and more efficient (Figs. 6 and 7).

The below graph shows that for punch holding force 32,220 N, the maximum punch force 89,481.1 N is obtained (Fig. 8).

Table 4 Experiment result

Figure	Details	Reasons
	<p>Blank holding force: 7.66 Tonne/75,189.63 N Stacking sequence: AC Lubrication: yes Thickness: 1 mm</p>	<p>Blank holding force is more than the desired value, so the deep drawing is not possible and component failed</p>
	<p>Blank holding force: 0.55 Tonne/5370 N Stacking sequence: CA/AC Lubrication: yes Thickness: 1 mm</p>	<p>Blank holding force is less than the desired value, so the wrinkles appear on the flange portion and also some wrinkles on the upper part of the cup wall</p>
	<p>Blank holding force: 1.09 Tonne/10,740 N Stacking sequence: AC Lubrication: yes Thickness: 1 mm</p>	<p>Blank holding force is less than the desired value, so the wrinkles appear on the flange portion</p>
	<p>Blank holding force: 3.28 Tonne/32,220 N Stacking sequence: AC Lubrication: yes Thickness: 1 mm</p>	<p>It appears almost defect free as the blank holding force is applied as per requirement</p>

(continued)

Table 4 (continued)


Figure	Details	Reasons
	<p>Blank holding force: 3.28 Tonne/32,220 N Stacking sequence: CA Lubrication: yes Thickness: 1 mm</p>	<p>It appears almost defect free as the blank holding force is applied as per requirement</p>

Table 5 Mechanical properties of Al–Cu composite

Material	Yield tensile strength (MPa)	Modulus of elasticity (GPa)	Ultimate tensile strength (MPa)	Elongation (%)	Poisson ratio	Shear modulus (GPa)
Copper	120	117	350	50	0.35	47.7
Aluminium	55	68	72	30	0.33	26

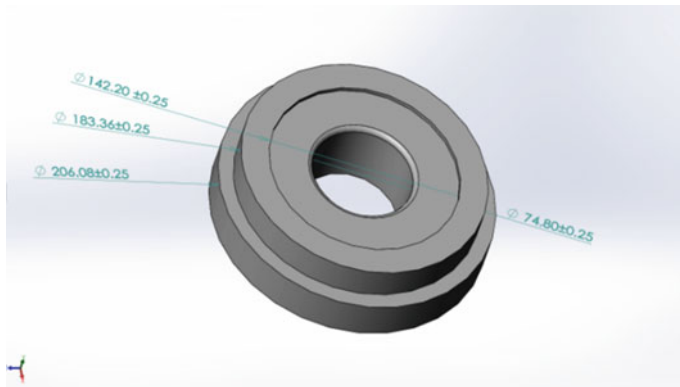


Fig. 4 Die design

5 Comparison

After processing experiment and simulation work, obtained data were with each other compared. Value of stress obtained from both experiment and simulation data is shown in Fig. 9. As per figure, it is clear that for different values of blank holding force, similar trend for experiment stress and simulation stress is obtained. As per graph, it was studied that there is minimum deviation in the result. Figure 10 shows the comparison of bottom thickness of product in experiment work and in simulation.

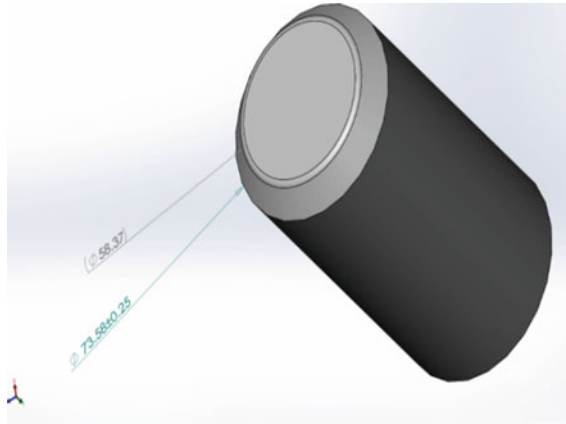


Fig. 5 Punch design

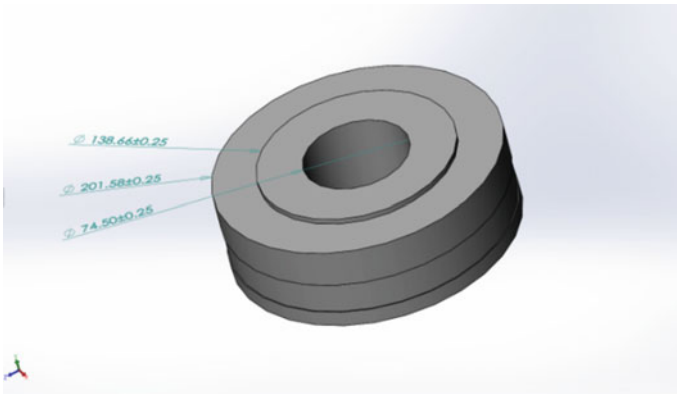


Fig. 6 Blank holder design

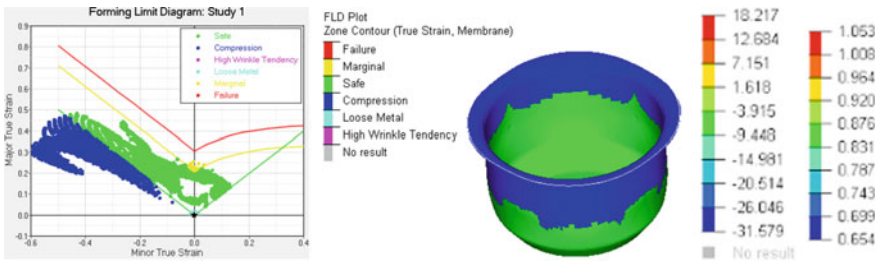


Fig. 7 Material deformation for blank holding force 32,220 N

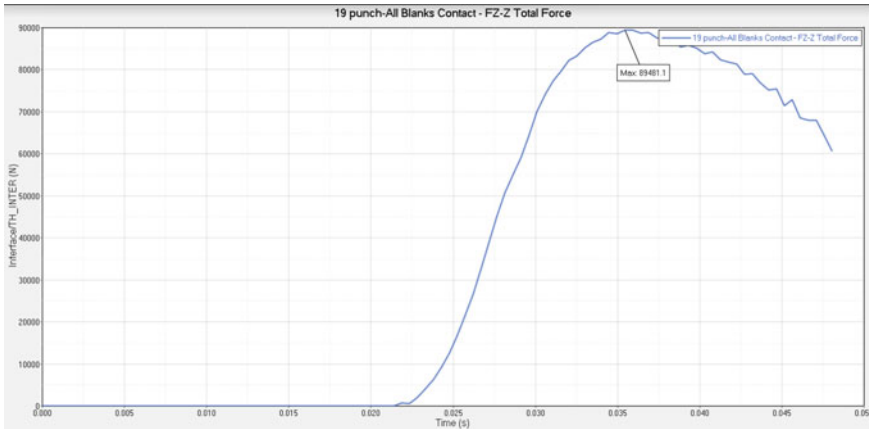


Fig. 8 Punch to blank force graph

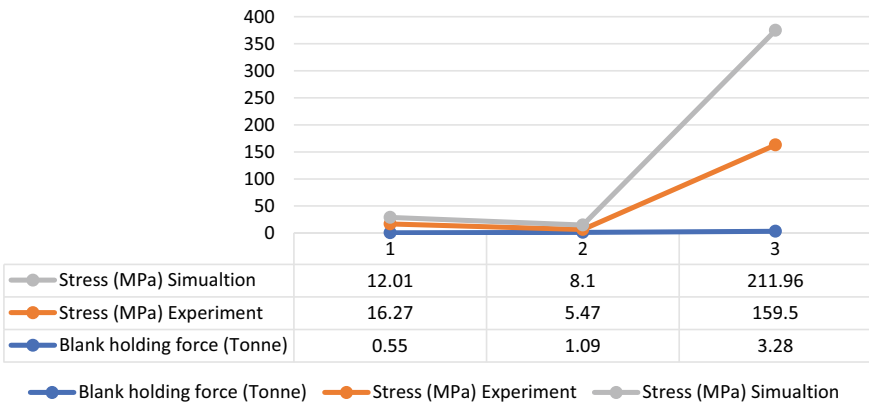


Fig. 9 Stress of experiment and simulation result

From the graph, it is noted that percentage of error between experiment and simulation data is less (Table 6 and Fig. 11).

6 Discussion

It was found that the most important parameter to perform deep drawing was lubrication without which the product cannot be formed. Another important thing is blank holding force. Less blank holding force would cause the wrinkle. Taking 0.55 tonne force, wrinkles appeared on the flange and top portion of the cup. By increasing this force to 1.09 tonne, still some wrinkles appear. When force was changed to

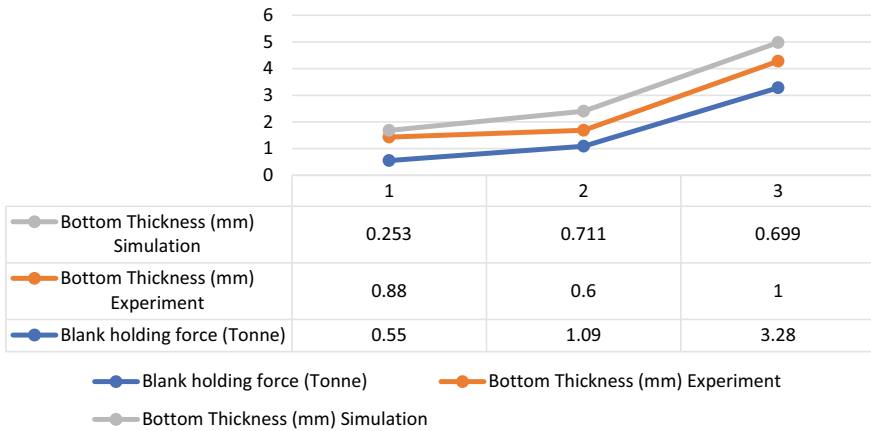


Fig. 10 Bottom thickness of experiment and simulation result

3.28 tonne, desired cup without wrinkles was formed. On taking blank holding force 7.66 tonne, material failed as the force would not allow the component to flow further. Thus, more or less blank holding force results in component failure. Number of times the material is drawn also affects the appearance. More number of redraw results in uniform material, while single draw is uneven draw. It can be seen by the shine at the bottom of cup in single drawn. Die radius and punch radius are also important parameter. Less die radius than 5 mm will not allow the material flow. Type of material used is also necessary to note down, aluminium will not allow the die to fail. It fails by itself but will save the die. On the other side if stainless steel is used, holding force cannot be taken more or less than desired due to die failure. Also, more blank holding force is required than taken for aluminium–copper.

7 Conclusion

Deep drawing was performed on layered Al–cu composite (bimetal sheet) using different parameters. Different observations were come across by changing the parameters. Altair Hyperworks software was used to check the simulation results. It helped to form a defect free cup. Lubrication also played the important role. Stacking sequence did not show much variation in results. The experimental and software results are almost the same. Some variation is there as the exact force used in the Hyperworks cannot be applied to the mechanical press, as the mechanical press uses the bolt tightening and loosening to increase or decrease the load. Another reason is friction that is different in a real situation and the one applied to software. There can be slight variation in the dimension of die, punch, and binder that was measured and then used for simulation. Velocity for the mechanical press cannot be changed and is

Table 6 Effect due to variation in blank holding force on the performance of deep drawing process

Result obtained	Experimental	Simulation result (Hyperworks)
Blank holding force 5370 N		
Flange thickness (mm)	1.5	–
Side wall thickness (mm)	0.8	0.244
Bottom thickness (mm)	0.88	0.253
% thinning in flange	– 50	–
% thinning in side wall	20	8.5
% thinning in bottom	12	12.883
Stress (MPa)	16.27	12.01
Strain	0.2	0.230
Blank holding force 10,740 N		
Flange thickness (mm)	2	–
Side wall thickness (mm)	1.1	1.038
Bottom thickness (mm)	0.6	0.711
% thinning in flange	–100	–
% thinning in side wall	–10	–9.1105
% thinning in bottom	40	18.23
Stress (MPa)	5.47	8.1
Strain	0.2	0.262
Blank holding force 32,220 N		
Flange thickness (mm)	1.5	–
Side wall thickness (mm)	1	0.787
Bottom thickness (mm)	1	0.699
% thinning in flange	–50	–
% thinning in side wall	21.3	20.5
% thinning in bottom	30.1	31.57
Stress (MPa)	159.5	211.96
Strain	0.2	0.224

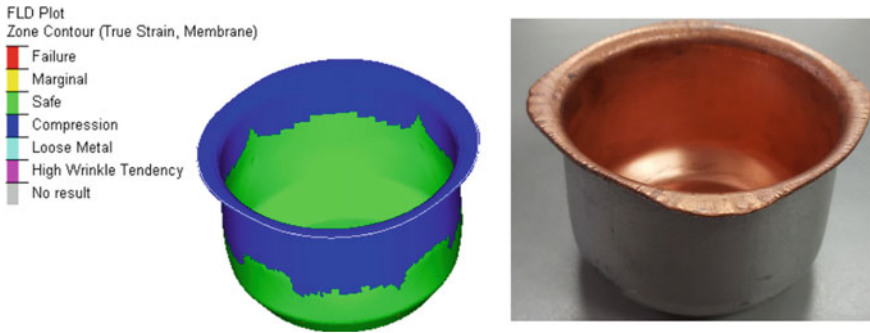


Fig. 11 Final part in simulation and experiment

constant. Repeated working on the machine results in heating of the die which needs to be taken care while working on machine. This thing does not happen in software.

Acknowledgements The research is supported by the Ahmedabad University under the part of project. The simulation part was carried out in trial version of manufacturing Software Altair Hyperworks (2017), Altair Engineering. Software available at <https://www.altair.com/hyperworks/>

References

1. Deep drawing of sheet metal—TheMech.in. TheMech.in (2014). <https://themech.in/deep-drawing-sheet-metal/>. Accessed: 24 May 2021
2. Groover M (2010) Fundamentals of modern manufacturing. Wiley, New York
3. Jia F, Zhao J, Luo L, Xie H, Jiang Z (2017) Experimental and numerical study on micro deep drawing with aluminium-copper composite material. *Procedia Eng* 207:1051–1056
4. Atrian A, Fereshteh-Saniee F (2013) Deep drawing process of steel/brass laminated sheets. *Compos B Eng* 47:75–81
5. https://www.researchgate.net/figure/The-true-stress-strain-curve-for-pure-aluminum-and-copper_fig4_257757496/download. Accessed: 24 May 2021

Anatomy of a Fused Filament Fabrication (FFF) 3D Printing System for High-Grade Polymers (HGPs)—An Overview



Chinmaya Prasad Padhy, S. Suryakumar, and N. Raghunath Reddy

Abstract Fused filament fabrication (FFF) or fused deposition modeling (FDM) is one of the most common extrusion-based technology used for additive manufacturing (AM). It differs from the subtractive manufacturing technique in its material utilization and ability to fabricate complex parts. FFF is found to be convenient and easy in many ways, e.g., associated manufacturing setup and process are non-toxic, cost-energy effective, latest technology driven, less time engineering, virtual inventory control, etc. In the past, many researchers worked on the improvement of process parameters on the functionality of FFF machines to enhance mechanical, thermal, and electrical properties of AM objects. On the other hand, few research groups have worked on the exploration of finding new materials used in medical industry, tissue engineering, dental parts, etc. The core part of the FFF machines are extruder system, and nozzle has been focused by few researchers. FFF led the expansion of many desktop 3D printers based on their material use. However, the design aspects of FFF machine components and their assembly were not much discussed by many in the past. The main focus of the current study is on discussing the design of different prime elements (anatomy) along with their functionality to handle high-grade (performance) polymers (HGPs). This paper confers the shortcomings of filament-based extruder system and also paves future scopes of FFF technology over the existing filament-based extrusion system (filament extruder).

Keywords Additive manufacturing (AM) · Fused filament fabrication (FFF) · 3D printer · Filament extruder · Software · Firmware · High-grade polymers (HGPs)

C. P. Padhy (✉)

Department of Mechanical Engineering, School of Technology, GITAM University, Hyderabad, India

S. Suryakumar

Department of Mechanical & Aerospace Engineering, Indian Institute of Technology, Hyderabad, India

e-mail: ssurya@mae.iith.ac.in

N. R. Reddy

Department of Mechanical Engineering, TOSHIBA, Hyderabad, India

1 Introduction

Industrial application of prototyping or rapid prototyping by means of material additive manufacturing (AM) process started a way back in the nineteenth century. However, with the recent development and advancement of prototyping in manufacturing technologies, where a solid geometry of any object is utilized for building an object by depositing its thin 2D planes of material along the other axis (layer-by-layer). This helps to save lot of efforts, energy, and cost. So far, we have a very few quite popular additive manufacturing technologies available for use, e.g., vat photo polymerization, sheet lamination, material extrusion, powder bed fusion, direct energy deposition, material jetting, and binder jetting which were developed based on liquid, powder, and solid form of materials. However, it is to be noted that among the seven available AM technologies, material extrusion is the one which is simple to use, cost-effective, and most adopted by many as it can handle materials in the abovementioned forms as well as it allows additives as per our requirement during the process and there is no downtime.

AM helps us in many ways, for example, limited material usage, manufacturing of complex geometry parts with dimensional accuracy, energy consumption, implementing change of design before its print, etc. Thus, additive manufacturing (AM) can certainly be compared with its counterpart subtractive manufacturing (SM). In earlier studies, Connor K. [1] studied application of additive manufacturing and the feasibility study of the disruption of traditional methods like injection molding. Parthasarathy et al. [2] discussed the injection molding with fused filament fabrication (FFF) 3D printing by creating a prototype and compared the energy consumed for manufacturing, fabrication time, cost of production, etc. Production (printing) time is an important parameter in AM which always reliant on the quality of the surface; in addition to this, it also eliminates dependencies on secondary processes, which ultimately saves a lot of money. Yoon et al. [3] discussed the energy consumption, material wastage, pollutants, etc., compared with subtractive manufacturing, where usage of auxiliary machines, equipment is more common in SM and which consume more energy than AM machines, also they found in SM use of cutting fluids which contain paraffinic oil are hazardous to environment. Tanisha et al. [4] studied the AM technologies and compared with the traditional methods to find that the capability of AM best to fit in low and high production volume products.

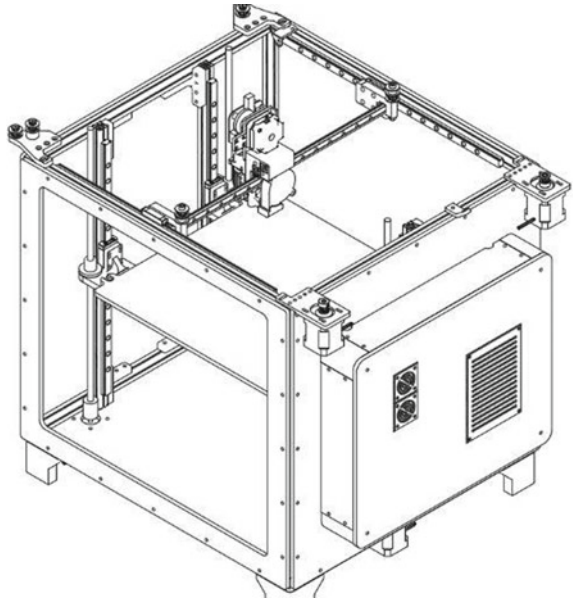
In this context, it is estimated that 3D printing has been a prevalent manufacturing technique with market value of \$9.9 billion USD in 2019 and expected to gain \$34.8 billion USD by 2024 [5–7]. Also, its believed that selective laser sintering (SLS) is going to take the most of the share in the global market, nonetheless material extrusion-based AM technology: FFF will be the 3rd one in the race to dictate the market share of nearly \$10.4 billion USD by 2024 [6, 8]. It is to be noted that FFF is well-liked for its modest design, create less amount of waste, innocuous, eco-friendly modeling facility, and more importantly reasonable cost among the existing 3D printing system in AM [9].

As in case of fused filament fabrication (FFF) technology, material is melted and fused through the heated printer extruder head and then is allowed to deposit in layers on a heated platform (build plate). Therefore, sometimes it is also popularly well-known as fused deposition modeling (FDM) [9, 10]. Extruder is considered to be one of the main mechanical component of any FDM machine, which is responsible to control the feeding of the materials (filament or pellet type) to the hot end for melting before depositing on the platform [11–13]. This technology is very simple to implement, and also allows small type of overhangs in the printed parts. Usually, feed filaments are made up of thermoplastic materials, e.g., PLA, ABS and can also be extended to the high-grade polymers (HGPs), e.g., PEEK, Ultem (PEI), ASA, etc., whose properties depend on their crystallization phenomenon connected with their melting history and exposure to the thermal treatment [14]. Beside thermoplastics, there are many more feed materials, e.g., metals, ceramics, composites, drugs, etc., are available for the use in this category. However, there are certain demerits like poor surface finish and close tolerance dimensional accuracy are inevitable [11–13]. FFF technology might be considered as one of the potential techniques to help the energy sector to shift toward green energy by improvising the process parameters aims to reducing the cost [12]. By now, the 3D printing technologies are widely seen in the applications domains, viz., automobile, aerospace, medical, food, fashion, and education industry, etc. [15, 16]. In recent past, a number of works [16–21] are done on its process parameters, e.g., nozzle dia., bead width, layer thickness, raster angle, printing speed, etc., for improvising surface quality, mechanical, electrical, and thermal properties of the printed job.

Das et al. [19], Marina et al. [22], and Morino et al. [23] examined build orientation (raster angles) in improving the volumetric error, surface finish, and accuracy of printed part which consumes less filament and achieves less printing time. Another important theme in FFF is the search for new feedstock materials, in addition to thermoplastics. Recently, Dennis et al. [24] studied about the waste plastics recycling process with the help of AM technologies for the community of fab labs and they succeed on that. Byron et al. [25] worked on an extrusion system meant for biopolymers using pellets. Trenton et al. [26] worked on shape memory polymers by using direct pellet extrusion to print the products. Rossana et al. [27] succeed with continuous fiber composite and confirmed that combining the topology and fiber orientation optimization techniques enables a significant weight reduction of the 3D printed parts.

FFF technology has contributed a lot in defense, pharma, medical industry, e.g., prosthetic, bone, cartilage, tissue engineering, dental parts, etc. [16, 28]. So, there are many versions of FFF printers available to handle different aspects of engineering and medical parts as per their use and demand. This is possible only with the help of modifying the existing system suitably or acquiring/constructing a new model for this. More importantly, FFF's extruder system and nozzle are one of the most important part as discussed and constantly attracted by many researchers in the past [29–31]. So, it is felt that a systematic study about the parts and components, of their design and functionality, would surely help in this direction. As discussed above, various aero, automobile, medical usage parts require high-grade polymers (HGPs)

Fig. 1 Schematic diagram of a HGP's FFF Cartesian 3D printer



for their uses because of their superior, resistance to corrosion, wear, creep, strength-to-weight ratio, and sustainable under high harsh environments. Therefore, an attempt has been made for the detailed study (anatomy) of the components laid architecture used and their functionality in a FFF printer specially planned for HGPs. Below (refer Fig. 1) shows the schematic diagram of a FFF-based Cartesian 3D printer for high-grade polymers (HGPs).

2 Main Components of a FFF 3D Printer for High-Grade (Performance) Polymers

Beside a dedicated printing chamber (enclosure), FFF printing system for high-grade polymers (HGPs) mainly consists of—(1) mechanical component parts, (2) electrical and electronics component parts, and (3) supporting software/firmware. Basically, mechanical components help for both as of a giving a support structure along with the needed kinematic setup for movement of different components. However, electrical and electronics component parts aid the control system for desired motion of the stepper motor, belts, extruder head, build plate, and whereas supporting software/firmware deals with the user's command.

2.1 Mechanical Components

The mechanical system of a FFF high-grade polymers 3D printer mainly involves of three components, i.e., (1) outer frame to support (2) linear rail and carriage for extruder movement, and (3) transmission system. Frame (refer Fig. 2) is an essential component of high-grade polymers FFF 3D printer consist of a rigid structure made up of heat-treated steel (refer Fig. 3) or extruded anodized aluminum profiles (refer Fig. 4). A rail mechanism is essential for easy drive of extruder-hot-end-nozzle along the designated linear axes. Therefore, linear rails usually laid down as shown in Fig. 5 for the easy drive of the components, viz., rectangular guide rail (refer Fig. 5) and cylindrical guide rail made up of smooth linear rods (refer Fig. 3). Sometimes, aluminum profiles (V-shape) are of choice for many manufacturers (refer Fig. 6), and for this, materials like heat-treated aluminum 2020 and 2040 are of good options which is of good strength, stiffness, and durable. Carriage is an important component with carriage plate, made up of aluminum along with wheels (POM V-wheels bearing 625ZZ) which move on laid linear rails (refer Fig. 6) and to attach this arrangement usually nuts-bolts-screw-washer-M5 socket head cap (refer Fig. 8) combination is used (Fig. 7).

In order to convert rotational movement of the motor shaft into linear motions, we use transmission systems. There are two forms of transmission system is used in case of FFF 3D printer, (1) pulley-belt driven (2) lead screw driven. In belt driven

Fig. 2 Frame

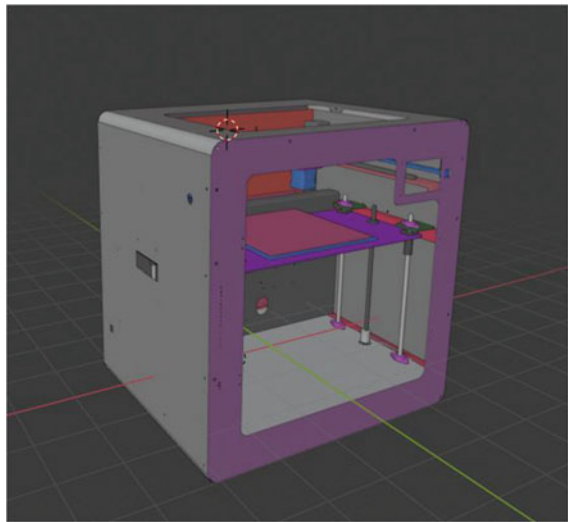


Fig. 3 Smooth steel rod



Fig. 4 Extruded anodized aluminum rod

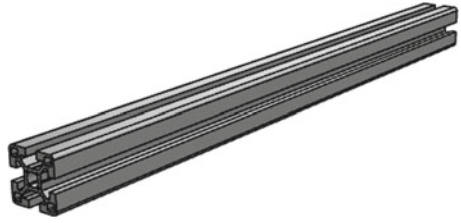


Fig. 5 Linear guide rails

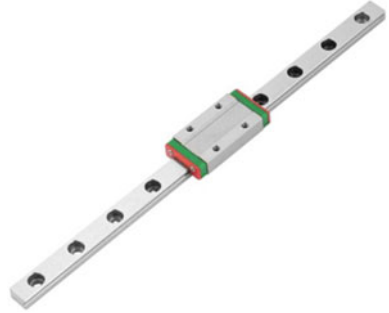


Fig. 6 V-shaped linear guide rails along with carriage



Fig. 7 Small deep groove ball bearing

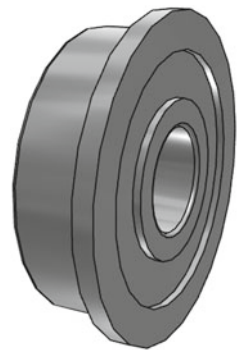


Fig. 8 M5 socket head cap



transmission system, carriage is connected by a high torque timing belt, preferably 2GT/3GT 6 mm high temperature timing belts: which are made up of fiber glass tensile cord (refer Fig. 9) having uniquely designed small pockets on it (refer Fig. 20) and it's been placed in a confined closed loop in such a way that a specialized timing pulley, preferably 20 teeth GT2 with 5-mm dia. (refer Fig. 10) with arranged pockets helps to fit the belt tightly in its grip and gives ease for drive the carriage system to its desired position accurately. On the other side, screw transmission concept is similar to movement of rack-pinion mechanism, thus the movement of lead screw (sometimes also known as 'ball screw' or 'power screw') which has a special threading used for transfer of motion to the connected carriage, and this type of transmission systems are more precise than the traditional belt system and expensive (refer Fig. 11). However,

Fig. 9 Timing belt



Fig. 10 Timing pulley

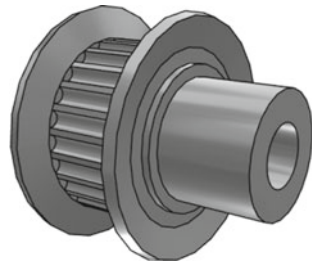


Fig. 11 Precision ball screw

this arrangement not only reduces deformation, wear, calibration, etc., but also lowers the amount of maintenance to a measurable extent.

Reinforced nylon PA66 cable drag chain cable carrier (refer Fig. 12) is used to carry all the electrical wires connected to the stepper motor, extruder, and controller of the printing head. They are usually high temperature resistant, wear resistant, corrosion resistant, and can sustain heavy loads also cause less noise while in operation. Linear rail shaft axis clamping guide end support (refer Fig. 13) for X-Y-Z axis to block the respective movement. Flanged linear bushings (refer Fig. 14) are used in combination with linear shaft, which can help to attain pure linear motion with lower friction and high accuracy movement of print bed and carriage plate. Knurled nuts (refer Fig. 15) are used to hold the carriage plate with the structural arms. Urethane rubber bumpers (refer Fig. 16) are used to provide the cushioning effect to the ceramic print bed for providing an excellent shock absorbing medium. Induction hardened (58 HRC) end shape tapped smooth linear shafts (refer Fig. 17) are arranged perpendicularly to the carriage to provide the desired linear motion along the z-axis. Linear ball bearings (refer Fig. 18) are tube-like, flanged, or pillow boxes, and all have ball bearings along their inside diameter where they run on a

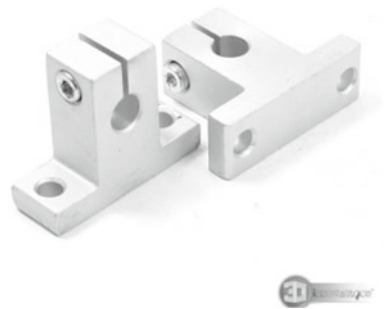
Fig. 12 Cable carrier**Fig. 13** Guiding blocks

Fig. 14 Flanged linear bushing

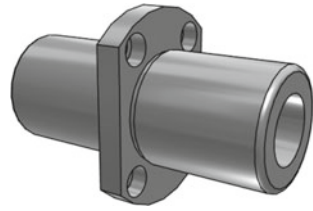


Fig. 15 Knurled nuts

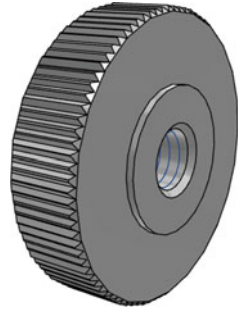


Fig. 16 Rubber bumper

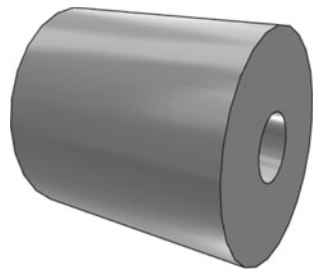


Fig. 17 Smooth linear shaft



linear shaft results in rolling motion rather than sliding. To fix the precision ball screw rigidly, support-units like FK10 (refer Fig. 19) may be attached on its top.

Now days, most 3D printers have very few sensors, and all kind of sensors are usually fallible after certain use, so sometimes a 3D printer will start behaving in

Fig. 18 Linear bearing**Fig. 19** Support units**Fig. 20** Emergency stop button

an uncontrolled way. So, it may be advisable to have a physical button ('Emergency Stop' button) attached to the printer on the frame appropriately to stop immediately from its on-going function (refer Fig. 20).

2.2 *Electrical and Electronics Components*

Essentially, electrical and electronics components of a FFF 3D printer play very crucial role for controlling mechanical components and responsible for their movements, functionality, and ultimately quality of the print. The important components are discussed below:

Extruder of a high temperature 3D printer is one of the most important component in the class of FFF-based 3D printers. It defines the characteristic of a FFF 3D printing

system. So, it is important to discuss its individual elements (sub-components) and their desired functionality in detail. The most usual used functional parts of an FFF extruders are as follows: (1) the hot end, which softens and melts the filament, and (2) the extrusion drive, which pushes the filament into the hot end [9]. However, there are two types of extruder drives are usually seen in case of FFF printers, (1) Bowden type drive and (2) Direct type drive. If the extrusion drive is attached far away from the hot end, and it only allows to feed the filament to the hot end, then the extruder is known as Bowden type drive. On the other hand, if the extrusion drive is attached directly to the hot end and is placed just above the hot end, then this kind of arrangement is known as direct type extrusion drive (Figs. 21 and 22).

As shown in Fig. 23, nozzle is mounted toward the closure of the extruder. The molten material then flows to the print bed through this small hole. Generally, the diameter of the nozzle hole ranges from 0.30 to 0.80 mm, which ultimately decides the output of the printed part. As its been learned most of the nozzle materials used to be brass, however for high temperature 3D printers (preferably for high-grade polymers) vanadium is preferable because of its superior thermal and physical properties over brass (Fig. 25) and is fixed to the hot end through screw mechanism. Hot end is a section (lower section) of the extruder made up of aluminum which heats the barrel by a series of cassette heater wrapped over the barrel body along with the internal ceramic channels, more specifically designed to reduce friction between viscous polymers and inner walls of the channel to facilitate extrusion. The hot end

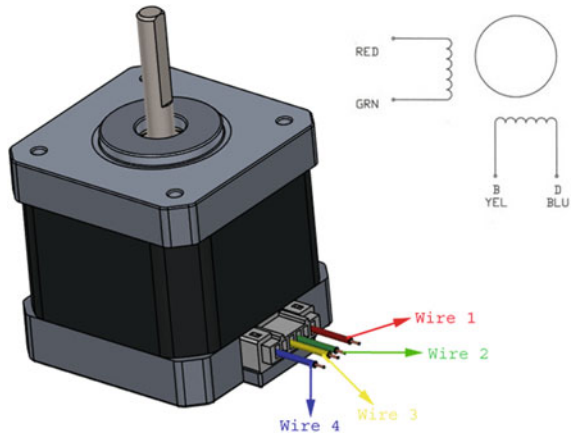
Fig. 21 Extruder with hot-end



Fig. 22 Extruder with hot end and nozzle



← nozzle

Fig. 23 Stepper motor

contains a thermistor to measure the temperature and provide a regulatory feedback so that temperature of the hot end shall be maintained in accordance with the working conditions. But with a note, in case of high temperature 3D printer, the temperature of hot end usually maintained at above 300 °C. Therefore, in this context, ‘Mosquito Magnum’ hot end (refer Fig. 24) may be used to serve the purpose. The melt zone of this hot end is extended proximally upward to maintain a small form factor and acts as a ‘heat break’ whereas a thermal insulator given to protect the extended melt zone from the effects of active cooling and radiative heat loss. Upper section of the hot end attached with a cooling fan, known as the cold end. Basically, it has two functions to do with, firstly to blocking at the hot end the heat transfer leading to the upper parts of the extruder system and next to maintain designed safe gap between preheated and melted filaments by which the extruder shall be more accessible and preventing the extrusion system from any unwanted blockage of the material.

A stepper motor is attached to the extruder with the defined gear-ratio and with proper splines supplies sufficient force to move forward the filament. Bondtech BMG-M’s extruder (refer Figs. 21 and 22) found to be preferable in case of high temperature 3D printers, and this extruder delivers high performance and high resolution material

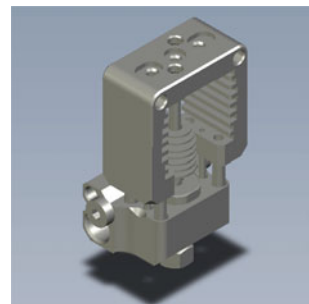
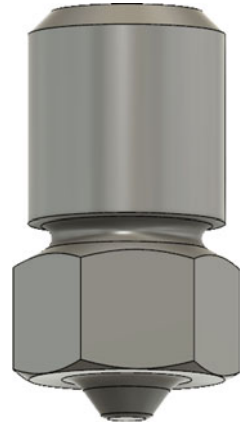
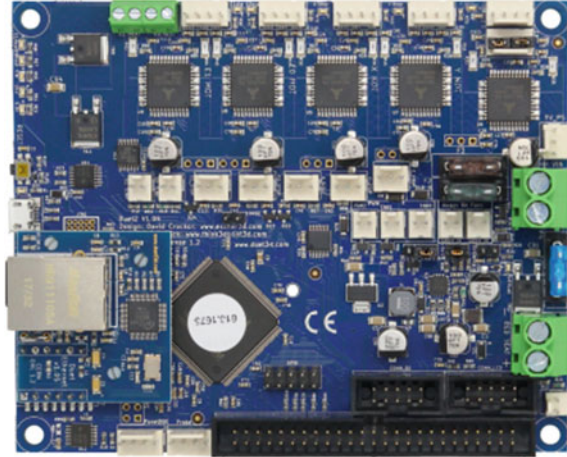
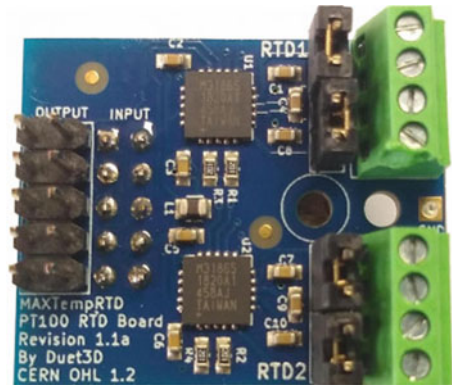
Fig. 24 Extruder hot end

Fig. 25 Extruder nozzle

feeding for print. This is possible because of its dual drive technology along with Ni-coated hardened steel drive gears, which helps to get flawless and precision material feeding to the hot end. A 24 V/50 W heater cartridge and thermistor pumps up high power into the 3D printer which can handle high grade of polymers like Nylon 66, Ultem (PEI), PEEK, and ASA.

Stepper motors (refer Fig. 23) are important part of CNC machine hoods, and they provide the desired rotational motion to the shaft. They are unique in that they can move to a known position stepwise and hold that position for a calculated amount of time. Ultimately, they make the shaft of the motor rotate in a précised controlled manner. A connection between the microcontroller and stepper motor establishes via. a stepper motor driver which sends a fixed amount of electricity or pulses with phases in a precise sequence to the stepper motor, for precise rotary movement of the drive shaft in a calculated manner [32, 33] LDO class ‘H’ high temperature stepper motors are more preferable in the class of high temperature FFF 3D printers, as can operate in winding temperature of about 1800 and can make a step of 0.90 step-angles, means one complete revolution occurs with 400 steps. In general, a stepper motor driver comes as an integral part of the control board (motherboard).

Control board (refer Fig. 26) is the main board, can be treated as the brain of the FFF 3D printer and is comprises of number of active microcontrollers, which has the chips inside them and does all the necessary computing, such that they usually take the inputs (G-code) and outputs with instructions of ‘*what to do*’ to the rest of the printer’s mechatronics. In most of the high temperature 3D printing system for HGPs, Duet 2 Ethernet control board is most preferable, which is having an advanced control board (32 bit) equipped with super quiet and high power (approx. 2.8 A) stepper-driver along with ferrules for heater and power terminals and plugs compatible with molex and crimps as well. Also, all the high temperature 3D printers are equipped with an additional control board called ‘daughter board’ (refer Fig. 27), they specifically designed for the better temperature control through the sensors attached to it. Touch screen board is the control arrangement used to communicate

Fig. 26 Main control board**Fig. 27** Daughter board

directly without the help of any personal computer, which is preferred to place on the outer frame of the 3D printing system. For example, Duet3D PanelDue 5i or 7i are the color screen (5 or 7 in.) control panels with 800×480 -pixel resolution. The G-code files can be transferred to the system using a standard SD card without the need for a continuous connection to a computer.

The hot end usually attached the below part (lower side) of the extruder and is responsible for liquefying the feed material, while the other side (upper side) of the extruder having the extrusion drive (gear drive) through which filament is fed toward the hot end. As it is highly requiring to maintain the extrusion drive working temperature to normal for its smooth operation and thus to prevent any heat transfer from hot end to normal end (cold end), essentially a cooling fan is attached [9]. A DC 12 V 2 pin 40×10 cooling fan may be used, which circulates the cold air to exhaust heat and maintains its temperature lower to normal.

It is required to support a constant temperature inside printing enclosure (heated chamber) throughout the printing process; therefore, for this, it is advised to use industrial positive temperature coefficient (PTC) fan ceramic heater (refer Fig. 28) 700–1000 W 220 V AC incubator (heat material: PTC thermistor) is suitably used at the bottom corner of the printing cabinet, where inside circulatory air is allowed to getting heated through heat radiation process during printing, which helps to avoid any possible shielding phenomena leading to a defect called warpage, that would usually occur with a unidirectional flow. High current AC loads can be controlled by a device called solid state relay (SSR), refer Fig. 29. A SSR having dielectric strength of 4000VAC, 50/60 Hz may be preferable. A high temperature probe can be used with a mechanical switch in combination with a servo motor to probe the bed for better printing results. The servo motor is outside the enclosure and retracts the probe pin by pulling on a steel string inside a spring guide tube. Also, a high precision digital temperature sensor (DHT22, Model: AM2302) having a resolution of 0.1 °C calibration can be planned to measure the cabinet temperature accurately.

The first layer of HGPs (usually, having high shrink rate) is extruded onto the high temperature build plate. After the material is deposited on the build plate, there is a possibility that the printed object’s edges start cooling down with higher rate as compared to object’s central (core) position, results warpage [10]. So, to address

Fig. 28 PTC fan ceramic heater



Fig. 29 Solid state relay (SSR)



this temperature gradient phenomena tactfully and in order to maintain a constant temperature throughout the print process, a high temperature heated bed (attached silicone heaters) can be used.

2.3 *Supporting Software/Firmware*

3D printer's microcontrollers run by a preselected firmware and it usually comes with the purchase of unique motherboard. Firmware is what it connects software and hardware of a 3D printer. Its purpose is to transform the machine path information in the form of G-codes into signals for precise and individual control of various elements. 3D printer's configuration variables are required to be setup as per the demand before installation of firmware in the microcontroller. RepRap is the most popular and open source firmware available for all the users. However, other firmwares, viz., Marlin, Smoothie, Klipper can also be used in FFF-based 3D printers preferably. So, the firmware controls the various machine elements like motors, heaters, display, information readers along with speed limits and thermal regulation.

3 Conclusion

A complete anatomy of a FFF-based 3D printing system for high-grade (performance) polymers—HGP is discussed elaborately. Most of the relevant mechanical, electrical and electronics components/sub-components and software firmware have been discussed along with their technical specification and working principles. It entails the complete design and facilities required for a high-grade FFF-based 3D printer. It also gives a clear understanding that FFF-based 3D printers are affordable and simple in their design. So, that it can reach to any individual based on the lying demand and interest. As the demand grows and technology facilitates, there is a need to look beyond filament-based fabrication. So, there is also increasing trend toward using pellets as feed stock material in the place of filament, extending the scope of low running cost, flexibility for additives and having no down time. Additionally, this can avoid the step of converting the raw material into wire form first, and also, it will help the user to choose the material as per their requirement and availability of such materials in pellet form, more importantly in this process we can skip the making of the filaments and make use of higher flexibility in material variety.

Acknowledgements This work is supported by the Science and Engineering Research Board (SERB)—DST, Government of India (GoI) under its Teachers Association for Research Excellence (TARE) scheme [Grant number: TAR/2020/000160].

References

1. Kress C (2015) An experimental and theoretical analysis of additive manufacturing and injection molding. A Master thesis, The University of Toledo
2. Parthasarathy G, Subramanyam B, Vineeta TV, Bharadwaj N, Shashank PS (2018) Comparative analysis of additive manufacturing over conventional manufacturing. *IOP Conf Ser: Mater Sci Eng* 455:1–11
3. Yoon H, Lee Jang Y, Kim Min S, Kim Eun SN, Shin Yong J, Chu Won S, Ahn Sung H (2014) A comparison of energy consumption in bulk forming, subtractive, and additive processes: review and case study. *Int J Precis Eng Manuf Green Technol* 1:261–279
4. Tanisha P, John VK, Johan P (2019) A comparison of traditional manufacturing versus additive manufacturing, the best method for the job. *Procedia Manuf* 30:11–18
5. McWilliams A (2019) Global markets for 3D printing: MFG074A. BCC Publishing. <https://www.bccresearch.com/market-research/manufacturing/3d-printing-market-report.html>
6. Shah J, Snider B, Clarke T, Kozutsky S, Lacki M, Hosseini A (2019) Large-scale 3D printers for additive manufacturing: design considerations and challenges. *Int J Adv Manuf Technol* 104(9–12):3679–3693
7. Cosson B, Anh L, Chateau A (2021) Simulation of large-scale additive manufacturing process with a single-phase level set method: a process parameters study. *Int J Adv Manuf Technol* 113:3343–3360
8. 3D Printing Global Market Size, Share, Trend & Research Report (2015) <https://www.bccresearch.com/market-research/instrumentation-and-sensors/global-markets-for-3d-printing.html>
9. Swapnil V, Soham T, Deepak P, Shailendra K (2019) Fused deposition modelling: a review. *Rapid Proto J* 26(1):176–201
10. Swapnil V, Soham T, Deepak P, Shailendra K (2020) Experimental study of surface roughness, dimensional accuracy and time of fabrication of parts produced by fused deposition modelling. *Rapid Proto J* 26(9):1535–1554
11. Masood SH (2014) “Advances in fused deposition modelling”, *Advances in additive manufacturing and tooling*. *Comprehens Mater Process* 10:69–91 (Elsevier)
12. Mwema FM, Akinlabi ET (2020) Basics of fused deposition modelling (FDM). In: *Fused deposition modeling*. Springer, pp 1–15
13. Zhao P, Liu S, Wu S, Zhang C, Fu J, Chen Z (2019) A pellet 3D printer: device design and process parameters optimization. *Adv Polym Technol* 1–9 (Wiley)
14. Zhiyi Z, Hanmin Z (1993) Effects of thermal treatment on poly(ether ether ketone). *POLYMER* 34(17):33648–3652 (Butterworth-Heinemann Ltd.)
15. Moreau C (2020) The state of 3D printing. <https://www.sculpteo.com/blog/2020/06/02/download-our-state-of-3d-printing-2020-for-free>
16. Mohammad A, Deborah O, Georgia K, Abu Z, Md. Shahadat H, Tasnim S (2020) Polymers for extrusion-based 3D printing of pharmaceuticals: a holistic materials-process perspective. *Pharmaceutics* 12(124):1–34 (MDPI)
17. Popescu D, Zapciu A, Amza C et al (2018) FDM process parameters influence over the mechanical properties of polymer specimens: a review. *Polym Testing* 69:157–166
18. Dizon JRC, Espera AH Jr, Chen Q, Advincula RC (2018) Mechanical characterization of 3D-printed polymers. *Addit Manuf* 20:44–67
19. Dey A, Yodo N (2019) A systematic survey of FDM process parameter optimization and their influence on part characteristics. *J Manuf Mater Process* 3:64–77
20. Das P, Mhapsekar K, Chowdhury S et al (2017) Selection of build orientation for optimal support structures and minimum part errors in additive manufacturing. *Comput-Aided Des Appl* 14:1–13
21. Spoerk M, Gonzalez-Gutierrez J, Sapkota J, Schuschnigg S, Holzer C (2017) Effect of the printing bed temperature on the adhesion of parts produced by fused filament fabrication. *Plast Rubber Compos* 47:17–24
22. Braconnier DJ, Jensen RE, Peterson AM (2020) Processing parameter correlations in material extrusion additive manufacturing *Addit Manuf* 31:100924

23. Matos MA, Maria A, Rocha AC, Pereira AI (2020) Improving additive manufacturing performance by build orientation optimization. *Int J Adv Manuf Technol* 1–13 (Springer)
24. Moroni G, Syam WP, Petro S (2015) Functionality-based part orientation for additive manufacturing. *Procedia CIRP* 36:217–222
25. Dennis JB, Aubrey LW, Robert BO, Matthew JF, Samantha LS, Joshua MP, (2019) Green fab lab applications of large-area waste polymer-based additive manufacturing. *Additive Manuf* 27:515–525
26. Byron JB, Arif KM, Steven D, Johan P (2017) Robot-assisted 3D printing of biopolymer thin shells. *Int J Adv Manuf Technol* 89:957–968
27. Trenton C, Alexis C, Callan H, Eric M, Pedro C (2021) 3D printed shape memory polymers produced via direct pellet extrusion. *Micromachines* 12(87):1–12 (MDPI)
28. Rossana RF, Nekoda van de W, Pratik K, Timothy Y, Ali YT, Mehran T (2021) Experimental investigation of additively manufactured continuous fiber reinforced composite parts with optimized topology and fiber paths. *Additive Manuf*
29. Han X, Yang D, Yang C, Spintzyk S, Scheideler L, Li P, Li D, Geis-Gerstorfer J, Rupp F (2019) Carbon fiber reinforced PEEK composites based on 3D-printing technology for orthopedic and dental applications. *J Clin Med* 8:240
30. Abilgazyev A, Kulzhan T, Raissov N, Hazrat Ali Md, Match WLKO, Mir-Nasiri N (2015) Design and development of multi-nozzle extrusion system for 3D printer. In: International conference on informatics, electronics & vision (ICIEV). IEEE
31. Shakor P, Nejadi S, Paul G (2019) A study into the effect of different nozzles shapes and fibre-reinforcement in 3D printed mortar. *Materials* 12(10):1708 (MDPI)
32. Krishnanand, Shivam S, Mohammad T (2020) Design and assembly of fused filament fabrication (FFF) 3D printers. *Mater Today: Proc* (Elsevier)
33. Faizal Arya S, Tajuddin W, Tiara Dwi A, Mi MNZ (2014) Three-phase inverter using microcontroller for speed control application on induction motor. In: Makassar international conference on electrical engineering and informatics (MICEEI), 26–30 Nov. IEEE, pp 81–86

Appropriateness Investigation on Three Different Layers Fashion of Specially Treated Banana/Epoxy/Fiberglass Hybrid Composite for Bio-medical Appliances



T. Malyadri, Afreen Begum, Nagasrisaihari Sunkara,
and M. S. Srinivasa Rao

Abstract Even though the metal implants have the risk of corrosion and the release of ions, the medical-grade titanium metal alloys and ceramics are widely used in orthopedic applications like plates, bars which fix for healing of fractured bones. This paper made an attempt to develop such risk-free choice, i.e., the hybrid composite for those orthopedic applications. The natural fibers of banana treated with the specially prepared chemical solution. The chemical solution consists of: volumetric percentages of 10% NaOH, 10% SLS, and 80% distilled water solution. The hybrid composite is obtained by compounding the natural fiber with artificial or synthetic fibers in the reinforcement phase. For the current work, the natural fibers of banana are combined with glass fibers in various layer fashions. The fiber weight fraction of 40% banana fibers and 60% fiberglass was preferred. The banana/glass fiber is reinforced in the matrix of epoxy. Specimens characterized as per standard of ASTM and compared with strength required for femur bone. Best suitable hybrid composite choice was identified and suggested for orthopedic applications.

Keywords Chemical treatment · Banana · Fiberglass · Epoxy · Femur Bone · NaOH

1 Introduction

Composite materials are nowadays choice for engineering, medical, construction industries, and other industries in considering its significant properties. In particular, the research for biomedical applications is a hot area of the research [1]. Some inherent properties of metals and metal matrix composites like corrosive, magnetic,

T. Malyadri (✉) · N. Sunkara · M. S. S. Rao
Mechanical Engineering Department, VNRVJIET, Hyderabad, Telangana 500090, India

A. Begum
Department of Humanity and Sciences, Shadan Women's College of Engineering and Technology,
Hyderabad, Telangana, India

and compressibility factors, and the orthopedic surgeons look for alternative materials for fixing issues like bone fractures. Though the selective materials, SS, titanium, cobalt chrome, etc. The issue still exists [2]. So this research focuses the polymer composites and their appropriateness for fixing bone fracture issues. Some of the composites reported in the literatures [3] Composted composites with different fiber fraction of 30, 40, and 50% and recommended that 30% banana gives best mechanical properties with jute and fiberglass-reinforced hybrid composite [4]. The proposed composites of contents of 12% sisal, 24% jute, and 36% hump to form the composite for bone applications. And [5] suggested treatment of banana fibers for enhancement of mechanical properties. This research is unique by the layer fashion consideration and treated banana fiber used for synthesizing the composites

The stiffness of bone is not uniform for all human beings, and it is not constant for same human being at all the time. But metallic plate which fix for curing long bone fracture the mismatch of stiffness happened in some cases. Such mismatch effects for stress shielding that is implanted lose due to mismatch of load transfer to plate and bone. So selective use of stiff material will be the best choice for resolving those issues. In this work, various weight fraction of fibers, pretreated natural fibers, selective layer fashion, improved fabrication technique were considered to obtain superior properties to suggest a right choice of hybrid composite material for bone plate applications.

2 Materials and Methods

2.1 Research Design

This research aims to support biomedical applications in particularly bone plate applications. The research on composite materials development is hot topic recent years. This research proposed to replace metallic bone plate by introducing natural and artificial fiber hybrid composite. This research considered the hybrid of natural fiber and synthetic fibers for balancing the properties and hence to obtain superior material than recently suggested for the bone plate application. The selection of reinforcement materials, matrix, hybrid composite fabrication, and the methods of characterization were done based on the research history and ASTM standards. Volume fraction and weight fraction are two terms of fraction used in composite design and fabrication. For fabrication, the composite engineer or fabricator used weight fraction. So in this research the weight fraction is used in design and fabrication for avoiding ambiguity.

Fig. 1 Woven fiber 600 gsm

2.2 Hybrid Composite Matrix

The natural fibers of banana and the synthetic fiber of fiberglass preferred for reinforcement in the matrix of epoxy resin.

2.3 Fiberglass (Synthetic Fiber)

The fiberglass woven roving is made by fiberglass direct roving, good electrical insulation and mechanical properties, high strength. Glass fiber woven roving offers weight and strength in all forms, paramount control over thickness and wide range. The 600 gsm of woven fiberglass (Refer Fig. 1) preferred in this study.

2.4 Treated Banana Fiber (Natural Fiber)

The natural fiber banana is identified based on its high strength with random orientation. In this study, the banana fibers were treated with the chemical solution consisting of NaOH 10% and 10% sodium lauryl sulfate and the remaining 80% distilled water for improving mechanical properties of the fiber and its adhesion properties. The treated banana fibers are shown in Fig. 2.

2.5 Epoxy Matrix

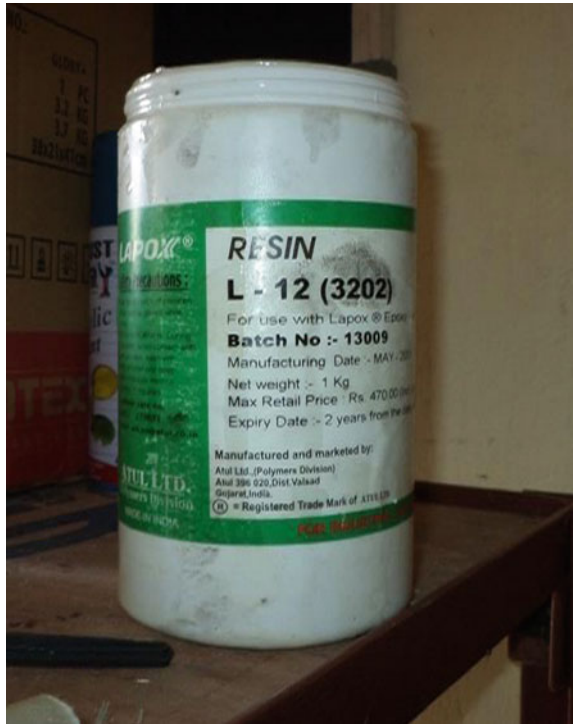
An epoxy matrix was preferred for this composite for the primary consideration that the epoxy established successful composite for bone plane applications in the



Fig. 2 Treated banaba fibers

research history [6], and secondarily the epoxy is economical in developing this new alternate materials. The epoxy of brand L 12- (3202) with suitable hardener was preferred for using at room temperature with the ratio of one part of hardener for ten parts of resin of epoxy (Fig. 3).

Fig. 3 Epoxy resin



3 Synthesize of Banana/Glass/Epoxy Hybrid Composite

The natural fiber hybrid with glass fibers in the epoxy matrix was done in terms of weighted fraction from 40 to 60%. In which the fibers fraction the weight of fibers according to the fiber percentage 40% banana and 60% fiberglass for 2 banana layers and 3 glass layer fashions and 60% banana and 40% fiberglass for 3 banana layers and 2 glass layer fashions for obtaining better matrix and desired properties. The sequences followed are: alternate layer fashion [G/B/G/B/G] and sandwich types like [G/B/B/B/G] and [B/G/G/G/B] preferred. This sequence is preferred and a treated banana fiber is used for obtaining better surface finish, lamination strength and improves the mechanical properties. The woven glass fibers sheets were cut into size of 300 × 300 (Refer Fig. 4). The hybrid composite was developed layer by layer of glass fiber and treated banana fiber (random) with epoxy matrix in specified weighted fraction. The beginning and finishing layer was glass fiber layer. Finally, the hybrid composite matrix was placed on the compression testing machine in between well-finished metallic plates for compacting with the applied pressure up to 0.5 kN/mm² load at room temperature for 90 min to promote the bonding strength, eliminate voids formation, obtain flatness, uniform thickness, and achieve desired mechanical properties of hybrid composite plate.

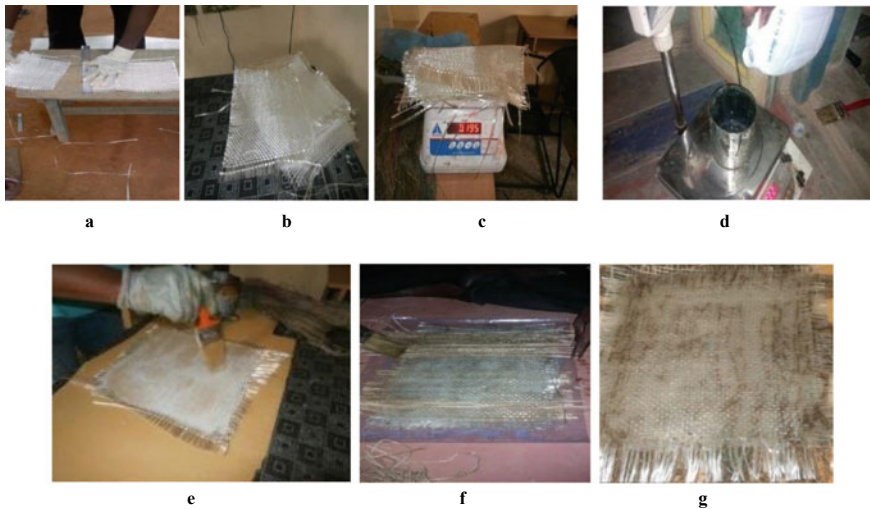


Fig. 4 Banana/glass/epoxy hybrid composite fabrication process. **a** Preparing the glass fibers to required size. **b** Prepare glass fibers for fabrication. **c** Weighing fibers for obtaining weight fraction. **d** Weighing of resin and hardener for obtaining weight fraction. **e** Preparing composite with epoxy resin, hardener. **f** Fabrication of hybrid composite with the alternate sequence of banana fiber and glass fiber with epoxy on surfaces. **g** Laminated banana/glass/ epoxy hybrid composite plate

Table 1 Tensile strength of Banana/ Epoxy/Glass hybrid fiber composites

Hybrid composite description	Breaking load KN	Tensile strength of composite (KN/mm ²)	Required tensile strength for femur bone (KN/mm ²)	Factor of safety
Alternate layer [G/B/G/B/G]	15.9	0.204	0.0434 ± 0.0036	4.340426
Sandwich structure [G/B/B/B/G]	11.2	0.139	0.0434 ± 0.0036	2.957447
Sandwich structure [B/G/G/G/B]	14.1	0.163	0.0434 ± 0.0036	3.468085

4 Investigation of Properties

4.1 Investigation on Tensile Strength Requirement

Investigation of Tensile properties is indispensable in composite material. The ASTM D-3039-76 standard was followed to prepare specimens of laminated banana/glass/epoxy hybrid composite. A wire hacksaw cutting employed for fabricating the specimens for investigating the properties of synthesized composite in tensile load. The specimen geometric features are 120 mm long, 15mm wide, and 5mm thick. The operating parameters are 50 KN load cell loading condition, 2mm/min testing speed. The tensile strength of proposed composites and required strength is given in Table 1.

$$\text{Tensile Strength} = \frac{L_t}{wt}$$

L_t = Tensile Load in N; w = width of the specimen and t = Thickness of the specimen.

4.2 Investigation on Compression Strength Requirement

As it is thin, flexible sample, the compressive strength investigation found somewhat difficult than metal testing. Sample often buckled and broke and more number of samples and utmost care need to perform this investigation. For the application aimed for this composite, the compressive strength estimation is must. The compression test was carried out according to the standard for polymer matrix composite D3140. The results are given in Table 2

Table 2 Compressive strength of Banana/Epoxy/Glass hybrid fiber composites

Hybrid composite description	Breaking load (KN)	Compressive strength of composite (KN/mm ²)	Required compressive strength for femur bone (KN/mm ²)	Factor of safety
Alternate layer [G/B/G/B/G]	7.32	0.214	0.11530 ± 0.0129	1.669267
Sandwich structure [G/B/B/B/G]	3.04	0.142	0.11530 ± 0.0129	1.107644
Sandwich Structure [B/G/G/G/B]	3.92	0.156	0.11530 ± 0.0129	1.216849

4.3 Investigation on Flexural Strength Requirement

The three-point bending test was carried out on specimens according to ASTM D 790. The length, width, and thickness of the specimen are 130 mm long, 12 mm wide, and 4 mm thick. The loading nose and its circular contact were 3 millimeter radius. The specimens here fixed horizontally and loading was done perpendicular to longitudinal axis of the specimen which is supported in a fixture with spanning to thickness ratio of 30:1 as per ASTM specification. The larger ratio preferred for minimizing effects of out-of-plane shear in bending properties calculations. The quasi-static transverse loading of 5 KN was done with the speed rate of 10mm/min in each specimen when testing. The flexural strength and requirements are furnished in Table 3.

Table 3 Flexural strength of banana/glass epoxy hybrid fiber composites

Hybrid composite description	Flexural strength of composites (KN/mm ²)	Breaking load (KN)	Required flexural strength for femur bone (KN/mm ²)	Factor of safety
Alternate layer [G/B/G/B/G]	0.172	4.358	0.08389 ± 0.009896	1.833962
Sandwich structure [G/B/B/B/G]	0.163	4.310	0.08389 ± 0.009896	1.737999
Sandwich structure [B/G/G/G/B]	0.169	4.296	0.08389 ± 0.009896	1.801975

5 Results and Discussions

The specially treated banana fibers reinforced hybrid composites in three different layers fashion fabricated and tested. The tensile compressive bending behaviors are understood from the plot of computerized composites testing facilities. All three kinds of hybrid composites were included in the investigation.

The displacement response for tensile load on the alternate layer [G/B/G/B/G] hybrid composite under tensile load-based investigation is shown in Fig. 5. Similarly for sandwich structures of [G/B/B/B/G] and [B/G/G/G/B] are shown in Figs. 6 and 7. The tensile strengths of the proposed composites are found higher than the required strength. And the maximum and minimum of factor of safety obtained are 4.340426 and 2.957447, respectively.

The displacement response for compressive load on the alternate layer [G/B/G/B/G] hybrid composite under compressive load-based investigation is shown in Fig. 8. Similarly for sandwich structures of [G/B/B/B/G] and [B/G/G/G/B] are shown in Figs. 9 and 10. The compressive strengths of the proposed composites are found higher than the required strength. And the maximum and minimum of factor of safety obtained are 1.669267 and 1.107644, respectively.

The displacement response for bending load on the alternate layer [G/B/G/B/G] hybrid composite under bending load-based investigation is shown in Fig. 11. Similarly for sandwich structures of [G/B/B/B/G] and [B/G/G/G/B] shown in Figs. 12 and 13. The flexural strength of the proposed composites is found higher than the required strength. And the maximum and minimum of factor of safety obtained are 1.669267 and 1.107644, respectively.

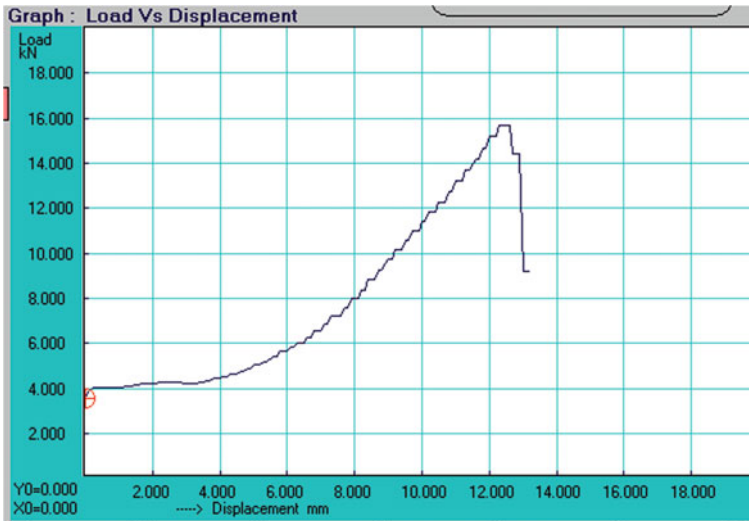


Fig. 5 Load versus displacement for alternate layer [G/B/G/B/G] hybrid composite under tensile load-based investigation

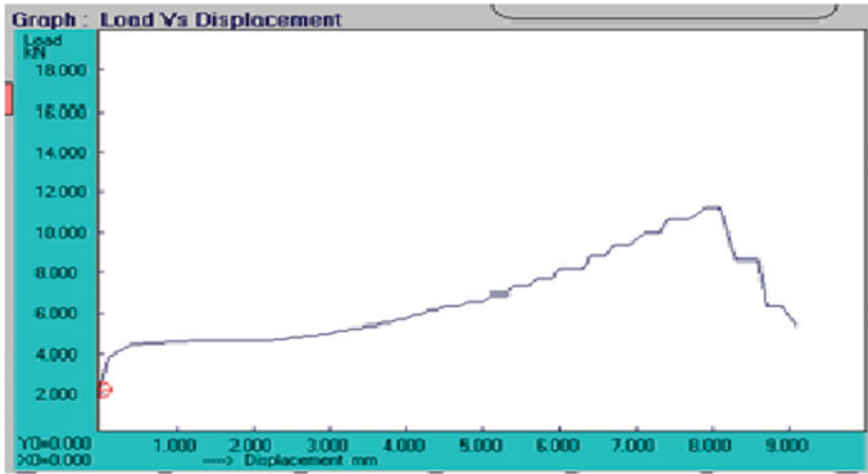


Fig. 6 Load versus displacement for sandwich structure [B//G/G/G/B] hybrid composite under tensile load-based investigation

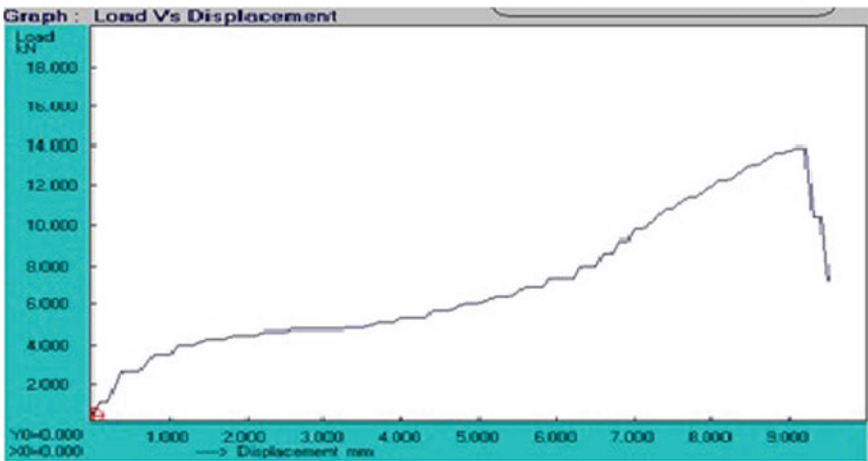


Fig. 7 Load versus displacement for sandwich structure [G/B/B/B/G] hybrid composite under tensile load-based investigation

6 Conclusion

The attempt of alternate material for femur bone plate is discussed in this study. The study preferred the polymer matrix composites in which the specially treated banana fibers and fiberglass-reinforced in epoxy resin matrix with three different fashions fabricated and characterized in terms of bending compression and tensile strengths and compared with required strengths. Based on the results found higher

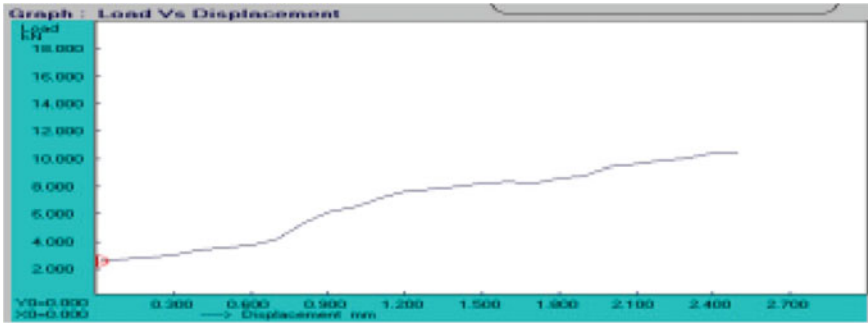


Fig. 8 Load versus displacement for alternate layer [G/B/G/B/G] hybrid composite under compressive load-based investigation

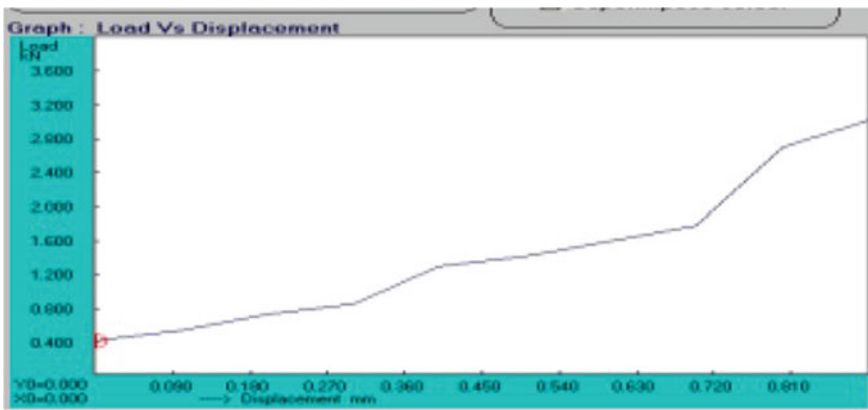


Fig. 9 Load versus displacement for sandwich structure [G/B/B/B/G] hybrid composite under compressive load-based investigation

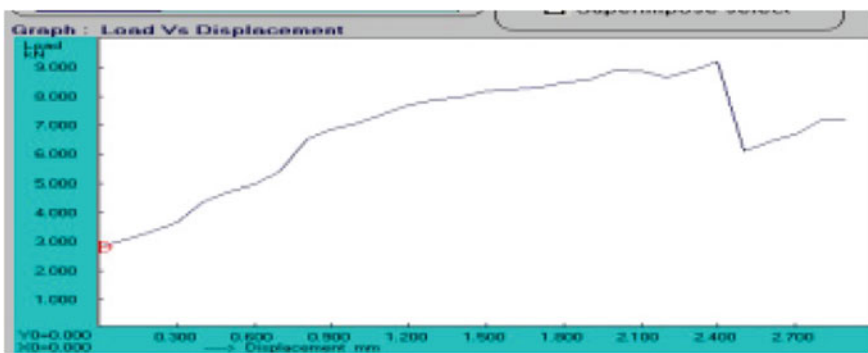


Fig. 10 Load versus displacement for sandwich structure [B//G/G/G/B] hybrid composite under compressive load-based investigation

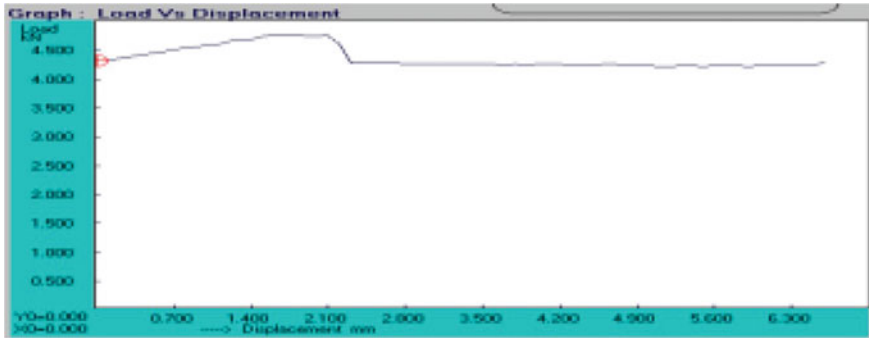


Fig. 11 Load versus displacement for alternate layer [G/B/G/B/G] hybrid composite under bending load-based investigation

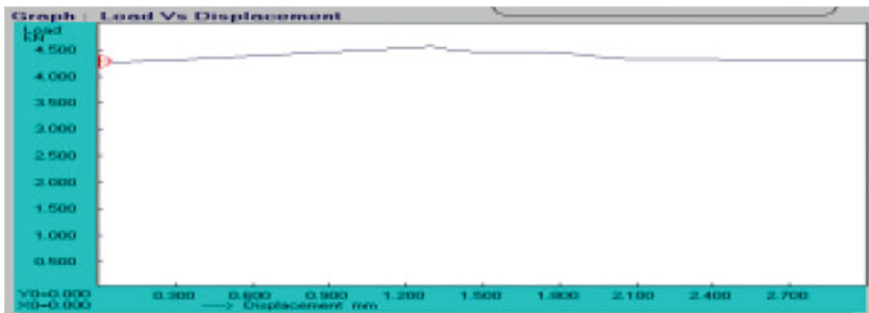


Fig. 12 Load versus displacement for sandwich structure [B//G/G/G/B] hybrid composite under bending load-based investigation

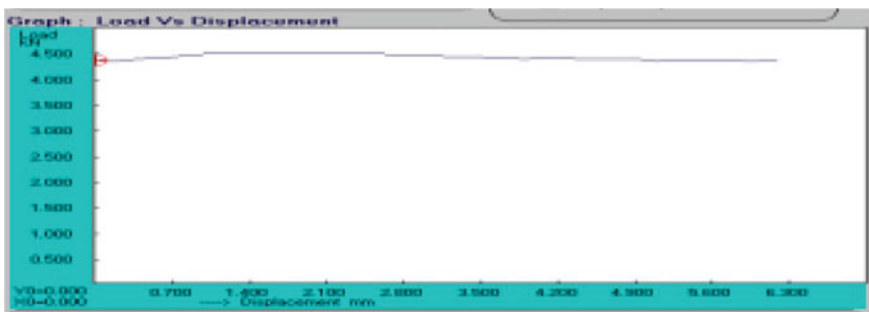


Fig. 13 Load versus displacement for sandwich structure [G/B/B/B/G] hybrid composite under bending load-based investigation

than the required strength. The proposed composites satisfied the requirements and factor of safety also found satisfactory levels. The further development of this work is: the composites to be tested with bio-fluids to know the volumetric changes and properties changes by absorbing the human bio-fluid. It will consume more time but the result may give one of the grand successes in the medical field.

References

1. Scholz M-S, Blanchfield JP (2011) The use of composite materials in modern orthopedic medicine and prosthetic devices: a review. *Compos Sci Technol* 71:1791–1803
2. Zheng-Ming Huang A, Fujihara K (2005) Stiffness and strength design of composite bone plates. *Compos Sci Technol* 65:73–85
3. Gopalakrishnan T, Jayakanth JJ, Gnanavel C Sridhar R (2018) Analysis of hybrid natural fiber composite for biomedical application. *Int J Emerging Technol Eng Res (IJETER)* 6(4):274–277. www.ijeter.everscience.org ISSN 2454-6410
4. Devarajan C, Krishnaswamy M (2011) Natural fiber bone plates as substitutes for orthopedic alloy plates. *Invited Rev Biotechnol Bioinf Bioeng*
5. Chandramohan D, Marimuthu K (2011) Bio composite materials based on bio polymers and natural fibers—Contribution as bone implants. *Int J Adv Med Sci Appl Res* 1(1)
6. Ali et al (1990) Application of the three-dimensional finite-difference time-domain method to the analysis of planar microstrip circuits

Automation Advancements in Wind Turbine Blade Production: A Review



K. P. Desai, D. Binu, A. V. V. D. Pavan, and A. P. Kamath

Abstract Wind turbine blade production involves intricate processes that require skilled labour, reliability and time. The automation of blade production processes in context with wind turbines aids in decreased cycle times and enhanced accuracy in the finished components. Automating the lay-up or material deposition process solely does not offer significant cost reductions, with rest of the processes remaining labour intensive. It may thus seem advantageous to establish a complete automated process chain for wind turbine blade production. This article enlists numerous automation methodologies which can be found suitable for a sequence of processes. The primary objective of this study lies in recognizing the advancements and the potential for automation in various operations associated with blade production. Besides helping to analyze the overall impact, this review shall assist researchers in realizing the challenging aspects of such self-driven processes as well.

Keywords Wind turbine · Blade production · Automation · Lay-up · Material deposition

1 Introduction

Harnessing energy from renewable resources has gained increased attention over the recent decades. In specific terms, wind energy is one of the cleanest and environmentally friendly resources, the wind power sector has witnessed rapid growth lately. With the requirement to tap more energy, the blades of wind turbines are being made larger and more efficient. On a standard basis, a utility scale wind turbine blade is found to have a length of 50 m approximately, while there are blades measuring

K. P. Desai · D. Binu · A. V. V. D. Pavan · A. P. Kamath (✉)
Department of Mechanical Engineering, Sardar Vallabhbhai National Institute of Technology,
Surat 395007, India

K. P. Desai
e-mail: kpd@med.svnit.ac.in

© The Author(s), under exclusive license to Springer Nature Singapore Pte Ltd. 2022
H. K. Dave et al. (eds.), *Recent Advances in Manufacturing Processes and Systems*,
Lecture Notes in Mechanical Engineering,
https://doi.org/10.1007/978-981-16-7787-8_15

209

even beyond 70 m in length [1]. With technological advancements, the efficiencies of harnessing energy from wind can be increased from 8 to even 50% [2].

The prime focus of blade manufacturers has been in cutting costs and cycle times for production of blade components, with no compromise to their performance and quality [3]. The urge to meet the foregoing needs is accomplished by automating a wide range of processes that are indulged in blade production. For instance, the fabric lay-up process for the Vacuum Assisted Resin Transfer Moulding (VARTM) is highly tedious and can be conveniently replaced by automating this manual process [1]. Similarly, continuous direct textile lay-up showcases an improved potential for cost reductions in comparison with currently used manual production processes [4]. It is worthwhile to note that automation techniques curb the proneness of workers to various health hazards during grinding or even finishing processes such as surface coating and painting [5]. Moreover, such techniques ensure improved quality control and reduce dimensional uncertainty, thereby leading to lower scrap rates during blade component production [6].

The generalized process chain for wind turbine blade production commences with the supply of raw materials, followed by handling processes that transfer the fed material in its unusable state. Material handling techniques further involve cutting, pick-up, positioning and lay-up, draping and fixation of material. Successively, primary manufacturing process such as vacuum infusion, prepreg or filament winding technology follows. This is accompanied by bonding and finishing techniques, which involve applying adhesives to blade halves and surface coating to mitigate the impact of natural factors respectively. The present paper is aimed to review the plausible methodologies of automation in blade production processes listed above. In addition, the article gives adequate focus to recognize the economic viability and draws attention to the challenges faced by the automation techniques.

2 Automation Processes in Blade Production

There are a wide number of techniques for automation, suitable for adoption in wind turbine blade production. In order to extract more energy from wind, blade profile plays a key role. Hence, its accuracy must be well assured [7, 8]. The methods for automation may broadly be categorized into processes accompanying supply along with handling of raw materials, primary manufacturing, assembly and finishing of blade components. These are reviewed in detail in the subsequent sections.

2.1 Supply and Handling of Materials

With advancements in materials, the technologies for supplying and handling raw materials to produce wind turbine blade components have drastically evolved. Polyurethane based materials are being incorporated for the sheets and preforms

in order to produce blades with optimal strength to weight ratio [9]. A variety of flexible automated methods have been developed to adapt to such materials and their properties. The initial processes of feeding and cutting of fabric are in general, carried out using conveyors, automatic cutting tables carrying straight and round knife cutters [10]. A non-crimp fabric (NCF) roll with a standard width of around 1.27 m is preferable for the automated process [11].

Fantoni et al. [12] put forward solutions for self-driven handling of materials by portraying different gripping devices. Based on the study, Bernoulli gripper is found to be relatively convenient as it operates based on airflow between the gripper and part and is a contactless handling technique. Reinhart and Straßer [13] also conducted a study on flexible gripping methods and developed a technology that uses a low vacuum suction principle with actuators for closing apertures on the perforated plate. Being suitable for limp materials, this technology is seen to remain advantageous over existing principles and can be widely used in the wind turbine blade production industry. Additionally, the Adaptive Robot End-effector (AEE) is a specialized technique that functions on hydro adhesive principle for the pick and place process using parallelogram kinematics and cryo grippers [14].

The prevailing methods of automating the lay-up process for blades include Automated Fibre Placement (AFP), Automated Tape Lay-up (ATL) and filament winding technologies. The intent of the lay-up process is to allow the fabric to make the shape of the blade mould through deforming and deposition, once picked and placed. The deposition rates for filament winding and ATL are reported to go up to 13 kg/h and 90 kg/h for complex parts respectively [1]. Specifically, ATL process is found convenient with a range of tool operations and may require just a quarter of the man hours needed. This has been verified for aerospace blade applications and may thus hold suitable for wind turbine blades [15]. It has been determined that a combination of ATL and AFP offers the added advantage of aiding in fibre orientations for the blade spar [6]. Sherwood and Polcari [16] and Siqi [1] described an automated lay-up concept of shifting which involves preforming the fabric based on mould shape and then depositing the fabric onto it. The study emphasized the ability to manipulate NCF without causing any out of plane deformations.

It has been stated that automation of composite lay-up process requires sensing mechanism for gathering initial information, intelligent decision making capacity and efficient material handling system which can effectively perform operations [17]. Franke et al. [4] highlighted a continuous direct textile lay-up technique, named Automated Dry Material Placement (ADMP). It is determined to deposit textiles of 100–2000 mm width and 0.25–2.5 mm thick. Having proven to be effective in automating the production of aerospace parts, the technique finds analogous application in producing parts of wind turbine blades. Another suitable technique involved using Large Area Robot (LAR) to automate the lay-up for spar cap of wind turbine blade by using integrated positioning sensors. Line lasers may be equipped to monitor the position of the laid-up fabric [18].



Fig. 1 Drape gripper with hexagonal pixels [21]

The draping operation must ensure accurate fixing of NCF deposited on the blade mould. Automated draping avoids the risks associated with manual draping techniques in terms of time constraints and health hazards due to the fabrics being pre-impregnated with toxic epoxy resins. Potter [19] considered automating the draping process through vacuum forming technology, which later proved to be impractical for large parts due to economic reasons. In an effort to automate the process, the Institute of Integrated Product Development (IPD) developed a module comprising a draping head and vacuum grippers for gentle handling of NCF. The module is capable of reshaping and draping the fabric appropriately [20].

As draping is to be performed right after fabric deposition onto the mould, incorporating draping elements in the effector is recommended. Forster et al. [21] introduced a pixel-based draping and gripping unit which contain sensors for monitoring and controlling draping (Fig. 1). The Danobat group incorporated a draping head to offer the required pressure surge against mould surface during the draping operation. To further enhance the adaptability of draping head to the complex mould contour, Direct Textile Placement (DTP) effector, a subproject of BladeMaker, was developed with a design that can vary the applied pressure to a certain limit [4].

Automation in fixation involves robotized spraying of hot melt adhesives and use of effectors for gel-like adhesives. Fixation of NCF is much needed to prevent the material from slipping after it has been deposited using adhesives. The Institute for Integrated Product Development (BIK) implemented a reproducible spray of adhesive using a gun coupled with the gantry robot system [4].

2.2 Manufacturing

Post et al. [22] conducted a study on the implementation of additive manufacturing in the wind energy sector and considered the Big Area Additive Manufacturing (BAAM) system (Fig. 2), developed by Cincinnati Incorporated. The system contains an extruder which is traversed by a gantry system and enables the extruder to move in all three axes, delivering 45 kg/h of thermoplastic materials. This gantry system can achieve 5 m/s peak velocities and 1.64 m/s^2 accelerations with position accuracy of 0.05 mm. Moreover, Ingersoll Machine Tool Company is developing the Wide and High Additive Manufacturing (WHAM) system with the ability to machine, print and coat. It is expected to start with a production rate at around 450 kg/h and can be scaled higher. Implementing Internet of Things (IoT) in additive manufacturing will be a major contribution towards reduction of scrap during blade production, thus increasing the overall efficiency of the process chain.

Griffin [23] presented a study dealing with the combination of automated preforming technologies and infusion processes which would avoid human intervention, reduce cycle time and also prevent distortion of fibres. Oriented sprayed fibre preforms are considered suitable for automated preform manufacturing for large wind turbines. The study covered various techniques of automated preform manufacturing for wind turbine blade structures and compared them using Analytic Hierarchy Process (AHP).



Fig. 2 Big Area Additive Manufacturing (BAAM) [46]

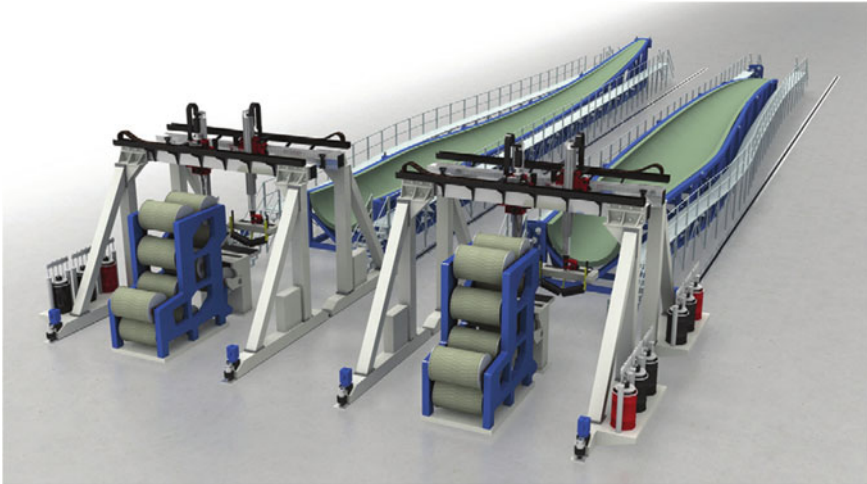


Fig. 3 Rapid material placement system (RMPS) [24]

Stewart [24] studied the applicability of Rapid Material Placement System (RMPS) (Fig. 3), a CNC controlled system containing multiple axes end effectors fitted onto a gantry. The system is capable of assisting the blade manufacturing process and can even perform operations like spraying and addition of adhesives onto the blade halves. It is reported that a dual gantry system, positioned next to each other takes only 2 h to produce a 45-m blade shell.

Another automation equipment, the Reaction Injection Moulding (RIM) machine is used to manufacture polyurethane wind turbine blades that lie in close proximity with wind power plants. The machine injects isocyanate and its reactive components into the mould. After compression and curing by radiation, the polyurethane blade is producible. Similarly, the Long Fibre Injection (LFI) machine injects both isocyanates, its reactive components along with long fibres which then compresses and cures, producing the polyurethane blade [25]. These machines curb difficulties associated with transportation of large blades as the entire process is performed in close proximity to the wind power plant.

2.3 Assembly

For movements between assembly stations, the use of Automated Guided Vehicles (AGV) is advisable. AGV makes use of tracks for movement, allowing them to traverse along the whole location using signals detected by sensors embedded on them [5]. Kruger et al. [26] have very well described man–machine cooperation in assembly lines. Various robotic assembly systems could prove to ease the transportation of blade components from one station to another. Moreover, integration of advanced

machinery to form systems capable to carry out multiple operations leads to decreased number of assembly stations, avoiding balance delays.

Roberts et al. [27] patented a concept of joining blade components through improved methods that consumes lesser adhesives. The study suggested a method of printing and depositing 3D grid structures at the first joint area of the blade using CNC machine. This is followed by blade add-on components being placed onto the rotor blade; an adhesive is provided partially to fill the grid which secures the components to the blade. These grid structures are known to offer buckling resistance, assisting to reinforce the joint areas of the blade. The printed grid structures have tight gaps; hence, the usage of adhesives for bonding is limited in comparison with conventional blades. The latter makes use of excess bonding due to intricate profiles near joint areas, making the usage of printed grid structures preferable.

Mironov [28] solved the problem of limited accessibility of longitudinal movement of robots over the blade mould to spray gelcoat, place dry fibreglass and apply bonding adhesives to the blade halves prior to joining them. It suggested engaging a gantry over the moulds provided with a robot that can slide longitudinally over the blade halves using servo drive motors. After the application of adhesives, the halves are joined using turnover hinge devices which rotate one half over the fixed mould half with no hindrance to the gantry track. Interlocking the removable bridge sections and gantries is facilitated through a Programmable Logic Controller (PLC).

2.4 *Finishing*

The blade components produced through automated techniques are to be precisely finished. These may involve sanding, painting, surface coating, etc. The factors influencing finishing process and its associated costs are mainly the size of finished component and amount of finishing work to be performed [29]. Blade finishing which impact quality and productivity rates involve risks of manual tool and heavy machinery handling as well as exposure to hazardous blade materials such as GFRP and Epoxy resins. This poses a detrimental impact on the health of workers. Automating surface treatment and finishing of blades make various tedious operations relatively simple to be implemented. Moreover, it improves the quality of finish as robots are able to travel across entire blade length in a continuous manner, improving the blade quality in terms of resistance to weather, corrosion and mechanical stresses [5].

Liebherr Automation Systems carried out automated blade trimming and fibre layout techniques on a blade length of 60 m. They implemented robotized polishing of blade surfaces, enabling large time and cost savings [30]. The complex blade contours make programming a robot difficult for trimming and sanding operations. EINA of Spain managed to tackle the concern through a system capable of tracking changing contours and placing the sand tool normal to the blade surface at all times [31].

Tebulo Robotics, a Dutch firm, developed an Automatic Mobile Robot (AMR), capable of a 360° rotation to follow and coat blade contours precisely by making use of the Externally Guided Motion (EGM) technology. The advanced technology imparts the capability to guide complex blade contours effortlessly with least programming needed for the robotic system. Besides, the AMR is suitable to be deployed for surface cleaning, precision polishing as well as non-destructive blade inspections. It is estimated to coat a 100-m blade in 90 min [32]. The patented AccuFind technology developed by Dynamic Robotic Solutions (DRS) locates and processes the root end of blade and provides a self-driven solution for excess blade material to be identified and subsequently ground and sanded [33].

Table 1 summarizes various principles and techniques of automating different processes which are involved in the production of wind turbine blades. Further details

Table 1 Automation methods for various blade production processes

Process	Operation	Automation method	References
Supply and handling	Feeding and cutting	Conveyor Automatic cutting table	Vilumsone [10] Vilumsone [10]
	Pick-up	Bernoulli gripper Low vacuum suction principle	Fantoni et al. [12] Reinhart and Straßer [13]
	Position and lay-up	AEE AFP ATL Filament winding Shifting ADMP LAR	Kordi et al. [14] Siqi [1] Siqi [1] Siqi [1] Sherwood and Polcari [16] Siqi [1] Franke et al. [4] Franke et al. [4] Rolbiecki et al. [18]
		Draping	Vacuum forming technology DTP effector
Manufacturing	Fixation Deposition, Infusion, Machining	Robotized sprayer BAAM WHAM RMPS AGV	Franke et al. [4] Post et al. [22] Post et al. [22] Stewart [24] Sainz [5]
Assembly	Transportation Bonding	3D printed grid structures Gantry with robotized sprayer	Roberts et al. [27] Mironov [28]
Finishing	Sanding Painting and coating	AccuFind technology AMR	Abrams et al. [33] Tebulo Robotics [32]

regarding practices of various such advanced blade production technologies may be referred to using the tabular summary.

3 Economic Analysis

The primary objective of automating wind turbine blade manufacturing is to diminish the expenses of harnessing energy by reducing labour costs, production time, increasing reproducibility and volume of production. The predominant factors of analyzing the economic viability of blade production include cost of tooling, maintenance and labour, which are relatively high at low manufacturing levels [6]. Chen et al. [34] stated that the most efficient way to decrease the operation and maintenance cost of blade production is to find out the blade defects by reducing the cost of inspection and by automating the entire sequence of processes. Benjamin [35] developed a winding system that is automated. The system is capable of winding NCF plies around a mandrel at a low cost without affecting the quality when compared to other processes.

Murray et al. [36] presented a study owing to the major contribution of production costs to materials and direct labour. The study depicted that 11.4% of material costs are from scrap materials. Based on these findings, incorporating an automated process chain in blade manufacturing may be considered to be a dominating step towards cost reduction by avoiding material wastage and ensuring tighter dimensional tolerances while manufacturing.

Schubel [6] adopted a Technical Cost Modelling (TCM) approach to contrast production costs of a 40-m wind turbine blade shell set and spar using different manufacturing techniques. The comparison included six processes, namely hand lay-up prepreg, Vacuum Infusion (VI), Light Resin Transfer Moulding (LRTM), ATL, AFP and overlay braiding (Figs. 4 and 5). On comparing the automated fibre deposition strategies, i.e. ATL, AFP and braiding, it is found that braiding adds tremendous expenses and time due to its failure to put filaments along the length. It depicts a 21% expense surge over manual techniques. On contrary, ATL and AFP appear to decrease fabricating costs by around 8%. ATL shows a decrement in expenses up to 4% over hand lay-up prepreg, being monetarily effective beyond production of 750 PPA. AFP is considered to have the added advantage of being more adaptable in comparison with ATL, making this technique more feasible.

Through automated preform techniques, blade manufacturers undergo reduced handwork costs, improved control over fibre orientation along with significant degree of consistency, helping to produce complex blade geometries with low misuse of crude materials and reduced time for production [23].

Franke et al. [4] studied the reduction of manufacturing and labour costs in the lay-up process of the BladeMaker project. Gantry robots coupled with effectors incorporated within the automation system carried out the process of continuous direct material deposition. An investigation in context with the BladeMaker concluded cost savings of 17.3–23.1% by utilizing the automation arrangements and systems.

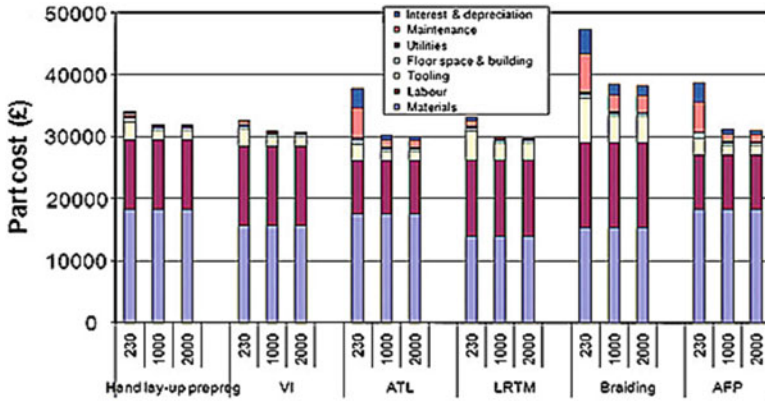


Fig. 4 Comparison of part costs for blade shell production via different processes [6]

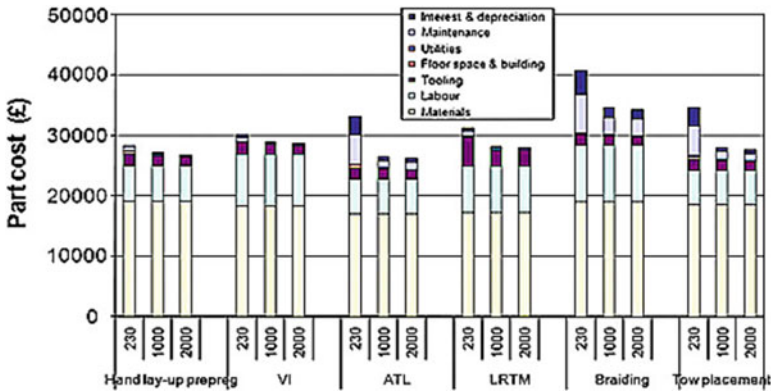


Fig. 5 Comparison of part costs for blade spar production via different processes [6]

The literatures reviewed emphasize that the economic perks of automation technologies for wind turbine blade production are numerous. However, these tend to be largely reliant on the blade production volumes and the extent up to which the plant is automated. Expense reduction via partial automation of blade production may likely be compensated by a range of labour costs for rest of the processes.

4 Challenges

A key challenge faced during the automated feeding and cutting processes lies in establishing speeds of unwounded material roll and conveyor belt at par [37]. Manual

processes are still being carried out handling and draping of dry fibres to manufacture prepreg, making it time consuming [38]. Manufacturing of wind turbine blades consists of geometric and time constraints, due to which automation techniques like AFP and filament winding principles become cumbersome to be carried out [1]. For instance, the curved profile of blade mould requires a handling unit with smaller width material roll for the automated lay-up process which would lead to an increased production time [4]. ATL and AFP face complexities to manufacture small parts like ribs, spars and blade corners [39]. Detection of small parts and contour details becomes inconvenient because of small course lengths [40].

With competencies to harness more energy from wind, the loads on wind turbines have been rising with the blade sizes [41]. The blades are to be designed light in weight, precisely manufactured to possess adequate strength and sustain heavy loads [1]. There is still scope for further research in developing concepts to restrain the extreme load conditions to which the blades are subjected, along with improvising the energy production [42]. Besides, there lie concerns in the transportation of bulky finished blade components. Peeters et al. [43] discussed the concept of segmented production of turbine blades, which not only offers convenience to 3D printing of blade components but also eases transportation of large blades. However, this technique does face difficulties in resisting high loads. Furthermore, self-monitoring of wind turbine blades becomes difficult under such unfavourable conditions [44].

Recent advancements attributed toward Future Emerging Technologies (FET) appear superior over the need to automate blade production. FETs such as Airborne Wind Energy (AWE) and offshore floating wind concepts are likely to be developed and put to practical use in the near future [45]. On account of reduced loads of these tethered systems, their operation could be relatively convenient with reduced capital expenses. It must be taken into account that difficulties associated with a weighted analysis and modelling between the convenience and costs of automation impede blade manufacturers from transforming into a completely automated process chain for blade component production.

5 Conclusion

A review on the automation advancements in blade production for wind turbines has been performed, highlighting the scope for technology-driven production plants in the wind power sector. This article enlists various automation techniques in a sequential process wise approach of producing wind turbine blades based on the survey of literature available.

As wind turbine blades continue to increase in their sizes, there is a need to develop advanced production techniques to boost production rates. There are countless automation techniques that suffice the demands of enhancing the efficacy of blade production. Different automated handling and manufacturing techniques discussed throughout the paper appear to ease the production process. Systems such as BAAM, WHAM and RMPS machines are developed to perform multiple operations such as

assisting primary manufacturing along with machining and coating within itself. This could help cut down production time, with the number of stations being reduced. However, the hesitancy of blade manufacturers in adapting to a complete automated process chain is mainly attributed to an unconvincing comparison between beneficial and non-beneficial impacts of automation.

Though future emerging technologies are expected to replace tower based wind turbines over the coming years, adequate attention must be diverted to simplify the production of wind turbine blades through automation.

References

1. Siqi Z (2013) An automated fabric layup machine for the manufacturing of fiber reinforced polymer composite. Graduate theses and dissertations. 13170
2. Rahman AS (2019) Design of cost-effective and efficient fiber-reinforced composite blades for wind turbines. *Reinf Plast* 63(1):21–25
3. Damiano M, Russo A, Sellitto A, Vecchio E, Stellato T, Riccio A (2021) Design of a composite wind turbine blade manufactured with the ONE SHOT BLADE® technology. *Mater Today: Proc* 34:103–105
4. Franke J, Ohlendorf JH, Thoben KD (2019) Automated production processes in the rotor blade industry—Solutions for a continuous direct textile layup. *Materialwiss Werkstofftech* 50(11):1326–1342
5. Sainz JA (2015) New wind turbine manufacturing techniques. *Procedia Eng* 132:880–886
6. Schubel PJ (2012) Cost modelling in polymer composite applications: case study—Analysis of existing and automated manufacturing processes for a large wind turbine blade. *Compos B Eng* 43(3):953–960
7. Hutchinson JR, Schubel PJ, Warrior NA (2011) A cost and performance comparison of LRTM and VI for the manufacture of large scale wind turbine blades. *Renew Energy* 36(2):866–871
8. Veers PS, Ashwill TD, Sutherland HJ, Laird DL, Lobitz DW, Griffin DA, Richmond JL (2003) Trends in the design, manufacture and evaluation of wind turbine blades. *Wind Energy: Int J Progr Appl Wind Power Convers Technol* 6(3):245–259
9. Hupka F, Schornstein M, Neffzger H (2018) U.S. Patent No. 9,920,175. U.S. Patent and Trademark Office, Washington, DC
10. Vilumsons-Nemes I (2018) Industrial cutting of textile materials. Woodhead Publishing
11. ISO 11093-4 (2016) Paper and board—Testing of cores—Part 4: Measurement of dimensions
12. Fantoni G, Santochi M, Dini G, Tracht K, Scholz-Reiter B, Fleischer J, Verl A (2014) Grasping devices and methods in automated production processes. *CIRP Ann* 63(2):679–701
13. Reinhart G, Straßer G (2011) Flexible gripping technology for the automated handling of limp technical textiles in composites industry. *Prod Eng Res Devel* 5(3):301–306
14. Kordi MT, Husing M, Corves B (2007) Development of a multifunctional robot end-effector system for automated manufacture of textile preforms. In: 2007 IEEE/ASME international conference on advanced intelligent mechatronics. IEEE, pp 1–6
15. Grimshaw MN, Grant CG, Diaz JM (2001) Advanced technology tape laying for affordable manufacturing of large composite structures. In International sampe symposium and exhibition, pp 2484–2494
16. Sherwood J, Polcari M (2017) Automation for wind blade manufacturing. In: Automated composites manufacturing—Third international symposium
17. Newell GC, Khodabandehloo K (1995) Modelling flexible sheets for automatic handling and lay-up of composite components. *Proc Inst Mech Eng Part B: J Eng Manuf* 209(6):423–432

18. Rolbiecki M, Worthmann F, Maass R, Müller DH, Thoben KD (2009) Large area robot—Flexibel automatisierte Produktion großflächiger Faserverbundstrukturen durch mobile Fertigungseinrichtung (02PK2052). In: Institut für integrierte Produktentwicklung
19. Potter K (2002) Beyond the pin-jointed net: maximising the deformability of aligned continuous fibre reinforcements. *Compos A Appl Sci Manuf* 33(5):677–686
20. Rolbiecki M, Franke J, Ohlendorf JH (2016) Draping module for draping textile webs on a forming tool, apparatus therewith, and methods for automatically depositing and draping textile webs (DE 10 2015 108 943 A1)
21. Förster F, Ballier F, Coutandin S, Defranceski A, Fleischer J (2017) Manufacturing of textile preforms with an intelligent draping and gripping system. *Procedia CIRP* 66:39–44
22. Post BK, Richardson B, Lind R, Love LJ, Lloyd P, Kunc V, Jenne D (2017) Big area additive manufacturing application in wind turbine molds. *Solid Freeform Fabrication*
23. Griffin D, Global Energy Concepts LLC (2002) Blade system design studies volume I: Composite technologies for large wind turbine blades (No. SAND2002-1879). Sandia National Laboratories
24. Stewart R (2012) Wind turbine blade production—New products keep pace as scale increases. *Reinf Plast* 56(1):18–25
25. Pyles RA, Matsco J (2012) U.S. Patent Application No. 13/392,967
26. Krüger J, Lien TK, Verl A (2009) Cooperation of human and machines in assembly lines. *CIRP Ann* 58(2):628–646
27. Roberts D, Althoff NK, Nielsen MW, Tobin JR, Mccalip A (2019) U.S. Patent Application No. 15/935,304
28. Mironov G (2012) U.S. Patent Application No. 13/497,845
29. Eker AA, Eker B (2013) General assessment of fiber-reinforced composites selection in wind turbine blades. Mechanical Engineering Department, Yıldız Technical University, İstanbul, Turkey, p 20
30. Wind turbine rotor blade manufacturing with Liebherr automation systems (2012) RP LVT. <https://www.liebherr.com/shared/media/gear-technology-and-automation/broschures/automation/robot-integration/liebherr-wind-turbine-rotor-blade-manufacturing-en.pdf>
31. Handelsman M, Zald R (2010) An automated approach to blade manufacturing. *Wind Syst Mag*. http://www.windsystemsmag.com/media/pdfs/Articles/2010_March/FG-KMT_0310.pdf
32. Tebulo Robotics (2021) Autonomous mobile robot (AMR). <https://www.tebulorobotics.com/exclusive-robot-trial-looks-to-speed-up-production-for-large-wind-turbine-blades>
33. Abrams CA, Kuhn J, Handelsman MW (2010) Vision guided real time locating and trimming of flash (WO2010151621A1)
34. Chen X, Shihavuddin AS, Madsen SH, Thomsen K, Rasmussen S, Branner K (2020) AQUADA: automated quantification of damages in composite wind turbine blades for LCOE reduction. *Wind Energy*
35. Wollner BA (2011) Development of a fabric winding system for the automated manufacture of prefabricated wind turbine blade roots
36. Murray RE, Jenne S, Snowberg D, Berry D, Cousins D (2019) Techno-economic analysis of a megawatt-scale thermoplastic resin wind turbine blade. *Renew Energy* 131:111–119
37. Ohlendorf JH, Richrath M, Franke J, Brink M, Thoben KD (2020) Towards automation of wind energy rotor blade production: a review of challenges and application examples. *Adv Manuf: Polym Compos Sci* 1–18
38. Reinhart G, Ehinger C (2013) Novel robot-based end-effector design for an automated preforming of limb carbon fiber textiles. In: *Future trends in production engineering*. Springer, Berlin, Heidelberg, pp 131–142
39. Paton R (2007) Forming technology for thermoset composites. In: *Composites forming technologies*. Woodhead Publishing, pp 239–255
40. Dirk HJ, Ward C, Potter KD (2012) The engineering aspects of automated prepreg layup: history, present and future. *Compos B Eng* 43(3):997–1009
41. Mishnaevsky L, Branner K, Petersen HN, Beauson J, McGugan M, Sørensen BF (2017) Materials for wind turbine blades: an overview. *Materials* 10(11):1285

42. Capuzzi M, Pirrera A, Weaver PM (2014) A novel adaptive blade concept for large-scale wind turbines. Part I: Aeroelastic Behav Energy 73:15–24
43. Peeters M, Santo G, Degroote J, Paepegem WV (2017) The concept of segmented wind turbine blades: a review. Energies 10(8):1112
44. McKenna R, Leye PO, Fichtner W (2016) Key challenges and prospects for large wind turbines. Renew Sustain Energy Rev 53:1212–1221
45. Watson S, Moro A, Reis V, Baniotopoulos C, Barth S, Bartoli G, Wiser R (2019) Future emerging technologies in the wind power sector: a European perspective. Renew Sustain Energy Rev 113:109270
46. Chesser P, Post B, Roschli A, Carnal C, Lind R, Borish M, Love L (2019) Extrusion control for high quality printing on Big Area Additive Manufacturing (BAAM) systems. Addit Manuf 28:445–455

Characterization of Damage Behavior During Hot Forging



Ahmed A. M. Okasha, Hussein M. A. Hussein, Mostafa Shazly,
and Osama M. Dawood

Abstract During hot forging process, surface cracks may be deformed in several positions. These cracks may have repeated during production process which may have an impact on the life of the product. Deforming conditions (forming temperature, strain rate, and stress triaxiality) may be responsible for these cracks' formation. This work is an effort to study the effects of the forming conditions on the damage behavior and develop models using the stress–strain curves of steel C45 material as a case study. It is found that; Raising the formation temperature at constant strain rates reduces damage initiation strain and fractural stress but increases fractural strain. Also increasing the strain rates leads to reduction of the fractural strain (complete fracture), at the same time causing increase of the flow stresses and the damage initiation strain (at ultimate point). It was observed that increasing the stress triaxiality reduced the damage strains (initiation and complete fracture). A finite element model on a tension test was conducted to locate and explain the damage initiation and complete fracture in a cutting plane that passes through the necking zone and to show the damaging effect on the material strength. It was noticed that the damage started at the central elements and the damage reduced the material stiffness after damage initiation.

Keywords Ductile damage · Fractural strain · Forging temperature · Strain rate · Stress triaxiality

A. A. M. Okasha (✉) · H. M. A. Hussein · O. M. Dawood
Mechanical Engineering Dept., Faculty of Engineering, Helwan University, Cairo, Egypt

H. M. A. Hussein
e-mail: husein@h-eng.helwan.edu.eg

H. M. A. Hussein
Mechanical Engineering Dept., Ahram Canadian Univ., 6th of October City, Giza, Egypt

M. Shazly
Mechanical Engineering Dept., The British University in Egypt, Elshorouk City 11187, Egypt
e-mail: mostafa.shazly@bue.edu.eg

1 Introduction

Metal forming processes may experience cracks (or fractures) during these processes due to the accumulation of plastic deformation especially at high strain rates with extended strain and relatively low temperatures. The cracking phenomena are related to -so called- material damage models which can be classified generally into brittle (cleavage), ductile, intergranular, and fatigue damages [1, 2].

The ductile damage model proposes from macroscopic point of view that the damage initiation starts at the instability zone (necking zone) [2, 3]. Also, this model proposes that the damage occurs in six steps; (1) inclusions or/and second phase in a ductile matrix, (2) void nucleation around the second phase or/and inclusions, (3) void growth, (4) strain localization between voids, (5) necking between voids, and (6) void coalescence and fracture [2, 4].

It is well-known that the necking starts at the ultimate strength in the engineering stress–strain curve [3]. After this point, the true stress drops to a new value of stress which is called damaged stress and the damage evolution starts to accumulate after the point of ultimate stress. The damage variable (D) is the measured parameter that can describe the amount of damage after damage initiation. At the onset of necking, the damage variable D is equal to zero but the ductile damage initiation criteria (ω_D) reaches the critical value = 1 [5]. At complete fracture, the damage variable (D) is equal to an experimental value which can be specified to (D_f). This model also proposes that the damage initiation criteria depend on strain rate, stress triaxiality, and forming temperature.

Bridgman [6], Davidson and Ansell [7] proved a relation between ductility and pressure (P). McClintock [8] and Rice and Tracey [9], deduced an expression relating between the stress triaxiality and the strain to fracture by a study of the void growth. The damage proposed occurs when the plastic strain causes a local instability in the form of localized strain bands [10, 11]. Bai et al. considered the studies of void growth as the basis of the modern ductile fracture mechanics [12, 13]. Bao [14] proved that increasing the stress triaxiality decreases the fractural strain for Steel C45. Mohanraj et al. [15] proved that increasing the stress triaxiality decreases the complete fractural strain for steel C45 by using notched specimens to show the effect of stress triaxiality.

The temperature and strain rate effects on damage strains were studied by Johnson and Cook [16] and Johnson and Holmquist [17] using the Split-Hopkinson tension-bar test on AISI 4340 steel to prove a model containing three brackets that cover the effect of temperature (linear function), strain rate effect (logarithmic function), and stress triaxiality effect (exponential function). This model contains five constants that need to be determined for each material (model calibration). Abed et al. [18, 19] used coupled model which consisted of J-C strength model and energy model to express the damage at different temperatures and different strain rates using microscopic scans for the fractured specimens during tensile test. Su-Tang et al. [20] studied the effect of strain rate and temperature on flow stress and complete fractural strain by using tensile test data.

Obviously, the damage data has been obtained historically from tensile tests, which not only represent the uniaxial state but also can represent multi-axial state using notched specimens with different radii to control the stress triaxiality. This makes the obtained data valid for complex metal forming processes as forging, bending, and deep drawing.

In this paper, a trial to create trends and statistical models to express the effects of the forming conditions on the damage behavior using the stress–strain curves of steel C45 as a material case study. Therefore, in this work, the damage behaviors were obtained conventionally-from tensile test results carried out on un-notched specimens at different temperatures and strain rates [20] and tensile tests carried out on notched specimens on steel C45 [15].

2 Problem Description and Motivation

During any hot forging process (especially, for the complex shape products), some surface cracks may be nucleated. Therefore, the motivation of this work is determining relations between the forming conditions (forming temperature, forming strain rate, and forming stress triaxiality) and crack nucleation parameter that is expressed as the plastic strain at damage initiation and the fractural plastic strain. Also, this work aims to obtain the trends that relate the forming parameters with the damage initiation strain and fractural strain. Also, it is a trial to create statistical models to relate the damage strains (damage initiation strain and fractural strain) to the forming parameters. Thus; these models can predict (forecast) the forming conditions (out of experimental data) that may cause these crakes.

3 Methodology

The methodology which was used to achieve the previous aim of this work is, first, specifying a suitable damage model which can deal with the hot forging process. The most suitable model is the ductile damage model that involves obtaining the plastic strain at damage initiation. According to (2) and (3), the damage starts at the necking zone that starts to form at the engineering ultimate point due to voids nucleation until complete fracture at voids coalescence. Therefore the way in determining the ultimate and fractural points from engineering curves using Eqs. (1) and (2) therefore, deducing the damage initiation strains (corresponding to ultimate point) and fractural strains (corresponding to fractural endpoint) at the different forming conditions by using the Eq. (3). The experimental stress–strain curves for C45 steel-as a case study- were available in [15, 18]. The results of true plastic strain at engineering ultimate point and at fractural point were analyzed and plotted against the different forming conditions to obtain the effect of these forming conditions on damage strains and stresses including general trends and approximated statistical models which can

relate them. These models can predict the damage initiation strain and fractural strain at other forming conditions which were out of the available experimental data and inside the experimental range.

$$\sigma_{\text{eng.}} = \frac{\sigma_{\text{true}}}{1 + \varepsilon_{\text{eng.}}} \quad (1)$$

$$\varepsilon_{\text{eng.}} = (e^{\varepsilon_{\text{true}}} - 1) \quad (2)$$

$$\varepsilon^{\text{pl}} = \varepsilon_{\text{true}} - \frac{\sigma_{\text{true}}}{E} \quad (3)$$

$$d_c = L_c \left(\varepsilon_f^{\text{pl}} - \varepsilon_0^{\text{pl}} \right) \quad (4)$$

where

$\sigma_{\text{eng.}}$	Engineering Stress
σ_{true}	True Stress
E	Young's Modulus
ε^{pl}	True Plastic Strain
ε_{eng}	Engineering Strain
$\varepsilon_{\text{true}}$	True Strain
$\varepsilon_f^{\text{pl}}$	True plastic strain at fracture
$\varepsilon_0^{\text{pl}}$	True plastic strain at ultimate.

At constant stress triaxiality, the experimental stress–strain data at temperatures range (from 298 to 923 °K), and different strain rates (from 0.0015 to 885 S⁻¹) for steel C45 were extracted from Ref. [18] using Get data Graph Digitizer software. However, the data which study the stress triaxiality effect were extracted from another review [15] as a (stress triaxiality–fractural strain) curve at room temperature.

At constant stress triaxiality: the engineering stress–strain data were calculated using Eqs. (1) and (2) leading to determination of engineering ultimate points strain and engineering fractural points strain which was transformed into the plastic true one using Eq. (3) to get; damage initiation strain, $\varepsilon_0^{\text{pl}}$, damage fractural strain, $\varepsilon_f^{\text{pl}}$, and the element displacement ratio. True plastic strain difference between the damage fracture strain and initial damage strain was calculated using Eq. (4).

4 Results Analysis and Discussion

4.1 Engineering Ultimate and Fractural Point's Results

Engineering stress–strain curves were obtained using Eqs. (1) and (2) and, the results were summarized in Table 1.

Table 1 Engineering ultimate and fractural points at different temperatures and strain rates

Strain rate	Temperature	Engineering ultimate point		Engineering fracture point	
		Stress	Strain	Stress	Strain
0.0015	298	844.3673	0.0481	759.1095	0.0890
	523	836.9600	0.0556	687.0961	0.1163
	723	509.3845	0.0445	259.1772	0.1238
	923	201.0202	0.0432	45.9844	0.2668
0.015	298	874.0914	0.0476	824.2929	0.0796
0.15	298	926.4845	0.0515	921.5375	0.0623
	523	833.9754	0.0613	754.9342	0.0779
	723	702.6436	0.0587	515.5113	0.1252
	923	293.0745	0.0460	145.9961	0.2609

4.2 Forming Temperature Effect

The influence of forming temperature on the damage initiation strain (ϵ_0^{pl}) and fractural strains (ϵ_f^{pl}) can be expressed by different trends as follows.

4.2.1 Damage Initiation Strain at Different Temperatures

The values of damage initiation strains at different temperatures were calculated using Eq. (3) and summarized in Table 2. The results were plotted to represent the temperature effect on damage initiation strain and corresponding true stresses at engineering ultimate point as shown in Figs. 1 and 2.

Table 2 True plastic strains and true stresses at damage initiation

Strain rate	Temperature	True plastic strain at damage initiation	True stress at engineering ultimate point
0.0015	298	0.0349	885.0000
	523	0.0266	883.4951
	723	0.0232	532.0388
	923	0.0200	209.7087
0.15	298	0.0382	974.2389
	523	0.0331	885.1300
	723	0.0328	743.8933
	923	0.0250	306.5495

Fig. 1 The forming temperature effect on the damage initiation strain

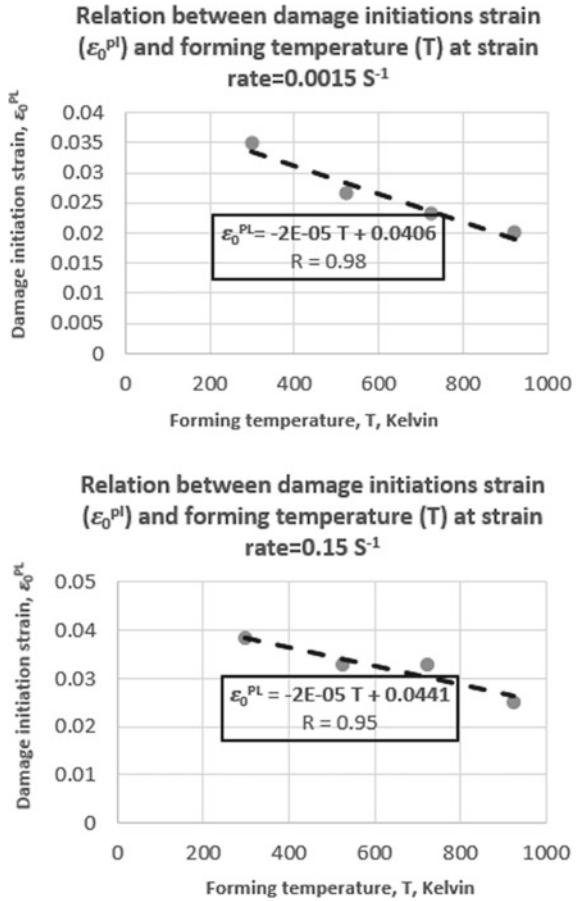
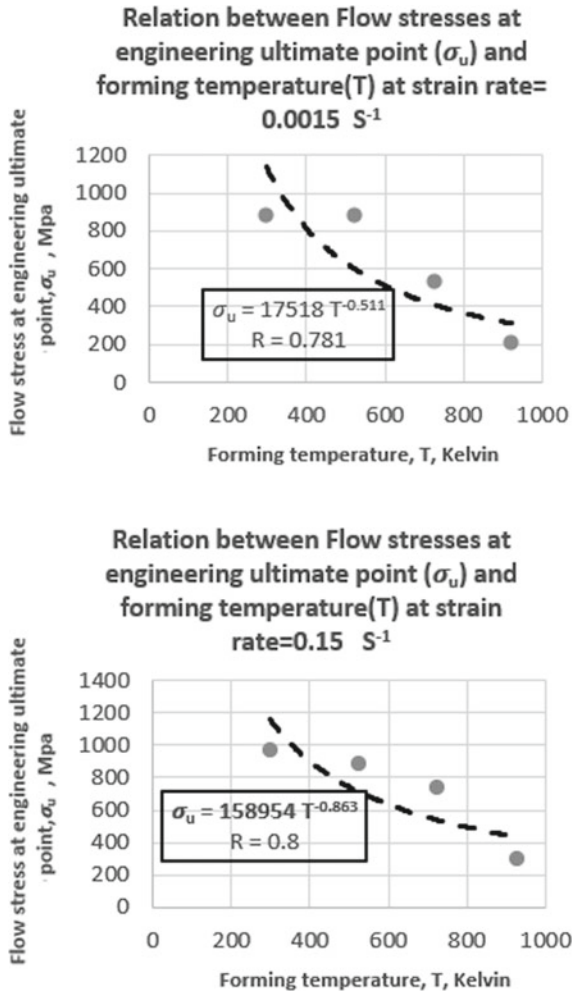


Figure 1 shows the relationship between the damage initiation strain (ϵ_0^{pl}) and forming temperature (T). It can be represented by proportional inverse linear relationship. The influence of the formation temperature on the flow stress at the ultimate point (σ_u) was shown in Fig. 2. This relationship can be expressed as an inverse power relationship.

This reverse relationship between forming temperature and the strain at the onset of damage (voids nucleation) may be physically explained based on that the increase in the temperature enlarges the grain size which makes the void formation about it more readily (2). Once the voids are nucleated, the necking (damage initiation) starts (Sect. 1). Also, the temperature rising increases the activation energy which can overcome the cohesion between the material matrix and the second phase grains (act as impurities or inclusions in steels). Therefore, this creates free surfaces around the second phase (2) where the voids are nucleated. Hence, the damage starts to occur. The two previous reasons explain the small strain which occurs before the onset

Fig. 2 The forming temperature effect on the flow stress at engineering ultimate point



of damage when the forming temperature rises. Also, this may clarify the reason for decreasing the ultimate strength due to interface decohesion between grains, therefore the bonding force decreases.

4.2.2 Fractural Strain at Different Temperatures

The values of fractural strains at different temperatures were calculated using Eq. (3) and summarized in Table 3 therefore the results were plotted in Figs. 3 and 4.

The influence of forming temperature (T) on the fractural strain (ϵ_f^{pl}) behavior was presented in Fig. 3. It can be expressed as a direct linear proportional relationship.

Table 3 Forming temperature effect on true plastic strain and true stress at complete failure

Strain rate	Temperature	True plastic strain at complete failure	True plastic strain difference	True stress at fracture
0.0015	298	0.0740	0.0391	826.6979
	523	0.0861	0.0595	766.9903
	723	0.1056	0.0824	291.2621
	923	0.2303	0.2103	58.2524
0.15	298	0.0483	0.0101	978.9227
	523	0.0507	0.0176	813.7300
	723	0.0990	0.0663	580.0613
	923	0.2198	0.1948	184.0824

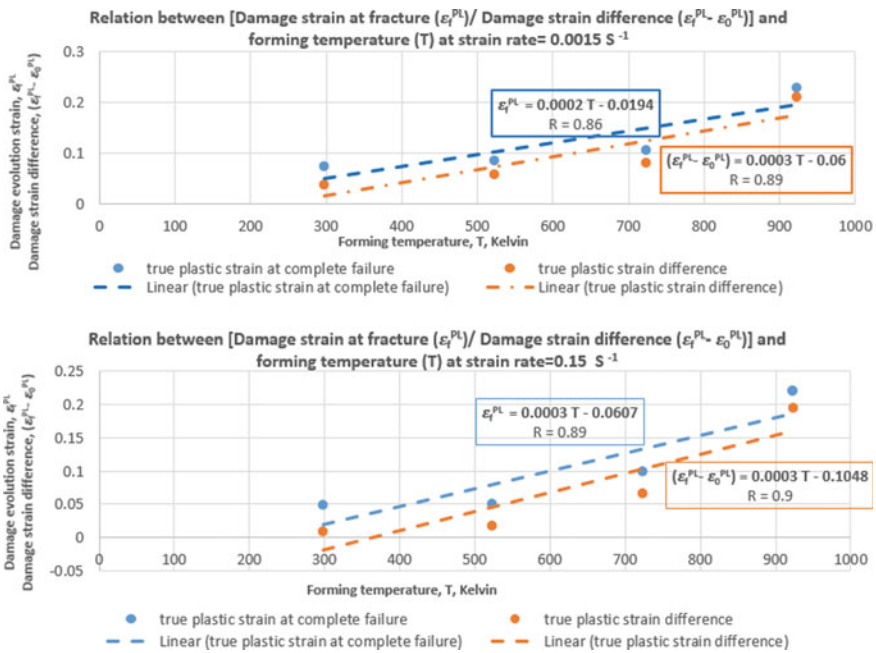


Fig. 3 The forming temperature effect on the fractural strain behavior

Figure 3a represents the fractural strain (ϵ_f^{pl}) at strain rate (0.0015 S⁻¹) but Fig. 3b indicates the fractural strain (ϵ_f^{pl}) at strain rate (0.15 S⁻¹). The influence of forming temperature (T) on the fractural flow stress (σ_f) is presented in Fig. 4 and can be presented by a reverse power relationship.

The results of the forming temperature (T) and fractural strain (ϵ_f^{pl}) may be explained starting from that, in general, the voids—which previously were deformed—grow under the effect of hydrostatic stress and further strain until the

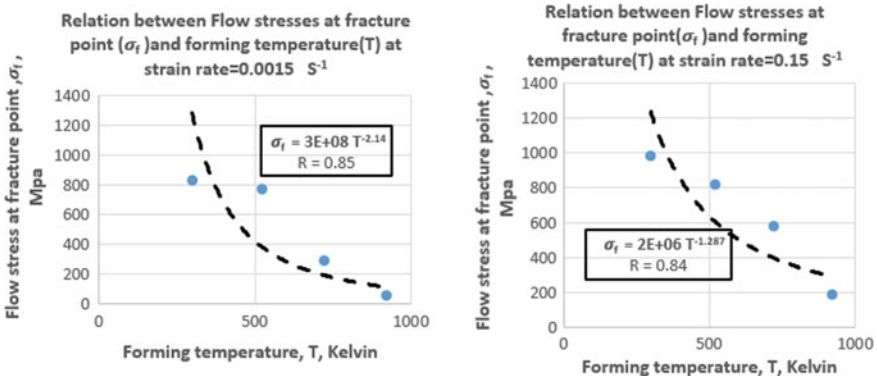


Fig. 4 The forming temperature effect on the fractural flow stress

coalescence occurs (complete fracture). However, with the temperature increasing, the grain size increases under the effect of hydrostatic stress and temperature. This increase in the grain size may overcome the void growth around the grain, therefore restricting the coalescence effect (as a barrier). Also increasing the temperature increases the ductility which exhibits larger strains in grains than in voids. This may explain the large strain before coalescence occurs (complete fracture).

The statistical models which describe the temperature effect were summarized in Table 4.

The results of fractural strain agree –in trend type- with the results obtained by Chiou et al. [19]. Also, the fractural stress results were obtained by Reza et al. [21].

The obtained statistical models are in agreement with the temperature term in Johnson–Cook damage model [16] and Johnson–Cook strength model. The above models were concluded at two strain rates (0.0015 and 0.15 S⁻¹) and at the temperature range from 298 to 923 °K.

Table 4 The statistical models which relate the forming temperature with damage strains and stresses at $T = 298^\circ, 523^\circ, 723^\circ,$ and 923°K on two different strain rates

Dependent parameter	Strain rate (S ⁻¹)	
	0.0015	0.15
ϵ_0^{PL}	$\epsilon_0^{PL} = -0.00002T + 0.0406$	$\epsilon_0^{PL} = -0.00002T + 0.0441$
ϵ_f^{PL}	$\epsilon_f^{PL} = 0.0002T - 0.0194$	$\epsilon_f^{PL} = 0.0003T - 0.0607$
$(\epsilon_f^{PL} - \epsilon_0^{PL})$	$(\epsilon_f^{PL} - \epsilon_0^{PL}) = 0.0003T - 0.06$	$(\epsilon_f^{PL} - \epsilon_0^{PL}) = 0.0003T - 0.1048$
σ_u	$\sigma_u = 17,518T - 0.511$	$\sigma_u = 158,954T - 0.863$
σ_f	$\sigma_f = 3(10)^8 T - 2.14$	$\sigma_f = 2(10)^6 T - 1.287$

Table 5 Strain rate effect on true plastic strain and true stress at damage initiation at different temperatures

Temperature	Strain rate	True plastic strain at damage initiation	True stress at engineering ultimate point
298	0.0015	0.0349	885.0000
	0.015	0.0352	915.6909
	0.15	0.0382	974.2389
	620	0.0193	1185.7296
	767	0.0200	1205.7869
	885	0.0274	1266.1206
523	0.0015	0.0266	883.4951
	0.15	0.0331	885.1300
723	0.0015	0.0232	532.0388
	0.15	0.0328	743.8933
923	0.0015	0.0200	209.7087
	0.15	0.0250	306.5495

4.3 Strain Rate Effect

The strain rate affected the damage initiation strain ($\varepsilon_0^{\text{pl}}$) and the damage evolution strain $\varepsilon_f^{\text{pl}}$ by different trends as following later.

4.3.1 Damage Initiation Strain at Different Strain Rates

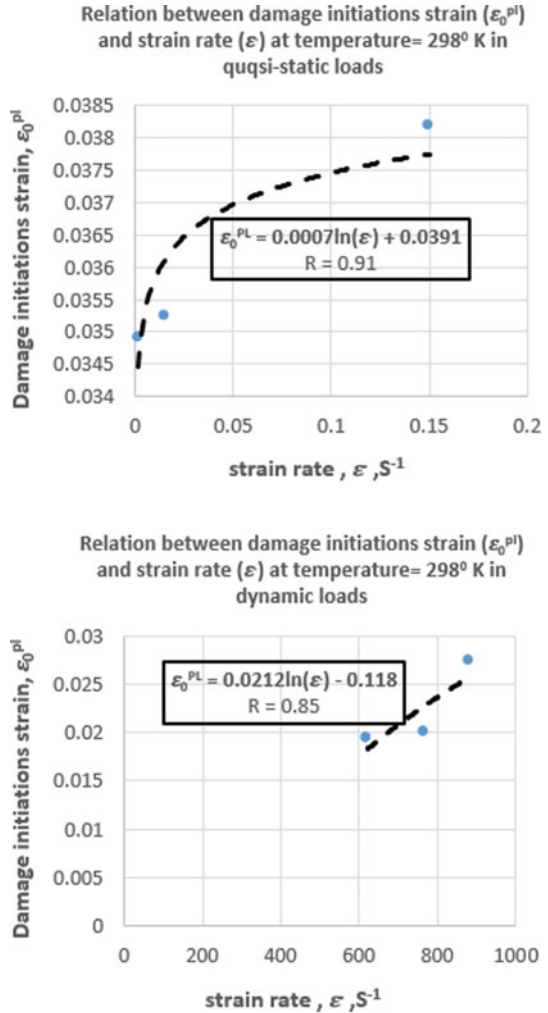
The values of damage initiation strains at different temperatures were calculated using Eq. 3 and summarized in Table 5. The results were plotted to show the temperature effect as shown in Figs. 5 and 6.

Figure 5 shows the relationship between strain rate and the damage initiation strain ($\varepsilon_0^{\text{pl}}$) at constant formation temperature (298 K). It can be noticed that there is a direct proportional logarithmic relationship. The influence of the strain rate on the flow stress at the geometric endpoint is shown in Fig. 6. This relationship can be expressed as a direct proportional as logarithmic relationship.

4.3.2 Fractural Strain at Different Strain Rates

The values of fractural strains ($\varepsilon_f^{\text{pl}}$) at different strain rates were calculated using Eq. (3) and summarized in Table 6. The results were plotted in Fig. 7. The relationship between strain rate and fractural strain is shown in Fig. 7. In general, these relations can be expressed as inversely proportional logarithmic functions. Figure 7a represents

Fig. 5 The effect of strain rate on the damage initiation strain at $T = 298\text{ }^\circ\text{K}$ in the quasi-static and dynamic loads

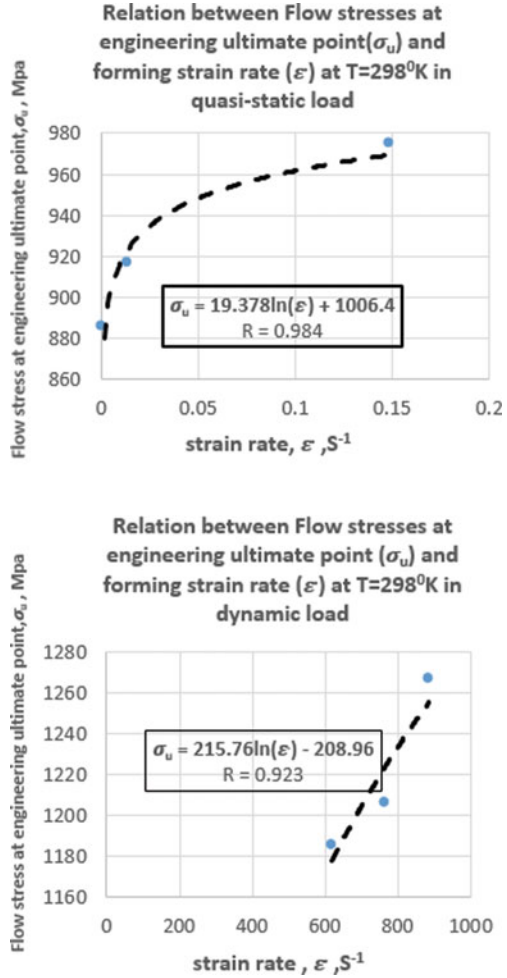


the fractural strain (ϵ_f^{pl}) at quasi-static test and Fig. 7b indicates the fractural strain (ϵ_f^{pl}) at dynamic tests.

The relationship between strain rate and fractural strain is shown in Fig. 7. In general, these relations can be expressed as inversely proportional logarithmic functions. Figure 7a represents the fractural strain (ϵ_f^{pl}) at quasi-static test and Fig. 7b indicates the fractural strain (ϵ_f^{pl}) at dynamic tests.

Figure 8 shows the strain rate ($\dot{\epsilon}$) effect on the fractural flow stress. It can be noticed that the relation between the forming strain rate ($\dot{\epsilon}$) and the true stress at ultimate (σ_u) and fractural (σ_f) points are relatively direct proportional and can be expressed by logarithmic function as summarized in Table 7. Table 7 Shows the

Fig. 6 The effect of strain rate on the flow stress at the engineering ultimate point at $T = 298 \text{ }^\circ\text{K}$ in the quasi-static and dynamic loads



statistical models which relate forming strain rate with damage strains and stresses at $T = 298 \text{ }^\circ\text{K}$ on two groups of strain rates.

The reverse relation between fractural strain (ϵ_f^{pl}) and strain rate perhaps due to the high velocity in forming which may cause high dynamic energy that can produce high hydrostatic pressure which fastens the growth and coalescence of voids.

The previous results of strain rate effects correspond—in function type—with [16]. Also the results of fractural strain and fractural stress match—in trend type—with the results obtained by Woei-Shyan and Chou [22]. As well, the fractural stress results coincide with the results conducted by Reza et al. [21]. Also, the ultimate stress results match with the results gained by Lin and Liu [23] but the results of ultimate and fractural stresses are in agreement with the results taken out by Chiou et al. [19].

Table 6 True plastic strain and true stress values at complete failure at different strain rates

Temperature	Strain rate	True plastic strain at complete failure	True plastic strain difference	True stress at fracture
298	0.0015	0.0740	0.0357	826.6979
	0.015	0.0657	0.0304	889.9297
	0.15	0.0483	0.0101	978.9227
	620	0.2839	0.2646	185.7612
	767	0.2554	0.2354	349.1729
	885	0.2465	0.2191	449.5790
523	0.0015	0.0861	0.0595	766.9903
	0.15	0.0507	0.0176	813.7300
723	0.0015	0.1056	0.0824	291.2621
	0.15	0.0990	0.0663	580.0613
923	0.0015	0.2303	0.2103	58.2524
	0.15	0.2198	0.1948	184.0824

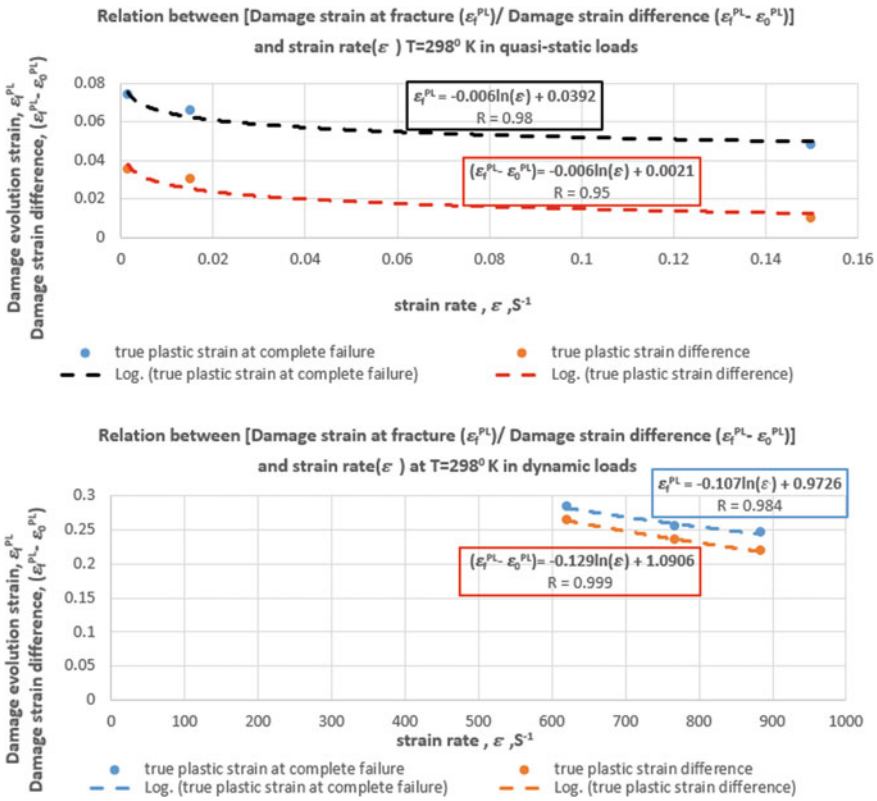


Fig. 7 The strain rate effect on the fractural strain behavior

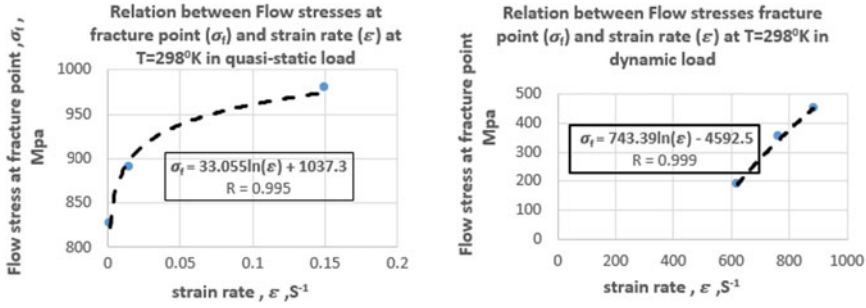


Fig. 8 The strain rate effect on the fractural flow stress

Table 7 Statistical models which relate forming strain rate with damage strains and stresses

Dependent parameter	Temperature (K)	
	298 °K (at: strain rates = 0.0015, 0.015, and 0.15 S ⁻¹)	298 °K (at: strain rates = 620,767, and 885 S ⁻¹)
ϵ_0^{PL}	$\epsilon_0^{PL} = 0.0007 \ln(\epsilon) + 0.0391$	$\epsilon_0^{PL} = -0.00002T + 0.0441$
ϵ_f^{PL}	$\epsilon_f^{PL} = -0.006 \ln(\epsilon) + 0.0392$	$\epsilon_f^{PL} = -0.107 \ln(\epsilon) + 0.9726$
$(\epsilon_f^{PL} - \epsilon_0^{PL})$	$(\epsilon_f^{PL} - \epsilon_0^{PL}) = -0.006 \ln(\epsilon) + 0.0021$	$(\epsilon_f^{PL} - \epsilon_0^{PL}) = -0.129 \ln(\epsilon) + 1.0906$
σ_u	$\sigma_u = 19.378 \ln(\epsilon) + 1006.4$	$\sigma_u = 215.76 \ln(\epsilon) - 208.96$
σ_f	$\sigma_f = 33.055 \ln(\epsilon) + 1037.3$	$\sigma_f = 743.39 \ln(\epsilon) - 4592.5$

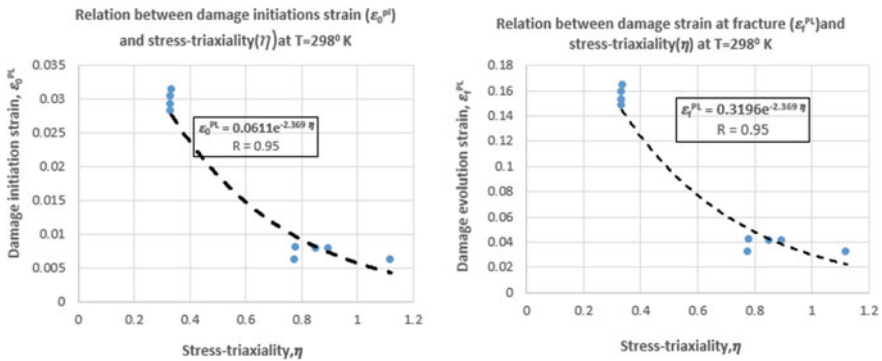


Fig. 9 The effect of stress-triaxiality on damage initiation strain and fractural strain at T = 298 °K

Table 8 Statistical models relate the forming stress triaxiality with damage strains

Dependent parameter	Temperature(K)
	298 °K
ϵ_0^{PL}	$\epsilon_0^{PL} = 0.0611 e^{-2.369\eta}$
ϵ_f^{PL}	$\epsilon_f^{PL} = 0.3196e^{-2.369\eta}$

4.4 Stress Triaxiality Effect

Figure 9 indicates that the relation between the forming stress triaxiality (η) and the damage initiation strain (ϵ_0^{pl}) and the fractural strain (ϵ_f^{pl}) is inverse proportional by exponential functions.

This reverse relation between stress triaxiality and the fractural strains may be explicated based on the definition of stress triaxiality which is the ratio between the average of the principal stresses (σ_m) and the equivalent Von-Mises stress (σ_e). The increasing of this ratio means increasing (σ_m) and/or decreasing (σ_e). This may be achieved by high positive three principal stresses ($\sigma_1, \sigma_2, \sigma_3$) which leads to interface decohesion between pre-existing second phase and the material matrix.

The statistical models which relate the forming stress triaxiality with damage strains at $T = 298 \text{ }^\circ\text{K}$ were summarized in Table 8.

These statistical models are similar to stress triaxiality term in Johnson–Cook damage model [16] and similar to the model proved by Bai [14].

4.4.1 Finite Element Case Study (on Stress Triaxiality Effect)

This case study aims to show and simulate the effect of stress triaxiality on the damage criteria.

A. Modeling Procedure

The model was designed on a specimen with the shown geometry and in Fig. 10. The material was described elastically and plastically. The damage initiation strain and fractural strain were defined at different stress triaxiality (Sect. 4.4). The lower cell was set as fully constrained but the upper one was set to be free in the axial direction. First, the meshing size optimization was conducted to determine a suitable size of the elements.

B. Damage Criteria Results

The visualization results of the artificial tensile test were focused on the first elements which reached the critical value of damage criteria (Figs. 11 and 12). The value of ductile damage criteria for this damaged element was assigned to the corresponding values of axial plastic strain and the stress triaxiality in the time domain (Figs. 13 and 14). Also, the effect of damage on the strength of this element was clarified (Fig. 15).

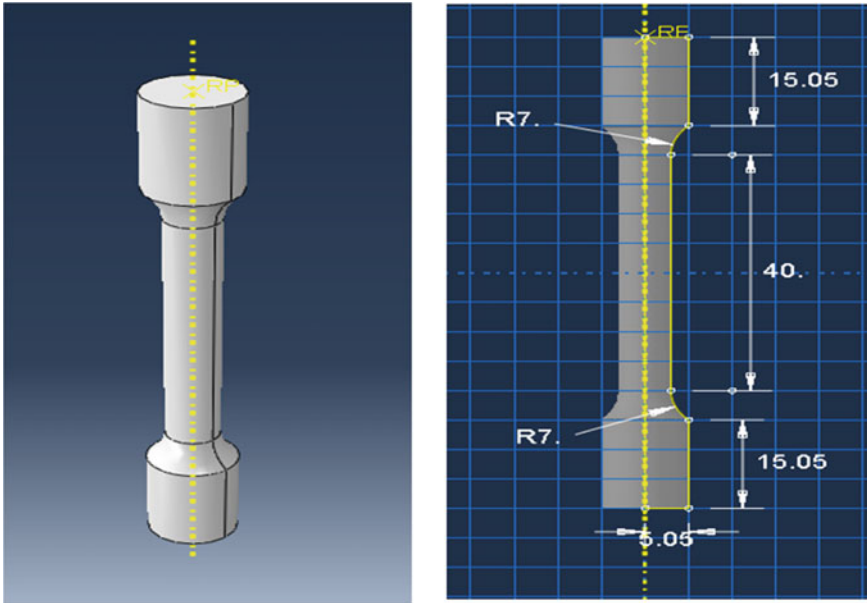


Fig. 10 The geometry and dimensions of the specimen

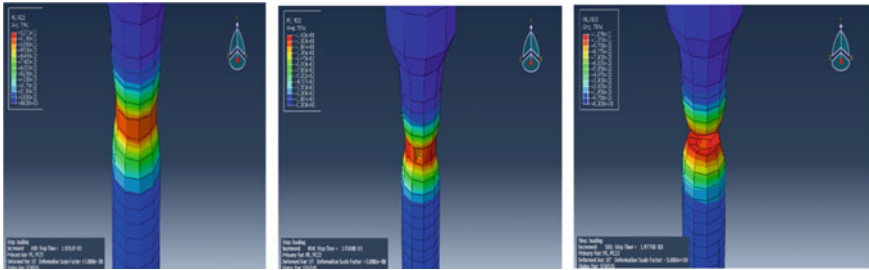


Fig. 11 The visualization results of the tensile test

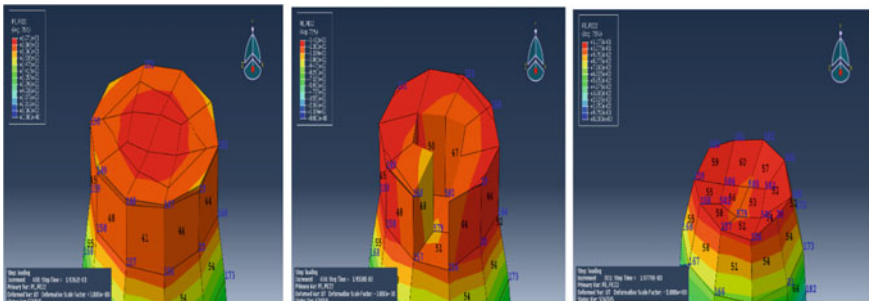


Fig. 12 The visualization results at a cutting plane passes through the removed elements (41, 43, and 46)

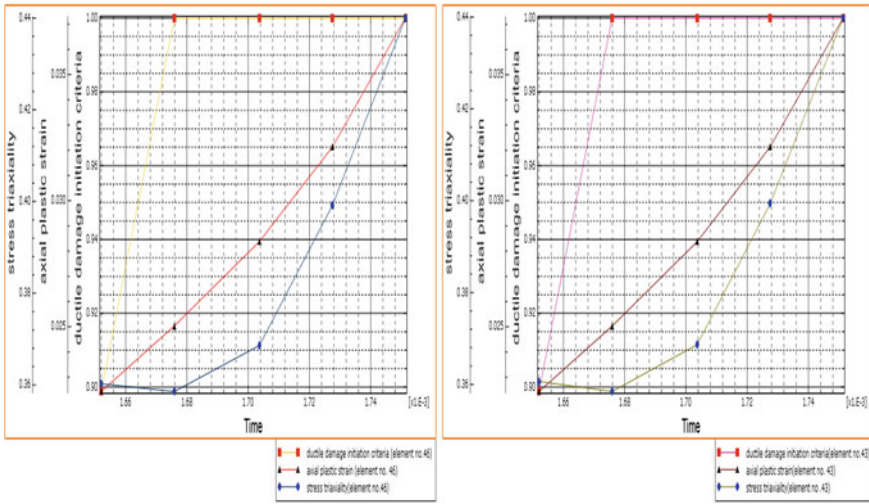


Fig. 13 The first two elements (43 and 46) which reaches the critical value of damage initiation criteria

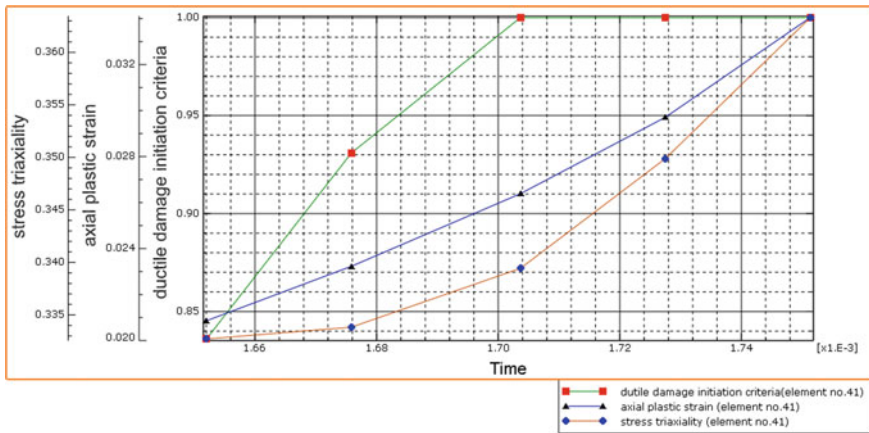


Fig. 14 The third element which reaches the critical value of damage initiation criteria

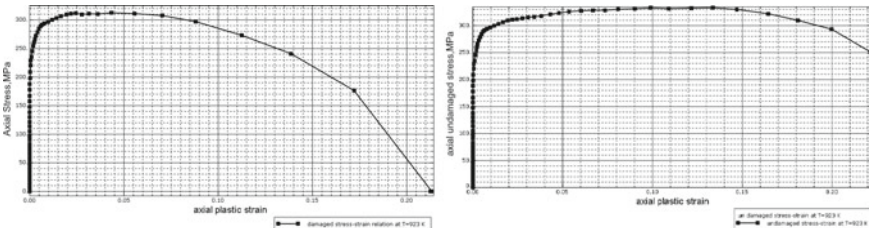


Fig. 15 The effect of damage on the strength values for elements (43 and 46)

(1) Stress Triaxiality Effect on Damage Criteria

Figures 11a and 12a show all elements before damage at a cutting plane passes through the removed elements but Figs. 11b and 12b show the first three removed elements which reach the critical values of damage criteria. Figures 11c and 12c clear that all the other elements of this section were removed soon later. Therefore, outputs of this model (damage initiation criteria, stress triaxiality, and plastic strain) were extracted from the field outputs in time domain to clear and explain the previously mentioned shortage. Therefore, these results were plotted against time (Figs. 14 and 15) for the three elements.

Figure 13 demonstrates the first two elements (43 and 46) reached the critical value of the damage initiation criteria at time equal to $1.677E-3$ s., stress triaxiality equal to 0.36, and axial plastic strain equal to 0.025 but Fig. 14 shows that the third element (41) reached the critical value of the damage initiation criteria at time equal to $1.71E-3$ s., stress triaxiality equal to 0.339, and axial plastic strain equal to 0.0265. At the first time ($1.677E-3$ s.), the third element (41) was at stress triaxiality equal to 0.33 which is smaller than its value (0.36) for elements (43 and 46).

These results may be explained based on that the first two elements (43 and 46) are central elements in the section and are bounded by other elements. This increases the pressure on them more than the edge circumferential elements which have free surfaces, therefore these central elements have a higher value of stress triaxiality. This makes them more prepared for damage initiation. This explanation may agree with the statistical inverse exponential function in Table 8. This may explain the cup-cone fractural shape in the necking zone.

(ii) Damage Effect on Strength

Figure 15a clarifies that the damage began at axial plastic strain equal to 0.025 and the full fracture (zero stress) occurred at axial plastic strain equal to 0.21. The accumulation of damage started from strain 0.025 until strain 0.21(fracture).this accumulation reduced the strength values after strain 0.025 but Fig. 15b shows that after this strain (0.025) the strength increased as usual in case of neglecting the damaging effect.

This result can be interpreted as a result of stiffness degradation in the material matrix due to the void growth and interface decohesion.

5 Conclusions

1. Increasing forming temperature increases the fracture plastic strain and the displacement after the damage initiation until the fracture. At the same time reduces the true stress at ultimate and fracture points and reduces the damage initiation plastic strain.
2. Increasing the forming strain rate decreases the fracture plastic strain and the displacement after the damage initiation until the fracture occurs.

3. Increasing in the forming stress triaxiality decreases the fractural strain and the damage initiation strain.
4. The statistical models obtained in this paper have the same types of function which were proved by Johnson and Cook in their constitutive models (strength and damage models).
5. The finite element models may help in determining the location of the first damage in the necking zone where the higher stress triaxiality exists.

References

1. Meyers MA (2002) Constitutive description of dynamic deformation: physically-based mechanisms. *Mater Sci Eng A* 322:194–216
2. Anderson TL (2008) *Fracture mechanics—Fundamentals and applications*, 3rd edn. Taylor & Francis
3. Callister WD, Rethwisch DG (2010) *Fundamentals of materials science and engineering*, 4th edn.
4. Tvergaard V (1982) On localization in ductile materials containing spherical voids. *Int J Fract* 18(4):237–252
5. Abaqus/CAE user's manual, version 6.14 edition
6. Bridgman PW (1952) *Studies in large plastic flow and fracture*, vol 177. McGraw-Hill, New York
7. Davidson T, Ansell G (1968) The structure sensitivity of the effects of pressure upon the ductility of Fe-C materials. *ASM Trans Quart* 61(2):242–254
8. McClintock FA (1968) A criterion for ductile fracture by the growth of holes. *J Appl Mech* 35(2):363–371
9. Rice JR, Tracey DM (1969) On the ductile enlargement of voids in triaxial stress fields. *J Mech Phys Solids* 17(3):201–217
10. Gurson AL (1977) Continuum theory of ductile rupture by void nucleation and growth: Part I—Yield criteria and flow rules of porous ductile media. *J Eng Mater Technol* 99:2–15
11. Tvergaard V (1989) Material failure by void growth to coalescence. *Adv Appl Mech* 27:83–151
12. Bai Y, Teng X, Wierzbicki T (2009) On the application of stress triaxiality formula for plane strain fracture testing. *J Eng Mater Technol* 131(2)
13. Bai Y, Wierzbicki T (2008) A new model of metal plasticity and fracture with pressure and Lode dependence. *Int J Plast* 24(6):1071–1096
14. Bai Y, Wierzbicki T (2005) On the cut-off value of negative triaxiality for fracture. *Eng Fract Mech* 72(7):1049–1069
15. Murugesan M, Jung DW (2019) Johnson Cook material and failure model parameters estimation of AISI-1045 medium carbon steel for metal forming applications. *Materials* 12:609
16. Johnson GR, Cook WH (1983) A constitutive model and data for metals subjected to large strains, high strain rates and high temperatures. In: Paper presented in the proceedings of the 7th international symposium on ballistics, pp 541–547
17. Johnson GR, Holmquist T (1989) Test data and computational strength and fracture model constants for 23 materials subjected to large strains, high strain rates, and high temperatures. Los Alamos National Laboratory, Los Alamos, NM, Report No. LA-11463-MS
18. Abed FH, Saffarini MH, Abdul-Latif A, Voyiadjis GZ (2017) Flow stress and damage behavior of C45 steel over a range of temperatures and loading rates. *J Eng Mater Technol Trans ASME* 139:1–8.
19. Chiou S-T, Tsai H-L, Lee W-S (2007) Effects of strain rate and temperature on the deformation and fracture behavior of titanium alloy. *Mater Trans Jpn Inst Metals* 48(9):2525–2533

20. Abed FH, Abdul-Latif A, Yehia A (2018) Experimental study on the mechanical behavior of EN08 steel at different temperatures and strain rates. *Metals* 8:736
21. Ferdowsi MRG, Nakhaie D, Benhangi PH, Ebrahimi GR (2014) Modeling the high temperature flow behavior and dynamic recrystallization kinetics of a medium carbon microalloyed steel". *JMEPEG ASM Int* 23:1077–1087
22. Lee W-S, Chou J-K (2005) The effect of strain rate on the impact behavior of Fe-2 mass% Ni sintered alloy. *Mater Trans Jpn Inst Metals* 46(4):805–811
23. Lin YC, Liu G (2010) A new mathematical model for predicting flow stress of typical high-strength alloy steel at elevated high temperature. *Comput Mater Sci* 48(54):58

Cutting Force Assessment in HSM of Inconel 718 Aided with Water Vapour as an Eco-Friendly Cutting Fluid



Ganesh S. Kadam and Raju S. Pawade

Abstract The need to comply for higher production rate with desired quality but with incorporating green manufacturing practices has been continually pressurising the manufacturers. This can be partially achieved by employing high-speed machining (HSM) using eco-friendly cutting fluids and keeping vigilant process control. In this context, the current paper examines machinability characteristics in turning of exotic superalloy Inconel 718 at high speed using coated carbide tools and eco-friendly cutting fluid being water vapour. Experiments have been performed following response surface methodology involving central composite design by varying three process parameters, viz. cutting speed, feed rate and water vapour pressure. A special tool holder having in-built fluid supply channel has been used as tooling for facilitating precise delivery of cutting fluid as water vapour onto machining zone. Measurement and analysis of the cutting forces were carried out as the same is one of the crucial indicators of process mechanics. Analysis showed that response surface quadratic model for cutting force is statistically significant. The feed rate, water vapour pressure as well as the interaction between feed rate and water vapour pressure was highly dominating factors influencing cutting force correspondingly having contributions of 19.64%, 20.97% and 40.03%, respectively. Increase in water vapour pressure was highly helpful towards lowering of cutting forces on account of better penetrability and performance of water vapour into machining zone. Overall usage of water vapour cutting fluid in feasible HSM parametric range may enable in achieving better surface integrity and higher tool life for machining Inconel 718, thus fulfilling the requirements of higher productivity, better quality and green machining.

Keywords Inconel 718 · Water vapour · HSM · Eco-friendly · Turning · Cutting forces

G. S. Kadam (✉) · R. S. Pawade
Mechanical Engineering Department, Dr. Babasaheb, Ambedkar Technological University,
Lonere, Raigad, Maharashtra, India

R. S. Pawade
e-mail: rspawade@dbatu.ac.in

1 Introduction

Manufacturers worldwide have been constantly seeking methods for increasing productivity. In machining, the productivity can be appreciably enhanced through incorporation of high-speed machining (HSM). Basically in HSM, very high cutting speeds as well as feed rates are involved in contrast to traditional machining. The nickel-based superalloy Inconel 718 finds suitability to broad array of applications as in defence, marine equipment, aerospace, nuclear reactors, gas turbines, petrochemical plants and food processing equipment particularly on account of its exceptional high-temperature strength, low thermal conductivity and better corrosion resistance [1]. However, Inconel 718 further is known for its machining difficulty too as a result of properties leading to poor machinability like preserved strength during machining, exorbitant strain rate sensitivity and poor thermal conductivity [2]. Majority of the problems during machining primarily originate on account of higher cutting temperatures and the control over it can be exercised by proper selection as well as delivery of cutting fluids. Also, due to stringent environmental laws imposed by governments worldwide for manufacturing industries, there imposes a necessity to use eco-friendly cutting fluids. A variety of researchers recently have directed their attention on machining of Inconel 718, wherein different cutting fluids and application methods ranging from conventional to eco-friendly grades like wet [3–10], high-pressure jet cooling [7, 8, 10–12], minimum quantity lubrication (MQL) [9, 11, 13–17], and cryogenic cooling [3, 4, 9, 11, 15] have been explored, and the benefits noted through attainment of better surface finish, improved tool life, reduced cutting forces, etc.

Podgorkov and Godlevski around 1990s proposed using the cutting fluid as water vapour in machining [18]. Water vapour is absolutely pollution-free and cheap as can be made easily available. Till date, very few studies have been reported on usage of cutting fluid being water vapour as in machining of steels [18–20], Ti6Al4V [21] and Inconel 718 [22]. Water vapour basically serves both as coolant and lubricant in machining. Water vapour forms lubrication film of low shear strength on underside of chip thus alleviating friction at chip-tool interface and hence reduces cutting temperature. Additionally, the water vapour assists in expelling away heat from the machining zone due to temperature gradients thus making it act as a coolant too. It can be concluded from past work that water vapour as cutting fluid in machining aids in lowering friction coefficient, cutting forces and tool wear as a result enhancing surface finish in comparison to other machining environments like dry, wet, compressed air and gases. Thus, exploration of water vapour from green machining point-of-view for Inconel 718 needs to be given due emphasis as negligible amount of work has been reported on this aspect. Present paper discusses the use of water vapour within HSM regime with due focus on exploring the effects of process parameters on resulting cutting forces having further causal effects towards surface integrity for Inconel 718 machining.

2 Experimental Work

Considering perspective of manufacturers' goal to achieve productive and sustainable manufacturing, it was decided to incorporate HSM of Inconel 718 using eco-friendly cutting fluid as water vapour. The experimental design established on RSM (response surface methodology) was adapted for conducting and analysing of experiments. The work particularly involved experiments at high-speed turning formulated on CCD (central composite design) of RSM. The three process parameters being cutting speed, feed rate and water vapour pressure were varied. The levels of these process parameters are given in Table 1 [23]. Selection of these machining parameters was through wisdom from literature and past experience. Cutting force was selected as the response as it a crucial indicator of machinability thus impacting process mechanics and subsequently tool wear and surface integrity.

Inconel 718 specimen in round bar form with diameter 25 mm and length 100 mm was employed as the work material. The chemical composition of Inconel 718 was Ni–Cr–Fe–Nb–Ti–Co–Al–Si–C as 54.95–17.90–16.54–4.85–0.92–0.92–0.52–0.08–0.03. The cutting tool used was carbide inserts with PVD TiAlN coating having specification CNMG120408MS and grade KCU10 from Kennametal. From recent research [23–25], it was learnt that usage of through tool cutting fluid delivery assists in precise fluid jetting onto the insert tip and further enhances the performance of cutting fluid in the zone of machining. Hence, a new special tool holder PCLNL2525M12HP (make Sandvik) having in-built channel and nozzle for cutting fluid delivery was used. The experiments on turning were carried out on production grade CNC lathe from Micromatic Ace and model being Jobber XL. In order to supply the cutting fluid as water vapour in the core machining zone, the steam generation device was brought into operation (Fig. 1).

For eliminating any of the effects of workpiece inhomogeneity on experimental results, a skin cut of 1 mm was taken over full length of the workpiece prior to every experiment. The water vapour pressure could be precisely controlled and fixed at a specific level due to aid of sophisticated controls embedded in steam generation device. Usage of fresh cutting tip was done for every experiment. Online monitoring and measurement of cutting forces were done during machining with the help of piezo-electric dynamometer from Kistler, model being 9257 A. Average cutting force

Table 1 Process parameters along with their levels

Levels	Coded levels	Cutting speed V_c (m/min)	Feed f (mm/rev)	Pressure P (bar)
1	–2	72.96	0.05	0.20
2	–1	90	0.07	0.30
3	0	115	0.10	0.45
4	+1	140	0.13	0.60
5	+2	157.04	0.15	0.70

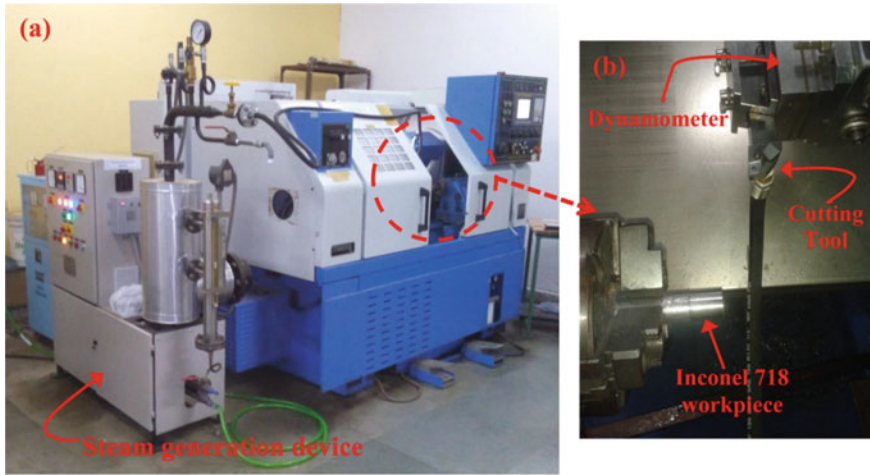


Fig. 1 a Steam generation device and cutting fluid water vapour's supply in the zone of machining of CNC turning lathe from hose, and b Jet of water vapour precisely directed onto insert tip through special tool holder

was taken as the main response. Design Expert software was employed for statistical analysis and to generate the 3D surface graphs.

3 Results and Discussion

The cutting force quantifies a crucial role in understanding machining process characteristics. It is well known that lower cutting forces imply machining with ease and consequently may lead to lower tool wear and better surface integrity. Needless to say, higher cutting forces shall imply the converse and are thus detrimental. The analysis of variance (ANOVA) for cutting force is given in the Table 2. Quadratic model of response surface for cutting force yields out as highly significant on statistically basis.

In terms of actual factors, the empirical model for cutting force (F_c) is as given below,

$$\begin{aligned}
 F_c = & -419.23096 + 0.84144(V_c) + 6247.75972(f) + 1336.23983(P) \\
 & - 20.68833(V_c \times f) + 1.77100(V_c \times P) - 9862.50(f \times P) \\
 & + (1.27991 \times 10^{-3})(V_c^2) + 6812.81224(f^2) - 797.26150(P^2) \quad (1)
 \end{aligned}$$

From ANOVA, it is revealed that the feed rate, water vapour pressure as well as the interaction between feed rate and water vapour pressure are the most important factors significantly influencing the cutting force. Percentage contribution of feed

Table 2 ANOVA for cutting force

Source	Sum of squares	DoF	Mean square	F value	P-value
Model	39,775.85	9	4419.54	3.71	0.0319
A	158.01	1	158.01	0.13	0.7239
B	7730.05	1	7730.05	6.50	0.0312
C	8252.54	1	8252.54	6.94	0.0272
AB	1926.03	1	1926.03	1.62	0.2351
AC	352.85	1	352.85	0.30	0.5993
BC	15,757.56	1	15,757.56	13.24	0.0054
A ²	9.21	1	9.21	0.007	0.9318
B ²	541.38	1	51.38	0.46	0.5169
C ²	4633.71	1	4633.71	3.89	0.0799

A—Cutting speed, B—Feed rate, C—Pressure

rate, pressure and interaction between feed rate and pressure on the resulting cutting force was 19.64, 20.97 and 40.03, respectively. However all the factors, viz. cutting speed, feed rate and pressure as well as their interactions affect the resulting cutting forces to varying levels. The same can be clearly inferred from 3D surface graphs shown in Figs. 2, 3 and 4 for the cutting force.

The combined effect of cutting speed and feed rate on cutting force is as shown in Fig. 2. It can be seen that there is slight increase in cutting force as cutting speed increases especially at lower feed rates. Further at average feed rate regimes, the cutting forces remain constant irrespective of variation in cutting speeds. However at higher feed rates, cutting force reduced with increase of cutting speed which can be attributed to higher cutting temperatures leading to ease in material removal.

Fig. 2 Effect of cutting speed and feed rate on cutting force

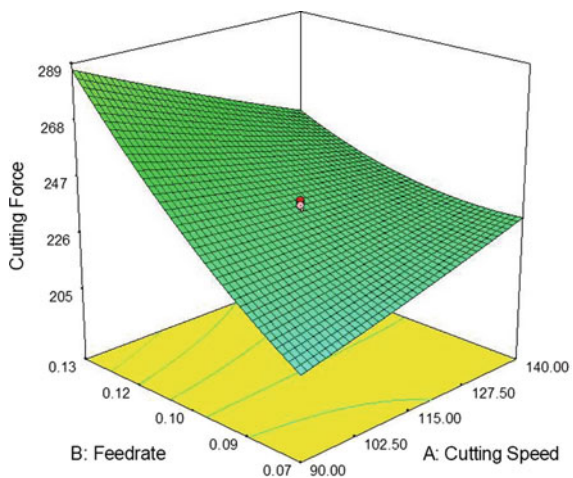


Fig. 3 Effect of cutting speed and pressure on cutting force

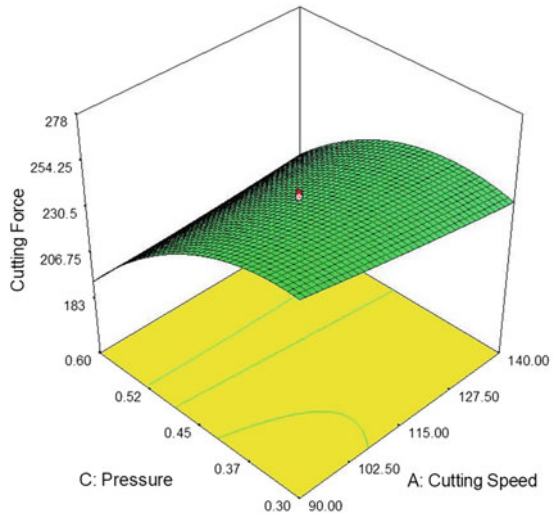
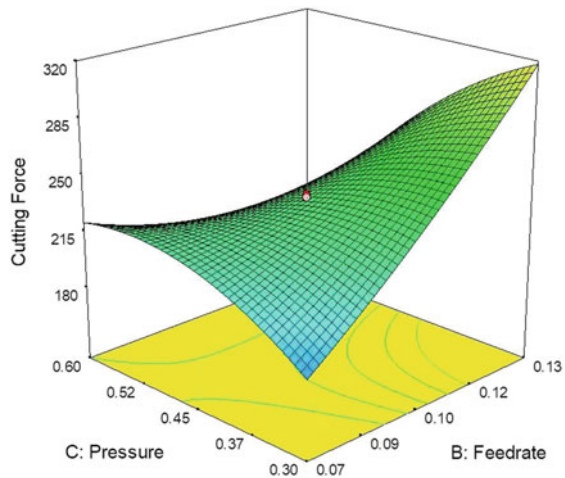


Fig. 4 Effect of feed rate and pressure on cutting force



Moreover, the trend on effect of feed rate on cutting force is reverse as observed for cutting speed. It is seen that as feed rate is increased, the cutting force also increases. Further, this trend is common for all cutting speed regimes. But, at lower cutting speeds, this trend is comparatively steeper than that observed for cutting speeds which are much higher. This is because at higher cutting speeds, the cutting fluid water vapour is unable in completely accessing the interface between chip-tool for providing necessary cooling and lubrication. This leads to increased cutting temperatures and thermal softening of work material. Consequence of this, effort expended by tool towards the removal of material is less eventually leading to lower cutting forces.

Figure 3 reveals the effect of cutting speed and water vapour pressure on cutting force. It is seen that increment of cutting speed leads to slight decrease of cutting force. In general, the cutting forces can be assumed to be constant at all cutting speeds. However, the cutting forces are lower in magnitude at higher water vapour pressures for all cutting speeds than that at lower water vapour pressures. This is because of the effectiveness of water vapour in providing the necessary lubrication particularly at higher pressures. Further, considering the water vapour pressure's effect on cutting forces, comparatively lower cutting forces are observed for water vapour pressures which are higher than at lower water vapour pressures. The decreasing trend of cutting forces with increasing water vapour pressure is due to better water vapour effectiveness into machining zone. High-pressure water vapour quickly accesses and completely penetrates the chip-tool interface and thus provides the necessary lubrication and cooling function. This trend is almost similar at all ranges of cutting speed, although slight lower magnitude of cutting force is evident particularly for cutting speeds that are high.

The feed rate as well as water vapour pressure's effect on the resulting cutting force is shown in Fig. 4. It is observed that at low water vapour pressure regimes the cutting force increases as the feed rate increased. However with water vapour pressure being increased, this trend gradually shows diminishing pattern, and at higher pressure, the cutting force seems to be almost constant with increase in feed rate. Further considering water vapour pressure's effect on cutting forces, at lower feed rate the cutting force increased minutely along with increment of water vapour pressure. However with further increments in feed rate, this trend gets drastically reversed. It could be seen that rise in pressure of water vapour resulted into lower cutting forces, and this is more evident at higher feed rates.

Finally, model adequacy check was carried out through few sample tests. Table 3 shows the comparison between the cutting force values predicted from the empirical model and the experimentally observed ones. It is clearly seen that cutting forces predicted values are very much close to experimentally obtained values. Overall, the error is less than 10% for all the confirmatory tests conducted. Thus, the model can be accurately used for estimation of the cutting force values within the range of process parameters.

Table 3 Results of confirmatory test

Test	V_c (m/min)	f (mm/rev)	P (bar)	F'_c (N)	F_c (N)	Error (%)
1	90	0.07	0.3	187.08	203.72	8.90
2	115	0.15	0.45	293.83	288.42	1.84
3	140	0.07	0.3	188.03	181.62	3.41
4	90	0.13	0.3	354.46	379.66	7.11
5	115	0.1	0.7	176.35	183.77	4.21

F'_c —Predicted value, F_c —Observed value.

4 Conclusions

The following conclusions can be arrived at from the experimental investigations.

- Higher cutting speeds in order to have higher material removal rates are feasible so as to get lower cutting forces, but provided the feed rates are kept lower.
- Increase in water vapour pressure helped in appreciably lowering the cutting forces on account of better penetrability and performance of water vapour cutting fluid into machining zone.
- The feed rate, water vapour pressure as well as the interaction between feed rate and water vapour pressure were the dominant factors influencing cutting force with a contribution of 19.64%, 20.97% and 40.03%, respectively.
- The quadratic model of response surface for cutting force was found to be statistically significant, and the same can be precisely used for predicting the cutting forces within the range of explored process parameters.
- Water vapour supplied at higher pressure in HSM range is beneficial in obtaining lower cutting forces and may possibly enable in achieving better surface integrity and higher tool life for machining Inconel 718, thus fulfilling the requirements of higher productivity, better quality and green machining.

Acknowledgements Authors humbly acknowledge the financial assistance rendered by MHRD Government of India towards acquisition of production grade CNC lathe under TEQIP Phase-I and sophisticated steam generation device under TEQIP Phase-II for developing the setup of experimentation in DBATU, Lonere.

References

1. Pawade RS, Joshi SS, Brahmanekar PK (2008) Effect of machining parameters and cutting edge geometry on surface integrity of high-speed turned Inconel 718. *Int J Mach Tools Manuf* 48:15–28
2. Mohsan AUH, Liu Z, Padhy GK (2017) A review on the progress towards improvement in surface integrity of Inconel 718 under high pressure and flood cooling conditions. *Int J Adv Manuf Technol* 91:107–125
3. Khanna N, Agrawal C, Dogra M, Pruncu CI (2020) Evaluation of tool wear, energy consumption, and surface roughness during turning of Inconel 718 using sustainable machining technique. *J Market Res* 9:5794–5804
4. Hribersek M, Pusavec F, Rech J, Kopac J (2018) Modeling of machined surface characteristics in cryogenic orthogonal turning of Inconel 718. *Mach Sci Technol* 22(5):829–850
5. Anthony XM, Manohar M, Patil MM, Jeyapandiarajan P (2017) Experimental investigation of work hardening, residual stress and microstructure during machining Inconel 718. *J Mech Sci Technol* 31(10):4789–4794
6. Zeilmann RP, Fontanive F, Soares RM (2017) Wear mechanisms during dry and wet turning of Inconel 718 with ceramic tools. *Int J Adv Manuf Technol* 92:2705–2714
7. Polvorosa R, Suarez A, Lopez de Lacalle LN, Cerrillo I, Wretland A, Veiga F (2017) Tool wear on nickel alloys with different coolant pressures: comparison of Alloy 718 and Waspaloy. *J Manuf Process* 26:44–56

8. Fang Z, Obikawa T (2017) Turning of Inconel 718 using inserts with cooling channels under high pressure jet coolant assistance. *J Mater Process Tech* 247:19–28
9. Tebaldo V, Confiengo GG, Faga MG (2017) Sustainability in machining: “Eco-friendly” turning of Inconel 718 Surface characterisation and economic analysis. *J Clean Prod* 140(3):1567–1577
10. Suarez A, Lopez de Lacalle LN, Polvorosa R, Veiga F, Wretland A (2017) Effects of high-pressure cooling on the wear patterns on turning inserts used on alloy IN718. *Mater Manuf Process* 32(6):678–686
11. Behera BC, Alemayehu A, Ghosh S, Rao PV (2017) A comparative study of recent lubri-coolant strategies for turning of Ni-based superalloy. *J Manuf Process* 30:541–552
12. Hoiera P, Klement U, Alagan NT, Beno T, Wretland A (2017) Flank wear characteristics of WC-Co tools when turning Alloy 718 with high-pressure coolant supply. *J Manuf Process* 30:116–123
13. Deshpande YV, Andhare AB, Padole PM (2018) Experimental results on the performance of cryogenic treatment of tool and minimum quantity lubrication for machinability improvement in the turning of Inconel 718. *J Braz Soc Mech Sci Eng* 40(6):1–21
14. Hegab H, Umer U, Soliman M, Kishawy HA (2018) Effects of nano-cutting fluids on tool performance and chip morphology during machining Inconel 718. *Int J Adv Manuf Technol* 96:3449–3458
15. Bagherzadeh A, Budak E (2018) Investigation of machinability in turning of difficult-to-cut materials using a new cryogenic cooling approach. *Tribol Int* 119:510–520
16. Behera BC, Chetan SD, Ghosh S, Rao PV (2017) Spreadability studies of metal working fluids on tool surface and its impact on minimum amount cooling and lubrication turning. *J Mater Process Technol* 244:1–16
17. Marques A, Suarez MP, Sales WF, Machado AR (2019) Turning of Inconel 718 with whisker-reinforced ceramic tools applying vegetable-based cutting fluid mixed with solid lubricants by MQL. *J Mater Process Technol* 266:530–543
18. Liu J, Han R, Sun Y (2005) Research on experiments and action mechanism with water vapor as coolant and lubricant in Green cutting. *Int J Mach Tools Manuf* 45:687–694
19. Liu J, Han R, Zhang L, Guo H (2007) Study on lubricating characteristic and tool wear with water vapor as coolant and lubricant in green cutting. *Wear* 262:442–452
20. Junyan L, Huanpeng L, Rongdi H, Yang W (2010) The study on lubrication action with water vapor as coolant and lubricant in ANSI 304 stainless steel. *Int J Mach Tools Manuf* 50:260–269
21. Pawade RS, Reddy DSN, Kadam GS (2013) Chip segmentation behaviour and surface topography in high-speed turning of titanium alloy (Ti–6Al–4V) with eco-friendly water vapour. *Int J Mach Mach Mater* 13:113–137
22. Kadam GS, Pawade RS (2017) Surface integrity and sustainability assessment in high-speed machining of Inconel 718—An eco-friendly green approach. *J Clean Prod* 147:273–283
23. Kadam GS (2019) Investigations on surface integrity in high-speed machining of inconel 718 under different machining environments. Unpublished thesis report. DBATU, Lonere, Raigad, M.S., India
24. Kadam GS, Pawade RS (2018) Chip Deformation Aspects in Relative Eco-friendly HSM of Inconel 718. *Procedia Manuf* 20:35–40
25. Kadam GS, Pawade RS (2020) Machining induced residual stresses in green machining of Inconel 718. In: Pawar P, Ronge B, Balasubramaniam R, Vibhute A, Apte S (eds) *Techno-societal 2018*. Springer, Cham. https://doi.org/10.1007/978-3-030-16962-6_58

“Design and Development of S Band Radio Frequency (RF) Cavity Filter Using Carbon Fibre Reinforcement Polymer (CFRP) Material for Communication Satellites”



Dipak Chopda, Vijay Kumar, Komal Dave, Prempal Kumar, Prashant Kumar, Nitin Kumar, and Hemendra Kansara

Abstract RF filter is critically tuned cavity structure, which has broadly two main functions, i.e. to pass the desired frequencies and to reject as much of the undesired frequencies such as noises. In this study, a new material, i.e. carbon fibre reinforcement polymer (CFRP), is introduced for realization of “S band radio frequency cavity filter” for high-power RF transmission and filtering, for communication satellites. The realization approach covers all the aspects, i.e. from material characterization to actual hardware testing. It starts with detailed CAD modelling of the device, mould design, appropriate layout sequence of CFRP to gain optimized mechanical and thermal properties, mechanical tooling for critical alignment for assembly, metallization like silver plating for improving electrical conductivity and RF performance. To assist and support the design, FE analysis for structural and thermal loads has been done and design margins are calculated which are well within the limit. For RF performance of this filter, performance network analyser (PNA) is used. Measured values of main RF parameters like return loss, insertion loss and frequency drift are 13 db, 0.9 db and 0.7 MHz, respectively.

Keywords Radio frequency (RF) · Coefficient of thermal expansion (CTE) · Total mass loss (TML) · Collected volatile condensable mass (CVCVM) · Glass transition temperature (T_g)

1 Introduction

In today’s time, usage of satellite links for telecommunication broadcasting, navigations as well as strategic communication is at highest peak. It helps in link establishment in many areas like television broadcasts, telephone calls and high-speed Internet

D. Chopda (✉) · V. Kumar · P. Kumar · P. Kumar · N. Kumar · H. Kansara
Space Applications Centre, ISRO, Ahmedabad, India

K. Dave
L.D. College of Engineering, Gujarat Technological University, Ahmedabad, India
e-mail: dave_komal123@ldce.ac.in

© The Author(s), under exclusive license to Springer Nature Singapore Pte Ltd. 2022
H. K. Dave et al. (eds.), *Recent Advances in Manufacturing Processes and Systems*,
Lecture Notes in Mechanical Engineering,
https://doi.org/10.1007/978-981-16-7787-8_18

data exchange. For realizing these satellite components, selection of materials plays important role. These materials need to possess a number of unique properties to be effective in space environment so that their functionality and integrity in micro-gravity remain as desired. For a material to be feasible for space usage, properties like low density, high specific strength and high specific stiffness, excellent corrosion resistance, excellent mechanical and thermal properties are essential. Launching cost can be considerably reduced by minimizing the payload mass.

The additional material properties required considering the functional aspects for high RF power transmission are high thermal conductivity (κ), high electrical conductivity (σ) and excellent thermo-structural stability for in-orbit environment. Riley et al. [1] characterized CFRP material for RF application. Mehdipour et al. [2] used conductive carbon fibre composite materials for antenna and microwave applications. RF power-filtering devices, i.e. S band RF cavity filter in payloads, are conventionally fabricated from “Invar” material. The scope of this research work is to realize S band RF cavity filter from CFRP material to overcome density drawback of Invar. Use of Invar results in high mass penalty on payloads, which ultimately results in high launch cost. Exploring the various options of available space-grade materials, CFRP prepreg is the obvious choice considering its excellent mechanical as well as thermal properties [3–6]. Density of CFRP is almost five times lesser than Invar. Thermal aspects considering the heat dissipation within the packages are also considered in the design phase. Electrical conductivity of the filter cavity is achieved through metallization on CFRP surface.

2 Experimental Procedure

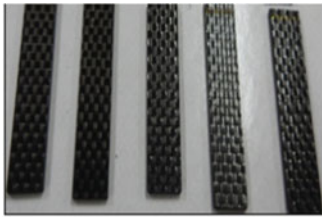
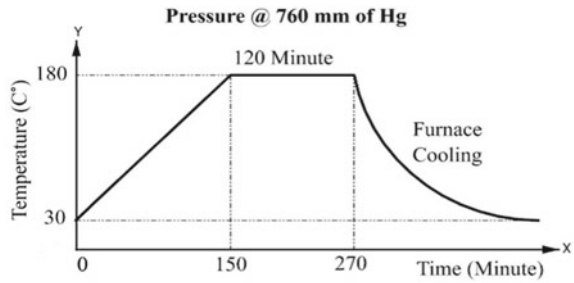
Experimental procedure includes CFRP material characterization, CAD model generation, finite element (FE) analysis, tool design, composite processing and CFRP metallization.

2.1 Material Characterization

The raw material selected for processing is HexPly® M18/32%/43090, which is carbon fibre reinforced woven prepreg. Test specimens for evaluation thermal and mechanical properties are prepared using hand-layup techniques. These samples are cured with standard vacuum-bagging and oven curing cycle as shown in Fig. 1. The test specimens are prepared as per the ASTM standards as shown in Fig. 2.

Characterized specimens show that CTE value of CFRP is better than Invar, but thermal conductivity is poor. Remaining parameters are excellent in comparison to Invar, which gives confidence to convert the existing metallic cavity filter into composite cavity filter. Table 1 shows measured properties for CFRP composite.

Fig. 1 Typical CFRP curing cycle



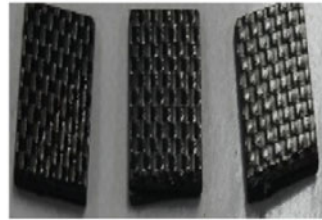
(a) For flexure test



(b) For tension test



(c) For CTE



(d) For Thermal conductivity

Fig. 2 a–d Specimen readiness for various property measurements

2.2 Generation of CAD Model and Fabrication Drawings

A detailed CAD model is generated for S band filter. The cylinder diameter, length and thickness are considered as 102 mm, 82 mm and 0.8 mm, respectively. Fabrication drawings are generated using same CAD tool, and subsequently, machining and dimensional inspection are carried out. Figure 3a, b shows exploded view for various components and assembled view for S band cavity filter.

Table 1 Measurement of various properties

Test category	Test method	Measuring unit	Measuredvalue
Tensile strength	ASTM D3039	Mpa	505
Tensile modulus		Gpa	157
Flexure strength	ASTM D790	Mpa	485
Flexure modulus		GPa	120
CTE (α)	ASTM E228	$\mu\text{m}/\text{m}/^\circ\text{C}$	-1.1610
Specific heat@ 125 °C	ASTM E1269	J/kg/K	1.25
Thermal diffusivity	ASTM E1461	cm^2/s	0.0068
Density	-	g/cm^3	1.7
Thermal conductivity (κ) @ 125 °C	ASTM E1461 ASTM E1269	w/m/K	1.15
TML and CVCM	ASTM E595	-	0.31 and 0.1%
T_g	ASTM D3418	$^\circ\text{C}$	205

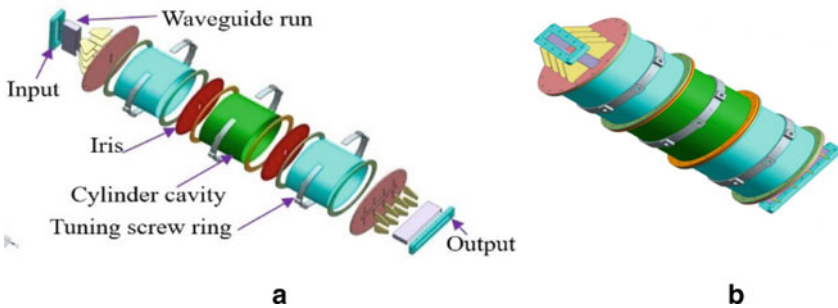


Fig. 3 a Exploded view of S band cavity filter. b Assembled view

2.3 Finite Element Analysis

For the FE analysis of S band cavity filter, HyperWorks (version 2017) software is used with OptiStruct as a solver. Pre-processing, processing (solver) and post-processing steps are followed for the analysis. All the properties obtained from characterized samples are given as input for analysis. Support mounts of the cavity filter are retained as metallic. Modal analysis has been carried out for estimation of natural frequency. The major design and loading specifications are as per environment test-level specification (ETLS) guidelines of the spacecraft by ISRO, which says the first fundamental mode of assembly shall be >100 Hz and quasi-static load conditions shall be 20 g in plane and 30 g out of plane. All base mounting locations are considered as fully fixed, i.e. all 6 DOFs constrained to simulate the actual boundary conditions. Based on FE simulation, results are extracted in form of eigenvalues, composite layer stresses and displacements which are shown in Fig. 4a–c. Stresses

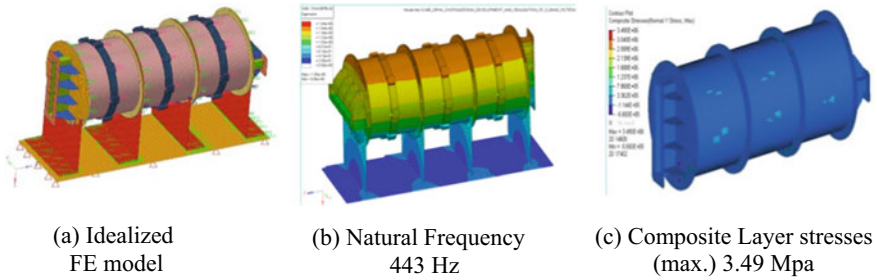


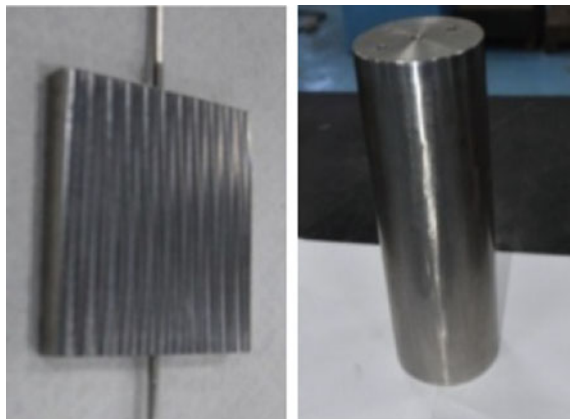
Fig. 4 a–c FE analysis model, normal mode and layer stress using HyperWorks software

are evaluated for composite elements as well as metallic support mounts. Sufficient margins are available against the allowable values. Margins are also calculated at the joint locations.

2.4 Mould Design and Fabrication

Zhang et al. [7] studied the geometry design using FEA. Here stainless steel (SS-304L) is selected as mould material for the cylindrical parts, and Invar is selected for the rectangular waveguide cavity as shown in Fig. 5. The main selection criterion for both the materials is their CTE values near to CFRP. During design of mould, adequate draft has been provided to ensure smooth release of cured component. Moulds are machined and inspected. All other parts are processed on flat surface plate, which are later machined to achieve required dimensions.

Fig. 5 Moulds for rectangular and cylindrical cavity



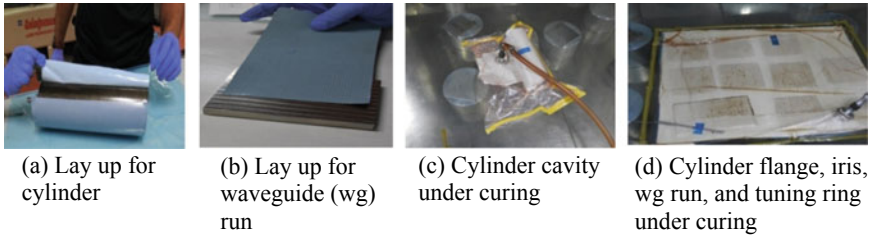


Fig. 6 a–d Hand-lay-up and vacuum-bagging and oven curing process for components

2.5 Lay-Up of Prepregs and Subsequent Curing Process

Hand-layup process is used for product realization as shown in Fig. 6a–d. Fibre orientation for cylinder cavity is considered as $(0^\circ/0^\circ/+60^\circ/-60^\circ)$, with symmetric and balanced lay-up up to its thickness. Standard vacuum-bagging and oven curing process is followed as per the curing cycle shown in Fig. 1. For monitoring temperature and vacuum level during curing cycle, standard data acquisition systems are used and logged.

2.6 Dimension Sizing for Component

Amini et al. [8] enhanced dimensional accuracy and surface integrity by helical milling of carbon fibre reinforced polymer. Using same philosophy, all components are machined and sized to final dimensions using milling and turning machines as per fabrication drawings. Figure 7a–d shows components after machining.

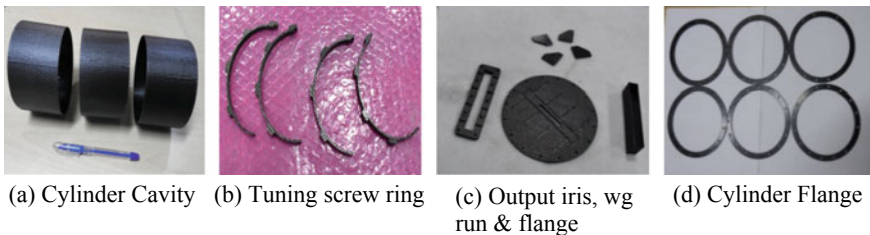


Fig. 7 a–d Various components after machining and sizing from cured laminates

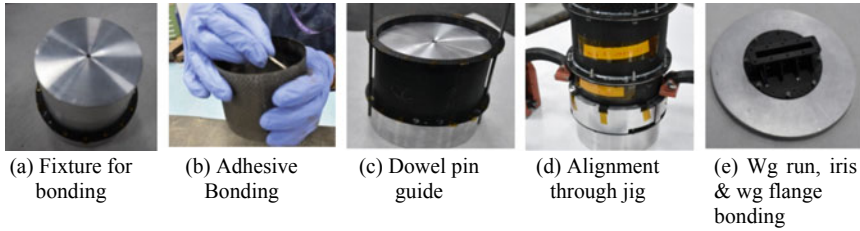


Fig. 8 a–e Assembly of subcomponents by adhesive bonding

2.7 Assembly and Adhesive Bonding of S Band Filter

Loctite EA E-120HP epoxy-based adhesive is used for subcomponent bonding, i.e. cylinder cavity to cylinder flange and tuning screw ring. To ensure accurate alignment of adhesive bonded components, jig and fixture are used. Provision of dowels is also given to minimize the assembly errors. Fasteners are used for filter cylindrical cavity-to-cavity assembly with cross-iris, cylindrical cavity to input output iris for final assembly. Figure 8a–e shows assembly process of various components.

2.8 Metallization on CFRP Components

Miomir et al. [9] observed the effect of silver on aluminium and its alloy. Kozlov et al. [10] found the electroless silver plating on aluminium. Similar approach is followed on CFRP components to make the surface electrically conductive for better RF power handling with minimum RF losses. Deposition methods, electroplating and electroless plating have been utilized to attain metallic plating on composite surfaces. Surface preparation, electroless copper plating, electroless nickel plating and silver electroplating are followed sequentially to make the surface electrical

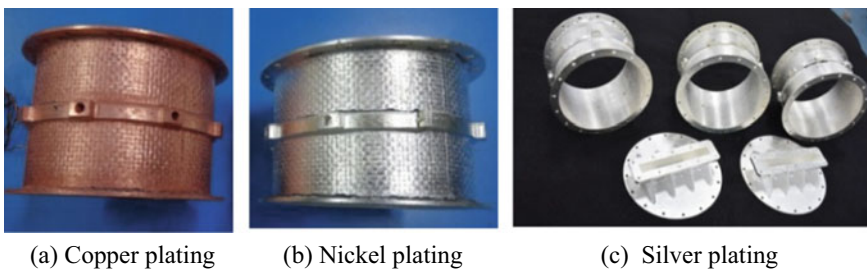
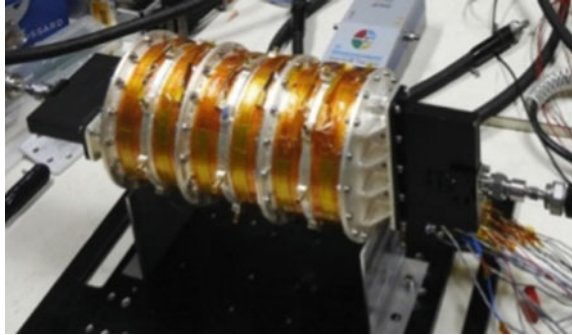


Fig. 9 a–c Various stages of metallization process on CFRP material

Fig. 10 S band cavity filter assembly with tape heater mounts



conductive. Figure 9a–c shows various stages of plating. Overall, dimensional variation is observed up to 100 μm , which is well within the tolerance limit of S band cavity filter.

2.9 Assembly and RF Test Preparation

All the components are assembled as per sequence defined in the assembly drawing. M3 SS fasteners are used to carry out joint assembly among cylinders, and M4 SS fasteners are used for base plate and support bracket assembly. These assemblies are carried out ensuring stress free condition. Additional tuning screws are provided on the tuning screw ring mounts to minimize the effect of dimensional errors; those are detrimental for RF performance. These mounts are at the middle of the each cylinder as shown in Fig. 10. Realized hardware is integrated to the base platform for RF simulation and testing.

3 RF Power Test Results

To simulate the actual condition, S band cavity filter is tested on performance network analyser (PNA) instrument for measurement of S parameters. Frequency drift analysis is measured for operating temperature range from 25 to 125 $^{\circ}\text{C}$. This temperature range is achieved by mounting tape-type resistive heater on external surface of the cylinder cavity as shown in Fig. 10. Applying external heat on surface in controlled mode, RF electrical characteristics like insertion loss, return loss and frequency drift are measured using PNA as shown in Fig. 11. Data are recorded and logged in the various temperature ranges, i.e. from ambient to 50, 80, 100 and 125 $^{\circ}\text{C}$. Table 2 shows RF parameters' comparison, and Fig. 12 shows impact of temperature on RF parameters.

Fig. 11 RF test set-up for insertion loss, return loss and frequency drift measurement

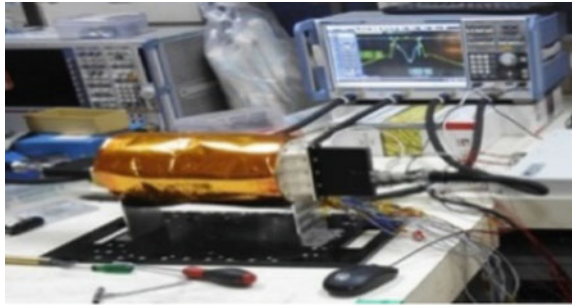
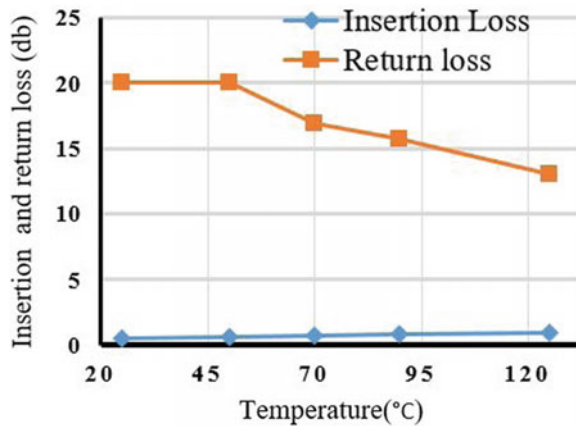


Table 2 Measured RF parameters Invar vs CFRP at centre frequency of 2565 MHz

Parameters	Unit	Invar @85 °C	CFRP @125 °C
Frequency drift	MHz	0.6	0.7
Insertion loss	db	0.6	0.9
Return loss	db	17	13

Fig. 12 Insertion loss and return loss versus temperature



4 Conclusion

On the basis of estimated design margins, sophisticated realization approach and test results, it can be stated that most of the RF parts can be realized using composite instead of conventional metallic materials. All the specification compliances are met, and results are within the acceptable limits. Structural design simulation shows a very good margin against the specified loads. Stresses are very benign, and deformations are within the range. Being polymer, the outgassing properties are also evaluated and those comply the specifications. Considering its functional aspects, the RF results show a good match between estimated and tested results. The losses are within the range and very much comparable to the metallic Invar-based design. However, few

challenges are also faced during design, mould realization and surface metallization on CFRP. In the mould and tool design phase, one has to consider the shrinkage allowances of mould during curing and cooling and the taper allowances of the mandrels. A tight tolerance-based jig and fixture design is used to ensure stress-free bonding.

Considering the metallization aspects, bond line is very critical, i.e. when two components are bonded with each other, one has to ensure the adhesives are not oozed out from the bond line area; otherwise, it will lead to intermittent coating phenomenon. In addition to this, adhesive's compatibility to be ensured with the chemical agents, which are required to be used during coating process. For better surface finish at the time of lay-up, processing shall be carried out on highly polished surfaces. During metallization process, minor degradation in surface finish is observed; therefore, there is still scope of reducing the roughness of the plated surface. Impact of deformation caused by differential CTE on RF performance is within acceptable limit. RF electrical parameter performance is also found satisfactory, and frequency drift in test is within acceptable range. RF tests conclude that insertion loss varies from 0.6 to 0.9 db as the temperature changes from ambient to 125 °C. Return loss is recorded 20 db at ambient condition to 13 db at 125 °C. Frequency drift observed is up to 0.7 MHz from centre frequency at 125 °C. Hence, it can be concluded that the CFRP-based cavity filter design is meeting the structural as well as RF requirements with enormous amount of weight saving. Further weight and cost can be further curtailed if such components are realized on mass scale.

Acknowledgements The authors wish to place on record their gratitude to all colleagues in Space Applications Centre (SAC), ISRO, for their invaluable contributions in these developmental efforts. The authors also thank workshop facilities for fabrication support, HPTD and MFD divisions for RF parameters test and STPD for metallization process. The authors also thank Shri Nilesh M. Desai, Director, SAC, Ahmedabad, for his continuous encouragement, guidance and support for advanced R&D activities.

References

1. Riley EJ, Lenzing EH, Narayanan RM (2014) Characterization of carbon. In: Ranney KI, Doerry A (eds) Radar sensor technology XVIII, Proceedings of SPIE, vol 9077
2. Mehdipour A, Sebak AR, Trueman CW, Rosca ID, Hoa SV (2012) Conductive carbon fiber composite materials for antenna and microwave applications. In: Paper presented at 29th national radio science conference (NRSC 2012), 10–12 Apr 2012. Faculty of Engineering/Cairo University, Egypt
3. Liu L, Zhang B-M, Wang D-F, Wu Z-J (2005) Effect of cure cycles on void content and mechanical properties of composite laminates. *Compos Struct* 73(3):303–309
4. Qian C, Weare R, Pasco C, Kourra N, Attridge A, Williams M, Kendall K (2020) Numerical and experimental studies of multiply woven carbon fibre prepreg forming process. In: Bambach M (ed) *Procedia manufacturing*, 23rd international conference on material forming (ESAFORM 2020). Elsevier, pp 93–99
5. Schlothauer A, Pappas GA, Ermanni P (2020) Material response and failure of highly deformable carbon fiber composite shells. *Compos Sci Technol* 199(2020):108378

6. Olivier P, Cottu JP, Ferret B (1995) Effects of cure cycle pressure and voids on some mechanical properties of carbon/epoxy laminates. *Composites* 26(7):509–515
7. Zhang W, Gao J, Cao J (2020) Blank geometry design for carbon fiber reinforced plastic (CFRP) preforming using finite element analysis (FEA). In: Fratini L, Ragai I, Wang L (eds) 48th SME North American manufacturing research conference, NAMRC 48. *Procedia manufacturing*, vol 48. Elsevier, pp 197–203
8. Amini S, Baraheni M, Hakimi E (2019) Enhancing dimensional accuracy and surface integrity by helical milling of carbon fiber reinforced polymers. *Int J Lightweight Mater Manuf* 2(4):362–372
9. Pavlovic MG, Tomic MV, Pavlovic LJ (2005) Electroplating of silver on to aluminium and its alloys. *Zastita Materijala* 46(2):23–27
10. Kozlov AS, Palanisamy T, Narasimhan (2002) Electroless silver plating. US 6387542 B1, United States Patent, 14th May 2002

Design and Manufacturing of a Test Rig for Experimental Studies on Misalignment Effect Between Rotors



Mili Hota and V. D. Dhiman

Abstract Most machines utilize mechanical couplings between the drive and load. A common malfunction that happens after load unbalance in rotating machines is the shaft misalignment, which might be because of incorrect assembling of machine, thermal distortion together with asymmetry in load. However, during assembly, care must be taken to keep it inside a tolerable limit. The alignment condition of the machines varies because of the asymmetry in loads, thermal distortion, unequal foundation settlement, and various other static loading. It leads to the development of reactive forces in the coupling and often a major cause of vibration and brings about poor efficiency of the rotating machines, which in turn culminates to failure. It will be helpful during diagnosis to have a meticulous study about the vibration characteristics on misalignments. To study the misaligned rotors dynamics, a set up is modelled and constructed. An investigation is carried out to study the effect of provoked misalignments and also steady-state vibration reaction on integer fraction of the initial bending Natural Frequency (NF). Additionally, the effects on Parallel Misalignments (PM), Angular Misalignments (AM), and combination of AM and PM both are analysed.

Keywords Misalignment · Natural frequency · FFT analyzer · Flexible coupling

1 Introduction

In machine assembly, positioning the rotational centres of two shafts in a manner such that they are collinear at normal operating condition is termed as shaft alignment. The perfect alignment of the machine bearings and shaft centres is described by means of the Total Indicator Reading (TIR) of coupling hubs or shafts. Harmonic forces

M. Hota (✉)

Gujarat Technological University, Ahmedabad, Gujarat 382424, India

V. D. Dhiman

Mechanical Engineering Department, Dr. S. & S.S. Ghandhy Government Engineering College, Surat, Gujarat 395001, India

are created when the shafts are misaligned. High stress is generated by these forces on the stationary elements along with the rotating machine components. The intense shaft misalignment cases induces bending stress to the shaft which will break and fracture the shaft.

As per “Bognatz [1]” and “Gibbons [2]”, about 70% rotating machine vibration issues are caused by misalignment. Sometimes, offset misalignment is called as parallel misalignment (PM), which is the distance connecting the shaft rotational centres gauged on the power transmission plane. Its measurement is generally performed on the coupling centre.

The angular misalignment (AM) may be expressed in terms of slope or angle in degree. The angle is represented most popularly in regards to gap per diameter. The gap is calculated by dividing gap by the diameter that is termed as coupling or working diameter. The relationship among gap and diameter is important. “Perez [3] clarifies that the prime indicator of any sort of alignment problem is vibration.” “Singiresu [4] suggest that both the high axial vibration levels (VL) at the machine’s thrust end along with high radial vibration levels (VL) on the machine’s coupling end are the best indicators of alignment problems. At the 1X or 2X frequency, vibration associated alignment usually appear.”

“Piotrowski [5], Shaft Alignment Handbook, 1995, it is stated that various combination of frequency was revealed by various kinds of flexible couplings in the vibration response under same kind of misalignment condition.”

“Lee and Lee [6] modelled a design to aim at the flexible coupling–rotor–ball bearing system. Anisotropies of bearing stiffness had been propounded as the indicator of misalignment as of orbital analysis”. “Redmond and Al-Hussain [7] designed a pliable coupling in a radially firm, pinned joint having rotational stiffness.”

“Lees [8] analysed the misalignment’s effect in firmly coupled rotors. The connecting bolts’ kinematics had been presented instinctively for PM.” “Redmond and Al-Hussain [3] stated coupled lateral-torsional 1X vibration aimed at PM.”

“Fengqi and Meng [9], and Patel and Darpe [10] discovered the whole spectrum analysis”. Work of “Lees [8] was relevant in this concern. For the misalignment’s diagnosis, the 2X filtered orbit’s major axis inclination in the misalignment’s direction had been recommended. It insinuates that the precise vibration response aimed at misalignment is still surrounded by mystery. A strong 2X harmonic is expected in diagnosis of misalignment amongst diverse vibration symptoms portrayed by different researchers.” “Sekhar [11] used a rotor bearing system to model the higher order system through finite elements by considering deflection, slope, shear force, bending moment with eight degrees of freedom per node. They analysed reaction forces, moments developed due to flexible coupling misalignment.”

“Xu and Marangoni [12] modelled the rigid coupling in two ways: a frictionless joint and a joint with stiffness and damping. The continuous wavelet transform (CWT) was been used as a tool to extract the time response of the rotor system.”

“Hujarea and Karnik [13] presented the results of Harmonic analysis of the Aluminium (Al) shaft rotor bearing system with rigid coupling, under parallel misalignment, using FEA. The paper showcases vibration spectrum due to the

misalignment. The results are compared with experimental results based on FFT analyzer for different sub critical speeds.”

“Lal and Tivari [14], developed a test rig and used for experimentation in which different levels of misalignment was introduced. After estimating the Multiple Fault Parameters, then the accuracy was checked through an impact test on the rotor test rig. The effect of different levels of misalignments on estimated parameters was studied.”

The existing literature are either related to theoretical analysis or experimental investigation related to rigid coupling. Attempt is made to carry out experimental investigation on a setup designed such that to accommodate all the three types of misalignment in the perpendicular planes. The investigational study of misaligned rotors coupled with flexible coupling support on single row ball bearings is focused in this work. Steady-states vibration reaction is attained at integer fraction of the critical speeds. The special test rig that permits the study of misalignment by the measurement of vibration response for all the three kinds of misalignment (parallel, angular and combined) is presented here. By inducing different amount of misalignment in the vertical and horizontal plane, the combination of AM along with PM has been explored. The study supports in the evaluation that merely a strong 2X frequency vibration do not conclude misalignment; and it provides a well-defined diagnosis technique. The study scrutinizes in which the direction (Radial or Axial) there is high frequency due to the specific type of misalignment. Most of the literature are predicting 2X dominance, attempts to conclude that only 2X dominance is not an indication of misalignment is made.

2 The Test Rig

Because of the tremendous expansion of Turbo Generator (TG) units, machines with flexible rotors became commonplace. In place of enormous concrete machines, lightweight manufactured steel structures are becoming popular. The steel foundations are low tuned, which means that their critical speed is several natural frequency lower than the machine’s operational speed. The bearing response forces are responsive to Lateral Misalignment (LM). A special misalignment rig is being modelled and commissioned to corroborate these theoretical predictions.

This test rig can introduce a wide variety of lateral alignment as well as angular alterations, and its key features result in predictions for the natural frequency (NF) of vibration in all three directions. The whole structure (including shaft, rotor, together with Base Plates (BP)) is made carefully in manifold parts.

2.1 Description of the Set up

As shown in Fig. 1, the testing rig set up consists of a coupled rotor setup with two rotors connected by flexible coupling. The vibration-measuring equipment, the drive unit, and the base plates are all included. Table 1 lists the specifications and dimensions of the rotor.

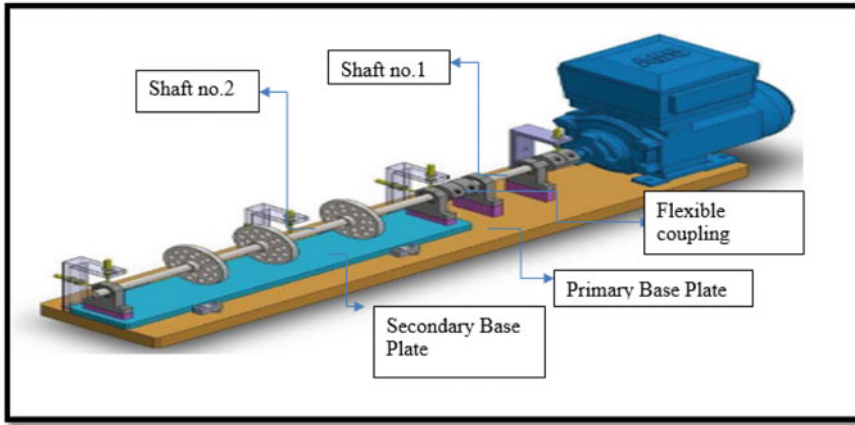


Fig. 1 The solid model of experimental set up

Table 1 Rotor bearing-pedestal specifications

Shaft length no. 1, 2	600,135 mm
Shaft major diameter	15 mm
No. of shafts	2
Shaft material	4137 Alloy steel
Mass of each shaft	689.10 g
No. of discs	3
Diameter of each disc	100 mm
Mass of each disc	523.66 g
Rotor speed	3000 rpm
Bearing diameter	25 mm
Bearing length	9 mm
Length between the bearing pedestals	426 mm
Coupling max diameter	32 mm
Coupling length	41 mm

2.2 Coupling Characteristics and Misalignment Condition

The amount of misalignment of the secondary base plate decides the, the coupling characteristics. The range of the misalignment to be included is further chosen centred on the coupling boundaries.

The tolerance of the coupling are:

- Lateral $dx = 1 \text{ mm } (\pm 0.5)$ (Axial Misalignment)
- Vertical $dy = 0.3 \text{ mm}$ (Lateral Misalignment)
- Angular $\theta = 3.5^\circ$ (Angular Misalignment)

Based on the angular and offset misalignment ranges in the perpendicular planes required to be induced, the coupling selection is done. For angular misalignment (AM), the shaft's axis is inclined in relation to the other shaft in the vertical plane by properly moving the pedestal. However, by placing pre-machined shims or filler gauges or slip gauges of defined thickness between the stoppers connected to the base plates in the horizontal and vertical direction, the offset misalignment could conveniently be attained.

2.3 Base Plates

To ensure the absolute flatness and appropriate alignment as for the plate, the primary and secondary base plate is made of plain pre-machined carbon steel. The plate's net-weight is approximately around 100 kg. By moving rotor-2 relative to rotor-1, the misalignment can be caused (Fig. 2). This may be possible as the rotor-2 is attached

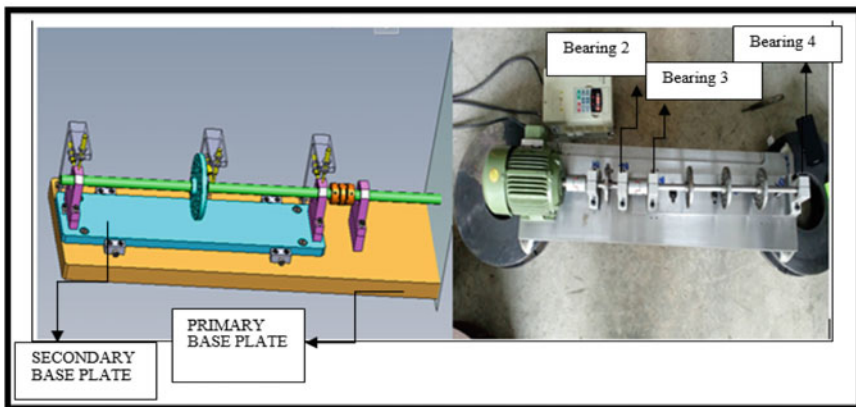


Fig. 2 Rotor-2 mounted on secondary base plate

to primary base plate using the secondary base plate. Moving base plate will most likely generate linear misalignment.

The horizontal motion of the secondary base plate could be rendered utilizing the four nut-bolt sets given on both the surface of the plate as exhibited in Fig. 2. The forward/backward motion of this bolts regarding the fixed nuts resulted in the horizontal motion of the plane. However, before that base plate is released from primary base plate.

The vertical movement of the base plate is attained as the vertical jacking bolt given at extreme ending of the plate for AM. For the misalignment in the vertical plane, the shims of proper thickness are placed between the base plate and the platform. This might be observed that this setup only allows the motion of rotor-2 in relation to rotor-1.

2.4 Precaution in Fabrication

All significant elements of the test rig are constructed with high accuracy (As per VDI/DGQ 3441) CNC machines with,

- Positioning Uncertainty (P): 0.01 mm
- Repeatability (Ps medium): 0.005 mm
- Every plates (i.e. main and the secondary base plates) as well as spacers are machined and earthed to ensure flatness and parallelism within 0.02 mm.

To ensure the test repeatability, the Hardened ground dowel pins and liner bush are utilized. In the standard metrology laboratory, the assembly and examination are done and the elements are chosen from the standard catalogue.

2.5 Instrumentation

The vibrations sensors are mounted on the bearings. Output of these sensors are recorded and stored in a FFT analyzer for further analysis.

3 Pilot Testing Steps

The test rig is fabricated and then the testing is carried out as follows:

Step.1. As specified by Piotrowski in Shaft Alignment Handbook [5], the shafts and motor are arranged within acceptable alignment tolerances. In this completely aligned condition the vibration levels are recorded by fixing magnetic base accelerometers along with hand handled FFT analyzer (Fig. 4).The aligned condition is firstly tested with programmed frequency drive for a run-up and run

down of speed from 500 to 2800 RPM. The shaft, couplings are checked for any permanent deformation during this test. This test is further carried out for specific frequencies and FFT recorded.

Step.2. After the aligned condition testing the angular misalignment (AM) is created by shifting the shaft axis from bearing 4 pedestal keeping reference toggle pin at the centre, the shaft axis is misaligned by 1° in X -direction from the coupling half. Vibration levels (VL) to be recorded at various frequencies.

Step.3. The test is repeated by misaligning the shaft by 1 mm by lifting the secondary base plate in Y - direction and inserting pre-machined shims of required thickness.

Step.4. The last test is carried out now by creating the combined misalignment of 1 mm along the Y -direction as well as 1.5° along the X -direction. This test rig facilitates this combination due to the unique design of base plates as shown in Figs. 2 and 3.

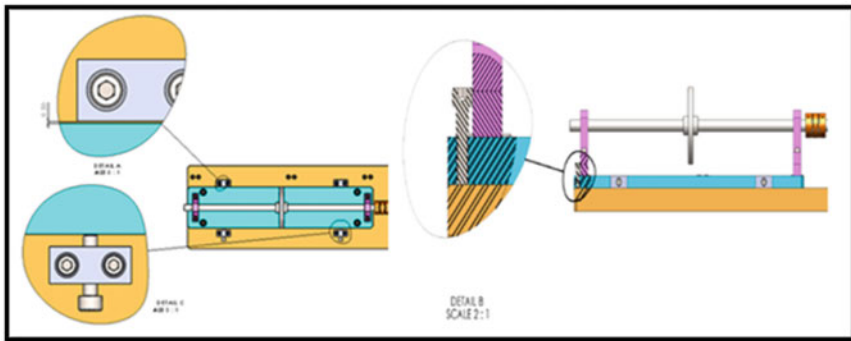


Fig. 3 The secondary base plate

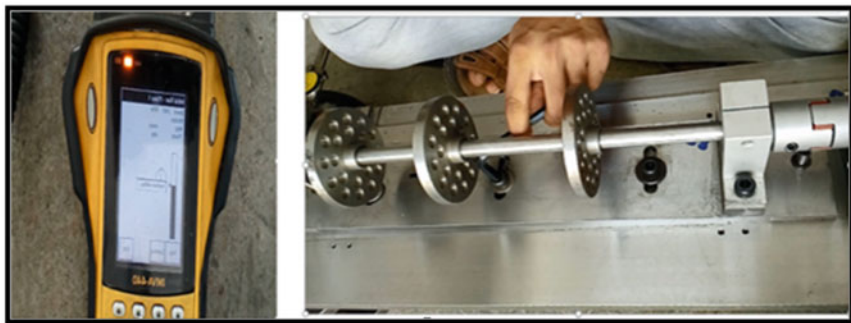


Fig. 4 Inducing misalignment and cross phase testing through FFT analyzer [Vibrasound Processor: IMVA-440™]

3.1 Recording the Response

The vibration responses are captured on the FFT analyzer. Sample test data is exhibited in Fig. 5a, b.

The three bearing houses are taken for recording the FFT curves in which one is in axial direction and two are in radial direction are been recorded by the FFT curves. The readings from the Tables 2, 3, 4 and 5 have frequency up to 3X for all direction at high frequency of rotor rotation. To get the more significant Peak Acceleration (PA) in all the three directions, the FFT curves are analysed up to 10X frequencies.

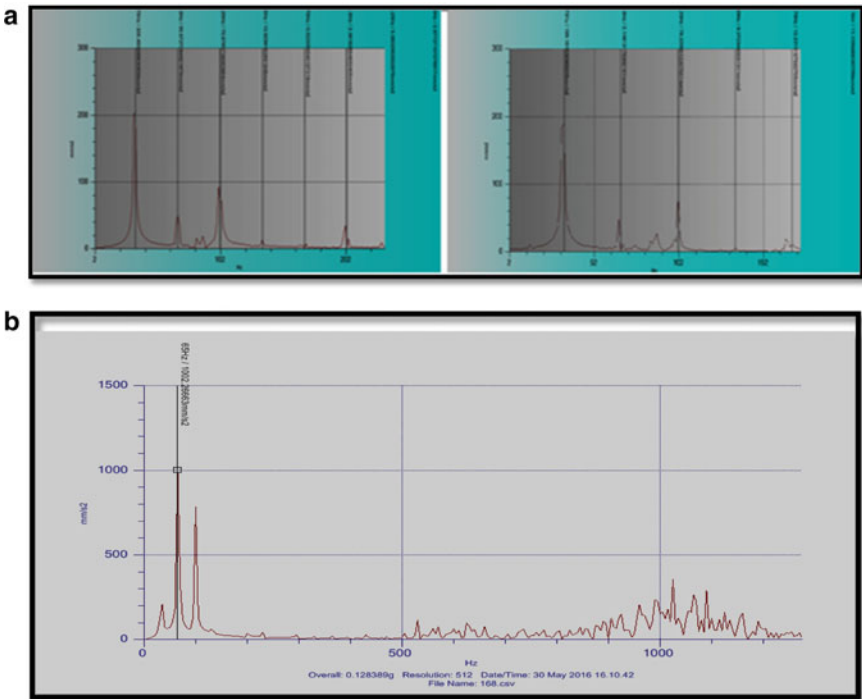


Fig. 5 a Sample FFT curves for completely aligned system (at 2000 rpm i.e.: 33.33 Hz). b Sample FFT curves for angular misalignment of 1 degree (at 2000 rpm i.e.: 33.33 Hz)

Table 2 The peak acceleration for fully aligned condition

Speed	Acceleration peak ups	Bearing 2			Bearing 3			Bearing 4		
	mm/s ²	1X	2X	3X	1X	2X	3X	1X	2X	3X
2000	Horizontal	205.5	50.7	70.7	145.4	80.7	143.8	39.2	114.2	245.4
	Vertical	183.9	6.2	8.2	130.4	8.0	113.7	9.2	9.8	82.9
	Axial	53.0	6.5	12.0	59.9	47.2	183.6	56.3	41.2	111.0
2500	Horizontal	422.0	72.5	6.1	361.4	16.4	21.8	111.7	10.4	7.6
	Vertical	327.3	48.8	14.3	261.3	73.5	9.4	113.5	62.6	5.3
	Axial	53.0	6.5	12.0	59.9	47.2	183.6	56.3	41.2	111.0
2800	Horizontal	493.8	43.6	8.7	414.0	43.8	3.1	217.6	10.5	10.2
	Vertical	439.7	41.5	3.9	293.8	60.2	12.5	151.6	23.1	8.8
	Axial	238.3	47.4	15.0	55.9	22.9	7.9	170.1	43.7	6.3

Table 3 The peak acceleration for the AM for 1°

Speed	Acceleration peak ups	Bearing 2			Bearing 3			Bearing 4		
	mm/s ²	1X	2X	3X	1X	2X	3X	1X	2X	3X
2000	Horizontal	228.6	1.7	53.3	172.7	10.3	132.1	65.9	51.5	55.8
	Vertical	245.9	6.1	79.0	27.4	19.5	400.4	57.2	35.4	47.9
	Axial	106.5	2.1	13.2	6.6	13.4	203.6	112.5	47.8	2.6
2500	Horizontal	434.3	148.2	33.8	371.1	108.2	20.7	105.0	333.9	80.9
	Vertical	392.1	430.2	126.7	275.2	508.8	52.3	11.0	161.6	52.6
	Axial	34.0	2.9	13.1	94.7	128.5	17.3	139.7	107.3	22.0
2800	Horizontal	536.5	29.7	34.9	456.8	70.0	22.8	259.5	54.5	47.4
	Vertical	487.5	241.4	55.0	360.3	370.1	40.5	50.6	102.3	30.1
	Axial	190.6	69.0	21.3	114.9	40.3	14.2	164.2	76.1	10.9

Table 4 The peak acceleration for the PM for 1 mm in Y-direction

Speed	Acceleration peak ups	Bearing 2			Bearing 3			Bearing 4		
	mm/s ²	1X	2X	3X	1X	2X	3X	1X	2X	3X
2000	Horizontal	51.9	1319.7	26.9	87.5	2041.5	122.5	149.7	3796.4	118.2
	Vertical	149.7	3796.4	118.2	359.8	351.3	716.6	268.7	126.5	348.3
	Axial	59.6	1278.6	49.2	43.9	295.5	15.8	268.7	126.5	348.3
2800	Horizontal	450.1	169.3	282.4	518.4	864.6	535.7	515.5	711.9	665.7
	Vertical	3907.0	350.1	704.5	4161.7	605.7	2198.1	1083.0	550.6	2284.1
	Axial	774.4	41.2	127.2	1195.9	131.1	518.5	359.8	351.3	716.6

Table 5 The peak acceleration for the combined misalignment for 1.5° X-direction and 1 mm in Y-direction

Speed	Acceleration peak ups	Bearing 2			Bearing 3			Bearing 4		
	mm/s ²	1X	2X	3X	1X	2X	3X	1X	2X	3X
2000	Horizontal	210.1	311.4	131.1	210.1	311.4	131.1	30.5	110.2	44.6
	Vertical	254.2	488.3	242.2	299.6	494.6	166.7	66.4	39.4	83.0
	Axial	167.0	53.6	95.9	140.2	307.3	76.5	38.7	29.9	74.6
2800	Horizontal	300.7	330.1	567.0	300.7	330.1	567.0	700.6	738.0	315.0
	Vertical	1844.0	558.8	344.6	354.5	254.0	23.1	484.2	114.3	529.4
	Axial	999.8	188.6	146.5	1796.3	676.0	190.6	1039.9	176.2	146.2

4 Comparison of the Results

4.1 Aligned Condition

The rig’s critical speed was calculated as 4500 rpm with the design parameters listed in Table 1. The rig was tested for a run-up and run down for 500–2800 rpm. The aligned condition vibration level exhibits that 1X is dominant. With the rise in speed, the acceleration value intensifies at 1X. When analysed with the vertical and axial direction, the pickups in the horizontal (radial) direction were higher than the axial directions (Fig. 6).

4.2 Angular Misalignment by 1° in the Horizontal Plane

It can be noted that 2X is dominant at some speed. When analysed with the horizontal reading, vertical and axial readings were low. With the amplification in speed, the vibration level (VL) increases at all the three bearings. Sometimes, even 3X was dominating at bearing 3. However, notable outcomes were exhibited by 1X and 2X (Fig. 7).

4.3 Parallel Misalignment of 1 mm in Vertical Plane

In here as well, the 1X and 2X are dominant. The level increases extremely high compared to the angular misalignment at higher speed (Fig. 8).

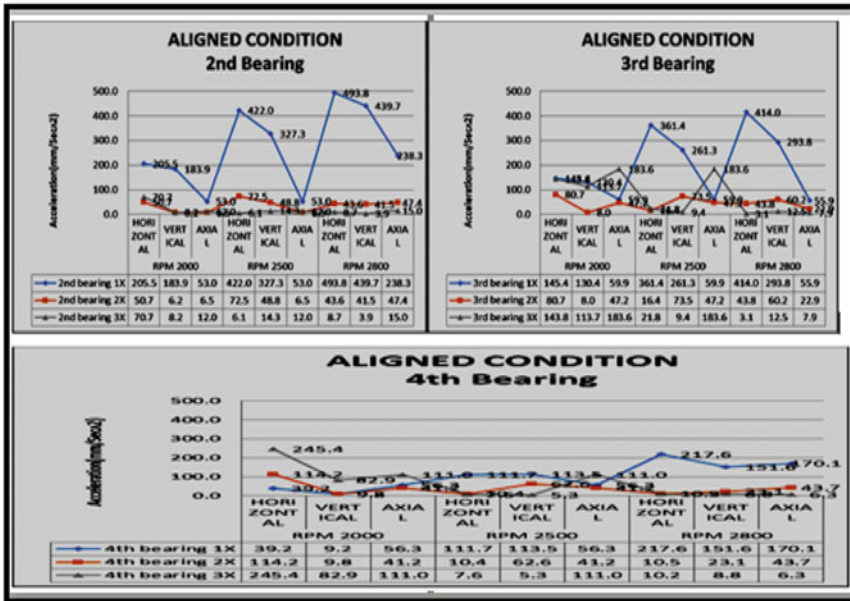


Fig. 6 Peak Acceleration values on all the three bearings in aligned condition

4.4 Combined Misalignment for 1.5° Horizontal Plane and 1 mm in Vertical Plane

The combined misalignment created in both perpendicular planes induces very high level of vibrations. The coupling is seen heated extremely. The results plotted shows the peak acceleration comparatively very high (Fig. 9).

5 Observations

- After intentional misalignment, it is observed that the set up showcases dominant acceleration at 1X as well as 2X frequency, while recording the vibration data by means of the hand handled FFT analyzer.
- With the increment in speed, the vibration level (VL) rises and the peak acceleration values noted in the Tables 3, 4, 5 compared to values in Table 2 shows that the intentional misalignment of the axis of the shaft from the coupling does cause harmonic forces induced which leads to rise in the VL at all the three bearings.
- The 3X attains dominance in the radial direction at few specified speeds, which concludes that only 2X dominance cannot conclude misalignment. In this specific case of flexible coupling though the initial vibration levels do not indicate

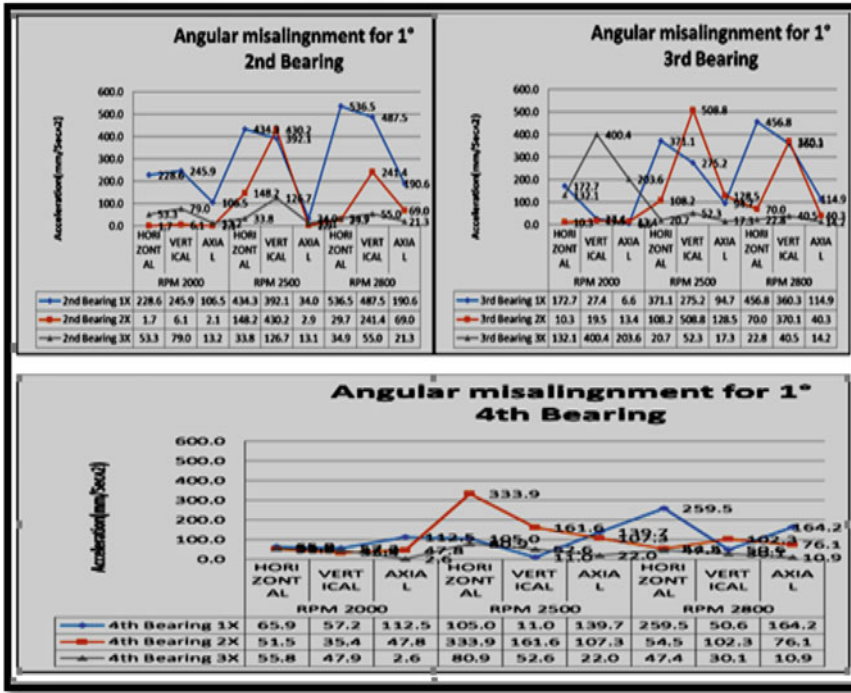


Fig. 7 Peak Acceleration values on all the three bearings with 1° misalignment in horizontal plane

misalignment but the misalignment in the vertical direction and the combined misalignment induce shows the attainment of 3X peaks.

- The radial measurements presents greater peaks than the axial direction during the angular misalignment in the horizontal plane. The main reason for this can be the flexible coupling is allowing angular misalignment especially in the plane parallel to the axis of rotation.
- The axial direction readings are comparatively low during the angular misalignment, but on experimenting further it is found that during parallel misalignment in the vertical direction the axial response also peak. The possible reason for this can be the amount of misalignment absorbed by the flexible coupling in the horizontal direction is high and so the axial readings are very low. But as the system is misaligned in the vertical plane the axial harmonics are induced and so high axial peaks are seen.
- Much higher vibration variation is exhibited by the combined misalignment.
- On account of heat generation, the coupling got impaired at the run-up test’s end.
- A 180° phase shift is noticed in the radial direction crosswise on the coupling halves. By the sensor’s movement from horizontal to vertical direction on the same bearing, the FFT shows a phase shift of 0°–180°.

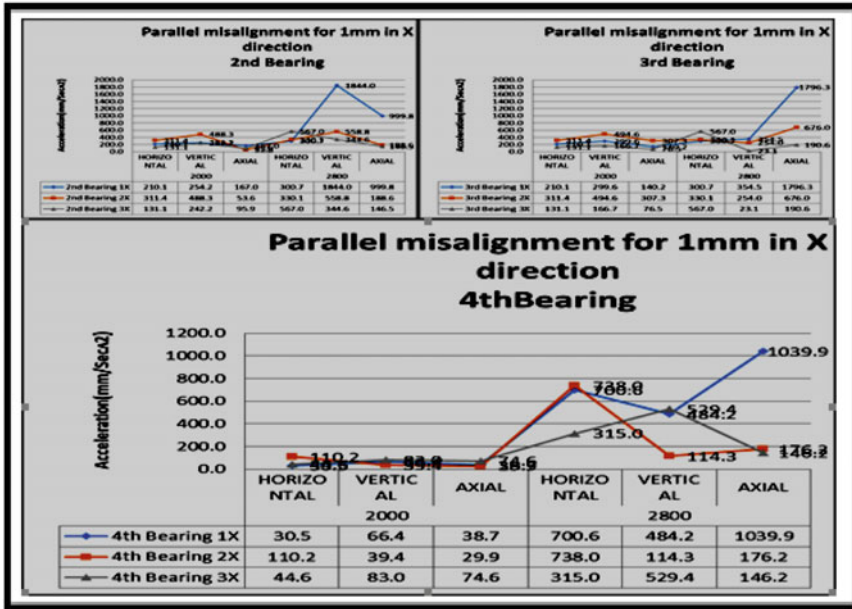


Fig. 8 Peak Acceleration values on all the three bearings with 1 mm misalignment in vertical plane

6 Conclusions

The study here on flexible couplings reveals that 2X dominance is not indicating misalignment and the results conclude greater peaks in the radial direction than in the axial directions due to misalignment, in contrast to the general traditional thinking. The measurement of cross phase across the misaligned coupling is facilitated by the test rig and a 0°–180° phase shift was noted on each bearing which also indicates that the phase shift between the harmonic forces generated in the three directions.

While inducing the misalignment in both the planes for creating the combined misalignment of parallel and angular misalignment, the observed variation in the harmonic response is much high.

Extensively huge amount of vibration level variation is obtained at the last bearing on the load end.

In the radial and axial direction reading, the percentage changes from 20 to 600%.

The 2X dominance cannot be seen clearly in the combined misalignment case. This also shows that in the industrial rotating structures the misalignment of the axis of the rotating shaft is not in a particular angular direction or parallel direction. So FFT indicating 1X and 2X peak does not conclude misalignment.

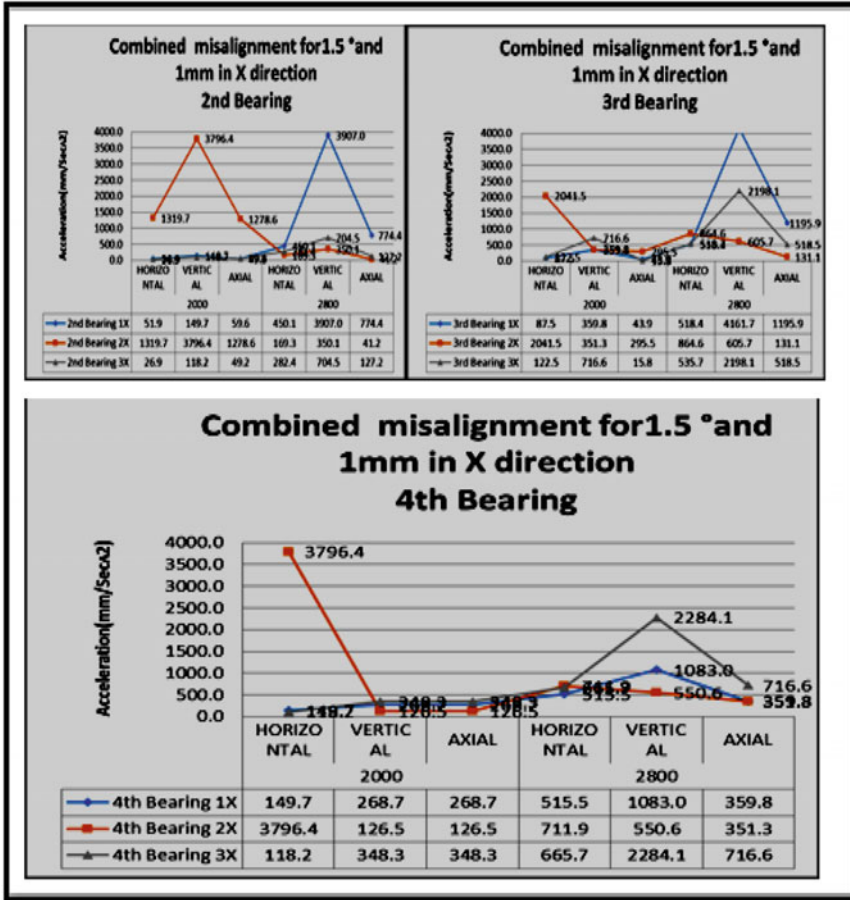


Fig. 9 Peak Acceleration values on all the three bearings in with combined parallel misalignment in vertical plane and angular misalignment in horizontal plane

References

1. Bognatz SR (1995) Alignment of critical and non-critical machines. Orbit 23A25
2. Gibbons CB (1976) Coupling misalignment forces. In: Proceedings of the 5th turbo machinery symposium. Gas Turbine Laboratory, Texas A & M University, pp 111–116.
3. Perez RX (2011) Is my machine ok?—A field guide to assessing process machinery
4. Singiresu RS (2004) Mechanical vibrations, 4th edn, international edition. Pearson Education, Inc., University of Miami, USA
5. Piotrowski J (1995) Shaft alignment handbook. Marcel Dekker Inc., New York
6. Lee YS, Lee CW (1999) Modelling and analysis of misaligned rotor ball bearing systems. J Sound Vibr 224:17–32
7. Al-Hussain KM, Redmond I (2002) Dynamic response of two rotors connected by rigid mechanical coupling with parallel misalignment. J Sound Vib 249(3):483–498

8. Lees AW (2007) Misalignment in rigidly coupled rotor. *J Sound Vibr* 305:261–271
9. Fengqi W, Meng G (2006) Compound rub malfunctions feature extraction based on full-spectrum cascade analysis and SVM. *Mech Syst Signal Process* 20(8):2007–2021
10. Patel TH, Darpe AK. Experimental investigations on vibration response of misaligned rotors. *Mech Syst Signal*. <https://doi.org/10.1016/j.ymssp.2009.04.004>
11. Sekhar A (1995) Effects of coupling misalignment on vibrations of rotating machinery. *J Sound Vib* 185(4):655–671. <https://doi.org/10.1006/jsvi.1995.0407>
12. Xu M, Marangoni RD (1994). Vibration analysis of a motor-flexible coupling-rotor system subjected to misalignment and unbalance Part I: theoretical model and analysis. *J Sound Vibr* 176(5):663–679
13. Hujarea DP, Karnik MG (2018) Vibration responses of parallel misalignment in AI shaft rotor bearing system with rigid coupling. *Mater Today: Proc* 5:23863–23871
14. Lal M, Tiwari R (2018) Experimental identification of shaft misalignment in a turbo-generator system *Sadhana (Acad Proc Eng Sci)* 43:80

Design, Modeling, and Simulation of Low-Cost Magnetorheological Fluid-Based Prosthetic Leg



Ganapati Shastry, Ashish Toby, Seung Bok Choi, Vikram G. Kamble, and T. Jagadeesha

Abstract This paper deals with designing and modeling a prosthetic leg with MR damper to control the knee joint for above-knee amputees. A four-bar mechanism has been selected for the knee joint of the prosthetic leg. A twin-tube MR damper was chosen for this work because of its better performance compared with other dampers, mainly due to the mobility of the magnetic core. The MR fluid selected for the purpose was the commercially available MRF 140CG. The entire modeling and simulation (motion analysis) of the prosthetic leg were done using SOLIDWORKS. This was done using the various relations of the natural human gait cycle. To find out the torque required to walk appropriately, dynamic analysis was done on a natural human leg's free body diagram (FBD). A curve was obtained between torque at knee and hip angle by combining the results of FBD and SOLIDWORKS simulation FBD and SOLIDWORKS simulation results. To understand the behavior of the MR damper, magnetic analysis, and CFD was done using COMSOL and ANSYS, respectively. Various results like variation of the magnetic field with coil wire diameter, variation of pressure, and velocity were obtained. Using these obtained results, a relation

G. Shastry · A. Toby · T. Jagadeesha (✉)

Department of Mechanical Engineering, National Institute of Technology, Calicut, Kerala 671603, India

e-mail: jagdishsg@nitc.ac.in

G. Shastry

e-mail: ganapati_b170859me@nitc.ac.in

A. Toby

e-mail: ashish_b170614me@nitc.ac.in

S. B. Choi

The State University of New York Korea (SUNY Korea), 119 Songdo Moonhwa-Ro, Yeosu-Gu, Incheon 21985, Korea

e-mail: seungbok.choi@sunkorea.ac.kr

V. G. Kamble

Department of Elastomers, Leibniz Institute for Polymer Research, 01069 Dresden, Germany

Faculty of Mechanical Science and Engineering, Institute of Materials Science, Technical University Dresden, 01069 Dresden, Germany

between the yield stress and current was obtained. This will further be used to obtain a relation between required torque and current. The control strategy for this leg is the use of a PID controller. The obtained relation between hip angle and current will be stabilized using a PID controller by tuning suitable gains.

Keywords Magnetorheological fluid · Prosthetic leg · Above-knee amputees · MR damper

Abbreviations

I_θ	Moment of inertia about knee joint
I_\emptyset	Moment of inertia about hip joint
V	Coriolis torque
G	Gravitational torque
τ_k	Torque at knee
θ	Knee angle
\emptyset	Hip angle
I_s	Moment of inertia of shank
m_t	Mass of thigh
l_s	Length of shank
m_s	Mass of shank
r_a	Distance of point of contact of the ankle and joint
r_s	Distance of center of mass of shank
k	Angle between sole of foot and ankle
r_t	Distance of center of mass of the thigh
W	Upper bodyweight of the person

1 Introduction

India has a high count of around 23,500 amputees each year, with 29% being post-femoral amputees. Approximately, 70% of the amputees in our country hail from rural areas with low incomes [1]. Active prosthesis, generally being expensive, cannot be afforded by a considerable section of society. Although less expensive, a passive prosthesis cannot outperform or provide enough aid for regular human activities or work [2–4]. Therefore, it is essential to develop a prosthetic leg that is not as expensive as an active leg but can provide adequate torque for walking. This paper aims at illustrating the design of a prosthetic leg using an intelligent material called MR fluid. MR fluid or magnetorheological fluid is a smart material that changes its viscosity and shear stress according to its magnetic field. A piston-cylinder mechanism can provide adequate damping force and the torque at the knee necessary for walking properly

inside a damper. Apart from this, the MR damper serves another purpose. Fluid is present inside the knee in a natural human leg that provides damping or shocking absorption while walking. An amputated leg wouldn't have this. Therefore, with the help of an MR damper, this can also be achieved [2–8].

An MR damper can be easily controlled with the help of a PID controller. A relationship between current and required torque must be found out, stabilized by tuning suitable control gains [9–18]. Magnetorheological fluids are intelligent materials that vary their viscosity and shear stress depending on the magnetic field acting on them [19]. MR materials (MR fluids, MR foam, and MR elastomers) [20]. It usually consists of a carrier fluid with ferromagnetic particles. The fluid quality depends on various factors, the cost, the density, the sensitivity to the magnetic field, the sedimentation rate, etc. MR fluids are a suspension of ferromagnetic particles in a carrier fluid. Under the action of a magnetic field, they aggregate and align themselves with the magnetic field, leading to a change of state for a Newtonian fluid to a non-Newtonian fluid, like toothpaste. Under normal conditions, it acts as a carrier fluid with suspended particles in it. The magnetic field changes the viscosity and yield stress of the fluid, depending on the direction and magnitude of the field applied.

A vast number of models have been defined to explain the working of the MR fluid. From Buoc-Wen and Bingham models to Dahl and visco-elastic–plastic models, many models theorized to numerically quantify the variations of properties of MR fluids [21]. Compared to their counterpart electrorheological fluids, MR fluids have shorter response times, a broader working temperature range, higher maximum yield stress, higher maximum field, has tolerance to impurities and changes after the application of magnetic fields are visible almost instantly [22, 23]. Due to its control over properties, MR fluid became a part of many devices, mainly as dampers, in brakes, clutches, and now in prosthesis [19, 24]. Modern medicine is currently researching the use of MR materials for multiple ways of treatment [25]. Due to its property variation, the damping coefficients and the damping forces can be controlled by changing the magnetic field.

MR fluids consist of three essential components: the carrier fluid (oil, water, grease etc.), the ferromagnetic particles, and additives. The primary parameters that need to be optimized while manufacturing MR fluids are the operating temperature range, the sedimentation rate, the response time, the hysteresis, chemical stability, magnetic saturation, and sensitivity [23, 24]. Sedimentation is the property of dispersions to settle down, leading to a heterogeneous mixture that affects the fluid's performance. A fluid with a lower sedimentation rate is usually preferred. The difference in yield stress and viscosity with and without the magnetic field should be significant to maximize its versatility [24, 26]. All these parameters are a function of the carrier fluid, the ferromagnetic particles (material, type, size, and shape) [27], additives, the relative quantities in the mixture, and the working environment [25, 26].

Another property of MR fluid that needs to be considered is the in-use-thickening. On continuous usage under high shear and stress, the fluid starts to thicken over time to a paste-like semisolid, rendering the MR fluid unsuitable for mechanical operations, similar to gear oil or butter [28]. Erosion is a problem that is caused due to interparticle contact, which results in a change in the shape and structure of the

ferromagnetic particles. This phenomenon leads to the thickening of the MR fluid, which is not reversible. Great attention needs to be given to the surface finish of the particle to make it last longer [26, 29]. Clumping is when the MR fluid is subjected to high magnetic field magnitudes for extended periods, resulting in chain-like agglomerations. This clumping phenomenon occurs due to induced magnetic field in the particles and residual magnetic field in the ferromagnetic particles. Eventually, the MR fluid aggregates to form something known as the ‘hard cake’, which reduces the increase in squeeze force due to the rise in the magnetic field [30].

There are several ways by which the stability of MR fluid is controlled: using additives like surfactants and stabilizers, using nanoparticles like nanowires and nanospheres, different carrier fluids, coating the ferromagnetic particles, etc. Additives like γ -Fe₂O₃ nanoparticles improve sedimentation stability and improve the MR characteristics of the MR fluids [31]. When added to MR fluids, poly (vinyl butyral) improves its sedimentation stability even at low particle concentration, reduces corrosion, and helps maintain stable yield stress at different shear rates [32]. Guar gum on adding to MR fluids reduces the density and improves the sedimentation stability [33]. Stearic acid on adding with MR fluid forms an emulsion with the silicon oil present, improving the sedimentation stability but increasing the initial viscosity, which is opposed to what is preferred for multiple industrial applications [34]. In addition of lecithin powder to the MR fluid, settling rate and agglomeration reduces [35]. There are several other methods of coating and additives that help stabilize the MR fluid and improve its performance [24, 26, 36, 37]. Another important factor deciding the quality of the MR fluid is the carrier fluid used. For this, the liquid should have a low viscosity that does not change with temperature [38]. Some of the standard fluids used are silicon oil, synthetic hydrocarbon oil, mineral oil, water, and glycerol [22, 23]. Silicon has good temperature stability, chemical stability, high flash point, making it an ideal and suitable carrier fluid. In this paper, the various relations are obtained assuming the MR fluid used to be MRF 140CG from Lord Corp [23].

2 Design and Modeling Aspects of MR Damper

2.1 Design of a Twin-Tube MR Damper

A variety of designs and sizes of MR dampers are commercially available. Each of them has a unique purpose. If an MR damper is to be used in a prosthetic leg, its primary requirements would be that it shouldn't be too bulky or else it would cause discomfort to the amputee. It should provide the necessary damping force and torque so that the prosthetic leg feels the same as the natural leg while walking. Apart from this, the design of the MR damper should be such that the entire MR fluid gets magnetized. Therefore, a twin-tube MR damper was found to be suitable for the prosthetic leg. The twin-tube MR damper consists of the following parts: upper-end

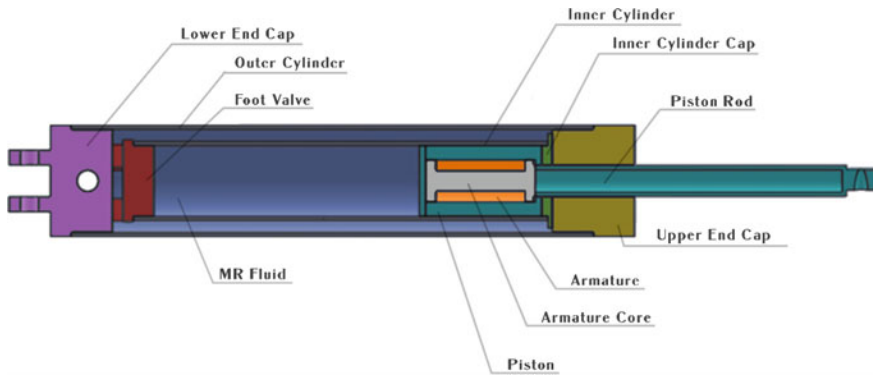


Fig. 1 Sectioned view of the designed MR damper

cap, lower-end cap, outer shock tube, inner shock tube, foot valve, piston, piston rod, piston cap, inner cylinder cap, and the armature core.

The armature core wound by the coil windings houses inside the piston to provide required magnetic field near the piston. This aids in keeping the magnetic losses to the minimum as the armature core itself would be reciprocating along with the piston. The piston also contains three holes so that the fluid can flow through it as well. The piston rod is attached to the end of the piston. The other end of the piston rod would be attached to the knee joint. The fluid is housed inside the inner shock tube or the inner cylinder. When the piston moves, it will enter the outer shock tube or the outer cylinder through the foot valve. The lower and the upper-end cap are provided at either end of the damper to close it. The inner cylinder cap acts as a seal. Figure 1 shows the sectioned view of the designed MR damper.

2.2 Analytical Model of the Prosthetic Leg

To get adequate torque at the knee of the prosthetic leg, it is necessary to find out the torque acting at the knee of a natural human leg. This can be done analytically by performing dynamic analysis of the FBD of the human leg. The amputee is assumed to move the hip joint; therefore, the torque at the hip joint is not necessary. The net torque acting at the knee joint can be divided into four major components: two inertial, one Coriolis, and one gravitational. As evident from the FBD, the various forces in play are the weight of thigh and shank, the moments of inertia of mass and shank, and the weight of the upper part of the human body. The centers of mass of the thigh and shank are also important parameters. The values chosen for calculation are the average values of the masses and lengths of a human leg. Figure 2 shows the free body diagram of the leg and the damping force acting on the prosthesis. Table 1 shows the free body diagram elements and dimensions.

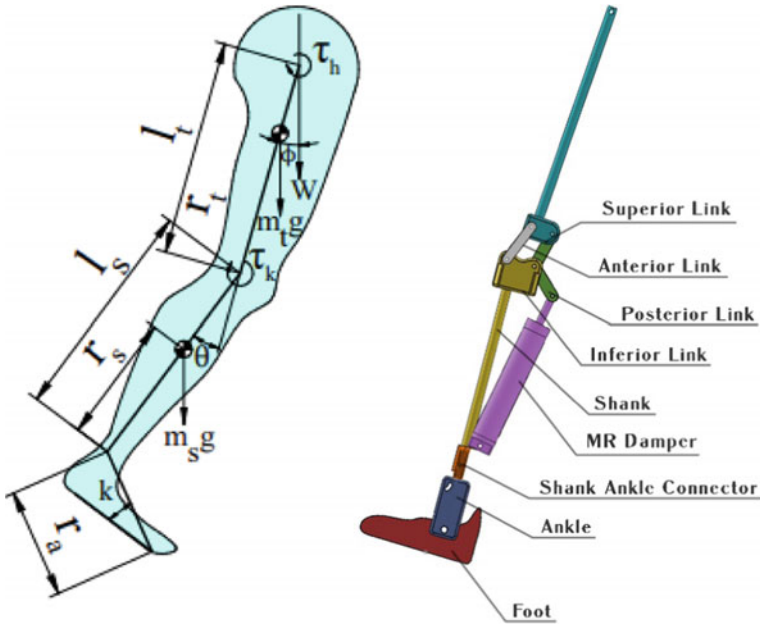


Fig. 2 Free body diagram of the leg and damping force acting on the prosthesis

Table 1 The free body diagram elements and dimensions

Parameters	Unit	Values
Length of thigh	m	0.43
Length of shank	m	0.41
Distance of center of mass of the thigh	m	0.19
Distance of center of mass of the shank	m	0.18
Distance of point of contact of the ankle and joint	m	0.275
Mass of thigh (m_t)	kg	5.7
Mass of shank (m_s)	kg	5
Moment of inertial of the thigh (I_{θ})	kg m ²	0.0982
Moment of inertial of the shank (I_{θ})	kg m ²	0.0402
Upper bodyweight of the person	kg	50

Using the free body diagram and using moment and force balances, we can derive the following equations. The MR damper works only in the stance phase of gait cycle (therefore making it a semi-active prosthetic leg), and hence, these equations are valid only for stance phase.

$$I_{\theta} \ddot{\theta} + I_{\theta} \dot{\theta} + V + G = \tau_k$$

$$\begin{aligned}
I_{\theta} &= I_s + m_t l_s^2 + m_s r_a^2 + m_t r_a^2 + m_s r_s^2 + 2(m_s l_s + m_t r_s) r_a \sin(k) \\
I_{\emptyset} &= I_s + m_t l_s^2 + m_s r_a^2 + m_t r_a^2 + m_s r_s^2 + m_t l_s r_t \cos(\theta) \\
&\quad + 2(m_t l_s + m_s r_s) r_a \sin(k) + m_t r_t r_a \sin(k + \theta) \\
V &= -m_t r_t (r_a \cos(k + \theta) - l_s \sin(\theta)) \dot{\emptyset}^2 \\
G &= g((m_s r_a + m_t r_a) \cos(k + \theta + \emptyset) - (m_t l_s + m_s r_s) \sin(\theta + \emptyset)) \\
&\quad - Wg(r_a \cos(k + \theta + \emptyset) - l_s \sin(\theta + \emptyset))
\end{aligned}$$

2.3 Total Assembly of the Prosthetic Leg

The entire assembly of the prosthetic leg has been made in SOLIDWORKS. The components of the total body are the thigh, the knee joint, which is a four-bar mechanism, the shank, the twin-tube MR damper, and the ankle joint. The methodology chosen to perform a motion study on this prosthetic leg was as follows: Two prosthetic legs were created in SOLIDWORKS. The entire gait cycle of the right and left leg could be simulated together. These two legs were connected with a rod. Also, a floor was given at the bottom so that contact could also be made. Motors were attached at the hip joint, the knee joint (inferior part), and the ankle joint, given angular displacements of joints according to the natural gait cycle. A force was applied at the top equal to the average upper body weight. Gravity was used, and contact was given between the foot and the floor. This gives the linear velocity of the piston as a function of time during the entire gait cycle, which when used with the torque at the knee obtained from the analytical model, gives the values of the damping force and damping coefficient required. Figure 3 shows the total assemble of one and two prosthetic legs.

2.4 Magnetic and CFD Analysis on the Twin-Tube MR Damper

Magnetic analysis was performed on the twin-tube MR damper using COMSOL. This was done to determine the variation of the magnetic field induced in the MR damper with coil diameter and the current. It was found out that the magnetic flux density continuously decreases with the increase in wire diameter. Also, the magnetic flux density increases linearly with an increase in current. The materials used for MR fluid, magnetic core, wire, and the rest of the structure were MRF 140CG, iron, copper, and steel, respectively. The materials were chosen to get the best possible results, considering their electrical conductivity, magnetic permeability, etc. The magnetic analysis was performed on the MR damper using COMSOL. Variation of the magnetic flux density for an area of wire 1 mm^2 and 0.5 mm^2 is shown in Figs. 4

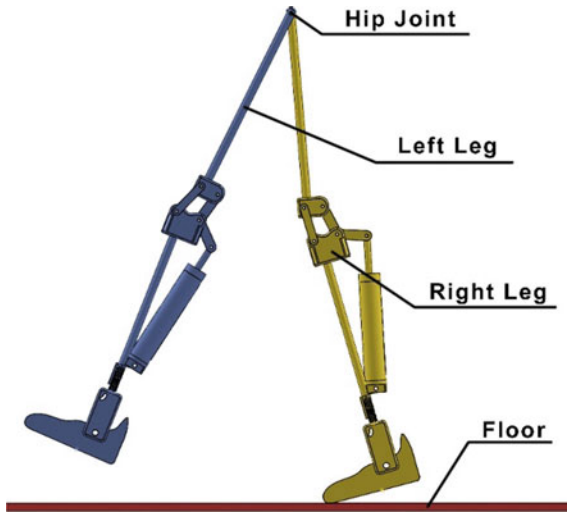


Fig. 3 Total assembly of one and two prosthetic leg

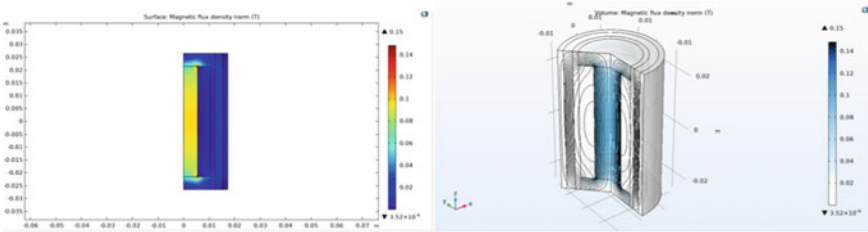


Fig. 4 Variation of magnetic flux density 2D and 3D ($A = 1 \text{ mm}^2$)

and 5, respectively. Continuous variation of magnetic flux density with wire area for a current of 1 A is shown in Fig. 6. The variation of magnetic flux density with the current for varying wire size is shown in Fig. 7.

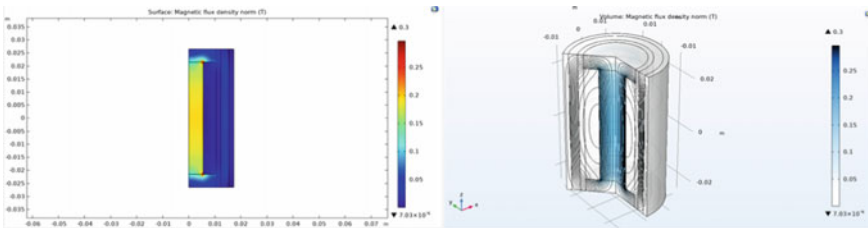


Fig. 5 Variation of magnetic flux density 2D and 3D ($A = 0.5 \text{ mm}^2$)

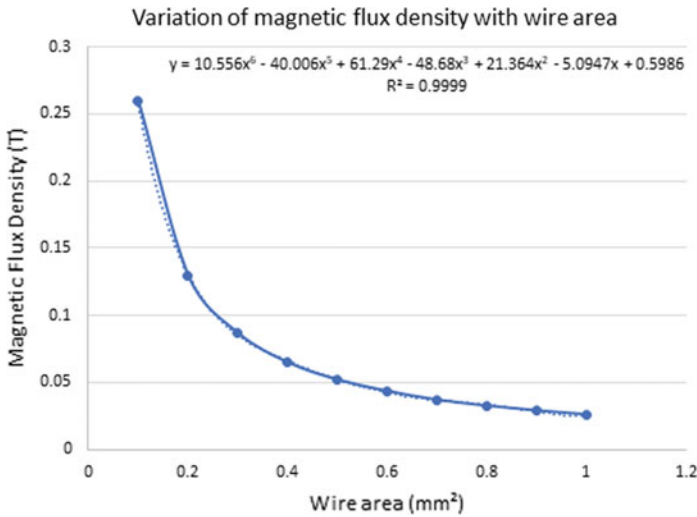


Fig. 6 Continuous variation of magnetic flux density with wire area for a current of 1 A

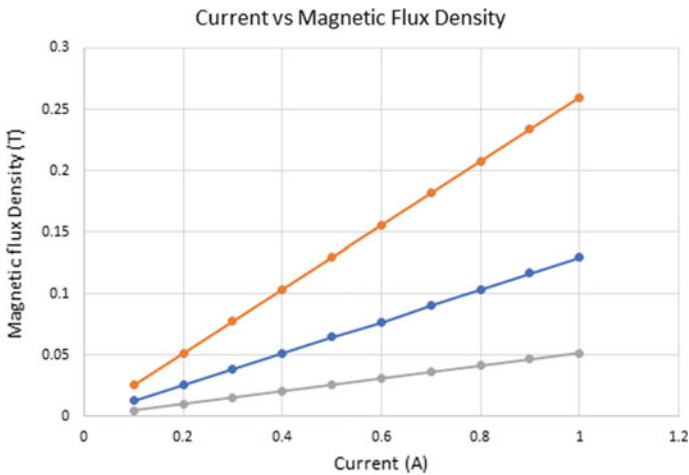


Fig. 7 Variation of magnetic flux density with the current for varying wire size

CFD was performed on the twin-tube MR damper to understand the flow patterns of the MR fluid. The piston moves reciprocate inside the inner tube, which houses the MR fluid. As mentioned earlier, the armature core is inside the piston, which energizes the MR fluid. When the piston starts reciprocating, one major component of the damping forces is the pressure difference. When the piston gets compressed, the fluid flows through the inner tube first. It then flows through the foot valve through which it goes to the outer box. When the piston begins its reverse motion, the fluid

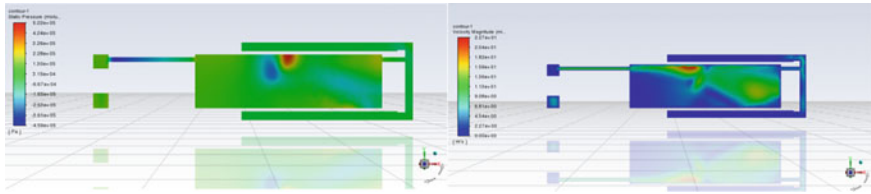


Fig. 8 Variation of pressure (left) and velocity (right) of MR fluid inside the damper

follows the same path backward, i.e., from the outer tube, goes to the foot valve and then comes into the inner tube. This repeats continuously until the piston remains in motion. To develop a required controller for the prosthetic leg, various relations of the constituents of the legs have to be found out. For instance, the dependence of magnetic field inside the MR fluid on the current flowing through the armature coil, the support of shear stress of the MR fluid on the current, etc. However, the final aim is to determine the dependence of torque at the knee on the current. Figure 8 shows the variation of pressure and velocity inside the MR damper.

3 Results and Discussion

3.1 Rheological Properties of MR Fluid

As mentioned above, the MR fluid chosen is MRF 140-CG by lord corporation. The variation of shear stress with magnetic field strength and magnetic field strength (H) with magnetic flux density (B) was taken from MRF 140CG. The equations were, however, obtained by plotting these graphs in MS Excel and fitting the curve. The graph of magnetic flux density vs current was found out by simulation on COMSOL as mentioned above. Using the three graphs, the relationship between shear stress and the current was obtained and was plotted in MS Excel to fit the curve and get the equation. It can be seen that the obtained relation is a sixth-order polynomial with a perfect fit. Variation of shear stress of MR fluid is shown in Fig. 9. Variation of magnetic flux density with respect to current is shown in Fig. 10. Variation of yield strength with respect to current is shown in Fig. 11.

3.2 Variation of Posterior Torque with Respect to Hip Angle

The model was given the gait angles as input, and the various acceleration and velocities were calculated. Also, the torque at the posterior of the four-bar mechanism was found with respect to time and hip angle. This is later used to calculate the yield stress required to generate the necessary amount of torque and then calculate the

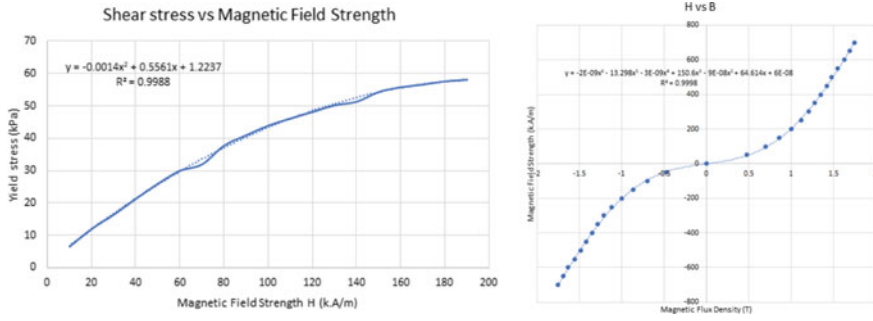


Fig. 9 Variation of shear stress of MR fluid MRF 140CG with respect to the magnetic field

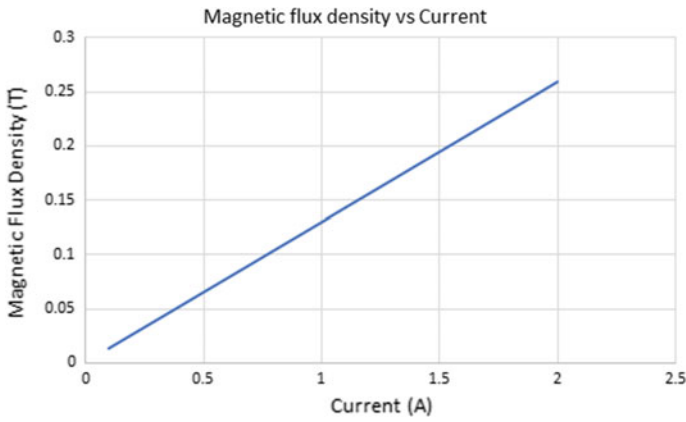


Fig. 10 Variation of magnetic flux density with respect to current

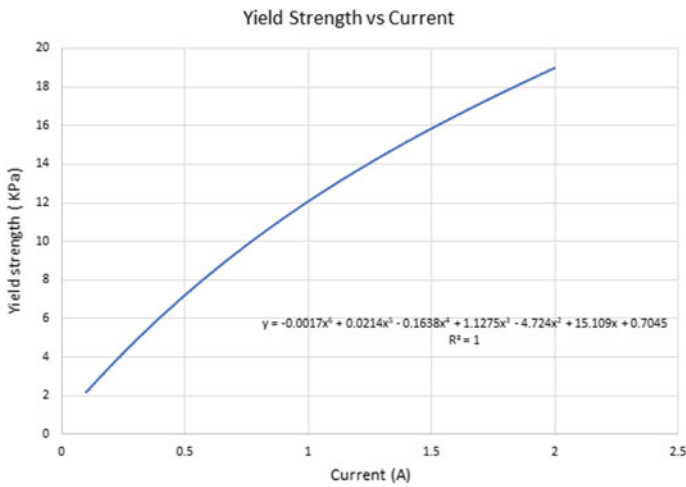


Fig. 11 Variation of yield strength with respect to current

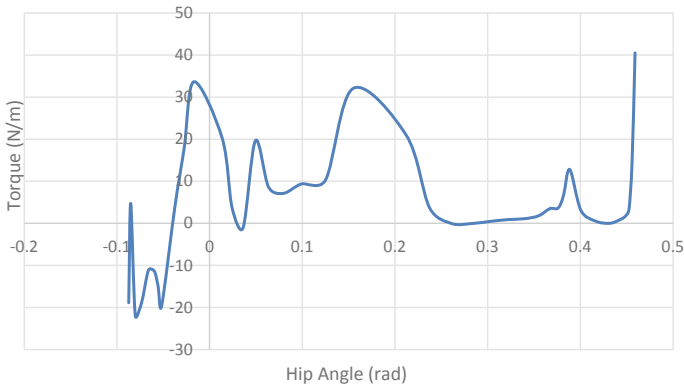


Fig. 12 Variation of torque required with respect to hip angle

current needed to create the magnetic field to yield that amount of yield stress. As mentioned above, the MR fluid chosen is MRF 140-CG by lord corporation. The variation of shear stress with magnetic field strength and magnetic field strength (H) with magnetic flux density (B) was taken. Variation of yield strength with respect to current is shown in Fig. 12.

4 Conclusions

Magnetorheological fluid is a smart material that can be conveniently used in prosthetic devices. By its magnetic properties, it renders to be advantageous material. The obtained results prove that MR fluid can be effectively used to control the knee joint. The MR fluid is also very cheap and easy to synthesize. This makes the overall cost of the prosthetic leg less expensive. A four-bar mechanism is a good choice for knee joints because of its flexibility and range of motion. The proposed MR damper can easily be controlled with the help of a PID controller by tuning suitable gains to stabilize the relation between current and hip joint (or torque). This work can further be extended to optimize the topology and various other parameters. This can be tested for multiple MR fluids with different carrier fluid and additives. Additionally, the effect of using a fuzzy PID controller instead of a PID controller can be studied.

References

1. Mohan D (1986) A report on amputees in India. *Orthot Prosthetics* 40(1):16–32
2. Daniele B (2020) Evolution of prosthetic feet and design based on gait analysis data. In: *Clinical engineering handbook*. Academic Press, pp 458–468

3. Kumar PK, Charan M, Kanagaraj S (2018) Trends and challenges in lower limb prosthesis. *IEEE Potentials*. <https://doi.org/10.1109/MPOT.2016.2614756>
4. Azocar AF, Mooney LM, Duval JF, Simon AM, Hargrove LJ, and Rouse EJ (2020) Design and clinical implementation of an open-source bionic leg. *Nat Biomed Eng*. <https://doi.org/10.1038/s41551-020-00619-3>
5. Xie HL, Liang ZZ, Li F, Guo LX (2010) The knee joint design and control of above-knee intelligent bionic leg based on magneto-rheological damper. *Int J Autom Comput*. <https://doi.org/10.1007/s11633-010-0503-y>
6. Park J, Yoon GH, Kang JW, Choi SB (2016) Design and control of a prosthetic leg for above-knee amputees operated in semi-active and active modes. *Smart Mater Struct*. <https://doi.org/10.1088/0964-1726/25/8/085009>
7. Baser O, Kizilhan H, Kilic E (2020) Employing variable impedance (stiffness/damping) hybrid actuators for lower limb exoskeleton robots for stable and safe walking trajectory tracking. *J Mech Sci Technol*. <https://doi.org/10.1007/s12206-020-0534-4>
8. Kim JH, Oh JH (2001) Development of an above knee prosthesis using MR damper and leg simulator. *Proc IEEE*. <https://doi.org/10.1109/ROBOT.2001.933191>
9. Metered H, Elsawaf A, Vampola T, Sika Z (2015) Vibration control of MR-damped vehicle suspension system using PID controller tuned by particle swarm optimization. *SAE Int J Passeng Cars Mech Syst*. <https://doi.org/10.4271/2015-01-0622>
10. Mataušek MR, Šekara T (2011) PID controller frequency-domain tuning for stable, integrating and unstable processes, including dead-time. *J Process Control*. <https://doi.org/10.1016/j.jprocont.2010.09.007>
11. Talib MHA, Darus IZM (2013) Self-tuning PID controller with MR damper and hydraulic actuator for suspension system. In: *Proceedings of international conference on computational intelligence, modelling and simulation*. <https://doi.org/10.1109/CIMSim.2013.27>
12. Ab MH, Talib (2020) Vibration control of semi-active suspension system using PID controller with advanced firefly algorithm and particle swarm optimization. *J Ambient Intell Hum Comput*. <https://doi.org/10.1007/s12652-020-02158-w>
13. Zeng GQ, Xie XQ, Chen MR, Weng J (2019) Adaptive population extremal optimization-based PID neural network for multivariable nonlinear control systems. *Swarm Evol Comput*. <https://doi.org/10.1016/j.swevo.2018.04.008>
14. Choe WW (2015) Intelligent PID controller and its application to structural vibration mitigation with MR damper. *Trans Korean Inst Electr Eng*. <https://doi.org/10.5370/KIEE.2015.64.8.1224>
15. Kasemi B, Muthalif AGA, Rashid MM, Fathima S (2012) Fuzzy-PID controller for semi-active vibration control using magnetorheological fluid damper. *Procedia Eng*. <https://doi.org/10.1016/j.proeng.2012.07.304>
16. Talib MHA, Darus IZM (2013) Self-tuning PID controller with MR damper and hydraulic actuator for suspension system. In: *Fifth international conference on computational intelligence, modelling and simulation*. <https://doi.org/10.1109/CIMSim.2013.27>
17. Geng GQ, Xie XQ, Chen MR, Weng J (2019) Adaptive population extremal optimization-based PID neural network for multivariable nonlinear control systems. *Swarm Evol Comput*. <https://doi.org/10.1016/j.swevo.2018.04.008>
18. Li HL, Yong C, Qi H, Jian LI (2009) Fuzzy pid control for landing gear based on magnetorheological (MR) damper. In: *2009 International conference on apperceiving computing and intelligence analysis, ICACIA 2009*, pp. 22–25. <https://doi.org/10.1109/ICACIA.2009.5361162>
19. Carlson JD, Catanzarite DM, St. Clair KA (1996) Commercial magneto-rheological fluid devices. *Int J Mod Phys*. <https://doi.org/10.1142/S0217979296001306>
20. Carlson JD, Jolly MR (2000) MR fluid, foam and elastomer devices. *Mechatronics*. [https://doi.org/10.1016/S0957-4158\(99\)00064-1](https://doi.org/10.1016/S0957-4158(99)00064-1)
21. Braz Cesar M, Barros RD (2012) Properties and numerical modeling of MR dampers. In: *ICEM-15, 15th international conference on experimental mechanics*, p 1199
22. Kumbhar BK, Patil SR (2014) A study on properties and selection criteria for magnetorheological (MR) fluid components. *Int J ChemTech Res* 6(6):3303–3306

23. Data T (2008) MRF-140CG magneto-rheological fluid. *Lord Prod Sel Guide Lord Magnetorheol Fluids* 74(1):5–6
24. Kumar JS, Paul PS, Raghunathan G, Alex DG (2019) A review of challenges and solutions in the preparation and use of magnetorheological fluids. *Int J Mech Mater Eng.* <https://doi.org/10.1186/s40712-019-0109-2>
25. Guerrero-Sanchez C, Lara-Ceniceros T, Jimenez-Regalado E, Raşa M, Schubert US (2007) Magnetorheological fluids based on ionic liquids. *Adv Mater.* <https://doi.org/10.1002/adma.200700302>
26. Ashtiani M, Hashemabadi SH, Ghaffari A (2015) A review on the magnetorheological fluid preparation and stabilization. *J Magn Magn Mater.* <https://doi.org/10.1016/j.jmmm.2014.09.020>
27. Bell RC, Miller ED, Karli JO, Vavreck AN, Zimmerman DT (2007) Influence of particle shape on the properties of magnetorheological fluids. *Electrorheol Fluids Magnetorheol Suspens.* https://doi.org/10.1142/9789812771209_0109
28. Carlson JD (2002) What makes a good MR fluid? *J Intell Mater Syst Struct.* <https://doi.org/10.1106/104538902028221>
29. Claracq J, Sarrazin J, Montfort JP (2004) Viscoelastic properties of magnetorheological fluids. *Rheol Acta.* <https://doi.org/10.1007/s00397-003-0318-7>
30. Huang J, Wang P, Wang G (2012) Squeezing force of the magnetorheological fluid isolating damper for centrifugal fan in nuclear power plant. *Sci Technol Nucl Install.* <https://doi.org/10.1155/2012/175703>
31. Jang DS, Liu YD, Kim JH, Choi HJ (2015) Enhanced magnetorheology of soft magnetic carbonyl iron suspension with hard magnetic $\gamma\text{-Fe}_2\text{O}_3$ nanoparticle additive. *Colloid Polym Sci.* <https://doi.org/10.1007/s00396-014-3475-6>
32. Jang IB, Kim HB, Lee JY, You JL, Choi HJ, Jhon MS (2005) Role of organic coating on carbonyl iron suspended particles in magnetorheological fluids. *J Appl Phys* <https://doi.org/10.1063/1.1853835>
33. Wu WP, Zhao BY, Wu Q, Chen LS, Hu KA (2006) The strengthening effect of guar gum on the yield stress of magnetorheological fluid. *Smart Mater Struct.* <https://doi.org/10.1088/0964-1726/15/4/N04>
34. Ashtiani M, Hashemabadi SH, Shirvani M (2014) Experimental study of stearic acid effect on stabilization of magnetorheological fluids (MRFs). In: 8th International chemical engineering congress and exhibition (IChEC 2014), p 4
35. Powell LA, Hu W, Wereley NW (2013) Magnetorheological fluid composites synthesized for helicopter landing gear applications. *J Intell Mater Syst Struct.* <https://doi.org/10.1177/1045389X13476153>
36. López-López MT, Kuzhir P, Bossis G, Mingalyov P (2008) Preparation of well-dispersed magnetorheological fluids and effect of dispersion on their magnetorheological properties. *Rheol Acta.* <https://doi.org/10.1007/s00397-008-0271-6>
37. Bombard AJF, Antunes LS, Gouvêa D. Redispersibility in magnetorheological fluids: Surface interactions between iron powder and wetting additives. *J Phys Conf Ser.* <https://doi.org/10.1088/1742-6596/149/1/012038>
38. Kciuk M, Kciuk S, Turczyn R (2009) Magnetorheological characterisation of carbonyl iron based suspension. *J Achiev Mater Manuf Eng* 33(2):135–141

Development and Comparison of Natural Fiber Composite Boards Made Using Water Hyacinth Fiber



Tony Varghese, Muhzin Ibnu, Mathews K. Tom, Mathew Joseph, and Rony Sebastian

Abstract Water hyacinth, otherwise called as *Eichhornia crassipes* belongs to hydrophytes group, floats freely on water. These perennial plants has fleshy stem, thick and ovate leaves with stems which can grow up to one meter in height. Water hyacinth is an aquatic weed that deteriorate the quality as well as purpose of water-bodies in many part of the world and thus became a social menace. The complete eradication of the plant is not possible due to the exponential growth rate. In this regard, utilization of the plant is found to be the only possible solution to control its growth. Water hyacinth has long, spongy, and bulbous stalks and happens to contain a combined cellulose and hemicellulose content around 70% which can be utilized by combining it with a binder to obtain composite boards which has wood-like properties. Combining the bundle of fibers of water hyacinth with various binders like coir pith, starch, and artificial resin offers good binding properties and gives strength to the composite boards. The primary objective was to minimize the ecological issues caused by water hyacinth by utilizing the plant in an effective manner and also to compare the properties of the developed product with various similar products available in market. Various weight proportions of the resins and fibers were used to produce the particle boards of dimension 150 mm × 150 mm × 10 mm using hot pressing. The visual comparison and water absorption test revealed that the particle board with higher resin concentration showed better water resistant characteristics.

Keywords Water hyacinth · Particle board · Epoxy resin · Water absorption

1 Introduction

Water hyacinth (WH) (*Eichhornia crassipes*) has been considered as a noxious water weed across the world due to the adverse effect of the plant on water bodies and related infrastructure. WH grows rapidly and forms a cover over the water bodies and causes a number of issues including the restriction of sunlight into water, depleting the water

T. Varghese (✉) · M. Ibnu · M. K. Tom · M. Joseph · R. Sebastian
Department of Mechanical Engineering, Amal Jyothi College of Engineering, Koovappally, India
e-mail: tonyvarghese@amaljyothi.ac.in

© The Author(s), under exclusive license to Springer Nature Singapore Pte Ltd. 2022
H. K. Dave et al. (eds.), *Recent Advances in Manufacturing Processes and Systems*,
Lecture Notes in Mechanical Engineering,
https://doi.org/10.1007/978-981-16-7787-8_21

295

quality underneath it and thereby affects the underwater fauna. Eventually, as the plant dies out, it decay and thereby depletes the oxygen content in water. The low oxygen level affects the aquatic life and slowly kills the fishes and other aquatic animals in the water. These contaminated water which are low in oxygen content act as a breeding place of mosquitos. Apart from this, the exponential as well as congested growth rate of the plant has made it beyond controllable. Over the years, the local as well as the central government bodies tried many measures to eliminate this species of plant from water bodies, but none of them came up successful. Among these eradication measures, two prominent methods adopted were the chemical eradication and the physical eradication. The former method had many drastic and long lasting side effects, whereas the later one was not economically viable. In addition to this, mechanical removal of plant from the water bodies requires high tech machineries and equipment's, which make them less feasible. Moreover, the mechanical removal is beneficial only for a short period of time [1].

Even though the plant has many drawbacks on its own, there are certain other benefits associated with it. The fibrous stem which is rich in cellulose and hemicellulose attracted many scientist to work on it to make a useful product. Even though the plant contain 95% water, the fibrous stem, cellulose as well as lignin content can be utilized for making fiber boards, basket work, handicraft, biogas production, cattle feed, fertilizers. [1, 2].

The fibers used for the production of composite boards are generally chemically treated using sodium hydroxide solutions to obtain better bonding as well as mechanical properties. Tensile strength of treated fibers was reported far superior when compared with the untreated one [3]. In addition to that, the water absorption property was low in treated fibers [3]. Various resins were used to make composite boards helped to attain more reliability and rigidity. Among the various binders used, LDPE and natural rubber were found to have better bonding property with the fibers [4]. A similar behavior was reported for unsaturated polyester (UPR) resin, where the treated fibers showed better flexural, tensile strength, and good resistance against moisture [5]. The WH fibers offer higher pressing strength in the order of 600 kPa and reported to have a resistance up to a temperature of 105 °C [6]. In certain studies, WH fibers were often used with tapioca starch, where it was found that the micro fibers added to the matrix enhanced the tensile strength considerably and can be considered as a reinforcement [7].

Pulp-based and particle-based composites were also studied to identify the thermal insulation as well as strength properties, and it was reported that the cement-based particle board showed the lowest thermal conductivity. Considering all the facts mentioned, this work focused on the effectiveness of using epoxy in different concentrations as a binder and their resistance toward moisture.

2 Experimental Procedure

Water hyacinth plants are widely available in the backwater of Kerala, especially in the Vembanadu Lake. The collected plants were cleaned properly, and the roots and leaves were removed. The drying process was carried out by keeping the water hyacinth fiber under sunlight for seven days where the moisture content got reduced to the lowest percentage. When the moisture content reached below 10%, the stems were retrieved and chemically treated with NaOH to withstand rotting. These WH fiber was crushed to small particles to ensure the proper interaction and missing with other components in the matrix.

Coir pith, one of the selected binding agent, a waste product of the coir industry, has very high lignin content and possesses high absorption capacity. The differential absorption ability enhances bonding between fiber and matrix. At elevated temperature above 160 °C, the lignin content in the coir pith oozes out and can act as a binder.

Purchased corn starch along with resorcinol formaldehyde (prepared by mixing resorcinol, formaldehyde and HCL solution in definite proportion) was used as another binder. A small amount of glycerol was added to the corn starch solution to reduce the brittleness of the composite board. A thermoset resin epoxy (LY556), density of 1.15 g/cm³ along with hardener (HY951), was the third resin used for the experiment. Considering the above binders in to account, the following set of experiments were carried out in Table 1.

In the initial sequence, no artificial resin as used, instead the coir pith was used to act as a binder. Cone starch and coir pith can produce composite boards with natural components and can be termed as eco-friendly composite board.

The dried WH fibers were crushed to small pieces using a crusher, Fig. 1. These crushed fibers and the weighted proportions of the binders were measured using an electronic weighing balance and mixed manually. The heavier coir pith in comparison with the WH fiber had a tendency to settle down which can lead to non-uniform mixing of components. A small amount of moisture added offered a cohesive force between fiber and the coir pith to get uniformly distributed in the matrix. Due to crushing of fiber, more amount of cellulose and hemi-cellulose detached from the bundle of fiber and got evenly distributed in the matrix. After a through mixing of

Table 1 Sequence of experiments conducted

	Weight percentage			
	Water hyacinth	Coir pith	Cone starch	Epoxy resin
A	70	30		
B	30		70	
C	30			70
D	20			80
E	10			90

Fig. 1 Crushed water hyacinth



the components, the constituents were placed in a metal mold with a cavity of 150 mm \times 150 mm \times 10 mm. The entire mold got hot pressed at 1500 psi for 30 min in a hot press and then cooled down to room temperature.

3 Results and Discussions

3.1 *Thermo-Gravimetric Analysis (TGA)*

TGA investigates the change in weight of a material with respect to the increase in temperature or at constant temperature (isothermal) and as a function of time when the material is maintained at a gaseous medium of nitrogen, helium, other gases, or vacuum. These measurements help to understand the physical phenomena as well as chemical phenomena happening during the process. Physical phenomena includes absorption, desorption, and phase transformation where the chemical phenomena involves oxidation and reduction. TGA is conducted on an instrument referred to as thermo-gravimetric analyzer. A thermo-gravimetric analyzer records instantaneously the change in mass of the material when the temperature changes over time. The three-base measurement in the analysis includes time, temperature, and mass, where all the other parameters can be derived from these three fundamental variables. The dried stem of water hyacinth is kept as an untreated specimen. The treated water hyacinth is prepared by dipping the dried specimen in NaOH solution for 5 h and keeping it for sun dry for two days. From Figs. 2 and 3, it can be read that at a temperature of 100 °C the weight loss was high in untreated fibers. The same behaviors were also observed at elevated temperatures. The gradation in the material mass was slow in treated fiber when compared with untreated fibers. The graph shows steep slope which indicates a sudden gradation of mass at elevated temperatures. The mass deterioration has started at a temperature and can be taken as a limiting temperature for hot pressing.

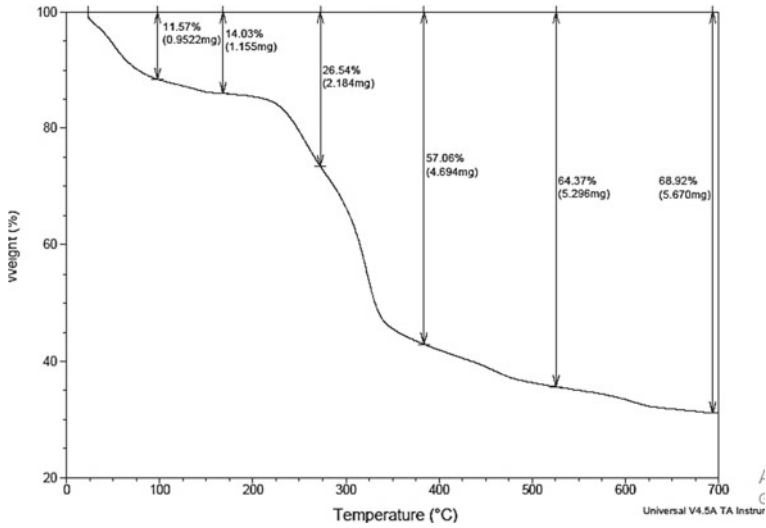


Fig. 2 TGA of untreated fiber

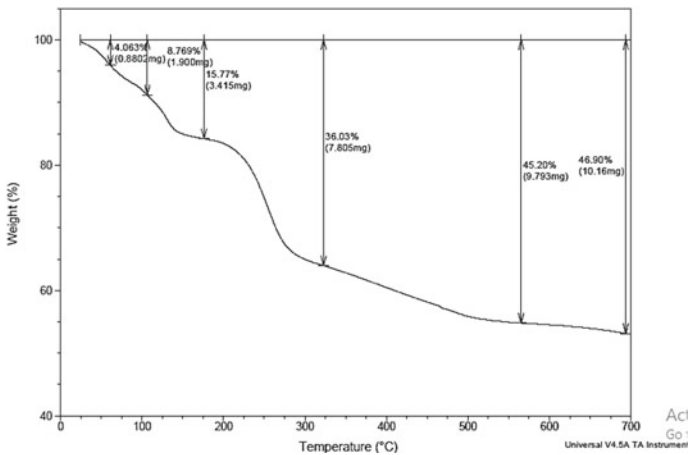


Fig. 3 TGA of treated fiber

3.2 Composite Boards Developed

The composite board made using 70% fiber and 30% coir pith was compressed in a hydraulic hot press at a temperature of 150 °C for 30 min. A temperature of 170 °C was essential to bring out the lignin in the coir pith so that it can act as a binder. But, the disintegration of fibers started at 100 °C and because of which the hot pressing temperature cannot be further raised. Due to this differential temperature resistance

of components in the matrix, lignin present in the matrix didn't act as a binder. Due to the hot compression at elevated pressure helped the components to compact together and form a solid particle board with moderate surface finish Fig. 4a. The visual inspection showed that the edges were wavy and was not intact, and the inter-bonding between the components was minimal. It was observed that the distribution of the coir pith was uniform throughout the matrix, and any kind of sedimentation was not observed.

The composites boards made of corn starch as resin were flexible; the inter-bonding was poor and were often difficult to get detached from the mold Fig. 4b. Epoxy was considered due to the limitation in obtaining a completely natural composite board. The weight percentage of the resins varied from 90% to 70% as given in Table 1 sequence C–E. The higher concentration of epoxy resin resulted in a rigid composite board with good surface finish. The surface was glossy and indicated that the concentration of resin was excess Fig. 4c, and the fibers were immersed in

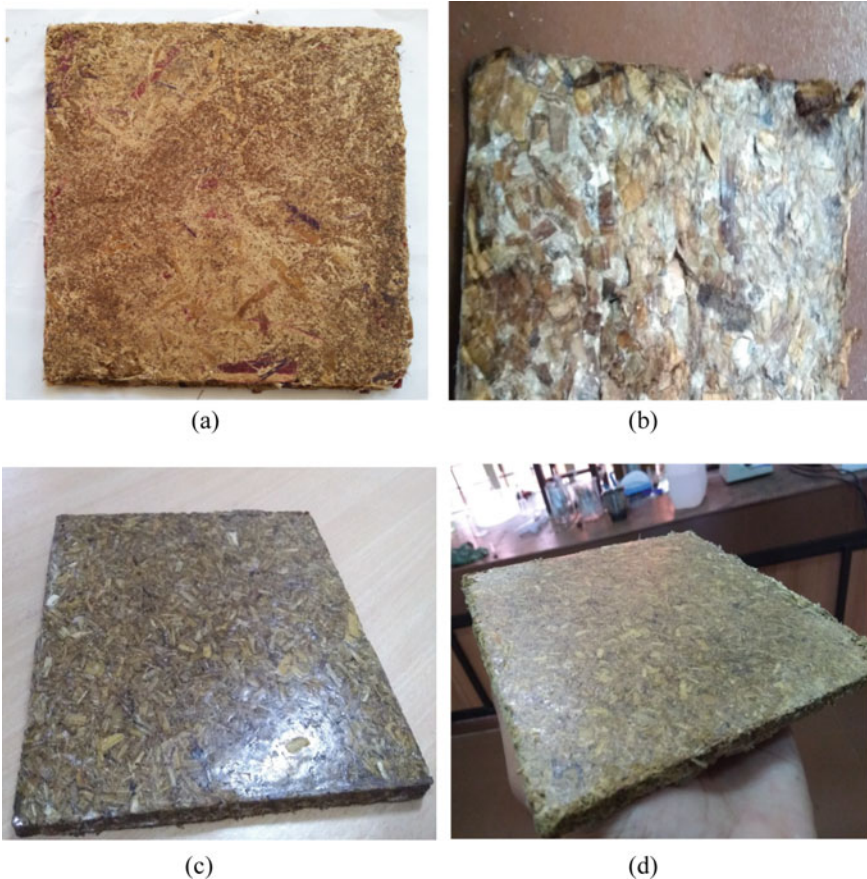


Fig. 4 Board made using 70% fiber and 30% coir pith

the matrix. The optimum use of resin is always advisable to limit the production cost to minimal. Particle board made with lesser concentration of resin also showed good bonding between the fiber and matrix. Even though the surface finish was reduced, the rigidity was not compromised Fig. 4d. It has to be noted that the fiber used was inferior in strength which make them a filler material instead of a reinforcement.

3.3 Water Absorption

The amount of water absorption is an essential criteria which enables the composite boards to compete with the board available in market. Factors affecting water absorption include the type of fiber, additives used, nature of matrix/binder, temperature, and length of exposure. ASTM D 4442–92 standard was followed to check the water absorption characteristics of the manufactured fiber boards. From the sequence of trials, it was found that the boards made using epoxy was better in finish and strength. Therefore, the epoxy-fiber board and the board made from fiber and coir pith were compared with the commercially available plywood's. Small pieces of samples were made out from WH board made with 90% epoxy, 80% epoxy, 70% epoxy, commercial plywood, particle board (fiber and coir pith), and bamboo fiber reinforced composite board.

Initial weight of samples were measured using a weighing balance and the samples were immersed in water which was maintained at 27 °C. The weight of the samples were taken every 30 min. The water absorbed was taken after 24 h, 48, and 72 h, and Fig. 5 indicates the behavior of each specimen prepared, and Fig. 6 shows the resistance to water.

From the graph, it can be seen that the board made with fiber and coir pith absorbed more water when compared with other samples. All the components used in the manufacturing especially the coir pith absorbed more moisture and maintains the absorbed water content, whereas the commercially available plywood also showed more water affinity.

The plywood used was also having high water affinity, and the moisture absorption rate is close to the particle board. All the other boards which were fabricated using the epoxy resin showed good water repulsion. The resin used was resistant to water and prevented the exposure of fiber to moisture thereby prevented or reduced

Fig. 5 Samples made for water absorption test



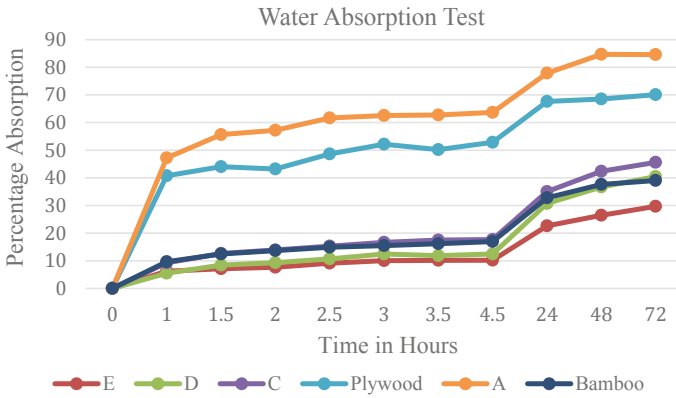


Fig. 6 Water absorption of samples

moisture intake. The composite board that contained the higher percentage of resin offered higher resistance to water, and the same level of resistance was observed in the bamboo reinforced composite. In the commercially available bamboo-based composite board, the bamboo fiber act as a reinforcement due to its higher strength and the bamboo fiber also resisted the water absorption. As the amount of resin concentration decreased, the moisture absorption also increased and vice versa. The percentage of water absorbed by composites boards (C, D, E) was in the close lower range, and the further reduction of resin may not affect the water repellent nature drastically. It can also be noted that the nature of water absorption is also similar, and the slope of all the curve were same.

4 Conclusion

Water hyacinth, an aquatic weed, can only be controlled by the effective utilization of the plant to develop various value added products and other building material substitute. One such solution is by utilizing the plant to produce composite boards using a resin as a binder. The use of coir pith as a binder is not an effective method since the boards manufactured was inferior in strength and offered poor water resistance. Higher temperatures were required to bring out the lignin content in coir pith which would have resulted in the burn out of WH fibers. The use of epoxy resin as a binder provided rigidity as well as inter-bonding between the fibers. The weight percentage of resin can be further optimized to make the composite boards which are cost-effective and reliable when compared with the boards available commercially. The percentage water absorption in the composite boards made using the resin were far less when compared with the particle board as well as the plywood. The rate of moisture intake in the composite boards showed a linear behavior and the quality of the board didn't deteriorate.

Acknowledgements We like to thank the Environmental Science Department of Mahatma Gandhi University for the TGA analysis.

References

1. Ilangovan VGM, Anantha Prasad MG, Reddy N (2017) Water hyacinth: a unique source for sustainable materials and products. *ACS Sustain Chem Eng* 2017(5):4478–4490
2. Flores Ramirez N, Sanchez Hernandez Y, Cruz de Leon J, Vasquez Garcia SR, Domratheva LvovaL, Garcia Gonzalez L (2015) Composites from water hyacinth (*Eichhornea crassipe*) and polyester resin. *Fibres Polym* 16(1):196–200
3. Supri AG, Lim BY (2009) Effect of treated and untreated filler loading on the mechanical, morphological, and water absorption properties of water hyacinth fibers- low density polyethylene composites. *J Phys Sci* 20(2):85–96
4. Supri AG, Tan SJ, Ismail H (2011) Effect of poly(methyl methacrylate) modified waterhyacinth fibre on properties of low density polyethylene/natural rubber/water hyacinth fibre composites. *Polym-Plastics Technol Eng* 50:898–906
5. Abrial H, Kadriadi D, Rodianus A, Mastariyanto P, Ilhamdi Arief S, Sapuan SM, Ishak MR (2014) Mechanical properties of water hyacinth fibers—Polyester composites before and after immersion in water. *Mater Des* 58:125–129
6. Bagnall LO et al (1976) Pressing characteristics of water hyacinth. *J Aquat Plant Manage* 14:71–75
7. Bagnall LO (2018) Characterization of tapioca starch biopolymer composites reinforced with micro scale water hyacinth fibers. 70(7–8) (Special Issue: Carbohydrate Polymer Composites)

Development of Al₂O₃ Nanoparticulates AA6061-T6 Aluminium Alloy Functionally Graded Composites via Friction Stir Processing: Effect of Tool Pin Profile on Mechanical and Tribological Properties



M. D. Sameer, B. Archith Reddy, Ch. Sai Kumar, N. Saiteja, and J. Dhanush

Abstract In the present study, AA6061-T6 reinforced with Al₂O₃ nanoparticulates composite functionally graded materials (FGM) is designed and manufactured via multi-step friction stir processing. The functionally graded material (FGM) was produced by two different tools of different pin geometry and by changing the weight percentage of alumina nanoparticles that are embedded in the grooves. The composite was produced by varying pin length, and a constant rotational speed of tool and traverse speeds are used. All the experiments are performed at room temperature. The microstructural features of the FGM and mechanical properties were analysed for the study of the effect of tool pin profiles. The highest average hardness in the nugget zone of 118 HV and tensile strength of 308 MPa was found in the square pin profile prepared functionally graded composite. The coefficient of friction was also least for square pin profile composite with 0.24 microns.

Keywords Friction stir processing · AA6061 aluminium alloy · Al₂O₃ · Functionally graded material

1 Introduction

In the developing world, materials play an important role; day-by-day researchers are finding different ways to improve materials. The most researched works are alloys, composite materials, functionally graded material, etc. They have found many ways to create such materials, and one of the methods is through additive reinforcement particles by using friction stir processing (FSP). It is one of the variants developed from the friction stir welding (FSW) technique to convert a heterogeneous microstructure to a homogeneous, refined microstructure [1]. FSP is used where the material undergoes severe plastic deformation, and it is a solid-state processing

M. D. Sameer (✉) · B. A. Reddy · Ch. S. Kumar · N. Saiteja · J. Dhanush
MED, KITS, Warangal, India
e-mail: mds.me@kitsw.ac.in

method (i.e. no melting of material takes place). As the process is solid-state, cracks or air voids in the processed zone are minimal. Many researchers conducted several kinds of research on different materials and fabricated functionally graded materials. Bikkina et al. [2] have investigated and found that a graded structure was developed by varying the volume fraction of SiC from 6 to 10%. The manipulation of process parameters has enhanced the properties of functionally graded Al/SiC composites in grain size of 5.3 μm and microhardness of 147HV. Ikumapayi et al. [3] worked on producing AMMHs and analysing their improved properties. They found a lot of potentials to improve the FSP technique by uniformly distributed reinforcement particles in the processed area which further improves mechanical properties and metallurgical properties. Patil et al. [4] in their research have done a comparison of three different types of patterns like zigzag pattern, linear pattern, groove pattern out of these three patterns, and they found linear pattern has highest microhardness compared to the other two patterns. Bharti et al. [5] reviewed the FSP of surface composites; they analysed different process parameters like the number of passes, speed and feed. They also found from their study that multiple passes in FSP result in good reinforcement distribution, and it also helps in attaining material superplasticity and perfect grain refinement. However, this depends on the tools speed and profile of the Pin. Gotawala et al. [6] in their investigation, the ideal FSW parameters are determined for experimentation purposes. The preferred pin profile is cylindrical-shaped, and ideal parameters are 710 rpm of rotational speed; traverse speed equal to 28 mm per min; D/d ratio which is 3; and square pin profile with 6 mm side was considered with rotational speed which is equal to 1000 rpm; 40 mm/min as traverse speed. They have concluded that cylindrical and square pin profiles are preferred by Mahamood et al. [7] have reviewed functionally graded materials and their applications; they developed different types of FGM among them are porosity gradient, chemical gradient and microstructure gradient. They also discussed applications of functionally graded materials in many areas like automobiles and biomedical. Mukhopadhyay et al. [8] investigated the behaviour of material when it is added with aluminium powder with the process of friction stir manufacturing by adding the aluminium powder to the material, there was an improvement in terms of mechanical properties when compared with initial composition AA1060 aluminium.

In the present study, an effort was made to improve and investigate the mechanical as well as tribological properties of functionally grades AA6061 aluminium alloy reinforced with nanoparticles Al_2O_3 through friction stir processing with varying two tool pin profile that is cylindrical and square pin profiles.

2 Experimental Procedure

2.1 Materials Used

In general, there are many strong and light alloys but a very commonly used extruded material with good weldability is AA6061 aluminium alloy. AA6061 is a precipitation-hardened alloy of aluminium having magnesium and silicon taking the lion share in alloying elements [9]. This material has decent mechanical properties like tensile strength thermal conductivity and melting temperature. The dimensions of the plate are length is 150 mm, width is 75 mm, and thickness is 5 mm. The chemical properties of AA6061 are presented in Table 1, and the mechanical properties were clearly shown in Table 2.

The tool material used is H13 tool steel; two different types of pin geometries are used in the current investigation, i.e. cylindrical pin profile and square pin profile which can be observed in Fig. 1. The tool dimensions are presented in Table 3.

Friction stir processing (FSP) was performed using a vertical milling machine made by Hindustan Machine Tools Ltd., as shown in Fig. 2.

Table 1 Chemical composition of AA6061

Alloy	Al	Cr	Cu	Fe	Mg	Mn	Zn
Wt%	97.67	0.064	0.19	0.25	0.8	0.12	0.11

Table 2 Mechanical properties of 6061

Alloy	Yield strength (MPa)	Ultimate Tensile Strength (MPa)	% Elongation	Hardness
AA6061	144	239	14	65 V

Fig. 1 FSW tools used

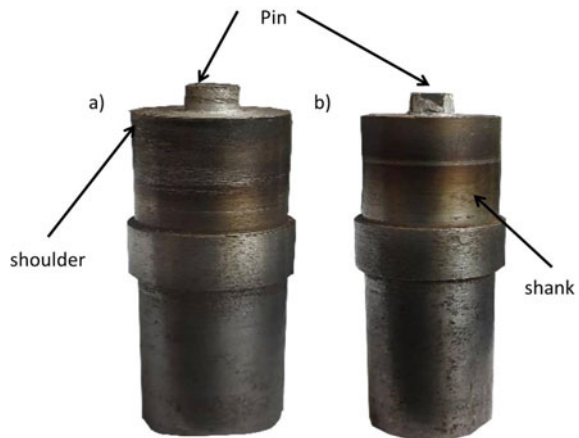
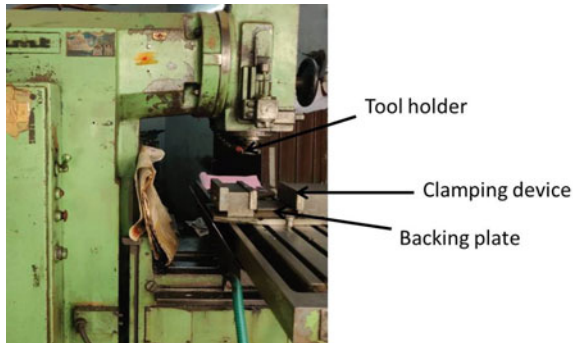


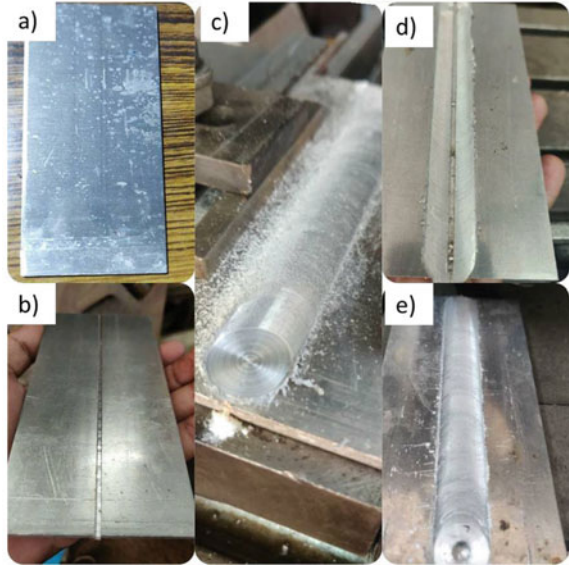
Table 3 Tool dimensions

Tool	Cylindrical		Square	
	Tool A (mm)	Tool B	Tool A	Tool B
Diameter of shoulder	18	18	18	8
Diameter of pin	6	6	–	–
Probe length	4.7	2.7	4.7	2.7
Square side	–		6	6

**Fig. 2** FSW machine

Tool rotational speed which is 900 rpm and tool traverse speed equal to 40 mm/min is used for the fabrication of the processed materials [2]. The other parameters were tool tilt angle 1° , and 0.2 plunge depth were maintained constant. The fabrication of the functionally graded samples was done first by making a groove on AA6061-T6 material with a depth of 4 mm and width which is 1 mm by wire EDM and compacted with Al_2O_3 nanoparticles with 10% volume. Initially, a tool that has no pin called the pin-less tool was used to seal the nanoparticles at the groove surface. As the sample is sealed with a pin-less tool, and Tool A was made to pass through the sealed groove. To obtain the functionally graded (FG) composite, the Tool A passed sample is again grooved with the depth of 3 mm and width of 0.5 mm and reinforcement nanoparticles are filled with 8% volume and compacted with the pin-less tool again. The tool B is passed along the sealed groove again. As mentioned above, two samples were prepared with two different tool pin profiles one with the cylindrical pin configuration and the other with the square pin configuration. The in-process procedure for fabricating the FG material is shown in Fig. 3.

Fig. 3 Friction stir processing procedure. **a** As-received AA6061 sample, **b** groove made on the sample before processing, **c** filled in Al₂O₃ nanoparticles processed with Tool A, **d** again groove made on the Tool A processed sample and **e** Tool B is processed on the sample filled with Al₂O₃ nanoparticles



2.2 Metallographic Procedure

Microstructural observations were made on two processed samples with two different pin configurations. The samples were sectioned normally in the direction of processing. Keller reagent was used as the etchant to expose the microstructure of the processed samples.

2.3 Mechanical Properties Procedure

The strength of the developed FG nanocomposite was studied by employing the electronic tensile machine of Instron make with a crosshead speed equal to 0.5 mm per min. The tensile specimen is cut normal to the processing direction as per guidelines of ASTM: E8/E8M-11 by using a wire-cut EDM. The sectioned specimen is shown in Fig. 4.

Microhardness was performed using a Vickers microhardness testing machine across the nugget with a load of 15 gm and a time duration of 15 s. A wear test was carried on the pin-on-disc tribometer according to ASTM G99 standard procedure. The samples to be tested are cut from the nugget zone prismatic with an 8 mm diameter. The wear tests are dry sliding with rpm of 983 rotational speed of the disc and with a constant load of 20 N and sliding speed of 3.4 m/s. The tribometer equipment used and prepared wear samples are shown in Fig. 5.

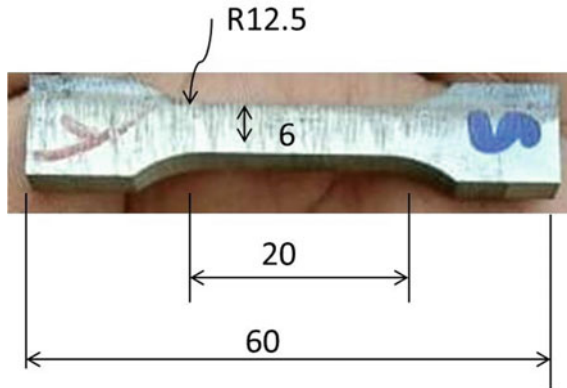


Fig. 4 Tensile specimen

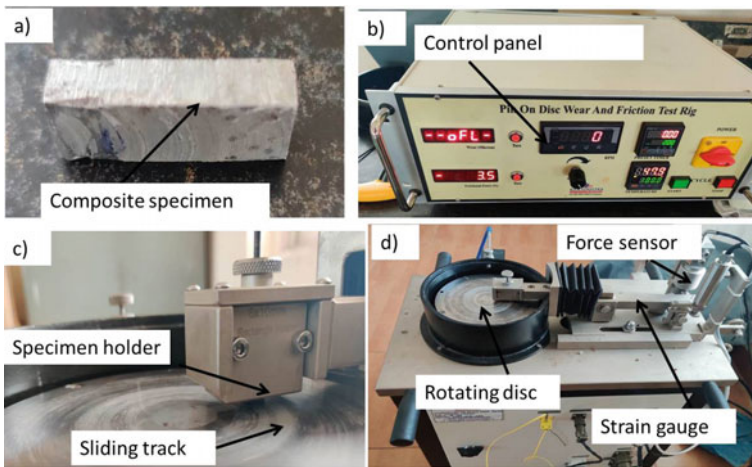


Fig. 5 a composite specimen, b wear testing control panel, c in-process wear test of sample, d wear test machine

3 Results and Discussion

3.1 Examination of Microstructure

Microstructural examination of the nugget zone of the two processed samples is done by an optical microscope. Figure 6a represents the nugget zone of sample processed with cylindrical pin and (b) square pin. Reinforcement particles are agglomerated in the sample processed by cylindrical pin, whereas the homogeneous distribution of reinforcement particulates was achieved at square pin profile. Uniform distribution of the nanoparticles at the nugget zone of the square pin profile fabricated FG composite

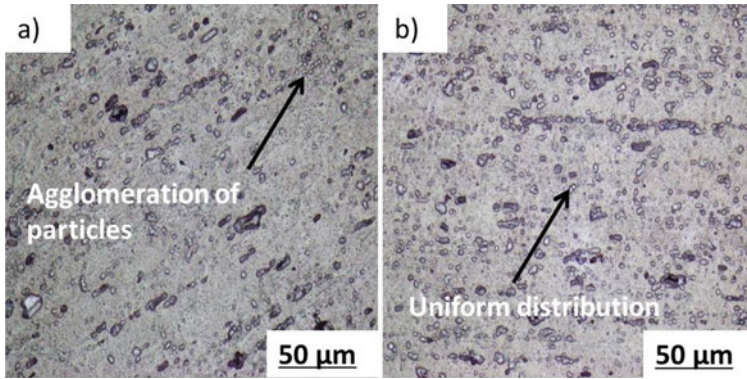


Fig. 6 Microstructure **a** cylindrical pin, **b** square pin

can be imputed to the flatness and more pulsating nature of a tool pin profile which resulted in material flow as a result enhanced properties [10]. Similar studies were reported by Shojaefard et al. [11]; they found that for pin profile of cylindrical there is no pulsating effect and also concluded that cylindrical pin profile when compared to square pin profile, the static and dynamic drawing of the material during stirring are same, whereas, for the square pin profile, there is a significant difference between static and dynamic drawing.

3.2 *Microhardness analysis*

Microhardness profiles of the two FG samples are shown in Fig. 7. Four different regions from top to bottom are considered for microhardness. The average microhardness of cylindrical and square pin FG composite is 113 HV and 118 HV, respectively. In both, the profiles of hardness are gradually reducing from the top region to the bottom region. The highest microhardness of 133.2 HV is observed for square pin profile fabricated FG composite. The decrease in hardness could be due to the uneven distribution of Al₂O₃ nanoparticles as the concentration of nanoparticle are more at one region the average the hardness is also decreasing [12]. It was also evident from the hardness studies that square pin profile fabricated FG has high hardness due to good material stirring which resulted in a distribution that is uniformly throughout by reinforcement particles subsequently enhanced the mechanical properties. Another reason for the increment in the hardness in the nugget zone can be attributed to dynamic recrystallization.

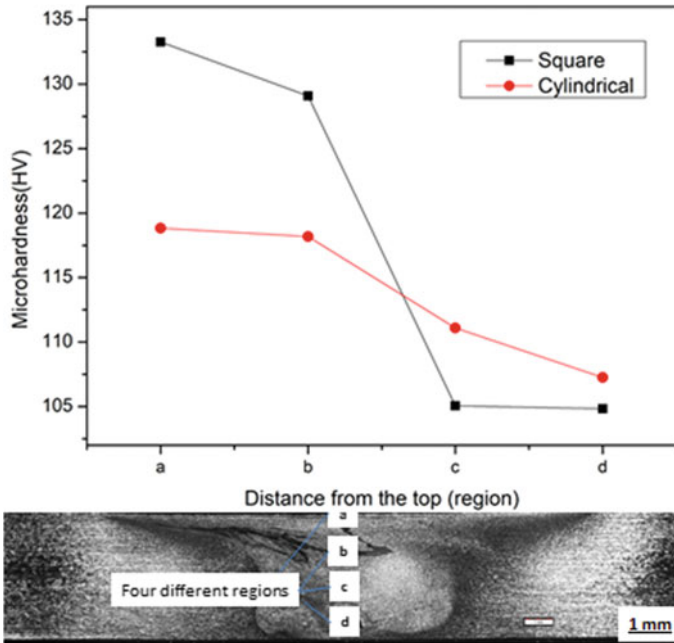


Fig. 7 Hardness profiles of two samples

3.3 Tensile Strength

The stress vs strain curves of the two FG composites and as-received base material can be seen in Fig. 8. The tensile properties of the friction stir processed FG composites mainly depend upon the grain size, particle distribution and interfacial bonding between reinforcement particles and matrix materials [13]. From Fig. 7, the elongation of the FG composites prepared with cylindrical and square pin profile has decreased compared to the as-received base material but the tensile strength of square pin profile prepared FG composite has increased. This may be attributed to the addition of reinforcement particles. The distribution of reinforcement particles restricts the dislocation motion and significantly reduces the elongation. It can be observed that square pin profile fabricated FG composite has a great tensile strength of 308 MPa when compared to that of cylindrical FG composite of 286 MPa.

3.4 Wear Test

Figure 9 shows the coefficient of friction (COF) of cylindrical pin profile prepared FG composite and square pin profile prepared FG composite compared to that as-received base material. It can be observed that square pin profile FG composite exhibited the

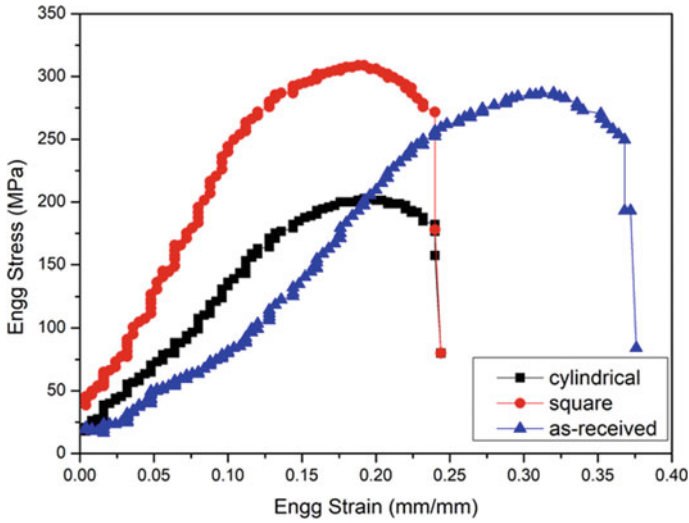
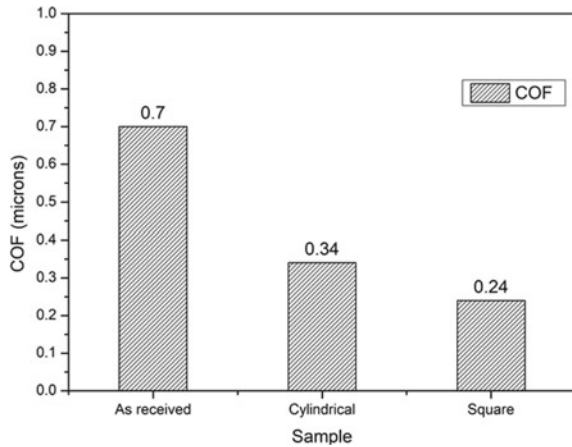


Fig. 8 Stress–strain curves of FG composites and as-received material

Fig. 9 Coefficient of friction (COF) of different samples



least coefficient of friction 0.24 microns, whereas the as-received base material has the highest coefficient of friction 0.7 microns. As per Archard’s equation wear rate generally decreases when there is an increase in hardness value [14]. Therefore, it can be observed that the pin profile highly affects the wear properties of the processed nanocomposite. From Fig. 8, it can also be observed that square FG has the least COF when compared to cylindrical FG composite. Square pin profile prepared FG composite has high hardness; at the same time, there is a low coefficient of friction due to the addition of Al₂O₃ nanoparticles. The FG composite prevents wear and high material removal from the surface of the composite when in contact with other

materials. The Al_2O_3 nanoparticles added to the matrix provide good lubrication and increase the hardness of the material [15, 16]. The reinforcement particles obstruct the penetration and shearing off the surface by the counter material when in contact with it. Therefore, it can be concluded that square pin configured FG composite has improved microstructure, microhardness, tensile and wear properties when compared to cylindrically configured pin profile FG composite.

4 Conclusions

In the present study, Al_2O_3 nanoparticles are reinforced to the AA6061 metal matrix via friction stir processing. The effect caused by a pin profile on mechanical and wear properties is investigated extensively and the following conclusions are drawn.

- Friction stir processed functionally graded materials using square and cylindrical pin profiles are successfully fabricated.
- Uniform distribution of Al_2O_3 nanoparticles in the nugget of square pin profile FG composite is more compared to cylindrical pin profile FG composite.
- The highest average hardness of 118 HV in the nugget zone was found for square pin profile fabricated FG composite.
- Functionally graded composite tensile strength depends on the mixing of reinforcement particles uniformly in the nugget zone; tensile strength of square pin profile FG composite is highest with 308 MPa.
- The coefficient of friction is found to be least for square pin profile fabricated functionally graded composite with 0.24 microns and the highest for as-received base materials. The flatness and pulsating effect caused by the square pin profile has enhanced the mechanical properties.

References

1. Mishra RS, Mahoney MW, McFadden SX, Mara NA, Mukherjee AK (1999) High strain rate superplasticity in a friction stir processed 7075 Al alloy. *Scripta Mater* 42:163–168
2. Bikkina V, Talasila SR, Adepu K (2020) Characterization of aluminum based functionally graded composites developed via friction stir processing. *Trans Nonferr Metals Soc China* 30(7):1743–1755
3. Ikumapayi OM, Akinlabi ET, Pal SK, Majumdar JD (2019) A Survey on reinforcements used in friction stir processing of aluminium metalmatrix and hybridcomposites. *Procedia Manuf* 35:935–940
4. Patil NA, Safwan A, Pedapati SR (2020) Effect of deposition methods on microstructure and mechanical properties of Al7075 alloy rice husk ash surface composites using FSP. <https://doi.org/10.1016/j.matpr.2020.05.639>
5. Bharti S, Ghetiya ND, Patel KM (2021) A review on manufacturing the surface composites by friction stir processing. *Mater Manuf Process* 36(2):135–170. <https://doi.org/10.1080/10426914.2020.1813897>

6. Gotawala N, Shrivastava A (2020) Analysis of material distribution in dissimilar friction stir welded joints of Al 1050 and copper. *J Manuf Process* 57:725–736
7. Mahamood RM, Akinlabi ET (2017) Types of functionally graded materials and their areas of application. Springer. https://doi.org/10.1007/978-3-319-53756-6_2
8. Mukhopadhyay A, Saha P (2020) Mechanical and microstructural characterization of aluminium powder deposit made by friction stir based additive manufacturing. *J Mater Process Technol*. <https://doi.org/10.1016/j.jmatprotec.2020.116648>
9. Opprecht M, Garandet JP, Roux G, Flament C, Soulier M (2020) A solution to the hot cracking problem for aluminium alloys manufactured by laser beam melting. *Acta Mater*. <https://doi.org/10.1016/j.actamat.2020.07.015>
10. Sameer MD, Birru AK (2020) Effect of tool pin profiles using tungsten carbide tool on microstructure and tensile properties of friction stir welded AA 6082-T6 thin aluminium alloy joints. In: *Advances in additive manufacturing and joining*. Springer, Singapore. <https://doi.org/10.1007/978-981-32-9433-2>
11. Shojaeefard MH, Akbari M, Khalkhali A, Asadi P (2018) Effect of tool pin profile on distribution of reinforcement particles during friction stir processing of B4C/aluminum composites. In: *Proceedings Inst Mech Eng Part L: J Mater: Design Appl* 232(8):637–651. <https://doi.org/10.1177/1464420716642471>
12. Khojastehnezhad VM, Pourasl HH, VatankhahBarenji R (2019) Effect of tool pin profile on the microstructure and mechanical properties of friction stir processed Al6061/Al₂O₃—TiB₂ surface hybrid composite layer. *Proc Inst Mech Eng Part L: J Mater: Des Appl* 233(5):900–912
13. Saadatmand M, Mohandesi JA (2015) Modeling tensile strength of Al—SiC functionally graded composite produced using friction stir processing (FSP). *Trans Ind Inst Metals*. <https://doi.org/10.1007/s12666-014-0459-7>
14. Bharti S, Dutta V, Sharma S, Ghetiya N (2020) Investigating the effect of tool speed on the mechanical properties of Al5052 processed by friction stir processing. *Mater Today: Proc* 33:1605–1609
15. Gupta MK (2020) Analysis of tribological behavior of Al/Gr/MoS₂ surface composite fabricated by friction stir process. *Carbon Lett*. <https://doi.org/10.1007/s42823-019-00109-w>
16. Thankachan T, Soorya Prakash K, Kavimani V (2019) Investigating the effects of hybrid reinforcement particles on the microstructural, mechanical and tribological properties of friction stir processed copper surface composites. *Compos B Eng*. <https://doi.org/10.1016/j.compositesb.2019.107057>

Development of Part Build Orientation Algorithm for FDM 3D Printing



Rushikesh P. Urunkar and Sachin Mastud

Abstract FDM 3D printing is one of the most widely used 3D printing techniques. The mechanical properties and overall quality of part produced by FDM are highly dependent on the build orientation. There are numerous methods presented by researchers to get the optimized orientation for the part. Due consideration is given to individually optimize parameters like surface finish, supports requirement, printing time and printing cost. Existing part orientation softwares do not provide the flexibility to priorities any of these parameters. Additionally, these softwares require higher computational power and they are time-consuming. Therefore, this work aims to improve the overall part quality and printing time by developing algorithm which can orient the part as per specific needs of the customer like surface finish, support material requirement and built height. Developed algorithm is implemented using a Python-based software which has easy-to-use interface and customized settings to get desired result. Additional feature of the software is customized adjustable weights to surface finish, supports and height parameters. Result obtained with the algorithm shows that this algorithm works better than the commercial softwares in terms of required printing material and in some of the cases printing time.

Keywords Fused deposition modelling · 3D printing · Build orientation · Surface finish · Overhanging · Support

1 Introduction

Rapid prototyping is promising in today's precise manufacturing scenario with a capability to print materials from eatable cakes to metals. Rapid prototyping helps

R. P. Urunkar (✉)
M.Tech Machine Design, VJTI, Matunga, Mumbai 400019, India

S. Mastud
Department of Mechanical Engineering, VJTI, Matunga, Mumbai 400019, India
e-mail: samastud@me.vjti.ac.in

not only in saving the actual production time but also the overall product development cost. In rapid prototyping, parts are built by depositing material layer-by-layer. Fused deposition modelling (FDM) is one of the widely used additive manufacturing techniques to print thermoset plastics and other materials. In FDM 3D printing or in any layered manufacturing technique, build orientation affects many printing characteristics such as surface finish, support material requirement and printing time. Therefore, efficient method to properly orient the 3D component is need of hour. This study highlights development of algorithm and further a software to optimize the orientation of parts as per specific requirement of users.

Selecting a proper build orientation is one of the prominent factors to get improved surface finish, minimum support material and minimum printing time [1]. It is essential to capture the anatomy of the part and orient it with predefined rules. Staircase effect is inherent in 3D printing of materials. Orientation of part must minimize the overall staircase effect. Pandey et al. [1] in their work determined methods to calculate the average part surface roughness with adaptive slicing and surface roughness model. According to this method, one can find out that, a relatively minimum surface roughness is observed when the surface is either perpendicular or parallel to build plate. Overhanging area is also an important factor for minimizing support material required. Pandey et al. [2] in further work attempted to determine the optimal part deposition orientations by considering two objective functions at a time, namely average part surface roughness (average part surface quality) and build time. They used multicriteria genetic algorithm to simultaneously minimize these two objective functions.

Alexander et al. [3] developed a cost estimation model for layered manufacturing processes, and they found out that printing cost can be reduced by lowering printing time and lowering support requirement. They also stated that, support requirement can lead to degrade the surface finish when supports get removed in post-processing. Lan et al. [4] provided a tool to obtain orientation before executing stereolithography software with various attributes like surface finish, printing time, support structure which was coded in c language. In one of the algorithms, it suggested that printing time can be reduced by reducing number of layers that are indirectly reducing printing height. Masood et al. [5] developed a genetic algorithm which works for staircase effect reduction with the help of volumetric error estimation. It can give the best orientation for surface finish and the accuracy for the part. Bastien Ga et al. [6] proposed a methodology which works simultaneously on volume of support, surface quality, building time and cost with weights given to each by the user to give the best part orientation. Schranz developed a python module called Tweaker [7], which can give optimal orientation working on geometry of part, like simply considering the overhanging area and the base area of the part. It is unable to give tailored orientation based on user requirement. Lin et al. [8] developed a mathematical model to predict the layered process error and also an optimization algorithm to define orientation with minimum process error. In their three case studies, the proposed method was implemented and results were used to validate the accuracy of the developed model and the algorithm. The algorithm ultimately suggested that the layered process error will be zero for perpendicular surfaces of the part to be printed. Cheng et al. [9] developed

a system which considers dimensional accuracy and build time as the objectives, using different weight factors for accuracy objective few orientations were determined, and one or two among these orientations were selected as per the build time objective. Das et al. [10] developed an optimization model to obtain build orientation which will minimize the support structure volume and support contact area. Various aspects like cylindricity, flatness, parallelism and perpendicularity tolerances and their effect on build orientation were analysed and developed. Supports were calculated by voxel-based approach, and ray-tracing approach is used to find removable supports.

The 3D printing users must have the knowledge of basic rules for selecting part orientation. Else, there should be some software with inbuilt intelligence to auto-orient the part as per required characteristics of part. Till date, there are very few software available in open source which provides liberty to users to apply the weightages to different criteria such as surface roughness and print quality. Very few software have been developed, and the literature review along with market survey has made it clear that, there is a scope for the development of user-friendly software for orientation of part and which require minimum computational capabilities. Also, existing software does not incorporate weightages for parameters like surface finish, minimum supports, etc. Taking into consideration these issues, it is decided to work on develop an algorithm and an executable software which fulfils these needs with an easy-to-use interface.

2 Methodology

The operations to import the 3D file in the software and the further processing to select the optimized orientation of part involves simple steps. The following heading shows the operation process and the user interface along with the detailed program structure.

2.1 *Operation and User Interface*

The interface of the developed software is shown in Fig. 1. This software is named as 'Orienter'. The following steps summarize the basic steps involved in obtaining optimized orientation of part:

1. Import the 3D geometry of the part in software by clicking 'Open a file to orient'.
2. Adjust the 'attribute settings' using vertical sliders for each module and adjust the dials for 'surface finish quality' and 'maximum overhanging angle'.
3. Results are shown with the rendering image of the file.

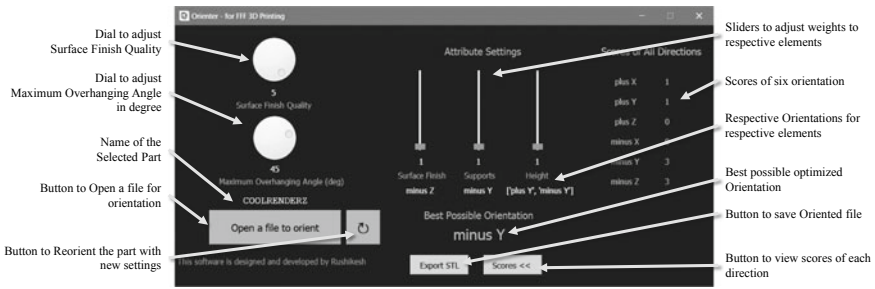


Fig. 1 User interface

2.2 Program Structure

There are mainly three attributes which can be set on the software. These are surface finish, supports and height. As can be seen from the interface diagram shown in Fig. 1 that, user has the flexibility to set the weightages for these criteria. If surface finish is the highest important for functional aspects of part, then slider on ‘surface finish’ parameter can be set at highest values. To obtain an optimized orientation of part, separate algorithm is developed and applied to six axes as like voxel-based approach. The basic flow of program is shown in Fig. 2.

2.2.1 Surface Finish

In FDM 3D printing or in general any layered manufacturing process, staircase effect is one of the important factors deciding and affecting the surface finish. Pandey et al. [1] suggested that, facets which are parallel to build plate and perpendicular to build plate tend to have minimum surface roughness compared to tilted facets with respect to build plate. Facets are the triangles in STL file which are denoted with normals and vertices. Sample file is shown in Fig. 3a–c. A STL file format (Stereolithography) is widely used 3D printing file format which contains the geometric information of 3D file in terms of triangles, and it can be opened in text editor. It contains normals and vertices of all triangles (facets). Different algorithms are developed to get properties

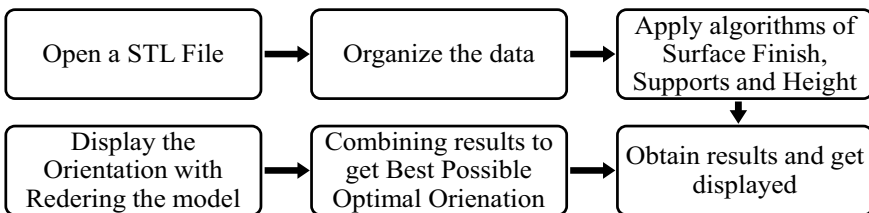


Fig. 2 Flowchart of overall process

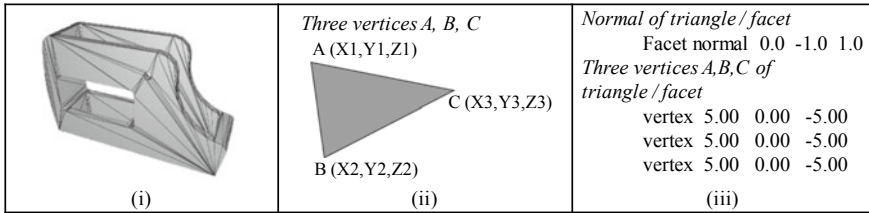


Fig. 3 a Rendering of STL file, b triangle/facet in STL file, c elaboration of STL file

of geometry by working on the coordinates of these normals and vertices, e.g. surface area, volume, relative dimensions of geometry.

The part build orientation is one of the principal process parameters which has a direct influence on the staircase effect and volume of support structure required for building the part [3]. These factors eventually contribute to the surface finish, dimensional accuracy and the post-processing requirements. Masood et al. [5] optimized the volumetric error in 3D printing by reducing the tilted surface area by increasing the parallel and perpendicular areas. This states that, the volumetric error reduction results in reducing staircase effect. All these aspects of optimization are implemented in algorithm developed in this study. The algorithm given in Fig. 4a

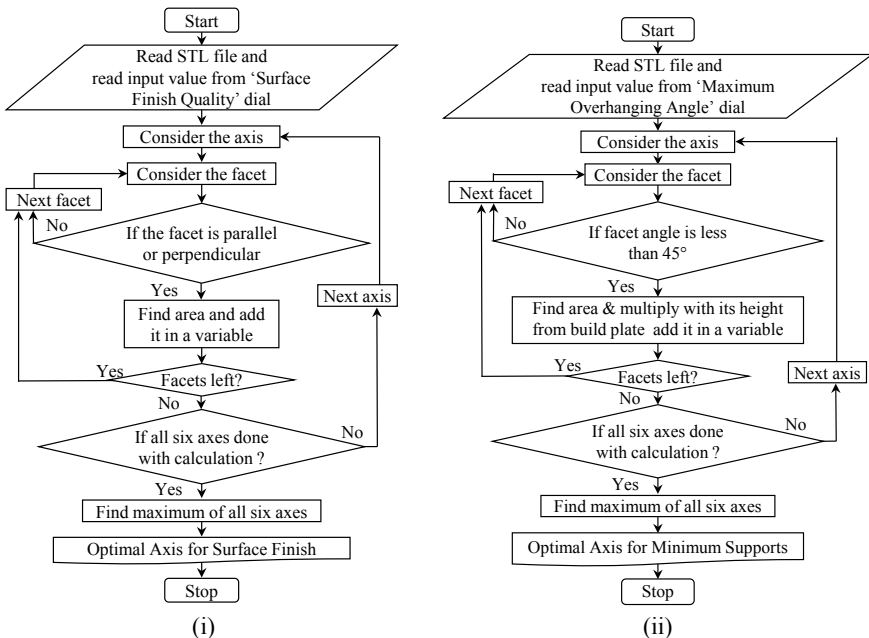


Fig. 4 a Algorithm for maximum surface finish, b algorithm for minimum supports, c algorithm for minimum height, d algorithm for optimal orientation

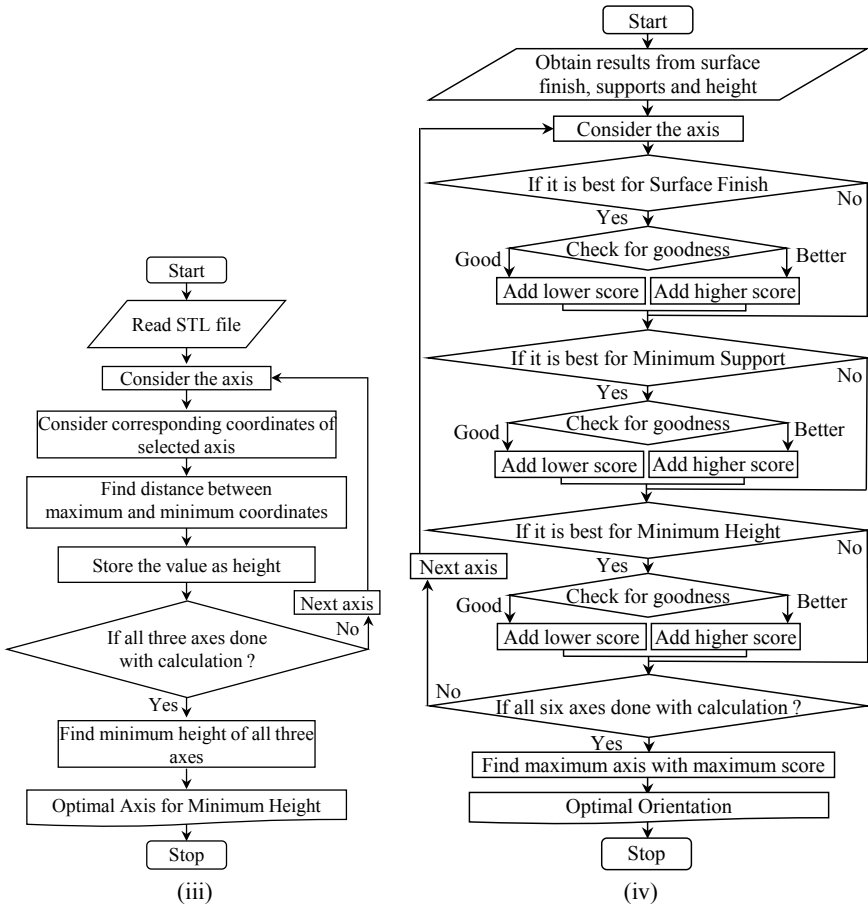


Fig. 4 (continued)

shows the flow of algorithm used to get best surface finish on component. In this method, staircase effect is minimized by increasing the area which is either parallel to build plate or perpendicular to build plate. So, this algorithm determines the orientation which will have the maximum surface area with facets parallel to build plate and perpendicular to build plate. Also, prior experience suggests that bottom surface has the best surface finishing. Additionally, algorithm with calculation of maximum bottom area is integrated with the surface finishing method which is not shown here in the algorithm.

2.2.2 Supports

The primary aim to optimize supports requirement is to minimize the overhanging surface area in order to reduce the support material requirement and avoiding a damage to the surfaces during post-processing. The algorithm shown in Fig. 4b is designed in such a way that, areas of facets with angle less than 45° to the build plate are calculated and further multiplied this area with its height from build plate. As these facets will get considered under the overhanging area and will require supports [6]. Now, the output of this multiplication indicates the approximate volume of support material required during printing. Though it is not a direct evaluation of support volume, it will provide a way to compare the overhanging volume for all six axes. Minimum value from these six orientation directions is considered as optimized direction for minimum support requirement.

2.2.3 Height

The printing height is the height of the part in building direction. Numerous studies have established a relation of the printing height and a printing time [1–4]. It is found that printing height is proportional to the printing time. In the algorithm developed for minimum height shown in Fig. 4c, the part height in all six directions is calculated with the help of vertices. For all three axes, the distance between maximum and minimum vertices is found out. Now, the minimum distance calculated among these three axes will show the minimum height. The minimum printing height orientation will ultimately reduce the printing time and also apply to constrain on the working space height.

2.3 *Optimal Orientation*

After using various techniques for different parameters, the obtained orientations can be evaluated to get the single best orientation. The optimized orientation would be the best possible combination of all parameters. This orientation is calculated empirically. Each axis will be assigned with a score based on its suitability; e.g. if one of the axes is having minimum height, it will get a lower score. Furthermore, if this minimum height is less than the half of the average height of all three axes, it is more suitable for minimum printing height, and hence, it will get a higher score. The algorithm shown in Fig. 4d suggests the optimal orientation from all six axes. Moreover, an extra feature is given to adjust the weightage for each of these modules. User can easily change the attribute settings to get a customized result. There are three sliders given which can be adjusted to get custom values for surface finish, supports and height, respectively.

2.3.1 Surface Finish Quality

While calculating the surface finish orientation, a method is proposed which can adjust the obliquity of vertical and horizontal surfaces. This will not only affect the finishing quality, but at the same time it will consider a greater number of facets under the accuracy criterion. User can adjust this feature in 'surface finish quality' dial given on the interface. When the dial is set on '1', surfaces which are slightly tilted either parallel or perpendicular to build plate will get considered under good surface finishing area. If the dial is set on '5', then algorithm will only consider the exactly parallel and perpendicular surfaces to the build plate under good surface finish area. In other words, this dial is simply a way to change the amount of strictness of surface finish method.

2.3.2 Maximum Overhanging Angle

The angle between facet and the build plate is known as overhanging angle. The general study shows that, 45° is the most widely accepted maximum overhanging angle and beyond 45° , it is required to get the extensive supports. Though when user changes some printing parameters, the maximum overhanging angle required to support the facets can change in considerable manner [3]. Also, in designing step, sometimes model can be designed in such a way that, very little or no supports are required. This change of maximum overhanging angle can be achieved in the 'Orienter' software by using the 'maximum overhanging angle' dial.

2.3.3 Scores

Each of the six axes would be having its own score based on the developed algorithm. These scores determine the printability of axis with respect to given parameters, e.g. if the axis is best under the multiple criteria of surface finish and height, it will get more score than the other axes. The scores are also given on the basis of the goodness of the criterion for the axis. More the axis is good for a criterion, more the score it will get for that criterion. Further, if the user is not satisfied with the given orientation, the next possible orientation based on given scores can be chosen for printing.

2.3.4 Export

The oriented file can be saved in desired format of STL. One can save it in either ASCII format or in Binary format. User just needs to click on 'Export' button and in next window, select the format which the user required.

3 Testing and Result

The testing can be done in four different ways. Firstly, one can judge the orientation based on his/her previous work experience, i.e. judgmental method. However, this method needs good experience with FDM 3D printing. The second way is to perform actual printing on FDM printer and compare result. One can print the same object six times with all the six orientations and followed by comparing the data. The third way is to simulate the process of printing in slicing software and compare the results within the software using its inbuilt feature of printing time and printing material requirement. The Ultimaker Cura [11] software is widely used by 3D printing professionals. To evaluate the performance of developed software, part orientation obtained from Ultimaker Cura is used as benchmarking. Printing time and printing material required for all six orientations are compared. The first orientation as in Fig. 5a was taken as it is designed in CAD software. Second orientation in Fig. 5b was optimally oriented in Orienter, and third orientation as in Fig. 5c was optimal oriented with Tweaker, as in [7].

Table 1 shows the result compared for the three orientations. It clearly shows that the optimally oriented Fig. 5b orientation requires less amount of time and less amount of printing material compared to Fig. 5a which was the default orientation and Fig. 5c which was oriented with Tweaker.

The fourth way is to compare results with pre-established softwares like Stratasys's Catalyst [12], Ultimaker Cura. Cura optimally orientates the part using the same Tweaker method using a plugin. The Catalyst's way of orientation is arbitrary, which means it can orient the part in more than six axes. It finally gives three orientations: A, B and C via its 'Auto Orient' inbuilt feature. The orientation given

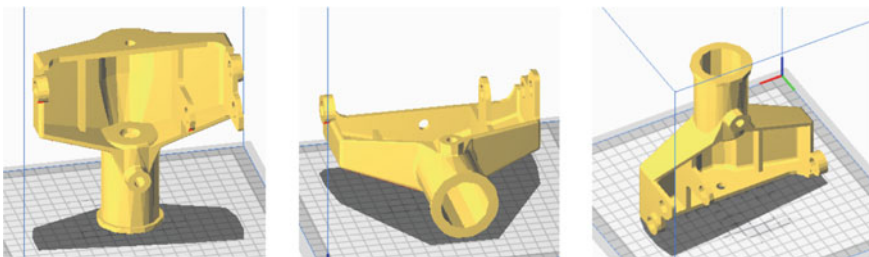


Fig. 5 a Default orientation as per CAD design, b optimally oriented in Orienter, c optimally oriented with Tweaker

Table 1 Comparison of printing parameters for orientations as in Figs. 5a–c in Cura

Part orientation	Printing material required (m)	Printing time required
Figure 5a	15.69	7 h 50 min
Figure 5b	10.27	5 h 28 min
Figure 5c	11.48	5 h 44 min

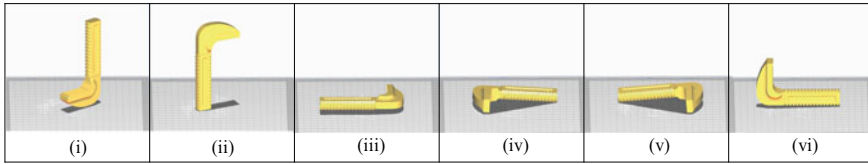


Fig. 6 **a** Default orientation as per CAD design, **b** Optimally oriented with Tweaker, **c** Optimally oriented in Orienter, **d** optimally oriented in Catalyst; Catalyst A, **e** Catalyst B, **f** Catalyst C

Table 2 Comparison of the printing parameters for orientation as in Fig. 6a–f in Cura

Part orientation	Printing material required (m)	Printing time required
Default, Fig. 6a	9.57	4 h 48 min
Tweaker, Fig. 6b	17.92	8 h 29 min
Orienter, Fig. 6c	8.31	3 h 20 min
Catalyst A, Fig. 6d	8.17	3 h 26 min
Catalyst B, Fig. 6e	8.16	3 h 25 min
Catalyst C, Fig. 6f	8.11	4 h 02 min

by Catalyst, Cura, i.e. Tweaker and Orienter, is given in Fig. 6a–f. The results were compared again in the Cura, and the comparative data is shown in Table 2. It shows that, orientation given by Tweaker is requiring more material. Also, it can be noticed with an obvious intuition. Further, ‘Catalyst C’ orientation requires lesser material but it also requires higher printing time than Orienter’s orientation. Also, ‘Catalyst A’ and ‘Catalyst B’ did not take care of the surface finishing; as it can be seen that, it is tilted with some angle and hence subjected to staircase effect as in Fig. 6d, e. So, considering these all factors, Orienter gives better results compared to Catalyst and Tweaker.

4 Conclusion

The proper orientation is necessary for FDM 3D printing for achieving better quality of part and overall improvement in printing process. One can achieve good surface finish, minimum supports and minimum printing time with the help of the ‘Orienter’ algorithm. This empirical algorithm works very well for CAD parts with moderate data, and result can be achieved with lesser calculations. The testing done showed that, it works comparatively better than available software for some parts in terms of minimum supports and printing time. Also, in terms of software it is having user-friendly interface with unique features like attribute settings and scores of other orientations.

References

1. Pandey PM, Reddy NV, Dhande SG (2003) Real time adaptive slicing for fused deposition modelling. *Int J Mach Tools Manuf.* [https://doi.org/10.1016/S0890-6955\(02\)00164-5](https://doi.org/10.1016/S0890-6955(02)00164-5)
2. Pandey PM, Thrimurthulu K, Reddy NV (2004) Optimal part deposition orientation in FDM by using a multicriteria genetic algorithm. *Int J Prod Res.* <https://doi.org/10.1080/00207540410001708470>
3. Alexander P, Allen S, Dutta D (1998) Part orientation and build cost determination in layered manufacturing. *Comput Aided Des.* [https://doi.org/10.1016/S0010-4485\(97\)00083-3](https://doi.org/10.1016/S0010-4485(97)00083-3)
4. Lan PT, Chou SY, Chen LL, Gemmill D (1997) Determining fabrication orientations for rapid prototyping with stereolithography apparatus. *Comput Aided Des.* [https://doi.org/10.1016/S0010-4485\(96\)00049-8](https://doi.org/10.1016/S0010-4485(96)00049-8)
5. Masood SH, Rattanawong W, Lovenitti P (2003) A generic algorithm for a best part orientation system for complex parts in rapid prototyping. *J Mater Process Technol.* [https://doi.org/10.1016/S0924-0136\(03\)00190-0](https://doi.org/10.1016/S0924-0136(03)00190-0)
6. Ga B, Gardan N, Wahu G (2019) Methodology for Part Building Orientation in Additive Manufacturing. *Compu-Aided Des Appl.* <https://doi.org/10.14733/cadaps.2019.113-128>
7. Schranz C (2016) Tweaker—Auto rotation module for FDM 3D printing. <https://doi.org/10.13140/RG.2.2.27593.36966>
8. Lin F, Sun W, Yan Y (2001) Optimization with minimum process error for layered manufacturing fabrication. *Rapid Proto J.* <https://doi.org/10.1108/13552540110386691>
9. Cheng W, Fuh JYH, Nee AYC, Wong YS, Loh HT, Miyazawa T (1995) Multi-objective optimization of part-building orientation in stereolithography. *Rapid Proto J.* <https://doi.org/10.1108/13552549510104429>
10. Das P, Mhapsekar K, Chowdhury S, Samant R, Anand S. Computer-aided design and applications. <http://dx.doi.org/https://doi.org/10.1080/16864360.2017.1308074>
11. Ultimaker BV with community (2011–2021) Ultimaker Cura [open-source software]. <https://ultimaker.com/software/ultimaker-cura>
12. Prairie E, MN (1991–2010) Stratasys Inc. CatalystEX [software] <https://catalystex.software.informer.com>

Development of Twin Fin Extension Liquefier Design for FFF 3D Printers Through Finite Element Analysis



Ashish Agrawal, Mansingh Armo, Deepak Kumar, Siddharth Singh, Krishnanand, and Mohammad Taufik

Abstract The intention of the present study is aimed at modeling and analyzing a new FFF 3D printer thermal liquefier. This paper focuses on the improvement of thermal liquefier performance for low melting point materials and to avoid its existing issue of overheating. Heat dissipation is a big concern with 3D printers because if heat is dissipated in the direction of feed velocity, then it can affect the parts of the printer, which are made of ABS plastic and other materials. As the fins regulate heat dissipation, so work focuses on the detailed discussion and analysis on how the new design will increase the local heat transfer coefficient. So that heat is predominantly dissipated by fins and released into the atmosphere, with less heat reaching the 3D printer's upper sections. Therefore, in this paper, model of thermal liquefier with a new heat sink design called "Twin Fin Extension" has been developed through geometrical modeling and finite element analysis. It is found that twin-extended fins are having more value of local heat transfer coefficient which indicates more value of Nusselt number. More value of Nusselt number has more heat dissipation through fins which favor the working conditions of a 3D printer. Hence, twin-extended fins are more appropriate for a 3D printer due to the high value of the local convection heat transfer coefficient. The efficient design of the liquefier governs the temperature which controls the continuous flow of material and blockage at the nozzle tip and heat sink. It also maintains the desired minimum temperature at top of the liquefier which prevents the lifecycle and functioning of surrounding hardware from overheating.

Keywords Fused filament fabrication (FFF) · Twin fin extension · Nusselt number · Simulation

A. Agrawal · M. Armo · D. Kumar · S. Singh · Krishnanand · M. Taufik (✉)
Department of Mechanical Engineering, Maulana Azad National Institute of Technology,
Madhya Pradesh, Bhopal 462003, India
e-mail: mohammad.taufik@manit.ac.in

© The Author(s), under exclusive license to Springer Nature Singapore Pte Ltd. 2022
H. K. Dave et al. (eds.), *Recent Advances in Manufacturing Processes and Systems*,
Lecture Notes in Mechanical Engineering,
https://doi.org/10.1007/978-981-16-7787-8_24

329

1 Introduction

Additive manufacturing (AM) is one of the latest and advanced manufacturing technique of Industry 4.0 which resolves many issues present in conventional and some non-conventional manufacturing process. Materials having a high melting point, strength, and brittleness cannot undergo casting, machining, rolling operations but can be processed using additive manufacturing. It is a layer-by-layer deposition process [1] and can produce “complex metal net shape parts” which means a solitary product in one component only, instead of manufacturing different components separately and then assembling. It is economical and reduces the wastage of material and resources. It has got wide range of uses in industries such as automotive, tooling and functional applications, aerospace, and medicine [2].

In extrusion-based additive manufacturing, fused filament fabrication (FFF), as shown in Fig. 1, is a type of manufacturing process, in which a thermoplastic-based (ABS) filament in wire form is fed through feed rollers on top of liquefier passing via heat sink and heat break and reaches heat block where it melts and then transforms into the semi-molten form which further gets extruded from nozzle mouth and deposited in a layer-by-layer manner to form adjacent finite length “roads” [3].

Melting of filament accompanied by its extrusion occurs in liquefier, and later, its cooling and solidification occur after deposition. Thus, liquefier is an essential component in FFF 3D printers, and its geometry and design have a significant effect on filament melt behavior. As shown in Fig. 2, liquefier has four major parts [2, 4]:

1. Heat Sink: It dissipates heat by convection.
2. Heat break or barrier: This reduces heat conduction upstream from the heating block and is made up of stainless steel.
3. Heat block: It helps to keep a uniform extrusion temperature.
4. Nozzle: It extrudes out melted filament material.

Fig. 1 Fused filament fabrication process [3]

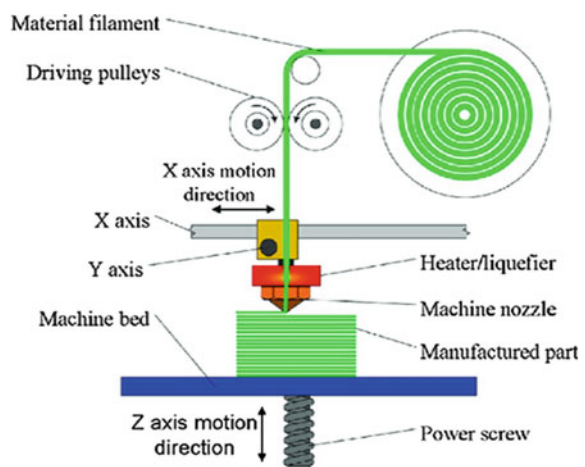
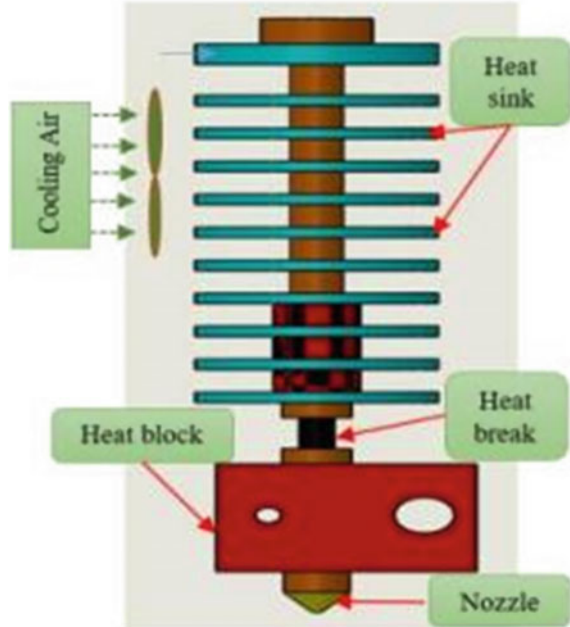


Fig. 2 Parts of liquefier [5]



Some others parts are fins, external fan, thermistor, and heating element.

After exploring this research journal which compares three separate 3D printer liquefier in terms of thermal behavior [6] along with its references, it could be realized how much significance a temperature control holds in the 3D printing process. Although many researchers have done plenty of work on thermal analysis on 3D printers with the aim that it affects the bonding strength and mechanical properties of a fabricated part. Still, one topic remains less discovered, i.e., the optimization of heat dissipation mechanism of liquefier, i.e., fins which becomes the main goal of this studied journal. Fins have many industrial applications, to enhance the rate of convection heat transfer and their design plays an especially significant role in this work. This study proposes two alternative designs (x-truder and twist 3D) of BC nozzle liquefier in which the only change done in alternative design is the design of fin, and then, the comparison is done between the proposed alternative design and the original one in terms of their temperature profiles acquired by FEM analysis and experiment and concluded two things. First, extruder even being a simpler design gives incredible results. It decreases the temperature more effectively at the top of the liquefier as compared to the other two designs. Second, 20% PWM fan speed becomes the optimized speed for the fan.

The temperature differential between the inner and outer parts of the extruded filament is smaller when the diameter of the filament is smaller; as a result, in the same layer between filaments, adhesion quality is better [7]. Better cooling control could have a big impact on the characteristic properties of the manufactured part made with the FDM [8]. It is found that the road-to-road contact, road shape, and the

“route”, have a remarkable impact on the properties and results of the finished part [9]. The mesostructured and all-inclusive quality of the adhesion strength between roads is strongly influenced by the envelope temperature and variations in convective conditions within the building chamber [10]. According to FEM analysis, stresses and deflections of the component are majorly affected by the deposition pattern [11]. The short-raster tool route produces higher residual stresses, and as a result, potentially greater deformation than the alternate-raster design and long raster design, which have identical deformation features and stress allocations [12]. As compared to the Maddock melting model, the dispersive melting model has several benefits [13].

More studies into the effects of overheating may disclose the maximum permissible temperature at the top of the liquefier, allowing the fan to operate less and save energy [14]. The fused deposition modeling (FDM)/fused filament fabrication (FFF) technology is a widely preferred advanced digital manufacturing system. The governing component of heating and deposition of the FFF system should manage the quality of product and energy saving. The quality of the final product also depends upon the proper heating, melting, and deposition of material. A thermal liquefier is one of the most influencing components of FFF for governing filament feed and heat energy saving. To increase the efficiency and to maintain proper working conditions, it is necessary to increase the rate of heat loss which is achieved here by modeling and analyzing an innovative design of fins and finally compares it with old existing fins.

2 Methodology

The studied paper [6] proposes a comparison between two alternative geometrical designs of liquefier as shown in Fig. 3 and makes a comparison between the proposed designs and BC nozzle liquefier in terms of their temperature profile and power consumption to get an improved design. Initially, temperature curves were obtained

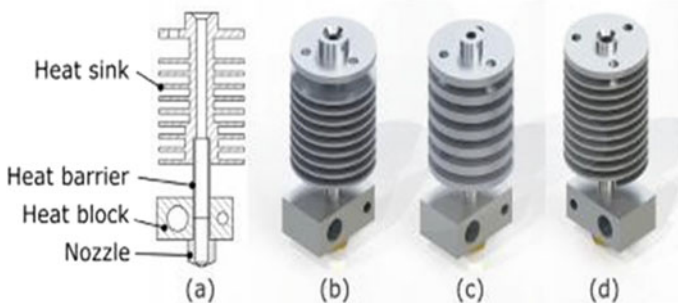


Fig. 3 Geometries of the liquefiers. **a** Cross-sectional representation of BC nozzle model liquefier. **b** External design of BC nozzle liquefier. **c** thickened fin-twisted 3D liquefier. **d** helical-shaped twisted 3D nozzle liquefier [6]

(in Fig. 4) from both finite element modeling analysis and experimental set up for their analyzed geometrical design of liquefier on five different speeds of the fan which were then compared individually to get the final results [6]. Once the temperature profiles were acquired in FEM analysis, temperatures at 0, 15, 22, and 30 mm heights were recorded.

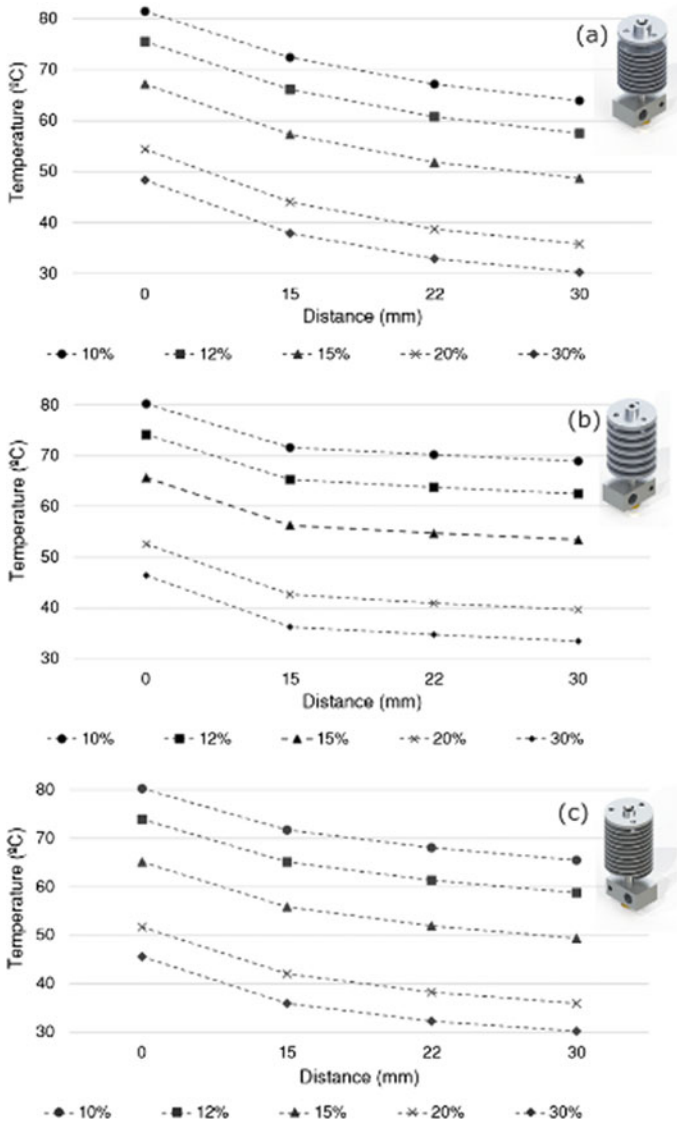


Fig. 4 Temperature profiles derived from FEM analysis for the three geometries under consideration. a BC nozzle, b x-truder, c twisted-3D [6]

While performing the experiment, liquefier and fan were kept attached to a support structure by putting the fan at the distance of 20 mm from the heat sink to imitate the actual arrangement in a real 3D printer. Thermocouples were attached at four distinct levels of the heat sink to record the temperatures once the steady state is reached with the aid of the PLW recorder; this data are then stored and visualized in a computer. By analyzing temperature profiles through both FEM and experimental setup, it was discovered that the extruder can lower the temperature at the upmost part of the liquefier as efficiently as the other two prototypes at a fan speed greater than 10%, despite being produced in less time. The temperature difference between the profiles while increasing the fan velocity from 10 to 20% is much than increasing it from 20 to 30% still power consumption is lesser in each of 10–20%. Thus, it is not advisable to increase the fan velocity by higher than 20%.

3 New Proposed Design and Its Analysis

Recently, temperature profiles for different types of nozzles are reviewed, but in this paper, an attempt is made to adjust the fin measurements with the primary goal of studying the change in the local wall heat transfer (dissipation) coefficient of the fins wall. For greater heat dissipation, the local heat transfer (dissipation) coefficient of the fins must be enhanced, so here, a normal annular fins structure is compared to the proposed model on Ansys workbench 17.2. Figure 5 shows the cross-sectional views of both the standard and new models.

The new design has been modeled using SolidWorks 16. The measurements of the base cylinder were 8 mm diameter with 4.2 mm endoring and the spacing between fins was 1.5 mm. The extension was 2.2 mm and 1.6 mm in length as measured from the tip of the fin at 5.6 mm and 4.3 mm, respectively. The inner and outer diameters of the fins were 8 mm and 22.3 mm, respectively, and the thickness of the fin was

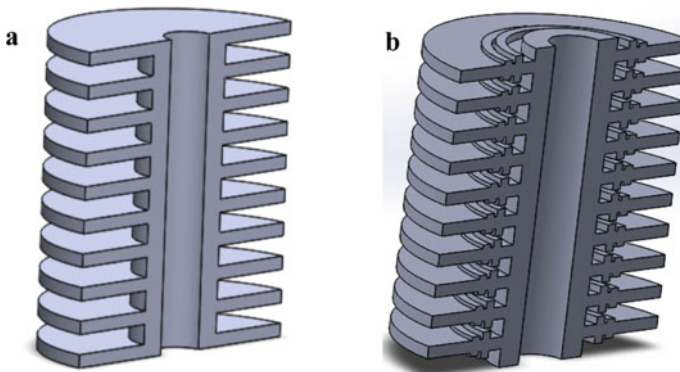


Fig. 5 Cross-sectional views. **a** Standard model, **b** twin extension fins model

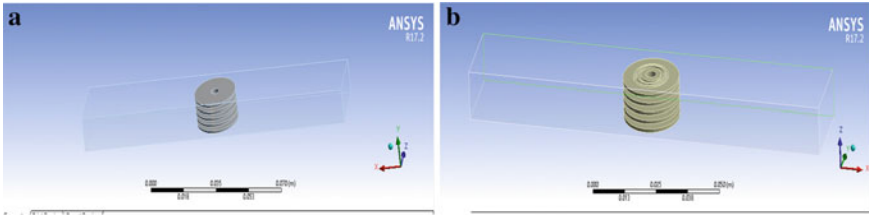


Fig. 6 Enclosure of **a** standard model and **b** modified model

1 mm. Ansys workbench 17.2 was used to analyze the fins. The fluid flow (fluent) was chosen for the evaluation of the rigid surface surrounded by a fluid medium. Thermal examination of fins was performed in a variety of ways.

3.1 Design of Enclosure

To define the airflow and the orientation of the air inlet and outlet over the fins, an enclosure was built around them. This enclosure was created concerning fin dimensions as shown in Fig. 6.

3.2 Mesh Generation

For more precise results, finer elements of the mesh are taken as depicted in Fig. 7. The size of the element was taken $5 * 10^{-3}/(5e - 003)$. The boundary state parts were described as inlet, exit, fins, and base cylinder.

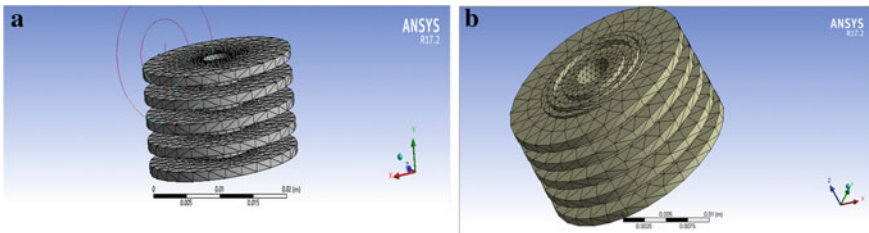


Fig. 7 Meshing of **a** standard model, **b** modified model

Table 1 Properties of air and aluminum

Parameters	Units	Aluminum	Air
Mass density	(Kg/m ³)	2718	1.225
Specific heat	(J/Kg K)	870	1005.42
Thermo-electric conductivity	(W/m K)	203.1	0.0242
Viscosity of medium	(Kg/m s)	NA	1.7849×10^{-5}

3.3 Input Parameters

For analysis of fins, some input variables which are provided to find local heat transfer coefficient are discussed here. Heat flux through the cylinder is assumed to be constant (5000 W/m²) keeping the cylinder temperature at 573 K. Air inlet velocity is kept at 1 m/s (max) with air inlet temperature of 300 k. The material of the fins is chosen to be aluminum and enclosure considered as fluid (air) medium. Properties of air and aluminum have been given in Table 1. model calculations are performed by selecting the energy model, and the k-epsilon model and solution have been initialized under hybrid initialization. For fins, the equations for momentum, and kinetic energy were all of order 2. There is no phase change phenomenon between air inlet to an outlet.

4 Results and Discussion

After performing the thermal analysis using Ansys workbench 17.2 with the help of assumed input parameters, results of local wall heat transfer coefficient variation for both models are obtained, which are shown in Fig. 8 and Table 2.

From the above results, it is noticed that the twin extended fins have a higher value of local convection heat transfer coefficient as compared to the standard old design of fins. More value of convection heat transfer coefficient indicates more value of

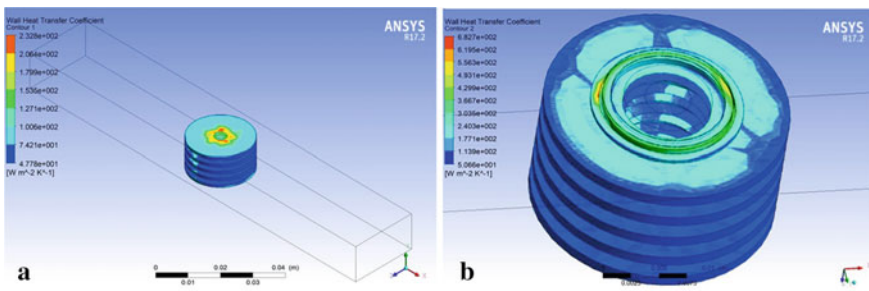


Fig. 8 Simulation outcome of **a** standard model, **b** modified model

Table 2 Range of wall heat transfer coefficients

Standard model	Twin fins extended model
(47.8–232.8) W/m ² k	(50.66–682.7) W/m ² k

Nusselt number because there are no significant changes in coefficient of thermal conduction, and hence, the convection heat transfer increases largely as compared to conduction heat transfer in twin extended fins. As the Nusselt number increases, the rate of convective heat dissipation through fins will increase which favors the appropriate working conditions for a 3D printer.

$$\text{Convection: } q_{\text{conv}} = h\Delta T \tag{1}$$

$$\text{Conduction: } q_{\text{cond}} = \frac{k\Delta T}{L} \tag{2}$$

$$\frac{q_{\text{conv}}}{q_{\text{cond}}} = \frac{h\Delta T}{K \frac{\Delta T}{L}} = \frac{hL}{K} = Nu_L \tag{3}$$

$$Nu_L = \frac{\text{convective heat transfer}}{\text{conductive heat transfer}} = \frac{hL}{K} \tag{4}$$

Thus from the above equations, it is evident that the Nusselt number increases with an increase in characteristic length (L), convective heat transfer (h), and decrease in conductive heat transfer (K).

5 Conclusions

It can be concluded that the new contemporary design of twin-extended fins proposed and discussed here is a better choice to increase the lifecycle of FFF 3D printers as compared to the old design of fins because:

- It increases the convection heat dissipation rate through the exposed area of fins.
- It has a high value of local wall heat transfer coefficient (convection) and a high Nusselt number.
- It will provide much better working conditions for FFF 3D printers by moderating the temperature inside the liquefier.

The result obtained shows that the coefficient of local wall heat transfer of fins was low in the standard model because of which the convection heat dissipation rate was comparatively slow. However, the new contemporary design (twin extended fin) will enhance it and make the process easier as evident from simulation results. Further, improvement in the design can be achieved in future work based on experimental analysis and available research and technology.

Acknowledgements This research was supported by Start-up Research Grant (SRG) through Science and Engineering Research Board (SERB)—DST, New Delhi-India (Project Number: SRG/2019/000943). The authors would like to acknowledge the funding agencies.

References

1. Taufik M, Jain PK (2013) Role of build orientation in layered manufacturing: a review. *Int J Manuf Technol Manage* 27:47–73
2. Krishnanand, Taufik M (2021) Fused filament fabrication (FFF) based 3D printer and its design: a review. In: *Lecture notes in mechanical engineering*, pp 497–505
3. Adel M, Abdelaal O, Gad A, Nasr AB, Khalil AM (2018) Polishing of fused deposition modeling products by hot air jet: evaluation of surface roughness. *J Mater Process Technol* 251:73–82
4. Krishnanand, Soni S, Taufik M (2020) Design and assembly of fused filament fabrication (FFF) 3D printers. *Mater Today: Proc* (in press)
5. Awasthi P, Srivastava R, Dev S (2019) Modelling and analysis of 3D printer thermal liquefier. *Int J Sci Res* 24–29
6. Jerez-Mesa R, Gomez-Gras G, Travieso-Rodriguez JA, Garcia-Plana V (2018) A comparative study of the thermal behavior of three different 3D printer liquefiers. *Mechatronics* 56:297–305
7. Domingo-Espin M, Borros S, Agullo N, Garcia-Granada AA, Reyes G (2014) Influence of building parameters on the dynamic mechanical properties of polycarbonate fused deposition modeling parts. *3D Printing Additive Manuf* 1:70–77
8. Bellehumeur C, Li L, Sun Q, Gu P (2004) Modeling of bond formation between polymer filaments in the fused deposition modeling process. *J Manuf Process* 6:170–178
9. Bellini A, Güçeri S, Bertoldi M (2004) Liquefier dynamics in fused deposition. *J Manuf Sci Eng Trans ASME* 126:237–246
10. Sun Q, Rizvi GM, Bellehumeur CT, Gu P (2008) Effect of processing conditions on the bonding quality of FDM polymer filaments. *Rapid Proto J* 14:72–80
11. Nickel AH, Barnett DM, Prinz FB (2001) Thermal stresses and deposition patterns in layered manufacturing. *Mater Sci Eng A* 317:59–64
12. Zhang Y, Chou Y (2006) Three-dimensional finite element analysis simulations of the fused deposition modelling process. *Proc Inst Mech Eng Part B: J Eng Manuf* 220:1663–1671
13. Huang H-X, Peng Y-C (1993) Theoretical modeling of dispersive melting mechanism of polymers in an extruder. *Adv Polym Technol* 12:343–352
14. Jerez-Mesa R, Travieso-Rodriguez JA, Corbella X, Busqué R, Gomez-Gras G (2016) Finite element analysis of the thermal behavior of a RepRap 3D printer liquefier. *Mechatronics* 36:119–126

Effect of Corrosion Behaviour of Microplasma Arc Welded Stainless Steel 316L Thin Sheet



Dipankar Saha, Abhradip Pal, Chandan Das, and Sukhomay Pal

Abstract The purpose of this work is to study the corrosion behaviour on microstructural changes of stainless steel 316L thin sheet (0.5 mm thickness) welded by microplasma arc welding. The welded metallurgical specimen exhibits that the welded zone contains delta-ferrite phase in the austenitic matrix. The electrochemical potentiodynamic polarization test exhibits excellent corrosion resistance of the fusion zone compared to the base metal in 1 M hydrochloric acid solution at ambient temperature. The immersion test of both base and fusion zone after 120 and 260 h are examined by field emission scanning electron microscope.

Keywords Thin sheet · Stainless steel 316L · Microplasma arc welding · Potentiodynamic polarization test · Immersion test

1 Introduction

Stainless steel 316L is significantly used in biomedical [1, 2], automotive industry, chemical industry, and water treatment plant [3] due to its superior mechanical properties at cryogenic temperature and elevated temperature. This material also shows excellent corrosion resistivity as well as creep-rupture properties [2]. The welding

D. Saha (✉) · S. Pal

Department of Mechanical Engineering, Indian Institute of Technology Guwahati, Assam 781039, India

e-mail: dipankar.saha@iitg.ac.in

S. Pal

e-mail: spal@iitg.ac.in

A. Pal · C. Das

Department of Chemical Engineering, Indian Institute of Technology Guwahati, Assam 781039, India

e-mail: p.abhradip@iitg.ac.in

C. Das

e-mail: cdas@iitg.ac.in

technique is widely used to transform raw material into industrial structural components. Different fusion welding techniques demonstrated accessible results on the mechanism of solidification behaviour and the formation of various delta-ferrite structures morphology in stainless steel weldment [3–7]. Dwibedi et al. [8] studied the relation of corrosion behaviour with the increasing heat input in the weld zone. They found that lower heat input weldment of austenitic steel shows higher corrosion resistance. Several welding techniques are used for the welding of thin sheet metal, but microplasma can weld with a minimal amount of welding current [8–10] that lead to less heat input.

The heat input during welding in the fusion zone alters the mechanical and metallurgical properties of stainless steels. In fusion welding techniques, chromium carbide precipitation and other intermetallic compound formation result in deteriorating mechanical strength in the welded joint. The austenitic phase is formed as a primary phase in austenitic steel under an equilibrium solidification condition. But, the transform from delta-ferrite to austenite structure does not complete in the welded zone because of the rapid solidification. So, the delta-ferrite structure remains in the welded zone, which prevents hot shortness and solidification cracking.

Cui et al. [4] explained the initial corrosion behaviour in austenite steel. The formation of microsegregation of the dendritic structure in the welded zone extracts chromium from the austenitic matrix, resulting in increased corrosion behaviour in the austenitic matrix. Ramkumar et al. [3] explained that the higher ferrite in the weld zone shows greater corrosion resistivity of the fusion zone. Mirshekari et al. [11] studied that increasing the number of weld passes increases ferrite count, which shows higher corrosion resistivity. Some spherical particles precipitation are observed in the austenitic matrix and grain boundaries of heat affected zone [12]. The temperature range of 873–1173 K is microstructurally unstable for the austenitic matrix, and decomposition occurs during welding. This condition is suitable for the formation and precipitation of chromium carbide phases and other intermetallic compounds. The formation of chromium carbides and other intermetallic compound lowers the corrosion resistivity of austenitic stainless steel and making them susceptible to intergranular corrosion [5, 13]. The mechanism behind the intergranular corrosion is known as the sensitization phenomenon of steels [14].

This research investigates the corrosion behaviour of weld and base metal of thin sheet material welded by microplasma arc welding process. For corrosion study, electrochemical potentiodynamic polarization test was performed. The corrosion behaviour of different phases was examined through an immersion test.

2 Experimental Procedure

The butt joining technique for thin sheet was adopted from the author previous publication [9] to weld 0.5 mm stainless steel 316L sheet material. Microplasma arc welding with a parameter setting of 11A current, 0.4 L/min plasma gas flowrate, 5 L/min shielding gas flowrate and 2.75 mm/s welding speed were used for the

current study. The metallographic samples and corrosion specimens were cut from the welded sheet. The metallographic specimens polished with 120 to 2500 grit size SiC emery papers. Further, these specimens were polished using alumina powder in a velvet cloth, and the microstructure was revealed with an etched solution (HNO_3 : HCl : Glycerol = 1:2:1). The corrosion specimens were also ground with emery paper and polish with aluminium powder in a velvet cloth to reveal a mirror-polished surface for use as a working electrode surface during the polarization test.

The potentiodynamic polarization technique was used to evaluate the corrosion behaviour of the base metal and the weld metal. The corrosion test's main parameters are current density (i_{corr}), corrosion potential (E_{corr}), corrosion rate, and polarization resistance. The equipment was used an electrochemical workstation Autolab Model PGSTAT302N potentiostat with the nova software interface. The test was carried out using an electrochemical cell with a wetted area of 0.03 cm^2 , which made it possible to assess the constricted area of the weld metal (limited width of 0.5 mm sheet weld joint).

The reference electrode silver/silver-chloride (Ag/AgCl) was used for macro-scale experiment. This was installed at a position near the working electrode (7.2 mm approximately) to measure the working electrode's potential. The platinum counter electrode (diameter of wire was 0.2 mm) was installed between the working and the reference electrodes and placed in an optimal position. This optimum position was expected to get the best electrical signals. All the measurements were programmed to begin after 15 min of open circuit potential, starting from a potential of $-500 \text{ mVAg}/\text{AgCl}$ and ending at $500 \text{ mVAg}/\text{AgCl}$, with a scanning rate of 0.5 mV/s . The electrolyte was used 1 mol/L hydrochloric acid (HCl) solution at room temperature.

The macro area was considered here to study the corrosion behaviour of the weld zone is about 0.03 cm^2 . Figure 1 shows the macro channel made by Teflon to allow electrolyte only in the weld zone. The macro electrochemical cell formed by three parts: the electrolyte containing cell, the flexible electrodes in the cell and the

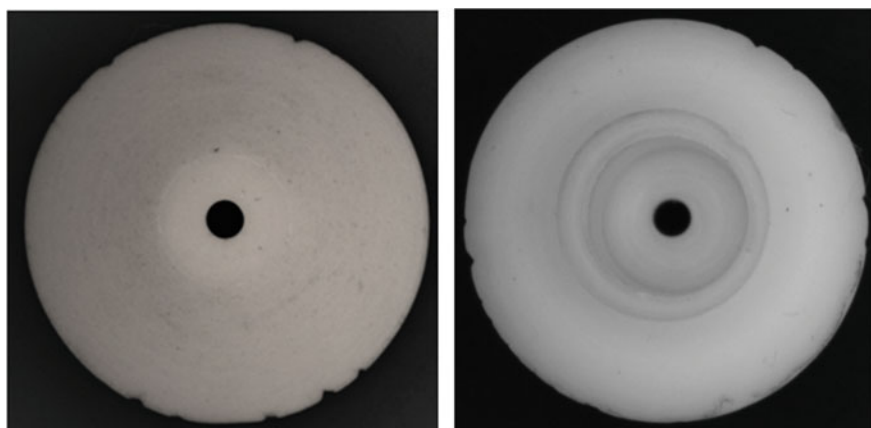


Fig. 1 Teflon made macro channel to expose the working electrode

macro area channel. The electrolyte circulates in the cell through the macro channel's upper inlet (diameter of 8 mm) and exits through the bottom outlet (diameter of 1.9 mm). Hence, a suction effect was developed by the reduction section continuously regulates corroded chemical species above the working electrode surface and allows fresh electrolyte flow. The disturbing phenomenon of possible bubbling formation then gets reduced. Finally, there was no requirement to use a joint sealant over the working electrode's surface. The Teflon microchannel was acting as a sealant, and no leakage had been observed during analysis. The weld and base metal specimens were immersed in 1 M hydrochloric acid (HCl) solution for 120 and 260 h. The corroded surface morphology was investigated under the field emission scanning electron microscope.

3 Results and Discussion

3.1 Microstructure

Figure 2a shows that the fusion zone contains delta-ferrite phases in the austenitic matrix. Due to the rapid solidification of molten material in the fusion zone, the delta-ferrite phase could not transform into the austenite phase. The high amount of delta-ferrite phase in the austenitic matrix helps to differentiate weld metal from base metal prominently (shown in Fig. 2a and 2b). The base metal (Fig. 2b) contains significantly less amount of delta-ferrite. Saha et al. [9] studied that delta-ferrite phase contains high amount of chromium than the base metal austenitic phase. It is well known that a higher percentage of chromium contain phases help to increase corrosion resistance.

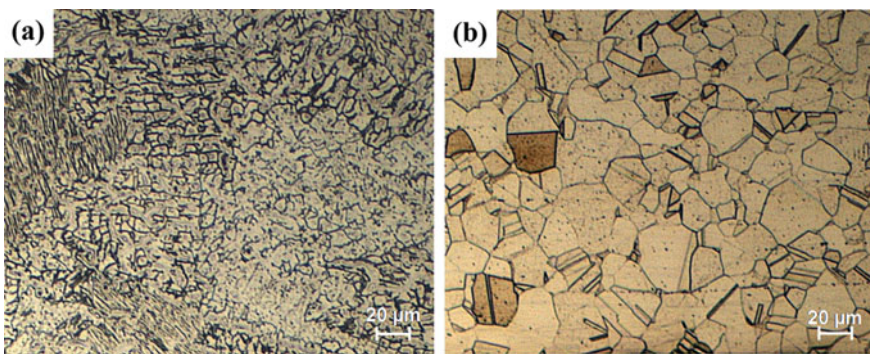


Fig. 2 a Weld metal containing delta-ferrite phases in the austenitic matrix, (b) base metal of stainless steel 316L

Fig. 3 Tafel polarization curves of stainless steel 316L weld and base zone metal

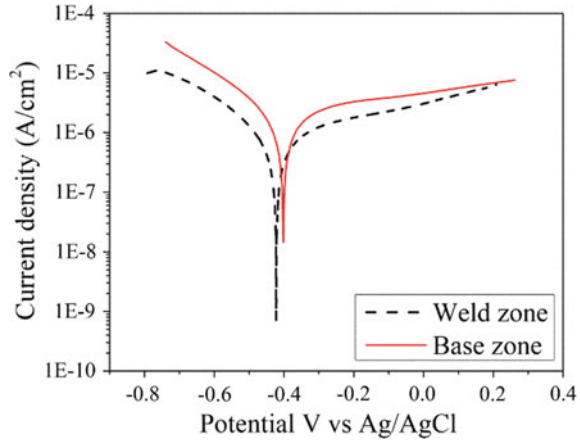


Table 1 Electrochemical corrosion tested results of weld and base zone

Parameters	Units	Base metal	Weld metal
i_{corr}	$\mu\text{A}/\text{cm}^2$	12.02	5.16
E_{corr}	mV	-401.29	-423.98
Corrosion rate	mm/year	14×10^{-2}	6×10^{-2}
Polarization resistance	M Ω	1.09	2.38

3.2 Electrochemical Potentiodynamic Polarization Test

The potentiodynamic polarization plots of weld and base metal specimens are shown in Fig. 3. Table 1 shows the results of corrosion behaviour such as corrosion current densities (i_{corr}), corrosion potentials (E_{corr}), corrosion rate and polarization resistance (M Ω). These values were evaluated from the potentiodynamic polarization curves (Fig. 3) with the help of the Tafel extrapolation method. The results show that the weld metal exhibits higher corrosion resistance with a lower corrosion rate than the base metal. AghaAli et al. [6] found a similar phenomenon: the base metal shows high corrosion and breakdown potential than the weld metal. This is due to the higher percentage of delta-ferrite phase formation in the austenitic matrix during welding (Fig. 2a shows delta-ferrite are present in the austenitic matrix). Saha et al. [9] explained that the delta-ferrite phase contains higher chromium than the austenitic phase in the welded zone.

3.3 Immersion Test

The weld metal and base metal were immersed in a 1 M HCl solution for 120 and 260 h to examine the corrosion behaviour of austenitic and ferritic phases. Figure 4 shows

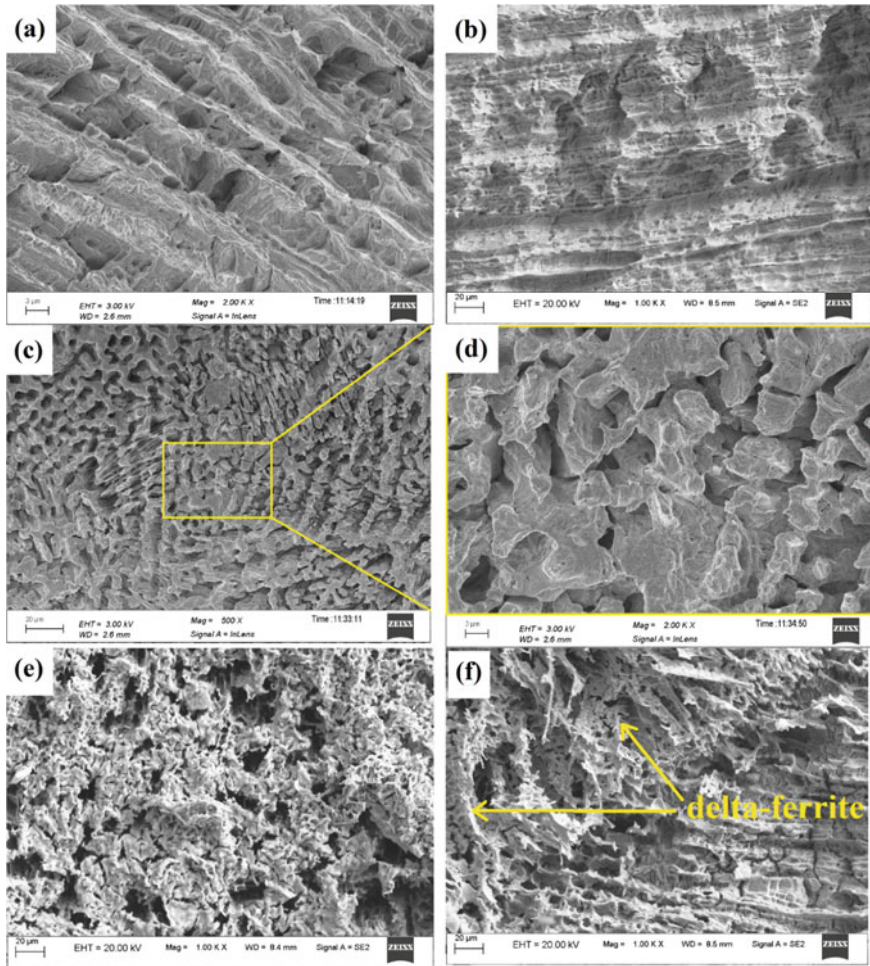


Fig. 4 FESEM images of corroded samples of **a** base metal after 120 h, **b** base metal after 260 h, **c** weld metal after 120 h, **d** higher magnification of weld metal after 120 h, **e** middle of weld metal zone after 260 h, **f** near the fusion boundary after 260 h

that all types of zones lose their protective surface passive layer in the immersion test. The base zone covers full of austenitic phase, which contains a low percentage of chromium than the delta-ferrite phase. This may be a reason that the base metal is the most preferential site for the breakdown of passivity. Figure 4a shows that the consistent removal of austenitic phase material from all over the base metal zone. Hereafter 120 and 260 h, no grain boundary pitting corrosion was observed. Figures 4a, b indicate that the removal of material was a continuous process over the increasing of time. Welded zone after 120 h immersed condition shows lots of pitting corrosion in austenitic phases (Fig. 4c, d). This behaviour of localized pitting

corrosion was promoted by the difference of potential electrochemical behaviour, caused by the percentage of chromium ratio of delta-ferrite/austenitic phase in the weld zone. Cui et al. [4] also studied immersion test, and they found pitting corrosion in the austenitic phase of weld metal. Dwibedi et al. [8] reported that delta-ferrite content high chromium than the austenitic phase, which helps in improving corrosion resistance in the fusion zone. Figure 4e, f show the middle of the weld zone and transition zone between the fusion and heat affect zones. These images (Fig. 4e, f) confirmed that the delta-ferrite phases are still present after 260 h immersion test.

4 Conclusions

The corrosion behaviour of microplasma arc welded thin stainless steel 316L sheet and base metal are studied in this research work. The following conclusions can be drawn:

- The electrochemical potentiodynamic polarization test of the weld metal shows superior corrosion resistance compared to the base metal zone.
- In immersion test, it is found that the delta-ferrite phase has high corrosion resistivity.
- Different electrochemical potential behaviours between the delta-ferrite and austenitic phase in the fusion zone are responsible for depleting austenitic phases.

References

1. Lodhi MJK, Deen KM, Greenlee-Wacker MC, Haider W (2019) Additively manufactured 316L stainless steel with improved corrosion resistance and biological response for biomedical applications. *Addit Manuf* 27:8–19
2. Kannan S, Balamurugan A, Rajeswari S (2005) Electrochemical characterization of hydroxypapatite coatings on HNO₃ passivated 316L SS for implant applications. *Electrochim Acta* 50:2065–2072
3. Ramkumar KD, Reddy PMM, Arjun BR, Choudhary A, Srivastava A, Arivazhagan N (2015) Effect of filler metals on the weldability and mechanical properties of multi-pass PCGTA weldments of AISI 316L. *J Mater Eng Perform* 24(4):1602–1613
4. Cui Y, Lundin CD (2007) Austenite-preferential corrosion attack in 316 austenitic stainless steel weld metals. *Mater Des* 28(1):324–328
5. Shaikh H, Rao BPC, Gupta S, George RP, Venugopal S, Sasi B, Jayakumar T, Khatak HS (2002) Assessment of intergranular corrosion in AISI type 316L stainless steel weldments assessment of intergranular corrosion in AISI Type 316L stainless steel weldments. *Br Corr J* 39(2):129–140
6. AghaAli I, Farzam M, Golozar MA, Danaee I (2014) The effect of repeated repair welding on mechanical and corrosion properties of stainless steel 316L. *Mater Des* 54:331–341
7. Kianersi D, Mostafaei A, Mohammadi J (2014) Effect of welding current and time on the microstructure, mechanical characterizations, and fracture studies of resistance spot welding joints of AISI 316L austenitic stainless steel. *Metall and Mater Trans A* 45A:4423–4442

8. Dwibedi S, Bag S (2021) Development of micro-plasma arc welding system for different thickness dissimilar austenitic stainless steels. *J Inst Eng (India) Ser C*. <https://doi.org/10.1007/s40032-021-00696-6>
9. Saha D, Pal S (2019) Microstructure and work hardening behavior of micro-plasma arc welded AISI 316L sheet joint. *J Mater Eng Perform* 28(5):2588–2599
10. Prasad S, Pal S, Robi PS (2020) Analysis of weld characteristics of micro plasma arc welded thin stainless steel 306L sheet. *J Manuf Process* 57:957–977
11. Mirshekari GR, Tavakoli E, Atapour M, Sadeghian B (2014) Microstructure and corrosion behavior of multipass gas tungsten arc welded 304L stainless steel. *Mater Des* 55:905–911
12. Silva CC, Farias JP, de Sant'Ana HB (2009) Evaluation of AISI 316L stainless steel welded plates in heavy petroleum environment. *Mater Des* 30(5):1581–1587
13. Matula M, Hyspecka L, Svoboda M, Vodarek V, Dagbert C, Galland J, Stonawska Z, Tuma L (2001) Intergranular corrosion of AISI 316L steel. *Mater Charact* 46(2–3):203–210
14. Devine TM (1990) The mechanism of sensitization of austenitic stainless steel. *Corros Sci* 30(2–3):135–151

Effect of Electrode Vibration Welding on Impact and Tensile Strength of 1018 Mild Steel Weld Joints



Bade Venkata Suresh, Y. Shireesha, and P. Srinivasa Rao

Abstract In past, so many decades welding technology attained its priority in production area. It is highly utilized all types of applications related to production. During the process of welding, welding defects are identified such as distortions and residual stress. To minimize these defects post weld heat treatment is introduced. But this method consumes more time and difficult to do. To Replace Post weld heat treatment processes, Mechanical vibrations are introduced during welding to refine the grain structure and mechanical properties of weldments. Based on this principle in this paper welding is done under the influence of electrode vibration. The welding with electrode vibrations is done to 1018 Mild steel specimens at different voltages and frequencies. As per ASTM Standards the specimens are prepared for tensile test, impact test and also performed SEM analysis to understand the effect of grain refinement in the weldments on mechanical properties. The results at various input parameters of the vibration welding will be observed and analysed to understand the advantages as well as disadvantages of this technique. The results show that the grain refinement is the cause for the improvement in mechanical properties. The properties of weldments are maximum at 4450 Hz, there is an increase in impact strength by 40% and the tensile strength by 12.4% (maximum) at 4450 Hz in comparison to that of without vibrations.

Keywords Vibration welding · Weld pool refinement · Mechanical properties · Microstructure

B. V. Suresh (✉) · Y. Shireesha
Department of Mechanical Engineering, GMR Institute of Technology, Rajam, Andhra Pradesh
532127, India
e-mail: suresh.bv@gmrit.edu.in

Y. Shireesha
e-mail: Shirisha1248@gmail.com

P. S. Rao
Department of Mechanical Engineering, Centurion University of Technology and Management,
Paralakhemundi, Odisha 761211, India

1 Introduction

Welding joints are widely used in automotive industries to assemble various products and also to repair damaged products. The major advantages of welding structures are high joint efficiency, water and airtight joints and low costs of fabrication compared to other means of fabrication methods. Welding provides a permanent joint but it normally affects the metallurgy of the components (weldments) results in decrement of the mechanical properties. The properties can be increased or residual stresses can be minimized with the help of post weld heat treatment for most of the components. But due to high input of heat during the process plastic deformation is generating. A welding joint can be performed with lesser weight than the bolted or riveted joint. Welding parameters in welding process results the quality of the weld and the life span of that weld joint. The parameters like welding current, electrode size, arc length, welding current, welding voltage and weld travel speed have lot of effect on weld bead quality. As every process in fabrication will have its pros and cons, besides being widely used and effective joints. Welding has a large heat effected zone, due to the concentration of large amount of heat produced during welding process over a small area, there may be a chance for generation of residual stresses in the joints. As residual stresses are a major problem during welding, much research work is going on. Heat treatment and mechanical processing are the most commonly used stress relieving techniques. But these are both costly and time consuming and involves a lot of hard work.

The vibratory stress relief (VSR) technique which is applied after the welding, with resonant and non-resonant cyclic loading treatments of low alloys of mild steel is used to improve mechanical properties such as hardness and tensile strength, as well as there is decrease in fatigue strength of the specimens with non-resonant cyclic loads welded with vibration assisted welding, which shows a drawback of the technique [1]. VSR is applied for stainless-steel weld specimens, has the total weight of base plate is over 34 tonnes examined for the cyclic stress and strain. The VSR process effectiveness is evaluated using frequency and amplitude. The variations are about 11% decrement in longitudinal residual stresses [2, 3]. The VSR process is most commonly used for minimising residual stresses in any other manufacturing process and their variations in microstructures are clearly visible where “tensile strength, fatigue and yield strength” have all improved and this VSR can be extended to significant applications for acceptable performance [4]. The hoist machine drum and SS-plate in nuclear core reactor are used as specimens for vibratory stress relief (VSR) method. The results are shown that there is decrement in residual stress almost 56% for hoist machine and almost 31% for SS-plate with VSR method. And it is chosen as an alternative process for PWHT [5]. The simulation of the VSR process was performed on 304L stainless-steel welded specimens with the material testing system and applied tensile-compress cyclic loading to study the cyclic strain and stress. The experimental test results revealed that dynamic-strain has cyclic creep characteristics. The “creep and creep speed” were influenced by cyclic loading [6]. The influence of rigid body motion was tried to find out during vibratory welding,

performed at two frequencies (50 and 500 Hz) to know the variation in the properties. The longitudinal and transverse residual stresses decrease and increase without any pattern at low frequencies. And at high frequency residual stresses were unchanged. As a result, both frequencies of rigid body motion are found to be unsuccessful in reducing residual stresses [7]. To observe the difference in the effect of the torsional vibration on residual stresses produced during welding, the three types of specimens were treated. Homogeneous shaft welded on the spot-welded and circumferential line of the shaft [8]. The effect of vibratory stress on the weld joint microstructures and the distribution of residual stress was investigated. The residual stress perpendiculars to weld line were measured. The results shown that the stress levels decrease about 75 MPa in the first 5 s of vibration [9].

The effects of frequency and amplitude of transverse oscillations on properties of mild steel were investigated. The results of oscillatory prepared welds show that the grain refinement, which is evident from the micrograph is the cause to improve mechanical properties within a frequency range of 80–400 Hz and the amplitude ranges of 5 to 30 μm [10]. The stress relief method with the introduction of vibrations during welding was compared due to PWHT [11]. The residual stress between ferritic steel and the buttering layer is about 160 MPa, while the residual stress between the weld metal and ferritic steel without the buttering layer is around 280 MPa [12]. The vibration welding results shows microstructure improvement, complete fusion structure and hardness increment compared to welding without vibration [13]. To improved quality of a completely welded valve finds an approach by the application of VWC (“vibratory weld conditioning”). It involves in prepping the specimens by normal SAW (Submerged Arc Welding) and vibratory SAW processes. The conclusions are residual stresses are reduced, Improved Weld strength [14, 15]. To understand the influence of vibration on the secondary microstructure of welds for (SAW) Submerged Arc Welding process a research work was performed. The results obtained reveals the microstructure and weld difference produced without imparting vibration and reheating reduced impact toughness more than in the case where the weld had been produced with vibration. Vibration with its mechanical energy supports the formation of aligned microstructures [16]. Vibratory welding condition describes the solidification behaviour and requiring less capital, being easier to operate, producing less pollution and taking less time to produce. The work piece vibrates during the welding process, which primarily affects welding solidification to improve efficiency [17]. To relieve and redistribute residual pressures, the vibratory stress relief technique is used. It is investigated how vibrational energy affects the microstructure of welds and Charpy toughness. During the “Electro Gas Welding (EGW) and Flux Cored Arc Welding (FCAW)” processes, vibration has a beneficial effect on impact energy and microstructure. That is, vibrational stress causes changes in ferrite microstructure alignment and grain refinement [18, 19].

The quality valuation performed on the tensile tests and the SEM (Scanning Electron Microscopy) analysis was conducted to observe the microstructure of the specimen and formation of the grain boundaries after the optimization were analysed and concluded with pictorials of microstructure with indications of changes at Heat Affected Zones and the welded regions [20, 21].

By introducing vibration to the weld pool, fine grain refinement and better material properties are observed. Because of these vibrations the PWHT process is completely eliminated.

2 Methodology

The principle of vibratory welding is changing mechanical form energy into the heat form of energy. In this procedure, heat is produced between the two surfaces because of frictional contact, these surfaces elements go in solid state part wherever material is heated till the molten point is achieved. Depending on the resistance properties of the material and process parameter frequency, amplitude and pressure the heat is generated. In the transition section layer of liquefied material will increase because of shear heating within the viscous section and thickness of viscous layer increases, heating decreases. The melting rate equals the outward flow rate in the steady-state melt flow phase. When this stage is achieved, the thickness of the liquid phase ends up steady. The consistent state is kept up until a specific “melt down-depth” is come to, at which the vibration is halted. Presenting of mechanical vibrations amid welding improves the mechanical just as metallurgical properties of material. To produce vibrations with required frequency, amplitude and acceleration regarding voltages, vibratory hardware is to be created.

2.1 Material Properties

Mild steel, otherwise called plain carbon steel is the most broadly utilized type of steel as it is generally more affordable and have better properties for some applications.

(a) **Mild steel:**

Mild steel is most regularly accessible of all alloy steels. It is commonly accessible in round-bar, square bar and rectangular bars. It has blended characteristics, for example, strength, little ductility and similarly simplicity of machining. The chemical combination is stated in the Table 1.

Chemical Composition of the MS Material:

Table 1 Chemical composition of mild steel

Chemical composition	Iron	Carbon	Manganese	Phosphorous	Sulphur
	98.81–99.26%	0.18%	0.6–0.9%	0.04% max	0.05% max

2.2 Electrode Vibrator-Welding Setup

To put the workpieces, a welding table is utilized as in ordinary welding process. The vibrating set up incorporates a small DC Motor, PWM-controller and an AC to DC adapter as main components. The connector converts a 220 V AC supply to a 20 V DC supply and the controller measures the voltage difference. The controller will adjust the voltage of DC Motor from a range of 12 to 20 V. As DC-Current is transferred to the DC Motor so that electrode vibrates since it is mechanically attached to it. The Fig. 1 shows the line diagram and experimental setup of electrode vibration welding.

The weld joints are delivered using manual metal arc welding methodology in this investigation. In any case, the vibrations that a matter produces are delivered and the weld-specimen is prepared on the flat platform. The work piece material for this project is mild steel. The vibration equipment is driven and steel plates are mounted on the weld table flat platform. The electrode vibration prepares the weld joint and the electrode generates the arc and the dimensions are shown in Fig. 2. After estimation of various frequencies, accelerations and amplitudes of electrode to which motor is associated, electrode with holder is taken to specimen.

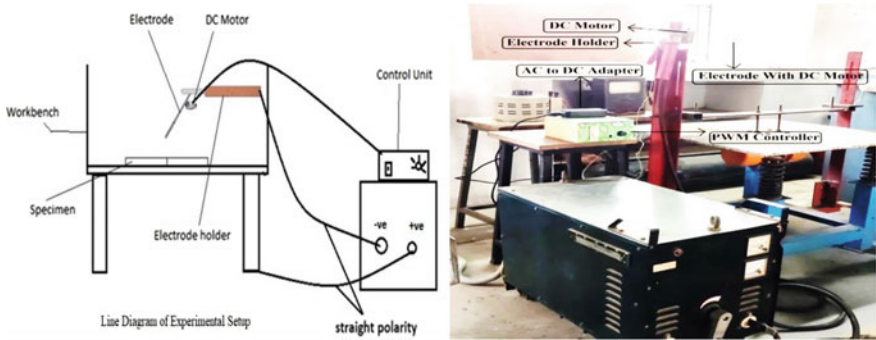


Fig. 1 Line diagram and experimental setup of electrode vibration welding

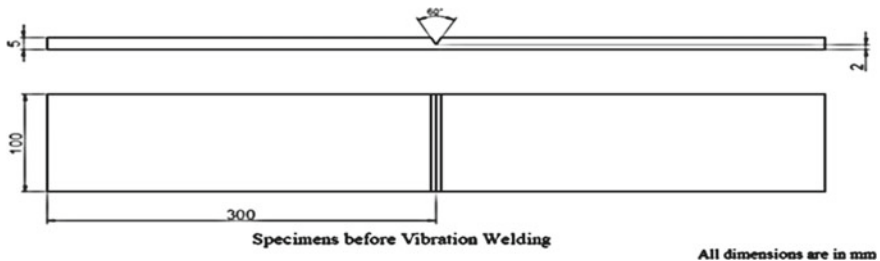


Fig. 2 Weld joint dimensions

2.3 Weld Joint Preparation

See Fig. 2.

2.4 Vibratory Welding Parameters

By utilizing the vibrometer, numerous frequencies and the relevant factors on the frequency are recognized. A scope of frequencies is distinguished between the operating range and the qualities are organized beneath Table 3. Here the DC Motor voltage is ranges from 12 to 18 V and the frequency of the electrode is ranges from 1071 to 5450 Hz shown in Table 2. In between these DC Motor voltages and electrode frequencies the welding is done and identified the various change in properties of impact and tensile strength is compared with the conventional welding process.

The blend of parameters picked between voltage, current and frequencies are arranged in the table underneath. The frequencies of the electrode along with the dependent parameters of the frequency like acceleration, velocity and displacement are shown in Table 3.

Table 2 DC motor voltage and frequency

Exp. No.	DC motor voltage (V)	Frequency (Hz)
1	12.80	1071
2	12.94	1625
3	13.08	2292
4	13.69	2469
5	13.97	2828
6	15.24	3452
7	16.19	4450
n	17.24	5450

Table 3 Frequencies of the electrode and its dependent parameters

Exp. No.	Frequency (Hz)	Displacement (m)	Velocity $\times 10^{-5}$ (m/s)	Acceleration (m/s ²)
1	1071	0.005431	5.0760	2.691892
2	1625	0.006124	5.7951	3.182112
3	2292	0.007187	6.1758	4.025392
4	2469	0.009145	6.9795	4.12369
5	2828	0.010356	8.3754	4.29895
6	3452	0.010864	10.1943	4.376166
7	4450	0.0112364	13.5783	4.487418
8	5450	0.0118619	18.6210	4.680458

3 Results and Discussion

3.1 Tensile Test

The provision of the test specimens is determined by the research objectives as well as the applicable test procedure or specification. A tensile specimen is normally a cross-section of a standardized sample. The tensile test is normally performed using a predetermined test fixture on a universal measuring machine (UTM). This unit has two crossheads, one of which is adjustable for specimen length and the other of which is operated to apply strain to the test specimen. Hydraulic and electromagnetically driven machines are the two groups. The computer must be capable of handling the test specimen being examined. Force power, speed, precision and accuracy are the four key parameters. The machine's force potential refers to its ability to produce sufficient force to achieve the fracture in specimen [22]. Finally, the unit must be able to calculate the gauge length and applied forces accurately and precisely (Fig. 3).

Figure 4 shows the tensile test specimen of mild steel 1018 as per the standards before testing and after testing is shown in Fig. 4.

The results of tensile test specimens prepared at different frequencies' are tabulated in Table 4. Here the range of frequencies is considered to form 0 to 5450 Hz.

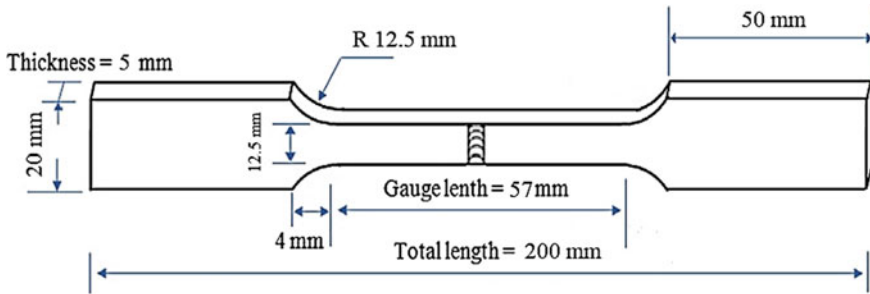


Fig. 3 Tensile test sample dimensions

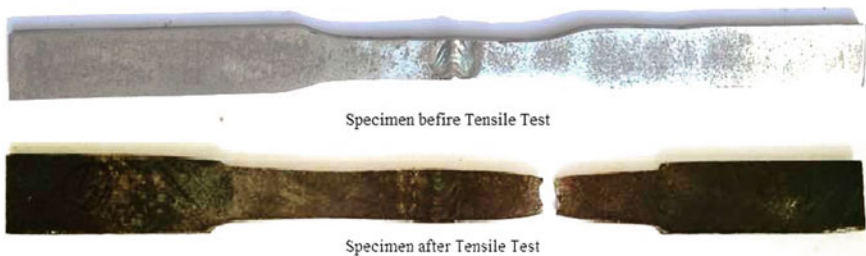


Fig. 4 Specimens before and after tensile test

Table 4 The results for Tensile test specimens

Exp. No.	Frequency (Hz)	Ultimate tensile strength (N/mm ²)	Tensile test at yield point (N/mm ²)
1	0	435.98	368.24
2	1071	454.84	392.75
3	1625	455.77	380.15
4	2292	480.19	391.62
5	2469	483.81	408.97
6	2828	490.09	411.82
7	3452	496.93	401.71
8	4450	497.71	402.95
9	5450	474.12	384.72

The 0 Hz frequency represents the welding process done in a conventional way and increased frequency over 0–5450 Hz represents the welding process with vibrations. And the results are tabulated.

The result of conventional and vibrational welding shows a huge difference in tensile strength. With conventional process that is at 0 Hz, the tensile strength is obtained as 435.98 and 368.24 N/mm² of ultimate and yield point of specimens respectively. And by imparting the vibrations that are at 1071 Hz frequencies the tensile strength is obtained as 454.84 and 392.75 N/mm² of ultimate and yield point of specimens respectively, here the tensile strength is enhanced with vibrations. The enhancement of tensile strength is continued up to 4450 Hz frequencies and the tensile strength is obtained as 497.71 and 402.95 N/mm² of ultimate and yield point of specimens respectively. Variations of Tensile stress at yield point and Ultimate Tensile Stress (UTS) with respect to frequency are shown in Fig. 5.

And from the above graph, it is identified that further enhancement of frequency causes a decrease in tensile strength that is at 5450 Hz. Here the tensile strength is obtained as 474.12 and 384.72 N/mm² of ultimate and yield point of specimens respectively. The decreased tensile strength is due to the high amplitude during welding, whenever the amplitude cross 0.5 mm displacement the arc gap increases rapidly and the imperfect weld bead is produced.

3.2 Impact Test

The impact test is carried out for welded specimens on the Charpy impact testing machine. As per ASTM (E23) the specimens were prepared and the dimensions are shown in Fig. 6. A specimen with notch is inserted in machine and the heavyweight pendulum is permitted to strike the workpiece from a stationary height. The specimen after impact test is shown in Fig. 7.

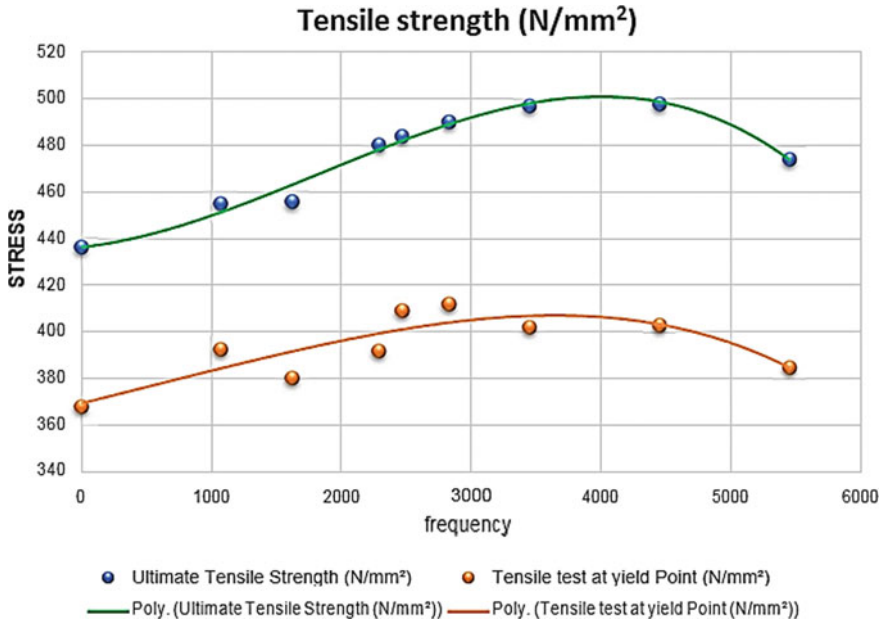


Fig. 5 Variation of Tensile stress at yield point and Ultimate Tensile Stress (UTS) with respect to frequency

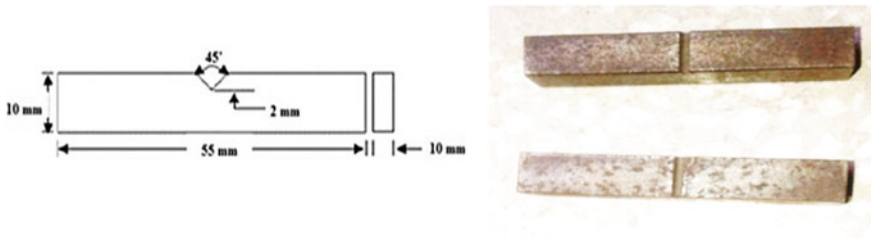


Fig. 6 Impact test specimen as per standards

Fig. 7 Specimen after impact test

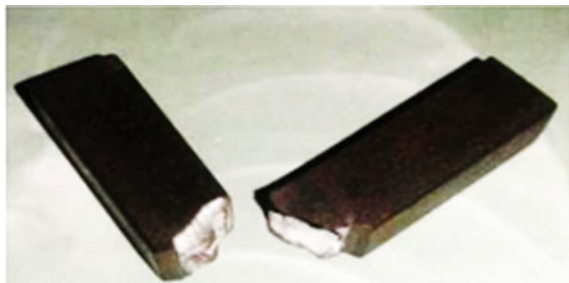


Table 5 The results for impact test at different frequencies

Exp. No.	Frequency (Hz)	Impact strength (J)
1	0	40
2	1071	41
3	1625	44
4	2292	48
5	2469	50
6	2828	52
7	3452	54
8	4450	56
9	5450	46

The results of impact test specimens prepared at different frequencies’ are tabulated in Table 5. Here the range of frequencies is considered to form 0 to 5450 Hz. The 0 Hz frequency represents the welding process done in a conventional way and increased frequency over 0–5450 Hz represents the welding process with vibrations. And the results are tabulated.

The result of conventional and vibrational welding shows a huge difference in tensile strength. With conventional process that is at 0 Hz, the impact strength is obtained as 40 J. And by imparting the vibration that is at 1071 Hz frequencies the impact strength is obtained as 41 J, here the impact strength is enhanced with vibrations. The enhancement of tensile strength is continued up to 4450 Hz frequencies and the impact strength is obtained as 56 J. Variations of impact strength with respect to frequency are shown in Fig. 8.

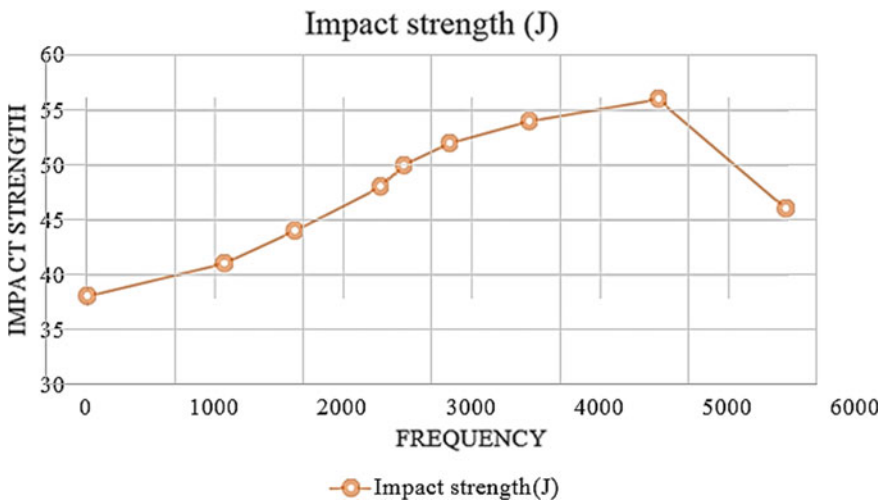


Fig. 8 Variation of impact strength with respect to frequency

And from the above graph, it is identified that further enhancement of frequency causes a decrease in impact strength that is at 5450 Hz. Here the impact strength is obtained as 46 J. The decreased impact strength is due to the high amplitude during welding, whenever the amplitude cross 0.5 mm displacement the arc gap increases rapidly and the imperfect weld bead is produced.

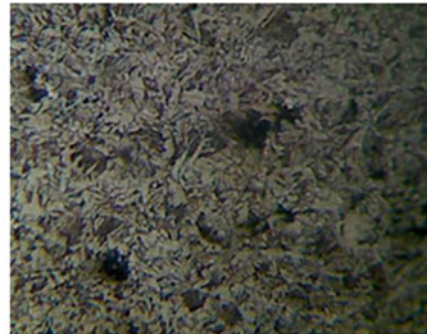
4 Microstructure Analysis

4.1 Microstructural Analysis of Welded Specimens at Different Frequencies

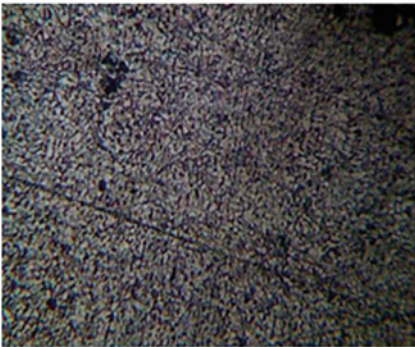
From the microstructure analysis, it is identified the reason for enhancing tensile strength and impact strength with vibrations. In the above Fig. 9, it is observed the microstructure of different weld specimens at different frequencies at 100 μ m.



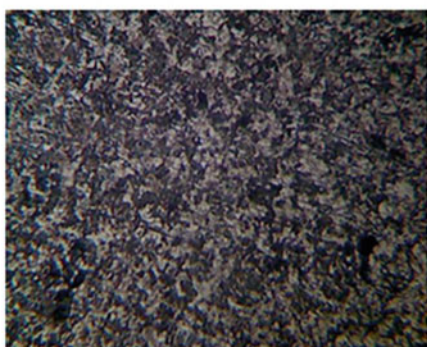
(a) Microstructure of weldment at 0Hz



(b) Microstructure of weldment at 1071Hz



(c) Microstructure of weldment at 4450 Hz



(d) Microstructure of weldment at 5450 Hz

Fig. 9 Microstructure of weldments vibrated at different frequencies

scales [22]. From the microstructure analysis at 0 Hz frequency that is without any vibrations, the weld bead grain size is very large and fine distribution of grains also does not happen. The large dendrites are clearly visible with conventional welding process. And by observing the 1071 Hz frequency specimens, the large size dendrites are started breaking into small sizes and it is continued up to 4450 Hz frequency. In 4450 Hz frequency, the large size dendrites in the weld bead are completely broken down into small dendrites and grain refinement is observed. Due to this reason, the tensile and impact strength is gradually increasing with vibrations and observed the maximum strength at 4450 Hz. After 4450 Hz that is at 5450 Hz again, the size of the dendrites is increasing due to increased amplitude of 0.5 mm. This results in decreasing tensile and impact strength. So with the microstructure analysis, the vibrations are improving the grain structure and increasing the properties of the weldments.

5 Conclusions

The practical experimentation exhibit (bring up) that there is considerable frequency on tensile tests of welded specimens during random vibrations and without vibration to the electrode. The tensile test results and impact test results are kept on increased up to the frequency level of 4450 Hz. As the observation of above result of tensile test and impact specimens, we concluded that value of tensile strength and impact test results of electrode vibration of welded specimens found more compared to the without vibration to the electrode. The increased value in the tensile strength and impact strengths is 12.4% and 40% (maximum) respectively at 4450 Hz in comparison to that of without vibration. The microstructure analysis reveals the fine grain structure weld pool refinement is achieved by imparting vibrations, this result in increasing tensile strength and impact strength.

References

1. Walker CA, Waddell AJ, Johnston DJ (1995) Vibratory stress relief—an investigation of the underlying processes. *Proc Inst Mech Eng Part E J Process Mech Eng* 209(1):51–58
2. Rao D, Wang D, Chen L, Ni C (2007) The effectiveness evaluation of 314L stainless steel vibratory stress relief by dynamic stress. *Int J Fatigue* 29(1):192–196
3. Jurčius A, Valiulis AV, Černašėjus O (2010) Effects of vibration energy input on stress concentration in weld and heat-affected zone of S355J2 steel. *Solid State Phenom* 165(1):73–78
4. Wang JS, Hsieh CC, Lai HH, Kuo CW, Wu PTY, Wu W (2015) The relationships between residual stress relaxation and texture development in AZ31 Mg alloys via the vibratory stress relief technique. *Mater Charact* 99(1):248–253
5. Rao DL, Zhu ZQ, Chen LG, Ni C (2005) Reduce the residual stress of welded structures by post-weld vibration. *Mater Sci Forum* 490(1):102–106
6. Kuo CW, Lin CM, Lai GH, Chen YC, Chang YT, Wu W (2007) Characterization and mechanism of 304 stainless steel vibration welding. *Mater Trans* 48(9):2319–2323

7. Munsif ASMY, Waddell AJ, Walker CA (1999) Vibratory weld conditioning—the effect of rigid body motion vibration during welding. *Strain* 35(4):139–143
8. Sakthivel P, Sivakumar P (2014) Effect of vibration in Tig and arc welding using AISI 316 stainless steel. *Int J Eng Res Sci Technol* 3(4):116–130
9. Pučko B, Gliha V (2005) Charpy toughness of vibrated microstructures. *Metalurgija* 44(2):103–106
10. Tewari SP (1999) Effects of transverse oscillation on tensile properties of mild steel weldments. *ISIJ Int* 39(6):570–574
11. Munsif ASMY, Waddell AJ, Walker CA (2001) Vibratory stress relief—an investigation of the torsional stress effect in welded shafts. *J Strain Anal Eng Des* 36(5):453–464
12. Pučko B, Gliha V (2006) Charpy toughness and microstructure of vibrated weld metal. *Sci Technol Weld Joining* 11(3):289–294
13. Bagheri B, Abbasi M, Dadaei M (2020) Mechanical behavior and microstructure of AA6061-T6 joints made by friction stir vibration welding. *J Mater Eng Perform* 29(2):1165–1175
14. Xu J, Chen L, Ni C (2007) Effect of vibratory weld conditioning on the residual stresses and distortion in multipass girth-butt welded pipes. *Int J Press Vessels Pip* 84(5):298–303
15. Zhu ZQ, Chen LG, Rao DL (2005) Relieving welding residual stress by applying vibratory weld conditioning. *Mater Sci Forum* 490(1):475–480
16. Qinghua L, Ligong C, Chunzhen N (2008) Effect of vibratory weld conditioning on welded valve properties. *Mech Mater* 40(7):565–574
17. Węglowska A, Pietras A (2012) Influence of the welding parameters on the structure and mechanical properties of vibration welded joints of dissimilar grades of nylons. *Arch Civ Mech Eng* 12(1):198–204
18. Hussein AR, Jail NAA, Abu Talib AR (2011) Improvement of mechanical welding properties by using induced harmonic vibration. *J Appl Sci* 11(2):348–353
19. Rao PG, Rao PS, Krishna AG, Sriram CV (2013) Improvement of tensile strength of a butt welded joints prepared by vibratory welding process. *Int J Mech Eng Technol* 4(2):53–61
20. Aoki S, Nishimura T, Hiroi T (2005) Reduction method for residual stress of welded joint using random vibration. *Nucl Eng Des* 235(14):1441–1445
21. Kalpana J, Rao PS, Rao PG (2016) Influence of amplitude on the tensile strength of welded joints fabricated under vibratory weld conditioning. *J Mech Eng Res Dev* 39(3):757–762
22. Bade VS et al (2020) The effect of vibratory conditioning on tensile strength and microstructure of 1018 mild steel. *World J Eng* 17(6):837–844. <https://doi.org/10.1108/WJE-07-2020-0296>

Effect of Low Temperature Treatments on the Stabilization of Transition Class Steel Used in Satellite Launch Vehicles



Tony Varghese, K. Sreekumar, K. Thomas Tharian, and Saju Sebastian

Abstract In steels, the conversion of austenite to a harder martensite phase, starts with a well-defined martensite start (Ms) temperature and finishes with martensite finish (Mf) temperatures. When the Mf or even Ms Temperatures are lower than the ambient, the steel may undergo a partial transformation to martensite, while the remaining structure being austenite, christened as retained austenite (RA). Mf is below room temperature in steels containing more than 0.30% C. Significant amounts of retained austenite, may be present, intermingled with martensite at room temperature. Under the influence of mechanical stresses, a gradual transition of RA can take place in material which in turn results in volume change and more importantly affect the dimensional stability of components made out of it. Such kind of instability can lead to catastrophic failure and is not welcomed in space applications. To reduce the retained austenite content, shallow as well as deep cryogenic treatments were proposed on steels in austenite martensite class which is used for space applications. Low temperature treatments were carried along with the conventional heat treatment cycles. Apart from the low temperature, there are many other parameters like soaking time, tempering temperature, and time that has a significant influence on the transition of retained austenite to secondary martensite. 07X16H6 steel which belongs to the transition class was subjected to study was given both shallow as well as deep cryogenic treatment at -80 and -196 °C respectively. The results revealed that the deep cryogenic treatment was suitable for the complete conversion of RA to ensure the dimensional stability of components. Mechanical characterization also revealed that the tensile strength got enhanced after deep cryogenic whereas, affected the impact resistance.

Keywords Cryogenic treatment · Retained austenite · Martensite transformation

T. Varghese (✉) · K. Sreekumar · S. Sebastian
Department of Mechanical Engineering, Amal Jyothi College of Engineering, Koovappally, India

K. T. Tharian
Liquid Propulsion System Center, ISRO, Valiyamala, Trivandrum, India

1 Introduction

During the heat treatment process, the dislocation movement, change in solubility of atoms, variation in grain size, formation of new grains, and change in crystal structure cause a change in atomic structure and microstructure. It's evident that heat treatment has a very significant role in almost all properties of a material. In Steel, the complete conversion of austenite to a harder phase-Martensite is not possible due to the limitation in the quenching temperature and quenching medium. Quenching temperature gradient offered by the quenching medium determines the rate of transformation of austenite to martensite in the material. In steels, the transformation from austenite to martensite begins at a well-defined temperature between the martensite start temperature (M_s) and martensite finish temperature (M_f). Sometimes the M_f or even M_s Temperatures can be lower than room temperature, and as a result, the partial transformation of austenite to martensite takes place with the remaining structure being named as retained austenite [1]. In order to ensure maximum conversion of retained austenite a lower temperature is needed which can be achieved by using.

- (a) Shallow cryogenic treatment, (SCT) sub-zero treatment ($-80\text{ }^\circ\text{C}$)
- (b) Deep cryogenic treatment. DCT ($-196\text{ }^\circ\text{C}$)

In Deep cryogenic treatment (DCT), the material is cooled down slowly to extremely low temperatures called cryogenic temperatures and keeping the material soaked for a specific time period at those temperatures. Further, the material is brought back to room temperature and tempered to release any forms of thermal shocks or residual stresses [2]. Some of the major advantages of cryogenic treatment involve the maximum conversion of retained austenite into martensite [2, 3], enhancement and uniform distribution of carbide density in the material [4, 5], and the precipitation of fine η -carbides [6]. The above benefits are said to be the mechanisms that enhance the mechanical properties in such steels [7, 8].

Apart from the above-said advantages, certain other benefits were also observed after DCT which include, enhanced wear and fatigue resistance, increase in hardness and toughness, and precipitation of ultra-fine carbide. All these advantages help the materials to attain dimensional stability which is a crucial requirement in aerospace applications, especially in satellite launch vehicles. Carbide precipitation kinetics changes during DCT which in turn enhances their precipitation. As a result, 22% more carbides were precipitated per unit volume after DCT when compare with the traditional heat treatment [8]. Although a notable change in tensile property, corrosion resistance, and fatigue life were reported, an atomic level study can shed more light on the effect of cryo treatment on the material [9, 10].

The parameters that influence the cryogenic treatment are cooling rate, soaking period, and soaking temperature. Among these parameters, the influence on various properties varies from material to material [11]. Most of the researchers reported that the low temperature treatment is an efficient method to stabilize the retained austenite content left with after room temperature quenching. During the process of DCT, the RA, which exists in Face Centred Cubic (FCC) transforms to Body

Centered Cubic (BCC) martensite and then to Body Centered Tetrahedron (BCT). Further upon tempering, the material becomes free from residual stresses and thermal shocks. Any significant amount of RA present in the matrix will get transformed to martensite under the influence of mechanical loads and as a result, due to the difference in the volume of FCC and BCT structures, a considerable enhancement in volume of components takes place which affects the dimensional stability of components. The austenite martensite class material 07X16H6 is mainly used in aerospace applications, especially in fuel transmission lines and nozzles. So the components used in the above application should offer dimensional stability while in operation. The paper focus on the effect of deep cryogenic treatment on the transition class material, 07X16H6, on the stabilization of retained austenite and its influence on mechanical properties.

2 Experimental Procedure

The chemical composition of the material 07X16H6 is given in Table 1. The steel was supplied in round forms and in normalized conditions. The tensile and impact test specimens were prepared using ASTM E8 [12] and E23 [13] standards respectively.

Influence of DCT can only be evaluated when studied along with the conventional heat treatment process. So the traditional method was taken as a reference. The specimens fabricated were given a standard heat treatment cycle which includes hardening at 990 °C for 1 h in a muffle furnace followed by air quenching (AQ). The DCT was conducted on tailor made cryogenic chamber which has a capacity of 60 L and uses liquid nitrogen (LN₂) as cooling medium. Three thermocouples were embedded in the system to measure the chamber temperature and specimen temperatures. The prepared specimens were cooled down slowly to the cryogenic temperature at – 196 °C using liquid nitrogen and the soaking period was set for 2 and 4 h so as to study the effect of soaking period on the transformation of RA. DCT was carried out after air quenching without much delay. The above process was followed by a tempering operation to relieve the thermal shocks and residual stresses. Tempering was carried out at two different temperatures, 250 and 410 °C for 1 and 2 h. Six different sequences of heat treatments cycles were planned to study the influence of DCT on the material which had a sub-zero treatment also as given in Table 2.

Mechanical characterization of the above samples involved X-ray diffraction, tensile test, and impact test, and hardness analysis. Micrographs of the samples were also evaluated to substantiate the findings. X-Ray diffraction was carried out on

Table 1 Chemical composition of 07X16H6

C	Mn	Si	S	P	Cr	Ni
0.067	0.44	0.4	0.00389	0.013	17.11	6.15

Table 2 Heat treatment cycles

Sample	Hardening	Sub-zero at – 80 °C	Cryogenic at – 196 °C	Tempering	
		Time (h)	Time (h)	Temperature (°C)	Time (h)
A1	990 °C–1 h-AQ	2		250	1
A2	990 °C–1 h-AQ	2		410	1
A3	990 °C–1 h-AQ		2	250	1
A4	990 °C–1 h-AQ		2	410	1
A5	990 °C–1 h-AQ		4	250	2
A6	990 °C–1 h-AQ		4	410	2

PANalytical analyzer, Universal Testing Machine series Unitek 9400 was used to evaluate the tensile test and the impact machine utilized was FIE Impact Tester-Model IT-30. Specimens were polished, etched and the optical micrographs were taken using Leica optical micrograph. In XRD, rotating anode method was used to identify the austenite peak. The obtained data were analyzed and compared with the JCPDS files to find the unit cell parameters and finally the volume percentage.

3 Results and Discussions

3.1 Retained Austenite

XRD- X-ray diffraction technique revealed that the sample in the as received condition contained a RA content of 29% and all the other samples which underwent low temperature treatments showed reduction in austenite content. Although six sequences of heat treatment were carried out on the samples, the retained austenite content showed the lowest value of 6% on the samples treated at –196 °C for 4 h followed by the tempering at 250 °C for 2 h Table 3. The volume percentage of retained austenite in the DCT samples attained the lowest values (sequence A3–A7) as compared to the sub-zero treated samples (sequence A1 and A2).

Fig 1 shows the peak list obtained for sequence 5, where the maximum intensity of an austenite peak was obtained at 44.5° (Fig. 2) and all the other austenite peak was either subtle or weak.

The XRD analysis revealed that the interference peak was from the plane (1 0 0) which belongs to the austenite class and study also pointed out that the retained

Table 3 Retained austenite percentage in various samples

Sequence	A1	A2	A3	A4	A5	A6
RA-%	18	14	8	10	6	9

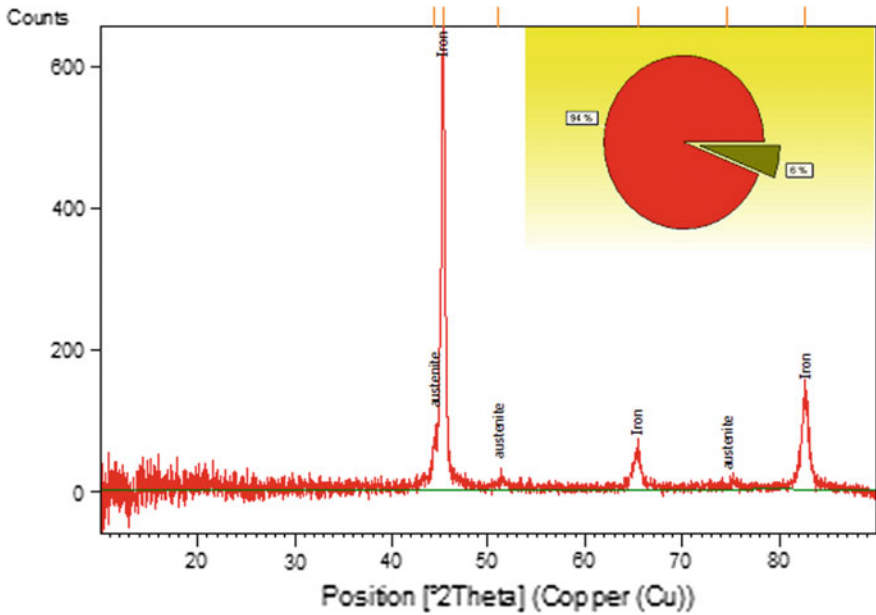


Fig. 1 XRD peak list of sequence A5

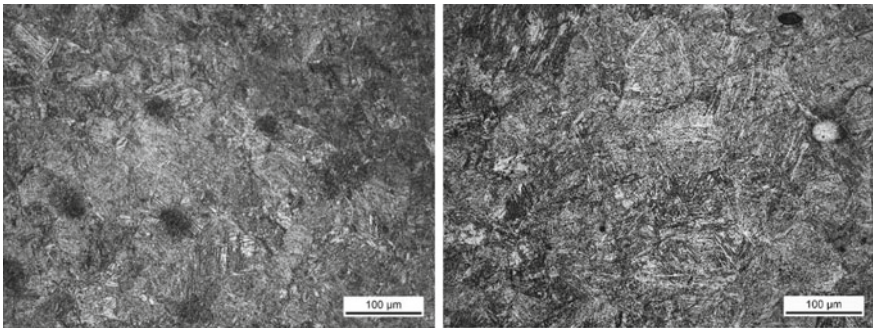


Fig. 2 Micro Structure of cryogenic treated 07X16H6

austenite structure was cubic. All the other peaks in the patterns were from plane (2 0 0) and (2 1 1) which belong to the iron peak. Even if there was precipitation of carbides, the XRD didn't report the presence of the same as their concentration might be low or not evenly dispersed in the matrix. The volume percentage around 5–7% is not good enough to cause a significant change in dimensional stability and so is read as zero and lower percentages are difficult to get identified in XRD analysis.

Table 4 Tensile Test of 07X16H6

	A1	A2	A3	A4	A5	A6
0.2% YS (MPa)	920	880	1299	1327	1306	1358
US (MPa)	1112	1085	1335	1355	1334	1372

3.2 Tensile Properties

The material in the as received condition was reported to have a tensile strength of 900 MPa and the same set of values were obtained after the experiment for tensile strength. The material showed a yield and ultimate tensile strength of 920 MPa and 1112 MPa respectively on samples tested at sub-zero temperature (A1 and A2 sequence) Table 4. The samples subject to DCT at $-196\text{ }^{\circ}\text{C}$ for 4 h showed an enhanced of 47% in yield stress from 920 MPa and reported 1358 MPa as final yield stress. It can be noted that a 17% difference between the yield and ultimate values on samples treated at sub-zero temperature (A1 and A2), got reduced to 1% after the DCT (sequence A3–A6). It was noted that, along with increase in tensile strength, the yield strength of the material also enhanced after DCT and the reported values were close to the ultimate tensile strength. Along with these enhancements, the ductility of the materials has not been compromised. The result pointed out that the variation in tempering temperature and time did not affect the tensile strength of the material.

Secondary martensite formed during the DCT along with the uniform precipitation of carbides can be inferred as the reason for an increase of 23% in tensile strength. As the carbide precipitation increases, the dislocation motion gets interfered, and thereby the yield strength and ultimate strength values enhance and came close to each other.

3.3 Impact Properties

The impact resistance of the base metal got reduced to 89 J when it was subjected to sub-zero treatment and further reduced to 59 J after cryogenic treatment. It can be noted that there is a considerable reduction of 33% in the impact resistance after the cryogenic treatment compared to the sub-zero treatment. Newly formed secondary martensite and carbides were brittle and have contributed to deterioration of impact resistance. Even though two tempering temperatures (250 and $410\text{ }^{\circ}\text{C}$) and time (1 h–2 h) were used to study the effect of the same on the mechanical properties, it can be observed that the impact resistance was lower in magnitude and close to each other. During tempering process, and increases in the precipitation of secondary carbides took place and the same was a reason for the low impact resistance. From Table 5 the hardness value of the cryogenically treated samples were ranging from 416 to 435VHN and is higher when compared with the sub-zero treated samples. The hardness values of the samples showed an increase as the soaking period increased

Table 5 Vickers hardness

Vickers hardness						
Batch	A1	A2	A3	A4	A5	A6
Hardness (VHN)	390	385	416	414	430	435

from two hours to four hours and can be inferred as due to the precipitation of above mentioned carbides. After the maximum possible conversion of retained austenite in the matrix, even if we increase in the soaking period, the hardness may remain constant.

3.4 Microstructure

Low temperature treatment of the material resulted in the transformation of retained austenite to secondary martensite and the precipitation of carbides along the grain boundaries can be inferred as the reason for the low RA value in XRD analysis. The presence of RA in such low percentage is difficult to get detected in the microstructure of bulk material. Moreover, the microstructure of the material showed complete martensitic structure with plate as well as lath martensitic formation Fig. 2. The presence of any such lower percentage of carbides and RA can only be evaluated with the help of sophisticated process using SEM or TEM. Even the use of feritoscope may not fetch the exact amount of RA in the material.

4 Conclusions

07X16H6- which belonged to an austenite martensite class had a retained austenite content of 29% and got reduced to 6% after cryogenic treatment. Retained austenite content close to 5% does not affect the dimensional stability of the parts manufactured using 07X16H6. When compared with the sub-zero treatment, cryogenic treatment proved to be a promising treatment method for the conversion of retained austenite. Standard tempering temperature and time were found to be sufficient for the precipitation of carbides along the grain boundaries and to toughening the material. These conversions of retained austenite to martensite and the precipitation of carbides have contributed to the enhancement of 47% in the yield stress value. The impact energy absorbed was low in the cryo treated specimens which again substantiated the formation of secondary martensite. The hardness value doesn't show any notable variation. The microstructure looks more or less the same for all the samples and the majority of the matrix showed a martensitic structure formation. The lower percentage of retained austenite as well as the carbide precipitates was not visible or detected in the microstructure. From the results obtained, it is concluded that the

cryogenic treatment is highly recommended for the conversion of retained austenite with significant improvement in tensile strength.

Acknowledgements We are grateful to RESPOND-ISRO for the funding offered and materials division VSSC for providing timely support for the XRD analysis.

References

1. Avner AH (1982) Introduction to physical metallurgy. McGraw-Hill, New York
2. Zhirafar S, Rezaeian A, Pugh M (2007) Effect of cryogenic treatment on the mechanical properties of 4340 steel. *J Mater Process Technol* 186:298–303
3. Darwin JD, Mohan Lal D, Nagarajan G (2008) Optimization of cryogenic treatment to maximize the wear resistance of 18% Cr martensitic stainless steel by Taguchi method. *J Mater Process Technol* 195:241–247
4. Barron RF (1973) Effect of cryogenic treatment on lathe tool wear. *Prog Refrig Sci Technol* 1:529–533
5. Preciado M, Bravo PM, Alegre JM (2006) Effect of low temperature tempering prior cryogenic treatment on carburized steels. *J Mater Process Technol* 176(1–3):41–44
6. Molinari A, Pellizzari M, Gialanella S, Straffelini G, Stiasny K (2001) Effect of deep cryogenic treatment on the mechanical properties of tool steels. *J Mater Process Technol* 118:350–355
7. Yan XG, Li DY (2013) Effects of the sub-zero treatment condition on microstructure, mechanical behaviour and wear resistance of W9Mo3Cr4V high speed steel. *Wear* 302(1–2):854–862
8. Das D, Dutta KA, Toppo V, Ray KK (2007) Effect of deep cryogenic treatment on the carbide precipitation and tribological behaviour of D2 steel. *Mater Manuf Process* 22(4):474–480
9. Baldissera P (2010) Deep cryogenic treatment of AISI 302 stainless steel: Part I hardness and tensile properties. *Mater Des* 31(10):4725–4730
10. Baldissera P, Delprete C (2010) Deep cryogenic treatment of AISI 302 stainless steel: Part II - Fatigue and corrosion. *Mater Des* 31(10):4731–4737
11. Gruber M, Ressel G, Ploberger S, Marsoner S, Ebner R (2006) Characterization of the effect of cryogenic treatment on the tempering behavior of a secondary hardening high Co-Ni steel. <https://iopscience.iop.org/article/https://doi.org/10.1088/1757-899X/119/1/012018/meta>
12. ASTM E8 Standard Test Methods for Tension Testing of Metallic Materials, American Association State Highway and Transportation Officials Standard, AASHTO No.: T68
13. ASTM E23 Standard Test Methods for Notched Bar Impact Testing of Metallic Materials

Effect of Nozzle Geometry on Melt Flow of Eutectic Sn–Bi Low-Melting Point Alloy in Fused Deposition Modeling



Alok Kumar Trivedi, P. S. Robi, and Sukhomay Pal

Abstract Fused deposition modeling (FDM) process is a low cost and widely used extrusion-based additive manufacturing (AM) process. FDM is generally used for printing thermoplastic materials like PLA, ABS, etc. This present study aims to extend the application of the FDM technique for printing low-melting point (LMP) alloys. The melt flow behavior (MFB) of molten material through liquefier plays a vital role in the deposition characteristic and calculation of feeding force or torque. This present study analyzes the melt flow behavior of eutectic Sn–Bi LMP alloy through the nozzle. The MFB parameters, i.e., pressure drop and melt flow velocity across the nozzle have been investigated. This study has been carried out using two methods: one analytical method and the other finite element analysis (FEA). The investigation has been carried out with varying nozzle angles and nozzle exit diameters. The results show that nozzle geometry has a significant impact on the MFB. Both pressure drop across the nozzle and nozzle exit velocity decreases with increase in nozzle angle and nozzle exit diameter resulting in a smooth flow.

Keywords Fused deposition modeling (FDM) · Melt flow behavior (MFB) · Low-melting point alloy (LMP) · Eutectic Sn–Bi alloy

1 Introduction

In recent decades, additive manufacturing (AM) has been the focus of attention among researchers working in advanced manufacturing technology. AM process is

A. K. Trivedi (✉) · P. S. Robi · S. Pal
Department of Mechanical Engineering, IIT Guwahati, Assam, India
e-mail: alok18@iitg.ac.in

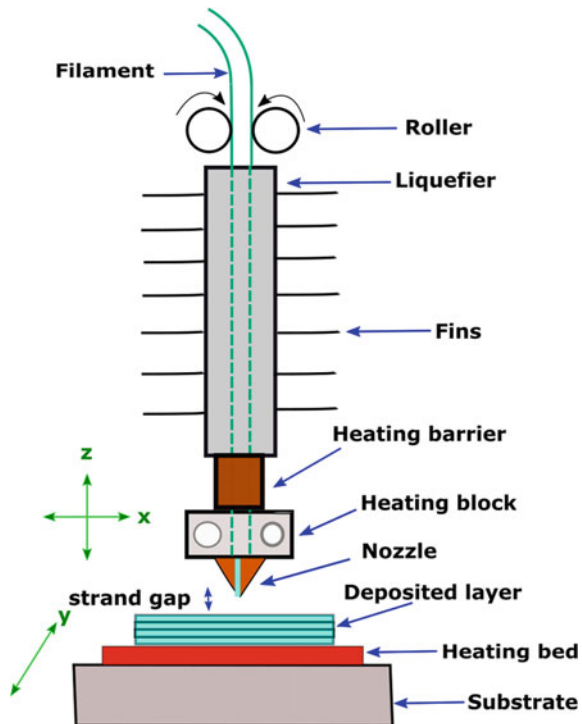
P. S. Robi
e-mail: psr@iitg.ac.in

S. Pal
e-mail: spal@iitg.ac.in

the process of manufacturing 3D objects or components directly from the computer-aided design (CAD) model by adding material layer by layer without the aid of expensive tools, molds, dies, jigs, fixtures, etc. [1]. In contrast to the subtractive manufacturing process, since in the AM process material is deposited one above the other in layers, material wastage is almost eliminated leading to a reduction in the final cost of the product. The first working 3D printer was the “stereolithography apparatus” made in 1984 by Charles W. Hull of 3D System Corp. This technology was expensive and not feasible by the general market at the early stages [2]. The components produced by the continuous 3D printing process have good strength and dimensional accuracy as obtained by the conventional manufacturing method [3]. Several AM techniques exist for metals, like selective laser sintering (SLS), selective laser melting (SLM), electron beam melting (EBM), laser engineering net shaping (LENS), etc. These processes are not cost effective because of high cost involved for the laser or electron beam units, which are used as a heat source for melting the metals in addition to the fact that the production of metal powder is also expensive [4–6].

The most widely used AM process is the fused deposition modeling (FDM) process [7, 8]. FDM is most popular for thermoplastic materials like polylactic acid (PLA), acrylonitrile–butadiene–styrene (ABS), etc. The basic mechanism of the FDM process is shown schematically in Fig. 1. In this process, raw material in

Fig. 1 Schematic view of FDM



the form of solid filament is feed by a roller to a liquefier and subsequently through a heating block to a nozzle. The heating block is heated slightly above the melting temperature of the filament. The filament material gets melted and is extruded out in the form of thread or wire from the nozzle and deposits on the substrate where it gets solidified. The temperature of the liquefier above the heat barrier is lower than the heating block temperature, hence known as cold zone. The temperature of the liquefier below the heat barrier is high, hence referred to as the hot zone. Melting of the material takes place at hot zone of the liquefier [9, 10]. The advantage of FDM includes simple design, cost effective, easy to operate and control. Though FDM is used for depositing thermoplastic materials, this technique has great potential for applying to other materials including ceramics, composites, and metallic alloys. Recent reports reveal that experimental attempts were made to deposit few layers of low-melting point alloys by FDM process. Mireles et al. [11, 12] experimentally demonstrated the layer deposition of different low-melting point alloys, including Bi58Sn42 at 220 °C temperature and nozzle diameter of 1.588 mm. Simulation studies will provide firsthand information regarding the effect of various parameters on the MFB of the depositing materials during the FDM process, thereby eliminating many expensive trial experiments.

With this objective, this present work was taken to investigate the effect of nozzle geometry on the MFB of eutectic Bi58Sn42 low-melting point alloy during its passage through the nozzle. Eutectic Bi58Sn42 alloy is the most widely used alloy in electronic industries due to the advantages like low-melting point, low cost, environment friendly, and zero shrinkage during solidification [13, 14]. This alloy is generally used as a pattern for casting and electronic industry because of its good electrical and thermal conductivity [15, 16]. This present investigation has been carried out by analytical method and finite element analysis (FEA) using Ansys Fluent software.

2 Materials and Method

This present study investigates the melt flow behavior of Bi58Sn42 at a temperature of 250 °C with variable nozzle geometry. The material properties of Bi58Sn42 alloy and nozzle material were taken from the literature [17–20] and are shown in Table 1.

The assembled view of hot end of the liquefier is illustrated in Fig. 2a. A resistance heater is embedded inside first hole of the heating block that increases block temperature and ultimately heat the nozzle. A thermistor is embedded in second hole for sensing and temperature control of the heating block. The temperature of the heating block and the nozzle are assumed to be same since brass is a very good conductor of heat. The heating block is connected to the liquefier through a heat barrier which restricts the heat transfer from the heating block to the liquefier. The heat barrier and fins shown in Fig. 1 are mainly for maintaining lower temperature for the liquefier. As the temperature below the heat barrier is higher, it is assumed that the alloy melts only inside the nozzle. This present investigation assumes that the

Table 1 Thermophysical properties of the materials

Bi58 Sn42 alloy	
Density [17]	8560 kg/m ³
Specific heat [17]	201 J/kg K
Thermal conductivity [18]	18.2 W/m K
Viscosity [19]	2.1 mPa s,
Nozzle material (brass)	
Density [20]	9490 kg/m ³
Specific heat [20]	380 J/kg K
Thermal conductivity [20]	109 W/m K

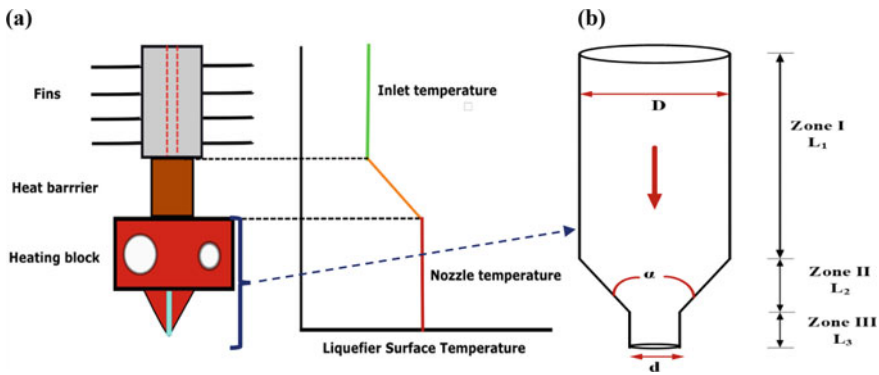


Fig. 2 a Geometry of hot end of the liquefier and liquefier surface temperature distribution, b 2D nozzle geometry used for numerical analysis

nozzle is maintained at a constant temperature. Bi58Sn42 LMP alloy has achieved the nozzle temperature and in a molten state at the inlet of the nozzle.

The nozzle geometry considered for the simulation is shown in Fig. 2b. The nozzle geometry is subdivided into three zones: Zone I is a cylindrical section of diameter “D” and length L_1 , zone II is conical section of cone angle “ α ” and length L_2 , and zone III is a capillary section with diameter “d” and length L_3 . The inlet diameter “D” of the nozzle and length “ L_1 ” of the cylindrical section of zone I were kept constant 2 mm and 11 mm, respectively, as recommended in the previous study [21]. Similar nozzle geometry has been used for the simulation of MFB analysis of polymeric materials and composites [22–24]. Variables considered for the study are nozzle exit diameter (d), nozzle angle (α), and filament inlet velocity (V). Nozzle diameter studied varies from 0.4 mm to 0.8 mm with an increment of 0.1 mm and nozzle angles considered are 60°, 90°, and 120°. Flow behavior is investigated at filament inlet velocities 1 mm/s, 2 mm/s, and 3 mm/s.

2.1 Analytical Method

It is essential to estimate pressure drop for calculating the amount of force required to feed the filament inside the liquefier. The analytical method used was following formulation of Bellini et al. [25] and Roxas et al. [26]. The pressure drop across the nozzle was derived from the momentum balance equation assuming the following [27]: (i) The melt is incompressible, (ii) flow is laminar and steady, (iii) no-slip condition at the boundary, and (iv) flow is fully developed. These general equations are derived using power-law relationship of viscosity;

$$\Delta P_1 = 2L_1 \left(\frac{v}{\phi}\right)^{\frac{1}{m}} \left(\frac{m+3}{(D/2)^{m+1}}\right)^{\frac{1}{m}} \exp\left[\alpha\left(\frac{1}{T} - \frac{1}{T_\alpha}\right)\right] \tag{1}$$

$$\begin{aligned} \Delta P_2 = & \left(\frac{2m}{3 \tan(\frac{\alpha}{2})}\right) \left(\frac{1}{(\frac{D}{2})^{m+3}} - \frac{1}{(\frac{d}{2})^{m+3}}\right) \left(\frac{v}{\phi}\right)^{\frac{1}{m}} \\ & \times \left(\frac{D}{2}(m+3)2^{m+3}\right)^{\frac{1}{m}} \times \exp\left[\alpha\left(\frac{1}{T} - \frac{1}{T_\alpha}\right)\right] \end{aligned} \tag{2}$$

$$\Delta P_3 = 2L_3 \left(\frac{v}{\phi}\right)^{\frac{1}{m}} \left[\frac{(m+2)(\frac{D}{2})^2}{(\frac{d}{2})^{m+3}}\right] \exp\left[\alpha\left(\frac{1}{T} - \frac{1}{T_\alpha}\right)\right] \tag{3}$$

The total pressure drop inside the nozzle,

$$\Delta P = \Delta P_1 + \Delta P_2 + \Delta P_3 \tag{4}$$

where L_1 , L_2 , and L_3 are the lengths of respective zones, D and d are inlet and exit diameter of the nozzle, respectively, α is the nozzle angle, ϕ is the fluidity, m is the power-law index, T_α is the temperature at which melt flow property is calculated, and T is the working temperature. In this present study, $T_\alpha = T$ is assumed. The viscosity of molten metal is independent of shear rate, unlike polymer melt. For this present study, Newtonian flow behavior through the nozzle is considered. The value of the power-law index (m) is taken 1 for a Newtonian fluid. The fluidity (ϕ) is the reciprocal of viscosity of the melt. Hence, the total pressure drop inside the nozzle can be calculated by using the above Eqs. 1–4.

2.2 Finite Element Analysis Modeling

In this present work, finite element analysis software Ansys Fluent was used to simulate the melt flow through the nozzle. 2D axisymmetric nozzle geometry, created by the Ansys model, was used for the simulation. Nozzle dimensions such as inlet

diameter (D), length of the cylindrical section (L_1), and capillary length (L_3) are 2 mm, 11 mm, and 0.5 mm, respectively, were set as a constant parameter [21, 24]. Three variable parameters including nozzle angle (α), nozzle exit diameter (d), and filament inlet velocity (V). The following assumptions were made for the simulation: Melt flow is considered steady-state flow; flow is fully developed and laminar; no-slip boundary condition at the wall and temperature of the nozzle is constant. The Navier–Stokes momentum equations and continuity equation (conservation of mass) are the primary governing equations for the finite element analysis. It was assumed that the Bi58Sn42 alloy has attained the temperature of the nozzle and is completely molten at the inlet of the nozzle. The velocity boundary condition was applied at the inlet, and constant pressure boundary condition was set at the nozzle exit. Molten metal enters the nozzle with constant filament inlet velocity. The constant pressure of 1 atm was set at the exit of the nozzle. The nozzle wall was maintained at a constant temperature of 250 °C. Acceleration due to gravity $g = 9.81 \text{ m/s}^2$ was also considered that acting along the flow direction. For meshing the 2D axisymmetric nozzle geometry, quadrilateral mesh elements were used for the accurate result [28]. The simulation was performed at different mesh element size as results dependents on the mesh size. The simulation was performed at varying mesh sizes $8 \times 10^{-6} \text{ m}$, $7 \times 10^{-6} \text{ m}$, and $6 \times 10^{-6} \text{ m}$. No significant change was observed in nozzle exit velocity with the increase in number of mesh elements, whereas a significant difference was observed for pressure drop. The model was optimized at $7 \times 10^{-6} \text{ m}$ mesh size and 232,597 elements for the nozzle of 0.4 mm diameter and 120° nozzle angle, beyond which no significant change was observed. Hence, all the simulations were performed at an optimized quadrilateral mesh size of $7 \times 10^{-6} \text{ m}$. The steady-state simulations were carried out at convergence criteria of 10^{-7} RMS.

3 Results and Discussion

The melt flow characteristics that have been investigated in present study are pressure drop across the nozzle and melt flow velocity through the nozzle. The results were obtained for varying nozzle angle (α), nozzle exit diameter (d), and filament inlet velocity (V) as mentioned in Sect. 2.

3.1 Results of Analytical Method

The total pressure drop (ΔP) inside the nozzle is an algebraic sum of pressure drop in each zone of the nozzle, as discussed in Sect. 2.1. The pressure drop was calculated for varying nozzle angles; 60°, 90°, and 120° at constant filament inlet velocity of 1 mm/s. For each nozzle angle, nozzle exit diameters (d) were varied as 0.4, 0.5, 0.6, 0.7 mm, and 0.8 mm. It was observed that pressure drop decreases with increase in nozzle exit diameter and nozzle angle, as shown in Fig. 3a. It was

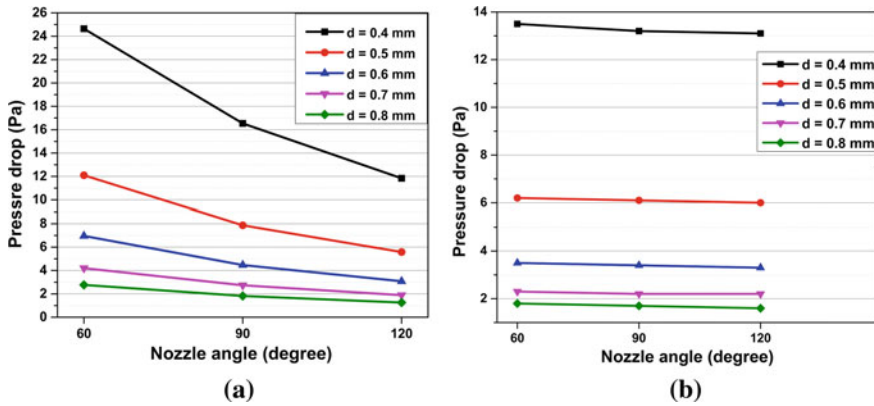


Fig. 3 Pressure drop results: **a** analytical method, **b** finite element analysis

observed that the trends of pressure drop variation for each nozzle angle are similar for all nozzle exit diameters. The equations used for calculation are ideal, subjected to many assumptions, and very sensitive to the minor changes in flow property and nozzle geometry. According to Roxas et al. [26], analytical technique does not model actual flow behavior, hence only analytical technique is not appropriate to estimate the pressure drop.

3.2 Results of Finite Element Analysis

2D axisymmetric melt flow through the nozzle was simulated using finite element software, Ansys Fluent. The pressure drop was computed for different nozzle angles and nozzle diameter as mentioned in Sect. 2 at varying filament inlet velocity 1, 2, and 3 mm/s. It was observed that pressure drop decreases with increase in nozzle diameter for constant nozzle angle. The change in pressure drop with increase in nozzle diameter from 0.4 to 0.6 mm is more, but further increase in nozzle diameter from 0.6 to 0.8 mm change in pressure drop is less. So, it can be concluded that 0.6 mm nozzle diameter is optimized nozzle diameter for better deposition. For constant nozzle exit diameter, pressure drop decreases with the increase in nozzle angle but not much significant than the change in nozzle diameter, as shown in Fig. 3b. Figure 4a shows the comparison of pressure drop results between FEA simulation and analytical method for 1 mm/s filament velocity. To avoid congestion, the pressure drop results of 0.4, 0.6, and 0.8 mm nozzle exit diameter only are compared for better visualization. For 0.4 mm nozzle exit diameter, the significant difference of pressure drop was observed between analytical technique and simulation results because mathematical equations are ideal derived within assumptions, frictional loss is not considered [26]. With the increase of nozzle exit diameter, the deviation of analytical results from finite element analysis is less. For higher nozzle exit diameter (0.8 mm), analytical

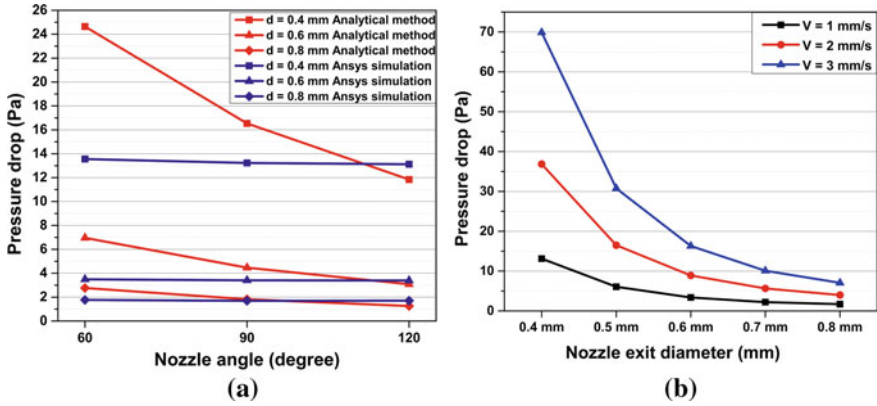


Fig. 4 a Comparison of pressure drop results between analytical technique and finite element analysis for a filament inlet velocity of 1 mm/s, b finite element analysis: Pressure drop versus nozzle exit diameter for different filament inlet velocity

results have good agreement with FEA results. For 120° nozzle angle, the average percentage error of pressure drop across the nozzle was approximate 9%.

It was observed that filament inlet velocity has a significant impact on pressure drop. For filament inlet velocity 3 mm/s, a small change of nozzle diameter from 0.4 to 0.6 mm causes a remarkable variation in the pressure drop from 69.87 to 16.3 Pa, as shown in Fig. 4b. The pressure contour map showed that initially, melt flow pressure was maximum at the inlet and maintained until it reached the conical zone. Then, dropped to preset pressure boundary condition at the exit of the capillary zone, as

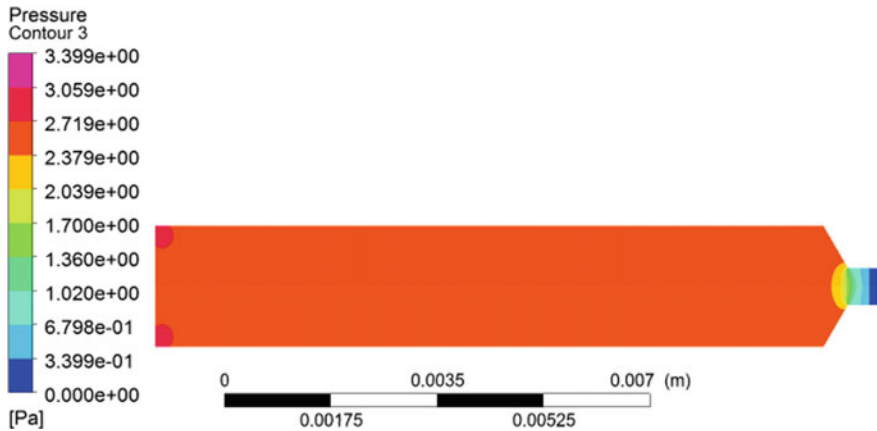


Fig. 5 Pressure distribution along the length of the nozzle for 0.6 mm nozzle diameter, 120° nozzle angle, and 1 mm/s filament inlet velocity

shown in Fig. 5. It was observed that major pressure drop takes place at capillary length (zone III) of nozzle geometry.

Nozzle exit velocity decreases with increase in nozzle exit diameter. The nozzle angle has no significant effect on nozzle exit velocity, as shown in Fig. 6a. As the nozzle diameter increases, the effect of filament inlet velocity on pressure drop across the nozzle and nozzle exit velocity decreases, as shown in Fig. 6b.

Figure 7 shows melt flow velocity profiles through the nozzle for 120° nozzle angle and 1 mm/s filament inlet velocity. Simulation results showed that melt flow through

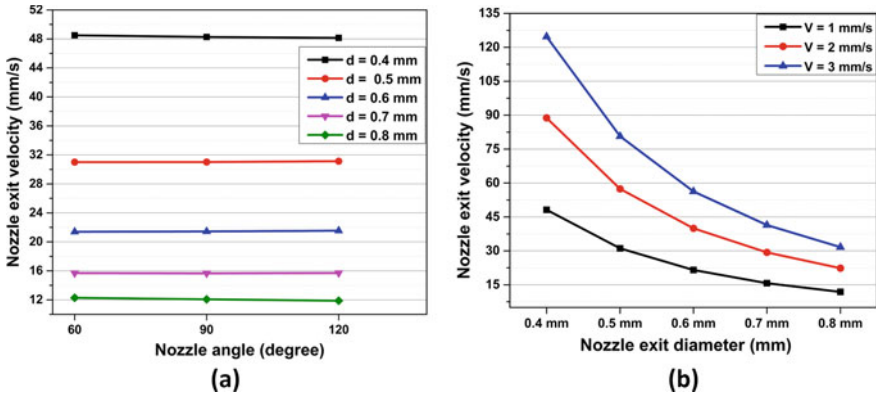


Fig. 6 FEA results: a nozzle exit velocity versus nozzle angle plot for different nozzle diameter, b nozzle exit velocity versus nozzle exit diameter plot for different filament inlet velocity

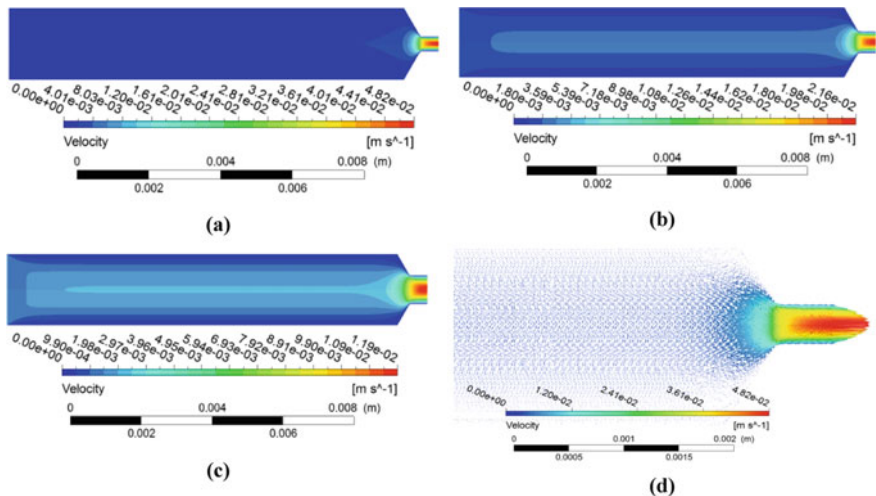


Fig. 7 Velocity contour map for 120 nozzle angle and 1 mm/s filament velocity: a 0.4 mm nozzle diameter, b 0.6 mm nozzle diameter, c 0.8 mm nozzle diameter, and d velocity vector map of 0.4 mm nozzle diameter

the nozzle was smooth and no backflow was observed. For 0.4 mm nozzle diameter, melt flow velocity is constant till near the conical section, then velocity changes rapidly and attains maximum value in capillary section. While as the nozzle exit diameter increases, velocity profiles vary from the inlet itself and reach a maximum value at the capillary section. It was observed that velocity near the wall is zero due to the no-slip condition, and the wall is stationary. Maximum melt flow velocity was observed at the center of the nozzle, as shown in Fig. 7d.

4 Conclusion

The melt flow behavior (MFB) of eutectic Sn-Bi LMP alloy through the nozzle has been investigated using analytical technique and finite element analysis. Pressure drop across the nozzle calculated by analytical method has deviation with finite element analysis results. A significant deviation was observed for 0.4 mm nozzle exit diameter because equations used in the analytical method are ideal, the frictional loss is not considered and very sensitive for minor changes. The deviation of analytical results with finite element analysis results decreases with the increase of nozzle exit diameter. It was observed that for the higher nozzle exit diameter, 0.8 mm, the analytical results have good agreement with finite element analysis.

From both analytical method and finite element analysis, it was observed that pressure drop decreases with increase in nozzle angle and nozzle exit diameter. It was observed that nozzle exit diameter significantly affects both pressure drop and nozzle exit velocity than nozzle angle. FEA results show that maximum melt flow pressure was observed at the inlet of the nozzle and remains constant till conical zone and subsequently drops at zone II and zone III of the nozzle. It was also observed that filament velocity has a significant effect on pressure drop. FEA results show that melt flow through the nozzle was smooth, and no backflow was observed for all nozzle angles and nozzle diameters with varying filament velocity. Velocity profile shows that melt flow velocity was maximum at the center and zero at the wall due to no-slip condition and the wall was stationary. It was also observed that significant changes in melt flow velocity took place at the nozzle's conical zone and capillary zone.

References

1. ASTM F2792-12a Standard terminology for additive manufacturing technologies. ASTM International, West 2012 Conshohocken, PA, USA
2. Bogue R (2013) 3D printing: the dawn of a new era in manufacturing. *Assem Autom* 33(4):307–311
3. Günther D, Heymel B, Günther JF, Ederer I (2014) Continuous 3D-printing for additive manufacturing. *Rapid Prototyping J* 20(4):320–327

4. Kruth J-P, Mercelis P, Van Vaerenbergh J, Froyen L, Rombouts M (2005) Binding mechanisms in selective laser sintering and selective laser melting. *Rapid Prototyping J* 11(1):26–36
5. Mueller B, Kochan D (1999) Laminated object manufacturing for rapid tooling and pattern-making in foundry industry. *Comput Ind* 39:47–53
6. Kudelski R, Cieslik J, Kulpa M, Dudek P, Zagorski K, Rumin R (2017) comparison of cost, material and time usage in FDM and SLS 3D printing methods. In: XIIIth international conference on perspective technologies and methods in MEMS design (MEMSTECH), IEEE Xplore, pp 12–14
7. Ning F, Cong W, Qiu J, Wei J, Wang S (2015) Additive manufacturing of carbon fiber reinforced thermoplastic composites using fused deposition modeling. *Compos B* 80:369–378
8. Hwang S, Reyes EI, Moon K, Rumpf RC, Kim NAMSOO (2015) Thermo-mechanical characterization of metal/polymer composite filaments and printing parameter study for fused deposition modeling in the 3D printing process. *J Electron Mater* 44(3):771–777
9. Jerez-mesa R, Travieso-Rodriguez JA, Corbella X, Busqué R, Gomez-Gras G (2016) Finite element analysis of the thermal behavior of a RepRap 3D printer liquefier. *Mechatronics* 36:119–126
10. Serdeczny MP, Comminal R, Mollah T, Pedersen DB, Spangenberg J (2020) Numerical modeling of the polymer flow through the hot-end in filament-based material extrusion additive manufacturing. *Addi Manuf* 36:101454
11. Mireles J, Kim H, Espalin D, Medina F, Macdonald E, Wicker R (2013) Development of a fused deposition modeling system for low melting temperature metal alloys. *J Electron Packagaging* 135:1–6
12. Mireles J, Espalin D, Roberson D, Zinniel B, Medina F, Wicker R (2012) fused deposition modeling of metals. In: *Proceeding*, pp 836–845
13. Gorgievski M, Mitrovica K (2018) Study of microstructure and thermal properties of the low melting Bi–In–Sn eutectic alloys. *Mater Res* 21(6):1–8
14. Kamal M, Mazen S, El-bediwi AB, Kashita E (2006) Microstructure, electrical, mechanical and thermal properties of melt-spun bismuth–tin eutectic alloy. *Radiat Eff Defects Solids* 161(2):143–148
15. Wang F, Chen H, Huang Y, Liu L, Zhang Z (2019) Recent progress on the development of Sn – Bi based low-temperature Pb-free solders. *J Mater Sci Mater Electron* 30(4):3222–3243
16. Ribas M et al (2015) Comprehensive report on low temperature solder alloys for portable electronics. In: *Proceedings of SMTA international*, Rosemont, IL, pp 176–183
17. Deng Y, Jiang Y, Liu J (2021) Low-melting-point liquid metal convective heat transfer: a review. *Appl Thermal Eng* 193:117021
18. Dutchak YI, Osipenko VP, A, Izvestiya PV (1968) Thermal Conductivity of Sn-Bi alloys in the solid and liquid states. *Izvestiya VUZ. Fizika* 11(10):154–156
19. Lee JHO, Lee DN (2001) Use of thermodynamic data to calculate surface tension and viscosity of Sn-based soldering alloy systems. *J Electron Mater* 30(9):1112–1119
20. Papon MEA, Haque A, Ali M, Sharif R (2017) Effect of nozzle geometry on melt flow simulation and structural property of thermoplastic nanocomposites in fused deposition modeling, American society of composite, thirty-second annual technical conference, Purdue Stewart center, 23–25 Oct 2017
21. Nienhaus V, Smith K, Spiehl D, Dörsam E (2019) Investigations on nozzle geometry in fused filament fabrication. *Addi Manuf* 28:711–718
22. Peng F, Vogt BD, Cakmak M (2018) Complex flow and temperature history during melt extrusion in material extrusion additive manufacturing. *Addit Manuf* 22:197–206
23. Sukindara NA, Ariffinb MKA, Baharudinb HTH, JaafarCNA, Ismail MIS (2016) Analyzing the effect of nozzle diameter in fused deposition modeling for extruding polylactic acid using open source 3D printing. *Jurnal Teknologi* 10:7–15
24. Wan Muhamad WM, Saharudin MS, Abd Wahid KA, Saniman MNF, Reshid M (2020) Nozzle design for fused deposition modeling 3D printing of carbon fibre reinforced polymer composite component using simulation method. *PalArch's J Archaeol of Egypt/Egyptology* 17(9):4192–4204

25. Bellini A, Bertoldi M (2004) Liquefier dynamics in fused deposition. *J Manuf Sci Eng* 126:237–246
26. Roxas M, Ju S (2008) Fluid dynamics analysis of desktop-based fused deposition modeling rapid prototyping. University of Toronto
27. Michaeli W (1992) *Extrusion dies for plastics and rubber: design and engineering computation*, second edition. Hanser ed, New York
28. Phan DD, Horner JS, Swain ZR, Beris AN, Mackay ME (2020) Computational fluid dynamics simulation of the melting process in the fused filament fabrication additive manufacturing technique. *Addi Manufa* 33:101161

Effect of the Rolling Direction on the Mechanical and Microstructural Properties of AISI 316L Stainless Steel Welded Joint



Vivekananda Haldar and Sukhomay Pal

Abstract The present work discusses the effect of rolling direction on the micro plasma arc welded joint of austenitic AISI 316L stainless steel (SS) sheet. The methodology of this work is entirely based on experimental analysis. The base metal samples are prepared based on the rolling direction, i.e., parallel to the rolling direction, diagonal direction, and transverse direction. After that, the sheets are butt welded by using micro plasma arc welding with particular welding parameters. Weld strength and ductility are measured and compared with the parent metal. A metallography test is carried out to correlate joint strength and elasticity to the microstructural variation. In addition, joint hardness and fractography tests are conducted. From the experimentation, it is observed that the sample welded in the diagonal direction displayed maximum ductility. Whereas the welded joint in the transverse direction has maximum strength and hardness, compare to others.

Keywords Rolling direction · Micro plasma arc welding · AISI 316L · Stainless steel

1 Introduction

The austenitic 316L stainless steel (SS) is popular for its high corrosion resistance property in corrosive applications. It contains chromium (Cr) and molybdenum (Mo) as alloying elements, which enhance its corrosion resistivity [1]. The austenitic 316L SS also contains a high amount of manganese (Mn) and nickel (Ni), which makes it stable at room temperature and cannot be hardened by heat treatment operation [2]. Austenitic SS are among the most widely used components in the applications of kitchen appliances, spacecraft [3], etc. They also have a large range of applications,

V. Haldar (✉) · S. Pal
Department of Mechanical Engineering, IIT Guwahati, Guwahati, Assam 781039, India
e-mail: vivek176103115@iitg.ac.in

S. Pal
e-mail: spal@iitg.ac.in

from room temperature to cryogenic temperature. But at cryogenic temperature, it loses its ductility [4]. There are some limitations of this steel in the field of structural materials and in critical engineering components due to its low yield strength. However, it has excellent cold workability, which enables us to use the work hardening phenomenon to improve their strength. During the fabrication of the sheet from the ingot, microstructure of the sheet gets deformed along the rolling direction and develops deformation twinning and dislocation density [5]. Hence, the steel gets strain hardened and it shows an anisotropic behavior in different directions. Many research works have been studied in the field of strain hardening behavior of AISI 316L SS [6, 7]. Peng et al. [8] investigated the effect of pre-strain on tensile behavior of austenitic 316L SS. They found that due to pre-strain operation, the strain hardening property got reduced. They also found that the dislocation density and number of twinning increased in the pre-strained samples.

The welded joint of these steel sheets is used in the automobile, petrochemical, food processing industries, etc. However, due to the welding operation, the mechanical and microstructural properties of the joint were modified. Hence, welding such thin rolled sheet is a challenging task for maximum ductility and strength point of view. Micro plasma arc welding is popular for thin sheet welding, and it can able to weld up to 0.1 mm sheets [9]. So, many authors have investigated micro plasma arc welding of thin sheet materials [10, 11]. Sahu et al. [12] studied on dissimilar joining of 316L SS and Inconel 718. They found that weld bead measurements obtained numerically and experimentally showed strong accuracy. Prasad et al. [13] optimized the process parameters for joining 316L SS sheets by micro plasma arc welding. They found that the welding speed has the greatest impact on the weld bead profile. Saha et al. [14] studied the work hardening behavior of 316L SS micro plasma arc welded joint. They observed highest hardness value in the fusion zone due to the presence of ferrite-austenitic matrix. They also found that the strain rate has a significant impact on the tensile properties of the welded joints.

Based on the literature review, the following conclusions can be drawn that many investigations have been carried out for the joining of austenitic 316L SS by using micro plasma arc welding. Most of the investigations are based on mechanical and metallurgical characterizations. There is the least literature found on the effect of rolling direction of micro plasma arc welded joint. Therefore, the motivation of the current research work is to investigate the effect of rolling directions, namely parallel to the rolling direction (RD), diagonal to the rolling direction (DD), and transverse to the rolling direction (TD) on the micro plasma arc welding of austenitic 316L SS sheets.

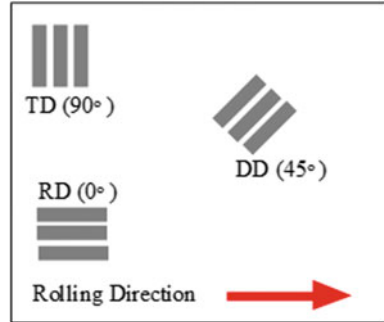
2 Experimental Procedure

Thin AISI 316L SS sheets with a dimension of 0.5 mm thick, 110 mm length, and 60 mm width were butt welded by micro plasma arc welding. The chemical composition of the base metal is presented in Table 1. Three different directions of

Table 1 Chemical composition of AISI 316L stainless steel (wt.%)

Cr	Ni	Mn	Mo	Si	Nb	Co	W	S	P	Al	C	Fe
17.2	9.9	2.0	1.8	0.4	0.4	0.3	0.3	0.2	0.1	0.1	0.03	67.3

Fig. 1 Layout of sheet orientation for cutting



base metal sheets were prepared, i.e., in RD (0°), DD (45°), and TD (90°) as presented in Fig. 1. The welding process was conducted by a medium current capacity (50 A) and a water-cooled micro plasma arc welding machine (model EWM-50). The welding torch was operated at straight polarity with a DC power source and the operating voltage of the device was constant (25 V). Pure 99.8% Ar gas was used as plasma as well as a shielding gas. The welding parameters considered in this research are mentioned in Table 2. At the time of welding, the torch was fixed and the workpiece moved with a constant travel speed. Before welding, the parent sheets were cleaned with acetone to remove the foreign particles and oils from the surfaces.

A microstructural study was carried out to determine the joint morphology of the welded specimens by using an optical microscope. The average grain size of the base metal and heat affected zone (HAZ) were measured by line intercepting method. The field-emission scanning electron microscope was used to study the fractography characteristics of the fractured samples.

The tensile specimens were prepared according to the ASTM-E8M standard along RD, DD, and TD for both the base and joint sheets. The tensile test was carried out on a 250 kN universal testing machine with a constant strain rate of 1 mm/s for both the base metal and welded samples. In each direction, at least three tensile samples were tested. During the test, the load–displacement data was recorded and used to

Table 2 Welding parameters used during joining processes

Welding parameters	Value
Current (A)	10.5
Travel speed (mm/s)	3.5
Stand of distance (mm)	1.7
Nozzle diameter (mm)	1.2

study the mechanical behavior of the base material and joint specimens. Furthermore, the hardness of the base zone (BZ), HAZ, and fusion zone (FZ) were measured by Vickers microhardness tester using 0.2 kg load. The hardness test was carried along a straight line in the cross section of the welded joint.

3 Results and Discussion

3.1 Microstructural Analysis

The microstructural analysis of the austenitic 316L showed that the base metal consists of an austenite structure with equiaxed grain distribution. The average grain size in RD, DD, and TD was found to be 12.91 μm , 12.03 μm , and 9.67 μm (Fig. 2), respectively. Annealing twins were observed in all the three above-mentioned cases. The delta ferrite was deposited at the austenite boundary due to the presence of alloying elements like Cr and Mo during the primary processing of the metal [15]. Three different zones can be visualized in the welded joint, i.e., FZ, HAZ, and unaffected BZ. The FZ of every sample had a duplex structure of ferrite and austenite, shown in Fig. 3a–c. The morphology of ferrite in the weld center was vermicular ferrite. However, some directionality was observed in the microstructural morphology as one moves closer to the transition line from the weld center. This happened due to the variation in solidification type and grain growth at the weld center and near to transition line [16]. The volume fraction of ferrite at the FZ of the specimens was measured as 17.98%, 15.34%, and 20.62% for the RD, DD, and TD cases, respectively. The variation in the volume fraction of ferrite structure appeared due to the different sheet orientations [17].

From Fig. 3d–f it was found that there was no grain growth at the HAZ of the welded specimens. As the austenitic 316L SS has molybdenum, vanadium is allowing elements, which were the main responsible for preventing the grain growth at the HAZ [1]. Moreover, the 316L sheets used for this experiment were annealed heat-treated, and this was another reason to intact the grain at the HAZ [15]. Some amount of

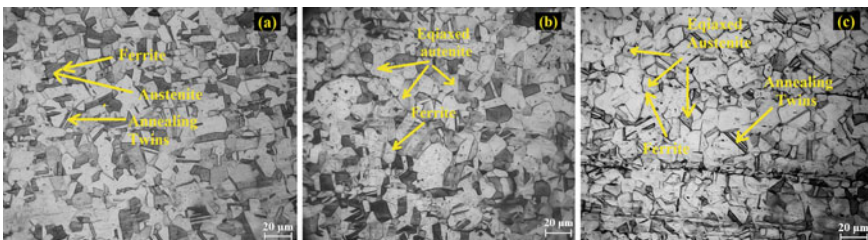


Fig. 2 Microstructure of the base material in **a** rolling direction, **b** diagonal direction, and **c** transverse direction

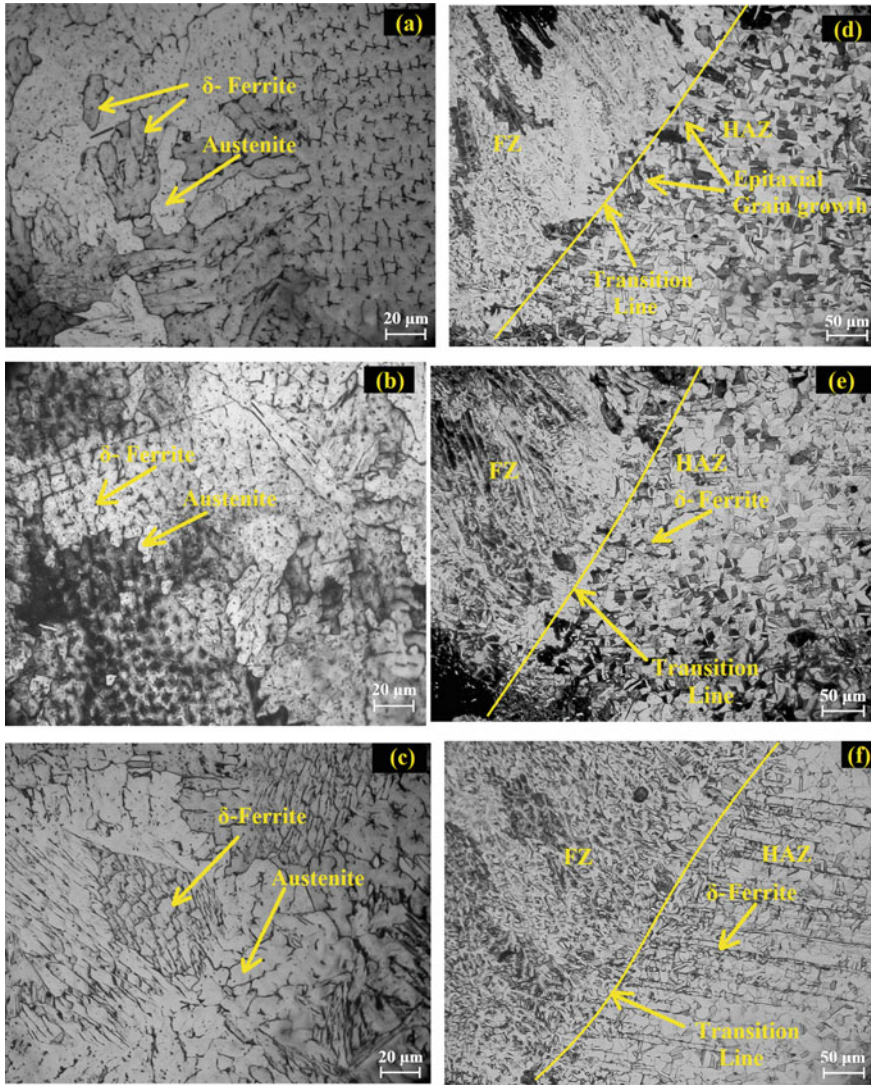


Fig. 3 a–c morphology of FZ and d–f morphology of HAZ of the welded joints in RD, DD, and TD, respectively

ferrite can be observed at the HAZ microstructure (Fig. 3d–f). Because the austenite got heated up to the solidus temperature; as a result, the formation of ferrite took place.

3.2 Uniaxial Tensile Test

The uniaxial tensile test was performed and the engineering stress–strain curve for the base metal and the welded sample is shown in Fig. 4. It was found that the base metal in TD has maximum elongation (~ 67%). The base metal in RD was found minimum elongation (~ 57%) and maximum ultimate tensile strength (~ 684 MPa). The DD sample exhibited average elongation (~ 60%) and minimum UTS (~ 647 MPa).

The welded tensile samples, i.e., the cross-weld specimens, were collected from the transverse portion of the weld joints. The welded specimens in RD were found with minimum ductility (~ 30%) and minimum joint strength (~ 618 MPa). The sample in DD exhibited maximum ductility (~ 53%), which was 88% of the base material ductility. The welded joint in TD showed average ductility (~ 33%) and maximum joint strength (~ 648 MPa), 95% of the base material strength. The strain hardening exponent (n) and strain hardening coefficient (K) were also calculated using a plot between the log of true stress and true strain at the plastic region.

The variation of the ‘ n ’ values for the above-mentioned directions of the base materials was more than the welded samples. The base material in RD and TD samples were found with an equal magnitude of ‘ n ’ value (~ 0.45). On the other hand, the base material in DD showed a minimum ‘ n ’ value (~ 0.43). The welded joint in DD had a maximum ‘ n ’ value (~ 0.45) and RD and TD had equal ‘ n ’ values (~ 0.38). The variations of ‘ n ’ occurred due to the microstructural changes at the fusion zone, which is discussed earlier. The obtained ‘ K ’ values for the welded joint in RD, DD, and TD were 1232 MPa, 1326 MPa, and 1252 MPa, respectively.

The failure of the welded tensile samples took place from the fusion zone, shown in Fig. 4b. The failure mode of the welded joint is described in Fig. 5. Lots of voids, microvoids, and dimples are found on the fracture surfaces, which indicates

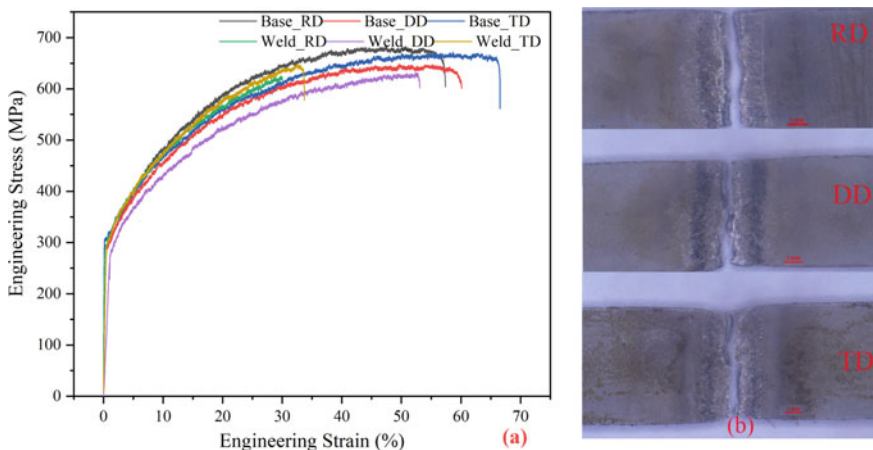


Fig. 4 a Engineering stress–strain curve for 316L SS base and welded samples in different orientation b macro view of tensile failure welded specimens in RD, DD, and TD

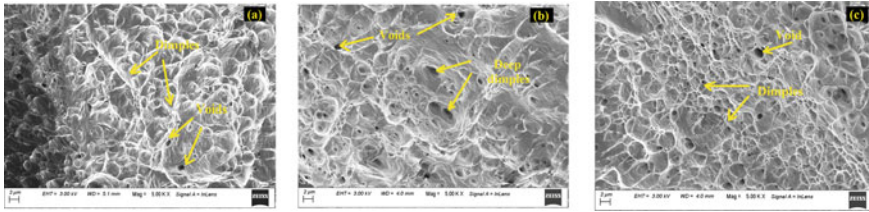


Fig. 5 Fractography of the fracture surface in a RD b DD and c TD

the ductile mode of failure. From Fig. 5b, it can be visualized that the DD specimen fracture surface had more narrow and deep dimples as compared with other directions.

3.3 Microhardness

The average microhardness values of the base materials in RD, DD, and TD were (~ 166 Hv), (~ 163 Hv), and (~ 169 Hv), respectively (shown in Fig. 6). The large fluctuations in microhardness were observed at the FZ. This happened due to the different microstructure at different positions of the welded joint. In all samples, the FZ microhardness was higher compared with the HAZ and unaffected BZ. The average microhardness of the FZ in TD was maximum (~ 200 Hv) and in DD was minimum (~ 189). The δ -ferrite consists of a body-centered cubic structure which is

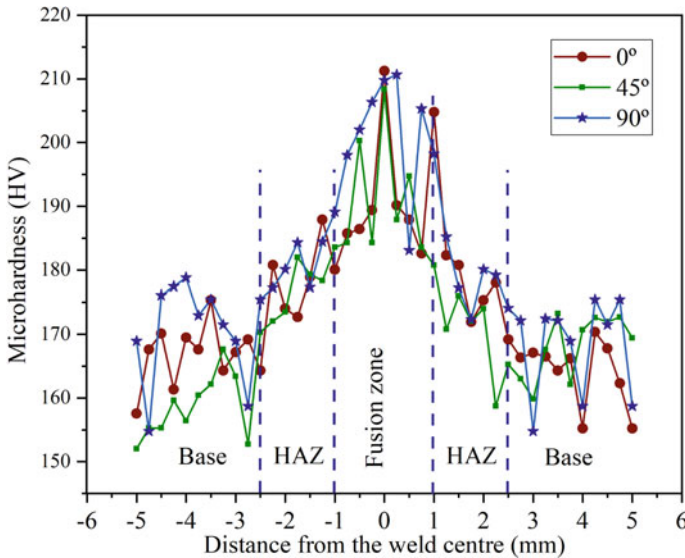


Fig. 6 Microhardness profiles of the welded joint across the cross section

harder than that of the face-centered cubic austenite phase. Hence, due to the different ferrite fractions, the hardness variation took place for the different specimens. The hardness at the HAZ was greater than that of the base material for all samples. It was happened due to the significant amount of ferrite content and lack of grain growth at the HAZ.

4 Conclusions

In this investigation, austenitic 316L SS sheets were butt welded using micro plasma arc welding in different rolling orientations (0°, 45°, 90°). The mechanical and microstructural investigations were carried out to evaluate the weld quality. Following are the major conclusions of the study.

1. The defect-free weld joint is achieved by using micro plasma arc welding of a thin 0.5 mm austenitic 316L SS sheet.
2. The microstructural analysis exhibits that the base material has an equiaxed grain orientation with austenite and ferrite phases. The annealing twinning boundary is more visible along with the RD specimen. The FZ consists of a predominant austenitic microstructure with δ -ferrite. There is no grain growth observed at the HAZ, and some amount of ferrite is observed at this zone. The fractography analysis confirmed that the failure of weld specimens is ductile in nature.
3. The welded joint in DD has maximum elongation. On the other hand, the TD welded joint shows maximum joint strength with average elongation, and this happens due to the microstructural changes at the FZ.
4. The microhardness result shows that the fusion zone is more brittle than the BZ and HAZ. The HAZ hardness is more than that of unaffected BZ because of the presence of ferrite. Higher hardness is observed in the TD sample.

References

1. Sánchez-Tovar R, Montañés MT, García-Anton J (2010) Effect of different micro-plasma arc welding (MPAW) processes on the corrosion of AISI 316L SS tubes in LiBr and H₃PO₄ solutions under flowing conditions. *Corros Sci* 52(4):1508–1519
2. Soltani HM, Tayebi M (2018) Comparative study of AISI 304L to AISI 316L stainless steels joints by TIG and Nd: YAG laser welding. *J Alloy Compd* 767:112–121
3. Lo KH, Shek CH, Lai JKL (2009) Recent developments in stainless steels. *Mater Sci Eng R Rep* 65(4–6):39–104
4. Paredes M, Grolleau V, Wierzbicki T (2020) On ductile fracture of 316L stainless steels at room and cryogenic temperature level: an engineering approach to determine material parameters. *Materialia* 10:100624
5. Belyakov A, Odnobokova M, Kipelova A, Tsuzaki K, Kaibyshev R (2018) Microstructural evolution and strengthening of stainless steels during cold rolling. In: Muruganant M, Chiraj A,

- Raj B (eds) *Frontiers in materials processing, applications, research and technology*. Springer, Singapore, pp 341–347
6. Xie XF, Jiang W, Chen J, Zhang X, Tu ST (2019) Cyclic hardening/softening behavior of 316L stainless steel at elevated temperature including strain-rate and strain-range dependence. experimental and damage-coupled constitutive modelling. *Int J Plast* 114:196–214
 7. Kale AB, Alluri P, Singh AK, Choi SH (2021) The deformation and fracture behavior of 316L SS fabricated by SLM under mini V-bending test. *Int J Mech Sci* 196:106292
 8. Peng J, Li K, Peng J, Pei J, Zhou C (2018) The effect of pre-strain on tensile behaviour of 316L austenitic stainless steel. *Mater Sci Technol* 34(5):547–560
 9. Tseng KH, Hsieh ST, Tseng CC (2003) Effect of process parameters of micro-plasma arc welding on morphology and quality in stainless steel edge joint welds. *Sci Technol Weld Joining* 8(6):423–430
 10. Baruah M, Bag S (2016) Microstructural influence on mechanical properties in plasma microwelding of Ti₆Al₄V alloy. *J Mater Eng Perform* 25(11):4718–4728
 11. Saikia T, Baruah M, Bag S (2019) On the effect of heat input in plasma microwelding of maraging steel. *Proc Inst Mech Eng Part B J Eng Manuf* 233(3):807–822
 12. Sahu AK, Bag S (2019) Finite element modelling and experimental verification of dissimilar joining between Inconel 718 and SS 316L by micro-plasma arc welding. In: Narayanan RG, Joshi SN, Dixit US (eds) *Advances in computational methods in manufacturing*. Springer, Singapore, pp 231–243
 13. Prasad S, Pal S, Robi PS (2020) Analysis of weld characteristics of micro plasma arc welded thin stainless steel 306 L sheet. *J Manuf Process* 57:957–977
 14. Saha D, Pal S (2019) Microstructure and work hardening behavior of micro-plasma arc welded AISI 316L sheet joint. *J Mater Eng Perform* 28(5):2588–2599
 15. Lippold JC, Kotecki DJ (2005) *Welding metallurgy and weldability of stainless steels*. John Wiley and Sons, Canada
 16. Kulkarni A, Dwivedi DK, Vasudevan M (2020) Microstructure and mechanical properties of A-TIG welded AISI 316L SS-Alloy 800 dissimilar metal joint. *Mater Sci Eng A* 790:139685
 17. Kannan AR, Sankarapandian S, Pramod R, Shanmugam NS (2021) Experimental and numerical studies on the influence of formability of AISI 316L tailor-welded blanks at different weld line orientations. *J Braz Soc Mech Sci Eng* 43(3):1–26

Effect of Tool Movement in Electro-Discharge Machining Process—A Review



Sudhanshu Kumar and Dilip Sen

Abstract Electro-discharge machining (EDM) is a non-contact material removal process having some unique capabilities like there is no need for further machining, easily machine hard materials, no thermal stresses, etc. EDM is used as the reproductive process of shaping, in which the shape of the electrode is imaged in the workpiece. There are lots of parameters that need to be considered in the course of EDM. Flushing of eroded material, surface finish, and material removal rate (MRR) all are imperative parameters for EDM. In the present work, various tool movements are studied, and their impacts on several others parameters with their effects on the machining process are probed. The current study is dedicated to tool movement around the axis, along the horizontal direction, and on the axis.

Keywords EDM · Tool movements · Orbit · Rotation · Linear

1 Introduction

EDM is a mostly used non-contact process of machining for difficult to machine materials. This machining deals easily with complex geometries by providing a high accuracy level. The most distinctive feature is the use of electric spark for removal of material for the machining of electrically conductive objects without hardness which is being concerned. This technique is primarily applied for the manufacturing of dies and molds, where it deals from as small as few microns to few centimeters [1].

In the process of material erosion in the EDM, electrical energy is transformed into thermal energy and applies continuous electric sparks between the workpiece and electrode submerged in a dielectric medium at a particular location. No contact between workpiece and electrode during machining eliminates vibration problems, mechanical stresses, and chatters during machining [2]. The spark produced between electrode and workpiece generates a plasma channel of high-temperature range from 8000 to 12,000 °C or maximum up to 20,000 °C. This high temperature initiates

S. Kumar (✉) · D. Sen
Mechanical Engineering Department, Maulana Azad NIT, Bhopal, India

the melting and heating of material from the workpiece when the spark is turned off the channel of plasma breakdowns. After this, the dielectric fluid reduces the high temperature, and the flow of dielectric fluid in between the gap of workpiece and electrode flushed out the molten material in the form of tiny debris [3]. As reported by the researchers [4–6], electric discharge machining can be performed in gas also. In this method, a thin wall pipe electrode is used for the flow of high-pressure gas which flushes the removed materials from the surface of the workpiece. The ultimate advantage of this method is having almost zero tool electrode wear ratio. With the help of 3D shape tools like cylindrical and tube electrodes, machining can be done very precisely [4].

Conventionally EDM process uses a formed electrode, material is removed by sinking a 3D shape electrode into the workpiece and hence creates a negative impression of the tool into the workpiece. The tool is maintained at a particular distance, and a spark is produced between the gap of the workpiece and electrode [7]. For the production of a particular shape die or mold, a different mirror electrode of die or mold is required.

For the generation of the desired cavity, tool movement in a specific direction is required. During the process of deep holes in the EDM, eroded material does not come out easily from the working gap between the workpiece and tool. By providing motion to the electrode flushing difficulties can be overcome, the motion to the tool increases the flushing action of debris. If the spark is generated at a particular location, localized material removal will be taken place. This will result in uneven material removal from the workpiece. By providing rotary motion to the tool, spark will be distributed evenly over the entire surface and even material removal will be taken place. This will also result in even tool wear. Hence, it can be seen that the rotary motion of the tool provides various benefits in the EDM process like improvement in flushing, machining, even cavity can be generated, even sparking can be produced, etc.

If there is a need for machining in the EDM process by using a very less diameter electrode, it is very difficult to machine the workpiece because a very less diameter tool will melt during sparking in the process of EDM. Alternatively, the rotary motion of the tool allows us to machine a workpiece at a high ampere. The rotary motion of the tool is also beneficial for the generation of deep holes.

There are some restrictions to the rotary motion of the tool. Rotary motion is restricted to circular or cylindrical tool electrodes only. For the generation of rectangular, square, or any other cavity, rotary motion cannot be provided. There is also a problem with the rotary motion of the tool of a very small diameter.

To obtain a particular shape using the EDM process, tool movement according to the geometry of the shape is required. In the current investigation, the focus is on better utilization of tool electrode movements in the EDM process. CNC EDM machine which is free form surfaces is a novel area for researchers and is becoming prevalent [8]. This paper represents the critical tool movements in the EDM process. Tool movements in EDM support debris surfing or eroded particles flushing during machining, which increases MRR along with the surface quality of surfaces.

Before actuation of the tool movement in the EDM, first need to identify the required tool movement for the generation of a cavity. In this regard, tool movement needs to be defined and tool movement selection plays an important role in achieving appropriate dimensional accuracies and surface finish. Die-sinking EDM performance has been enhanced by orbiting motion of the electrode. In this regard, various studies have been done to find better machining capabilities for the motion of tools around the axis. Further discussion on this is illustrated below in the present work.

2 Tool Movements

The study of tool movements can be done via subdivided into three categories, i.e., tool movement around the axis, and on the axis, and in the horizontal direction (Fig. 1).

2.1 Tool Movement Around the Axis

The motion of the tool around the axis is also known as orbital tool movement. Orbital movement of the tool is started along a helical path and spiral for the generation of a cavity as shown in Figs. 2 and 3. By introducing an orbital mechanism in the EDM process, X–Y axis tool movements can be controlled independently. The mechanism can be performed on the helix path by simultaneously moving on all three axes and on the spiral path in which the tool starts moving on X–Y axes after the electrode movement up to the well-defined depth in the direction of the Z-axis. Orbital motion can be defined as a circular translation of the tool electrode.

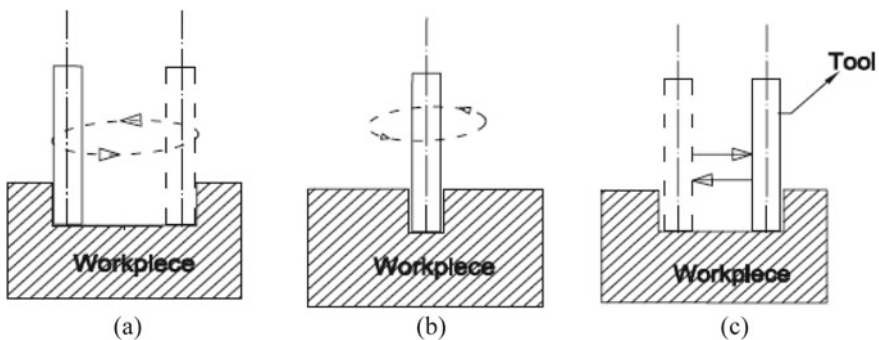


Fig. 1 Schematic representation of tool movements in EDM process **a** around the axis **b** on the axis **c** along the horizontal direction

Fig. 2 Helical tool movement

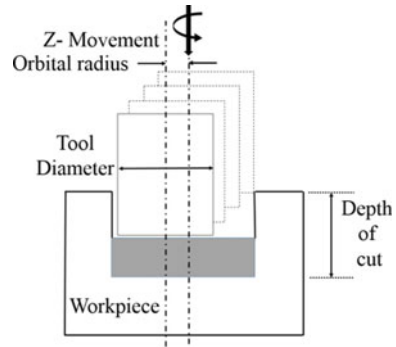
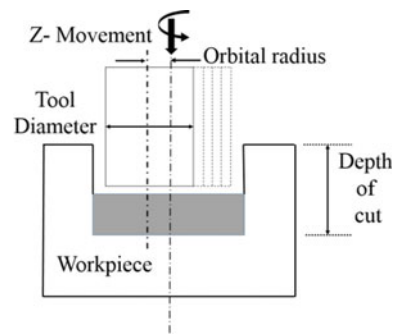


Fig. 3 Spiral tool movement



It is feasible to drill big size holes by using small size electrodes in the trepanning method of electro-chemical discharge machining (ECDM). In this method, ceramic materials which are high strength as well as high temperature resistant non-conductive, are easily machined using the orbital motion of the tool. During machining of ceramics, micro-cracks develop on the upper phase of the surface, and to overcome this problem and for enhancement of machining performance, a cylindrical electrode of abrasive with spring-fed mechanism has been used. The results of this research revealed that pulsed DC voltage reduces the cracking for non-conductive material, and these types of materials abrasive electrodes provide better machining and can drill deep holes compare to copper electrodes. Abrasive particles over the tool improve surface integrity and dimensional accuracy of machined surfaces. This research showed techniques to improve the quality of holes using ECDM [9]. Dave et al. [1] suggested a multi-response optimization method for EDM orbital tool movement. The cited works of the literature suggest that the orbital tool movement provides efficient and stabilized sparks that improve MRR, TWR, and surface roughness. Taguchi loss function, signal-to-noise ratio (S/N), and ANOVA technique are used, and the proposed optimization method's effectiveness is identified by conducting some experiments. The results concluded that orbital radius and current both are the utmost major parameters that affect orbital tool movement in EDM. It has been found that by assigning weight factors to MRR, TWR, and surface

roughness, their combinations have a marginal effect on parameters. It is determined that the multi-response optimization method used in the study helps to watch out TWR, MRR, and SR at the same time during the orbital tool actuation in the EDM process.

Before actuation of the tool movement in the EDM, first, need to identify the required tool movement for the generation of the cavity. In this regard, tool movement needs to be defined and tool movement selection plays an important role in achieving appropriate dimensional accuracies and surface finish. Die-sinking EDM performance can be enhanced by orbiting motion of the electrode. EL taweel and Hewidy [10] studied and validated spiral and helix mode of circular planetary EDM between different parameters like machining time, MRR, dimensional accuracy, and surface finish. The study revealed that the planetary tool motion controls the shape of the workpiece with several dimensional tolerances and SR quality. By increasing the tool eccentricity for helix mode, roundness error can be improved than spiral mode. These results of the analysis are beneficial to get better dimensional accuracy, surface quality, and machining time.

As MRR, TWR, surface roughness, dimensional stability, and tolerances are important elements that need to consider for performance enhancement of EDM. Besides these factors, flushing is also an important parameter need to draw attention to at the time of machining. Ziada and Koshy [11] studied and provided a scheme that enables flushing by providing motion between the electrodes. Kinematics of Reuleaux triangle (RT) is used for flushing through synchronous orbiting of rotating curvilinear tool. The tool route recommended and the curvilinear tool used in this study is inspired by the principle of RT. This arrangement helps the machining of regular as well as non-regular polygonal shapes with sharp corners. As reported in the literature RT cannot be directly for machining of square shapes with sharp corners, some modifications need to be done in the RT. By modifying the geometry, the equilateral sides of RT are replaced by three circular arcs. This modified geometry of RT can generate sharp corners within a square. RT has been used in modern engineering applications such as a mechanical drill and the Wankel engine for machining of square holes.

In the process of die-sinking EDM, every time a new tool is required to produce a new cavity. This is a very expensive process for the manufacturing of die and molds. To overcome this difficulty, researchers found a new way for the generation of different size cavities using a single electrode. This can be done by providing orbital movement to the electrode in the X–Y plane. Dave et al. [12] examined the orbital movement of the tool in EDM to understand the functioning of the orbital system. This investigation suggested that at a lower orbital radius and lower orbital speed, MRR can be enhanced with the orbital tool movement. Dave et al. [13] established a semi-empirical model for the prediction of MRR of Inconel 718 during the ED machining process. This model is developed for orbital tool movement by applying the dimensional analysis approach. Semi-empirical results are validated by conducting experiments on Inconel 718. The results revealed that MRR increases during orbital tool movement by increasing current without changing the setting of pulse ON time. It is also noticed that pulse ON time variations influence MRR slightly

at different current settings during the orbital process. During the orbital movement of the tool in the EDM, it is noticed that by increasing orbital radius, MRR decreases.

In the EDM process, the orbital tool movement provides various benefits over other tool movements. Dave et al. [14] examined orbital parameters effect with machine parameters on MRR and TWR. By applying Taguchi and ANOVA methods, results revealed that orbital radius along with duty factor and current influence MRR significantly. For TWR, pulse on time and current both are the most important parameters.

Dave et al. [15] examined the orbital parameters effect with machine parameters on SR and MRR. Taguchi and ANOVA techniques are applied and the S/N ratio is determined to know the significance level of process parameters on the response characteristics. After analyzing the results, it is found that current and orbital radius both influence MRR significantly, and pulse on time and current both influence SR significantly. It is also observed that if orbital radius increases, MRR reduces, and surface roughness increases.

Kumar et al. [16] have considered the effects of orbital tool movement for the EDM process and explored new ways to enhance the machining performance of EDM. Die-sinking EDM is a costly process due to the cost of tooling because in this process for every cavity that needs to generate, a different tool is required. This problem can be fixed by providing orbital motion to the electrode. Orbital tool movement provides various benefits over the die-sinking EDM process. It provides better control for shape, surface finish, and dimensional accuracy by using the same tool.

2.2 Tool Movement on the Axis

Various researchers have been carried out for tool actuation in the vertical direction. There are various techniques to improve the machining process of EDM as reported by researchers. Abdullah and Shabgard [17] presented machining of high mechanical strength material, i.e., cemented tungsten carbide using ultrasonic vibration (UV) of the tool on EDM. For obtaining high MRR, ultrasonic vibration of the tool provides better results working under low pulse times and discharge currents. This provides four times high MRR than the conventional EDM. During the study, it is observed that UV decreases open circuit pulses and arcing, also enhances the stability of the process. The vibration of an electrode tool improves the flushing and makes easy ionization between the sparking gap. This provides a higher surface roughness value and higher improvements in the finishing regimes than conventional EDM. This investigation concluded that ultrasonic vibration of tool better results fort machining of metallic composite materials.

Chiang and Wang [18] developed a method to determine the variation of overcutting, bottom overcut, and positioning accuracy of machines for the EDM process. Electrode wear, bottom overcut and machining depth are measured using the discharge circuit of EDM. In this investigation, variance analysis of electrode tool

wear, spark hole, and dimensions of the electrode is done. The results revealed that the coupling effect between spark hole diameter and electrode diameter plays an important role in the estimation of the variation of side overcut. During the investigation, it is observed that for lower TW and better SR, the polarity of the electrode should be positive.

Rajesh et al. [19] employed a hollow copper electrode for machining a hole on the Inconel 718 workpiece. In this investigation, it is observed that MRR is mostly influenced by pulse current, duty factor, and interaction of duty factor and flushing pressure produce minimum SR. To obtain a good surface finish for the machining of the Inconel 718, an inferior level set of gap control, sensitivity control, and pulse current, and reasonable flushing pressure process parameters values are advised.

There are various researchers have been carried out to increase MRR and to reduce the SR of the workpiece while machining on EDM. By providing vibrating motion, these properties can be enhanced as reported by researchers. Prihandana et al. [20] reported that many researchers used an ultrasonic range of vibration for experiments to get a good flushing effect, MRR, SR, etc. But ultrasonic vibration setup requires expensive devices and extensive tool settings. To overcome these difficulties, low vibration frequencies can be used. In the investigation, a copper electrode is used for machining of stainless steel workpiece and low-frequency vibrations are applied to the workpiece. The results revealed that applying vibrating motion to the workpiece MRR has increased by 23%, and it also enhances the flushing effect in the process of EDM. It is also observed that vibrating motion also decreases the TWR and SR.

It is observed that discharge current pulse influences the machinability in the process of EDM. Muthuramalingam and Mohan [21] considered the effect of discharge current pulse on MRR and SR in the process of EDM. It is reported that by modifying the current pulse generator, a good surface finish with higher MRR can be achieved. It is also observed that duty factor and discharge current considerably affect the machining characteristics.

EDM process can be performed by using gas as a dielectric medium as a replacement of liquid. Teimouri and Baseri [5] investigated the effect of the rotary magnetic field and vibrations of the workpiece for the dry electric discharge machining process. The results of the experiment revealed that a brass tool having two eccentric holes provides the maximum MRR compare to an existing tool. It is noticed that magnetic fields impose positive effects on SR and MRR and also ultrasonic vibration helps to improve the MRR. The vibration provided to the workpiece also improves the removal process of debris.

Singh et al. [22] established a mathematical model for the ultrasonic-assisted EDM process (UEDM) and also performed FEM analysis for flushing due to UEDM. By analyzing the results, it is revealed that vibrations provided to the workpiece improve the flushing and reduce the arcing. This also enhances the MRR in the process of UEDM.

UEDM can be performed using gas instead of the liquid dielectric medium, but in this process, thermal stresses can be developed on the workpiece after machining. Xu et al. [6] proposed UEDM in gas for machining of hard and brittle material and the thermal stress removal mechanism of cemented carbide and sintered Nd-Fe-B

magnetic material is discussed. After the detailed investigation, it is observed that the stress removal process has four sections, first one is thermal stress formation then micro-cracks formation, and then grains break, and then particles strips. So, it can be said that performing UEDM in gas thermal stresses from machined surfaces cannot be avoided.

Sivam et al. [23] created a regression model for the analysis of electrical parameter's effect on some machining responses in the process of EDM. In this analysis, a graphite tool is used for machining titanium alloy. From the detailed investigation, it is revealed that current and pulse on time both are the supreme critical factors that affect all other responses. It is observed that increasing the current MRR also increases and electrode cross-section area does not influence geometry only deviates entry and exit of the tool. SR is also independent of the cross-section area of the electrode tool, and it is only affected by pulse off time.

2.3 Tool Movement Along the Horizontal Direction

For this type of tool actuation, movement is given to the tool in a straight line, i.e., tool movement in the radial direction. In this approach, the tool starts moving from the center of the cavity to radially outward. The tool electrode removes the material during the forwarding tool motion and after removing material return back to its primary location. In this approach, the tool is placed initially at full depth of the hole and then starts removing material during radially outward motion.

For the boring operation in the EDM process, various tool motions can be provided to the tool electrode. Kumar et al. [24] investigated tool movement approaches in the EDM process and experiments are performed to find the best suitable strategies for boring operation. Three different types of tool movements are provided to the electrode, i.e., helical, radial, and die sinking. The results of the investigation concluded that radial tool movement provides several benefits over other tool movements. Radial orbital tool movement provides better feature tolerances, lower wear ratio, very less edge wear and overcut, generates cavity with minimum circularity error, and also provides the least radius of curvature at the bottom machined surface.

Tool movement along the horizontal direction for the boring operation can be provided by giving electrode movement in the radial direction. Kumar et al. [16] have reported that with the help of radial electrode movement-wide range of hole sizes can be created with a single tool electrode.

It is reported that horizontal EDM is a more accurate and productive technique than the verticle EDM process. M. Kunieda and T. Masuzawa [25] investigated that eroded particles easily flushed out from the working region due to the buoyancy of bubbles. This effect can be enhanced further by providing rotational motion to an electrode tool and workpiece to get fine machining accuracy.

Shih and shu [26] have performed experiments for electrical discharge grinding. In this rotational disk, the copper tool electrode is used which is mounted on a horizontal

spindle. The experimental results revealed that in this process higher MRR can be obtained with lower TWR.

Kaneko and Tsuchiya [27] reported that for the EDM process four-machining sequences are there, i.e., rough and medium machining, contour, and corner finishing. In every process, contouring is done by applying cutting motion in the horizontal direction, and then, feed is provided vertically. In this investigation, 3D numerically controlled EDM arrangement is developed for solving the problem of tool wear. This process monitors the deformation of an electrode and automatically applies compensation to the tool path. The results revealed that compensation length depends on the distorted shape of the tool with objective contour and offset length in the finishing process directly influences the machining accuracy of the process.

At various places flushing in the working gap poses some difficulties due to the shape need to be produced. When there is no possibility of holes in the electrodes flushing becomes very difficult. To overcome this difficulty, Koshy et al. [28] proposed a rotating disk electrode for machining in the EDM process. The results of the investigation revealed that rotation of tool electrodes on the horizontal axis improves flushing, MRR, and provides a better surface finish. From these findings, it can be said that the radial orbital tool movement strategy is beneficial for the enlargement of a circular cavity with great tolerance. From this approach, different sizes of large cavities can be generated using the same tool electrode.

3 Conclusion

Present research includes the study of EDM process incorporation with three tool electrode movement approaches, which are tool movement around the axis, on-axis, and along the axis. Based on the current investigation of research work, the following conclusions can be drawn.

1. EDM is a highly applicable process for machining of complex cavities that need to be generated on hard materials mainly used in automobile and die manufacturing industries.
2. The capacity and performance of EDM can be increased by modification of tool holding arrangements.
3. Tool movement arrangements influence the MRR, TWR, SR, and dimensional tolerances during the machining process.
4. Orbital tool movement reduces the tooling cost and various hole cavities can be generated using the same tool electrode.
5. Orbital tool movement provides better surface finish, dimensional accuracy than the die-sinking EDM process.
6. Providing vibratory motion to the tool MRR, flushing improves, and TWR, surface roughness decreases.
7. Radial tool movement provides better tolerances, very less overcut, and tool wear during machining.

The selection of proper tool movement for specific operations in EDM process is very important for better machining performance. But these tool movement strategies are only limited to symmetric kinds of cavities. For the generation of asymmetric kind of cavities using the process of EDM, further research is required.

Acknowledgements The authors gratefully acknowledge the Department of Science and Technology (DST) Gov. of India SERB under SRG scheme (SRG/2020/000675) for their financial support of this research.

References

1. Dave HK, Desai KP, Raval HK (2012) Optimisation of multiple response characteristics in orbital electro discharge machining of Inconel 718 using Taguchi's loss function. *Int J Manuf Technol Manage* 25(1–3):78–94
2. Sudhakara D, Naik BV, Sreenivasulu B. (2012). The experimental analysis of surface characteristics of inconel-718 using electrical discharge machining. *Int J Mech Eng Rob Res* 1(3)
3. Ho KH, Newman ST (2003) State of the art electrical discharge machining (EDM). *Int J Mach Tools Manuf* 43(13):1287–1300
4. Kunieda M, Yoshida M, Taniguchi N (1997) Electrical discharge machining in gas. *CIRP Ann* 46(1):143–146
5. Teimouri R, Baseri H (2013) Experimental study of rotary magnetic field-assisted dry EDM with ultrasonic vibration of workpiece. *Int J Adv Manuf Technol* 67(5–8):1371–1384
6. Xu M, Luo X, Zhang J (2011, January) Study on thermal stress removal mechanisms of hard and brittle materials during ultrasonic vibration assisted EDM in gas. In: 2011 third international conference on measuring technology and mechatronics automation, vol 3). IEEE, pp 597–600
7. Jha B, Ram K, Rao M (2011) An overview of technology and research in electrode design and manufacturing in sinking electrical discharge machining. *J Eng Sci Technol Rev* 4(2)
8. Ding S, Jiang R (2004) Tool path generation for 4-axis contour EDM rough machining. *Int J Mach Tools Manuf* 44(14):1493–1502
9. Chak SK, Rao PV (2007) Trepanning of Al_2O_3 by electro-chemical discharge machining (ECDM) process using abrasive electrode with pulsed DC supply. *Int J Mach Tools Manuf* 47(14):2061–2070
10. El-Taweel TA, Hewidy MS (2009) Enhancing the performance of electrical-discharge machining via various planetary modes. *Int J Mach Mach Mater* 5(2–3):308–320
11. Ziada Y, Koshy P (2007) Rotating curvilinear tools for EDM of polygonal shapes with sharp corners. *CIRP Ann* 56(1):221–224
12. Dave HK, Desai KP, Raval HK (2011, August) Effect of orbital tool movement on material removal rate during electro discharge machining. In: Proceedings of international conference on advanced trends in engineering materials and their applications, YM Haddad (Ed) (pp. 365–370)
13. Dave HK, Desai KP, Raval HK (2013) Development of semi empirical model for predicting material removal rate during orbital electro discharge machining of Inconel 718. *Int J Mach Mach Mater* 13(2–3):215–230
14. Dave HK, Desai KP, Raval HK (2013) A Taguchi approach-based study on effect of process parameters in electro discharge machining using orbital tool movement. *Int J Mach Mach Mater* 13(1):52–66
15. Dave H, Desai K, Raval H (2012) Experimental investigations on orbital electro discharge machining of Inconel 718 using Taguchi technique. *Int J of Mod Manuf Technol* 4(1):53–58
16. Kumar S, Dave HK, Desai KP (2015) Effect of orbital tool actuation during electro discharge machining process—a critical review. *J Assoc Eng India* 85(1 & 2):49–71

17. Abdullah A, Shabgard MR (2008) Effect of ultrasonic vibration of tool on electrical discharge machining of cemented tungsten carbide (WC-Co). *Int J Adv Manuf Technol* 38(11–12):1137–1147
18. Chiang HN, Wang JJ (2011) An analysis of overcut variation and coupling effects of dimensional variable in EDM process. *Int J Adv Manuf Technol* 55(9–12):935–943
19. Rajesha S, Sharma AK, Kumar P (2012) On electro discharge machining of Inconel 718 with hollow tool. *J Mater Eng Perform* 21(6):882–891
20. Prihandana GS, Mahardika M, Hamdi M, Mitsui K (2011) Effect of low-frequency vibration on workpiece in EDM processes. *J Mech Sci Technol* 25(5):1231
21. Muthuramalingam T, Mohan B (2013) Influence of discharge current pulse on machinability in electrical discharge machining. *Mater Manuf Processes* 28(4):375–380
22. Singh J, Walia RS, Satsangi PS, Singh VP (2011) FEM modeling of ultrasonic vibration assisted work-piece in EDM process. *Int J Mech Syst Eng* 1(1):8–16
23. Sivam SP, MichaelRaj AL (2013) Effects of electrical parameters, its interaction and tool geometry in electric discharge machining of titanium grade 5 alloy with graphite tool. *Proc Inst Mech Eng Part B J Eng Manuf* 227(1):119–131
24. Kumar S, Dave HK, Desai KP (2016) Experimental investigation on performance of different tool movement strategies in EDM process for boring operation. *Int J Adv Manuf Technol* 87(5):1609–1620
25. Kunieda M, Masuzawa T (1988) A fundamental study on a horizontal EDM. *CIRP Ann* 37(1):187–190
26. Shih HR, Shu KM (2008) A study of electrical discharge grinding using a rotary disk electrode. *Int J Adv Manuf Technol* 38(1–2):59–67
27. Kaneko T, Tsuchiya M (1988) Three-dimensional numerically controlled contouring by electric discharge machining with compensation for the deformation of cylindrical tool electrodes. *Precis Eng* 10(3):157–163
28. Koshy P, Jain VK, Lal GK (1993) Experimental investigations into electrical discharge machining with a rotating disk electrode. *Precis Eng* 15(1):6–15

Enhancement of Mechanical Properties Alkali-Treatment and Polylactic Acid Coated Woven Jute Fiber Reinforced Composites



P. Naresh Sagar, Naveen Reddy CH, and T. Malyadri

Abstract The main objective of present study is to lessen the limits of natural fibers. Woven jute fiber is used as a normal fiber, to develop the possessions of jute with alkali reaction and (PLA) eco-friendly coating. Mechanical strength of jute was studied in present work and manufactured with wet layup method fiber weight constant 30%. Mechanical strength tensile, flexural, and impact properties were studied. Coated by PLA shown the highest value compared with other natural fiber and treated composites. Chemical treated and coated with PLA (JL4) showed the highest value compared with natural jute fiber (JL1).

Keywords Natural jute fiber (JL1) · PLA (JL4) · Tensile · Flexural · Impact

1 Introduction

Different physical and chemical properties of materials are connected together to build a composite material. Properties of composite materials are depending on the ingredient materials, resin, and fiber used. Currently, advanced composite materials with their good mechanical properties are broadly used in the engineering field. Advantages are electric insulation, fatigue resistance, less weight, and is widely suitable for formation applications [1]. The global dumping of millions tons of plastics, universal ecological concern, increasing global hotness, decrease in polar ice caps, rapid deplete fuel resources, rising sea level, etc., contain a weight on atmosphere. Overhead mention is reasons for the condition to expand green and bearable goods they are gradually allowed to justifiable growth [2]. Green composites were divided into two categories for instance partially recyclable and completely recyclable complexes. Moderately green-complexes in which one of element used from natural resources similar to reinforcement as a normal fiber and epoxy as matrix, PLA, and strengthening are synthetic fibers. In fully degradable composite together the reinforcement and matrix are the normal like natural fiber as strengthening and

P. N. Sagar · N. R. CH · T. Malyadri (✉)

Department of Mechanical Engineering, VNR Vignana Jyothi Institute of Engineering and Technology, Hyderabad, India

normal polymer is PLA, PVA as a matrix [3]. Many researchers were working on synthetic resin and synthetic fibers for the development of industrialized goods. But with non-biodegradable behavior, there are a lot of problems to nature, reduction of fossil assets, global warming, and growing oil costs result in increased research for sustainable improvement. Totally above are the reasons for the researchers to develop the completely biodegradable in countryside and with good mechanical attributes [4]. In the green fibers, jute is frequently used normal fiber as strengthening. Indonesia, Nepal, Thailand, and Brazil produce good quality jute fiber. Jute plant grows height of 2–3.5m and very sensitive, with break to extension is low because high lignin content (up to 12–16%) [5, 6].

The limitations of natural fiber are overcome with surface modification by using chemical treatments. Woven jute fiber is eco-friendly and chemical treatments (alkaline, sodium hydrogen carbonate, and benzylation) and PLA covering are used to progress the performance [7]. PLA and Banana fiber biocomposites are made-up using compression molding. Both the modulus and tensile strength are increased for surface modified BF biocomposites which are found that there is an increased interfacial attachment between fiber and epoxy material [8]. It also absorbed that concentration of NaOH, immersion time and fiber loading are major factors of increasing and decreasing physical, mechanical, and thermal stability of alkali treated green composite [9]. Pre-treatment is used to change the structure and fiber surface morphology. With this decreased the moisture absorption and the dimension stability [10]. Thermoplastic polyurethane, PLA, and wood flour particles are as materials. The TPU taken from (0–50) % and WF is (10) % constant. These were prepared using thin screw extruder. The mechanical, dynamic analysis, and biodegradation were studied. Here is an enhancement in tensile strength and with impact strength around 147% and 870% were found from PLA50/TPU50/WF10 [11]. Nanofiber 2wt%, DMA were seen improved and thermal stability also increased due to incorporation of hemp nanofibers [12]. 30% weight jute fiber shows better results in Tg and load bearing capacity. Frequency increases the storage modulus also increased and with increasing frequency glass transition temperature/thermal stability reduced [13]. HCT3 shows better results in storage modulus, glass transition temperature, and maximum water absorption resistance [14]. Found that JT1 and JT2 decrease in its impact properties with negative effect of chemical treatment and further increased with coating. JT3 showed highest mechanical properties with strong bonding in between jute and matrix [15]. Fiber kept with constant weight of 20% and examined static, dynamic, and water absorption properties. The above tests coated with PLA improved its results compare with untreated and treated [16]. SC1 shows best results with less void and fiber matrix bonding control with chemical treat and coating [17]. In this article effects of weight fraction, surface treatment, orientation, geometry, and hybridization are presented. Better tensile and flexural properties are obtained with 30–40% with weight fraction and 20–50 mm fiber length [18].

Composite properties are not increased only with chemical treatments. Hence, there is a need for fresh treatment to increase the composite properties consequently they are used in advanced manufacturing and other requests. In present research

Table 1 Physical, chemical and mechanical attributes of jute

Properties	Jute fiber
Density (g/cm ³)	1.3
Hemi cellulose (%)	14–20
Lignin (%)	12–13
Moisture content (%)	12.6
Cellulose (%)	61–71
Tensile strength (MPa)	393–773
Elastic modulus (GPa)	26.5
wax (%)	0.5
Elongation at break (%)	1.5–1.8

overawed the main boundaries of JFRPCs with latest treatment as PLA covering on alkali treated woven jute fiber. Properties of jute are exposed in Table 1.

2 Materials and Methods

2.1 Materials

Jute fiber

Jute is from tilaceae blood and its methodical term is *Corchorus capsularis* and extracts from corchorus of the plant, this has less cost fiber. Throughout the world, jute produces 2300 × 103 to 2850 × 103 tones. Jute has large choice of applications in industry such as construction, textile, and automobile. Woven Jute fibers were purchased from Vruksha Composites and services, Guntur, Andhra Pradesh.

Resin and hardener

The polymeric material epoxy resin consists of higher properties they are good chemical, mechanical, easy processing, and corrosive resistance properties. Because of its large applications, epoxy was selected as matrix material for present study. The hardener additives serve as catalysts that speed up the curing process. In the fabrication AraliditeLY556 epoxy resin and hardenerHY951 is used for the preparation of the composite and is brought from Vruksha Composites and services, Guntur, Andhra Pradesh.

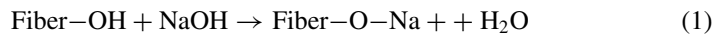
Alkaline treatment

Woven jute fiber is treated with 5% NaOH in the current work. 4 h with 30 °C jute fiber were placed in the alkaline solution. After that taken out from solution and cleaned with floating water numerous times and then placed into the HCL solution to eliminate NaOH adhere from the outside of fiber. Again fiber was cleaned with

Table 2 Physical and mechanical attributes of PLA

Properties	Values
Tensile strength (M Pa)	37
Density (g/cm ³)	1.29
Tensile modulus	27–16
Melting temperature (°C)	173–178
Tg	55–80
Impact strength (J/m)	13

water and dried in oven maintained at 60 °C for 24 h. The reaction of fiber with alkaline is provided under:



PLA coating on treated and untreated

PLA is a completely biodegradable, renewable, and fully biological and good processing capacity and mechanical strength. PLA manufacture through lactic acid during fermentation farming foods like corn, rice, potatoes, forming waste and sugar beet, etc. PLA properties are shown in Table 2. At first, PLA pellets with weight of 2% w/v were placed in chloroform mixture up to 8 h consequently, stirred the mixture to dissolve the PLA in chloroform solution and maintained 600 °C. After PLA solvent woven jute fiber was soaked for 5 mins. Lastly, coated fibers were dried 24 h at room temperature and dried at 600 C for 4 h in hot air oven. Schematic diagram provides below in Fig. 1. PLA pellets brought from Vruksha Composites and services, Guntur, AP.

2.2 Fabrication of Composites

The laminates of required dimensions are fabricated with the help rectangular shape mold made of hardened steel. The dimensions of the mold which is used to prepare the laminates are in the size of 200 mm × 200 mm and thickness 4 mm. In this project, hand layup technique is adopted for the preparation of composite laminates because of its flexibility in material design and good surface finish. Layers of jute fiber are marked and cut according to the mold dimensions. Based on the GSM of the fabric the quantity of resin is calculated. The low temperature curing epoxy resin LY556 and hardener HY951 is added to epoxy resin with percentage of 10:1 by weight % and mixed thoroughly with the support of vertical stirrer and weight of jute fiber is constant with 30%. The composite laminates made of different compositions of untreated, treated, coated, and treated and coated were named JL-1, 2, 3, and JL-4 are shown in Table 3. Finally, the laminates are cut with the help of hack saw in order to get the test specimens as per ASTM standards for characterization and testing.

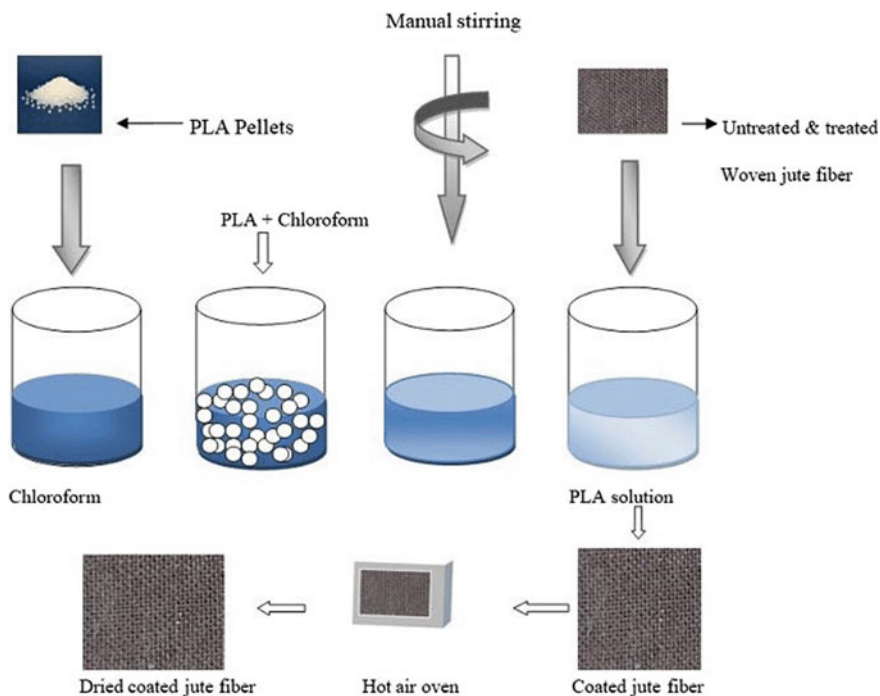


Fig. 1 PLA coating of Untreated and Treated woven jute fiber

Table 3 Nomenclature of composites

Composites	Jute fiber (wt) [%]	Alkaline treatment (wt) [%]	PLA covering (wt) [%]
JL1	30	–	–
JL2	30	5%	–
JL3	30	–	2
JL4	30	5%	2

Flow chart of production process of composites showed in Fig. 2 and nomenclature of composites in Table 3.

2.3 Mechanical Properties

Tensile Strength (T.S) of the specimens were conducted as per ASTM D 638 grade. INSTRON make UTM-3369 machine has been employed for evaluating the T.S on the specimens. To evaluate the tensile strength of the laminates were cut into 165 x

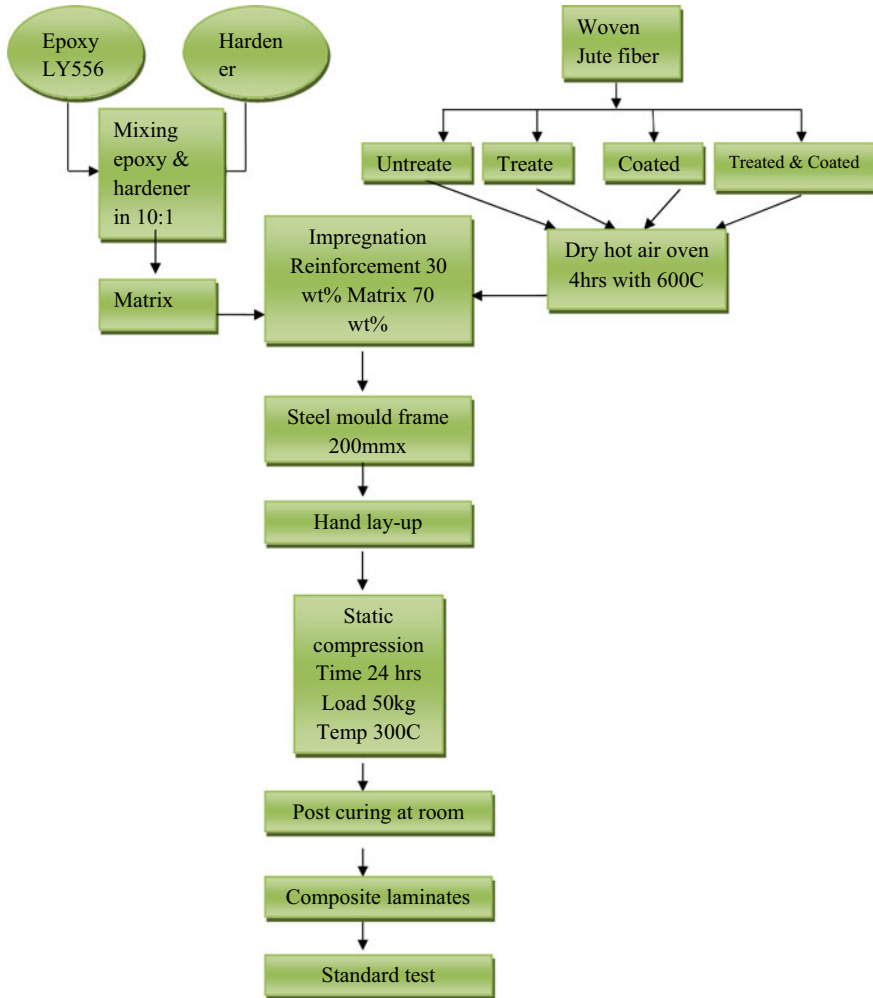


Fig. 2 Flow chart for manufacture process of composites

20 x 3 mm³ size.. The characterization of T.S was done with a cell load of 30 kN, 10 mm/min speed of the crosshead (CHS), temperature at 270 °C, and 60% humidity [19]. For each laminate type, 3 undistinguishable laminates were verified and the average value is stated as the stuff of particular composite.

Flexural Strength (F.S): To evaluate the flexural properties according to ASTM D 790. F.S specimens were cut to 80 × 13 × 3 mm³ with a constant cell load of 2 kN, CHS travel of 5 mm/min, temperature at 270 °C, and 60% humidity [19]. Results were used to calculate the flexural properties strength and modulus.

Impact Strength: Impact tests were performed at room temperature 270 °C and 60% humidity as the ASTM D 256 grade dimension of 65 × 13 × 3 mm³ [19].

Impact energy of each specimen is directly noted on the pointer. Three specimens of each laminate were investigated and average value was reported as its property.

3 Results and Discussion

Mechanical Properties: The partition describes the characterization of mechanical attributes mainly, Tensile properties, Flexural strength and modulus, and impact strength of manufactured composites with 5%wt NaOH treatment and 2%wt PLA coating specimens.

Tensile properties: Tensile testing value gained with tensile load versus displacement untreated, treated with coated composites shown in Fig. 3. The tensile values are closed to previously published works. The chemically treat and PLA covered composites enhanced the tensile properties of woven jute composites. Treated and coated composites JL4 have highest value compared with all other composites JL1, JL2, and JL4. Only coated with PLA have less value compare with JL2 and JL4 because of average bonding between matrix and fiber composites. Tensile strength and the modulus of coated and treat are presented in Table 4. The alkaline treated coated with PLA have advanced tensile strength and with modulus compare with

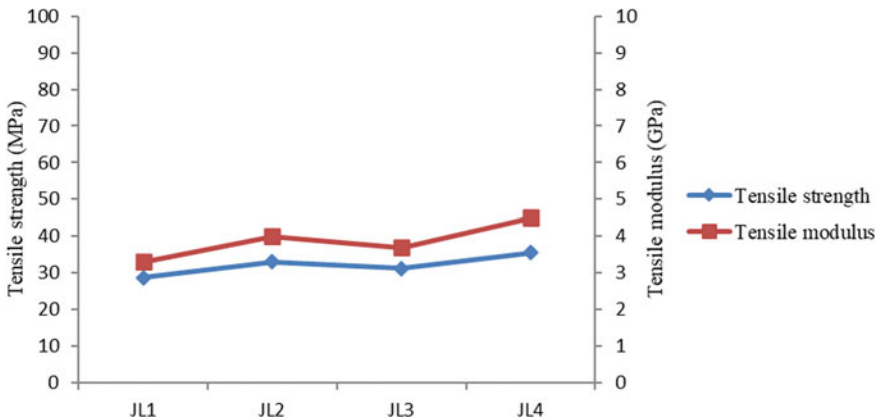


Fig. 3 Tensile strength and modulus of untreated and improved Woven jute fiber composites

Table 4 Tensile attributes of chemical treated and modified jute composites

Composites	Tensile strength (MPa)	Tensile modulus (GPa)
JL1	28.7	3.3
JL2	33	4.0
JL3	31.2	3.7
JL4	35.6	4.5

untreated JL1. This with removing contamination by alkaline treatment leads to solid attachment among fiber and epoxy material and increases tensile characteristics. The overall composite laminates JL4 have highest value of tensile value is (35.6 MPa) and with tensile modulus value (4.5 GPa) compare with other laminates. With alkaline treatment remove the unwanted material (lignin, wax, and hemicelluloses) and reduce thickness and increase the attached surface between the fiber and matrix. Alkaline treatment increase the tensile properties are found in 8, 9, and 11. The highest tensile properties are absorbed JL4 due to both the effect alkaline treatment and PLA coating.

Flexural properties: Flexural strength and modulus of entreat and changed jute composites are provided in Table 5. Same as alike tensile properties, flexural properties results are obtained. The laminate JT2 has 9.2% and 6% extra flexural strength and modulus than JC1, correspondingly, where has composite JT3 has maximum results of flexural strength (86.3 MPa) and modulus (7.6 GPa) this are 16.3% and 11% greater later JC1, respectively. Grater values of flexural properties in laminate JT4 with good interfacial attachment among fibers and epoxy matrix primes to efficient stress handover from matrix to jute fibers. Flexural properties increased with PLA coating of jute fiber with non-polar behave and well adhesion of matrix. Coated jute fiber has in between properties JL2 and JL4. Maximum flexural properties are absorbed in JL4. The increase in flexural properties is $JL4 > JL2 > JL3 > JL1$ is shown in Fig. 4.

Table 5 Flexural attributes of chemical treated and untreated jute composites

Composites	Flexural strength (MPa)	Flexural modulus (GPa)
JL1	70	6.5
JL2	79.2	7.1
JL3	72.3	6.9
JL4	86.3	7.6

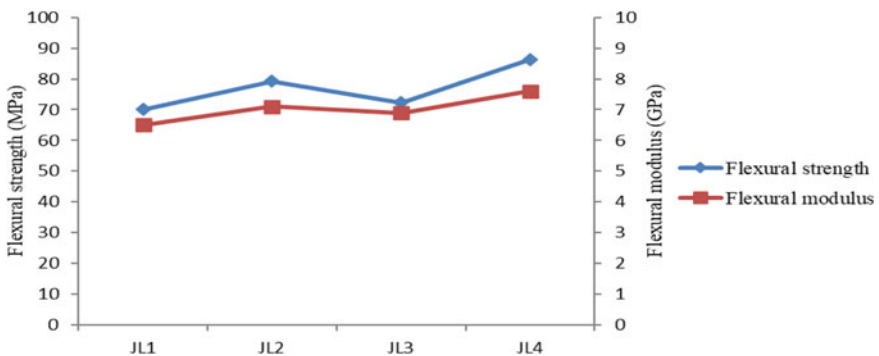


Fig. 4 Flexural strength and flexural modulus of untreated and improved Woven jute fiber composites

Table 6 Impact attributes of chemical treated and untreated jute composites

Composites	Impact energy (kJ/m ²)
JL1	6.1
JL2	4.4
JL3	4.8
JL4	6.3

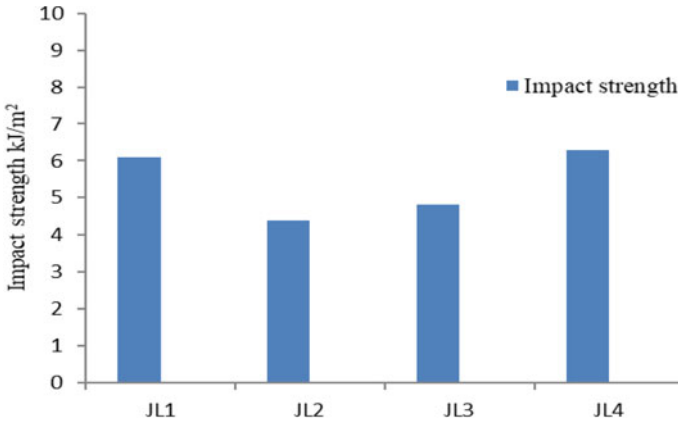


Fig. 5 Impact strength of untreated and improved Woven jute fiber composites

Impact properties: Impact strength of untreated and modified woven jute fiber is shown in Table 6. Impact strength JL2 is reduced compared with treated JL1. Similar results were absorbed in 8, 9, and 17. During the impact test process mainly concentrate on the fiber pull-out process. With alkaline treatment, the fiber pull-out reduces with the strong bonding in between the matrix and fiber. Jute composite laminate JL3 is higher value than the JL2 and lower value than the JL1. The jute composites JL4 have maximum impact strength compared with other composites JL1, JL2, JL3, and JL4 are shown in Fig. 5.

4 Conclusion

In this current research, chemical treatment and PLA covering are applied on woven jute fiber and mechanical properties are presented. Limitations of woven jute fiber are reduced with treatment and coating shown good mechanical properties. Alkali treat and PLA covered woven jute fiber composite (JL4) highest mechanical properties. Chemical treatment and PLA improve the properties but in some cases impact properties are reduced with the treatment shown in JL2. Though, composite JL4 shown enhanced impact strength also. The strong attachment between the fiber and

epoxy material is shown highest mechanical attributes in JL4 composite compared with JL1. Natural fibers are completely bio-degradable with PLA coating because PLA itself is a bio-degradable polymer. PLA covering as a fresh treat can encourage researchers for latest and progressive requests of NFRPCs.

Acknowledgements The writers are thankful to Dr. K. S. Rao M.D Kelvin labs and Vruksha composites from Chennai providing PLA pellets.

References

1. Singh H, Singh JIP, Singh S, Dhawan V, Tiwari SK (2018) A brief review of jute fibre and its composites. *Mater Today Proc* 5(14):28427–28437
2. Thakur VK, Singha AS (2011) Thakur MK 2011 green composites from natural cellulosic fibers. GmbH & Co. KG, Germany
3. Bajpai PK, Singh I, Madaan J (2012) Comparative studies of mechanical and morphological properties of polylactic acid and polypropylene based natural fiber composites. *J Reinf Plast Compos* 31(24):1712–1724
4. Bajpai PK, Singh I, Madaan J (2014) Development and characterization of PLA-based green composites: a review. *J Thermoplast Compos Mater* 27:52–81
5. Faruk O, Bledzki AK, Fink H-P, Sain M (2012) Biocomposites reinforced with natural fibers: 2000–2010. *Progress Polym Sci* 37:1552–1596
6. Kozłowski R, Mieleniak B, Helwig M, Przepiera A (1999) Flame resistant lignocellulosic-mineral composite particleboards. *Polym Degrad Stabil* 64:523–528
7. Yadav A, Gupta MK (2019) Development and characterization of jute composites for sustainable product: effect of chemical treatments and polymer coating. *Mater Res Express* 7(1):015306
8. Jandas PJ, Mohanty S, Nayak SK, Srivastava H (2011) Effect of surface treatments of banana fiber on mechanical, thermal, and biodegradability properties of PLA/banana fiberbiocomposites. *Polym Compos* 32(11):1689–1700
9. Sahu P, Gupta MK (2020) A review on the properties of natural fibres and its bio- composites: effect of alkali treatment. *Proc Inst Mech Eng Part L J Mater Des Appl* 234(1):198–217
10. Kabir MM, Wang H, Lau KT, Cardona F (2012) Chemical treatments on plant-based natural fibre reinforced polymer composites: an overview. *Compos Part B Eng* 43(7):2883–2892
11. Pandey K, Antil R, Saha S, Jacob J, Balavairavan B (2019) Poly (lactic acid)/thermoplastic polyurethane/wood flour composites: evaluation of morphology, thermal, mechanical and biodegradation properties. *Mater Res Express* 6(12):125306
12. Rana SS, Gupta MK (2018) Dynamic mechanical properties of hemp nanofibre reinforced epoxy composite. In: IOP conference series: materials science and engineering, vol 455, issue no 1. IOP Publishing, p 012013
13. Rana SS, Gupta MK, Srivastava RK (2017) Effect of variation in frequencies on dynamic mechanical properties of short sisal fibre reinforced epoxy composite. *Mater Today Proc* 4(2):3387–3396
14. Gupta MK, Gond RK, Bharti A (2018) Effects of treatments on the properties of polyester based hemp composite. *Indian J Fibre Text Res (IJFTR)* 43(3):313–319
15. Gupta MK (2020) Investigations on jute fibre-reinforced polyester composites: effect of alkali treatment and poly (lactic acid) coating. *J Ind Text* 49(7):923–942
16. Gupta MK, Singh R (2019) PLA-coated sisal fibre-reinforced polyester composite: water absorption, static and dynamic mechanical properties. *J Compos Mater* 53(1):65–72

17. Sahu P, Gupta MK (2020) Lowering in water absorption capacity and mechanical degradation of sisal/epoxy composite by sodium bicarbonate treatment and PLA coating. *Polym Compos* 41(2):668–681
18. Khan MZR, Srivastava SK, Gupta MK (2018) Tensile and flexural properties of natural fiber reinforced polymer composites: a review. *J Reinf Plast Compos* 37(24):1435–1455
19. Sgriccia N, Hawley MC, Misra M (2008) Characterization of natural fiber surfaces and natural fiber composites. *Compos A Appl Sci Manuf* 39(10):1632–1637

Designing and Developing of a Renewable Agrobot to Enhance Harvest Productivity and Reduce Water Consumption



Arafa S. Sobh, Hussein M. A. Hussien, and Ali Abd El-Aty

Abstract The aim of the work shows the designing steps and implementation of a new version of Agrobot that combines most activities done in farming filed. This new version installs special mechanical mechanisms to control seeds feeding and reduce water consumption. By selecting suitable lightweight materials and using renewable energy through solar panels, electric power can be saved and high working hours during morning and night can be achieved. Therefore, increase the productivity. In order to achieve these goals, an integration of hard components with Arduino UNO unit, Bluetooth module HC05, battery 12 V, relay (2channels-12 V), DC motor, stepper motor, pump, breadboard, and jumpers. Thus, algorithms are implemented for maximum power output and speed control to guide the agricultural robot. The proposed design of the new version of renewable Agrobot has environmental and social impacts. It can be considered not only as a step to replace the human being activities by a robot but also more suitable for people and places that suffering from few water resources. In addition, food self-sufficiency and the green areas can be extended with little effort of human.

Keywords Agrobot · Renewable energy · Design · Environmental impact · Control

1 Introduction

Food self-sufficiency needs extension of green areas. However, this mission is difficult to countries that have small number of water resources. On the other hand, exporting foods from other countries is an alternative. But, this alternative needs foreign currency. Also, during these period of life that world face of COVID-19

A. S. Sobh · H. M. A. Hussien · A. Abd El-Aty (✉)
Mechanical Engineering Department, Faculty of Engineering-Helwan, Helwan University, Cairo, Egypt
e-mail: aliabdelaty@h-eng.helwan.edu.eg

H. M. A. Hussien
e-mail: hussien@h-eng.helwan.edu.eg

© The Author(s), under exclusive license to Springer Nature Singapore Pte Ltd. 2022
H. K. Dave et al. (eds.), *Recent Advances in Manufacturing Processes and Systems*,
Lecture Notes in Mechanical Engineering,
https://doi.org/10.1007/978-981-16-7787-8_32

which make this alternative more difficult to implement. Therefore, most international orientation is to get food self-sufficiency by fast and little cost Agrobot. There are different points of views of Agrobot classification; mechatronics and electronics, locomotion, manipulators, and robotic vision [1].

This previous classification based on the type of technology is involved in the robot hardware structure. However, most developed Agrobots can be classified as farm robots, fruits, and vegetables robots and animal husbandry robots [2]. In addition, Nidhi and Ritula [3] classified agriculture processes as seeding, irrigation, weeding, fertilizing, and harvesting. Some researchers oriented to develop weeding robot with advanced image processing techniques to identify and position the bad weeds [4, 5].

Harvesting robots come into the list of interests, and autonomous robots are attached by cutters to pick up the plants [6–8]. Recently, smart autonomous harvest robots were developed to perform more than one function like Manikandan and Sreenivasan [9] who constructed a flying robot to observe the crops by combination of mechanical, electrical, and computer sciences. In addition, Ramesh and Pasupathy [10] developed a decision-making system by collecting soil moisture and temperature data from the land and stored it to a cloud system. Amith et.al. [11] established water management concept in Agrobot module to save water wastes.

However, seeding autonomous agriculture robot is the most type of robots that has different trials of researches. For example, Keerthana et.al. [12] introduced a precision robot which perform a seeding process only. Chetan et.al. [13] developed a robot perform operations like automatic ploughing and seed dispensing processes. Rubens et.al. [14] studied the kinematic of the mechanical structure by constructing a virtual prototype. Francesco and Andrea [15] designed a multibody Agrobot of small size and kinematic model was verified. Aldis and Vitalijs [16] presented a multifunction Agrobot in real farm. In addition, Luis et.al. [17], they investigated the fleets of robots for different topologies. They proposed architecture-based centralized main controller and advanced sensory systems that provide some advantages for a future sensor vision.

From the previous literature survey, it can be noticed that there are some researches oriented to handle and solve individual problem of farming processes like digging, seeding, or irrigation. On the other hand, others concerned with reducing the existence of farmer by developing multifunction Agrobot to increase productivity by updated designs. However, there are few trials to solve the problems of the three farming processes and merge these processes in one Agrobot. In addition, it seems that solar energy, as source of renewable energy, is not handled in surveyed studies. Therefore, developing an Agrobot with good control, low cost, and power consumption is needed. This search is a trial prototype of Agrobot which does all farming processes with little consumption of power using solar cells to increase the productivity.

2 Agrobot Concept

The proposed prototype can perform the three farming processes, i.e., digging, seeding, and irrigation by three different mechanisms as shown in Fig. 1. The digging mechanism at the front of the Agrobot is consisting of two V shape diggers connected to rack and pinion gears in order to reduce stresses acted on the diggers and make the process easier as shown in Fig. 2.

The seeding mechanism used to feed down the seeds one by one and two plastic funnels as shown in Fig. 3. The distance between the two funnels equal to the distance between the two rows of plants. Down the funnels a slider connected by the stepper motor to open and close one time during half cycle of motor rotation to allow two seeds enter the two holes produced by two diggers.

There is a delay for the second half cycle of motor to control the feeding the two other seeds when the robot comes to the desired location. Then, ploughing process,

Fig. 1 The proposed prototype of Solar Agrobot

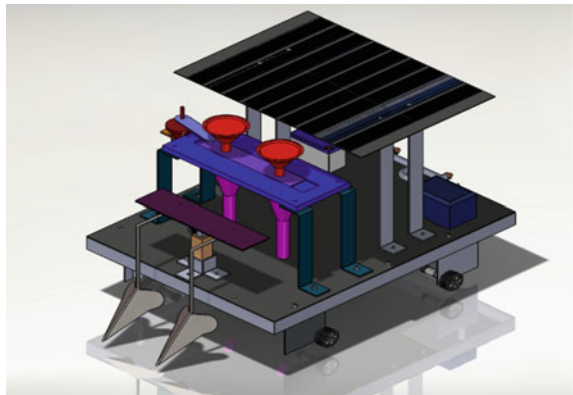


Fig. 2 Digging mechanism

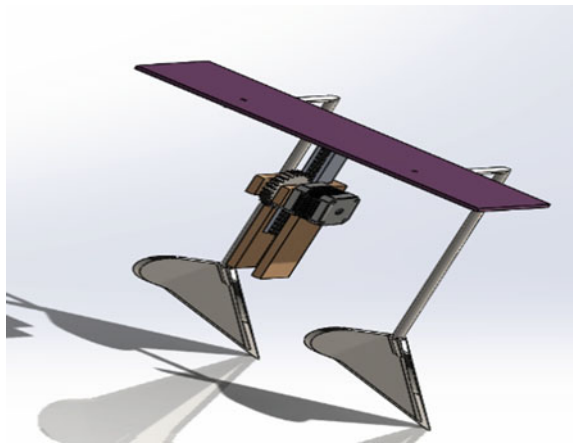


Fig. 3 Seeding mechanism

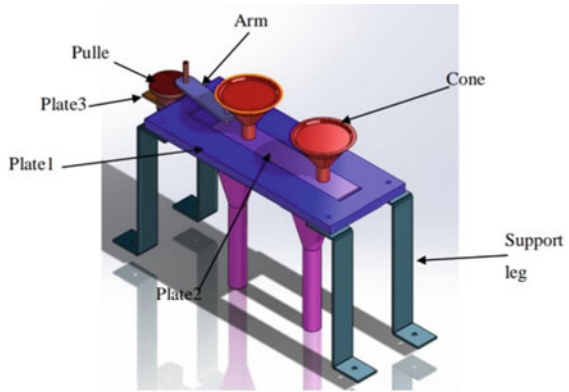
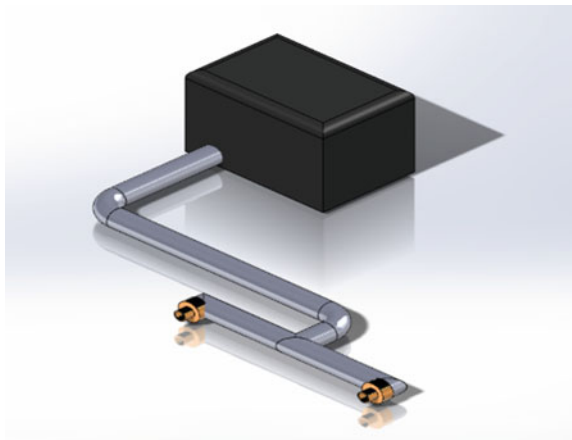


Fig. 4 Irrigation mechanism



to cover the seeds, performed by mechanism similar to digging mechanism attached at back of the robot. Irrigation process is the next that happened by pumped tunnels, as shown in Fig. 4, directed to the location of the tow covered seeds. The required power supplied by battery that charged by solar panels to make the farming processes continued during morning and night.

2.1 Hardware Design and Materials Selection

Robot’s design was based on replacing the farmers and their tasks in agriculture process, i.e., digging, seeding, and irrigation. In order to achieve these tasks, design phase pass through different stages, i.e., control system and mechanical system. The control system consists of an Arduino UNO unit, Bluetooth module HC05, battery 12 V, relay (2 channels-12 V), DC motor, stepper motor, pump, breadboard and

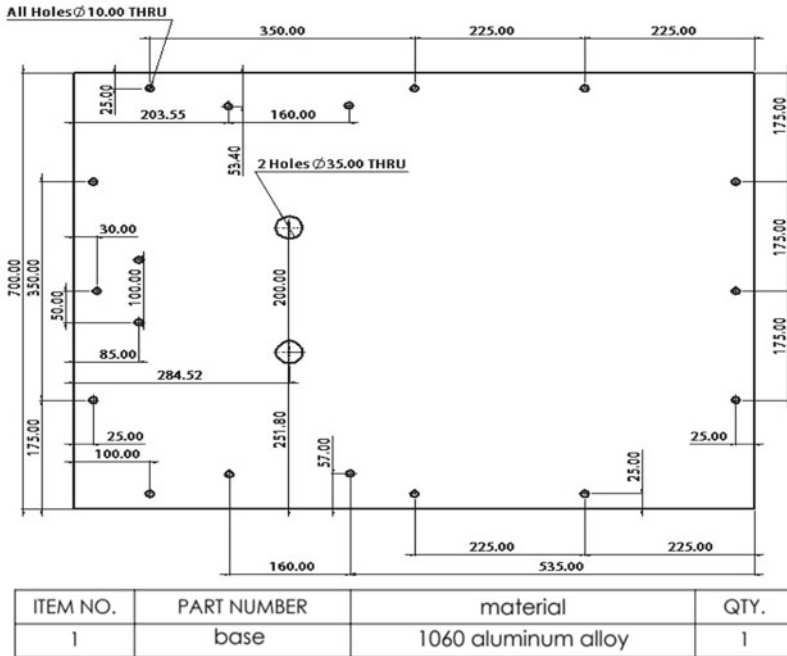
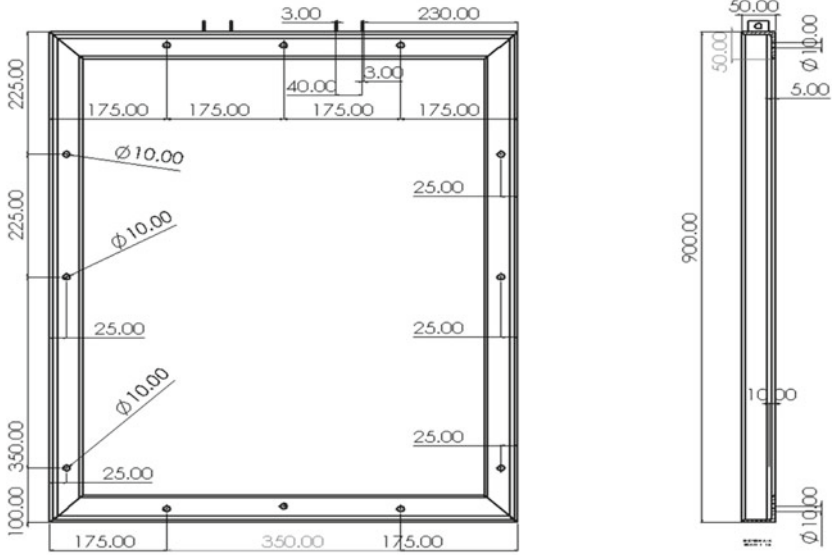


Fig. 5 Base description

jumpers. On the other hand, the assembled mechanical system, Figs. 5, 6, 7, 8, 9, 10, 11, 12 and 13 consists of seeding mechanism, digging mechanism, irrigation mechanism, and soil returner (Plougher). In order to get balanced system of control and mechanical system, a simulation of designed software is performed using solid works software to determine the size and shape of each part and the nature of loading (static, dynamic, shock, thermal, uniform distributed or non-uniform distributed). Finally, select the appropriate material for parts to perform their functions well.

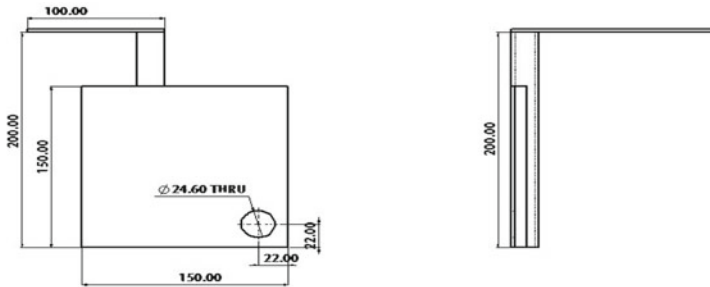
2.2 Control System

he proposed prototype equipped by Arduino UNO (Microchip ATmega328P micro-controller) that can be considered as an open-source microcontroller board. The board has sets of digital and analog input/output (I/O) pins that may be interfaced to various expansion boards and other circuits, as shown in Fig. 14. The board attached by USB cable or by an external 9-V battery. The role of Arduino board is to control the input signals and produces the right outputs to allow motors to rotate. In addition, HC-05 Bluetooth component is installed as transparent wireless serial connection. Its function used to interface with the controller or PC. HC-05 Bluetooth module



ITEM NO.	QTY.	DESCRIPTION	LENGT H	material	QT Y.
1	1	50x50x5	900	steel	1
2	1	50x50x5	700	steel	1
3	1	50x50x5	900	Steel	4
4	1	50x50x5	700	steel	1

Fig. 6 Frame description



ITEM NO.	QTY.	DESCRIPTION	MATERIAL
1	1	wheel supporter	1060 Aluminum alloy

Fig. 7 Wheels supporter description

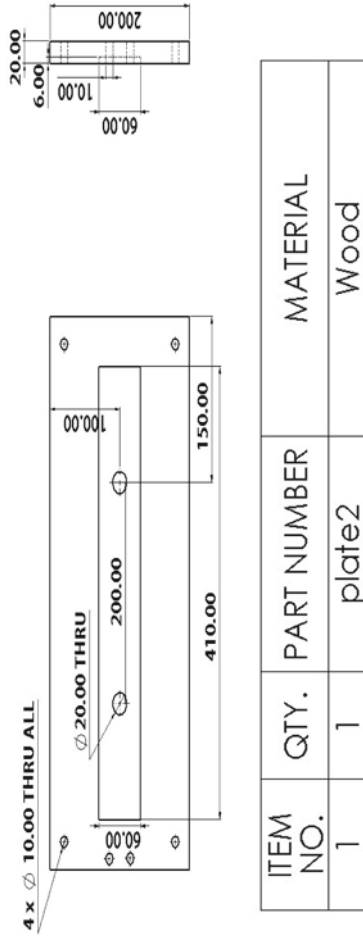


Fig. 8 Seeding plate1 description

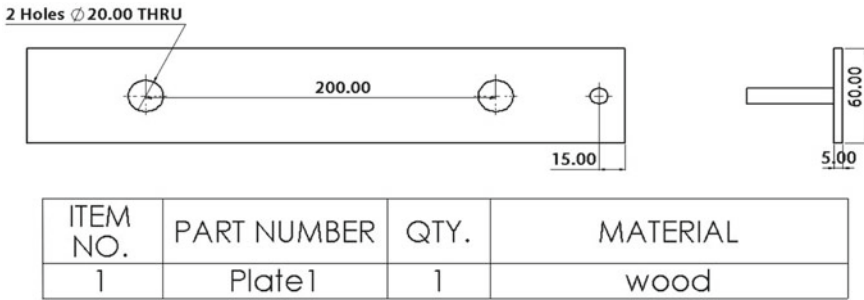


Fig. 9 Seeding plate2 description

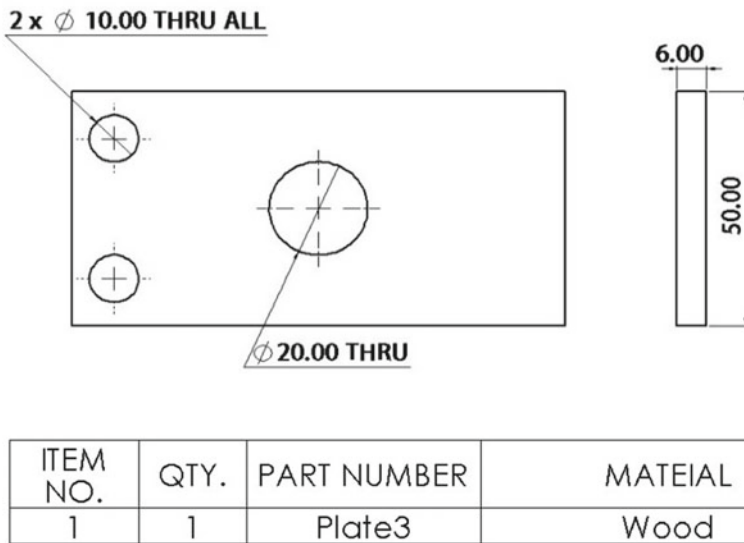


Fig. 10 Seeding plate3 description

provides switching mode between master and slave mode, which means it is able to use neither receiving nor transmitting data. Bluetooth module transfers the inputs from mobile application (RC controller) and sends it to Arduino, as shown in Fig. 15.

The channel 5 V relay module, as shown in Fig. 16, is a relay interface board, and it can be controlled directly by a wide range of microcontrollers such as the Arduino, AVR, PIC, ARM, and so on. It uses a low-level triggered control signal (3.3-5VDC) to control the relay. It is frequently used in an automatic control circuit. Its role is adapting voltage value from battery to give motors and Arduino board. Here, the prototype attached by is seven relays; six for motors, and one for the pump. Also, there are six DC motors, four DC motors for the main motion beside one motor for seeding mechanism, and the last one for digging mechanism.

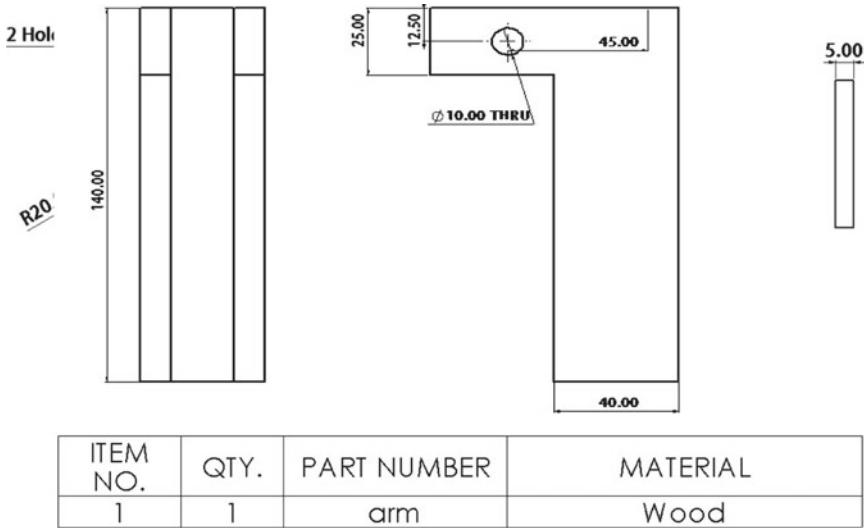


Fig. 11 Arm description

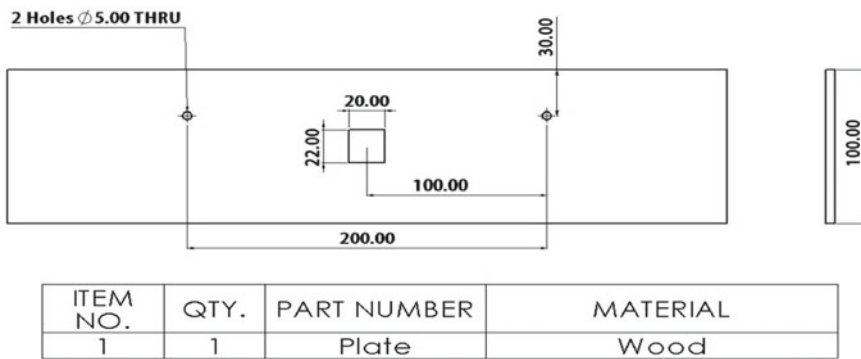
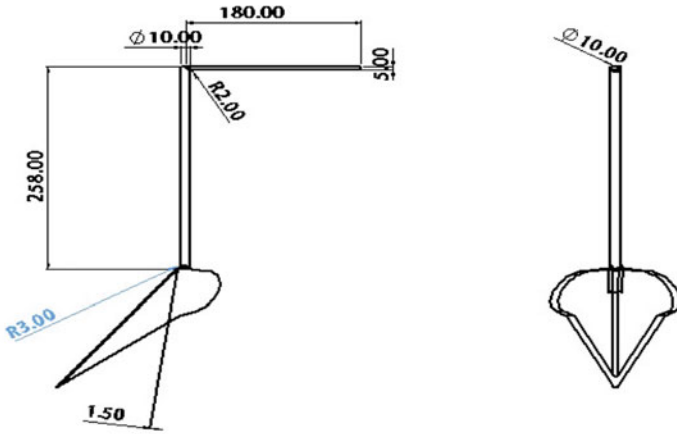


Fig. 12 Digging plate description

2.3 Solar Energy Calculations

A solar panel can be considered as tool used to convert thermal energy into electrical energy. It used to charge Agrobot battery to increase production time. The panel consists of a layer of silicon cells that are a nonmetal with conductive properties that allow it to absorb and convert sunlight into usable electricity. When light hits a silicon cell, the light causes electrons in the silicon to be set in motion, initiating a flow of electric current. This is known as “photovoltaic effect,” and it describes the general functionality of solar panel technology. There are three major types of solar panels: monocrystalline, polycrystalline, and thin-film. Each type has its own



ITEM NO.	PART NUMBER	MATERIAL	QTY.
1	degger	steel	1
2	degger arm	steel	1

Fig. 13 Digger description

Fig. 14 Bluetooth RC controller application

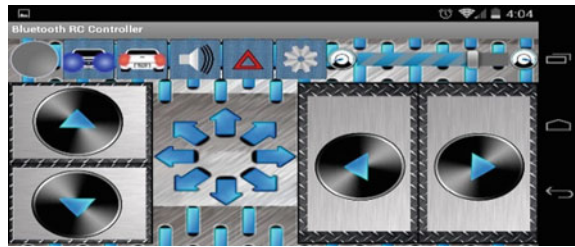


Fig. 15 Bluetooth connection with Arduino

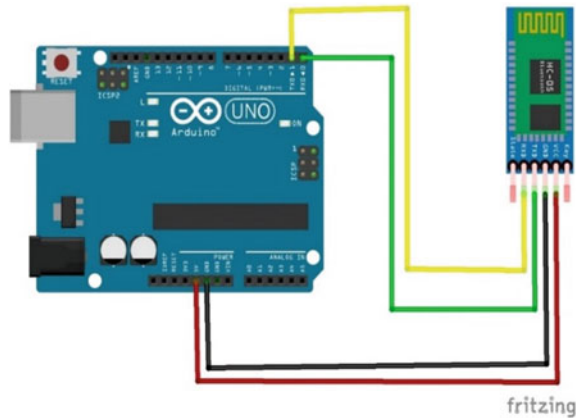
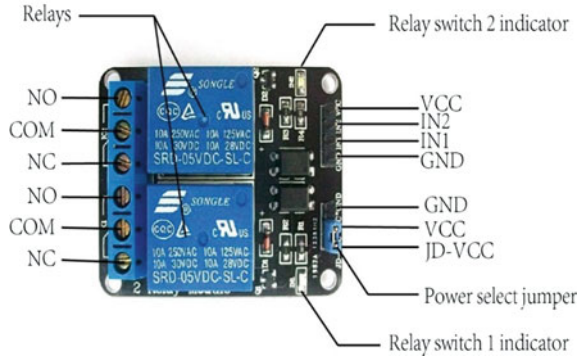


Fig. 16 Relay connections



unique advantages and disadvantages, and the solar panel type best suited for your installation will depend on factors specific to your own property and desired system characteristics. The proposed prototype installed by monocrystalline type of 130 W and 12 V of size 29.9 * 21.2 * 1.1 inches. The selection of the selected panel is based on some calculations as shown below:

Calculation of the required power of the proposed Agrobot:

Starting point of main motion:

$$P = (\text{No of motors} \times V \times I \times \text{factor of safety})$$

$$P = 4 \times 12 \times 1.8 \times 1.2 = 103.68 \text{ W}$$

Starting point for seeder and digging mechanisms:

$$P = (\text{No of motors} \times V \times I) \text{ for main motion} + (\text{No of motors} \times V \times I \times \text{factor of safety})$$

$$P = (4 \times 12 \times 1.8) + (2 \times 12 \times 1.5 \times 1.2) = 129.6 \text{ W}$$

So the proposed Agrobot needs solar panels at least 130 watts.

3 Conclusion

The proposed design of renewable Agrobot has an environmental and social impacts by achieving food self-sufficiency and extension of green areas. The proposed Agrobot can save electric power by choosing lightweight materials suitable to the working conditions. Implementation of the proposed Agrobot has significant increasing of production and savings of casts, water consumption, and farmers' efforts. Also, controlling can be achieved by wireless mobile application, and panels can charge the battery that makes the proposed robot which can work during all the day.

References

1. Vidyasagar C, Hemalatha J, Velmurugadass P, Anand SS (2019) Use of robotics in agricultural field and its applications: short commentary. *Adv Robot Autom* 8
2. Jiang L, Zhang Y (2018) Making agriculture more intelligent: progress of agricultural robots. *Robot Autom Eng J* 4
3. Agarwal N, Thakur R (2016) Agricultural robot: intelligent robot for farming. *Int J Sci Eng Technol* 3
4. Hansen KD, Garcia-Ruiz F, Kazmi W (2013) An autonomous robotic system for mapping weeds in fields. *Int Fed Autom Control* 10
5. Behmanesh M, Hong TS, Kassim MSM, Azim A, Dashtizadeh Z (2017) A brief survey on agricultural robots. *Int J Mech Eng Robot Res* 6
6. Nielsen SH, Bøggild A, Jensen K, Bertelsen KK, Jørgensen RN (2019) Implementations of FroboMind using the robot operating system framework. <http://www.njf.nu/site/seminarRedirect.asp?intSeminarID=441&p=1004>
7. Pfaff J, Baur J, Schütz C, Buschmann T, Ulbrich H (2014) Design of drive units for agricultural robots. In: International conference of agricultural engineering
8. Celen IH, Onler E, Kilic E (2015) A design of an autonomous agricultural robot to navigate between rows. In: International conference of electrical, automation and mechanical engineering
9. Manikandan K, Sreenivasan S (2014) Composition of agricultural robotic technology. *Int J Agric Environ Sci* 1
10. Ramesh AP, Pasupathy N (2019) Design and implementation of remote sensing robotic platform for precision agriculture. *Int J Innov Technol Exploring Eng* 8
11. Kulkarni AA, Dhanush P, Chetan BS, Thamme Gowda CS, Shrivastava PK (2019) Applications of automation and robotics in agriculture industries: a review. In: International conference on mechanical and energy technologies
12. Keerthana A, Kirubaharan P, Krishnamoorthy S, Rajeswari K, Syed Zabiullah G (2018) Agriculture robot for seeding and forming. *Int Res J Eng Technol* 5
13. Patil C, Deshmukh V, Deshmukh S, Rai G, Bute P (2018) Design and fabrication of multipurpose agro system. *Int J Curr Eng Sci Res* 5
14. Tabile RA, Godoy EP, Pereira RRD, Tangerino GT, Porto AJV, Inamasu RY (2011) Design and development of the architecture of an agricultural mobile robot. *Eng Agríc Jaboticabal* 31
15. Mocera F, Nicolini A (2018) Multibody simulation of a small size framing tracked vehicle. *Procedia Struct Integrity* 8
16. Pecka A, Osadcuks V (2018) Conceptual design of modular multi functional agricultural mobile robo. *Res Rural Dev* 1
17. Emmi L, Gonzalez-de-Soto M, Pajares G, Gonzalez-de-Santos P (2014) New trends in robotics for agriculture: integration and assessment of a real fleet of robots. *Sci World J* 2014

Estimation of Mechanical Properties of Kenaf Fiber Reinforced Polyester Composites



Shilpa S. Bhambure and Addanki S. Rao

Abstract Nowadays, in fiber reinforced composites, natural fibers are used as better alternative to synthetic fibers due to their properties such as biodegradability, high stiffness, strength and low density, low cost. It was observed that one of the plant fibers, kenaf fiber had wide possibilities in replacing the conventional fibers. This realization has motivated all the researchers for the development of new innovative bio-based composites. In present study, the composites were prepared by varying length of kenaf fiber. The mechanical properties such as tensile, bending, and impact strength of plain polyester and kenaf fiber reinforced composites were analyzed experimentally. Composite prepared with 10 cm kenaf fiber length shows maximum tensile strength of 40.765 MPa and impact strength of 4.686 kJ/m². Composite prepared with 15 cm kenaf fiber length shows maximum bending strength of 63.44 MPa and bending modulus of 2.657 GPa.

Keywords Kenaf fiber · Polyester resin · Tensile strength · Bending strength · Impact strength

1 Introduction

Composite is very fascinating mixture which is not found in nature directly. It is combination of different nature materials to fabricate advanced materials with new properties as needed [1]. The matrix is reinforced with different materials strengthen its physical and mechanical properties. Composite mechanical properties vary depending on the matrix and reinforcing material used for it [2]. Nowadays, because of growing environs consciousness, polymer composites reinforced with natural fibers is making researchers and scientists attentive in consequence of

S. S. Bhambure (✉) · A. S. Rao
Department of Mechanical Engineering, VJTI, Mumbai, India
e-mail: shilpabhambure@somaiya.edu

A. S. Rao
e-mail: asrao@me.vjti.ac.in

advantages namely low density, low cost, less health risk, partially or completely recyclable, easy availability, admissible specific strength, and biodegradability over traditional fibers [3, 4]. But some of the natural fiber limitations such as dimensional stability, water absorption, and poor adhesion with resin need to be considered for further improvement [5]. Cellulose-based natural fibers are cheap, light, strong, and available in ample amount. Recently, polyester composites reinforced with natural fibers found several applications in areas of sporting goods, electrical, automotive, industrial, and construction due to their desirable characteristics such as environment friendly, have high specific stiffness, and strength [6].

This interest encompasses an extensive variation of materials varying from synthetic to natural, orderly to attain the need of fabricating composites with required characteristics. In many engineering applications, the inclusion of fillers and fibers into composites provide a way of enhancing the composite properties which can fulfill the demands. [7]. So natural fiber-reinforced polymer composites have an emerging future as upcoming substitute for plastics or metals in various applications [8]. Some researchers have done the survey on energy required for extraction of natural and glass fibers and found that using natural fibers instead of glass fiber can save 60% energy per ton of fiber. Also uses of natural fibers not only help us in environment balance but can provide employment to the people in rural areas where natural fibers are available in ample amount [9]. Current research shows that natural fibers can very well utilized in place of glass fibers in polymer composites. The composites are relatively inexpensive to manufacture as many manufacturing processes are available. Exchanging steel with composites can save component weight by 60–80% [10].

Biocomposites are generally fabricated with non-biodegradable or biodegradable polymers as matrix and lignocellulosic natural fibers such as sisal, hemp, and abaca jute, as reinforcement because of their moderate specific mass and adequate mechanical properties [11]. In literature, some authors predicted the tensile strength of biocomposites by varying the length of fiber and commented that increasing fiber length has notable improvement in tensile strength of composite [12]. The strength of natural fiber is mainly affected by factors, namely cellulose content, microfibrillar angle, and aspect ratio. Low microfibrillar angle and more cellulose content provide higher strength to fiber [13]. At present, natural fibers make up above 14% part of reinforcing material; although the share is predicted to arise 28% by totaling to around 8,30,000 tons of natural fibers [14].

Kenaf is mostly grown in India, Malaysia, China, and Bangladesh. Its origin is Africa and has found good future in many biocomposite applications. Kenaf fiber has low density and high mechanical properties which make it as good alternative in fiber reinforced composites. Energy required to produce 1 kg of glass fiber is 54 MJ, whereas it takes just 15 MJ for 1 kg kenaf fiber. Our research work aims to prepare kenaf fiber reinforced composite with simple hand lay-up technique and to estimate its mechanical properties such as tensile, bending, and impact strength experimentally.

2 Materials and Methods

Matrix material used in this study unsaturated polyester resin, catalyst methyl ethyl ketone peroxide (MEKP), and initiator cobalt oxide were purchased from Manish Resins & Polymers Pvt. Ltd, Mumbai, India. Unsaturated polyester has numerous benefits compared to other resins such as low pressure and room temperature molding capabilities which make it useful for large component manufacturing at comparably low cost [6]. The kenaf fibers were collected from Yavatmal district, Maharashtra, India. Kenaf fiber was first dried at 100 °C in an oven to remove moisture. Then, fibers were cut into 5, 10, 15, 20, and 25 cm length. First the mold release agent was applied on mold. Cut kenaf fibers were randomly placed in the mold with 30 cm × 30 cm outer dimensions and 25 cm × 25 cm inner dimension. After adding 3% of cobalt oxide and MEKP each to the polyester resin, it was poured manually over the kenaf fibers kept in mold. It was then covered with thin plastic sheet, and steel hand roller was used to remove trapped air if any and excess of resin. The top mold was then kept on sample along with the dead weight of 25 kg on it. The sample was allowed to cure for 24 h and then removed from mold. The post curing was done at 80°C in hot air oven for 5 h. All the samples of fiber varying length were prepared in the similar way with hand lay-up method.

3 Mechanical Testing

3.1 Tensile Test

ASTM D638 Type IV standard shown in Fig. 1 was used to cut tensile test specimens out of sheet. The tests were conducted at ambient conditions using 5 kN capacity Tinius Olsen machine shown in Fig. 2 with crosshead speed of 5 mm/min. The tensile strength was reported in MPa.

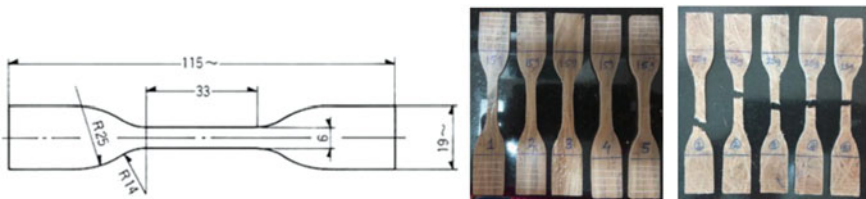


Fig. 1 ASTM D638 for tensile test specimen



Fig. 2 Tensile testing machine

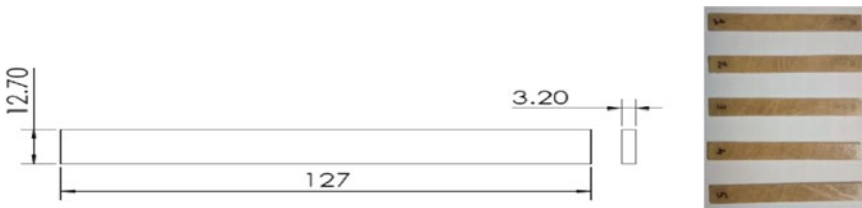


Fig. 3 ASTM D790 for bending test specimen

3.2 *Bending Test*

ASTM D790 standard shown in Fig. 3 was used to cut bending test specimens. The three-point bending test was conducted on Tinus Olsen machine shown in Fig. 4 with span length of 80 mm for all specimens and crosshead speed of 5 mm/min.

3.3 *Impact Test*

ASTM D256 standard shown in Fig. 5 was used to cut the impact test specimen. The V notch was prepared with triangular file. The test was carried out at room temperature using Izod impact testing machine shown in Fig. 6.



Fig. 4 Three-point bending test

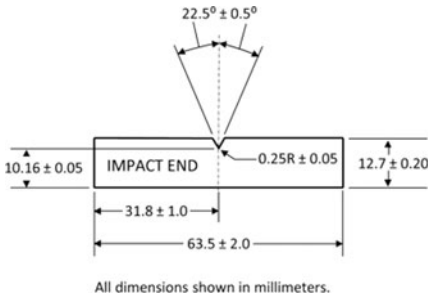


Fig. 5 ASTM D256 for impact test specimen

4 Results and Discussion

The plain polyester sheet was prepared in the same mold and allowed to cure for 24 h at room temperature, and post-curing was done at 80 °C for 5 h. The test specimens were then cut according to ASTM standard. The literature values for Young’s modulus, tensile, bending, and impact strength of plain polyester were compared with experimental values given in Table 1.

Fig. 6 Impact testing machine

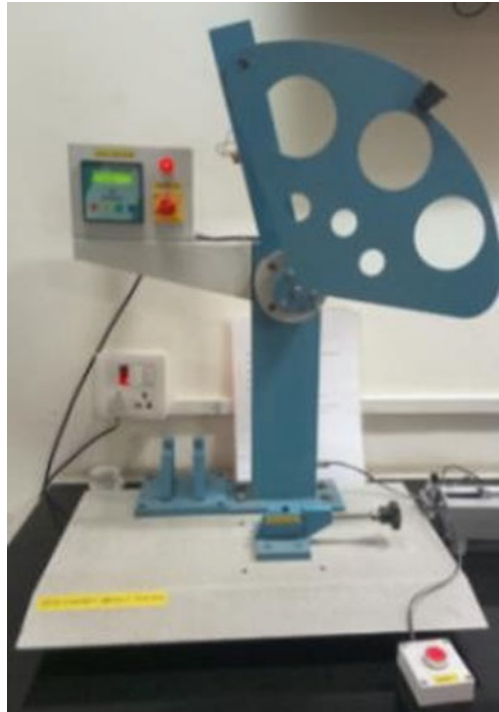


Table 1 Mechanical properties of plain polyester

Plain polyester				
	Tensile strength (MPa)	Young's modulus (GPa)	Bending strength (MPa)	Impact strength (KJ/m ²)
Literature value	55	2.8	90	3.85
Experimental value	53.889	2.36	80.415	3.75

4.1 Tensile Strength

Figure 7 shows tensile strength of plain polyester as 53.889 MPa and maximum tensile strength for composite with 10 cm fiber length as 40.765 MPa. It was observed that with further increase in fiber length, tensile strength of composite decreases.

Fig. 7 Tensile strength of polyester and kenaf fiber reinforced polyester composites

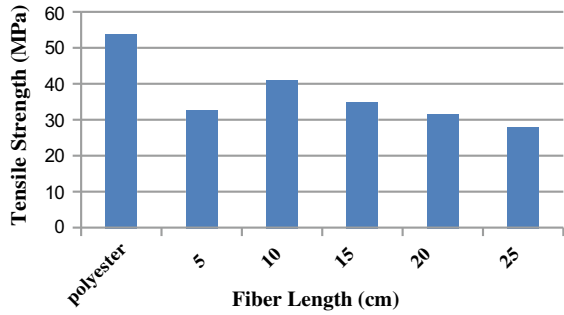
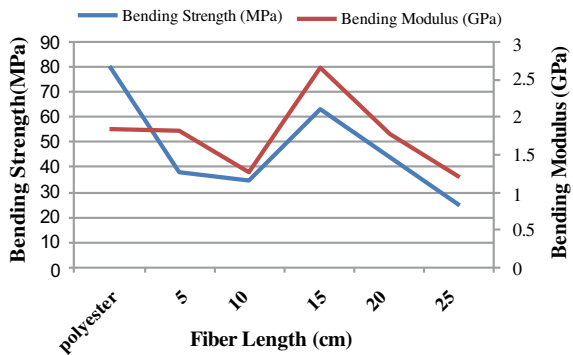


Fig. 8 Bending strength and modulus of polyester and kenaf fiber reinforced polyester composite



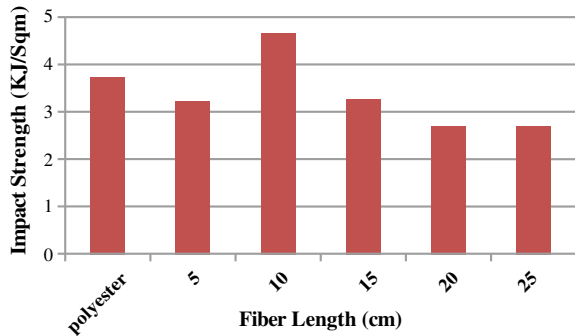
4.2 Bending Strength

Figure 8 shows bending strength and bending modulus for plain polyester and kenaf fiber reinforced polyester composites. Among prepared composites 15 cm kenaf fiber reinforced composite shows maximum bending strength of 63.44 MPa and bending modulus of 2.657 GPa.

4.3 Impact Strength

Figure 9 shows impact strength for plain polyester and kenaf fiber reinforced polyester composites. The 10 cm kenaf fiber length reinforced composite shows maximum impact strength of 4.686 kJ/m².

Fig. 9 Impact strength of polyester and kenaf fiber reinforced polyester composite



5 Conclusion

The raw kenaf fiber reinforced polyester composites prepared by varying the length of fiber shows considerable effect on mechanical properties such as tensile, bending, and impact strength. Compared to plain polyester kenaf, fiber reinforced composites show less tensile and bending. Strength, whereas composite with 10 cm fiber length shows around 20% increase in impact strength. Composite prepared with 15 cm fiber length shows significant increase in bending modulus.

References

1. Suharty NS, Ismail H, Diharjo K, Handayani DS, Firdaus M (2016) Effect of Kenaf fiber as a reinforcement on the tensile, flexural strength and impact toughness properties of recycled polypropylene/halloysite composites. *Procedia Chem* 19:253–258. <https://doi.org/10.1016/j.proche.2016.03.102>
2. Fahim IS, Elhaggar SM, Elayat H (2012) Experimental investigation of natural fiber reinforced polymers. *Mater Sci Appl* 3(2):59–66. <https://doi.org/10.4236/msa.2012.32009>
3. Ku H, Wang H, Pattarachaiyakoop N, Trada M (2011) A review on the tensile properties of natural fiber reinforced polymer composites. *Compos Part B Eng* 42(4):856–873. <https://doi.org/10.1016/j.compositesb.2011.01.010>
4. Badrinath R, Senthilvelan T (2014) Comparative investigation on mechanical properties of banana and sisal reinforced polymer based composites. *Procedia Mater Sci* 5:2263–2272. <https://doi.org/10.1016/j.mspro.2014.07.444>
5. Yahaya R, Sapuan SM, Jawaid M, Leman Z, Zainudin ES (2016) Effect of fibre orientations on the mechanical properties of kenaf–aramid hybrid composites for spall- liner application. *Def Technol* 12(1):52–58. <https://doi.org/10.1016/j.dt.2015.08.005>
6. Rashdi AAA, Salit MS, Abdan K, Megat MMH (2010) Water absorption behaviour of Kenaf reinforced unsaturated polyester composites and its influence on their mechanical properties. *Pertanika J Sci Technol* 18(2):433–440
7. Akil HM, Omar MF, Mazuki AAM, Safiee S, Ishak ZAM, Abu Bakar A (2011) Kenaf fiber reinforced composites: a review. *Mater Des* 32(8–9):4107–4121. <https://doi.org/10.1016/j.matdes.2011.04.008>

8. Romli FI, Alias AN, Rafie ASM, Majid DLAA (2012) factorial study on the tensile strength of a coir fiber-reinforced epoxy composite. AASRI Procedia 3:242–247. <https://doi.org/10.1016/j.aasri.2012.11.040>
9. Mishra V, Biswas S (2013) Physical and mechanical properties of bi-directional jute fiber epoxy composites. Procedia Eng 51:561–566 (no. NUiCONE). <https://doi.org/10.1016/j.proeng.2013.01.079>
10. Gopinath A, Senthil Kumar M, Elayaperumal A (2014) Experimental investigations on mechanical properties of jute fiber reinforced composites with polyester and epoxy resin matrices. Procedia Eng 97:2052–2063. <https://doi.org/10.1016/j.proeng.2014.12.448>
11. Rajesh G, Prasad AVR (2014) Tensile properties of successive Alkali treated short Jute Fiber reinforced PLA composites. Procedia Mater Sci 5:2188–2196. <https://doi.org/10.1016/j.mspro.2014.07.425>
12. Capela C, Oliveira SE, Pestana J, Ferreira JAM (2017) Effect of fiber length on the mechanical properties of high dosage carbon reinforced. Procedia Struct Integr 5:539–546. <https://doi.org/10.1016/j.prostr.2017.07.159>
13. Kumar R, Ul Haq MI, Raina A, Anand A (2019) Industrial applications of natural fibre-reinforced polymer composites—challenges and opportunities. Int J Sustain Eng 12(3):212–220. <https://doi.org/10.1080/19397038.2018.1538267>
14. Rwawiire S, Tomkova B, Militky J, Jabbar A, Kale BM (2015) Development of a biocomposite based on green epoxy polymer and natural cellulose fabric (bark cloth) for automotive instrument panel applications. Compos Part B Eng 81:149–157. <https://doi.org/10.1016/j.compositesb.2015.06.021>

Evaluating Torsional Properties of FDM Components for Various Layer Heights



Prasad A. Hatwalne and S. B. Thakare

Abstract In the below presented work, the steps are taken to evaluate torsional strength of parts developed using fused deposition modelling (FDM). For this test, samples were 3D printed using ABS material and then investigated to understand the influence of layer height on the torsional strength of components. The parts were fabricated and tested as per ASTM standards with varying the layer height of 0.14 mm, 0.16 mm and 0.22 mm. Further, the parts were applied with acetone bath treatment and its effect on torsion strength is also investigated. The obtained values of torsional properties were compared with the injection moulded parts from literature. The results show that torsional properties of components manufactured by FDM are significantly influenced by variation in layer height. Comparatively, injection moulded parts were found to have better torsional properties.

Keywords Fused deposition modelling (FDM) · Injection moulding · Torsional strength

1 Introduction

Fused deposition modelling is additive manufacturing methods in which the components are produced by layer-wise deposition of the thermoplastic material. In FDM, firstly, the 3D CAD model is developed using appropriate designing software. For more complex, geometry scanned images are directly used. The developed CAD model is changed to STL format which is suitable for the machine. The software of the FDM printer evaluates the geometry of the CAD model and accordingly develops the toolpath for component fabrication. As per the developed toolpath, heated extruded nozzle moves across the X – Y direction and deposits the layer of semi-molten thermoplastic material. This deposited layer solidifies instantly and then the extrusion

P. A. Hatwalne (✉)

Department of Mechanical Engineering, YCCE Nagpur, Nagpur, India

S. B. Thakare

Department of Mechanical Engineering, PRMIT&R, Badnera, India

nozzle is raised vertically upward (Z direction) relative to deposition platform, and then, the next layer of semi-molten material is deposited. [1] There are many industrial applications of FDM such as aviation industry, automobile industry, medical and electronics industry [2].

Initially, the additive manufacturing (AM) was invented as a tool for rapid prototyping of a product. The parts produced AM technology was used for prototyping, visualization and validation of design [3]. But with continuous development in this field and applications growing in diversity of 3D printed parts, the paradigm has shifted to rapid manufacturing from rapid prototyping. But the FDM technology has its limitations like the requirement of support material for overhanging and hollow structures, lower mechanical properties of parts due to anisotropic nature, staircase effects at curves, poor surface finish, less sensitivity to dimensional accuracy, etc. [3]. A critical review of the literature suggests that the processing parameters like layer height, raster angle, extrusion temperature, air gap raster width, built orientation, etc., strongly influence the quality of the part being printed [4]. Accordingly, many researchers have been conducted in last two decades to address the above-mentioned challenges through the optimization of the process parameters.

Prithvi shubham et al. in their research work considered the variation in layer thickness to analyze its impact on the tensile properties of ABS parts. In their work, they observed that ultimate tensile strength decreases as the layer height increases [5].

Ashu garg et al. analyzed the mechanical properties of FDM parts with X -, Y - and Z -axis build orientation and with raster angle 0° , 30° , 60° and 90° . They found that parts built along the X - and Y -axis direction with raster angle 60° have more tensile strength than Z -axis built direction parts. Further, he found that application of acetone treatment results in slight reduction in mechanical strength of parts [6].

Sandeep raut et al. investigated the impact of variation in built orientation on tensile strength and bending strength of FDM printed parts and their findings suggested that specimen fabricated along Y -axis with 0° gives maximum tensile strength, and maximum bending strength was observed for X -axis at 0° orientation [7].

T. Nancharaiah et al. investigated the effect of road width, layer thickness, air gap and raster angle on dimensional accuracy and surface finish [8].

Aboma wagori et al. used full factorial ANOVA design of experiments and evaluated the tensile strength of ULTEM 9085 specimen for variations in raster angle, air gap, contour width, contour numbers. They concluded that as the raster angle increases, tensile strength also increases [9].

Cristiana Valen et al. conducted their research on PLA specimens to investigate the effect of spatial orientation and layer height on tensile strength. Their findings suggested that increase spatial orientation reduces the tensile strength by about 8% [10].

MST Fouja Afrose in his research work found that PLA printed specimen exhibits maximum tensile strength along X direction as compared to Y direction and 45° orientated specimen [11].

After reviewing the literature critically, it was observed that the problems of mechanical properties such as bending strength, tensile strength, compressive

strength and fatigue strength have been addressed so far by many researchers. The effect of various processing parameters on torsional strength of FDM parts has found to be very little explored till date. As the applications of FDM continue to grow on diversity such as gears and bearings, it is necessary to understand the performance of FDM components under these loading conditions also. So in the present work, the specimens were printed with three different layer heights and its effect on torsional strength of FDM components is investigated experimentally.

2 Methodology

2.1 Sample Preparations

The specimen to be tested is printed as per ASTM–E143 standard. The CAD models of test specimens are created in CATIA software as per the guidelines in ASTM–E143 standard. All the test specimens were printed using acrylonitrile butadiene styrene thermoplastic material (ABS) with a layer thickness of 0.14 mm, 0.18 mm and 0.22 mm (Fig. 1).

The effect of layer thickness and acetone bath treatment on torsional strength was investigated independently. Layer height is the thickness of layer deposited by nozzle. Samples with different thicknesses (0.12 mm, 0.14 mm and 0.16 mm) were printed using ABS material. Additionally, three samples with the same layer thickness were printed and they were subjected to acetone vapour treatment to investigate the effect of this post acetone treatment on torsional strength. The other printing parameters were

Fig. 1 FDM printer



Table 1 Printing parameters values for printing

Control factors			Fixed factors		
Factors	Level	Unit	Factors	Value	Unit
Layer height	0.14	mm	Built orientation	0	
	0.18	mm	Raster angle (RA)	0	°
	0.22	Mm	Extrusion temperature	210	°C
			Air gap	0	Mm

Fig. 2 ABS specimen with different layer thickness acetone treatment



Fig. 3 ABS specimen with a different layer thickness (without acetone treatment)



kept fixed at the level as shown in Table 1. Accordingly, total of six test specimens were fabricated as shown in Figs. 2 and 3.

2.2 Torsional Testing

To evaluate the effect of layer height and acetone treatment on FDM components, the built specimens were tested as per ASTM standard on torsional testing machine as shown in Fig. 4. Monotonic torsional test was performed at the speed of one degree per second. The real-time data recorded were load applied in Kgf and corresponding angle of twist. For each specimen, the shear stress τ (Mpa), modulus of rigidity G and shear strain produced γ calculated.

Fig. 4 Torsional testing setup



3 Result and Discussions

3.1 Impact of Variation in Layer Thickness on Torsional Properties of ABS Specimen

As shown in Table 2, the values of shear stress (τ) Mpa, modulus of rigidity (G) and shear strain (γ) for the ABS samples with and without post chemical bath treatment of acetone. It can be noted that the maximum shear stress is obtained for ABS material for 0.18 m layer thickness in both cases, i.e. without chemical bath and with a chemical bath. The corresponding value of shear stress is found to be 22.29 Mpa and 24.88 Mpa. But from these results, it can be seen that chemical treatment has very little effect on the torsional strength of the parts manufactured using FDM.

Similarly, if we compare the values of modulus of rigidity (G) for ABS, the maximum value of G is observed for the layer thickness of 0.18 mm and shear strain values are found to be maximum for 0.28 mm layer thickness with acetone treatment (Fig. 5).

Table 2 Various torsional for different layer thickness and post acetone treatment

Sr. No	Type of specimen	Shear stress τ (Mpa)	Modulus of rigidity (G) Mpa	Shear strain produced (γ)
1	ABS 0.14	16.44	71.29	2.152
2	ABS 0.18	22.29	73.23	2.9088
3	ABS 0.22	12.44	72.28	1.628
4	ABS 0.14 chemical bath	22.22	65.29	2.908
5	ABS 0.18 chemical bath	24.88	70.28	3.25
6	ABS 0.22 chemical bath	15.11	71.30	1.97

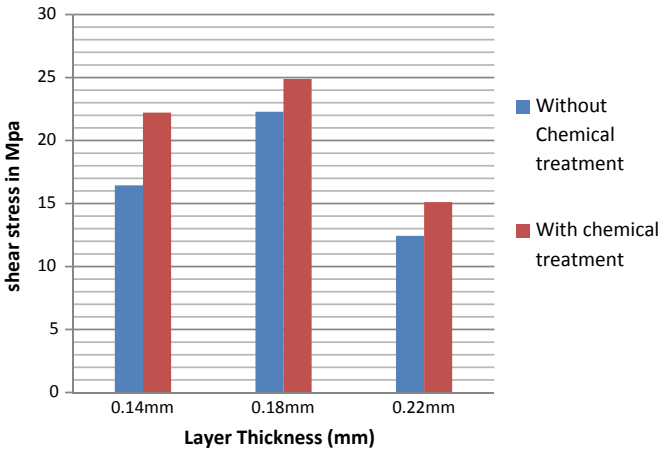


Fig. 5 Variation of shear stress with layer thickness

Overall, if these values are compared with the values of the same parameters of parts manufactured by injection moulding process, it can be said that the layer height affects the torsional properties of FDM specimen. When these observations compared with values obtained by other researchers for similar experimentation [12], it can be said that extent of influence of layer thickness and acetone treatment on torsional properties of ABS parts is almost the same as that of some other variables like built orientation and raster angle. But for through characterization under torsional loading conditions, the effect of other parameters on the same must be investigated.

4 Conclusion

In the research work carried out as above, the impact of layer height and post-processing chemical treatment of acetone on torsional properties of ABS specimen printed by fused deposition modelling is investigated.

- (1) When the obtained results are compared with the values of the same parameters of parts manufactured by injection moulding, it can be concluded that layer thickness and post acetone treatment affect the torsional properties significantly. Injection moulded parts have comparatively greater values.
- (2) When the obtained results are compared with results of other similar experimentation in which the influence of built orientation and raster angle is investigated, it can be concluded that variation in layer thickness and acetone treatment quantitatively has the almost same effect that built orientation and raster angle have on torsional properties.

- (3) If the influences of acetone treatment on torsional properties are observed, then it can be concluded that acetone treatment does not affect the said properties to much extent as compared to without acetone treatment parts.

Overall from the present investigation, it can be concluded that the effect of layer height and acetone treatment of torsional properties of ABS specimen is quantitatively the same as the effect of raster angle and built orientation. For through characterization, the effect of other processing parameters on torsional properties of FDM parts must be investigated. This will help to explore the potential of the FDM process to manufacture the parts which are subjected to torsional load.

References

1. Dey A, Yodo N (2019) A systematic survey of FDM process parameter optimization and their influence on part characteristics. *J Manuf Mater Process* 3(3):64–70
2. Rajpurohit SR, Dave H (2018) Effect of process parameters on tensile strength of FDM printed parts. *Rapid Prototyping J* 24(8):1317–1324
3. Alafaghani A, Qattawi A, Alrawi B, Guzman A (2017) Experimental optimization of fused deposition modelling processing parameters: a design-for-manufacturing approach. *Procedia Manuf* 10:791–803
4. Garg A, Bhattacharya A, Batish A (2017) Chemical vapor treatment of ABS parts built by FDM: Analysis of surface finish and mechanical strength. *Int J Addit Manuf technology* 89:2175–2191
5. Shubham P, Sikidar A, Chand T (2016) The influence of layer thickness on mechanical properties of the 3D printed ABS polymer by fused deposition modeling. *Key Eng Mater* 706:63–67
6. Gerg A, Bhattacharya A, Batish A (2016) On surface finish and dimensional accuracy of FDM parts after cold vapor treatment. *Mater Manuf Process* 31(4):522–529
7. Rauta S, Jattib VKS, Khedkar NK, Singh TP (2014) Investigation of the effect of built orientation on mechanical properties and total cost of FDM parts. In: *Procedia materials science, 3rd international conference on material processing and material characterisation vol 6*, pp 1625–1630
8. Nancharaiah T, Raju DR, Raju VR (2010) An experimental investigation on surface quality and dimensional accuracy of FDM components. *Int J Emerg Technol* 1(2):106–111
9. Gebisa AW, Lemu HG (2019) Influence of 3D printing process parameters on tensile property of ULTEM 9085. In: *Procedia manufacturing, 14th global congress on manufacturing and management, vol 30*, pp 331–338
10. Vălean C, Marşavina L, Mărghita M, Linul E, Razavi J, Berto F (2020) Effect of manufacturing parameters on tensile properties of FDM printed specimens. In: *Procedia structural integrity, MedFract1 the 1st mediterranean conference on fracture and structural integrity, vol 26*, pp 313–320
11. Afrose MF, Masood SH, Iovenitti P, Nikza M, Sbarski I (2016) Effects of part build orientations on fatigue behaviour of FDM-processed PLA material. *Prog Addit Manuf* 1:21–28
12. Balderrama-Armenariz CO et al (2018) Torsion analysis of the anisotropic behavior of FDM technology. *Int J Adv Manuf Technol* 96:307–317

Experimental Investigation in Wire Cut EDM of Inconel 718 Superalloy



Ayanesh Y. Joshi, Vaishal J. Banker, Kenil K. Patel, Kashyap S. Patel, Devarsh M. Joshi, and Madhav R. Purohit

Abstract Wire cut electric discharge machining (WEDM) possesses capabilities of manufacturing complex shapes which are of hard materials, carbides, tool steels, or superalloys. The present work deals with investigation of surface roughness (SR) and material removal rate (MRR) in WEDM of Inconel 718 alloy. Taguchi's L27 orthogonal array is utilized for carrying out the experimentation having input parameters as pulse on time, peak current, duty cycle, and wire feed rate. It is observed that as pulse on time was the most significant parameter for the responses which were surface roughness (SR) and material removal rate (MRR). Analysis of variance (ANOVA) was also carried out for the results and values of R^2 and R^2 (adj) deduced that model developed was accurate.

Keywords WEDM · Taguchi method · Inconel 718 · Surface roughness · MRR · ANOVA

1 Introduction

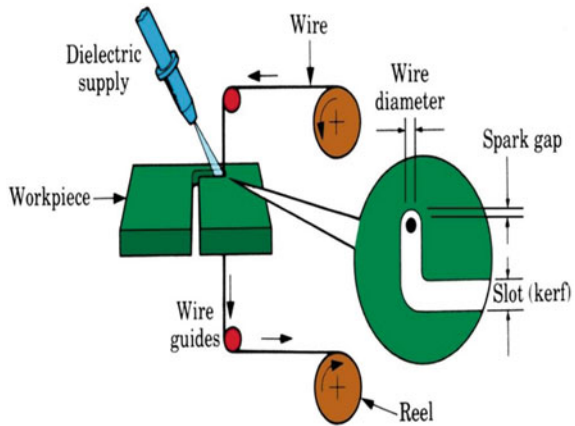
WEDM is an electro thermal manufacturing process wherein a thin metal wire in combination with deionized water allows the wire to cut through metal by using the heat developed from electrical sparks and is frequently used where low residual stresses are anticipated. Major applications are to cut plates which can be thick as 300 mm and to make machine tools like punches, cutting tools, and dies from hard metals that are difficult to machine with other methods. The part and wire are kept in a dielectric fluid which also cools and flushes the debris away shown in Fig. 1. Inconel 718 is a hard-to-cut alloy superalloy having various industrial applications in

A. Y. Joshi (✉) · V. J. Banker · K. K. Patel · K. S. Patel · D. M. Joshi · M. R. Purohit
Mechanical Engineering Department, A D Patel Institute of Technology, New Vallabh
Vidyanagar, Anand 388121, Gujarat, India
e-mail: ayjoshi@adit.ac.in

V. J. Banker
e-mail: me.vaishal@adit.ac.in

© The Author(s), under exclusive license to Springer Nature Singapore Pte Ltd. 2022
H. K. Dave et al. (eds.), *Recent Advances in Manufacturing Processes and Systems*,
Lecture Notes in Mechanical Engineering,
https://doi.org/10.1007/978-981-16-7787-8_35

Fig. 1 Working principle of WEDM process [2]



jet engine and high-speed airframe parts, including wheels, fasteners, bolts, spacers, and buckets.

It is observed from the previous studies that surface roughness plays a pivotal role in Inconel 718 parts and is largely affected by wire feed rate and head feed rate [1]. A proper shape accuracy is achieved if normal-to-feed direction is met in machining of Inconel 718 alloy [2–6]. Various parameters like pulse on time, pulse off time, peak voltage, spark voltage, and dielectric flow pressure are used to carry out experimentations. Significance of water pressure, wire feed is found to be the least by review of effects of different process parameters [7–12].

Over the years, works on understanding different effects of input parameters in machining of Inconel 718 alloy and measuring its toughness, hardness, impact resistance, etc., are published throughout the world. Very few works are found for studying effect process parameters on surface roughness (SR) and material removal rate (MRR) which remain desirable in case of turbine manufacturing and also a prime application of Inconel 718. Therefore, in the present work, an effort has been made to study effect of different machining parameters like pulse on time, peak current, duty cycle, and wire feed rate on machining characteristics of superalloy.

2 Materials and Method

2.1 Design of Experiment

Taguchi's method was utilized for design of experiments having process parameters and levels shown in Table 1. The number of experiments were reduced to 27 from 81 using L27 orthogonal array using MINITAB 19 software [13]. Duty cycle was calculated using the following Eq. 1

Table 1 Input parameters used for experimentation and their levels

Input parameters	Levels		
	I	II	III
Pulse on time (T_{on})	40 μ s	70 μ s	110 μ s
Peak current (I_p)	2 A	4 A	6 A
Duty cycle	0.6	0.7	0.8
Wire feed rate (W_f)	0 (50 mm/min)	1 (100 mm/min)	2 (150 mm/min)

$$\text{Duty cycle} = \frac{T_{on}}{T_{on} + T_{off}} \tag{1}$$

Values of pulse off time (T_{off}) were taken as given in Table 3.

2.2 Methodology and Experimental Setup

Figure 2 shows the flowchart of process deployed for experimentation and WEDM setup used at Lalguru Engineering Unit-2 located in Vitthal Udhyanagar, Anand, and Gujarat. Specifications of the experimental setup used are given in Table 2. Inconel 718 having length as 300 mm and diameter of 22 mm were utilized for workpiece

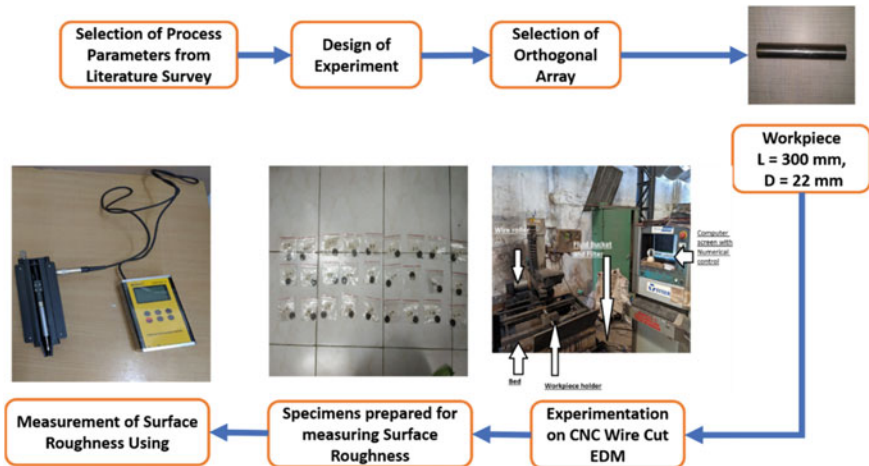


Fig. 2 Flowchart for experimentation

Table 2 Machine specifications

Description	Remark
Deionized water used for each experiment	20 L
Gel used	J3RA ointment
<i>X Y</i> axis	360 × 250 mm
Net weight	2300 kg
Coolant tank system	30 L
Max size of working piece	725 × 560 × 220 mm
<i>XY</i> feed rate	Max 800 mm/min
Motor system	AC servo motor

as visible in Fig. 2. Deionized water with a soluble gel was used for the experimentation. Material of wire was molybdenum having diameter of 0.2 mm. After the experimentation was complete, a surface roughness measurement instrument Metrix SurfTest 10 was used for measurement of surface roughness as described in Fig. 2 having a cutoff length of 2.5 mm.

3 Results and Discussion

There were 27 experiments conducted for the various set of process parameters as given in Table 3. The analysis of the design, main effects plots, and the plots for S/N ratios was made in MINITAB 19 software. The ratio “smaller the better” of Taguchi’s method was used for minimizing the surface roughness, while for material removal rate, the ratio “larger the better” was used. It is calculated by Eqs. 2 and 3 given below where n is the number of variables, and y_i is the value of output desired. Analysis of variance (ANOVA) is utilized to find out the utmost significant parameter affecting the output responses, and the model was developed in MINITAB 19 software, where a confidence level was set at 95%.

Larger the better S/N ratio

$$\eta = -10 \log \left[\frac{1}{n} \sum \left(\frac{1}{y_i^2} \right) \right] \quad (2)$$

Smaller the better S/N ratio

$$\eta = -10 \log \left[\frac{1}{n} \sum (y_i^2) \right] \quad (3)$$

Table 3 Results of surface roughness (μm) and MRR (mm^3/min) in WEDM of Inconel 718 superalloy

Sr. No.	T_{on} (μs)	T_{off} (μs)	I_p (A)	Duty cycle	W_f (mm)	SR (μm)	SR S/N ratio	Cutting time (min)	MRR (mm^3/min)	MRR S/N ratio
1	40	27	2	0.6	0	2.52	-8.0801	8.27	7.98	18.04006
2	40	27	2	0.6	1	2.6	-8.2947	9.2	7.17	17.11038
3	40	27	2	0.6	2	2.8	-8.9316	10.18	6.48	16.2315
4	40	17	4	0.7	0	4.95	-13.921	4.47	14.76	23.38173
5	40	17	4	0.7	1	4.57	-13.983	5.5	12	21.58362
6	40	17	4	0.7	2	4.6	-13.552	8.35	7.89	17.94154
7	40	10	6	0.8	0	4.91	-13.216	5.18	12.72	22.08974
8	40	10	6	0.8	1	5.22	-14.534	6.08	10.83	20.69257
9	40	10	6	0.8	2	5.91	-15.317	6.15	10.71	20.59579
10	70	30	2	0.7	0	3.43	-10.059	8.3	7.95	18.00734
11	70	30	2	0.7	1	3.2	-10.03	9.2	7.71	17.74109
12	70	30	2	0.7	2	3.03	-9.6285	11.37	5.79	15.15357
13	70	18	4	0.8	0	5.7	-15.175	5.26	12.54	21.96595
14	70	18	4	0.8	1	5.54	-14.802	5.55	11.88	21.49633
15	70	18	4	0.8	2	4.6	-13.252	6.36	10.35	20.29881
16	70	47	6	0.6	0	4.06	-12.105	5.05	13.05	22.31221
17	70	47	6	0.6	1	4.1	-12.257	5.5	12	21.58362
18	70	47	6	0.6	2	4.62	-13.228	7.1	9.27	19.34159
19	110	28	2	0.8	0	4.16	-12.319	9.01	7.32	17.29022
20	110	28	2	0.8	1	3.8	-11.557	9.1	7.23	17.18277
21	110	28	2	0.8	2	3.7	-11.364	11.5	5.73	15.26309

(continued)

Table 3 (continued)

Sr. No.	T_{on} (μ s)	T_{off} (μ s)	I_p (A)	Duty cycle	W_f (mm)	SR (μ m)	SR S/N ratio	Cutting time (min)	MRR (mm^3/min)	MRR S/N ratio
22	110	73	4	0.6	0	4.83	-13.689	5.04	13.08	22.33215
23	110	73	4	0.6	1	4.87	-13.706	5.3	15.9	24.02794
24	110	73	4	0.6	2	4.6	-13.252	5.52	11.94	21.54009
25	110	47	6	0.7	0	5.3605	-14.541	4.2	15.69	23.91246
26	110	47	6	0.7	1	5.5	-14.873	4.34	15.18	23.62544
27	110	47	6	0.7	2	5.75	-15.134	5.2	12.69	22.06923

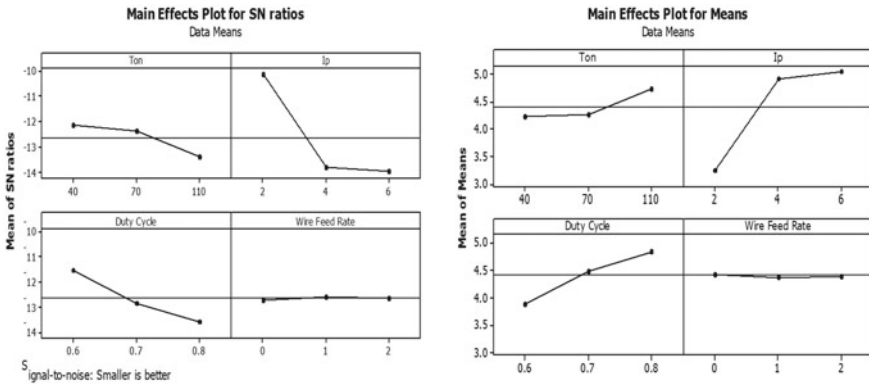


Fig. 3 Main effects plot for surface roughness

3.1 Results for Surface Roughness (SR)

The results after carrying out experiments are presented in Table 3 and it displays its corresponding S/N ratios. It can be concluded from Table 3 that the ideal conditions for minimum surface roughness were found for trial no. 1 where the minimum S/N ratio = -8.080 is obtained. The analysis results state that the optimal machining conditions were observed when EDM was done at pulse on time = 40 μs, input current = 2A, duty cycle = 0.6, and wire feeding rate = 50 mm/min.

It can be deduced from the main effects plot in Fig. 3 for SN ratio that the input current has highest slope and thus the highest significance. It is also seen that surface roughness (SR) increases with rise of input current but reduces with surge of wire feed. As increased pulse current will increase the amount of heat released in the inter electrodiagonal gap, which intern produces deeper craters. As a result, surface roughness also increases. Residual plots as shown in Fig. 4 suggest that values are nearer to the normal probability showing that the errors are distributed normally. It is justified from Table 4 that most dominant parameter is input current as it has the highest *f-value*. Also, the values of R^2 and R^2 (adj) are 92% and 88.44% (between 80 and 100%) concluding model developed for ANOVA as adequate.

3.2 Results for Material Removal Rate (MRR)

The results after carrying out experiments are presented in Table 3 and it also displays its corresponding S/N ratios. It can be seen from Table 3 that the ideal conditions for maximum MRR were in expt. no. 23 where the maximum S/N ratio = 24.02794 was found. The corresponding optimal conditions were seen when pulse on time was 110 μs. Input current was 6A, duty cycle was 0.7, and wire feed was one level (100 mm/min) of machine.

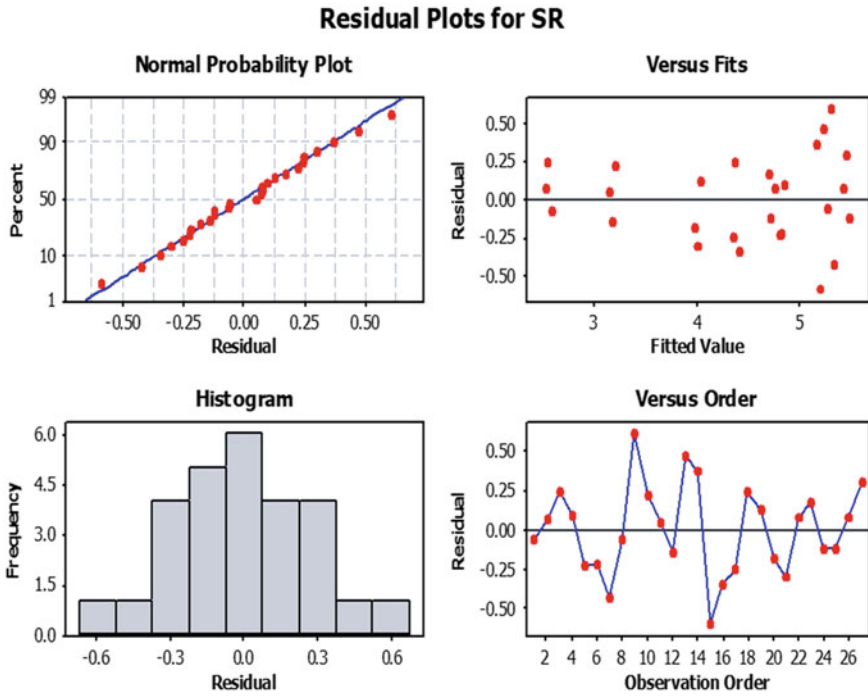


Fig. 4 Residual plots for surface roughness

Table 4 ANOVA for surface roughness in WEDM of Inconel 718 superalloy

Source	DF	Seq SS	Adj SS	Adj MS	F	P
Ton	2	1.4301	1.4301	0.7151	6.24	0.000
Ip	2	18.149	18.1149	9.0575	79.04	0.000
Duty cycle	2	4.1448	4.1448	2.0724	18.09	0.000
Wire feed rate	2	0.0152	0.0152	0.0076	0.07	0.936
Error	18	2.0626	2.0626	0.1146		
Total	26	25.7676				
$S = 1.20299$		$R^2 = 92.00\%$	$R^2(\text{adj}) = 88.44\%$			

Material removal rate (MRR) was calculated using the equation (Eq. 4) given below

$$MRR = F \times D_w \times H \tag{4}$$

$$MRR = \frac{\text{Diameter of Workpiece}}{\text{Cutting Time}} \times D_w \times H$$

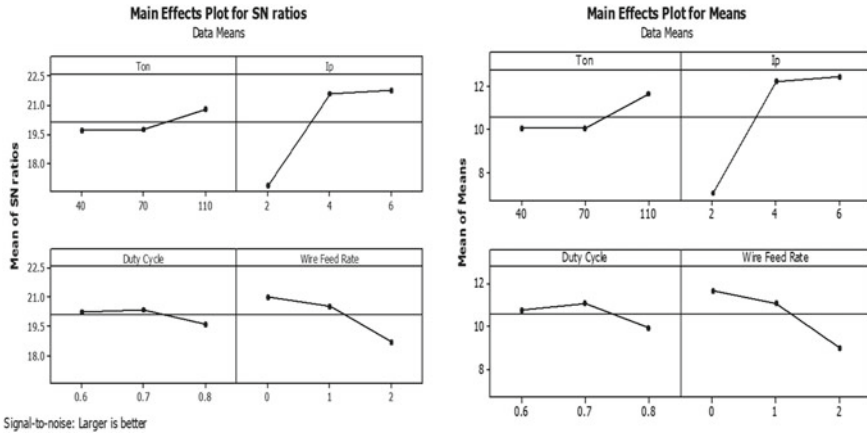


Fig. 5 Main effects plot for MRR

$$MRR = \left(\frac{22}{8.27} \right) \times 0.2 \times 5 = 7.98 \text{ mm}^3/\text{min} \text{ (For 1st Experiment)}$$

where

- F* Machine feed rate (mm/min)
- D_w* Diameter of feed wire, mm = 0.2 mm
- H* Height / thickness of cutting workpiece, mm = 5 mm.

It can be concluded from the main effects plot in Fig. 5 for SN ratio that the input current has highest slope and thus the highest significance. It is also perceived that MRR surges with rise of input current and pulse on time but reduces with rise of wire feed and duty cycle. As increase in pulse on time and pulse discharge, current increases the bulk heating and vaporization of the metal. This results in increase in material erosion from the workpiece. Residual plots as shown in Fig. 6 suggest that values are nearer to the normal probability showing that the errors are distributed normally. It is justified from Table 5 that most dominant parameter is input current as it has the peak *f-value*. Also, the values of *R*² and *R*² (adj) are 89.73% and 85.16% (between 80 and 100%) concluding the model developed for ANOVA as adequate.

4 Conclusion

In the present research work, the effects of various process parameters have been analyzed in WEDM of Inconel 718. The workpiece material and Inconel 718 are a superalloy having large range of industrial applications like jet engine and high-speed airframe parts. It was observed that most dominant parameter affecting surface

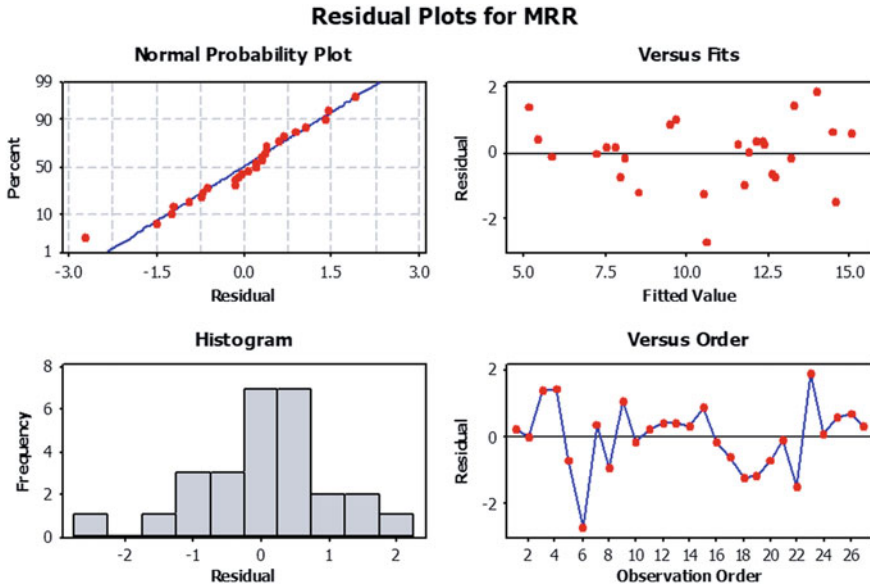


Fig. 6 Residual plots for MRR

Table 5 ANOVA for MRR in WEDM of Inconel 718 alloy

Source	DF	Seq SS	Adj SS	Adj MS	F	P
Ton	2	14.978	14.978	7.489	5.17	0.017
Ip	2	169.994	169.994	84.997	58.73	0.000
Duty cycle	2	6.373	6.373	3.186	2.20	0.140
Wire feed rate	2	36.201	36.201	18.100	12.51	0.00
Error	18	26.049	26.049	1.447		
Total	26	253.595				
$S = 1.20299$	$R^2 = 89.73\%$		$R^2(\text{adj}) = 85.16\%$			

roughness (SR) and material removal rate (MRR) is pulse on time. The parameters setting at pulse on time = 40 μs , input current = 2 A, duty cycle = 0.6, and wire feed = 50 mm/min delivered the optimum surface finish. The MRR was found maximum when WEDM was operated at pulse on time = 110 μs , input current = 6A, duty cycle = 0.7, and wire feed = 100 mm/min. The higher pulse duration caused higher material removal by increasing energy at discharge causing craters of large size. Wire feed showed very negligible change in the MRR and SR for Inconel 718. ANOVA was also developed for the validity of experiments and values of the values of R^2 and R^2 (adj) are 92% and 88.44% for surface roughness, and the values of R^2 and R^2 (adj) are 89.73% and 85.16% for MRR showing the adequacy of the experimentation and results.

References

1. Beranoagirre A, Urbikain G, Calleja A, López de Lacalle LN (2018) Hole making by electrical discharge machining (EDM) of γ -TiAl intermetallic alloys. *Metals* 8(7):543
2. Świercz, R., Holubek, R. (2020). Experimental investigation of influence electrical discharge energy on the surface layer properties after EDM. *Welding Technology Review*, 92
3. Świercz R, Oniszczyk-Świercz D, Chmielewski T (2019) Multi-response optimization of electrical discharge machining using the desirability function. *Micromachines* 10(1):72
4. Kulkarni VN, Gaitonde VN, Karnik SR, Manjiaiah M, Davim JP (2020) Machinability analysis and optimization in wire EDM of medical grade NiTiNOL memory alloy. *Materials* 13(9):2184
5. Chalisgaonkar R, Kumar J (2016) Investigation of the machining parameters and integrity of the work and wire surfaces after finish cut WEDM of commercially pure titanium. *J Braz Soc Mech Sci Eng* 38(3):883–911
6. Chaudhari R, Vora JJ, Patel V, López de Lacalle LN, Parikh DM (2020) Surface analysis of wire-electrical-discharge-machining-processed shape-memory alloys. *Materials* 13(3):530
7. Świercz R, Oniszczyk-Świercz D, Nowicki R (2018) Wire electrical discharge machining nickel super alloy. *Mechanik* 91(3):220–222
8. Muralova K, Benes L, Zahradnicek R, Bednar J, Zadera A, Fries J, Kana V (2020) WEDM Used for Machining High Entropy Alloys. *Materials* 13(21):4823
9. Oniszczyk-Świercz D, Świercz R, Nowicki R, Kopytowski A, Dąbrowski L (2018, October) Investigation of the influence of process parameters of wire electrical discharge machining using coated brass on the surface roughness of Inconel 718. In: *AIP conference proceedings*, vol 2017, No 1. AIP Publishing LLC, p 020020
10. Klocke F, Welling D, Dieckmann J, Veselovac D, Perez R (2012) Developments in wire-EDM for the manufacturing of fir tree slots in turbine discs made of Inconel 718. In: *Key engineering materials*, vol 504. Trans Tech Publications Ltd., pp. 1177–1182
11. Newton TR, Melkote SN, Watkins TR, Trejo RM, Reister L (2009) Investigation of the effect of process parameters on the formation and characteristics of recast layer in wire-EDM of Inconel 718. *Mater Sci Eng, A* 513:208–215
12. Tonday HR, Tigga AM (2019) An empirical evaluation and optimization of performance parameters of wire electrical discharge machining in cutting of Inconel 718. *Measurement* 140:185–196
13. Montgomery DC (2017) *Design and analysis of experiments*. Wiley

Experimental Investigation of Average Surface Roughness and Chip Morphology in End Milling of Aluminium Alloy 6151 Using Uncoated and TiAlN-Coated HSS Tools



I. Suresh Kannan

Abstract The present work is aimed to investigate the impact of TiAlN coating on the high-speed steel tool top surface and cutting velocity in end milling of Aluminium alloy 6151 under a dry machining environment. The performance was assessed by the average surface roughness, scanning electron microscopic imaging of end mill cutters and chip morphology. The TiAlN-coated HSS end mill cutter experienced the very least amount of chip adhesion at all feed rates of cutting velocity: 30 m/min. However, such favourable condition was not observed at and above the cutting speed–feed combination: 60 m/min–200 mm/min. It was reflected in the escalation of average surface roughness and variation of chip morphology under the same chip load per tooth conditions. The average surface roughness obtained at the machining condition ($V_c = 30$ m/min – $f = 100$ mm/min) was $1.691 \mu\text{m}$, which increased by 60% and 75% at the same chip load per tooth conditions 60–200 and 90–300, respectively. The uncoated HSS was considered as reference tool material for all the cutting conditions, which was not shown any improvement in machining performance at all the machining conditions than TiAlN-coated one.

Keywords Aluminium 6151 · Surface roughness · Chip morphology · Chip adhesion · Built-Up Edge (BUE) · Built-Up Layer (BUL)

1 Introduction

Aluminium and its alloys are widely used in structural and transportation applications due to its exceptional properties like high strength-to-weight ratio, high fatigue and corrosion resistance [1]. Although aluminium and its alloys are having lower shear strength when compared with other structural materials, they are categorized as difficult-to-machine materials. The major problem in the machining of aluminium and its alloy is the adhesion of the chip on the cutting tool [2]. The adhesion of the chip material in the form of bulk volume is known as Built-Up Edge (BUE), and the

I. S. Kannan (✉)

Department of Mechanical Engineering, SRM Institute of Science and Technology, Vadapalani, Chennai 600026, India

chip material leaves a fine layer on the rake face of the cutting tool which is referred to as Built-Up Layer (BUL) [3]. The nature of adhesion is depending on the chemistry of the workpiece material, tool material, cutting parameters and cutting environment [4]. The BUE and BUL could deteriorate the surface finish, alteration of cutting tool geometry, fluctuation of cutting force due to the unstable nature of adhered material on the cutting tool [5]. Many attempts were made by different research groups, to reduce or arrest the BUE or BUL in the machining of these materials. Suitable surface coating on the cutting tool is an easily adaptable technique to reduce the BUE/BUL formation by providing better lubricity and chemical inertness towards the work material [6]. Diamond-coated tools are a more promising solution to machine aluminium. Although diamond is more chemical inert towards aluminium [7], its microcrystalline nature causes BUL formation due to mechanical interlocking of the chip. Moreover, diamond tooling is very expensive when compared with other coated tools which restrict their use in small- and medium-scale industries. It was found that most of the transitional metal-based nitride and carbide-coated tools failed to arrest BUE/BUL formation under dry and wet machining conditions [8]. In contrast, it has been reported that the use of TiAlN/VN- and TiAlCrYN-coated tool experienced no BUE in high-speed milling of Al-7010-T7651 [9, 10]. Burr formation on the workpiece is another problem in machining soft ductile materials using uncoated carbide tools. Such burr formation can be delayed by the use of advanced tool materials. Ti(C₇N₃) cermet end mill cutter delayed the burr formation on the AA2024 workpiece 7 min when compared with the tungsten carbide tool [11]. However, the scope of multilayered transition metal-based coated tools in dry machining of aluminium is not explored in the wider range of cutting conditions.

In the present work, the machinability of AA6151 by TiAlN-coated HSS end mills has been investigated in terms of average surface roughness, chip morphology and SEM images of end mill cutters.

2 Materials and Experimental Procedure

The work material used in this investigation was extruded Aluminium alloy 6151, which is widely used in aircraft, automobile and marine structures. The chemical elements present in the work material are listed in Table 1, which was accessed by optical emissive spectroscopy (OES). End milling experiments were performed on the AA6151 using a vertical machining centre under the dry machining environment. The cutting tool utilized for machining was uncoated and TiAlN-coated high-speed steel (HSS) end mill cutters. The experimental conditions are detailed in

Table 1 Chemical composition of work material (AA6151)

Element	Si	Mg	Fe	Mn	Cu	Zn	Cr	Ti	Al
Wt %	0.61	0.5	0.33	0.22	0.2	0.18	0.13	0.11	Remaining

Table 2 Experimental details

Machine tool	Vertical machining centre Make and model: Bharat Fritz Verner (BMV) & BMV 51 TC24
Workpiece material	AA6151
Cutting tool	Four fluted 10-mm-diameter HSS end mill cutter having helix angle of 30°
Machining conditions	Cutting velocity (V_c): 30, 60, 90 m/min
	Feed (f): 100, 200, 300 mm/min
	Depth of cut (doc): 0.5 mm

Table 2. The average surface roughness (R_a) of the machined surface was measured by a computerized profilometer, and the set cut-off length was 0.8 mm. The post-machining condition of the end mills and chips was observed under high-resolution scanning electron microscope (Make & Model: FEI Quanta FEG 200).

3 Results and Discussion

Aluminium alloy 6151 was machined using both HSS and TiAlN-coated HSS end mills under a dry environment at the cutting velocity ranges from 30 to 90 m/min in the steps of 30 m/min and feed rate varied from 100 mm/min to 300 mm/min in the steps of 100 mm/min and constant axial depth of cut 0.5 mm. Average surface roughness (R_a), post-machining observation of cutting tools and chip morphologies were observed under SEM and compared at identical chip load conditions.

3.1 On Average Surface Roughness (R_a)

The surface quality of the machined surface plays an important role in the mechanical behaviour of the material such as fatigue strength, friction, etc. It is mostly influenced by machining conditions, surface chemistry of tool and work material and machining environment. In the present investigation, surface roughness produced by TiAlN-coated end mill cutters was compared with uncoated HSS under identical cutting conditions and machining environment. Figure 1 shows the variation of R_a values of the machined surface produced by uncoated and TiAlN-coated HSS end mills under identical machining conditions. R_a of the machined surface was decreased with cutting velocity and increased with feed rate. The smeared layer of adhered material caused the irregularities in the machined surface which predominantly influenced the surface roughness over the lay pattern on the machined surface. Surface roughness produced by TiAlN-coated HSS tool was lower than that produced by uncoated

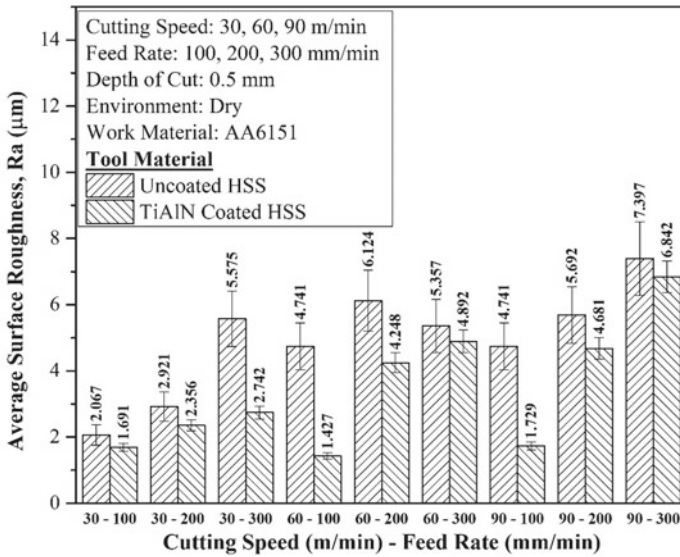


Fig. 1 Average surface roughness of the AA6151 after machining with end mill cutters

HSS at all machining conditions. TiAlN-coated tool also deteriorate the surface quality at severe machining conditions. The quality of machined surface produced by TiAlN-coated tool at the lower feed rate (100 mm/min) was relatively smoother when compared with the other two feed rates at all cutting velocities. Under same chip load per tooth conditions (cutting velocity (m/min) – feed rate (mm/min)), 30–100, 60–200 and 90–300, the surface roughness should be the same if the machining is free from BUE and wear or chatter. The surface roughness produced by TiAlN-coated HSS at machining condition 30–100 was 1.691 µm which was increased to 60% and 75% at 60–200 and 90–300 conditions, respectively.

The increased cutting velocity has raised the temperature at the sliding interface between tool and chip, which facilitate the adhesion of aluminium by the mechanism of diffusion of aluminium atoms into the tool material.

3.2 SEM Images of the End Mills After Machining AA6151

Figure 2 shows the SEM images of uncoated and TiAlN-coated HSS end mills after machining AA6151 at cutting velocity: 90 m/min and feed: 300 mm/min. At this condition, both the tools were received a severe BUE on the rake face. High cutting velocity and feed rate accelerated the temperature in the primary and secondary shear zone. This condition favoured the diffusion of aluminium across the Fe matrix which is present in the HSS end mill cutters. TiAlN-coated tool experienced a little trace of BUL at cutting velocity: 30 mm/min for all three feed rates. The level of

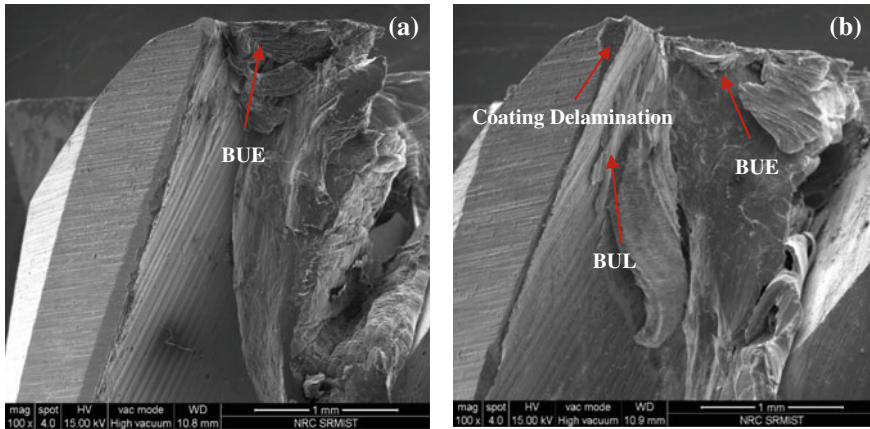


Fig. 2 SEM images of **a** uncoated and **b** TiAlN-coated HSS end mill cutters after machining AA6151 at Vc: 90 m/min, f: 300 mm/min and doc: 0.5 mm

aluminium adhesion was increased with cutting velocity and feed rate. The presence of Ti and Al in the TiAlN formed the tribo-oxide layers on the tool surface thus reduced the BUE/BUL formation when compared with HSS. However, at higher cutting velocities, coating delamination due to the intermittent nature of the process increased the chip adhesion on the tool.

3.3 Chip Morphology

Chips of selected cutting conditions were observed under SEM. Figure 3 shows the SEM micrograph of AA6151 chips formed by HSS and TiAlN-coated HSS end mills at 30–100 and 60–200 conditions. It was observed that the chip produced at 30–100 condition by the uncoated tool was subjected to tearing and a considerable amount of chip clogging. However, at the same condition, TiAlN-coated HSS produced a chip smooth under surface and very least side flow. At Cutting velocity: 60 m/min and feed rate 200 mm/min, both the tools caused a considerable amount of side flow which is evidenced by tear marks on the chips. At this condition as a cutting velocity was doubled, the temperature generated at the tool–chip interface become severe due to high friction between them, and thus, it favoured the interdiffusion of aluminium spices into the elements of cutting tool material. This would be further improved by providing soft and lubricous coating over the hard TiAlN coating.

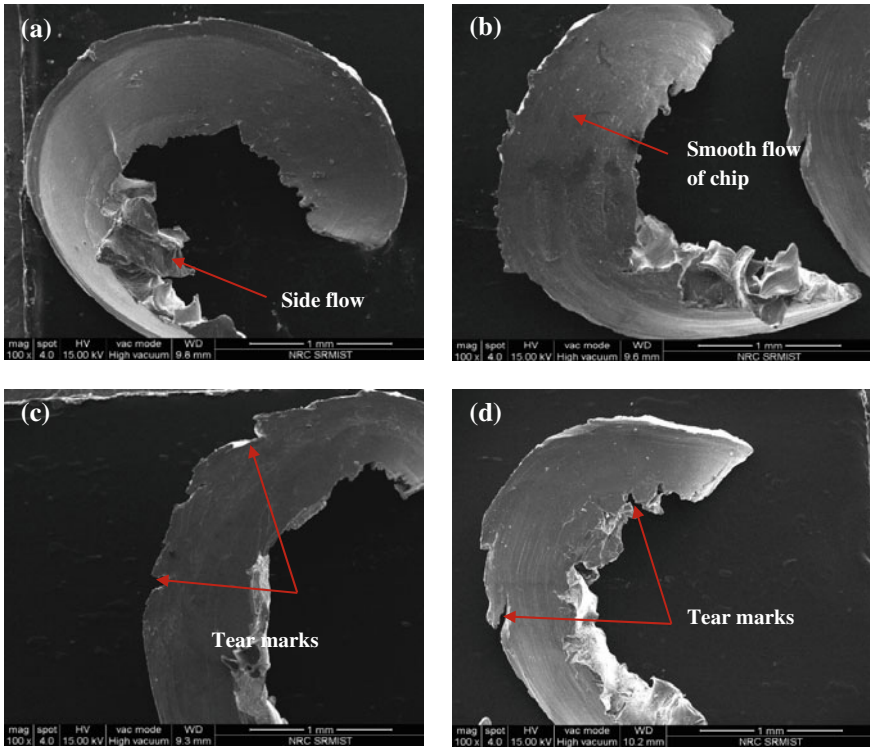


Fig. 3 Scanning electron microscopic images of AA6151 chip produced by **a, c** uncoated HSS and **b, d** TiAlN-coated HSS at V_c - f : 30–100 and 60–200 conditions

4 Conclusion

Dry machining performance of Aluminium alloy 6151 by HSS (without any coatings and surface coated with TiAlN) end mills was experimentally investigated, and the following conclusion was drawn.

- The average surface roughness of the Aluminium alloy 6151 machined using TiAlN coated HSS was lower than uncoated HSS produced one at all combination of experimental conditions.
- TiAlN coating on HSS end mills proved its good machining characteristics at all the feed rates of cutting velocity: 30 m/min. However, such characteristics were not pronounced at higher cutting velocities under the same chip load conditions due to high-temperature activated diffusion at the tool–chip interface. The surface roughness produced by TiAlN-coated HSS at machining condition 30–100 was $1.691 \mu\text{m}$ which increased to 60% and 75% at 60–200 and 90–300 conditions, respectively.

- Rake face of the uncoated HSS end mill cutters subjected to severe aluminium chip adhesion at all the experimental conditions due to strong interdiffusion of the aluminium element in work material and iron element in HSS. Although TiAlN-coated HSS proved its BUE-free machining at lower cutting velocity, it was also received a severe chip material built upon the cutting tool at higher cutting velocities (at and above 60 m/min) and under same chip load conditions and consequently deteriorated the surface quality of the workpiece.
- BUE formed end mill cutters caused a severe flank side flow and tearing of chips especially at and above the cutting velocity: 60 m/min which deteriorated the surface finish due to redeposition of chip material on the machined surface.
- It is recommended that TiAlN-coated HSS tools can be utilized to machine the aluminium at a cutting velocity lesser than 30 m/min. It would help a small-scale industry; those who are not able to afford a diamond tooling is perfect tooling to machine aluminium.

References

1. Mukhopadhyay P (2012) Alloy designation, processing, and use of AA6XXX series aluminium alloys. *ISRN Metallurgy*.
2. Sugihara T, Enomoto T (2012) Improving anti-adhesion in aluminum alloy cutting by micro stripe texture. *Precis Eng* 36(2):229–237
3. Sánchez JM, Rubio E, Álvarez M, Sebastián MA, Marcos M (2005) Microstructural characterisation of material adhered over cutting tool in the dry machining of aerospace aluminium alloys. *J Mater Process Technol* 164:911–918
4. Nouari M, List G, Girot F, Gehin D (2005) Effect of machining parameters and coating on wear mechanisms in dry drilling of aluminium alloys. *Int J Mach Tools Manuf* 45(12–13):1436–1442
5. Gómez-Parra A, Álvarez-Alcón M, Salguero J, Batista M, Marcos M (2013) Analysis of the evolution of the built-up edge and built-up layer formation mechanisms in the dry turning of aeronautical aluminium alloys. *Wear* 302(1–2):1209–1218
6. Coldwell HL, Dewes RC, Aspinwall DK, Renevier NM, Teer DG (2004) The use of soft/lubricating coatings when dry drilling BS L168 aluminium alloy. *Surf Coat Technol* 177:716–726
7. Chattopadhyay AK, Roy P, Ghosh A, Sarangi SK (2009) Wettability and machinability study of pure aluminium towards uncoated and coated carbide cutting tool inserts. *Surf Coat Technol* 203(8):941–951
8. Lahres M, Müller-Hummel P, Doerfel O (1997) Applicability of different hard coatings in dry milling aluminium alloys. *Surf Coat Technol* 91(1–2):116–121
9. Luo Q, Robinson G, Pittman M, Howarth M, Sim WM, Stalley MR, Leitner H, Ebner R, Caliskanoglu D, Hovsepian PE (2005) Performance of nano-structured multilayer PVD coating TiAlN/VN in dry high speed milling of aerospace aluminium 7010–T7651. *Surf Coat Technol* 200(1–4):123–127
10. Hovsepian PE, Luo Q, Robinson G, Pittman M, Martin Howarth D, Doerwald R, Tietema WM, Sim A, Zeus DT (2006) TiAlN/VN superlattice structured PVD coatings: a new alternative in machining of aluminium alloys for aerospace and automotive components. *Surf Coat Technol* 201(1–2):265–272
11. Xu K, Zou B, Wang Y, Guo P, Huang C, Wang J (2016) An experimental investigation of micro-machinability of aluminum alloy 2024 using Ti(C₇N₃)-based cermet micro end-mill tools. *J Mater Process Technol* 235:13–27

Experimental Investigation of Mechanical Properties of AA 7075-T6 by Friction Stir Processing



A. D. Wable and S. B. Patil

Abstract The present work shows the Taguchi approach to analyze the optimum parameters for processing the speed of rotation, tilt angle of tool and transverse speed output as an optimum ultimate tensile strength (UTS), percentage of elongation, and hardness on AA7075-T6. The primary and interaction influences of the process parameters were examined using the L9 orthogonal array and analysis of variance. The results demonstrate that the operating rotational speed of tool, transverse speed, and angle of tilt all have a considerable impact on UTS, % elongation, and hardness, with respective contributions of 99.76, 0.07, and 0.09%. FSP surface observed free from defects and delimitation at optimized process parameters. The valuable recommendations given to select the suitable process parameters in FSP for AA 7075-T6 using ANOVA analysis are presented in this paper. By research, it is found that optimum combination of parameters is speed of rotation 1180 rpm, transverse speed of 38 mm/min, and angle of tilt 3° produce surface treatment optimum tensile strength 492 MPa, % elongation 11%, and microhardness 135 HV.

Keywords Friction stir processing · ANOVA · Orthogonal array · Grain refinement

1 Introduction

Friction stir processing is a solid-state surface treatment procedure that alters the microstructure of a material in order to improve its mechanical properties. This approach involves inserting a rotating tool with a shoulder and a pin at the bottom into the material for localized microstructural alteration to improve a material's specific attribute. It causes extensive plastic deformation and thermal exposure in the process zone, leading in microstructure refinement and uniformity. This approach is used in

A. D. Wable (✉)

Department of Production Engineering, COEP, Pune, Maharashtra, India

S. B. Patil

Department of Mechanical Engineering, COEP, Pune, Maharashtra, India

e-mail: sbp.mech@coep.ac.in

the fabrication of fine-grained structures and surface composites [1]. Its key benefit is that it allows you to alter mechanical qualities by optimizing process parameters. Researchers have recently attempted to improve FSP process parameters such as speed of rotation, speed of transverse, and others in order to achieve high tensile strength of the generated surface [2]. Using the Taguchi approach and ANOVA analysis, Bayazid et al. [3] investigated the effect of speed of rotation, speed of transvers, and plate placements on different 6063–7075 joint strength. Preethi et al. [4] analyzed weldability of hybrid aluminum composite using input parameters speed of rotation, speed of transverse, and output response as a hardness. “Taguchi method shows that tool rotation speed has a major contribution (57.3%) on hardness, and all input parameters show a significant effect on the hardness by ANOVA analysis. The multiple response problems taken with three independent variables, and it was formulated by grey relational analysis method, factor analysis method, DEA rank-based method, assignment weight age method and compared by their own procedure using FSW experimental data. These methods can be used to predict the welding parameters within the experimental design” [5]. The FSW process conditions are altered to enhance the tensile strength of the joint. 900 rpm, 80 mm/min, and 7 kN were found to be the best speed of rotation, speed of transverse, and axial force levels, respectively [6, 7]. Kumar et al. [8] used “FSW to examine the effect of process factors on joint A6061 and A6082, and found that rotational speed is the most important process parameter for hardness and tensile strength, followed by tool pin profile and tool tilt angle”. Salehi et al. [9] “studied the effect of transverse speed, rotational speed, tool penetration, and pin profile on ultimate tensile strength. Optimize the process parameter using ANOVA, and results show that rotational speed is the most influential parameter. Also, the higher the rotational speed, the lower the transverse speed”.

Aluminum alloys are commonly utilized in the transportation and aerospace industries due to their low density and high strength-to-weight ratio. Aluminum-based metal matrix composites (MMC) typically have a high elastic modulus, high strength, and increased wear, creep, and fatigue resistance, making them useful as a structural material in a variety of sectors [10]. Without changing the bulk material, FSP alters the process zone along the path the tool travels. Due to the existence of tool settings, the process zone suffered from low toughness and ductility, which limited their widespread uses to some extent (Fig. 1).

In this study, AA 7075-T6 material is treated, and the impact of tool speed of rotation, speed of transverse, and angle of tilt on mechanical properties is explored experimentally.

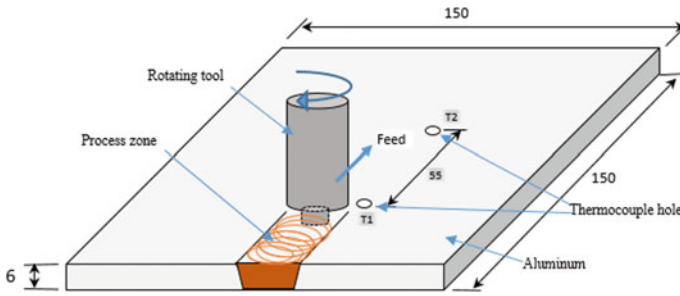


Fig. 1 Friction stirrs processing (FSP/FSW) schematic

Table 1 Chemical properties of Al 7075-T6 aluminum alloy

Si	Fe	Cu	Mn	Mg	Zn	Ti	Al
0.088	0.097	1.73	0.015	2.16	5.61	0.038	Bal

Table 2 Mechanical characteristics of AA 7075-T6 alloy

Tensile strength (MPa)	Elongation (%)	Microhardness (HV) _{0.1}
530	17.67	172

2 Materials and Methodology

2.1 Materials Used

The material used in this study is an AA 7075-T6 aluminium alloy with a high strength. It arrived as rolled plates with a thickness of 6 mm and a metallurgical temper of T6 (solution heat treatment). Tables 1 and 2 demonstrate the chemical properties and mechanical characteristics of Al 7075-T6 aluminium alloy plates with dimensions of 150 × 150 × 6 mm cut from the sheet using AWJ machining.

2.2 Friction Stir Processing

The plates were subjected to FSP at a tool speed of rotation of 710–1180 rpm, speed of transverse of 38–64 mm/min, and angle of tilt 1–3°. Figure 2 shows FSP experimental setup for experiments was conducted on conventional milling machine with 20 HP of motor was used to process AA 7075-T6 aluminum alloy with a M6 × 1.5 mm threaded pin of height 5.5 mm and a flat shoulder 20 mm in diameter. The

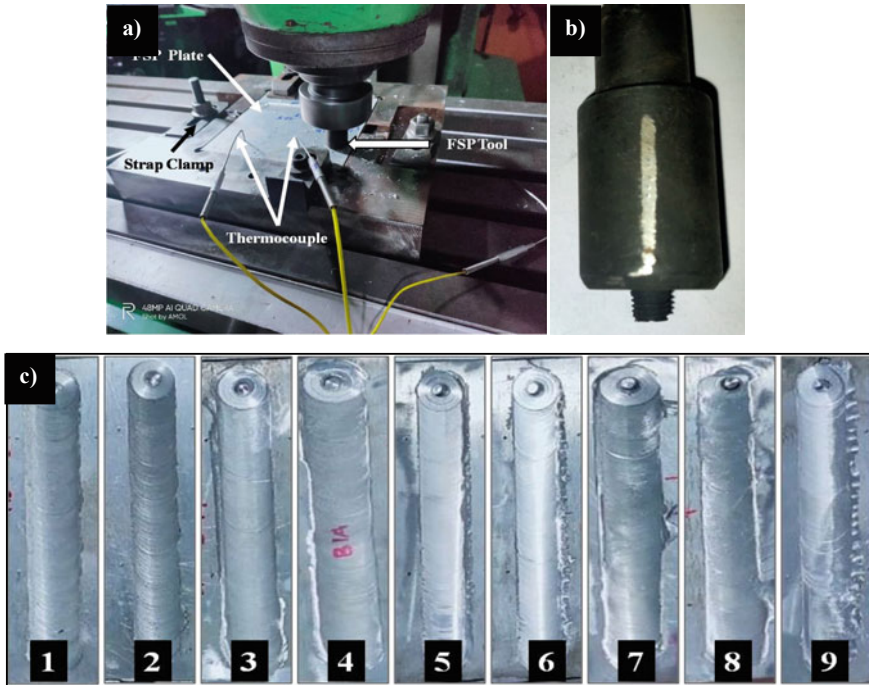


Fig. 2 Experimental setup for FSP **a** Conventional milling machine, **b** FSP tool and **c** top surface images of the FSP specimen

plunge depth of the shoulder was regulated at 0.2 mm with a tool angle of tilt 1–3°. The friction stir processing (FSP) was employed in the working media, in normal condition.

2.3 Taguchi Method

“The Taguchi method is a robust design of experiment (DoE) technique to decrease the number of trials significantly by a specially planned orthogonal array (OA), which can accommodate the selected manufacturing parameters for the analysis. Furthermore, signal-to-noise ratio (S/N) reflecting both the amount of variation present, and the mean response of several repetitions can be used in the Taguchi method to measure the variability in the response data. The S/N can minimize the effects of noise and identify control factors settings, thus reducing the sensitivity of the system performance to a source of variation. The Taguchi method has been actively used to examine the contributing effects of processing parameters on the enhancement of surface treatment performance” [6].

Table 3 Control of machine parameters and levels

Sr. No.	Control parameters	Level 1	Level 2	Level 3
1	Rotational speed (rpm)	710	900	1180
2	Speed of transverse (mm/min)	38	49	64
3	Angle of tool tilt (°)	1	2	3

3 Experimentation Plan

3.1 FSP Operating Parameters and Levels Specified

In order to maximize the FSP for high mechanical properties of surface treatment for AA 7075-T6 heat-treated aluminium alloy, it is vital to figure out what the best operating parameters are. Using literature review and trial experiments for the FSP process parameters range, selected tool rotational speed is 710, 900, and 1180 rpm. [7, 10]. In case of FSP traverse speed, the range selected is 38, 49, and 64 mm/min, and angle of tilt range selected is 1, 2, and 3°. Table 3 lists the selected control machine process parameters and their associated levels for developing surface treatment with the goal of achieving high mechanical qualities, as illustrated in Fig. 3.

3.2 FSP of Design of Experiments and Data Analysis

A set of nine experiments based on the L9 orthogonal array are done using the three machine control parameters and three levels indicated in Table 4. The S/N ratios computed and the ultimate tensile strength (UTS), percent elongation, and microhardness (HV) derived from experiments are tabulated.

3.3 Mechanical Characterization

A material's ultimate tensile strength (UTS) is the maximum tensile stress it can sustain before breaking. The tensile test specimen was made according to the ASTM E8 (sub-size) standard. Specimens with lengths of 100 mm, widths of 6 mm, thicknesses of 6 mm, and gauge lengths of 32 mm were tested at a strain rate of 10^{-3} seconds. The MTS landmark testing solution with computer-controlled universal testing machine used in tensile testing is shown in Fig. 4a; stress-strain curve as shown in Fig. 4b, and tensile test specimen is illustrated in Fig. 4c. The tensile specimens at each FSP condition were test three times for average tensile test.

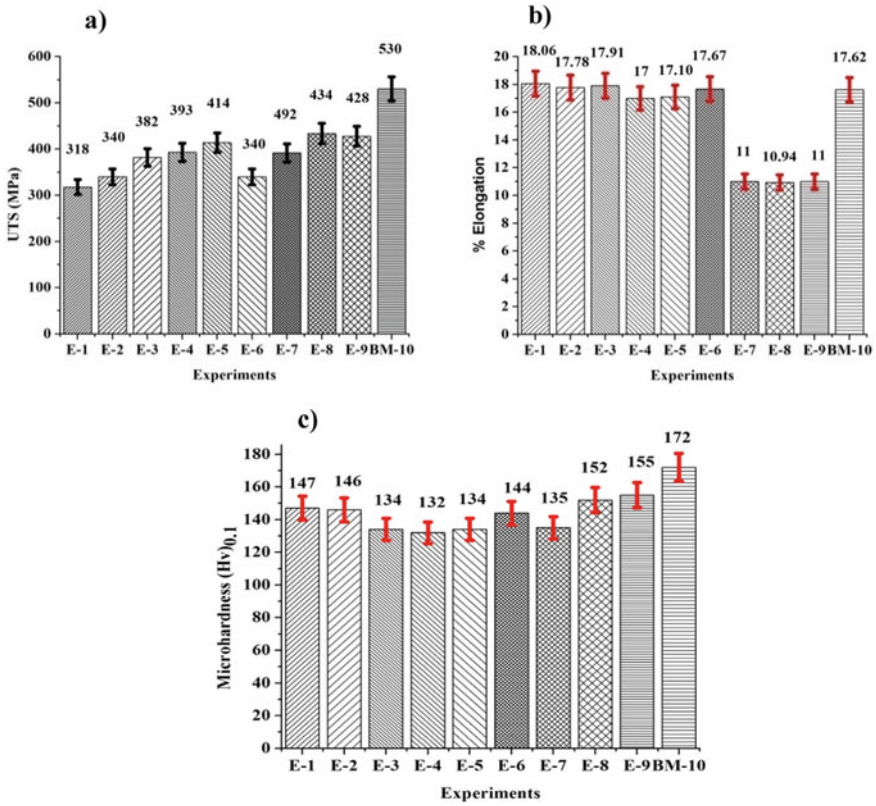


Fig. 3 Histogram for UTS, % E and microhardness of FSP

4 Results and Discussion

4.1 Analyzed of Optimum Parameters for FSP

The influence of friction stir processing operating parameters on UTS, % elongation, and microhardness may be seen in Fig. 5. Response tables for UTS signal-to-noise ratio, percent elongation, and microhardness were assessed using MINITAB 18 software to examine FSP parameters, as shown in Table 5. The ideal volume fraction for UTS, percent elongation, and microhardness, as well as their related optimum process parameter levels, are determined using signal-to-noise ratio analysis and are listed in Table 6.

Table 4 The L9 orthogonal array used in the experiment

Expt. No	Rotational speed (rpm)	Transverse speed (mm/min)	Angle of tool tilt (°)	UTS (MPa)	% E	Hardness (HV)	UTS S/N	% E	Hardness (HV)
1	710	38	1	318	18.06	147	50.04	25.13	45.51
2	710	49	2	340	17.78	146	50.62	24.99	45.56
3	710	64	3	382	17.91	134	51.64	25.06	45.04
4	900	38	2	393	17	132	51.88	24.60	44.95
5	900	49	3	414	17.10	134	52.34	24.65	45.11
6	900	64	1	340	17.67	144	50.62	24.94	45.46
7	1180	38	3	492	11	135	53.83	20.82	45.30
8	1180	49	1	434	10.94	152	52.74	20.78	46.14
9	1180	64	2	428	11	155	52.62	20.82	45.28

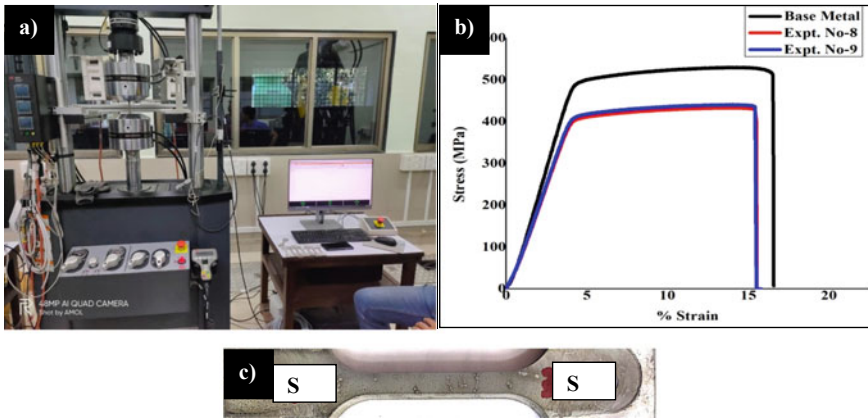


Fig. 4 Photograph for a tensile test machine, b stress–strain curve, c tensile test specimen

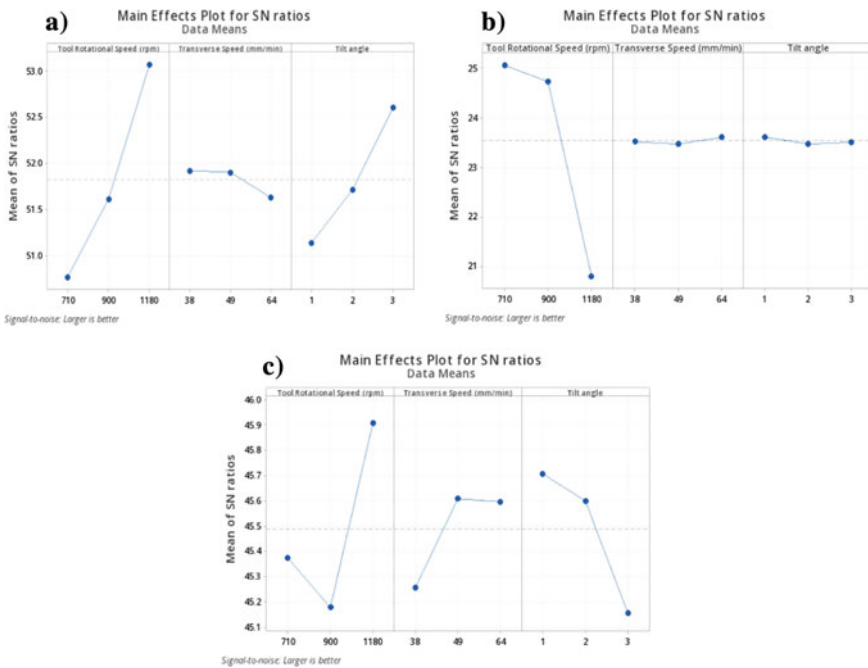


Fig. 5 Photograph for main effects plot of S/N ratio for UTS, % E and microhardness

4.1.1 Effect of FSP Parameters on UTS, % E and Microhardness

The signal-to-noise ratio Table 5 shows that most significance process parameter for tool rotational speed, second significance process parameter for angle of tool

Table 5 Response table for UTS, % E, and microhardness signal-to-noise ratios

UTS (MPa)			
Level	Speed of rotation (rpm)	Speed of transverse (mm/min)	Angle of tool tilt (°)
1	50.77	51.93	51.14
2	51.62	51.91	51.72
3	53.07	51.63	52.61
Delta	2.30	0.29	1.46
Rank	1	3	2
% Elongation			
1	25.06	23.52	23.62
2	24.74	23.48	23.48
3	20.81	23.61	23.52
Delta	4.25	0.13	0.14
Rank	1	3	2
Microhardness (HV)			
1	45.38	45.26	45.71
2	45.18	45.61	45.60
3	45.91	45.60	45.16
Delta	0.73	0.35	0.55
Rank	1	3	2

Table 6 Optimum process parameters of FSP for Al 7075-T6 alloy

Parameters	Level	Optimum value		
		UTS (MPa)	% Elongation	Microhardness
Speed of tool rotation (rpm)	3,1,3	53.07	25.06	45.91
Speed of transverse (mm/min)	1,3,2	51.93	23.61	45.61
Angle of tool tilt (°)	3,1,1	52.61	23.62	45.71

tilt, and third one speed of transverse. The optimum friction stir processing parameters for enhanced ultimate tensile strength were found at tool speed of rotation of 1180 rpm, speed of transverse of 38 mm/min, and angle of tilt 3° according to signal-to-noise ratio. The effect of speed of rotation on ultimate tensile strength is shown in Fig. 5a. According to signal-to-noise ratio, optimal friction stir processing parameters for higher % elongation were speed rotation of 710 rpm, speed of transverse of 64 mm/min, and angle of tool tilt 3°. Figure 5b shows the effect of tool speed rotation on % elongation. According to signal-to-noise ratio, optimal friction stir processing parameters for higher microhardness were speed of rotation 1180 rpm, speed of transverse 49 mm/min, and angle of tool tilt 1°. Figure 5c shows the effect of speed of rotation on microhardness. Speed of tool rotation has a 99.76% contribution to UTS, % elongation and microhardness, while speed of transverse has a

Table 7 Mechanical properties of FSP for surface treatment

Expt. No	Average UTS of FSP surface treatment (MPa)	Average % E of FSP surface treatment	Average microhardness of FSP surface treatment (HV)
1	318	18.06	147
2	340	17.78	146
3	382	17.91	134
4	393	17	132
5	414	17.10	134
6	340	17.67	144
7	492	11	135
8	434	10.94	152
9	428	11	155
BM	530	17.62	172

0.07% contribution to UTS, % elongation and microhardness, and angle of tool tilt has a 0.09% contribution to UTS, % elongation, and microhardness. On the basis of Fig. 5, Table 6 indicates the optimum % of FSP for the highest ultimate tensile strength (UTS), percent elongation, and microhardness.

4.2 Analysis for Mechanical Properties

Tensile test was conducted for FSP surface treatment developed using optimum FSP parameters for AA 7075-T6 base material. Table 7 lists the UTS, % E, and microhardness of FSP surface treatment and base material.

4.3 Analysis of Variance (ANOVA) Results

The UTS, percent elongation, and microhardness were evaluated using the ANOVA method to determine the effect of process factors at a 95% confidence level using F (variance ratio) statistics, as shown in Table 8. For machining process parameters, like speed of tool rotation, speed of transverse, and angle of tool tilt, F calculated is greater than ($\alpha = 0.005, 6$). A minor change in these parameters causes a significant change in ultimate tensile strength (UTS), % E, and microhardness. As a result of the ANOVA, it is clear that speed of tool rotation, speed of transverse, and angle of tool tilt is important process variables. F calculated, on the other hand, is less than ($\alpha = 0.005, 6$) for tool rotating speed.

Table 8 Analysis of variance for FSP UTS, % E, and microhardness

Source	DF	Seq SS	Adj SS	Adj MS	F	P
Tool rotating speed (rpm)	2	32.7579	32.7579	16.3789	1821.61	0.001
Transverse speed (mm/min)	2	0.0260	0.0260	0.0130	1.45	0.409
Tool tilt angle	2	0.0327	0.0327	0.0163	1.82	0.355
Residual error	2	0.0180	0.0180	0.0090		
Total	8	32.8345				

4.4 Analysis for Interaction Effect of UTS, % E and Microhardness

The interaction between angle of tool tilt and speed of tool rotation is greater than the interaction between speed of transverse and speed of tool rotation and the interaction between angle of tool tilt and speed of transverse. The interaction plot for ultimate tensile strength (UTS) as shown in Fig. 6a. Increase angle of tool tilt and speed of rotation to increase UTS. Increase speed of transverse and speed of tool rotation to decrease UTS. The speed of transverse 38 mm/min and increase tilt tool angle increase to increase UTS, increase tool tilt angle up to 2°, and increase transverse speed up to 49 mm/min to increase UTS after that decrease the UTS.

The interaction effect between angle of tool and speed of transverse, as well as the interaction effect between angle of tool and rotating speed, is stronger than the

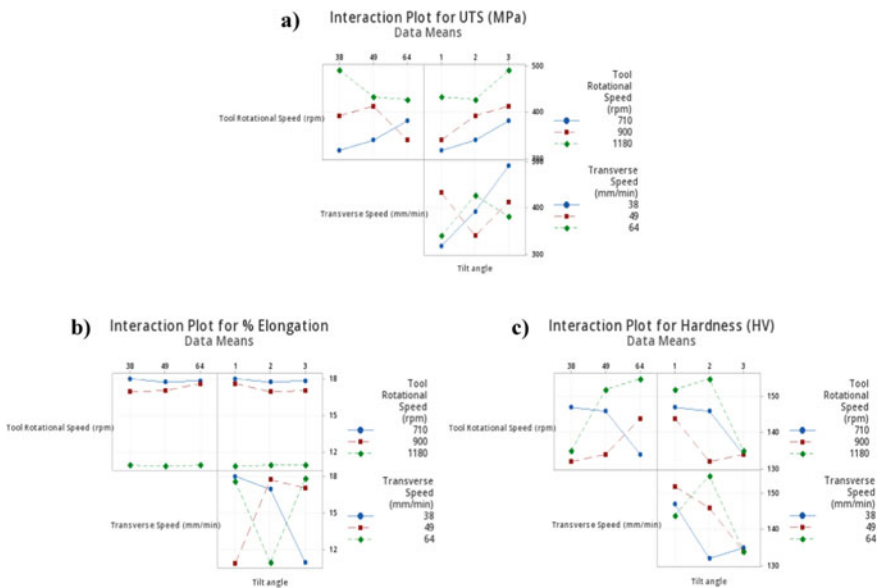


Fig. 6 Interaction plot for FSP UTS, % E and microhardness

interaction effect between angle of tool and speed of transverse. The interaction plot of percent elongation is presented in Fig. 6b. Increase transverse speed and tool rotational speed to increase % elongation. Increase tool tilt angle and tool rotational speed to increase % elongation. The transverse speed 38 mm/min and increase tool tilt angle to decrease % elongation. Increase tool tilt angle up to 2° and 49 mm/min transverse speed to increase % elongation after that decrease the % elongation. Decrease tool tilt angle up to 2° and 64 mm/min transverse speed to decrease % elongation after that increase the % elongation. Furthermore, the ANOVA values and the interaction plot in Fig. 6c reveal that there is no significant interaction impact between rotating speed of tool and transverse speed, as well as between transverse speed and tool rotating speed.

5 Conclusions

In this study, FSP of AA 7075-T6 was successfully achieved by friction stir processing. Analysis of mechanical properties for friction stir processing of AA 7075-T6 alloy.

- The AA 7075-T6 aluminum alloy was successfully friction stir processing using a cylinder pin with M6×1.5 mm threaded pin of height 5.5 mm and a plain shoulder 20 mm in diameter at a speed of tool rotation 1180 rpm and speed of transverse 38 mm/min produce good surface quality of FSP surface treatment.
- The UTS, % E, and microhardness of FSP are maximized by optimizing the FSP process parameters. The best speed of tool rotation, speed of transverse, and angle of tool tilt, respectively, was found to be 1180 rpm, 38 mm/min, and 3°.
- FSP reported optimum tensile strength 492 MPa, % elongation 11%, and microhardness 135 HV using optimum process parameters of speed of tool rotation 1180 rpm speed of transverse 38 mm/min, and angle of tool tilt 3°.
- The UTS, % E, and microhardness of FSP reaches to 92.83%, 102.43%, and 96.51% of the base metal UTS, % E, and microhardness.

Acknowledgements The Testing Laboratory, IIT Bombay, Maharashtra, India, provided extensive mechanical and metallurgical test facilities to the writers. The authors are grateful to the Director of the College of Engineering in Pune, Maharashtra, India, for allowing them to conduct hardness testing.

References

1. Ma ZY (2008) Friction stir processing technology: a review. *Metall Mater Trans* 39A:642–657
2. Murthy V, Dileep KS, Saju KK, Rajaprakash BM, Rajashekar R (2019) Optimization of friction stir processing parameters for manufacturing silicon carbide reinforced aluminum 7075–T651

- surface composite. *Mater Today: Proc* 18:4549–4555. <https://doi.org/10.1016/j.matpr.2019.07.427>
3. Bayazid SM, Farhangi H, Ghahramani A (2015) Investigation of friction stir welding parameters of 6063–7075 aluminum alloys by Taguchi method. *Procedia Mater Sci* 11:6–11
 4. Preethi V, Daniel Das A (2020) Optimization of friction stir welding parameters for better hardness in weld nugget of hybrid aluminium composite. *Mater Today: Proc* 1–5
 5. Anganan K., S. Prabakaran, S. Marimuthu. (2020) An experimental study and analysis of various cylindrical pin diameters in friction stir welded AA7075-T6 and A3840-T6 aluminium alloys of butt joint. *Mater Today: Proc* 1–5
 6. RaviKumar S, KajaBanthaNavas R, Sai SP (2019) Multiple response optimization studies for dissimilar friction stir welding parameters of 6061 to 7075 aluminium alloys. *Mater Today: Proc* 16:405–412. <https://doi.org/10.1016/j.matpr.2019.05.108>
 7. Gupta S, Pandey KN (2013) Application of Taguchi method for optimization of friction stir welding process parameters to joining of Al alloy. *Adv Mater Manuf Charact* 3(1):1–6
 8. Kumar S, Kumar S, Kumar A (2012) Optimization of process parameters for friction stir welding of joining A6061 and A6082 alloys by Taguchi method. *Proc Inst Mech Eng C J Mech Eng Sci* 227(6):1150–1163
 9. Salehi M, Saadatmand M, Aghazadeh MJ (2012) Optimization of process parameters for producing AA6061/SiC nanocomposites by friction stir processing. *Transa Nonferrous Metals Soc China* 22(5):1055–1063
 10. Vijayan D, Seshagiri RV (2014) A multi response optimization of tool pin profile on the tensile behavior of age-hardenable aluminum alloys during friction stir welding. *Res J Appl Sci Eng Technol* 7(21):4503–4518

Experimental Investigation on Mechanical Properties of Friction Stir Dissimilar Welded Joints of Al AA6063 and SS 304 Alloys



Debashis Mishra and Anil Kumar Das

Abstract The sheet metals of the aluminum alloy (AA 6063-T6 grade) and stainless-steel alloy (AISI 304L) were friction stir welded by using various factors like feed, tilting angle, and tool rotating speed. Two unique types of rotating tool structural profiles were chosen as hexagonal and squared. The hexagonal structured tool profile was produced better results than the squared profile. The tensile strength and flexural strength of the fabricated dissimilar welded joint were reported like 56 N/mm² and 2.61 MPa, respectively, with the use of a hexagonal structured profile. The dissimilar welding of the chosen metal sheets by using the friction welding process by changing the pin profiles such as hexagon and squared was addressed in this experimental investigation to suggest the best profile to achieve the desired mechanical properties.

Keywords Aluminum alloy (AA6063-T6) · Flexural strength · Friction stir welding · Hexagonal profile · Squared profile · Stainless-steel alloy (AISI 304L) · Tensile strength

1 Introduction

The welded joints are generally produced by the action of a rotating tool at a certain pressure in the friction stir welding technique. Moreover, frictional heat is created due to the rubbing of a rotating tool over the metal surface under tremendous pressure. The welded joints are commonly produced without liquefying the sheet metal and that is at solid-state conditions. The process is having a tremendous advantage over the arc and other welding techniques. This process was evidenced to be a competent and governable method of joining dissimilar as well as similar metals particularly for the use of aluminum and its alloys. The dissimilar welded joint properties were affected

D. Mishra (✉) · A. K. Das

Department of Mechanical Engineering, National Institute of Technology, Patna, Bihar 800005, India

e-mail: debashism.ph21.me@nitp.ac.in

A. K. Das

e-mail: akdas@nitp.ac.in

by the proceeding speed [1, 2]. The process was also called green technology and has the potential to join highly reactive metals like aluminum and magnesium which was very difficult by most traditional welding techniques [3]. An exclusively structured pin profile and shoulder were implanted at high pressure progressed through the adjoining sections of the well-clamped two metal pieces and navigated further to produce a strong and solid joint. The proper selection of the tool and its profile was very important as it produces major tasks during the welding, i.e., heating and subsequently material flow to produce a high strength welded joint. The process was optimized to produce aluminum 6061 alloy welded joints by optimizing the chosen factors [4]. Dissimilar aluminum alloys such as A356 and 6061 were friction welded. The finding from the investigation was reported as the weld zone structure was governed and directed through the preceding section. Fine structure with low stresses can be obtained with the proper selection of rate of speed [5]. The effect of the factors on welds of aluminum has been investigated, and significant enhancement in properties was reported by following the optimization techniques [6, 7]. The tool pin profile and its geometrical features are having a major influence on the quality of the welded joints as material flow and its amalgamation throughout the welded joints [8, 9]. The rate of the translational and rotational speed accelerates the flow of material from retreating to the advancing side [10]. A good mechanical property can be obtained by correlating it with the weld travel speed. The frictional heat was generated because of the proper rotation and traverse speed of the tool [11, 12]. The selection of process parameters and their welding limits was reported for the production of aluminum welds. The optimization of chosen experimental conditions was performed to eliminate the defects and errors. The effects of the factors have been understood, and the significance of experimental model terminologies was reported statistically [13, 14]. The production of dissimilar weld joints of chosen alloys of aluminum and stainless steel was addressed in this experimental investigation. The tensile strength, flexural strength, and microstructural examinations of the friction welded joints were presented significantly. The experimental investigation is giving an insight into the difficulties in producing the dissimilar welded joints.

2 Materials and Method

The aluminum alloy (AA6063-T6) and stainless-steel alloy (AISI 304L) of thickness 8 mm are widely used for various structural applications. The size of the chosen metal sheets before welding was 150 mm in length and 150 mm in width. The friction stir welding technique was used to prepare the dissimilar weld joint by taking various considerable factors, and it is given in Table 1. The experimental setup which was exercised to fabricate the dissimilar welded joints is represented in Fig. 1. The edge preparation was followed by reducing 3 mm from both the sides of chosen metal sheets for the final welding and clamped rigidly on the fixture for successful welding. The high-speed steel (HSS) rotated tool having pin profile was chosen as hexagonal and squared, as shown in Fig. 2. The fabricated welded joint images are shown in Fig. 3.

Table 1 Selected process parameters for the dissimilar welded joints

Chosen factors of the friction stir welding	Welding limits
The tool rotational speed	900 rpm
The feed	40 mm/min
Tilt angle	0.5°
Tool pin profile	The hexagonal and squared profiles

**Fig. 1** Friction stir welding setup**Fig. 2** Hexagonal and squared structured tool profiles respectively used in the welding

3 Outcomes from the Experimental Investigation

The fabricated welded joints were examined for the tensile, flexural, and microstructural examinations. The tensile specimens were collected following the ASTM standard E8M-08. The collected samples were examined for their tensile properties. The tensile strength was achieved as 56 N/mm^2 and 28 N/mm^2 for hexagonal and squared pin profiles, respectively. The specimens were observed to be broken at the



Fig. 3 Fabricated welded joint by using of hexagonal and squared structured profiles, respectively

weld zone. That means the strength obtained was the strength of the welded joint. The flexural strength was obtained as 2.61 MPa and 1.41 MPa in the cases of hexagonal and squared pin profiles, respectively. The specimens were observed to get broken at the weld zone. The results are shown in Table 2. The tensile and flexural welded samples are shown in Figs. 4, 5, 8 and 9, respectively. The load versus displacement graph obtained after tensile testing is shown in Fig. 7. The tensile and flexural specimens after testing are shown in Figs. 6 and 10, respectively. The microstructure of the welded joints was collected at a magnification of 100X. The wet etchant named hydrofluoric acid was used to etch out the surface to develop the microstructure of the welded joints. The elongated grains were observed in the direction of stirring with very coarse intermetallic particles in the case of hexagonal structured pin profile. The elongated grains were observed in the direction of stirring with the fine

Table 2 Tensile and flexural testing results

Tool pin profile	Ultimate load (kN)	Tensile strength (N/mm ²)	Load (N)	Flexural strength (MPa)
Hexagonal	2.095	56	163	2.61
Squared	1.120	28	88	1.41



Fig. 4 Tensile specimen fabricated by using the hexagonal profiled tool



Fig. 5 Tensile specimen prepared by using the squared profiled tool

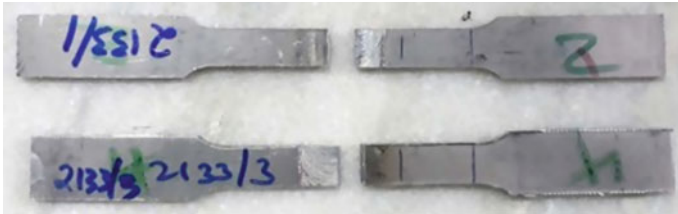


Fig. 6 Tensile tested pieces

intermetallic particles in the case of a squared structured pin profile. The developed microstructures are shown in Fig. 11.

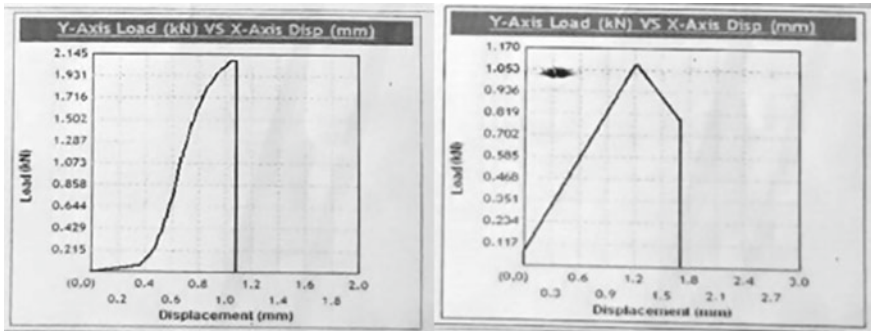


Fig. 7 Load versus displacement graph for hexagonal and squared profiles, respectively



Fig. 8 Flexural welded specimens—hexagonal profile



Fig. 9 Flexural welded specimens—squared profile

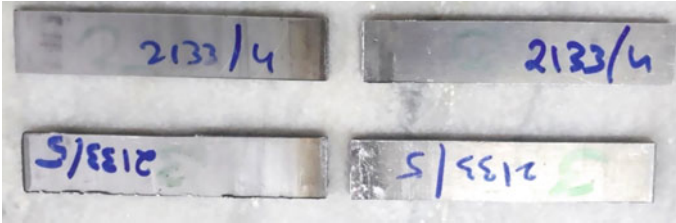


Fig. 10 Flexural test specimens after the testing

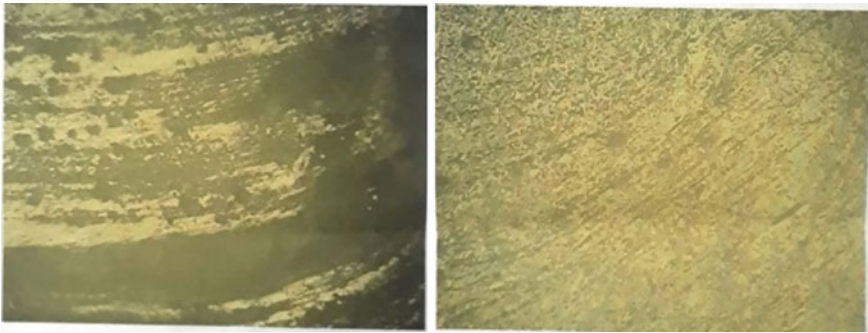


Fig. 11 Microstructural images for hexagonal and squared profiles, respectively

4 Conclusion

The dissimilar welded joints were produced fruitfully. The observations made from the experimental investigation are expressed below.

1. The strength of the weld zone was reported as 56 N/mm^2 and 28 N/mm^2 , in the case of hexagonal and squared structured profiles, respectively.
2. The flexural strength was reported as 2.61 MPa and 1.41 MPa, respectively.
3. The elongated grains were observed in the path of stirring action with very coarse intermetallic particles by exercising the hexagonal structured pin profile.
4. The elongated grains were noticed in the course of the stirring zone with the fine intermetallic particles by employing the squared structured pin profile.

5. The rotating tool with the hexagonal structured profile is found suitable in the fabrication of the dissimilar welded joint and to achieve the desired weld properties.

References

1. Boumerzoug Z, Helal Y (2017) Friction stir welding of dissimilar materials aluminum Al6061-T6 ultra-low carbon steel. *Metals* 7:42. <https://doi.org/10.3390/met7020042>
2. Padhy GK, Wu CS, Gao S (2018) Friction stir based welding and processing technologies—processes, parameters, microstructures, and applications: a review. *J Mater Sci Technol*. <https://doi.org/10.1016/j.jmst.2017.11.029>
3. Ma ZY, Feng AH, Chen DL, Shen J (2017) Recent advances in friction stir welding/processing of aluminum alloys: microstructural evolution and mechanical properties. *Crit Rev Solid State Mater Sci*. <https://doi.org/10.1080/10408436.2017.1358145>
4. Mohamadreza N, Abbas SM, Spiro Y (2011) Taguchi optimization of process parameters in friction stir welding of 6061 aluminum alloy: a review and case study. *Sci Res* 3:144–155. <https://doi.org/10.4236/eng.2011.32017>
5. Ghosh M, Kumar K, Kailas SV, Ray AK (2010) Optimization of friction stir welding parameters for dissimilar aluminum alloys. *Mater Des* 31:3033–3037. <https://doi.org/10.1016/j.matdes.2010.01.028>
6. Rajesh KG, Das H, Tapan KP (2012) Influence of processing parameters on induced energy, mechanical and corrosion properties of FSW Butt joint of 7475 AA. *J ASM Int* 21:1645–1654. <https://doi.org/10.1007/s11665-011-0074-2>
7. D'Urso G, Ceretti E, Giardini C, Maccarini G (2009) The effect of process parameters and tool geometry on mechanical properties of friction stir welded aluminium butt joints. *Int J Mater Forming* 2(Suppl. 1):303–306. <https://doi.org/10.1007/s12289-009-0480-2>
8. Reza-E-Rabby M, Tang W, Reynolds A (2013) Effect of tool pin features and geometries on quality of weld during friction stir welding. In: Mishra R, Mahoney MW, Sato Y, Hovanski Y, Verma R (eds) *Friction stir welding, and processing VII*. Springer, Cham. https://doi.org/10.1007/978-3-319-48108-1_17
9. Hattingsh DG, Blignault C, Van Niekerk TI, James MN (2008) Characterization of the influences of FSW tool geometry on welding forces and weld tensile strength using an instrumented tool. *J Mater Process Technol* 203:46–57. <https://doi.org/10.1016/j.jmatprotec.2007.10.028>
10. Zhang Z, Zhang HW (2007) Material behaviors and mechanical features in friction stir welding process. *Int J Adv Manuf Technol* 35:86–100. <https://doi.org/10.1007/s00170-006-0707-z>
11. Sakthivel T, Sengar GS, Mukhopadhyay J (2009) Effect of welding speed on microstructure and mechanical properties of friction-stir-welded aluminium. *Int J Adv Manuf Technol* 43:468–473. <https://doi.org/10.1007/s00170-008-1727-7>
12. Treadgill PL, Leonard AJ, Shercliff HR, Withers PJ (2009) Friction stir welding of aluminium alloys¹. *Int Mater Rev* 54(2):49–93. <https://doi.org/10.1179/174328009X411136>
13. Kanwer SA, Sunil P, Michael S, Rajneesh K (2010) Effect of process parameters on friction stir welding of aluminum alloy 2219–T87. *Int J Adv Manuf Technol*. <https://doi.org/10.1007/s00170-010-2560-3>
14. Cavliere P, Campanile G, Panella F, Squillace A (2006) Effect of welding parameters on mechanical and microstructural properties of AA6056 joints produced by friction stir welding. *J Mater Process Technol* 180:263–270. <https://doi.org/10.1016/j.jmatprotec.2006.06.015>

Experimental Investigations to Enhance the Rheological Properties of Vegetable Oils Blending with Mineral Oil



Santhosh Kumar Kamarapu, M. Amarnath, and B. Suresha

Abstract Biodegradable lubricants are gaining importance due to their unique characteristics such as biodegradability, renewability, and environmental friendliness. The major drawbacks of these lubricant oils are poor oxidative and thermal stabilities which cause a negative impact on their industrial applications. However, by changing the vegetable oil base stock with methods such as interesterification and transesterification, chemical alteration, additive reformulation, and oil crop generic modification, these limitations can be reduced. Experiments were conducted in order to improve the rheological properties of vegetable oils such as palm and castor oils by mixing them with mineral oil in the current study. The increase in the rheological properties of blended oil samples was demonstrated in tribological tests using a four-ball tribometer. The friction and wear characteristics of vegetable oils, mineral oil, and mineral oil blends were highlighted in the findings. The friction coefficient values and wear rate of the specimen lubricated with mineral–vegetable oil blends were significantly reduced.

Keywords Blend lubricants · Four-ball tribometer · Tribological properties · Lubrication mechanism

S. K. Kamarapu · M. Amarnath (✉)

Tribology and Machine Dynamics Laboratory, Department of Mechanical Engineering, PDDM Indian Institute of Information Technology Design and Manufacturing Jabalpur, Jabalpur, Madhya Pradesh, India

e-mail: amarnath@iiitdmj.ac.in

B. Suresha

Department of Mechanical Engineering, The National Institute of Engineering, Mysore, Karnataka, India

e-mail: sureshab@nie.ac.in

1 Introduction

The machine elements subjected to power or motion transmission generate friction and wear under various operating conditions. Lubricants used in engineering applications are available in various form, viz liquid, solid particles, pressurized air or in gaseous stages. The desired lubricant properties, such as thermal stability, high viscosity index, and anti-wear properties, result in a substantial reduction of wear and friction on the load-bearing contact surface of machine elements. Mineral and synthetic oils are extensively used to serve lubrication requirements in industries. There are several issues in handling and disposal of mineral and synthetic lubricants [1–3]. Numerous researchers have paid their attention in the development of alternatives to replace or minimize the usage of mineral oils. The alternatives include modifications of vegetable oil properties by considering interesterification, transesterification, chemical alteration, additive reformulation, and oil crop generic modification. Research articles proposed blending of nanoparticles into the vegetable oils, blending mineral oil in vegetable oil in appropriate proportion based on the requirements [4–9]. Vegetable oils contain triglycerol and fatty acid composition. The fatty acids in vegetable triglycerides have a carbon chain that ranges from 8 to 24 in length depending on the unsaturation level of oil. Vegetable oil contains fatty acids that allow molecules to bind to metallic surfaces. However, this bonding mechanism changes with operating parameter, viz temperature, applied load, speed, etc. Selecting a suitable vegetable oil, mineral–vegetable oil, or nanomaterial-blended lubricants results in a substantial reduction in coefficient of friction and wear on metallic surfaces [10–13]. The tribological performance of vegetable oil, mineral oil, and a blend of mineral oil and vegetable oil was investigated in this study. Using a four-ball tribometer, friction and wear tests were carried out. The mineral and vegetable blended oil samples resulted in a major drop in coefficient of friction and wear on the contact surfaces of chromium steel ball specimen mounted in the four-ball tribometer.

2 Experimental Procedure and Apparatus

Figure 1 depicts the four-ball tribometer used in friction and wear tests. This machine consists of steel oil cup, thermocouple which measure variations in temperature of oil samples. A constant torque was applied to the system, a control panel is coupled to the test rig which records the output parameter such as temperature, torque, and friction. The oil test rig was enclosed in a chamber to avoid oil spillages from the system to surroundings during its high-speed operating conditions.

The experimental test procedure was followed as per ASTM D 4172 [14], and to investigate the wear phenomenon, the test steel balls of 12.7 mm diameter with 64–66 HRC polished surface were considered in the experiments. The rotational speed and load for each experiment were 1200 rpm and 392 N, respectively, and the temperature of the oil samples was measured at 75 °C. The lubricants considered

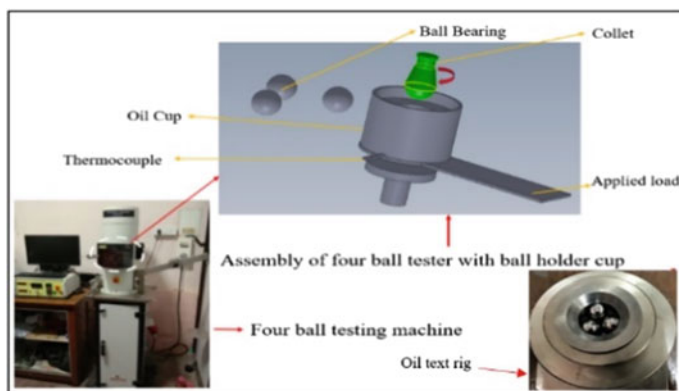


Fig. 1 Four-ball tester

Table 1 Test parameter details

Test parameters	Unit	Values
Normal load	N	392
Lubricant temperature	°C	75
Lubricant volume	mL	10 ± 2
Speed	rpm	1200 ± 1
Experiment time	min	60

in the experiment were mineral oil and vegetable oils such as palm (PO), castor oil (CO), and blends of mineral and individual vegetable oils. The mineral and vegetable oils were blended at 2/3 ratio. The blended lubricant samples were prepared using a magnetic stirrer, and the samples were heated up to 80 °C, stirred about 2 h at 1000 rpm. The acetone was used to clean the steel balls which is need to observe wear images clearly. As indicated in Fig. 1, three balls are positioned in a steel cup and tightened, with one more ball fixed to the collet (Table 1).

3 Results and Discussion

The specimen lubricated by using castor oil showed a substantial drop in coefficient of friction than the other oil samples as depicted in Fig. 2. The coefficient of friction values obtained by plain vegetable oil and blended oil samples show a considerable reduction than the mineral oil as shown in Fig. 2. The friction coefficient value obtained from mineral–palm blended oil sample showed about 6% reduction than the plain palm oil which can be attributed to a gradual reduction in carbonyl group free fatty acids present mineral–vegetable blended oil samples; however, mineral oil additives present blended oil form a protective layer between rolling contact surfaces

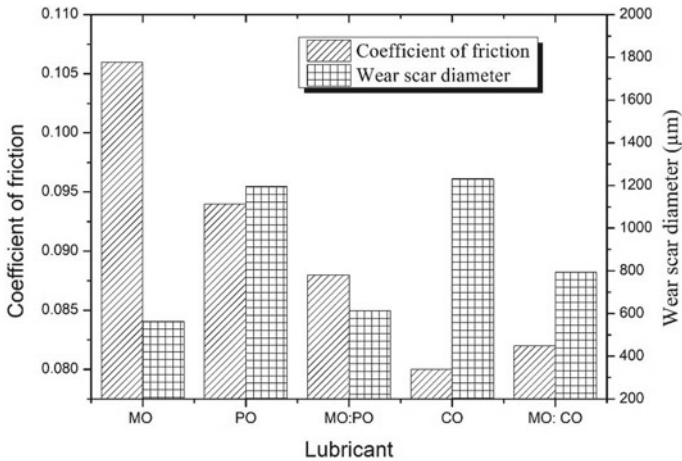


Fig. 2 Coefficient of friction and wear scar at 40 kg for all samples

[15, 16]. As compared to mineral oil, the existence of unsaturated fatty acids such as oleic, linoleic in palm oil, and ricinolein in castor oil results in a significant reduction in friction coefficient values.

The diameter of the wear scar was measured using a high-resolution microscope, as shown in Fig. 3. Due to increase in load cycle, the severity of wear increases that reflects an increase in scar diameter of balls. Elasto-hydrodynamic lubrication regime is achieved when fatty acids in the working lubricant form a soap film on top of the contact surfaces thereby causing a considerable reduction in wear severity on the contact surfaces. As the amount of load cycles on the spherical ball contact surfaces increases, the temperature of the plain oil rises gradually. As a result, unsaturated fatty acids in the plain vegetable oil form peroxides, increasing the degree of wear on the rolling contact surfaces. Under operating conditions, due to increase in temperature, the blended oil sample becomes volatile which influence the additives present in the mineral oil to produce a thin shielding layer on rolling contact surfaces. The chemical reaction occurred between mono and poly unsaturated fatty acids of vegetable oil and saturated hydrocarbon chain present in mineral oil result a decrease in terms of wear scar diameter on top of the rolling contact surfaces.

4 Conclusion

Experiments were conducted to examine the suitability of mineral oil and vegetable oil blends in minimizing friction and wear in steel ball specimen mounted in four-ball tribometer. From the experimental findings, the following conclusions were taken.

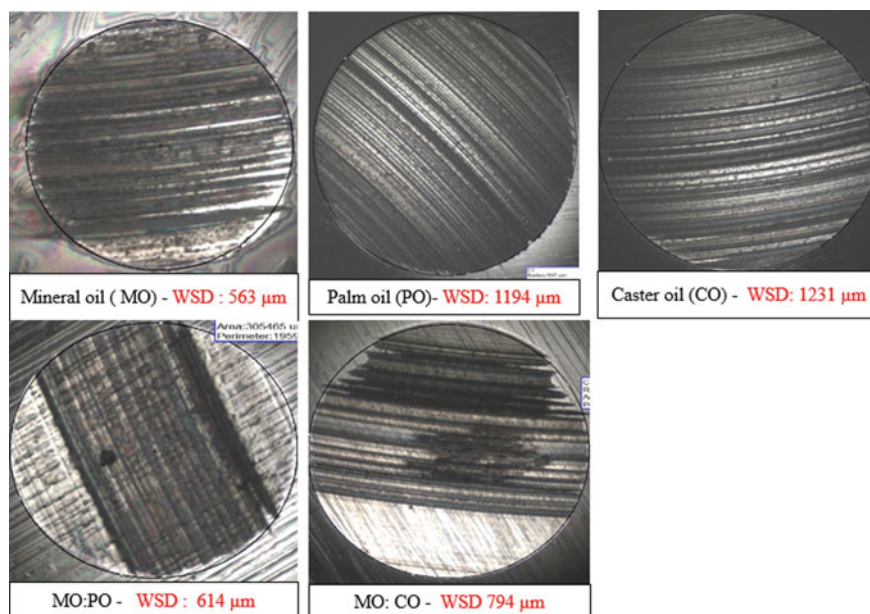


Fig. 3 Wear scar images of different samples

1. The performance of palm and castor oils were evaluated in minimizing friction and wear of steel balls mounted in four-ball tribometer. Blend compositions of vegetable and mineral oil were used to enrich lubricant performance.
2. Palm oil consists of linear chain structure which provide a fine interaction of polar heads between rolling contact surfaces thereby causing a significant reduction in friction.
3. The blended mineral–vegetable oil samples produced a considerable reduction in friction coefficient and wear scar diameter on rolling contact surfaces.

Additionally, attempts are being made to bring down the friction and wear in application stage such as bearings, gears, cams and many rolling/sliding contact machine elements.

References

1. Gebeshuber IC (2016) Ecotribology: development, prospects, and challenges. In: Ecotribology. Springer, Cham, pp 1–39
2. Bartz WJ (1998) Lubricants and the environment. *Tribol Int* 31(1–3):35–47
3. Madanhire I, Mbohwa C (2016) Environment and the economics of long drain interval. In: Mitigating environmental impact of petroleum lubricants. Springer, Cham, pp 149–164

4. Sabarinath S, Rajendrakumar PK, Prabhakaran Nair K (2019) Evaluation of tribological properties of sesame oil as biolubricant with SiO₂ nanoparticles and imidazolium-based ionic liquid as hybrid additives. *Proc Inst Mech Eng Part J: J Eng Tribol* 233(9):1306–1317
5. Campanella A, Rustoy E, Baldessari A, Baltanas MA (2010) Lubricants from chemically modified vegetable oils. *Biores Technol* 101(1):245–254
6. Wagner H, Luther R, Mang T (2001) Lubricant base fluids based on renewable raw materials: their catalytic manufacture and modification. *Appl Catal A* 221(1–2):429–442
7. Karmakar G, Ghosh P (2015) Soybean oil as a biocompatible multifunctional additive for lubricating oil. *ACS Sustain Chem Eng* 3(1):19–25
8. Adhvaryu A, Biresaw G, Sharma BK, Erhan SZ (2006) Friction behaviour of some seed oils: biobased lubricant applications. *Ind Eng Chem Res* 45(10):3735–3740
9. Bahari A, Lewis R, Slatter T (2018) Friction and wear response of vegetable oils and their blends with mineral engine oil in a reciprocating sliding contact at severe contact conditions. *Proc Inst Mech Eng Part J: J Eng Tribol* 232(3):244–258
10. Zulhanafi P, Syahrullail S (2019) The tribological performances of super olein as fluid lubricant using four-ball tribotester. *Tribol Int* 130:85–93
11. Murakami T, Sakamoto H (2003) Lubricating properties of vegetable oils and paraffinic oils with unsaturated fatty acids under high-contact-pressure conditions in four-ball tests. *J Synth Lubr* 20(3):183–201
12. Qucinchia LA, Delgado MA, Valencia C, Franco JM, Gallegos C (2009) Viscosity modification of high-oleic sunflower oil with polymeric additives for the design of new bio lubricant formulations. *Environ Sci Technol* 43(6):2060–2065
13. Alves SM, Barros BS, Trajano MF, Ribeiro KSB, Moura EJTI (2013) Tribological behaviour of vegetable oil-based lubricants with nanoparticles of oxides in boundary lubrication conditions. *Tribol Int* 65:28–36
14. ASTM D4172-18 (2018) Standard test method for wear preventive characteristics of lubricating fluid (four-ball method). ASTM International
15. Sharma BK, Adhvaryu A, Erhan SZ (2009) Friction and wear behaviour of thioether hydroxy vegetable oil. *Tribol Int* 42(2):353–358
16. Bowden FP, Gregory JN, Tabor D (1945) Lubrication of metal surfaces by fatty acids. *Nature* 156(3952):97–101

Experimental Study on Tensile Behavior of Tri-axial Hybrid Fiber Composites



Yegireddi Shireesha and Govind Nandipati

Abstract Concerns about environmental degradation and deterrence of non-biodegradable and non-renewable resources have drawn investigators trying to create novel products and eco-friendly materials based on sustainability concepts in today's fast-developing world. Natural fibers have undeniable benefits over synthetic reinforcing materials including low density, non-toxicity, low cost, comparable power, and minimal waste discarding issues. The current study involves the use of tri-axial laminates to prepare jute-banana hybrid composites. The composites were prepared using the traditional hand-layup technique. Composites were prepared in different laminate sequences, i.e., B-B-B-B, B-J-J-B, J-B-B-J, J-J-J-J. And also, the tensile power of these triaxle composites is examined in the direction of fiber orientation with different stacking sequences. Form this study, it is observed that fiber in 0° orientations is showing the slightly increasing in tensile strength. According to the staking sequences, the B-J-J-B sequence showing the high tensile strength compare to reaming stacking sequences.

Keywords Natural fibers · Fiber orientation · Composite sequence · Mechanical study · Tri-axial laminates

1 Introduction

Since 1900, the reinforced material for composites has produced natural fibers, Today's world, fiber composites are used in a variety of applications as a replacement for metal composites due to benefits such as low cost, scarcity, high specific strength, high stiffness, and perishability [1]. The emphasis on the production of natural fibers is to investigate their use in small load conditions. Composites, a tremendous material

Y. Shireesha (✉)

Department of Mechanical Engineering, GMRIT, Rajam, Andhra Pradesh, India

e-mail: y.shireesha@gmr.it.edu.in

G. Nandipati

Department of Mechanical Engineering, RVR & JC College of Engineering, Guntur, Andhra Pradesh, India

© The Author(s), under exclusive license to Springer Nature Singapore Pte Ltd. 2022

H. K. Dave et al. (eds.), *Recent Advances in Manufacturing Processes and Systems*,

Lecture Notes in Mechanical Engineering,

https://doi.org/10.1007/978-981-16-7787-8_40

having light-weight, rigidity, and high strength/weight properties have made great progress in replacing traditional materials such as metals and woods. Steel can be replaced with composites to save 60–80% of component weight, while aluminum parts can save 20–50% of component weight. For their light weight and good mechanical/tribological solutions, polymer-based composite materials are becoming more popular [2]. However, composites have issues such as delamination, matrix splitting, and fiber fracturing. In comparison to these problems, fiber cracking and matrix cracking play a significant role in tensile stress [3–6]. Following the production of composites to address the demands of the aerospace industry, researchers have concentrated on the desires of industrial, domestic applications. The rich availability of all natural fibers has fueled the growth of natural fiber composites. To meet and reduce the expense of housing needs, fiber composite boards have been used in the preparation of doors and separators. Roofing sheets are also developed with sisal and jute fiber-hybridized glass fiber that increases composite strength. Supreme applications of fiber composites such as buildings, partition boards, car outdoor parts, car seating panels, false ceilings, panels, automobile parts, packaging, and sports industries because of low cost and eco-friendly. Researchers also found that natural fiber composites can also be used as reinforcement which can also replace the glass fiber in polymer-based composites. Low-weight fiber cabinets, panel, and soft doors, plywood are made with jute fiber mixed with coir composites [7, 8]. Furthermore, the use of jute fiber in glass improves the composites' mechanical strengths. As a result, jute fiber has an efficient and value-added use. Polyester mixed jute composites are used to make suitcases, pipes, post-boxes, bath units, paperweights, tub, helmets, lampshades, electrical appliances, covers, panels for partition, grain storage silos and false ceilings, roof tiles bio-gas containers, and low-cost mobile and pre-fabricated buildings for use during traditional disasters. The primary focus of fiber strengthening is its increased availability in a wide range of applications [9–16]. Banana fiber is derived from waste stems of banana processing, so there is no additional cost to produce these fibers for industrial purposes [17]. Polyester-mixed banana fiber composites have high dynamic mechanical behavior and also found that fiber volume fraction effect the composites mechanical properties. Optimum strength is found in composites with a fiber loading of 40%, which is chosen as the important fiber loading [18]. Epoxy-mixed banana peel fiber range varying from 0 to 30% composites were prepared. Compare to all fiber loading 20% fiber loading shows best mechanical performance [19].

From the literature, the work on composites is focused on uni- and bi-directional composites. There is very less work concentrates on tri-axial composites. Due to this, the current work mainly focusing on preparation of tri-axial composites and studied about its strength along the fiber orientation.

2 Materials

Preparation of composites has done using jute and banana fibers along with epoxy resin. The epoxy LY 556, which is chemically part of the epoxy family used as matrix material, is reinforced in jute and banana fiber. Jute fiber mats are prepared in tri-axial direction, i.e., yarns are placed in 60° to each other. Similarly, banana fiber mats are also prepared.

Features of epoxy (LY556):

- Epoxy resin has chemical and corrosion resistance
- Good grip (bond) to various substrate
- Excellent thermo-mechanical possessions
- Excellent electrical-insulating strength
- Low shrinkage
- Highly electrical resistance
- Density—1.15 kg/cm³
- Viscosity—10,000 to 12,000 mpa-s
- Low thermal conductivity.

2.1 Fiber Materials

2.1.1 Jute Fiber

Jute material is an excellent fabric for burlap, sacking, and string, which is utilized as a tufted carpet backing material. It aids in the production of high quality to industrial yarn, sacks, cloth/net. It is one of the most versatile natural fibers, with applications in packaging, non-textiles, textiles, manufacturing, and agriculture. As yarn is bulked, it has a lower breaking tenacity and a higher breaking extensibility when blended as a ternary blend. Jute fiber, among other natural fibers, is a promising reinforcement for use in composites due to its easy availability, renewability, low cost, much lower energy demand for processing, lack of health risk, and high specific properties. Many works on the possibilities for jute fibers in polymer composites have been published. FRP-composites properties are identified by many of the factors like fibers properties, fibers concentration, fibers matrix, fibers orientation, and properties of matrix. While increasing the reinforcement volume, the strength and stiffness also enhances for the composite.

2.1.2 Banana Fiber

Natural banana fiber is one which have important advantages like low density, high mechanical properties, appropriate stiffness, and great renewability. Moreover, they are recyclable and bio-degradable. Banana fiber obtained from the pseudo stem of

Table 1 Banana fiber properties

Properties	Value
Parsistance	29.87 g/denier
Fineness	17.21
Moisture regain	13%
Elongation	6.57
Alco-ben extractives	1.8%
Total cellulose	81.7%
Alpha cellulose	61.7%
Residual gum	41.8%
Lignin	16%

banana plant, which is vast fiber with relatively good mechanical properties and high disposability and renewability. Banana plant is a big permanent grass with pseudo-stem sheaths.

Features of banana fiber (Table 1):

- It is one of the strong fiber.
- It looks very shiney, depending on the process of expulsion and spinning.
- Light in weight.
- It has very strong moisture absorption.
- It is bio-degradable, and it is not showing any adverse result on environment.
- Average fineness of fiber is 2400 Nm.

2.2 Preparation of Fiber Mats

Jute fiber and banana fiber mates are prepared in tri-axial direction as shown in Fig. 1. The fiber yarns are placed 60° of orientation to each other. Like this, the preparation of jute and banana mats was completed.



Fig. 1 Tri-axial jute and banana mats

Fig. 2 J-J-J-J sample tensile test at different % of fiber loading

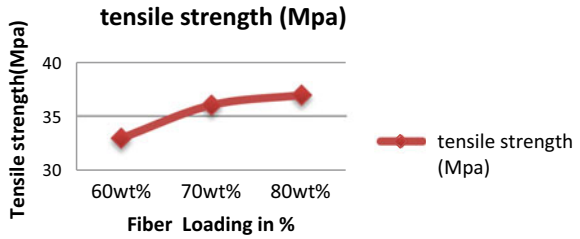
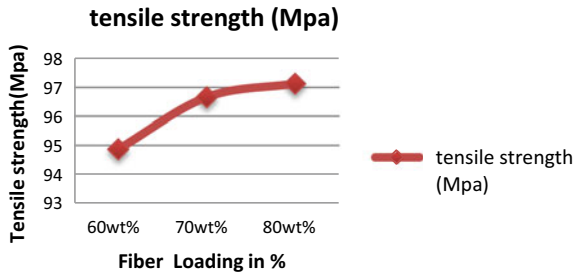


Fig. 3 B-B-B-B tensile test at different % of fiber



2.2.1 Sample Preparation

Tensile tests were performed on sample composites of pure jute and pure banana at three different weight ratios, namely 60, 70, and 80 wt%. According to the study, 80 wt% composites have the best tensile properties, but the bonding strength in laminates composites is decreases. Due to this, 70 wt% fiber composites are manufactured, which shows as similar strength to 80 wt% composites, but the bonding strength in these composites is high.

From the above study (Figs. 2 and 3), it is observed that constant weight ratio 70% weight considered for preparation of the hybrid jute-banana composites in different alignments, i.e., B-B-B-B, B-J-J-B, J-B-B-J, J-J-J-J.

2.3 Preparation of Composite

2.3.1 Mould Preparation

For the mold preparation, sheet-boxes (galvanized iron) of 55 × 55 × 8 mm have been used. Through the HAND LAY-UP technique, the prepared tri-axial laminates sheets are placed into a square box, into which the resin, and hardener mixture is poured.

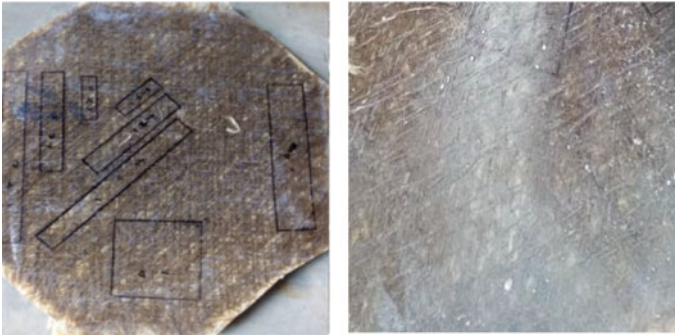


Fig. 4 Composites of jute and banana

2.3.2 Composite

Initially, pure jute and pure banana composites are prepared which are overlapped in a sequence of 0° , 60° , 120° , 0° . Now, the hybrid composites are prepared in a sequence of B-J-J-B and J-B-B-J with given orientations. With the aid of the rollers support, leveling was performed to evenly fill the cavity. Curing took about 24 h at room temperature (Fig. 4).

3 Mechanical Analysis and Results

The processed composites are sliced into 25×25 cm dimensions, after which the specimens are sectioned according to ASTM specifications, and the reinforced composites have the classification ASTM D3039-14 for tensile properties testing. The universal testing machine is used for to determine the mechanical properties like: strength and the stress, strain elongation of the given standard specimen made up of the different combinations. Flat specimens are often used for stress testing. For specimen geometry, the dog bone shape is most widely used. The tensile test is carried out on a straight-sided specimen in this analysis. The specimens are cut in all the three fiber directions for tensile properties study (Figs. 5 and 6; Table 2).

4 Results

Specimen with different orientations versus loads J-J-J-J (Figs. 7, 8, 9 and 10).

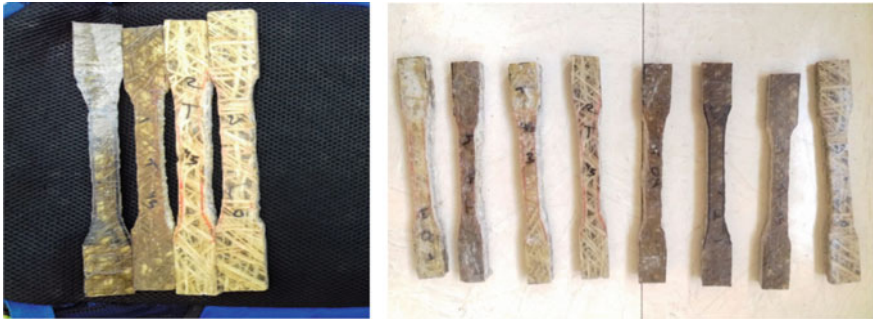


Fig. 5 Jute and banana specimens for tensile property

Fig. 6 Tensile test machine

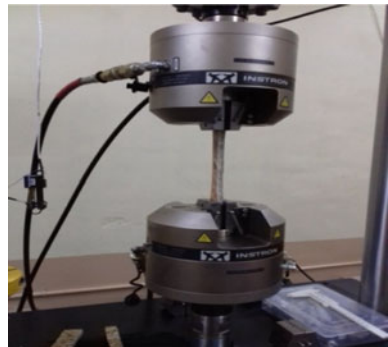


Table 2 Tensile test specimen loads

S. No.	Specimen	Tensile strength (Mpa) 1st orientation (0°)	Tensile strength (Mpa) 2nd orientation (60°)	Tensile strength (Mpa) 3rd orientation (120°)
1	J-J-J-J	32.98	32.49	32.38
2	B-B-B-B	96.66	96.91	95.8
3	J-B-B-J	61.6	60.9	60.4
4	B-J-J-B	96.86	96.21	96.16

Fig. 7 J-J-J-J composites at different orientations versus load

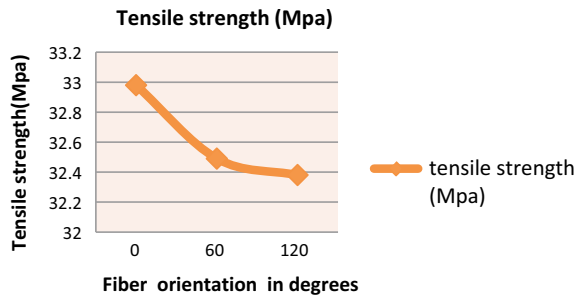


Fig. 8 B-B-B-B composites at different orientations versus load

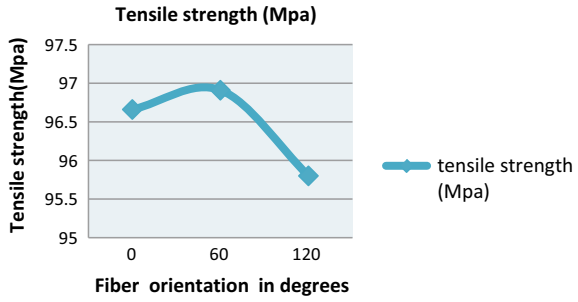


Fig. 9 J-B-B-J composites at different orientations versus load

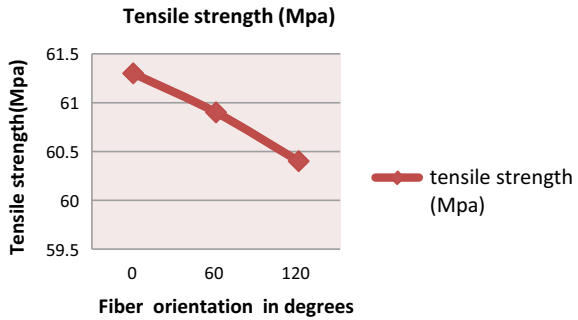
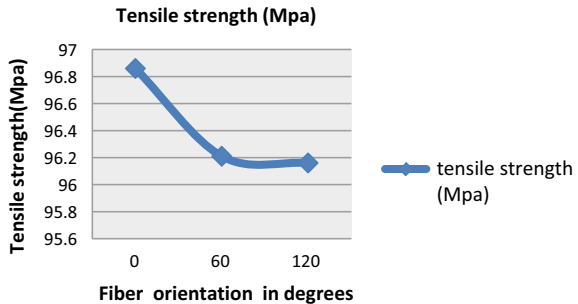


Fig. 10 B-J-J-B composites at different orientations versus load



5 Conclusions

The study resulted in the preparation of a new set of tri-axial composites, and the tensile properties of these composites in various fiber orientations and staking sequences were identified.

According to the results, composites with 70 wt% fiber have the best tensile strength and inter laminate bonding when compared to composites with the remaining wt% fiber.

In addition, compared to pure composites, hybrid composites produce high strength in all stacking sequences. From this work, we finalized that fiber orientation doesn't (not much) effecting the strength of the composites.

But, stacking sequences affect the tensile strength of the composites. From the results, it is concluded that B-J-J-B sequenced composite with 0° fiber orientation produces the high tensile strength.

References

1. Ma X, Yu J, Kennedy JF (2005) Studies on the properties of natural fibers-reinforced thermoplastic starch composites. *Carbohyd Polym* 62(1):19–24
2. Yadav RC, Chaturvedi S. An investigation of mechanical and sliding wear behavior of glass fiber reinforced polymer composite with or without addition of Silica (SiO_2)
3. Richardson MOW, Wisheart MJ (1996) Review of low-velocity impact properties of composite materials. *Compos A Appl Sci Manuf* 27(12):1123–1131
4. Paliwal MK, Chaturvedi SK (2010) An experimental investigation of tensile strength of glass composite. In: Proceedings of the world congress on engineering 2010, vol 2. WCE 2010, London
5. Cantwell WJ, Morton J (1991) The impact resistance of composite materials-a review. *Composites* 22(5):347–362
6. Bibo GA, Hogg PJ (1996) The role of reinforcement architecture on impact damage mechanisms and post-impact compression behaviour. *J Mater Sci* 31(5):1115–1137
7. Mueller DH, Krobjilowski A (2003) New discovery in the properties of composites reinforced with natural fibers. *J Ind Text* 33(2):111–130
8. Shaikh AA, Channiwala SA (2010) To study the characteristics of jute polyester composite for randomly distributed fiber reinforcement. In: Proceedings of the world congress on engineering, vol 2
9. Khan MA, Khan RA, Haydaruzzaman, Ghoshal S, Siddiky MNA Saha M (2009) Study on the physico-mechanical properties of starch-treated jute yarn-reinforced polypropylene composites: effect of gamma radiation. *Polym-Plast Technol Eng* 48(5):542–548
10. Scarponi C, Pizzinelli CS (2009) Interface and mechanical properties of natural fibers reinforced composites: a review. *Int J Mater Prod Technol* 36(1–4):278–303
11. Gopinath A, Kumar MS, Elayaperumal A (2014) Experimental investigations on mechanical properties of jute fiber reinforced composites with polyester and epoxy resin matrices. *Procedia Eng* 97:2052–2063
12. Vilaseca F, Mendez JA, Pelach A, Llop M, Canigueral N, Girones J, Mutje P (2007) Composite materials derived from biodegradable starch polymer and jute strands. *Process Biochem* 42(3):329–334
13. Zaman HU, Khan AH, Hossain MA, Khan MA, Khan RA (2009) Mechanical and electrical properties of jute fabrics reinforced polyethylene/polypropylene composites: role of gamma radiation. *Polym-Plast Technol Eng* 48(7):760–766
14. Li X, Panigrahi S, Tabil LG (2009) A study on flax fiber-reinforced polyethylene biocomposites. *Appl Eng Agric* 25(4):525–531
15. Yang HS, Kim HJ, Park HJ, Lee BJ, Hwang TS (2006) Water absorption behavior and mechanical properties of lignocellulosic filler-polyolefin bio-composites. *Compos Struct* 72(4):429–437
16. Jamil MS, Ahmad I, Abdullah I (2006) Effects of rice husk filler on the mechanical and thermal properties of liquid natural rubber compatibilized high-density polyethylene/natural rubber blends. *J Polym Res* 13(4):315–321

17. Joseph S, Sreekala MS, Oommen Z, Koshy P, Thomas S (2002) A comparison of the mechanical properties of phenol formaldehyde composites reinforced with banana fibers and glass fibers. *Compos Sci Technol* 62(14):1857–1868
18. Idicula M, Malhotra SK, Joseph K, Thomas S (2005) Dynamic mechanical analysis of randomly oriented intimately mixed short banana/sisal hybrid fiber reinforced polyester composites. *Compos Sci Technol* 65(7–8):1077–1087
19. Shireesha Y, Nandipati G (2019) State of art review on natural fibers. *Mater Today: Proc* 18:15–24

Forming Simulation of Bump Foils Used in Complaint Gas Foil Bearings



Rakesh K. Sahoo, Debabrata Mohapatra, and Suraj K. Behera

Abstract Complaint gas foil bearings are used in turbomachines. One among the various applications includes cryogenic turboexpander for the liquefaction of gas. Gas foil bearings provide enhanced temperature capability and eliminate the use of oil systems for lubrication purposes thereby reducing weight and lowering maintenance costs. Complaint gas foil bearings are self-acting hydrodynamic bearings of at least two layers of sheet metal foils. The complaint gas foil bearing traps the gas flowing between the collars of a shaft and the top foil. The shaft load is supported by the innermost “top foil” by trapping a gas pressure film while the outer bump foil provides an elastic foundation. This elastic foundation is a bump type structure called bump foil which is welded to the bearing base. Bump foil provides an additional level of cushioning effect increasing the bearing stiffness. Forming is the most popular process used to manufacture bump foils. The major problem faced during forming process of bump foil is the spring back effect. This paper presents a simulation method to predict the spring back generated in the bump foil during its forming process and propose suitable conditions under which spring back can be minimized.

Keywords Gas foil bearing · Bump foil · Spring back effect · Turboexpander

1 Introduction

Gas foil bearing is a self-acting bearing that separates the moving part of a machine from the part in rest, supporting the load and accommodating the shaft misalignment with the help of the gas present in the bearing. Air or other gas is present as a thin film

R. K. Sahoo (✉) · D. Mohapatra · S. K. Behera
National Institute of Technology Rourkela, Rourkela, Odisha, India
e-mail: 716ME4109@nitkl.ac.in

D. Mohapatra
e-mail: 115ME0450@nitkl.ac.in

S. K. Behera
e-mail: beherask@nitkl.ac.in

in the bearing which acts as a lubricant preventing contact between the moving parts. This type of bearing also eliminates the problem of oil contamination of process gas which is the case in general bearings. Here, the same working fluid is used in the bearing itself. The usefulness and significance of gas foil bearings in turbomachine applications are quite remarkable. Until now, a small amount of research and development is only done in this bearing. One of the major problems faced in forming bump foils is spring back effect. Spring back effect refers to the change in geometrical shape of the bump foil when the top die has been unloaded from the bump foil at the end of forming process. Also, the developed works present a complex procedure, simulation, and modeling technique which make them difficult to use for different applications. In this thesis, a prudent attempt is made to design and develop a smooth, straightforward, and transparent simulation procedure of the bump foils. Due to the elastic–plastic properties of the sheet metal, during loading process, the shape imparted by top die will be a combination of elastic and plastic deformation. At the end of unloading process, there will be permanent plastic deformation in the bump foil whereas the release of elastic deformation causes spring back effect in the bump foil.

Nowadays, turboexpanders with excellent efficiency have been constructed which are used in industries, medicine manufacturing, and research facilities. The increasing demand for these turbomachines requires the development of bearing which can be efficiently used in them. The most suitable type of bearing used for this application is the gas foil bearing with a bump foil structure. There are different kinds of bearings that can compete for this purpose, but gas foil bearing with bump type foil structure bearings are the most preferred ones due to their simple and efficient operation. They prevent major operating problems like oil contamination, misalignment, lower bearing stiffness, and lower load carrying capacity. Turbomachines rotate at very high speeds which demands a bearing having excellent load carrying capacity and higher bearing stiffness necessary for supporting the rotating shaft.

Bump foil structure under top foil provides an additional level of cushioning effect which takes the sudden load by the high-speed rotors and aligns them back into their proper positions. Top foil is made smooth in order to reduce friction during the starting and stopping of the rotation of the shaft. Top foil is constructed in a manner to give a converging shape to the gas flowing between itself and the collar. This wedging action results in a gas film with increased pressure capable of carrying the thrust load. The research was done by Agrawal [1] on overview of foil air/gas bearing technology where he summarized the various air foil bearing designs used for turbomachinery purposes during last 25 years. In this paper merits of air foil bearings that are currently used in industry. It was concluded that air foil bearings can be used in various turbomachines involving high-temperature operations which will increase efficiency and reduce the cost of these machines. Research was done by Dellacorte et al. [2] on Design, Fabrication, and Performance of Open Source Generation I and II Compliant Hydrodynamic Gas Foil Bearings which provided literature review on design and manufacturing process of both first and second generation bump-style foil bearings. Simple bearing design has lower load capacity while shaft misalignment provided load capacity more than simple bearing.

The research was performed by Xiong et al. [3] on the development of air foil journal bearings for a high-speed cryogenic turboexpander. They have designed high-speed cryogenic expander and analyzed the vibration performance of bearings by varying foil stiffness and the optimum foil stiffness is determined which provides sufficient stability at a rotational speed greater than 230,000 rpm. A research thesis was done on manufacturing of a Gas Foil Bearing for Palm-Sized turbomachinery by Creary [4] in which mini gas foil bearings have been manufactured by using silicon parts and micro-fabrication technique called LIGA (German acronym meaning Lithography, Electroplating, and Molding). The bearing made for impulse turbine test setup has elastic foundation of 200 μm , 1 mm depth and the top foil was created using precision machine. The performance of gas foil bearing was analyzed using the orbit simulation method. A research was performed by Shalash [5] on various gas foil bearing manufacturing processes. Monte Carlo simulation method was used to analyze the static performance of bump foil bearing and DOE (Design of Experiment) technique was used to determine the effect of various manufacturing parameters. Mathematical model of bump foil was created and finite element analysis of forming process of bump foil was performed. It was inferred that reducing the curvature of bump reduces the spring back effect generated at the end of forming process.

A research on comparative evaluation of gas foil bearings was done by Shalash [6] with different compliant structures to improve the manufacturing process. Monte Carlo simulation method of bump foil bearing was performed to determine the effect of various manufacturing parameters on performance of bearing. Moreover, two types of compliant structures were used to compare the ease of manufacturability such as sinusoidal foil and cantilever bump foil. Another research was performed by Zhou et al. [7] on numerical and experimental investigation of dynamic performance of bump foil journal bearing based on journal orbit. In this research paper, the minimum film thickness and dynamic stiffness of bump foil bearing were determined using journal orbit, and the results of simulations were validated by experimental results. Finite element analysis of forming process of bump foil of compliant gas foil bearing made up of phosphorus bronze foils was performed by Behera et al. [8] where the equivalent stress, deformation, damage, and spring back was determined. Forming simulation of bump foil bearing was investigated at varying loading and unloading speeds of top die, and the optimum speed was observed at 4.8 mm/s.

Combining the ideas, concepts, and research work done in all the papers discussed above, a simple method of forming simulation is presented in the current research paper for the design and fabrication of bump foil needed for various applications. A bright, uncomplicated, and transparent methodology is conferred in the thesis to simulate the forming process of bump foils used in complaint gas foil bearings. The author believes that the documented steps of computational and fabrication methodology will be helpful for the researchers to develop a bump foil.

2 Methodology

2.1 Simulation Process Parameter

The rigid or metal die with corrugated bump shape is used to make bump foils. Rigid dies are taken as application of heat during bump forming operation is possible to reduce spring back effect and maintain uniformity in the bump height. The FEM analysis for bump formation is carried using DEFORM 3D software. The 3D models for foil, top, and bottom dies are created using SOLIDWORKS software. The profile of bumps on the bottom die is kept the same as the bump dimension. However, the profile of bumps on the top die is reduced to minimize the spring back effect. This software package helps to predict the forming load needed for bump formation, stress distribution over bump foil, and damage to bump foils for various forming parameters. For studying the plastic deformation behavior of a given metal homogeneous deformation of bump foil is considered. The flow stress of material can be considered as the yield stress of material under uni-axial conditions which is a function of strain ($\bar{\epsilon}$), strain rate ($\dot{\bar{\epsilon}}$), and temperature (T). The metal foil will undergo deformation plastically when the stress induced in the metal is above the yield stress or flow stress of material. The DEFORM3D software uses a different method of flow stress which is predefined in the software as shown below:

$$\bar{\sigma} = \bar{\sigma}(\bar{\epsilon}, \dot{\bar{\epsilon}}, T)$$

where,

$\bar{\sigma}$ = flow stress

$\bar{\epsilon}$ = effective plastic strain

$\dot{\bar{\epsilon}}$ = effective strain rate

T = Temperature.

The above method is a more accurate way to determine the flow stress as it is equal to the true behavior of a material. This method takes into account linear weighted average of tabular flow stress data points. The Von-Mises function type is used as yield function and it specifies an isotropic material model. A three bump analysis is done for the forming process to get accurate results from the deformation of the middle bump which can be later extended for the forming of multiple bumps. The thin foil is placed in between the metal top and bottom die. Table 1 shows all the

Table 1 Dimensions of bump for journal bearing

Bump parameters	Values
Thickness (t), mm	0.1
Radius (R), mm	1.75
Height of bumps (H), mm	0.60
Pitch (P), mm	4.20
Width (W), mm	16

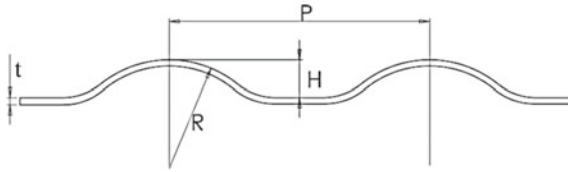


Fig. 1 Parameters of journal bump foil

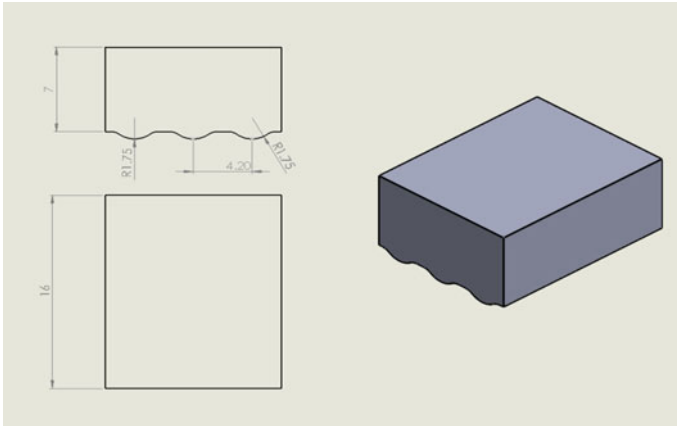


Fig. 2 Top rigid die for fabrication of bump journal foil

bump parameters and Fig. 1 shows all the parameters for the designed bumps.

Fabrication of bump needs a pair of dies and a thin foil. The thin foil is pressed by placing it between the dies. Prior research has already been done on fabrication methodology of bump foil using a rigid bottom die and a flexible top die. Figure 2 shows the design of the top die used along with all its dimensions used for forming the desired bump and Fig. 3 shows the design of the Bottom die used along with all its dimensions used for forming the desired bumps. Figure 4 shows the design of the sheet used along with all its dimensions used for forming the desired bump.

2.2 Convergence Test

A convergence test is performed to determine the optimum number of mesh elements and forming load required for finite element analysis. The mesh is refined till no difference in results (load) is seen. Figure 5 shows the flow chart of convergence test [9].

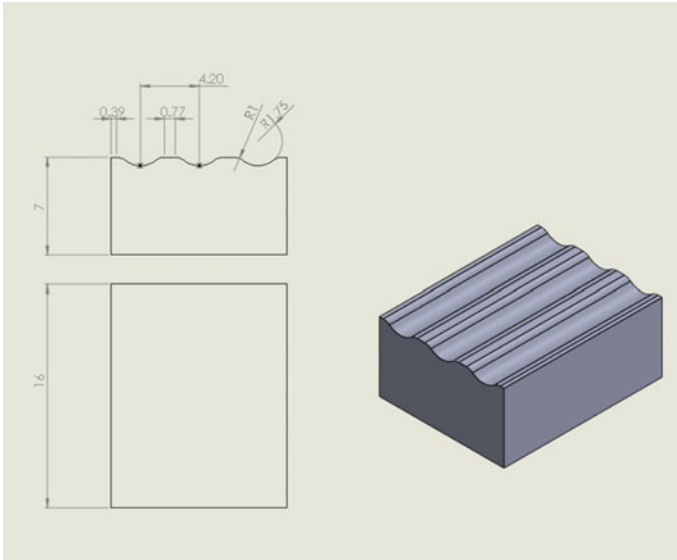


Fig. 3 Bottom rigid die for fabrication of bump journal foil

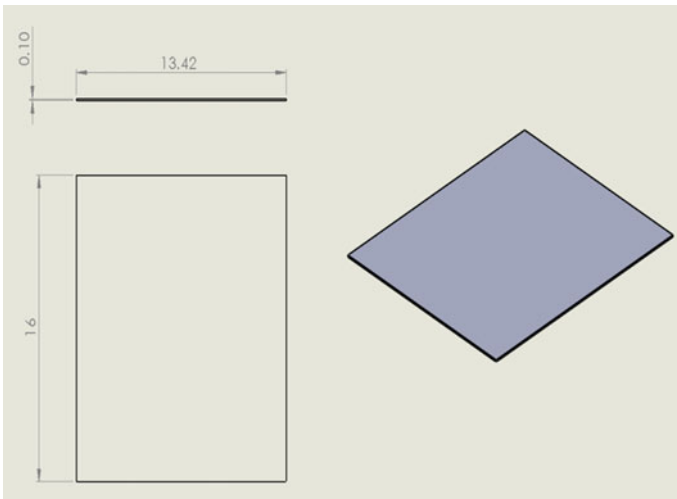


Fig. 4 Sheet for fabrication of bump journal foil

The convergence test is done to get the optimized meshing size. Then the simulation test is done for various die speeds to get the deformed bump foil under loaded conditions. Thereafter, another simulation is done where the top die moves in reverse direction to simulate the unloading process. The spring back is calculated after the completion of the entire process and the optimum stroke speed of top die is proposed

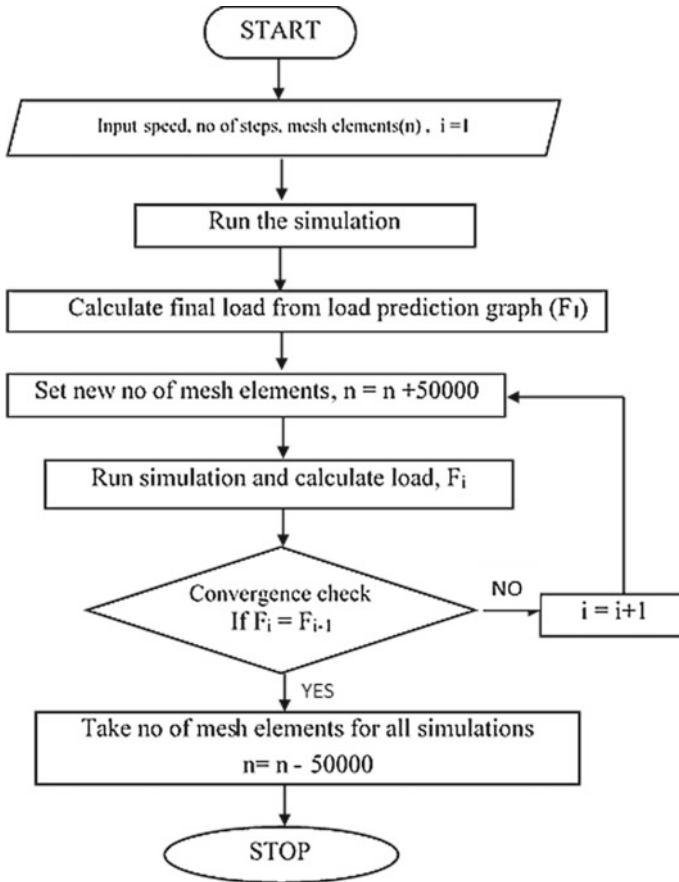


Fig. 5 Flow chart of convergence test

for minimum spring back. Table 2 shows the initial input parameters for simulation of bump foil formation and these parameters were used to simulate the load prediction on the top die. The speed is initially taken to be the total deformation per second.

Initially number of mesh elements were taken 100,000. The convergence test is conducted and Table 3 shows convergence test results.

So, changing number of mesh elements from 150,000 to 250,000, i.e., by 200% only changes the result by 0.1%. Thus number of elements of 150,000 is an optimum number of mesh elements needed for accurate results. To calculate the accurate value of residual stress and spring back at the end of forming process convergence test is performed. To observe the material response during the unloading, direction of the primary die is reversed and the simulation is done in small steps.

Table 2 Parameters required for forming simulation of bump foil

S. No.	Input parameter	Values
1	Workpiece materials	Phosphor bronze
2	Top die/Primary die	Rigid
3	Bottom die	Rigid
4	Movement of the workpiece	Vertically downward
5	Movement of top die	Vertically downward
6	Movement of bottom die	Fixed
7	Stroke speed of the top die	0.06 mm/s
8	No. of steps	100
9	Stop conditions	Release the forming load after traveling 0.6 mm
10	Flow stress	$\bar{\sigma} = \bar{\sigma}(\bar{\epsilon}, \dot{\bar{\epsilon}}, T)$
11	Yield function type	von-Mises
12	Hardening rule	Isotropic
13	Mesh type	Tetrahedral mesh
14	Friction co-efficient	0.12

Table 3 Results of forming simulation done for convergence test

S. No.	Number of mesh element	Run time (min)	Load (kN)
1	100,000	71	59.19
2	150,000	97	57.87
3	200,000	146	57.89

2.3 Bump Foil Material

The material chosen for forming simulation is phosphor bronze. Phosphor bronze is an alloy of copper with 0.2% phosphorus and 5% of tin. It is suitable for use in cryogenics applications as it has good electrical conductivity and low thermal conductivity that allows the making of electrical connections to devices at ultra-low temperatures without adding excessive heat. The tin increases the corrosion resistance and strength of the alloy while the phosphorus increases the wear resistance and stiffness of the phosphor bronze alloy. Some important properties of phosphor bronze are: (a) It has excellent elasticity thus providing the required cushioning effect to the gas bearing, (b) It has outstanding malleability thus can be easily deformed, (c) It has no seasonal cracking or age hardening, (d) It has high strength and wear resistance which is required in cryogenic turboexpander, (e) It has high electrical conductivity, and (f) It has high resistance to chemical corrosion. Table 4 shows the mechanical and physical properties of phosphor bronze.

Table 4 Properties of phosphor bronze

S. No.	Properties	Values
1	Density, g/cc	8.8
2	Hardness, Rockwell B	85
3	Yield strength, MPa	550
4	Elongation at break	33%
5	Poisson's ratio	0.341
6	Young's Modulus, Gpa	110
7	Co-efficient of thermal conductivity, $\mu\text{m}/\text{m}^\circ\text{C}$	18.2
8	Electrical resistivity, ohm-cm	1.33e-05
9	Heat capacity, $\text{J}/\text{g}^\circ\text{C}$	0.38
10	Thermal conductivity, $\text{W}/\text{m}-\text{K}$	62
11	Melting point, $^\circ\text{C}$	880-1025

3 Results and Discussion

3.1 Comparative Study of Forming Process at Various Die Speed

The forming simulation is done for various top die velocities. The starting velocity is taken such that the operation is finished in one second as the foil dimensions are very small. The velocity is doubled after each simulation and the load prediction on the top die, deformation, effective stress, and damage of the workpiece or bump foil is compared for various speeds to get the optimal speed for forming process. Table 5 shows the common input parameters for simulation of bump foil formation and Table 6 shows the time step for each speed. The time step is taken differently for every calculation so as to keep the number of simulation steps constant. Time step can be found out by dividing total displacement of top die per unit stroke speed with total number of steps.

The values for flow stress for phosphor bronze is plotted for various value of Strain and Strain Rate is shown in Fig. 6.

This flow stress plot of phosphor is taken from the material database of DEFORM 3D software for material Silicon Bronze which has similar flow stress data as of Phosphor Bronze. This method takes a linear weighted average between tabular flow stress data points. Figures 7 and 8 show plots for average damage, Stress effective versus stroke velocity of top die.

Yield Strength for phosphor bronze is 450 MPa. So, if effective stress induced in the bump foil is greater than yield strength major part of bump foil after loading will be in plastic region and won't change its shape upon unloading thus minimizing spring back effect. Figure 9 shows that for stroke velocity 4.8 mm/s, the major part of bump foil is in plastic region thus satisfying our condition. Moreover, after unloading, the

Table 5 Common input parameters for all simulation

S. No.	Input parameter	Values
1	Workpiece materials	Phosphor bronze
2	Top die/Primary die	Rigid
3	Bottom die	Rigid
4	Movement of the workpiece	Vertically downward
5	Movement of top die	Vertically downward
6	Movement of bottom die	Fixed
8	No of steps	100
9	Stop conditions	Release the forming load after traveling 0.6 mm
10	Flow stress	$\bar{\sigma} = \bar{\sigma}(\bar{\epsilon}, \dot{\bar{\epsilon}}, T)$
11	Yield function type	von-Mises
12	Hardening rule	Isotropic
13	Mesh type	Tetrahedral mesh
14	Friction co-efficient	0.12

Table 6 Input parameter for different stroke speeds

S. No.	Stroke speed (mm/s)	Time step (s/step)
1	0.6	0.01
2	1.2	0.005
3	2.4	0.0025
4	4.8	0.00125
5	6.0	0.001
6	10.0	0.0006
7	153.6	0.0000390625

average effective stress is less than the yield strength. So after unloading, maximum part of bump foil is in elastic region. As the bump foil is in elastic region it provides cushioning effect to the journal air foil bearing.

3.2 Study of Loading Simulation at Optimum Speed

It is seen that the combination of least damage and required effective stress is obtained when forming of bump foil is done with top die velocity falling within the range of 0.6–4.8 mm/s. The nodal percentage distribution is also studied to get the average value of effective stress, damage after the forming process. Figures 9 and 10 give the plot of damage, effective stress after the forming process.

During loading maximum damage takes place in the area present between the bump of the top die and bump of the bottom die and the maximum effective stress

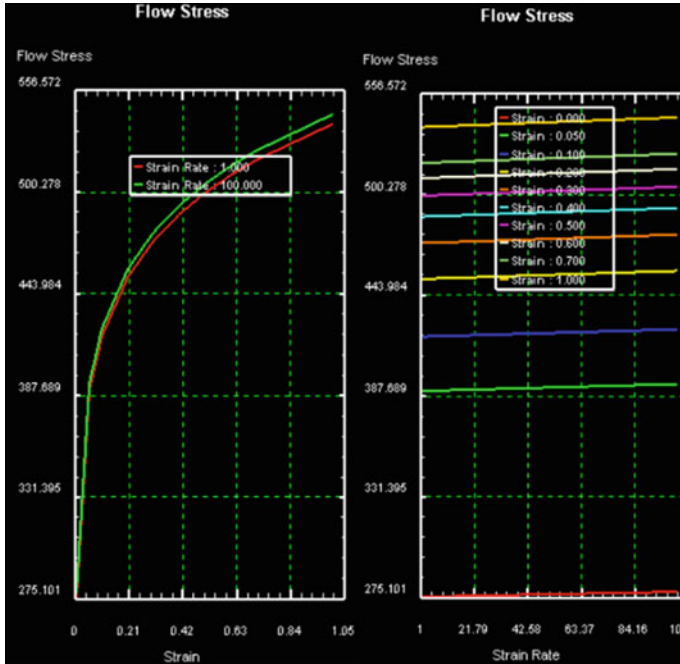
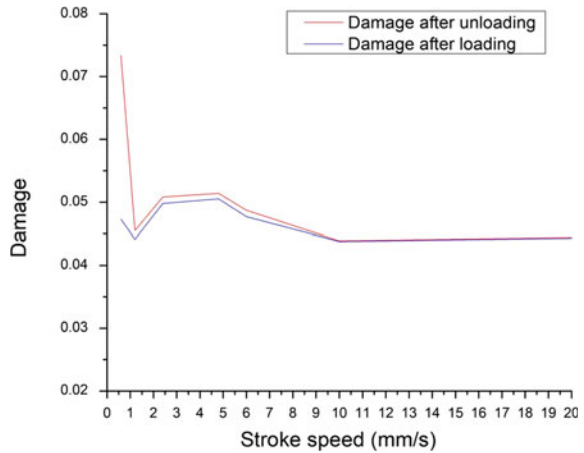


Fig. 6 Graph of flow stress of phosphor bronze versus strain and strain rate

Fig. 7 Graph of damage of bump foil versus stroke speed after unloading



to be present at the places where damage is maximum. It can be inferred from the figure that most part of the bump foil (red region) has undergone plastic deformation and ideally will not show spring back effect. The peripheral region is in the region of elastic deformation and may show some spring back effect. The release of elastic deformation is the spring back in the bump foil often observed at the end of a forming

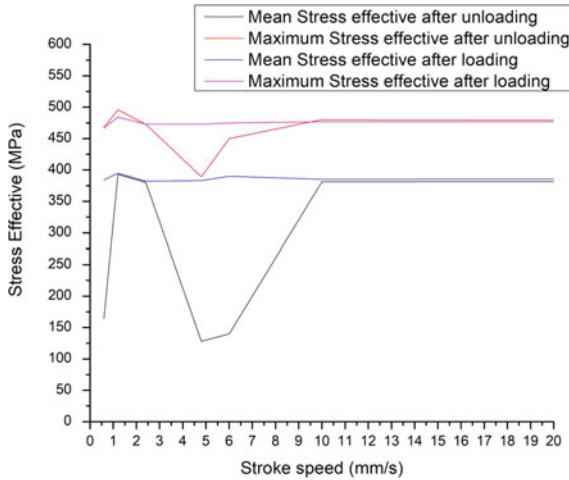


Fig. 8 Graph of Stress effectiveness of bump foil versus stroke speed after unloading

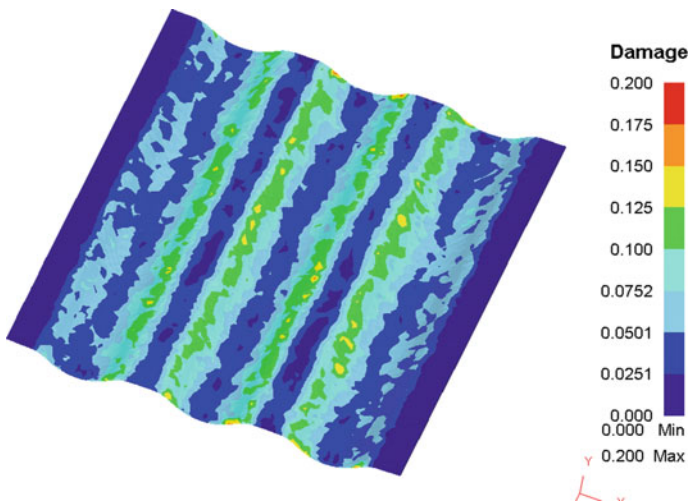


Fig. 9 Simulated damage for phosphor bronze journal bump foil

process. We observe an unequal distribution of effective stress in the bump foil after loading condition. The distribution of various output parameters is studied and the spring back is calculated. Figure 11 and 12 gives the nodal distribution of damage, effective stress after the forming process. The X-axis representing the output parameters are divided into 40 divisions and the Y-axis represents the percentage of total nodes with respect to a specific value of output parameter.

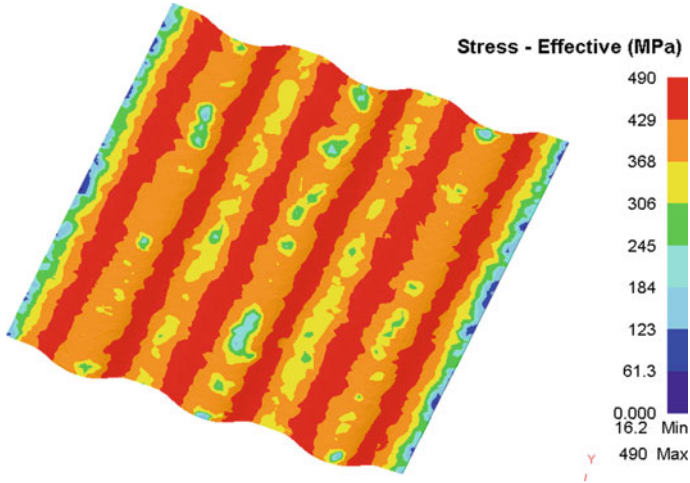


Fig. 10 Simulated effective stress for phosphor bronze journal bump foil

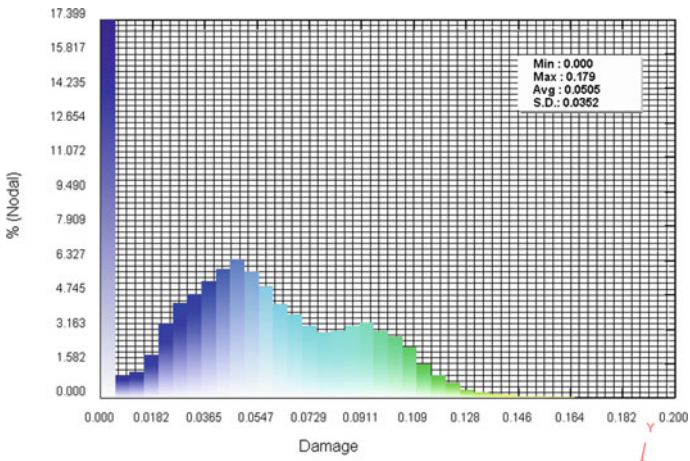


Fig. 11 Histogram of nodal distribution of damage for bump foil

3.3 Study of Unloading Simulation at Optimum Speed

To calculate the spring back during unloading process, a simulation is done. To observe the material response during the unloading, direction of the primary die is reversed and the simulation is done in small steps. Figures 13 and 14 shows give the plot of damage, effective stress after the forming process.

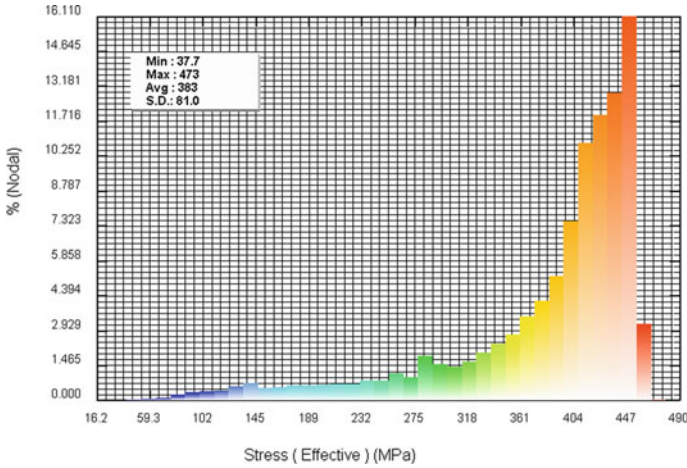


Fig. 12 Histogram of nodal distribution of effective Stress for bump foil

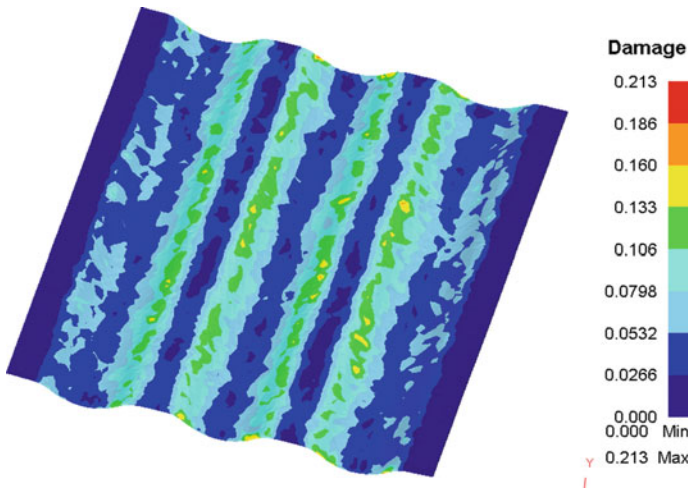


Fig. 13 Simulated damage for bump foil after unloading

The initial input parameters for simulation of spring back in bump foil formation and the parameters used to simulate the displacement, effective stress on the work-piece or bump foil after top die is removed is taken to be same as input parameters for loading simulation as mentioned in Table 5 above except that the stopping condition of top die displacement is taken as 1.2 mm. Unloading the top die over the workpiece gives a uniform distribution of stress in the bump foil which is the desired result. This is favorable as maximum elements in the bump foil are elastic now as required in their operation in airfoil bearings. During unloading, the bump foil rises above the fixed

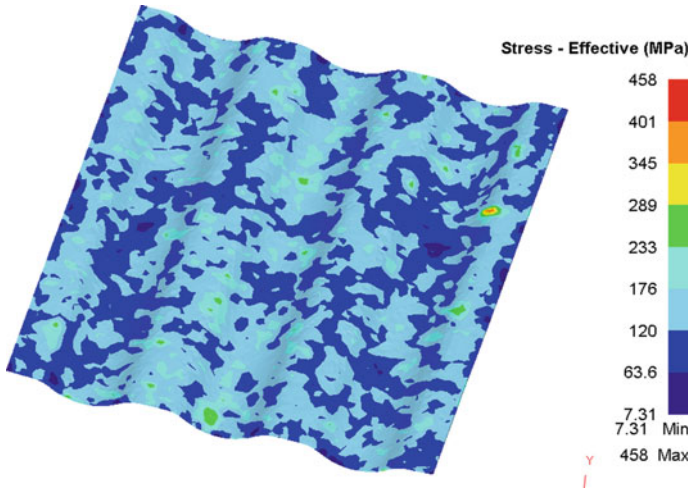


Fig. 14 Simulated Stress effective for bump foil after unloading

bottom die and the average thickness is also around 90% of the required thickness thus this process is acceptable for the fabrication of phosphor bronze journal bump foil. Figures 15 and 16 give the nodal distribution of damage and effective stress after the forming process in the form of histogram. The X-axis representing the output parameters are divided into 40 divisions and the Y-axis represents the percentage of total nodes with respect to a specific value of output parameter.

The motion of the upper die during loading operation was downwards and so should be the direction of displacement of the foil. But in Fig. 17, it is seen the

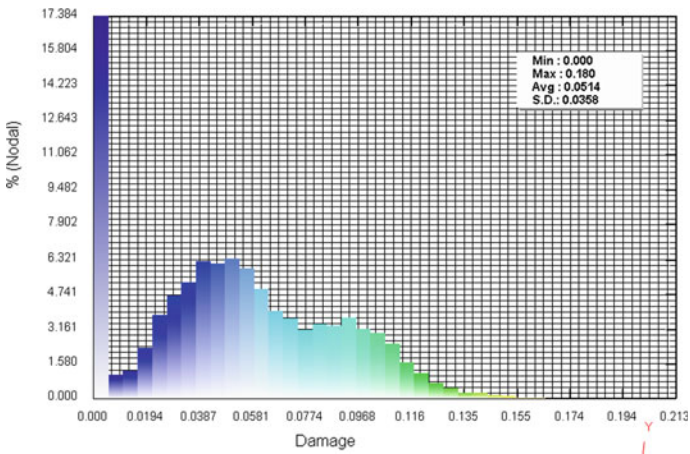


Fig. 15 Histogram of nodal distribution of damage for phosphor bronze journal bump foil after unloading

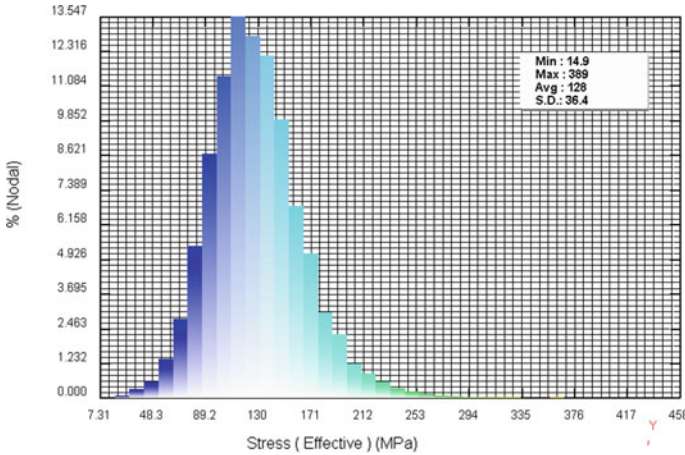


Fig. 16 Histogram of nodal distribution of Stress effective for phosphor bronze journal bump foil after unloading

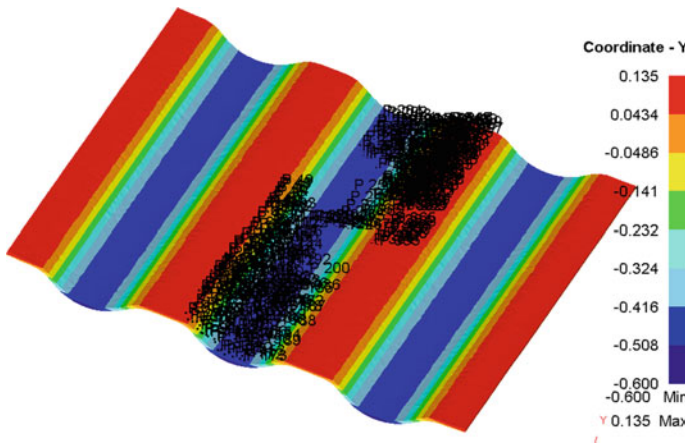


Fig. 17 Selected points on phosphor bronze journal bump for point tracking

direction of displacement of the nodes between two bumps is in an upward direction. So, these are the areas where the spring back will be majorly found. To calculate spring back we use the Point Tracking feature of Deform3D software. Point tracking shows displacement of points in the material. Using point tracking we can find the Y coordinate of each marked point after every step. After point tracking is done the data is saved in the form of the data sheet and the absolute value of the difference between the Y-coordinates of points between first and final step gives the spring back for that particular point. Four Hundred random points are marked on the middle bump of the simulated bump foil after loading condition (Step 100). Two hundred points

are marked on the top side of the middle bump while the other two hundred points are marked on the bottom side. The total surface of the bump is divided into seven regions according to the Y-coordinate plot. The point distribution is done according to the length of these regions.

The average spring back for the various regions is provided in Tables A.1 and A.2 under Appendix section. Region A, I, and H, O being the longer regions are marked with 50 points while the rest are marked with twenty points. Moreover, from Fig. 17 it was observed that the probability of occurrence of spring back is in region A, I so the number of points are taken in this region to get accurate results of spring back. The percentage of spring back value is calculated with respect to the maximum deformation of the workpiece that is 0.6 mm. The average spring in the middle bump of the bump foil is found by taking the average of the spring backs of all the four hundred marked points. The maximum value of spring back was found to be 0.0095 mm. The value of average spring back is found to be 0.00052 mm and the percentage spring back is 0.087%.

The average spring back found by point tracking method is highest in region A. The average spring back for the entire middle bump is 0.00052 mm and the percentage spring back relative to maximum deformation is 0.09%. As the tolerance value for the fabrication of bump foil is assumed to be 0.1% so this method of fabrication is acceptable. For the lesser value of spring back the geometry of the upper die may be changed. The gap between the upper die and lower die in the closed position should be less than the thickness of the bump foil in the region between two bumps to compensate for the effect of spring back and increase the accuracy of the process if needed. The output parameters of forming process during loading and unloading conditions such as mean damage, mean stress effective, maximum stress effective, mean strain effective, mean strain rate effective, mean thickness of bump foil, and average spring back values are shown in Table 7.

4 Conclusion

The thesis presented gives us a way to understand the modeling and simulation of bump foils. The parameters are stated for a smooth, straightforward, and transparent forming procedure of the bump foils. It was concluded that:

- (a) The forming process is one of the easiest and preferable methods for the manufacturing of bump foil. The parameter which guides the deformation process and controls the spring back majorly is the stroke speed of top die.
- (b) For speed greater than the critical speed plastic deformation takes place and spring back is considerably reduced. The critical speed for the forming operation is found to be 4.8 mm/s. The speed should be risen above the critical speed considering the increasing damage and the reduction in thickness of the bump foil during the forming process with increasing speed.

Table 7 Output parameters of bump foil after loading and unloading condition

S. No.	Output parameter	Values
<i>After loading condition</i>		
1	Mean damage	0.0505
2	Mean stress effective (MPa)	383
3	Maximum stress effective (MPa)	473
4	Mean strain effective (mm/mm)	0.0916
5	Mean strain rate effective (mm/mm)/s	20.4
6	Mean thickness of bump foil (mm)	0.0918
<i>After unloading condition</i>		
1	Mean damage	0.0514
2	Mean stress effective (MPa)	128
3	Maximum stress effective (MPa)	389
4	Mean thickness of bump foil (mm)	0.0919
5	Average spring back (mm)	0.000522129

Table A.1 Simulated spring back for various regions on the top side of bump foil

S. No.	Region	Point to be taken	Coordinate range (mm)	Average spring back (mm)	% Average spring back
<i>Top side of the foil</i>					
1	A	50	0.135 to 0.0434	0.001675909	0.279318233
2	B	20	0.0434 to – 0.0486	0.000854146	0.142357646
3	C	20	–0.0486 to – 0.141	0.000400919	0.06681976
5	E	20	–0.232 to –0.324	0.00034909	0.058181602
6	G	20	–0.324 to –0.416	0.000219217	0.036536091
7	H	50	–0.416 to –0.600	0.000235585	0.039264144

(c) The average spring back found by point tracking method is 0.00052 mm and the percentage spring back relative to maximum deformation is 0.09%. As the tolerance value for the fabrication of bump foil is assumed to be 0.1% so this method of fabrication is acceptable.

Table A.2 Simulated spring back for various regions on the bottom side of bump foil

S. No.	Region	Point to be taken	Coordinate range (mm)	Average spring back (mm)	% Average spring back
<i>Bottom side of the foil</i>					
8	I	50	0.135 to 0.0434	0.000256309	0.04271824
9	J	20	0.0434 to – 0.0486	0.000267351	0.044558424
10	K	20	–0.0486 to – 0.141	0.000284129	0.047354844
11	L	20	–0.141 to –0.232	0.000149091	0.024848427
12	M	20	–0.232 to –0.324	0.000104211	0.017368469
13	N	20	–0.324 to –0.416	0.000274173	0.045695582
14	O	50	–0.416 to –0.600	0.000754589	0.125764757

Appendix

References

1. Agrawal GL (1997) Foil air/gas bearing technology an overview. In: International gas turbine and aerospace congress and exhibition, no. ASME paper 97-GT-347. American Society of Mechanical Engineers. <https://doi.org/10.1115/97-GT-347>
2. DellaCorte C, Radil KC, Bruckner RJ, Adam Howard S (2008) Design, fabrication, and performance of open source generation I and II compliant hydrodynamic gas foil bearings. *Tribol Trans* 51(3):254–264
3. Xiong L-Y, Wu G, Liu L-Q, Ling M-F, Chen C-Z (1997) Development of aerodynamic foil journal bearings for a high speed cryogenic turboexpander. *Cryogenics* 37(4):221–230
4. Creary AJ (2009) Manufacturing of a gas foil bearing for palm-sized turbomachinery. Master's Thesis, Florida State University
5. Shalash K, Schiffmann J (2017) On the manufacturing of compliant foil bearings. *J Manuf Process* 25:357–368
6. Shalash K, Schiffmann J (2017) Comparative evaluation of foil bearings with different compliant structures for improved manufacturability. In: Proceedings of the ASME turbo expo 2017: turbomachinery technical conference and exposition, vol 7A. Structures and Dynamics, Charlotte, North Carolina, USA, 26–30 June 2017
7. Zhou Y, Shao L, Zhanz C, Ji F, Liu J, Li G, Ding S, Zhang Q, Farong D (2020) *Chin J Aeronaut* 34(2):585–600
8. Kumar BS, Debabrata M, Kumar SR (2019) Finite element analysis of bump forming process on thin phosphorus bronze foils used in complaint gas foil bearings. In: International conference on recent advances in materials & manufacturing technologies (IMMT 2019). Dubai, UAE, 20–22 November 2019
9. Mohapatra D (2019) Forming simulation of bump foils used in complaint gas foil bearings. B. Tech Thesis, National Institute of Technology Rourkela

Friction Stir Welding of Heat-Treated Inconel 718 Alloy, and Its Mechanical and Microstructural Analysis



Sanjay Raj and Pankaj Biswas

Abstract In this paper, the mechanical and microstructural properties of the welded joints of heat-treated Inconel 718 alloy were investigated. For this purpose, the friction stir welding (FSW) technique was used with the WC-10%Co FSW tool at a rotational speed of 450 rpm and welding speed of 70 mm/min. Before the welding, heat treatment of the Inconel 718 plate was performed at temperature 1030 °C followed by water quenching and precipitation hardening for 18 h. As a result, good friction stir weld with significant refined grain 13–20 μm in the stir zone (SZ) was found due to dynamic recrystallization. The SEM and TEM investigation revealed secondary phases in the SZ due to precipitation of the niobium (Nb) rich phases during the joining. The EDS analysis of the SZ of the high strength welded sample reveals tungsten (W) and Cobalt (Co) elements in the welded region. The presence of carbide particles and precipitates formation led to the enhancement of mechanical properties of the weld region. The microhardness of the weld zone increased by 21%, whereas the tensile strength of the welded sample found 77% of the base material.

Keywords Inconel 718 · FSW · Heat treatment · TEM analysis · FESEM-EDS analysis · Mechanical and microstructure analysis

1 Introduction

The friction stir welding (FSW) technique was developed by “The Welding Institute” in 1991 mainly for low strength materials, such as aluminum and its alloy [1]. It is an advanced solid-state joining process, where frictional heat is generated below the melting heat of the materials. The principle behind the joining of materials is using the thermo-mechanical effect produced by the friction of the FSW tool [2].

S. Raj (✉) · P. Biswas
Department of Mechanical Engineering, Indian Institute of Technology Guwahati, Guwahati,
Assam 781039, India

P. Biswas
e-mail: pankaj.biswas@iitg.ac.in

Compared with the fusion welding technique, the friction stir welding technique is highly significant in minimum heat input, low energy consumption, and less welding time. After developing high strength and high wear resistive tool material at an elevated temperature, some researchers have used the friction stir welding process to join high melting point materials such as nickel and titanium alloy [3]. Ni-alloy remains the main material for industrial applications in high-temperature work fields such as nuclear power plants, aerospace industries, cryogenic tankage industries, and industrial turbine engines [4]. In the field of Ni-alloy, Inconel 718 has excellent properties in strength, toughness, and thermal fatigue up to 700 °C in the working field.

Joining Inconel alloy with conventional fusion welding techniques such as laser beam and tungsten inert gas welding produces difficulties like solidification cracking, forming a brittle compound with Nb element, and thermal defects in the heat-affected zone (HAZ) [5, 6]. Therefore, the alternative to the fusion welding of Inconel 718 is the low heat input joining process known as the FSW process used in this work. Joining Ni-based alloys by FSW process has limited literature that focused on process parameters. Ahmed et al. [4] and Song et al. [7] successfully joined Inconel 718 sheets by the FSW process. They studied the enhancement of mechanical and microstructure properties with grain refinement.

The above literature shows few researchers work on the joining of Ni-alloy with FSW process, and limited study observed on mechanical and microstructure properties with the process parameters, heat treatment, and precipitates formation. Therefore, in this study, the joining of 3 mm thick heat-treated Inconel 718 plates has been performed by FSW. After welding, the mechanical and microstructural properties of the weld joint were investigated.

2 Experimental Procedure

In this present work, cold-rolled Inconel 718 sheets with dimensions 200 mm × 80 mm × 3 mm were used. The heat treatment of the cold-rolled sheets was performed as per the time–temperature schedule shown in Fig. 1. The heat treatment of Inconel 718 was performed in a muffle furnace at temperature 1030 °C followed by water quenching. After solution treatment, precipitation hardening was performed with a heating rate of 10 °C/min at 720 °C for 8 h, followed by furnace cooling (cooling rate 2.5 °C/min) to 620 °C and holdings for 8 h. In the last stage, Inconel 718 plates were furnace cooled (cooling rate 0.55 °C/min) up to room temperature.

After heat treatment, position controlled friction stir welding machine was used for joint formation. The WC-10%Co FSW tool with shoulder diameter 25 mm and pin height 2.6 mm, was used in this experiment, shown in Fig. 2. The used tool pin was taper with dimensions 7: 5 mm (at the shoulder face: free end). Further, a tool tilt angle 2° with tool plunge depth 0.2 mm was taken from vertical to obtain sound welds. The welding was performed with a constant rotational speed of 450 rpm and a 70 mm/min welding speed under 35 kN downward axial force.

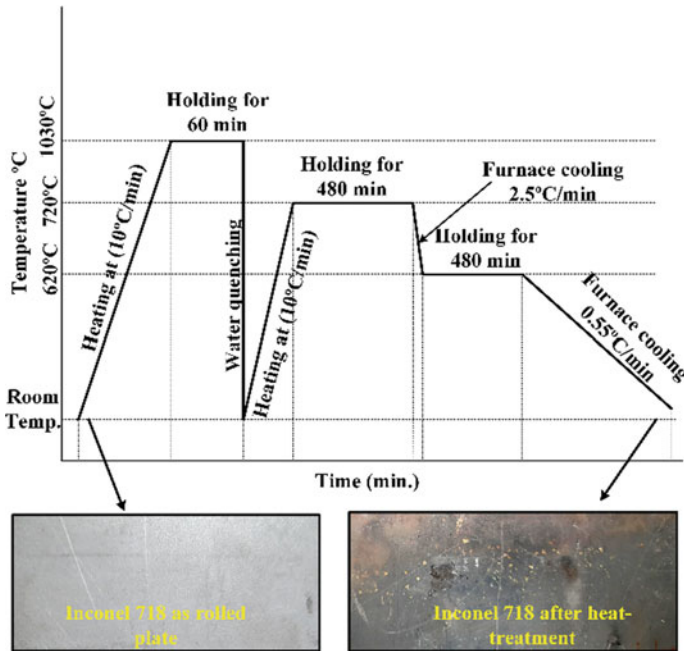


Fig. 1 Heat treatment process diagram of Inconel 718

After the welding, to observe the mechanical and microstructural properties of the welded joint, specimens were cut with the wire-cut EDM. The finely polished samples were etched with Kalling's reagent for 180 s to reveal grains under the microstructure analysis. An optical microscope (OM) was used for macrostructure and microstructure analysis. Scanning electron microscopy (SEM) equipped with electro-dispersive spectroscopy EDS was used to analyze the presence of external elements and carbide particles (i.e., MC-type) in the microstructure of the welded joint. For investigation of precipitates formation and microstructural phases, transmission electron microscopy (TEM) was used (Make: JOEL, Model: 2100F) at 200 kV.

Furthermore, the tensile tests and microhardness tests were conducted to examine the mechanical properties of the joint. The Instron 8801 universal tensile machine (UTM) was used on the sub-sized tensile samples (as per ASTM E8 standard) at a deformation speed of 1 mm/min, in the perpendicular direction of the friction stir weld line. In addition, a Vickers microhardness tester (Make: Omni Tech) with a standard load of 0.5 kgf for a 10 s time interval was used to measure the hardness on the cross-section of the welding zone.

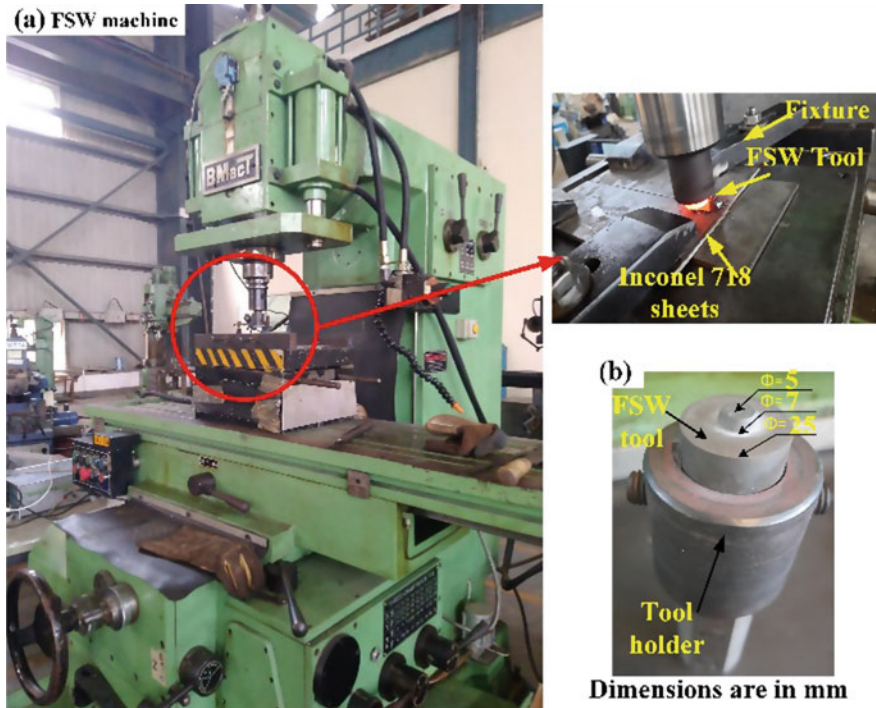


Fig. 2 a FSW machine setup and b FSW tool

3 Results and Discussion

3.1 Macro and Microstructural Characterizations

Figure 3 shows the top view and cross-sectional macrostructure appearance of the FS welded butt joints of heat-treated Inconel 718 sheets. The welding parameters for the joining of heat-treated Inconel 718 were taken at rotational speed 450 rpm and welding speed 70 mm/min after several trials. Figure 3a shows the welded specimen, which was without any surface defect. Figure 3b shows the cross-sectional view of the welded specimen reveals a 2.7 mm depth of penetration from the top surface with a weld cavity in the advancing side (AS). Furthermore, a small region thermo-mechanically affected zone (TMAZ) was observed without a heat-affected zone (HAZ). The band structure in the center of the weld region was also detected, as shown in Fig. 3b. The presence of band structure was similar to the previous study reported by Song et al. [7] in his research. The formation of the band structure in the center of the nugget zone (i.e., stir zone) was observed due to the degradation of the tool during welding.

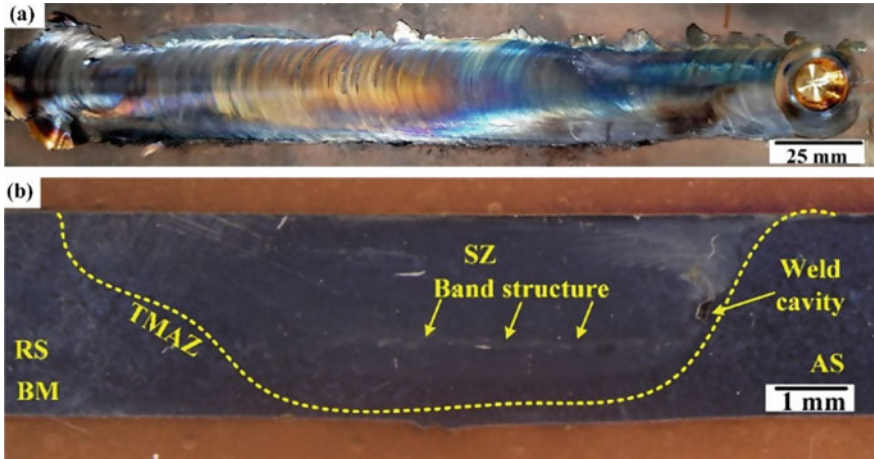


Fig. 3 a Top view appearance of the welded sample and b macrostructure of the weld zone

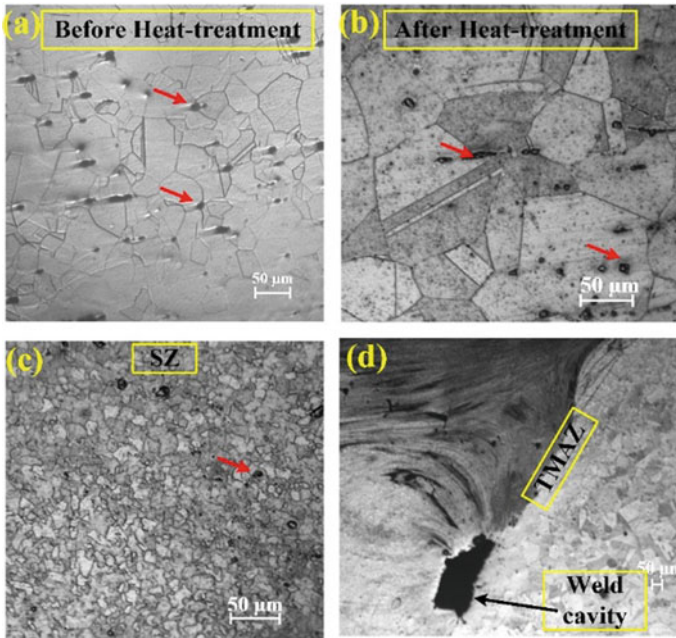


Fig. 4 Microstructure of a base metal before heat treatment, b base material after heat treatment, c SZ of the welded sample, and d TMAZ of the welded sample with weld cavity in the advancing side

Figure 4 shows the variation of grains obtained in the different weld zone. The grain size distribution in different weld zone was measured by the linear intercept method in 'Image J' software. The grain size of the as-received base metal (BM) was in the range of 25–155 μm (Fig. 4a), whereas after heat treatment, the grain size significantly increased in the range of 45–195 μm , as shown in Fig. 4b. Significant growth in the grain size of the BM after heat treatment is also reported in the previous literature [8]. Furthermore, Fig. 4b shows the MC-type carbide (red arrows in the microstructure) and annealing twins distribution in the grains and grain boundaries. The size of the randomly distributed carbide in the heat-treated base material was in the range of 5–10 μm (Fig. 4b). During friction stir welding, the high distortion of the grains in the stir zone was observed due to the dynamic recrystallization and stirring action of the material [9]. The grains in the stir zone (SZ) and TMAZ were found more refined in the range of 13–20 μm and 15–22 μm , respectively, as compared with the coarse grains in the base material (Fig. 4c–d). MC-type carbide particles similar to the base material were observed in a more refined form in the stir zone. In the advancing side (AS), the microstructure of the weld nugget, near the bottom of the TMAZ, weld cavity defects observed, which may be due to insufficient heat input led to lack of intermixing of material [10]. The defect in the weld zone affects the mechanical and microstructural properties of the weld zone.

Figure 5 shows the SEM images and point electro-dispersive spectroscopy (EDS) analysis of the base metal and stir zone. Spectrum point 1 of the base material shows the basic chemical composition. In contrast, spectrum point 3 of the stir zone (SZ) found W and Co external elements in the basic elements of Inconel 718. External elements in the weld nugget were from the FSW tool, which conforms to high tool wear during the FSW process [6]. In the base material, MC carbides such as NbC and (Nb, Cr, Ti)C were observed in the range of 5–10 μm in the grains and their boundaries, which conformed from the spectrum point 4 and 2, respectively. However, MC carbide in the stir zone was more refined, as shown in microstructure with point 4.

Figure 6 shows the TEM image and the diffraction pattern of the weld nugget zone of the FS welded sample. In the stir zone, the presence of δ -phase was observed due to heat treatment of Inconel 718. The intermetallic phases such as Ni_3Nb and M_6C in the stir zone were identified with the diffraction pattern. The previous researcher also reported the improvement of mechanical properties with precipitates [4, 6].

3.2 Mechanical Properties

The mechanical test was performed to examine the weld strength and microhardness of the welded samples. The hardness value in the weld zone was obtained at the middle of the cross-section. A large variation of microhardness was observed across the weld line. Figure 7a shows the hardness variation of the weld sample obtained at welding speed 70 m/min. It was observed that measured hardness values of the stir zone were higher than the base material due to grain refinement. The stir zone was

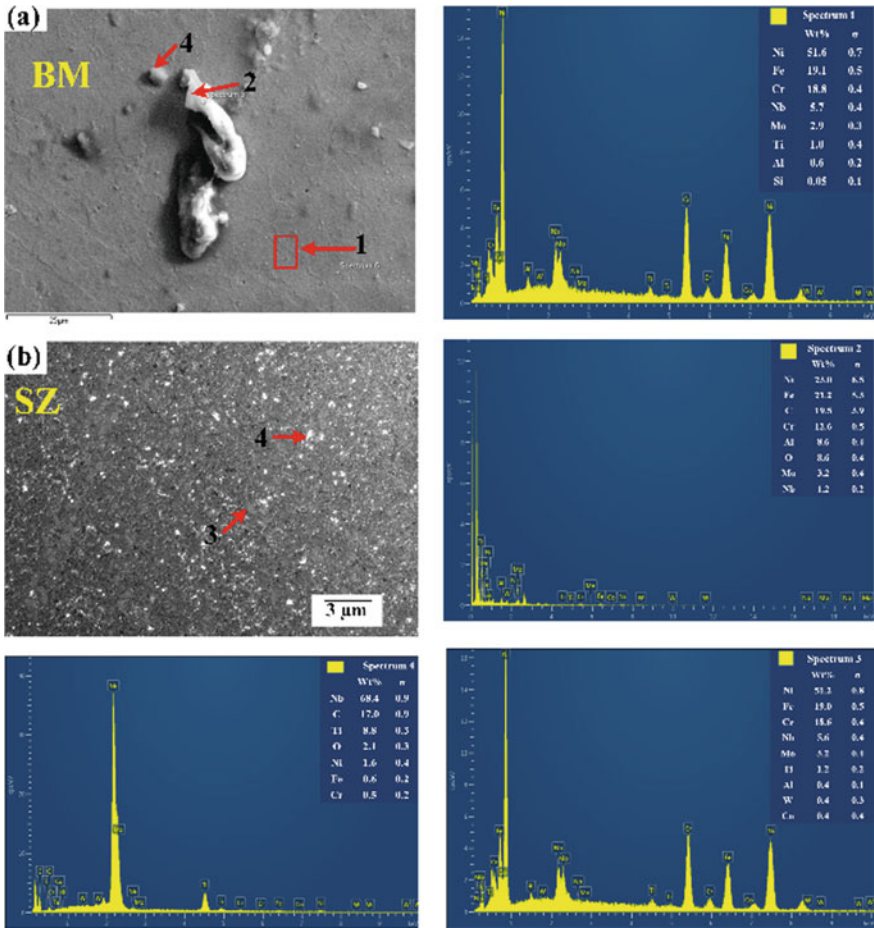


Fig. 5 FE-SEM images and EBSD point spectrum of a BM and b SZ

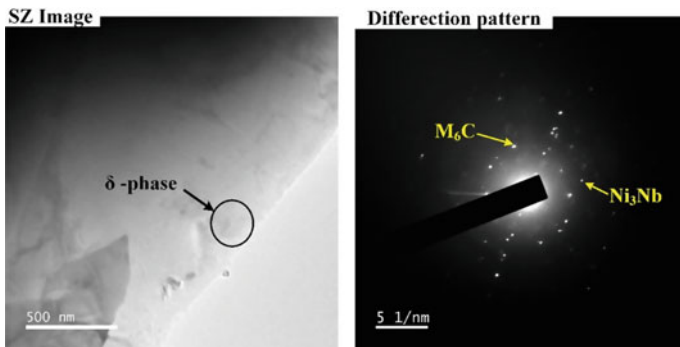


Fig. 6 The TEM image and its diffraction pattern of the SZ

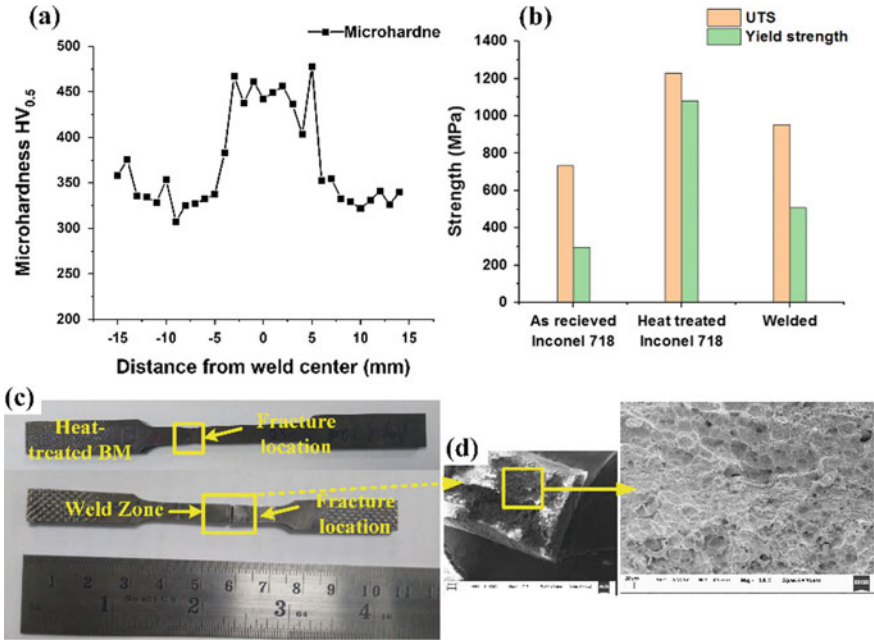


Fig. 7 a Hardness distribution in the weld zone, b weld strength in terms of UTS and yield strength, c tensile sample, and d fractured tensile SEM image

Table 1 Chemical compositions (wt%) of the Inconel 718 and its mechanical properties before and after heat treatment

Chemical composition (wt%)							
Ni	Fe	Cr	Nb	Mo	Ti	Si	Al
51.82	19.1	18.8	5.7	2.96	1	0.05	0.5
Mechanical properties of BM (As-received material)							
UTS (MPa)		σ _y (MPa)		Elongation (%)		Hardness (HV _{0.5})	
735		297		33		215	
Mechanical properties of BM (After heat treatment)							
UTS (MPa)		σ _y (MPa)		Elongation (%)		Hardness (HV _{0.5})	
1230		1080		5		375	

455 HV_{0.5}, whereas it was 375 HV_{0.5} in the base material. An increase of hardness value was observed due to refined grain appearance in the weld nugget zone [10, 11]. It can also observe that the hardness value of base material (375 HV_{0.5}) in case of heat treatment was increased compared to the as-received Inconel 718 material (215 HV_{0.5}). The formation of precipitates and carbide particles in the grain was responsible for incrementing the hardness value in the heat-treated Inconel 718.

Table 1 shows the average measured tensile properties of the base metal before and after heat treatment. The ultimate tensile strength (UTS) and 0.2% yield strength of the as-received material were 735 MPa and 297 MPa, respectively, whereas, in the case of heat-treated Inconel 718, it was 1230 MPa and 1080 MPa. After heat treatment of the base material, the tensile properties significantly increased due to precipitates formation [6]. The UTS and yield strength of the welded samples was 954 MPa and 507 MPa, respectively, which was lower than the heat-treated base material, as shown in Fig. 7b. The location of the fractured tensile samples was inside the weld zone and near the advancing side (AS), as shown in Fig. 7c. The formation of weld defects such as weld cavities was the cause of the decrease of weld strength. The fractured SEM image of the tensile sample reveals a mixed-mode of failure with only 5% elongation. The reduction of elongation in welded tensile specimen confirmed the maximum part was brittle failure occurred, as shown in Fig. 7d.

4 Conclusions

The present study gives the following outcome.

Successful welding of heat-treated Inconel 718 was performed at traverse speed 70 mm/min. As a result of dynamic recrystallization, the microstructure of the SZ was refined with an average grain of 16 μm from a base grain of 120 μm . The grain size of TMAZ on the retreating side was finer than the advancing side because higher heat input in the advancing side led to large grain. Heat treatment of the Inconel 718 resulted in increment of the grain size. In the weld zone, grain refinement and precipitates formation with carbide particle effectively enhanced mechanical properties. The microhardness value of the SZ was significantly increased 21% from the base material (375 $\text{HV}_{0.5}$). The ultimate tensile strength of the welded sample was 77% of the heat-treated Inconel 718 alloy (1230 MPa), whereas the elongation and yield strength of the welded sample was lower than the heat-treated base material. The weld strength reduction was due to the weld cavity and void formation in the advancing side of the weld zone. Furthermore, the presence of intermetallic δ -phase and MC carbides at elevated temperature, mechanical properties enhanced.

Acknowledgements The authors are thankful to the IIT Guwahati (IITG), India, to provide experimental support in this work.

References

1. Mishra RS, Ma ZY (2005) Friction stir welding and processing. *Mater Sci Eng R Rep* 50(1–2):1–78
2. Lemos GVB, Hanke S, Dos Santos JF, Bergmann L, Reguly A, Strohaecker TR (2017) Progress in friction stir welding of Ni alloys. *Sci Technol Weld Joining* 22(8):643–657

3. Tiwari A, Pankaj P, Biswas P, Kore SD, Rao AG (2019) Tool performance evaluation of friction stir welded shipbuilding grade DH36 steel butt joints. *Int J Adv Manuf Technol* 103(5):1989–2005
4. Ahmed MMZ, Wynne BP, Martin JP (2013) Effect of friction stir welding speed on mechanical properties and microstructure of nickel based super alloy Inconel 718. *Sci Technol Weld Joining* 18(8):680–687
5. Gordine J (1971) Some problems in welding Inconel 718. *WELD J* 50(11):480
6. Song KH, Kim WY, Nakata K (2012) Evaluation of microstructures and mechanical properties of friction stir welded lap joints of Inconel 600/SS 400. *Mater Des* 35:126–132
7. Song KH, Nakata K (2010) Microstructural and mechanical properties of friction-stir-welded and post-heat-treated Inconel 718 alloy. *J Alloy Compd* 505(1):144–150
8. Prasad KS, Panda SK, Kar SK, Murty SN, Sharma SC (2018) Effect of solution treatment on deep drawability of IN718 sheets: experimental analysis and metallurgical characterization. *Mater Sci Eng A* 727:97–112
9. Mahto RP, Kumar R, Pal SK, Panda SK (2018) A comprehensive study on force, temperature, mechanical properties and micro-structural characterizations in friction stir lap welding of dissimilar materials (AA6061-T6 & AISI304). *J Manuf Process* 31:624–639
10. Pankaj P, Tiwari A, Biswas P, Rao AG, Pal S (2020) Experimental studies on controlling of process parameters in dissimilar friction stir welding of DH36 shipbuilding steel–AISI 1008 steel. *Weld World* 64(6):963–986
11. Tiwari A, Singh P, Pankaj P, Biswas P, Kore SD, Pal S (2019) Effect of tool offset and rotational speed in dissimilar friction stir welding of AISI 304 stainless steel and mild steel. *J Mater Eng Perform* 28(10):6365–6379

Heat Transfer Model of Coil in a Bell Annealing Furnace



Deepoo Kumar, Nurni N. Viswanathan, and Partha Sarathi Sarkar

Abstract Batch annealing furnace is used for stress relieving and recrystallization of cold rolled coils. Six to eight coils are stacked and heat treated under inert atmosphere for about 50–60 h. The optimization of such a furnace is desired for both quality and productivity purposes. Several researchers have worked on this problem to develop models based on heat transfer, microstructure evolution, and/or data analysis. In this work, a simplified heat transfer model is developed incorporating continuous measurement of hydrogen gas temperature. The model is validated with exhaustive temperature measurement campaigns. The validated model is being used to optimize batch annealing furnace operation. This model has been useful in reducing both energy consumption and rejection rate at the plant.

Keywords Batch annealing · Optimization · Heat transfer · Soaking time · Model validation · Coil geometry · Mechanical properties

1 Introduction

Cold rolled coils need to be annealed before further processing for final use. The annealing can be achieved as a batch or a continuous process. In batch annealing, coils are stacked and annealed under inert atmosphere (N_2 or H_2). The rolled coils are typically 0.5–4.0 mm thick and weigh 4.5–5.5 MT. In a batch, typically 6–8 coils are stacked over one another, with convector plates placed between two coils. Poor radial thermal conductivity, due to entrapped air between rolled sheets, and large thermal

D. Kumar · N. N. Viswanathan

Metallurgical Engineering and Materials Science, Indian Institute of Technology Bombay,
Mumbai, India

e-mail: deepook@iitb.ac.in

N. N. Viswanathan

e-mail: vichu@iitb.ac.in

P. S. Sarkar (✉)

Theis Precision Steel India Pvt. Ltd, Navsari, Gujarat, India

e-mail: p.sarkar@theis.in

mass of these coils require very long heating cycle, 50–60 h to make sure that entire stack receives minimum required soaking time at the required soaking temperature. Thermal gradients within the coil exist due to conduction resistance mainly in the radial direction. The optimization of such a heat treatment process is of interest due to two reasons: (1) due to large difference in soaking time and temperature in the stack, final microstructure could be different that may lead to spatial variation in mechanical properties, and (2) optimized cycle time can help in reducing energy consumption of the furnace.

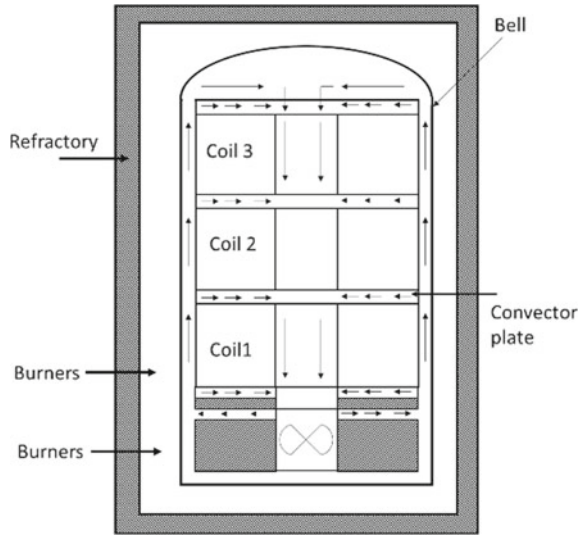
Significant research has been carried out to optimize the heat treatment process in such furnaces. In particular, researchers have considered one of these three approaches: (1) modeling of heat transport in the furnace, stack, and within coil [1–4], (2) heat transfer model coupled with recrystallization models [5, 6] and (3) data driven models such as those based on artificial neural networks [7–10]. One of the early works in this area was done by Jaluria [1]. He reported the development of a comprehensive mathematical model for heat transfer in a batch annealing furnace considering heat transport through various parts of a bell annealing furnace: through wall, flue gas, cover, convector plate, and within the coil. Finally, all heat transport equations were coupled to calculate spatial and temporal variation in the temperature in the stack of coils.

In this work, the aim is to develop a similar heat transfer model but the focus is to use available plant data to simplify the model in order to reduce the number of unknowns and make it more user friendly for the plant. For the batch annealing operation at Theis Precision India Pvt. Ltd., the PNG gas burners are controlled by measuring hydrogen temperature at the base of the furnace. Therefore, a heat transfer model is developed considering hydrogen temperature as input. The model is validated by measuring temperature within the coil present at three locations of the stack: bottom, mid and top. Temperature was also measured within the coil at three locations: outside, mid, and inside. The validated model is being used to optimize the process for different grades.

2 Process Description

Schematic of a typical bell annealing furnace is shown in Fig. 1. Rolled and coiled sheets are clamped and stacked as shown in the schematic. In this schematic, only three coils are shown stacked but there could be more coils during the actual annealing process. The stacked coils are then covered with a stainless-steel hood known as the bell of the furnace. Inside of the bell is first purged with nitrogen to flush out air. Heating hood is placed over this coil-bell arrangement. The bell containing stacked coil is heated due to burners installed at two levels as shown in the schematic. Heat transfer from the burner to coil occurs in three steps: (1) external convection and radiation heat transfer from flue gas/refractory wall to the external surface of the bell, (2) conduction heat transfer from external to internal surface of the bell, (3) convection heat transfer from inner surface of the bell to the inert gas ($N_2 + H_2$) and

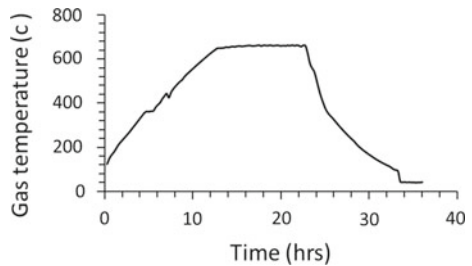
Fig. 1 Schematic of a bell annealing furnace



(4) convection heat transfer from the inert gas to the coil and radiation heat transfer from the inner surface of the bell to the outer surface of the coil. It should be noted that the convection heat transfer from inner surface of the bell to the coil through inert gas is further improved by installing convecter plates in between two coils (see Fig. 1). The inert gas is recirculated during the process with the help of a fan installed at the bottom.

A typical heating cycle is shown in Fig. 2 in terms of the inert gas temperature. It should be noted that the burners operate in the pulse mode to maintain the set inert gas temperature. The gas is typically heated to soaking temperature of 620–700 °C depending on the product properties requirement. The furnace is maintained at soaking temperature for desired period, typically 15–30 h. After soaking the coil is cooled in three steps: (1) furnace cooling, (2) air cooling (with heating hood removed) and (3) rapid cooling. Rapid cooling is achieved by recirculating inert gas through a heat exchanger. The bell is removed when gas temperature is under 100 °C. The coils are expected to follow the inert gas temperature with a time lag during both

Fig. 2 Heating and cooling profile for inert gas



heating and cooling cycles. However, the soaking period is expected to vary within a coil as well as along vertical position of the coil. The modeling aspect is discussed in the next section.

3 Model Setup

Since hydrogen temperature is continuously measured and maintained during actual operation, it was provided as an input to the model. Temperature variation within a coil was calculated by numerically solving a one-dimension transient conduction equation as shown in Eq. (1).

$$\frac{\partial T}{\partial t} = \frac{1}{r} \left(\frac{\partial}{\partial r} \left(r k_{\text{eq}} \frac{\partial T}{\partial r} \right) \right) \quad (1)$$

where T is the temperature of the coil which varies with time and radial position.

Equivalent thermal conductivity of the coil was calculated considering thermal conductivity of the rolled strip and interfacial resistance to conduction using a method suggested by Park et al. [11], see Eq. (2). The equivalent thermal conductivity does vary with radial position due to temperature gradient in the radial direction at any time.

$$k_{\text{eq}} = \frac{t}{\left\{ \frac{t_s}{k_s} + \left[\frac{1.13k_s \tan \theta}{\sigma_p} A^{0.94} + \frac{(1-A)k_a}{t_a} + 4(1-A)\epsilon ST^3 \right]^{-1} \right\}} \quad (2)$$

where t is the total thickness (steel sheet + air gap), t_s is the thickness of an individual steel sheet, k_s is the thermal conductivity of the steel, $\tan \theta$ is the mean of the absolute slope of the profile, σ_p is the standard deviation of the surface profile height, A accounts for the fractional contact area at the interface, k_a is the thermal conductivity of air in the gap and t_a is the thickness of the air gap, ϵ is the emissivity of the steel sheet, S is the Stephan-Boltzmann constant and T is the local temperature in °kelvin.

Thermal conductivity of the steel was varied with the temperature: $k_s = 54.4 - 0.0033 \times T$ (in °C). It should be noted that (2) does not consider the thickness of oxide layer as suggested by Park et al. [11]. Since the coil is being heated under H_2 atmosphere, oxidation of steel sheet is not expected. Table 1 provides the values of relevant variables in Eq. (2). It should be noted that the value of A depends on the hardness of steel and compressive stress applied due to clamping. Hence, it is expected to vary with the steel grade and operating practice with respect to coiling.

Table 1 Data used to calculate effective thermal conductivity

$\tan \theta$	σ_p (μm)	A	t_a (μm)	ϵ
0.08554	3.22	0.98	20.2	0.2

The emissivity is considered to be lower due to absence of any oxide layer under the reducing operating condition.

Heat transfer from hydrogen gas to the coil was modeled by considering convective boundary conditions at the inner and outer surfaces of the coil. Due to difficulty in measuring the velocity of inert gas close to the coils, convection heat transfer coefficient was estimated from measured temperature data, see next section. However, the effect of coil thickness was considered by assuming inverse of square root dependence of the convection heat transfer coefficient on the size of the coil ($Nu \propto Re^{0.5}$, where Nu and Re are Nusselt numbers and Reynolds number).

Equation 1 was discretized taking $\Delta r = 10$ mm and $\Delta t = 60$ s. Temperature profile in the radial direction was numerically calculated for each time step for each coil considering temperature of inert gas, coil and strip dimensions, and appropriate thermal properties. The model was implemented using C programming language. A user has to provide following information for a fixed grade and operating conditions:

- (1) Number of coils
- (2) Specification of each coil: weight, strip thickness, strip width, inner and outer diameter of the coil
- (3) Heating cycle: heating rate, soaking temperature, and soaking time
- (4) Cooling cycle: time and temperature corresponding to furnace cooling, air cooling, and rapid air cooling.

Output of the model is temperature at inner, intermediate, and outer surface of each coil with respect to time.

4 Industrial Trials

Temperature gradient along the radial direction is expected to cause different heat treatments to steel sheets within each coil, which may lead to variation in their microstructures and hence mechanical properties. In order to directly assess this variation, temperature was measured at three locations (inner, core/intermediate, and outer) in the coil as shown in Fig. 3. The coils were stacked and flexible K-type thermocouples were attached at three locations in three coils: bottom coil, middle coil, and top coil (see Fig. 4). For example: in a stack of eight coils, thermocouples were attached in 1st (bottom), 4th (middle), and 8th (top) coils. Thermocouples were identified according to vertical position of the coil and radial position of the thermocouples. For example, BO thermocouple was present at the outer point of the bottom (1st) coil. Hydrogen gas temperature was measured at the bottom using a fixed thermocouple. It should be noted that under normal operating conditions, only gas temperature is measured that acts as feedback to burner operation. Temperatures were noted every 15 min during these trials.

Typical results of such a thermal mapping exercise are shown in Fig. 5. In this figure, data from thermocouples only at the core of top, middle, and bottom coils are shown for better clarity. In the inset, the temperature variation from top to bottom

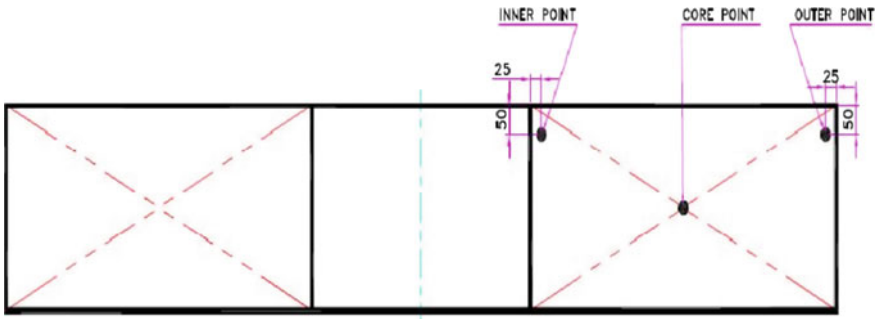
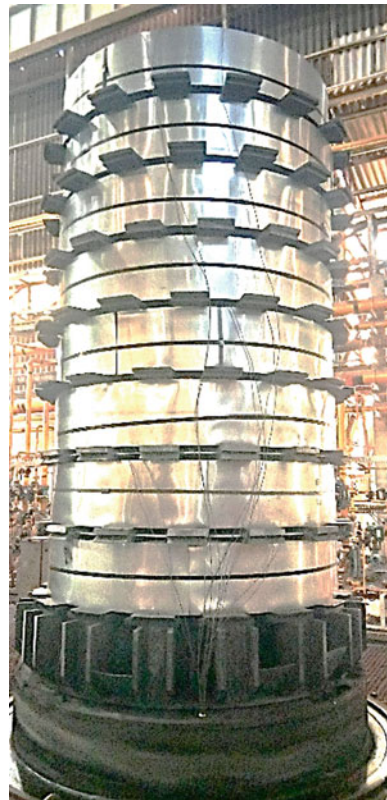


Fig. 3 Thermocouple location in each coil

Fig. 4 A typical stack of coil with flexible thermocouple attached to coils at different locations



coil is shown; the difference varies from 15 to 30 °C. In total, eight such trials were conducted for different grades and different coil arrangements.

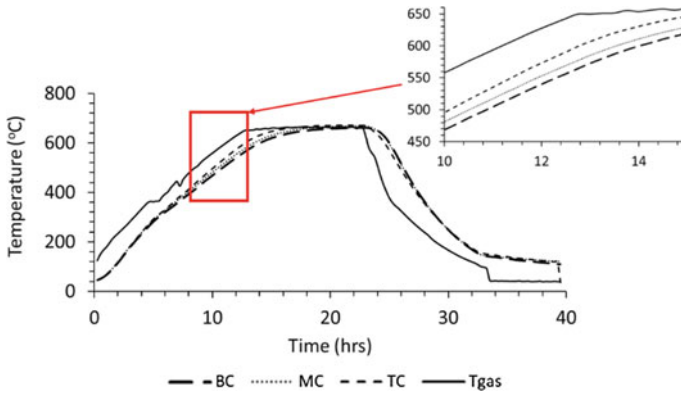


Fig. 5 Typical results from thermal mapping trials showing temperature variation at the center of bottom (BC), middle (MC), and top (TC) coils

5 Model Validation

Data from several trials were used to validate the model and estimate convection heat transfer coefficient. Model results for one batch annealing process will be discussed here. Coil geometry and its position are described in Table 2. Coil 1 was at the bottom and coil 8 was at the top of the stack. Last column of the table shows whether thermocouples were attached or not in the coil. It should be noted that the thermocouples were attached at three positions within each coil as shown in Fig. 3.

Figure 6 summarizes the model validation using one example batch annealing process as described in Table 2. Figure 6a shows the target temperature profile; the dashed line shows measured hydrogen temperature using bottom thermocouples. This was used to provide input hydrogen temperature to the model. Heating cycle was considered as a combination of linear temperature profiles but the cooling cycle was modeled as combination of linear and exponential temperature profiles.

Table 2 Coil details in the stack; the inner diameter of all coils was 508 mm and strip thickness was 0.7 mm

Coil #	Weight (kg)	Strip width (mm)	Coil, O.D. (mm)	Thermocouple attached
1	5330	328	1701	Yes
2	5340	329	1700	Yes
3	5300	328	1603	No
4	5300	329	1601	Yes
5	5280	328	1600	No
6	5260	328	1599	No
7	5260	328	1597	No
8	5220	329	1590	Yes

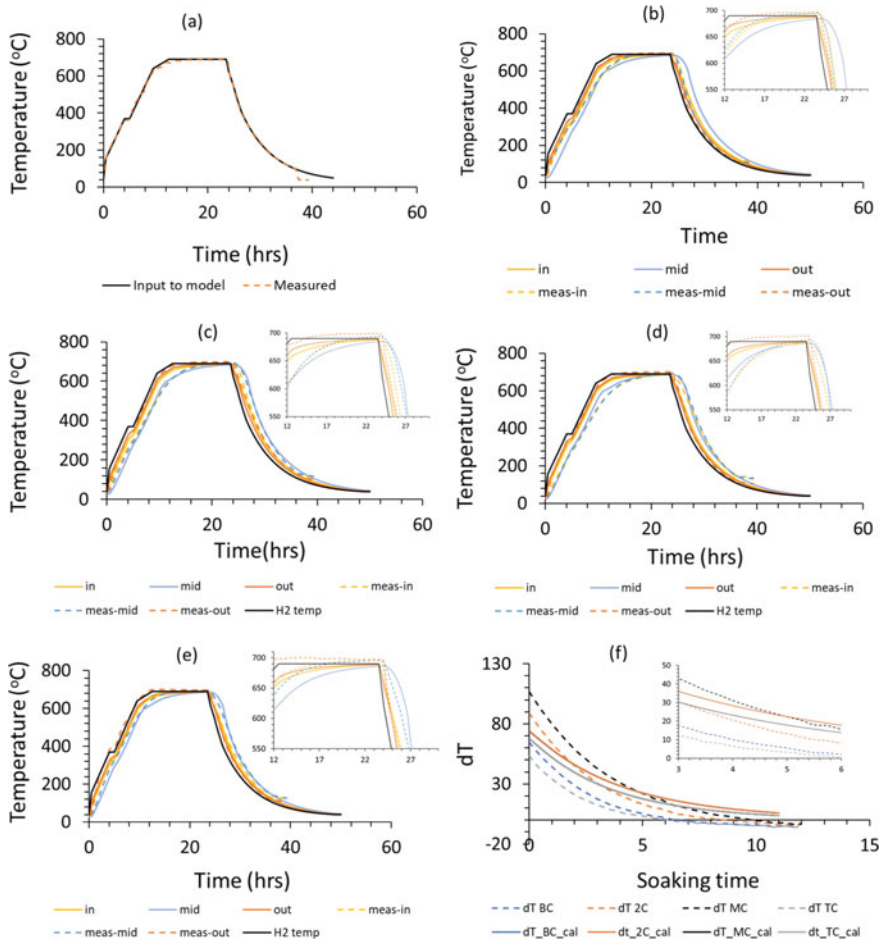


Fig. 6 Model validation: **a** Input hydrogen temperature based on target heat treatment cycle, **b–e** comparison of measured and calculated temperature of bottom, 2nd, middle, and top coils, and **f** difference between target temperature and coil center temperature during soaking period

Figure 6b-e show the comparison between measured and calculated temperature at inside, core and outside location of bottom (1st), 2nd, mid (4th), and top coils. In these graphs, solid lines represent calculated results, and dashed lines represent measured temperature. General agreement between the model and trend can be seen from these results. Temperature difference in soaking time is very important from mechanical properties point of view. This difference is highlighted by showing calculated and measured temperature in the inset of each graph; solid black line is the input hydrogen temperature as shown in Fig. 6a. Calculated temperature is within ± 20 °C of measured temperature at the early times of the soaking period; the difference further diminishes as expected. The core temperature is expected to be lower due

to conduction thermal resistance between hot gas and core of the coil. This effect is nicely captured in both measured and calculated temperature profiles during the soaking period. Measured temperature at the core for four coils shows that the core temperature of the top coil was closest to the target temperature at the beginning of the soaking period. In addition to conduction thermal resistance, change in hydrogen temperature along the z -direction (moving up on the outer surface and moving down on the inner surface of the coil), is also expected to affect the core temperature of the coil. In the present model, the variation in hydrogen temperature in the z -direction is not considered, hence the model can only capture the variation due to thermal resistance. Calculated core temperature for bottom (1st) coil and second coil at the beginning of the soaking period is approximately 610 °C and that of mid (4th) and top (8th) coil is 615 °C. This is likely due to different thicknesses of these coils. As shown in Table 2, O.D. of coils 1 and 2 are close to 1700 mm and that of coil 4 and 8 are close to 1600 mm. This effect is clearly shown in the plot of deviation from target soaking temperature at the core of these coils during the soaking period, see Fig. 6f. The calculated results show only two lines as there are coils having either ~ 1600 mm O.D. or ~ 1700 mm O.D. Hence, the model may be further improved by incorporating variation in hydrogen temperature along vertical direction.

6 Practical Implications

Coil annealing model developed in this work is being used to optimize the annealing process at the plant. It is desirable to know actual soaking time at different locations within each coil. Over-soaking or under-soaking in terms of temperature and time can lead to undesirable mechanical properties that may lead to rejection. Here, we demonstrate the use of model with an example of coil annealing of C40E grade as per DIN EN 10132–3.

Eight coils were stacked for sub-critical annealing. Bottom coil (coil 1) is expected to have the cold spot from dimensional viewpoint. As per plant's operating procedure, 24–34 h of soaking time is needed at an annealing temperature between 690 and 700 °C in order to achieve desired mechanical properties as specified in Table 4. A trial was conducted for a stack of eight coils; coil geometry is described in Table 3.

Coil annealing model was used to predict soaking time with respect to coil position and at three (inside, mid, and outside) positions for each coil. As mentioned earlier, hydrogen temperature with time was provided input to the model. Soaking period, as per hydrogen temperature, was kept at 34 h (at a temperature in the range of 690–700 °C). Local soaking temperature, as calculated from the model, is shown in Fig. 7. As expected, the center of the coil goes through the shortest soaking period, and outside of the coil goes through the longest soaking period. Median soaking temperature for these 24 locations is considered as the soaking period of the stack. In this case, median soaking time was found to be equal to 29.5 h. As shown in Table 4, this soaking period was enough to achieve desired mechanical properties at all locations of the coil. As shown through this example, the model can be used to

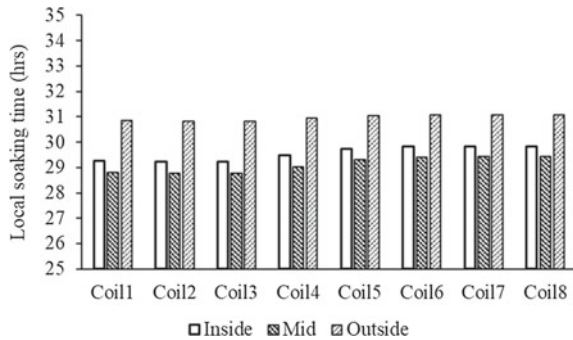
Table 3 Coil geometry used for optimization trial; strip thickness = 1.5 mm and coil I.D. = 508 mm for all coils

Coil No.	Width (mm)	Weight (Kg)	OD (mm)
Coil 1	360	5570	1671.67
Coil 2	330	5090	1669.32
Coil 3	360	5550	1668.95
Coil 4	330	5060	1664.85
Coil 5	310	4790	1641.05
Coil 6	360	5220	1623.30
Coil 7	360	5200	1620.50
Coil 8	330	4760	1619.47

Table 4 Desired and measured mechanical properties

Parameters	Unit	Desired values	Measured values
Hardness	HV	150 max	138–146
Yield Strength	Mpa	440 max	271.63–334.17
Tensile Strength	Mpa	550 max	437.32–493.80
Elongation @80 mm GL	%	22 min	26.09–32.60

Fig. 7 Local soaking time in the stack



find local soaking time. The combination of mechanical properties measurement and model calculation can be used to design and optimize heat treatment cycles for coil annealing. In last year, through the spheroidization annealing process optimization by using this heat transfer model there was a reduction in rejection due to poor mechanical properties by 62.51%.

7 Conclusions

A heat transfer-based model was developed to predict temperature variation within cold rolled coil during batch annealing furnace operation. The model was validated using temperature measured within bottom, mid, and top coils in the stack. The agreement between measured and calculated temperature was within ± 20 °C. The agreement can be further improved by considering variation in hydrogen temperature along axial direction. The validated model is being used to optimize the batch annealing furnace operation at the plant for different grades. The model implementation is being further supported by measuring mechanical properties of the samples taken from the coil at different locations in the stack. Such a model is found to be helpful in reducing both the energy demand of the plant and the rejections.

References:

1. Jaluria Y (1988) Numerical simulation of the transport processes in a heat treatment furnace. *Int J Numer Methods Eng* 25(2):387–399. <https://doi.org/10.1002/nme.1620250209>
2. Fang CJ, Wu LW (2015) Batch annealing model for cold rolled coils and its application. *China Steel Tech Rep* 28:13–20
3. Saboonchi A, Hassanpour S, Abbasi S (2008) New heating schedule in hydrogen annealing furnace based on process simulation for less energy consumption. *Energy Convers Manage* 49(11):3211–3216. <https://doi.org/10.1016/j.enconman.2008.05.024>
4. Sahay SS, Kumar AM (2002) Applications of integrated batch annealing furnace simulator. *Mater Manuf Process* 17(4):439–453. <https://doi.org/10.1081/AMP-120014227>
5. Sahay SS, Krishnan K, Kulthe M, Chodha A, Bhattacharya B, Das AK (2006) Model based optimisation of highly automated industrial batch annealing operation. *Ironmak Steelmak* 33(4):306–314. <https://doi.org/10.1179/174328106X94799>
6. Sahay SS, Kumar AM, Chatterjee A (2004) Development of integrated model for batch annealing of cold rolled steels. *Ironmak Steelmak* 31(2):144–152. <https://doi.org/10.1179/030192304225010990>
7. Liu QL, Wang W, Zhan HR, Wang ZG, Liu RG (2005) Optimal scheduling method for a bell-type batch annealing shop and its application. *Control Eng Pract* 13(10):1315–1325. <https://doi.org/10.1016/j.conengprac.2004.11.017>
8. Mehta R, Sahay SS, Datta A, Chodha A (2008) Neural network models for industrial batch annealing operation. *Mater Manuf Process* 23(2):204–209. <https://doi.org/10.1080/10426910701774759>
9. Pal D, Datta A, Sahay SS (2006) An efficient model for batch annealing using a neural network. *Mater Manuf Process* 21(5):567–572. <https://doi.org/10.1080/10426910600599356>
10. Singh RKr, Sudharshan R, Mehta PKr, Chandrawanshi M, Mishra D (2018) Optimization of annealing stack using design of experiment method in batch annealed HSLA steel. *Mater Today Proc* 5(2):7055–7060. <https://doi.org/10.1016/j.matpr.2017.11.369>
11. Park SJ, Hong BH, Baik SC, Oh KH (1998) Finite element analysis of hot rolled coil cooling. *ISIJ Int* 38(11):1262–1269. <https://doi.org/10.2355/isijinternational.38.1262>

Hybridized Nanotubes and Graphene Oxide in CFRP Development for Space Use



J. D. Solanki, D. A. Vartak, Y. S. Ghotekar, N. A. Deshpande, N. Kumar,
B. Satyanarayana, A. K. Lal, and P. M. Bhatt

Abstract Multi-walled Carbon Nanotubes (MWCNT) and Graphene Oxide (GO) are potential nano materials for fabrication of conductive Carbon Fiber Reinforced Polymers (CFRP). The conductive CFRP in terms of electrical and thermal properties is well suited for space components to replace conventional materials like Invar, Kovar and Aluminum alloy. This paper discusses the fabrication of CFRP samples for developing space grade components using hybridization of MWCNT and rGO. Different concentration of MWCNT and rGO enhances electrical and thermal conductivity. Moreover, the characterization of the CFRP samples with this hybrid

J. D. Solanki (✉)

L. D. College of Engineering, Ahmedabad, India

D. A. Vartak · B. Satyanarayana
QAMD, SAC-ISRO, Ahmedabad, India
e-mail: dhaval@sac.isro.gov.in

B. Satyanarayana
e-mail: bsatyanarayana@sac.isro.gov.in

Y. S. Ghotekar
PMQD-M, SAC-ISRO, Ahmedabad, India
e-mail: yogeshghotekar@sac.isro.gov.in

N. A. Deshpande
TED, SAC-ISRO, Ahmedabad, India
e-mail: nandinigodhe@sac.isro.gov.in

N. Kumar
CDFG, SAC-ISRO, Ahmedabad, India
e-mail: nitinsharma@sac.isro.gov.in

A. K. Lal
SRA, SAC-ISRO, Ahmedabad, India
e-mail: aklal@sac.isro.gov.in

P. M. Bhatt
Silver Oak University, Ahmedabad, India

nano fillers are carried out in terms of thermal expansion and shielding effectiveness. This paper presents best suitable concentration for fulfilling the set of criteria required for enhancing the electrical and thermal properties for use in RF system.

Keywords Multi-walled carbon nanotubes · Graphene oxide · CFRP · Electrical conductivity · Thermal conductivity · Thermal expansion · Shielding effectiveness

1 Introduction

Carbon nano fillers such as Single-walled Carbon Nanotube (SWCNT), Multi-walled Carbon Nanotube (MWCNT), Graphene Oxide (GO) and their combinations are promising materials for improving electrical conductivity and the thermal conductivity [1, 2]. Enhancement in the electrical as well as the thermal properties of composite will enable the material to replace the existing high density metals for space. Electrical conductivity of the composite allows electroplating of high conductivity metals on the CFRP laminates which benefits for the Radio Frequency (RF) applications. Electrical conductivity is an important factor for electrical performance compliance and electromagnetic shielding for payload components. Different CNT concentration embedment in CFRP demonstrates varying electrical conductivity. Similarly, thermal conductivity is also a very important parameter to achieve the thermal balance. Thermal conductivity helps to improve heat dissipation, which is generated by payload components. Hybridization of MWCNT and rGO enhances the thermal conductivity due to the formation of C–C covalent bonds. Phonons transport speedily in covalent bonds which is not the case in non-covalent Van der Waals bonds due to the reflection and scattering of phonons. Transportation of phonons are directly proportional to thermal conductivity [3].

Graphene offers large contact area for MWCNT due to its multiple internal layers and it shows active participation in phonon transport with minimum coupling loss. Moreover, concentration of graphene leads to weaken the surface energy of CNT and form the π - π interaction between rGO and side wall of the MWCNT [4, 5]. This results into formation of bridges between rGO and MWCNT. The uniform dispersion of MWCNT/rGO complexes with no precipitation at room temperature indicates good stabilizing quality of GO for MWCNT [6]. However, it is observed that with increase in MWCNT content over rGO in a hybrid system, the thermal conductivity decreases in in-plane direction but it increases in the through-plane direction, whereas electrical conductivity increases. Higher ratio of MWCNT/rGO offers maximum thermal conductivity in through-plane direction, whereas minimum value in in-plane direction with such hybrid system having highest electrical conductivity [7].

The objectives of this paper are to (1) Enhance electrical and thermal conductivity of CFRP by inclusion of different concentration of MWCNT and rGO (2) To explore potential nano fillers to be added to CFRP. This will further explore potential space application like RF reflectors, carrier plates and feed horns. The fabrication of the

samples with different concentrations of MWCNT and rGO followed by thermal and electrical characterization. This data is useful for fabricating the RF components for space use [8].

2 Materials and Fabrication of Composite

- Carbon fabric sheet: Bi-axial, Plain weave, Thickness 0.300 mm, Density 1.7 g/cc
- Multi-walled Carbon Nanotubes (MWCNTs): Purity 99%, Diameter 5–20 nm, length 10 μm
- Reduced Graphene Oxide (rGO): Purity > 99%, No of layers 3–6, Thickness 0.8–2 nm, Length 1–2 μm
- Epoxy: Lapox ARL-135 LV, Density 1.3 g/cc
- Hardener: Lapox AH-422, Density 0.9 g/cc
- Solvent: Acetone Grade AR.

Carbon nano fillers like Multi-walled Carbon Nanotube (MWCNT) and reduced Graphene Oxide (rGO) are used with the different concentration in the epoxy for fabricating the CFRP samples. Solution mixing method is used for fabricating the samples as shown in Fig. 1. Hybrid of MWCNT and rGO are added with respect to epoxy by percentage weight method as shown in Table 1. An appropriate quantity

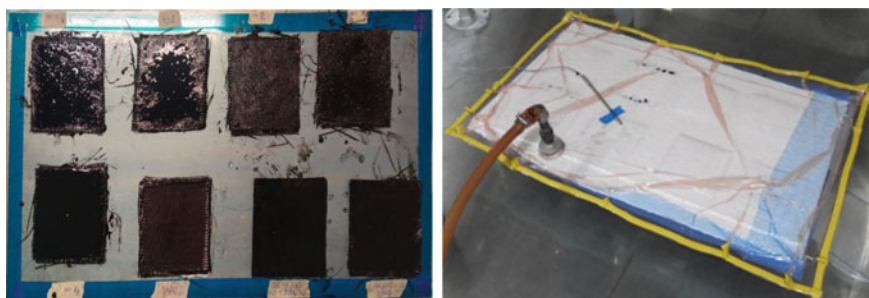


Fig. 1 Fabrication of samples

Table 1 CFRP samples with different concentration

Sr. No.	Nano filler	Composition
1	No filler	Bare CFRP
2	Hybrid MWCNT + rGO	0.75 wt% + 0.75 wt%
3	Hybrid MWCNT + rGO	0.25 wt% + 0.25 wt%
4	Hybrid MWCNT + rGO	0.25 wt% + 0.75 wt%
5	Hybrid MWCNT + rGO	0.75 wt% + 0.25 wt%
6	Hybrid MWCNT + rGO	0.50 wt% + 0.50 wt%

of acetone is used for sonication process. Hardener is added to this nano filler-epoxy solution and the uniform dispersion of the mixture is achieved with the help of magnetic stirrer. Samples are prepared by hand layup technique as shown in Fig. 1 followed by curing at room temperature for two hours. Later, it is post-cured at elevated temperature for six hours in vacuum chamber.

Electrical and thermal properties are evaluated by testing these samples. This characterization is significantly important for the qualification of the material before the use in space payload applications [9]. The results obtained are compared with bare CFRP sample.

3 Electrical Characterization

Carbon nanotubes and rGO have extraordinary electrical properties making it suitable material to improve electrical properties of non-conductive polymer composite. Epoxy has very low electrical conductivity. These filler materials are the additives to improve the electrical conductivity which in turn will enhance the electromagnetic shielding of the composite.

Electrical characterization is carried out by measurement of sheet resistivity as per ASTM D257-07 [10] and measurement of shielding effectiveness as per ASTM D4935-18 [11].

3.1 Resistivity and Shielding Effectiveness

Electrical conductivity and Electromagnetic Interference (EMI) are the important parameters for the materials to be used for RF components in space. PRS-801 Resistance System is used for DC resistivity measurement. The samples with different concentration of MWCNT/rGO including the bare CFRP sample are measured for electrical resistivity in in-plane and through-thickness direction. There is significant reduction in electrical resistivity in both in-plane and through-thickness direction for MWCNT/rGO samples than that of the bare CFRP sample. Surface electrical conductivity decreases with an increase in hybrid filler content and highest value is obtained at lower filler loading with 0.25 wt% MWCNT and 0.25 wt% rGO. It is assumed that with an increase in filler content rGO is unable to create uniform dispersion with MWCNT and tends to saturate the mixture. MWCNT remains in form of close bundle due to its strong Van der Waals interaction among CNTs themselves instead of absorption onto rGO sheet to establish a conductive path. Enhancement of electrical conductivity in through-thickness is significantly noticed with concentration of 0.25 wt% MWCNT and 0.75 wt% rGO as shown in Fig. 2. Moreover, the sample with 0.75 wt% MWCNT and 0.25 wt% rGO showed considerably good electrical conductivity than other samples. These samples with 12–14 Ω measured

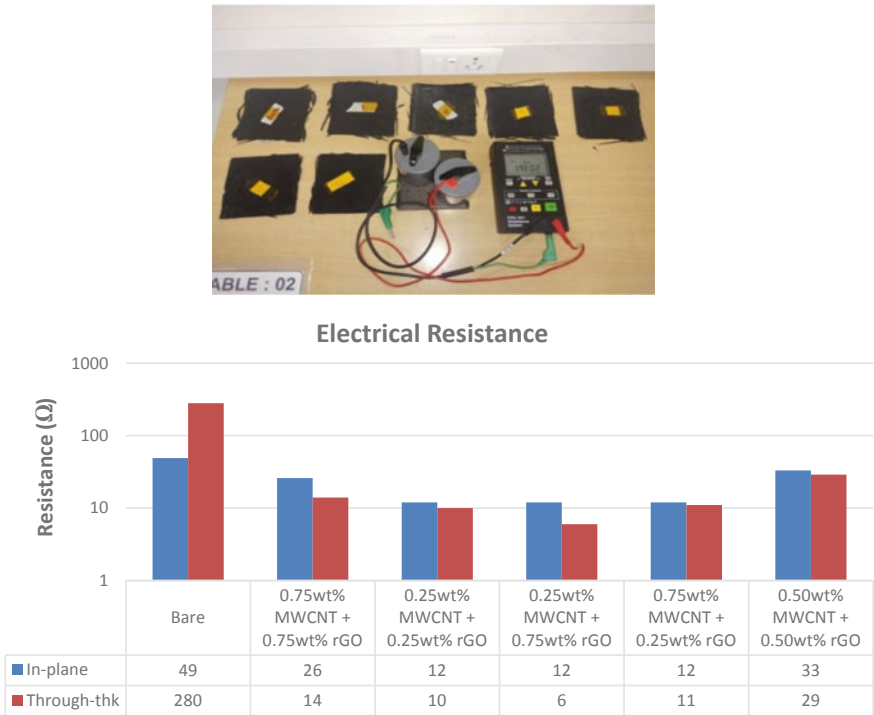


Fig. 2 Measurement of electrical resistivity

resistance can directly electroplate without activating the surface due to increment in electrical conductivity.

It was observed that electrical conductivity will increase with MWCNTs content and its maximum value was achieved, when the MWCNTs nanoparticles dominates the total nano filler content [12]. Apart from electrical conductivity space material must also have better Shielding Effectiveness (SE) to avoid unwanted electromagnetic interface and provide electromagnetic compatibility with sufficient isolation. SE is measured on the samples with different concentrations of rGO and MWCNT, using the waveguide method. The sample with 0.75 wt% MWCNT and 0.25 wt% rGO revealed an improvement in SE in frequency band of 10–27 GHz; measured values are compared to bare CFRP sample and are as shown in Fig. 3.

4 Thermal Characterization

Space payload components are subjected to thermal load during its testing and service life. Poor thermal conductivity can increase the temperature of the components and reduce the rate of heat dissipation. Thermal properties like thermal conductivity can

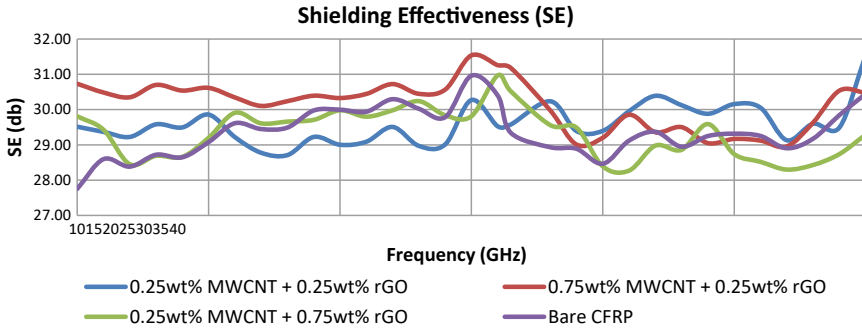
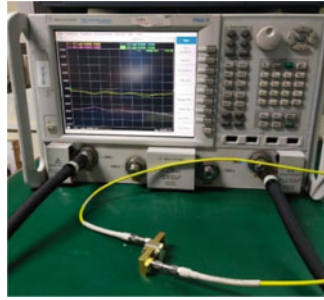


Fig. 3 Measurement of shielding effectiveness

be deduced from thermal diffusivity as per ASTM E1461-13 [13], co-efficient of thermal expansion as per ASTM E228-17 [14] and specific heat capacity as per ASTM E1269-11 [15], the same are measured and characterized.

4.1 Thermal Expansion

The co-efficient of thermal expansion (CTE) is evaluated by measuring the change in length with respect to change in temperature as shown in Fig. 4. CTE of 0.75 wt% MWCNT and 0.25 wt% rGO composite sample indicates negative value ($-0.1454 \text{ ppm}/^\circ\text{C}$) whereas the composite sample with 0.25 wt% MWCNT and 0.75 wt% rGO indicates positive value ($0.2916 \text{ ppm}/^\circ\text{C}$) near to zero as shown in Fig. 4. CTE data on bare CFRP sample is more than $0.783 \text{ ppm}/^\circ\text{C}$ between the temperature range of -100°C to $+150^\circ\text{C}$ [16].

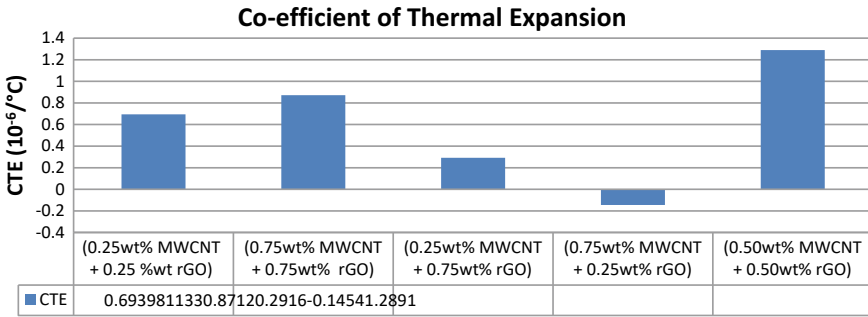


Fig. 4 Measurement of co-efficient of thermal expansion

4.2 Thermal Conductivity

Thermal conductivity of a bare CFRP sample is 0.3 W/mK to 0.5 W/mK over the temperature range of $-100\text{ }^{\circ}\text{C}$ to $+150\text{ }^{\circ}\text{C}$ [16], whereas the sample with 0.75 wt% MWCNT and 0.25 wt% rGO concentration has higher thermal conductivity than other samples as shown in Fig. 5. The ratio of MWCNT/rGO plays significant role in improving through-thickness thermal conductivity and it increases with increase in the ratio of MWCNT/rGO [7]. Thermal conductivity is greatly influenced by rGO content, the sample with lower loading of rGO over MWCNT offers highest thermal conductivity due to decrease in the level of defectiveness (impurities in the form of oxidized carbons and other defects) associated with rGO [17]. The increase in thermal conductivity is due to the formation of 3-dimensional thermal paths formed by the addition of MWCNT. There is a chance of increase in phonon scattering due to the

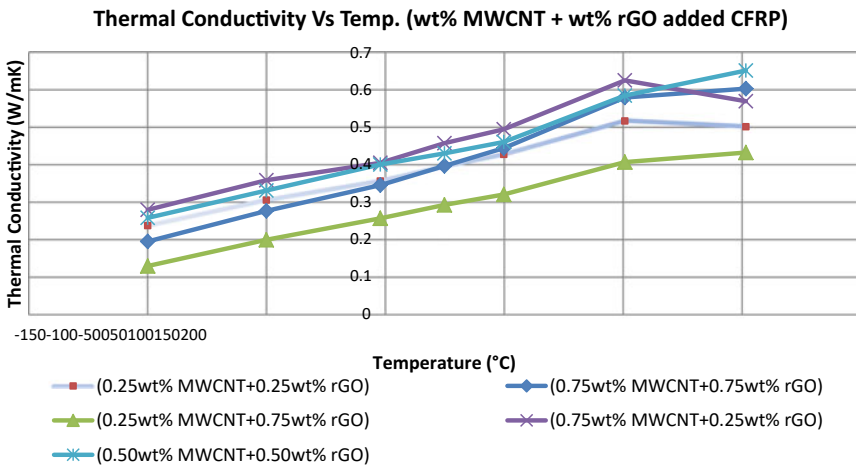


Fig. 5 Measurement of thermal conductivity

highest concentration of MWCNT, which results in decreased thermal conductivity [18].

5 Observation and Conclusion

- There is a significant improvement in the electrical conductivity by addition of hybrid 0.25 wt% MWCNT and 0.75 wt% rGO in through-thickness direction by 54 folds, and with hybrid 0.75 wt% MWCNT and 0.25 wt% rGO in in-plane direction by 4 folds as compared to bare sample. The enhancement of electrical conductivity leads to improved SE values. Hybrid sample with 0.75 wt% MWCNT and 0.25 wt% rGO achieves maximum SE in the range of 10–27 GHz. This offers advantage in RF conductivity, which is essential requirement of payload components and its functionality index. Improvement in electrical conductivity is also beneficial for direct electroplating of the component without surface activation.
- In the hybrid sample with different concentration of MWCNT/rGO, the thermal conductivity increases with increase in the ratio of MWCNT/rGO for hybrid sample with 0.75 wt% MWCNT and 0.25 wt% rGO in the range of 0.28–0.62 W/mK as compared to hybrid sample with 0.25 wt% MWCNT and 0.75wt% rGO having the range of 0.12–0.43 W/mK. The increase in the ratio also offers transition of CTE from positive value (0.2916 ppm/°C) to negative value (–0.1454 ppm/°C), minimizing strain transfer due to thermal load.
- Silver electroplating is carried out on these samples as a surface treatment process, which are tested under space environmental conditions. The peel test is carried out as per ASTM D3359-17 [19], no plating degradation is observed.
- This characterization is useful to evaluate limited space qualification of CFRP with different concentration of MWCNT and rGO for enhanced thermal and electrical characteristics. These results provide the confidence for the composite material with MWCNT and rGO to be evaluated further for space applications. Also this data is essential for the fabrication of low power carrier plates and feed horns for future space projects.

Acknowledgements We are heartily thankful to Shri Sharad Shukla, Head ECPTF, V.M. Shah, Engr MQAD, Shri A.T. Parmar Sr. Technician-PMF of SAC-ISRO, Ahmedabad for their technical support. We would also like to express our heart-felt gratitude to Shri H.R. Kansara, Deputy Director, MESA, Shri N.M. Desai, Director, SAC-ISRO, Ahmedabad for their concern toward our work and abundance of motivation.

References

1. Musto P, Russo P, Cimino F, Acierno D, Lupò G, Petrarca C (2015) Dielectric behavior of biopolymer based composites containing multi wall carbon nanotubes: effect of filler content and aspect ratio. *Eur Polymer J*. <https://doi.org/10.1016/j.eurpolymj.2015.01.010>
2. Gojny FH, Wichmann MHG, Fiedler B, Kinloch IA, Bauhofer W, Windle AH, Schulte K (2006) Evaluation and identification of electrical and thermal conduction mechanisms in carbon nanotube/epoxy composites. *Polymer*. <https://doi.org/10.1016/j.polymer.2006.01.029>
3. Chen J, Walther JH, Koumoutsakos P (2015) Covalently bonded graphene-carbon nanotube hybrid for high-performance thermal interfaces. *Adv Func Mater*. <https://doi.org/10.1002/adfm.201501593>
4. Zhang C, Ren L, Wang X, Liu T (2010) Graphene oxide-assisted dispersion of pristine multi-walled carbon nanotubes in aqueous media. *The Journal of Physical Chemistry C*. <https://doi.org/10.1021/jp103745g>
5. Tian L, Meziani MJ, Lu F, Kong CY, Cao L, Thorne TJ, Sun YP (2010) Graphene oxides for homogeneous dispersion of carbon nanotubes. *ACS Appl Mater Interfaces*. <https://doi.org/10.1021/am100687n>
6. Kwon YJ, Kim Y, Jeon H, Cho S, Lee W, Lee JU (2017) Graphene/carbon nanotube hybrid as a multi-functional interfacial reinforcement for carbon fiber-reinforced composites. *Compos B*. <https://doi.org/10.1016/j.compositesb.2017.04.005>
7. Pan TW, Kuo WS, Tai NH (2017) Tailoring anisotropic thermal properties of reduced graphene oxide/multi-walled carbon nanotube hybrid composite films. *Compos Sci Technol*. <https://doi.org/10.1016/j.compscitech.2017.07.015>
8. Vartak DA, Satyanarayana B, Munjal BS, Vyas KB, Bhatt PM, Lal AK (2020) Potential applications of advanced nano-composite materials for space payload. *Aust J Mech Eng*. <https://doi.org/10.1080/14484846.2020.1733176>
9. Vartak DA, Ghotekar Y, Munjal BS, Bhatt PM, Satyanarayana B, Lal AK (2021) Characterization of tailored multi-walled carbon nanotubes based composite for geo-space payload components. *Journal of Electrical Materials*. <https://doi.org/10.1007/s11664-021-08978-6>
10. ASTM D257-07 (2007) Standard test methods for DC resistance or conductance of insulating materials. ASTM International. <https://doi.org/10.1520/D0257-07>
11. ASTM D4935-18 (2018) Standard test method for measuring the electromagnetic shielding effectiveness of planar materials. ASTM International. <https://doi.org/10.1520/D4935-18>
12. Kostromin S, Asandulesa M, Podshivalov A, Bronnikov S (2019) Effect of rGO MWCNTs ratio on electrical conductivity of polyazomethine/rGO: MWCNTs nanocomposites. *Mater Res Express*. <https://doi.org/10.1088/2053-1591/ab46f8>
13. ASTM E1461-13 (2013) Standard test method for thermal diffusivity by the flash method. ASTM International. <https://doi.org/10.1520/E1461-13>
14. ASTM E228-17 (2017) Standard test method for linear thermal expansion of solid materials with a push rod dilatometer. ASTM International. <https://doi.org/10.1520/E0228-17>
15. ASTM E1269-11 (2018) Standard test method for determining specific heat capacity by differential scanning calorimetry. ASTM International. <https://doi.org/10.1520/E1269-11R18>
16. Vartak DA, Ghotekar Y, Deshpande N, Munjal BS, Bhatt P, Satyanarayana B, Vyas KB, Lal AK (2021) New horizons of space qualification of single-walled carbon nano tubes-carbon fibre reinforced polymer composite. *J Phys*. <https://doi.org/10.1088/1742-6596/1854/1/012001>
17. Colonna S, Monticelli O, Gomez J, Novara C, Saracco G, Fina A (2016) Effect of morphology and defectiveness of graphene-related materials on the electrical and thermal conductivity of their polymer nanocomposites. *Polymer*. <https://doi.org/10.1016/j.polymer.2016.09.032>
18. Im H, Jooheon K (2012) Thermal conductivity of a graphene oxide-carbon nanotube hybrid/epoxy composite. *Carbon*. <https://doi.org/10.1016/j.carbon.2012.07.029>
19. ASTM D3359-17 (2017) Standard test method for rating adhesion by tape test. ASTM International. <https://doi.org/10.1520/D3359-17>

Investigation on Effect of Different Tool Configurations on Heat Generation During Friction Stir Welding (FSW) of AA 6061 T6



Nisarg Patel, Shalin Marathe, and Harit Raval

Abstract The Friction Stir Welding (FSW) process is a solid-state joining process that is extensively used to join the materials like aluminum, steel, copper and titanium. The FSW of material having high melting point involves a lot of challenges due to the excessive heat generation during the welding. Due to the heat generation, the life of the welding tool and the parts of the welding machine tool is affected. In the present investigation, experimental and simulation study on FSW process has been attempted and study on heat generation during the FSW process has also been studied. The different configuration of welding tool has been selected and its effect on the heat generation on spindle, tool holder and tool has been explored. The tools having geometrical features and coating are selected in the present investigation. It has been found that the geometrical features incorporated on the welding tool result in significant heat transfer to the atmosphere. To reduce the excessive heat during the welding tool diameter can also be reduced. The thermal barrier coating applied between tool shank and the spindle yielded adequate insulation between tool and the spindle.

Keywords Friction stir welding · Simulation study · Finite element analysis · Thermal efficiency · Conventional tool

1 Introduction

Friction Stir Welding (FSW) process was invented particularly for the joining of aluminum materials. In this process, a rotating tool having cylindrical shoulder and pin is inserted into the joining line followed by the transverse movement of the

N. Patel · S. Marathe (✉) · H. Raval
Department of Mechanical Engineering, S. V. National Institute of Technology, Surat, Gujarat
395007, India

H. Raval
e-mail: hkr@med.svnit.ac.in

welding tool. This process has different stages involved in the welding, plunge stage, tool feed stage and tool retraction stage.

The effectiveness of the process depends upon different process parameters like tool rotational speed, tool feed, tool type, pin type, tool plunge depth, shoulder and pin diameter ratio and tool tilt angle. It has been also reported that to join different parent materials, different tool pin profiles can result in the good quality of joints. Fujii et al. [1] conducted such a study on different tool types and it was reported that for AA 1050-H24 triangular prism shape tool and the effect of tool shape to join AA 6061 T6 material is insignificant. Marathe and Mistry [2] performed an experimental investigation on FSW process to join the AA 6061 material of 6 mm thick. The effect of tool pin profile, tool rotational speed and tool feed on joint strength was investigated. Full factorial study and ANOVA was adopted and it was reported that 15 mm/min of tool feed, 2750 tool rotational speed and tapered pin profile yielded maximum strength of the joints. Rumalla et al. [3] performed parametric investigation on joining of AA 6061 T6 material. It was reported that as the tool rotational speed and tool feed increased, the force on the welding tool increased. Marathe et al. [4] performed experimental investigation on FSW process to join AA 6061 material of 6 mm thick. Different configurations of tool pin profiles were selected during the investigation. The three different levels of tool rotational speed and tool feed were also selected. All the parameters selected for investigation had a significant effect on the tensile strength of the FSW joints. A similar investigation was performed [5] and it was observed that the tool shoulder diameter had a significant effect on the weld quality of the FSW process. Li et al. [6] investigated the effect of different tool configurations on welding thermal efficiency. The tools like hollow tool, fluted tool and thermally insulated tool were selected for the study. It was found that the thermally insulated tool resulted in maximum thermal efficiency of 96%. Patel et al. [7] showed that the tool rotational speed, tool feed and tool pin profile control the heat generation during the FSW process and ultimately affects the quality of the joints produced using the FSW process. Rodrigues et al. [8] showed that for cold weld conditions low axial loads led to significant internal and surface defects, whereas for hot weld conditions high axial load values led to tool destruction due to excessive plunge depth in the softened material. A special twin-tool setup was used to fabricate the joints using the FSW process. The twin-tool setup yielded high heat during the joining process leading to high plastic deformation in the weld zones [9]. Chao et al. [10] reported that the quality of the weld, residual stress and distortion of the workpiece is affected by heat transfer to the workpiece. The amount of heat conducted to the tool dictates the life of the tool and the capability of the tool for the joining process. It was reported that the maximum heat is transferred to the faying surfaces and a very insignificant amount of heat is conducted into the tool material.

The FSW of parent materials having a very high melting point involves many challenges regarding excessive heat generation. The excessive heat generated during the welding can reduce the tool life, tool holder life and can affect the part of the welding machine tool also. The spindle bearings of the machine tool can also get affected

due to the heat generation during the FSW process. In the present investigation, the FSW tools are developed with geometrical features to deal with the excessive heat generated during the welding process.

2 Simulation Study

The simulation of FSW process was done using the ABAQUS/Explicit simulation tool. The different parts required to be modelled for simulation of FSW process are aluminum base plate (Lagrangian 3D deformable), Eulerian plate (Eulerian 3D deformable), Tool (Lagrangian-3D deformable), Tool spindle holder (Lagrangian-3D deformable). The heat produced during the FSW process is transferred to the tool spindle and tool holder and that can affect the life of the spindle bearings and other components. To investigate the effect of different tool designs, total five tool configurations were developed during the simulation study as represented in Fig. 1.

The tool material was considered as H13 and tool holder material was considered as C45 carbon steel. The parent material was considered as AA 6061 T6 of 2 mm thickness and its plastic and fracture behaviour was determined from the Johnson–Cook model. The constants used in the Johnson–Cook model are presented in Table 1. The thermal and mechanical properties of the different materials are shown in Table 2.

In the present simulation study, coupled Eulerian–Lagrangian plate was used for the analysis and the advantage of this combination is only the Eulerian plate is required to mesh. For meshing, multi-material thermally coupled element type EC3D8RT (8 node) is used.

The interaction between FSW tool and faying surface was general explicit contact with 0.3 as the coefficient of friction. Surface film condition type interaction has been used to define convective heat transfer ($h = 10 \text{ W/m}^2\text{K}$) between external surface of the model and surrounding environment [6]. During the simulation, the plates being welded were encastre from the edges and tool was given rotational movement (1000 RPM) along with tool feed (40 mm/min). The initial temperatures of tool, tool holder and plates were given as 25 °C.

3 Experimental Study

In the experimental investigation, similar to simulations study, five different configurations of tools were developed. In addition to the geometrical feature, coatings were also applied to the tool to deal with the excessive heat developed during the welding. In this work, a Y_2O_3 stabilized ZrO_2 was used as thermal barrier (3 mm thick) coating on tool shank surface. This thermal barrier coating was plasma sprayed on the shank surface of conventional tool. The conventional tools and coated tools are shown in Fig. 2.

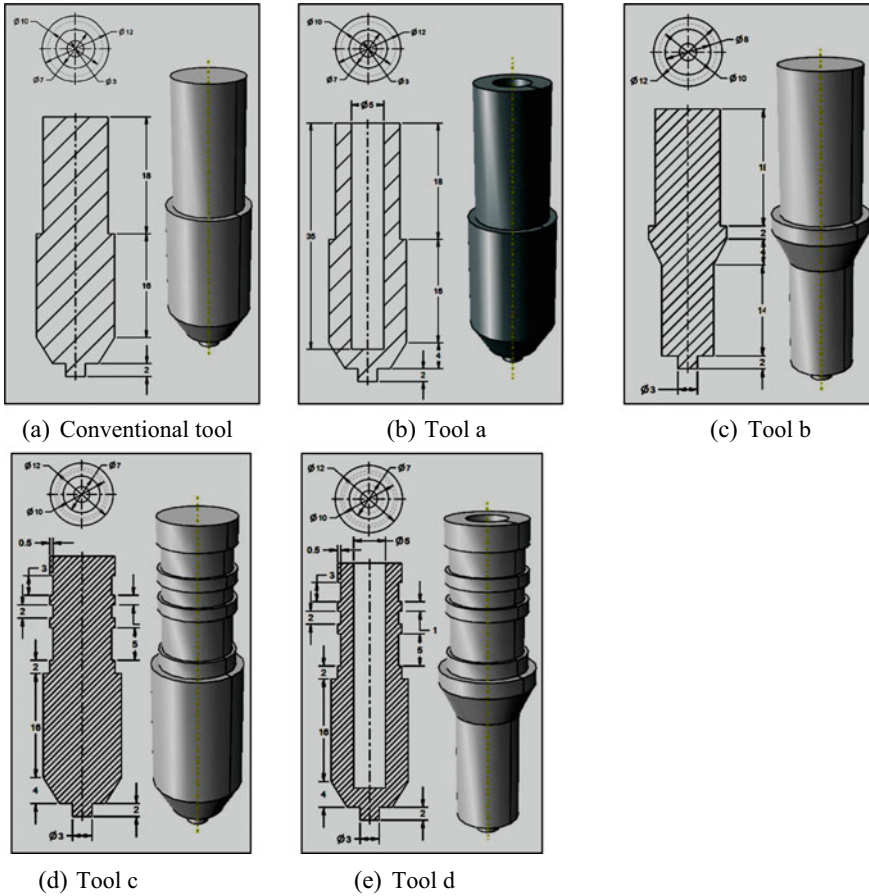


Fig. 1 Different configurations of FSW tool (All the dimensions are in mm)

Table 1 Constants of Johnson–Cook model

Material	T_{melt} (°C)	A (MPa)	B (MPa)	c	n	m
Al 6061-T6	588	285	94	0.002	0.41	1.34

Table 2 Thermal and mechanical properties of FSW parts

Material	Density (ton/mm ³)	Young’s modulus (MPa)	Poisson’s ratio	Thermal conductivity (W/m°C)	Specific heat (kJ/ton°C)
Al 6061-T6 [6]	2.72×10^{-9}	68,900	0.33	167	896×10^6
H13 [11]	7.80×10^{-9}	210,000	0.30	24.7	460×10^6
C45 [6]	7.86×10^{-9}	200,000	0.30	41.2	536×10^6

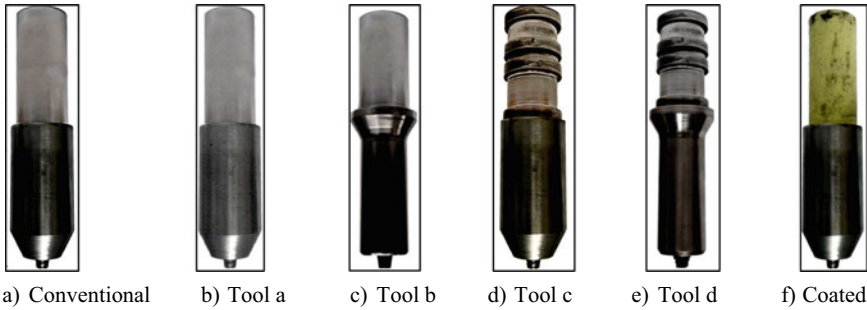
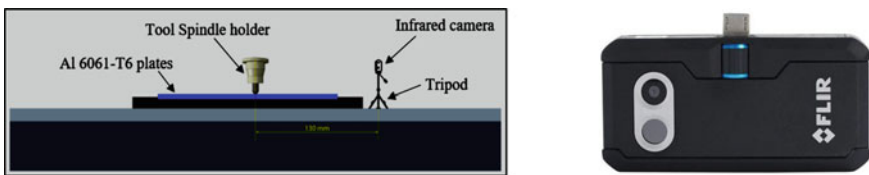


Fig. 2 Different configurations of tool used in the experimental study



(a) Schematic view of set up of infrared camera (b) Infrared thermal Imager

Fig. 3 Experimental setup to measure the temperature during the welding process

The experimental work was performed on the milling machine and the temperature on the spindle was measured with the non-contact type thermal imager. The experimental setup to measure the temperature and the equipment used to measure the temperature are depicted in Fig. 3. To ensure the accuracy of the temperature measurement, the surfaces subjected to measurement were painted with black paint.

4 Results and Discussions

In this section, the results of simulation and experimental study are reported along with the comparison between them.

4.1 Simulation Results

The results of simulation study are presented in Fig. 4. The NT11 is field output request which shows Nodal temperature in the ABAQUS/Explicit module. For measurement, five different nodes in the spindle, from the bottom end of the spindle at a distance of 2.5, 7.5, 12.5, 25, 37.5 mm were selected. In addition to this, the

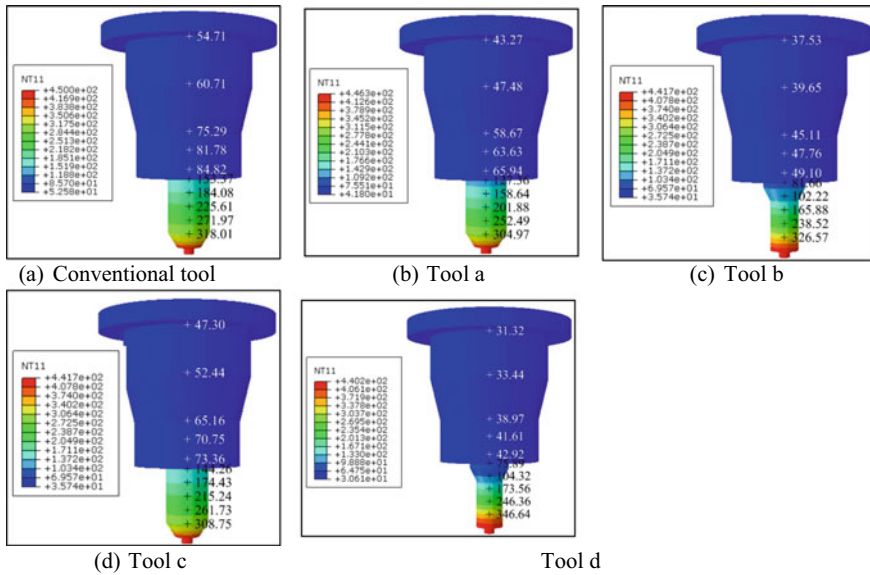


Fig. 4 Temperature distribution in the tool and tool holder for simulation conditions

difference of temperature in all tools with respect to the conventional tool is compared in Table 3.

It has been observed that the temperature recorded for all the tools is lower than the temperature recorded in the spindle of the conventional tool. It has been also observed that the temperature in the spindle recorded for tool d is very low in comparison to the conventional tool. This indicates that the reduction in the diameter of tool and the hollow tool design is the solution to reduce the heat transfer to the tool holder and spindle. Hence, the FSW of material having a very high melting point can be done

Table 3 The temperature (°C) at each measuring point of the spindle tool holder and the percentage (%) of the temperature change with respect to the conventional tool

FSW tools	Conventional tool	Tool (a)	Tool (b)	Tool (c)	Tool (d)
Point 5	54.71	43.27 (-20.90%)	37.53 (-31.40%)	47.30 (-13.55%)	31.32 (-42.74%)
Point 4	60.71	47.48 (-21.79%)	39.65 (-34.69%)	52.44 (-13.62%)	33.44 (-44.91%)
Point 3	75.29	58.67 (-22.08%)	45.11 (-40.09%)	65.16 (-13.45%)	38.97 (-48.23%)
Point 2	81.78	63.63 (-22.19%)	47.76 (-41.60%)	70.75 (-13.48%)	41.61 (-49.12%)
Point 1	84.82	65.94 (-22.26%)	49.10 (-42.12%)	73.36 (-13.51%)	42.92 (-49.40%)

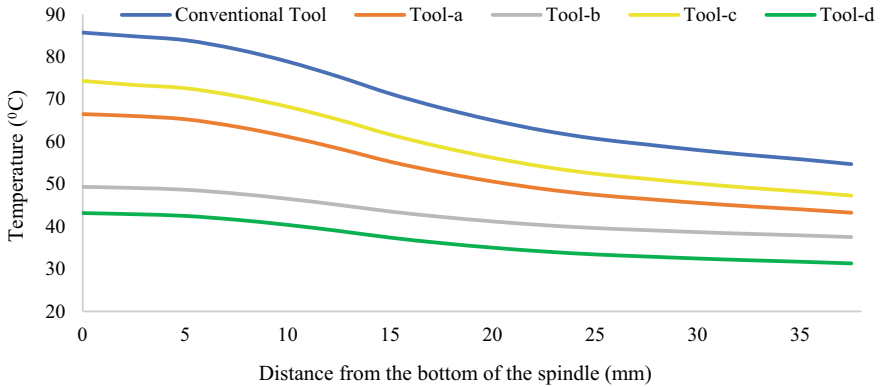


Fig. 5 Comparison of temperature variation in all the different FSW tools

by the tool having geometrical features for heat transfer insulation. The comparison of temperature recorders in the spindle for different tool configurations is presented in Fig. 5.

From Fig. 5, it can be observed that at the end of spindle, the minimum temperature is observed for the tool (d) in comparison to all other tool configurations. The geometrical features added to tool d are responsible for this kind of behaviour. In addition to the temperature distribution on the spindle and tool holder, the temperature variation in the tool at different points from the shoulder was also investigated (see Fig. 6). The temperature recorded for all the tools at all the different locations is represented in Table 4. Similar to the results of temperature for the tool holder and spindle, the temperatures for the different tools were observed. The maximum difference of temperature between point I and V was recorded for tool b and tool d

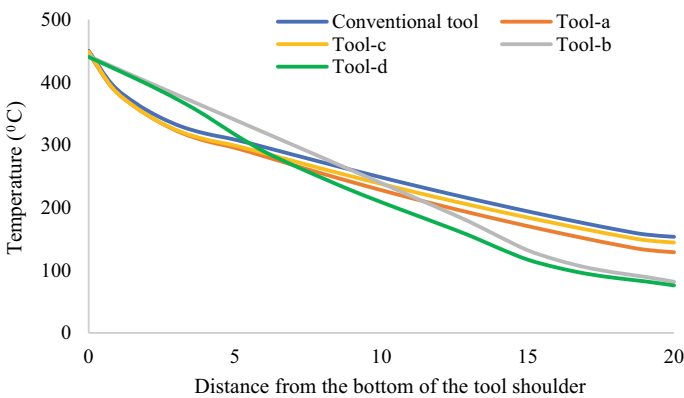


Fig. 6 Graphical comparison of temperature trendline of all tools

Table 4 The temperature (°C) at each measuring point of the tool

Point on tool surface	Conventional tool	Tool-a	Tool-b	Tool-c	Tool-d
Point I	318.01	304.97	326.57	308.75	346.64
Point II	271.97	252.39	238.52	261.73	246.36
Point III	225.61	201.88	165.88	215.24	173.56
Point VI	184.08	158.64	102.22	174.43	104.32
Point V	153.37	127.36	81.66	144.26	75.89

indicating that the heat is dissipated to the atmosphere and not transferred to the tool spindle and tool holder.

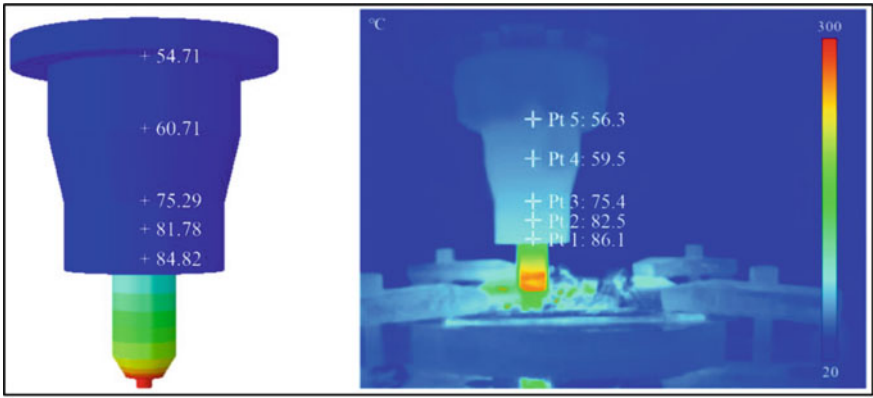
Similar to the previous results, in tool d, the temperature variation between tool shoulder to the uppermost end of tool is maximum in comparison to all other tools. This result indicates the reduction in shoulder diameter and appropriate geometrical features can reduce the transfer of heat from the faying surfaces to the spindle of the machine.

4.2 Experimental Results

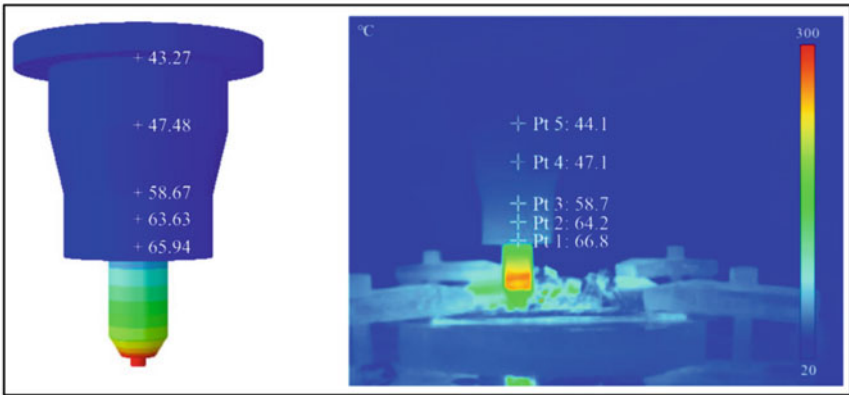
The experimental work on FSW process was performed with six different tools. Similar to the simulations study, five tools were developed with different geometrical features. In addition to these tools, one more tool was fabricated with coating. The results of temperature recorded in experimental and simulation studies are compared in Fig. 7. It can be observed that the value of temperature recorded at the bottom of the spindle is higher and at the top of the spindle, lower temperatures are recorded. The results of experimental and simulation studies showed good agreement.

During the experimental study, the comparison of temperature distribution between conventional tools and thermal barrier coated tools was performed (see Fig. 8). It can be observed that the coated tool yielded significant temperature loss during the welding in comparison to the conventional tool.

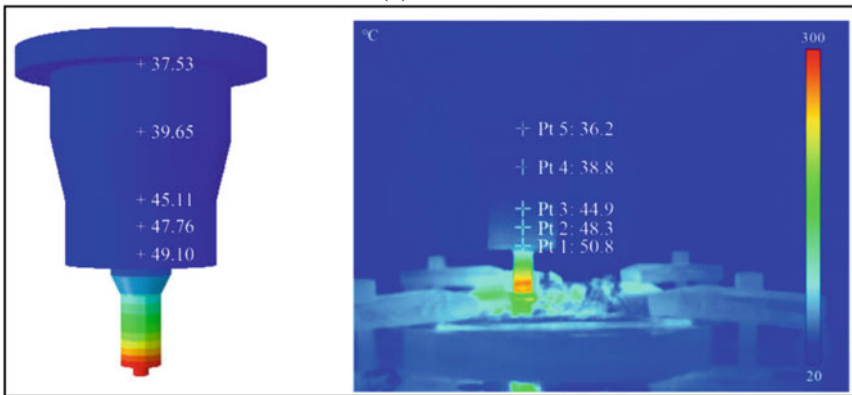
The temperature recorded for different tools is compared and the change with respect to the conventional tool regarding the temperature is presented in Table 5. It is observed that the temperatures noted for the coated tool are significantly low in comparison to the conventional tool and other tools with geometrical features. This indicates that the coating between tool shank and the spindle can be used as a solution to deal with the excessive heat generated during the welding. The comparison of experimental results and simulation results regarding temperature distribution in the spindle and tool holder is presented in Fig. 9 which shows good agreement between the two-study adopted.



(a) Convectional tool

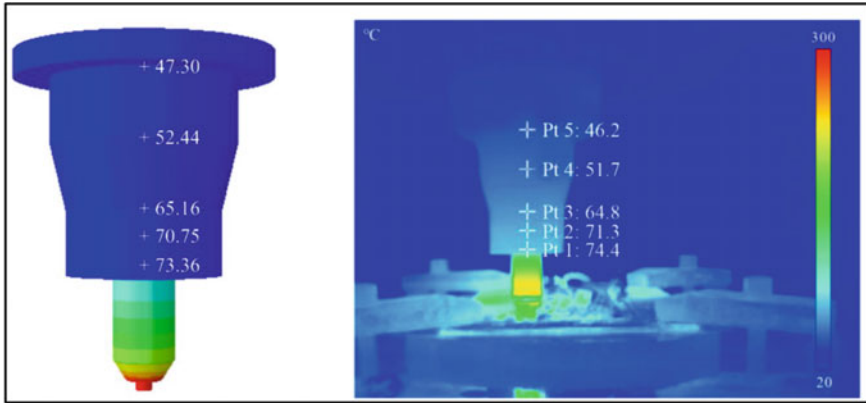


(b) Tool a

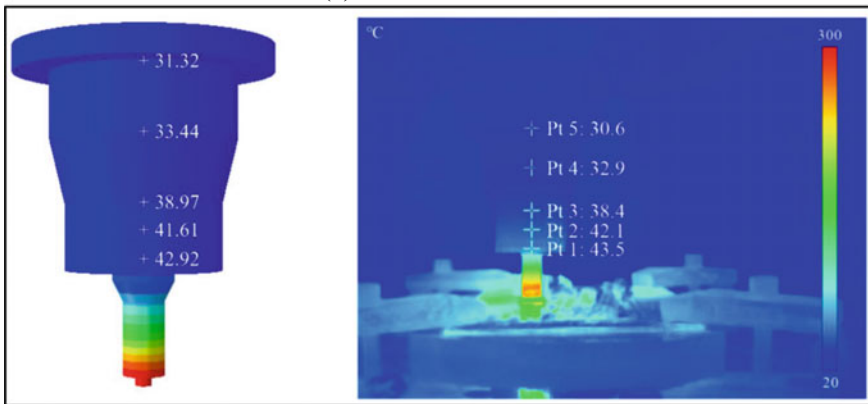


(c) Tool b

Fig. 7 Comparisons of simulation FE model and temperature contour obtain from infrared camera

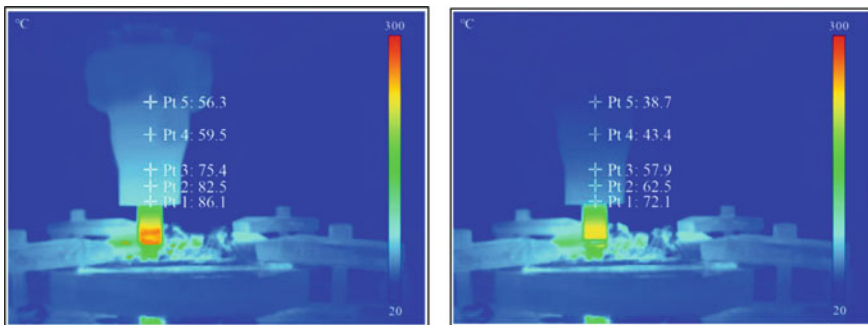


(d) Tool c



(e) Tool d

Fig. 7 (continued)



(a) Conventional tool

(b) Coated tool

Fig. 8 Comparison of temperatures of five points between conventional tool and coated tool during the experimental study

Table 5 The temperature (°C) at each measuring point of the spindle tool holder and the percentage (%) of the temperature change with respect to the conventional tool

Temperature measurement	Conventional tool	Tool-a	Tool-b	Tool-c	Tool-d	Coated tool
Point 5	56.3	44.1 (-21.7%)	36.2 (-35.7%)	46.2 (-17.9%)	30.6 (-45.7%)	38.7 (-31.3%)
Point 4	59.5	47.1 (-20.8%)	38.8 (-34.8%)	51.7 (-13.1%)	32.9 (-44.7%)	43.4 (-27.1%)
Point 3	75.4	58.7 (-22.2%)	44.9 (-40.4%)	64.8 (-14.1%)	38.4 (-49.1%)	57.9 (-23.2%)
Point 2	82.5	63.8 (-22.1%)	48.3 (-41.4%)	71.3 (-13.6%)	42.1 (-49.0%)	62.5 (-24.2%)
Point 1	86.1	66.8 (-22.4%)	50.8 (-41.0%)	74.4 (-13.6%)	43.5 (-49.5%)	72.1 (-16.3%)

4.3 Approximation of Temperature Equation for Tool

The polynomial curves were plotted for all the different tool initial conditions of simulation. The polynomial curve was found to be covering all the points of simulation curve (see Fig. 10). For all the different tool configurations, the equations of polynomial curve were generated and it was found that the equation and nature of polynomial curve were different for all the tool configurations.

There was a minute disagreement between the polynomial curve and simulation curve at a distance of 20 mm from the bottom of the shoulder. This is a region of tool spindle cylindrical surface contact interface. There are two points at the same length at 20 mm representing tool surface temperature and spindle surface temperature. As there is radial heat transfer through tool to spindle there is temperature drop from tool surface to spindle surface which can be viewed by the vertical line at 20 mm in the graph.

4.4 Comparison of Temperature from Equation with Experimental Temperature

The derived polynomial equation was adopted to predict the value of temperature for all the tool configurations and predicted value was compared with the experimental values and good agreement was observed between the predicted values and the experimental values (see Fig. 11).

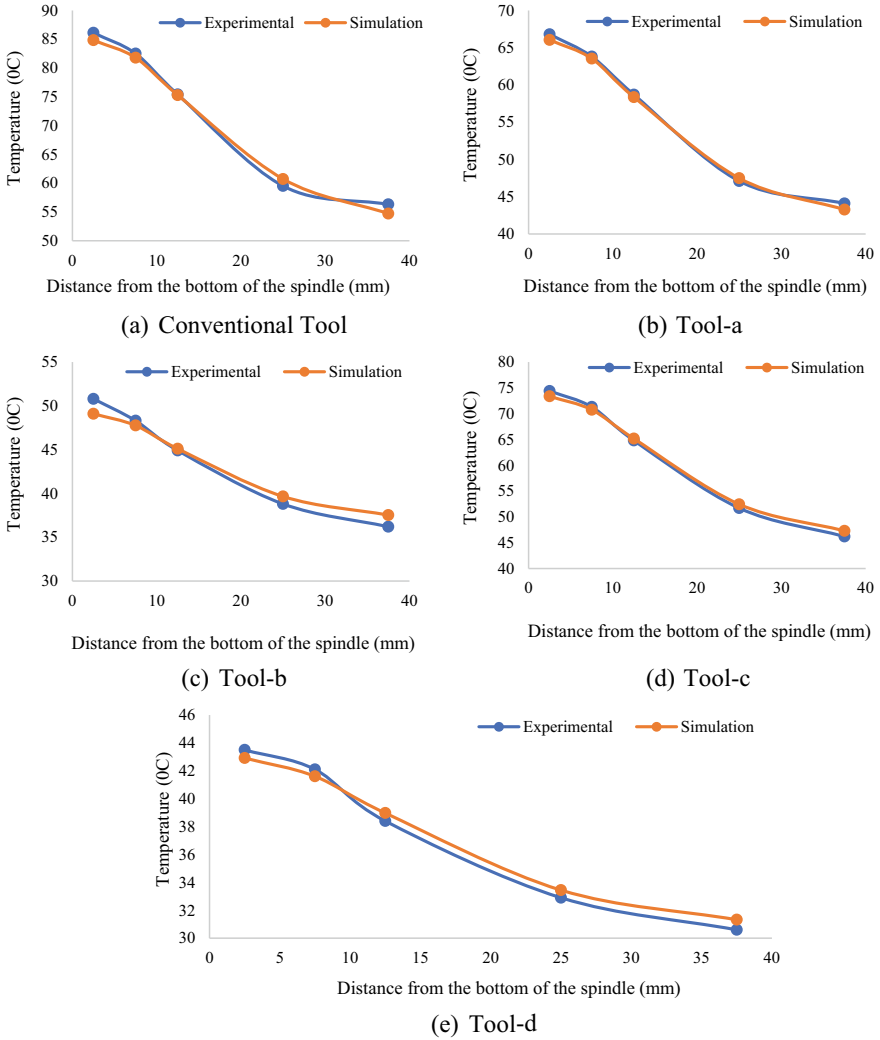


Fig. 9 Comparison of experimental and simulation results for temperature at different points in spindle and tool holder

4.5 Welding Thermal Efficiency

The welding thermal efficiency between the different tool configurations was calculated and compared. The welding thermal efficiency was calculated by the following equation,

$$\eta = \frac{Q_1}{Q_1 + Q_2} = \frac{Q_1}{Q} \tag{1}$$

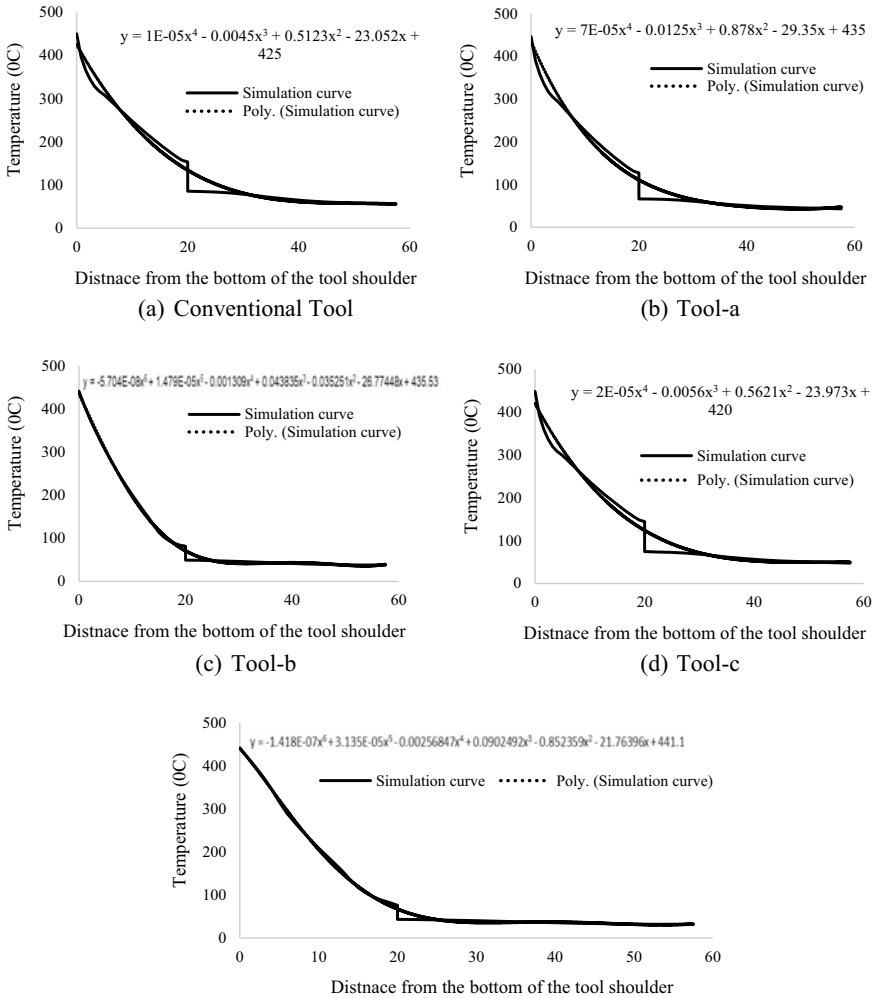


Fig. 10 Simulation curve and polynomial curve for different configurations of curve

where the total heat Q is the sum of the workpiece heat input Q_1 and heat flowing into the FSW tool Q_2 . The comparison of welding thermal efficiency is shown in Table 6.

Out of all the tools, FSW Tool-d gives temperature drop by 54.29% with respect to conventional tool and the thermal efficiency increased to 96.0% from 91.6%. From Table 6, Tool-b gives temperature drop by 53.61% with respect to conventional tool which slightly lesser than temperature drop by using Tool-d. Tool having small diameter is most efficient for reducing heat flow. But if reducing the diameter of the tool, strength of the tool will be decreased and there may be a chance of failure of the tool. So, up to some extent, decreasing the diameter of the tool is advisable.

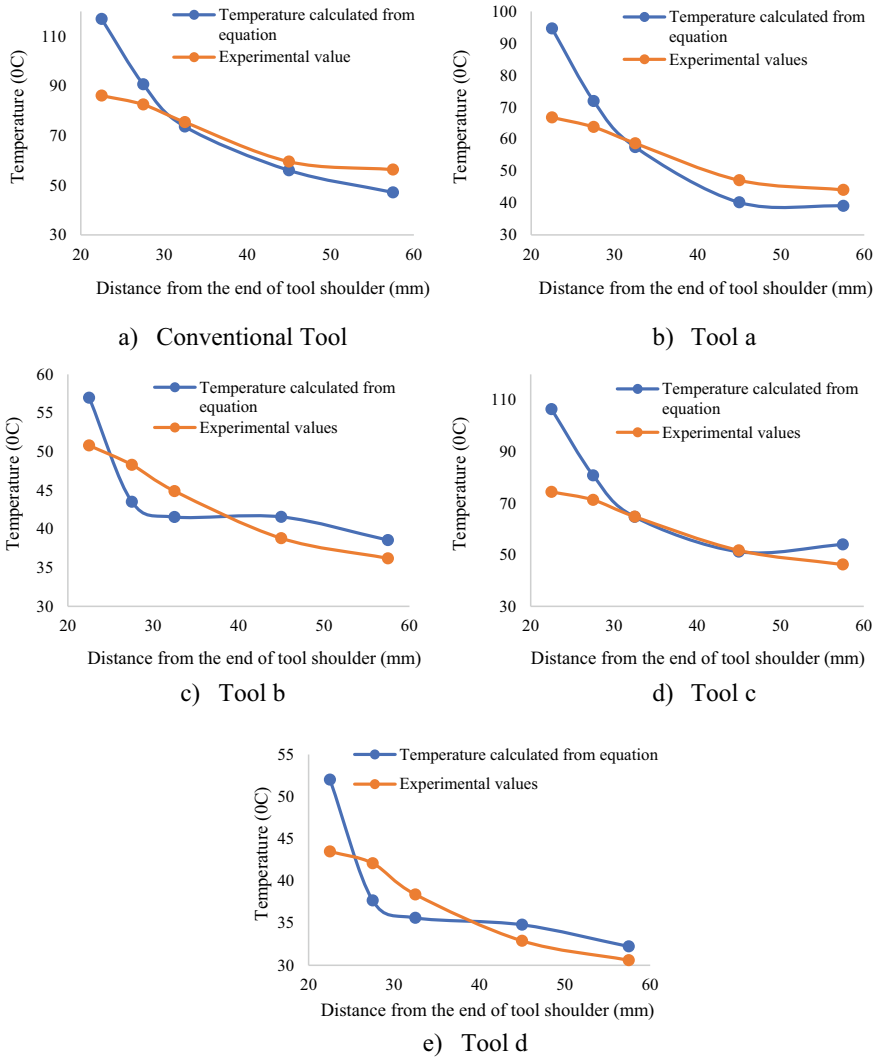


Fig. 11 Comparison between temperature (°C) calculated from the equation and experimental values for all five tools

Therefore, there is a compromise in the strength of the tool to increase the welding efficiency. The hollow tool also gives a notable temperature drop of 49.8% with respect to conventional FSW tools. But further reducing the tool diameter is not possible, hollow tool or hollow tool with smaller diameter tool can be used.

Table 6 Thermal efficiency and percentage of heat into tool change with respect to conventional tool calculated using simulation result values

FSW tool	Heat flow to the tool (Q_2) (W)	Total heat (Q) (W)	Q_1/Q	Thermal efficiency (%)
Conventional tool	88.41	1049.89	0.915	91.6
Tool-a	44.43 (-49.8%)	1049.89	0.958	95.8
Tool-b	41.01 (-53.61%)	1004.94	0.959	95.9
Tool-c	69.54 (-21.38%)	1049.89	0.934	93.4
Tool-d	40.44 (-54.29%)	1004.94	0.960	96.0

5 Conclusions

In the present investigation study on the thermal efficiency of the FSW process has been investigated. The study involved different tools with different geometrical features and coatings and its effect on the temperature distribution on the spindle, tool holder and tool were studied. Following are the conclusive remarks from the present simulation and experimental study.

The geometrical features applied on the welding tool yielded in the reduction of temperature on spindle, tool holder and tool indicating that heat dissipation to the atmosphere increased with the inclusion of geometrical features. The tool d (hollow tool with smaller diameter and fluted shank) is found to be most effective for which the thermal efficiency was 96%. The smaller diameter of the tool and hollow tool were found effective in reducing the heat from towards tool spindle. The experimental study revealed that the tool with heat insulation can reduce the spindle temperature leading to safe operation of spindle bearings and other parts. The thermal barrier between tool shank and the spindle was also found significant in reducing the flow of heat from tool material to spindle during the welding process. The approximation equation to predict the temperature was also developed for all the tools. The temperature predicted by the developed equation was in good agreement with the experimental temperature values.

References

1. Fujii H, Cui L, Maeda M, Nogi K (2006) Effect of tool shape on mechanical properties and microstructure of friction stir welded aluminium alloys. *Mater Sci Eng, A* 419(1–2):25–31
2. Shalin M, Hiten M (2018) Experimental analysis on effect of tool transverse feed, tool rotational speed and tool pin profile type on weld tensile strength of friction stir welded joint of AA 6061. *Mater Today Proc* 5(1):487–493
3. Ramulu PJ, Babu AS, Narayanan RG, Prasad SD, Rao PS (2013) The behavior of friction stir welded (FSW) sheets of AA6061-T6 during in-plane stretching test. *Procedia Eng* 1(64):862–867

4. Marathe SP, Mistry HJ, Raval HK (2016) Parametric study of friction stir welding (FSW) of AA 6061 using Taguchi method. In: Proceedings of national workshop on industrial problems on machines and mechanical similar materials: “challenges in manufacturing”. NIT, Nagpur
5. Hou JC, Liu HJ, Zhao YQ (2014) Influences of rotation speed on microstructures and mechanical properties of 6061–T6 aluminum alloy joints fabricated by self-reacting friction stir welding tool. *Int J Adv Manuf Technol* 73(5):1073–1079
6. Li H, Qin W, Liu D, Li Q, Wu Y (2018) Design of friction stir welding tools reducing heat flow into spindle. *Int J Adv Manuf Technol* 94(5):1925–1932
7. Patel S, Marathe S, Desai K, Raval H (2021) Effect of friction stir welding process parameters on tensile strength and forming height of tailor welded blanks. In: *Advances in manufacturing processes*. Springer, Singapore, pp 123–134
8. Rodrigues DM, Leitao C, Louro R, Gouveia H, Loureiro A (2010) High speed friction stir welding of aluminium alloys. *Sci Technol Weld Joining* 15(8):676–681
9. Kumari K, Pal SK, Singh SB (2015) Friction stir welding by using counter-rotating twin tool. *J Mater Process Technol* 1(215):132–141
10. Chao YJ, Qi X, Tang W (2003) Heat transfer in friction stir welding—experimental and numerical studies. *J Manuf Sci Eng* 125(1):138–145
11. Surekha K, Els-Botes A (2012) Effect of cryotreatment on tool wear behaviour of Bohler K390 and AISI H13 tool steel during friction stir welding of copper. *Trans Indian Inst Met* 65(3):259–264

Investigation on Mechanical Properties of 3D Printed PETG Material



T. Malyadri, Nagasrisaihari Sunkara, and M. S. Srinivasa Rao

Abstract Additive Manufacturing using 3D Printing plays a very predominating role in the manufacturing industry by providing alternative solutions to existing conventional manufacturing methods. 3D Printed components strength is still in initial stages in the current research areas. Modified version of PET is Polyethylene terephthalate glycol modified (PETG) which is most commonly used plastic in the present world. It is a recyclable and biodegradable material and in Fused Deposition Modelling (FDM) based 3D printing modelling it is one of the most flexible materials. Investigations are carried out by testing PETG material according to the ASTM standards. In the present work, specimens have been printed according to ASTM standards on a 3D FDM printer using the PETG material and conducted tensile, compression tests respectively by varying the layer height parameters and infill percentages respectively. The experimental results are then to be validated with simulating software. The difference in the experimental and simulation values should be calculated. These results will be compared with the effect of change in every parameter on strength will be carried out and optimized parameters for high strength need to obtain.

Keywords PETG · FDM · 3D printing · Tensile · Compression

1 Introduction

Rapid prototyping is a technology in which parts are produced with the help of Computer Aided Design (CAD) data. Traditional manufacturing method is a subtractive method whereas, this method is an advanced method that is capable of reducing the manufacturing time, simplified process and reducing material waste. The first methods of rapid prototyping are available from the 1980's. Now due to vast improvement in rapid prototyping, it is playing a crucial role in industrial sector with improvements in design and applications, thus reducing the physical part preparation and

T. Malyadri (✉) · N. Sunkara · M. S. Srinivasa Rao
Mechanical Engineering Department, VNRVJIET, Hyderabad, Telangana 500090, India

conceptual design time. The errors in design can be reduced by making changes to the components that are to be manufactured and can be tested immediately.

Tensile test is a material test that belongs to the category of quasi-static and destructive tests. Mechanical and deformation properties of the specimen are determined in parallel to tension with the desired velocity. ASTM D638 standard covers the tensile properties of reinforced and unreinforced plastics. Type IV in ASTM D638 is chosen because of its short length and is most widely used for plastic strength tests. The Universal Testing Machine (UTM) is used to perform these tests. The compression test is performed as per the ASTM D695 standard. It determines the mechanical properties and compression strength of rigid plastics when applied load in compression testing machine at low uniform rates of strain and loading.

Polyethylene terephthalate (PET) is the most commonly used plastic in the 3D printing world. PETG is the modification of PET only. Here 'G stands for glycol modified'. It is used for manufacturing thousands of consumer products like delivering and packaging food beverages. These components are made using traditional manufacturing processes like blow moulding. They can also be made using additive manufacturing processes like 3D printing which uses PETG as raw material and is deposited in the form of layer by layer from the extruder. It is very important that the strength of the 3D printed parts are known for proper functioning and applications. To test the strength of 3D printed PETG parts, 2 ASTM standards are available; for tensile testing, ASTM D638 standard is used and for compression testing, ASTM D695 standard is used. For ASTM D638 there are four sub-types; however, it has been noticed ASTM D638 is widely used. In this work, it is proposed to perform tests to evaluate tensile strength of PETG 3D printed specimens as per ASTM standards. Compressive specimens are to be printed using ASTM D695 standard for evaluating compressive strength in order to have a relative comparison.

2 Methodology

The project idea is to achieve tensile and compressive strength of PETG specimens printed in 3D printer as per type the ASTM type IV standards for tensile tests and compression test according to ASTM D695 and. Dimensions are chosen as per standards and drafted using CATIA V5 software and generated a .stl file. The .stl file is imported into the SIMPLIFY 3D software to rectify errors and generate supports if any. The error free file is then exported to SIMPLIFY 3D software. This software slices the model into number of consecutive layers which is sent to 3D printer for printing. SIMPLIFY 3D desktop software also generates tool path for the printer to the creative part as well. Two specimens were to be printed for each tensile and compressive test as per the ASTM standards by changing two parameters for each and two sample specimens that need conditioning at a temperature of 21–25 °C. The conditioned specimens are to be then tested using UTM to find tensile and compressive strengths of specimen. The tests in the UTM machine are again conducted for

the specimens that are printed by varying the layer height and the infill percentage of the material.

The methodology involved in the modelling using CATIA V5 and validation of the specimens for compression, tensile tests under the ASTM D695 and ASTM D638 standards has been discussed and explained in detail.

3 Modelling and Analysis of Test Specimens

The test specimen for doing compression test is modelled as per ASTM designation D695 as shown in Fig. 1. Overall length of specimen is 79.4 mm and thickness of specimen is 4 mm and gauge length is 38.1 mm (Fig. 2).

The analysis was done using the ANSYS 16.2 workbench. Simulation is done in static structural analysis module, with one of the ends is fixed. Figure 3 shows an overview of analytical procedure followed in ANSYS software. ANSYS analysis is performed to check for random errors.

Stress at 1245.44 N is maximum than all the loads applied. This is because the applied load is more in the affecting area which leads to high concentration of stresses at gauge length area (Fig. 4; Table 1).

Amongst all the loads applied and deformations recorded the deformation is maximum at the 1245.44 N load. The reason behind the maximum deflection is the concentration of load applied on the specimen is maximum and is prone to deflection (Fig. 5; Table 2).

For a load of 1245.44 N, the stress is maximum than at all the other loads applied. This is because of the fact that applied load is affecting the area which is less and length is more. This leads to high concentration of strain at a point. The maximum strain is 0.025 (Fig. 6; Table 3).

Stress at 246.61 N load is greater at all the loads applied. This is because of the fact that applied compressive load is affecting that area which is leading to the high

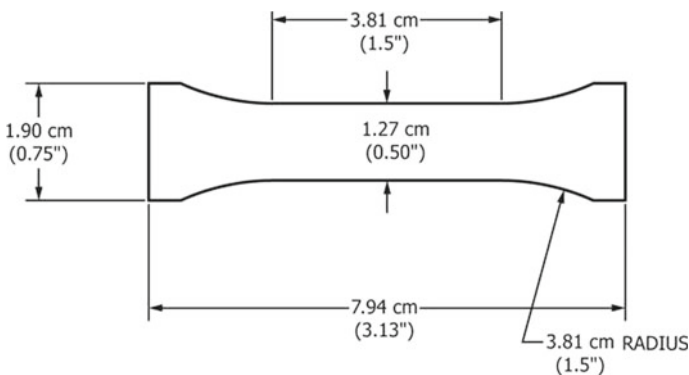


Fig. 1 Detailed dimensions of tensile specimen

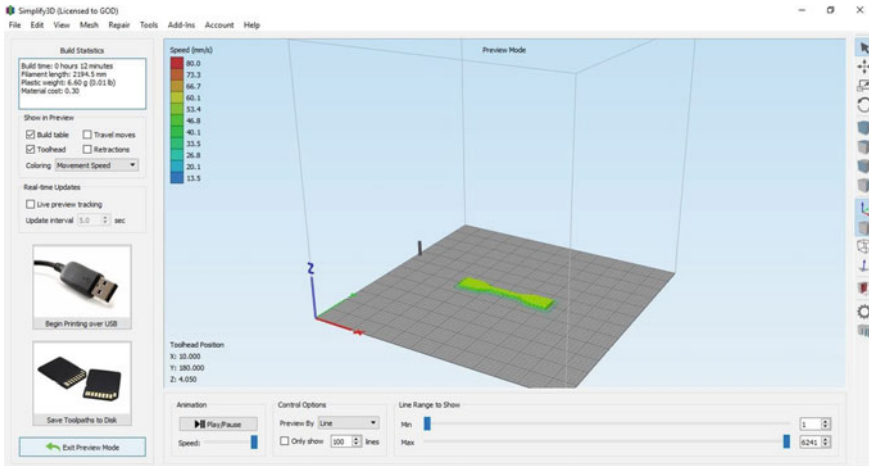


Fig. 2 Orientation of tensile specimen

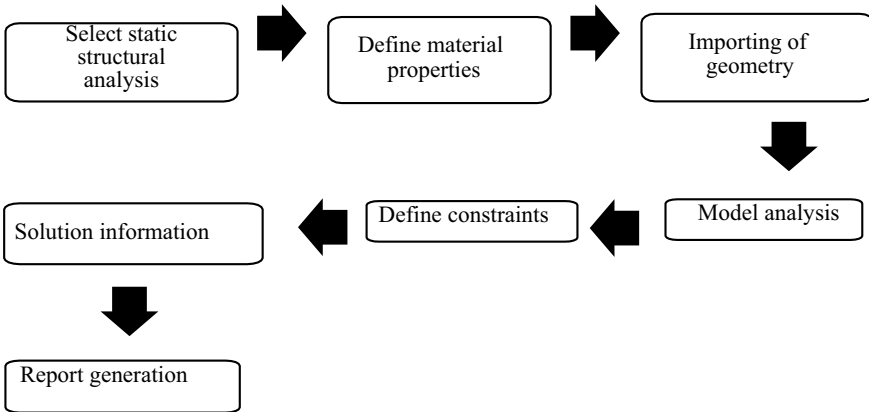


Fig. 3 Steps involved in static structural analysis

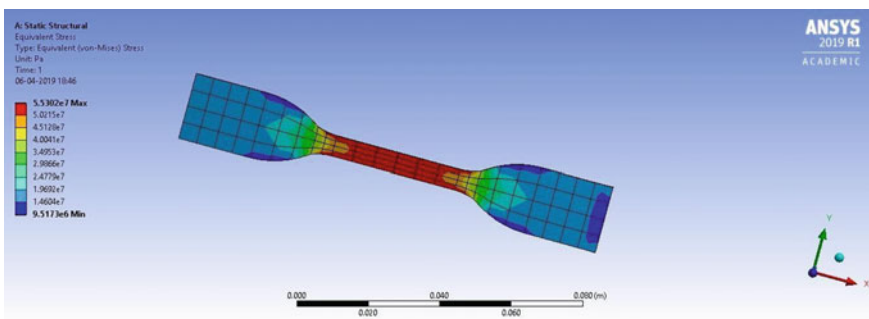


Fig. 4 Stress analysis for tensile load

Table 1 Stress values for different tensile loads

Layer thickness	Specimen	Load (N)	Stress (N/mm ²)
0.1	1	1214.06	55.30
	2	1245.44	56.73
0.3	1	1043.33	47.53
	2	995.37	45.34

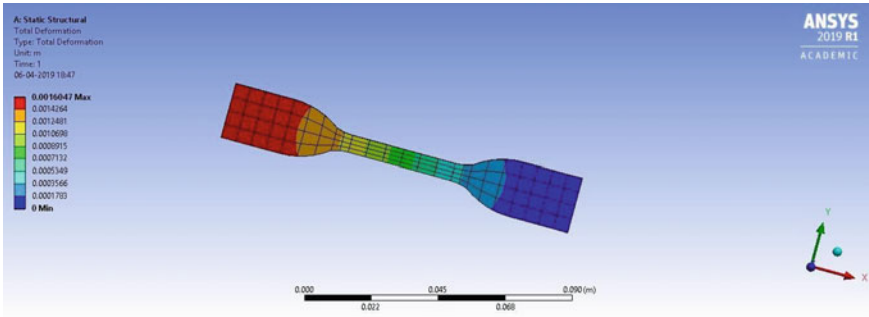


Fig. 5 Deformation analysis for tensile load

Table 2 Deformation values for different tensile loads

Layer thickness	Specimen	Load (N)	Deformation
0.1	1	1214.06	1.61
	2	1245.44	1.64
0.3	1	1043.33	1.37
	2	995.37	1.31

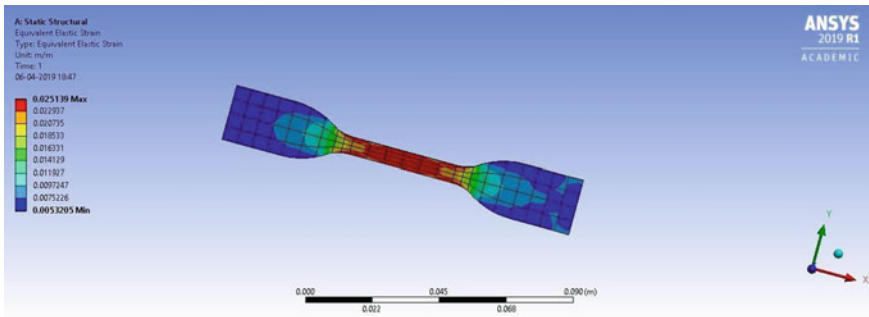


Fig. 6 Strain analysis for tensile load

Table 3 Strain values for different tensile loads

Layer thickness	Specimen	Load (N)	Strain (%)
0.1	1	1214.06	2.51
	2	1245.44	2.58
0.3	1	1043.33	2.16
	2	995.37	2.06

concentration of stresses on the specimen. The stress for 0.1 mm thickness is much high than the 0.3 mm due to the fact that it is withstanding thrice the load which 0.3 mm specimen is able to bear (Fig. 7; Table 4).

Among all specimens analyzed the deformation at 246.61 N has recorded the highest value. This is due to the reason that there is a higher concentration of compressive load acting on that region (Fig. 8; Table 5).

For a load of 1245.44 N, the stress is maximum than at all the other loads applied. This is because of the fact that applied load is affecting the area which is less and length is more. This leads to high concentration of strain at a point. The maximum strain is 0.025 (Fig. 9; Table 6).

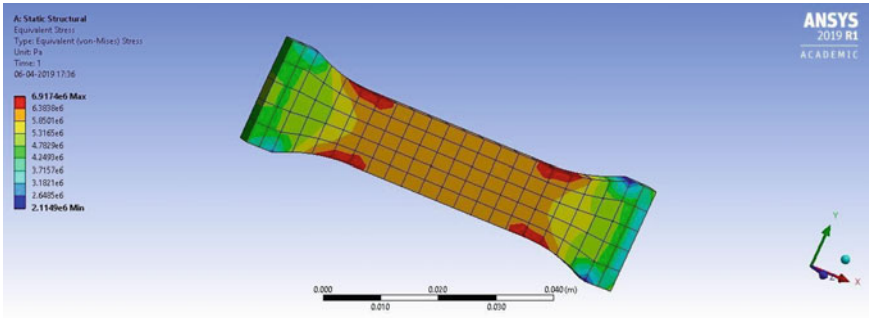


Fig. 7 Stress analysis for compressive load

Table 4 Stress values for different compressive loads

Layer thickness	Specimen	Load (N)	Stress (N/mm ²)
0.1	1	241.78	6.91
	2	246.61	7.05
0.3	1	74.34	2.12
	2	83.14	2.38

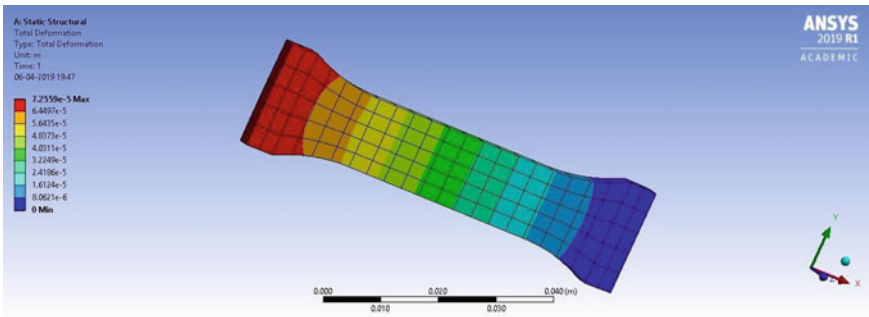


Fig. 8 Deformation analysis for compressive load

Table 5 Deformation values for different compressive loads

Layer thickness	Specimen	Load (N)	Deformation
0.1	1	241.78	2.11
	2	246.61	2.15
0.3	1	83.14	0.65
	2	74.34	0.72

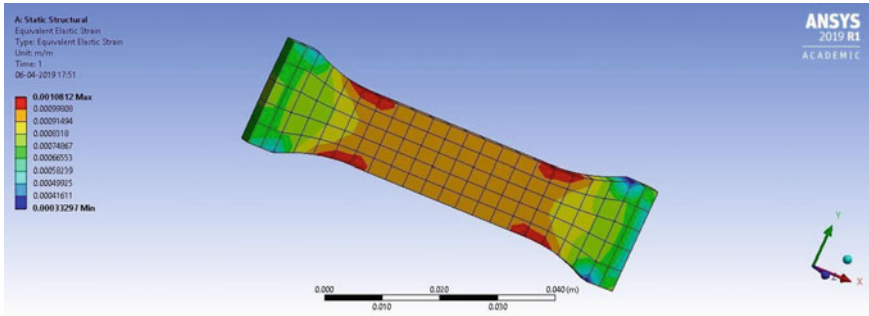


Fig. 9 Strain analysis for compressive load

Table 6 Strain values for different compressive loads

Layer thickness	Specimen	Load (N)	Strain
0.1	1	1214.06	0.0031
	2	1245.44	0.0032
0.3	1	246.78	0.00009
	2	241.61	0.00108

4 Experimental Validation

Tensile and compressive tests are performed using the Universal Testing Machine (UTM) and the data has been derived to obtain stress, strain values. The step by step procedures is carried out to obtain these results (Figs. 10, 11, 12; Table 7).

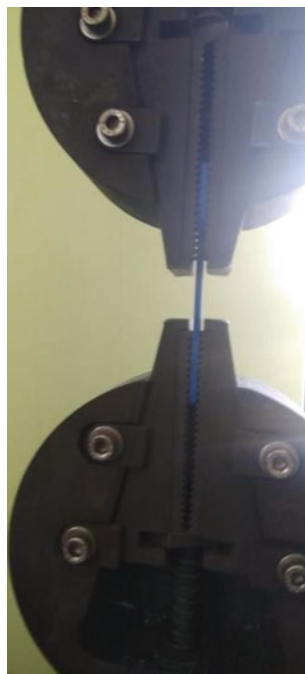
Following are the results observed for compression and tensile tests for different varied 3D printing parameters.

For 100% infill and 0.1 mm layer thickness Maximum tensile stress of 56.73 N/mm² and 51.21 N/mm² was found for a load of 1245.44 N in simulated conditions and UTM respectively. For 100% infill and 0.1 mm layer thickness Maximum tensile elastic strain of 2.58% and 14% is found for a load of 1245.44 N in simulated conditions and UTM respectively. For 100% infill and 0.3 mm layer thickness the Maximum tensile stress is 47.53 N/mm² and 42.90 N/mm² obtained for the load of 1043.33 N in simulated conditions and UTM respectively. For 100% infill and 0.3 mm layer thickness Maximum tensile elastic strain of 2.16% and 3.9% was observed for the load of 1043.33 N in simulated and UTM conditions respectively.

Fig. 10 Performing compression test



Fig. 11 Performing tensile test



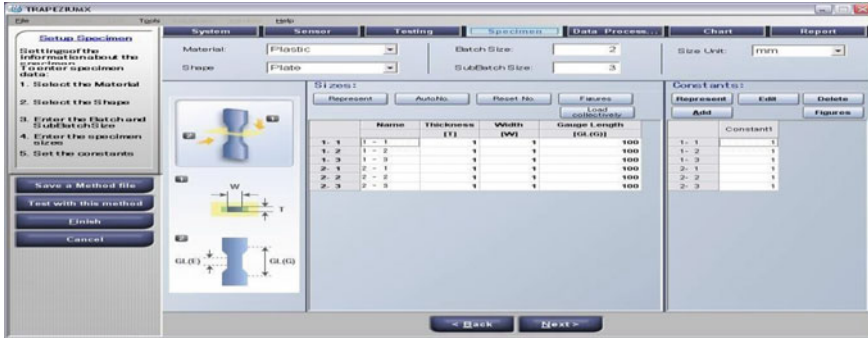


Fig. 12 Setting the test parameters in UTM

Table 7 Tensile test results

S. No	Results	Value
1	Area	24.3200 mm ²
2	Yield force	1148.76 N
3	Break force	1214.1 N
4	Tensile strength at yield	47.24 N/mm ²
5	Yield elongation	3.87 mm
6	Tensile strength at break	49.92 N/mm ²
7	Modulus of elasticity	402.04 N/mm ²
8	Tensile strength at max	49.92 N/mm ²
9	% elongation	12.37%
10	Break elongation	4.33 mm
11	Max force	1214.06 N
12	Max elongation	4.33 mm

The tensile strength of 51.21 N/mm² and 47.53 N/mm² obtained is similar to that of the results obtained by other researchers for the PETG material. The strain induced in the specimens during experimental test is higher when compared to that of simulated conditions. For 100% infill and 0.1 mm layer thickness Maximum compressive stress of 7.05 N/mm² and 7.73 N/mm² is found for a load of 246 N in simulation and UTM respectively. For 100% infill and 0.1 mm layer thickness Maximum deformation of 2.15 mm and 1.06 mm is attained for a load of 246.61 N under simulated and UTM testing’s respectively for compressive specimens. For 100% infill and 0.3 mm layer thickness Maximum compressive stress of 2.38 N/mm² and 2.61 N/mm² are found for a load of 83 N in simulation and UTM respectively (Tables 8, 9, 10, 11, 12, 13, 14 and 15).

There has been a clear decrease in the tensile strength of the components when there is a change in the %infill and the increase in layer thickness. The change has been gradual but not exponential.

Table 8 Results obtained for tensile test for 100% infill and 0.1 mm layer thickness

Parameters 100% infill 0.1 mm) (Units)	Maximum force (N)	Maximum stress (N/mm ²)	Maximum strain (%)
1	1245.44	51.21	13.14
2	1214.1	49.92	12.37
Mean	1229.77	50.57	12.76

Table 9 Results obtained for tensile test for 100% infill and 0.3 mm layer thickness

Parameters (100% infill 0.3 mm) (Units)	Maximum force (N)	Maximum stress (N/mm ²)	Maximum strain (%)
1	1043.33	47.53	12.64
2	995.37	40.73	15.09
Mean	1019.35	44.13	13.87

Table 10 Results obtained for tensile test for 50% infill and 0.1 mm layer thickness

Parameters (50% infill 0.1 mm) (Units)	Maximum force (N)	Maximum stress (N/mm ²)	Maximum strain (%)
1	857.1	35.24	14.06
2	937.5	38.55	11.31
Mean	897.3	36.90	12.69

Table 11 Results obtained for tensile test for 50% infill and 0.3 mm layer thickness

Parameters (50% infill 0.3 mm) (Units)	Maximum force (N)	Maximum stress (N/mm ²)	Maximum strain (%)
1	640.37	26.33	8.09
2	589.38	24.23	8.91
Mean	615.38	25.28	8.50

Table 12 Results obtained for compression test for 100% infill and 0.1 mm layer thickness

Parameter (100% infill 0.1 mm) (Units)	Maximum force (N)	Maximum displacement (mm)	Maximum stress (N/mm ²)
1	241.78	0.76	7.58
2	246.61	1.06	7.73
Mean	244.20	0.91	7.65

Table 13 Results obtained for compression test for 100% infill and 0.3 mm layer thickness

Parameter (100% infill 0.3 mm) (Units)	Maximum force (N)	Maximum displacement (mm)	Maximum stress (N/mm ²)
1	74.34	1	2.33
2	83.14	0.84	2.61
Mean	78.74	0.92	2.47

Table 14 Results obtained for compression test for 50% infill and 0.1 mm layer thickness

Parameter (50% infill 0.1 mm) (Units)	Maximum force (N)	Maximum displacement (mm)	Maximum stress (N/mm ²)
1	126.39	0.96	3.88
2	112.01	0.72	3.51
Mean	119.2	0.84	3.695

Table 15 Results obtained for compression test for 50% infill and 0.3 mm layer thickness

Parameter (50% infill 0.3 mm) (Units)	Maximum force (N)	Maximum displacement (mm)	Maximum stress (N/mm ²)
1	51.96	1.10	1.63
2	62.88	1.41	1.97
Mean	57.42	1.26	1.80

The order of tensile strengths obtained are:

$$50\% \text{ infill}(0.3 \text{ mm}) < 50\% \text{ infill} (0.1 \text{ mm}) < 100\% \text{ infill} (0.3 \text{ mm}) \\ < 100\% \text{ infill} (0.1 \text{ mm})$$

The order of compression strengths obtained are:

$$50\% \text{ infill}(0.3 \text{ mm}) < 100\% \text{ infill} (0.3 \text{ mm}) < 50\% \text{ infill} (0.1 \text{ mm}) \\ < 100\% \text{ infill} (0.1 \text{ mm})$$

Strength of the 3D printed PETG specimens are almost equal to conventionally produced specimens, we can use 3D printed PETG in place of conventional ones in food packaging industries, medical implants, etc. The tensile and compressive strength tests have been experimentally performed and the validation has been done using static structural analysis in ANSYS software. There will be a 10% error in the simulated values which are reflected in the final results. The experimental and simulated values are varied up to 5% (which is acceptable).

5 Conclusion

The attempt for evaluation of tensile and compressive strengths of the 3D printed specimens made from PETG material using the ASTM D638 and ASTM D695 standards is carried out. Based on this work the following conclusions have been drawn. In tensile testing maximum strength was found for 100% infill and 0.1 layer thickness. In compression testing, maximum strength was found for 100% infill

and 0.1 layer thickness. Validation of the experimental values is done using the ANSYS software and it was observed that ANSYS values and the experimental values obtained are very close and an error between 5 and 8% is observed. It was observed that layer thickness has more effect than infill percentage on mechanical properties of PETG. The PETG specimens can be tested for hardness, impact strength, flexural strength, etc. in future.

References

1. Karavaikin PA. The effect on mechanical performance of 3D printed polyethylene terephthalate glycol structures through differing infill pattern
2. Es-Said OS, Foyos J, Noorani R, Mendelson M, Macmoth R, Pregger BA (2000) Effect of layer orientation on mechanical properties of rapid prototyped samples. *Mater Manuf Process J* 5(1):107–122
3. <https://jps.library.utoronto.ca/index.php/cpoj/article/view/32038/24453>
4. Tymrak BM, Kreiger M, Pearce JM (2014) Mechanical properties of components fabricated with open-source 3D printers under realistic environmental conditions. *Mat Des J* 58:242–246
5. Ullu E, Korkmaz E, Yay K, Ozdoganlar OB, Kara LB (2015) Enhancing the structural performance of additively manufactured objects through build orientation optimization. *J Mech Des* 137:111410–111419
6. Joshi SC, Shcikh AA (2015) 3D printing in aerospace and its long-term sustainability. *Virtual Phys Prokityping J* 101175–101185
7. Yan Y, Li S, Zhand R, Lin F, Wu R, Lu Q, Xiong Z, Wang X (2009) Rapid prototyping and manufacturing technology principle, representative technics, applications, and development trends. *Tsinghua Science and Technology*, pp 1–12
8. Letcher T (2014) Material property testing of 3D printed specimen in PLA on an entry level 3D printer. *Int Mech Eng Congr Exposition Montreal IMECE* 2:1–8
9. Ramya A, Vanapalli SL 3D printing technologies in various applications. *Int J Mech*
10. Jaya Christiyam KG, Chandrasekhar U, Venkateswarlu K (2014) Influence of raster orientation and layer thickness on mechanical properties of ABS material using FDM process. *Int J Adv Res Sci Eng* 3:1–6
11. Mohamed OA, Masood SH, Bhowmik JL (2015) Optimization of fused deposition modeling process parameters: a review of current research and future prospects. *Adv Manuf* 3:42–53

Mechanical Behavior of Inconel 625 and 17-4 PH Stainless Steel Processed by Atomic Diffusion Additive Manufacturing



Balaji M. Jagtap, Ganesh M. Kakandikar, and Samidha A. Jawade

Abstract 3D printing or rapid prototyping are other terms for additive manufacturing (AM). AM is a technique that involves layering materials to create a three-dimensional object. AM is critical for producing complex geometric objects with high precision. The exponential development of additive manufacturing over the last decade has shown significant potential in cost-effective manufacture of high-quality product. It is difficult to produce superalloys like Inconel 625 using traditional methods, but it is much simpler with AM. Atomic diffusion additive manufacturing (ADAM), a layer-by-layer process for metals based on material extrusion, was recently patented by Markforged. An indirect additive production technique such as ADAM uses a metal powder filament encased inside a plastic binder. The plastic binder is separated after the fabrication of a green part by washing and sintering post-treatments. Fabrication of four separate standard tensile specimens for metal 17-4 PH stainless steel with different process parameters as well as four parts are printed for metal Inconel 625. The tensile test is carried on UTM with these eight parts. As a result, the weight reduction due to infill density is 20%, resulting in a loss of 10–15% of the part's strength, and the UTS of the part varies due to layer orientation.

Keywords Additive manufacturing · Markforged · Inconel 625 · 17-4 PH stainless steel · Metal X · Infill density

B. M. Jagtap (✉) · G. M. Kakandikar · S. A. Jawade
School of Mechanical Engineering, Dr. Vishwanath Karad MIT-WPU, Pune 411038, India

G. M. Kakandikar
e-mail: ganesh.kakandikar@mitwpu.edu.in

S. A. Jawade
e-mail: samidha.jawade@mitwpu.edu.in

1 Introduction

Additive manufacturing (AM) has evolved from the rapid prototyping industry during the last decade and is now widely recognized as a manufacturing option for a wide range of products. Due to its many possible advantages, such as more geometric flexibility, shorter design to product time, reduced process phases, part mass reduction, and material versatility, AM has gotten a lot of attention in the aerospace, automotive, and biomedical sectors [1]. As the advantages of AM are hoped to be exploited, an increasing number of businesses are expressing interest. For this to happen, extensive research into the microstructure and mechanical properties of engineering alloys is needed, from component manufacturing to post-processing procedures including finishing and heat treatment [2].

The amount of metal used on the inside of the print is determined by the infill density. A higher infill density indicates that more metal is present on the inside of the print, resulting in a more durable item. On both Inconel 625 and 17–4 PH SS parts, we used a 37% triangular infill density [3].

The aim of this research is to see how processing conditions, such as wall layer thickness as well as layer directions (orientation of print), influence the mechanical property (i.e., tensile strength) of printed materials. According to the research, only certain specimens with a thinner wall layer thickness and Z-orientation layer direction would have low mechanical properties.

2 Literature Review

This chapter provides a description of metal additive manufacturing (AM) as well as an introduction to superalloys in AM. Also, the introduction of the atomic diffusion additive manufacturing (ADAM) that process is based on the material extrusion additive manufacturing. This topic discusses the process parameters that influence the mechanical strength of ADAM manufactured components and also analyze tensile strength of parts with same process parameters with two different printing materials.

Out of the seven additive manufacturing processes following, five are used for metal AM.

- Binder Jetting;
- Sheet Lamination;
- Direct Energy Deposition;
- Powder Bed Fusion;
- Material Extrusion.

Binder Jetting: Binder jet additive manufacturing, also identified as “Powder bed and inkjet” or “drop-on-powder” printing, is a form of 3D printing that uses a binder jet. It is a fast prototyping and additive manufacturing technique for making objects from digital data like a CAD file [4].

Sheet Lamination AM: It is a solid-based metal additive manufacturing technique in which on the cutting bed metal sheet is fix, by using the adhesive, metal sheet is bonded in place on the previous layer. With use of laser beam, cut the metal sheet as required shape, and next layer is added. Layer lamination technique include laminated object manufacturing (LOM) and also ultrasonic consolidation (UC) [5].

Direct Energy Deposition (DED): It is one the type of metal 3D printing technology that objects are made by melting a powdered material or a wire with a concentrated energy source and depositing it on a surface with a nozzle. Although DED is used for create different part, it is most commonly used to repairing and reconstruct broken ones [6].

Powder Bed Fusion (PBF): It is a powder-based metal additive manufacturing technique that works on the same general concept as milling in that rather than subtracting material, parts are made by adding it. The PBF process starts with input 3D CAD model that is numerically cut into multiple distinct layers. Since the heat source is typically an energy beam, each layer has different scan path of heat source, which specifies the moving path of beam as well as the fill sequence, which is usually a contour pattern (e.g., laser beam).

After that, each layer is sequentially bound on top of the others. Powdered material is spread across the newly joined layer through PBF methods, preparing it for another next layer's application, resulting in isolated rather than continuous production (despite the fact that each layer is completely integrated to the layers above it). The powdered material fed into a hopper and then applied evenly on the powder bed creates powder layer by using roller or brush. Based on the manufacturing conditions and the materials used, the optimal thickness of each spreading powder layer varies, although values between 25 and 100 μm are common [7].

Material Extrusion: Material extrusion is a process of additive manufacturing in which to produce a 3D object, a continuous stream of material is pressed through a heated nozzle and selectively added layer by layer [8]. Fused filament fabrication (FFF) is one technique, and fused deposition modeling (FDM) is another material extrusion technique.

Atomic Diffusion Additive Manufacturing (ADAM): This is metal AM technique recently invented by the Markforged which is completely based on a material extrusion additive manufacturing. A wire is composition of metal powder and plastic binder used in an indirect additive manufacturing procedure known as ADAM [9]. After printing of green part, next step is removing plastic binder from the green part by post-treatments such as washing and sintering which is shown in Fig. 1. In this, study is to characterize the ADAM process using the Markforged Metal X printer [8].

From above literature survey, we can conclude that atomic diffusion additive manufacturing process is completely new in metal additive manufacturing. As research point of view, this area has wide scope for new researcher because initially material extrusion AM process is only use for polymer, but Markforged Metal X has invented new technique for metal printing also.

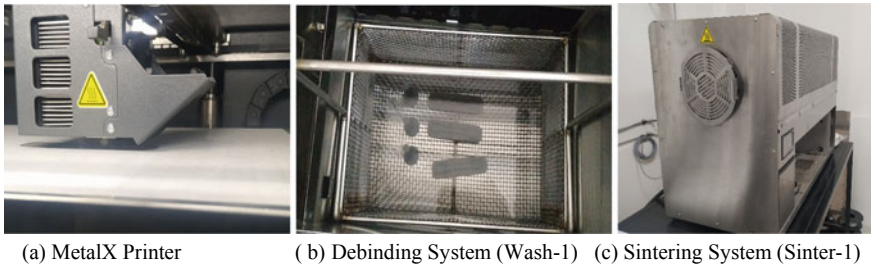


Fig. 1 Three Stages of Markforged Metal X printer

Objective of this study is finding the optimum value of the process parameter to increase the mechanical strength of the printing component. Since Inconel 625 and 17-4 PH stainless steel alloys are used in aerospace applications, it is crucial to minimize weight without compromising the part's strength (using triangular infill parameter in AM).

3 Materials and Methods

3.1 Material and Equipment

Inconel 625 is a nickel-based superalloy [10] that gets its strength from the refractory metal's niobium and molybdenum solid-solution hardening in a nickel–chromium matrix [11]. With superior strength at high temperatures, the alloy is highly resistant to heat, corrosion, wear, fatigue, and also good weldability [12].

Markforged has patented the Metal X printer for metal additive manufacturing. Input form of metal alloy in the MetalX printer is required in wire form and which has following composition, i.e., Inconel 625 and 17-4 PH SS material are given in Table 1 [13] and Table 2 [14], respectively.

The machine's building dimension are height 300 mm, length 220 mm, and width 180 mm. But the largest component size which can be installed with dimension of height 250 mm, length 183 mm, and width 150 mm only. At the start of each task top surface of the build plate, vacuum-sealed sheet is mounted to aid in product adhesion during installation and detachment at the end. Design of leveling mechanism and base of building such that it can sustain maximum load of 10 kg. During the printing of part, both building base and complete chamber are heated. The printed part from this process is known as green part.

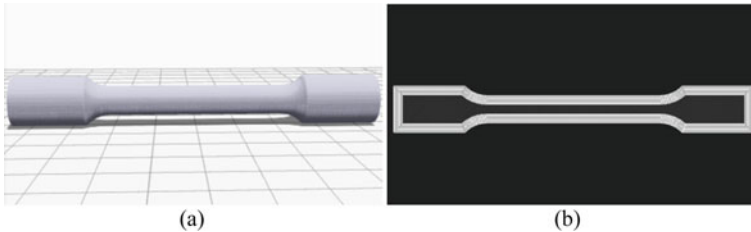
As a debinding method, it is second most important step in ADAM, for that Markforged WASH-1 was used. The washing vat volume is $356 \times 254 \times 203 \text{ mm}^3$ with Opteon Sion as the washing solvent.

Table 1 Inconel 625 Supper alloy composition

Cr	Mo	Fe	Nb	Co	Mn	Si	Al	Ti	C	P	S	Ni
20-23%	8-10%	5%	3.15-4.15%	1%	0.5%	0.5%	0.4%	0.4%	0.1%	0.015%	0.015%	Bal

Table 2 17-4 PH stainless steel composition

Cr	Ni	Cu	Si	Mn	Nb	C	P	S	Fe
15–17.50%	3–5%	3–5%	1% max	1% max	0.150–0.450%	0.070% max	0.040% max	0.030% max	Bal

**Fig. 2** Eiger software: The tensile specimen CAD file, **a** part view and **b** internal view

The sintering process is last step of ADAM process. It was completed in a Mark-forged Sinter-1 furnace. It can reach temperatures of 1300°C and inside of chamber, inert gas, i.e., argon (Ar) and nitrogen (N), is used for operating an inert environment. The cylindrical chamber has dimensions which is a length of 305 mm and diameter of 141 mm [8].

Eiger Software: Eiger, a proprietary software, automatically designs the size of the component and process parameters. Eiger is a CAM program that controls the whole operation, from architecture to sintering. The user's access to the app has been disabled. As a result, the process parameters are unknown and cannot be changed by the operator, with the exception of the layer thickness, which represents the machine's resolution. The final geometry to be printed is then given, as well as the minimum time needed for polymer debinding. Figure 2(a) shown is part view which is uploaded STL file format of Tensile specimen in Eiger software, and Fig. 2(b) shows that internal view of tensile specimen in which we get total time required for printing green part, etc.

3.2 Metal 3D Printing of Specimen with Its Geometrical Configuration

The dimensions of all eight tensile specimens were the same. The schematic diagram of the E8 standard tensile specimen is shown in Fig. 3.

Fig. 3 E8 standard tensile specimen

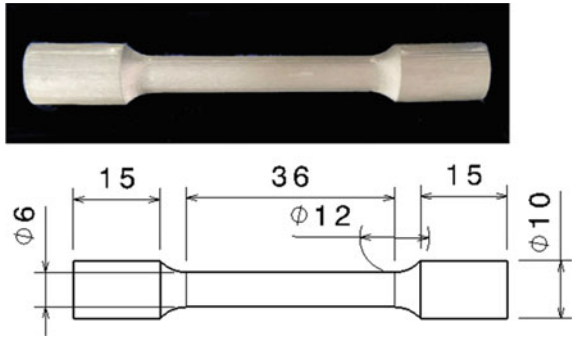


Table 3 Process parameters

Sr. no	Process parameter	Level 1	Level 2
1	Wall layer (mm)	1.00 (4 Layer)	1.99 (8 Layer)
2	Infill density (%)	37	100

Table 4 Experimental combination

No. of experiment	Infill density (%)	Orientation	Wall layer (mm)
1	37	X	1.00
2	37	X	2.00
3	100	X	2.00
4	100	X	1.00

3.3 Printing/Experimental Setup

Varying process parameter like wall layer thickness (mm) and infill density (%) with two level of value which is given in Table 3. For that, two process parameters and level of value, we get four different possible experimental combination which is given in Table 4.

For, wall layer 1 mm thickness (4 layer) = Roof and floor 1 mm thickness (8 layer), and wall layer 1.99 mm thickness (8 layer) = Roof and floor 1.99 mm thickness (16 layer).

3.4 Component Failed in Z-Orientation

Table 4 shown four different experimental combination for all X-orientation that we had printed successfully, but all similar four parts of Z-orientation are failed due low strength of green part in sintering process.

To overcome this problem, we added extra support which is shown in Fig. 5. But still, all part fails during sintering.

4 Result and Discussion

After completion of printing, we go for tensile testing of eight parts in which four are 17-4 PH SS and other are Inconel 625. Printed all parts E8 std. tensile specimen which is shown in Fig. 4. These parts are printed with different process parameter and different level of value as per Table 3.

4.1 Tensile Testing

All tensile sample are tested on UTM which has maximum load capacity that is 100KN is shown in Fig. 6 and the tensile properties of specimens fabricated by ADAM with various experimental parameters are given in Table 4. As a result, obtained in tensile testing, the tensile strength and yield strength vary with different process parameters change like infill density and wall layer (Table 5).

Part no. 01 Inconel 625 (solid infill and wall layer 1 mm) and part no. 02 Inconel 625 (solid infill and wall layer 2 mm) have almost the same volume of material, but the wall layer affects the tensile strength, which is 777.844 MPa and 768.79 MPa, respectively, and yield strength, which is 365.986 MPa and 615.011 MPa.

In Part no. 3 and 4 which is Inconel 625 (37% infill density and wall layer 1 mm) and Inconel 625 (37% infill density and wall layer 2 mm), tensile test result is



Fig. 4 Printed tensile specimens for mechanical investigations with two different metals: **a** Inconel 625, **b** 17-4 PH SS

Fig. 5 Printed green Z-orientation part with different support



Fig. 6 Tensile testing performed on M100 UTM

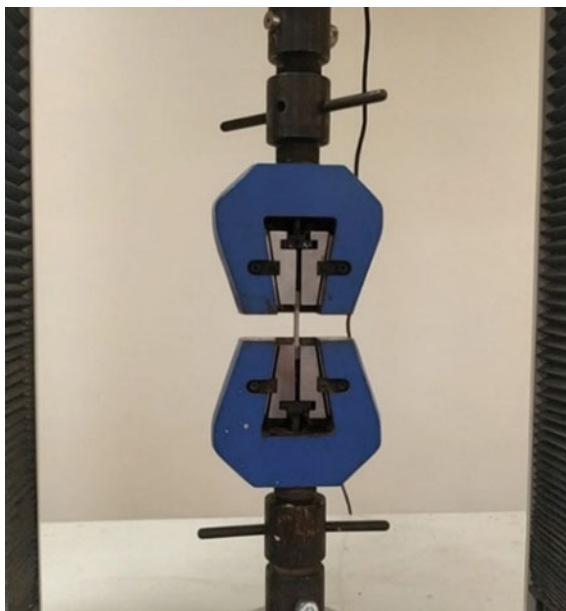


Table 5 Comparison of tensile properties of Inconel 625 and 17-4PH SS parts

Part no	Tensile specimen	Tensile strength (MPa)	Yield stress (MPa)	% Reduction area	% Elongation	Load at peak (KN)	Elongation at peak (mm)
1	Inconel 625 100% 1 mm	777.844	365.986	21.97	38.57	21.993	22.113
2	Inconel 625 100% 2 mm	768.79	615.011	19	23.75	21.737	15.51
3	Inconel 625 37% 1 mm	332.952	166.618	3.31	11.64	9.414	11.079
4	Inconel 625 37% 2 mm	524.717	327.364	3.31	16.48	14.836	10.846
5	17-4PH SS 100% 1 mm	1049.964	837.12	3.31	7.99	29.687	7.294
6	17-4PH SS 100% 2 mm	1077.232	861.135	3.31	4.29	30.458	7.524
7	17-4PH SS 37% 1 mm	531.154	424.803	3.31	8.94	15.018	4.78
8	17-4PH SS 37% 2 mm	896.008	715.031	3.31	2.13	25.334	6.531

332.952 MPa and 524.717 MPa and also yield strength changes to 166.618 MPa to 327.364 MPa. Percentage reduction area of solid infill part is part no. 1 and 2 which is more compared to all other part. And the graph obtained for material 17-4 PH stainless steel is same pattern, but strength is higher than Inconel 625; these are shown in Fig. 7.

5 Conclusion

In this paper, the ADAM process was used to test the tensile strength of Inconel 625 and 17-4 PH stainless steel. For the experiment, two process parameters with two levels of value are selected. There are four possible experimental combinations based on the two process parameters and two levels of value. The first four parts were printed with Inconel 625 material, and the second four parts were printed with 17-4 PH stainless steel. Tensile testing is done on eight printed components. The following conclusions were drawn from tensile testing results.

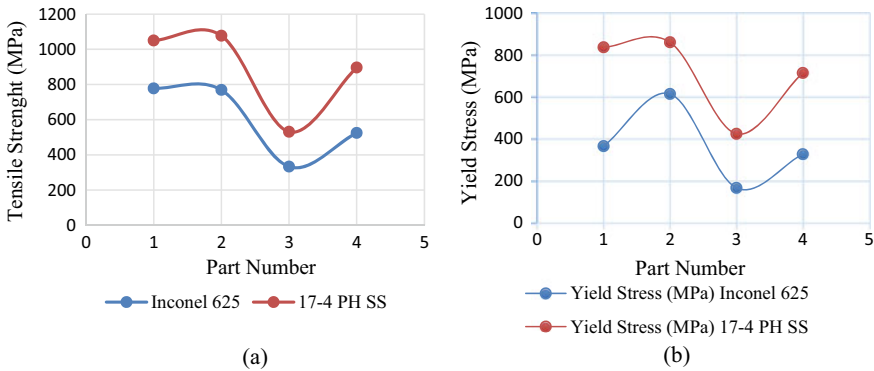


Fig. 7 Results: **a** UTS versus part number and **b** yield Stress versus part number of the Inconel 625 and 17-4PH SS parts

- The specimens were printed with two different wall layer thicknesses. According to the study, the layer thickness has a significant effect on the mechanical properties of the printed element.
- As a result, the part’s weight is reduced by 20% due to infill density, resulting in a loss of 10–15% of its strength, and the part’s UTS varies due to layer orientation.
- Low mechanical properties can only be seen in specimens with a thinner wall layer and Z-orientation (layer direction) parts.

References

1. DebRoy T, Wei HL, Zuback JS, Mukherjee T, Elmer JW, Milewski JO, Beese AM, Wilson-Heid A, De A, Zhang W (2018) Progress in materials science additive manufacturing of metallic components—process, structure and properties. *Prog Mater Sci* 92:112–224
2. Mohanavel V (2020) Mechanical and microstructural characterization of AA7178-TiB2 composites. *Mater Test* 62(2):146–150
3. Lieberwirth C, Sarhan M, Seitz H (2018) Mechanical properties of stainless-steel structures fabricated by composite extrusion modelling. *Metals* 8(2). <https://doi.org/10.3390/met8010084>
4. Yusuf SM, Cutler S, Gao N (2019) Review: the impact of metal additive
5. Alghamdi SS, John S, Choudhury NR, Dutta NK (2021) Additive manufacturing of polymer materials: progress, promise and challenges. *Polymers*. <https://doi.org/10.3390/polym13050753>
6. Gibson I, Rosen D, Stucker B (2015). Directed Energy Deposition Process. https://doi.org/10.1007/978-1-4939-2113-3_10
7. Wang YC, Lei LM, Shi L, Wan HY, Liang F, Zhang GP (2020) Scanning strategy dependent tensile properties of selective laser melted GH4169
8. Galati M, Minetola P (2019) Analysis of density, roughness, and accuracy of the atomic diffusion additive manufacturing (ADAM) process for metal parts. *Materials*. <https://doi.org/10.3390/ma12244122>

9. Kurose T, Ishigami A, Abe Y, Santos M, Tanaka S, Ito H (2020) Influence of the layer directions on the properties of 316L stainless steel parts fabricated through fused deposition of metals. *Materials*. <https://doi.org/10.3390/ma13112493>
10. Kotzem D, Beermann L, Awd M, Walther F (2019) Mechanical and microstructural characterization of Arc-welded Inconel 625 alloy. *Materials* 12(22). <https://doi.org/10.3390/ma12223690>
11. Gonzalez JA, Mireles J, Sta SW, Perez MA, Terrazas CA, Wicker RB (2019) Characterization of Inconel 625 fabricated using powder-bed-based additive manufacturing technologies. *J Mater Process Technol* 264:200–210
12. Yangfan W, Xizhang C, Chuanchu S (2019) Microstructure and mechanical properties of Inconel 625 fabricated by wire-arc additive manufacturing. *Surf Coat Technol* 374:116–123
13. Markforged. Inconel 625 material datasheet. Available online: <https://static.markforged.com/downloads/Inconel-625.pdf>. Accessed 26 May 2021
14. Markforged. 17-4 PH stainless steel material datasheet. Available online: https://static.markforged.com/downloads/markforged_datasheet_17-4_ph_stainless_steel.pdf. Accessed 26 May 2021

Mechanical Behavior of Nylon Load Bearing Structures Fabricated by Fused Deposition Modeling



Sanket S. Jagtap, Ganesh P. Borikar, and Snehal B. Kolekar

Abstract Fused deposition modeling (FDM) is an additive manufacturing (AM) technique used to create complex models, parts for demonstration and operational components/products. In FDM, process control parameters have a significant impact on the mechanical properties of the components produced. Layer thickness, infill density and raster angle are the control parameters investigated in current research. The mechanical behavior of the FDM component are evaluated using tensile and flexural strength as touchstones in this paper. The Taguchi design was used to ensure the desired process parameters for the production of Nylon material parts. The process parameters are analyzed using orthogonal array, primary effect, signal to noise ratio (S/N) along with analysis of variance (ANOVA) methods. Flexibility and durability of Nylon helps in obtaining thin walls with strength in 3D printing objects. Its low friction coefficient with a high melting point makes it extremely abrasion resistant and allows components such as practical interlocking gears to be used in printing.

Keywords Additive manufacturing (AM) · Process parameters · Taguchi methodology · (S/N) ratio · Analysis of variance

1 Introduction

The growth of a country depends heavily on its manufacturing sector. Manufacturing sectors are driving economic strength. The core technology methods used in manufacturing are Subtractive, Formative, and Additive. The finished product is produced

S. S. Jagtap (✉) · G. P. Borikar · S. B. Kolekar
School of Mechanical Engineering, Dr. Vishwanath Karad MIT-World Peace University, Pune,
India

e-mail: 1032181749@mitwpu.edu.in

G. P. Borikar
e-mail: ganesh.borikar@mitwpu.edu.in

S. B. Kolekar
e-mail: snehal.kolekar@mitwpu.edu.in

by extracting material from the raw material, known as subtractive processing. The finished product is produced with the help of the punch and die system in formative production. Raw material is added/deposited in successive layer patterns in additive manufacturing to create the finished product. In the last decade, the advancement of additive manufacturing (AM) technologies has seen rapid growth. Additive development is collaboratively formed by layer construction of a part derived directly from its 3D CAD model and using various operations and processes. Laser sintering, stereolithography, laminated manufacturing and extrusion modeling, are some of the preferred methods that are part of additive manufacturing. AM may be used for the manufacture of components on any production scale, i.e., customized production, along with both batch and mass production. AM is used in nearly all major fields, such as aerospace, healthcare, education, engineering, and machinery. FDM makes use of content extrusion. The material is heated to the point that it begins to melt, depositing the semi solid material through a printing nozzle/head on the print bed. The deposited material quickly settles and cools down. The expected component is generated by such successive layers. In FDM, products with strong plasticity, such as polylactic acid (PLA), nylon, and polycarbonate are preferred.

FDM's machine set-up is streamlined and lightweight. One can also set-up FDM machines on a small surface area. The management of its set-up is simplified one. The print head, which is motor driven, has the freedom to travel vertically and horizontally while the print head/tool route is programmed by a CAM software. FDM uses much less time needed for new design and development lead time, so it is very easy to introduce new customized models and produce finished components. The operation is noiseless and clean; as modern printing machines use advanced technology based print head along with other elements. It results in very less amount of material wastage during printing of component.

2 Literature Review

Raney et al. [1] worked to find a mesostructure specimen effect on categoric tensile performance for FDM manufactured ABS components. Infill percentage and orientation of the parts, parameters were considered for study. They found that the direction of construction has a strong impact on power when the outputs are calculated in terms of mechanical strengths. The sample strength measured along the layers is greater than the sample strength tested against the layers. The inconsistency in strength is due to weak layer bonding.

Rahman et al. [2] investigated the impact of six parameters [2] on the dimension-accuracy and surface roughness of FDM-fabricated parts. Material used for testing is ABS and the following process parameters are taken into consideration: nozzle and bed temperature, print velocity, density of infill, layer height along with loop count. The machine used is an AHA 3D Innovations Proto Center 999 from India. The program used is KISSlicer PRO. The measurements of the fabricated parts are determined by CMM. Surface roughness is determined using SURFTEST SJ10. The

Taguchi technique is used to schedule experiments. In the parts generated by using the scaling factor, better accuracy was found.

Alafaghania et al. [3] studied the effect of process regulating parameters on the repeatability of dimensional accuracy as well as the strength attributes of manufactured components. For the manufacturing of experimental components, PLA material is used. Layer height, extrusion temperature, and build temperature process parameters are studied during research. In the form of dimensional precision and mechanical properties, the results are obtained. They concluded that better dimensional accuracy results in lower extrusion temperature and layer height.

The optimization methods, for determining optimum process parameters were analyzed by Mohamed et al. [4]. The environment in which FDM operations take place is critical for improving dimensional accuracy along with surface roughness; mechanical strength properties, material behavior and production time. Different papers have been analyzed in which the above parameters are investigated and the review is presented. Here they addressed how the dominant optimization approaches are the Taguchi technique and ANOVA procedure. The Taguchi method was applied to find best concoction of process parameter levels, with their interaction impacts on the components produced. The Taguchi Design method can be used to effectively optimize FDM process parameters. Taguchi method can be used to improve product quality while keeping costs low. The Taguchi technique is easy, dependable, and efficient. The Taguchi method allows for a reduction in the number of experiments. Taguchi method will increase the product's quality at a low cost. The ANOVA method provides the necessary process parameters.

The techniques for printing polymer composites using FDM technology were investigated by Bryll et al. [5]. The fact finding primarily refers to the printing of preliminary and composite filaments. It shows that, compared to composites produced by regular methods, manufacturing the components with 2 heads shows inferior mechanical properties.

Wang et al. [6] explored the synopsis of AM methodologies and properties for polymer composite materials. The performance and possible application of AM printed components in fields such as biomedical, electronics and aerospace engineering are also included. Particle Reinforced Composites (Barium titanate + ABS, ABS + TPE), Fiber Reinforced Polymer Composites (Carbon Fiber + ABS, PLA + Carbon Fiber), Nanocomposites are the forms of composites illustrated in the paper (Carbon Nanotubes, Graphene, Graphite, Ceramics, and Metal Nanoparticles). The scaffolds were often prepared by combining polymer matrix with blended TCP or HA to improvise the power of the scaffolds.

If the polymer matrix is combined with electrically conductive material, it can be used in electronic devices such as piezo-resistive sensors and capacitive sensors. The existence of void in printed parts is used to justify poor mechanical performance. Due to poor interfacial bonding with the matrix, additional reinforcement will result in porosity. No guarantee is provided as to the reproducibility and stability of the parts produced by AM. The construction area of the FDM machine is small, so the development of large volume components is difficult.

On the basis of mechanical evidence, Bagsik et al. [7] examined the effect of construction direction and studied the formation of toolpaths for manufactured components. Polyetherimide (Ultem*9085) material is used in present case. By utilizing a negative raster air gap for all the orientations, the best results were achieved. The mechanical properties of FDM test pieces built up were investigated depending on the build orientation.

In current research, the process parameters and material were finalized from the literature analysis. Ultimaker nylon material is chosen for testing because there is much less research work done on it. The study is performed to find mechanical behavior of nylon part. The analysis of important process parameters and the final combination of optimized process parameter configuration were obtained in this paper to increase tensile strength and flexural strength.

3 Taguchi Method

This approach offers a versatile design in which the performance not only falls within the parameters, but also powerful. The Taguchi process flow is defined as in Fig. 1.

Taguchi notes that when the production moves away from the average, the consumer often loses. This is done not only by modeling the controllable variables as in standard DOE, but also the “uncontrollable” variables. This leads to:

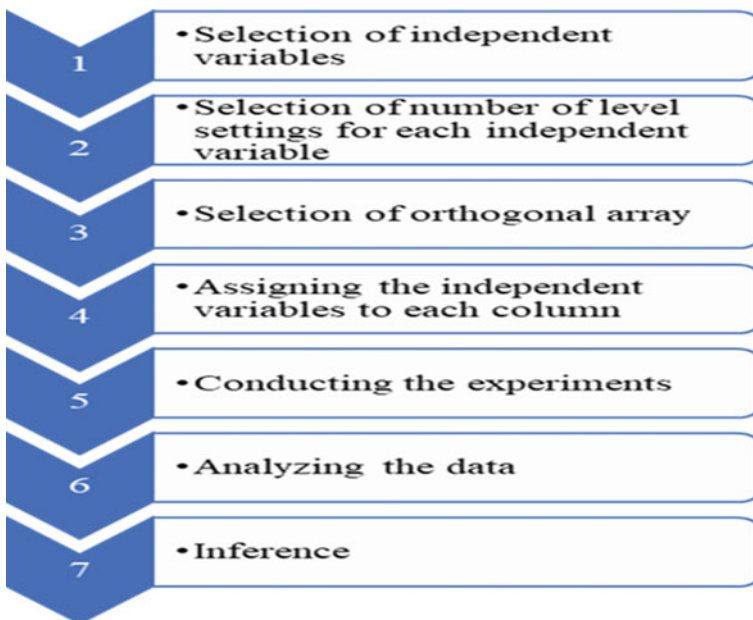


Fig. 1 Taguchi method steps [10]

- The aim of the design is to get the best possible correlation between the output feedback and the input signal parameter.
- Taguchi’s method employs orthogonal arrays to produce the best results with the fewest trials at the lowest expense (The concept of Orthogonal Arrays was first initiated by CR Rao in 1947).

The Experimental Research Approach is consists of following two steps i.e. process parameter selection and experiment specimen preparation. Here most affecting process parameters were taken into consideration to manufacture the specimen and in second step the standard test specimen’s preparations were performed.

3.1 Process Parameter Selection

Slicing of CAD modeled components was done with the Ultimaker Cura 4.5 software. Table 1 shows the 3 control parameters (layer height, infill density, and raster angle) that were taken into account for investigation purpose and each of which has three levels. The Ultimaker Cura software interface and a raster angle as 0°/90° in the specimen is as shown in Fig. 2.

The setting’s temperature and humidity are maintained at a constant level. When selecting an orthogonal series for the tests, the cumulative degrees of freedom is the most important thing to note. Degrees of freedom (DOF) are distinctions between process criteria that must be made to determine which degree is superior to others and by how much. A method parameter with three stages has 2 DOF. An overall DOF are calculated as follows:

$$\text{Total DOF} = \text{DF} \times n$$

where, DF = DOF of each control parameter, n = Number of parameters.

As a result, this experimentation has three control parameters, each with 2 DOF, totaling 6 DOF. According to a basic theorem, the number of DOF for the orthogonal sequence should either be \geq the number of method parameters. The standard L9, which has 3 columns and 9 rows, was simply the better orthogonal array in present study. The L9 orthogonal array used in this study is shown in Table 2.

Table 1 FDM control parameters with levels (L1, L2, L3)

Control parameter	Symbol	Units	L1	L2	L3
Layer thickness	A	mm	0.1	0.2	0.3
Infill density	B	%	20	60	100
Raster angle	C	°	0/90	± 45	30/60

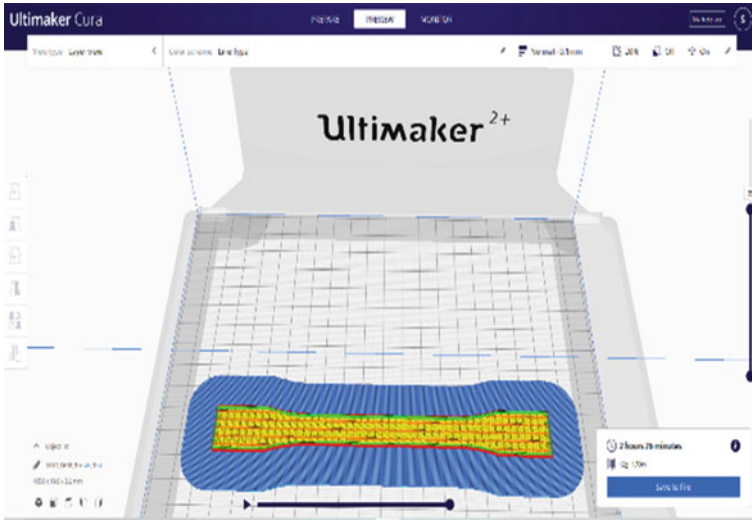


Fig. 2 Ultimaker Cura 4.5 Interface

Table 2 L9 orthogonal array experimental layout [10]

No. of experiment	A	B	C
1	1	1	1
2	1	2	2
3	1	3	3
4	2	1	2
5	2	2	3
6	2	3	1
7	3	1	3
8	3	2	1
9	3	3	2

3.2 Experiment Specimen Preparation

The specimen section is designed as per ASTM standards for tensile strength and flexural strength [9] analysis. The components' CAD models are created in Autodesk Fusion 360 and translated to .stl files, which are then imported into the Ultimaker Cura 4.5 slicing software to create "G code" files for the FDM machine. The FDM Printer Ultimaker 2+ is used to make the specimens for each experiment and the filament pool used for experimentation components is Nylon. Nylon's material properties are mentioned in Table 3.

Table 3 Nylon [8] material properties

Material Property	Unit	Values
Specific gravity	–	1.14
Tensile modulus	MPa	579
Tensile strength	MPa	27.8
Flexural modulus	MPa	463.5
Flexural strength	MPa	24
Elongation at yield	%	20
Melt mass-flow rate (MFR)	g/min	6.2/10
Thermal shrinkage	%	12 ± 2

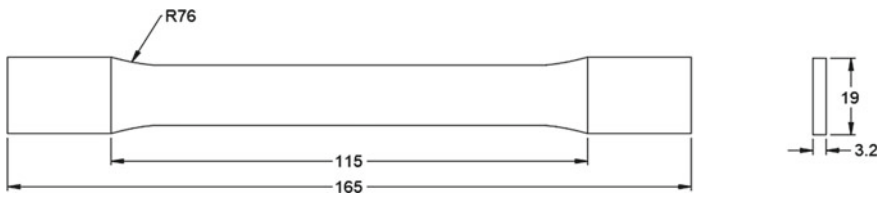


Fig. 3 Specimen 1

3.2.1 Tensile Strength Experiment Specimen

Schematic diagram and dimensions of tensile strength component (Specimen 1) are shown in Fig. 3. ASTM D638 standard is followed for designing experimentation component.

3.2.2 Flexural Strength Experiment Specimen

The recommended illustrational details of the flexural test component (Specimen 2) is shown in Fig. 4. The ASTM D790 standard is used to design the experimentation component.

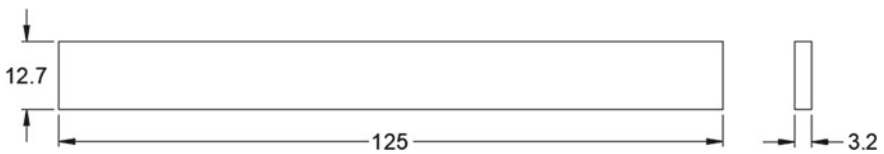


Fig. 4 Specimen 2

4 Results and Discussion

The outcomes were obtained by experimenting all the nine test components for Tensile strength and Flexural strength obtained (Figs. 5 and 6). Every component manufactured represents each experiment as per orthogonal array (Table 2). The tensile strength and flexural strength of the components obtained during its performance test are shown in Table 4. The findings were then analyzed using main effects, analysis of variance and signal to noise (S/N) ratio measurements, all of which were performed using MINITAB tools.

4.1 Tensile Strength

4.1.1 Analysis of Variance (ANOVA)

ANOVAs judge the significance of 1 or more factors by comparing the output variable means at the different parameter levels. The null conjecture states that all factor level means are same while the alternative conjecture states that at least one is different.

An ANOVA is only possible if a continuous feedback variable is available and at least one categorical parameter with 2 or more levels. The neighborhood of normally distributed populations with similar variances between parameter levels are required for ANOVAs. The P value is observed in ANOVA tables which indicates the significance of the process parameters in the specimen. Whichever process parameter has the P value less than 0.05 it is considered most effective.

The infill density is more effective in this case. In Table 5, ANOVA output is illustrated.

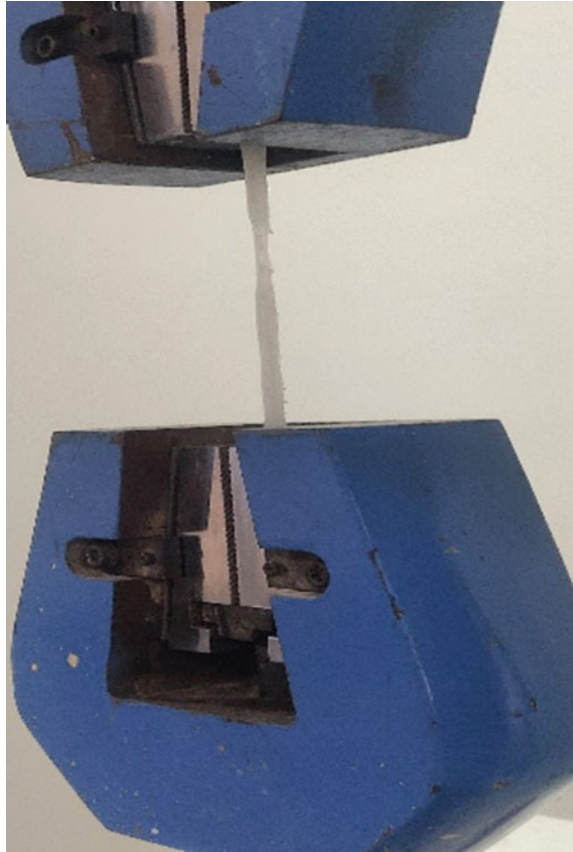
Where, DF and Seq SS are Degree of freedom and Sequential sums of squares, respectively.

Whereas Adj SS and Adj MS are Adjusted sums of squares and Adjusted mean square.

Table 4 Tensile strength and flexural strength obtained during experimental test runs

Experiments	Tensile strength (MPa)	Flexural strength (MPa)
1	16.407	21.128
2	24.762	17.349
3	32.833	21.456
4	15.969	20.187
5	17.882	14.257
6	24.613	15.695
7	9.588	22.762
8	12.291	13.436
9	22.841	17.218

Fig. 5 Tensile strength testing



$F = \text{variation between sample means} / \text{variation within the samples}$

The p -value is a probability that indicates how strong the proof is against the null hypothesis. Lower possibilities indicate that the null statement is more likely to be true.

4.1.2 Signal to Noise Ratio

The S/N ratio is a robustness parameter that can be used to determine control parameter settings that minimize noise's influence on performance. In the Taguchi design, Minitab calculates an individual S/N ratio for each concoction of control parameter stages. In each and every case, the maximization of the S/N ratio is considered. There are four kinds of S/N ratios MINITAB provides: Larger is better, two Nominal is best ratios and, Smaller is better. For tensile strength and flexural strength, larger is better criteria is selected.

Fig. 6 Flexural strength testing

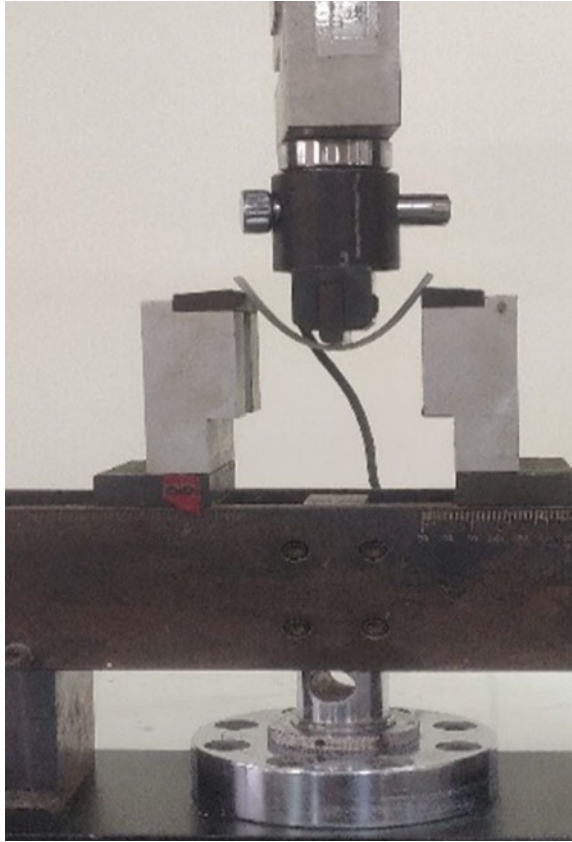


Table 5 ANOVA output

Source	DF	Seq SS	Adj SS	Adj MS	F	p
Laser thickness	2	143.774	143.774	71.887	56.91	0.017
Infill density	2	253.491	253.491	126.745	100.35	0.010
Raster angle	2	18.595	18.595	9.298	7.36	0.120
Residual error	2	2.526	2.526	1.263		
Total	8	418.386				

A general precept by using base 10 log for the condition larger is better S/N ratio is:

$$\text{Signal to Noise Ratio} = -10 * \log(\Sigma(1/Y^2)/n)$$

where Y = Value of i th experiment and n = Number of parameters.

Table 6 Responses of S/N ratios

Level	Layer thickness	Infill density	Raster angle
L1	27.50	22.67	24.62
L2	25.65	24.89	26.37
L3	22.85	28.44	25.00
Delta	4.65	5.77	1.75
Rank	2	1	3

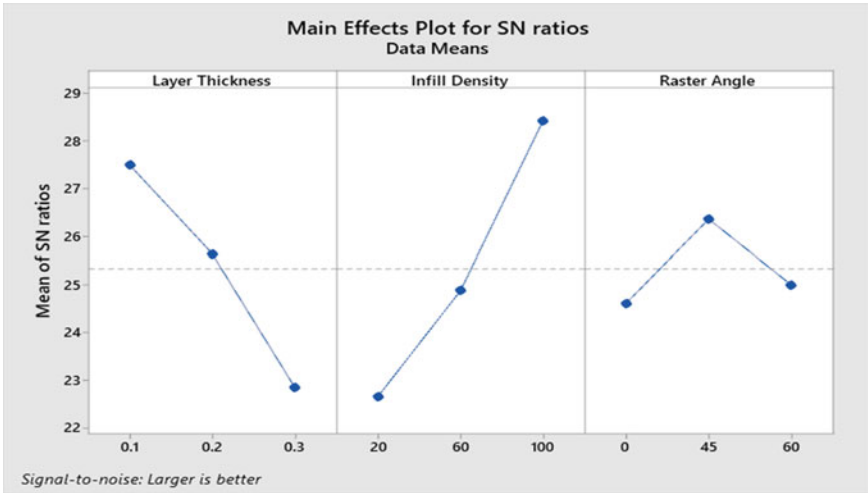


Fig. 7 Tensile strength MEP of S/N Ratios

Table 6 contains a response table of S/N ratios. Figure 7 shows a main effect plot (MEP) with S/N ratios. The highest value is chosen from the S/N ratio plots. From the response table, it is also observed and checked.

From Table 6 and Fig. 7, it can be found that layer thickness and infill density are the significant parameters that affect the tensile strength. Therefore, based on the S/N and ANOVA analyses, the optimum parameters for Tensile strength are layer thickness at level 1, the infill density at level 3, and raster angle at level 2.

4.1.3 Results

In case of tensile strength combination lesser layer thickness, higher infill density are considered. Process parameter settings are tabulated as shown in Table 7.

Table 7 Control parameters settings

Control parameters	Unit	Settings
Layer thickness	mm	0.1
Infill density	%	100
Raster angle	°	45/−45

Table 8 ANOVA output

Source	DF	Seq SS	Adj SS	Adj MS	<i>F</i>	<i>p</i>
Layer thickness	2	16.570	16.570	8.2851	8.81	0.102
Infill density	2	60.397	60.397	30.1983	32.13	0.030
Raster angle	2	11.284	11.284	5.6419	6.00	0.143
Residual error	2	1.880	1.880	0.9399		
Total	8	90.130				

4.2 Flexural Strength

4.2.1 Analysis of Variance (ANOVA)

The infill density is more effective in case of flexural strength. The ANOVA for flexural strength in Table 8 illustrates this.

4.2.2 Signal to Noise Ratio (S/N)

Table 9 contains a response table of S/N ratios. Figure 8 as MEP for S/N Ratios. The highest value is chosen from S/N ratio plots. From the response table, it is also observed and checked.

From Table 9 and Fig. 8, it can be observed that layer thickness and infill density are the significant parameters which affect flexural strength. Therefore, as per S/N and ANOVA analysis, the optimum parameters for flexural strength are layer thickness at level L1, the infill density at level L1, and raster angle at level L3.

Table 9 Response table of S/N Ratios

Level	Layer thickness	Infill density	Raster angle
1	25.97	26.58	24.33
2	24.37	23.48	25.20
3	24.81	25.09	25.62
Delta	1.61	3.10	1.29
Rank	2	1	3

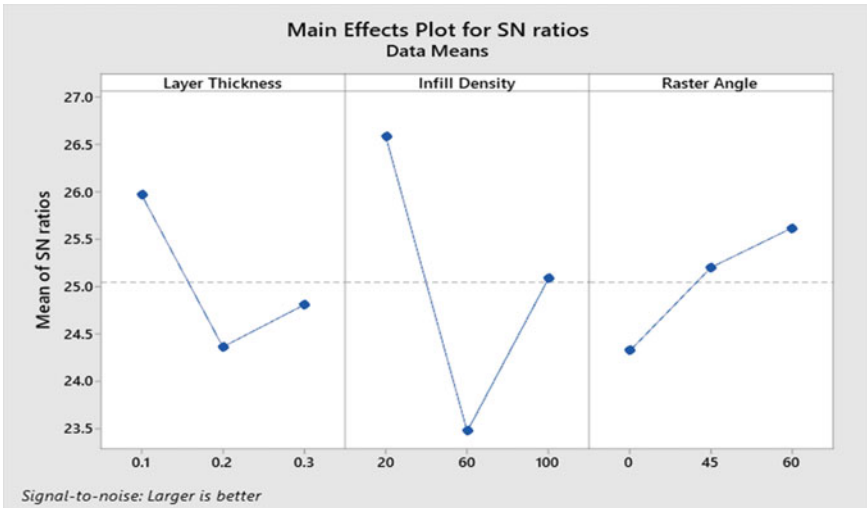


Fig. 8 Flexural Strength MEP of S/N Ratios

Table 10 Control parameters settings

Control Parameters	Unit	Settings
Layer thickness	mm	0.1
Infill density	%	20
Raster angle	°	30/60

4.2.3 Result

In case of flexural strength combination lesser layer thickness, lesser infill density are considered. Process parameters settings are tabulated in Table 10.

5 Conclusions

Experimental investigation was performed for finding out significant process parameters and its optimum combination for maximum tensile and flexural strength of components. The Nylon material components printed by FDM leads to following conclusions.

- Infill density has significant impact in case of tensile as well as flexural strength.
- In relation with tensile and flexural strength, layer thickness acts as is second important parameter.
- Raster angle has negligible impact in case of both, i.e., tensile and flexural strength.

- The highest tensile strength (32.833 MPa) is obtained by 0.1 mm layer thickness, 100% infill density and 45/–45-degree raster angle.
- The highest flexural strength (22.762 MPa) is obtained by 0.3 mm layer thickness, 20% infill density and 30/60-degree raster angle.

References

1. Raney K, Lani E, Kalla DK (2017) Experimental characterization of the tensile strength of ABS parts manufactured by fused deposition modeling process. *Mater Today Proc* 4(8):7956–7961
2. Rahman H, John TD, Sivdasan M, Singh NK (2018) Investigation on scale factor applicable to ABS based FDM additive manufacturing. *Mater Today Proc* 5(1):1640–1648
3. Alafaghania A, Qattawia A, Alrawia B, Guzman A (2017) Experimental optimization of fused deposition modelling processing parameters: a design-for-manufacturing approach. *Procedia Manuf* 10
4. Mohamed OA, Masood SH, Bhowmik JL (2015) Optimization of fused deposition modeling process parameters: a review of current research and future prospects. *Adv Manuf* 3:42–53
5. Bryll K, Piesowicz E, Szymanski P, Slaczka W, Pijanowski M (2018) Polymer composite manufacturing by FDM 3D printing technology, Chapter 2: material engineering. *MATEC Web Conference*, vol 237
6. Wang X, Jiang M, Zhou Z, Gou J, Hui D (2017) 3D printing of polymer matrix composites: a review and prospective. *Compos B Eng* 10:442–458
7. Bagsik A, Schoppner V (2011) Mechanical properties of fused deposition modeling parts manufactured with ULTEM*9085. *DMRC*
8. <https://ultimaker.com/download/74598/UMTDSNylonRBV10.pdf>
9. <https://www.sciencedirect.com/science/article/pii/S2214785319341173>
10. Roy RK (2010) A primer on the Taguchi Method, society of manufacturing engineers

Mechanical Characterization of Composite Material Fabricated by Friction Stir Processing Technique



V. Pradeep, Anil Kumar Bodukuri, and Madeeha Zoufeen

Abstract Composite materials have been pertinent among different materials owing to their exhibition of excellent properties. All materials have some variability in the strength capacity of individual pieces which are similarly manufactured. As a result, sufficient steps must be considered to control and recognize the both mechanical and microstructural properties of composite materials in order for them to satisfy the requirements in the best possible way. This undertaking comprehensively shows about assessing the mechanical properties of composite material explicitly tensile strength, impact strength and studying microstructure of MMC prepared by using the friction stir processing (FSP) procedure. An aluminium AL 5083 base plate was used with titanium carbide and zirconium dioxide as powder to reinforce inside the base metal through FSP, both the reinforced materials were taken in the form of 1:1 ratio by utilizing 10 g of TiC and ZrO₂. Two specimens were fabricated with two pass FSP and four pass FSP machining, and results were acquired from both the specimens. It is noticed that two pass FSP specimen truly and reasonably gives the great upsides of mechanical properties, and grain refinement is additionally expanded comparing with four pass FSP machining specimen.

Keywords Microstructure · Surface composite · MMC · Stir zone · Grain refinement · Friction stir processing

1 Introduction

Composite materials are contrived by coordinating at least two materials which belongs to different properties. Over late many years numerous new composites have been grown, some with entirely significant properties. Via cautiously picking

V. Pradeep (✉) · M. Zoufeen
Department of Mechanical Engineering, KITS, Warangal, Telangana, India
e-mail: vpd.me@kitsw.ac.in

A. K. Bodukuri
Kakatiya University, Warangal, Telangana, India

© The Author(s), under exclusive license to Springer Nature Singapore Pte Ltd. 2022
H. K. Dave et al. (eds.), *Recent Advances in Manufacturing Processes and Systems*,
Lecture Notes in Mechanical Engineering,
https://doi.org/10.1007/978-981-16-7787-8_49

the support, the lattice, and the assembling interaction that unites them, architects can tailor the properties to meet explicit necessities.

The best benefit of composite materials is strength and solidness joined with delicacy. By picking an appropriate mix of help and organization material, producers can make properties that decisively fit the necessities for a particular development for a particular explanation. The present-day avionics, both military and common, is a great representation. It would be substantially less productive without composites. Indeed, the requests made by that industry for materials that are both light and strong have been the principal power driving the improvement of composites. The essential purposes behind picking composites are: increase in strength, weight decrease, durability and support, added usefulness, design.

Aluminium is the most abundant metal in the world. It is found as aluminium oxide in metal called bauxite. Aluminium 5083 is known for excellent execution in outrageous conditions. Zirconium dioxide (ZrO_2) is an oxide of zirconium in the form of white glass powder and available in a typically monoclinic structure. It is essentially used in the making of hard earthenware, for instance, in dentistry. Titanium carbide is an incredibly hard stubborn artistic material, like tungsten carbide. It resembles dark powder with the sodium chloride precious stone design. In general, Cermets which are made up of TiC are used as tools for machining of steel materials at high cutting speeds.

1.1 Friction Stir Processing Technique

Surface composite (SC) can be prepared by changing its microstructure with the aid of novel FSP solid-state technique. Friction stir welding (FSW) innovation is critical to the advancement of this process. Mishra et al. (1999) introduced the FSP as a variety of erosion mix welding (FSW), a steady of cess composed at the welding organization (TWI), UK in 1991. Plastic aluminium blends with ultrafine grain size and high grain limit disorientations were used at first for the process of FSP.

For encountering surface communications, layer composites are suitable materials for planning applications. Rubbing mix handling is arising as a significant method for this. FSP can improve properties like toughness, hardness, strength, disintegration opposition, weakness without affecting the mass properties of the material. Aluminium and mg-based amalgams were prepared at first by using the FSP. Later it is also used for titanium-based alloys and steel for experiments. SCs are prepared with various combinations of process parameters like tool traversing speed, tool angular rotation speed and also with number of passes.

Rana et al. produced the SC by using Al-7075 as base plate and B4C as reinforcement particles on base plate. As Al 7075 has a wide range of applications in engineering fields and exhibits superior mechanical properties. The hardness and wear resistance of prepared composite are enormously increased. Traversing speed had minor influence in distribution of reinforcement particles on the matrix plate [1].

Eskandari et al. fabricated hybrid SC with the aid of the FSP technique. Microstructural analysis of A-TiB₂-Al₂O₃ hybrid surface nano-composites layers exposed that ceramic particles were well-dispersed in the Al matrix, with strong bonding to the Al matrix. Hybrid SC exhibits superior micro-hardness with TiB₂/Al₂O₃ particles. They obtain superior mechanical properties at 800 rpm of tool angular speed [2]. Ranjith Bauri et al. studied the influence of the geometry of the tool with various specifications. For obtaining a defect-free stir zone tool parameters as 1200 rpm as tool rotation and of 0.4 mm/s were considered [3].

Ramesh et al. described how to make Al 7075-B4C SC with better surface hardness and wear resistance using (FSP). Al 7075-B4C SC hardness was discovered to be 62 per cent higher than the base metal Al 7075—T651. The fine distribution of B4C particles in Al 7075 matrix caused to the increase in hardness [4].

E.R I. Mahmud et al. Fabricated Al-based hybrid SC with SiC and Al₂O₃ as ceramic reinforcements of 1.25 μm size in Aluminium A 1050-H24 Matrix by FSP. Proper dispersion of reinforcements was achieved and identified by microstructural study. Wear analysis was done on ball-on-disc apparatus at ambient temperature with different loads. At a normal load of 5 N, SC of 80 per cent SiC reinforced with 20% Al₂O₃ outperformed when compared to any other hybrid ratio in terms of wear resistance, while at a normal load of 10 N, the wear resistance was unaffected by the reinforcement ceramic type and was very close to the unreinforced FSP sample [5]. A. A. Zadeh et al. detailed the material utilized for contact mix preparing was projected with Aluminium 356 with silicon carbide powder, having normal molecule size of 30 μm with 5 μm normal molecule size as half and half support [6].

Gholami et al. analysed the influence of post-process ageing temperatures and duration on microstructure, wear behaviour and mechanical characteristics using microscopic and SEM analysis of the friction stir treated 7075 Al alloy. The findings show that homogeneous, equi-axed and tiny particles are produced [7].

1.2 Working Principle of FSP

FSP in its most effortless design involves a non-consumable pivoting apparatus, that is dove into workpiece and a short time later moved towards interest. Figure 1 shows the principle of the FSP in which two fundamental limits are served by the equipment: (a) warming (b) distortion of specimen material. The glow is made predominantly from scouring of the turning shoulder. The warmed material is blended by rotating test or pin with the specimen. It is then unwinds and streams around the turning pin. It by then fills the hole at the rear of the instrument. Genuine plastic miss happening and warm receptiveness is presented by the material that streams around the instrument. This causes a fundamental structural refinement in the looked-after zone. Mix zone (SZ) implies the zone blended by the mechanical assembly test. The unique recrystallization (DRX) is the rule framework and also for age of a fine and grains in the SZ. Regardless, in high stacking shortcoming energy materials, for instance, aluminium and its mixtures, unique recuperation go before DRX.

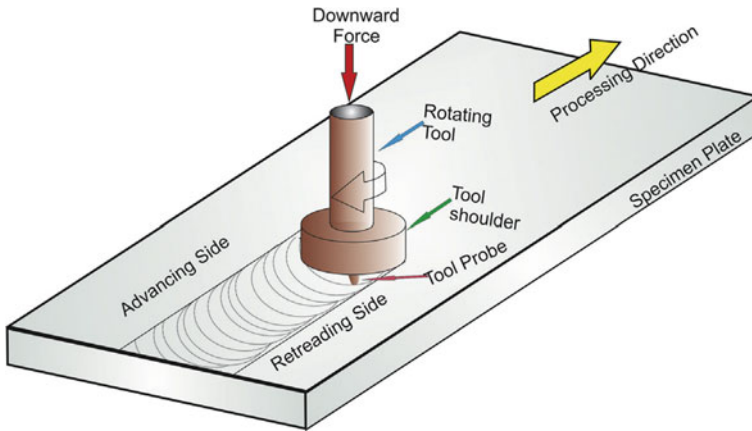


Fig. 1 Principle of friction stir processing

1.3 Effect of Multiple Passes or Introduction to Multiple Machining Passes

Capability of composites is influenced by the significant issue of bunching of support materials in composite creation. In nano-sized reinforcements grouping is more articulated. The grain size of the composite diminishes by using the multi-pass, and also, it decreases in size of bunch and uniform dissemination of support particles. In FSP specimen, support molecule dissemination principally relies upon number of passes. This is ascribed to the higher grain limit area available after each pass as grain limits and interfaces among the particles, framework are wellsprings of dislocations. More dislocations are produced by the disfigurement at the time of resulting machine pass, while high stacking shortcoming energy of aluminium prompts dynamic recuperation and development of low angle sub-grain limits [8–10].

2 Experimental Procedure

Aluminium alloy 5083 plate of measurements 100 mm × 50 mm × 10 mm is utilized in this task. The strategy for penetrating openings on a superficial level and installing support powders inside the SC is utilized in this undertaking. Openings are bored at one end of the specimen by accepting focus line (centre line) as reference and 2.5 mm distance on the two sides from focus line and profundity of the openings (depths) are 5 mm. 10 g of titanium carbide powder and 10 g of zirconium dioxide powder are utilized in the range 1:1 proportion and are embedded inside the bored openings of the specimen. The weight machine is utilized for masterminding the 1:1 extent of titanium carbide and zirconium dioxide, and it is combined as one as one

powder. This blended powder is inserted inside the bored openings of the specimen of profundity 2.5 mm. FSP tool without pin is utilized, and it is moved along the specimen to close the bored openings or for shutting the surface. A pin-less tool was at first utilized to cover the bored holes of the furrow subsequent to loading up with spasm particles to keep the particles from dissipating during FSP. The FSP tool had a shoulder measurement of 25 mm, pin distance across of 3 mm. The FSP was done on a natively constructed FSW machine. The FSP parameters considered were: tool rotational speed of 1800 rpm, navigate speed of 25 mm/min and pivotal power of 10 KN. This closing of the outer surface is necessary, and it is done on the specimen to avoid the escape of the reinforced powder from the drilled holes (Fig. 2).

At that point, the FSP handling technique is done on a superficial level composite by utilizing a strung tip instrument and this apparatus is brought close to the surface to contact, and afterwards, the device gets embedded inside the surface with the profundity of 6 mm as the device profundity is 6 mm and the openings profundity is 2.5 mm. The openings profundity consistently relies upon the apparatus profundity, and it is bored as needs be to that. The instrument is moved along the specimen, and the contact is produced in the middle of the surface and the device pin; this develops a high temperature between the two surfaces (this high temperature is generated due to the friction between the surface plate and the tool) and the plastic deformity of the specimen happens which changes the properties of the metal. This totally legitimizes the assertion of the FSP innovation that it is a totally strong state measure procedure and the solitary plastic deformation happens which totally changes the properties, microstructures without changing the shape and size and look of the specimen. At the hour of friction generation temperatures were likewise recorded with the assistance of sensor thermometer. The greatest shown temperature at the



Fig. 2 Movement of the tool during the machining of surface

hour of interaction is 500 °C. The various temperatures which were recorded are 440, 450, 490 and 430 °C. Every one of these temperatures is well underneath the recrystallization temperatures of the materials. Liquefying temperature of zirconium dioxide is 2715 °C, and dissolving temperature of titanium carbide is 3160 °C.

This is likewise the point that covers the meaning of the FSP strategy that it is a novel strong state preparing innovation where just microstructures and properties of the materials are changed without changing the shape and size of the specimen and just plastic disfigurement happens (Fig. 3).

Temperatures are also recorded after completion of process up to 50 min at centre pass and also at side pass. The highest temperature recorded at centre pass is **54 c** and at side pass is **49 c**.

Machine variables:

- (1) Tool rotational speed: 1800 rpm.
- (2) Tool tilt angle: 2 degree.
- (3) Tool plunge depth: 6 mm.
- (4) Feed: 25 mm per minute.

Tool design variables:

- (1) Shoulder diameter: 22 mm.
- (2) Shoulder height: 35 mm.
- (3) Probe diameter: 3 mm.
- (4) Probe profile: threaded tool (Fig. 4).

Two specimens were fabricated by using the multiple passes machining strategy of the friction stir processing. One specimen is manufactured with the two pass



Fig. 3 Recording of temperature during FSP



Fig. 4 FSP tool

machining of the method, and the other specimen is created with four pass machining of the strategy with a similar technique, same instrument factors, and same strung apparatus and with a similar synthesis. Temperatures were additionally recorded as needs to be and continually with the progressing time. Two pass and four pass fabricated specimens are shown in Figs. 5 and 6.



Fig. 5 Two pass specimen

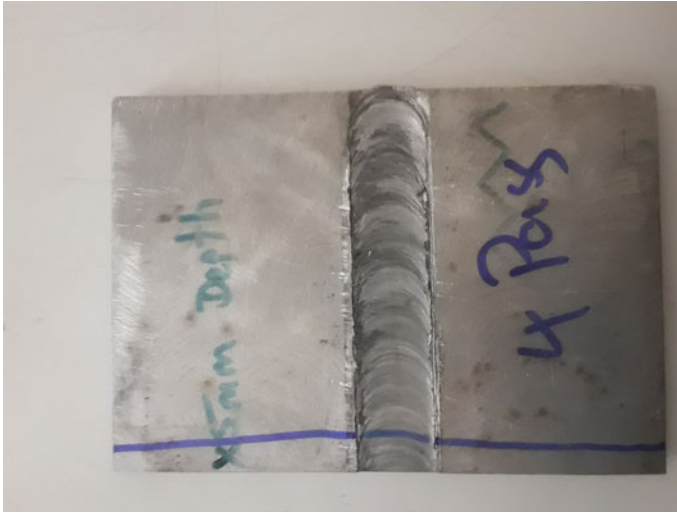


Fig. 6 Four pass specimen

3 Mechanical Characterizations

3.1 Tensile Test

The machine used for tensile test is **MCS/ UTE- 20 T**. The test procedure used for this test is **ASTM B 557: 2015**. Material specification is **AL ALLOY AA 5083** (Fig. 7).

The results obtained from the test are:

See Tables 1 and 2.

3.2 Impact Test

The equipment used in this project for conducting impact test is **KRYSTAL EQUIPMENTS**. The test procedure used for this is **CHARPY- V** method. The standard used for this procedure is **IS 1757 (PART- 1)2014**. Notch depth is 2 mm, and notch angle is 45 degree (Fig. 8).

The results obtained from the test are:

See Table 3.



Fig. 7 Tensile test specimens of two pass and four pass

Table 1 Results of tensile test of four pass specimen

Specimen dimensions	Results
Type of the specimen: flat	Ultimate load: 13,480 N
Width of the Specimen: 12.8 mm	UTS: 98.791 N/mm ²
Thickness of the specimen: 10.66 mm	Elongation: 6.360%
Cross section are: 136.448 mm ²	Yield load: 12,380 N
Original gauge length: 50 mm	Yield stress: 90. 729 N/mm ²
Final gauge length: 53.18 mm	

Table 2 Results of tensile test of two pass specimen

Specimen dimensions	Results
Type of the Specimen: flat	Ultimate load: 15,880 N
width of the specimen: 12.78 mm	UTS: 116.124 N/mm ²
Thickness the specimen: 10.7 mm	Elongation: 6.200%
Cross section area: 136.746 mm ²	Yield load: 14,900 N
Original gauge length: 50 mm	Yield stress: 108.958 N/mm ²
Final gauge length: 53.1 mm	



Fig. 8 Impact test samples of two pass and four pass

Table 3 Impact test results of two pass and four pass specimen

S. No.	Composition	Impact test in joules	
		2—pass machining	4—pass machining
01	1:1	36	30

3.3 Study of Microstructure

Used magnification in this test is 100X, and the used etchant is: KELLERS REAGENT. THE RESULTS OBTAINED UNDER MICROSCOPE ARE (Figs. 9 and 10):

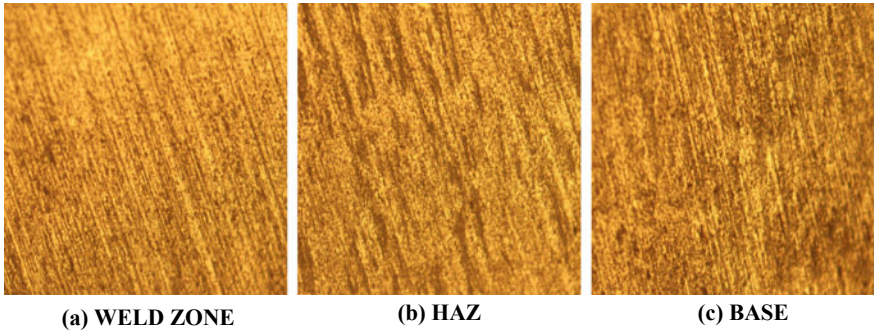


Fig. 9 a, b, c Microstructure of the two pass specimen

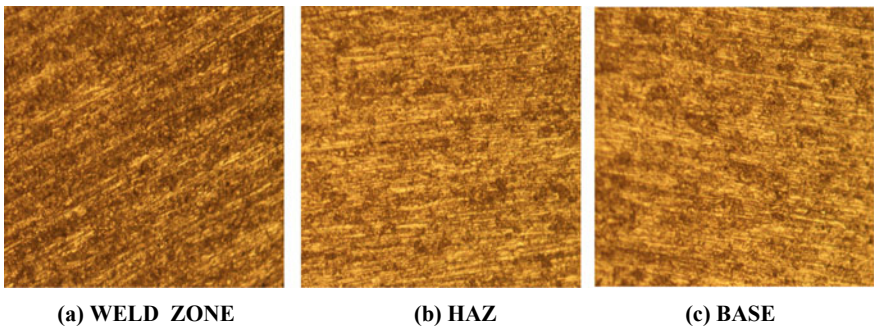


Fig. 10 a, b, c Microstructure of the four pass specimen

4 Results and Discussion

In this research work, from the testing of impact strength, it is noticed that the effect esteem in two pass machining specimen is great as in first effect. It very well may be said that support of the metals in the base framework truly helped the composite specimen and the worth has been expanded. It is additionally noticed that four pass machining specimen value esteem is marginally diminished contrasting with two pass machining. Here likewise it tends to be noticed that expansion in the passes of the machining on the specimen marginally diminishes the property’s estimation of the specimen (Table 4).

4.1 Tensile Test Result

Here in this analysis of testing tensile strength, the consequences of four pass machining and two pass machining of the specimen are gotten. In this outcome,

Table 4 Results of tests performed on the specimens

S. No.	No. of passes	Composition in 1:1 ratio			
		Ultimate tensile strength in N/mm ²	Impact strength in joules	Yield stress in N/mm ²	Displacement in mm
01	Two pass	116.124	36	108.958	8.9
02	Four pass	98.791	30	90.729	8.0

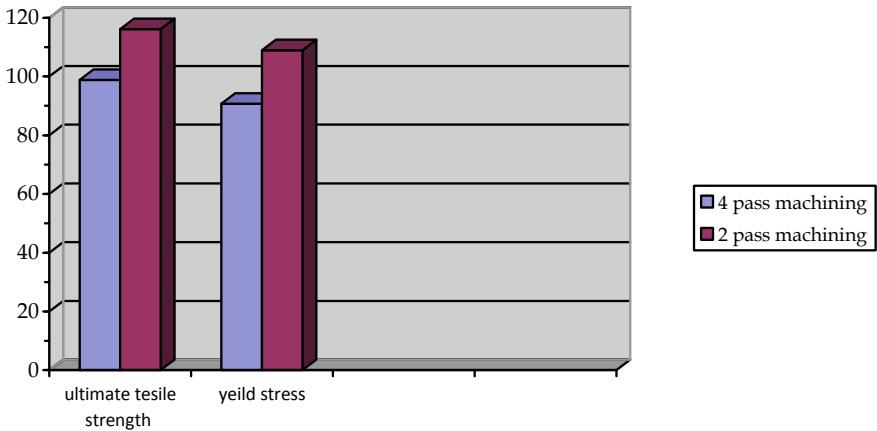


Fig. 11 Tensile strength property results in bar graph in N/mm²

as structured presentation shows there is a slight expansion in a definitive strength of the specimen in two pass machining as it is 116.124 N/mm². The normal incentive for this test was 120 N/mm². Along these lines, it very well may be informed that the worth of the outcome is close to the true form worth and it can likewise be informed that four pass machining of the specimen simply diminishes the strength and two pass machining makes the malleable property of the specimen better and gives the normal worth (Fig. 11).

4.2 Impact Test Result

See Fig. 12.

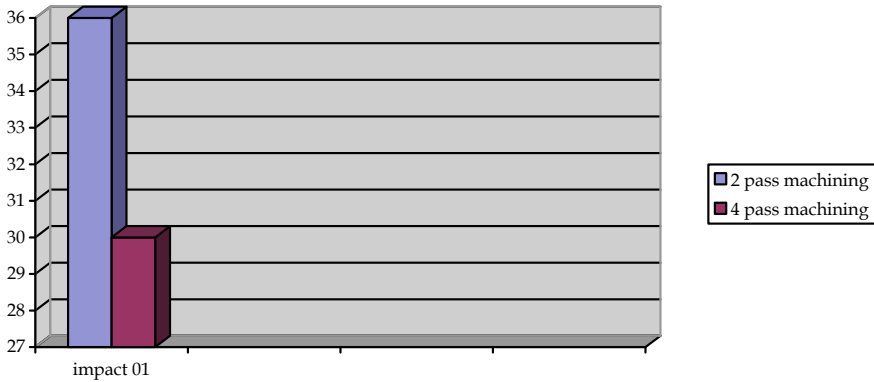


Fig. 12 Results of impact test in bar graph, values in joules

4.3 Study of Microstructure

In the above figures of the microstructure of weld zone, HAZ, base zone in the four pass machining and two pass machining it is seen that:

The three zones for specimen in weld zone, heat influenced zone (HAZ) and in base zone the microstructures are completely upset and generally haphazardly are in moving condition. While in two pass machining it is noticed that in each of the three regions, for example, heat influenced zone, weld zone and base zone, the microstructure particles are very much gotten comfortable the locale and there is no aggravation around there. Furthermore, it is likewise noticed that the weld zone and warmth-influenced zone in both machining measure is for the most part influenced spaces of built up particles as the surface isn't clear. It is additionally seen that there is a more than somewhat distinction in both base zone of the two pass specimen and four pass specimen.

5 Conclusions

The accompanying ends or the conclusion derived from this project (study) are as follows:

Preparation or manufacture of Aluminium AA5083 has been done effectively by utilizing supported materials like titanium and zirconium by taking the synthesis (composition) as 1:1 proportion (taken as 10 g of both titanium and zirconium). The manufacture of the metal matrix composite is effectively done by using the friction stir processing strategy. It is likewise reasoned that the enormous permanent strain in friction stir processing essentially provides the circulation and movement of molecules on a superficial level. Mechanical properties (portrayal) tests have been effectively done on both two pass machining specimen and four pass machining

specimen. It is noticed that adding supported particles to the base plate of aluminium AA5083 unquestionably expands the mechanical properties of the specimen. It is likewise seen that in the whole tests, two pass machining specimen gave better and expected outcomes and it is in expanded structure contrasting with the four pass machining specimen. The tensile, impact strength of the two pass machining specimen is better and true to form. So it is noticed that expanding number of passes on the specimen marginally diminishes the properties of the example.

References

1. Rana HG, Badheka VJ, Kumar A (2016) Fabrication of Al7075/B4C surface composite by novel friction stir processing and investigation on wear properties. *Procedia Technol* 23:519–528
2. Eskandari H, Taheri R (2015) A Novel Technique for Development of Aluminium Alloy Matrix/TiB₂/Al₂O₃ Hybrid Surface Nanocomposite by Friction Stir Processing. *Procedia Mater Sci* 11:503–508
3. Bauri R, Ram GDJ, Yadav D, Kumar CNS (2015) Effect of process parameters and tool geometry on fabrication of Ni particles reinforced 5083 Al composite by friction stir processing. *Mater Today Proceedings* 2:3203–3211
4. Ramesh R, Murugan N (2012) Production and characterization of aluminium 7075-T651/B4C surface composite by friction stir processing. *IJEAT*, ISSN: 2249–8958, 2(1)
5. Mahmoud ERI, Takahashi M, Shibayanagi T, Ikeuchi K (2010) Wear characteristics of surface hybrid MMCs layer fabricated on aluminum plate by friction stir processing. *Wear* 268:1111–1121
6. Abdollah-zadeh A, Alidokht SA, Soleymani S, Assadi H (2011) Microstructure and tribological performance of an aluminum alloy based hybrid composite produced by friction stir processing. *Mater Design* 32:2727–2733. <https://doi.org/10.1016/j.matdes.2011.01.021>
7. Gholami S, Emadoddin E, Tajally M, Borhani E (2015) Friction stir processing of 7075 Al alloy and subsequent aging treatment. *Trans Nonferrous Met Soc China* 25:2847–2855
8. Surface composites by friction stir processing: A review by Sharma V, Prakash U, Kumar BVM, Department of Metallurgical and Materials Engineering, Indian Institute of Technology, Roarkee, India
9. Production of surface composites by friction stir processing—a review by Sudhakar M, Srinivasa Rao CH, Meera Saheb K
10. Surface modification of Al6061—SiC surface composite through impregnation of grapheme, graphite and carbon nanotubes via FSP: A tribological study by Sharma A, Narsimhachary D, Sharma VM, Sahoo B, Paul J

Mechanical Characterisation of Nano Hybrid Composites



A. Vinay, T. Malyadri, and Lanka Sandeep Raj

Abstract In this research work, the impact of nanoparticles silicon oxide (SiO_2) and titanium dioxide (TiO_2) fillers on the tensile, impact and flexural, properties of epoxy/basalt(B)/kenaf(K)/Kevlar(KV)/glass(G) laminates was studied. The vacuum bagging process improves the tensile, impact and flexural properties of hybrid composite laminates. Construction, defence and vehicle applications are growing request for exclusive material manufacture innovation imitation reinforced composite remains replacing traditional materials are cost-effective, recyclable and cost-effective capacity, now the hybrid composites are fabricated by basalt(B)/kenaf(K)/Kevlar(KV)/glass(G) reinforced with L-12 epoxy resin as matrix. In the presence of nanoparticles, the tensile, flexural, then impact strength, the L-12 epoxy resin/hybrid laminates improved dramatically. As compared to epoxy + BKGK fibre composites, the epoxy + BKGK + 0.48 wt per cent nanoparticles composites had improved tensile and flexural performance. Due to nanotechnology, nanoparticles are now being seen as a possible filler material for enhancing the properties of existing composite materials. The polymer composite has improved in performance. Fillers, which are factory that are often recognised, come in a variety of forms, including silicon oxide (SiO_2) and titanium dioxide (TiO_2). As nanofiller-added composites were compared to and without filler-added composites, it was discovered that the effects were higher. It is used as a low-cost adsorbent for the reduction of organic complexes and also a light-weight polymer material for building construction. However, there is little available information about ability as a nanofiller for polymer composites.

Keyword Nanotechnology · Vacuum bagging method · Basalt/kenaf/glass/Kevlar fabrics · Nanosilicon oxide (SiO_2) and titanium dioxide (TiO_2) · Composite roof sheet · Epoxy resin hybrid composites

A. Vinay · T. Malyadri (✉) · L. S. Raj
Department of Mechanical Engineering, VNR Vignana Jyothi Institute of Engineering and Technology, Bachupally, Nizampet (S.O), Hyderabad, Telangana 500090, India

© The Author(s), under exclusive license to Springer Nature Singapore Pte Ltd. 2022
H. K. Dave et al. (eds.), *Recent Advances in Manufacturing Processes and Systems*,
Lecture Notes in Mechanical Engineering,
https://doi.org/10.1007/978-981-16-7787-8_50

623

1 Introduction

Nanotechnology is the establishment of new materials, devices and systems to induced desirable improvements in the macroscopic material properties. In recent years, investigation and development happening the usage of nanotechnology have increased in spite of would-be cost and health fears related to the use of nanoparticles. As of their special properties, such as high strength to weight ratio, hybrid composites, ceramics and plastics, are valuable materials. Composites have a greater benefit because they are created by manufacturing methods and are mostly used to decrease weight and thereby improve performance. A composite material is made up of two or more components, each of which is in a separate phase. The reinforcement refers to the discontinuous phase, which is normally tougher and heavier than that of the continuous phase, whilst the matrix refers to the continuous phase. Nanoparticles, polymers and even ceramics can be used as matrix materials. The composite is known as a polymer matrix composite because the matrix is a polymer (PMC). Fibrous and non-fibrous reinforcement phases are available. In recent years, composite structures have become increasingly prevalent with novel features such as the very simple rigidity and resilience of metals and alloys in aerospace and civil and subsea applications. Fibre reinforcement polymer (FRP) composites have been one of the most significant material developments in current years because of its benefits. Due to its low cost and other benefits, the vacuum bagging moulding method is commonly used now the research of composites. It is crucial towards know how to properly place dry fibre into the mould. Ply stacking is a typical method of spreading single sheet reinforced fabric hooked on mould independently in order near attain desired thickness then shape of finished product. Fabrics must typically be blended with in edge locations when preparing composites, particularly those with complex geometry form structures. Fabrics can be deformed during the bending phase. Since there are several layers of clothing, they will interfere with one another, causing friction or slipping that may be the origin of the fabric phenomenon. Artificial and natural fabric strengthened L-12 epoxy polymer matrix composites were also developed by way of an over-all part of current years, natural fibre-reinforced composites (NFRC) are now thought to be the most promising materials for long-term product production as well as a potential substitute for conventional fibre-reinforced composites [1–3]. Polymer composites have many compared to synthetic fibres, including expense, low weight, accessibility and moderate comprehensive strength, as well as market awareness such as biodegradability and recyclability. The tensile strength and flexural values of the hybrid composite are higher than those of the jute/glass or epoxy resin hybrid composites. Manufacturers are similar to natural fibres such as banana, cotton flax, okra, jute, hemp, sisal, bamboo and kenaf for applications such as vehicle, domestic door panels, boot lining, C column trim, aerospace and structural components [4–7].

The basalt, Kevlar, kenaf and glass fabric as well as the vacuum bagging process were hybridised in order to create hierarchical composite specimens [3]. Compared to the epoxy hybrid composite, basalt/glass hybrid composites provide

improved mechanical properties. A few studies were conducted with structural pieces to research the environmental, sustainable and economic aspects. Hybrid filler composites with improved results and a better strength and mechanical characteristics of weight per cent nanofillers with a number of fibre forms. The mechanical properties to wt% nanofillers with a range of fibre forms include hybrid filler composites with better results and better strength and solar mirroring of other composites [8]. Nano TiO₂ and SiO₂ filling materials were light, abundantly available as best filling materials mechanical properties, [9] due to their many benefits, including comparatively low processing costs and increased strength [10] and the various types of composite applications. Epoxy resins were of exceptional, mechanical properties and have an average nano TiO₂ and SiO₂ particle size between 20 and 30 nm.

In addition to composites mechanical properties such as tensile, bending and impacting and density, the nanofillers TiO₂ and SiO₂ were added to each of the compounds in different percentages (0.5, 0.48 and 0.47). The basalt/kenaf/glass/Kevlar hybrid epoxy resin composite sheets of basalt/kenaf/glass/Kevlar fabrics are prepared in four different forms. In this, focus of research is to examine the effects on mechanical properties such as tensile, flexural and impact properties of nanofillers TiO₂ and SiO₂ and basalt/kenaf/glass/Kevlar fabrics reinforced epoxy hybrid composites [11].

2 Experimental Investigation

2.1 Materials

The nanoparticle material used in this analysis has been obtained from regional Hyderabad dealers. The materials involved in this investigation are L-12 epoxy resin, K-6 hardener, basalt (B), kenaf (K), glass (G), Kevlar (KV), as shown in the Figs were bought by local market distributors in Hyderabad, India. The first and the second L-12 epoxy resin have a density of between 1.16 and 1.20 g/cm³ and a density of between 10,000 and 12,000 cps at 25C. Market demand over the forecast at higher permeability and room temperature is the properties of the K-6 hardener. The K-6 hardener is 110 C and 0.98 0.99 g/cm³ at density and flashpoint [12] (Figs. 1 and 2 and Table 1).

2.2 Nanofillers

TiO₂ region is 50 + 15 m², 80 in antae crystal and 200 crystals, with an average 30 nm particle size. Powder with SiO₂ nano. It had totally 98 pure particles and 62–70 nm particles [9] (Fig. 3 and Table 2).



Fig. 1 Basalt and kenaf fabrics

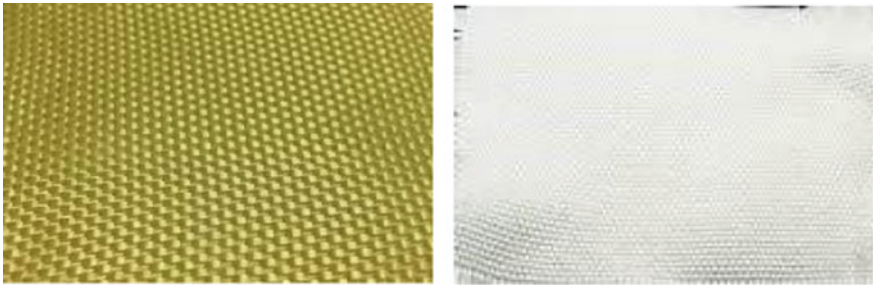


Fig. 2 Kevlar and glass fabrics

Table 1 Properties of fibres

Property	Density (g/cm ³)	Tensile strength(MPa)	Modulus of elasticity (gap)	Elongation at break (%)
Basalt fibre	2.67	3100–4840	85–87	3.15
Kenaf fibre	1.4	284–800	21–60	1.62
Glass fibre	2.44	200–3500	70	2.5
Kevlar fibre	1.47	2758	62	1.26
Epoxy	1.36	60–70	-	3–7

2.3 Hardener, Fabrics and Epoxy Resin

Usually, the hybrid composite is layers of basalt (B), Kenaf (ke), G, Kevlar (KV) and L-12 epoxy resin. The hybrid composite is a substance of basalt (B), kenaf (K) or glass (G), Kevlar (KV) [13] and the remaining 60% by weight of a L-12 epoxy resin and K-6 hardens, each of which is 100% by weight fraction, and 40% by weight. Therefore, the weights are 878 g and 1223 g for basalt (B), kenaf (K), glass (G), Kevlar (KV) and L-12 epoxy resins and for K-6 hardener. The matrix in composite of polymer materials of L-12 Epoxy resin or K-6 hardener (Fig. 4).

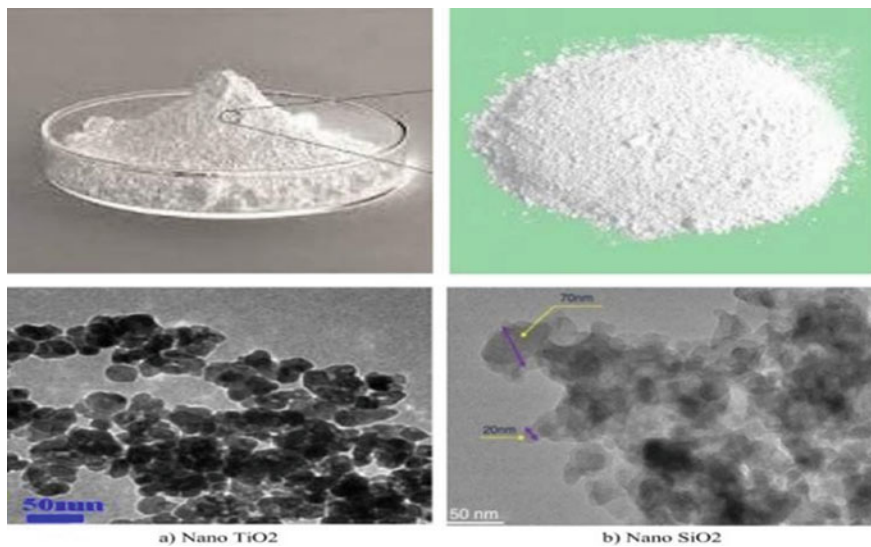


Fig. 3 Nanofillers SiO₂ and TiO₂

Table 2 Properties of nanofillers (SiO₂ and TiO₂)

Property	SiO ₂	TiO ₂
Purity	99.8%	99.9%
Colour	White	White
Size outer diametre	20–30 (nm)	100(nm)
Specific surface area	180–600 m ² /g	85 m ² /g
Bulk density	<0.10 g/cm ³	0.65 g/cm ³
True density	24 g/cm ³	g/cm ³

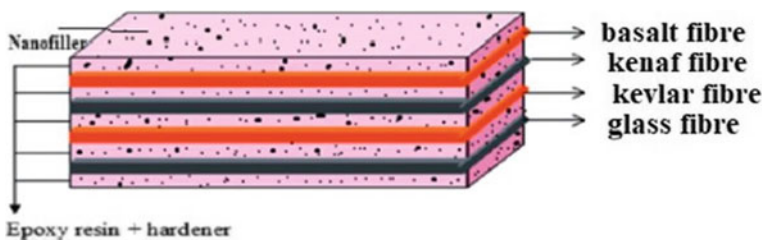


Fig. 4 Hybrid composites image

3 The Hybrid Composite Laminate Fabrication Procedure

A small spreader layer is used to evenly distribute the resin hardener mixture on the Mylar sheet, ensuring that the adjacent cloth is fully saturated. We apply one cloth sheet at a time, spreading the mixture evenly between them. If you do not scatter in the direction of the fibres, you will disrupt the fabric's fibres, as seen in Figure. Now place a peel ply fabric to easily peel out the laminate once it has fully dried, as well as a perforated sheet that absorbs excess resin through perforates, followed by two layers for breather sheets (shown in Figure) to absorb the air trapped between the mould and the bagging sheet (shown in Figure), as well as to eliminate the formation of flange impressions observed after the casting. The top side of this configuration has a flange to give it weight and to guide the excess resin to the capture jar. Place the bagging sheet over this arrangement so that it passes through the flange's topside gap. Check the bagging sheet's sealing of tacky tape along the edges. Attach the infusion tube between the flange and the catch pot using a clamp and lock it. The excess resin is stored in a collection cup that is put within the trap container. A polytec pressure gauge is attached to the top surface of the catch pot and is connected to the ALUE vacuum pump via a simple return valve. When the pump is turned on, it begins swallowing air and waste resin. Listen for a brief sound coming from the fabrication rig to search for air leakage. Spread the bagging sheet out evenly so that sucking will go as smoothly as possible. Wait before the pressure drops to -95 kPa on a -100 kPa gauge or -28 in Hg on a -30 in Hg gauge. Shut down the vacuum pump and check to see if the pressure is stable. Finally, the greater the consistency of pressure, the higher the product quality and it means that no air has been drawn back into the laminate, indicating that no voids have formed (Fig. 5).

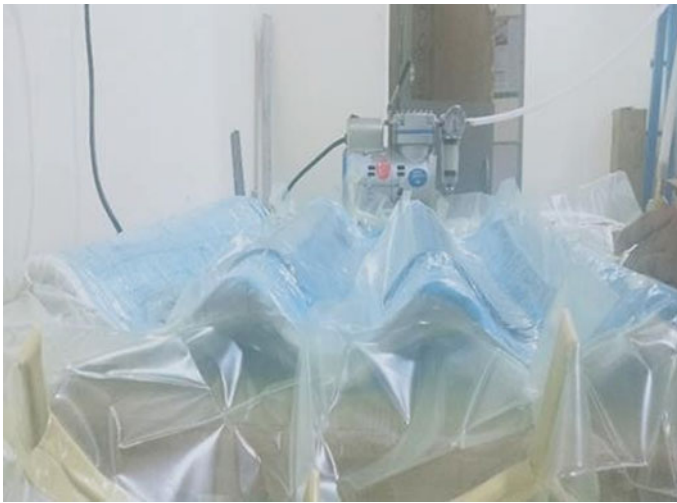


Fig. 5 Image of the vacuum bagging process

Table 3 Hybrid composites tensile strength

Composite samples	Tensile strength (mpa)
Epoxy resin	22.50
Basalt/kenaf/glass/Kevlar + 0% nanoparticles	57.13
Basalt/kenaf/glass/Kevlar + 0.5% nanoparticles	100.64
Basalt/kenaf/glass/Kevlar + 0.48% nanoparticles	118.39
Basalt/kenaf/glass/kevlar + 0.47% nanoparticles	87.96

4 Results and Discussion

4.1 Tensile Testing

The ASTM D3039 standard using to test the tensile strength of hybrid composite laminates. The style samples were cut from the laminate that had been fabricated. A universal test device with cross head speed of 4 mm per minute and measuring length of 100 mm has been used for tensile testing. Table 3 illustrates how hybrid composites have achieved their tensile power. The traction specimen is seen in the Figure after inspection.

This effect on tensile strength of applying nanofiller to basalt/kenaf/glass/Kevlar fabrics is obvious. Pure epoxy's tensile strength is 22.5 MPa, whilst the basalt/kenaf/glass/Kevlar hybrid composites have a tensile strength of 57.13 MPa. The hybrid composites of the fabrics are filled with different weights of 0.5, 0.48 and 0.47 and nanofillers. The tensile strengths of basalt/kenaf/glass/Kevlar fibre hybrid composites after the addition of 0.47, 0.5 and 0.48 nanofiller are 87.96 MPa, 100.64 MPa and 118.39 MPa, respectively. Figure 6 clearly shows a notable improvement in tensile strength up to 0.48 wt per cent nanofiller inclusion but without adding nanofiller to hybrid on fabrics, hybrid basalt/kenaf/glass/Kevlar composites also reach above 0.48 wt per cent tensile strength increase, but tensile strength difference is reduced between 0.5 wt per cent to 0.47 wt per cent nano-tensile strength increase. This may have been due to a lack of sufficient bonding between the nanoparticles and the thermo-set polymer matrix materials (Fig. 7).

4.2 Flexural Test

Flexural tests are carried out in accordance with ASTM D790 principles, by a load capacity of 20 kN with 5 mm/min transverse speed, and 125 12.7 mm sample size

Fig. 6 Fractured specimens of tensile test



cut from the hybrid composite laminate produced. Table 4 displays the results. The diagram Fig. 8 After flexural inspection, the broken specimens are seen.

The effect of adding nanofiller to basalt/kenaf/glass/Kevlar fabrics hybrid composites on flexural strength is clearly visible. The flexural strength of pure epoxy resin is 47 MPa, whilst the flexural strength of basalt/kenaf/glass/Kevlar fabrics hybrid composites is 95.67 MPa, as seen in Fig. The basalt/kenaf/glass/Kevlar fabrics hybrid composites are filled with different weight per cents of nanofiller (0.5, 0.48 and 0.47). The flexural strengths of basalt/kenaf/glass/Kevlar fabrics hybrid composites after nanofiller inclusion are 181.73Mpa, 231.1Mpa and 99.94Mpa, respectively. The Fig. 8 clearly shows that adding nanofiller to basalt/kenaf/glass/Kevlar fabrics hybrid composites increase flexural strength up to 0.48 wt per cent, and without

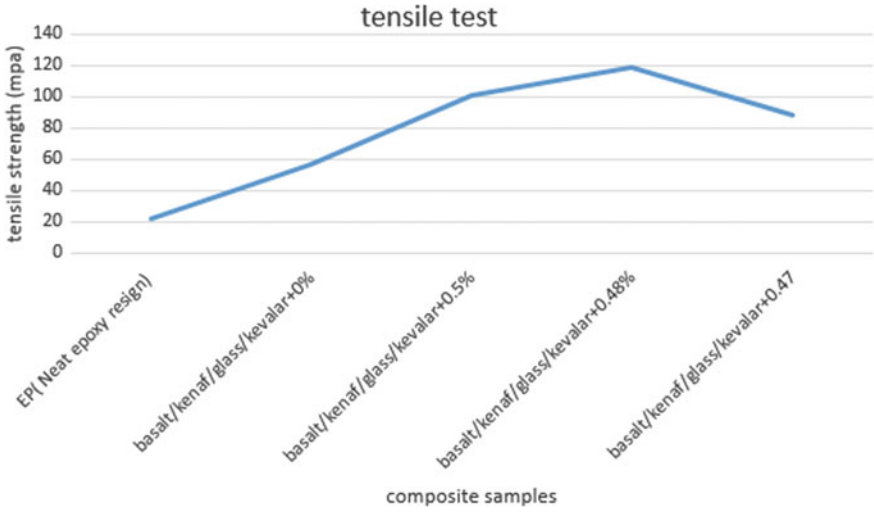


Fig. 7 Tensile strength of nanofiller hybrid composites

Table 4 Flexural test results

Composite Samples	Tensile strength (MPa)
EP(neat epoxy resin)	47
Basalt/kenaf/glass/Kevlar + 0% nanoparticles	95.62
Basalt/kenaf/glass/Kevlar + 0.5% nanoparticles	99.94
Basalt/kenaf/glass/Kevlar + 0.48% nanoparticles	231.1
Basalt/kenaf/glass/Kevlar + 0.47% nanoparticles	181.73



Fig. 8 Fractured specimens of flexural test

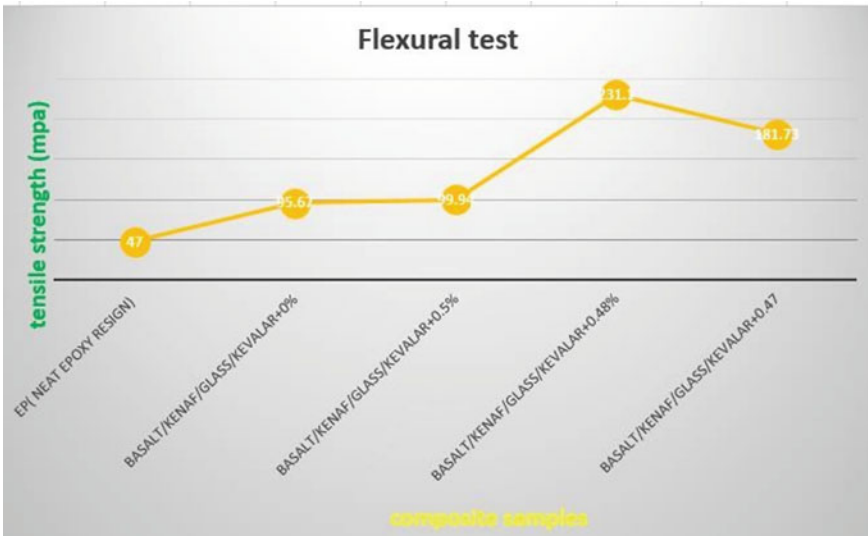


Fig. 9 Flexural strength of hybrid composites

adding Nanofiller to basalt/kenaf/glass/Kevlar fabrics hybrid composites increase flexural strength beyond 0.48 wt per cent, but flexural strength decreases from 0.5 wt per cent to 0.47 wt per cent. This may be due to insufficient nanoparticle bonding and irregularities by the polymer matrix (Fig. 9).

4.3 Charpy Impact Test

The Kroger 3/70 Charpy effect test kit was used to conduct Charpy testing in accordance with ISO 179/92 standards. Test specimens measuring 55 × 10 mm, both notched and unnotched (Figs. 10 and 11 and Table 5).

Fig. 10 Fractured specimens of impact test



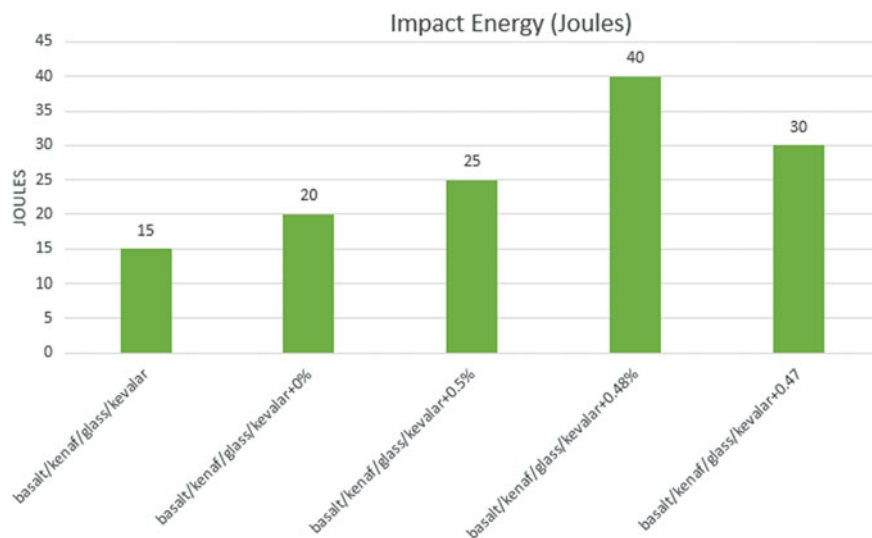


Fig. 11 Impact strength hybrid composites with nanofiller effect

Table 5 Impact test results

Composite samples	Charpy impact energy (J/m)
Basalt/kenaf/glass/Kevlar	15
Basalt/kenaf/glass/Kevlar + 0% nanoparticles	20
Basalt/kenaf/glass/Kevlar + 0.5% nanoparticles	25
Basalt/kenaf/glass/kevlar + 0.48% nanoparticles	40
Basalt/kenaf/glass/kevlar + 0.47% nanoparticles	30

5 Conclusions

A synthetic composite made from basalt/kenaf/glass/Kevlar fabrics mechanical behaviour. The hybrid composites were made using a vacuum bagging process and testing followed the ASTM research protocol. The research presented in this experimental study draws the following conclusions.

- i. TiO_2 and SiO_2 nano-filing result on basalt/kenaf/glass/Kevlar tensile and flexural properties, the use of numerous basalt/kenaf/glass/Kevlar fabrics was tested for reinforced epoxy composites. The findings demonstrate explicitly that the addition of nanofiller to the mix enhances tensile, bending and effect properties.

- ii. The fabrics basalt/kenaf/glass/Kevlar strengthened composites epoxy hybrid with 0.48 weight per cent nano TiO_2 and SiO_2 filler outperform the fabrics basalt/kenaf/glass/Kevlar strengthened hybrid epoxy composites with significant tensile properties.
- iii. The 4 wt per cent nanoparticles BKGK hybrid composites are a better replacement for basalt/kenaf/glass/Kevlar fabrics reinforced epoxy hybrid composites where flexural properties appear protuberant.
- iv. Basalt/kenaf/glass/Kevlar epoxy incorporated with hybrid nanofillers was analysed for impact properties. According to the findings, the 0.48% wt. reinforced composites had a higher impact power. The addition of SiO_2 and TiO_2 fillers resulted in a higher impact energy, indicating that impact energy improved.
- v. An in-depth investigation of the performance of basalt/kenaf/glass/Kevlar hybrid composite fabrics by innovative nanofillers might remain interesting subject aimed at coming research.

References

1. Mility J, Kovacic V (2006) "Structure and properties of basalt filaments." *Journal*
2. Ochi S (Apr–May 2008) "Mechanical properties of kenaf fibers and kenaf/PLA composites" 40(4–5):446–452
3. Lu SR, Hongyu J, Zhang HL, Wang XY (2005) "Wear and mechanical properties of epoxy/ SiO_2 - TiO_2 composites". *J Mater Sci*
4. Yang Y, Jin Q, Mao D, Qi J, Wei Y, Yu R, Li A (2015) "Dually ordered porous TiO_2 -rGO composites with controllable light absorption properties for efficient solar energy conversion." *Journal*
5. Zhu H, Wu G, Zhang L, Zhang J, Hui D (2014) "Experimental study on the fire resistance of RC beams strengthened with near-surface-mounted high-Tg BFRP bars." *Journal*
6. Composites for structural applications: a review. *Compos B Eng* 133:112–121 (2017)
7. Mazur K, Kuciel S, Salasinska K (2019) Mechanical, fire, and smoke behavior of hybrid composites based on polyamide 6 with basalt/carbon fibres. *J Compos Mater* 53(28–30):3979–3991
8. Wang H, Zhong J, Feng D, Meng J, Xie N (2013) Nanoparticles-modified polymer-based solar-reflective coating as a cooling overlay for asphalt pavement. *Int J Smart Nano Mater* 4(2):102–111
9. Levinson R, Akbari H, Berdahl P (2015) "A novel technique for the production of cool coloured concrete tile and asphalt shingle roofing products." *Journal*
10. Lopresto C, Leone I, De Iorio (2011) "Mechanical characterisation of basalt fibre reinforced plastic." *Journal*
11. Jawaid M, Khalil HPSA, Bakar AA (2011) Hybrid composites of oil palm empty fruit bunches/woven jute fiber: chemical resistance, physical, and impact properties. *J Compos Mater* 45(24):2515–2522
12. Vijayakumar S, Palanikumar K (2019) Mechanical property evaluation of hybrid reinforced epoxy composite. *Mater Today: Proc* 16:430–438
13. Kim JG et al (2015) Tensile behavior of aluminum/carbon fiber reinforced polymer hybrid composites at intermediate strain rates. *J Compos Mater* 49(10):1179–1193

Mechanical Properties of 3D-Printed ABS with Combinations of Two Fillers: Graphene Nanoplatelets, TiO₂, ATO Nanocomposites, and Zinc Oxide Micro (ZnOm)



N. Vidakis, M. Petousis, E. Velidakis, and A. Maniadi

Abstract This work is focused on researching new polymer nanocomposites' mixing and fabrication methods and to investigate nanomaterials' interactions with the polymer matrix with the sole goal of enhancing the polymer's mechanical properties. This research was focused on increasing the mechanical stability of three-dimensional (3D) printed parts by fabricating novel microcomposite and nanocomposite filaments. Those filaments were created by melt mixing and melt extrusion processing. Specimens were fabricated with commercially available 3D printers and further characterized. Graphene nanoplatelets (GnP), zinc oxide micro (ZnOm), titanium dioxide (TiO₂), and antimony tin oxide (ATO) were selected to be combined with an acrylonitrile butadiene styrene (ABS) matrix at preselected concentrations. Mechanical test specimens were fabricated, in accordance with international standards for tension and flexion. It was proven that these combinations of nanomaterials at the selected concentrations slightly decrease the mechanical stability of the polymer matrix due to possible agglomerations. Transmission electron microscopy (TEM) and scanning electron microscopy (SEM) were used to identify any possible structural flaws and to assess the overall nanomaterial distribution inside the polymer matrix.

N. Vidakis · M. Petousis (✉) · E. Velidakis
Mechanical Engineering Department, Hellenic Mediterranean University, 71410 Heraklion, Crete, Greece

e-mail: markospetousis@hmu.gr

N. Vidakis

e-mail: vidakis@hmu.gr

E. Velidakis

e-mail: mvelidakis@hmu.gr

A. Maniadi

Department of Materials Science and Technology, University of Crete, 700 13 VassilikaHeraklion, VoutesCrete, Greece

e-mail: maniadi@materials.uoc.gr

Keywords Three-dimensional (3D) printing · Nanocomposites · Acrylonitrile butadiene styrene (ABS) · Material characterization · Graphene nanoplatelets (GnP) · Titanium dioxide (TiO_2) · Zinc oxide micro (ZnOm) · Antimony tin oxide (ATO)

1 Introduction

3D printing technology nowadays is constantly gaining ground in the industries, thus creating interest in research regarding novel materials for 3D printing applications. In the additive manufacturing (AM) and more specifically in fused filament fabrication (FFF) 3D printing processes, selected materials in the form of filament strands are deposited layer by layer to produce a 3D structure [1]. Research on the field of 3D printing showed that the mechanical properties of FFF parts can vary depending on the printing process parameters used among other factors, such as printing orientation and printing speed, in addition to the fact that 3D printing introduces anisotropy to the final produced parts [2]. Regarding the filament materials used, among the most popular and commonly-used materials are acrylonitrile butadiene styrene (ABS), with polymer's mechanical and physical properties being thoroughly reported in literature [3–8].

Another research finding is that the physical, mechanical, and electrical properties of the 3D printed parts can be altered or even increased by introducing nanofillers in the initial polymer matrix [9]. Most common nanofillers that literature reports to increase the mechanical stability in ABS matrices specifically are zinc oxide [10], titanium dioxide [11, 13], antimony tin oxide [11], and graphene [12].

Literature in this field is nowadays focused on researching new, novel materials, and composite filaments, with increased mechanical and physical properties [13]. Moreover, nanocomposite filaments are of high interest due to increased surface area interactions between the nanofillers and the polymer matrix, offering in some cases, higher mechanical stability to 3D printed parts [13].

In this work, nanocomposite ABS filaments reinforced with titanium dioxide (TiO_2), antimony tin oxide (ATO), zinc oxide micro (ZnOm), and graphene nanoplatelets (GnP) were fabricated by means of melt extrusion. These nano and micro fillers were chosen according to the previous research done [9] that proved that adding each of these fillers alone in the ABS polymer matrix can highly increase the mechanical properties of the matrix. The next step was to combine these nano and micro materials to test the interactions between two fillers and the polymer matrix. Testing specimens were fabricated via 3D printing to evaluate the mechanical properties in tension, flexion, and microhardness. Scanning electron microscopy (SEM) and transmission electron microscopy (TEM) were used to identify any possible structural flaws and to assess the overall nanomaterial distribution inside the polymer matrix. The overall results showed a slight degrading in mechanical properties of the

nanocomposites when compared to pure ABS specimens, due to possible agglomerations and structural faults in the specimens, it developed with the specific method followed.

2 Methodology

2.1 Materials

2.1.1 Matrix

The polymeric matrix selected for the current research was industrial grade, high pressure acrylonitrile butadiene styrene (ABS), with a brand name Terluran Hi-10, purchased from INEOS Styrolution (Frankfurt, Germany) in powder form.

2.1.2 Nanomaterials

The nanomaterials preselected as fillers were the future graphene nanoplatelets (GnP) with <5 nm width and $5 \mu\text{m}$ thickness, nanografi zinc oxide micro (ZnOm) with average particle size of $20 \mu\text{m}$ (nanografi Ankara, Turkey), the brand-named Degussa Evonik P25 titanium dioxide (TiO_2) (Essen, Germany) with an average particle size of 25–50 nm, and antimony tin oxide (ATO) received from nanografi (nanografi Ankara, Turkey) with an average particle size <28 nm. The above nanomaterials were selected to be combined with the ABS matrix in three (3) different combinations; 1. ABS with 0.5% wt. GnP and 5% wt. ZnOm, 2. ABS with 5% wt. GnP and 0.5% wt. ZnOm, and 3. ABS with 2.5% wt. TiO_2 and 0.5% wt. ATO.

These combinations, with the exact percentages of each filler, were derived from previously implemented research that proved that adding each of these fillers alone in the ABS matrix can highly increase the mechanical properties of the matrix by up to 20% [10].

2.2 Nanocomposite Filaments' Fabrication and 3D Printing

Initially, the ABS matrix material was mechanically mixed in with the GnP, the ZnOm, the TiO_2 , and the ATO nanomaterials according to their abovementioned selected combinations and percentages.

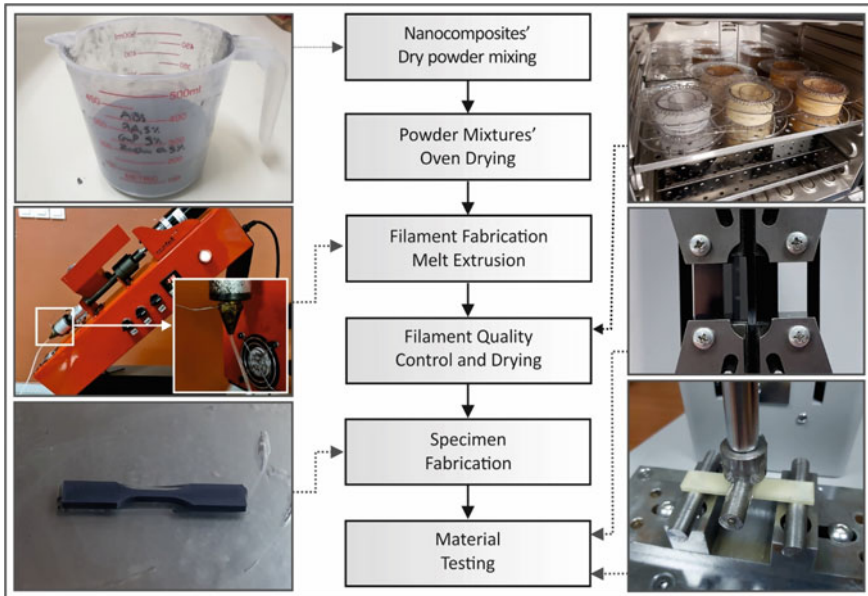


Fig. 1 Nanocomposite and microcomposite filament's and specimen's fabrication methodology

The micro and nanocomposite filaments were fabricated by melt extrusion, using a desktop single-screw extrusion system, Noztek Pro (Noztek, UK). The extruding temperature used was 230–235 °C. The filament fabrication temperature varied depending on the filler concentration in each case. The aforementioned nano and microcomposite materials, in the form of powder mixtures, were fed into the extrusion system. The fabricated filaments then were qualitatively analyzed and used to 3D print tensile and flexure test specimens. The overall procedural steps followed are depicted in Fig. 1.

A commercially available 3D printer was used an Intamsys HT 3D printer (Intamsys Technology Co Ltd, Shanghai, China) to 3D print all the test specimens with the same printing parameters. The printing temperature was set at 235 °C, while the printing orientation was 45°. Heat bed temperature was set at 70 °C, and the specimens were built full solid (100% infill).

2.3 Tensile Testing

Specimens 3D printed for tensile testing experiments were fabricated according to ASTM D638-02a standard with specific dimensions. For each combination studied, seven specimens were printed according to the ASTM D638-02a standard. The tensile experiments were conducted using an Imada MX2 (Northbrook, IL, USA) tensile

test machine, equipped with grips according to the international standard. The chuck of the tensile test machine was set at a 10 mm/min speed for all the experiments, and all tests were conducted in room temperature ($\sim 22^\circ\text{C}$).

2.4 Flexural Testing

Specimens for flexural testing experiments were fabricated according to ASTM D790-10 with specific dimensions. Seven specimens were 3D printed for each composite studied. The flexural experiments were performed using an Imada MX2 (Northbrook, IL, USA) tension/flexion test apparatus, with an experimental setup according to the standard that requires a three-point bending test with 52 mm support span. The chuck of the tensile test machine was set at a 10 mm/min speed for all the flexion experiments, and all tests were conducted in room temperature ($\sim 22^\circ\text{C}$).

2.5 Microhardness Measurement

For evaluating, the microhardness Vickers of the 3D printed specimens studied the ASTM E384-17 standard was followed. The test apparatus was set with 0.2 kg force scale (1.962 N) and 10 s indentation time. An Innova test 400-Vickers (Maastricht, The Netherlands) apparatus was used to identify the microhardness of the specimens and all tests were conducted in room temperature ($\sim 22^\circ\text{C}$).

2.6 Morphological and Structural Characterization

The printed specimens' internal/external structure and interlayer fusing were examined using a scanning electron microscopy (SEM) characterization. The SEM analysis was performed using a JEOL JSM 6362LV (Jeol Ltd., Massachusetts, USA) electron microscope in high-vacuum mode at 5 kV acceleration voltage on uncoated samples.

For the structural analysis, the agglomeration, and nanomaterials' distribution analysis, transmission electron microscopy (TEM) was used using a JEOL JEM-2100 (Jeol Ltd., Massachusetts, USA) at 200 kV full vacuum. In conjunction with a microtome, nanocomposite slices were cut approximately 250–400 μm in thickness. Images at 1 μm and 500 nm were taken and analyzed.

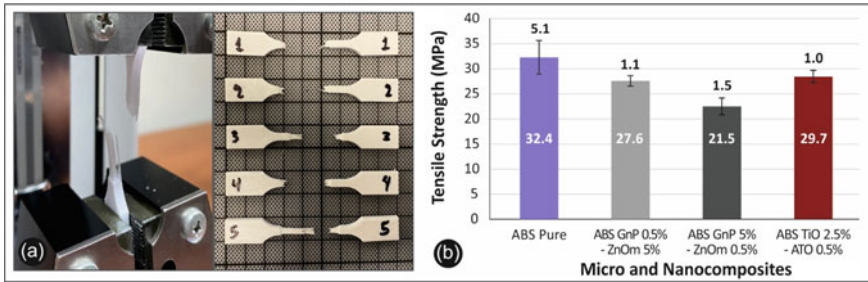


Fig. 2 Tensile experiments: **a** The tensile test setup with the broken specimens, **b** tensile test results for the composites studied

3 Results and Discussion

3.1 Tensile Testing

Regarding the tensile experiments, the results are shown in Fig. 2.

The experimental data showed a slight reduction in the tensile strength of 34% in the case of ABS GnP 5% and ZnOm 0.5%, while the case of ABS GnP 0.5% and ZnOm 5% had a decrease of 15% in comparison with pure ABS specimens. On the other hand, the case of ABS TiO₂ 2.5% with ATO 0.5% showed a reduction of only 11% as compared to pure ABS.

Literature is not yet enriched enough regarding the combination of not only one but two nanofillers in an ABS matrix and especially regarding their effect on 3D printed specimens.

3.2 Flexural Testing

Regarding the flexural experiments, the results are shown in Fig. 3.

The flexural test results showed similar trend with the tensile test results presented above. More specifically, the flexural test results showed a reduction in the flexure strength of 20% in the case of ABS GnP 5% and ZnOm 0.5%, while the case of ABS GnP 0.5% and ZnOm 5% had a decrease of 10% when compared with pristine ABS specimens. Instead, the case of ABS TiO₂ 2.5% with ATO 0.5% showed a reduction of only 12% as compared to pure ABS.

Literature is not yet enriched enough regarding the combination of not only one but two nanofillers in an ABS matrix and especially regarding their effect on 3D printed specimens.

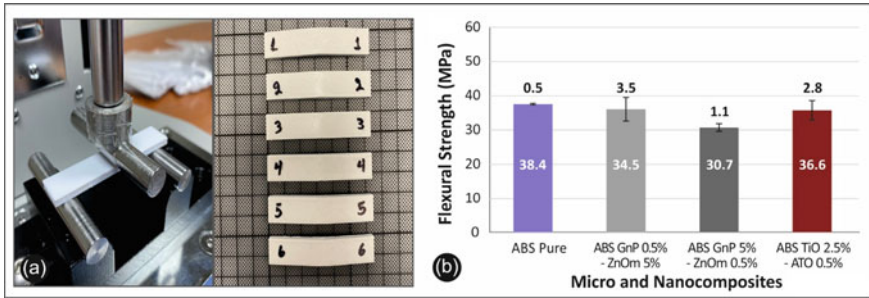


Fig. 3 Flexural experiments: **a** The flexural test setup with the broken specimens, **b** flexural test results for the composites studied

3.3 Microhardness Measurement

About the microhardness Vickers, the test data for all the nanocomposites studied are presented in Fig. 4

In the microhardness measurements, the highest value was observed on the case of ABS TiO₂ 2.5% with ATO 0.5% with an increase of 26% when compared to pure ABS. In the case of ABS GnP 0.5% and ZnOm 5%, it was shown that the microhardness is the same as the pure ABS specimens, while in the case of ABS GnP 5% and ZnOm 0.5%, there is a slight reduction of 9%.

These results showed that there is a correlation between the filler concentration in the case of GnP filler percentage and the overall filler percentage presents in the polymer matrix.

Literature is not yet enriched enough regarding the combination of not only one but two nanofillers in an ABS matrix and especially regarding their effect on 3D printed specimens.

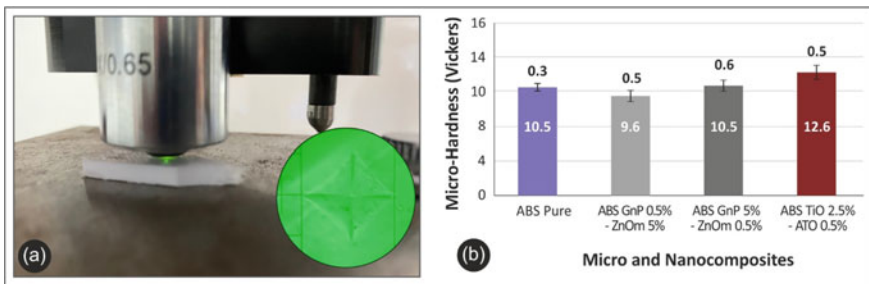


Fig. 4 Microhardness Vickers experiments: **a** The microhardness Vickers test setup, **b** results for the nanocomposites studied

3.4 *Morphological and Structural Characterization*

Figure 5 presents the SEM images of the fracture areas of randomly selected tensile test specimens for all cases studied in this work.

From the SEM images and the fracture type of the test specimens, it became evident that while pure ABS seems to fracture in a ductile manner, the rest of the nanocomposites fracture in a more brittle way with signs of poor layering interfusion especially in the cases of ABS with GnP and ZnOm. Moreover, the case of ABS with TiO₂ and ATO seems to have the “cleanest” and the most brittle fracture as compared to the other cases. These results can be correlated with the microhardness Vickers results presented above.

In Fig. 6, the TEM images for each case studied in this work are presented. The TEM images revealed agglomeration regions in the cases of ABS with GnP and ZnOm. This was more profound on the case of ABS GnP 5% with ZnOm 0.5%.

The overall nanofiller distribution in the polymer matrices appeared to be homogeneous in all cases studied but the homogeneity is rather compromised in the cases of ABS with GnP. The possible reason behind the agglomerating regions in ABS with GnP is the non-functionalized graphene that was mixed with the ABS [9].

4 Conclusion

In this work, nanocomposite ABS filaments reinforced with various nano and microfillers such as titanium dioxide (TiO₂), antimony tin oxide (ATO), zinc oxide micro (ZnOm), and graphene nanoplatelets (GnP) were fabricated by means of melt extrusion. Test specimens were fabricated via 3D printing to evaluate their mechanical properties in tensile, flexural, and microhardness tests.

It was found that the overall mechanical stability, both in tension and in flexion experiments, was slightly reduced due to nanofillers agglomerations that further introduced structural faults to the 3D printed specimens leading to weak interlayering fusion. Further, research is needed to identify the main cause of these agglomerations and to further improve the overall nanofiller distribution in the polymer matrix regarding the combination of two or more nanofillers inside the matrix.

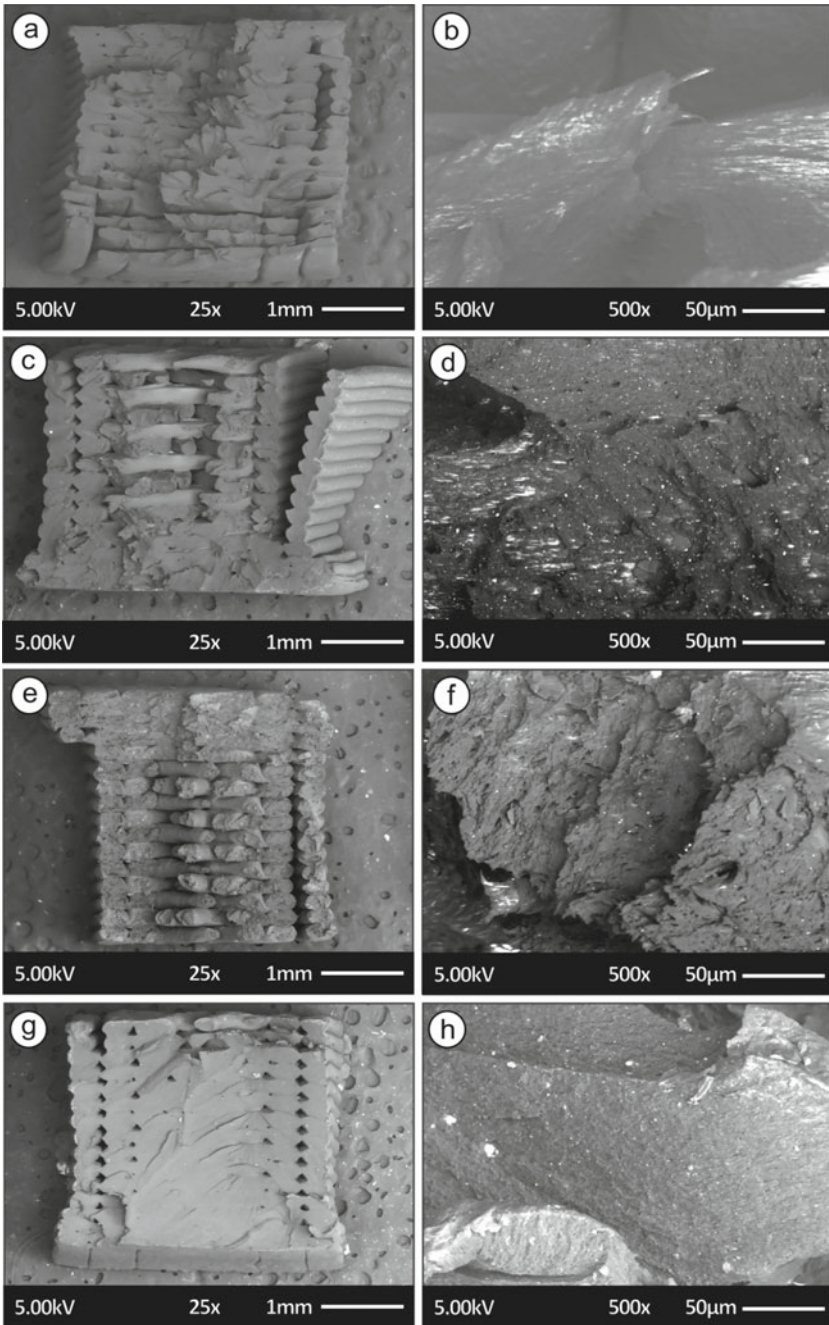


Fig. 5 SEM images on the fracture surface area of the tensile test specimens; a-b: pure ABS, c-d: ABS with 0.5% wt. GnP and 5% wt. ZnOm, e-f: ABS with 5% wt. GnP and 0.5% wt. ZnOm, and d-h: ABS with 2.5% wt. TiO₂ and 0.5% wt. ATO

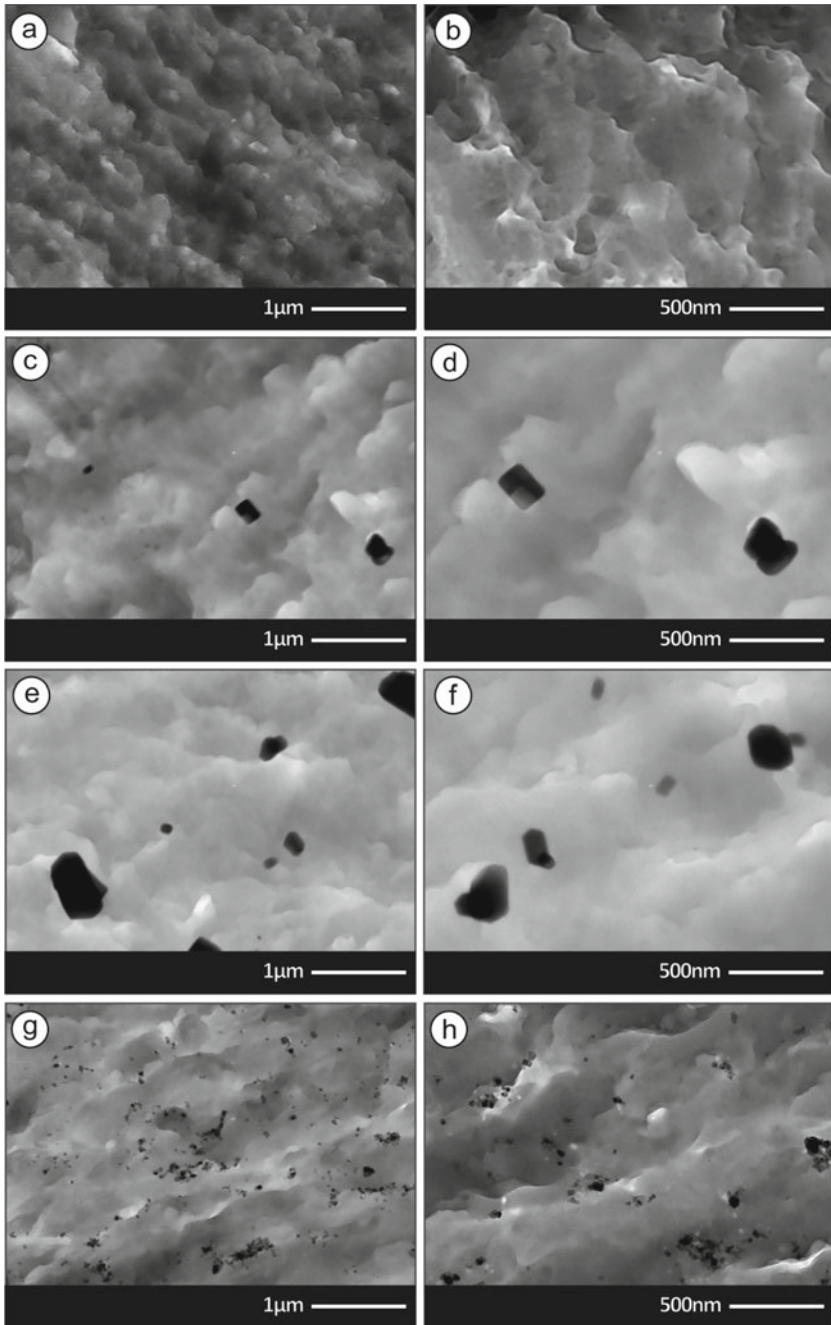


Fig. 6 TEM images on 3D printed specimens' nano-slices; a-b: pure ABS, c-d: ABS with 0.5% wt. GnP and 5% wt. ZnOm, e-f: ABS with 5% wt. GnP and 0.5% wt. ZnOm, and d-h: ABS with 2.5% wt. TiO₂ and 0.5% wt. ATO

References

1. Huang SH, Liu P, Mokasdar A, Hou L (2013) Additive manufacturing and its societal impact: a literature review. *Int J Adv Manuf Tech* 67:1191–1203
2. Ivanova O, Williams C, Campbell T (2013) Additive manufacturing (AM) and nanotechnology promises and challenges. *Rapid Prototyp. J.* 19:353–364
3. Vidakis N, Vairis A, Petousis M, Savvakis K, Kechagias J (2016) Fused deposition modelling parts tensile strength characterisation. *Acad J Manuf Eng* 14:87–94
4. Sood AK, Ohdar RK, Mahapatra SS (2012) Experimental investigation and empirical modeling of FDM process for compressive strength improvement. *J Adv Res* 3:81–90
5. Rodrõ AF, Thomas JP, Renaud JE (2001) Mechanical behavior of acrylonitrile butadiene styrene (ABS) fused deposition materials Experimental investigation. *Rapid Prototyp J* 7:148–158
6. Ahn SH, Montero M, Odell D, Roundy S, Wright PK (2002) Anisotropic material properties of fused deposition modelling ABS. *Rapid Prototyp J* 8:248–257. <https://doi.org/10.1108/13552540210441166>
7. Vidakis N, Petousis M, Vairis A, Savvakis K, Maniadi A (2017) On the compressive behavior of an fdm steward platform part. *J Comput Design Eng* 4:339–346. <https://doi.org/10.1016/j.jcde.2017.06.001>
8. Vidakis N, Petousis M, Maniadi A, Koudoumas E, Vairis A, Kechagias J (2020) Sustainable additive manufacturing: mechanical response of acrylonitrile-butadiene-styrene over multiple recycling processes. *Sustainability* 12(9):3568. <https://doi.org/10.3390/su12093568>
9. Maniadi A, Vamvakaki M, Suche M, Tudose IV, Popescu M, Romanitan C, Pachiu C, Ionescu ON, Viskadourakis Z, Kenanakis G, Koudoumas E (2020) Effect of graphene nanoplatelets on the structure, the morphology, and the dielectric behavior of low-density polyethylene nanocomposites. *Materials* 13(21):4776. <https://doi.org/10.3390/ma13214776>
10. Vidakis N, Petousis M, Maniadi A, Koudoumas E, Kenanakis G, Romanitan C, Tutunaru O, Suche M, Kechagias J (2020) The mechanical and physical properties of 3d-printed materials composed of abs-zno nanocomposites and abs-zno microcomposites. *Micromachines*, 2 11(6):615. <https://doi.org/10.3390/mi11060615>
11. Vidakis N, Petousis M, Maniadi A, Koudoumas E, Liebscher M, Tzounis L (2020) Mechanical properties of 3d-printed acrylonitrile–butadiene–styrene TiO₂ and ATO nanocomposites. *Polymers* 12(7):1589. <https://doi.org/10.3390/polym12071589>
12. Vidakis N, Maniadi A, Petousis M et al (2020) Mechanical and Electrical properties investigation of 3d-printed acrylonitrile–butadiene–styrene graphene and carbon nanocomposites. *J Mater Eng Perform* 29:1909–1918. <https://doi.org/10.1007/s11665-020-04689-x>
13. Skorski M, Esenther J, Ahmed Z, Miller A, Hartings M (2016) The chemical, mechanical, and physical properties of 3D printed materials composed of TiO₂-ABS nanocomposites. *Sci Technol Adv Mater* 89:89–97

Mechanical Testing and Optimization of Bamboo and Tamarind Fiber Composites



Gowdagiri Venkatesha Prasanna, Achyutuni Venkata Naga Sri Harsha, Vemula Sunil Kumar, and Rapolu Srilekha

Abstract The robustness and hardness of biofiber composites produced of bamboo and tamarind fibers were investigated in this study. In contrast to synthetic fibers, these fibers are inexhaustible, lightweight, cost-effective, and biodegradable. While natural fibers have several advantages over synthetic fibers, one disadvantage is that they are hydrophilic. The hydrophilic aspect of fibers makes it difficult for the matrix and fibers to fuse well. So the fibers are chemically processed with sodium hydroxide, potassium permanganate, acrylic acid, and benzene diazonium chloride to improve their cohesiveness. These treatments change the surface texture and biocomposition, allowing fibers and resin to adhere properly. The fabrication process is completed using the hand layup method. The specimens were made with varying weight ratios of fiber composition (10, 20, 30, 40, and 50%). The specimens were tested for strength using ASTM standards. Chemical procedures changed the fiber structure and improved the composite's performance, according to the study. 40% fiber weight composite specimen handled with benzene diazonium chloride had superior strength properties to untreated and chemically handled fibers. The moisture content of untreated and treated fibers was tested, and the results showed that the fibers treated with benzene diazonium chloride had less moisture. The dielectric strength test results revealed that 40% wt of fiber treated with benzene diazonium chloride has a higher dielectric strength.

Keywords Bamboo fiber · Tamarind fiber · Mechanical test · Chemical treatment

1 Introduction

Composites are the most appealing materials, since they are created by incorporating two or more natural or artificial products to create a composite that is stronger as a whole and adds to the most desirable characteristics such as weight, performance, and longevity. Due to advantageous properties such as strong damping power, high

G. Venkatesha Prasanna (✉) · A. V. N. Sri Harsha · V. Sunil Kumar · R. Srilekha
Department of Mechanical Engineering, CVR College of Engineering, Hyderabad, Telangana
501510, India

© The Author(s), under exclusive license to Springer Nature Singapore Pte Ltd. 2022
H. K. Dave et al. (eds.), *Recent Advances in Manufacturing Processes and Systems*,
Lecture Notes in Mechanical Engineering,
https://doi.org/10.1007/978-981-16-7787-8_52

647

specific modulus, and high specific pressure, these are now widely utilized in the automotive industry. Due to their outstanding properties such as water resistance, light weight, high resilience, chemical resistance, electrical resistance, high strength, fire resistance, and corrosion resistance, fiber reinforced composites have been extremely common in the aircraft and automotive industries. The majority of FRP fibers are made up of synthetic fibers such as glass fibers and carbon fiber. However, there are a few drawbacks of using artificial fibers, including the reality that they are non-renewable, non-biodegradable, and noxious to the earth because the processing of these fibers release a large amount of carbon dioxide into the atmosphere, as well as their energy-intensive fabrication method. As a result, natural fibers must be adapted. These fibers are used to render composites lighter, and they have a number of benefits over artificial fibers, including their variety, low weight, reduced damage to manufacturing equipment, cost effectiveness, superior relative mechanical properties like flexural and tensile modulus, and superior surface strength of formed parts composites. The most important aspect in composites is insulation, which can endure the full load placed on the material. That it must withstand the weight, it must be porous and have superior hardness. Matrix is an adjoining structure that preserves and strengthens the reinforcement. We may obtain a wide variety of physical properties by combining the correct amount of matrix and reinforcing, lending composites to a myriad of applications. Polymer is used as the matrix for its extensive range of physical properties like strong power, low shrinkage, outstanding adhesion properties, simplicity of shape, and decent electrical and thermal insulation. Natural fibers are used as insulation to compensate for the polymer matrix's poor strength and stiffness. Natural fibers have a number of benefits, including biodegradability, low expense, quick supply, no health effects, and renewability, but they still have a few disadvantages such as poor wettability and moisture tolerance, which decreases the bonding between the reinforcement and matrix. This lead to the evolutions of composites with poor mechanical properties. As a result, composites with weak mechanical properties evolved. To address this disadvantage, chemical treatment of the composites may be used to remove the repulsive quality and improve the properties of the composites by changing the microstructure and refining the wettability, tensile strength, and surface morphology of fibers, thus enhancing the adhesive property of fibers with matrix and making them less hydrophilic.

2 Experimentation

2.1 Materials

Fibers: Bamboo and tamarind fibers (Figs. 1 and 2, Table 1).

Resins: Vinyl ester and unsaturated polyester.

Fig. 1 Bamboo fiber**Fig. 2** Tamarind fiber**Table 1** Natural fiber composition

Fiber	Ash (%)	Hemicellulose (%)	Lignin (%)	Pectin (%)	Cellulose (%)
Bamboo fiber	0.20	12.49	12.49	0.37	73.8
Tamarind fiber	2.19	64.5	59	18.21	64.5

2.2 Surface Alteration of Natural Fibers

Just a few issues occur at the interface during the fortification of natural fibers into the resin mix due to the proximity of natural fibril hydroxyl groups. Since natural fiber absorbs water, it is tough to hold strands in a resin mix. Pectin, oil, waxy dirt, and grease present in the fibers act as a buffer between the resin blend and the reinforcement. To increase interfacial holding capability between fibers and resin, fiber surfaces must be treated with various chemicals.

2.3 Chemical Treatments

Various chemical therapies, binding agents, and reaction supplements must be added to the fiber surface to boost interfacial adhesiveness. Surface handling creates redundant reflex sections on the fiber surface, making matrix union possible.

2.3.1 Alkali Treatment

The fibers were dewaxed after being soaked in a 2:1 combination of benzene and ethanol for 72 h. At 30 to 32 °C, these fibers were immersed in a 6% sodium hydroxide solution for 1 h. The solution's total amount is 15 times the wt of the fibers. They are then dissolved in an alkaline solution for 36 h at 30 to 32 °C, washed, and neutralized with a 2% (CH₃COOH) acetic acid solution. Finally, they are washed under water to remove any residual acid that has adhered to them, bringing the pH of the fiber to nearly 7. Eventually, alkali-treated fibers are acquired by dehydrating them at room temperature for 48 h.

2.3.2 Acrylic Acid Treatment

Acrylic acid has been used for treatment. Bamboo and tamarind fibers were soaked in a 1% acrylic acid solution for 1 h at 50 °C, then thoroughly washed with seltzer water until being shriveled in a 70 °C oven for 24 h.

2.3.3 Permanganate Treatment

After 30 min of immersion in 6% sodium hydroxide, the fibers were thoroughly cleansed with seltzer water. These alkali-treated fibers are treated with 0.5% potassium permanganate in C₃H₆O solution for 2 min, then cleaned using water and dehydrated at 80 °C in an oven.

2.3.4 Preparation of Benzene Diazonium Chloride

8cm³ of concentrated HCL was applied to a boiling tube comprising 10cm³ of water and 3cm³ of aniline, and the blend was shaken until the amine was dissolved. The mixture was then cooled in an ice bath at 5 °C, and then a solution of NaNO₃ (3 g in 8cm³ of water), formally luke warmed to 5 °C, was poured at the time of blending the blend temperature was conserved to less than 10 °C.

2.3.5 Benzene Diazonium Treatment

The bamboo and tamarind fibers were cut to 10 mm lengths, cleaned using seltzer water, and dehydrated at 70 °C in an oven for 24 h. The fibers were then soaked in a 2L glass beaker containing a 6% sodium hydroxide solution for 10 min at 5 °C. The newly made diazo solution was then allowed into the beaker and continuously stirred. Finally, the fibers were stripped and cleaned with clean water and soap solution, followed by dehydration in the open air for 48 h.

2.3.6 Fabrication of Blended Hybrid Biocomposites.

For easy removal of composites, the mold cavity is filled with a dense layer of solid wax. Lean liquor arranged POLYVINYL ALCOHOL (PVA) was added immediately after the wax was re-established. The hand layup method is used to assemble the bio-fibrils crossover composite. Cross-breed biostrands of treated and untreated tamarind bamboo fibers are reinforced to network mix to required biocomposite execution and mechanical requirements at that stage. After that, air bubbles are gently removed with delicate spinning rollers. The objective of the post-cure in the temperature of 800 oC for about two hours by putting the specimen in a hot oven is to cure composite samples fully. Biocomposite specimen samples are checked after they have been completely cured, both raw and refined (Figs. 3 and 4).

Fig. 3 Fabrication of blended hybrid biocomposites



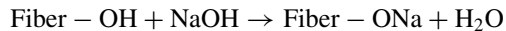
Fig. 4 Universal testing machine



3 Chemical Treatment of Fibers

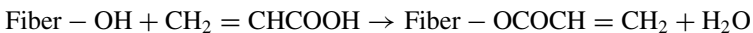
3.1 Alkali Treatment

The morphology of bamboo and tamarind is significantly altered by alkali therapy, which helps in the expulsion of hydrogen bonding in the fiber network, resulting in a reduction in moisture absorption. It decreases the width of the thread, resulting in a higher aspect ratio. The interfacial adhesion is improved as the aspect ratio is increased, which increases the mechanical properties. Enhancing the surface roughness improves mechanical interlocking and the amount of cellulose on the fiber surface. This allows for increased fiber wetting by increasing the number of appropriate reaction sites. It also increases the amount of amorphous cellulose, resulting in a decrease in crystalline cellulose.



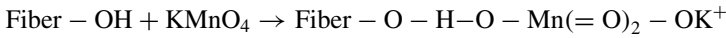
3.2 Acrylation Treatment

This treatment made the fibers more hydrophobic by reducing the absorption of water through them. Bamboo and tamarind fibers treated with acrylic acid absorbed less moisture. It is because the hydroxyl group has been replaced by hydrophobic water groups.



3.3 *Permanganate Treatment*

Extremely, reactive permanganate ions interact with cellulose hydroxyl groups to form cellulose manganate in this treatment. Chemical interlocking at the surface improves, as a result, resulting in better matrix-fiber attachment. It lowers the fiber's hydrophilic value.



3.4 *Benzene Diazonium Chloride Treatment*

This treatment aids in the reduction of fiber water absorption by improving matrix-fiber adhesion. The coupling reaction of benzene diazonium chloride with OH groups produces diazo cellulose in this treatment.

4 Results and Discussion

4.1 *Tensile Strength Properties*

Composite specimens with measurements of $150 \times 15 \times 3 \text{ mm}^3$ were prepared, in accordance with ASTM D 3039 requirements (Universal Testing Machine). The interfacial bonding between matrix and fiber would not be accurate due to the existence of hydroxyl groups in fiber and the inclusion of undesirable substances such as oil, grease, pectin, and waxy powder. Chemical treatments were used to resolve these issues such as, alkali treatment decreases fiber diameter, raises aspect ratio, enhances stress transfer capability, and improving tensile strength, while permanganate treatment roughens the surface, offering strong interlocking at the interface and increasing adhesion between fiber and matrix, increasing tensile strength. The stress transmission quality at the fiber interface improves as a result of the acrylation of the fiber by increasing the tensile power. Chemical treatments have an effect on fiber strength, as seen in Fig. 5 the analysis shows that at 10, 20, 30, 40 and 50% fibril quantity biocomposites, $[\text{C}_6\text{H}_5\text{N}_2] \text{Cl}$ -treated fiber composites exhibit higher and optimum values than sodium hydroxide treated, acrylic acid-treated, potassium permanganate treated, and untreated fiber composites [1, 4, 9]. The strength values increased from 10 to 40% due to rich fiber distribution. Owing to a lack of adequate adhesion between the matrix and fibers, inadequate stress transfer, weak fiber distribution, less fiber splitting, and tensile strength drop after 40%. As opposed to all chemically cured fiber composites, the untreated fiber composites have poor tensile power, as seen in Fig. 5. The hydrophilic design of the untreated fibers explains

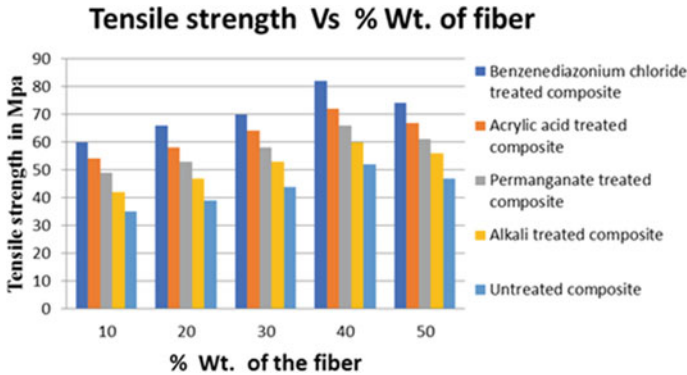


Fig. 5 Tensile strength

this. As a result, the matrix and fiber are incompatible. In either case, alkali-treated tamarind- bamboo fibrils composites had a strong visible tensile power, and $[C_6H_5N_2]Cl$ -treated tamarind-bamboo fibrils composites had a vital increment. According to the findings, chemical processes generated a strong interface with fibril cell walls, and pairing response between $[C_6H_5N_2]Cl$ and fibril cellulose results in the development of diazo cellulose compounds, which are supposed to watch the essential increase of composite tensile property. Surface treatment with $[C_6H_5N_2]Cl$, sodium hydroxide, allows one to expel unwanted materials, thus improving fibril distribution in matrix blends, resulting in improved mechanical properties [1, 3, 4, 6, 10].

4.2 Compressive Strength Properties

ASTMD695–15 stipulations are used to prepare and test composite samples in order to determine their compressive power. Figure 6 shows the changes in estimations for compressive content properties for fibril volumes without and with surface modification. Similarly, $[C_6H_5N_2]Cl$ tested bio-fibrils composites have higher compressive properties and perfect conditions than alkali tested, acrylic acid-treated, potassium permanganate raw biocomposites [1, 4, 9]. The optimal and superior conditions are attributed to ideal fibril stacking and chemical handling, which advanced strong interfacial keeping between filaments framework mix, resulting in adequate stress transfer and execution [1, 4, 6]. Acrylic treated fiber composites remove more harmful materials than alkali, permanganate-treated fiber composites, but not as much as benzene diazonium chloride-treated fiber composites. The previous research has discovered that material treatment decreases the gap between fibrils and broadens the roughness of the surface [3, 7, 9]. At 50% fibril magnitude, there is a smaller drop in compressive properties of composites. The reduction in compressive properties at 50% fibril material handled and untreated composite (higher fibril loads) shows low fibril-grid interfacial gripping and small scale breakage at interface prompt inadequate

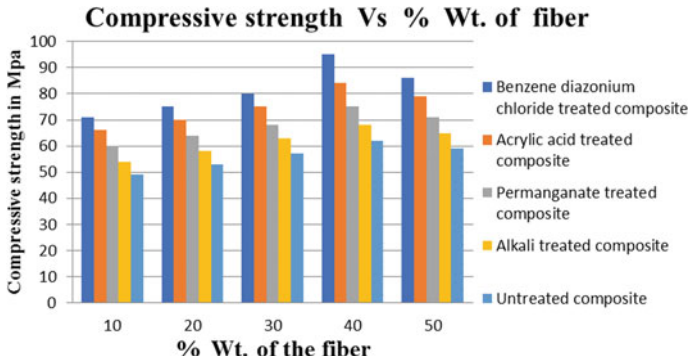


Fig. 6 Compressive strength

stress transfers. The compressive intensity of 40% fibril stackings was particularly impressive. The $[C_6H_5N_2] Cl$ therapy, on the other hand, fills the voids in the fibril resulting in higher compressive strength [1, 3, 5].

4.3 Flexural Strength Properties

To determine the flexural property, 150mmx15mmx3mm specimens were produced and checked according to the ASTM D 5943–96 standard. Figure 7 depicts the disparity of flexural content estimations of composites. As flexural properties of 40% fibril amounts, $[C_6H_5N_2] Cl$ -treated biofibrils composites were more compared to acrylic acid-treated, potassium permanganate treated, sodium hydroxide treated, untreated at 10, 30, 20, 40, and 50% fibril amounts composite [1, 3, 4] due to proper

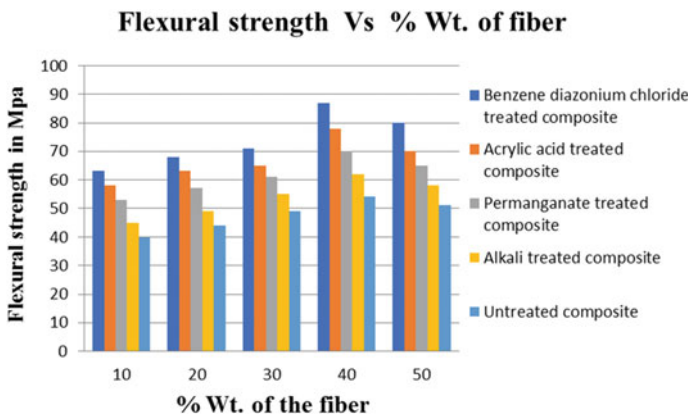


Fig. 7 Flexural strength

fiber distribution and load transfer. It was observed that the values increased from 10% fiber weight to 40% fiber weight and a decrease after 40% due to poor fiber distribution. Alkaline treatment improves the stress transmission capability of the fiber, while permanganate treatment improves the interlocking at the interface and increases fiber and matrix adhesion. Acrylic acid-treated biofibers composites had better fibril-matrix compatibility, collaboration, and handling than potassium permanganate and sodium hydroxide-treated biofibers composites [2, 4, 6, 7]. Compared to treated bio-fibrils composites and untreated bio-fibrils composites, $[C_6H_5N_2] Cl$ -treated bio-fibrils composites exhibited more significant and noticeable production of fibril dissemination matrix, stress, and aspect ratio transfer capability.

4.4 Moisture Content Testing

Figure 8 displays the rate of moisture ingestion by untreated fibril composites, alkali-treated composites, potassium permanganate, acrylic acid, and $[C_6H_5N_2] Cl$ -treated composites produced to ASTM D 543–87 standards. Bio-fibrils composites are made up of fibrils that have hydrophilic properties [7, 9]. In any case, alkali-responsive hydroxyl groups in molecules are dissolved, which combines with OH-H molecules at points and transfers from fibril formations. As a result, alkali and $[C_6H_5N_2] Cl$ treatment reduced hydrophilic hydroxyl groups and increased moisture blockage qualities outside the fibril. [1, 2, 4]. The presence of hydroxyl groups in fibers makes them capable for the formation of hydrogen bonding with water resulting in hydrophilic nature. These fibers when treated with alkali, ONa groups replace the hydroxyl groups resulting in the decrease of moisture absorption in $[C_6H_5N_2] Cl$ -treated fibers. Unprocessed fibril composites absorb more moisture than alkali-treated, acrylic acid-treated, potassium permanganate-treated, and $[C_6H_5N_2] Cl$ -treated composites [1, 2, 9].

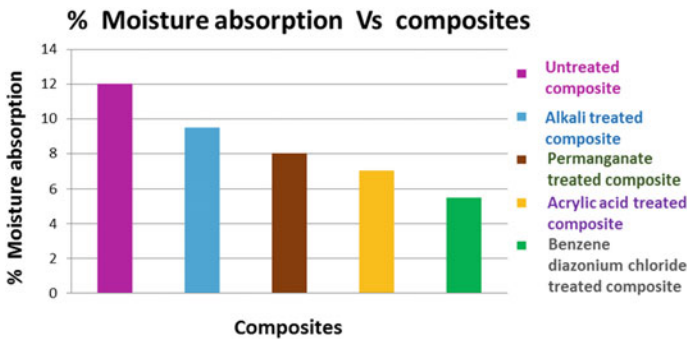


Fig. 8 Moisture content testing

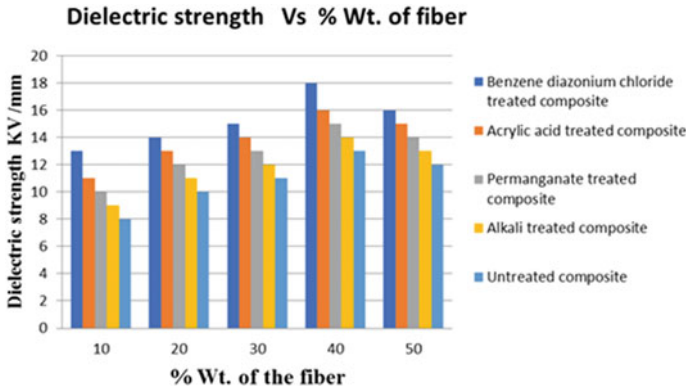


Fig. 9 Dielectric strength

4.5 Dielectric Strength

These composites samples were produced with ASTM-D-149 steps to contemplate dielectric properties of untreated, acrylic acid, potassium permanganate alkali treated, and $[C_6H_5N_2]$ Cl-treated composites. A composite with dimensions of $120 \times 120 \times 3\text{mm}^3$ is reinforced with strands that are 120 mm long and stranded in one direction. For five of the specimens, dielectric splitting voltage is discovered and the mean value is used in the investigations. The test is performed at 50 Hz recurrence and ambient temperature. To determine the thickness of the composite at specific stages, a digital micrometer with a 0.001 mm least count was used. The fiber distribution is maximum at 40% wt of fiber, and the expulsion of unwanted materials is more at $[C_6H_5N_2]$ Cl-treated fibers at 40%, so the dielectric strength is maximum at 40% wt benzene diazonium-treated fibers. It is also worth noting that the dielectric content of crossover fibril composites improves when the percentage wt of fibril rises from 10 to 40%, but decreases at 50% fibril magnitude composites [3, 7, 9]. The lack of interfacial holding between strands and resins blend resulted in a decrease in dielectric quality at 50% fibril magnitude composites [1, 2, 4, 8] (Fig. 9).

5 Conclusion

From the above research by observing the results, we can conclude that the chemical treatments done on fibers imparted that the treatments impact their surface and their biochemical composition. The benzene diazonium chloride treatment has more impact on the fibers than the acrylic acid, potassium permanganate, NaOH treatments. In the tensile strength test, the benzene diazonium-treated fiber specimens have higher strength value followed by acrylic acid-treated specimens. The compressive results show that the benzene diazonium-treated fiber specimens have the highest

value than other treated and untreated composites. Even in the flexural strength tests, the benzene diazonium-treated fibers have the highest value. Other than the strength tests, the dielectric strength results show that the benzene diazonium chloride treated specimens have higher strength. The moisture content results depict that the fibers treated with benzene diazonium chloride have less moisture. Hence, we can come to a point that benzene diazonium treatment has a better impact on the fibers to lose their hydrophilic nature and improve the overall strength of the composite.

References

1. Venkatesha Prasanna G, Venkata Subbaiah K, Varada Rajulu A (2012) Chemical resistance, impact, flexural, compressive properties and optimization of fibers of natural fibers reinforced blend composites. *Scholarly J Eng Res* 1(6):85–89
2. Kalia S, Kaith BS, Kaur I (2009) Pretreatments of natural fibres and their application as reinforcing material in polymer composites—a review. *Polymer Eng Sci* 49:1253–1272
3. Venkatesha Prasanna G, Sunil Kumar V, Srilekha R, Sri Harsha AVN, Sai Abhi Chandan V (2021) Hybridization and influence of chemical treatment on the morphology and optimization of composites, Elsevier, *Materials today proceedings*, 4833–4837
4. Alamgi MK, Monimul MH, Islam RM, Bledzki AK (2010) *BioResources* 5:1618–1625
5. Rahman MR, Islam MN, Huque MM, Hamdan S, Ahmed AS (2010) *BioResources* 5:854
6. Punyamurth R, Sampath Kumar D, Bennehalli B, Badyankal P, Vekateshappa SC (2014) Surface modification of abaca fiber by benzene diazonium chloride treatment and its influence on tensile properties of abaca fiber reinforced polypropylene composites. *CienciaTechnologia dos materiais* 26(2):142–149
7. Composites and its recycle. *J Biol Sci* 7:393–396 (2007)
8. Yu T, Ren J, Li S, Yuan H, Li Y (2010) Effect of fibre surface-treatments on the properties of poly (lactic acid)/ramie composites. *Composites Part A: Appl Sci Manuf* 41:499–505
9. Venkatesha Prasanna G, Sri Harsha AVN, Srilekha R, Sunil Kumar V, Sai Abhi Chandan V (2020) Chemical treatment and fiber length, their effect on the mechanical properties of blended composites, Elsevier, *materials today proceedings*, 4862–4866
10. John MJ, Anandjiwala RD (2008) Recent developments in chemical modification and characterization of natural fiber-reinforced composites. *Polym Compos* 29:187–207

Mechanical, Degradation, and Flammable Behavior of VALOX_{100-x}—X Wt. % Polycarbonates Composite Materials for Electrical Plugs, Sockets, and Extension Applications



Khalid Algadah, Subbarayan Sivasankaran, and Abdulaziz S. Alaboodi

Abstract In the present research work, new VALOX composite materials have designed, developed, and investigated as per Saudi Standards, Metrology and Quality Organization (SASO) requirements. The newly developed materials have consisted of pure VALOX (Polybutylene terephthalate, PBT mixed with 30 wt.% glass fiber) and different weight percentage of polycarbonate (PC) granules. Pure VALOX 420 grade was incorporated with 5, 10, and 15 wt.% of polycarbonate granules which these composite materials consist of two soft thermoplastic matrices and one glass fiber of ceramic phase. The developed materials were designated as VALOX-0 wt.% PC, VALOX-5 wt.% PC, VALOX-10 wt.% PC, and VALOX-15 wt.% PC. These composite materials can be recommended to use in electrical plug, electrical socket, and electrical extension boxes applications. These composite materials were manufactured by mechanical grinding/milling method and then consolidated the powder samples to bulk by hand-operated injection molding machine. Samples were prepared as per ASTM/ISO testing standards for conducting compression test, mechanical degradation test, and flammability test. The test results have shown that the VALOX + 5 wt.% PC composite samples exhibited improved mechanical strength, mechanical degradation-ability, and good in flammability compared to other samples.

Keywords VALOX composite materials · Mechanical grinding method · Hand-injection molding · Mechanical testing · Degradation · Flammability

1 Introduction

It is well known that polybutylene terephthalate (PBT) is the most commercially used thermoplastic-based polymers in the world which can be easily molded into any

K. Algadah · S. Sivasankaran (✉) · A. S. Alaboodi
Department of Mechanical Engineering, College of Engineering, Qassim University, Buraidah
51452, Saudi Arabia
e-mail: sivasankaran@qec.edu.sa

A. S. Alaboodi
e-mail: alaboodi@qec.edu.sa

© The Author(s), under exclusive license to Springer Nature Singapore Pte Ltd. 2022
H. K. Dave et al. (eds.), *Recent Advances in Manufacturing Processes and Systems*,
Lecture Notes in Mechanical Engineering,
https://doi.org/10.1007/978-981-16-7787-8_53

shapes. PBT is usually in semicrystalline nature or amorphous form which depends on the selection of cooling rate and forming techniques [1, 2]. PBT exhibits improved properties, namely high mechanical strength, excellent abrasion resistance, good in heat resistance, excellent in chemical resistance, and possessing good dimensional stability when PBT is reinforced with glass fiber (VALOX materials). This VALOX materials are developed by SABIC which are (for instance): VALOX 508 SABIC 30% Glass Fiber, VALOX 553 SABIC 30% Glass fiber, and VALOX 745 SABIC 30% Mineral. This PBT possesses several engineering applications such as electrical field (electrical plug, relays, switches, distribution boxes), fiber optic cable (jackets), and some automotive components. However, the fracture toughness value of PBT polymers is lower one which affect/decreases the impact resistance. To improve the available properties of VALOX materials (PBT polymers), some other thermoplastic materials can be blended. Among several thermoplastics, polycarbonate (PC) is the best thermoplastic blend which can easily mix with the PBT polymers. Due to the blending of PC in PBT, several properties can be improved, namely flexibility and easy for processability consequently any intricate shapes with dimensional stability and corrosion resistance in chemical environment can be achieved compared to the present one. Assembly of matter into micro-/nano-metric scale provides unimaginable improved properties from the materials especially by adding some reinforcements called as nanocomposites [3, 4] which is recent scenario for the research community. This can be achieved in polymers based nanocomposites. The incorporation of soft polycarbonates (PC) with the PBT and glass fiber produces multi-structured materials. Due to nanostructures/multi-structures, the physical, electrical, thermal, mechanical and chemical properties can be changed in to expected industrial/market demand [5]. These polymer nanocomposites consist of matrix materials and dispersion of second phase ceramic particles which VALOX materials are under the category of polymer composites [6].

SABIC discovered several innovative plastics (SABIC-IP) for various products (PET bottles, electrical parts). For electrical appliances, SABIC uses polybutylene terephthalate (PBT) mixed with glass fibers and minerals which are called as VALOX materials [7]. Showaib and Elsheikh [8] have investigated the mechanical strength of VALOX 420 joined parts (PBT polymers mixed with 30% GF) by linear friction method after the surface preparation. The VALOX 420 pellets were produced by injection molding. Thongsong et al. [9] developed polybutylene adipate-co-terephthalate (PBAT) polymer mixed with polyethylene terephthalate (PET)-based material. The authors have investigated the mechanical and thermal properties. In addition, titania (TiO₂) and zinc oxide (ZnO) surface treatment over the PBAT-PET polymers were done and studied the mechanical properties. The results demonstrated that enhanced mechanical properties were obtained by incorporating 2 wt.% ZnO. Hernández-López [10] developed biodegradable-based PBAT/PLA (poly-lactic acid) material which consist of 60% PBAT and 40% PLA produced by extrusion. Choi et al. [11] developed a polymer-based nanocomposite material which consist of PBT polymer mixed with multi-wall carbon nanotubes (MWCNTs) by in-situ method of transesterification. The authors have explored the electrical and mechanical properties. Ma'eder et al. [12] have investigated the adhesive, interphase properties, and

mechanical performance of PBT mixed with the glass fiber (GF). Ivanič et al. [13] investigated the mechanical and structural properties of PBAT mixed with thermo-plastic starch (TPS). Ferreira et al. [14] developed PBT polymers mixed with different weight percentage of polycarbonates (PC). The authors have characterized the several PBT/PC polymers using FTIR. Schmidt et al. [15] have used PBT granules of 2–3 mm and converted it into products using additive manufacturing technology (via laser beam melting, recent technique). Zhao et al. [16] have used nano-fibrillation technology for developing PBT mixed with poly-propylene (PP) polymers for electrical and automotive applications. The authors have investigated the thermal properties via TGA, mechanical properties in terms of compressive strength and rheological properties. Olmos et al. [17] have developed nanocomposites which consist of high-density polyethylene (HDPE) mixed with titania (TiO₂). Jung et al. [18] have synthesized HDPE/nano-BN (boron nitride) nanocomposite via mechanical milling method. The results explained that effective dispersion of BN over HDPE was achieved by mechanical milling. From the literature review, there are not much studies related to the manufacturing of VALOX 420 grade mixed with different weight percentage of polycarbonates prepared by mechanical blending/grinding followed by hand-operated injection molding techniques. In the present research, the development of new VALOX composite multi-material structures by solid-state mechanical grinding method, investigation of its mechanical properties by compression test, exploration of the mechanical degradation-ability by varying the temperature with a constant load over the samples, and determination of the fire capturing and time taken for complete burning of the developed materials using flammability test were carried out and reported.

2 Experimental Methods

2.1 *Synthesis of VALOX_{100-x}—X Wt.% PC (X = 0, 5, 10, and 15 Wt.%) Multi-Material Structures*

VALOX granules were mixed with different weight percentages of polycarbonate granules. The incorporated PC granules were 0, 5, 10, and 15 wt.% over VALOX material producing multi-materials structures. The detailed chemical composition of developed composites of multi-materials is shown in Table 1. Figure 1a, b shows the macrograph of as-received VALOX 420 grade granules and polycarbonate granules, respectively. Mechanical mixer/grinder was used to manufacture the VALOX 420 grade incorporated with different weight percentage of polycarbonates of multi-material structures. The charged materials as per chemical composition mentioned in Table 1 was mechanically ground at a speed of 2000 rpm for 10 min. After 10 min, all the incorporated granules were converted into the form of powders. The multi-structured powders were then fed into a hand-operated plastic injection machine (Fig. 2a). Before injecting the composite melt, a temperature of 275 °C was set,

Table 1 Chemical composition of developed VALOX + x wt.% PC composite multi-structures

Sample specification	Weight of VALOX granules, g	Weight of Polycarbonate, g
VALOX + 0 wt.% PC	100	0
VALOX + 5 wt.% PC	95	5
VALOX + 10 wt.% PC	90	10
VALOX + 15 wt.% PC	85	15



Fig. 1 Macrograph of as-received: **a** VALOX 420 grade granules; **b** Polycarbonates

heated until 275 °C, and hold it for 10 min to attain the melt stage. Once reach the melt stage, the lever was operated toward downward direction to inject the plastic melt over the mold for fabricating the samples.

2.2 *Mold Design and Sample Preparation for Mechanical Testing*

To conduct the mechanical behavior of developed composites of multi-materials, a mold was designed and fabricated from H13 steel. A cylindrical sample was fabricated with the dimensions of diameter 10 and 17 mm height which was under ASTM E39 standard for compression test. The prepared samples were subjected to compression until fracture with the cross head speed of 3 mm per minute (Fig. 2b). The load cell and the actuating sensors have given the applied load and shortening of samples during test, respectively. The data obtained from the machine was used to determine the mechanical properties such as yield strength, strain at yield, ultimate strength, and strain at ultimate point. The yield strength was estimated at 0.2% offset strain.

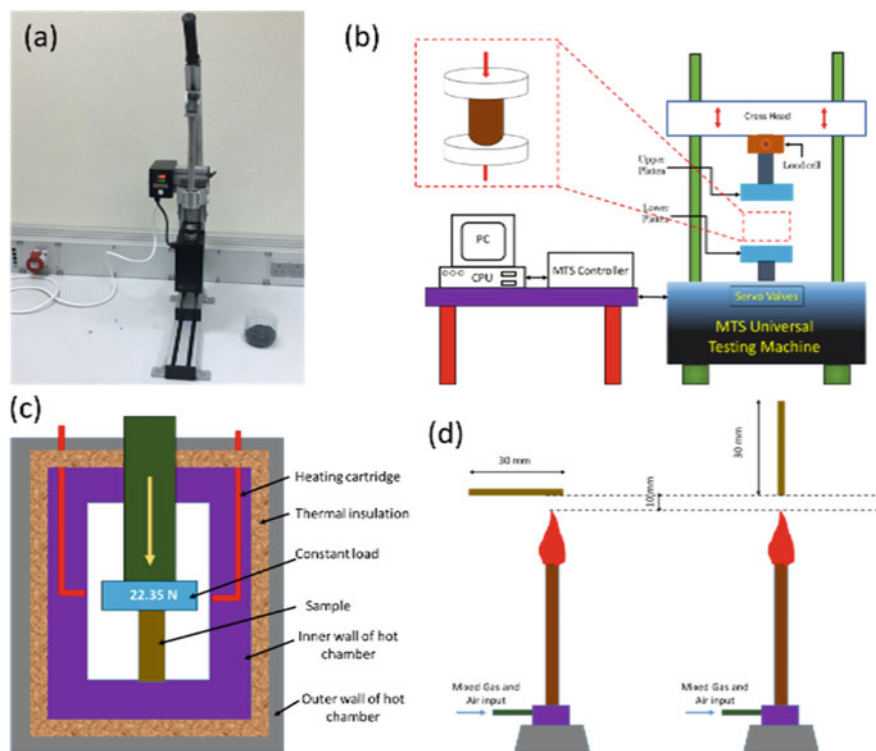


Fig. 2 **a** Photograph of used hand-operated plastic injection molding machine; **b** Schematic of compression test conducted in a MTS universal testing machine; **c** Schematic of mechanical degradation test; **d** Schematic of Flammability test

2.3 Mechanical Degradation Test

Mechanical degradation test over the fabricated VALOX + x wt.% PC composites of multi-materials samples was conducted by varying the temperature with a constant load. This test was conducted to determine the temperature withstanding ability of the developed materials. Figure 2c shows the schematic of mechanical degradation test in which a constant load of 22.35 N was applied due to the weight of fixture. This mechanical degradation setup consists of inner chamber, outer chamber, and moveable plunger with head. Three heating cartridge inserts were fixed in the inner chamber with maximum heating capability of 500 °C. VALOX + X wt. % PC samples ($X = 0, 5, 10, \text{ and } 15 \text{ wt.}\%$) with the dimensions of 10 mm in diameter and $17 \pm 1.5 \text{ mm}$ height were used in mechanical degradation test. The prepared sample was put inside the heating chamber, heating was started from room temperature to degradation temperature with the average heating rate of $1.5 \text{ }^\circ\text{C}/\text{min}$. At least, two to three trials were used in each composition and the average was used for investigation.

2.4 Flammability Test Over VALOX + x Wt.% PC Samples

Flammability test is an important one in the electrical parts by which the sample burning rate, complete burning characteristics, smoking behavior, sample ignition characteristics, how the samples burning quickly, etc., can be determined. In general, two types of flammability test are the common one such as horizontal flammability test and vertical flammability test. Figure 2d shows the schematic of flammability test of both horizontal and vertical types. In the present work, vertical-type flammability test was conducted over the samples for which around 30 mm extruded samples from the nozzle was used. At least, three samples in each composition were used and the average was used for investigation. A stop watch was used to find-out the complete burning time of each sample.

3 Results and Discussion

VALOX-x wt.% PC composites of multi-materials ($x = 0, 5, 10,$ and 15 wt.%) were fabricated successfully. The mechanical properties in terms of uniaxial compression test, mechanical degradation test, and flammability test were conducted, and the results and discussion are given in the subsequent sections.

3.1 Examination of Mechanical Behavior of VALOX—X Wt.% PC Composites of Multi-Materials

The mechanical performance of VALOX-x wt.% PC composites multi-materials of three replicas is shown in Fig. 3. The results of Fig. 3a illustrate that pure VALOX of 0 wt.% PC samples has produced an average yield compressive strength and ultimate compressive of 22.3109 ± 0.8253 MPa and 25.6267 ± 1.2183 MPa, respectively. Pure VALOX has produced the compressive strain at ultimate point was around 0.0374 ± 0.0054 mm/mm which was less than 5% indicating that pure VALOX possesses brittle characteristics. To improve the properties of pure VALOX-0 wt.% PC samples, different weight percentage of PC were incorporated by blending and grinding process as explained in the previous sections.

The mechanical performance of VALOX-5 wt.% PC composites multi-materials of three replicas is shown in Fig. 3b. The results of Fig. 3b illustrate that VALOX of 5 wt.% PC samples have produced an average yield compressive strength and ultimate compressive of 37.2131 ± 5.843 MPa and 43.5775 ± 5.133 MPa, respectively. Both yield strength and ultimate strength of VALOX-5 wt.% PC were increased by around 68.89% and 68.18% compared to pure VALOX sample. This was attributed to uniform dissolution of polycarbonate thermoplastic compound in the VALOX (polybutylene and glass fiber composite matrix) matrix. VALOX—5 wt.% PC

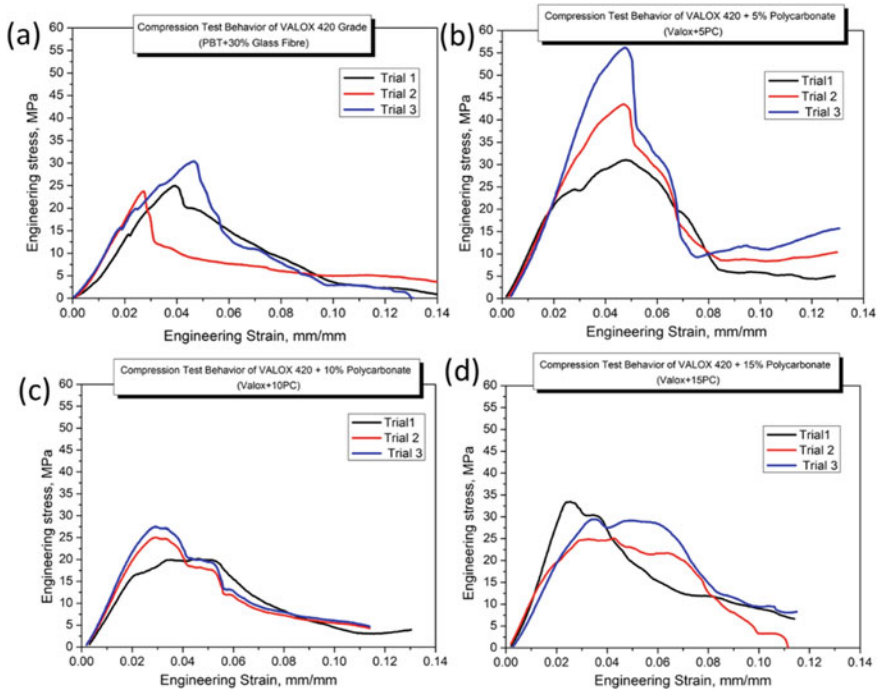


Fig. 3 Room temperature mechanical performance of composite multi-materials with three replicas: **a** pure VALOX-0 wt.% PC composites; **b** VALOX-5 wt.% PC; **c** VALOX-10 wt.% PC; and **d** VALOX-15 wt.% PC

sample has produced the compressive strain at ultimate point was around 0.0477 ± 0.0002 mm/mm which was more in around 28% compared to the pure VALOX. Hence, the incorporation of polycarbonate was expected to increase the mechanical strength and toughness (evidence from strain increment). The mechanical performance of VALOX-10 wt.% PC composites multi-materials of three replicas is given in Fig. 3c. The results of Fig. 3c illustrate that VALOX of 10 wt.% PC samples have produced an average yield compressive strength and ultimate compressive of 21.7585 ± 1.8687 MPa and 24.2436 ± 1.5344 MPa respectively. Both yield strength and ultimate strength of VALOX-10 wt.% PC were decreased compared to pure VALOX and VALOX-5 wt.% PC samples. This was expected to the domination of non-uniform dissolution of polycarbonate thermoplastic compound in the VALOX (polybutylene and glass fiber composite matrix) matrix. VALOX- 10 wt.% PC sample has produced the compressive strain at ultimate point was around 0.0349 ± 0.0042 mm/mm which was lower value compared to pure VALOX and VALOX-5 wt.% PC samples. The mechanical performance of VALOX-15 wt.% PC composites multi-materials of three replicas is shown in Fig. 3d. The results of Fig. 3d illustrate that VALOX of 15 wt.% PC samples have produced an average yield compressive strength and ultimate compressive of 26.0597 ± 2.6226 MPa and 29.2513 ± 1.7546 MPa, respectively.

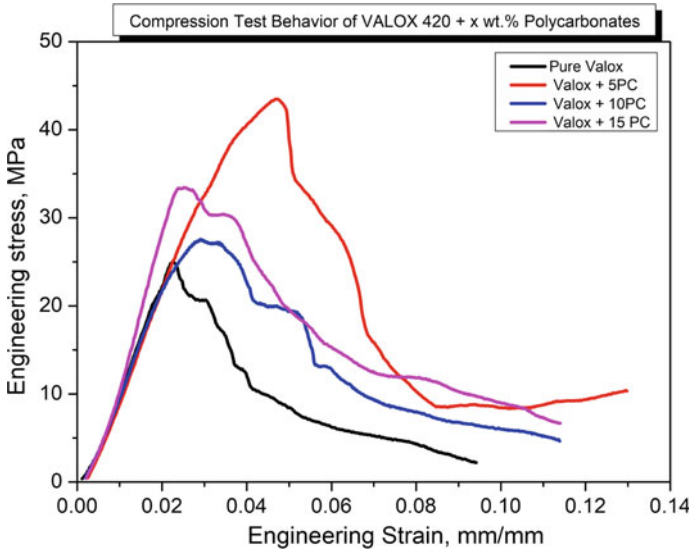


Fig. 4 Comparison of room temperature mechanical performance of VALOX-x wt. % PC composites of multi-materials

Both yield strength and ultimate strength of VALOX-15 wt.% PC were slightly increased compared to pure VALOX and VALOX-5 wt.% PC samples. This was expected to the uniform dissolution and more amount of polycarbonate of thermoplastic compound in the VALOX (polybutylene and glass fiber composite matrix) matrix. VALOX- 15 wt.% PC sample has produced the compressive strain at ultimate point was around 0.0309 ± 0.0021 mm/mm which was lower value compared to pure VALOX, VALOX-5 wt.% PC, and VALOX-10 wt.% PC samples.

The comparison of room temperature mechanical performance of VALOX – x wt.% PC composites of multi-materials is shown in Figs. 4 and 5, and Table 2. The results explained clearly that the incorporation 5 wt.% PC in the VALOX materials has improved the mechanical strength and strain; consequently, the toughness of was also increased. Hence, VALOX-5 wt.% PC samples can be recommended to use it for electrical parts and applications.

3.2 Investigation of Mechanical Degradation of VALOX-X Wt.% PC Composite of Multi-Materials

Mechanical degradation test with varying temperature was performed over VALOX-x wt.% PC composites of multi-materials. The temperature was increased from room temperature (25 °C) until its failure/rupture.

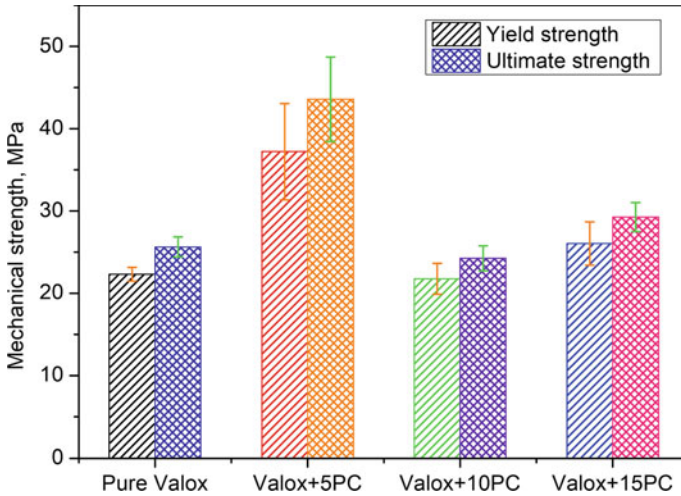


Fig. 5 Variation of yield strength and ultimate compressive strength of VALOX—x wt.% PC composites of multi-materials

Table 2 Comparison of room temperature mechanical properties of VALOX—x wt.% PC composites of multi-materials

Sample name	Yield strength, Mpa	Strain at yield	Ultimate strength, Mpa	Strain at ultimate point
Pure VALOX	22.3109 ± 0.8253	0.0298 ± 0.0045	25.6267 ± 1.2183	0.0374 ± 0.0054
VALOX + 5PC	37.2131 ± 5.8433	0.0325 ± 0.0037	43.5775 ± 5.1333	0.0477 ± 0.0002
VALOX + 10PC	21.7585 ± 1.8687	0.0237 ± 0.0008	24.2436 ± 1.5344	0.0349 ± 0.0042
VALOX + 15PC	26.0597 ± 2.6226	0.0238 ± 0.0024	29.2513 ± 1.7546	0.0309 ± 0.0021

Figure 6 shows the mechanical degradation behavior of pure VALOX—0 wt.% PC samples with 5 replicas. The results have explained that with the increasing of temperature up to around 200 °C, the samples retained its mechanical strength. Once the temperature has reached around 200 °C, the samples have exhibited to degrade by itself suddenly. Pure VALOX-0 wt.% PC sample possess the average mechanical degradation temperature was around 206.2 ± 2.902 °C. To compare the mechanical degradation behavior of all the developed VALOX-x wt.% PC composites of multi-materials, best three replicas in each sample composition were taken, and the average results were used for examination. Table 3 and Fig. 7 have explained the results of comparison of mechanical degradation temperature with the incorporation of different percentage of polycarbonates in the VALOX 420 grade. The results have

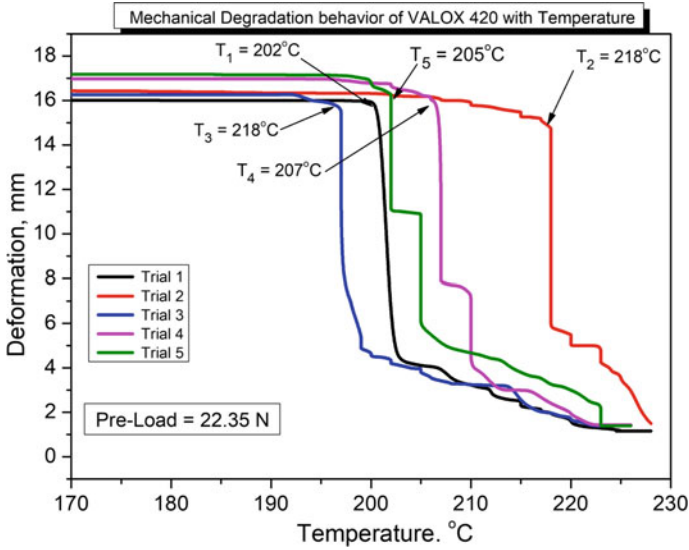


Fig. 6 Mechanical degradation behavior of pure VALOX—0 wt.% PC samples with the function of temperature

Table 3 Comparison of mechanical degradation results of VALOX-x wt.% PC composites of multi-materials

Name of sample	Replica	Sample height before mechanical degradation, mm	Mechanical degradation temperature, °C	Average degradation temperature	Standard deviation	Standard error
Pure VALOX	Trial 1	16	202	204.6667	2.0548	1.1863
	Trial 2	17	207			
	Trial 3	17	205			
VALOX + 5PC	Trial 1	19	219	220.3333	1.2472	0.7201
	Trial 2	19	222			
	Trial 3	19	220			
VALOX + 10PC	Trial 1	19	211	213.0000	1.6330	0.9428
	Trial 2	17	215			
	Trial 3	18	213			
VALOX + 15PC	Trial 1	16	218	215.0000	2.9439	1.6997
	Trial 2	14	211			
	Trial 3	17	216			

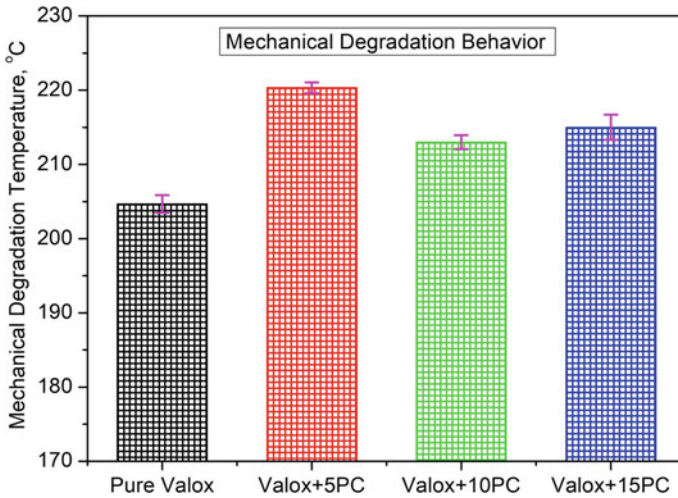


Fig. 7 Average mechanical degradation temperature with the function of incorporation of different weight percentage of polycarbonate compounds in VALOX 420 grade

shown that VALOX-5 wt.% PC sample possesses the highest mechanical degradation temperature of around 220.3333 ± 0.7201 °C. This was attributed to that the incorporation of 5 wt.% PC might have expected dissolve properly in the VALOX composite matrix consequently the sample exhibited to withstand more temperature compared to other samples. However, the incorporation of PC beyond 5 wt.% produced to lower mechanical degradation temperature. But, all the PC incorporated VALOX samples exhibited more mechanical degradation temperature.

3.3 Flammability Behavior of VALOX-X Wt.% PC Composites of Multi-Materials

The flammability of developed VALOX-x wt.% PC composites ($x = 0, 5, 10,$ and 15 wt.%) of multi-materials was carried out to identify that which materials compositions retained more temperature, which materials composition starts to burn quickly and the smoking behavior. Table 4 and Fig. 8 explain the flammability results of developed VALOX-x wt.% PC composite of multi-materials. The results have explored that the incorporation of PC up to 5 wt.% has decreased the flammability by around 41% compared to pure VALOX materials which mean, VALOX-5 wt.% PC sample has taken more time for complete burning which can be recommended for electrical parts. However, with the increasing of PC with the VALOX 420 grade composite matrix, the flammability was increased considerably due to the presence of more amount of lower melting point of polycarbonates. The average flammability speed of VALOX-5 wt.% PC sample has produced 28.7705 ± 2.5617 mm/min which was

Table 4 Flammability results of VALOX-x wt.% PC composites of multi-materials

Sample	Replica	Sample Length (mm)	Time for complete burning in sec	Time in min	Flammability speed, mm/min	Average Flammability, mm/min	Standard Deviation	Standard error
Pure VALOX	Trial-1	30	45.07	0.75	39.94	40.7704	1.7594	1.0158
	Trial-2	30	45.97	0.77	39.16			
	Trial-3	30	41.65	0.69	43.22			
VALOX + 5PC	Trial-1	23	57.20	0.95	24.13	28.7705	4.4370	2.5617
	Trial-2	30	65.60	1.09	27.44			
	Trial-3	28	48.35	0.81	34.75			
VALOX + 10PC	Trial-1	30	36.40	0.61	49.45	49.7754	0.8677	0.5010
	Trial-2	30	36.80	0.61	48.91			
	Trial-3	30	35.32	0.59	50.96			
VALOX + 15PC	Trial-1	30	39.54	0.66	45.52	44.4849	0.9553	0.5516
	Trial-2	30	41.65	0.69	43.22			
	Trial-3	30	40.26	0.67	44.71			

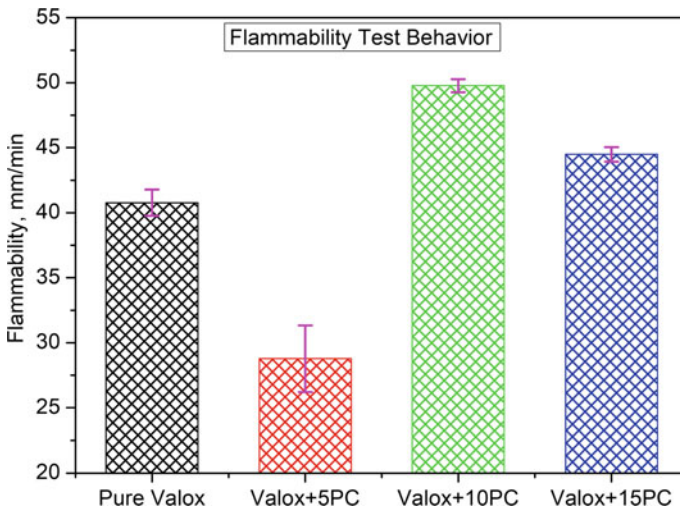


Fig. 8 Flammability behavior of VALOX-x wt.% PC composites of multi-materials

the lowest value compared to other samples. The obtained flammability test results were from vertical flammability test type.

4 Conclusions

In the present research work, several VALOX-based materials incorporated with different weight percentage of polycarbonates composites of multi-materials were designed, developed, and fabricated successfully. The following achievements were made through this research work.

- VALOX-0 wt.% PC, VALOX-5 wt.% PC, VALOX-10 wt.% PC, and VALOX-15 wt.% PC composites samples have manufactured by mechanical blending/grinding followed by manual hand-operated extrusion techniques.
- The mechanical behavior in terms of uniaxial compression test, mechanical degradation behavior, and flammability behavior of all the developed samples were executed, investigated, and reported.
- From the mechanical compression test, VALOX-5 wt.% sample exhibited the highest yield strength (37.213 MPa), ultimate compressive strength (43.577 MPa), and more value of compressive strain (4.77%, indicating more toughness).
- From the mechanical degradation test, VALOX-5 wt.% PC composite sample produced highest mechanical degradation temperature of around 220.333 °C which was highest value when compared to all other samples.
- VALOX-5 wt.% sample has shown the lowest flammability speed of around 28.7705 mm/min meaning that this sample has taken more time for complete burning in the same sample length.
- Based on the present research work, VALOX-5 wt.% composite sample can be recommended for its usage in manufacturing of various electrical parts like adaptors, electrical sockets, and plugs.

Acknowledgements The authors gratefully acknowledge M/S Saudi Standards, Metrology and Quality Organization (SASO), Saudi Arabia, on the financial support for conducting this research work.

References

1. Pious CV, Thomas S (2016) Polymeric materials—structure, properties, and applications. Print Polym William Andrew Publ 21–39
2. Thomas S, Visakh PM (2011) Handbook of engineering and specialty thermoplastics, vol 3: Polyethers and Polyesters. Vol 63. Wiley
3. Olkhov AA, Liaw DJ, Fetisov GV, Goldschtrakh MA, Kononov NN, Krutikova AA et al (2013) On polymer nanocomposites. Prog Org Phys Chem Struct Mech 32:223–234. <https://doi.org/10.1201/b13964-18>
4. Chawla KK (2012) Composite materials: science and engineering. Springer Science and Business Media
5. Yina Y, Talapin D (2013) The chemistry of functional nanomaterials. Chem Soc Rev 42:2484–2487. <https://doi.org/10.1039/c3cs90011h>
6. LeBaron PC, Wang Z, Pinnavaia TJ (1999) Polymer-layered silicate nanocomposites: an overview. Appl Clay Sci 15:11–29

7. Baroth A (2011) Environmental benefits of post-consumer recycled PET based Valox iQ resin * vs. Valox * resin using life cycle assessment approach environmental benefits of post-consumer recycled PET based Valox iQ resin * vs . Valox * resin using Life Cycle Assessment
8. Showaib EA, Elsheikh AH (2020) Effect of surface preparation on the strength of vibration welded butt joint made from PBT composite. *Polym Test* 83:106319. <https://doi.org/10.1016/j.polymertesting.2019.106319>
9. Thongsong W, Kulsethanchalee C, Threepopnatkul P (2017) Effect of polybutylene adipate-co-terephthalate on properties of polyethylene terephthalate thin films. *Mater Today Proc* 4:6597–6604. <https://doi.org/10.1016/j.matpr.2017.06.173>
10. Hernández-López M, Correa-Pacheco ZN, Bautista-Baños S, Zavaleta-Avejar L, Benítez-Jiménez JJ, Sabino-Gutiérrez MA et al (2019) Bio-based composite fibers from pine essential oil and PLA/PBAT polymer blend. Morphological, physicochemical, thermal and mechanical characterization. *Mater Chem Phys* 234:345–353. <https://doi.org/10.1016/j.matchemphys.2019.01.034>
11. Choi EY, Kim SW, Kim CK (2016) In situ grafting of polybutylene terephthalate onto multi-walled carbon nanotubes by melt extrusion, and characteristics of their composites with polybutylene terephthalate. *Compos Sci Technol* 132:101–107. <https://doi.org/10.1016/j.compscitech.2016.07.003>
12. Mäder E, Gao SL, Plonka R, Wang J (2007) Investigation on adhesion, interphases, and failure behaviour of cyclic butylene terephthalate (CBT®)/glass fiber composites. *Compos Sci Technol* 67:3140–3150. <https://doi.org/10.1016/j.compscitech.2007.04.014>
13. Ivanič F, Kováčová M, Chodák I (2019) The effect of plasticizer selection on properties of blends poly(butylene adipate-co-terephthalate) with thermoplastic starch. *Eur Polym J* 116:99–105. <https://doi.org/10.1016/j.eurpolymj.2019.03.042>
14. Ferreira AC, Diniz MF, Babetto Ferreira AC, Sanches NB, da Costa Mattos E (2020) FT-IR/UATR and FT-IR transmission quantitative analysis of PBT/PC blends. *Polym Test* 85. <https://doi.org/10.1016/j.polymertesting.2020.106447>
15. Schmidt J, Sachs M, Fanselow S, Zhao M, Romeis S, Drummer D et al (2016) Optimized polybutylene terephthalate powders for selective laser beam melting. *Chem Eng Sci* 156:1–10. <https://doi.org/10.1016/j.ces.2016.09.009>
16. Zhao C, Mark LH, Chang E, Chu RKM, Lee PC, Park CB (2020) Highly expanded, highly insulating polypropylene/polybutylene-terephthalate composite foams manufactured by nanofibrillation technology. *Mater Des* 188:108450. <https://doi.org/10.1016/j.matdes.2019.108450>
17. Olmos D, Domínguez C, Castrillo PD, Gonzalez-Benito J (2009) Crystallization and final morphology of HDPE: Effect of the high energy ball milling and the presence of TiO₂ nanoparticles. *Polymer (Guildf)* 50:1732–1742. <https://doi.org/10.1016/j.polymer.2009.02.011>
18. Jung J, Kim J, Uhm YR, Jeon JK, Lee S, Lee HM et al (2010) Preparations and thermal properties of micro- and nano-BN dispersed HDPE composites. *Thermochim Acta* 499:8–14. <https://doi.org/10.1016/j.tca.2009.10.013>

Methods and Parameter Optimization of Manufacturing Process Using Alginate-Based Hydrogel Bioinks



M. B. Łabowska, P. Szymczyk-Ziółkowska, I. Michalak, and J. Detyna

Abstract The application of additive manufacturing (AM) technology in biomedicine offers many advantages due to the possibility of personalization and precision in shape accurate reproduction or dose of drug selection. AM technique enables the use of a wide variety of biocompatible materials, which can be applied even in the form of hydrogel. However, the use of sodium alginate as a bioink is encountered with some difficulties, for example, problem with shape retention during fabrication before being cross-linked. In this paper, methods used in extrusion-based method that contributes to maintaining the precision and quality of the print by reducing the spill ability of alginate hydrogel are described. This paper presents one of the methods, which supports the alginate hydrogel manufacturing process—freeform reversible embedding of suspended hydrogels (FRESH), as well as the optimization of the manufacturing process parameters to improve the quality of prints.

Keywords Additive manufacturing · Bioprinting · Sodium alginate · Hydrogel bioink · Manufacturing parameters · FRESH method

M. B. Łabowska (✉) · J. Detyna

Department of Mechanics, Materials and Biomedical Engineering, Faculty of Mechanical Engineering, Wrocław University of Science and Technology, Wrocław, Poland
e-mail: magdalena.labowska@pwr.edu.pl

J. Detyna

e-mail: jerzy.detyna@pwr.edu.pl

P. Szymczyk-Ziółkowska

Center for Advanced Manufacturing Technologies (CAMT/FPC), Faculty of Mechanical Engineering, Wrocław University of Science and Technology, Wrocław, Poland
e-mail: patrycja.e.szymczyk@pwr.edu.pl

I. Michalak

Department of Advanced Material Technologies, Faculty of Chemistry, Wrocław University of Science and Technology, Wrocław, Poland
e-mail: izabela.michalak@pwr.edu.pl

1 Introduction

Sodium alginate is an anionic linear polysaccharide obtained from brown seaweeds, which has the ability to create hydrogel in the presence of water. Cross-linking of alginate solution by the addition of divalent or trivalent metal ions (e.g., calcium, magnesium, barium, aluminum, iron) leads to a transformation into water-insoluble hydrogel. The retention of a significant amount of water in hydrogel is caused by the presence of hydrophilic groups on the polymeric backbone. The maximum water uptake of an alginate hydrogel depends on many factors, e.g., the cross-linking time or concentration of cross-linker and varies from 50–90% [1–3]. Unique properties and biological activity make alginate hydrogel widely used in many fields, especially in the biomedical sector. This material is non-toxic, biodegradable, therefore is commonly used as a drug carrier (e.g., oral, ocular, nasal) or wound dressing [1, 3]. Alginate hydrogel is also used for encapsulation of cells, genes, proteins, or vaccines. Moreover, soft and flexible structure of alginate hydrogel, likewise similar to extracellular matrix (ECM) gives the potential to the utilization in tissue engineering and regenerative medicine (e.g., scaffold) [2, 4].

The extrusion-based technique is one of the additive manufacturing (AM) technologies, which allow three-dimensional bioprinting using hydrogel materials. AM technologies provide numerous benefits directly related to personalization, freedom of complex structure creation, and quite high accuracy of dimension representation, but also, the selection of an appropriate dose of the active substance used in the drug delivery systems, depending on the patient's needs. However, the use of hydrogel as a bioink requires the proper selection of process parameters that will affect the quality and final properties of the manufactured object [5, 6]. The process ability of soft, low viscosity materials (gels, hydrogels) is a challenge in bioplotting due to the difficulty in maintaining shape and the possibility of deformations during the fabrication process [7]. Sodium alginate is often used as a bioink due to its feasibility in bioengineering applications. Unfortunately, its properties, including low viscosity, make it difficult to obtain precise structure. In most cases, the utilized bioink does not maintain integrity during the production process and spills, which creates a problem in achieving an accurate shape [8].

The challenge of achieving accurate shape representation during the manufacturing process has been undertaken by many researchers. Methods based on ink additives or sacrificial materials have been proposed to prevent bioinks from spilling before their cross-linking. The combination of alginate and additives such as methylcellulose, gelatin, carrageenan improves printability and provides greater mechanical strength of manufactured objects [5, 9]. The second technique is based on the utilization of support materials such as Pluronic F127, which can be used as an outline for the printed hydrogel. Pluronic F127 is characterized by reverse thermal gelation, whereby after completing fabrication of the target object, it can be easily removed by melting. Moreover, this material is non-toxic; therefore, it can be successfully used for applications in the biomedical field [10, 11]. Other sacrificial materials taken into

consideration, such as nanoclay, ion-sensitive carbopol microgels, gelatin, are excellent candidates for support bath material [12]. Freeform reversible embedding of suspended hydrogels (FRESH) is one of the methods using support bath material. It consists of extruding the hydrogel bioink in a bath of thermo-reversible support gel, where extruded hydrogel has to rapidly gelation into filament. The supported gel can be formulated from thermosensitive gelatin in combination with the cross-linking solution. This mixture creates an environment in which the suspended sample cross-links, resulting in high shape retraction. The printed object can be easily removed from supported baths by raising the temperature and melting gelatin [8, 13].

3D bioplotting is based on similar principles to traditional additive manufacturing methods—a three-dimensional object of arbitrary shape is created layer-by-layer using a semi-liquid material. To fabricate an element using the AM technology, a hydrogel needs to be injected from an extrusion nozzle under appropriate pressure and distributed by moving print head. The next parameter affecting manufacturing quality is the diameter of the extrusion nozzle. It determines the flow of the material and, as a result, the thickness of the layer. Proper selection of these parameters (diameter of extrusion nozzle, pressure, and speed of the print head) will allow to control the material's flow and to obtain the desired result—an accurate dimension of the imprint [14].

The aim of this paper is to present methods that allow the production of alginate hydrogel-based imprints using extrusion-based technique and to determine the influence of process parameters (i.e., nozzle diameter, pressure, and speed of printing). In this study, a technique using the FRESH, which allows the suspension of the printout in the support bath is described. Optimization of parameters of manufacturing process was also performed to obtain imprints with a high-quality shape and dimension representation.

2 Materials and Methods

In this study, alginic acid sodium salt (Sigma-Aldrich, USA) with a viscosity of 15–25 cP 1% in H₂O was used. Sodium alginate was dissolved in distilled water to create an alginate solution at a concentration of 4%. The hydrogel was cross-linked by solution of anhydrous calcium chloride (Avantor Performance Materials Poland S.A., Poland) in the concentration of 0.1 M, in a support bath during process manufacturing.

2.1 Fabrication Using the FRESH

Samples of alginate hydrogel were prepared in the three-dimensional cuboid with dimension of 5 × 5 × 1 mm used BioX bioplotter (Cellink, USA). Dry powder of LifeSupport™ (2 g of gelatin and gum Arabic mixture)—support material for FRESH

3D bioprinting (Cellink, USA) and 0.1 M of calcium chloride (20 ml) (Avantor Performance Materials Poland S.A., Poland) were used for the FRESH bioprinting support bath production. Then, it was placed in a petri dish and positioned on the cooling table of the bioplotter. After printing, the hydrogel was cross-linked for 5 min, subsequently, the petri dish was placed in warm water (40 °C) to melt the support bath and remove the alginate imprint.

2.2 Manufacturing Parameters

Parameters of the manufacturing process were tested depending on the extrusion nozzle selected (nozzle with diameter 0.25 mm and needle with diameter 0.2 mm). Various values of print speed (V ; mm/s) and pressure (p ; kPa) were taken into consideration, which were selected based on a background study. Table 1 summarizes the selected parameters used in the sample production, which showed the best shape reproduction. The temperature of the alginate solution was 23 °C, the same as in the working space, and the worktable was cooled to 20 °C due to maintaining the stiffness of the support bath. The humidity present in the working space was 47%.

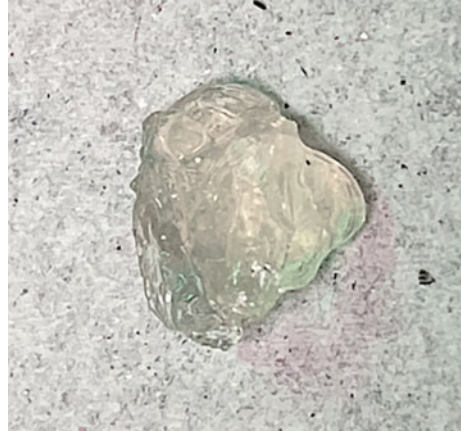
3 Results and Discussion

Alginate outprints were left in a support bath for 5 min after process manufacturing to cross-link the alginate hydrogel. Depending on the duration of exposure to calcium chloride, the samples became more rigid and better retained their shape, thus they gain better mechanical properties. Samples were measured to determine the accuracy of the manufacturing process and reproducibility of shape and dimensions. After cross-linking of samples, LifeSupport™ was melted by a warm water bath; then, the samples were removed.

Table 1 Process parameters of production of sodium alginate-based hydrogel samples

Process parameters	(Nozzle) 0.25 mm		(Needle) 0.2 mm		
	p [kPa]	V [mm/s]	Sample	p [kPa]	V [mm/s]
Sample			Sample		
S1	2	3	S4	20	2
S2	3	4	S5	25	3
S3	4	5	S6	30	3

Fig. 1 Excessive material flow out of the nozzle (incorrectly selected process parameters of bioplotting) (own source)



3.1 Manufacturing Parameters

The selection of process parameters is the next important aspect besides the choice of manufacturing technique to improve print quality (dimensional and shape precision). In addition to the extrusion nozzle diameter, which determines layer thickness, these parameters include print pressure and print speed. Pressure is responsible for the amount of the material extrusion and printing speed determines the movement of the print head. All these parameters are correlated and need to be strictly controlled in order to release the optimum amount of bioink in the appropriate location and time. Table temperature is also significant for materials sensitive to temperature changes. Incorrectly chosen printing parameters can lead to excessive overflow of material from the nozzle or poor outflow of material from the nozzle, resulting in the deformation, creation of air bubbles, lack of connection of the material. An example of overflowing material from the extrusion nozzle is shown in Fig. 1.

In order to optimize the bioplotting of sodium alginate-based hydrogel, process parameters were selected for FRESH method. LifeSupport™ allowed fabrication of hydrogel samples retaining their shape without spilling the alginate, which resulted in obtaining printouts with accuracy close to the model. The choice of process parameters is closely dependent on the density and viscosity of sodium alginate, which influenced the choice of nozzle diameter. Decreasing the diameter to 0.2 mm requires increasing the pressure to 30 kPa. However, the printing speed cannot be too rapid, to avoid breaking the applied layer. Figure 2 shows the effect of process parameter optimization.

Two printing nozzles (nozzle 0.25 mm and needle 0.2 mm) were used to prepare alginate prints. The dimensions of the alginate samples were measured after being removed from the support bath and are presented in Table 2. The dimensional inaccuracies and the deviation from the model dimensions ($5 \times 5 \times 1$ mm) may be caused not only by chosen parameters but also by the evaporation of water from the alginate hydrogel.

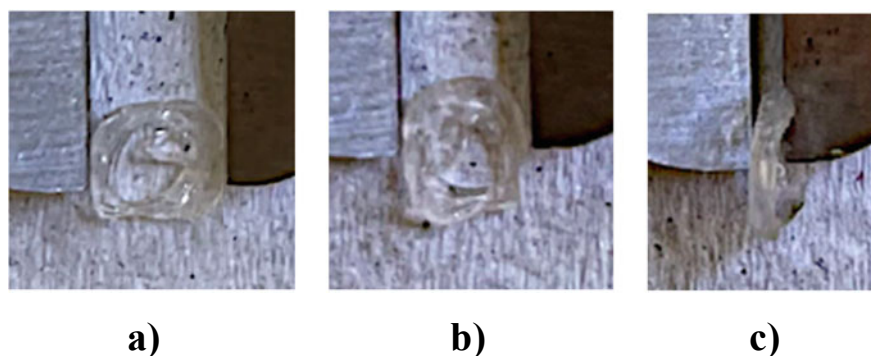


Fig. 2 Optimization of bioprinting process parameters to achieve accuracy of the manufactured hydrogel **a** length, **b** width, **c** thickness

Table 2 Dimensions of alginate samples fabricated on bioplotter after optimization of process parameters

Dimensions [mm]	(Nozzle) 0.25 mm			Sample	(Needle) 0.2 mm		
	width	depth	height		width	depth	height
Sample				Sample			
S1	5.11	4.70	0.78	S4	4.25	4.30	0.76
S2	4.11	5.31	1.32	S5	4.05	4.17	0.81
S3	5.23	6.12	1.5	S6	4.11	4.5	0.89

During increasing one of the process parameters—pressure, the head speed needs to be also increased to ensure the evenly outflow of material. However, the feed rate should not be excessive, as it can lead to a displacement of the sample and thus to dimensional deviations. The most accurate shape reproduction was obtained for needles with a diameter of 0.2 mm.

4 Conclusions

A major challenge of tissue engineering and regenerative medicine is the production of progressively smaller and dimensionally more precise tissues, scaffolds, and cellular matrices. Additive manufacturing offers this opportunity through a wide choice of biomaterials, as well as the possibility of a personalized approach to the patient. Methods of manufacturing hydrogels are becoming more and more refined, resulting in manufactured objects with high accuracy and complex structure.

The manufacturing of hydrogel imprints based on sodium alginate requires an adequate approach due to their properties. The choice of printing parameters influences the dimensional and shape quality, and the selection of cross-linking method

and also an appropriate cross-linking time can influence shape retention as well as mechanical properties improvement. Therefore, various techniques have been invented to help achieve the desired results. One of them is the method used in this paper, FRESH, which with assistance of a support bath, maintains the shape of the print throughout the manufacturing process. A forward-looking attitude toward miniaturization of the fabricated object will enable improving their application in the biomedical field by creating porous, intricate, and accurate structures that will not only support cell culture, drug, or protein delivery but perhaps also contribute to a new generation of organ and tissue manufacturing.

References

1. Sachan NK, Pushkar S, Jha A, Bhattacharya A (2009) Sodium alginate: the wonder polymer for controlled drug delivery. *J Pharm Res* 2(8):1191–1199
2. Borumand MR, Mirak AZ, Duonighi NM, Damavandi M, Rahnamafard H (2015) Preparation of sodium alginate nanoparticles containing bovin serum albumin (BSA). *Int J Biol Pharm Allied Sci* 4(12):6702–6711
3. Chaturvedi K, Ganguly K, More UA, Reddy KR, Dugge T, Naik B, Aminabhavi TM, Noolvi MN (2019) Sodium alginate in drug delivery and biomedical areas. In: Md Hasnain S, Nayak AK (eds) *Natural polysaccharides in drug delivery and biomedical applications*, Elsevier Inc, pp 59–100
4. Lee KY, Mooney DJ (2012) Alginate: properties and biomedical applications. *Prog Polym Sci* 37(1):106–126
5. You F, Eames BF, Chen X (2017) Application of extrusion-based hydrogel bioprinting for cartilage tissue engineering. *Int J Mol Sci* 18(7):1597
6. Boularaoui S, Al Hussein G, Khan KA, Christoforou N, Stefanini C (2020) An overview of extrusion-based bioprinting with a focus on induced shear stress and its effect on cell viability. *Bioprinting*, e00093
7. Hinton TJ, Jallerat Q, Palchesko RN, Park JH, Grodzicki MS, Shue H-J, Ramadan MH, Hudson AR, Feinberg AW (2015) Three-dimensional printing of complex biological structures by freeform reversible embedding of suspended hydrogels. *Sci Adv* 1(9):e1500758–e1500758
8. Shah PP, Shah HB, Maniar KK, Ozel T (2020) Extrusion-based 3D bioprinting of alginate-based tissue constructs. *Procedia CIRP*, 95:143–148
9. Kim MH, Lee YW, Jung W-K, Oh J, Nam SY (2019) Enhanced rheological behaviors of alginate hydrogels with carrageenan for extrusion-based bioprinting. *J Mech Behav Biomed Mater* 98:187–194
10. Suntornnond R, Tan EYS, An J, Chua CK (2017) A highly printable and biocompatible hydrogel composite for direct printing of soft and perfusable vasculature-like structures. *Sci Rep* 7:16902
11. Askari M, Naniz MA, Kouhi M, Saberi A, Zolfagharian A, Bodaghi M (2021) Recent progress in extrusion 3D bioprinting of hydrogel biomaterials for tissue regeneration: a comprehensive review with focus on advanced fabrication techniques. *Biomater Sci* 9:535–573
12. Ding H, Chang RC (2018) Printability study of bioprinted tubular structures using liquid hydrogel precursors in a support bath. *Appl Sci* 8:403
13. Lee A, Hudson AR, Shiwarski DJ, Tashman JW, Hinton TJ, Yerneni S, Bliley JM, Campbell PG, Feinberg AW (2019) 3D bioprinting of collagen to rebuild components of the human heart. *Science* 365(6452):482–487
14. Naghieh S, Sarker MD, Sharma NK, Barhoumi Z, Chen X (2019) Printability of 3D printed hydrogel scaffolds: influence of hydrogel composition and printing parameters. *Appl Sci* 10(1):292

Microstructural and Mechanical Properties Analysis of Fibre Laser Welding of Dissimilar AA6061 and AA2024 Aluminium Alloy



Pradyumn Kumar Arya, Vivek Kumar, Dan Sathiaraj, I. A. Palani, and Neelesh Kumar Jain

Abstract The present research work evaluates the butt joints of 2-mm-thick dissimilar aluminium alloy plates AA6061 and AA2024 were welded using a 2 KW laser fibre welding machine. The impact of different laser power on the evaluation of microstructure, phase and mechanical properties has been examined. According to this analysis, low laser power leads to insufficient heat diffusion and defective surface morphology. Maximum tensile strength of 189.1 MPa was achieved with 1.6 KW of laser power, which is approximately 67.5% of the tensile strength of AA6061 Al alloy. Weld zone near the side of AA2024 Al alloy had the highest hardness value, while the HAZ near the side of AA6061 Al alloy had the lowest hardness value. The XRD pattern verified the presence of Al phase and Mg_2Si in laser welding joints. The analysis of microstructural shows that grain size in the fusion region becomes finer than the heat-affected region and reference Al alloy. Hence, it is necessary to evaluate the weldabilities of these materials due to their use of aluminium alloys in many manufacturing processes.

Keywords Laser welding · Dissimilar aluminium alloys · Microstructure and tensile properties

P. K. Arya (✉) · V. Kumar · D. Sathiaraj · I. A. Palani · N. K. Jain
Department of Mechanical Engineering, IIT Indore, Indore, India
e-mail: mtphd2006103001@iiti.ac.in

V. Kumar
e-mail: mtech1902103007@iiti.ac.in

D. Sathiaraj
e-mail: dansathiaraj@iiti.ac.in

I. A. Palani
e-mail: palaniia@iiti.ac.in

N. K. Jain
e-mail: nkjain@iiti.ac.in

1 Introduction

Aluminium alloys were being utilized extensively in the production, aerospace, automotive, defence and medical industries because of their high strength, hardness and low weight [1]. Welding of different aluminium alloys has gained popularity and is being used most frequently in the lightweight design of industries [2]. Porosity forming, residual stresses, low distortion and hot cracking have mostly been discovered when joining dissimilar aluminium alloys using fusion welding methods [3, 4]. Fusion welding is one of the most widely used in different manufacturing fields for joining dissimilar aluminium alloys [5], steel [6], metal matrix composite [7] and coated Al alloy [8]. Also, various welding methods such as TIG, MIG, CMT, laser welding and FSW have been used to join aluminium alloys [9]. Laser welding seems to be a viable technique for joining various materials because of its lower heat input, high localization capability, higher weld speed, high durability, good weld strength and high efficiency [10, 11]. Very few studies have studied welding similar and dissimilar aluminium alloys from the groups of 2XXX, 5XXX and 6XXX via laser welding techniques [12, 13]. Haboudou et al. [14] evaluated the laser welding of dissimilar aluminium alloy AA356 and AA5083. According to the results, porosity formation was influenced by low Mg vaporization point and process instability. Nie et al. [15] utilized pulse MIG welding to explore the microstructural and mechanical characteristics of AA6061/AA356 aluminium alloy. It showed that the accumulation of brittle phases and pits in MIG weld joints would significantly reduce joint properties. Khodabakhshi et al. [16] could minimize crack faults in Al with Mg dissimilar alloys joints by using Ni barrier layer to facilitate material intermixing. Besides, Liu et al. [17] studied microstructural and corrosion analysis of Al alloys to Al matrix composites. Microstructure mainly contains Al, Al₂Ti, Fe₂Si and Al_{0.5}Fe₃Si_{0.5}, and TiB₂ particles become dissolved and interacted with melted Al, and excessive TiB₂ particles moved towards the grain boundaries. Yan et al. [18] modifying laser welding variables, defect-free welded joints of different Al alloys could be achieved. According to microstructure analysis, the fusion zone has wide precipitates, lower dislocation density and coarse grains. Pores and inclusions seem to be the primary cause of fatigue strength degradation. Adisa et al. [19] showed that refined grains with a mean size of $2 \pm 0.26 \mu\text{m}$ were found in a laser welded sample with Al-5Ti-B filler metal, and the welded joint's strength had been reported to be approximately 97% of the base materials. Although several studies reported, the effect of various laser power on microstructural and mechanical characteristics of distinct aluminium alloy AA2024 and AA6061 is still missing and needs to be addressed. In this scenario, the primary goal of this research needs to examine different laser power effects on microstructural and mechanical characteristics of laser welding of dissimilar aluminium alloys AA2024-AA6061 joints.

2 Material and Methods

In this investigation, all-welded samples of AA6061 and AA2024 Al alloys with 30 mm length, 30 mm width, and 2 mm thickness and welding proceeded in the transverse direction. First, AA6061 and AA2024 aluminium alloy plates were sprayed with acetone distilled water and washed to remove the surface oxides. Next, samples were welded using a fibre laser welding machine (Model: Mehta, with a 2 KW power output Make: India), and clamping fixtures were used to support the back and front sides of the welded samples. Three groups of different laser welding power parameters were evaluated using the experiments listed in Table 1 after specific trial experiments. Welding speed and nitrogen flow rate were set to 1.2 m/min and 5 L/min, respectively, throughout all experiments. Metallographic specimens and tensile specimens with standard dimensions were extracted using a wire-cut electrical discharge machine after laser welding. Then welded samples were mounted in epoxy and grounded by using sandpaper 400, 800, 1000, 1500, 2000 gradually and were finally polished with 1 μm polishing suspensions, using a diamond paste, cleaned with the ultrasonic cleaned in alcohol.

In this work, an indigenously designed and procured computer numerical controlled (CNC) machine for laser welding was used to fabricate the joints, and Fig. 1 shows laser welding machine and fixture setup.

After diamond polishing, the specimens were dipped in Keller's solvent (2.5 ml HNO_3 + 1.5 ml HCL + 1 ml HF + 10 ml DI water) for 12–16 s to reveal the microstructure. Microstructure and fracture analysis were done using the optical microscope (Model: LEICA, Germany) and field emission scanning electron microscope (Model: Zeiss Ultra PLUS, Germany). In addition, the phase analysis was done by using an XRD-X-ray diffractometer (Model: Bruker D8 advance, USA). On a Vickers micro-hardness tester, micro-hardness values were calculated at the central thickness area of the different zones of the weld joints using an indenting load of 0.01 kg for a dwell time of 15 s. Finally, tensile testing was performed for each weld sample with a 12 mm gauge length and strain rate of 10^{-4} s $^{-1}$ (Model: Instron 5540 micro tester, UK).

Table 1 Experimental parameter for fibre laser welding

Sample No.	Laser weld speed (m/min)	Power (KW)
1	1.2	1.4
2	1.2	1.6
3	1.2	1.8

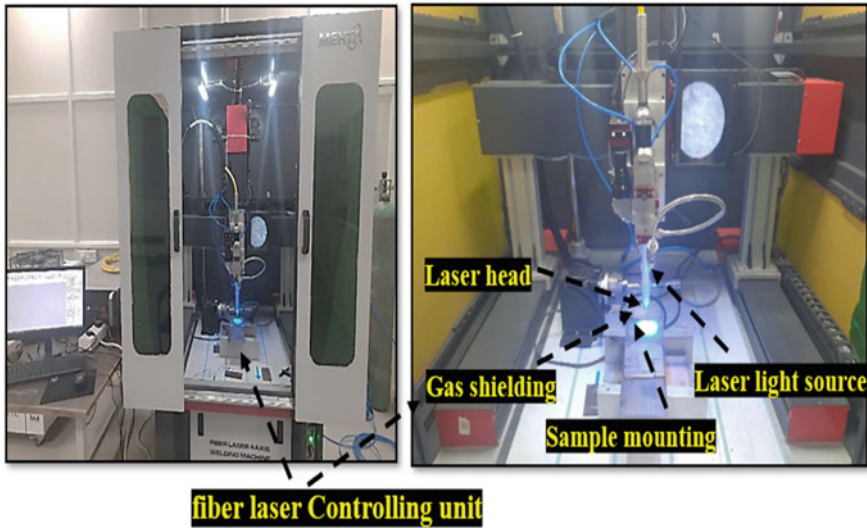


Fig. 1 Laser welding machine

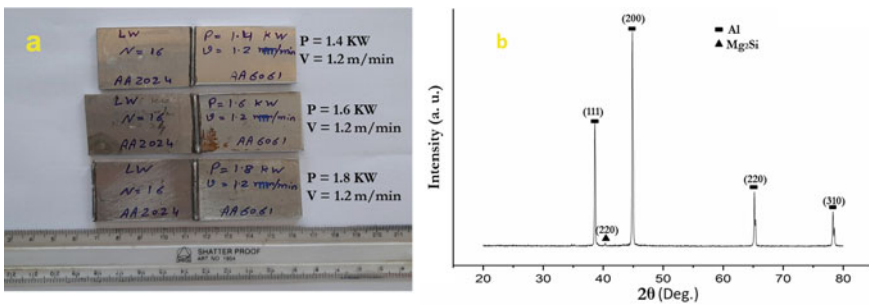


Fig. 2 a Surface morphologies of the welded samples b XRD analysis of AA2024-AA6061 welded samples

3 Results and Discussions

In this section, surface morphologies, microstructure analysis and mechanical characteristics (ultimate tensile strength and micro-hardness) of laser-welded AA6061 and AA5052 concerning different laser power have been discussed.

3.1 Microstructure Analysis

Figure 2a shows the surface morphologies of laser welding samples produced by various laser powers. It was observed that a laser-welded sample with laser power of 1.6 KW and laser weld speed of 1.2 m/min seems to provide adequate depth to weld zone to cover the bottom surface, while the sample with low laser power of 1.4 KW provides inadequate depth to the weld zone. Defects-free weld was produced using 1.6 KW laser power but some macroscopic defects occurred at low and high laser power. At low laser power of 1.4 KW, the heating rate became lower to enable proper fluidity of alloys to attain proper welding. However, at a higher laser power of 1.8 KW, extreme laser interference causes the alloys to over melt and partially evaporate. X-ray diffraction (XRD) evaluation was carried out on transverse cross sections of laser welding, and the corresponding patterns for laser welding joints are shown in Fig. 2b. The existence of Al phase and Mg_2Si in laser welding joints was verified using XRD peaks. Owing to the existence of the intermetallic compound Mg_2Si , all laser welding dissimilar joints showed reasonable strength to base material alloys.

Figure 3 shows the microstructure of various locations, i.e. fusion region (FZ), heat-affected region (HAZ) and reference material of the laser-welded of different AA6061-AA2024 aluminium alloys. The microstructure of the base alloys did not change significantly, but heat generation seems to have a significant impact mostly

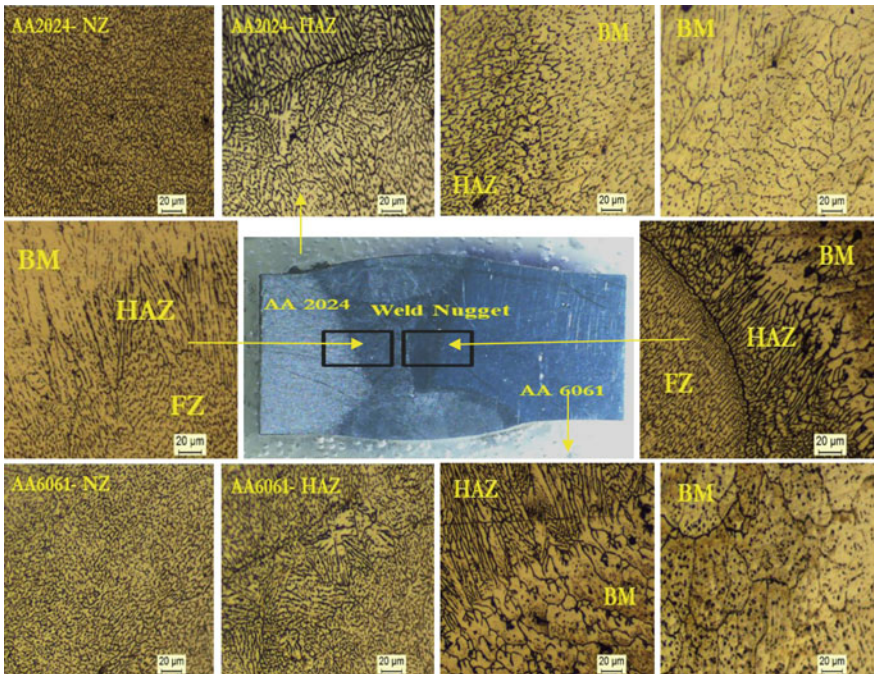


Fig. 3 Microstructure of various locations, i.e. FZ, HAZ and BM

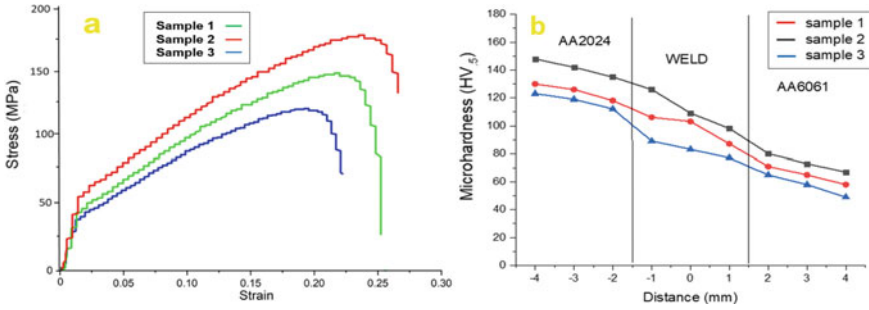


Fig. 4 a Stress–strain curve of the laser welded sample b micro-hardness variation

on microstructural of HAZ and the fusion zone. Microstructure clearly shows that such fusion regions, heat-affected regions and reference materials zones are separated by a clear grain boundary, as shown in Fig. 3. The accumulation of finer equiaxed grains was caused by extreme deformation and a high heating rate in laser-welded fusion region. The accumulation of fine grains in the laser-welded fusion region was observed, improving the weld joint’s strength. Due to less heat generation in the heat-affected regions, grain sizes are larger in this zone.

3.2 Tensile Strength Analysis

Figure 4a shows the stress–strain graph of the laser welding specimen at different laser powers. The weld generated with 1.8 KW of laser power demonstrated a minimum joint strength of 121 MPa due to surface cracks in the welding zone. In addition, over-melting and partial evaporation at higher laser power might be the reason for the lower tensile strength and poor bonding between both dissimilar alloys. Due to stronger mixing and improved materials flowing among two dissimilar alloys, the joint produced with 1.6 KW laser power displayed a maximum joint strength of 189.1 MPa. All the welded samples of different laser power have fractured at weak connection region, i.e. at heat-affected zone.

3.3 Micro-Hardness Analysis

Figure 4b shows the variation of micro-hardness measured in 1 mm increments across the cross section of a weld joint’s fusion zone using different laser powers.

Hardness variation occurs because the difference in heat generation during laser welding and hardness mainly depends on the precipitate distribution such as Mg₂Si. In the weld fusion region, the hardness value was lower than that of AA2024 aluminium alloy but greater than AA6061 aluminium alloy. Owing to the presence

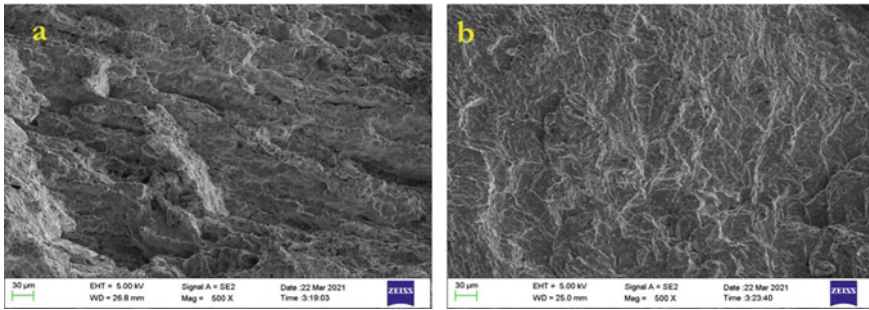


Fig. 5 Fracture morphology of tensile sample

of macroscopic defects, weak bonding, and over-melting of alloys, the fusion zone has the smallest hardness value at 1.8 KW laser power. On the other hand, due to effective intermixing and strong bonding of both dissimilar alloys, the maximum hardness value was observed at 1.6 KW laser power welded sample.

3.4 Fractography of Tensile Sample

Figure 5 shows SEM images of fracture morphology observed at 1.6 KW laser power from the fractured surface of a laser-welded sample. Location of fracture in the tensile specimen of weld joints at different laser power was observed in heat-affected region. From Fig. 5, the fracture surface shows large dimples with some of those featureless flat surfaces.

4 Conclusions

Effects of different laser power on microstructural and mechanical properties of laser welding dissimilar aluminium alloys AA6061-AA2024 were investigated in this research.

Following is the conclusion that can be drawn from the current research:

Laser welded sample with laser power of 1.6 KW and laser weld speed of 1.2 m/min appears to provide sufficient weld zone depth and defect-free welding. Microstructure clearly shows that such fusion zone, base materials regions and heat-affected region were separated by a clear grain boundary. Fine grains were observed in the laser-welded fusion region, but grain sizes were larger in the heat-affected regions (HAZ). The existence of Al phase and Mg₂Si in laser welding joints was verified using XRD peaks. Joint produced with 1.6 KW laser power displayed a maximum joint strength of 189.1 MPa due to proper intermixing and good bonding between both base alloys. In the weld fusion region, the hardness value was lower than

that of AA2024 aluminium alloy but greater than AA6061 aluminium alloy. Tensile fracture surface shows large dimples with some of those featureless flat surfaces.

References

1. Mathers G (2002) *The welding of aluminium and its alloys*. Woodhead publishing
2. Khan NZ, Siddiquee AN, Khan ZA (2017) *Friction stir welding: dissimilar aluminium alloys*. CRC Press
3. Kah P, Rajan R, Martikainen J, Suoranta R (2015) Investigation of weld defects in friction-stir welding and fusion welding of aluminium alloys. *Int J Mech Mater Eng* 10(1):1–10
4. Naik AB, Reddy AC (2018) Optimization of tensile strength in TIG welding using the Taguchi method and analysis of variance (ANOVA). *Thermal Sci Eng Progress* 8(3):27–39
5. Patel VK, Kumar P, Bhattacharya S (2018) Mechanical, microstructural and sliding wear properties of friction stir welded AA6063-T6 and AA5052-H32 aluminium alloys. *Mater Focus* 7(1):50–58
6. Arya PK, Gupta G, Rajput AK (2016) A review on friction stir welding for aluminium alloy to steel. *Int J Sci Eng Res* 7(5):119
7. Arya PK (2015) A review on friction stir welding for aluminium alloy composite. *Int J Res Appl Sci Eng Technol* 3(6):216–221
8. Bahuguna S, Arya PK, Patel VK (2020) Mechanical and abrasive wear properties of friction stir welded joints of aluminium alloy AA6061-T6 with/without nickel coating. *Strojnický Casopis-J Mech Eng* 70(2):21–36
9. Arya PK (2021) Investigation on microstructural, mechanical properties and corrosion behaviour of Al 6061–T6 welded joints fabricated by TIG, MIG CMT and FSW. *AIJR Abstracts* 6:120
10. Sánchez-Amaya JM, Delgado T, De Damborenea JJ, Lopez V, Botana FJ (2009) Laser welding of AA 5083 samples by high power diode laser. *Sci Technol Weld Joining* 14(1):78–86
11. Kuo TY, Lin HC (2006) Effects of pulse level of Nd-YAG laser on tensile properties and formability of laser weldments in automotive aluminum alloys. *Mater Sci Eng A* 25;416(1–2):281–289.
12. Abe N, Tsukamoto M, Maeda K, Namba K, Morimoto J (2006) Aluminium alloy welding by using a high-power direct diode laser. *J Laser Appl* 18(4):289–293
13. Yan J, Zeng X, Gao M, Lai J, Lin T (2009) Effect of welding wires on microstructure and mechanical properties of 2A12 aluminium alloy in CO₂ laser-MIG hybrid welding. *Appl Surf Sci* 255(16):7307–7313
14. Haboudou A, Peyre P, Vannes AB, Peix G (2003) Reduction of porosity content generated during Nd: YAG laser welding of A356 and AA5083 aluminium alloys. *Mater Sci Eng A* 363(1–2):40–52
15. Nie F, Dong H, Chen S, Li P, Wang L, Zhao Z, Li X, Zhang H (2018) Microstructure and mechanical properties of pulse MIG welded 6061/A356 aluminium alloy dissimilar butt joints. *J Mater Sci Technol* 34(3):551–560
16. Khodabakhshi F, Shah LH, Gerlich AP (2019) Dissimilar laser welding of an AA6022-AZ31 lap-joint by using Ni-interlayer: novel beam-wobbling technique, processing parameters, and metallurgical characterization. *Opt Laser Technol* 112:349–362
17. Dai J, Yu B, Jiang W, Htun HM, Liu Z (2019) Laser welding of dissimilar metal joint of 6061 Al alloy and Al matrix composite. *Adv Mater Sci Eng*
18. Yan S, Qin QH, Chen H, Zhong Z (2020) Hybrid laser welding of dissimilar aluminium alloys: welding processing, microstructure, properties and modelling. *J Manuf Process* 56:295–305
19. Adisa SB, Loginova I, Khalil A, Solonin A (2018) Effect of laser welding process parameters and filler metals on the weldability and the mechanical properties of Al alloy AA7020. *J Manuf Mater Process* 2(2):33

Modelling Factors Influencing Company Decision on Distribution Structure Using Interpretive Structure Modelling (ISM)



Mudit Kumar Rawat and Rajiv Kumar Sharma

Abstract This study includes Distribution structure, identification of new factor which are affecting distribution structure decisions, i.e. centralised or decentralised in logistics. In logistics Distribution structures include layout of transportation system and storage system used to transfer product from company to consumer locations. Product has higher inventory cost affect company to preferred centralised distribution system similarly product has higher transportation cost affect company to preferred decentralised distribution system. Based on literature review eight factors are identified which influences distribution structure decision. Further structural relationship is modelled between different factors which is performed by interpretive structure modelling (ISM) methodology. MICMAC analysis is implemented on factors to identify driving power and dependence power. The result of study show that Organisation factor is the key factor among all factors having highest driving power. Organisation factor is of higher preference for company to selection of distribution structure locations. The factors demand level, service level, logistics cost having higher dependence power. Hence, company should focus on these for the development and profit of company.

Keywords Distribution structures · Interpretive structure modelling · MICMAC analysis

1 Introduction

Supply chain is a network which involves the activities from transferring the raw material to good finished and delivering the finished product to customer. Logistics involves the process of transferring of good from origin point to delivering point of

M. K. Rawat (✉) · R. K. Sharma

Department of Mechanical Engineering, National Institute of Technology, Hamirpur, Himanchal Pradesh, India

R. K. Sharma

e-mail: rksfme@nith.ac.in

customer to meeting customer requirement and information flow from customer to company. Logistics management involves the activities of managing warehousing, inventory control and management, proper packaging and order fulfilment for the delivery of finished goods at the given time to right customer. Distribution structure include spatial layout of transportation and storage system through which good is used to move from company to end consumers location. For the distribution of goods from company to Consumers Company could use direct channel, i.e. centralised distribution system as The PC company dell shipped its PC to consumer directly [1] while the PC company HP uses indirect channel, i.e. decentralised distribution system as it is distributed through resellers [2]. Company uses different distribution system is mainly depend on service level of customer and logistics cost [1]. For the compromise between service level and logistics Cost Company choose optimal distribution system. Logistics cost incorporate vehicle cost, inventory expense, warehousing cost, capital expense and service level incorporate lead time adaptability, responsiveness, delivery recurrence and dependability [3].

There are several factors which affect distribution structure decision. In centralised distribution system company transport finished good directly to consumer or company may uses one distribution centre location to sell their product to other country. Centralised distribution allow them saving of inventory and warehousing cost. For high value high density Product Company uses centralised layout. Drawbacks of centralised distribution is transportation cost is high and services level is low, i.e. lead time is high. In decentralised layout which involve more than one DC location. Decentralised layout is used for high demand product and high service level. Advantage of decentralised layout is lead time reduction and reduction in higher outbound transportation cost but it includes additional inventory and warehousing cost. Company implement hybrid distribution layout, i.e. combining centralised and decentralised layout for goods for effective and efficient supply chain [5]. There are several factor which are important for distribution structure decision.

2 Literature Review

In logistics, the selection of distribution channel is important for company profit. There are various factor which affect selection of Distribution channel. Onstein et al. [4] recognised 7 principle factor and their sub factor that influence dynamic in distribution structure for example Demand level, service level, item characteristics, logistics cost, labour and land accessibility, Location accessibility and organisation factors. Draw a structure that shows the connection between these variables. Onstein et al. [4] identified logistics cost is the main factor followed by service and Demand level. A. T. C. Onstein et al. [6] identified one new factors business strategy and effect of these factors in distribution structure design in three industry, i.e. fashion, Consumer electronic, online retail. Chopra [1] discuss the different choice of distribution structure and their weakness and strength. According

to product variety and customer requirement identify the suitable distribution structure. Company choose decentralised layout for high volume and spatial dispersed product demand to improve service level and to reduce transportation cost [3]. For High value and high packaging density Product Company used centralised distribution to reduced inventory and handling cost [7]. Decentralised layout is used to provide good service level but it increase logistics cost [1]. There is a compromise between logistics cost and service level. Logistics cost include transportation cost and warehousing cost. Good service level increased warehousing cost but decrease transportation cost. There also trade-off between warehousing cost and transportation cost [7–9]. Location accessibility is access on location of distribution centre by train, air, motorways, ship. Parcel companies to reduced lead time of air cargo prefer location near to airports [10]. Decision maker do not give preference to rail location accessibility [11]. For real estate logistics growth land availability, labour and land cost is important resources for DC activities [12]. In urban area land area is limited therefore land availability is important factor [13] similarly is labour market is more important where labours are in limited. For lower labour and land Cost Company choose distribution location in peripheral areas and in peripheral areas further expansion of distribution location can be done [12]. Organisation characteristics include company size [14] and business strategy [15]. Company following customer intimacy strategy used decentralised structure to make supply chain more responsiveness. In operational excellence strategy company focuses on price of product which is competitive in market and low distribution cost. Product leadership strategy operation are flexible and the focuses on launching of innovative product. Organisation factor are legal and fiscal scheme which include various factor, i.e. zoning laws, Taxes, customs, International exchange conditions, presence of business park, insurance policies cost etc [16–19]. Zoning permits nearby governments to manage which territories under their locale may have land or land utilised for specific purposes. Company prefer locate DC periphery of country because taxes are higher than additional transport cost [12]. By using speedy customs and reduced moving good cost in international borders it attractiveness for DC location for higher value products and improves service level and reduced logistics cost.

Onstein et al. [4] derive framework of factors influencing distribution structure decision is developed by including seven factor. The level of importance of factor play important role in selection of distribution centre location. Interpretive structure modelling (ISM) is structural modelling technique used for analysing and establishing the relationship among enablers into a graphical model. As it is structural technique it simplify complex structure into simple structure by develop hierarchy of variables of system. ISM is used by all over world and by prominent corporations including NASA, IBM, and other organisation. In the below sections ISM strategy is utilised to discover structural connection between factors. MICMAC analysis is done on various factors to identify dependent and independent variables. Based on the result obtained from the final recommendations are made Future work is recommended.

3 Methodology

Interpretive structure modelling (ISM) is a technique for recognising connection between factors which characterized an issue. Larger number of factors having interaction which directly or indirectly affect the problem. They factors confuse the construction of framework which could conceivably be express a reasonable design of framework. ISM is used to define structure of system (Fig. 1 and Table 1).

3.1 Structural Self Interaction Matrix

SSIM matrix is formulated after identify relationship between each pair of factors from literature review. For the formulation of SSIM, four symbol V, A, X, O are utilised which address the directional relationship of each pair of components i, j where $i < j$ (Table 2).

- (1) V represent factor i affect to factor j .
- (2) A represent factor j affect to factor i .
- (3) X represent both factors i, j affect to one another.
- (4) O represent no relationship between factors i, j .

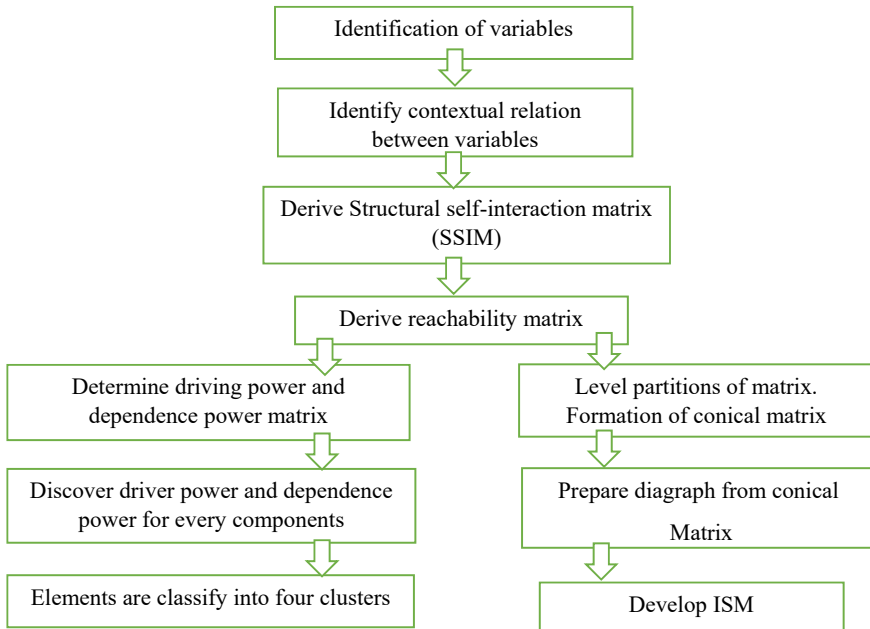


Fig. 1 Methodology of preparing ISM and MICMAC analysis

Table 1 Main factors of decision on distribution structure

S. No	Factors	Sub-factor
1	Demand level	Demand uncertainty Spatial demand pattern
2	Service level	Lead time adaptability Responsiveness Delivery recurrence Delivery dependability
3	Product characteristics	High and low value density product High and low Packaging density Perishability
4	Logistics costs	Transport costs Inventory costs Warehousing costs
5	Labour and land availability	Labour availability and cost Land availability and cost Expansion capability
6	Location Accessibility	Distance DC location from transport system Congestion
7	Organisation characteristics	Company size Business strategy (a) Customer intimacy, (b) Operational excellence (c) Product leadership
8	Organisation factors	Zoning laws, guidelines and arrangements Presence of a business park Cost of living and doing business Logistics land accessibility Local taxes and subsidies International exchange conditions Costs of insurance policies Customs execution Labour conditions

Table 2 Structural self-interaction matrix (SSIM)

Driver no	Driver for distribution structure decision	8	7	6	5	4	3	2	1
1	Demand level	O	O	O	O	X	O	X	-
2	Service level	A	A	A	O	X	A	-	
3	Product characteristics	O	V	O	O	V	-		
4	Logistics cost	A	A	A	A	-			
5	Labour and land availability	A	V	A	-				
6	Location accessibility	A	V	-					
7	Organisation characteristics	A	-						
8	Organisation factor	-							

3.2 Reachability Matrix

The following stage is to create a Reachability matrix. Initial reachability matrix is gotten from SSIM by subbing 1, 0 instead of V, A, X, and O.

The substitution rules are defined below-

1. In SSIM If (i, j) esteem is V, at that point In reachability lattice V changes to 1 for (i, j) and 0 for (j, i).
2. In SSIM If (i, j) esteem is A, at that point In reachability lattice A changes to 0 for (i, j) and 1 for (j, i).
3. In SSIM If (i, j) esteem is X, at that point In reachability lattice X changes to 1 for both (i, j) and (j, i)
4. In SSIM If (i,j) esteem is O, at that point In reachability lattice O changes to 0 for both (i, j) and (j, i).

3.2.1 Transitivity Check

There is a need of transitivity check in initial reachability Matrix. Transitivity rule expressed that if there is a connection between two elements 1 and 2 and another connection somewhere in the range of 2 and 3, transitivity infers that there is additionally connection between factors 1 and 3. Transitivity links are 5-4-1, 5-4-2 etc. 1* value is entered which factors follow transitivity. Last reachability lattice is achieved after implying transitivity check as shown in Table 3. In the below table driving power implies factors which affect other factors and itself and dependence power implies factor which dependent to other factor and itself.

3.3 Level Partitions

For the level allotments, for each factor reachability set and antecedent set are gotten from Final reachability lattice. The reachability set contain factors which it influence and itself moreover. The antecedent set contain factors which drive it and itself too.

Table 3 Final reachability matrix

Criterion	1	2	3	4	5	6	7	8	Driving power
1	1	1	0	1	0	0	0	0	3
2	1	1	0	1	0	0	0	0	3
3	1*	1	1	1	0	0	1	0	5
4	1	1	0	1	0	0	0	0	3
5	1*	1*	0	1	1	0	1	0	5
6	1*	1	0	1	1	1	1	0	6
7	1*	1	0	1	0	0	1	0	4
8	1*	1	0	1	1	1	1	1	7
Dependence power	8	8	1	8	3	2	5	1	

Table 4 (Iteration 1)

Enablers	Reachability set	Antecedent set	Intersection set	Level
1	1,2,4	1,2,3,4,5,6,7,8	1,2,4	I
2	1,2,4	1,2,3,4,5,6,7,8	1,2,4	I
3	1,2,3,4,7	3	3	
4	1,2,4	1,2,3,4,5,6,7,8	1,2,4	I
5	1,2,4,5,7	5,6,8	5	
6	1,2,4,5,6,7	6,8	6	
7	1,2,4,7	3,5,6,7,8	7	
8	1,2,4,5,6,7,8	8	8	

Table 5 Level of all enablers

Enablers	Reachability set	Antecedent set	Intersection set	Level
1	1,2,4	1,2,3,4,5,6,7,8	1,2,4	I
2	1,2,4	1,2,3,4,5,6,7,8	1,2,4	I
3	3	3	3	III
4	1,2,4	1,2,3,4,5,6,7,8	1,2,4	I
5		5,6,8	5	III
6	6	6	6	IV
7	7	3,5,6,7,8	7	II
8	8	8	8	V

The crossing point set contain same variables of reachability and antecedent set. The components which have same reachability and crossing point set starts things out level in the ISM progression. The variables which comes in the top chain of command is eliminated from consideration and same steps is followed until the level of all components is characterised. The level partition iteration and Level of all enablers is represented in Tables 4 and 5, respectively.

3.4 Conical Matrix

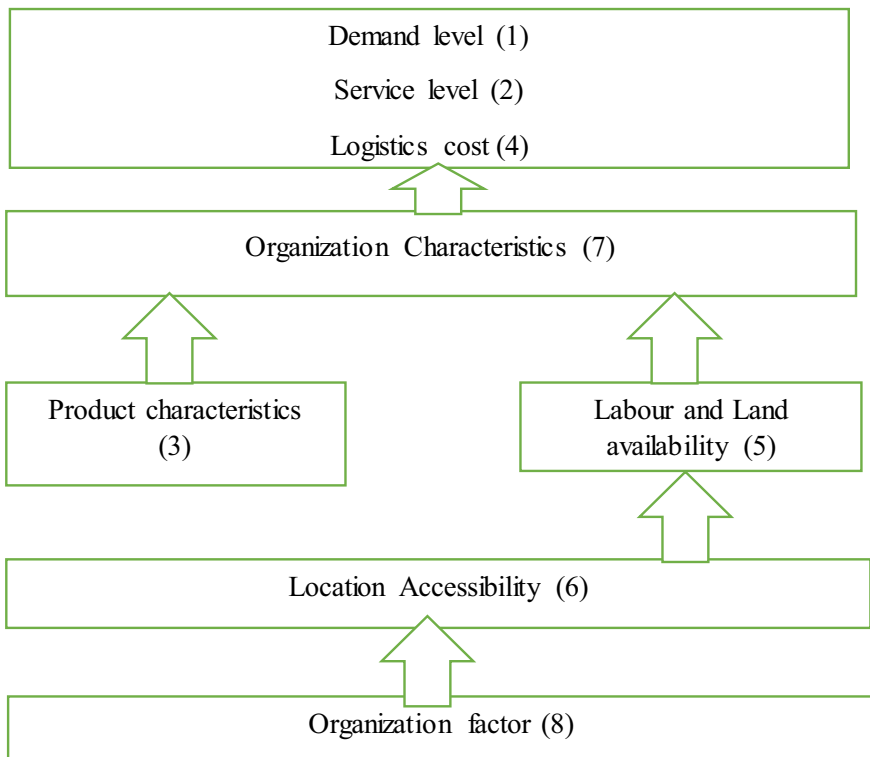
Conical matrix is also called lower triangular matrix. Conical matrix is obtained from final reachability lattice by revising the variables as indicated by their levels in level partitions. Conical Matrix is shown in Table 6.

Table 6 Conical Matrix

Criterion	1	2	4	7	3	5	6	8
1	1	1	1	0	0	0	0	0
2	1	1	1	0	0	0	0	0
4	1	1	1	0	0	0	0	0
7	1	1	1	1	0	0	0	0
3	1	1	1	1	1	0	0	0
5	1	1	1	1	0	1	0	0
6	1	1	1	1	0	1	1	0
8	1	1	1	1	0	1	1	1

3.5 ISM Based Model

From the level partitions given in the Tables 4, 5 and 6 and conical matrix ISM is developed for the factor which affect decision-making in distribution structure as shown below.



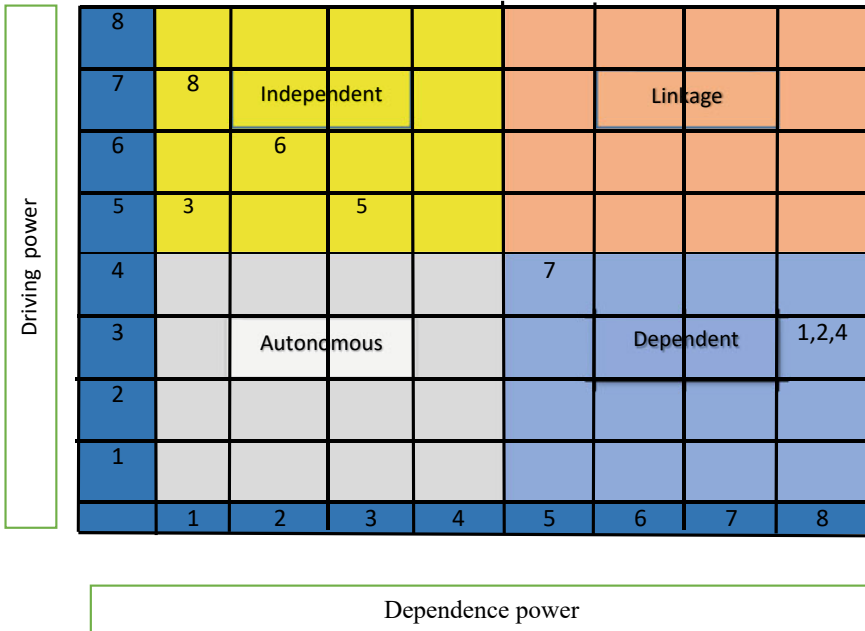


Fig. 2 Driving power and dependence power diagram

3.6 MICMAC Analysis

MICMAC analysis is graphical representation of the factors of ISM model as shown in Fig. 2. From the final reachability lattice, driving and reliance power is utilised to partition the diagram into four gatherings for example Autonomous, Dependent, Linkage, Independent enablers. The factor which drive other factors and dependency on other factors is less falls in independent enabler group, i.e. strong driving and weak dependence power. The independent enabler group includes location accessibility, labour and land availability, and organisational factor. Dependent enablers consist of factors which depend upon other factors and drive less factor, i.e. strong dependence and weak reliance power. Dependent enablers include demand levels, service levels, logistics costs, and product characteristics. The variables which drive different elements and furthermore reliant upon factors goes ahead linkage enablers, i.e. strong dependence and driving power. Autonomous enablers consist of factors which driving and dependency is less on other factors. There is no factors include in Linkage and Autonomous enabler groups.

4 Result

ISM model defined the structural relationship of factors affecting distribution structure decision. Variable Demand level, service level, logistics cost form the top hierarchy of ISM model and dependent variables in MICMAC analysis. These enablers strong dependency indicates for company profit and development Company mostly depend upon these variable. These three variables drive each other and other variables drive these variables. Organisation characteristics which is dependent on three lowermost hierarchy variables and drive top most hierarchy variables. Variable organisation characteristics falls second topmost in the ISM hierarchy and falls in the category of dependent variable in MICMAC analysis. Variable product characteristics which is independent, drive top 2 hierarchy variables, falls in middle level of ISM hierarchy. Variable Land and labour availability which is driven by lower hierarchy variables and drive upper hierarchy variables, falls with the same level of product characteristics. Product characteristics, labour and land availability falls in independent variables cluster in MICMAC analysis and same level in ISM hierarchy. Variables Location accessibility which drive all other top hierarchy variable is dependent on contextual factor, falls in the second lowermost level in the ISM hierarchy. Organisation factor has strong driving power least reliance power they structure the lowermost level in the ISM progression. Organisation factor does not subject to any factor. It drive all other variables which are in upper hierarchy.

Location accessibility and contextual factor falls on Independent enablers cluster in MICMAC analysis.

5 Conclusion and Future Scope

From the ISM model and MICMAC analysis organisation factor has strong driving power and weak reliance power comes in lowermost hierarchy. Decision on DC location the company manger should focus on the contextual factor. Demand level, service level, logistics cost has weak driver power and strong reliance power and comes in top most hierarchy. For the development and profit of company these three factors are most important. For futures scope more factors can be identified which affect distribution structure decision and structural relationship can be done.

References

1. Chopra S (2003) Designing the distribution network in a supply chain. *Transp Res Part E Logist Transp Rev* 39(2):123–140. [https://doi.org/10.1016/S1366-5545\(02\)00044-3](https://doi.org/10.1016/S1366-5545(02)00044-3)
2. Dell M (1998) The power of virtual integration: an interview with dell computer's Michael Dell. Interview by Joan Magretta. *Harv Bus Rev* 76(2):73–84

3. McKinnon AC (1984) "The spatial organization of physical distribution in the food industry," Dr. thesis, Univ. London
4. Onstein ATC, Tavasszy LA, van Damme DA (2019) Factors determining distribution structure decisions in logistics: a literature review and research agenda. *Transp Rev* 39(2):243–260. <https://doi.org/10.1080/01441647.2018.1459929>
5. Van Hoek RI, Commandeur H, Vos B (1998) Reconfiguring logistics systems through postponement strategies. *J Bus Logist* 19(1):33
6. Onstein ATC, Tavasszy LA, Rezaei J, van Damme DA, Heitz A (2020) "A sectoral perspective on distribution structure design." *Int J Logist Res Appl*, 1–29. <https://doi.org/10.1080/13675567.2020.1849074>
7. Behrenbeck K, Thonemann U, Merschmann U (2007) Soft secrets of supply chain success 7(2)
8. Chuang PT (2002) A QFD approach for distribution's location model. *Int J Qual Reliab Manag* 19(8):1037–1054. <https://doi.org/10.1108/02656710210438113>
9. Ashayeri J, Rongen JMJ (1997) Central Distribution in Europe: a multi-criteria approach to location selection. *Int J Logist Manag* 8(1):97–109. <https://doi.org/10.1108/09574099710805628>
10. Dablanc L, Rakotonarivo D (2010) The impacts of logistics sprawl: How does the location of parcel transport terminals affect the energy efficiency of goods' movements in Paris and what can we do about it? *Procedia Soc Behav Sci* 2(3):6087–6096. <https://doi.org/10.1016/j.sbspro.2010.04.021>
11. Bowen JT (2008) Moving places: the geography of warehousing in the US. *J Transp Geogr* 16(6):379–387. <https://doi.org/10.1016/j.jtrangeo.2008.03.001>
12. Hesse M (2004) "Introduction: the nature and the location of freight distribution." *Tijdschr voor Econ en Soc Geogr* 95(2):162–173, , [Online]. Available: https://orbilu.uni.lu/bitstream/10993/3469/1/tesg_landforlogistics.pdf
13. Klauenberg J, Elsner LA, Knischewski C (2020) Dynamics of the spatial distribution of hubs in groupage networks—the case of Berlin. *J Transp Geogr* 88:102280. <https://doi.org/10.1016/j.jtrangeo.2018.07.004>
14. Pedersen SG, Zachariassen F, Arlbjørn JS (May 2012) "Centralisation vs de-centralisation of warehousing: a small and medium-sized enterprise perspective." *J Small Bus Enterprise Develop* 19(2). Emerald Group Publishing Limited, pp. 352–369. <https://doi.org/10.1108/14626001211223946>
15. Wiersema F, Treacy M (1993) Customer intimacy and other value disciplines. *Harv Bus Rev* 71(1):84–93
16. Cidell J (2011) Distribution centers among the rooftops: the global logistics network meets the suburban spatial imaginary. *Int J Urban Reg Res* 35(4):832–851. <https://doi.org/10.1111/j.1468-2427.2010.00973.x>
17. Van Thai V, Grewal D (2005) "Selecting the location of distribution centre in logistics operations: a conceptual frame work and case study." 17(3):3–24
18. Warffemius PMJ (2007) Modeling the clustering of distribution centers around Amsterdam airport schiphol : location endowments, economies of agglomeration, locked-in logistics and policy implications
19. Melachrinoudis E, Min H (May 2000) Dynamic relocation and phase-out of a hybrid, two-echelon plant/warehousing facility: a multiple objective approach. *Eur J Oper Res* 123(1):1–15. [https://doi.org/10.1016/S0377-2217\(99\)00166-6](https://doi.org/10.1016/S0377-2217(99)00166-6)

Modern Processes Improvements and Capability Analysis of Friction Stir Welded Dissimilar Nonferrous Materials—A Review



Rajnish Singh and Yogesh Kumar

Abstract Friction stir welding (FSW) is a joining process where two metals are joined in solid-state. In, FSW, a non-consumable type tool is used to join two metal workpieces. It is important to note that the melting of workpiece materials does not take place in the case of friction stir welding unlike the other conventional methods of welding. This process was invented by the TWI UK in the year 1991. In the last two decades, various process improvements incorporated in FSW. The primary aim of process improvement was to facilitate weld strength and mechanical and microstructural properties. The placement of the base material in FSW of two dissimilar materials, for example, aluminum and copper, are significant and play important role in the weld quality and welding strength of joints. The aluminum and copper are welded by the FSW with the integration of ultrasonic vibrations. The roughness of base material reduces in the only Type I joint with the use of ultrasonic vibrations. The joints' strength increases with decreases in the intermetallic compound's thickness formation in Type I & II joints. The welding strength is better in tensile strength if the copper is placed on the retreating side. The electrical property of base material, like electrical conductivity, did not experience any changes during FSW. The back heating assisted processes improvements to improve cracking and tunnel defects. The microhardness of welding of NiTi/Ti6Al4V joints is higher than the base material. The underwater FSW has new advancements in process capabilities that improve the thermal cycle, tensile strength, and hardness of the welded sample. The controlled cooling enhances the microstructure of the base plate also. The hardness at the stir zone drops independently of parameters. At high tool pin temperature, the transition from brittle to ductile was observed.

Keywords UaFSW · UFSW · i-FSW · IMC · Type I · Type II

R. Singh (✉)

Mechanical Engineering Department, Kamla Nehru Institute of Technology, Uttar Pradesh, Sultanpur 228118, India
e-mail: rajnish.singh@knit.ac.in

Y. Kumar

Mechanical Engineering Department, National Institute of Technology Patna, Bihar 800005, India
e-mail: yogesh.me@nitp.ac.in

1 Introduction

Before the 1990s, we had various welding technologies such as gas welding, arc welding, etc., to join one substance to another, which may be similar or dissimilar with having different mechanical, chemical, and physical properties. But in this welding process, many disadvantages had been found, such as hot cracking, porosity, and residual stresses. The main problem was forming an oxide layer on the aluminum during arc welding and hardening of the aluminum surface. This hardened surface was difficult to machine for further improvements in the dimension. FSW was a new technique that reduces fusion defects and improves weldability. A Schematic diagram of FSW technique is shown in Fig. 1 [1]. FSW is a solid-state welding process. In FSW, a rotatory tool moves along the weld line. At one side of the workpiece plate, where rotation and translation of tool are in the same direction, is advancing side and another side is retreating side [2]. The materials are welded by the heat generated due to friction at the interface of the tool and workpieces. The frictional heat exceeds yield of material then the shear strength is reduced and result in the plastic deformation of the materials being welded. The amount of frictional heat generated depends upon the various process parameters and additional attachments. FSW may also be called as thermomechanical welding method [3]. The complete process details are shown in Fig. 1.

The convention FSW process was done on a similar and dissimilar material that needs some improvements in the processes for optimum mechanical as well as metallurgical properties. The conventional FSW was not used for hard materials like titanium alloys. The back assisted heat source was used for welding titanium alloys. A gas welding torch was attached with translating tool that follows the exact path as the tool, which improves the mechanical and microstructural properties of titanium alloys. There were three different zones were found in the microstructural as (a) Stir Zone (SZ), (b) thermomechanical affected zone (TMAZ), and (c) heat affected zone

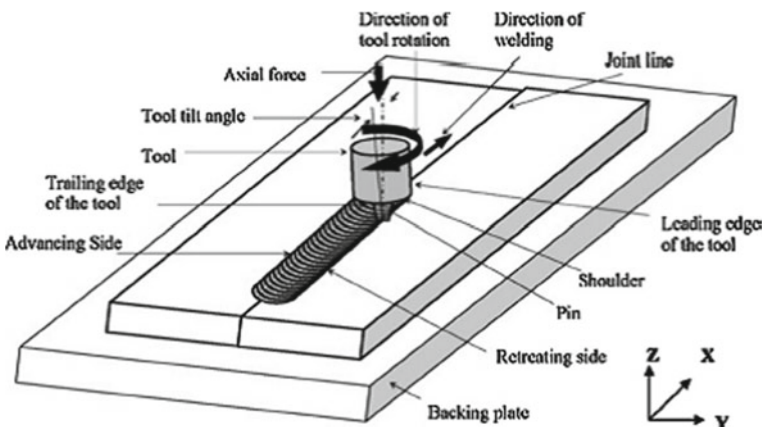


Fig. 1 Principle of Friction stir welding [4]

(HAZ) [11]. The effect of ultrasonic energy and placement of material was used that showed the extreme effect on the tensile strength and intermetallic compound (IMC) formation. An ultrasonic vibration mechanism was coupled with the tool as well as fixture the setup was known as UaFSW process. The objective is to reduce the problem associated with FSW of dissimilar Al/Cu material with ultrasonic vibration-assisted mechanism and placement of base material [9]. Other process improvements were also introduced known as i-FSW process which includes the induction heating of the job as well as of tool that reduces the mixing problem and IMC formation. The i-FSW initially was done on thermoplastic dissimilar material then extended to metallic material also. The frictional heat was not sufficient to reduce the shear strength of all materials. The induction heating tool was a very convenient and cheap method of improvement in FSW [4]. The effect of heat generation was also studied on aluminum alloys for tensile strength which shows improvement in the weld joint [8]. The fixture of FSW was submerged in the pool of water and welding was done in the same. The frictional heat was conducted in the water therefore preheating was done and the effect of preheating was also observed in the UFSW joint [5]. The mathematical modeling of UFSW was analyzed on the FEA method on dissimilar material and simulated the results of modeling with experiments [6]. Another process improvement was the placement of material. The joining of dissimilar material like Al/Cu, when Cu placed at advancing side placement was known as Type I joint similarly when Cu was placed at retreating side known as Type II joint. The effect of placement was necessary for dissimilar material having a huge difference in the melting point [12].

2 Methodology

The welding of UaFSW was done on the Al/Cu dissimilar materials. In this experimental investigation, pure copper and aluminum alloys 6061-T6 were used for dissimilar welding through the friction stir method. The melting point of aluminum was 585 °C and 1085 °C for pure copper. The selected workpiece dimensions are 200 mm × 65 mm × 2 mm for butt welding processes. The welding was performed to analyze the effect of ultrasonic vibration on copper and aluminum joints' weld strength. Another ultrasonic vibration mechanism was applied to the conventional friction stir welding machine. The process was converted into four different experimental processes with the different placing of material. The base materials used in the ultrasonic-assisted FSW are aluminum and copper. The properties of base material played an important in the welding and joining processes. There is a huge difference in melting point of base metals. The actual experimental setup with steel tools is shown in Fig. 2 [9].

The back assisted heating was introduced on the welding of titanium alloys and nitinol. The methodology and experimental setup are shown in Fig. 2c. The plate of 70 mm × 210 mm × 3 mm rolled NiTi and Ti6Al4V was welded with back heating arrangements at 200 °C fixed temperature at a constant speed. The concept

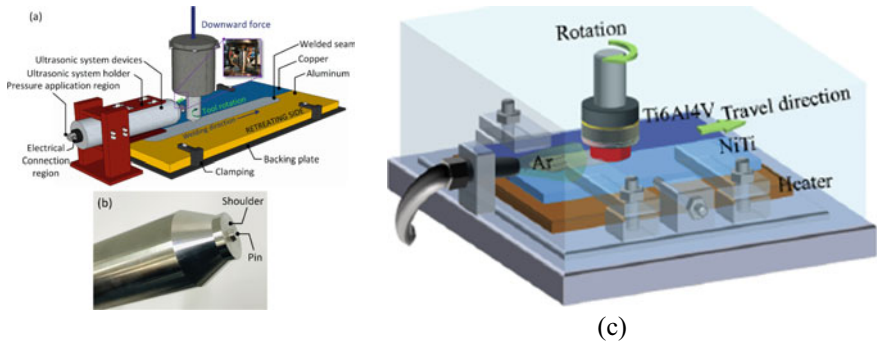


Fig. 2 a Joining of Al and Cu by FSW and UVaFSW processes, and b H13 steel tool used in FSW [9] c Back heating assisted FSW [11]

of placement of material was also investigated for mechanical and microstructural properties. The NiTi was placed at the retreating side [11].

The methodology for underwater friction stir welding (UFSW) was adopted as changing the fixture design and tool material. The complete welding was done in underwater conditions, and the effects of underwater were compared with friction stir welding, and mathematical modeling results were also compared. Significant results were obtained. The convention FSW process involved the effect of uncontrolled heating and cooling cycle. In UFSW, controlled heating and cooling improve the base material's mechanical and microstructure properties. The underwater condition also limits the brittle IMC formation in similar and dissimilar joints. The underwater environments improve surface quality [6]. The other process improvement facility has been incorporated to induce heating processes by induction effect named as the i-FSW process. The tool was rapped with the induction coil and heated by the variable current and voltage value. The three different temperature was selected for the observation of mechanical properties and microstructural evaluation. The microcontroller was used for the control of the heating in the specified temperature range. Only the tool is heated in this process, and no other elements like fixture and base plate were supposed to heat [4].

2.1 Base Materials

An aluminum plate is used for friction stir welding. The melting point temperature of aluminum was approximately 585 °C. Its melting point is comparatively less as compared to other metal and their alloy. Therefore, it can be more easily softened when H13 steel tool met it. Due to frictional heat generated, the aluminum alloy is softened. The rotating tool fuses the metal from one plate to another and is fused into one another and welding is completed. The mechanical composition of aluminum and pure copper is shown in Tables 1 and 2 respectively.

Table 1 6061-T6 aluminum alloy [9]

Al	Mg	Si	Fe	Cu	Cr	Zn	Ti	Mn	Remainder
95.85-98.56	08.-1.2	0.40-0.8	0.0-0.7	0.15-0.40	0.04-0.35	0.0-0.25	0.0-0.25	0.0-0.15	0.05 each, 0.15 total

Table 2 Copper C10100 alloy composition [9]

Cu	Pb	Zn	Fe	P	Ag	As	O	Sb	Te
99.99	0.0005	0.0001	0.0010	0.0003	0.0025	0.0005	0.0005	0.0004	0.0002

The Nitinol and Ti6Al4V are one of the widest used shape memory alloys used in the important field. They have excellent superplasticity and unique strength. The combination of these materials forms better properties that have wide applications. The thermoplastic materials were also used for the investigation of mechanical properties and microstructural behavior analysis.

2.2 Tool

The tool of friction stir welding was made by the H13 steel, die steel, carbide tool, and other alloys. The material should have various properties such as hardness, resistance to abrasion, and the ability to retain shape. The die steel rod is converted into a cylindrical-shaped tool using a lathe machine for performing friction stir spot welding. The diameter of the shoulder is kept at 20 mm. A pin is made below the shoulder, which has a dimension of 4.2 mm × 5.2 mm × 1.8 mm in length for UFSW. The tool was designed for conical pin and flat shoulder type. There was not any threading provided on the pin profile. The tool is placed 2 mm away from the weld centerline [7]. The heat treatment process is done on this tool to make it even harder. For this purpose, the die steel tool is heated to its crystallization temperature, and then it is cooled into the water. This process is called quenching [10].

2.3 Base Material Position

In the FSW process, a rotatory tool travels along the weld centerline, so there are two sides: advancing side and the other one is retreating side. If the direction tool movement and direction of tool rotation are same, the side is advancing side, and if the directions are alike, then the side is retreating side. So, if the aluminum is placed at the retreating side and the copper is placed at the advancing side, such a convention is known as Type I joint and vice versa is named Type II joint. The RS denotes the advancing side represented by AS and the retreating side. On the other hand, the ultrasonic vibration was incorporated in the FSW denoted by UaFSW, and without incorporating vibration the system was named FSW. Therefore, four combinations of placements and vibration were introduced for the experimental process. The actual representation of base material placement is shown in Fig. 3 [9].

The process parameters were selected for the experiential process. The main process parameters were tool rotational speed in rpm, tool translational speed along

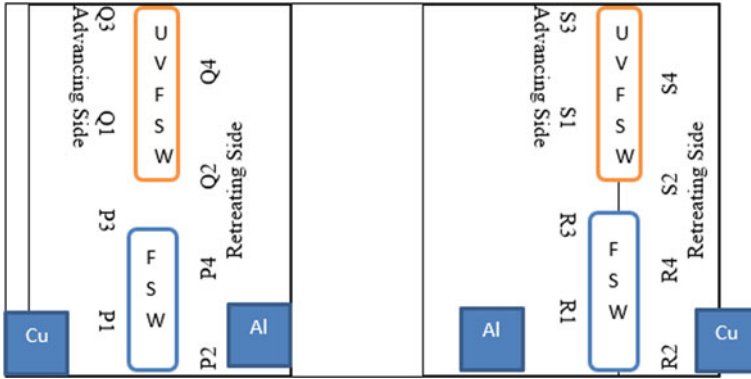


Fig. 3 The placement of base material in two types **a** Type I joint **b** Type II joint

Table 3 Process parameters of UaFSW and FSW [9]

Weld parameters	Rotation speed of tool (Rpm)	Linear welding speed (Mm/min)	Tool offset (Mm)	Shoulder plunge depth (Mm)	Tool tilt angle (Degree)
FSW-Al (RS)	600	40	2	0.1	2
UVaFSW-Al (RS)			2	0.1	2
FSW-Al (AS)			2	0.1	2
UVaFSW-Al (AS)			2	0.1	2

the weld line in mm/min. Tool offset was given to the placing of the base material. The tool tilt angle is the angle from vertical to tool for proper mixing of stir zone. The shoulder diameter and pin length are also given in Table 3.

3 Result and Discussion

3.1 Thermal Evaluation Behavior

The thermal analysis of UaFSW was investigated on Al/Cu. The analysis of thermal behavior was done by converting the surface of base material into four different points at each AS and RS. The temperature effects are measured with a thermocouple attached near the welding line. In Type, I joint point P1, P3, Q1, and Q3 was indicating the AS. The temperature of FSW joint was found lower as compared to UaFSW process. The temperature response time was also analyzed and found less time for equilibrium maximum temperature reaches in UaFSW process. The temperature rise

in UaFSW process was more which results in the improved plastic material flow and proper mixing at the stir zone was observed in the UaFSW process. Similarly, in Type II joint aluminum was placed at advancing side, the peak temperature and time was recorded for both FSW and UaFSW process. The copper is at RS and has a higher melting point. The temperature distribution is shown in Fig. 4 [9].

The Joint strength of nitinol and titanium alloys welded by the back assisted heating mechanism was found to be improved properties as tabulated below in Table 4. The welding after the back assisted temperature the average temperature of the weldable plate increases therefore the yield strength reduces and mixing of high melting point improves [11].

The thermal cycle of underwater welding and conventional friction stir welding were compared and found that maximum heat at FSW and UFSW was recorded by NT1 thermocouple and found lower magnitude in UFSW. The placements of materials also play an important role in heat generation magnitude. The retreating side reached the lowest temperature the experimental and simulation results were shown in Fig. 4. In all types of friction stir welding processes, thinning is always found in joints that reduce the strength of joints. This is due to the flow of plasticized material with uncontrolled process parameters but in the case of UFSW process lower probability of thing of the joint which processes less flash defect and improves the tensile strength (Fig. 5) [6].

Table 4 Heat assisted FSW

Rotational speed	Travel speed	Plunge depth (mm)	Title angle (Degree)	Back assisted heating	Shielding gas	Placement
750 rpm	23.5,30,60 mm/min	0.2	2	No	Ar	NiTi at retreating
475 rpm	23.5,30,60 mm/min	0.2	2	200°C	Ar	Niti at retreating

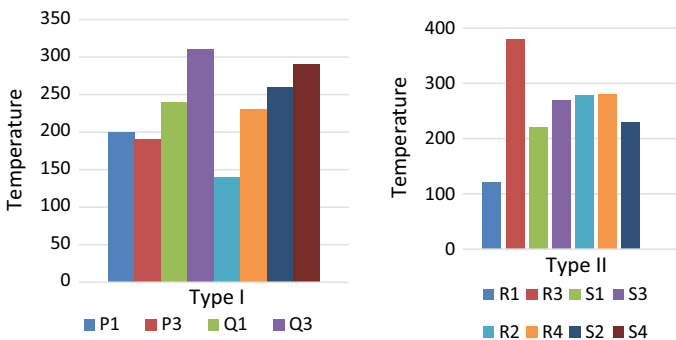


Fig. 4 The temperature distribution and time response are mentioned at the assigned location in both Type I and Type II joint

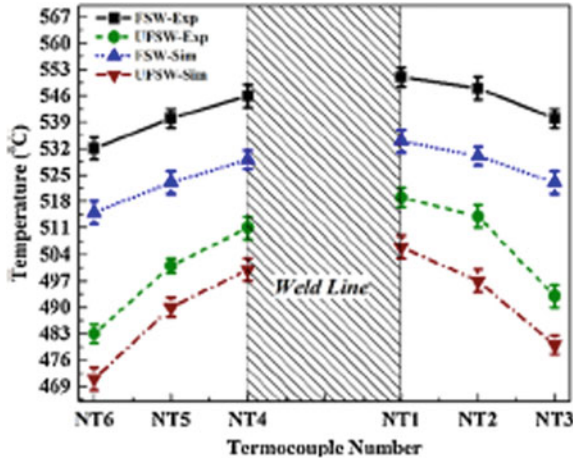


Fig. 5 The thermal behavior of underwater friction stir welding [6]

3.2 Weld Surface and Phase

The intermetallic layer distribution was analyzed with X-ray diffraction technics in the stir zone and results were shown in Fig. 6. The scanning electron microscopy images revealed that the Type I joints have a leaf-like structure which is evident

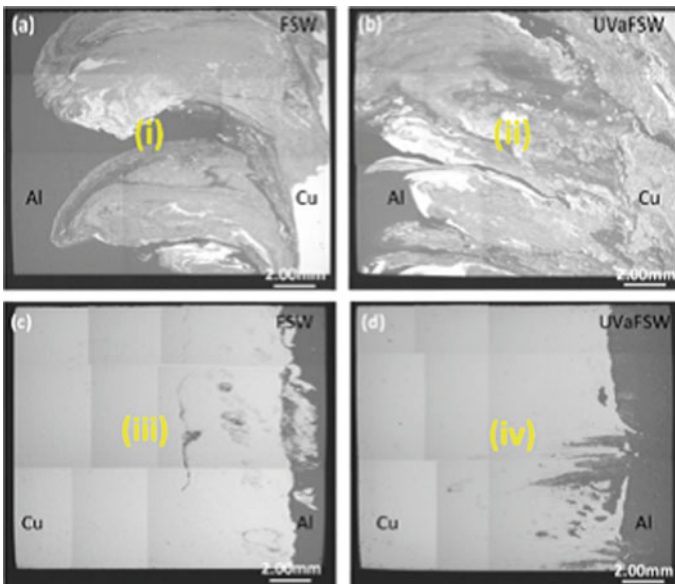


Fig. 6 SEM image of FSW and UVaFSW joints, a, b Type I joints, c, d type II joints [9]

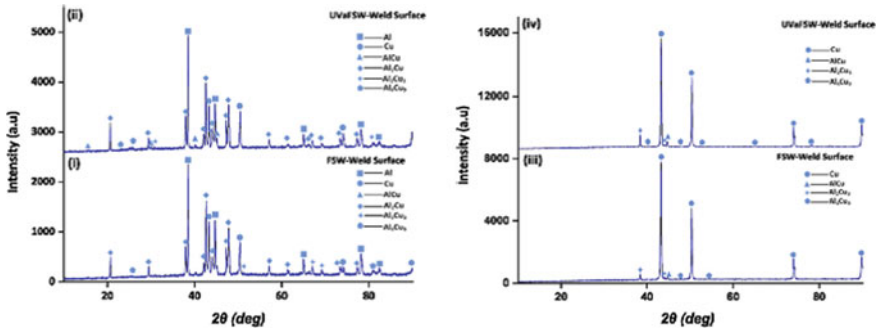


Fig. 7 X-ray diffraction of FSW and UVaFSW joints from Fig. 6 a–d for (I, ii) Type I joints, and (iii, iv) type II joints [9]

of complex mixing in FSW and UaFSW processes [3]. In Type II joint the evident of mixing was less as shown in scanning electron microscopy images. The X-ray images of Type I joint in UaFSW process the aluminum layer was more distributed on the top surface, and particles were distributed nonuniformly. The largest peak of aluminum was found in both FSW and UaFSW processes as shown in Fig. 6. The highest peak of aluminum is the evidence of the stir zone where predominant mixing of aluminum took place. In the Type II joint as shown in the XRD images copper was dominant in the stir zone. The scanning electron microscopy SEM images are shown in Fig. 6. The XRD results are represented in Fig. 7 for both Type I and Type II joints [9].

The effect of back-assisted heating was shown in the SEM images. The images of scanning electron microscopy of NiTi/Ti6Al4V are shown in Fig. 8. The interface consists of nitinol debris via tool flowed into the matrix & small nitinol debris transferred to the matrix. A micron-level IMC formed at the interface. The numerous IMC formed at the interface with different sizes. The XRD images predict that various IMC developed during welding of dissimilar materials at the interface of joints and disturb the joints' mechanical properties. The strength was improved by the back heating arrangements [11]. The transition zone was formed between weld and base material on the surface of heated tool (in i-FSW) on the welding of the thermoplastic form. This zone forms due to the formation of skin core structure in the welding zone [4].

3.3 Tensile Strength

The tensile strength of Al/Cu dissimilar material of Type I and Type II joint was investigated for welding strength of UaFSW. The UTS and YS of all four types of joint results are shown in Table 4. The welding strength of ultrasonic-assisted welding was found to be higher than the normal FSW process in both types I & II joints. The

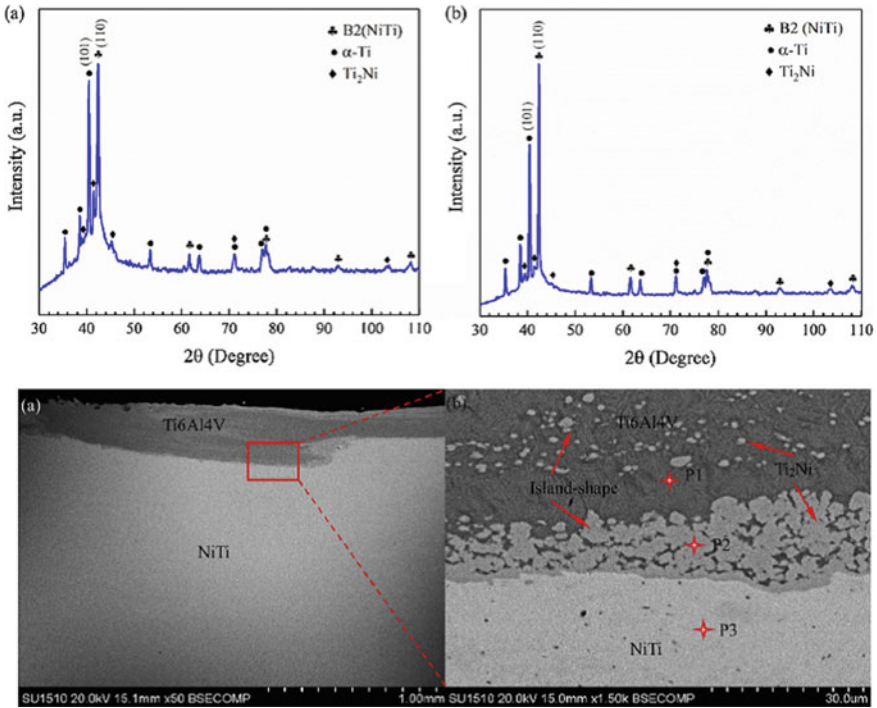


Fig. 8 SEM images and XRD images of NiTi/Ti6Al4V welded by back assisted heating sources [11]

yield strength of Type I joint lacks due to the inability of weld deform after yielding. The fracture strain was much small in both FSW and UaFSW processes. This is due to rapid fracture which occurs after the elastic limit. The yield strength in Type II joint found large plastic deformation after yielding and established large plastic strain as compared to Type I joint. However, yield strength and ultimate tensile strength in UaFSW Type II joint were increased by 12 and 28 MPa respectively compared to conventional FSW. All four samples were examined on a universal tensile tester machine. The results were tabulated. The thin layer of the intermetallic compound was promoted the weld quality of FSW joints. The intermetallic compound layer (IMC) in FSW and UaFSW vary differently. The thickness of IMC in UaFSW is small and increases the weld strength as compared to FSW in both Types I & II joints. In Type II joint the IMC is continuous and insignificance difference in Morphology in UaFSW and FSW as compared to Type I joint. The tensile strength as UTS and YS are tabulated in Table 5.

The back assisted heating mechanism also showed a significant effect on the weld strength. The tensile strength improvements by the process improvements capabilities in the nitinol alloys and respective placements found to be as mentioned below. When increasing the traverse speed forming tunnel defect and kissing bonding at interface

Table 5 Tensile properties of Al/Cu Joint [9]

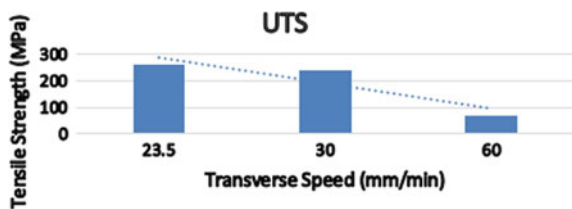
Weld	Yield strength (MPa)	Ultimate tensile strength (MPa)	Elongation (%)
FSW- Type I joint	117.10	123.35	10.56
UVaFSW- Type I joint	128.10	151.5	17.31
FSW- Type II joint	149.63	196.93	27.15
UVaFSW- Type II joint	140.10	199.57	35.28

of nitinol and titanium alloys and detreating mechanical properties of the joints. It is speculated by back assisted heating mechanism and plasticizes the material. The tensile strength was found to be improved by a constant heating source (Fig. 9) [11].

The tensile strength in all types of underwater friction stir welding processes improves due to the controlled heating and cooling process involved. The strength of the weld increases due to the controlled cooling effect. The experimental results predict the increased value of ultimate tensile strength in the case of UFSW as compared to FSW process. The fracture points are normally found at the stir zone in case of friction stir welding process but due to fast cooling the fracture point shift from the stir zone to heat affected zone in case of UFSW process. The shifting of fracture point is proved by the fractography test which is done by Scanning electron microscopy (Fig. 10).

The tensile strength in the case of induction heated friction stir welding (i-FSW) is influenced by the tool temperature and tool rotational speed. The tensile strength of the tool was found to be maximum for temperature range 40–45 °C. The tool rotational speed ranging from 1000 to 2000 rpm strength increases rapidly but further increases in tool rotational speed decreased in strength found. However higher rpm results in thinning of weld zone and flash defect. So that strength reduction was observed. The fracture mode was found to be at the stir zone, base material, and retreating side. The sample at low rpm fractured at the retreating side and minimum joint efficiency was found [4].

Fig. 9 The tensile strength variation in the back assisted friction stir welding



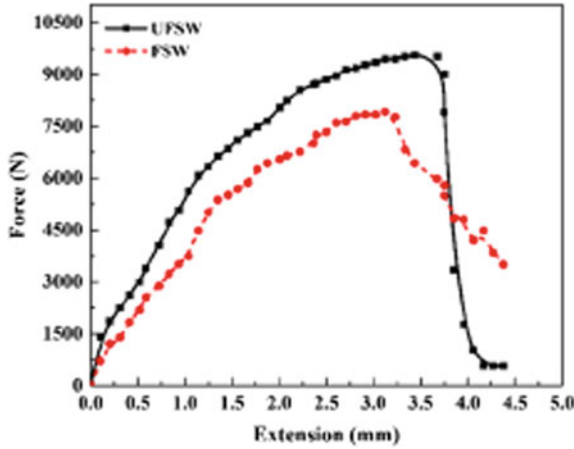


Fig. 10 The load extension curve of underwater welding [6]

3.4 Microhardness

The microhardness profile of FSW and UaFSW process was obtained in two different types of joint. The Type I joint showed a different pattern as compared to Type II. In the general process, if IMC formation was maximum then the microhardness peaks were obtained. Thus, it was evidence of IMC layer formation in FSW and UaFSW processes. The Type I joint showed limited stir zone width but having higher peaks were obtained in FSW process as compared to UaFSW process. It means the interaction pattern of Al & Cu enables the development of a stir mixed zone which evaluates several IMC layers. On the other hand, the stir zone had no lamellar structure and had a uniform distribution of copper particles. That was mentioned lower hardness peaks in the stir zone (Fig. 11).

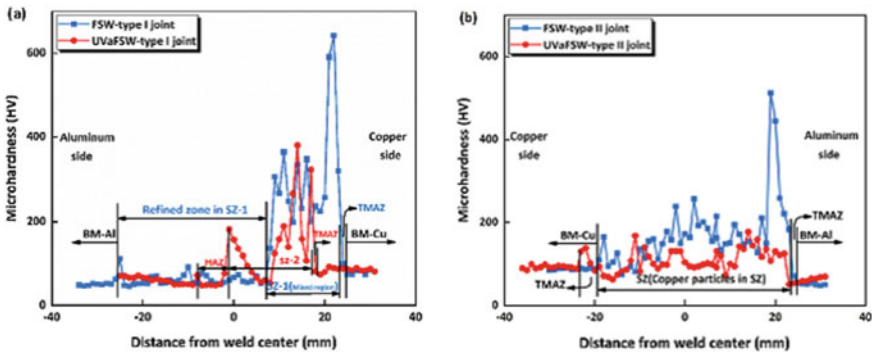


Fig. 11 The microhardness distribution is shown a Type I joint b Type II joint [9]

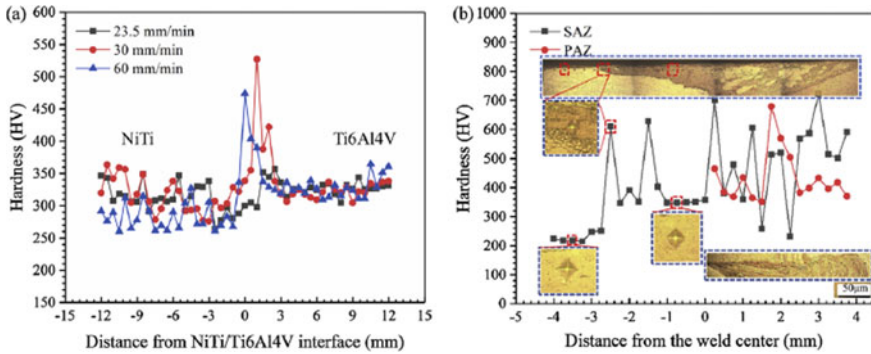


Fig. 12 Microhardness variation in the NiTi/Ti6Al4V [11]

The microhardness of the nitinol and their alloys welded by back assisted heating mechanism to display the fluctuation in the microhardness in the nitinol side relatively larger than on another side. The microhardness at the interface of the joint has significant fluctuation in magnitude, this is caused by the formation of IMC at the interface. The hardness of IMC is more than 3 to 4 times of normal nitinol. This improves the brittleness in the joints. That can be confirmed by fractography (Fig. 12) [11].

The microhardness in the case of the underwater welding process predicts the phase identification and the evaluation of the effect of water in the joint formation. It has been found that the microhardness of aluminum alloys welded by the UFSW process shows a higher magnitude value in magnitude. This is due to the fast cooling rate. And the pattern of hardness distribution will remain the same as the other process improvement process.

The microhardness behavior of welding similar and dissimilar thermoplastic showed a different pattern in the case of welding of induction heated tool. The softening of base material due to heated tool reduced hardness recorded. The tool temperature increases reduced hardness value recorded. The recorded pattern of hardness shows the ductile nature of the weld. To understand the better understanding of hardness a new term introduced hardness ratio (difference of hardness of base material and weld center to the base material hardness.) It was not found in the higher tool pin temperature and moderate tool rotational speed. The joint produced at 1000 rpm and low tool temperature failed in a brittle manner.

3.5 Electrical Conductivity

The electrical conductivity of the joints of FSW & UaFSW process was analyzed and found that there is no significant variation in the electrical conductivity irrespective

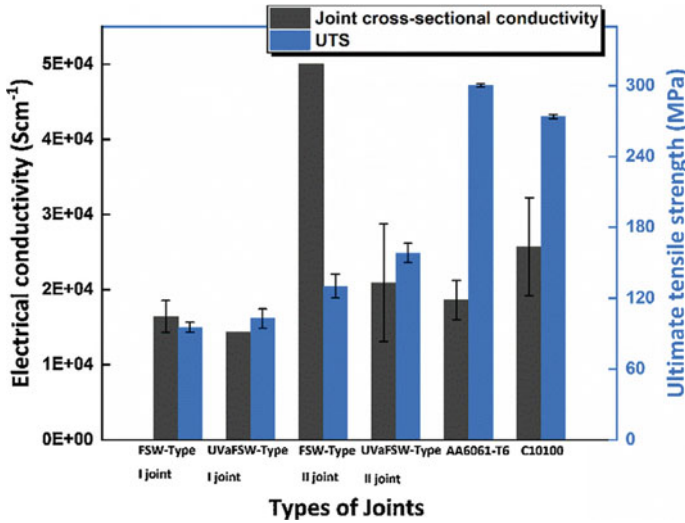


Fig. 13 Comparison of electrical conductivity in Type I & II joint with base material [9]

of the types of joints and process involved. It is a good sign that the vibration in the weld zone did not affect the electrical behavior of the material (Fig. 13).

4 Conclusion

The joint strengths of dissimilar copper and aluminum were increased with the decrease in intermetallic compound layer thickness for Type I joints. The reduction in particle sizes was also observed in Type II joints. Mixing mechanisms in FSW for Al/Cu joint led to the generation of IMC Lamare structure and coper particle distribution, which is used to determine the layer thickness and stir zone behavior. The fracture of the weld joint was found to fail at stir zone in Type I joint but failed at the boundary of stir zone and Cu in Type II joint. This was used for the behavior of mixing. There was no evidence of ultrasonic vibration was found for the electrical property improvement. The joining of Nitinol and Ti6Al4V with defect-free was obtained 269 MPa with back assisted heating. The microhardness was found maximum 710HV it was the evidence of brittle IMC formation that was the main cause of deteriorating the mechanical properties of joints. The induction heat effect on the welding of dissimilar and similar material showed minimum flash. The optimum condition was obtained at moderate temperature and moderate rotational speed of the tool. Too high heating retards the mechanical properties. The i-FSW shows a good mixing capability and a high level of crystallization. In UFSW methodology the water environment reduces the heat flow and improves the cooling rate which turns into the improvement of grain structure in the finer pattern. The tensile strength

increases up to 15% of the conventional friction stir welding. The back assisted heating methodology produces defect-free and fractured at bulk IMC zone.

References

1. Hou W et al (2021) "Enhancing metallurgical and mechanical properties of friction stir butt welded joints of Al–Cu via cold sprayed Ni interlayer." *Mater Sci Eng A* 809(November 2020):140992. <https://doi.org/10.1016/j.msea.2021.140992>
2. Song Q, Wang H, Ji S, Ma Z, Jiang W, Chen M (2020) Improving joint quality of hybrid friction stir welded Al/Mg dissimilar alloys by RBFNN-GWO system. *J Manuf Process* 59(October):750–759. <https://doi.org/10.1016/j.jmapro.2020.10.037>
3. Singha R, Rizvi SA, Tewari SP (2017) Effect of friction stir welding on the tensile properties of AA6063 under different conditions. *Int J Eng Trans A Basics* 30(4):597–603. <https://doi.org/10.5829/idosi.ije.2017.30.04a.19>
4. Vijendra B, Sharma A (2015) Induction heated tool assisted friction-stir welding (i-FSW): a novel hybrid process for joining of thermoplastics. *J Manuf Process* 20:234–244. <https://doi.org/10.1016/j.jmapro.2015.07.005>
5. Dong J, Zhang D, Luo X, Zhang W, Zhang W, Qiu C (2020) EBSD study of underwater friction stir welded AA7003-T4 and AA6060-T4 dissimilar joint. *J Mater Res Technol* 9(3):4309–4318. <https://doi.org/10.1016/j.jmrt.2020.02.056>
6. Talebizadehsardari P, Musharavati F, Khan A, Sebaey TA, Eyvaziana A, Derazkola HA (2021) "Underwater friction stir welding of Al-Mg alloy: thermo-mechanical modeling and validation." *Mater Today Commun* 26(December 2020):101965. <https://doi.org/10.1016/j.mtcomm.2020.101965>
7. Darmadi DB, Talice M (2020) "Improving the strength of friction stir welded joint by double side friction welding and varying pin geometry." *Eng Sci Technol An Int J xxxx*. <https://doi.org/10.1016/j.jestch.2020.11.001>
8. Singh R, Yadav A (2018) "Experimental study of effect of process parameters for heat generation in friction stir welding." *IOP Conf Series: Mater Sci Eng* 402(1). <https://doi.org/10.1088/1757-899X/402/1/012131>
9. Muhammad NA, Wu CS (2020) "Evaluation of capabilities of ultrasonic vibration on the surface, electrical and mechanical behaviours of aluminium to copper dissimilar friction stir welds." *Int J Mech Sci* 183(April):105784. <https://doi.org/10.1016/j.ijmecsci.2020.105784>
10. Cao F, Li J, Hou W, Shen Y, Ni R (2021) "Microstructural evolution and mechanical properties of the friction stir welded Al/Cu dissimilar joint enhanced by post-weld heat treatment." *Mater Characterization* 174. <https://doi.org/10.1016/j.matchar.2021.110998>
11. Deng H, Chen Y, Jia Y, Pang Y, Zhang T, Wang S, Yin L (2021) "Microstructure and mechanical properties of dissimilar NiTi/Ti6Al4V joints via back-heating assisted friction stir welding. *J Manuf Process* 64. <https://doi.org/10.1016/j.jmapro.2021.01.024>
12. Yu P, Wu CS, Shi L (2021) "Analysis and characterization of dynamic recrystallization and grain structure evolution in friction stir welding of aluminum plates." *Acta Mater* 207. <https://doi.org/10.1016/j.actamat.2021.116692>

Novel Hybrid Bio Composites of PLA with Waste Bio Fillers



D. V. Lohar, A. M. Nikalje, and P. G. Damle

Abstract Additive manufacturing or 3D printing is nowadays a more popular method for manufacturing complex shaped components. Researcher's aim of developing eco-friendly composites materials leads to developing biocomposites made of PLA and blended with waste bio fillers to enhance properties required for commercial applications. This research is the effort to prepare three types of filaments of PLA with blending of powder of walnut shell, powder of waste eggshell, and waste powder of white marble. The specimens were 3D printed as ASTM standards and testing was carried out for density, hardness, tensile strength, and flexural strength. The hardness is higher in case of PLA and powder of white marble biocomposite. Powder of walnut shell in PLA matrix declines density from 1.24 g/cm^3 to 1.044 g/cm^3 and it was 1.1903 g/cm^3 for PLA + White marble powder. The maximum tensile strength of 43.22 MPa was observed in PLA and walnut shell powder composite. The addition of eggshell powder has increased flexural strength to the value of 93.88 MPa which was almost 15% more compared to PLA without filler.

Keywords Biocomposites · PLA · Bio fillers · 3D printing

1 Introduction

The recent trends in manufacturing of complex shaped components adopted additive manufacturing as a better method and it is suitable for metals and non-metals like polymers.

Polymers are considered as most suitable lightweight materials and many products were already used in automobile, pharmaceutical, food packaging and interior decoration of vehicles, and many more. The biggest limitation of polymers is the issue of their degradation and pollution at all levels throughout the world. The environmental

D. V. Lohar (✉) · P. G. Damle
SSBT's College of Engineering, Jalgaon, Maharashtra, India

A. M. Nikalje
Government College of Engineering, Aurangabad, Maharashtra, India

protection rules and regulations are stringent and promoted to develop eco-friendly biodegradable materials as a substitute to replace the conventional polymers.

The various nature-friendly scientist and researchers strived for development of biocomposite materials which were originated from natural resources. Babagowda, Kadadevara Math, Goutham, Srinivas Prasad [1]. This work is devoted to blending recycled PLA materials pallets mixed consistently with pure PLA pallets before being subjected to extrusion of filaments. Five types of PLA and recycled PLA mixed filaments were manufactured with the variation of recycled PLA material in the range of 10–50% in the step of 10% respectively using extrusion by single screw technique. Author also carried out DOE and ANOVA analysis for thickness of layer during printing and percentage of recycled material in new PLA filament to observe their effects on output parameters such as flexural strength, tensile strength. The results were shown that optimized process parameters for achieving larger tensile strength are 10% additives in PLA and 0.1 mm layer thickness and for highest flexural strength are 20% additives in PLA with 0.1 mm layer thickness.

Ashok et al. [2] concluded that the tensile strength of the composite films of PLA and eggshell was greater than pure PLA and better with 4 wt.% ESP and then declined.

Diana Gregor-Svetec, Urska Stankovic Elesini, Rasa Urbas, Mirjam Leskovšek and Urska Vrabec Brodnjak [3] The research was dedicated on the HDPE and PLA polymers strengthened with waste cardboard dust which is by product of paper mill having 50 wt.% volume in the new composites. It shows that newly manufactured filaments are mainly nonhomogeneous and porous when subjected to morphology tests. Observation of SEM image shows cardboard dust gives a distribution in a heterogeneous manner and the pores were observed in the polymer matrix. The mixing of cardboard dust with the PLA polymer matrix has no influence on bending and toughness and has also improved the compression strength of the 3D printable filament. SEM image analysis has shown a more porous structure for the PLA /cardboard dust bio composite 3D printable filament, in comparison with the pure PLA 3D printable filament, which is also confirmed with its lower density.

Laszlo Lendvai, Tej Singh, Gusztav Fekete, Amar Patnaik, Gabor Dogossy [4] The waste dust of marble (MD) was added PLA to form new composites. Melt bending process was used for Samples preparation and waste marble dust was added up to containing up to 20 wt%. The research was dedicated to analyzing mechanical characteristics, morphological, wear resistance, and thermal properties of new PLA and marble dust composites. The tensile strength and flexural modulus were improved significantly, but mild negative impact was witnessed in deformability and strength. Impact toughness was rise up to 10% of waste marble dust and decreases with further increase in amount of waste marble dust. Wear resistance was superior with higher content of marble dust.

Michele Cali, Giulia Pascoletti, Massimiliano Gaeta, Giovanni Milazzo and Rita Ambu [5] In this research five different bioplastic compounds filaments, obtained by varying the organic by products named weed.hemp, carob, tomato, and pruned. The results shown in this study were hemp bioplastic composite has highest roughness while other composites have a better surface finish. The melting point is highest

at 150° c for tomato bioplastic composite and flexural modulus is highest in hemp bioplastic composite whereas lowest in tomato bioplastic composite.

Mohammed Hosseini Fouladi et al. [6] This research aims to produce 3D printed filaments composed of Polylactic acid (PLA) reinforced with 5 wt%, 10 wt%, and 15wt% of coconut fiber (CF) and coconut shell powder (CSP). These fillers were alkaline and silane treated in order to enhance the thermal properties. These fillers were characterized by FTIR, SEM, and TGA analysis. The SEM images show that there are structural changes in the fillers after successive treatments. TGA results show enhancement of thermal stability for CF by 10 °C whereas decreased by 10 °C for CSP. These fillers are melting blended with PLA as a polymer matrix and extruded as filaments. The filament which is reinforced with CSP holds good for 3D printing whereas, the filaments reinforced with CF clog during the process of 3D printing due to the large diameter of the filaments.

Rajpurohit and Dave [7] in their experimental work, analyzed the effect of process parameters of 3 d printing process on tensile characteristics of PLA. The parameters selected for study were height of layer, raster width, and raster angle. The specimens were prepared with reference to Type I ASTM D638 standards. The result shows that a 0° raster angle gives maximum tensile strength. Layer height of lower value has positive impact on higher tensile strength due to bonding area being more among the layers. Tensile strength is enhanced at larger value of raster width within limits but after that void may be formed which has negative effect on tensile strength.

Sehijpal Singh Khangura, Jai Inder Preet Singh, Vikas Dhawan [8] The research was devoted to green biodegradable composites blended with fibers of jute as strengthening element and matrix as a polylactic acid using method of film stacking. The input parameter is a curing temperature which has variations like 160 °C with 10 °C added each time up to 190 °C and its effect studied for different mechanical properties. Impact strength was reduced with rising in temperature of curing. Whereas improvement in tensile and flexural strength up to 180 °C, thereafter reduction in the same was observed. This research achieved to find optimum temperature of curing for jute fibers and PLA composites.

Valentina Mazzanti, Lorenzo Malagutti, Francesco Mollica [9] This review paper discussed that the cost of filaments can be reduced by addition of bio fillers without affecting mechanical properties of composites. However, there is no change in biodegradability when fibers of natural type were added to the bio-based polymer matrix. Some problems were identified related to bio fillers which are mainly moisture content or hydrophilic nature which affects poor adhesion of matrix and fillers. It is also important to ensure the quality of the biocomposite filaments before it was used for printing. The filaments should be free from any defects like small voids, stable diameter, morphology, and homogenous structure. The printed filaments can be tested using SEM, chemical testing using solvents, etc. The composites after 3D printing can also be tested for morphology, mechanical and thermal properties using suitable testing devices.

The authors also concluded that geometrical features of fillers are also playing a vital role in the mechanical characteristics of biocomposites. The average shape, size

of the filler can find out by sieve method and the ratio of filler length and diameter is vital parameter in fabrication of biocomposites and it needs more specific study.

Vignesh Sekar, Mazin Zarrouq, Satish Narayana Namasivayam [10] The research was focused on matrix of Polylactic acid (PLA) blended with Fiber of Empty Fruit Bunch of an Oil Palm and analyzed physical, mechanical, and thermal properties. PLA with fibers of Empty Fruit Bunch of an Oil Palm with 10–40% addition in the step of 10% prepared by melt blending process and effectively extruded as thin wire filaments. New composites filaments have less density with rising in tensile modulus, superior ecological behavior, and thermal degradation in comparison to PLA without fillers. Tendency of water absorption is high with decrease in tensile strength than PLA without fillers. Lower content of filler helps for better extrusion of filaments. Thin Filaments with 10 wt.% fibers of Empty Fruit Bunch were uninterruptedly printed but wires with greater fiber content blocked the nozzle.

Waleed Ahmed et al. [11] as per review of 80 articles by the authors, it has been noticed that there is no improvement in mechanical properties when addition of natural fibers in ABS and PLA -based materials for 3D printing applications. The strength properties are reduced as filler content increases. The stiffness was remain unchanged with low filler contents, whereas stiffness decreased with an increase in the amount of filler. Authors also recommended giving more focus on using industrial waste in the development of bio-based polymers, to prepare ecofriendly composites.

Xiaohui Song, Wei He, Shoufeng Yang, Guoren Huang, and Tonghan Yang [12] research was devoted to preparing 3D filaments using combination of PLA and powder of walnut shell. The walnut shell powder was subjected to pretreatment in two stages with NaOH and then by silane. The FTIR analysis was carried out for untreated and treated WSP. The test analysis shows that mechanical and thermal properties could be enhanced by regulating the silane concentration. Results of testing witnessed that the surface intermolecular adhesion of PLA with WSP was radically enhanced through KH550 treatment. The crystalline was enhanced from 1.46 to 2.84%, thermal gravity was enhanced from 60.3 °C to 61.3 °C, and thermal degradation temperatures of biocomposite was enhanced from 239.87 °C to 276.37 °C with treated WSP. The biocomposite tensile strength was improved by 8.07%, flexural strength by 14.66%, and compressive strengths were improved by 23.32%. PLA with 10–15 wt.% treated with determined saline treatment has tensile strength enhanced to 56.2 MPa, close to the value of pure PLA.

In this research work, PLA is blended with biowaste in the form of fine powder and is not used for any productive work. The fillers selected are powder of waste walnut shell, powder of eggshell, and powder of white marble available easily at local sources. PLA matrix is reinforced with powder of walnut shell, powder of eggshell, and powder of white marble separately to prepare new three types of thin wire filaments for 3D printing. The composites were prepared by 3D printing and performance is compared by conducting various types of tests like density, hardness, tensile strength, and flexural strength.

Table 1 Characteristics of waste bio-fillers

Sr. no	Type of bio filler	Wall nutshell powder (WSP)	Eggshell powder (ESP)	White marble powder (WMP)
1	Particle Size	70–90 microns	70–90 microns	70–90 microns
2	Density	1.397 g/cc	1.450 g/cc	2.324 g/cc
3	Content of moisture	5.47%	0.98%	0.33%

2 Material and Methods

2.1 Materials

2.1.1 PLA

In this study PLA pellets manufactured by Luminy® Total corbion, Thailand is used as polymer matrix. As per datasheet, it has 1.2–1.3 g/cm³ density and melting point of 150–230 °C.

2.1.2 Bio Fillers

The waste walnut shells and eggshells are collected from local sources. The powder of white marble grinding waste is collected from nearby marble suppliers. Walnut shells, eggshells, and marble dust were cleaned and washed with water to remove any contaminants and subjected to sun drying for 24 h. Fine powders were prepared by grinding and all powders are sieved by a set of sieves to prepare fine powder. The particle size measured and is in the range of 70–90 microns for homogeneous blending with PLA matrix.

2.1.3 Characteristics of Bio Fillers

See Table 1.

2.2 Manufacturing of PLA Filaments with Blending of Bio Fillers

The filaments were factory-made at Solidspace technology LLP located in Nashik, Maharashtra (India). An extruder of single screw type was used to extrude the new biocomposite filaments suitable for 3D printing. The diameter of screw of the extruder was 45 mm and the ratio of length to diameter was 30. The filaments are prepared

Table 2 Composition of PLA with bio fillers for hybrid PLA filaments

Sr. No	Filament type	PLA (No filler)	PLA + WSP	PLA + ESP	PLA + WMP
1	% weight of PLA Matrix	100	97	97	97
2	% weight Bio filler	0	3	3	3

to a commonly suitable specific diameter of 1.75 mm. New three types of filaments were prepared for biocomposites (Table 2 and Fig. 1).

Specifications of Extruder are

- a. Motor power: 6 Kw/8HP.
- b. Motor RPM: 1440.
- c. Maximum Screw Speed: 90 RPM.
- d. Extruder Die Diameter: 4 mm (Table 3 and Fig. 2).

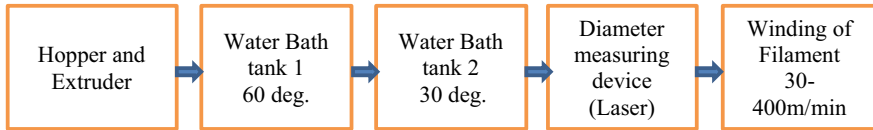


Fig. 1 Block diagram of Extruder set up for Bio composite filament extrusion

Table 3 Parameters for 3D printing filament extruder

Type of extruder	Single Screw, Screw diameter = 45 mm, L/D = 30:1
Barrel temperature	Input Feed zone: 195°C, Compression zone: 200° C, Mixing zone: 210° C
Die temperature (Extrusion)	210° C
Filament diameter	1.72 to 1.78 mm
Screw rotating Speed	45 RPM
Filament processing stages	1. Extrusion at 210°C 2. Hot water tank 60 °C 3. water tank 30 °C
Filament winding speed	30–400 m/min

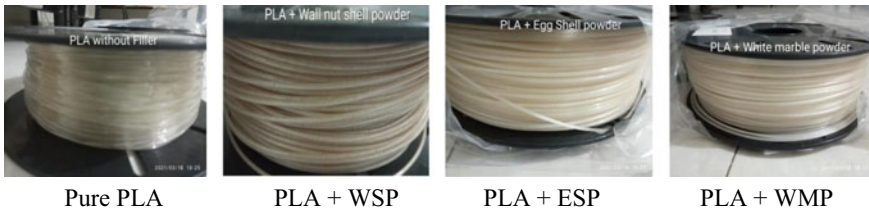


Fig. 2 Types of 3D Biocomposite filaments

2.3 Preparation of Specimens Using 3D Printing

The specimens were printed for tensile testing as per ASTM D-638 and flexural test as per ASTM–D790 on commercial 3D printer which available at Solidspace technology, Nashik and parameters during printing was nozzle temperature is 215° C, layer thickness 0.25 mm, Nozzle diameter is 0.6 mm, bed temperature is 60 °C, printing speed is 100 mm/sec with fan speed of 255 RPM, raster angle of orientation is 45 ° (Figs. 3 and 4).

Specifications of 3D Printer Used for Printing:

- Build volume: 220 × 220 × 300 mm.
- Min. Layer Height: 0.05 mm.
- Make: Creality.
- Nozzle Quantity: One.
- Nozzle diameter: 0.4 mm.
- Max. Print temperature: 260°C

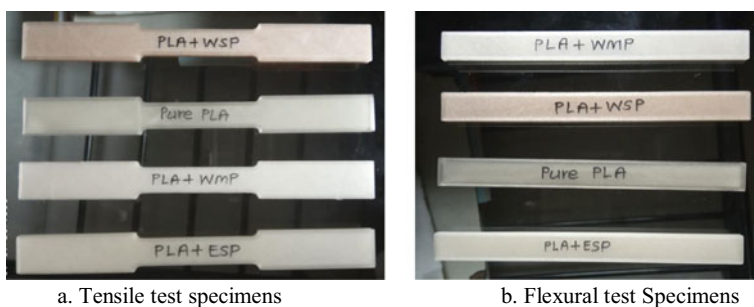


Fig. 3 Specimens for Tensile and Flexural test

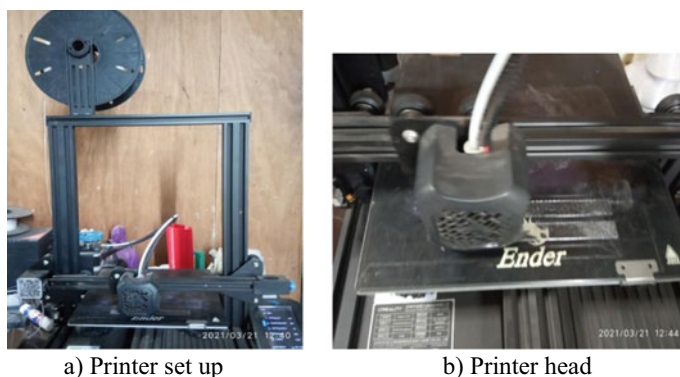


Fig. 4 3D printer used for specimens printing

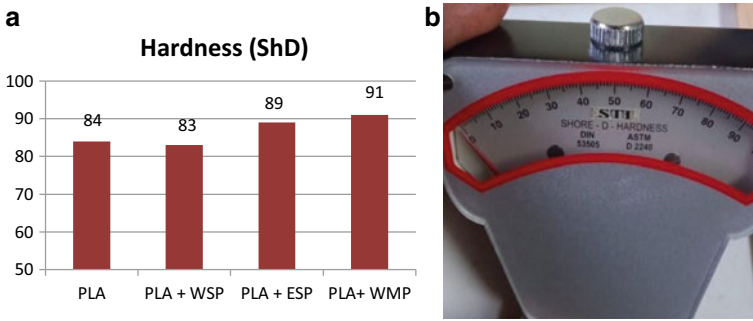


Fig. 5 a Comparison of hardness of biocomposites b. Shore D hardness tester

- g. Filament diameter: 1.75 mm (PLA/ABS/Wood/Flexible).
- h. Layer thickness: 0.1 to 0.4 mm.
- i. Precision: ± 0.1 mm.
- j. Max. Travelling speed: 180 mm/sec.
- k. File format: STL,OBJ,G-Code.

3 Testing of Biocomposites Specimens

3.1 Hardness

The biocomposites are tested for hardness as per ASTM D2240 using shore D scale. The hardness of PLA without any bio—filler is 83–85 ShD. The blending of 3% of wall nutshell powder has no substantial effect on hardness of new biocomposite. As powder of wall nutshell has low density and it is matching to wood powder. Even though the walnut shell is hard but after making powder, the particles will lose its hardness and it has identical characteristics of wooden powder. The hardness is maximum in PLA and powder of white marble biocomposite as marble particles are heavy with high density and contain calcium carbonate (CaCO_3) (Fig. 5).

3.2 Density

The waste bio fillers are not of same density and it has effect on density of PLA bio filler composites. The blending of powder of walnut shell in PLA matrix declines density from 1.24 g/cm^3 to 1.044 g/cm^3 . Walnut Shell powder is having less density compared to eggshell powder and white marble powder. Therefore PLA + eggshell powder has density of 1.073 g/cm^3 while it is 1.1903 g/cm^3 for PLA + White marble powder. The white marble powder has maximum density in bio filler blended PLA biocomposites (Fig. 6).

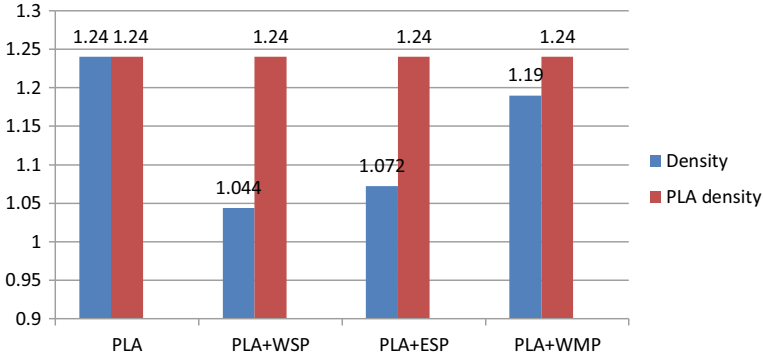


Fig. 6 Comparison of Density of Biocomposites with PLA

3.3 Tensile Strength

Tensile strength was tested on Universal testing machine TTM-01 available at material testing laboratory located at Nasik. It has maximum load capacity of 20KN. The tensile test is conducted as per ASTM D638 standard. The PLA + WSP has highest tensile strength of 43.22 MPa as the density of walnut shell is less and hardness of this biocomposite was also comparatively less. The lowest tensile strength among three bio filler added composites is observed in PLA + WMP which are nearer to the PLA Composite without filler. The eggshell powder filled PLA Composite has tensile strength of 42.17 Mpa which is more as compared to PLA Composite without filler. The eggshell particles are having density more than powder of wall nutshell. According to [12] The tensile strength of the composite films of PLA and eggshell was greater than pure PLA and better with 4 wt.% ESP and then declined. In present

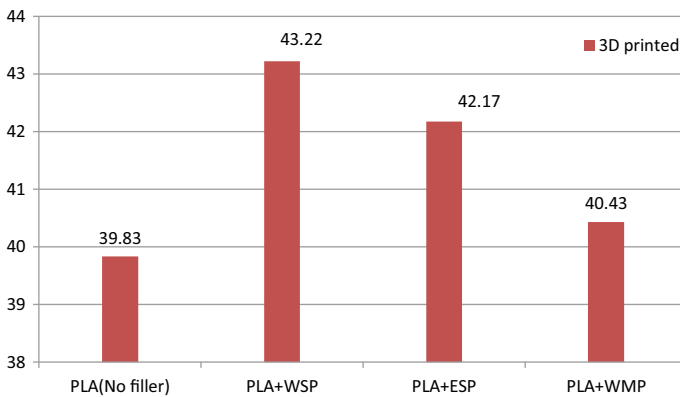


Fig. 7 Comparison of tensile strength of 3 D printed specimens

work, the ESP is 3% hence improvement in tensile strength was observed (Figs. 7, 8 and 9 and Table 4).

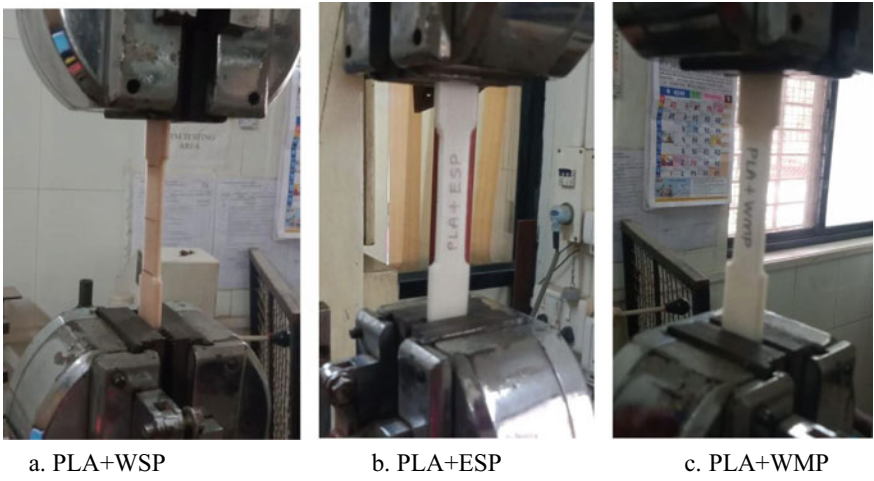


Fig. 8 Tensile testing of 3 D printed composites

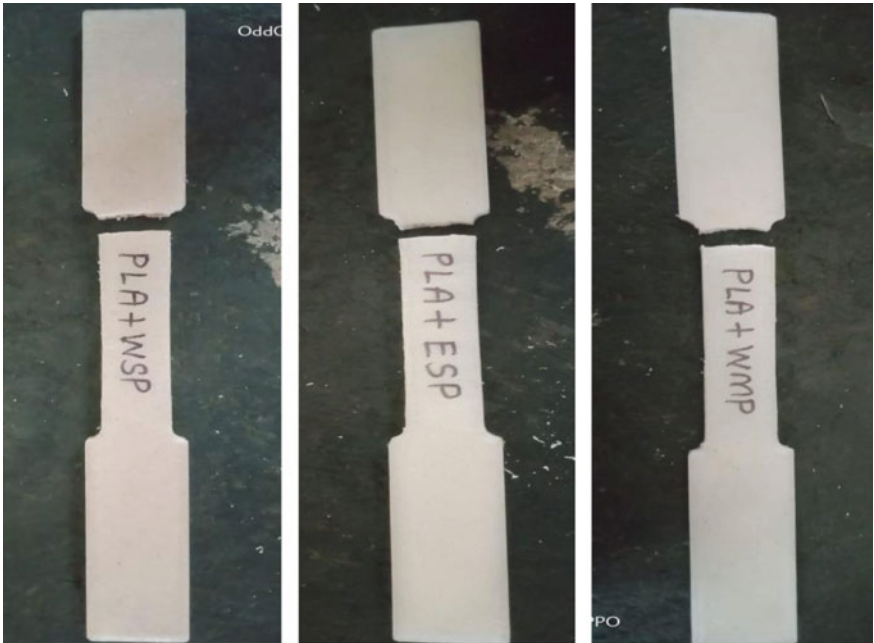


Fig. 9 Specimens after tensile testing

Table 4 Testing Results of Biocomposites specimens

Type of Test	PLA (No filler)	PLA + WSP	PLA + ESP	PLA + WMP
Tensile Strength (MPa)	39.83	43.22	42.17	40.43
Flexural Strength (MPa)	81.18	90.43	93.88	82.76

3.4 Flexural Strength

Flexural test was conducted for specimens prepared as per ASTM–D790 and the results of testing show that it was highest for PLA and eggshell power composite and lowest for composite having bio filler of waste white marble dust. The flexural strength of this composite is slightly higher compared to PLA without filler. The 3% powder of walnut shell when added to PLA it has improved flexural strength by 10% approximately. The addition of eggshell powder was increased flexural strength to the value of 93.88 MPa which was almost 15% improvement compared to PLA without filler (Figs. 10, 11 and 12).

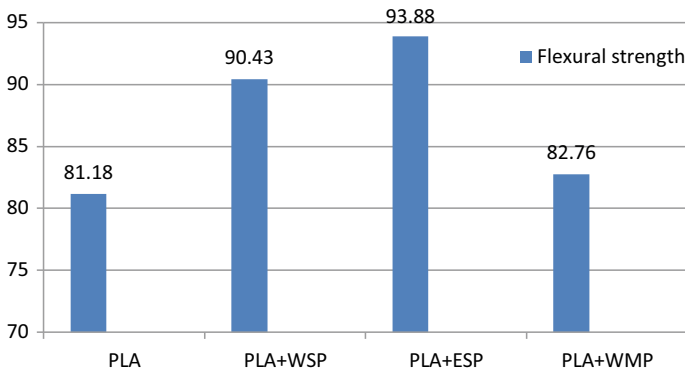


Fig. 10 Comparison of Flexural strength of 3D printed specimens



Fig. 11 Flexural testing of 3D printed composites

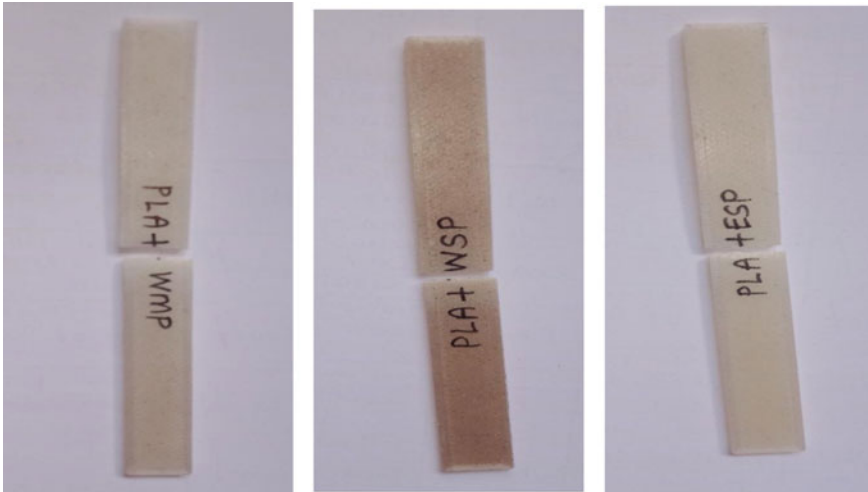


Fig. 12 Specimens after Flexural testing

4 Conclusion

The effects of biowaste fillers (3%), when blended with PLA matrix, are discussed in the following points.

1. The blending of 3% of wall nutshell powder has no substantial effect on hardness of new biocomposite. The hardness is higher in case of PLA and powder of white marble biocomposite as marble particles are heavy with high density. The addition of eggshell powder has also positive impact on hardness of PLA biocomposite.
2. The blending of bio fillers has negative impact on density of biocomposite. Powder of walnut shell in PLA matrix declines density from 1.24 g/cm^3 to 1.044 g/cm^3 , PLA + eggshell powder has density of 1.073 g/cm^3 and it was 1.1903 g/cm^3 for PLA + White marble powder. The white marble powder has maximum density in bio filler blended PLA biocomposites.
3. The lowest tensile strength of 40.43 MPa is observed in PLA + WMP composite among three bio filler added composites and it is nearer to the PLA Composite without filler. The maximum tensile strength of 43.22 MPa was observed in PLA and walnut shell powder composite.
4. The addition of eggshell powder has increased flexural strength to the value of 93.88 MPa which was almost 15% more compared to PLA without filler, while powder of walnut shell when added to PLA, it has improved flexural strength by 10% approximately.

Funding This research did not receive any specific grant from funding agencies in the public, commercial, or not-for-profit sectors.

References

1. Babagowda R, Kadadevara Math S, Goutham R, Srinivas Prasad KR (2018) Study of effects on mechanical properties of PLA filament which is blended with recycled PLA materials. International conference on advances in materials and manufacturing applications (IConAMMA-2017) 17–19 August 2017, Bengaluru, India, IOP Conf. Series: Materials Science and Engineering: Volume 310/1/012103
2. Ashok B, Naresh S, Obi Reddy K, Madhukar K, Cai J, Zhang L, Varada Rajulu A (2014) Tensile and thermal properties of poly (lactic acid) eggshell powder composite films. *Int J Polym Anal Charact* 19:245–255
3. Gregor-Sveteč D, Elesini US, Urbas R, Leskovšek M, Brodnjak UV (2019) The influence of cardboard dust on structural, morphological and mechanical properties of biocomposite PLA and HDPE filaments for 3D printing. *Acta Chim Slov* 66:614–621. <https://doi.org/10.17344/acsi.2019.5025>
4. Lendvai L, Singh T, Fekete G, Patnaik A, Dogossy G (2021) Utilization of waste marble dust in poly(lactic acid)-based biocomposites: mechanical, thermal and wear properties. *J Polym Environ*. <https://doi.org/10.1007/s10924-021-02091-9>
5. Fouladi MH, Namasivayam SN, Sekar V, Marappan P, Choo HL, Ong TK, Walvekar R, Baniotopoulos C (2020) Pretreatment studies and characterization of bio-degradable and 3d printable filaments from coconut waste. *Int J Nanoelectron Mater* 13(Special Issue):137–148
6. Cali M, Pascoletti G, Gaeta M, Milazzo G, Ambu R (2020) A new generation of bio-composite thermoplastic filaments for a more sustainable design of parts manufactured by FDM. *Appl Sci* 10:5852
7. Rajpurohit SR, Dave HK (2018) Effect of process parameters on tensile strength of FDM printed PLA part. *Rapid Prototyping J*. <https://doi.org/10.1108/RPJ-06-2017-0134>
8. Khangura SS, Singh JIP, Dhawan V (2018) Effect of curing temperature on mechanical properties of jute fiber reinforced polylactic acid based green composite. *Int J Indus Manuf Eng* 12(9):852–857
9. Mazzanti V, Malagutti L, Mollica F (2019) FDM 3D printing of polymers containing natural fillers: a review of their mechanical properties. *Polymers* 11:1094. <https://doi.org/10.3390/polym11071094>
10. Sekar V, Zarrouq M, Namasivayam SN (2021) Development and characterization of oil palm empty fruit bunch fibre reinforced polylactic acid filaments for fused deposition modeling. *J Mech Eng* 18(1):89–107
11. Ahmed W, Alnajjar F, Zaneldin E, Al-Marzouqi AH, Gochoo M, Khalid S (2020) Implementing FDM 3D printing strategies using natural fibers to produce biomass composite materials 13:4065. <https://doi.org/10.3390/ma13184065>
12. Song X, He W, Yang S, Huang G, Yang T (2019) Fused deposition modeling of poly (lactic acid)/walnut shell biocomposite filaments—surface treatment and properties. *Appl Sci* 9:4892. <https://doi.org/10.3390/app9224892>

Investigation on Formability of Tailor Welded Blanks (TWBs) During Single Point Incremental Forming (SPIF) Process



Gireesh Sripathireddy, Shalin Marathe, and Harit Raval

Abstract Tailor Welded Blanks is defined as two or more separate pieces of flat material, dissimilar thickness, and/or mechanical properties joined together before forming. TWBs are associated with limitations of weld line shift and reduced formability. To improve the formability of homogenous blanks, Single Point Incremental Forming (SPIF) has given good results. The present work aims to investigate the effect of SPIF process parameters on forming behaviour of TWBs using a simulation method. ABAQUS/Explicit is used as a simulation tool and SPIF process parameters like feed, spindle rotational speed and coefficient of friction are selected for investigation. The responses like thinning and weld line shift are studied for different conditions of SPIF process. It has been found that feed is the most significant parameter affecting the weld line shift, plastic equivalent strain and thinning of the TWBs. The significance of coefficient of friction and spindle speed is found negligible. During SPIF process, nature of weld line shift is sinusoidal and the shift of weld line is on both sides of the weld region. For weld line shift, tool dragging and deformation of weak material play important roles.

Keywords Tailor welded blanks · Single point incremental forming · ABAQUS/Explicit · Thinning · Weld line shift

1 Introduction

The Tailor Welded Blanks (TWB) is fabricated by joining two or more two materials that have different material properties or thicknesses. These welded blanks are then subjected to forming processes to form the desired shape using any forming process. The meaning of word “Tailor” indicates control on the location of the weld

G. Sripathireddy (✉) · S. Marathe · H. Raval
Department of Mechanical Engineering, S. V. National Institute of Technology, Surat, Gujarat
395007, India

H. Raval
e-mail: hkr@med.svnit.ac.in

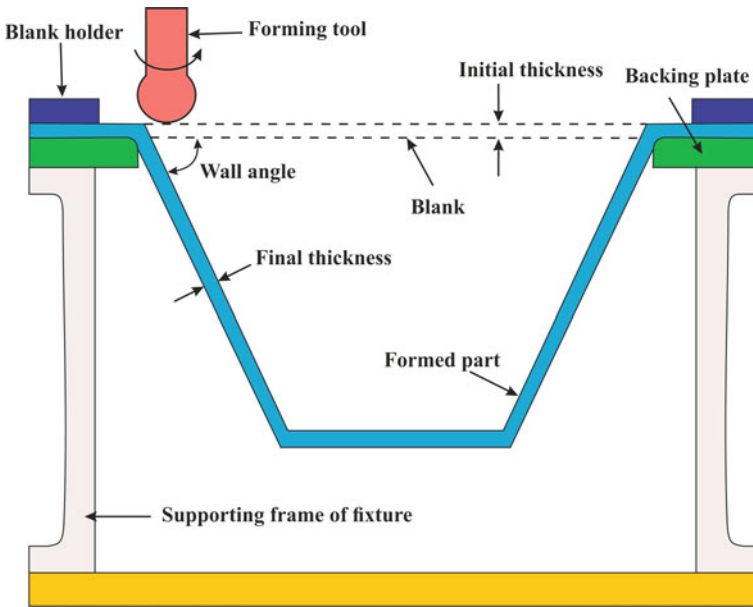


Fig. 1 Schematic representation of SPIF process

line and control on the properties of the weld material produced while fabrication of TWBs. Since TWB contains two materials having different properties and thicknesses, the deformation behaviour of both the parent materials will be different during the forming process. The strong/thick material will deform less in comparison to the weak/thin material resulting in the shift of weld line towards the strong material [1]. Because of this reason, the weak/thin material will experience excessive thinning leading to premature failure of the TWBs during forming. This reduces the formability of TWBs in comparison to the formability of the parent materials participating in it [1].

It has been stated that the formability and weld line shift of the TWBs depends upon the parameters like thickness ratio of the parent blanks [2]. To control the weld line shift, the deformation of strong/thick material should be increased. Such an attempt was made [3] wherein the split punch technology with heating source was used to heat the strong/thick material. Heating will reduce the flow stress of the strong/thick material and more deformation is experienced by strong/thick material resulting in less weld line shift during forming process.

Many efforts have been made by researchers to improve the formability of the process and as a result of that advanced forming process like Single Point Incremental Forming (SPIF) has come into existence. It has been found that SPIF process results in the improved formability of the homogeneous blanks in comparison to the conventional forming processes [4, 5].

Figure 1 represents the schematic of SPIF process. In SPIF process, localized and incremental deformations are provided on the blank with the help of a spherical or hemispherical tool. Due to the incremental and localized deformation, simultaneous stretching and bending take place during the SPIF process resulting in the improved formability of the homogeneous blanks [4, 5]. It has been also stated that the rate of growth of hydrostatic stress, responsible for failure of sheet material, is slow in SPIF process which also enhances the formability of this process for homogeneous blanks [6]. TWBs has the limitation of reduced formability while SPIF has the advantage of improved formability for the homogeneous blanks. So, the combination of TWBs and SPIF processes can be explored to study the forming behaviour of TWBs during the SPIF process.

Such combination was attempted [7] wherein the use of dummy sheet was done to protect the forming tool from the weld seam and it was reported that use of dummy sheet has no effect on the formability of the blank being formed. Similar effort was made [8] to study the formability of CO₂ laser welded blanks. Formability of TWBs made using FSW was investigated during SPIF process [9]. In this investigation, effect of FSW process parameters on formability of TWBs was investigated. Marathe and Raval, (2019) [10] performed a similar investigation and explored the effect of tool initial position on formability of TWBs during the SPIF process.

In earlier attempts to investigate the combination of SPIF and TWBs, the major focus was to study the effect of welding parameters and dummy sheets on the formability of the TWBs. So, in this work, a combination of SPIF and FSTWBs is investigated and emphasis is given to studying the effect of SPIF process parameters on formability behaviour of TWBs. The responses like weld line shift, thickness distribution and PEEQ are investigated. Full factorial design of Design of Experiment (DOE) and Analysis of Variance (ANOVA) are used to understand the significance of SPIF process parameters.

2 Methodology

2.1 Process Parameters and Target Geometry

In the present simulation study, three parameters are selected for investigation viz. tool feed (mm/min), spindle speed (RPM) and coefficient of friction between forming tool and blank being formed. For each parameter, three levels are chosen as tabulated in Table 1.

During forming of TWBs, an incremental depth of 0.5 mm [10] and a hemispherical forming tool [10] of 5 mm radius was used. Using the process parameters mentioned in Table 1, TWBs were converted into truncated square pyramids during SPIF process. The blank dimensions were 98 mm × 98 mm, the wall angle was 45° and the total forming height of the geometry was 20 mm. The target geometry is shown in Fig. 2.

Table 1 SPIF Process parameters

Level	Feed (mm/min)	Spindle speed (RPM)	Coefficient of friction
1	200	0	0.1
2	400	400	0.25
3	600	800	0.5

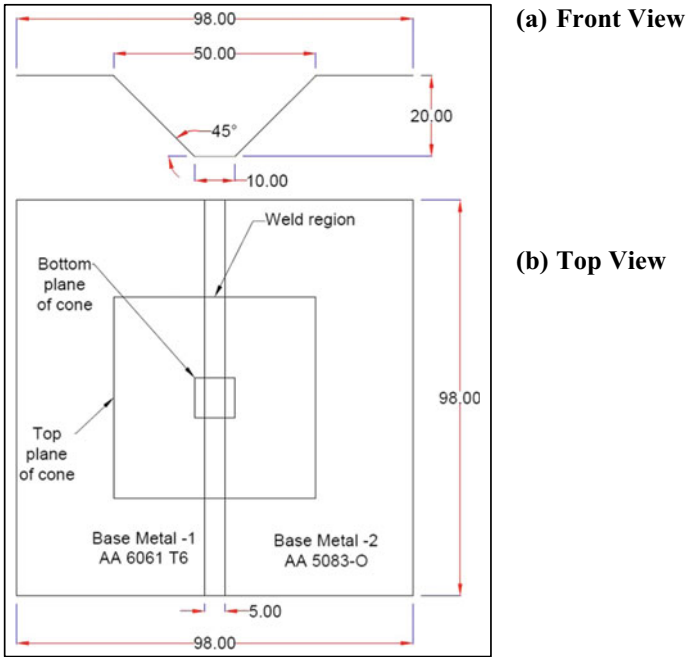


Fig. 2 Target geometry (All the dimensions are in mm)

2.2 Material Properties, Modelling of Parts and Boundary Conditions

The present investigation considers AA 6061 T6 and AA 5083-O as parent materials and the properties of these materials considered for simulations are reported in Table 2. ABAQUS/Explicit is used to perform the simulation of SPIF process for TWBs. The yield strength is experimentally derived for both materials. The strength coefficient and strain hardening index are derived from the true stress–strain curve of both the parent materials. The property of the weld material is considered an average of the properties of both the parent materials. To define the weld properties, weld zone approach is used in the present investigation. In weld zone approach, separate section is modelled for weld zone and separate individual properties are assigned to it [11]. The yield strength of AA 6061 T6 is more in comparison to yield strength

Table 2 Material Properties used during the simulation

Material	Thickness (mm)	Yield strength (MPa)	Strength coefficient (MPa)	Strain hardening index
AA 6061 T6	1	280	568.3	0.2071
AA 5083-O	1	150	623.82	0.3727
Weld material	1	215	596.06	0.2899

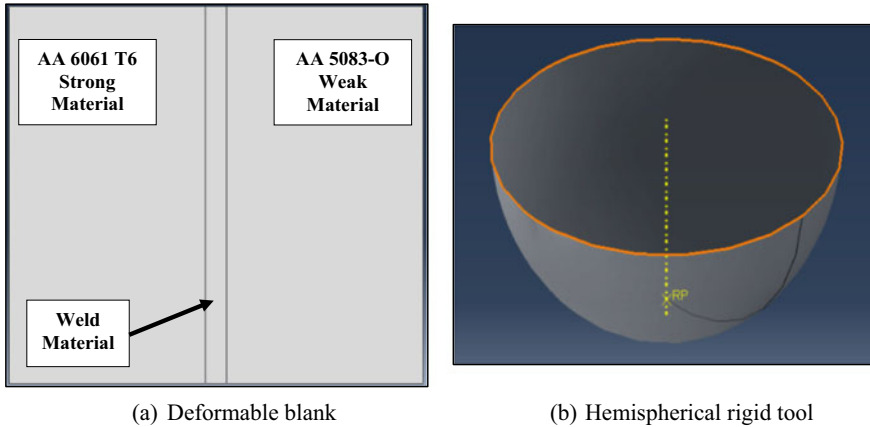
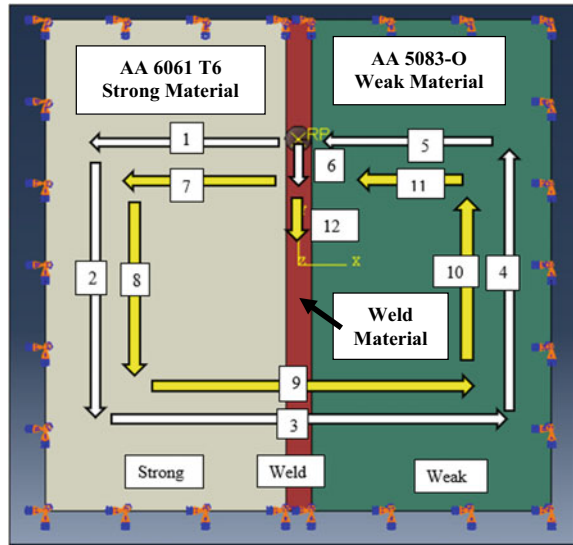


Fig. 3 Modelling of parts

of AA5083-O material and hence AA 6061 T6 and AA5083-O materials will be considered as strong and weak materials respectively.

During simulation, a deformable blank was modelled with three different sections to define parent materials and weld material as shown in Fig. 3a. A rigid hemispherical tool was also modelled as shown in Fig. 3b. Figure 4 shows the tool path used during the simulation study. The initial position of tool is on weld material and from that, it moves towards strong material. The weld material will be deformed after strong material and at the end of the cycle, weak material is deformed. After reaching the starting position, the incremental depth of tool will deform the sheet material. This cycle continues till the desired geometry is formed. This position of forming tool can be termed as Weld-To-Strong (WTS) condition of forming tool [10]. It has been already reported that WTS condition of forming tool results in the minimum weld line shift and minimum %thinning, WTS condition is adopted in the present investigation.

Fig. 4 Encastre boundary condition to the edges of the blank and direction of tool movement



2.3 Design of Experiments (DOE)

In the present investigation, full factorial DOE is adopted and for three levels of three parameters total of 27 simulations are performed as tabulated in Table 3. The formability of the TWBs has been investigated by studying the responses like Equivalent Plastic strain, %thinning and weld line shift. For all the responses, minimum the better characteristic is adopted and Analysis of Variance (ANOVA) is performed.

3 Results and Discussions

3.1 Formed Geometry

The TWBs were converted into truncated pyramids using the SPIF process and the formed geometry is shown in Fig. 5. In the present investigation, TWBs are considered to be made of AA 6061 T6 and AA 5083-O material which is strong and weak material respectively because the yield strength of the AA 6061 T6 is higher than the yield strength of AA 5083-O material. During Forming the weak AA 5083-O material will deform more in comparison to the strong AA 6061 T6 material. This pushes the weld line towards strong AA 6061 T6 material. For all the simulation runs, the weld line shift is measured and further analyzed.

The weld line shift is affected by the tool dragging effect and deformation of weak material as presented in Fig. 6. In the present investigation, WTS condition of tool is considered in which the repetitive deformations are provided on the weld material.

Table 3 Full factorial design matrix

Simulation no	Feed (mm/min)	Spindle speed (rpm)	Coefficient of friction
1	200	0	0.1
2	200	0	0.25
3	200	0	0.5
4	200	400	0.1
5	200	400	0.25
6	200	400	0.5
7	200	800	0.1
8	200	800	0.25
9	200	800	0.5
10	400	0	0.1
11	400	0	0.25
12	400	0	0.5
13	400	400	0.1
14	400	400	0.25
15	400	400	0.5
16	400	800	0.1
17	400	800	0.25
18	400	800	0.5
19	600	0	0.1
20	600	0	0.25
21	600	0	0.5
22	600	400	0.1
23	600	400	0.25
24	600	400	0.5
25	600	800	0.1
26	600	800	0.25
27	600	800	0.5

The deformation of weak material is more in comparison to the strong material and this deformation of weak material is always towards the strong material (see Fig. 6). In addition to this, due to the friction between forming tool and blank being formed, there is effect of tool dragging wherein the tool tries to drag the material in its direction of motion (see Fig. 6). Due to the combined effect of tool dragging and deformation of weak material, the nature of weld line shift for SPIF of TWBs is sinusoidal in nature and on both sides of the weld material which is unlike conventional forming processes. The detailed investigation on weld line shift is reported in the next section.

Fig. 5 Formed geometry after the forming process

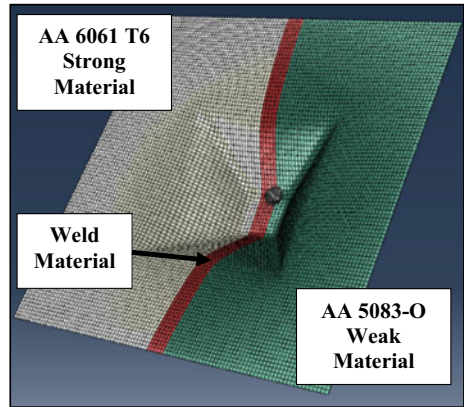
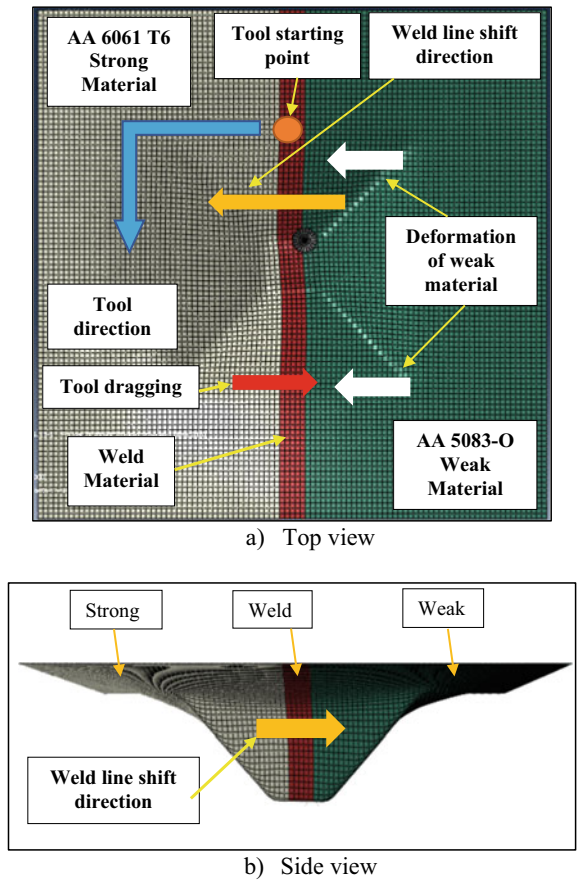


Fig. 6 Weld line shift in the formed cup



3.2 Effect of Process Parameters on Weld Line Shift

The weld line shift for different feed rates of tool is indicated in Fig. 7. As reported earlier, the nature of the weld line shift is sinusoidal which is due to the combined effect of tool dragging and deformation of weak material. If the deformation of weak material is not opposed by the tool dragging then it results in the maximum weld line shift as represented in Fig. 7. As the tool feed increases from 200 mm/min to 600 mm/min, the deformation of weak material will increase because for instance, 200 mm/min feed of tool will have more contact area in comparison to the 600 mm/min feed which results into the more deformation of weak material.

In section A, there is no tool dragging effect on the weld line because tool does not cross the weld line. In section A, maximum weld line shift is observed for 200 mm/min of tool feed because it results in more deformation of weak material. In section B, there will be tool dragging from strong material to weak material during forming. But the tool dragging will be opposed by the deformation of weak material leading to less weld line shift in comparison to section A. The resistance offered by the deformation of weak material will be maximum for tool feed of 200 mm/min because for 200 mm/min deformation of weak material is more. Hence, for 200 mm/min tool feed, the weld line shift is low in section B and it is towards strong material. For 600 mm/min of tool feed, the deformation of weak material will be less resulting in less resistance of deformation of weak material to tool dragging. This will lead to

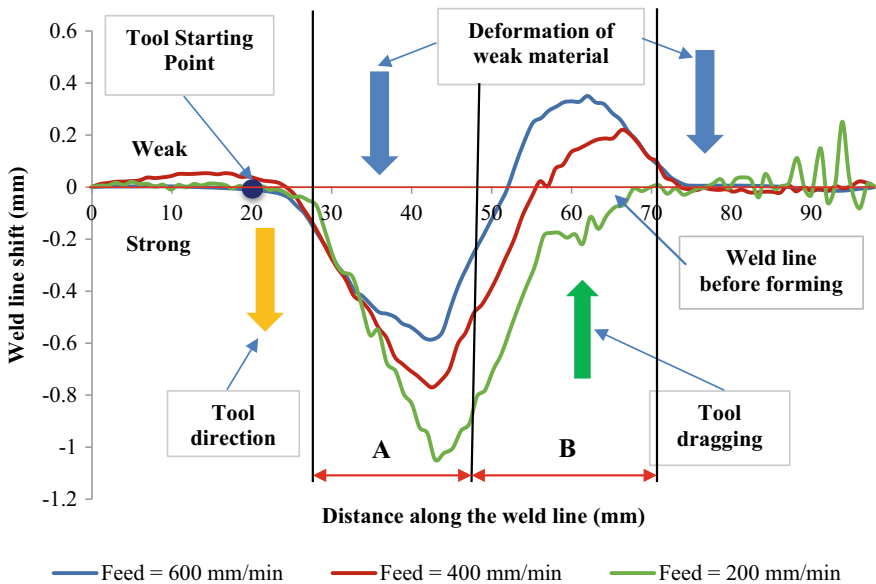


Fig. 7 Effect of feed rate (mm/min) on weld line shift (Spindle speed = 0 rpm, Coefficient of friction = 0.1)

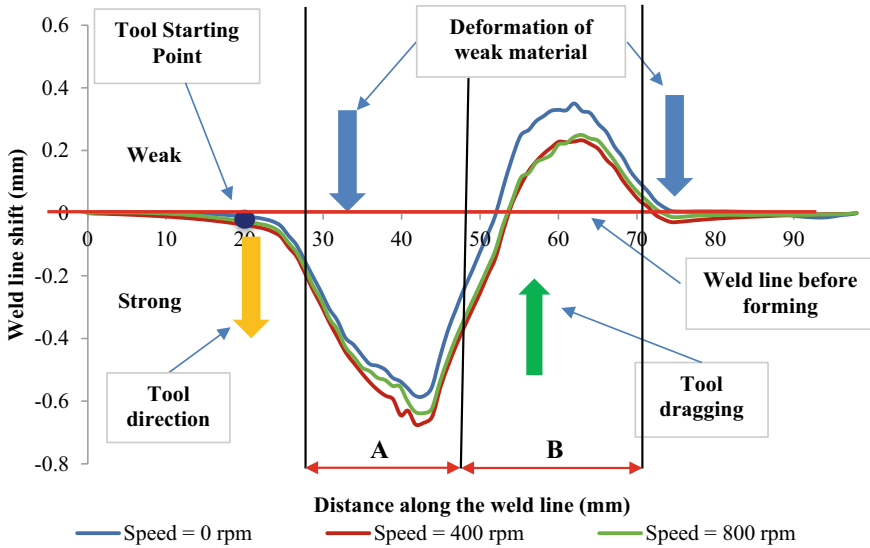


Fig. 8 Effect of spindle speed (RPM) on weld line shift (Feed = 600 mm/min, Coefficient of friction = 0.1)

maximum weld line shift for 600 mm/min of tool feed in section B and it is towards weak material.

Figure 8 depicts the effect of spindle speed on weld line shift for constant feed and coefficient of friction. Due to the friction between the forming tool and the blank being formed, localized heat is generated during the forming process. For 0 RPM of spindle speed, the generation of heat will be less in comparison to the 400 RPM and 800 RPM of spindle speed because the tool rotation will increase the generation of heat during forming. This additional heat generation will result in more deformation of weak material for 400 RPM and 800 RPM of spindle speed in comparison to the 0 RPM of spindle speed. Hence, in section A, the weld line shift for 0 RPM of tool is minimum. The weld line shift for 400 RPM and 800 RPM of spindle speed is not having much difference. The reason behind such result is that as the tool rotation increases from 400 to 800 RPM, the friction condition changes from sticking to sliding condition and that may not affect the heat generation. Therefore, for 400 RPM and 800 RPM of spindle speed, the shift in weld line is insignificant in both sections A and B. In section B, for 0 RPM of spindle speed, the weld line shift is maximum because the deformation of weak material will be less due to less heat generation. Less deformation of weak material will offer less resistance to the tool dragging resulting in the maximum weld line shift in section B for 0 RPM of spindle speed.

The results of weld line shift for different coefficients of friction are shown in Fig. 9. It indicates that the coefficient of friction has significant effect on the weld line shift. As the coefficient of friction increases, the friction between forming tool

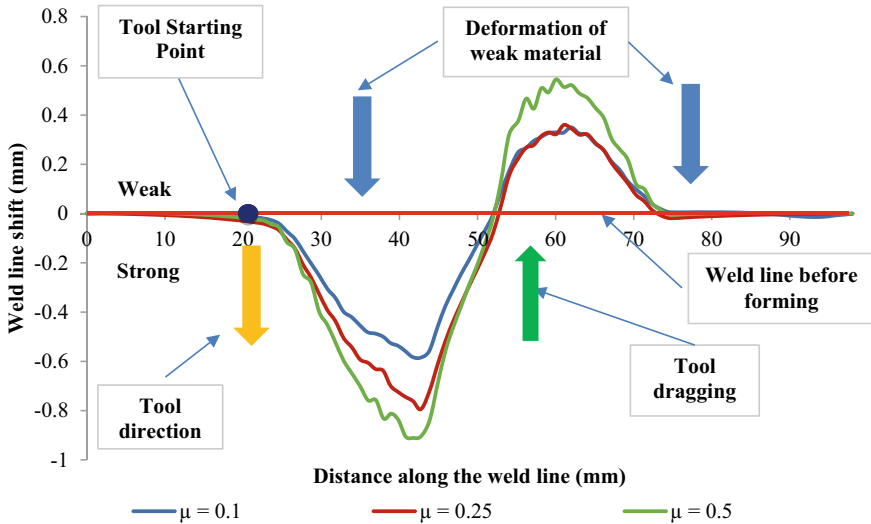


Fig. 9 Effect of coefficient of friction on weld line shift values (Feed = 600 mm/min, Spindle speed = 0 RPM)

and the blank being formed increases which increase the tool dragging effect during the forming process. Hence, the weld line shift will be more due to the increased tool dragging effect. Therefore, for high value of coefficient of friction, more weld line shift is observed.

The ANOVA was also performed for the response weld line shift and minimum the better characteristics was adopted for it. Table 4 represents the ANOVA table for the weld line shift. It can be stated that tool feed is the most significant parameter that affects the weld line shift in comparison to the spindle speed and coefficient of friction. As discussed earlier, the change in the feed of the forming tool has an effect on the deformation of weak material which indirectly affects the shift of weld line.

Table 4 ANOVA for weld line shift

Factor	Degree of freedom	Sum of squares	Mean square	F-Value	P-Value	%P
Feed	2	0.70787	0.353936	23.43	0.000	66.47
Spindle speed	2	0.05286	0.026430	1.75	0.199	4.96
Coefficient of friction	2	0.00195	0.000976	0.06	0.938	0.18
Error	20	0.30215	0.015108			28.39
Total	26	1.06484				100

3.3 Analysis of Plastic Equivalent Strain (PEEQ)

The PEEQ in the formed components represents the plastic strain in the material. The high value of PEEQ represents that the material has yielded and permanent deformation is achieved in the material. Figure 10 represents the PEEQ in the formed TWB.

It can be observed that the material at corner of the formed TWB is showing maximum PEEQ. The wall section is also showing the high value of PEEQ indicating that it has yielded during the forming process. The wall section of the formed component is subjected to simultaneous stretching and bending during forming operation resulting in more PEEQ in it. At the corner, the tool changes the direction of motion during forming, which may increase the effect of stress concentration leading to high value of PEEQ in the corner. From Fig. 10, it can be also observed that AA 5083-O material resulted in more PEEQ in comparison to the AA 6061 T6 because the yield strength of the AA 5083-O material is less in comparison to the AA 6061 T6 material. In addition to this, high value of PEEQ is also found near the boundary of weld and parent metal. At this boundary, there is a change in the properties which leads to the effect of stress concentration and hence, more PEEQ is observed at the boundary between parent and weld material. The maximum value of PEEQ for all the simulations was determined and ANOVA is performed as represented in Table 5.

The ANOVA for PEEQ showed that the feed is the most significant factor affecting the PEEQ, similar to the weld line shift. The significance of spindle speed and coefficient of friction was found negligible for the response PEEQ. As reported earlier, as the feed decreases, the deformation of material increases. More deformation of

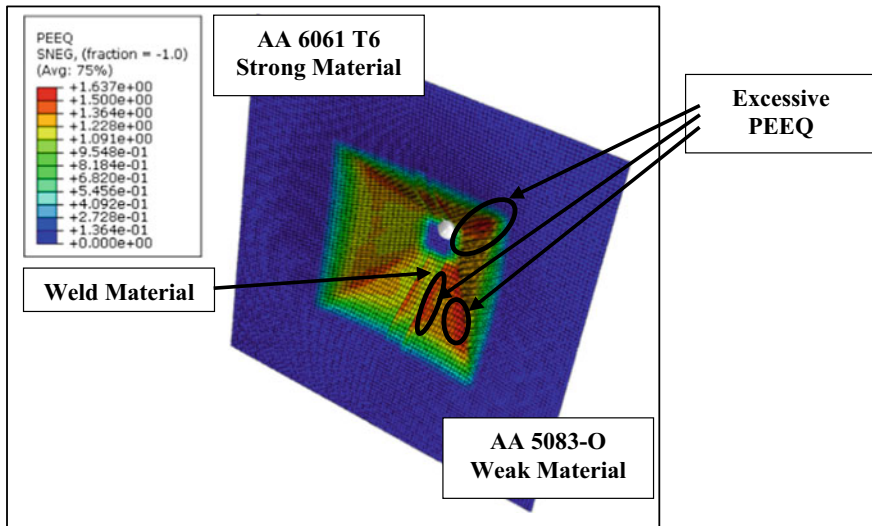


Fig. 10 PEEQ in the formed TWB

Table 5 ANOVA for PEEQ

Factor	Degree of freedom	Sum of squares	Mean square	F-Value	P-Value	%P
Feed	2	1823.99	911.99	25.64	0.00	70.66
Spindle speed	2	36.72	18.36	0.52	0.60	1.42
Coefficient of friction	2	9.14	4.56	0.13	0.88	0.35
Error	20	711.31	35.56			27.57
Total	26	2581.16				100

material leads to yielding of sheet material and ultimately that will result in more PEEQ in the material. Hence, the feed has maximum effect on the PEEQ in the formed TWBs. For the change in spindle speed and coefficient of friction, there is an insignificant change in the deformation of sheet material and because the significance of spindle speed and coefficient of friction is less.

3.4 Analysis of Thinning

SPIF process involves simultaneous stretching and bending operation and because of that, the material is subjected to thinning. During SPIF process, material in wall and corner is subjected to more thinning and because of that at these portions, less thickness is observed after completion of forming (see Fig. 11). Since the yield strength of AA 5083-O material is less, it experiences more thinning in comparison

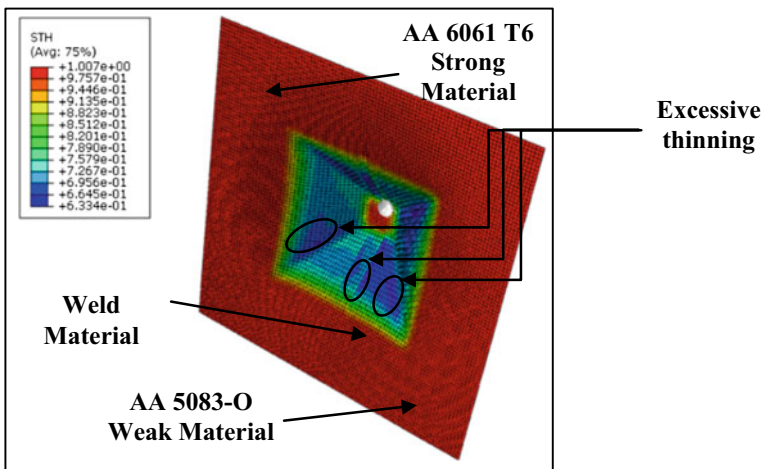


Fig. 11 Distribution of thickness in the formed TWB

to the AA 6061 T6 strong material. There is a sudden change of properties at the boundary between parent and weld material which leads to stress concentration effect resulting in more thinning at the boundary between parent and weld material. For %thinning of blanks, ANOVA was performed and reported in Table 6. Similar to the weld line shift and PEEQ, for %thinning of blanks, tool feed is found to be the most significant parameter and spindle speed and coefficient of friction are found insignificant. As reported earlier, the tool feed controls the deformation of sheet material during the SPIF process. Decrease in feed deform the sheet material more and that will increase the thinning of the material. Hence, the contribution and significance of tool feed are found more.

The thickness distribution in the formed component along the weld and across the weld was also investigated. For a simulation run, the thickness distribution along the weld is depicted in Fig. 12. In the present investigation, WTS initial position of tool is selected wherein the repetitive deformations are provided on the weld material. This will increase the thinning of the material at the initial position of the tool. Hence, low value of thickness is observed at the initial position of tool along the weld thickness distribution. At the centre portion of the blank, there is no deformation provided by

Table 6 ANOVA for % of Thinning

Factor	Degree of Freedom	Sum of squares	Mean square	F-Value	P-Value	%P
Feed	2	17.375	8.687	3.13	0.066	21.84
Spindle Speed	2	3.854	1.927	0.69	0.511	4.84
Coefficient of Friction	2	2.828	1.414	0.51	0.608	3.55
Error	20	55.491	2.775			69.77
Total	26	79.547				100

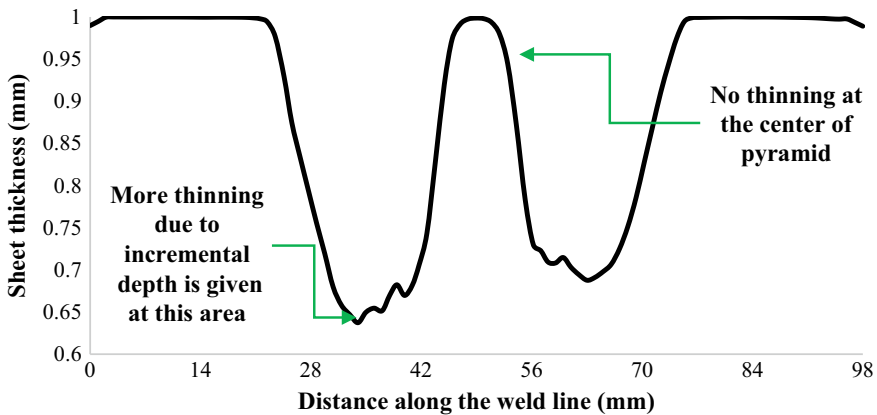


Fig. 12 Distribution of thickness along the weld line

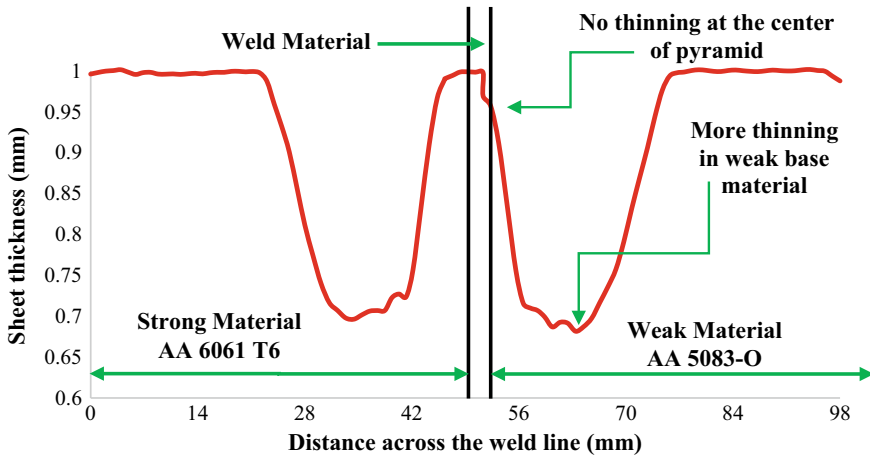


Fig. 13 Distribution of thickness across the weld line

the tool since there is no interaction between tool and the blank being formed. Hence, at the centre portion of the blank, no thickness reduction is observed.

The thickness distribution across the weld is also investigated and presented in Fig. 13. The study of thickness distribution across the weld indicates that weak material will show less thickness after forming because weak material has a low value of yield strength resulting in more thinning of the weak material. At the centre portion of the formed blank, there is no interaction between tool and blank resulting in no reduction in blank thickness.

4 Conclusions

In the present investigation, simulation study on SPIF of TWBs is reported. Effect of SPIF process parameters on formability of TWBs is investigated. To study the formability of TWBs, responses like weld line shift, PEEQ and thinning of blanks are investigated. The remarks from the presented study are as follows.

The forming of TWBs using SPIF process yields in the weld line shift on both sides of the weld zone, unlike conventional forming processes. For such results tool, dragging and deformation of weak material is responsible. For weld line shift, tool feed is found to be the most significant parameter and spindle speed and coefficient of friction are found insignificant. In the formed component more PEEQ and thickness reduction is found in weak parent material. In the formed geometry, wall sections and corners are subjected to maximum PEEQ and %thinning during the SPIF process. The boundary between weld material and parent material is also subjected to high PEEQ and thickness reduction and for that stress concentration effect is responsible. For PEEQ and %thinning, most significant parameter is tool feed and insignificant

parameters are spindle speed and coefficient of friction. Investigation on thinning showed that, more thinning in the material at the initial position of the tool is found due to the repetitive deformation of the forming tool. In the centre part of the formed component, there is no significant reduction in thickness is found because there is no interaction between the forming tool and the blank being formed at centre.

References

1. Parente M, Safdarian R, Santos AD, Loureiro A, Vilaca P, Jorge RN (2016) A study on the formability of aluminum tailor welded blanks produced by friction stir welding. *Int J Adv Manuf Technol* 83(9–12)
2. Chan SM, Chan LC, Lee TC (2003) Tailor-welded blanks of different thickness ratios effects on forming limit diagrams. *J Mater Process Technol* 132(1–3):95–101
3. Suresh VS, Regalla SP, Gupta AK (2017) Combined effect of thickness ratio and selective heating on weld line movement in stamped tailor-welded blanks. *Mater Manuf Processes* 32(12):1363–1367
4. Micari FA, Ambrogio G, Filice L (2007) Shape and dimensional accuracy in single point incremental forming: state of the art and future trends. *J Mater Process Technol* 191(1–3):390–395
5. Centeno G, Bagudanch I, Martínez-Donaire AJ, Garcia-Romeu ML, Vallengano C (2014) Critical analysis of necking and fracture limit strains and forming forces in single-point incremental forming. *Mater Des* 63:20–29
6. Silva MB, Skjødtt M, Atkins AG, Bay N, Martins PA (2008) Single-point incremental forming and formability—failure diagrams. *The journal of strain analysis for engineering design*. 43(1):15–35
7. Silva MB, Skjødtt M, Vilaça P, Bay N, Martins PA (2009) Single point incremental forming of tailored blanks produced by friction stir welding. *J Mater Process Technol* 209(2):811–820
8. Rattanachan K, Sirivedin K, Chungchoo C (2014) Formability of tailored welded blanks in single point incremental forming process. *Advanced materials research*. Trans Tech Publications Ltd, vol 979, pp 339–342
9. Alinaghian I, Ranjbar H, Beheshtizad MA (2017) Forming limit investigation of aa6061 friction stir welded blank in a single point incremental forming process: RSM approach. *Trans Indian Inst Met* 70(9):2303–2318
10. Marathe SP, Raval HK (2019) Numerical investigation on forming behavior of friction stir tailor welded blanks (FSTWBs) during single-point incremental forming (SPIF) process. *J Braz Soc Mech Sci Eng* 41(10):424
11. Zadpoor AA, Sinke J, Benedictus R (2009) Finite element modeling and failure prediction of friction stir welded blanks. *Mater Des* 30(5):1423–1434

Optimization of Design Parameters Under Compression and Shear Loading of FDM Fabricated Re-Entrant Auxetic Structure Using Failure Mode Map



Shailendra Kumar, Swapnil Vyavahare, and Kokani Nirmal

Abstract Auxetic structures have high strength, stiffness, and energy absorption capacity. These structures are used in aircraft, transportation, and automotive applications where weight minimization is an important parameter for cost-effective design. With recent advances in manufacturing techniques, fabrication of these complex structures is easily possible. In the present study, re-entrant auxetic structures of polyethylene terephthalate glycol (PET-G) material are manufactured using fused deposition modeling (FDM) technique and then tested under compressive and shear loading. Further, mechanical properties (strength and stiffness) obtained under these loading conditions are correlated with design parameters and relative density of the unit cell. A failure mode map (FMM) is developed using SCILAB software which shows the dominant failure modes for various design parameters and relative densities of the structure. Further, constant load lines are plotted on the FMM to get optimized value of design parameters and relative density for a specified load.

Keywords Re-entrant auxetic structure · Design parameters · Fused deposition modelling · Compressive loading · Shear loading

1 Introduction

Auxetic structure is a type of mechanical metamaterial which has high stiffness to weight ratio, strength to weight ratio, and energy absorption capability. They are widely used in many fields where light-weight components are essential such as aircraft and automotive industry [1]. Location of these structures is a core region of composite. As shown in Fig. 1, sandwich composite has two rigid face sheets which are connected by a light-weight core. The core enhances inertia of the sandwich beam with a small increment in the mass and it also helps the sandwich composite beam to resist bending and buckling load. The core can consist of various configurations of cellular or lattice solids; which are shown in Fig. 2 [2]. Analytical and experimental

S. Kumar (✉) · S. Vyavahare · K. Nirmal
Department of Mechanical Engineering, Sardar Vallabhbhai National Institute of Technology,
Surat, India

© The Author(s), under exclusive license to Springer Nature Singapore Pte Ltd. 2022
H. K. Dave et al. (eds.), *Recent Advances in Manufacturing Processes and Systems*,
Lecture Notes in Mechanical Engineering,
https://doi.org/10.1007/978-981-16-7787-8_60

747

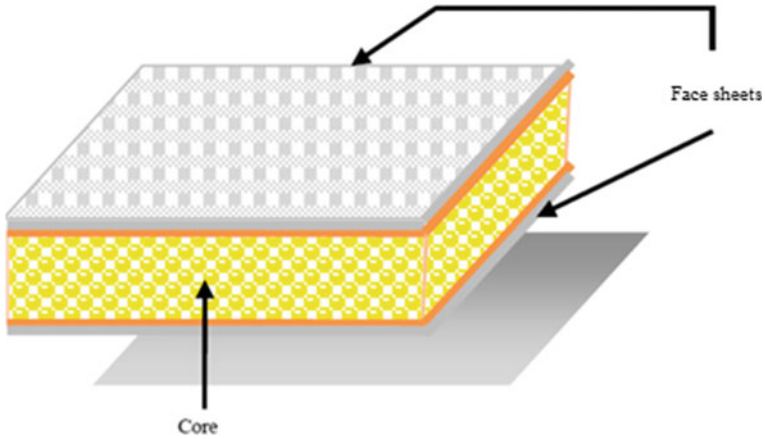


Fig. 1 Sandwich composite

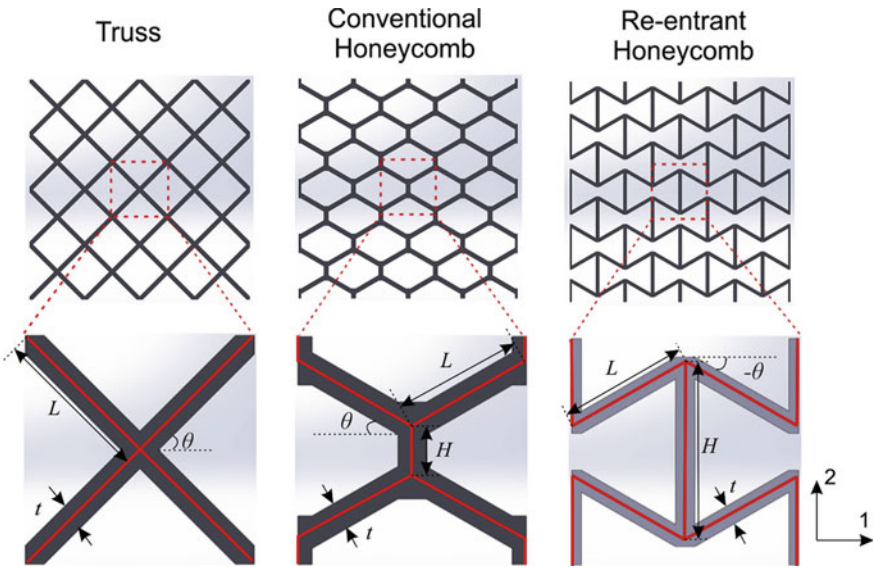


Fig. 2 Two-dimension unit cell structures

studies show that sandwich composites with ordered architected cellular core have high mechanical properties compared to a randomly porous foam core [3]. The most extensively studied and used ordered architected core structures are conventional and re-entrant structures. The re-entrant structure has a negative poisson ratio, with high-energy absorption capability and high impact resistance [2, 4].

Conventionally, the core structures are fabricated through the expansion or corrugation process. In the expansion process, the additive is applied at a selected location

on the sheet. The bundle of such sheets is prepared and then expanded. In the corrugation process, the sheet is formed using a rolling tool, and then these sheets are joined. These processes are able to fabricate simple core geometry which limits the improvement of the mechanical properties of sandwich composites. Recently developed additive manufacturing (AM) technology is able to manufacture complex core geometries. AM is based on the addition of material in the form of layers to create the desired workpiece [5]. Fused deposition modeling (FDM), is the popular AM technique due to its abundant availability of material, cost-effectiveness, and parts having good strength [6].

Various researchers investigated the domain of mechanical property improvement of sandwich composites [2, 7–11]. Li et al. [2] studied the impact of density and face sheet thickness on strength of sandwich panels on Poisson's ratio, bending strength, stiffness, the energy absorption capability of core re-entrant, truss, and honeycomb structure. The material used for the face sheet was Vero-White, woven CFRP, and unidirectional CFRP. They found that bending stiffness and strength of honeycomb and struss structure was higher compared to the re-entrant structure. The energy absorption capacity and force response were higher in the re-entrant structure. For re-entrant structure, the failure mode was global whereas in truss and honeycomb the local failure mode was present. Sarvestani et al. [4] studied the energy absorption capacity of the re-entrant core. The sandwich panel of re-entrant core structure was manufactured employing AM technology. They showed that the sandwich panel having a re-entrant core structure had 33% more energy absorption capacity. The re-entrant core structure also showed more impact resistance and less stress level in out-of-plane loading compared to other topologies. Triantafillou and Gibson [7] developed equations for various failure modes and constructed failure mode maps (FMM) for yielding face sheets and core material. They observed failures such as shear of core structure, yielding, and wrinkling in face sheets. Petras et al. [8] studied failure modes of sandwich beams made from glass fiber reinforced polymer (GFRP) laminate face sheet and honeycomb core. They described theoretical models of the mechanical properties of honeycomb and the sandwich beams. They also constructed an FMM for 3-point bending. They showed that the concept of an FMM was a useful design tool for optimization of performance of the sandwich panels. Belouettar et al. [9] studied static and fatigue properties of honeycomb sandwich composites of aramid fibers and aluminum cores under bending. They investigated the influence of core densities and the cell orientation on the maximum load and the damage processes. They also discussed damage and failure modes. Akour et al. [10] investigated the influence of stiffness of core material on the composite structure. The relative amount of modulus of elasticity of the core and face was investigated. They observed that the load-bearing capability of the structure increased as the stress in core material reaches above the yield stress value. Linul et al. [11] established failure modes of sandwich beams with different cores and different face sheets. Foams with 40 and 200 kg/m³ densities were used as core material, while GFRP, polyester, epoxy, and aluminum were used as the faces materials. Then, sandwich core morphology and cell dimensions are studied through scanning electron microscopy (SEM). Sadighi et. al. [12] built failure modes for sandwich beams with honeycomb structured core

combined with composite face sheets. They calculated FMMs using equations that were developed to predict the failure load of sandwich beams. Honeycomb sandwich beams were tested under flexural load for validation of the results. Zhu et al. [13] studied modes of failure of composite sandwich panels subject to quasi-static indentation and low-velocity impact. They observed that the face sheet thickness had vital contribution in development of failure mode and its corresponding ultimate load while core density is responsible for the failure mode but not its ultimate load. Wang et al. [14] analyzed the characteristics of the sandwich panels made of carbon fiber reinforced polymer (CFRP) under shear, compression, and flexural loading. They conclude that the delamination of faceplates was an important limitation for using composite material in the sandwich panel. Rajkumar al. [15] studied design factors of the core of the aluminum honeycomb core structure (AHCS). The theoretical calculations of core compression strength, crushing strength, shear strength is done in both longitudinal and lateral directions. They concluded that the stiffness was higher for smaller spans and it considerably reduced with an increase in span length. Stiffness values of AHCS panels were higher than solid beams. Wu et al. [16] studied the categorized lattice cores and sandwich panels by analytical modeling and numerical simulations. They constructed failure maps for these geometries by generation analytical expressions for strength for all failure modes under four types of static loadings.

The above literature review reveals that researchers studied failure modes in sandwich composites and then developed response models. But limited efforts have been made to design sandwich composites having a re-entrant core structure and subjected to strength and weight constraint. To accomplish this goal, the following objectives are identified for mechanical property maximization of the re-entrant core structure

- (i) to develop a FMM for sandwich panel having FDM fabricated re-entrant core structure
- (ii) to find the optimum design parameters of the sandwich panel for minimum weight by constructing a constant load line of the FMM.

2 Methodology

In the present study, firstly configurations to be modeled are decided by varying relative density of the structure in the range of 0.1 to 0.3. Then, computer-aided design (CAD) models are generated in the modeling software. Further, FDM specimens are fabricated from these CAD models. Lastly, experimental testing is performed.

In the present study, the re-entrant structure was used as a core. Figure 3 depicts unit cell of the re-entrant structure.

Mechanical characteristics of the re-entrant structure depend upon core angle (θ), edge length (L), edge height (H), edge thickness (t), and relative density. For re-entrant core structure, relative density is given by Eq. 1 [17].

Fig. 3 Re-entrant structure unit cell

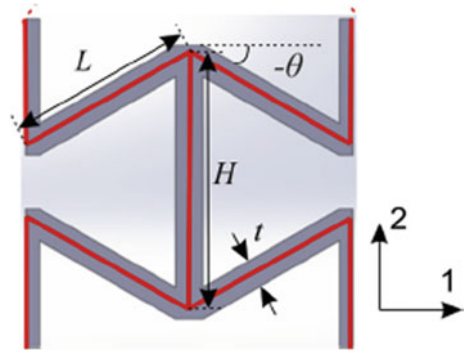


Table 1 Geometrical parameters of re-entrant core structure

Configuration no	Relative density	L (mm)	H (mm)	t (mm)
1	0.2	5.2	7.1	0.52
2	0.3	5.2	7.1	0.76
3	0.4	5.2	7.1	1.4

$$\frac{\rho^*}{\rho_s} = \frac{\left(\frac{t}{L}\right) \times \left(\frac{H}{L}\right) + 2}{2 \cos \theta \left(\left(\frac{H}{L}\right) + \sin \theta\right)} \tag{1}$$

Specimens are designed with three different relative densities as listed in Table 1, for evaluation of mechanical properties of the sandwich structure under compression and shear loading.

Three different configurations are modeled for compressive and shear loading using Solidworks 2019 (Dassault Systèmes). All the configurations are modeled by designing unit cells, arraying in XY plane, and then by extruding in Z-direction. For compressive testing, specimens are modeled with 4 × 2 unit cells and they have width of 30 mm. Upper and lower face sheet thickness is maintained as 5 mm for each configuration of the compression test specimen. For shear testing, specimens are modeled with 1 × 4 unit cells and they have width of 30 mm. Thickness of face sheets is 5 mm for all configurations of the shear test specimen. Shear test specimen is modeled in such a way that compressive load applied by compression testing machine (CTM) is converted into shear load on re-entrant core. The representative CAD models of compression and shear test specimen are in Fig. 4. All geometrical files are kept in STL file format.

Ultimaker CURA 4.2.1 is used for slicing and path generation to form a G-code file. In the current work, specimens are fabricated using a FDM machine (Deltawasp 2040, Wasp, Italy) with layer thickness 0.2 mm, wall thickness 0.3 mm, top and bottom thickness 0.3 mm, and printing speed 40 mm/s. The material used for the core structure is polyethylene terephthalate glycol (PET-G). PET-G is a good material for applications demanding high strength and moderate heat loads. This material is

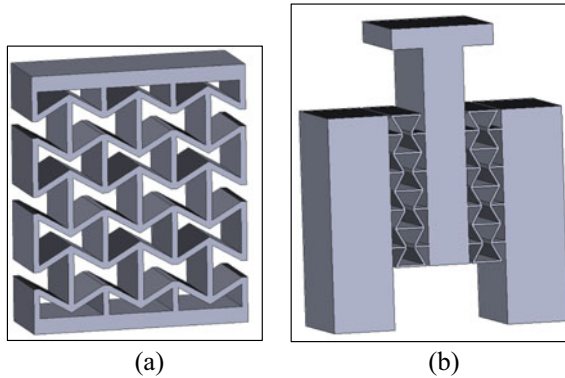


Fig. 4 Representative CAD models **a** compression test specimen **b** shear test specimen

more wear resistant and impact resistant than acrylonitrile butadiene styrene while still being very cost-effective for production applications.

Quasi-two-dimensional samples are manufactured which has equal number of unit cells. Two samples are manufactured for each configuration of the structure to minimize experimental error. So a total of 12 specimens are manufactured for compression and shear loading. Fabricated specimens for compressive and shear testing are shown in Fig. 5.

Compression tests of the re-entrant core structure are performed on a CTM as shown in Fig. 6. The specimen is placed between lower and upper plates of the CTM. During testing upper plate is fixed while lower plate is gradually moved at 5 mm/min speed upwards to apply load on the structure. The extensometer is kept touching the lower plates which measure displacement of lower plate during testing. Compression and shear tests are done by taking two replicas for each configuration. ASTM C365 standard ASTM C273 standard is used for the compression and shear testing of the specimens. The responses load and displacement are then transformed in stress and strain respectively by gauging measurements of the specimen. Using this stress–strain curve mechanical properties are calculated. Specimens for compressive and shear testing are shown in Fig. 7.

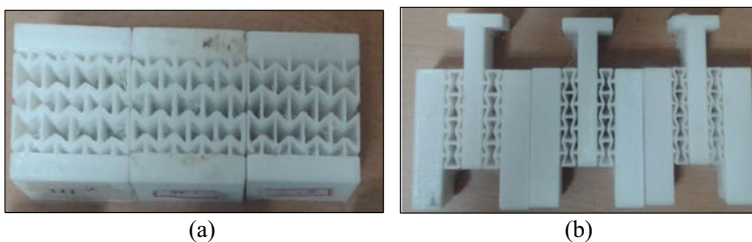


Fig. 5 Fabricated **a** compressive test specimens **b** shear test specimens



Fig. 6 Compression testing machine

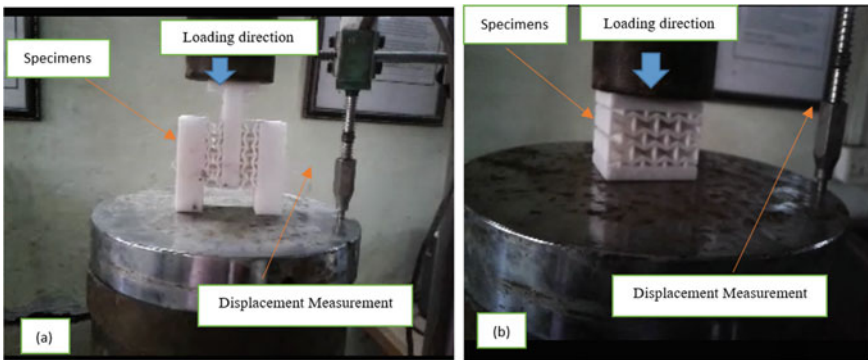


Fig. 7 Testing of manufactured specimens **a** shear loading **b** compression loading

3 Result and Discussion

Stress–strain curve of compression testing specimen configuration 1 is shown in Fig. 8. It comprises three regions namely linear region, plateau region, and densification region. In linear region, stress is proportional to strain. The proportionality constant obtained after dividing stress by strain is called modulus of elasticity. The second region is plateau region in which stress almost remains constant. And lastly, there is densification region in which rapid stress increment is observed with little strain increment.

For compressive and shear loading, mean values of strength and stiffness for each relative density are tabulated in Table 2. From Table 2, it is clear that as relative density increases modulus and strength increase for both types of loading.

Fig. 8 Representative stress–strain curve for configuration I compressive test specimen

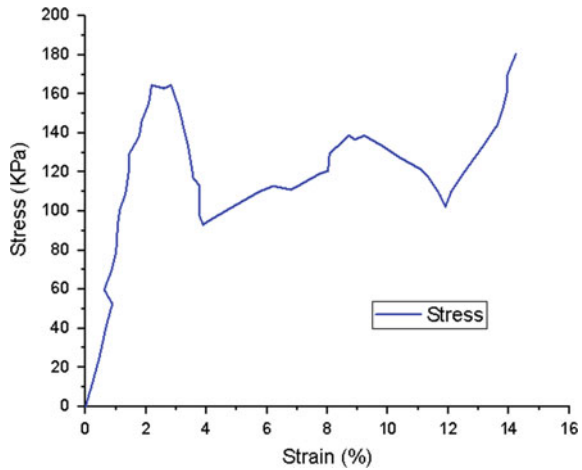


Table 2 Mechanical properties of the core structure

Relative density	Compressive		Shear	
	Strength (KPa)	Stiffness (KPa)	Strength (KPa)	Stiffness (KPa)
0.2	98	54	180	261
0.3	560	166	600	1260
0.4	1471	457	800	2936

3.1 Development of FMM

The FMM provides an outline of failure modes for all beam design parameters for an allotted loading condition. It also describes the reliance of failure mode on the ratio of skin thickness to span length and relative density. In the sandwich panel, several failure modes are present as in Fig. 9, and each failure mode is described by different equations [7]. To develop FMM, constants in the failure equations are required to be computed which are shown in Table 3 [18]. These constant values depend on core geometry, core material, and core density. In the present study, mechanical properties of solid PET-G material are taken from the literature [19].

Microsoft Excel 2013 software is used to calculate values of constants by applying power-law curve fitting to the equations listed in Table 3. These values of the constants are given in Table 4.

The FMM is the graphical representation of the strength of the sandwich composite beam. In present investigation, it is developed in SCILAB solver (ESI Group) after calculating the values of all the constants. Flowchart for SCILAB code of FMM is given in Fig. 10.

The sandwich beam can be failed by many failure modes like face yielding, face wrinkling, core shear, core yielding in compression, etc. The minimum failure

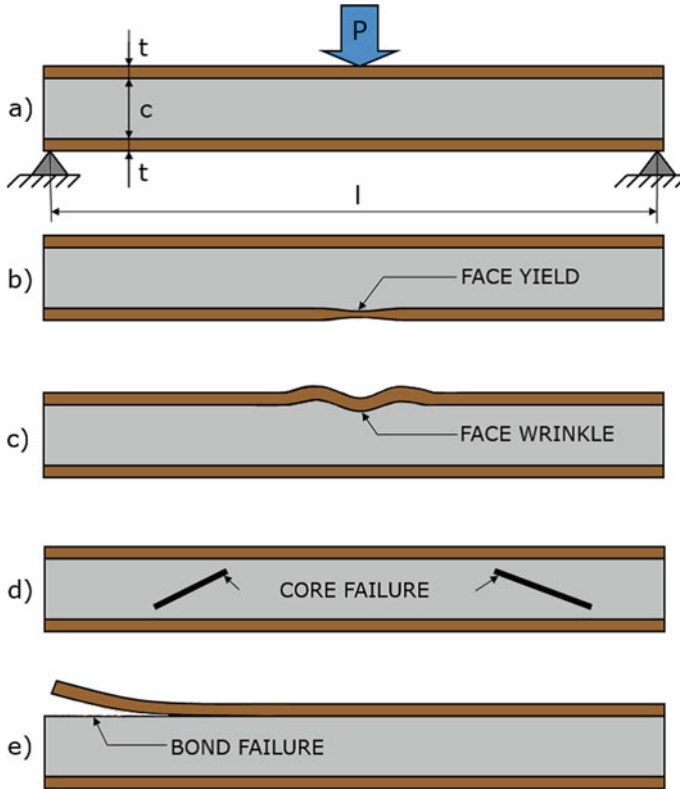


Fig. 9 Failure modes of sandwich beams or panels

Table 3 Equations of core properties [18]

$E_c = C_3 \left(\frac{\rho_c}{\rho_s}\right)^A E_s$	$\tau_c^* = C_4 \left(\frac{\rho_c}{\rho_s}\right)^B \sigma_{ys}$
$\sigma_{cc}^* = C_6 \left(\frac{\rho_c}{\rho_s}\right)^F \sigma_{ys}$	$G_c^* = C_7 \left(\frac{\rho_c}{\rho_s}\right)^E \sigma_{ys}$

where,

E_c = Modulus of elasticity of core material

E_s = Modulus of elasticity of solid material

τ_c^* = Yield strength of core material

σ_{ys} = Yield strength of solid material

σ_{cc}^* = Plastic compressive strength of core material

G_c^* = Shear modulus of core material

C_3, C_4, C_6, C_7 and A, B, F, E = constants (whose values depend upon core structure, core geometry, and core material)

Table 4 Constants for the re-entrant core structure

Constant	Value
C ₃	0.0035
C ₄	0.130
C ₆	1.08
C ₇	0.81
A	3.06
B	2.21
F	1.08
E	2.21

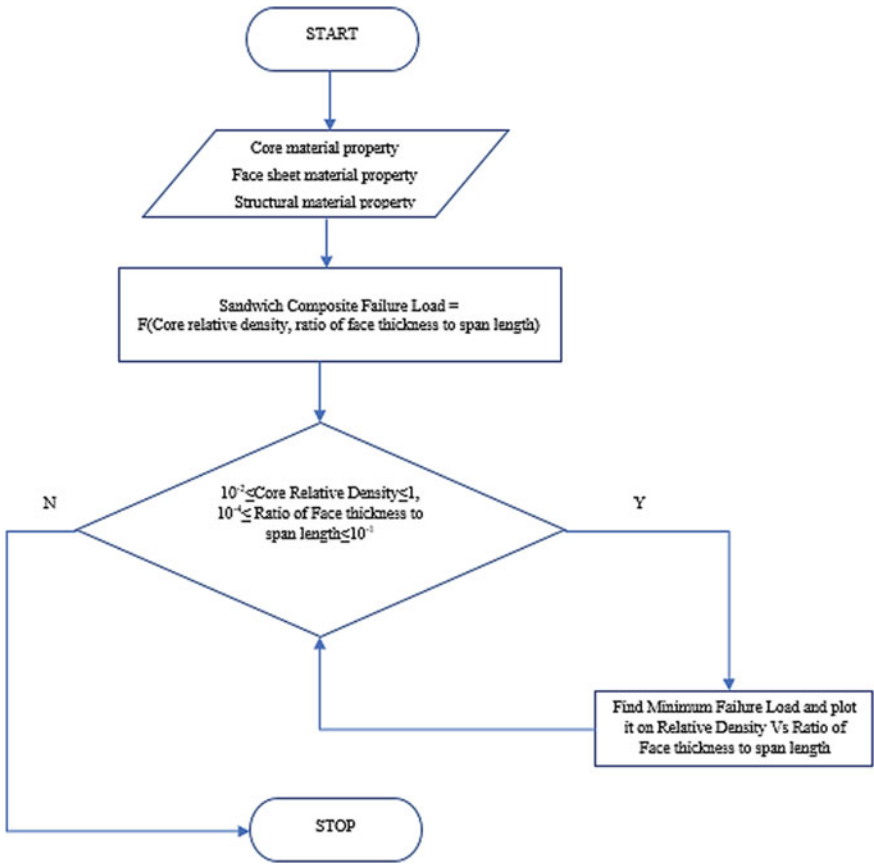


Fig. 10 Flowchart for Scilab code of FMM

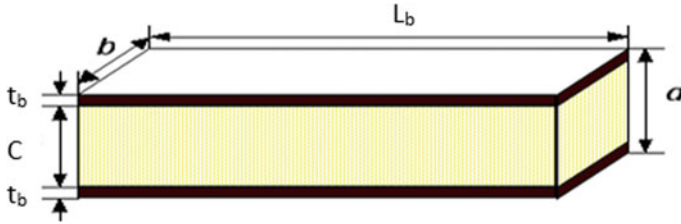


Fig. 11 Sandwich composite beam

load from all these failure modes is the strength of the sandwich beam. Mechanical properties of the sandwich composite beam depend upon thickness of face sheet (t_b), length of beam (L_b), width of beam (b), height of beam (d), core height (C) as shown in Fig. 11. For most of the sandwich beam (t_b/L_b) ratio is within 10^{-2} – 10^{-1} and relative density are within 10^{-1} – 1 ; therefore in present investigation, failure load is obtained within these ranges.

In present study, beam width and core thickness are taken as 25 mm. Generated FMM for the re-entrant core structure is presented in Fig. 12a. As depicted in Fig. 12a, the dominated failure modes are face wrinkling, core yielding in shear, and compression. At lower relative density and low (t_b/L_b) ratio core yielding in compression is the dominant failure mode. If relative density is increased at lower (t_b/L_b) ratio face wrinkling is dominated failure mode. For high relative density and (t_b/L_b) ratio core yield in shear is dominated failure mode. Figure 12b shows FMM of hexagonal honeycomb core structure [7].

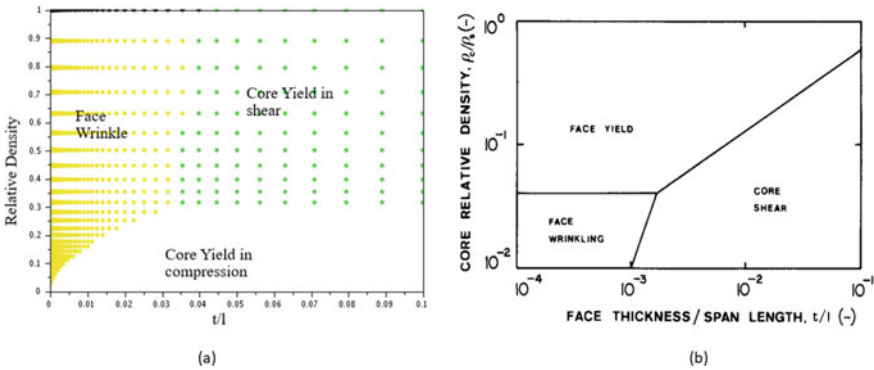


Fig. 12 a FMM of the re-entrant core, b FMM of the hexagonal honeycomb core

3.1.1 Comparison FMMs of Sandwich Beam Having Re-Entrant and Honeycomb Core

In this subsection, comparison of failure mechanism and FMMs of sandwich beam having re-entrant and honeycomb core is performed. Remarkable differences are observed between Fig. 12a, b. With application of load on sandwich composite beam, re-entrant unit cells are also get contracted in lateral direction due to inherent property of negative Poisson’s ratio; therefore face wrinkle failure mode is observed in case of re-entrant structure upper left region of Fig. 12a. In case of hexagonal honeycomb structure, unit cells get expanded in lateral direction with application of load due to positive Poisson’s ratio; which gives rise to face yield failure mode shown in Fig. 12b. Reason for high-energy absorption in auxetic structures is that they undergo large deformation (strain ~0.08) at nearly constant stress value (called plateau stress) which is lower than yield strength of the material. Therefore, area under stress–strain curve is high with low stress value, so that material does not break [17].

3.2 Optimum Design Parameter of the Sandwich Panel for Minimum Weight

In sandwich composites, weight and strength are important parameters. The strength of the sandwich composite is the lowest load where the sandwich composite fails. These failure mode equations for each type of failure are taken from the literature [7].

For optimization, a constant load line is imposed on the FMM to find optimum design parameter of the sandwich panel. The FMM with constant load line is shown in Fig. 13a. Number above line is the load (Unit—Newton) applied to the beam under flexural loading. The constant load line in core yield, in the shear and compression

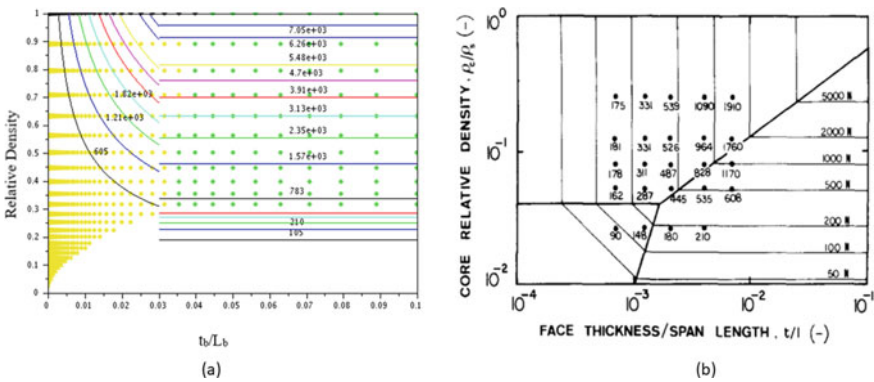


Fig. 13 FMM with constant load lines for a re-entrant core structure, b hexagonal core

region, is horizontal. Therefore, for a given load the thickness of the face sheet decreased up to boundary point without losing strength. So the optimum parameter is at boundary point for the given load. This is also true in the case of constant load line in face wrinkling region the optimum point lies at a boundary point. Out of all the design parameters depicted in Fig. 11, width of beam (b) and width of core (c) are considered as fixed parameters and their value is taken as 25 mm. Variable parameters such as sheet thickness (t_b), the relative density of the core, and length of the beam (L_b) are obtained from the FMM. These values provide the optimum weight of sandwich panel for the given strength. Figure 13b shows FMM with constant load lines for hexagonal honeycomb core structure available in the literature [7]. By comparing Fig. 13a, b, it is seen that the load-bearing capability of the sandwich composite with the re-entrant core is higher than the sandwich composite with the honeycomb core.

4 Conclusions

In the present investigation, the sandwich panel is designed using a re-entrant auxetic structure having a requirement of minimum weight and then subjected to the strength and stiffness constraint. The core structures are fabricated at different relative densities using the FDM technique using PET-G material and the mechanical characteristics of the re-entrant auxetic structures are obtained under compression and shear loading. Following are the findings of current work.

- (i) Mechanical properties of re-entrant core structure improve with increase in relative density.
- (ii) FMM shows dominant failure modes such as face wrinkle, core shear, and core compression.
- (iii) Core compression failure mode is dominant at lower relative density. As relative density increases face wrinkling and core shear failure are two most dominant failure modes.
- (iv) For low t_b/L_b ratio face wrinkle failure mode is dominant while for high value of this ratio core shear failure mode is dominant.
- (v) The constant load line in core shear and core compression is horizontal which shows that failure mode is independent of t_b/L_b ratio. Therefore, t_b/L_b ratio can be decreased without loss in load-carrying capacity.
- (vi) Optimum design points of the sandwich panel for minimum weight subjected to strength as constraints are lying at the boundary of the failure region.
- (vii) Using this FMM the optimum parameters of the sandwich composite with minimum weight are obtained.

The present study is certainly useful in finding dominant failure modes in different types of auxetic structures. Future work can be attentive in investigating strength, stiffness, and SEA under flexural loading for re-entrant auxetic structures.

References

1. Azmi MA, Abdullah HZ, Idris MI (2013) Properties of polyurethane foam/coconut coir fiber as a core material and as a sandwich composites component. *IOP Conference Series: Mater Sci Eng* 50(1):012–067
2. Li T, Wang L (2017) Bending behavior of sandwich composite structures with tunable 3D-printed core materials. *Compos Struct* 175:46–57
3. Ashby MF (2006) The properties of foams and lattices. *Philosophical Trans Royal Soc A: Math Phys Eng Sci* 364(1838):15–30
4. Sarvestani HY, Akbarzadeh AH, Niknam H, Hermenean K (2018) 3D printed architected polymeric sandwich panels: energy absorption and structural performance. *Compos Struct* 200:886–909
5. Gibson I, Rosen D, Stucker B, Khorasani M (2014) *Additive manufacturing technologies*, vol 17, New York, Springer, p 195
6. Vyavahare S, Teraiya S, Panghal D, Kumar S (2019) “Fused deposition modelling: a review”. *Rapid Prototyping J* 26(1)
7. Triantafillou TC, Gibson LJ (1987) Failure mode maps for foam core sandwich beams. *Mater Sci Eng* 95:37–53
8. Petras A, Sutcliffe MPF (1999) Failure mode maps for honeycomb sandwich panels. *Compos Struct* 44(4):237–252
9. Belouettar S, Abbadi A, Azari Z, Belouettar R, Freres P (2009) Experimental investigation of static and fatigue behaviour of composites honeycomb materials using four point bending tests. *Compos Struct* 87(3):265–273
10. Akour SN, Maaitech HZ (Jun 2010) Effect of core material stiffness on sandwich panel behavior beyond the yield limit. In *Proceedings of the world congress on engineering* (2)
11. Linul E, Marsavina L (2015) Assessment of sandwich beams with rigid polyurethane foam core using failure-mode maps. *Proc Romanian Acad A* 16(4):522–530
12. Sadighi M, Dehkordi AA, Khodambashi R (2010) A theoretical and experimental study of failure maps of sandwich beams with composite skins and honeycomb core. *J Modeling Simulation* 42(6):37–47
13. Zhu S, Chai GB (2013) Damage and failure mode maps of composite sandwich panel subjected to quasi-static indentation and low velocity impact. *Compos Struct* 101:204–214
14. Wang B, Zhang G, He Q, Ma L, Wu L, Feng J (2014) Mechanical behavior of carbon fiber reinforced polymer composite sandwich panels with 2-D lattice truss cores. *Mater Des* 55:591–596
15. Rajkumar S, Arulmurugan B, Manikandan M, Karthick R, Kaviprasath S (2017) Analysis of physical and mechanical properties of A3003 aluminum honeycomb core sandwich panels. *Appl Mech Mater* 867:245–253
16. Wu Q, Gao Y, Wei X, Mousanezhad D, Ma L, Vaziri A, Xiong J (2018) Mechanical properties and failure mechanisms of sandwich panels with ultra-lightweight three-dimensional hierarchical lattice cores. *Int J Solids Struct* 132:171–187
17. Gibson LJ, Ashby MF (1999) *Cellular solids: structure and properties*. Cambridge University Press
18. Gibson LJ (1984) Optimization of stiffness in sandwich beams with rigid foam cores. *Mater Sci Eng* 67(2):125–135
19. Szykiedans K, Credo W, Osiński D (2017) Selected mechanical properties of PETG 3-D prints. *Procedia Engineering* 177:455–461

Parametric Influences on Powder Mixed Dielectric in Wire EDM for Processing Ti6Al4V



Sadananda Chakraborty , Souren Mitra, and Dipankar Bose

Abstract Owing to brilliant mechanical properties, Ti6Al4V alloy is used in the advanced manufacturing sector broadly. Machining of the alloy is created many inherent issues by the conventional methods. Due to this, proper machining process selection is very much necessary for processing the Ti6Al4V alloy. The present investigation illustrated a hybrid machining process of wire EDM where the abrasive powder is mixed with the dielectric to achieve better accuracy in dimensional criteria. With powder in dielectric, the process becomes more stable and improves the machining performance of Ti6Al4V alloy such as MRR and surface roughness. Therefore, the study of the influence of powder properties along with other machining settings in wire EDM has been explored. Sensitivity analysis has been adopted in the present work to find out the significance level of each parameter. For modeling and optimizing the process variable, RSM is used. The relation between the input parameters such as peak current, pulse-off time, pulse-on time, and powder concentration is established to find the best optimal solution for the proposed work. The result concludes that Al₂O₃-mixed deionized water can improve surface roughness upto 61.37% and metal removal rate increased upto 31.52% compared with the conventional WEDM process.

Keywords Hybrid machining · Ti6Al4V · MRR · SR · Sensitivity analysis · RSM

1 Introduction

As per the structure of the metallurgical view of Ti6Al4V, it is known as α - β titanium alloy, and it has a high weight ratio, corrosion resistance, and wear resistance at elevated temperature. Those mechanical properties and other metallurgical properties make the material exceedingly more rigid and more stringent. Also, Ti6Al4V is

S. Chakraborty (✉) · S. Mitra

Production Engineering Department, Jadavpur University, Kolkata 700032, India

D. Bose

Mechanical Engineering Department, NITTTR, Kolkata 700106, India

known as a hard to cut material due to its low machinability and poor conductivity nature ([1, 2]). With the advancement of new technology in the field of more unique super alloy and hydride material, such as Ti-based, nickel-based, and chromium-based, Ti6Al4V alloy becomes very popular in different applications.

Therefore, the machining of the superalloy material is a challenging task in the manufacturing field. Plenty thermal-assisted non-conventional machining is available like EDM, LBM, and EBM, which have more capability to cut the hard material very smoothly. Among of them, electric discharge machining is one of the most efficient machining processes for processing Ti6Al4V material very precisely [3]. However, many researchers have discussed how to improve the machining capability of EDM with the help of different methodologies. EDM is a thermal-assisted process, so there is always a chance to produce surface defects on the machined surface. So, it is required to improve the machining process of EDM for better output. Hence, adding powder particle in the dielectric of EDM gives remarkable change on MRR and SR, but certain limitations and problems may occur during machining [4].

Process parameter, as well as an electrode material, also plays an essential role in performance. So, the choice of suitable electrode material is also influencing the machining criteria. Rahul et al. [5] presented an experimental work by using different electrode material to machine Ti6Al4V material by EDM process and found that cryogenically treated copper wire gives superior EDM performance. The effect of process parameters on EDM performance such as fatigue life, surface integrity has been investigated and stated that two contributing factors for fatigue performance are recast and heat effected zones [6]. Achieving high accuracy in curvature profile, basically in die-cutting operation with controlling the dimension sift and process parameter, is highly relevant to the research area for advanced material to produce micro part [7].

Shabgard and Khosrozadeh [8] utilized the carbon nanotubes in dielectric to elevate the machining efficiency of Ti6Al4V alloy using EDM process. The surface integrity and element compositions were investigated by SEM analysis. In addition of CNT powder with dielectric MRR significantly increases with long pulse duration. Better discharge can be achieved and the process becomes more stabilized by mixing powder particles in the dielectric of the EDM process. But, proper selection of powder size and powder concentration is a difficult task, and it is a challenging research topic. Bui et al. [9] investigated the PMEDM process by varying 50–60 nm size silver powder particles with concentration 0–25 g/l in dielectric fluid.

The most recent innovation in EDM process is known as powder mixed EDM, where the conductive powder generates a series of continuous spark in the dielectric. The primary mechanism of PMEDM is to improve the plasma channel because of reducing the insulating strength of dielectric fluid; as a result, the process becomes more stable and increases the efficiency of MRR and surface finish. Chakraborty et al. [10] reported the mechanism of PMWEDM and concluded that PMWEDM has an excellent application for getting a better response than conventional EDM.

Kumar et al. [11] investigated the effect of different powder like Al_2O_3 and Al powder mixed with deionized water on EDM performance characteristics such as MRR, SR, and surface topography. The result revealed that adding powder with

dielectric generates a larger size bubble and a maximum 0.139 mm interelectrode gap in EDM process. Nguyen et al. [12] analyzed the process parameter such as T_{on} , T_{off} , electrode polarity, current with different electrode material, and powder concentration (0–20 g/l) for better MRR, surface finish, and microhardness by using Taguchi-Topsis method. The size of the powder has a vital role in EDM process. Hourmand et al. [13] optimized the process variables by ANFIS and RSM methodology to machine difficult to cut material of Mg_2Si with PMEDM by adding nanopowder particle in dielectric. Nguyen et al. [14] established a 41.81% increment in microhardness value with 10 g/l concentration of Ti powder in dielectric while machining dies steel using powder mixed die-sinking EDM.

A hybrid technique approach of EDM is the best choice to produce micro-profile geometry on Ti6Al4V alloy. Tiwari et al. [15] made a micro-hole on Ti6Al4V material with Cu powder mixed deionized water and observed that EDM performance significantly improved after machining. Chakraborty et al. [16] explored the relationship of process variable on material removal and surface roughness of Ti6Al4V during B_4C abrasive mixed WEDM and found that 10 μm sizes, 6 g/l concentration is the optimum condition of mixing powder properties in the investigation.

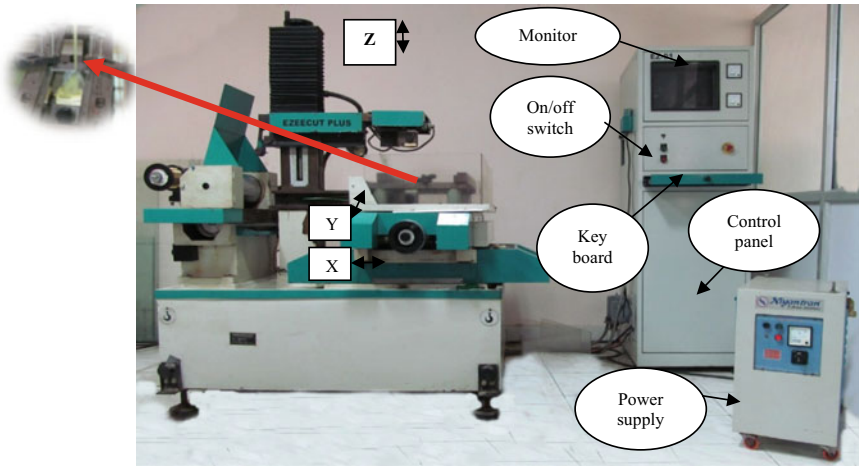
Past researchers have observed the powder's physical behavior adding in the dielectric of electric discharge machining process to analyze how to improve the plasma channel. It also concluded that different metal, non-metal, and abrasive powder have a remarkable effect on machining advanced materials. Fewer researches have been done on powder mixed WEDM process for its more complicated nature in the overall operation. In the present study, a hybridization of WEDM has been applied to get the best machining output of Ti6Al4V material. The contribution of each machining parameter to the responses has been carried out using sensitivity analysis. The research result shows the effectiveness of PMWEDM for the optimization of multiple outputs at a time using RSM methodology. Al_2O_3 abrasive powder mixed with deionized water along with three other inputs such as peak current, pulse-on time, and pulse-off time is taken into consideration in this work to find out the optimum condition and analyze the response variable.

2 Experimental Plan and Procedure

In the present research, experiments are conducted on high precision Ezee cut plus WEDM machine. Brass wire with a diameter of 250 μm is chosen as an electrode material, and another machining parametric condition with their level is shown in Table 1. Deionized water is used as dielectric fluid. Response surface methodology conducts the design of experiment to minimize the number of experiments. Minitab 19 software is used to create DOE as per experiment condition based on the RSM method. Thirty-one numbers of experiments are conducted by the central composite design method. A total of four input parameters of three levels of each, including powder concentration, are implemented in order to study the effect on responses like MRR and surface roughness.

Table 1 Selected parameter and their levels

Input parameters	Unit	Level 1	Level 2	Level 3
Peak current (I_p)	A	2	3	4
Pulse-on time (T_{on})	μs	30	50	70
Pulse-off time (T_{off})	μs	4	8	12
Powder concentration (PC)	g/l	2	4	6

**Fig. 1** Experimental setup view

Furthermore, MRR has been calculated by the weight-based method. Surface roughness is measured in terms of R_a by Mahr surf PS1 surface roughness tester with a cutoff length value of 0.8 mm. The experimental overview has been illustrated in Fig. 1.

3 Result and Discussion

As per the design of experiment, the obtained experiment results are presented in Table 2. Surface roughness is measured by taking an average of three different locations of the same machined sample. The experimental table shows that 19 no experiment has minimum surface roughness, and 25 no experiment has maximum MRR. Both the experiment pulse-off time and powder concentration is the effective parameter. The lower value of pulse-off time and powder concentration gives better surface texture, but the higher value gives a better metal removal rate as well as considerable surface roughness.

Table 2 Experimental data and obtained results

Std order	Run order	Peak current (X_1) A	Pulse-on time (X_2) μ s	Pulse-off time (X_3) μ s	Powder concentration (X_4) g/l	MRR (Y_1) mm ³ /min	SR (Y_2) μ m
10	1	4	30	2	6	5.332	2.485
11	2	2	70	2	6	4.487	2.277
31	3	3	50	6	4	6.732	2.426
19	4	3	30	6	4	6.139	2.305
9	5	2	30	2	6	3.194	2.078
2	6	4	30	2	2	5.968	2.128
14	7	4	30	10	6	5.151	2.574
1	8	2	30	2	2	4.575	2.353
26	9	3	50	6	4	6.225	2.326
8	10	4	70	10	2	7.298	2.386
13	11	2	30	10	6	4.45	2.106
17	12	2	50	6	4	5.498	2.183
29	13	3	50	6	4	6.155	2.326
6	14	4	30	10	2	5.492	2.138
28	15	3	50	6	4	6.135	2.563
4	16	4	70	2	2	6.165	2.243
27	17	3	50	6	4	6.355	2.316
25	18	3	50	6	4	5.655	2.126
23	19	3	50	6	2	3.691	1.929
15	20	2	70	10	6	7.663	2.326
21	21	3	50	2	4	7.238	2.61
20	22	3	70	6	4	7.838	2.528
3	23	2	70	2	2	5.108	2.355
7	24	2	70	10	2	7.741	2.337
22	25	3	50	10	4	8.439	2.645
30	26	3	50	6	4	6.755	2.026
18	27	4	50	6	4	6.377	2.41
24	28	3	50	6	6	3.363	2.108
12	29	4	70	2	6	6.64	2.906
5	30	2	30	10	2	5.59	2.313
16	31	4	70	10	6	8.027	3.017

3.1 Mathematical Modeling for MRR (Y_1), SR (Y_2) in PMWEDM

The mathematical modeling equation for metal removal rate (Y_1) and surface roughness (Y_2) during powder mixed in wire EDM has been presented in Eqs. (1) and (2). Based on the RSM methodology, the empirical modeling equation is used for correlating the machining parameters and the output measures such as MRR and SR.

$$\begin{aligned}
 Y_1 = & 0.30 + 2.235 X_1 - 0.2065 X_2 - 1.099 X_3 + 4.522 X_4 \\
 & - 0.246 X_1 * X_1 + 0.002013 X_2 * X_2 + 0.10346 X_3 * X_3 \\
 & - 0.6640 X_4 * X_4 - 0.00313 X_1 * X_2 - 0.0971 X_1 * X_3 \\
 & + 0.1077 X_1 * X_4 + 0.005246 X_2 * X_3 \\
 & + 0.00625 X_2 * X_4 + 0.01041 X_3 * X_4
 \end{aligned} \tag{1}$$

$$\begin{aligned}
 Y_2 = & 3.127 - 0.217 X_1 - 0.0319 X_2 - 0.2517 X_3 + 0.329 X_4 \\
 & - 0.0266 X_1 * X_1 + 0.000233 X_2 * X_2 + 0.01902 X_3 * X_3 \\
 & - 0.0762 X_4 * X_4 + 0.00244 X_1 * X_2 + 0.00522 X_1 * X_3 \\
 & + 0.0831 X_1 * X_4 + 0.000155 X_2 * X_3 \\
 & + 0.001397 X_2 * X_4 + 0.00142 X_3 * X_4
 \end{aligned} \tag{2}$$

3.2 Analysis of Variance (ANOVA) for MRR

Analysis of variance is a statistical approach used in design of experiment and regression analysis. In ANOVA, F -statistics and p -values mainly used to determine whether the predicted factors are significantly related to the response variable or not. The F value can be determined by dividing the individual factor mean squares value by the error mean squares value. The model F value of 64.42 (as in Table 3) indicates that the model is significant for MRR.

A 95% confidence level has considered for the experimentation. So, the p -value is less than 0.05 indicates that the factor is significant for the process. In the present investigation, the following factors are significant and taken into consideration for analysis such as X_1 , X_2 , X_3 , X_4 , X_2^2 , X_3^2 , X_4^2 , $X_1 * X_3$, $X_1 * X_4$, $X_2 * X_3$, $X_2 * X_4$, respectively. The determination of R^2 value shows the degree of fit and total deviation. Also, R^2 value near to the unity relates to the well fit of the model to the real data. In the present study, determined coefficient for MRR is 98.26%, which proposes that the recognized model is accomplished the variation on MRR. The predicted R^2 value (97.34%) is very close to the Adj R^2 value (96.73%), indicating the model is fitted for the present work.

Table 3 Analysis of variance for MRR

Source	DF	Adj SS	Adj MS	F-value	P-value
Model	14	53.0647	3.7903	64.42	0.000
Linear	4	23.8238	5.9559	101.23	0.000
X_1	1	3.6847	3.6847	62.63	0.000
X_2	1	12.6270	12.6270	214.62	0.000
X_3	1	6.8994	6.8994	117.27	0.000
X_4	1	0.6127	0.6127	10.41	0.005
Square	4	22.0890	5.5222	93.86	0.000
$X_2 * X_2$	1	1.6830	1.6830	28.61	0.000
$X_3 * X_3$	1	7.1108	7.1108	120.86	0.000
$X_4 * X_4$	1	18.3098	18.3098	311.21	0.000
2-Way Interaction	6	7.1519	1.1920	20.26	0.000
$X_1 * X_3$	1	2.4157	2.4157	41.06	0.000
$X_1 * X_4$	1	0.7426	0.7426	12.62	0.003
$X_2 * X_3$	1	2.8182	2.8182	47.90	0.000
$X_2 * X_4$	1	1.0015	1.0015	17.02	0.001
Error	16	0.9413	0.0588		
Lack-of-fit	10	0.0759	0.0076	0.05	1.000
Pure error	6	0.8655	0.1442		
Total	30	54.0060			

3.3 Analysis of Variance (ANOVA) for SR

The experimental result for surface roughness in terms of R_a has listed in Table 2 for further analysis. The quadratic model is determined by Minitab 19 software. After ANOVA, the results are summaries by eliminating non-significant variable in Table 4.

In the present investigation, the following factors are significant and considered for analysis such as $X_1, X_2, X_4, X_3^2, X_4^2, X_1 * X_4$, respectively. The average surface roughness deviation is extended up to 88.91% as the determined coefficient for SR is 88.91%. Also, a reasonable nearer value of the predicted R^2 value (84.58%) to the Adj R^2 value (78.64%). Therefore, the quadratic model can be used to forecast R_a inside the factor considered of maximum and minimum levels.

Table 4 Analysis of variance for SR

Source	DF	Adj SS	Adj MS	F-value	P-value
Model	14	1.53700	0.109786	8.89	0.000
Linear	4	0.58152	0.145380	11.77	0.000
X_1	1	0.21320	0.213204	17.26	0.001
X_2	1	0.19950	0.199501	16.15	0.001
X_4	1	0.15961	0.159612	12.92	0.002
Square	4	0.41425	0.103564	8.38	0.001
$X_3 * X_3$	1	0.24042	0.240417	19.46	0.000
$X_4 * X_4$	1	0.24083	0.240830	19.50	0.000
2-Way interaction	6	0.54123	0.090204	7.30	0.001
$X_1 * X_4$	1	0.44156	0.441560	35.75	0.000
Error	16	0.19763	0.012352		
Lack-of-fit	10	0.00563	0.000563	0.02	1.000
Pure error	6	0.19199	0.031999		
Total	30	1.73463			

3.4 Regression Analysis of MRR and SR in PMWEDM Process

For metal removal rate, peak current, pulse-on time, pulse-off time and powder concentration are the significant factors. The set of combination of all these parameters gives optimum result such as peak current (4A), pulse-on time (70 μ s), pulse-off time (9 μ s), and powder concentration (4g/l), respectively, as shown in Fig. 2.

In regression analysis, fitted values are essential in determining whether the investigation model fits the actual data. Graphically, representation of the fitted values is fitted in line plots of all x -values in the region space. These line plots are appropriate ways to compare fitted data to actual data values to evaluate the model fit. For surface roughness, the input variables such as peak current, pulse-on time, and powder concentration are the significant factors, and the set of combination of all

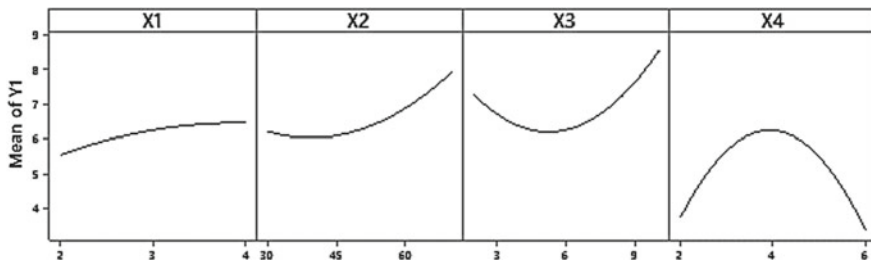


Fig. 2 Individual fitted graph for MRR

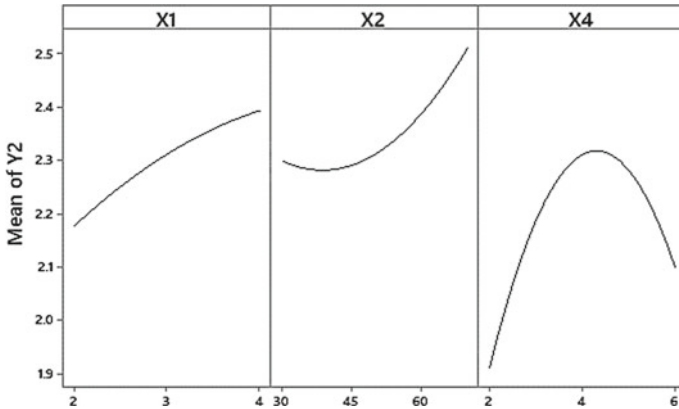


Fig. 3 Individual fitted graph for SR

these parameters gives optimum result such as peak current (2A), pulse-on time (50 μs) and powder concentration (2g/l), respectively, as in Fig. 3. Below, the fitted line plots for two different models are compared to see which model fits the data better.

3.5 Sensitivity Analysis

With the change in variation of response measures concerning the change in input variables, the sensitivity analysis is one the best methodology to determine each machining parameter’s contribution [17]. The sensitivity of the objective function for a design variable is carried out by derivation of the objective function. Therefore, Eq. (3) is the differential form of Eq. (1). Regarding change of peak current, the change in MRR is calculated when other constant parameters are considered as the central value. The sensitivities of MRR have been given in Eqs. (3)–(6), respectively, for the machining inputs of peak current, pulse-on time, pulse-off time, and powder concentration. Sensitivity of surface roughness has been given in Eqs. (7)–(10), respectively.

$$\frac{dY_1}{dX_1} = 2.235 - 0.492 X_1 - 0.00313 X_2 - 0.0971 X_3 + 0.1077 X_4 \quad (3)$$

$$\frac{dY_1}{dX_2} = -0.2065 + 0.004026 X_2 - 0.00313 X_1 + 0.005246 X_3 + 0.00625 X_4 \quad (4)$$

$$\frac{dY_1}{dX_3} = -1.099 + 0.20692 X_3 - 0.0971 X_1 + 0.005246 X_2 + 0.01041 X_4 \quad (5)$$

$$\frac{dY_1}{dX_4} = +4.522 - 1.3280 X_4 + 0.1077 X_1 + 0.00625 X_2 + 0.01041 X_3 \quad (6)$$

$$\frac{dY_2}{dX_1} = -0.217 - 0.0532 X_1 + 0.00244 X_2 + 0.00522 X_3 + 0.0831 X_4 \quad (7)$$

$$\frac{dY_2}{dX_2} = -0.0319 + 0.000466 X_2 + 0.00244 X_1 + 0.000155 X_3 + 0.001397 X_4 \quad (8)$$

$$\frac{dY_2}{dX_3} = -0.2517 + 0.03804 X_3 + 0.00522 X_1 + 0.000155 X_2 + 0.00142 X_4 \quad (9)$$

$$\frac{dY_2}{dX_4} = 0.329 - 0.1524 X_4 + 0.0831 X_1 + 0.001397 X_2 + 0.00142 X_3 \quad (10)$$

Figure 4 shows that the sensitivity of peak current on MRR and SR. The sensitivity calculations are done with a change in peak current value from 2 to 4A and taking the other constant parameters such as pulse-on time of 50 μs, pulse-off time of 6 μs, and powder concentration of 4 g/l. The sensitivity of MRR on peak current is higher than the SR. With an increase in peak current, both the responses are decreased. A higher peak current leads to higher spark energy. Due to this, a large number of discrete spark in the narrowest gap causes low MRR as well as low surface finish. At the same time, higher evaporation and impulse force affect mostly on responses.

Figure 5 represents the sensitivity of pulse-on time on MRR and SR. Initially, both the responses are minimal and negative. After that, the sensitivity value is positive. With the increase in pulse-on time, the MRR and SR values are increased. Therefore, higher motion and acceleration of the ion release higher thermal energy that increases the MRR. Also, it creates bigger craters and voids, which causes more elevated surface roughness.

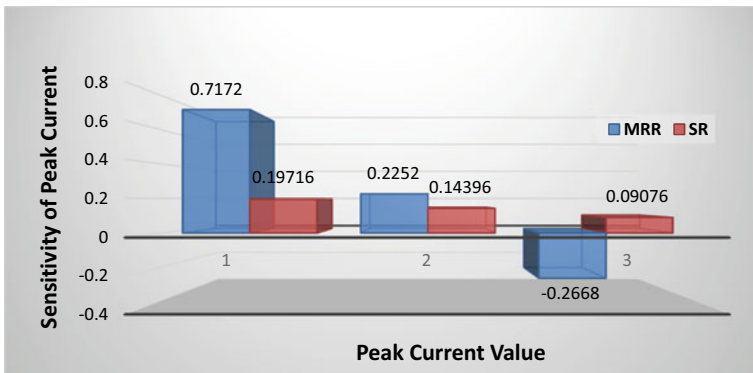


Fig. 4 Sensitivity analysis of peak current on MRR and SR

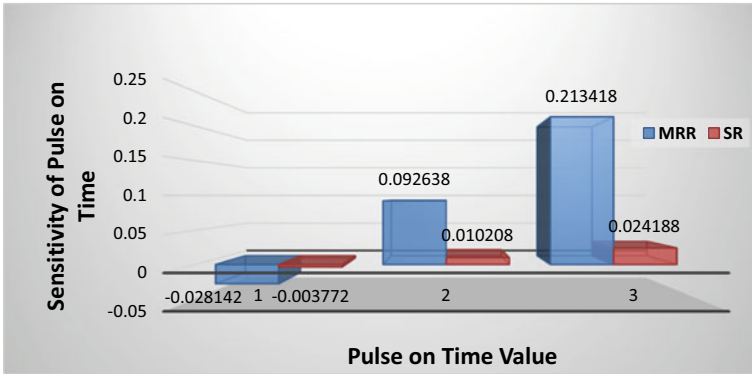


Fig. 5 Sensitivity analysis of pulse-on time on MRR and SR

Figure 6 represents the sensitivity analysis of pulse-off time on MRR and SR. The sensitivity calculations are done with a change in pulse-off time value from 2 to 10 μ s and taking the other constant parameters such as peak current of 3A, pulse-on time of 50 μ s, and powder concentration of 4 g/l. The sensitivity value is firstly negative and then positive. For both the cases, MRR and SR are increased. Higher pulse-off time up to a certain limit provides the suitable time to flash away debris from the gap zone. On the other hand, higher pulse-off time leads to higher cooling action that reduces MRR, and the debris particle stick on the machine surface causes poor surface finish.

Figure 7 represents the sensitivity analysis of powder concentration on MRR and SR. By varying powder concentration 2–6 g/l, the sensitivity has been calculated with considering the constant parameters such as peak current of 3A, pulse-on time of 50 μ s, and pulse-off time of 6 μ s. The graphical representation shows that the highest sensitivity is found for powder concentration on MRR. With an increase in powder

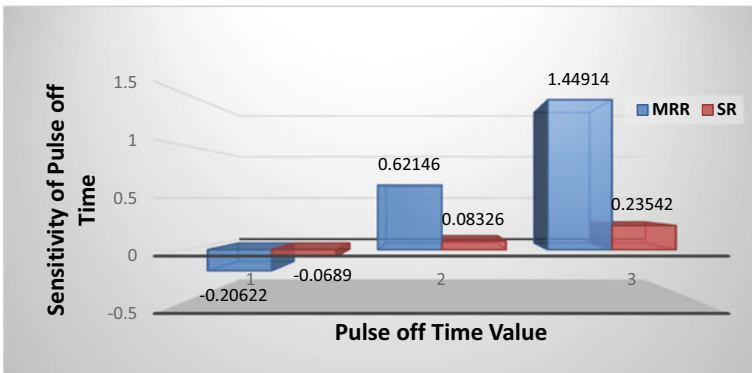


Fig. 6 Sensitivity analysis of pulse-off time on MRR and SR

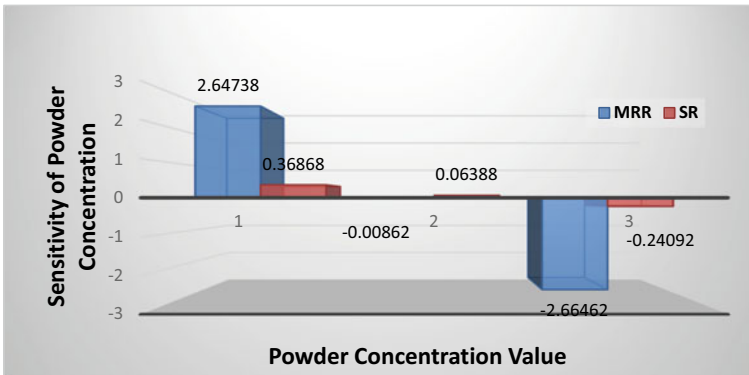


Fig. 7 Sensitivity analysis of powder concentration on MRR and SR

concentration, the MRR and surface finish are reduced. Higher amount of powder particles disturb to create the spark. When powder mixed with dielectric in the wire EDM process, the powder helps to reduce the insulating strength of the dielectric and increase discharge gap. As a result, increasing MRR and reducing impulse force create small size craters that indicate a better surface finish.

3.6 Multi-objective Optimization

Response surface methodology is one of the best choices to optimize the process variable and is suitable for multi-objective optimization. Response optimizer found out the input setting and satisfied the requirement for all responses by composite desirability. In the present study, the composite desirability (0.745 as in Fig. 8) is closer to 1, indicating the settings appear to achieve satisfactory results for all responses as a whole.

The optimum setting for both responses is as follows: Peak current = 2A, Pulse-on time = 70 μ s, Pulse-off time = 8.868 μ s, and Powder concentration = 2.929 g/l. The confirmation test (Table 5), a 3.36% error in SR, and a 2.12% error in MRR are found in powder mixed wire EDM. A total of 61.37% of surface roughness has improved in powder mixed WEDM compared to the conventional WEDM process. Also, 31.52% of MRR has been improved in powder mixed WEDM compared to the conventional WEDM process.

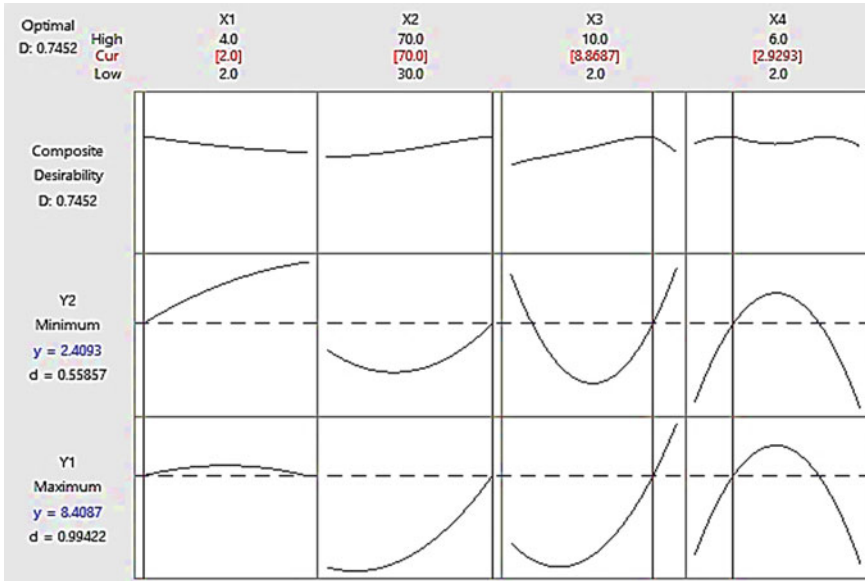


Fig. 8 Optimum parametric setting

Table 5 Confirmation test

Input parameter		SR			MRR		
		Predicted	Experimental	Error	Predicted	Experimental	Error
With powder	(I_p) 2A (T_{on}) 70 μ s (T_{off}) 8.868 μ s (PC) 2.929 g/l	2.409	2.493	3.36%	8.4	8.225	2.12%
Without powder	(I_p) 2A (T_{on}) 70 μ s (T_{off}) 8.868 μ s		4.023			5.632	

4 Conclusion

In the present study, following concluded remarks are presented as:

1. Powder with deionized water plays an essential role for enhancing the machining capability.
2. The contribution of each parameter on responses is explored by using sensitivity analysis. The results show that the highest contribution is found for powder concentration as an input variable and the other machining setting.
3. Al_2O_3 powder with dielectric provides maximum MRR and better surface topography on Ti6Al4V machined surface. Al_2O_3 with other defined parametric

settings can improve surface roughness upto 61.37% and MRR upto 31.52% compared with the WEDM process.

4. The defined set of input conditions is found using RSM methodology in the present study, such as peak current of 2A, pulse-off time of 70 μ s, pulse-on time of 8.868 μ s and abrasive concentration of 2.929 g/l. From the confirmation test, 3.36% error in SR and 2.12% error in MRR are found in powder mixed wire EDM, which is quite acceptable.

It can be concluded that the PMWEDM fulfilled bright promises of hybridization of the WEDM process, particularly with respect to quality as well as productivity. The proposed concept can be utilized for industrial application.

References

1. Li N, Yongzhong Z, Tong H, Xiaoxian C, Chenghui W (2014) β -Type Zr–Nb–Ti biomedical materials with high plasticity and low modulus for hard tissue replacements. *J Mech Behav Biomed Mater* 29:1–6
2. Ma Y, Li H, Yang L, Hu A (2018) Reaction-assisted diffusion bonding of Ti6Al4V alloys with Ti/Ni nanostructured multilayers. *J Mater Process Technol* 262:204–209
3. Nouari M, Makich H (2013) Experimental investigation on the effect of the material microstructure on tool wear when machining hard titanium alloys: Ti–6Al–4V and Ti-555. *Int J Refract Metal Hard Mater* 41:259–269
4. Chakraborty S, Mitra S, Bose D (2020) Performance analysis on eco-friendly machining of Ti6Al4V using powder mixed with different dielectrics in WEDM. *Int J Autom Mech Eng* 17(2):8128–8139. <https://doi.org/10.15282/ijame.17.3.2020.06.0610>
5. Rahul MDK, Datta S, Masanta M (2018) Effects of tool electrode on EDM performance of Ti–6Al–4V. *SILICON* 10:2263–2277
6. Pramanik A, Basak AK (2019) Effect of wire electric discharge machining (EDM) parameters on fatigue life of Ti–6Al–4V alloy. *Int J Fatigue* 128:1–9
7. Chakraborty S, Mitra S, Bose D (2021) An investigation on dimensional accuracy and surface topography in powder mixed WEDM using RSM and GRA-PCA. *Mater Today: Proc* 44(1):1524–1530
8. Shabgard M, Khosrozadeh B (2017) Investigation of carbon nanotube added dielectric on the surface characteristics and machining performance of Ti–6Al–4V alloy in EDM process. *J Manuf Process* 25:212–219
9. Bui VD, Wangi JWM, Schubert A (2019) Powder mixed electrical discharge machining for antibacterial coating on titanium implant surfaces. *J Manuf Processes* 44:261–270
10. Chakraborty S, Mitra S, Bose D (2020) Optimization of machining performance in PMWEDM of titanium alloy using hybrid technique (GRA-PCA). *Adv Mater Process Technol, TMPT* 1860500. <https://doi.org/10.1080/2374068X.2020.1860500>
11. Kumar A, Mandal A, Dixit AR et al (2020) Quantitative analysis of bubble size and electrodes gap at different dielectric conditions in powder mixed EDM process. *Int J Adv Manuf Technol* 107:3065–3075. <https://doi.org/10.1007/s00170-020-05189-x>
12. Nguyen H, Pham VD, Ngo NV (2018) Application of TOPSIS to Taguchi method for multi-characteristic optimization of electrical discharge machining with titanium powder mixed into dielectric fluid. *Int J Adv Manuf Technol* 98:1179–1198
13. Hourmand M, Sarhan AAD, Saeed F, Sayuti M (2019) Microstructure characterization and maximization of the material removal rate in nano-powder mixed EDM of Al–Mg2Si metal matrix composite—ANFIS and RSM approaches. *Int J Adv Manuf Technol* 101:2723–2737

14. Nguyen TD, Nguyen PH, Banh LT (2019) Die steel surface layer quality improvement in titanium μ -powder mixed die sinking electrical discharge machining. *Int J Adv Manuf Technol* 100:2637–2651
15. Tiwary AP, Pradhan BB, Bhattacharyya B (2018) Investigation on the effect of dielectrics during micro-electro-discharge machining of Ti–6Al–4V. *Int J Adv Manuf Technol* 95:861–874
16. Chakraborty S, Mitra S, Bose D (2019) Modeling & analysis of B4C powder mixed wire EDM process for improving performance criteria of Ti6Al4V. *IOP Conf Ser: Mater Sci Eng* 653:1–6
17. Kibria G, Doloi B, Bhattacharyya B (2013) Predictive model and process parameters optimization of Nd: YAG laser microturning of ceramics. *Int J Adv Manuf Technol* 65(1–4):213–229

Performance of a Single Point Cutting Tool with Textured Surfaces: A Comparative Study of Different Textured Patterns



Manoj Nikam, Anurag Karulkar, Aweek Chowdhury, Hasan Khalfay, and Darshan Rathod

Abstract Carbide Inserts are machining tools that are used for several machining operations such as turning, milling, boring, grooving, etc. Post conduction of experiments and calculations, surface texturing of a traditional carbide insert is deemed as a potential improvement in the performance of the tool under both dry and wet conditions. The current study presents a thorough investigation of how tool wear is affected by stress and its future impact on the operational life of the tool. This paper presents the influence of various micro textures on carbide inserts and how these textures affect the stress distribution at the tip and flank of the tool. The variation in stress concentration is assessed using a 3D Finite Element Model. The carbide insert undergoes a varied stress distribution for various textures on the upper surface of the tool while machining Mild Steel based on the Johnson–Cook Material Failure and Damage Criterion. Further ahead, these stress concentrations were validated by performing the same experiment on a CNC Lathe Machine, where volumetric wear was calculated theoretically for the initial and final weight of the inserts. The results of the study comprised of the stress distribution concerning the flank and crater wear of the tool and theoretical calculations of volumetric wear, in order to validate the most efficient micro texture which undergoes the least wear for specific machining parameters.

Keywords Carbide inserts · Micro textures · Wear · Stress distribution · Finite element model

M. Nikam (✉) · A. Karulkar · A. Chowdhury · H. Khalfay · D. Rathod
Mechanical Engineering, Bharati Vidyapeeth College of Engineering, Kharghar, Navi Mumbai
400614, India
e-mail: manoj.nikam@bvcoenm.edu.in

© The Author(s), under exclusive license to Springer Nature Singapore Pte Ltd. 2022
H. K. Dave et al. (eds.), *Recent Advances in Manufacturing Processes and Systems*,
Lecture Notes in Mechanical Engineering,
https://doi.org/10.1007/978-981-16-7787-8_62

777

1 Introduction

1.1 Background

Turning operation is one of the basic and widely employed machining processes in the industrial world [1]. Most common carbide inserts are fabricated of high-grade materials which have a specific tool life after which they cannot perform with the required finesse and need to be replaced [2]. Microtextures are shapes that are primarily etched onto the top face and leading edge of the tools. These textures change the volume and composition of the tool and cause variations in the stresses involved, thus influencing the tool life [3, 4].

1.2 Classification of Tool Wear

There are numerous types of wear, classified by the position of the wear on the tool and the degree of it. Cutting tool wear is classified into flank wear, crater wear, notch wear, abrasive wear, adhesive wear, etc. One of the most common tools wears is flank wear. Wear on the flank face (relief or clearance face) of the cutting tool is called flank wear [5]. Flank Wear is most commonly caused due to abrasion of the cutting edge against the machined surface. Flank Wear generally occurs when the speed of cutting is very high. Crater wear occurs on the device face at a short distance from the cutting edge due to activity of chip stream over the face at extremely high temperatures [6]. Nose wear destroys the instrument corner. If the wear is caused by hard particles or sharp tips on a surface the wear is called abrasive wear. The loss of material, in this case, is dominated by chip forming, brittle fracture, or fatigue. If a sharp tip from one surface ploughs a groove in the other surface it is denominated two-part abrasion. If it is a particle between two surfaces that causes the wear it is denominated three-part abrasion. Adhesive wear occurs when two solids are in sliding contact and the atomic bonding forces present between the materials on the interface are stronger than the strength of the surrounding area in either of the materials [4]. Already in the early works in tribology, it was recognized that the amount of wear is proportional to the applied load and sliding [7]. Adhesive wear is one of the most frequently encountered types of wear in dry cutting operations.

1.3 Effect of Micro Textures on Machining Operation

Micro Texturing is a well-established approach towards improved machining. Micro texturing involves various parameters such as pit diameter, pit depth and pitch between the pits. The textured inserts give a significant improvement in performance when compared to non-textured inserts. There is a major effect of surface

texturing of cutting tools on the reduction of friction force and the material adhesion between tool-chip interfaces [8]. It creates a big difference in tribological performance on the tool surface. Micro textures give several advantages over traditional non-textured tools [9]. Micro Textures give improved performance and better tool life for both dry and wet cutting conditions. There is an increment in wear resistance with a better stress distribution. The textures also act as reservoirs to store lubricant during wet condition machining and act as air pockets which helps aid cooling for the dry cutting conditions. Current study focuses on enhancing the turning operations, by using multiple micro-textured inserts where turning is performed by keeping the machining parameters constant for all textured inserts. The volumetric wear of the tool is measured post turning operation and the stresses are calculated by performing finite element analysis setting up the physical parameters in the ANSYS® application.

2 Methodology

2.1 Design and Characteristics of Material

The cutting insert used in current study is Widia CNMA 120404 THM. The workpiece used in the turning operation is of mild steel. Distinctive nine nos. of microtextures patterns were chosen and etched onto the cutting insert samples. These microtextures were selected as they were feasible to be fabricated and have been previously used on carbide inserts, as evident during literature survey. The tool itself and the microtextures for different shapes and dimensions were designed using the CAD software—PTC Creo® (Figs. 1 and 2; Tables 1 and 2).

The failure or fracture of mild steel is analyzed by considering the Johnson Cooks Material model of failure and Damage model [10]. It mainly depends on three factors altogether viz. deformation under strain, strain rate and temperature.

The model (equation) devised is:

$$\sigma = (A + B\varepsilon^n)(1 + C \ln \varepsilon^*)(1 + T * m) \tag{1}$$

where, σ is the (Von Mises) flow stress, A is the yield stress which is 217 MPa at reference temperature and reference strain rate, B is the coefficient of strain hardening

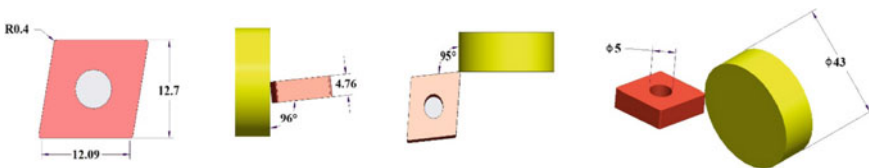


Fig. 1 3D model of assembly

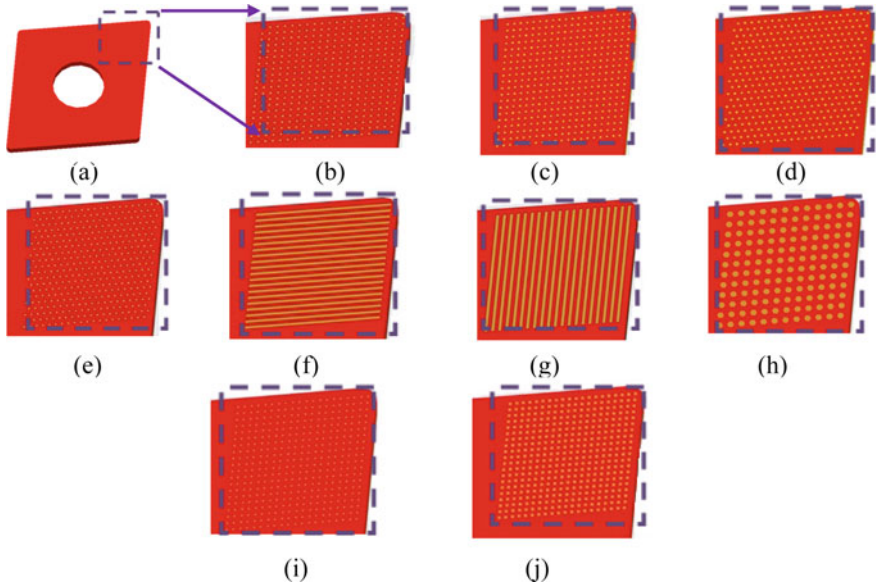


Fig. 2 a Non-textured, b circular pitted 1, c circular pitted 2, d circular cross pitted 1, e circular cross pitted 2, f parallel grooved, g perpendicular grooved, h hexagonal pitted, i triangular pitted, j square pitted

Table 1 Properties of tool and work piece

Physical properties	Work piece	Tool
Material	Mild steel	Carbide (WC = 96.4% and Co = 2.19%)
Density (g/cm ³)	7.85	15.2
Youngs modulus (Pa)	2×10^{11}	7.02×10^{11}
Poisson's ratio	0.3	0.21
Specific heat capacity (J/kg K)	510	350

which is 233.7 MPa, n is 0.66428 which is the strain hardening exponent, ϵ is the plastic strain, $\epsilon^* = \epsilon/\epsilon_{ref}$ is the dimensionless strain rate, C is 1 and m is the material constant which represents the coefficient of strain hardening and thermal softening and T^{*m} is the melting temperature which is 1530 °C. JC Damage model is obtained by introducing a scalar damage variable D1–D5 [11]. When $D = 0$ it indicates no damage and when $D = 1$ it indicates complete damage and the material has lost its load-carrying capacity. Where $D1 = 0.8$, $D2 = 2.1$, $D3 = -0.5$, $D4 = 0.0002$ and $D5 = 0.61$ are the scalar damage constants or model parameters.

Table 2 Micro-texture dimensions

Micro texture		Dimension (in μm)			
Pattern	Sample name	Side length/diameter (l)	Spacing (a)	Depth (d)	Width (w)
(a) Non-textured	S1	–	–	–	–
(b) Circular pitted-1	S2	100	200	20	100
(c) Circular pitted-2	S3	75	200	20	100
(d) Circular cross pitted-1	S4	100	200	20	100
(e) Circular cross pitted-2	S5	75	200	20	100
(f) Parallel grooved	S6	4000	200	20	100
(g) Perpendicular grooved	S7	4000	200	20	100
(h) Hexagonal pitted	S8	100	200	20	100
(i) Triangular pitted	S9	100	200	20	100
(j) Square pitted	S10	100	200	20	100

2.2 Simulation

Finite element analysis is carried out to determine and understand the stress distribution and maximum stress which is experienced by different micro-textured carbide inserts [12]. Explicit Dynamics Analysis is used in Ansys Mechanical, where the meshing considered for the tool and the work piece is tetrahedrons and adaptive meshing at the tool and work piece interface and fine meshing at the microtextures for close to accurate stress distribution [13]. Tetrahedron meshing is preferred over the hex mesh model to avoid the hourglass effect and distortion of the elements on contact. The contact and interaction between the two surfaces are considered to be frictional with the assumed standard coefficient of friction of 0.4 [14]. The tool was assumed to be rigid and elastic and the work piece was assumed to be visco-plastic. The machining conditions which were considered during the simulation and actual experiment where, spindle speed (S) = 500 RPM, Depth of Cut (ap) = 0.5 mm and Feed (f) = 0.2 mm/rev (Fig. 3).

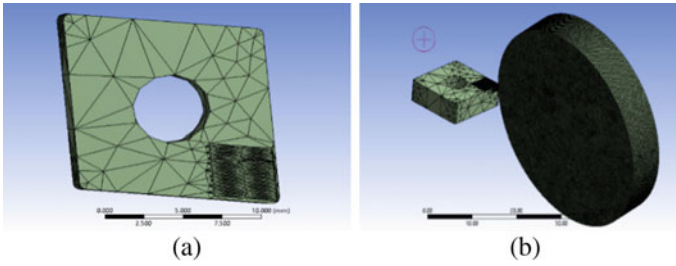


Fig. 3 a Meshing tool, b meshing assembly

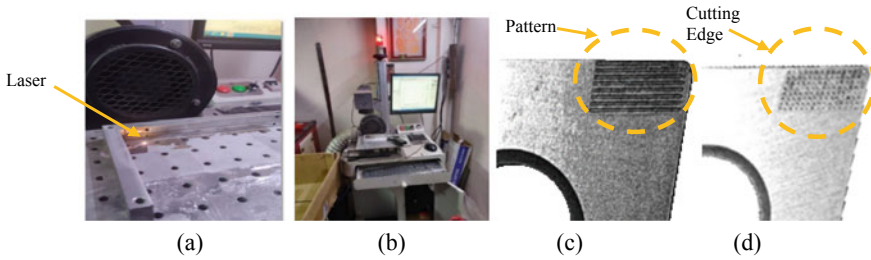


Fig. 4 a Laser process, b laser machine and control unit, c sample insert 1, d sample insert 2

2.2.1 Laser Cutting

Micro Texturing can be achieved by several techniques out of which laser cutting is the most prominent and accurate method. The laser used falls under the Marking and Engraving category, which was built by JPT Opto-Electronics. The laser was a fibre laser, which was operating on EZCAD[®] for importing .dxf and .plt files of the design. The laser was operating at power capacity, i.e. 20 W, 30 V at a frequency of 60 Hz. The loop count for the laser was 40 at a speed and height difference of 100 mm/s and 168 mm respectively (Fig. 4).

2.2.2 Experimental Setup

As a part of the initial setup, in order to find the volumetric wear due to machining conditions, the initial weight of each carbide insert after the micro texturing was noted down in order to compare with the resultant weight after the machining process using a weighing scale (in milligrams). The following table shows the weight and volume (calculated by density) of each carbide insert [15]. The selection of the carbide inserts for the experimental process was based on the least stress distribution and varied pattern shapes obtained through literature survey and finding the common pattern and grooves for the same machining parameters as in the simulation, i.e. Spindle

Speed (S) = 500RPM, Depth of Cut (a_p) = 0.5 mm and Feed (f) = 0.2 mm/rev (Fig. 5; Table 3).

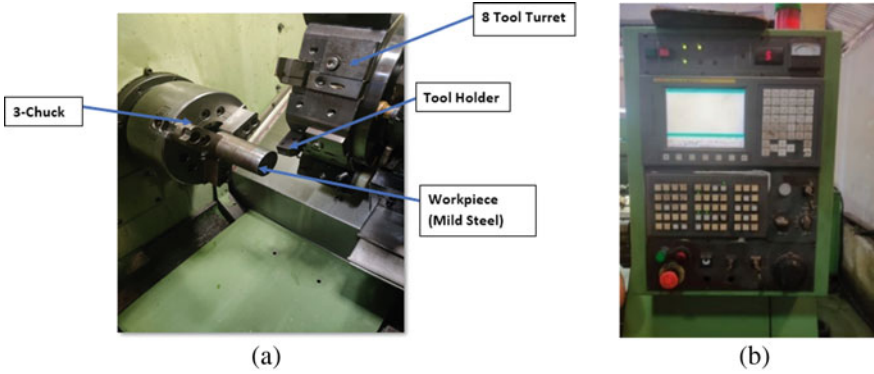


Fig. 5 a Turning operation, b control panel

Table 3 Observation table of turning operation

Sample No.	Wi (g)	Vi (mm ³)	Job diameter		LOC (mm)	Time (min)	Total time (min)
			Start (mm)	End (mm)			
S1	10.202	649.808	33	32	50	0.633	1.203
			32	31	50	0.659	
S2	10.070	641.401	43	42	50	0.6	1.203
			42	41	50	0.603	
S6	10.069	641.337	41	40	50	0.6	1.203
			40	39	50	0.603	
S7	10.193	649.235	39	38	50	0.6	1.203
			38	37	50	0.603	
S9	10.078	641.910	35	34	50	0.6	1.203
			34	33	50	0.603	
S10	10.180	648.407	37	36	50	0.6	1.203
			36	35	50	0.603	

3 Results and Discussions

3.1 FEM Simulation Results

As per the simulation conducted through FEM analysis using ANSYS® Mechanical for Explicit Dynamics were achieved for the given parameters for the assigned micro textures. The results for the non-textured Carbide Insert (S1) where the stress attained was maximum and the results for the triangular pitted tool (S9) can be seen in Fig. 6. With respect to the simulation carried out, it is seen that in Fig. 7a, b the stress and strain is highest for non-textured tool (S1) and is the lowest for triangular pitted tool (S9). The stress value plateaus for pitted tools (S2–S5, S8–S10) with a difference of ±10 MPa for the same. Apart from the least maximum Von Mises stress and strain observed, the most effective stress distribution has been observed for the circular pitted (S2). Both circular (S2) and circular cross pitted (S4) micro textures with diameter 100 μm have better stress distribution and lower stress values than Circular Pitted (S3) and Circular Cross Pitted (S5) with a diameter of 75 μm advocating the fact that bigger the pit diameter better the stress effect and distribution.

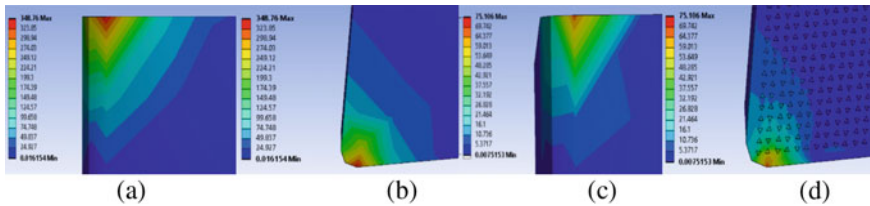


Fig. 6 Von Mises stress **a** Front view of non-textured tool, **b** top view of non-textured tool, **c** front view of triangle pitted tool, **d** top view of triangle pitted tool

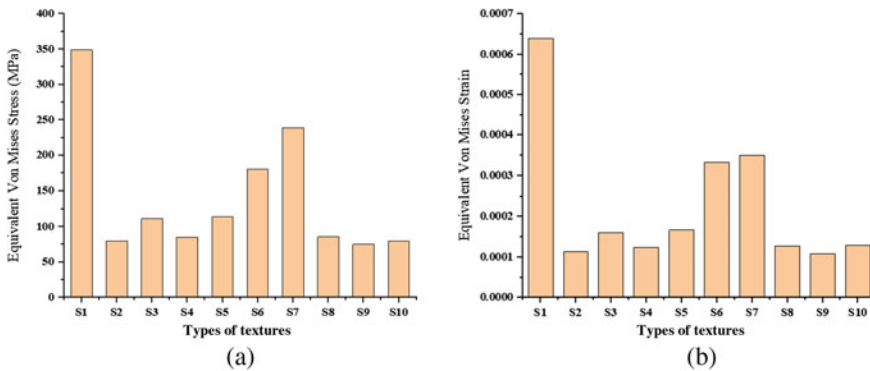


Fig. 7 **a** Graph of Equivalent Von Mises stress versus types of textures, **b** Equivalent Von Mises strain versus types of textures

Table 4 Experimental results of volumetric wear and wear rate

Sample No.	Wi (g)	Vi (mm ³)	Time (min)	% Change weight	% Change volume	Wear rate ($\frac{\text{mm}^3}{\text{min}}$)	Wear (mm ³)
S1	10.202	649.8	1.203	-0.025	-0.026	0.137	0.165
S2	10.070	641.4	1.203	-0.019	-0.019	0.105	0.127
S6	10.069	641.3	1.203	-0.023	-0.021	0.117	0.140
S7	10.193	649.2	1.203	-0.022	-0.022	0.121	0.146
S9	10.078	641.9	1.203	-0.018	-0.017	0.095	0.114
S10	10.180	648.4	1.203	-0.020	-0.019	0.100	0.121

3.2 Experimental Results and Calculations

With respect to the results achieved from the simulation, in this paper we consider the carbide inserts with the following patterns: Circular Pitted 1 (S2), Parallel Grooved (S6), Perpendicular Grooved (S7), Triangular Pitted (S9) and Square Pitted (S10) to calculate the volumetric wear [16] as per the formula:

$$\text{Volumetric Wear Rate} = \frac{W_i - W_f}{\rho T} \text{mm}^3/\text{min} \quad (2)$$

where W_f is the final weight, W_i is the initial weight, ρ is density in (g/mm³) and T is machining time in min. According to the formula above, the wear rate is calculated and compared with the results achieved from the FEM analysis (Table 4).

As per the experiment conducted, it can be observed that the triangular pitted tool (S9) undergoes the least amount of wear and carries the least wear rate under constant machining parameters. By understanding the effects of the stress using FEM analysis and considering the experimental results, it can be observed that the triangular pitted tool (S9) is the most effective micro texture concerning wear, wear rate and Von Mises stresses (Fig. 8).

3.3 Characterization of Wear

See Fig. 9.

As per the imaging done using the Alicona Surface Profilometer, a deep understanding of the topology of the tool face and flank has been carried out for each micro-textured insert. As seen in Table 5, the weight difference for the triangular pitted tool (S9) is the least and the maximum adhesion by weight is observed in the circular pitted tool (S2). But the weight difference for the non-textured tool (S1) is maximum, suggesting that adhesion through increasing the weight by milligrams, is not the only governing factor for tool wear. Since the weight difference is maximum

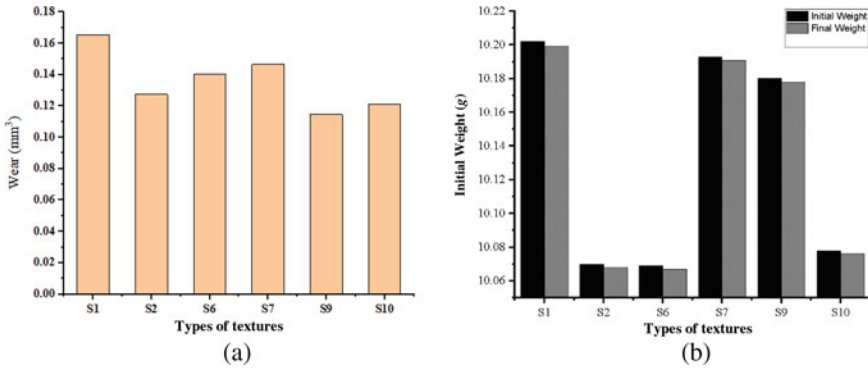


Fig. 8 a Graph of wear versus textures, b W_i W_f versus types of textures

for non-textured carbide insert, we can conclude that crater wear, flank wear has highly affected the non-textured insert and had the least effect on the triangular pitted tool. According to the imaging, it can be easily concluded how wear-adhesive, flank, crater and notch vary and behave as per the microtextures and their dimensions. It can be observed how adhesive wear plays a vital role and is an unwanted result due to dry cutting. It is advocated that in case of wet cutting, wear that occurred would have been of less magnitude and the adhesive wear that occurred would have been negligible. Adhesion of the work piece on the insert edge is an eventuality due to the high forces, high energy and heat generated during the machining process [4]. The adhesion that has occurred can be studied using processes such as the Energy Dispersive X-Ray Spectroscopy (EDS) or the X-Ray Diffraction Analysis (XRD) which helps to determine the intensity of the components present in a thin film (microns), layer, micro-body, etc. This study gives us the composition of the material which has been adhered to the tool edge, which is to be the imminent interface for the next machining process between the tool and the work piece.

3.4 Side Grooving Analysis

After certain experiments, studies and research of microtextures and their effect on tool wear and how the composition of adhesive wear can be studied, a new study regarding the placement of microtextures was considered. Microtextures, though traditionally have been etched and experimented with on the top face of the leading edge of the cutting tool, the implementation of these microtextures on the flank of the carbide tool has to be considered as well. This technique has been implemented in this study just as part of a FEM analysis, as the fabrication of microtextures on the flank of the carbide insert is complicated and not feasible. For simplification and ease of understanding the basics of this study, the microtextures considered within the experimental setup are recalled here with grooves on their flanks. The length of

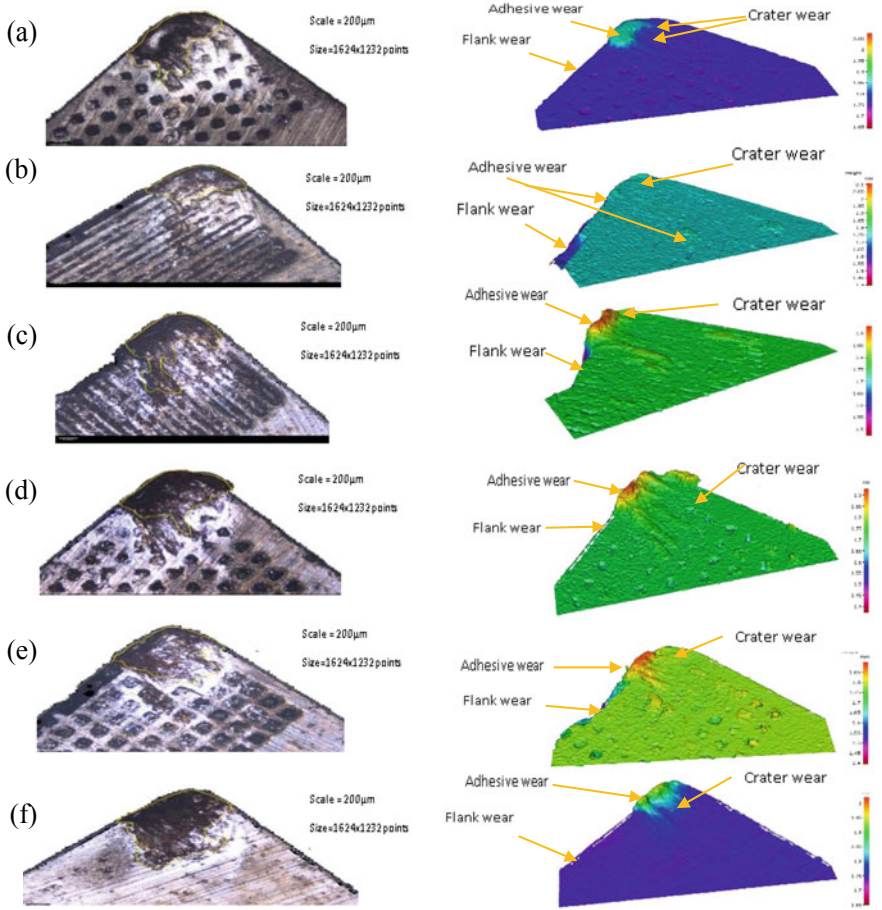


Fig. 9 Optical images of **a** Circular pitted, **b** parallel grooved, **c** perpendicular grooved, **d** triangular pitted, **e** square pitted, **f** Non-textured tool

Table 5 Characterization of adhesive wear

Sample	V_a (mm ³)	ρ (g/mm ³)	W_a (g)	W_f (g)	W_i (g)	W_a' (g)	W_{diff} (g)
S1	0.00354	0.0157	5.57E-05	10.1994	10.2021	10.199	0.00264
S2	0.00852	0.0157	13.38E-05	10.068	10.070	10.068	0.00186
S6	0.00164	0.0157	2.58E-05	10.0668	10.069	10.066	0.00237
S7	0.00709	0.0157	11.13E-05	10.1907	10.193	10.190	0.00218
S9	0.00735	0.0157	11.55E-05	10.0762	10.078	10.076	0.00168
S10	0.00556	0.0157	8.74E-05	10.1781	10.180	10.178	0.00191

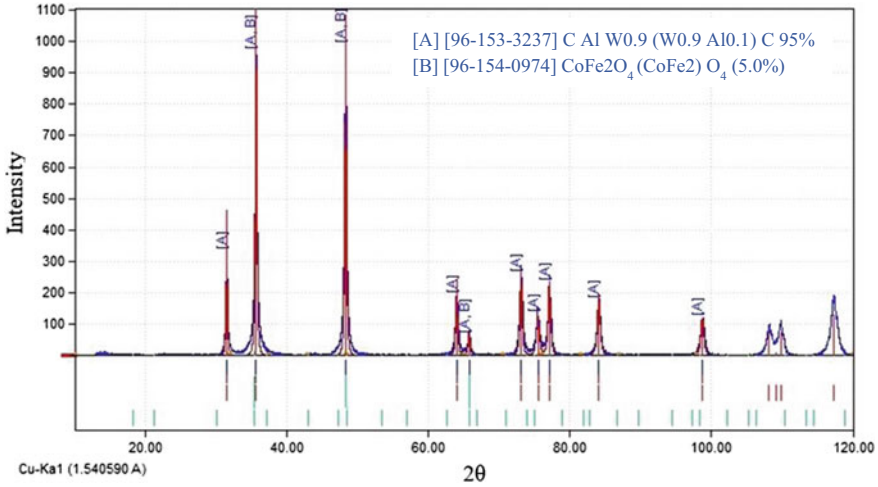


Fig. 10 XRD analysis

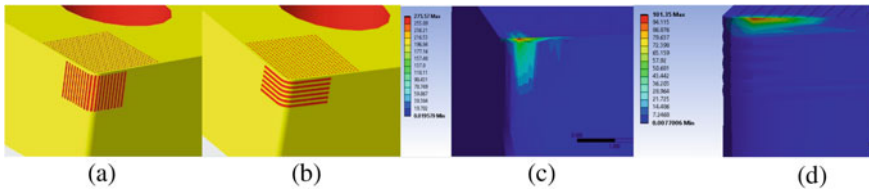


Fig. 11 a Circular pitted tool with vertical grooves, b Circular pitted with horizontal grooves

the grooves is 400 μm , width is 100 μm , depth is 20 μm , the centre distance between successive grooves is 200 μm and the total number of grooves are 6 (horizontal) and 20 (vertical) (Figs. 10 and 11).

4 Conclusion

As per the experiment and simulations performed, the following conclusions can be made and asserted regarding micro-textured carbide inserts and their behaviour with respect to machining operations, stress distribution and tool wear:

1. After observing the difference in maximum stress and stress distribution for circular pitted (S2, S3) and circular cross pitted (S4, S5) textures for diameters of 75 μm and 100 μm each, it can be concluded that greater the dimensions of the pit, lesser is the stress-induced and better is the stress distribution.
2. The experiment conducted for the micro-textured carbide inserts validates the relation between wear and stress-induced on the insert, as the triangular pitted

tool undergoes the least amount of volumetric wear and the non-textured insert undergoes the maximum amount of wear. From optical images, the types of wear observed on the leading edge of the tool were adhesive wear, flank wear and crater wear.

3. Adhesive wear is a result of the dry cutting operation, where adhesion of the work piece material takes place on the face and cutting edge of the tool. The mass and volume of the adhered material vary concerning the micro texture, where maximum adhesion by weight takes place for the circular pitted tool, but the crater and flank wear also play a vital role in the same, which results in the least amount of wear for triangular pitted tool and maximum amount of wear for the non-textured carbide insert.
4. Machining conditions play a significant role in determining tool wear; and tool life can be maximized by optimizing the machining parameters or by considering a wet operating condition, i.e. use of coolant which would result in a decrease in overall tool wear.
5. Micro Texturing of simple grooves on the flank or leading edge of the tool has a different and negative effect on the stress distribution and strain which generates on the tool during machining conditions and can be studied further by changing the dimension and type of grooves for the same.

Appendix

n	Strain Hardening Exponent
m	Thermal Softening Coefficient
$T^* m$	Melting Temperature
ϵ^*	Strain Rate
D1–D5	Scalar Damage Constants for Mild Steel
a	Centre Distance
l	Length/Diameter
d	Groove Depth
w	Groove Width
σ	Von Mises Stress (MPa)
A	Yield Stress (MPa)
B	Coefficient of Strain Hardening (MPa)
C	Strengthening Coefficient of Strain Rate
S	Spindle Speed (RPM)
ap	Depth of Cut (mm)
f	feed (mm/rev)
W_i	Initial Weight (g)
V_i	Initial Volume (mm ³)
W_f	Final Weight (g)
V_f	Final Volume (mm ³)

LOC	Length of Cut (mm)
ρ	Density (g/mm^3)
V_a	Volume of Adhesive Material (mm^3)
W_a	Weight of Adhesion (g)
W_a	Weight without Adhesion (g)
W_{dif}	Weight Difference (g)

References

1. Milling S, Aluminum OF (2015) Optimization of machining parameters in high. *Int J Sci Res Eng Technol* 4(8)
2. Umbert SM (2017) Cutting forces in turning operations. Dept. Mech. Ind. Engr. Nowegian Univ. Sci. Technol., p 74
3. Ma J, Duong NH, Lei S (2015) Finite element investigation of friction and wear of microgrooved cutting tool in dry machining of AISI 1045 steel. *Proc Inst Mech Eng Part J J Eng Tribol* 229(4):449–464
4. Siju AS, Gajrani KK, Joshi SS (2021) Dual textured carbide tools for dry machining of titanium alloys. *Int J Refract Met Hard Mater* 94(June 2020):105403
5. Tamizharasan T, Selvaraj T, Haq AN (2006) Analysis of tool wear and surface finish in hard turning. *Int J Adv Manuf Technol* 28(7–8):671–679
6. Devaraj S, Malkapuram R, Singaravel B (2021) Performance analysis of micro textured cutting insert design parameters on machining of Al-MMC in turning process. *Int J Light Mater Manuf* 4(2):210–217
7. Nikam MD, Shimpi D, Bhole K, Mastud SA (2019) Design and development of surface texture for tribological application. *Key Eng Mater*, pp 55–59
8. Nikam MD, Jadhav SP, Khetri SD, Sawant PK (2020) Surface texture to reduce friction coefficient. *Test Eng Manag* 82(7813):7813–7818
9. Li Q, Pan C, Jiao Y, Hu K (2019) Investigation on cutting performance of micro-textured cutting tools. *Micromachines* 10(6)
10. Vedantam K, Bajaj D, Brar S, Hill S (2006) Johnson–Cook strength models for Mild And. *Aerosp Eng*, pp 1503–1506
11. Rasae S, Mirzaei AH, Almasi D (2020) Constitutive modelling of Al7075 using the Johnson–Cook model. *Bull Mater Sci* 43(1)
12. Cakir MC, Isik Y (2005) Finite element analysis of cutting tools prior to fracture in hard turning operations. *Mater Des* 26(2):105–112
13. Sai Venkatesh S, Ram Kumar TA, Blalakumhren AP, Saimurugan M, Prakash Marimuthu K (2019) Finite element simulation and experimental validation of the effect of tool wear on cutting forces in turning operation. *Mech Mech Eng* 23(1):297–302
14. Wu Z, Bao H, Liu L, Xing Y, Huang P, Zhao G (2020) Numerical investigation of the performance of micro-textured cutting tools in cutting of Ti–6Al–4V alloys. *Int J Adv Manuf Technol* 108(1–2):463–474
15. Talib RJ, Zaharah AM, Selamat MA, Mahaidin AA, Fazira MF (2013) friction and wear characteristics of WC and TiCN-coated insert in turning carbon steel workpiece. *Procedia Eng* 68:716–722
16. Al Kindi Y, Murali RV, Salim RK (2018) Tool wear investigation in CNC turning operation. *Lect Notes Eng Comput Sci* 2236:457–461

Post Processing 3D Printed UAV Wing Enabling Trailing Edge Morphing Technology



Krunalkumar N. Patel, Anirudh Manoj, Mohammed Shams H. Sayed,
K. Shah Kaushal, Swayam J. Shah, and Harshit K. Dave

Abstract In recent years, significant researches focus on improving aircraft efficiency using morphing wing technology. Altering the camber of the wing during flight, it can be advantageous for controlling the aerial vehicle during specific flight conditions by changing the lift distribution along the wing. A flexible trailing edge can be used to achieve chord as well as spanwise differential camber variation with the same structural system. It can effectively replace the use of ailerons/elevons. The bell-shaped lift distribution (BSLD) has recently come into the limelight because of its design for minimum induced drag while at the same time having the added advantage of generating proverse yaw, i.e., yawing and rolling in the same direction. In general, wings that are designed on the BSLD to generate vortexes at the seventy percent span location and not at the tips of the wing. Due to this configuration, upwash is generated at the outer thirty percent of the wing. Fused deposition modeling (FDM) is an additive manufacturing (AM) technique used in the present work to fabricate the UAV wing. polylactic acid (PLA) feedstock filament is used as raw material for FDM printing. Post processing has been done on a 3D printed UAV part to get desired flexibility for enabling trailing edge morphing.

K. N. Patel · A. Manoj (✉) · M. S. H. Sayed · K. Shah Kaushal · S. J. Shah · H. K. Dave
Sardar Vallabhbhai National Institute of Technology, Surat, India
e-mail: u17me008@med.svnit.ac.in

K. N. Patel
e-mail: u17me019@med.svnit.ac.in

M. S. H. Sayed
e-mail: u17me006@med.svnit.ac.in

K. Shah Kaushal
e-mail: u17me017@med.svnit.ac.in

S. J. Shah
e-mail: u17me011@med.svnit.ac.in

H. K. Dave
e-mail: hkd@med.svnit.ac.in

Keywords UAV · Bell-shaped lift distribution · Proverse yaw · Fused deposition modeling · PLA · Trailing edge morphing · Post processing

1 Introduction

Ludwig Prandtl published “lifting line” theory, which allowed the computation of lift and drag for a given wing. Using this tool, the best span load for the least amount of induced drag for a particular span was determined [1]. However, in the later years, Prandtl published another research work where it was found that the previously derived solution was incomplete. Also, a much more superior spanload can be used to achieve minimum induced drag for a given structural weight/root bending moment. This newly derived bell-shaped spanload would create an 11% more efficient wing but 22% greater span than the previously derived elliptical span load [2]. Reimar Horten calculated the induced drag and studied the impact of BSLD, which eliminated the need for a vertical stabilizer all together due to the proverse yaw generated. The aircraft can thus be controlled by actuating control surfaces installed on the outer 30% of the wing span. This concept was recently validated under the project PRANDTL-D conducted by NASA Armstrong Flight Research Center [3]. Due to the upwash generated at the outer span, the control surfaces actuated here are responsible for maneuvering the aircraft (roll and yaw). Morphing airfoil ribs are used to have a more sensitive and smooth control over the maneuvers compared to the conventional control surfaces. The trailing edge morphing airfoil technology has been used to alter the symmetrical airfoil ribs [4].

This particular wing design involves a nonlinear variation of the geometric twist and interpolated airfoil geometries along the span of the wing with complex inner features that are challenging to fabricate using conventional manufacturing methods. The capability to fabricate complex inner features directly without the mold gives additive manufacturing (AM) an advantage over other manufacturing techniques [5]. Recent development in different 3D printing processes opens up new prospects of printing lightweight structures with better mechanical properties. AM processes being the manufacturing techniques where the parts are manufactured layer by layer. Researchers have used different AM processes for the aerospace applications to fabricate the part from metals, ceramics, and composites [6–8]. From the various AM techniques, Fused deposition modeling (FDM) is a widely used process. Many FDM printed parts have been implemented in NASA’s Mars rover due to their lightweight and better durability [9].

Several researchers have used the FDM technique to fabricate the various aerospace components. Carneiro and Gamba [10] used the FDM process to fabricate the wing ribs from polylactic acid (PLA) material. From the structural analysis of the ribs, they have concluded that stiffness of the part is limiting factor rather than the strength. Easter et al. [11] successfully 3D printed UAV parts using acrylonitrile butadiene styrene (ABS) filament with an FDM machine. They have conducted flight testing and found that the 3D printed parts had better survivability. Michelson

et al. [12] 3D printed strong wing ribs for the entomopter structure using FDM. The University of Sheffield Advanced Manufacturing Research Center (AMRC) used FDM to fabricate a blended-wing-body UAV. Their results showed that FDM made part resulted into lower cost and reduced processing steps [13]. Zhang et al. [14] 3D printed frame, tail, and gears for UAV using ABS material. However, they concluded that the ABS cannot provide sufficient strength to the parts. To improve the strength of the parts, they have used the reinforcement of carbon fiber and polyester films. The post processing of the FDM printed components is also an important aspect. Several researchers have applied the different post processing techniques to the FDM printed components for improving mechanical properties as well as part quality in terms of surface finish. Guduru and Srinivasu [15] investigated the effect of two different post processing methods viz., chemical treatment and heat treatment. They have found that though both post processing techniques improved the mechanical properties of the parts, chemical treatment gave better results as compared to the heat treatment. Galantucci et al. [16] used sand blasting as a post processing and found that the surface roughness can be improved by 96%. McCullough and Yadavalli [17] used acetone dipping for the surface finishing of FDM printed ABS samples.

From the literature study, it is observed that researchers have started using FDM as a manufacturing technique for aerospace application parts. Some post processing can also be applied in these parts to get required properties. Therefore, in the present research work, FDM was chosen to fabricate the airfoil ribs of the UAV. PLA feed-stock filament was used as a raw material. A novel post processing method that increases the flexibility of the rib in the desired regions was implemented.

2 Design and Validation

2.1 Airfoil Selection

The preliminary airfoil selection was made on the different requirements viz., low drag, moderate lift and near zero pitching moment. The airfoil for this tailless configuration aircraft is selected so that they have a pitching moment that is nearly equal to zero ($C_m = 0$) to aid the stability requirement. Since the aircraft is designed based on the bell-shaped spanwise lift distribution, the loads taper to zero toward the tips. The use of symmetric airfoil toward the tips helps to achieve zero lift by changing the AOA to counter the upwash and structural weight.

2.2 Preliminary Design Parameters

As shown in Table 1, the design parameters were fixed after careful evaluation of flight requirements and manufacturing constraints in terms of span.

Table 1 UAV design parameters

Wing area S [m ²]	0.19
Aspect ratio	11
Taper	0.4
Sweep LE [deg.]	20
Span b [m]	1.4
Real root chord [m]	0.1877
Tip chord [m]	0.0751
1/4 chord sweep [deg.]	18.003
Tip offset H [m]	0.2629

2.3 Lift Distribution and Twist Distribution

Prandtl's 1933 solution is stated in Eqs. (1) and (2)

$$L = (1 - x^2)^{(3/2)} \quad (1)$$

where “ L ” is the non-dimensional local load (this is also expressed as gamma), “ x ” is the span location between 0 and 1.

Subsequently,

$$DW = \frac{3}{2}(x^2 - 1/2) \quad (2)$$

where DW is the non-dimensional downwash (angle) of the flow. The lift approaches zero at the wingtip. The twist at various span locations was calculated using the lifting line theory for the bell-shaped lift equation as shown in Table 2.

2.4 XFLR5 Simulation

Using these parameters, a UAV model, as shown in Fig. 1 in XFLR5 [18], was modeled and wing analysis has been done to generate and validate various graph plots. Figure 2 shows the superimposition of BSLD on the UAV model. From Fig. 2, it is observed that a seamless bell shape has been achieved.

Moreover, the upwash/downwash results also validate the acclaimed upwash generation assertions as shown in Fig. 3. Vortexes were generated when downwash transcends into upwash. Thus, this result also proves the concept of vortex generation at around 70% of wingspan. After validating the design parameters, these parameters were used to model UAV using SolidWorks as shown in Fig. 4.

Table 2 Twist distribution across the span

	w upwash [m/s]	Alpha induced [°]	Span location	Local chord	Local LE offset [m]	Geometric twist [°]
Root	-0.506	1.9	0	0.187	0	7.09
2	-0.49	1.9	0.083	0.178	0.022	7.47
3	-0.47	1.8	0.1666	0.168	0.043	7.68
4	-0.44	1.71	0.25	0.158	0.065	7.69
5	-0.39	1.58	0.33	0.15	0.087	7.49
6	-0.33	1.29	0.416	0.14	0.109	7.06
7	-0.25	0.999	0.5	0.138	0.131	6.4
8	-0.16	0.66	0.583	0.12	0.153	5.47
9	-0.05	0.21	0.66	0.11	0.175	4.3
10	0.06	-0.2	0.75	0.1	0.1975	2.86
11	0.19	-0.7	0.83	0.093	0.213	1.24
12	0.34	-1.3	0.916	0.081	0.241	-0.55
Tip	0.5	-1.98	1	0.07	0.26	-1.9

Fig. 1 UAV model

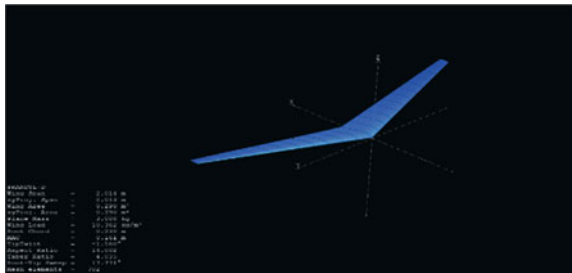


Fig. 2 Results of lift distribution using vortex lattice method

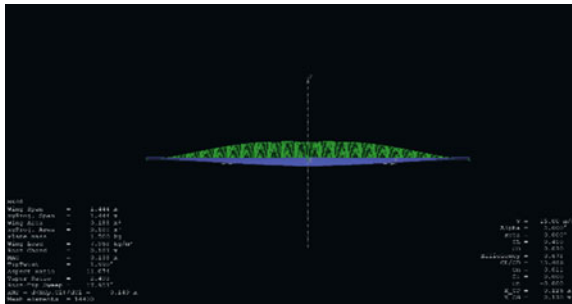


Fig. 3 Downwash/upwash distribution across span

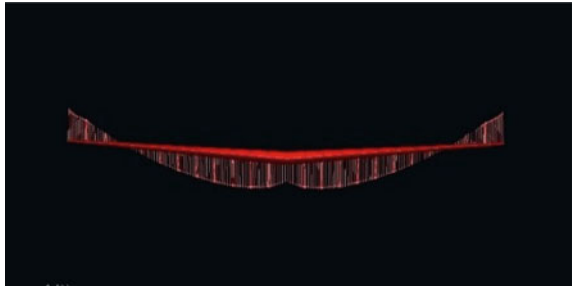
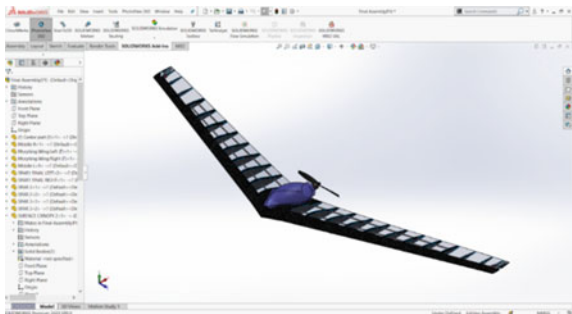


Fig. 4 UAV CAD model in SOLID WORKS



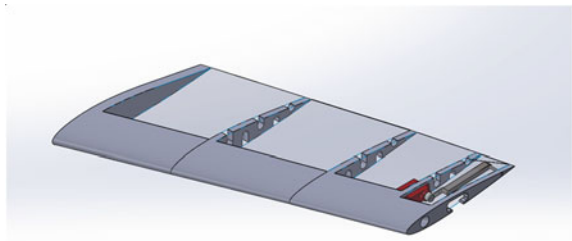
3 Morphing Wing for UAV

3.1 Morphing Wing Mechanisms

For this section of the wing, airfoil morphing with a variable chamber was used. The trailing edge of the last 30% of the wing was morphed using a simple servo actuated rocker arm mechanism. The morphing mechanism for PRANDTL-D is shown in Fig. 5.

This trailing airfoil morphing is used instead of elevons as a control surface. This is because typical ailerons cause discontinuity in the airflow and produce drag. So,

Fig. 5 Morphing mechanisms for PRANDTL-D



the advantage of using this type of morphing is a continuous airflow that does not cause flow separation while actuation [19]. The skin of the wing is stretched and separately assembled on the rib structure to provide the aerodynamic shape to the wing.

3.2 Morphing Wing Ribs Analysis

The control surface in the wing plays a vital role in piloting the aircraft, thereby making it essential to sustain the stresses generated. Therefore, Ansys structural analysis was carried out on the moving section of the part, which will be subjected to direct torque from the micro servo [20]. The maximum force that can be applied by the micro servo was found to be 0.94 N. Upon meshing the parts, the force was applied to the respective surfaces along with necessary fixed supports.

The results obtained from two different rib designs are shown in Figs. 6 and 7. The total deformation and von Mises stress generated in each of the moving parts are shown in the images. The total deformation as well as the von Mises stresses generated in the ribs for morphing wing were found to be within the limits for the particular application. However, it is observed that better flexibility was achieved in RIB1 as compared to RIB2.

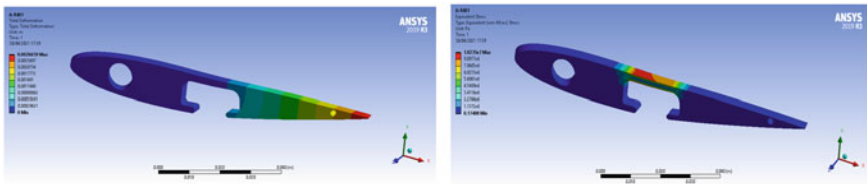


Fig. 6 Total deformation and equivalent von Mises stress for RIB1

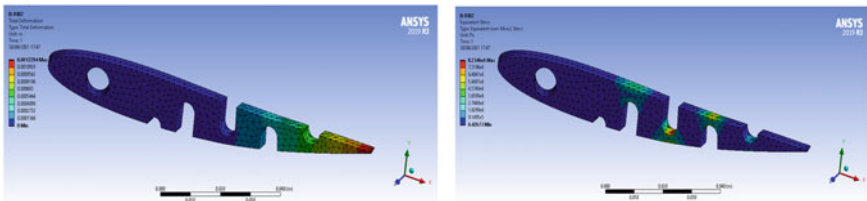


Fig. 7 Total deformation and equivalent von Mises stress for RIB2

4 Additive Manufacturing of Morphing Wing

After completing the design and modeling followed by an analysis of the UAV, 3D printing of the UAV has been carried out using the FDM process. Testing of the proposed morphing wing mechanisms was of utmost priority as the aircraft's dynamics, stability, and maneuverability were highly dependent on its performance. In general, the standard 3D printing filament used to fabricate flexible parts is TPU/TPE. However, considering the mechanical properties required by the wing to maintain its structural integrity, it was decided to 3D print with PLA with post processing instead of directly printing using flexible TPU filament.

4.1 FDM Process Parameters

The mechanical properties of FDM printed components were found to be primarily dependent on the orientation of printing as well as the infill percentage [21, 22]. For the ribs, 100% infill density was used for superior strength, and two different orientations viz., horizontal and vertical, were analyzed to determine the most optimum method. Figure 8 shows the horizontal and vertical orientation of the part.

The part in horizontal orientation was estimated to be 47 g, compared to the vertical part being 6 g heavier at 53 g, the increment in the latter part was because of the additional support structure that was required to complete the printing. Therefore, horizontal orientation was preferred. During printing, it was observed that the horizontal orientation resulted with parts that depicted errors such as shifting of layers and warpage to a great extent. Figure 9 shows the actual parts that were 3D printed in both orientations using FDM process.

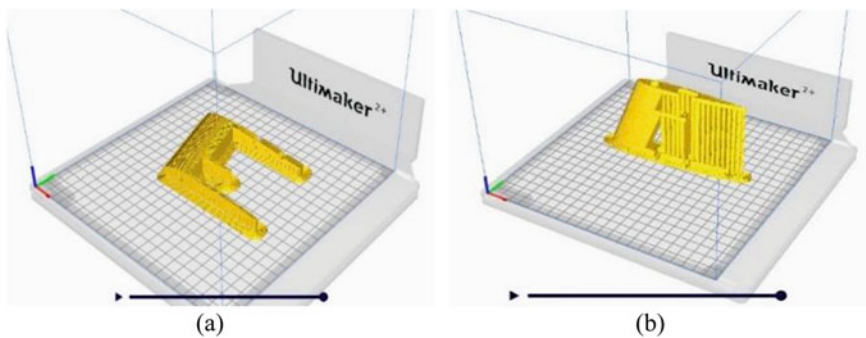


Fig. 8 Part orientation in **a** horizontal and **b** vertical direction

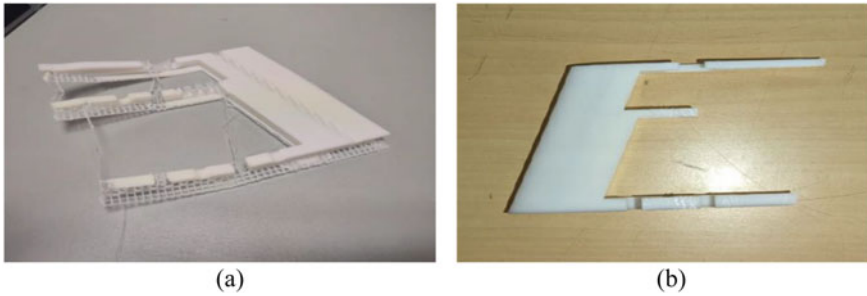


Fig. 9 3D printed part in **a** horizontal and **b** vertical orientation

4.2 Post Processing

The mechanical qualities of the finished print are a key challenge when creating solutions that use 3D printing. PLA transformed into brittle material after printing because the connections between the layers are weak, which contrasts dramatically with a stock material that is both strong and elastic. In order to cater to the flexibility requirements of executing a trailing edge morphing wing mechanism, appropriate material selection is critical to allow bending of the rib upon actuation. The bending is further improved by post processing with a reagent containing Xylene and Toluene. From the literature study about the post processing capabilities of PLA, it was found that it could be possible to use thermal and chemical treatment [9]. From practical experimentation, it was found that when PLA was treated with Xylene and Toluene, it behaved as a plasticizer that softens the PLA to a flexible state. Carburetor cleaner was used as the plasticizer as it contained both these organic components and was easily accessible. For this post processing, initially, a carburetor cleaner reagent bath was prepared in a well-ventilated room. After that, 3D printed part has been dipped in the bath, only immersing the area which needed to be made flexible. The flexibility of the part has been checked at the regular interval of 15 min. Once the desired flexibility was achieved, the part has been removed from the solution.

5 Results

Figure 10 shows the FDM printed part before and after post processing. It was observed that desired flexibility and toughness could be achieved with the post processing. The followings Figures depicted that part with post processing is having better flexibility. PLA being brittle, it is very difficult to bend/ deform and if excessive force is exerted, it fails. On post treatment with carburetor cleaner, it was observed that the flexibility was severely improved and that the rib was able to deflect as required.

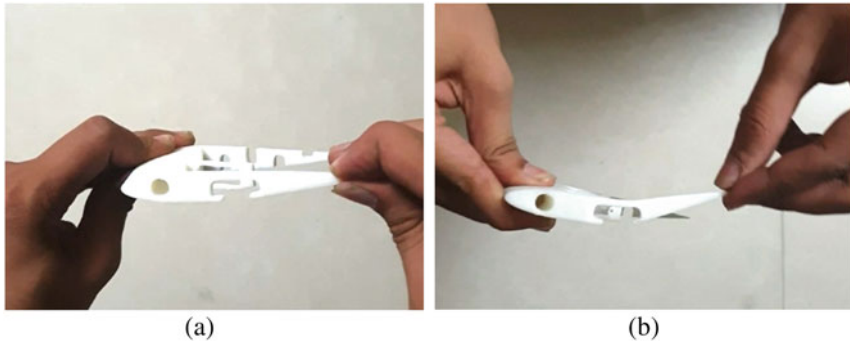


Fig. 10 FDM printed part **a** before post processing, **b** after post processing

The desired flexibility of the ribs was achieved after two cycles of treatment. Further, the micro servo was integrated at the slot provided and a simple lever rocker arm mechanism was used to actuate the control surface. The advantage of this particular post processing treatment is that flexibility can be imparted to only the desired area, thus leaving the remaining component properties unaffected.

6 Conclusion

In the present research work, design and validation have been done for a UAV wing and it is 3D printed with the FDM machine. Post processing treatment is also applied to the 3D printed part to enhance the flexibility.

The major conclusions of this work are following.

- The wing designed on BSLD exhibits superior efficiency than the ones designed on the conventional elliptical distribution, at the cost of around 22% increase in span. This improvement in efficiency results from vortex being generated inboard rather than at the wing tips.
- The upwash that is generated at the outward thirty percent of the wing is augmented with the help of morphing airfoil ribs to control the UAV. Aerodynamic forces can be controlled more efficiently by morphing control surfaces than by conventional ailerons.
- The feasibility and preferability of morphing flying have been established using PLA material with appropriate post processing treatment. This design has a large deflection that allows it to regulate in-flight forces as a continuous control surface.
- The process of making PLA flexible can be extended to the entire wing to create complete wing morphing, which would enable the wing loading to be adjusted for specific flight conditions.

References

1. Prandtl L (1923) Applications of Modern Hydrodynamics to Aeronautics, report University of North Texas Libraries, UNT Digital Library crediting UNT Libraries Government Documents Department
2. Hunsaker DF, Phillips W (2020) Ludwig Prandtl's 1933 paper concerning Wings for minimum induced drag, Translation and Commentary. In: AIAA Scitech 2020 Forum, p 0644
3. Albion H. Bowers (2016) On Wings of the Minimum Induced Drag: Spanload Implications for Aircraft and Birds, NASA/TP—2016–219072
4. Li D (2018) A review of modelling and analysis of Morphing Wings. Prog Aerosp Sci. <https://doi.org/10.1016/j.paerosci.2018.06.002>
5. Goh GD, Agarwala S, Goh GL, Dikshit V, Sing SL, Yeong WY (2017) Additive manufacturing in unmanned aerial vehicles (UAVs): challenges and potential. Aerosp Sci Technol. 63:140–151. <https://doi.org/10.1016/j.ast.2016.12.019>
6. Kobryn PA, Ontko NR, Perkins LP, Tiley JS (2006) Additive manufacturing of aerospace alloys for aircraft structures. Air Force Research Lab Wright-Patterson AFB OH Materials and Manufacturing Directorate
7. Travitzky N, Bonet A, Dermeik B, Fey T, Filbert-Demut I, Schlier L, Schlordt T, Greil P (2014) Additive manufacturing of ceramic-based materials. Adv Eng Mater 16(6):729–754
8. Compton BG, Lewis JA (2014) 3D-printing of lightweight cellular composites. Adv Mater 26(34):5930–5935
9. Strasys (2015) 3D printing a space vehicle—NASA's human supporting Rover Has FDM Parts
10. Carneiro PMC, Gamboa P (2019) Structural analysis of wing ribs obtained by additive manufacturing. Rapid Prototyping J 25(4):708–720
11. Easter S, Turman J, Sheffler D, Balazs M, Rotner J (2013) Using advanced manufacturing to produce unmanned aerial vehicles: a feasibility study. In: Ground/air multisensor interoperability, integration, and networking for persistent ISR IV, vol 8742. International Society for Optics and Photonics, p 874204
12. Michelson RC, Reece S (1998) Update on flapping wing micro air vehicle research-ongoing work to develop a flapping wing, crawling entomopter. In: 13th Bristol International RPV/UAV systems conference proceedings, Bristol England, vol 30, pp 30–31
13. Tim, FDM-printed fixed wing UAV Available <http://www.amrc.co.uk/featuredstudy/printed-uav/>
14. Zhang T, Zhou C, Su S (2015) Design and development of bio-inspired flapping wing aerial vehicles. In: 2015 International conference on advanced robotics and intelligent systems (ARIS). IEEE, pp 1–6
15. Guduru KK, Srinivasu G (2012) Effect of post treatment on tensile properties of carbon reinforced PLA composite by 3D printing, Mater Today: Proc. <https://doi.org/10.1016/j.matpr.2020.03.128>
16. Galantucci LM, Dassisti M, Lavecchia F, Percoco G, (2014), Improvement of fused deposition modelled surfaces through milling and physical vapor deposition, available at: www.poliba.it/Didattica/docs/scorepoliba2014_submission_187.pdf
17. McCullough EJ, Yadavalli VK (2013) Surface modification of fused deposition modeling ABS to enable rapid prototyping of biomedical microdevices. J Mater Process Technol 213:947–954
18. Septyana A, Hidayat K, Rizaldi A, Ramadiansyah ML, Ramadhan RA, Suseno PAP, Rasyadi A (2020) Analysis of aerodynamic characteristics using the vortex lattice method on twin tail boom unmanned aircraft. AIP Conf Proc 2226:020003. <https://doi.org/10.1063/5.0002337>
19. Dimino I, Amendola G, Amoroso F, Pecora R, Concilio A (2016) Morphing technologies: adaptive ailerons. In: Agarwal RK (ed) Recent progress in some aircraft technologies
20. Dharmendra P (2020) Design and analysis of an aircraft wing rib for different configurations. IRJET 07(06)

21. Ranganathan S, Kumar KS, Gopal S, Pradeep C (2020) The effect of print orientation and infill density for 3D printing on mechanical and tribological properties. SAE Technical Paper. <https://doi.org/10.4271/2020-28-0411>
22. Dave HK, Patadiya NH, Prajapati AR, Rajpurohit SR (2021) Effect of infill pattern and infill density at varying part orientation on tensile properties of fused deposition modeling-printed poly-lactic acid part. Proc Inst Mech Eng C J Mech Eng Sci 235(10):1811–1827

Preliminary Investigations of Low Plasticity Burnishing Process on Mechanical Properties of Aluminum Alloy



S. R. Thorat and A. G. Thakur

Abstract Surface modifications and surface treatments have a significant impact on the service life of so many critical parts of various materials being used in industrial applications. As a result, significant attention has been given to post-machining processes because traditional machining operations such as turning and milling and so on develop surfaces with inherent discrepancies and inadequacies. As a result, a surface finishing operation is required to eliminate these irregularities while also improving other surface properties such as surface roughness, corrosion resistance, and wear resistance. Low plasticity burnishing (LPB) process was used to enhance mechanical characteristics of components, which were subjected to low surface plastic deformation. In this present research work, sensitive analysis of low plasticity burnishing process parameters with different mechanical properties of aluminum alloy, i.e., AA6061T6 has been performed. The burnishing process parameters considered are speed, pressure, ball diameter, number of passes, and ball material. Mechanical properties considered for analysis are wear resistance, surface roughness, and corrosion resistance. The outcomes of sensitive analysis demonstrated that surface roughness has most significance in burnishing process. Wear resistance and corrosion resistance properties are having strong correlation with surface roughness. Each burnishing process parameter has specific significance for improvement in mechanical properties.

Keywords Surface roughness · Corrosion resistance · Wear resistance · Low plasticity burnishing · Fatigue life

S. R. Thorat (✉)

Mechanical Engineering Department, Sanjivani College of Engineering, Kopargaon, Kopargaon, Ahmednagar, Maharashtra (MS), India

A. G. Thakur

Sanjivani College of Engineering, Kopargaon, Kopargaon, Ahmednagar, Maharashtra (MS), India

1 Introduction

The manufacturing industry's expectations have risen in recent years as a result of the technological revolution. The component's expected service life has increased without increasing the assembly cost. As a result, the engineers were needed to develop and implement improved manufacturing processes to fulfill these requirements. According to recent research, the technological procuring and the wide range of surface enhancement techniques used have a significant impact on the service life and dependability of machine parts [1].

Burnishing is a surface modification technique that involves planetary rotating a tool over a bored or turned surface to produce a very smooth surface finish. This procedure does not require any material to be removed from the work pieces. Burnishing is a surface modification technique that involves planetary rotating a tool over a bored or turned surface to produce a very smooth surface finish. This procedure does not require any material to be removed from the work pieces.

Corrosion is an effect in which the component's material reacts with the environment around it. Wear is a regular occurrence in connecting parts. This decreases the machinery's operating costs and downtime. The burnishing method offers a significant benefit by increasing wear resistance.

2 Experimental Work

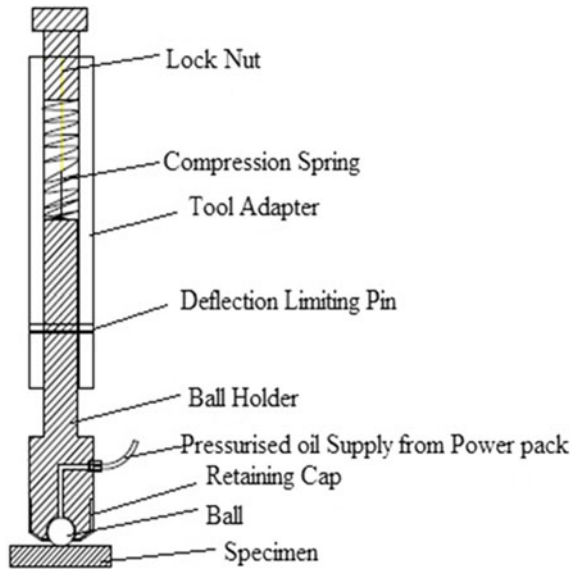
To the understanding of the authors, based on literature, very little or no data available in public research that would assist to resolve the barriers to design as well as development and thus produced an LPB tool successfully. Therefore, a suitable equipment for the specific purpose had to be designed, developed, and produced. Consequently, a new technique was developed for implementing this technology to common machine as lathe machine. The novel low plasticity burnished tool that can be mounted to any traditional machine tools like milling or lathe, designed, and developed to build a pressure on a ball with the help of fluid power. A ball which is protected by a spherical hydrostatic bearing consists of the simple LPB instrument.

2.1 *Burnishing Tool and Process Parameters*

According to design, the low plasticity burnishing tool has been manufactured. As shown in Fig. 1, this tool consists of various elements such as tool adapter, coolant power pack, spring, ball holder, retaining cap, lock nut, and deflection limiting pin.

The tool was developed to accommodate various ball diameters in the 6–12 mm range. In the current research work, balls of four various materials were used such as alumina, carbon chromium steel, tungsten carbide, and silicon carbide, each with

Fig. 1 Low plasticity burnishing tool



four possible diameters of 6, 8, 10, and 12 mm. A ball had mounted to a surface of a part/work material in perpendicular position. The power pack has been used to develop pressure in the recess to revolve the ball. The pressure arising by the ball induces plastic deformation that arises as the ball rolls over the surface of the specimen. As the majority of the materials restrict, the region that is deformed and is remaining in compression during the passing of a ball and retains the same. During the experiment, no content was removed.

In the current study, an effort has been made to simplify the technology, so that it was important to analyze the effectiveness of this invention, the future commercial implementation to general industries, and the implementation of such innovation to common work materials like steels. Aluminum (Al 6061T6) round bar is used as the work piece material in this research work. This material has been selected due to its relevance in companies and severity to deterioration when burnished, both on the surface and beneath the surface.

Aluminum alloys are especially well suited for components and mechanisms that require a high strength-to-weight ratio, and they are likely the most well-known materials mostly used in aircraft and truck wheels. Figure 2 shows AA6061T6 specimens prepared for the experimentation.

The burnishing process is controlled by a number of process parameters. To achieve the best results, all of these parameters must be optimized and controlled. Burnishing pressure, tool diameter (ball diameter), burnishing speed, tool material (ball material), and number of passes are most important variables. Five burnishing parameters with their four levels have been considered for experimentation. Low plasticity burnishing process variables and their levels have been given in Table 1.

Fig. 2 Aluminum specimen**Table 1** LPB process parameters and their levels [2]

Parameters	Level			
	1	2	3	4
Burnishing pressure (MPa)	0.5	1	1.5	2
Burnishing speed (rpm)	280	450	710	1120
Number of passes	2	3	4	5
Ball material	Chrome steel	Alumina	Silicon carbide	Tungsten carbide
Ball diameter (mm)	6	8	10	12

The work piece was then rotated by using the head stock. After that, the tool post has been shifted laterally until the roller makes contact with the rotating work material. To burnish the work piece surface, feed the tool post along the length of the work material. Figure 3 shows the burnishing process experimental setup.

2.2 Measurements

After conduction of experiments of burnishing process, specimens were cut into various sections for different tests such as surface roughness test, wear resistance test, corrosion resistance test, and fatigue test. Details of test have been explained below.

Fig. 3 Low plasticity burnishing process setup

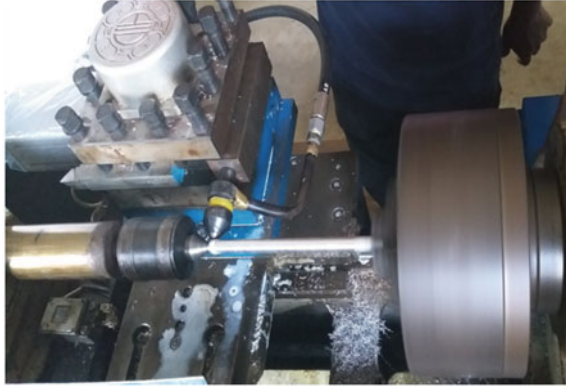


Fig. 4 Surface roughness measurement instrument



2.2.1 Surface Roughness Test

Surface finishing is the primary application for burnishing. Burnishing can be used to reduce the height of surfaces. As the pressure exerted by the burnishing tool is more than the yield strength of the workpiece, flow occurs from peaks to valleys reducing surface roughness. The SURFCOM130A surface roughness measuring instrument is used to check (Ra) surface roughness values as shown in Fig. 4. The average surface roughness (Ra) value is taken by three roughness tests [3, 4].

2.2.2 Wear Resistance

When parts wear, it begins to lose material from the surface. A digital weighing machine is used to calculate the mass of the work piece pre- and post-wear test. The difference in mass between pre and post the test gives a value of wear. The

Fig. 5 Wear resistance measurement setup



improvement in wear resistance can be determined by comparing the weight losses of the burnished and without burnished (only turned) specimens. The wear testing setup, i.e., (pin on disk), has been shown in Fig. 5.

The cylindrical wear specimens with a size of 12×5 mm cut from the unburnished and burnished specimen have been mounted on experimental setup as per provision [2, 5–7].

The wear rates of the materials were calculated by

$$W = \frac{\Delta w}{\rho t V_s F} \quad (1)$$

where

W —Specific wear rate (mm^3/Nm)

Δw —Weight loss (grams)

ρ —Density of the material (g/mm^3) ($0.0027 \text{ g}/\text{mm}^3$)

V_s —Sliding velocity in m/s (2.68 m/s)

t —Time duration in sec (180 s)

F —Applied load in N (10 N).

2.2.3 Corrosion Resistance

Gradual degradation or disintegration of metal parts caused by the reaction of the metal parts with foreign elements. Because the strength of the components deteriorates as a result of corrosion, this may result in mechanical failure of the machinery or structure. Burnishing is a method reducing the corrosion of parts. Specimens were prepared as per requirement of electrochemical corrosion setup machine (diameter -12 mm and thickness 5 mm). As we have to test influence of LPB process, so only cylindrical surface needs to be checked, according to that both side flat surfaces were coated to get corrosion of only required surface.

To ensure an accurate comparison, only-turned components were also checked. Burnished components are tested for corrosion resistance by using potentiostat Analyzer Gamry made as shown in Fig. 6.

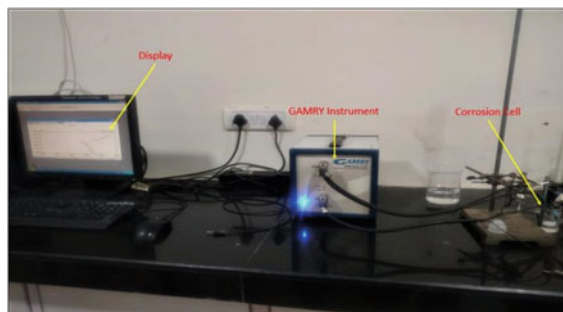


Fig. 6 Electrochemical corrosion test setup

Corrosion resistance can be expressed in a variety of ways, including weight loss percentage, mils per year penetration [8].

3 Results and Discussion

3.1 *Effect of the Fluid Pressure on the Surface Roughness, Wear Rate, and Corrosion Rate*

The influence of the burnishing pressure is displayed in the Fig. 7a, it shows that average value of the roughness rises as pressure improves. Higher pressure, as seen from above, tends to increase surface roughness as it influences the rate of plastic deformation. Lowering the asperity heights, which will occur at low pressure levels, produces more material flow, results in the material moving upwardly (Bougharriou A) [9], and large waviness, may degrade the surface finishing. Increased pressure can also produces surface flakes (El-Taweel et al.) [10], which increases surface roughness.

From Fig. 7b, it is clear that rate of wear is increased in accordance with increment in pressure at earlier stage. Later on, as the burnishing speed increases, the wear rate decreases. Furthermore, burnishing pressure rises the compressive stress at the surface layer, preventing crack growth, and wear delamination. In contrast, lesser burnishing force results in low improvement as inadequate pressure leads to imperfect deformity operation.

The influence of burnishing pressure on corrosion rate is described in Fig. 7c, which shows that the average value of corrosion rate increases as pressure increases. Excessive pressure can also cause surface flaking (El-Taweel et al.) [10] and (El-Tayeb) [11], increasing the corrosion rate.

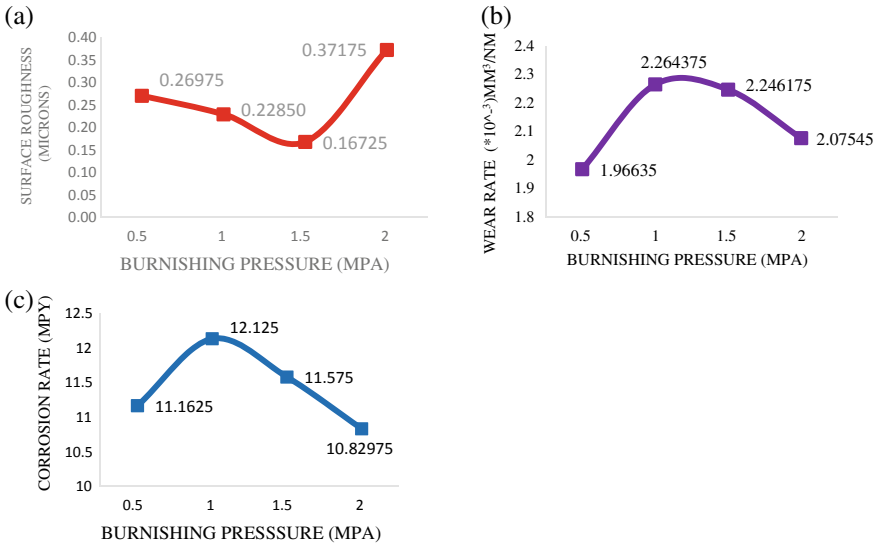


Fig. 7 a Effect of the burnishing pressure on the surface roughness, b effect of the burnishing pressure on the wear rate, c effect of the burnishing pressure on the corrosion rate

3.2 Effect of the Burnishing Speed on the Surface Roughness, Wear Rate, and Corrosion Rate

Whenever burnishing speed enhanced from 280 to 780 rpm, the surface finish decreases slightly at 450 rpm, whereas it improves when a speed is enhanced from 780 to 1120 rpm, as shown in Fig. 8a. It is because, immediately, at lower speed range, as the speed increases, burnishing ball has a greater probability of leveling out surface irregularities and thus reducing surface roughness. When the speed has been increased, it increases temperatures of both work material and the ball, because of the inadequacy of tool (El-Axir) [12]-(El-Taweel et al.) [10]. Nemat and Lyons [13] as well confirmed that because of chatter at higher speeds, the burnishing tool has less deformation time to stabilize out further discrepancies, increasing surface roughness.

As wear rate and corrosion rate are strongly depend on surface roughness [14]. As surface roughness decreases because of increase in speed results in decrease in wear rate and also corrosion rate as shown in Fig. 8b, c.

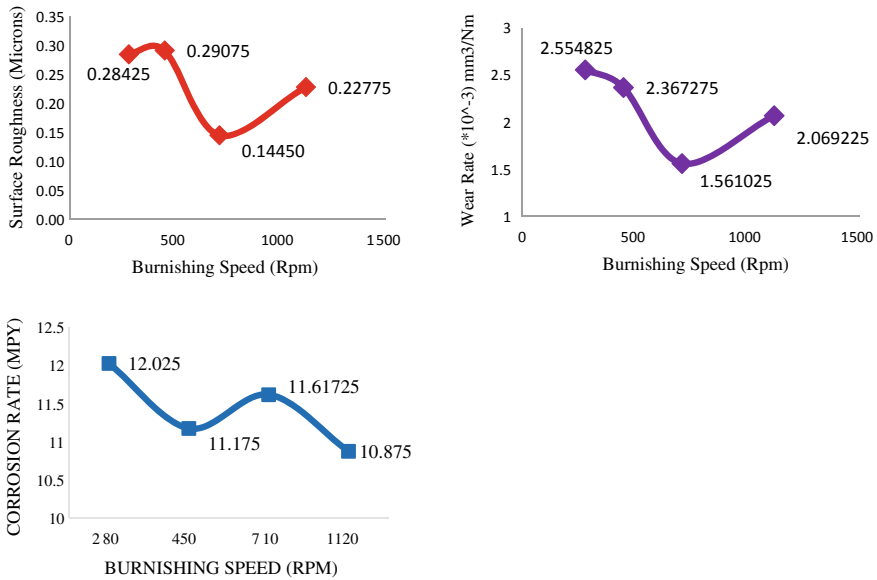


Fig. 8 a Effect of the burnishing speed on the surface roughness, b effect of the burnishing speed on the wear rate, c effect of the burnishing speed on the corrosion rate

3.3 Effect of the Ball Diameter on the Surface Roughness, Wear Rate, and Corrosion Rate

The normal force in this hydrostatic process is determined by the pump pressure and the ball diameter. Different sizes result in different burnishing pressures, resulting in different plastic deformation-affected zones after burnishing. As burnishing pressure increases, then surface roughness decreases as shown in Fig. 9a because of more plastic deformation results in more residual compressive stresses.

As wear rate and corrosion rate are strongly depend on surface roughness. As surface roughness decreases because of increase in ball diameter results in decrease in wear rate except at initial stage because of delamination as shown in Fig. 9b. Corrosion rate decreases as ball diameter increases as shown in Fig. 9c.

3.4 Effect of the Ball Material on the Surface Roughness, Wear Rate, and Corrosion Rate

The normal force in this burnishing process is determined by the pump pressure and the ball material. Different ball materials result in different burnishing pressures, resulting in various plastic deformation-affected zones after burnishing. As ball material SAE used, it shows less roughness but as material changes to Al₂O₃,

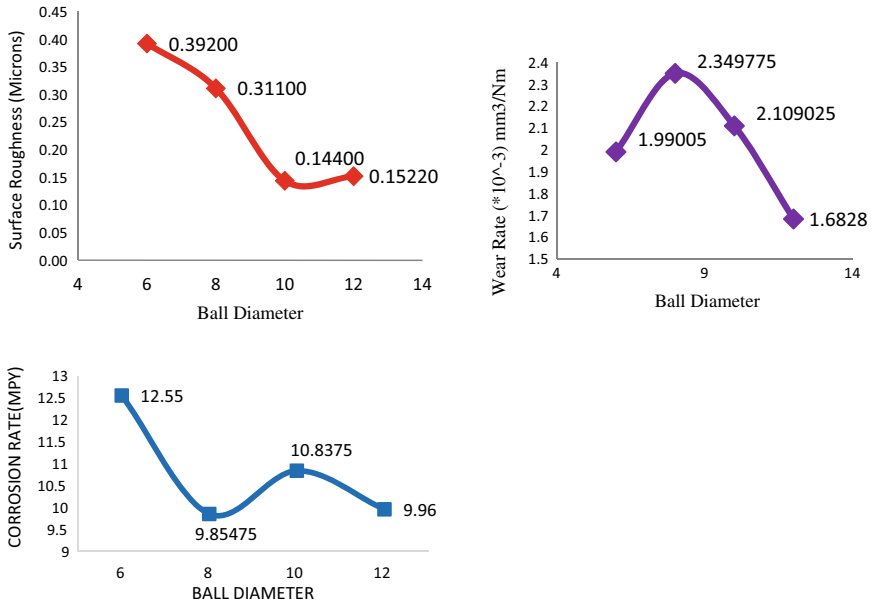


Fig. 9 a Effect of the ball diameter on the surface roughness, b effect of the ball diameter on the wear rate, c effect of the ball diameter on the corrosion rate

suddenly roughness increases, but for SiC and WC, it results in decrease in roughness as shown in Fig. 10a because of more plastic deformation results in more residual compressive stresses.

It is observed that wear rate decreases as material changes from SAE to Al₂O₃, SiC, and WC as shown in Fig. 10b. Corrosion rate also results in decreasing phenomenon as shown in Fig. 10c.

3.5 Effect of the Number of Passes on the Surface Roughness, Wear Rate, and Corrosion Rate

The surface roughness increases marginally whenever the number of passes is enhanced from two to three, but it decreases dramatically when the number of passes is continued to increase from three to four. As shown in Fig. 11, the enhanced surface finishes with a few more passes early on is due to more hardening (El-Taweel) [10]; (Nemat and Lyons) [13] (a). As a result of the foregoing analysis on surface roughness main effect plots, it is found that wear rate and corrosion rate follow the same trend as surface roughness. Figures 11(b, c) demonstrate this (c).

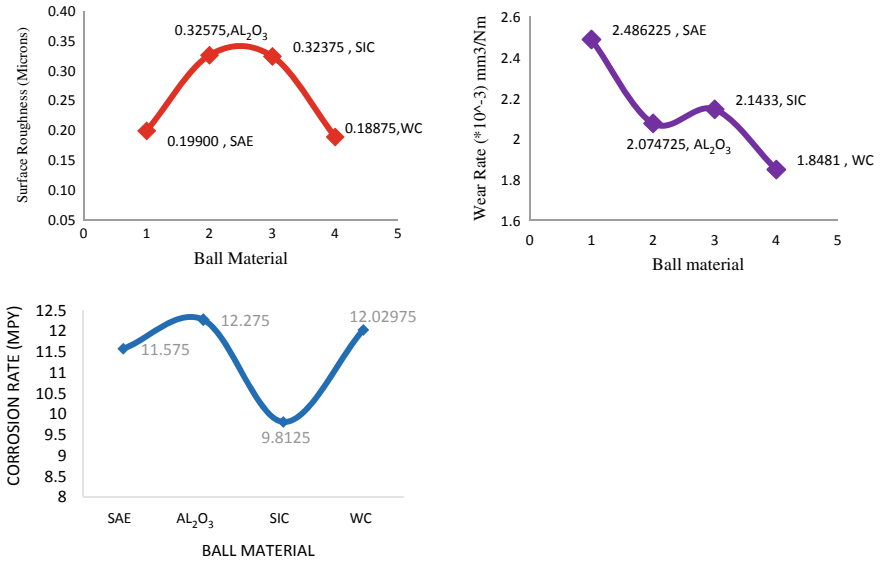


Fig. 10 a Effect of ball material on the surface roughness, b effect of ball material on wear rate, c effect of ball material on corrosion rate

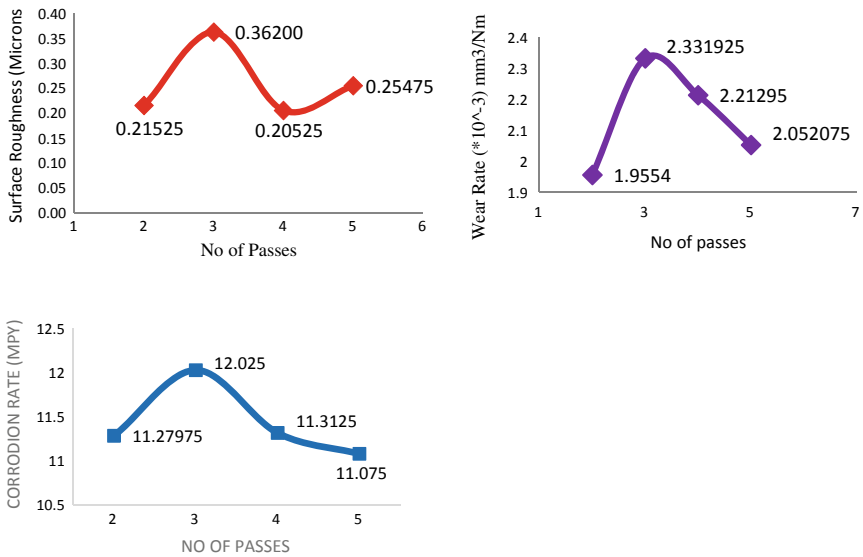


Fig. 11 a Effect of the passes on the surface roughness, b effect of the passes on the wear rate, c effect of passes on corrosion rate

4 Conclusion

The low plasticity burnishing process has been applied by considering different process parameters. Influence of each parameter on burnishing process for different mechanical properties such as surface roughness, wear resistance, and corrosion resistance investigated.

The developed burnishing tool can handle a wide range of ball diameters. The current apparatus provides outstanding and all-around properties such as enhanced cold work, improved surface, better finish, wear resistance, and corrosion resistance.

The findings aided in identifying parameters that have a significant impact on surface properties and in choosing main variables. After conducting research, the different LPB process parameters that influence the surface roughness, wear rate, and corrosion rate of aluminum alloy 6061T6. Surface roughness of 0.147 microns (Ra) and wear rate of 1.56 mm³/Nm were achieved. The database created from experimental investigation will be very effective for selecting the best possible process variables for low plasticity burnishing process.

Acknowledgements The authors are thankful to ASPIRE, Research Mentorship Program, Savitribai Phule Pune University, Pune for providing research support.

References

1. Seemikeri CY, Brahmanekar PK, Mahagaonkar SB (2008) Some studies on design and performance analysis of a new low plasticity burnishing tool. *IJMMM* 4(2/3):237. <https://doi.org/10.1504/IJMMM.2008.023195>
2. Thorat SR, Thakur AG (2021) Analysis of surface roughness and wear resistance in low plasticity burnishing process using multi-objective optimization technique. *Mater Today: Proc* 41:1082–1088
3. Thorat SR, Thakur AG (2018) Optimization of burnishing parameters by Taguchi based GRA method of AA 6061 aluminum alloy. *Mater Today: Proc* 5(2):7394–7403. <https://doi.org/10.1016/j.matpr.2017.11.410>
4. Seemikeri CY, Brahmanekar PK, Mahagaonkar SB (2008) Investigations on surface integrity of AISI 1045 using LPB tool. *Tribol Int* 41(8):724–734
5. Revankar GD, Shetty R, Rao SS, Gaitonde VN (2014) Analysis of surface roughness and hardness in ball burnishing of titanium alloy. *Measurement* 58:256–268
6. Designation: G 99–95a (Reapproved 2000), Standard Test Method for Wear Testing with a Pin-on-Disk Apparatus, pp 1–6
7. Revankara GD, Shetty R, Rao SS, Gaitonde VN (2016) Wear resistance enhancement of titanium alloy (Ti–6Al–4V) by ball burnishing process. *JMRTEC*-212, pp 1–20
8. Saldaña-Robles, Plascencia-Mora H, Aguilera-Gómez E, Saldaña-Robles A, Marquez-Herrera A, Diosdado-De la Peña JA (2018) Influence of ball-burnishing on roughness, hardness and corrosion resistance of AISI 1045 steel. *Surf Coat Tech* 339:191–198.
9. Bougharriou A, Saï WB, Saï K (2010) Prediction of surface characteristics obtained by burnishing. *Int J Adv Manuf Technol* 51:205–215
10. El-Taweel TA, El-Axir MH (2009) Analysis and optimization of the ball burnishing process through the Taguchi technique. *Int J Adv Manuf Technol* 41:301–310

11. El-Tayeb NSM, Low KO, Brevern PV (2009) On the surface and tribological characteristics of burnished cylindrical Al-6061. *Tribol Int* 42:320–326
12. El-Axir MH (2000) An Investigation into roller burnishing. *Int J Mach Tools Manuf* 40:1603–1617
13. Nemat M, Lyons AC (2000) An investigation of the surface topography of ball burnished mild steel and aluminium. *Int J Adv Manuf Technol* 16:469–473
14. Revankar GD, Shetty R, Rao SS, Gaitonde VN (2014) Selection of optimal process parameters in ball burnishing of titanium alloy. *Mach Sci Technol: An Int J* 18:464–483. <https://doi.org/10.1080/10910344.2014.897848>

Recent Advancements in Hybrid Investment Casting Process—A Review



C. V. Morsiya and S. N. Pandya

Abstract Investment casting process is the promising method for manufacturing of complex component with better surface finish and dimensional accuracy. Development of 3D printing or rapid prototyping has given opportunities for the mass customization and production of complex designs having CAD model. In past few years, rapid prototyping has been integrated to enhance efficacy of investment casting process called as rapid investment casting process or hybrid investment casting process. This present paper is focused on review of effect of fused deposition modeling (FDM) printing parameters on quality of printed pattern and use of 3D printable materials in different steps of investment casting process with their benefits and limitations to improve productivity, accuracy, mechanical properties, and surface finish of the final component. Applications and benefits of hybrid investment casting process to manufacture different industrial product are also considered. There are certain challenges in implementation of this process such as ceramic shell cracking, pattern burning temperature, and pattern quality. These are also discussed in detail. These challenges will become separate topic of research for further advancement in hybrid investment casting process.

Keywords 3D printing · Rapid prototyping · Hybrid · Investment casting · Applications · Benefits · Challenges

1 Introduction

Manufacturing field is a continuously developing and improving all over the globe. Current market demands variety of products with better quality and lower cost. Fourth industrial revolution leads to the digitalization of complex industrial tasks. This trend

C. V. Morsiya (✉) · S. N. Pandya
Mechanical Engineering Department, Sardar Vallabhbhai National Institute of Technology,
Ichchhanath, Surat, Gujarat 395007, India

S. N. Pandya
e-mail: s.pandya@med.svnit.ac.in

of industry 4.0 is also applies to the manufacturing industries which lead to integration of automation and artificial intelligence. Manufacturing automation consists of implementation of flexible manufacturing system using subtractive methods, injection molding, and additive manufacturing (AM). 3D printing or rapid prototyping (RP) is an additive manufacturing in which material is deposited layer by layer to fabricate complex geometries as 3D model. It develops opportunities of the mass manufacturing and customization of complex design having CAD model. Due to flexibility in design and its modification, variable requirements of consumer can easily be fulfilled [1, 2].

Investment casting (IC) is one of the important methods to produce complex shaped products with better dimensional accuracy and is well explained by Singh et al. [3]. This method can be used to manufacture multiple components of different shape and size by attaching a number of patterns to the wax tree [4]. In past few years, various methods have been developed to improve efficacy of investment casting process. With the advancement in RP technology, IC is beneficial to provide better quality component at faster rate and lower cost which are difficult to obtain by subtractive technology.

Nowadays, many varieties of 3D printing methods are available in the market to print complex structure with better quality. Fused deposition modeling (FDM) is the most widely used method which commonly uses polymer filaments to print the structure. It is mostly used in hybrid investment casting for preparation of patterns [5, 6]. Advantages of polymer include low cost, easy manufacturability, availability, and water resistance [2]. Some limitations are also there based on material used such as warping, poor surface finish, and low resolution [7]. Polymers such as thermoplastics, elastomers, thermosets, and biopolymers are used as raw materials in 3D printing. Some of the most widely used materials due to their characteristics are acrylonitrile butadiene styrene (ABS), polylactic acid (PLA), thermoplastic polyurethane (TPU), nylon, polyethylene terephthalate glycol (PETG), and high impact polystyrene (HIPS). Important properties and extrusion temperatures for these materials are listed in Table 1. But they all have certain limitations and mostly used for prototype preparation. Nowadays research is ongoing on reinforcing polymer with nanoparticles to increase mechanical, electrical, and thermal properties compare to the regular polymer. Detailed article reviewing the challenges involved in the preparation and printing of nanocomposites given by researcher Penumakala and team [8].

Properties of 3D printed parts not only depend on material used but also depends on printing parameters. Printing parameters affect the precision, accuracy, and properties of 3D printed parts. Figure 1 indicates classification of printing parameters [9].

Optimized structure-based parameters are required for different shape and size of component based on surface finish and dimensional accuracy needed. Nozzle size mostly used is 0.4 mm [17]. Diameter of standard filaments used is 1.75 and 2.85 mm [18]. Thickness of each layer deposited by nozzle is called layer thickness and its selection depends on nozzle diameter and material properties [19]. Infill geometry is inside geometry of printed component. It mostly affects mechanical properties of component and printing time. Generally, used infill pattern is linear, rectangular, and

Table 1 3D printable materials and important properties

Material	Extrusion temperature (°C)	Properties	References
ABS	210–250	Abrasion resistant, good impact strength, low weight	[9, 10]
PLA	180–230	Biodegradable pollution free polymer, more sensitive to heat than ABS	[10, 11]
PETG	220–250	Combines properties of ABS and PLA, good impact resistance, slightly softer surface	[10, 12]
Nylon	240–260	Hygroscopic, tough, semi flexible, high impact, and abrasion resistant	[10, 13]
TPU	220–250	Flexible, abrasion resistant, excellent interlayer adhesion	[14]
HIPS	250	Similar properties as ABS but slightly expensive	[15, 16]

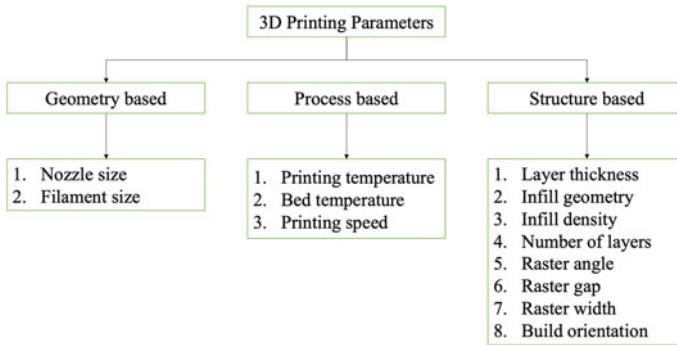


Fig. 1 Classification of printing parameters [9]

honeycomb [20]. Due to use of different infill geometry, density of component also changes called infill density. It affects strength and mass of printed parts. 100% infill density preferred for better properties of components but it will increase printing time [21]. Raster angle is another important parameter refers to the angle between X-axis of printer board and the nozzle direction. Mechanical efficiency and shape precision of component depend on it [22].

Using recent advancements in technology, traditional investment casting needs to be enhanced. 3D printing is effective method for integration with other traditional methods to improve productivity, accuracy, and to reduce cost of the component. This present paper is focused on integration of 3D printing with investment casting known as hybrid investment casting or rapid investment casting [23–25]. Use of 3D printable materials in different steps of investment casting process is discussed with their benefits and limitations to improve productivity, accuracy, mechanical

properties, and surface finish. Applications of hybrid investment casting process to manufacture different industrial product are also discussed.

2 Literature Review

Investment casting process consists of many steps from which most important step is preparation of wax pattern. Wax pattern requires preparation of injection molding die by machining. For every change in pattern design, new die is required to be designed, which is very costly when a smaller number of parts to be produced and customer needs flexibility in design. To overcome this problem, many researchers have worked on use of 3D printing method for pattern preparation. Some of the studies are also based on pattern die preparation using 3D printing method. There are many factors affecting pattern shape and dimensions such as pattern material, printing method, and parameters selected. In this section, effect of printing parameters and use of 3D printing in investment casting process has been reviewed in brief.

There are many printing parameters which affect properties of 3D printed part. For different materials, different sets of parameters are required for efficient printing. ABS shows surface roughness and waviness, if proper parameters not selected. Compared to ABS, PLA shows good surface performance [26]. Considering infill density as main criteria for FDM of ABS, Biach et al., validated that for tensile and bending applications low infill density result into low cost and its effect on strength remains very less. Compression test revealed that cost and strength performance is proportional to volume of material [27]. Ćwikła et al. [28] investigated that for lightweight and durable element, honeycomb pattern with 40–50% infill density, and shell thickness of 2–3 layer/lines gave better result. Dawoud et al. recommended a negative raster gap with combination of 45° orientation for high density FDM of ABS with enhanced mechanical properties [29]. ABS emits more particles compared to PLA due to its high melting temperature. Particle emission is affected by many parameters such as infill pattern, nozzle temperature, infill density, and printer age [30]. Ansari and Kamil reported that tensile strength of FDM printed PLA mostly affected by print speed. High printing temperature and low print speed resulted to minimum dimensional deviation [31]. Moradi et al. printed bronze—PLA specimen. They showed that mechanical properties of sample improved as the layer thickness and infill density increased [32]. Kumar et al. printed carbon fiber reinforced PETG using FDM. They reported that hardness and tensile strength can be controlled by infill density and print speed [33]. 3D printing is also used to develop die for pattern preparation termed as rapid tooling. Some of the attempts have also been made to prepare ceramic mold having cavity of desired shape [34]. Table 2 reviews ongoing research in the field of hybrid investment casting process.

Hybrid investment casting process is in focus of research community from last few years. FDM method of 3D printing was mostly used with investment casting process for the preparation of patterns. There are many factors which affect printed pattern's surface quality and dimensional accuracy such as infill density, infill pattern, build

Table 2 Ongoing research in the field of hybrid investment casting process

Printing method	Printing material	Comments	References
FDM	ABS	<ul style="list-style-type: none"> • Pattern prepared were checked for dimensional accuracy. Dimensional deviation reported was 0.01 – 0.03 mm • Suggested that injection molded wax patterns can be replaced with ABS patterns to achieve better dimensional accuracy • Used hybrid investment casting to manufacture biomedical implant 	[36]
FDM	ABS, ABS + Wax	<p>Concluded that,</p> <ul style="list-style-type: none"> • Thin coating of wax on ABS pattern helps to improve dimensional accuracy • For good dimensional accuracy, orientation of pattern suggested to be 90° in FDM machine 	[37]
FDM	ABS, ABS + Wax	<ul style="list-style-type: none"> • Found that to eliminate problem of shell cracking, surface of ABS patterns can be coated with thin layer of wax • Microstructure and hardness majorly affected by mold thickness • Observed that the volume to area ratio also affect hardness of the castings but build orientation and pattern density have no effect on hardness of the castings 	[38]
Stereolithography	ABS, Wax	<ul style="list-style-type: none"> • Shown that ABS can cause more severe shell breakage than wax resin. The resulting casting had varying defects • Stereolithography can create high-precision patterns for casting and enable manufacturers to accelerate mold production and reduce costs 	[39]

(continued)

Table 2 (continued)

Printing method	Printing material	Comments	References
FDM	ABS	<ul style="list-style-type: none"> • Used hybrid investment casting to fabricate hip joint • VS was used to improve pattern quality • Corrosion behavior of hip joint was observed. Majorly affecting parameters reported are pattern density and mold baking time 	[40]
FDM	ABS	<ul style="list-style-type: none"> • Observed that increase in drying time of primary coating removes moisture from ceramic shell which decreases surface roughness • Increase in mold thickness slightly decreases surface roughness due to change in heat transfer rate 	[41]
FDM	Wax	<ul style="list-style-type: none"> • Additive manufacturing of wax patterns and topology optimization of cast part proves significant potential for casting of lightweight and structurally optimized component for mechanical applications • Showed that for low volume production, hybrid investment casting can reduce cost and manufacturing time • Mentioned that due to use of polymer patterns, IC faces new problems such as pattern burning issues, chances of residual ash formation, and shell cracking 	[42]

(continued)

Table 2 (continued)

Printing method	Printing material	Comments	References
FDM	PLA	<p>Attempted to produce low-cost periodic cellular lattices by hybrid investment casting</p> <ul style="list-style-type: none"> • Observed that fine struts with low density can be produced by optimizing process parameters such as layer thickness and nozzle diameter • Suggested that nozzle having diameter 0.4 mm could be helpful to print struts with cross section of 0.6 mm • Due to round shape of nozzle exit, difficulty was observed in the production of square cross sections • Dimensional deviation and defects in PLA pattern could be minimized with the use of printers having tight tolerances and improved controls over process parameters • Also considered, hybrid investment casting as low-cost method compared to others to manufacture lattices 	[43]
FDM, Digital Light Processing	Castable resin, castable resin with 20% wax, polyvinyl butyral	<ul style="list-style-type: none"> • Manufactured specimens having 0.4 mm wall thickness • Castable resin during burnout showed cracking in prepared shell mold when heated up to 150 °C • FDM printed polyvinyl butyral was used to prepare ceramic shell mold, and no shell cracking was observed during burnout • Surface finish of pattern was improved by using isopropyl vapor in VS process 	[44]

orientation, print speed, raster angle, and raster gap [26]. Each of the above listed parameters have various effects on different polymeric materials. Effect of such parameters on ABS and PLA material investigated by many researchers [35] but newly available material such PETG, and carbon fiber reinforced polymeric material requires further research [33]. As quality of the final cast part depends on pattern quality in investment casting, vapor smoothing (VS) process has also been suggested to improve printed pattern quality [28].

3 Applications of Hybrid Investment Casting

Investment casting (IC) is mostly used to manufacture intricate shapes at low cost and in minimum time compared to other casting processes. There are various applications of hybrid investment casting process such as in manufacturing medical implants, jewelry casting, dentistry, micro casting, low volume production components such as turbine blades, fuel pumps [45], and cylinder heads etc.

The emergence of the new RP methods has major impact on traditional investment casting. Most dental prostheses are made by investment casting. RP patterns for dental prostheses generated using laser scanning method in most of the studies [46]. Wu et al. [47] attempted to integrate rapid prototyping with investment casting to cast titanium dental prostheses. Their result supports the use of RP with IC. Kheirollahi and Abbaszadeh [48] also investigated for applications of RP technology in dentistry. They have established a way for helpful integration of RP for fabrication of dental prostheses that otherwise difficult to fabricate by other methods. Torabi et al. [49], in their review, concluded that preparation of wax pattern using RP for dentistry is more affordable. They also reported that 3D printing directly produces ceramic shell for dental prostheses which reduces cost of die, pattern, and slurry preparation and also makes process faster compared to traditional investment casting. The method has also been applied effectively for fabrication of facial prostheses.

Bhosale and Sinde [50] attempted to manufacture patient specific implant models using hybrid investment casting. They developed femoral and tibial implant and reported that reliability and accuracy of component depends on pattern making process and accurate casting process. Deviation observed in dimension of metal implant was -2.00 to 1.40 mm. Kumar et al. [51] provided critical review of use of AM in biomedical field. Some of the applications are manufacturing of implants, surgical instruments, and cracked bone replacements. Major merits of integration of AM with investment casting in medical field are listed in Fig. 2. Kumar et al. [52] attempted to manufacture biomedical implant using hybrid investment casting and reported many factors affecting surface finish of the castings.

Charmeux [54] considered low cost and minimum time as main criteria while integrating RP and IC to manufacture meso/micro metallic parts with complex geometries. They reported that accuracy of final part depends on printing method selected, size of powder during ceramic shell printing, and pouring temperature. Jain and Kuthe

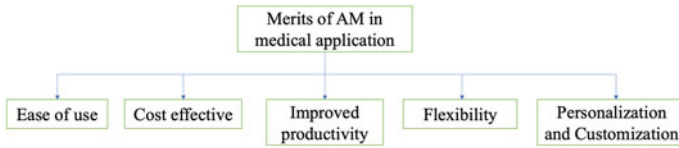


Fig. 2 Merits of use of AM in integration with investment casting process for medial application [53]

[55] manufactured middle disk of Oldham coupling using RP patterns in investment casting and sand casting. They used AUTOCAS-T-X to manufacture defect free casting. It was found that hybrid investment casting is useful to manufacture intricate parts in small quantity as per customers' description. 3D printing found its significance in jewelry casting also. Implementation of 3D printing helps to create complex and thin jewelry and multiple patterns can be created at once within very short time [56]. Wannarumon and Bohez [57] created ring model and mold using CAD and RP and reported that this technology offers the great benefit to jewelry industry. They concluded that during generation of STL files, CAD model should be based on solid modeling to avoid errors such as gaps, non-manifold solid, and flipped triangles. Cheah et al. [58] aimed at presenting detailed comparison of conventional investment casting and rapid prototyping and tooling assisted process and reported that hybrid investment casting saves cost and time both compared to traditional investment casting. Mondal et al. [59] used rapid tooling approach to fabricate mold for obtaining wax pattern of cylinder head. They reported that thin wall casing of cylinder head can be obtained by maintaining ceramic mold temperature and pouring temperature. Zhang et al. [60] manufactured impeller having 60 mm diameter and blade thickness 2 mm using hybrid investment casting method. Using Anycasting simulation software concluded that to obtain defect free excellent quality casting, side gating system should be used. Attempt has also been made to manufacture TiAl turbine blades using hybrid investment casting approach [61].

4 Hybrid Investment Casting Process—Challenges

Even though, there are many advantages and applications of hybrid investment casting process, there are certain challenges in its implementation. Major challenges faced are shell cracking during pattern removal, selection of effective pattern burning temperature, and pattern quality. In most of the cases, shell cracking and pattern burning temperature are related to each other.

Ceramic shell cracking observed during dewaxing step or pattern removal step. In traditional investment casting, wax is removed by heating the mold in furnace up to melting temperature of wax. During use of non-wax RP patterns, shell cracking also observed during pattern removal step. Mismatch in coefficient of thermal expansion of pattern and ceramic material induces stress on ceramic mold which leads to shell

cracking [62]. One of the effective solutions to prevent shell cracking is to use hollow structured pattern. Use of hollow structure reduces amount of printing material used and also reduces printing time. The concept of using hollow structure is that hollow structure would soften at lower temperature and collapses inside before critical stress level develops [58]. Yao and Leu [63] used internally webbed laser stereolithography patterns to study ceramic mold cracking behavior during pattern removal step in IC. Using finite element analysis, they observed that internal pattern geometry and shell thickness affect the ceramic mold cracking. Heating buckles more to the pattern having long Web span and lower moment inertia. Black et al. did detail study for using ABS pattern for investment casting based on burnout temperature, ash removal, thermal analysis, and casting issues [62]. During pattern burning, there are chances of presence of residual ash in complex components. Ash residues are many times removed from shell by using water or compressed air as a flushing medium. Singh et al. [64] provided a method to solve ceramic mold cracking issues in hybrid investment casting by integrating plastic patterns with wax sprues. To attach ABS patterns with wax sprue, they designed T-shaped joint. They also suggested new dewaxing method in which they placed pattern tree into furnace, increasing temperature gradually to 1120 °C. Using this proposed method, no shell cracking was observed. Sharma et al. [65] also attempted to study shell cracking behavior and to provide remedies for the same. They connected solid and hollow printed patterns using wax sprue, ingates, and riser. Trade name of polymer used was Accura-60. They produced shell of 8–10 mm thickness by coating it 8–9 times. Thermogravimetric analysis and differential thermal analysis (TGA-DTA) was done to find optimum burnout temperature for pattern material. From result, selected pattern burning temperature 600 °C left very less or almost no residue inside the mold without shell cracking.

FDM technique possesses significant difficulties in terms of dimensional accuracy and surface finish of the printed patterns. Pattern quality is always a main parameter affecting quality of casting produced by investment casting. Bual and Kumar [66] suggested four categories for improving surface finish. They are optimization of build orientation, slicing strategy, printing parameter optimization, and post treatment. Effects of printing parameters are discussed in the section of literature review. Relative surface roughness of RP pattern is due to stair stepping effect of FDM printers. So, post processing is required to improve the quality of patterns. In this literature, there is reported use of vapor smoothing process for surface finish of patterns. It was proposed that chemical exposure cycle substantially affects surface finish of the pattern [67]. Singh et al. [68] performed vapor smoothing process using acetone to improve surface quality of ABS patterns of biomedical implants. Rao et al. [69] optimized chemical treatment process in terms of solution concentration, exposure time, and temperature of chemical bath using design of experiments and ANOVA. During experiment, they used two chemicals, i.e., methyl ethyl ketone and acetone. After processing, they observed glossy finish on pattern and suggested maximum curing time 2–4 h based on size and shape of component. Rajan et al. [70] investigated the effect of vapor smoothing process parameters on surface roughness of PLA fabricated component. Parameters considered are process time and volume of

the tetra hydro flouride (THF) solution. After experimentation, they reported that VS process performed using 10 ml THF solution for 5 min decreased surface roughness by 78.13%.

5 Conclusions

Investment casting process enhanced with the integration of RP method termed as hybrid investment casting or rapid investment casting. Different 3D printing methods are useful for pattern preparation and rapid tooling from which FDM was mostly adopted due to its low cost and faster processing. From this present paper, the following conclusions can be made:

- i. There are many printing parameters and printing materials to be understood for effective utilization of FDM in investment casting. Detailed review on effects of printing parameters and applications of 3D printing gave significant information that ABS and PLA are mostly studied and used materials.
- ii. Parameters that were considered are infill density, infill pattern, raster angle, part orientation, extrusion temperature, and print speed. Impact of each parameter is different based on shape and size of the pattern and its application.
- iii. Hybrid investment casting found its application in many fields such as manufacturing of medical implants, jewelry casting, dentistry, micro casting, and many low volume production components such as turbine blades, fuel pumps, and many more.
- iv. Certain problems to be resolved are shell cracking during pattern removal, effective pattern burning temperature, and pattern quality.
- v. Shell cracking may be reduced by changing solid pattern to hollow Web type structure pattern and increasing shell thickness.
- vi. Pattern burning temperature can be optimized using TGA-DTA analysis.
- vii. Pattern quality improvement consists of many pre-processing and post processing treatment. Majorly used techniques are process parameter optimization and chemical finishing techniques such as vapor smoothing.

Other than these, use of newly available materials such as PETG and reinforced polymer materials as pattern material requires detailed investigation. Some of the casting parameters such as primary slurry drying time, viscosity of primary, and secondary slurry need to be investigated further for better quality of product along with low cost.

References

1. Ngo TD, Kashani A, Imbalzano G, Nguyen KTQ, Hui D (2018) Additive manufacturing (3D printing): a review of materials, methods, applications and challenges. *Compos B* 143(February):172–196. <https://doi.org/10.1016/j.compositesb.2018.02.012>
2. Shahrubudin N, Lee TC, Ramlan R (2019) An overview on 3D printing technology: technological, materials, and applications. *Procedia Manuf* 35:1286–1296. <https://doi.org/10.1016/j.promfg.2019.06.089>
3. Singh R, Singh S, Hashmi M (2016) Investment casting. *Mater Sci Mater Eng*, pp 1–18. <https://doi.org/10.1016/B978-0-12-803581-8.04163-1>
4. Olsen D (2020) What is investment casting and how does it work? *metaltek.com*. <https://www.metaltek.com/blog/what-is-investment-casting-and-how-does-it-work/> (accessed May 02, 2021)
5. Bhushan B, Caspers M (2017) An overview of additive manufacturing (3D printing) for microfabrication. *Microsyst Technol* 23(4):1117–1124. <https://doi.org/10.1007/s00542-017-3342-8>
6. Khan I, Kumar N (2020) Fused deposition modelling process parameters influence on the mechanical properties of ABS: a review. *Mater Today: Proc* xxx. <https://doi.org/10.1016/j.matpr.2020.10.202>
7. Boschetto A, Giordano V, Veniali F (2012) Modelling micro geometrical profiles in fused deposition process. *Int J Adv Manuf Technol* 61(9–12):945–956. <https://doi.org/10.1007/s00170-011-3744-1>
8. Penumakala PK, Santo J, Thomas A (2020) A critical review on the fused deposition modeling of thermoplastic polymer composites. *Compos Part B: Eng* 201(July):108336, 2020. <https://doi.org/10.1016/j.compositesb.2020.108336>
9. Manoj Prabhakar M, Saravanan AK, Haiter Lenin A, Jerin leno I, Mayandi K, Sethu Ramalingam P (2020) A short review on 3D printing methods, process parameters and materials. *Mater Today: Proc* xxx. <https://doi.org/10.1016/j.matpr.2020.10.225>
10. Hay Z (2021) Best 3D printing temperatures for PLA, TPU, ABS, & more. *all3dp.com*. <https://all3dp.com/2/the-best-printing-temperature-for-different-filaments/> (accessed Mar. 24, 2021)
11. Yao T, Ye J, Deng Z, Zhang K, Ma Y, Ouyang H (2020) Tensile failure strength and separation angle of FDM 3D printing PLA material: experimental and theoretical analyses. *Compos Part B: Eng* 188(February):107894, 2020. <https://doi.org/10.1016/j.compositesb.2020.107894>
12. Srinivasan R, Ruban W, Deepanraj A, Bhuvanesh R, Bhuvanesh T (2020) Effect on infill density on mechanical properties of PETG part fabricated by fused deposition modelling. *Mater Today: Proc* 27:1838–1842. <https://doi.org/10.1016/j.matpr.2020.03.797>
13. Simplify3D (2021) Nylon. *simplify3d.com*. <https://www.simplify3d.com/support/materials-guide/nylon/> (accessed Mar. 24, 2021)
14. Tractus3d (2021) TPU material. *tractus3d.com*. <https://tractus3d.com/materials/tpu/> (accessed Mar. 24, 2021)
15. Gokhare VG (2017) A review paper on 3D-printing aspects and various processes used in the 3D-printing. *Int J Eng Res Technol (IJERT)* 6(06):953–958
16. Alzahrani M (2017) Modification of recycled poly (ethylene terephthalate) for FDM 3D-printing applications
17. Magdum Y, Pandey D, Bankar A, Harshe S, Parab V, Kadam MS (2019) Process parameter optimization for FDM 3D printer. *Int Res J Eng Technol (IRJET)*, pp 1472–1477
18. Deb D, Jafferson JM (2021) Natural fibers reinforced FDM 3D printing filaments. *Mater Today: Proc*, xxx. <https://doi.org/10.1016/j.matpr.2021.02.397>
19. Arnold C, Monsees D, Hey J, Schweyen R (2019) Surface quality of 3D-printed models as a function of various printing parameters. *Materials* 12(12):1–15. <https://doi.org/10.3390/ma12121970>
20. Mishra PK, Senthil P, Adarsh S, Anoop MS (2021) An investigation to study the combined effect of different infill pattern and infill density on the impact strength of 3D printed polylactic acid parts. *Compos Commun* 24(April):100605. <https://doi.org/10.1016/j.coco.2020.100605>

21. Dey A, Yodo N (2019) A systematic survey of FDM process parameter optimization and their influence on part characteristics. *J Manuf Mater Process*
22. Wu W, Ye W, Wu Z, Geng P, Wang Y, Zhao J. (2017) Influence of layer thickness, raster angle, deformation temperature and recovery temperature on the shape-memory effect of 3D-printed polylactic acid samples. *Materials* 10(8). <https://doi.org/10.3390/ma10080970>
23. Lee CW, Chua CK, Cheah CM, Tan LH, Feng C (2004) Rapid investment casting: Direct and indirect approaches via fused deposition modelling. *Int J Adv Manuf Technol* 23(1–2):93–101. <https://doi.org/10.1007/s00170-003-1694-y>
24. Upadhyay M, Sivarupan T, El Mansori M (2017) 3D printing for rapid sand casting—a review. *J Manuf Process* 29:211–220. <https://doi.org/10.1016/j.jmapro.2017.07.017>
25. Pattnaik S, Karunakar DB, Jha PK (2012) Developments in investment casting process—a review. *J Mater Process Technol* 212(11):2332–2348. <https://doi.org/10.1016/j.jmatprotec.2012.06.003>
26. Alsoufi MS, Elsayed AE (2018) Surface roughness quality and dimensional accuracy—a comprehensive analysis of 100% infill printed parts fabricated by a personal/desktop cost-effective FDM 3D printer. *Mater Sci Appl* 09(01):11–40. <https://doi.org/10.4236/msa.2018.91002>
27. Manogharan G, Marie H, Baich L (2015) Study of infill print design on production cost-time of 3D printed ABS parts Liseli Baich, Guha Manogharan*. *Int J Rapid Manuf* 5:308–319
28. Paprocka I, Ociepa P, Ćwikła G, Grabowik C, Kalinowski K, The influence of printing parameters on selected mechanical properties of FDM / FFF 3D-printed parts. *IOP Conf Ser: Mater Sci Eng* 227(012033). <https://doi.org/10.1088/1757-899X/227/1/012033>
29. Dawoud M, Taha I, Ebeid SJ (2016) Mechanical behaviour of ABS: an experimental study using FDM and injection moulding techniques. *J Manuf Process* 21:39–45. <https://doi.org/10.1016/j.jmapro.2015.11.002>
30. Manoj A, Bhuyan M, Banik SR, Ravi Sankar M (2021) Review on particle emissions during fused deposition modeling of acrylonitrile butadiene styrene and polylactic acid polymers. *Mater Today: Proc*, xxxx. <https://doi.org/10.1016/j.matpr.2020.11.521>
31. Ansari AA, Kamil M (2021) Effect of print speed and extrusion temperature on properties of 3D printed PLA using fused deposition modeling process. *Mater Today: Proc*. <https://doi.org/10.1016/j.matpr.2021.02.137>
32. Moradi M, Moghadam MK, Shamsborhan M (2020) The synergic effects of FDM 3D printing parameters on mechanical behaviors of bronze poly lactic acid composites. *J Compos Sci* 4(17):1–16
33. Kumar MA, Khan MS, Mishra SB (2020) Effect of machine parameters on strength and hardness of FDM printed carbon fiber reinforced PETG thermoplastics. *Mater Today: Proc* 27:975–983. <https://doi.org/10.1016/j.matpr.2020.01.291>
34. Wu Kang J, Xian Ma Q (2017) The role and impact of 3D printing technologies in casting. *China Foundry* 14(3):157–168. <https://doi.org/10.1007/s41230-017-6109-z>
35. Petrus RE, Puşcaşu S, Pascu A, Bondrea I (2019) Key factors towards a high-quality additive manufacturing process with ABS material. *Mater Today: Proc* 12:358–366. <https://doi.org/10.1016/j.matpr.2019.03.136>
36. Singh R, Singh S, Singh G (2014) Dimensional accuracy comparison of investment castings prepared with Wax and ABS patterns for bio-medical application. *Procedia Mater Sci* 6(December):851–858. <https://doi.org/10.1016/j.mspro.2014.07.102>
37. Kumar P, Singh R, Ahuja IPS (2015) Investigations on dimensional accuracy of the components prepared by hybrid investment casting. *J Manuf Process* 20:525–533. <https://doi.org/10.1016/j.jmapro.2015.07.008>
38. Kumar P, Ahuja IS, Singh R (2016) Experimental investigations on hardness of the biomedical implants prepared by hybrid investment casting. *J Manuf Process* 21:160–171. <https://doi.org/10.1016/j.jmapro.2016.01.001>
39. Huang P, Huang W (2017) Processing design of miniature casting incorporating stereolithography technologies. *Int J Aerosp Mech Eng* 11(8):1403–1406

40. Singh D, Singh R, Boparai KS, Farina I, Feo L, Verma AK (2018) In-vitro studies of SS 316 L biomedical implants prepared by FDM, vapor smoothing and investment casting. *Compos B Eng* 132:107–114. <https://doi.org/10.1016/j.compositesb.2017.08.019>
41. Singh J, Singh R, Singh H (2018) Surface roughness prediction using Buckingham's Pi-theorem for SS-316L hip implant prepared as rapid investment casting. *Mater Today: Proc* 5(9):18080–18088. <https://doi.org/10.1016/j.matpr.2018.06.142>
42. Wang J, Sama SR, Lynch PC, Manogharan G (2019) Design and topology optimization of 3D-printed wax patterns for rapid investment casting. *Procedia Manuf* 34:683–694. <https://doi.org/10.1016/j.promfg.2019.06.224>
43. Carneiro VH, Rawson SD, Puga H, Meireles J, Withers PJ (2020) Additive manufacturing assisted investment casting: a low-cost method to fabricate periodic metallic cellular lattices. *Additive Manuf* 33(November, 2019):101085. <https://doi.org/10.1016/j.addma.2020.101085>
44. Körber S, Vökl R, Glatzel U (2021) 3D printed polymer positive models for the investment casting of extremely thin-walled single crystals. *J Mater Process Technol* (February):117095. <https://doi.org/10.1016/j.jmatprot.2021.117095>
45. Cooper KG, Wells D (2000) Application of rapid prototyping to the investment casting of test hardware (June)
46. Singh R, Singh R, Singh Dureja J (2019) CAD-CAM assisted investment casting for preparation of dental crowns. *Mater Today: Proc* xxxx, 2019. <https://doi.org/10.1016/j.matpr.2019.10.169>
47. Wu M et al (2001) Application of laser measuring, numerical simulation and rapid prototyping to titanium dental castings. *Dent Mater* 17(2):102–108. [https://doi.org/10.1016/S0109-5641\(00\)00037-3](https://doi.org/10.1016/S0109-5641(00)00037-3)
48. Kheirollahi H, Abbaszadeh F (2011) Application of rapid prototyping technology in dentistry. *Int J Rapid Manuf* 2(1/2):104. <https://doi.org/10.1504/ijrapidm.2011.040692>
49. Torabi K, Farjood E, Hamedani S (2015) Rapid prototyping technologies and their applications in prosthodontics, a review of literature. *J Dent* (Shiraz, Iran) 16(1):1–9. [Online]. Available: <http://www.ncbi.nlm.nih.gov/pubmed/25759851%0A>, <http://www.pubmedcentral.nih.gov/articlerender.fcgi?artid=PMC4345107>
50. Bhosale S, Shinde PVD (2018) Manufacturing of patient specific implant models by 3D printing assisted investment casting. *Int Res J Eng Technol (IRJET)* 5(7):64–68
51. Kumar R, Kumar M, Chohan JS (2021) The role of additive manufacturing for biomedical applications: a critical review. *J Manuf Process* 64(September 2020):828–850. <https://doi.org/10.1016/j.jmapro.2021.02.022>
52. Kumar P, Ahuja IS, Singh R (2016) Effect of process parameters on surface roughness of hybrid investment casting. *Prog Addit Manuf* 1(1–2):45–53. <https://doi.org/10.1007/s40964-016-0004-9>
53. Sanadhya S, Vij N, Chaturvedi P, Tiwari S, Arora B, Modi YK (2015) Medical applications of additive manufacturing. *Int J Sci Prog Res* 12:11–17. https://doi.org/10.1007/978-3-030-00665-5_152
54. Charmeux J-F (2007) Capabilities of the Investment Casting Process for producing meso/micro metal castings using Rapid Prototyping manufacturing routes
55. Jain P, Kuthe AM (2013) Feasibility study of manufacturing using rapid prototyping: FDM approach. *Procedia Eng* 63:4–11. <https://doi.org/10.1016/j.proeng.2013.08.275>
56. Redwood B (2021) Jewelry 3D printing applications. 3dhubs.com. <https://www.3dhubs.com/knowledge-base/jewelry-3d-printing-applications/> (accessed Apr. 07, 2021)
57. Wannarumon S, Bohez ELJ (2004) Rapid prototyping and tooling technology in jewelry CAD. *Comput-Aided Des Appl* 1(1–4):569–575. <https://doi.org/10.1080/16864360.2004.10738300>
58. Cheah CM, Chua CK, Lee CW, Feng C, Totong K (2005) Rapid prototyping and tooling techniques: a review of applications for rapid investment casting. *Int J Adv Manuf Technol* 25(3–4):308–320. <https://doi.org/10.1007/s00170-003-1840-6>
59. Mondal B, Kundu S, Lohar AK, Pai BC (2008) Net-shape manufacturing of intricate components of A356/SiCp composite through rapid-prototyping-integrated investment casting. *Mater Sci Eng, A* 498(1–2):37–41. <https://doi.org/10.1016/j.msea.2007.10.126>

60. Zhang Y, Li X, Zhang L, Rong B, Cai Q, Zhu R, Xu Y (2018) Simulation and optimization for investment casting of impeller based on 3D printing. *IOP Conf Ser: Earth Environ Sci* 186(5). <https://doi.org/10.1088/1755-1315/186/5/012016>
61. Brotzu A, Felli F, Mondal A, Pilone D (2020) Production issues in the manufacturing of TiAl turbine blades by investment casting. *Procedia Struct Integrity* 25:79–87. <https://doi.org/10.1016/j.prostr.2020.04.012>
62. Blake P, Fodran E, Koch M, Menon U, Priedeman B, Sharp S (1997) FDM of ABS patterns for investment casting. In: *Solid freeform fabrication proceedings*, September 1997, pp 195–202
63. Yao WL, Leu MC (1998) Shell cracking in investment casting with laser stereolithography patterns, pp 427–434
64. Singh S, Kumar P, Singh J (2021) An approach to eliminate shell cracking problem in fused deposition modeling pattern based investment casting process. *IOP Conf Ser: Mater Sci Eng* 1091(1):012035. <https://doi.org/10.1088/1757-899x/1091/1/012035>
65. Sharma A et al (2012) Study of shell cracking behavior and its remedies in investment casting process using quick cast rapid prototype polymer patterns. *Mater Sci Forum* 710:214–219. <https://doi.org/10.4028/www.scientific.net/MSF.710.214>
66. Bual GS, Kumar P (2014) Methods to improve surface finish of parts produced by fused deposition modeling. *Manuf Sci Technol* 2(3):51–55. <https://doi.org/10.13189/mst.2014.020301>
67. Singh R, Singh S, Preet I, Fabbrocino F, Fraternali F (2017) Investigation for surface finish improvement of FDM parts by vapor smoothing process. *Compos B* 111:228–234. <https://doi.org/10.1016/j.compositesb.2016.11.062>
68. Singh J, Singh R, Singh K (2020) Vapor smoothing process for surface finishing of FDM replicas. *Mater Today: Proc* 26:173–179. <https://doi.org/10.1016/j.matpr.2019.09.013>
69. Rao AS, Dharap M, Venkatesh JVL, Ojha D (2012) Investigation of post processing techniques to reduce the surface roughness of fused deposition modeled parts. *Int J Mech Eng Technol (IJMET)* 3(3):531–544
70. John Rajan A, Sugavaneswaran M, Prashanthi B, Deshmukh S, Jose S (2020) Influence of vapour smoothing process parameters on fused deposition modelling parts surface roughness at different build orientation. *Mater Today: Proc* 22:2772–2778. <https://doi.org/10.1016/j.matpr.2020.03.408>

Recent Advancements in TIG Cladding Process on Non-ferrous Alloys: A Review



Sujeet Kumar and Anil Kumar Das

Abstract Recently, quality improvement of the cladding layer deposited on non-ferrous metals/alloys such as aluminium, titanium, magnesium and its alloys, are mainly focused for the cladding industries and associated research department. The main focus of these industries is development of a new process of cladding that improves cladded layer quality, increase productivity with low cost. TIG cladding has been used to fulfil the requirements by changing the parameters of the cladding such as input current, voltage, shielding gas, standoff distance and scan speed can be strongly controlled. Aluminium, magnesium and titanium alloys have been frequently used in aerospace, automobile industries because of its low weight and high strength, improved properties at low temperature, good heat conductive and low corrosion tendency. Especially, magnesium alloys are replaced with plastic in electronic industries because of easy damping capacity and electromagnetic shielding properties. While its application is restricted in abrasive conditions due to its poor tribological properties and low hardness. Several researchers reported that surface properties of the non-ferrous alloys successfully enhanced using various metallic and non-metallic elements with or without ceramic materials deposited by tungsten inert gas cladding process. This paper compiled the effect of the reinforcement and matrix on the hardness, wear resistance and corrosion resistance. It also discussed the effect of process parameters of TIG cladding on the microstructure, cladding quality and surface properties of the cladded layer on the non-ferrous alloy especially aluminium, magnesium and titanium. The summary table also displays the effect of coating powder on the non-ferrous alloys.

Keywords TIG cladding · Microhardness · Non-ferrous alloy · Wear resistance · Friction coefficient · Coating

S. Kumar (✉) · A. K. Das
Department of Mechanical Engineering, National Institute of Technology Patna, Patna, Bihar
800005, India

A. K. Das
e-mail: akdas@nitp.ac.in

© The Author(s), under exclusive license to Springer Nature Singapore Pte Ltd. 2022
H. K. Dave et al. (eds.), *Recent Advances in Manufacturing Processes and Systems*,
Lecture Notes in Mechanical Engineering,
https://doi.org/10.1007/978-981-16-7787-8_66

833

1 Introduction

Aluminium alloys are frequently used in aircraft and automobile industries because of its very low corrosion and oxidation tendency as well as high strength with lightweight. Due to high strength of 2000 series of aluminium alloys, it is selected for the structural components of aerospace industries [1]. Magnesium alloys are also used in automotive transportation and aerospace industries because of its many advantages such as shock absorption, good heat dissipation capacity, low density and high strength. Lightweight, high resistance to corrosion, high strength and good properties at elevated temperature of Ti–6Al–4V alloys are widely utilized in biomedical industries, aerospace and petrochemical industries. Nevertheless, application of these alloys is restricted in extremely abrasive conditions because of relatively poor wear resistance [2–4]. Hence the surface modification techniques are required to eliminate the drawback of these alloys. There are various surface modification methods such as laser cladding, tungsten inert gas (TIG) cladding, plasma spraying and electron beam cladding which are employed to enhance the surface properties of the aluminium, magnesium, titanium and its alloys [5].

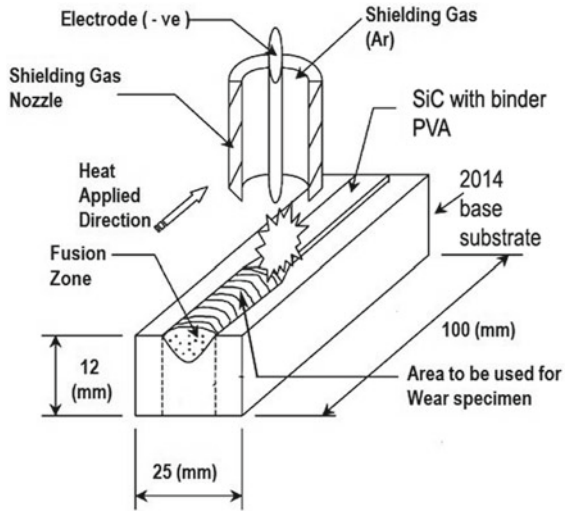
Several researchers reported that TIG cladding techniques are capable to provide better cladding quality and enhance surface properties of the substrate and are also used to repair the worn out surfaces of the components by depositing the new coating layer. The TIG cladding is considered an economical and high energy density technique compare to laser cladding that creates energy absorption problems and electron beam cladding that required vacuum chamber [6, 7]. The TIG heat input is function of voltage, current and scan speed of TIG torch, it may be controlled by the change in various parameters such as input current, voltage, distance between electrode tip and substrate, therefore, better cooling rate is achieved. Over the years, researchers have enhanced the surface properties by depositing the composite coating layer on the substrate using TIG cladding. Ardeshiri et al. [8] have enhanced the microhardness as well as reduced the wear loss of the A2618 aluminium using silicon and iron powder deposited by TIG coating process.

The present study contains an overview of the TIG cladding on non-ferrous alloys. The advantages and applications of TIG cladding techniques are also mentioned in this paper. The influence of the various process parameters of TIG cladding on tribological properties as well as surface properties of the newly deposited layer was discussed in this paper. The hardness value shows in the graph achieved by the authors using different coating materials. This paper provides the facility for the researchers to select the coating materials and process parameters for the TIG cladding.

2 TIG Cladding Process

Tungsten inert gas (TIG) cladding process is an affordable process than the other cladding process such as laser, plasma and electron beam cladding. The laser and

Fig. 1 Experimental setup diagram of TIG cladding [2]



electron beam cladding provide less dilution and precise coating layer but these are expensive processes whereas laser cladding required high skilled operators and high power to generate laser beam, as well as the electron beam, also required a vacuum chamber for operation. Therefore, nowadays TIG cladding process is frequently used to deposit the coating powder on surface of the substrate to modify the hardness, corrosion and wear resistance. This process also provides the facility for applying different shielding gas to shield the weld pool. Figure 1 [2] display the setup diagram of the TIG cladding. It also sows the preplaced layer, substrate, fusion zone, TIG torch, etc. The heat input of the TIG process can be calculated by Eq. 1 [9]:

$$\text{Heat input}(E) = (\eta \times I \times V)/(S) \quad (1)$$

where, I , V and S represent is input current, voltage and scan speed respectively, η represents the efficiency coefficient which is considered as 48%.

2.1 TIG Cladding on Aluminium Alloys

Tungsten inert gas coating process was successfully used to deposit the metal matrix composite coating on the aluminium alloys that make it usable in many industries such as aircraft industries, petrochemical, automobile industries. The addition of the matrix enhances the wetting properties between the reinforcements and substrate, it is reported by Lotfi et al. [9] deposited the new hard layer of the SiC ceramic with Al and Si matrix on the A380 aluminium alloy using TIG cladding. It was reported that the added Si content increase the wetting properties with aluminium powder and

enhance the adhesion process. Due to the formation of needle-shaped Al_4SiC_4 , the microhardness achieved was about 400 HV [9]. Shanmugasundaram et al. (2016) also deposited the SiC ceramic composite on AA 2014 aluminium alloy by TIG process. It was observed that the AA 2xxx alloy of aluminium alloy consists of copper as main alloying element and is selected for mechanical construction components. It was noticed that SiC particles in the aluminium matrix formed the high angle boundaries. During applying external load, high angle boundaries prevent the dislocation movement therefore hardness values increase and the strength of the coated layer also increases. It was reported that more wear loss was found for the heat treated AA 2014 aluminium alloy as compared to base metal of that alloys while the wear rate of the SiC coated layer was less than the base metal [2]. Shanmugasundaram et al. [2] also reinforced the SiC particles on AA 5086 melting by the TIG cladding techniques using different scanning speeds and current. The hardness value increases with increasing the travel speed of TIG torch. It was reported that the fine grain microstructure has been found at 150 A current whereas the coarser grain microstructure found at 175 A. The hardness at 150 A was more than the hardness at 175 A current due to refinement of the grains. The hardness value varies from fusion zone to right side and the left side because at the left side and right side the heat dissipation takes place easily while heat input is found constant and dispersion becomes nil at the centre of fusion zone [10]. Ardeshiri et al. [8] have produced the silicon and iron alloyed coating on A2618 aluminium alloy. Figure 2 [8] shows that at high input current the depth of alloyed layer increases due to dilution of the substrate. It was found that the cellular microstructure found at interface zone, aluminium dendrites as well as intermetallic compound of the Al-Si-Fe with needles shape found at alloyed zone. The maximum microhardness of the alloyed layer reached 210 HV owing to the presence of new different compounds such as Fe_5Si_3 , Al_5FeSi , $\text{Al}_8\text{Fe}_2\text{Si}$ and $\text{Al}_{13}\text{Fe}_4$. Because

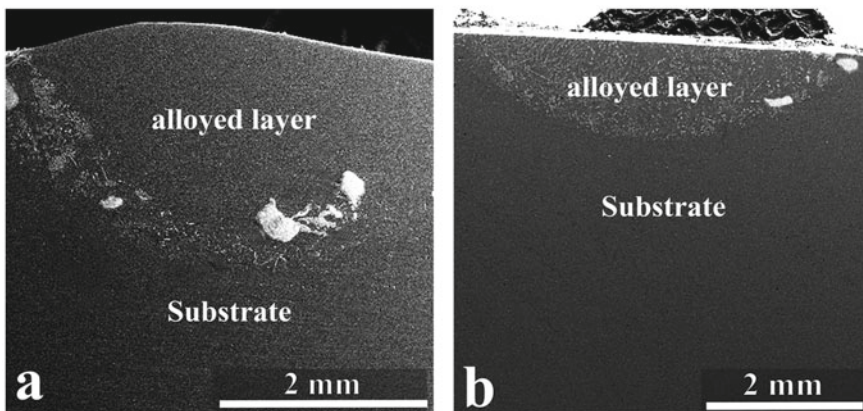


Fig. 2 Scanning electron microscope images of the Si-Fe alloyed layer deposited on the A2618 aluminium at **a** 200 A and **b** 150 A input current with constant speed [8]

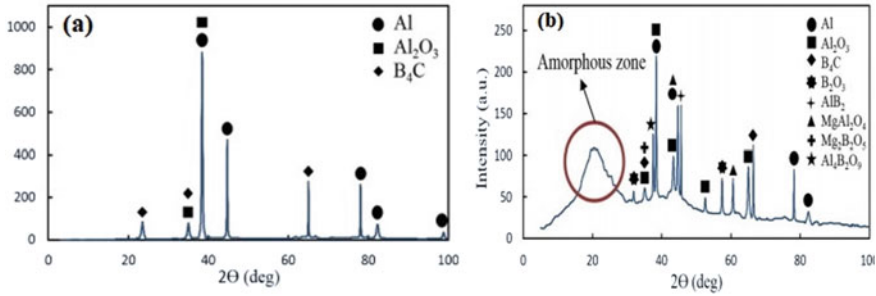


Fig. 3 XRD graph of Al/5 wt%B₄C coated layer produced by **a** flame spraying process and **b** TIG cladding process [11]

of the fabrication of hard new compounds in the alloyed layer, the wear rate decreases about half of the untreated layer [8].

Zabihi and Soltani [11] deposited the B₄C-Al-Mg coating on the Al-Mg plate by flame spraying process and then remelted this layer using TIG process. It was reported that due to high solidification rate the dense coating layer was obtained, which increases the hardness as well as wear resistance. The B₄C-Al mixture was deposited by flame spraying and formed intermetallic compounds such as B₄C and Al₂O₃. Then applied the TIG to produce dense coating and formed intermetallic compounds such as B₄C, B₂O₃, AlB₂, MgAl₂O₄, Al₄B₂O₉ and Mg₂B₂O₅ as shown in XRD Fig. 3 [11], due to presence of these phases increases the load bearing capacity as a result the maximum microhardness found 270 HV_{0.2} [11].

Liang et al. [12] compared the microstructure and geometry of coating tracks deposited by cold metal transfer (CMT) process and CMT-TIG hybrid process on the 6061 aluminium alloy at different scan speeds and current. They reported that the clad surface produced by the CMT process was not uniform because of low heat input provided by this process whereas defect free and uniform surface was deposited by the CMT-TIG process. The width and depth of the tracks increases with increasing TIG current (From sample 1 to sample 3) and it decreases with increasing scan speed (sample 4, 6 and 7) with constant CMT current as shown in Fig. 4 [12]. It was also reported that the width and depth of the tracks increased with increasing CMT current at the same time TIG current was kept constant as shown in Fig. 4 (sample 2, 4 and 5) [12].

2.2 TIG Cladding on Magnesium Alloys

Very little work has been done on the magnesium alloy by TIG process as much as available research papers collected and compiles the information about the TIG cladding and documented the effect of the process parameters of TIG cladding on magnesium alloys. Magnesium alloy possesses low density, good castability, good

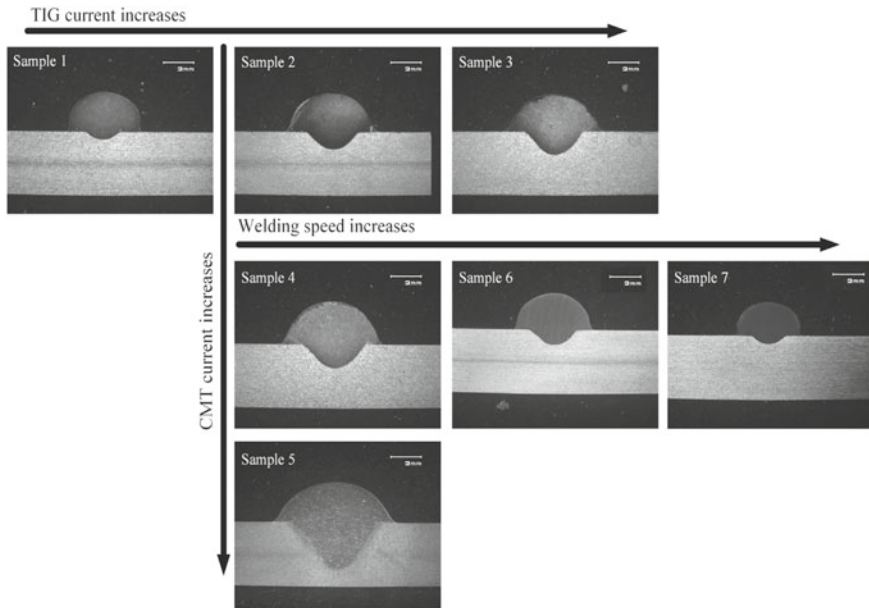
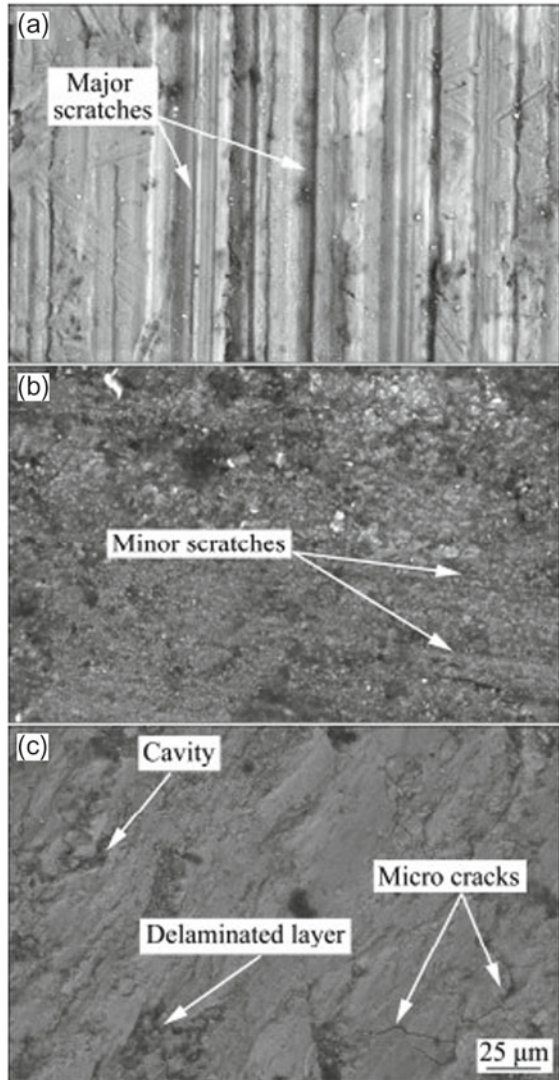


Fig. 4 Cross-section images of the specimen with increasing scan speed and current of TIG cladding and CMT process [12]

machinability, good ductility and high ambient temperature strength but suffers from poor surface quality. Surface properties of the magnesium alloy has been improved by adding hard phases using TIG cladding, reported by researchers. Padhee et al. [13] have improved the wear resistance of this alloy by depositing the Al–TiC composite coating. It was reported that the microhardness improved owing to the distribution of the TiC ceramic phases in the Al–Mg matrix, hardness value fluctuated in the coating due to TiC particles present non-uniformly. The depth of the cladded layer increases the TiC particles decreases as a result the microhardness decreases. The presence of TiC phases resist the deformation as well as prevent the removal of cladded layer during the wear test. Figure 5 [13] display the scanning electron microscope images of wear out of treated and untreated surfaces. The images show that large grooves and scratches present over the uncoated AZ91 magnesium alloy due to absence of any hard phases. Wear test after 3 min, minors scratches occurred on the Al–TiC coated Mg alloy while after 30 min of wear testing, some micro cracks and scratches formed on the Al–TiC coated Mg alloy. The existence of the hard phases in the coating surface, protect the coated layer against wear testing [13].

Elahi et al. [5] deposited the Al–Ni coating layer on the AZ91D magnesium alloy using tungsten inert gas melting process at different heat inputs. Due to the formation of the following intermetallic compounds Mg, $Mg_{17}Al_{12}$ and $AlNi_3$ the hardness value approaches 162 $HV_{0.01}$ that was higher than the substrate hardness 80 $HV_{0.01}$ [5]. Wenbin et al. [14] modified the microstructure and mechanical properties

Fig. 5 Scanning electron microscope pictures of the **a** uncoated AZ91 magnesium alloy and coated substrate with, **b** wear test duration 3 min, **c** wear test duration 30 min [13]



of AZ31 using SiC coating by gas tungsten arc (GTA) cladding. It was reported that the GTA coating depth increases with increasing processing current and depth decreases with scan speed increases. The current increases from 150 to 200 A, the melt depth increases and simultaneously decreases the SiC particles in the coating zone as a result wear rate of the treated AZ31 magnesium alloy at 200 A found high as compared to wear rate of treated AZ31 magnesium alloy at 150 A with increasing wear load (0.5–3.5 h) with constant temperature (20 °C) it also found high when wear test conducted at increasing temperature (from 20 to 260 °C) at constant wearing

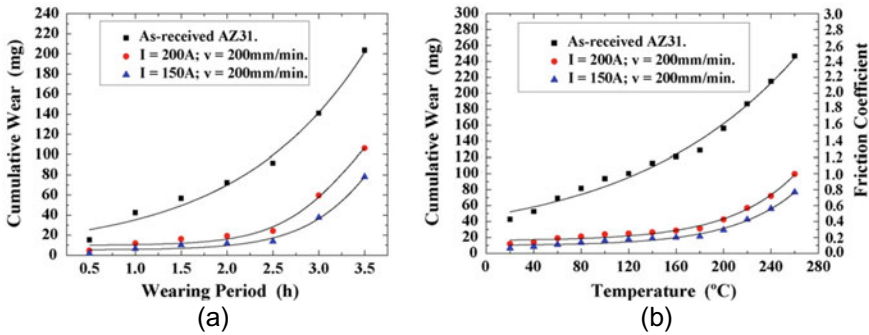


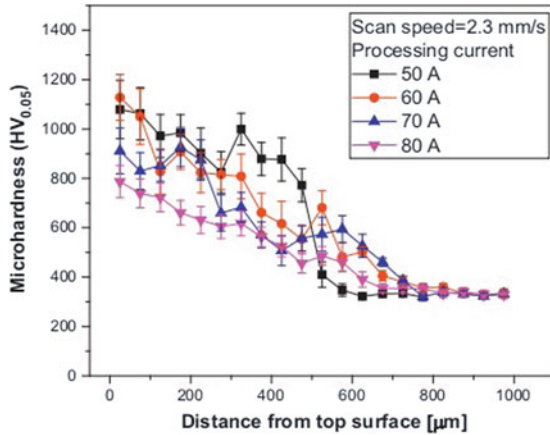
Fig. 6 The cumulative wear of the coated and uncoated samples with **a** Increasing wear test period at fixed temperature (20 °C) and **b** wear as well as friction coefficient with increasing temperature at fixed period (1 h) [14]

time (1 h) as shown in Fig. 6a, b. From the wear graph (Fig. 6 [14]), it is also clear that the wear of the as-received AZ31 alloy surface is more than the clad AZ31 surface. The friction coefficient of the as-received AZ31 substrate is more than that of the clad samples, it also decreases with decreasing in processing current [14].

2.3 TIG Cladding on Titanium Alloys

Many research groups had enhanced the surface properties such as wear resistance and microhardness of the Ti or Ti alloy using TIG cladding process. The researchers reported that the heat input of the TIG directly influences the coating layer quality, microstructure and surface properties. The surface properties of the coated titanium or Ti alloy are also influenced by the distribution of the coating powder or formation of hard phases, it is reported by Yang et al. [15] deposited the TiC-Ti composite layer using Ti, C and Al powder melting by TIG cladding on the Ti-6Al-4V alloy. It was mentioned, the TiC particles size decreases with depth increases therefore the microhardness decreases. The maximum microhardness approached about 1300 HV_{0.05} [15]. Waghmare et al. [4] analyzed the microstructure and surface properties performance of the NiTi cladding layer on titanium alloy. The authors reported that the presence of NiTi and NiTi₂ provide protection from oxidation, corrosion and wear for the Ti-6Al-4V alloy. At 40 A and 50 A lower processing current the microhardness approached at maximum value and reduces with increasing in processing input current [4]. It is also reported by Tijo and Masanta [16] and hardness graph shows in Fig. 7. The authors reported that at processing current of 50 A the surface of the substrate does not melt with the clad layer and uniform distribution of coating materials was achieved in the coated zone as a result uniform hardness achieved at this current in clad zone and suddenly drops in the substrate as shown in Fig. 7. At 60 A and 70 A, the substrate melted partially and the non-uniform distribution of

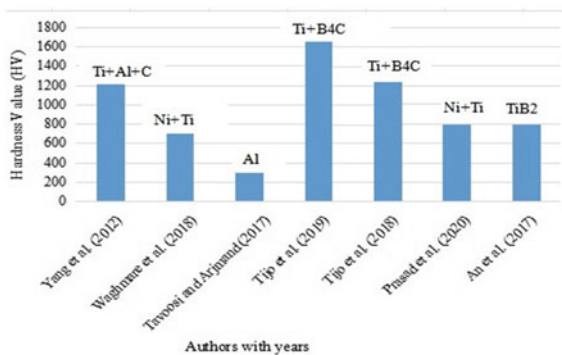
Fig. 7 Microhardness distribution on the polished cross-section area of the coated samples at different scanning speeds with constant scan speed [16]



the coating materials occurs therefore at this processing temperature hardness value varies randomly. While at 80 A current, more melting of the substrate occurs with slight decrease of the coating materials with the depth therefore microhardness is found with small reduction with the depth [16].

Tavoosi and Aejmam [17] deposited the Al coating on the pure titanium substrate that formed the Al₃Ti phases and found the hardness value of about 295 HV in the coating zone. Various research groups improved the surface properties of Ti–6Al–4V alloy utilized by various coating power melted by TIG cladding as shown in Fig. 8 [4, 15–20]. The hardness value depends upon the reinforcements and matrix materials, coating layer deposited using optimized parameters. From Fig. 8, it is noticed that hardness value of the cladded titanium or Ti alloy depends upon the distribution or formation of the hard phases in the coating zone. Ti and B₄C coating formed the hard phases such as TiB₂ and TiC synthesized on Ti–6Al–4V alloy and gives the higher hardness value about the 1680 HV as compared to the deposition of Al coating layer on pure titanium substrate that formed only Al₃Ti phases and found lower hardness

Fig. 8 The hardness value of the coated layer achieved by the authors using different coating materials on the Ti and its alloy



about 250 HV. NiTi coating layer also produces high hardness than the Al_3Ti coating but less than the TiB_2 and TiC composite coating.

2.4 Summary Table About TIG Coating on the Non-ferrous Alloys Substrate

Table 1 shows the summary of the reviewed research paper. The table also shows the hardness value and wear resistance of the coated layer using different coating powder deposited on non-ferrous alloys by TIG cladding.

3 Conclusion

After a review of many research papers available on TIG cladding on the aluminium, magnesium and titanium alloys following points had been summarized.

1. Using optimized process parameters of TIG cladding, it can be deposited the pore and voids free coating on the non-ferrous metals and alloys at low cost than the other cladding process.
2. The width and depth of the cladded tracks increase with increasing processing current but decreases with an increasing scan speed of the TIG torch.
3. The hardness was found maximum at the left and right side from the fusion zone because at the left and right side the heat transfer was high compared to the fusion zone.
4. The uniform distribution of the reinforcements leads to a reduced wear rate, prevent crack initiation and wear by delamination of the coated surface.
5. The coating of the hard phases on the non-ferrous alloy substrate provides high hardness as well as better wear resistance.

Table 1 Work done by the various research group on non-ferrous alloys

Authors	Substrate	Coating materials	Key findings	
			Microhardness (HV)	Wear resistance
Different coating powder deposited on aluminium alloys by TIG cladding process				
Lotfi e al. [9]	A380 Al alloy	Al, Si, SiC	190	Lower wear rate of the coated samples than substrate
Shanmugasundaram et al. [2]	AA 2014 Al alloy	SiC	177	Wear rate decreases 75% for SiC reinforced sample
Shanmugasundaram et al. [10]	AA 5086 Al alloy	SiC	101	Wear resistance of SiC reinforced sample improved 48% than the substrate
Zabihi and Soltani [11]	Al–Mg plate	Al–Mg–B ₄ C	270	Volume loss decreases about 48% of the sample
Ardeshiri et al. [8]	A2618 Al alloy	Fe-Si	210	Wear rate of the alloyed samples decreases about half than the substrate
Different coating powder deposited on magnesium alloys by TIG cladding process				
Elahi et al. [5]	AZ91D magnesium alloy	Al-Ni	162	Wear rate of the alloyed layer decreases about half than the substrate
Wenbin et al. [14]	AZ31 magnesium alloy	SiC	150	Wear resistance enhanced
Padhee et al. [13]	AZ91 magnesium alloy	Al-SiC	305	Wear of the coated sample found very less as compared to uncoated sample
Different coating powder deposited on titanium alloys by TIG cladding process				
Tijo and Masanta [16]	Ti–6Al–4V alloy	TiC-TiB ₂	1200	The wear resistance of the coated samples 3 times higher than compared to substrate

(continued)

Table 1 (continued)

Authors	Substrate	Coating materials	Key findings	
			Microhardness (HV)	Wear resistance
Tavoosi and Arjmand [17]	Pure titanium	Al	250	–
Waghmare et al. [4]	Ti–6Al–4V alloy	Ni, Ti	680 ± 60	Wear resistance increases of coated samples about 9.5 times than the substrate
Tijo and Masanta [18]	Ti–6Al–4V alloy	Ti, B ₄ C	1680	Wear resistance increases about 11 times
Prasad et al. [19]	Ti–6Al–4V alloy	Ni, Ti	800	Wear resistance increases with percentage of overlapping increases
An et al. [20]	Ti–6Al–4V alloy	Ti–6Al–4V, TiB ₂	728	Wear resistance of coated samples found better wear resistance

References

1. Starke J, Edgar A, Staley JT (1996) Application of modern aluminium alloys to aircraft. *Prog Aerosp Sci* 32(2–3):131–172
2. Shanmugasundaram A, Arul S, Sellamuthu R (2018) Effect of reinforcement of SiC and aging treatment on the hardness and wear property of AA 2014 using GTA as a heat source. *Mater Today: Proc* 5(8):16552–16564
3. Pei X, Li Z, Zhang Y, Wei S, Yang L, Wang Y (2019) A gradient Al/Ni–Cr–Al layer formed by direct current pulse metal inert gas welding combined laser cladding on AZ91D magnesium alloy. *Vacuum* 165:86–95
4. Waghmare DT, Padhee CK, Prasad R, Masanta M (2018) NiTi coating on Ti–6Al–4V alloy by TIG cladding process for improvement of wear resistance: microstructure evolution and mechanical performances. *J Mater Process Technol* 262:551–561
5. Elahi MR, Sohi MH, Safaei A (2012) Liquid phase surface alloying of AZ91D magnesium alloy with Al and Ni powders. *Appl Surf Sci* 258(15):5876–5880
6. Heydarzadeh Sohi M, Ansari M, Ghazizadeh M, Zebardast H (2015) Liquid phase surface nitriding of aluminium using TIG process. *Surf Eng* 31(8):598–604
7. Chen JH, Chen PN, Lin CM, Chang CM, Chang YY, Wu W (2009) Microstructure and wear properties of multicomponent alloy cladding formed by gas tungsten arc welding (GTAW). *Surf Coat Technol* 203(20–21):3231–3234
8. Ardeshiri A, Sohi MH, Safaei A (2017) Surface alloying of A2618 aluminium with silicon and iron by TIG process. *Surf Coat Technol* 310:87–92
9. Lotfi B, Rostami M, Sadeghian Z (2014) Effect of silicon content on microstructure of Al–Si/SiCp composite layer cladded on A380 Al alloy by TIG welding process. *Trans Nonferrous Met Soc China* 24(9):2824–2830

10. Shanmugasundaram A, Arul S, Sellamuthu R (2018) Study on the effect of GTA surface melting and SiC reinforcement on the hardness, wear and corrosion properties of AA 5086. *Mater Today: Proc* 5(2):6597–6606
11. Zabih A, Soltani R (2018) Tribological properties of B4C reinforced aluminium composite coating produced by TIG re-melting of flame sprayed Al-Mg-B4C powder. *Surf Coat Technol* 349:707–718
12. Liang Y, Hu S, Shen J, Zhang H, Wang P (2017) Geometrical and microstructural characteristics of the TIG-CMT hybrid welding in 6061 aluminium alloy cladding. *J Mater Process Technol* 239:18–30
13. Padhee CK, Masanta M, Mondal AK (2020) Feasibility of Al–TiC coating on AZ91 magnesium alloy by TIG alloying method for tribological application. *Trans Nonferrous Met Soc China* 30(6):1550–1559
14. Wenbin D, Haiyan J, Xiaoqin Z, Dehui L, Shoushan Y (2007) Microstructure and mechanical properties of GTA surface modified composite layer on magnesium alloy AZ31 with SiCp. *J Alloy Compd* 429(1–2):233–241
15. Yang R, Liu Z, Yang G, Wang Y (2012) Study of in-situ synthesis TiCp/Ti composite coating on alloy Ti6Al4 V by TIG cladding. *Procedia Eng* 36:349–354
16. Tijo D, Masanta M (2018) In-situ TiC–TiB₂ coating on Ti–6Al–4V alloy by tungsten inert gas (TIG) cladding method: Part-II mechanical performance. *Surf Coat Technol* 344:579–589
17. Tavooosi M, Arjmand S (2017) In situ formation of Al/Al₃Ti composite coating on pure Ti surface by TIG surfacing process. *Surf Interfaces* 8:1–7
18. Tijo D, Masanta M (2019) Effect of Ti/B4C ratio on the microstructure and mechanical characteristics of TIG clad TiC–TiB₂ coating on Ti–6Al–4V alloy. *J Mater Process Technol* 266:184–197
19. Prasad R, Waghmare DT, Kumar K, Masanta M (2020) Effect of overlapping condition on large area NiTi layer deposited on Ti–6Al–4V alloy by TIG cladding technique. *Surf Coat Technol* 385:125417
20. An Q, Huang L, Jiang S, Li X, Gao Y, Liu Y, Geng L (2017) Microstructure evolution and mechanical properties of TIG clad TiB reinforced composite coating on Ti–6Al–4V alloy. *Vacuum* 145:312–319

Reinforced Composites from Natural Fiber: A Review



Sagar Singh, Chitranjan Agarwal, M. S. Khidiya, and M. A. Saloda

Abstract Materials assume a significant part of every manufacturing sector. In modern times, natural composite fabrics replace synthetic materials as a result of the promising properties of common strands like light, water obstruction, high effect strength, harmless to the ecosystem, and so on. While typical natural fibers are not so strong as synthetic fibers made, they are richly accessible, low in thickness, minimum expense, inexhaustible and biodegradable. The objective of this review should provide a comprehensive survey of common fiber composites, usually suitable and used, including various forms of usable natural fibers, various manufacturing methods, and processes involved in the preparing of characteristic fiber composites are likewise assessed.

Keywords Natural composites · Methods · Hybridization · Applications

1 Introduction

Materials are known to be the pillar of every manufacturing sector. In current times, composite materials are commonly utilized in the various sector moreover, replace traditional materials positively due to its promising properties, such as high explicit strength, solid damping, high explicit gravity strength and stability, greater failure strength, and energy retention limit of impact, more notable erosion protection, burning, acids and typical unsafe conditions, longer life-time support, and lower total costs; In the 1940s fiber was first supplied with composite materials as a norm [1]. Composite materials are delegated multi-stage materials comprising of at least two segments with extraordinary properties [2]. The use of sufficient surface alterations which can increase the mechanical properties of the characteristic strands can improve protection against water absorption or dampness. [3, 4].

S. Singh (✉) · C. Agarwal · M. S. Khidiya · M. A. Saloda
Mechanical Engineering, College of Technology and Engineering, (MPUAT) Udaipur, Udaipur, India

© The Author(s), under exclusive license to Springer Nature Singapore Pte Ltd. 2022
H. K. Dave et al. (eds.), *Recent Advances in Manufacturing Processes and Systems*,
Lecture Notes in Mechanical Engineering,
https://doi.org/10.1007/978-981-16-7787-8_67

847

1.1 Natural Fiber Composite

Natural fibers are plants and animals rendered fibers [5]. Essential and optional plants foster characteristic filaments as per their usage. Plants developed fundamentally for their fiber are known as essential plants, while plants comprising of strands are alluded to as optional plants as bi-items. The essential plants fuse jute, cotton, sisal, kenaf, and the auxiliary plants are apple and coir. At current time, there has been enormous thought paid to the usage of ordinary filaments from sustainable and non-inexhaustible hotspots for instance sisal, oil palm, jute, and flax to manufacture composites. Plants that produce cellulose strands can be arranged as bast-filaments, grass and reed-filaments, and principle components, and wide scope of plants that produce cellular filaments (sisal, pinean-apples, and abacah) (wood and roots) [6]. Natural fibers are plants and animals rendered fibers [5]. In this analysis, we only address natural fibers dependent on plants.

1.2 Types of Natural Fiber

For the creation of characteristic fiber built up polymer composites, there are various assortments of normal filaments are existing as support. Some regular filaments with incredible execution, like reinforcement in polymer composites.

Natural fibers are ordered into the accompanying six sorts:

1. Reed: including wheat, maize, and rice.
2. Leaf: Pineapple, Abaca, and Sisal.
3. Bast: Kenaf, Jute, Ramie, Flax, and Hemp.
4. Seed: Cotton, Capricorn, and Coir.
5. Main: Kenaf, Jute, and Hemp.
6. Others: Roots and Woods (Table 1).

1.3 Methods of Processing

Various methods, such as hand lay-up procedure, molding by help of compression, by help of injection molding, and transmission of epoxy resin. Production processes require three-cycle steps: first is moisture separation, second is matrix combination, and at the end component manufacturing. A fundamental hand lay strategy [9] encourages the planning of a crossover multi-part composite. For the production of composites, injection molding technology is still used and is viewed as more exact than different techniques [10]. The combination of the formed fiber fabricating system and resin transfer molding processes has been created utilizing another strategy for natural fiber-reinforced composites. This innovation encourages us to effectively produce composites with a thickness of 5 mm [11] (Table 2).

Table 1 Significant fiber source, their production rates, and usage

S. No.	Name of source	Usage	Production rates (10 ³ t.)	References
1	Ramie	Pressing material, modern sewing string	100	[7]
2	Jute	Pressing, entryway edges, and shades	2300	[8]
3	Coir	Flush entryway shades, reflect packaging, material sheets	100	[7]
4	Sisal	Development enterprises like entryway, boards, material	378	[7]
5	Hemp	Table, chair paper industry, material industry	214	[7]
6	Flax	Window outline, snowboarding	830	[8]
7	Bamboo	Development and carpentry enterprises	30,000	[8]
8	Kenaf	Versatile cases, protections, sacks, pressing materials	970	[7]

Table 2 Distinctive blending and assembling measures dependent on common fiber and length

S. No.	Sources	Blending process	Method/processes	(mm) Length	References
1	Hemp	Manual mixing	Vacuum bagging method	3.4	[12]
2	Kenaf	Injected epoxy resin in mold at 1.3 bar pressure	Transfer of epoxy resin molding	6	[13]
3	Pineapple leave	Internal mixing	Compression molding	0.5	[6]
4	Banana	Epoxy was put into mold	Hand lay-up procedure	15	[14]
5	Kenaf	Extrusion	Molding by compression	6	[15]
6	Bamboo	Manual mixing	Dried in an Oven	15	[6]
7	Kenaf-PALF	Internal mixing	Compression molding	1.0	[6]
8	Basalt	Manual mixing	Compression molding	10	[6]
9	Agave	Stirring process	Compression molding	3	[6]

2 Hybridization of Materials

The combination of a few particular fibers. In a mixed composite, natural fiber and synthetic fibers are broadly utilized. This strategy is utilized broadly to create properties and limit composite expenses [16].

2.1 Fiber–Fiber

Ramesh et al. [17] find that sisal fiberglass increments tensile characteristics more than jute fiberglass, yet that jute fiberglass fiber composites are better accomplished in conditions where flexural qualities are available. Ahmed et al. [18] likewise tracked down that the mechanical properties of composite jute fiber supported the coordination of glass fiber. Reddy et al. [19] have seen the elastic and flexural nature of the jute composite, the tar fiber, and leaf of pineapple with a 1:1:1 extent. Bhoopathi et al. [20] noticed a higher tensile property for banana composites and a more prominent bending and impact than for other composite examples for banana-hemp composites.

Vaghasia et al. [21] additionally found that an improvement in the level of bamboo fiber up to 9 percent of the mechanical properties upgrades. A further ascent in fiber content adds to a deficiency of sap, which over in mechanical properties the long haul, in the end, prompts a diminishing. Girisha et al. [22] moreover demonstrated that regular fiber crossover composites have better properties relative to solitary support. Shanmugam [23] noticed that the capacity and misfortune modulus of palm jute cross breed composites expanded with a high substance of jute fiber, however, the estimation of Tand diminished with an expansion in content of jute. Salleh et al. [24] saw the impact of water retention on kenaf glass half and half composite and saw that the ingestion of composite dampness increases with the hour of drenching and grandstands a true to life conduct. Atiqah et al. [25] considered the rise in the thickness of the expanding and the absorption of water by expanding the fiber content and the dispersion, in light of the fiber content.

2.2 Filler-Fiber

The mixture of filler material into the composite fiber structure produces regular hybrid composites. The nanometers or subnuclear levels of these filler particles are. Filling materials are used to lower fiber costs and to reinvent composite materials' properties such as scraping area, stiffness, and shrinking. As customary and non-regular fillers, filler materials are required. Titanium dioxide, Alumina, Silicon carbide, Silicon dioxide, and unusual fillers are nano earth and modern waste, such as fly waste, red sludge, etc.

The aggregation in Jute Epoxy Compound of titanium dioxide particles of various wt% has improved tractable and flexural properties to a composite of 7.5% of TiO₂ Titanium dioxide particles, Bheemappa et al. [16] have observed. In the event of a weak hold of the fiber filler to the system structure, the higher filler composite reduces the mechanical properties. Ashik et al. [16] provided shot-jute epoxy composite effects to silica fillers and monitored them to show that the foldable and crack resistance properties of 5 wt of the composite were over 10 wt% ideal. The wear of the Jute epoch composite stacked with the silicon carbide/alumina filler was inspected by Ahmed et al. [26] and it was determined that its growth is added to an increase in the composite's properties. Composite loaded with alumina will wear more of it than silicon carbide.

3 Advantages and Disadvantages of Natural Composites

3.1 Composites Are Regularly Utilized in Different Ventures, with a Portion of the Huge Benefits [8, 27–31]

- Environmental affability, CO₂ neutrality, and biodegradability are the first and leading advantages of natural fibers.
- Abundantly usable and harmless toxins following improved energy recuperation by burning.
- Reduce the utilization of oil base materials by supplanting them with up to 50% common filaments for infusion trim and in excess of 50% for pressure forming.
- Natural strands are modest and can lessen the normal cost.
- Offering relatively cleaner creation measures and expanded work environment safety.
- Natural strands are delicate and hence improve the general life and execution of the preparing hardware/instrument.
- The strategies for preparing and reusing of NFRCs are naturally reasonable.
- The useful use of yield buildups leads to income and work possibilities.
- NFRCs have exceptional acoustic retention properties.
- Relatively low processing temperatures and NFRCs have decent sound and heat insulation.

3.2 Natural Fiber Composites also Suffer from the Following Disadvantages [32–36]

- Heavy ingestion of dampness adds to growing, subsequently affecting item consistency and toughness.

- Low wettability of characteristic strands likewise brings about terrible interfacial fiber-framework holding and diminishes properties.
- Some of the strands are not consistent with some polymer matrices.
- Large contrasts in fiber attributes and properties explicitly add to the enormous scattering of NFRC properties.
- Easily powerless against bother and contagious assaults.
- Relatively low-temperature decay and promptly combustible.
- Wide contrasts in regular fiber quality depend on temperature and states of development.
- Thermal conductivity of NFRCs is moderately not exactly that of built up glass fiber composites.
- Dynamic production network, provincial accessibility.
- Market and creation variances because of temperature and harvest yields.

4 Different Application of NFRC

The utilize composites filling progressively in engineering fields [37]. Different types of natural polymer composite have procured abundant importance in different sectors [38, 39] (Table 3).

Table 3 Summary of typical applications in different industrial sectors

Industrial sectors	Usage	References
Transport and auto motives	Inside entryway outlines, bodyboards, secondary lounge headphones, dashboards, vehicle protection, motor cover, deck	[40]
Construction and building	Connect, rooftop tiles, parcel boards, and bogus tiles, deck, segment sheets, board, deck, windows, and entryway modules	[40]
Electronics	Versatile cases	[41]
Materials handling	Capacity storehouses, compartments, fuel holders, Tables, seats	[41]
Household	Fencing segments, entryway outlines, inside boards, entryway outline profiles, food plate, parcels, bags, caps, pipes, ropes, Hessians, packs, mats, and floor coverings	[8, 41]
Sports	Toys, frames, bike outlines, snowboards, chairs, boats	[41]

Table 4 The usage in the automobile industry

Model	Usage	References
Volkswagen	Seatback, door frame, panel and boot liner	[42]
Audi	Boot-line, pneumatic replacement, side and rear frame, back seat	[42]
BMW	Chair back, headliner plate, door boards	[42]
Fiat	Door panel	[42]
Toyota	Interior boards	[42]
Volvo	natural foams, seat padding, and cargo	[43]
Ford	Door boards, trays and door inserts	[42]
Renault	Rear parcel shelf	[43]
Toyota	Floor tubes, take back panels and backrests	[43]
Mercedes Benz	The glove box, the instrument support for the panels, the insulation, the backrest board, backboard, and a surface/backrest seat	[42]
Truck	Interior motor mask, sun visor, inner padding	[44]

4.1 Indoor Automotive Uses of Natural Fiber Composites

The interior of vehicles, particularly seating, parcel shelving, boot liners, door linen for front and back, linens for Lorries and door panels [17].

A significant number of car creators around the globe have done many studies to insert natural composites into their vehicles. In the inside of vehicles, specifically, seating, package racking, boot materials, entryway cloth for front and back, materials for Lorries and door panels [17] (Table 4).

4.2 Usages in the Industry NFRC

In most NFPC implementations, indoor components in structural designing are not load-bearing as a result of their vulnerabilities to environmental attacks [45]. In its utilization for development, firstly, structural bio-composites and secondly non-structural bio-composites [46] (Table 5).

Research gap and opportunity to work

As improvement behavior continues to spread around the world, so does the interest for building materials and raw materials, therefore, needs broke down various sort of helpful properties are faster interaction time, lower production cost, quicker process and method and so on relative investigation giving benefits to use in business applications. In field of CAD/CAM modeling and simulation design need some valuable

Table 5 NFRC usages in the industry [47–51]

Name of source	Usage in building, production, etc.	References
Hemp	Production goods, paper & packaging	[49]
Oil palm	Siding, clamping, roofing, shielding and others	[48]
Wood	Fenster doors, panels, railings systems	[47]
Flax	Fencing, tennis racket, cycling framework, fork, sitting post, snowboarder	[49]
Rice husk	Construction tiles, briques, frames for walls, panels, decking	[47]
Bagasse	Fencing, tables, structures	[47]
Sisal	Building business, for example in the manufacture of panels, partitions	[51]
Stalk	Construction walls, panels of furniture, bricks, and sinks, and pipelines	[47]
Kenaf	Packs, insulations, clothing grade sleepers, soilless mixtures, animal bedding	[48]
Cotton	The garment and thread, goods, and cordage industry	[51]
Coir	Panels for construction, flush door shutters, roof boards, holding tanks, mirrors	[51]
Ramie	Use as commercial sewing threads, wrapping fabrics, fishing nets	[49]
Jute	Panels, door frames, door shutters, shipping, packing, geotextiles	[51]

information that can be considered by composite properties. For work opportunities, we can think about work for fluctuation of mechanical property and strength, long-term durability, decrease of expenses, codes and standards, market acceptance, etc.

5 Conclusion

From above discussion, it is reasonable to conclude that characteristic fibers are a strong competitor for replacing fibers as provision in polymer composites due to their superior properties. The primary reason characteristic composite materials are chosen for parts is weight, with something set aside for its overall firmness and strength with expanded utility in increased use of agricultural waste disposal.

- Polymer composite fibers have ideal properties such as low thickness, low cost, and reduced robustness, resulting in benefits for modern applications (car industry, structures, and developments).
- Natural fabrics can be used outdoors by hybridizing to enhance their properties. The technique is extremely straightforward however just the correct determination of the composite material is essential.

- The ability for users and its benefits and drawbacks must be resolved by natural fiber composites. Mechanical waste has a major responsibility to promote the property that allows for a satisfactory way of using waste as a value-added material, and there are various unique fibers available on the earth for the creation of modern natural fiber-based composite polymers.
- The future looks promising because they are cheaper, thinner, and more environmentally conscious than glass fibers. Future studies can therefore concentrate on the achievement of comparable or better technological efficiency, composites of natural fibers, different kinds of natural fibers, various manufacturing methods and processes involving the composites, and component life of natural fibers.

References

1. Wang X, Liu WS, Lu X, Lee PS (2012) Dodecyl sulfate-induced fast faradic process in nickel cobalt oxide-reduced graphite oxide composite material and its application for asymmetric supercapacitor device. *J Mater Chem* 22(43):23114–23119
2. Jia J, Tang M, Chen X, Qi L, Dong S (2003) Co-immobilized microbial biosensor for BOD estimation based on sol-gel derived composite material. *Biosens Bioelectron* 18(8):1023–1029
3. Alomayri T, Assaedi H, Shaikh FUA, Low IM (2014) Effect of water absorption on the mechanical properties of cotton fabric-reinforced geopolymer composites. *J Asian Ceram Soc* 2(3):223–230
4. Rajesh G, Ratna Prasad AV, Gupta AVSSKS (2019) Soil degradation characteristics of short Sisal/PLA composites. *Mater Today: Proc* 18:1–7
5. Ticoalu A, Aravinthan T, Cardona F (2010) A review of current development in natural fiber composites for structural and infrastructure applications. In: *Proceedings of the southern region engineering conference (SREC 2010)*. Engineers Australia
6. Jaafar J et al (2019) Important considerations in manufacturing of natural fiber composites: a review. *Int J Precis Eng Manuf-Green Technol* 6(3):647–664
7. Jariwala H, Jain P (2019) A review on mechanical behavior of natural fiber reinforced polymer composites and its applications. *J Reinf Plast Compos* 38(10):441–453
8. Faruk O, Bledzki AK, Fink HP, Sain M (2012) Biocomposites reinforced with natural fibers: 2000–2010. *Prog Polym Sci* 37(11):1552–1596
9. Patnaik A, Satapathy A, Biswas S (2010) Investigations on three-body abrasive wear and mechanical properties of particulate filled glass epoxy composites. *Malays Polym J* 5(2):37–48
10. Gupta A, Kumar A, Patnaik A, Biswas S (2011) Effect of different parameters on mechanical and erosion wear behavior of bamboo fiber reinforced epoxy composites. *Int J Polym Sci* 2011
11. Sarikaya E, Çallioğlu H, Demirel H (2019) Production of epoxy composites reinforced by different natural fibers and their mechanical properties. *Compos B Eng* 167:461–466
12. Pervaiz M, Sain M, Ghosh A (2006) Evaluation of the influence of fiber length and concentration on mechanical performance of hemp fiber reinforced polypropylene composite. *J Nat Fibers* 2(4):67–84
13. Ariawan D, Mohd Ishak ZA, Salim MS, Mat Taib R, Ahmad Thirmizir MZ (2017) Wettability and interfacial characterization of alkaline treated kenaf fiber-unsaturated polyester composites fabricated by resin transfer molding. *Polym Compos* 38(3):507–515
14. Sanjay MR, Arpitha GR, Laxmana Naik L, Gopalakrishna K, Yogesh B (2016) Studies on mechanical properties of banana/e-glass fabrics reinforced polyester hybrid composites. *J Mater Environ Sci* 7(9):3179–3192
15. Aji IS, Sapuan SM, Zainudin ES, Abdan K (2009) Kenaf fibers as reinforcement for polymeric composites: a review. *Int J Mech Mater Eng* 4(3):239–248

16. Gohal H, Kumar V, Jena H (2020) Study of natural fiber composite material and its hybridization techniques. *Mater Today: Proc* 26:1368–1372
17. Davoodi MM, Sapuan SM, Ahmad D, Aidy A, Khalina A, Jonoobi M (2011) Concept selection of car bumper beam with developed hybrid bio-composite material. *Mater Des* 32(10):4857–4865
18. Ahmed KS, Vijayarangan S (2008) Tensile, flexural and interlaminar shear properties of woven jute and jute-glass fabric reinforced polyester composites. *J Mater Process Technol* 207(1–3):330–335
19. Reddy MI, Kumar MA, Raju CRB (2018) Tensile and flexural properties of jute, pineapple leaf and glass fiber reinforced polymer matrix hybrid composites. *Mater Today: Proc* 5(1):458–462
20. Bhoopathi R, Ramesh M, Deepa C (2014) Fabrication and property evaluation of banana-hemp-glass fiber reinforced composites. *Procedia Eng* 97:2032–2041
21. Jesthi DK, Nayak S, Saroj S, Sadarang J (2021) Evaluation of flexural and vibration property of glass/bamboo/jute hybrid fiber composite in hydrothermal environment. *Mater Today: Proc*
22. Girisha C, Sanjeevamurthy G, Srinivas GR (2012) Sisal/coconut coir natural fibers-epoxy composites: water absorption and mechanical properties. *Int J Eng Innov Technol* 2:166–170
23. Shanmugam D, Thiruchitrabalam M (2013) Static and dynamic mechanical properties of alkali treated unidirectional continuous Palmyra Palm Leaf Stalk Fiber/jute fiber reinforced hybrid polyester composites. *Mater Des* 50:533–542
24. Salleh Z, Taib YM, Hyie KM, Mihat M, Berhan MN, Ghani MAA (2012) Fracture toughness investigation on long kenaf/woven glass hybrid composite due to water absorption effect. *Procedia Eng* 41:1667–1673
25. Atiqah A, Jawaid M, Ishak MR, Sapuan SM (2017) Moisture absorption and thickness swelling behaviour of sugar palm fiber reinforced thermoplastic polyurethane. *Procedia Eng* 184:581–586
26. Ahmed KS, Khalid SS, Mallinatha V, Kumar SA (2012) Dry sliding wear behavior of SiC/Al₂O₃ filled jute/epoxy composites. *Mater Des* 1980–2015(36):306–315
27. Mohanty AK, Misra MA, Hinrichsen GI (2000) Biofibers, biodegradable polymers and biocomposites: an overview. *Macromol Mater Eng* 276(1):1–24
28. Joshi SV, Drzal LT, Mohanty AK, Arora S (2004) Are natural fiber composites environmentally superior to glass fiber reinforced composites? *Compos A Appl Sci Manuf* 35(3):371–376
29. Eichhorn SJ, Young RJ (2004) Composite micromechanics of hemp fibers and epoxy resin microdroplets. *Compos Sci Technol* 64(5):767–772
30. Al-Maadeed MA, Labidi S (2014) Recycled polymers in natural fiber-reinforced polymer composites. *Nat Fiber Comp*, pp 103–114. <https://doi.org/10.1533/9780857099228.1.103>
31. Kerni L, Singh S, Patnaik A, Kumar N (2020) A review on natural fiber reinforced composites. *Mater Today: Proc* 28:1616–1621
32. Dicker MP, Duckworth PF, Baker AB, Francois G, Hazzard MK, Weaver PM (2014) Green composites: a review of material attributes and complementary applications. *Compos Part A: Appl Sci Manuf* 56:280–289
33. Koronis G, Silva A, Fontul M (2013) Green composites: a review of adequate materials for automotive applications. *Compos B Eng* 44(1):120
34. Martins C, Galetti PM (1999) Chromosomal localization of 5S rDNA genes in *Leporinus* fish (Anostomidae, Characiformes). *Chromosome Res* 7(5):363–367
35. Summerscales J, Dissanayake NP, Virk AS, Hall W (2010) A review of bast fibers and their composites. Part 1—fibers as reinforcements. *Compos Part A: Appl Sci Manuf* 41(10):1329–1335
36. Zini E, Scandola M (2011) Green composites: an overview. *Polym Compos* 32(12):1905–1915
37. Mohammed L, Ansari MN, Pua G, Jawaid M, Islam MS (2015) A review on natural fiber reinforced polymer composite and its applications. *Int J Polym Sci* 2015
38. Shalwan A, Yousif BF (2013) In state of art: mechanical and tribological behaviour of polymeric composites on natural fibers. *Mater Des* 48:14–24
39. Sassoni E, Manzi S, Motori A, Montecchi M, Canti M (2014) Novel sustainable hemp-based composites for application in the building industry: physical, thermal and mechanical characterization. *Energy Build* 77:219–226

40. Ramesh M, Palanikumar K, Reddy KH (2017) Plant fiber based bio-composites: sustainable and renewable green materials. *Renew Sustain Energy Rev* 79:558–584
41. Holbery J, Houston D (2006) Natural-fiber-reinforced polymer composites in automotive applications. *Jom* 58(11):80–86
42. Suddell BC (2008) Industrial fibers: recent and current developments. In: *Proceedings of the symposium on natural fibers*, vol 20, pp 71–82
43. Pickering K (ed) (2008) *Properties and performance of natural-fiber composites*. Elsevier
44. Bos HL (2004) The potential of flax fibers as reinforcement for composite materials. Technische Universiteit Eindhoven, Eindhoven
45. Azwa ZN, Yousif BF, Manalo AC, Karunasena W (2013) A review on the degradability of polymeric composites based on natural fibers. *Mater Des* 47:424–442
46. Uddin N (ed) (2013) *Developments in fiber-reinforced polymer (FRP) composites for civil engineering*. Elsevier
47. Ticoalu A, Aravinthan T, Cardona F (2010) A review of current development in natural fiber composites for structural and infrastructure applications. In: *Proceedings (SREC), engineers Australia*, pp 113–117
48. Tawakkal IS, Cran MJ, Bigger SW (2014) Effect of kenaf fiber loading and thymol concentration on the mechanical and thermal properties of PLA/kenaf/thymol composites. *Ind Crops Prod* 61:74–83
49. Sen T, Reddy HJ (2011) Various industrial applications of hemp, kinaf, flax and ramie natural fibers. *Int J Innov, Manag Technol* 2(3):192
50. Bongarde US, Shinde VD (2014) Review on natural fiber reinforcement polymer composites. *Int J Eng Sci Innov Technol* 3(2):431–436
51. Mwaikambo L (2006) Review of the history, properties and application of plant fibers. *Afr J Sci Technol* 7(2):121

Research Progress in Gas Tungsten Arc Cladding on Steel: A Critical Review



Md Sarfaraz Alam and Anil Kumar Das

Abstract The motivation behind this comprehensive review paper is to accentuate the key characteristics and developments of gas tungsten arc (GTA) cladding of steel. Steel parts are often worn out due to different types of wear, such as abrasion, impact, or corrosion. Surface modification by TIG torch as heat source is commonly used to combat such issues and thereby prolong the service life. Several previous studies have led to this conclusion, the application of various powders reinforced on steel substrate by gas tungsten arc cladding is discussed. Incorporating ceramic/metallic powders into molten surface of substrate to generate a metal-matrix-composite (MMC). It is a commonly used technique all over the world. MMC has been formed to meet the requirements of particular applications.

Keywords GTA cladding · Coating · Hardness · Wear resistance · Corrosion resistance

1 Introduction

Cladding is the method of altering or replacing a solid substrate's surface phase. Cladding is often used to enhance properties near the surface while maintaining core characteristics [1–4]. Cladding can be done on metals using a melting process that involves fusing the substrate's surface as well as the reinforcing particles with an intense energy source. When cladded layer and the substrate upper layer solidify, a strong metallurgical bond is established [5]. Scanning electron microscope, X-ray diffraction, transmission electron microscopy and electron probe micro analyser

M. S. Alam (✉) · A. K. Das
Department of Mechanical Engineering, National Institute of Technology Patna, Patna, Bihar
800005, India
e-mail: mda.phd19.me@nitp.ac.in

A. K. Das
e-mail: akdas@nitp.ac.in

© The Author(s), under exclusive license to Springer Nature Singapore Pte Ltd. 2022
H. K. Dave et al. (eds.), *Recent Advances in Manufacturing Processes and Systems*,
Lecture Notes in Mechanical Engineering,
https://doi.org/10.1007/978-981-16-7787-8_68

859

are generally employed to analyse the microstructure. Micro-hardness and fracture-toughness of the cladded layer often determined by Vickers's hardness testing technique. Pin-on-disc tribometer used to perform abrasive wear monitoring [6]. The micro-hardness, wear characteristics of composite cladded layer in the matrix was improved because of the higher hardness of TiC particles [7, 8]. TIG cladded surface modification is a feasible technique to enhance the resistance against wear and hardness of Ni-WC nanocomposite [9]. A continuous, uniform and free from defect interface is achieved between TiC/FeCrBSi cladded layer and substrate made of AISI 1045. In comparison to the substrate, the maximum hardness is nearly 5 times higher [10]. The suggested coatings find its suitability where corrosion resistance and resistance against wear are essential. The mechanical properties and microstructure of the cladding is significantly influenced by TiC powder content, thickness of preplaced layer, and input current. The TiC grains and Inconel 825 matrix have excellent adhesion because alloy of Ni has a better soaking behaviour with TiC and the emergence of different intermediate phases. Micro-hardness of coating achieved 1100 HV and particularly in comparison to AISI 304, there was a seven-fold reduction in wear [11]. Gas tungsten arc cladding is a metallurgical bonding process that involves first placing the powder on the substrate surface to be cladded and then melting it with source of heating energy [12].

As compared to other methods of surface modification. TIG arc cladding has many advantages.

- i. TIG torch has a low net heat intake, which means the minimal heat affected zone, thus allowing for very close surface modification without adverse effect on the mass substrate
- ii. Cladding time is minimal, and it is possible to automate the operation
- iii. There is no need for complicated support structures
- iv. Although the coating material can weaken the substrate to a degree, a free from flaws and porosity, interface between the substrate and coating with fairly strong metallurgical bond is achieved
- v. Uniform and continuous interface microstructure can be obtained by adjusting parameters like input current, traversing speed, power, and coating powder composition
- vi. High deposition rate
- vii. Economical
- viii. Easy operation.

2 Characteristics of the Coating Layer Through GTA Cladding

The following are the characteristics of GTA cladding.

- a. Coating height: The coating height above the substrate surface rises as the scan speed of GTA increases, while the melt depth inside the substrate decreases.

Increased power input causes the coating height to drop and the melt depth to rise.

- b. Dilution of layer coated: When arc heating is given to premixed clad powder placed on substrate, melt pool spreads over the substrate. Dilution affects the characteristics of GTA clad layers. The metallurgical bonding of the clad layer defines the resistance against wear, which is determined by dilution. As the enveloped area of dilution for the particular point under study is extended, the adhesion of the coating to the substrate looks to be improving. The clad layer arrangement with the highest coating material rate must be used in applications that need high corrosion or oxidation resistance.
- c. Roughness: A lack of finish on clad surface is indicated by roughness. Reduced roughness improves surface quality as a result.
- d. Hardness: The type of cladding material used and the traversing speed have an effect on the coating layer's hardness. With low traversing speed and steady current, the heat input is greater. During the treatment, the clad powder disintegrated into the surface layer's mass. Furthermore, the situation's reinforcing effect is greater along these lines. Because of uniform melting, microhardness increases as current increases at a constant scan speed.
- e. Wear resistance: Wear resistance is what determines how long the coated substrate lasts. It is determined by the ceramic material used for the substrate coating and the treatment parameters.
- f. Homogeneity: Coating layers with a chemical composition that is homogeneous and free of defects result from a thorough set of handling parameters.
- g. Porosity: Porosity refers to the presence of gaps in the coating sheet. The arrangement of trapped gas bubbles in the weld pool is the most common cause.

3 Methods for Applying Reinforcement in GTA Cladding

The following is a classification of GTA clad surface modification techniques.

- a. Preplaced powder Method: The main stage involves covering the substrate with preplaced powder, followed by the electric arc exchanging its need for the powdered metal and melting it. The second step is the transfer of heat to the confined area of substrate.
- b. Wire Feed Method: A wire feed is the second form of clad transportation. The wire is fed to the layer from a drum. Unpredicted behaviour molten drop at the wire's tip is the most important issue with wire feeding. The molten metal not able to move with ease on the substrate, causing the clad to become significantly weaker.
- c. Powder feeding: Cladding powder is usually metallic and ceramic in nature and is infused into the framework through coaxial or sidelong spouts. Melting occurs as a result of the interaction between the stream of metallic powder and the warmth, and called as the molten pool. This is saved to a layer, which is then shifted, allowing the melt pool to harden and form a solid metal track.

A negatively charged electrode made of tungsten and the substrate establishes arc, which in turn produces heat in the TIG process. Gases that provide protection such as argon, helium or a combination of both inert gases, and nitrogen are adopted to keep the molten pool free of contaminants. Surface layer then solidifies, creating a new microstructure with various wear and hardness properties.

4 Research Progress in TIG Cladding on Steel

Alloyed steels are commonly used as substrate materials in TIG cladding. On a micro alloyed steel surface, a MMC layer was satisfactorily developed by TIG torch cladding method, using Ti_2AlC particles as ceramic reinforcement [13]. TIG cladding by preplace TiC powder on alloyed carbon steel was investigated using traversing speed, current, arc gap, and shielding gas flow rate by Peng [14]. During his study, he discovered that the TIG surfacing technique's welding speed and welding current are more critical than the other processing variables. Ruckert et al. [15] used Silica powder coating on AISI304 substrate, they found that Weld penetrations are influenced by coating geometry and thickness. Two different types of coatings are investigated. The first design uses a continuous coating of 20 mm width in the coating zone, while the later uses two 1–7 mm apart parallel coatings spaced around the joint. Continuous coatings have a maximum thickness of about 50 μm , while 2 mm apart coatings have a maximum thickness of 70–200 μm . Muigai et al. [16] used stainless steel coating on mild steel substrate conclude that TIG system's hardness and DC current have an inverse relationship. Raja et al. [17] clad TiC powder on AISI 1020 substrate and concluded that it was possible to achieve wear resistant and a hard composite coating with improved TiC particle-to-steel matrix metallurgical bonding. During TIG cladding, wear and hardness properties of TiC cladding largely depends on heat input and is controlled by adjusting the current supply. Patel et al. [18] a maximum temperature of 375 °C was obtained on molten cladding surface of with or without SiC powdered microalloyed steel substrate in the 2nd–3rd of track, in either argon–helium or argon shielding atmosphere. In the resolidified SiC coated substrate decrease of hardness of 300 HV was noted over this short distance, and a cast iron's microstructure with cracks was observed. Mridha and Baker [19] clad 0.5 mm thick TiC powder layer on AISI-4340 and observed that the composite layer hardness was more than 800 HV. Unevenly distribution is also observed in tracks at the beginning and end during fusion. Wear nature of TiC reinforced AISI-4340 has been explored by Maleque et al. [20] and observed that the coated steel had a greater resistance against wear. TiC inclusion into the steel surface enhanced the steel's resistance against wear by minimising surface's ploughing and plastic deformation. The coating's micro-hardness profile showed a five-fold increase in hardness as compared to substrate. Maleque et al. [21] applied Taguchi Approach for the same as reported on [20] and the findings show that voltage greatly influence in reduction of wear rate, input current has the least impact on reduction in wear rate. Optimal conditions for TiC embedded coatings are voltage (30 V), traversing

speed (2.5 mm/s), assist gas flow rate (20 L/min) and input current (90 A), which result in the lowest wear rate. Finally, a confirmatory experiment was carried out to validate the optimised result, less than 4.7% error is observed between experimental and expected values. As a result, the validity of the optimum coatings condition is proven. At duplex stainless steel surface, cladding by preplaced SiC powder and TIG arcing method was fabricated by Lailatul and Maleque [22] with different working welding variables including input energy of 648, 768 and 1440 J/mm and welding currents of 80, 90 and 100 amperes. According to the results of the experiments 830 HV_{0.5} peak hardness of composite surface after resolidification was achieved and 250 HV_{0.5} hardness with 768 J/mm energy input was achieved. Due to complete fusion of SiC in the altered surface, dendrite formed in microstructure. Formation of dendrite leads to the material's increased hardness. Paraye et al. [23] TIG arcing was utilised to create an in-situ produced TiC reinforced steel matrix. The changed surface created at varied arcing currents of 80, 140, and 200 A was micro graphed using a scanning electron microscope (FESEM). The microstructures demonstrate that at any heat input the changed matrix generated with and without flux coating undergoes martensite phase transformation, interface is almost flaw free such as pores and cracks. Saroj et al. [24] employed AISI 304 stainless steel as the substrate and Inconel 825 cladding. It was revealed in the study that the dilution ratio, clad height, clad angle and clad track width could all be increased by varying TIG current. When comparing the clad track to the substrate material 100 HV higher micro-hardness observed reveals a steady enhancement. Under comparable test settings, wear test indicated minor depression (6 µm) in comparison to without clad steel (125 µm). Dyuti et al. [25] melted titanium powder in atmosphere of nitrogen on 0.2%C Mild steel confirms titanium nitride's dendritic microstructure. The surface hardness of the melt layer was around 1927 HV, with scattered TiN, Ti₂N dendrites that were more densely packed near the surface than in the deeper melt. Lower friction value 0.12 of the altered surface is achieved and the rate of wear is 0.007895×10^{-4} in comparison with unclad steel of 1.648×10^{-4} mm³/N/m. Buytoza and Ulutan [26] used SiC reinforcement with varying proportions and AISI 304 substrate. The process parameters were updated to see how they affected the microstructure of the coating. The results revealed that during the manufacturing process, the SiC powders are fully liquified. At lower powder concentrations dendrites microstructure formed. Small concentration of Fe, Cr, Si, and C as well as dendrites presence were associated with reduced dendritic microstructure hardness. Due to the progress of MMC, superior performing composite powder deposition on substrate materials of lower grade has lately been a key topic of study. Several carbides strengthened MMC cladding's have been fabricated to increase resistance against corrosion and wear. When Zhang et al. [27] fabricated In-situ VC strengthened Fe-based low carbon steel, the effect on grain size and cladding layer characteristics with the variation in colling conditions were analysed comparatively. The results showed that under water cooling conditions, ultra-fine grain coating layers can be produced in in-situ Fe-based nano vanadium carbide. Heat affected zone was narrower and the dilution rate was lower in vanadium carbide this cladding layer. The cladding layer has an average grain size of 1.90 µm. Wang et al. [3] uses graphite, Fe–Cr–B–Si and ferrotitanium powders to clad over

AISI 1045 steel surfaces, the findings showed that titanium carbide particles may be obtained through a reaction between graphite and ferrotitanium in the course of TIG cladding process. The bulk of TiC grains were equally spread across surface layer. Micro-hardness varied from the melting edge to the upper surface edge of the cladding in gradual manner, which was dependent on welding parameters and powder spread thickness. The cladded surface demonstrates a better hardness and a lesser rate of wear than the steel substrate because of the production of titanium carbides. Das et al. [28] used iron and titanium carbide powders in two different proportions 80–20% and 90–10% to clad over AISI 1020 steel substrate. The profile of micro-hardness depicts the fluctuation in the value of hardness for both the cladding zone and the substrate. The hardness value dropped as the distance from the cladded layer's top surface grew due to the difference in cooling temperatures. Kumar et al. [29] produced a Ti-SiC MMC cladding on AISI 304 steel, interface exhibits improvement in mechanical characteristics. A maximum micro-hardness obtained was 639 HV and 575 HV, whereas the mean micro-hardness of the substrate was 237 HV at 30 per cent SiC and 20 per cent SiC, respectively, in the cladded layer, using 400 grades SiC paper, the relative resistance against wear with respect to substrate was 3.4 and 2.3 times, respectively. Kumar et al. [30] deposited titanium diboride reinforced Fe-based composite cladding on AISI 304 substrate, with variation of TiB₂ amount in Fe-matrix was used to investigate the impact on morphology and micro-hardness of cladding. Six hundred and six HV is the highest hardness value recorded (30% TiB₂). Furthermore, interface cladding qualities were satisfactory; the micro-hardness improved 2.66 times over the substrate (227 HV), and a crack-free uniform distribution (TiB₂) was observed. In another study Kumar and Das [12] AISI 304 as substrate and Ti-SiC powder as reinforcement. EDX examination reported the existence of Fe, Ni, Si, and C in the modified layer. The morphology of the coating and the mode of wear mechanism were investigated using SEM. XRD diffraction patterns demonstrated the development of silicides of metal (Fe₂Si, Ni₃Si, NiSi and CrSi₂), carbides of iron (Fe₃C and Fe₂C), and inter-metallic compounds (NiFe). A maximum hardness, average hardness of 663, 507.7 HV in 30% SiC and 660.5, 499 HV in 20% SiC, respectively, is achieved in comparison to the substrate hardness of 220 HV. As compared to the substrate material (wear height loss 621.7 μm), the 20% SiC coating had the lowest wear loss (wear height loss 301.5 μm). In another study Kumar and Das [31] AISI 304 as substrate and Ni, SiC and Ni, Si, B₄C in different proportions of SiC and B₄C in coating mixtures taken as reinforcement. For the sample (85% Ni, 7.5% Si and 7.5% B₄C), FESEM shown fine microstructure of martensite produced. The coated layer's peak micro-hardness and mean hardness came out as 676 and 523 HV accordingly, whereas the substrate's mean hardness was 200 HV. In contrast to direct SiC inclusion in nickel-based MMC fabrication, the outcome indicates that Si + B₄C can be a suitable alternative to improve surface hardness substrate. Kumar et al. [32] cladded TiC–TiN and the substrate hardness rose by 3.38–3.82 times, when evaluated by micro-hardness analysis around the cross section. Tosun [33] Ni and WC mixed powder coating on AISI 1010 substrate and, the response of coating layer thickness and current on the alloyed surface's hardness and microstructure were studied. Harder phases were discovered to improve the alloyed

surfaces' hardness. Depending on the performance criteria, several microstructures were revealed. Thomson structure type pattern, ferrite, grain boundary ferrite, acicular ferrite, bainite, and a trace of martensite were discovered in the microstructures of the cladded surfaces. Tosun and Buytoz [34] cladded FeCrC and FeNb on AISI 4140 substrate, concluded that as the coating is applied with enough energy, it becomes metallurgically bound to the substrate. Hexagonal-shaped carbides consolidated in the (Fe, Cr) eutectic matrix of FeCrC coatings, while quadrangular-shaped NbC carbides consolidated in FeCrC/NbC composite coatings. As more FeNb was melted, the proportion of NbC in the micro structure grew. Singh et al. [6, 35] The microstructure and properties of the WC-10Co-4Cr nanostructured highly wear resistant cladding on an AISI 304 substrate were studied in relation to argon flow rate, current, and standoff size. Increased hardness and wear resistance were linked to longer standoff distances and higher argon flow rates. The extraction of tungsten carbide particles, as well as the yielding and extrusion of the CoCr binder, cause wear in the cladding [35]. The parameters of the TIG cladding process were optimised utilising a central composite design based on response surface technique. The outcome indicates that interface resistance against wear and hardness are greatly influenced by current, followed by traversing speed, gap between arc surface and electrode, and argon gas flow rate has least effect [6]. The goal of Shi et al. [36] on stainless steel substrate and cladded NiTi with/without Ni inter-layer was to improve resistance against cavitation erosion. NiTi and NiTi-Ni, TIG claddings are more resistant to cavitation erosion than SS substrate because they have higher micro-hardness and super-elasticity. In addition, a Ni inter-layer minimises the number of brittle inter-metallic complexes like Fe_2Ti and prevents fracture development, resulting in NiTi-Ni cladding having greater resistance to cavitation erosion than NiTi cladding. A Ni inter-layer can increase the resistance cavitation erosion of NiTi coating created using the TIG cladding process. The effect of SiC rate of reinforcement with and without NiBSi and NiBSi/SiC-X on micro-hardness, microstructure and resistance against wear of AISI 304 steel using TIG arcing has been investigated by Kilic et al. [37]. The microstructure was microphotographed and revealed a dendrite with diffused silicon carbide particles, suggesting that SiC reinforcement could increase micro-hardness. SiC & NiBSi/SiC coatings on AISI 304 had exceptional wear resistance and hardness. Sharma et al. [38] cladded Al and TiO_2 on alloy steel concluded that depending on the ratio of the powder mixture of the cladding, an increase in hardness of 1.88–2.24 times compared to substrate is possible.

5 Conclusion

After a rigorous critical review of various types of powder/ powder mixture cladding by GTA cladding technique, the method of pre-placing of powder for reinforcing ceramic/metallic particles onto substrate of steel, is the economic, clear, and versatile way to enhance the surface performance characteristics of steel materials. Process parameters like current, traversing speed, gap between surface and electrode, rate of

flow of shielding gas and others have an much effect on the properties of coating in TIG cladding. Also, coating material selection and design significantly affect the properties of coating.

References

1. Sahoo CK, Masanta M (2017) Microstructure and mechanical properties of TiC-Ni coating on AISI304 steel produced by TIG cladding process. *J Mater Process Technol* 240:126–137
2. Azimi G, Shamanian M, Firozi P (2012) Microstructure and wear properties of Fe-Cr-C and Fe-Cr-Nb-C clads on carbon steel by TIG surfacing process. *Int J Surf Sci Eng* 6(1/2):15–23
3. Wang X, Zhang M, Zou Z, Song S, Han F, Qu S (2006) In situ production of Fe–TiC surface composite coatings by tungsten-inert gas heat source. *Surf Coat Technol* 200(20–21):6117–6122
4. Azimi G, Shamanian M (2010) Effects of silicon content on the microstructure and corrosion behavior of Fe–Cr–C hardfacing alloys. *J Alloy Compd* 505(2):598–603
5. Sahoo CK, Masanta M (2017) Microstructure and tribological behaviour of TiC-Ni-CaF₂ composite coating produced by TIG cladding process. *J Mater Process Technol* 243:229–245
6. Singh J, Thakur L, Angra S (2020) An investigation on the parameter optimization and abrasive wear behaviour of nanostructured WC-10Co-4Cr TIG weld cladding. *Surf Coat Technol* 386:125474
7. Zhao LP, Liu ZD, Li B (2011) Microstructure and grain abrasion properties of (Ti, W)C-Ni cermet cladding layers prepared by tungsten inert gas cladding. *Appl Mech Mater* 80–81:133–136
8. Hojjatzadeh S, Halvae A, Sohi MH (2012) Surface alloying of AISI 1045 steel in a nitrogen environment using a gas tungsten arc process. *J Mater Process Technol* 212(11):2496–2504
9. Sabzi M, Dezfuli SM, Far SM (2018) Deposition of Ni-tungsten carbide nanocomposite coating by TIG welding: characterization and control of microstructure and wear/corrosion responses. *Ceram Int* 44(18):22816–22829
10. Xinhong W, Zengda Z, Sili S, Shiyao Q (2006) Microstructure and wear properties of in situ TiC/FeCrBSi composite coating prepared by gas tungsten arc welding. *Wear* 260(1–2):25–29
11. Saroj S, Sahoo CK, Masanta M (2017) Microstructure and mechanical performance of TiC-Inconel825 composite coating deposited on AISI 304 steel by TIG cladding process. *J Mater Process Technol* 249:490–501
12. Das AK, Kumar A (2020) Mechanical properties of Fe+SiC metal matrix composite fabricated on stainless steel 304 by TIG coating process. *Int J Mater Eng Innov* 11(3):181
13. Muñoz-Escalona P, Walker A, Ogwu A, Mridha S, Baker T (2019) Comparison of empirical and predicted substrate temperature during surface melting of microalloyed steel using TIG technique and considering three shielding gases. *Appl Surf Sci* 477:179–183
14. Peng D (2012) The effects of welding parameters on wear performance of clad layer with TiC ceramic. *Ind Lubr Tribol* 64(5):303–311
15. Rückert G, Huneau B, Marya S (2007) Optimizing the design of silica coating for productivity gains during the TIG welding of 304L stainless steel. *Mater Des* 28(9):2387–2393
16. Muigai M, Akinlabi E, Mwema F (2021) Influence of direct current (DC) on hardness of weld stainless steel coating—a model for mild steel repair. *Mater Today: Proc* 44:1133–1135
17. Sekhar BR, Nayak RK, Rout SR, Masanta M (2020) Wear characteristic of TiC coated AISI 1020 mild steel fabricated by TIG cladding method. *Mater Today: Proc* 26:3288–3291
18. Patel P, Mridha S, Baker TN (2014) Influence of shielding gases on preheat produced in surface coatings incorporating SiC particulates into microalloy steel using TIG technique. *Mater Sci Technol* 30(12):1506–1514
19. Mridha S, Baker TN (2014) Overlapping tracks processed by TIG melting TiC preplaced powder on low alloy steel surfaces. *Mater Sci Technol* 31(3):337–343

20. Maleque MA, Ghazal BA, Ali MY, Hayyan M, Ahmed AS (2015) Wear behaviour of TiC coated AISI 4340 steel produced by TIG surface melting. *Mater Sci Forum* 819:76–80
21. Maleque MA, Bello KA, Adebisi AA, Dube A (2017) Abrasive wear response of TIG-melted TiC composite coating: Taguchi approach. *IOP Conf Ser: Mater Sci Eng* 184:012018
22. Lailatul P, Maleque M (2017) Surface modification of duplex stainless steel with SiC preplacement using TIG torch cladding. *Procedia Eng* 184:737–742
23. Paraye NK, Neog SP, Ghosh PK, Das S (2021) Surface modification of AISI 8620 steel by in-situ grown TiC particle using TIG arcing. *Surf Coat Technol* 405:126533
24. Saroj S, Sahu A, Masanta M (2020) Geometrical assessment and mechanical characterization of single-line Inconel 825 layer fabricated on AISI 304 steel by TIG cladding method. *Surf Interfaces* 20:100631
25. Dyuti S, Mridha S, Shaha S (2011) Wear behavior of modified surface layer produced by TIG melting of preplaced Ti powder in nitrogen environment. *Adv Mater Res* 264–265:1427–1432
26. Buytoz S, Ulutan M (2006) In situ synthesis of SiC reinforced MMC surface on AISI 304 stainless steel by TIG surface alloying. *Surf Coat Technol* 200(12–13):3698–3704
27. Zhang H, Chong K, Xiao G, Sun Z, Zhao W (2018) TIG cladding in-situ nano vanadium carbide reinforced Fe-based ultra-fine grain layers under water cooling condition. *Surf Coat Technol* 352:222–230
28. Das AK, Kumar S, Chaubey MK, Alam W (2020) Tungsten inert gas (TIG) cladding of TiC-Fe metal matrix composite coating on AISI 1020 steel substrate. *Adv Mater Res* 1159:19–26
29. Kumar A, Kumar RR, Kumar Das A (2019) Mechanical characteristics of Ti-SiC metal matrix composite coating on AISI 304 steel by gas tungsten arc (GTA) coating process. *Mater Today: Proc* 17:111–117
30. Kumar A, Batham H, Das AK (2021) Microhardness of Fe-TiB₂ composite coating on AISI 304 stainless steel by TIG coating technique. *Mater Today: Proc* 39:1291–1295
31. Kumar A, Singh N, Nagar S, Das AK (2020) Microstructural and microhardness analysis of nickel-based ceramic composite coating on AISI 304 stainless steel by TIG coating method. In: *Proceedings of international conference in mechanical and energy technology*, pp 111–119
32. Kumar A, Singh RK, Rathore R, Das AK (2020) Microstructure and microhardness characteristics of TiC–TiN ceramics coating by TIG process on mild steel. *Adv Mech Eng*, pp 467–474
33. Tosun G (2013) Ni–WC coating on AISI 1010 steel using TIG: microstructure and microhardness. *Arab J Sci Eng* 39(3):2097–2106
34. Tosun G, Buytoz S (2020) Microstructural properties of Fe–Cr–C/NbC composite coating produced on medium carbon steel surface by TIG coating process. *Arab J Sci Eng* 46(3):2231–2241
35. Singh J, Thakur L, Angra S (2019) Effect of argon flow rate and standoff distance on the microstructure and wear behaviour of WC-CoCr TIG cladding. *J Phys: Conf Ser* 1240:012162
36. Shi ZP, Wang ZB, Wang JQ, Qiao YX, Chen HN, Xiong TY, Zheng YG (2019) Effect of Ni interlayer on cavitation erosion resistance of NiTi cladding by tungsten inert gas (TIG) surfacing process. *Acta Metall Sin (English Letters)* 33(3):415–424
37. Kilic M, Imak A, Kirik I (2021) Surface modification of AISI 304 stainless steel with NiBSi-SiC composite by TIG method. *J Mater Eng Perform* 30(2):1411–1419
38. Sharma D, Ghosh PK, Kumar S, Das S, Anant R, Kumar N (2018) Surface hardening by in-situ grown composite layer on microalloyed steel employing TIG arcing process. *Surf Coat Technol* 352:144–158

Review of Enhancement of Polymer for Material Extrusion Process by Combining with Filler Material



Mizab Ahmed E. A. Bardi, Shubham A. Bokade, Sushant L. Gunjal, Omkar R. Bedade, and Shreeprasad S. Manohar

Abstract Additive manufacturing or layer manufacturing is the development of a 3D object from a CAD or a digital 3D model of practically any shape with minimum wastage of material. Its principal advantage of layer-by-layer deposition can even eliminate post-production assembly too. Out of various methods, Fused Deposition Modeling (FDM) is one of the extensively used. One of the primary drawbacks of the FDM approach is the dearth of the strength of the component produced with it. Along these lines, for improving the properties of the polymer grid one of the most generally utilized techniques is to strengthen it by reinforcement of filler material. This paper opens up about numerous filler substances which may be reinforced within the polymer matrix to enhance its universal properties and the methodologies related to it. The paper initially discusses various natural fibers but, the results show that strengthening provided by most of them is not adequate hence, synthetic fibers comes into the picture. The focal point of this review paper is on the cellulose, Glass fiber (GF) and Basalt fiber (BF) and proposes to use silane and graphene oxide as coupling agents which can enhance interfacial bonding between the organic and inorganic substrate.

Keywords FDM · Layer manufacturing · Polymer · Silane coupling agent · Glass fiber · Basalt fiber · Composite

1 Introduction

Additive manufacturing in short AM is additionally also referred to as layer manufacturing. It is the process of mixing materials to fabricate a three dimensional (3D) object, layer-by-layer. The inputs are taken from the 3D CAD model which is modeled in a Solid Modeling software. Additive manufacturing is used in many manufacturing

M. A. E. A. Bardi (✉) · S. A. Bokade · S. L. Gunjal · O. R. Bedade · S. S. Manohar
Mechanical Department, Don Bosco Institute of Technology, Mumbai, India

S. S. Manohar
e-mail: shreeprasad.dbit@dbclmumbai.org

© The Author(s), under exclusive license to Springer Nature Singapore Pte Ltd. 2022
H. K. Dave et al. (eds.), *Recent Advances in Manufacturing Processes and Systems*,
Lecture Notes in Mechanical Engineering,
https://doi.org/10.1007/978-981-16-7787-8_69

industries like automotive, furniture, biomedical, construction, aerospace etc. Multi-step process and single-step process are the type of AM on the basis of ISO/ASTM 52900. Various 3D printing processes are classified into: material extrusion, binder jetting, directed energy deposition, material jetting and powder bed fusion. Based on the materials used in the Additive Manufacturing process, there are predominantly three types of 3D printing methods available and these are liquid-based, solid and/or extrusion-based and powder-based Additive Manufacturing. Stereolithography (SLA) and polyjet are liquid-based Additive Manufacturing processes. Fused deposition modeling (FDM) is extrusion-based AM process and laminated object manufacturing (LOM) is the example of solid-based AM process. Powder bed and inkjet head 3D printing (3DP), laminated engineered net shaping (LENS), prometal, electron beam melting and selective laser sintering (SLS) all are powder-based AM processes. For printing fiber-reinforced polymer composites FDM is the most conventional technique. Void formation between the deposition lines in 3D printed composites is one of the most prominent drawbacks of the FDM technique [1–3]. One significant advantage of FDM over other techniques consists of quick movement, high accuracy and less wastage of material. Additionally, as far as the geometry of the product is concerned, the 3D printer is free of limitations, and does not require additional apparatus [4]. A combination of variables like the extrusion nozzle diameter, printing orientation and temperature are some of the parameters which influence the mechanical properties [5].

The creation of 3D model using CAD file is the first step for FDM 3D printing. Then this file is converted into a specific surface file format which is called STL (standard tessellation language) format. This format is supplied to the slicing software. Slicing software allows to process this format and adds layer details and packs the file in the G-code format which is easily understood by the 3D printer. In order to make an object using 3D printer, a polymer plastic filament is fed through an extrusion nozzle with the help of feeding gear mechanism. This nozzle locally melts the filament. Meanwhile feeding gear keeps pushing material filament in, which increases the pressure inside the extruder and then material comes out of nozzle. It is made to fall on a glass plate also called as built plate. Both the build plate and the nozzle are controlled by a computer which can translate the object's geometry into (x, y, z) coordinates. The nozzle moves in a horizontal as well as vertical direction, creating a thin plastic layer, which sticks to the paper placed on the table, which gets cooled and hardened. When a specific layer is totally set out, the base is brought down to make space for the following layer of plastic. The size of the object being manufactured is the important factor on which the printing time depends [4, 6]. Out of various available 3D Printing techniques, Fused Deposition Modeling (FDM) creates a 3D geometry by depositing layer-by-layers of thermoplastic material which is extruded through its nozzle. Out of available thermoplastic materials, polylactic acid (PLA), polyvinyl alcohol (PVA), polyether-ether-ketone (PEEK), acrylonitrile butadiene styrene (ABS), Nylon, Copolyester (CPE), and Polypropylene (PP) are widely used FDM materials [7].

3D printers have very advantages but an important limitation is the limited library of materials. Pure thermoplastic when used to manufacture parts via FDM shows a

tendency of displaying inadequate strength at the time of performance of loading tests which restricts scope of application where 3D printing can be used which leads to enhancement of their properties. To overcome this limitation compatibilizers, fiber reinforcements, nanomaterials, etc. can be used [4]. General composite materials available are PLA + GF, PLA + CF, PEEK + CF, PP + GF, PEKK + CF.

2 Natural Fiber as a Reinforcement

Minerals, plants, and animals are the source of natural fibers. Higher ‘Specific Strengths’ and stiffness are the reasons because of which natural fibers are the most widely used as a reinforcement in composites [1]. A Comparative study was carried out between various natural fibers, and results depict the following:

- (1) Lignin and tannin—Reduction in tensile strength and improvement in thermal degradation [8, 9].
- (2) Abaca—Increment in brittleness [8, 9].
- (3) Pulp—Improvement in strength and rigidity, reduction in ductility and toughness [8, 9].
- (4) Harakeke—Increment in tensile strength up to 20% of the fiber content [8].
- (5) Kenaf—Increment in tensile strength up to 30% of fiber content [8].
- (6) Hemp—Increment in tensile strength upto 10% of fiber content and then strength decreases [8, 10].
- (7) Banana—Good specific strength properties as compared to Glass Fiber, as banana possesses lower density and good moisture intake capacity [10].
- (8) Cellulose—Improving PLA performance with cellulose + GF [11] (see Fig. 1 for cellulose fibers).
- (9) Basalt Fiber—possesses the qualities of good noise damping and high thermal resistance. The basalt fibers are produced from the melting of basalt stones obtained by crushing them at 1400 °C and drawing out the molten material. Two different kinds of basalt fibers can be distinguished—staple fibers and filaments. The staple fibers show unsymmetrical properties hence, industrial-grade is commonly used, i.e., basalt fiber filament produced by the spinneret process. For the preparation of fibers, silica content of 46% or more is required. Only under this precondition, it is possible to melt the stone completely without leaving any residues [12] (see Fig. 2 for Basalt Fibers).

On general basis, while comparing with pure polymers, properties of the 3D printed natural fiber composites do not increase significantly [1].

Fig. 1 Chopped cellulose fiber strands (250 μm diameter)



Fig. 2 Chopped silicized/silane treated basalt fiber for reinforcement (1 mm diameter and 3 mm length)



3 Synthetic Fiber and Elastomer as Reinforcement

Compared to the natural fibers, synthetic fibers show better mechanical properties [1], But natural polymers like PLA shows fewer negative effects and thus can be suggested as a replacement of petroleum-based counterparts [1]. Improved stiffness and strength are the key enhancements by carbon fibers (Fig. 3) hence they are one of the preferred choices as a reinforcing material. Other properties include lightweight nature and

Fig. 3 Raw black chopped carbon fiber (3 mm length) with 95% carbon content



excellent chemical resistance but cost is the disadvantage [13]. Introduction of GF increases strength, rigidity, toughness and thermal resistance of polymer matrix. Various fillers used for modification consists of some tough polymers and fibers. Addition of TPE in PLA increases ductility, but reduction in strength and stiffness was observed. Poly(hydroxybutyrate) PHB has the same effects on mechanical properties as that of TPE with a reduction in thermal resistance. Poly (ϵ -caprolactone) (PCL) enhances ductility of PLA when mixed with compatibilizing agents, and at the same time tensile strength as well as modulus is reduced.

4 Compounding of Polymer Matrix with Reinforcement and Methodologies

Varsavas et al. researched on the effects of addition of Thermoplastic Elastomer (TPU) in the composite matrix of polylactide and E-glass fibers, w.r.t. mechanical properties like strength and modulus. In Tension and flexural test, it is seen that respective strengths increases with addition of GF content upto 15 wt%. Increase in σ_{TS} and σ_{Flex} were upto 32% and 21%, respectively. Also, compared to neat PLA, addition of 15 wt%GF resulted in 48% and 100% increase in E and E_{flex} , respectively. It is observed that use of 10 wt% TPU causes loss in strength and modulus, but these losses are also recovered when PLA/TPU blend is reinforced with 15 wt% GF. PLA blend with 10% TPU shows more than three times increase in ductility whereas, 74% and 103% increase in G and K fracture toughness values, respectively [14].

Jaszkievicz et al. carried out their research work in this field by using GF, cellulose pulp from wood species and abaca fiber to precisely control the growth and mechanical properties of PLA. The PLA is predrilled and the cellulose fibers are placed in the oven, and GF are directly used. Thus, fibers and molten polymers are mixed in a twin-screw extruder and cut to 15 mm length and dried up, then these

are fed into a single screw extruder. PLA composite shows low impact strength. Cellulose fiber increases the stress-related properties and allows larger deformation, increase in tensile strength up to 1.9 times for PLA. Young's modulus for pure PLA, PLA/cell 30%, PLA/GF 30%, PLA/Abaca 30% obtained using experimentation were 3.4 GPa, 6.5 GPa, 9.8 GPa, 7.6 GPa, respectively. Mean values of a notch Charpy impact strength of PLA and PLA with 30 wt% fiber content of Cellulose, Abaca and GF observed were 1.6, 8.2, 3.7, 10.1 KJ/m², respectively. Increase in impact strength can be achieved by using short fibers [13].

Li et al., in their research, worked on the reinforcement of PLA with Cellulose and GF. Cellulose prepared with TEMPO oxidation method and GF was blended with PLA and spun into the reinforced PLA filament, respectively, which is applied to FDM printing technology. The oxygen atoms in PLA forms hydrogen bonds with cellulose but the cohesive force is small. Hence, PBAT solvent is used to improve the cohesion. The composite is manufactured through the following steps:

- (1) The particle powder is heated, dried and then melted
- (2) After mixing in twin-screw extruder filament is extruded and cooled
- (3) The coil is wound on the filament winder
- (4) Hardening of the spool is done.

It was observed that the toughness as well as the bending capacity of the cellulose blended PLA is much better than pure PLA. Improved hardness with a good surface finish could be obtained with reduced brittleness. The strength and hardness of the Glass Fiber reinforced PLA, are higher and the surface is extremely rough with increased brittleness. A comparative analysis between Glass Fiber (see Fig. 4 for Glass Fiber) and Cellulose Fiber gave the following:

- (1) 4% cellulose addition—improved material toughness, elasticity and bending capacity with reduced brittleness.
- (2) 8% cellulose addition—significant increase in hardness.
- (3) 4% Glass Fiber addition—increase in hardness, but toughness reduces.
- (4) 8% Glass Fiber addition—brittleness and hardness improve, but bending and curling is difficult [15].

Rameshwar Kendre tested a mix of PLA bio-composites with man-made cellulose and Abaca Fibers processed by extrusion coating process as well as injection molding. The Charpy impact strength at NTP conditions was observed to increase by a factor of 3.6. On addition of 30 wt% man-made cellulose, the tensile strength rose by a factor of 1.45 and stiffness by an approximate of 1.75. Reinforcing with Abaca Fibers up to 30 wt% resulted in an enhancement by factors of 1.2 and 2.4 in tensile strength and modulus of elasticity, respectively. The Charpy notch impact resistance of PLA/abaca could be enhanced by a factor of 2.4. The ductility of each composite declined, when compared to neat PLA. Reinforcement allowed better stress transfer from the matrix to the fiber. The highest value of the dynamic modulus could be achieved for PLA/abaca, then for PLA/cellulose and PLA [10].

The manufacturing process followed by Rahimizadeh et al. for creation of filament is described here: Double extrusion process was used for mixing glass fiber with PLA

Fig. 4 Raw plain chopped glass fiber (10 μm diameter and 3 mm length)



for FDM. Co-rotating twin-screw extruder was used for composite, as it can handle highly viscous fluid very easily and also provides more time for the base and filler material to bond together. They found that the recycled glass fibers have been used as these can enhance the properties to a large extent since, they are covered with an epoxy layer which results in the formation of a stronger bond. The method used for the formation of fibers was ‘mechanical grinding’ because it is comparatively more Eco-friendly. Moreover, these short fiber composites work well with the FDM process. GFRP blades were cut into 20×20 cm pieces and were fed to a hammer mill grinder since it can produce small granular fibers, which were then mixed with PLA. This mixture was then sieved, for separating fibers greater than 0.4 mm which could result in clogging of the nozzle. Even though the epoxy powder reduces the surface finish, which may lead to stress concentration and micro-crack formation, the main advantage is that it promotes mechanical interaction, which leads to molecular and chemical interaction, which improve the impregnation of glass fiber with PLA [16–18].

Gholamhossein Sodeifiana et al. observed that, PP GF made specimens had higher values of strength and modulus hence, lower flexibility and elongation at break. Their work suggested that dispersion of GF through the filament enhances the tensile strength and modulus, while reducing the flexibility of the material. Introduction of POE-g-MA at 10, 20 and 30%, enhances the overall flexibility of the material. As an elastomer, it tends to remain isolated from the surface of the glass fiber and PP, thereby

increasing the strength and Mechanical properties of the material through phase separation. At lower frequencies and lower temperature all specimens display more or less same rheological properties like storage modulus. But at higher temperature, POE-g-MA enhanced the storage modulus. Higher values of loss modulus were obtained on increasing of POE-g-MA content. As far as viscosity was concerned, the increase in viscosity with increasing POE-g-MA content was observed. Study of degree of crystallinity using x-ray diffraction analysis showed that, the addition of polyolefin increased the degree of crystallinity [4].

It was perceived by Wang et al. that, GFR PLA composite 20% GF in PLA shows, 2 times strength and rigidity whereas, 3 times enhanced impact toughness. PLA derived from corn and wheat displayed properties such as; good biodegradability, high stiffness and UV stability, highly brittle and poor temperature resistance. Stereo complex crystallization is an effective method to enhance the properties of PLA. Natural fibers result in higher water absorption content and increase in toughness, but the strength decreases. Results show that proper dispersion and good chemical bonding results in better enhancements [8, 9, 19]. J. G. Matisons has concluded that Silane coating can improve the interfacial bonding between polymer and filler material [20]. Proper dispersion reduces the chance of crack initiation and propagation. The fibers tend to orient along the melt flow direction. Up to 50 GFRP shows higher Young's modulus. As the temperature increases, a sudden drop can be seen in Young's Modulus. Higher the GF content, smaller is the melt flow index (flowability). As orientation depends on flow direction, flowability is not much compromised in extrusion and injection molding [8].

Wang et al. have manufactured the filament as follows:

- (1) The PLA pellets and GF in bundle form are dried and fed to the co-rotating twin-screw extruder.
- (2) To reduce breakage GF is fed at mid-range through the side-feeding system.
- (3) Extruded matrix is cooled in a water bath then chopped in a pelletizer. [In the pelletizer high-pressure steam is used to soften the composite matrix and then two rollers are used to force the matrix over a mesh which creates pellet according to mesh size].
- (4) The pellets need to be dried again before feeding to the injection molding machine for filament extrusion and the diameter of the filament depends on the die attached in front of the injection molder.
- (5) The filament is wound on a spool by a filament winder, finally the spool is cooled to harden the filament (which does not allow any unwinding).
- (6) The spool/filament is fed to a 3D printer to print specific shapes for testing the properties [8]. Table 1 [12, 13, 21, 22] shows stress and strain related to various polymers on reinforcement of 30% Glass Fiber.

Basalt fibers are obtained from a volcanic rock named as basalt rock which has similar composition as GF as it contains large amount of silica [23]. Basalt fiber is used as a good natural alternative to glass fiber. Aslan et al. experimentally found that the fibers of basalt are bio-inert and are harmless to human health. Basalt fibers show-case good noise dampening properties and have perfect thermal resistance, which is

Table 1 Composite for glass fiber content of 30%

Material	Strain (%)	Stress (MPa)
PLA	2	150
Nylon	–	145
PP	2	90
Polyester	1.7	70

Table 2 Comparison between GF, CF and BF on the basis of various properties

Glass fiber	Carbon fiber	Basalt fiber
(1) High tensile strength and dimensional stability (2) Good thermal conductivity and electrical properties (3) High durability and cheaper than Carbon fiber (4) Good fire and mechanical properties	(1) High stiffness and tensile strength (2) Lower density and low thermal expansion coefficient (3) High-temperature tolerance	(1) Superior noise damping properties, high thermal and chemical resistance (2) Economical in comparison to carbon and glass fiber (3) Lower humidity absorption than glass fiber (4) High tensile strength and Elastic modulus (5) Obtained naturally and is biodegradable

superior to the glass fibers. Moreover, the fibers of basalt are less expensive and show high mechanical properties when compared to glass. Aslan et al. have conducted some tests and have investigated that, untreated basalt fibers with reinforced PLA possess three times the strength and seven times the stiffness of neat PLA. Silane treated, extruded and injection molded composites show better properties. PLA composites with basalt fiber reinforcement show better mechanical properties with respect to PLA composites with glass fiber reinforcement [24–26]. Table 2 summarizes the properties which can be improved by various filler materials.

Sang et al. tried to develop a composite of PLA reinforced with KH550 treated basalt fiber, as a sustainable and cheaper 3D printable material. Initially, Aladdin reagent and Triethoxysilane are applied on basalt fiber for a greater bonding then, drying is done for 1.5 days at 60 °C. An internal mixer is used for blending by adding Half of PLA to the mixing chamber for 3 min at 180 °C and then, adding basalt fibers in a varying weight after 3 min each. After an interval of 10 min, the remaining half of PLA and BF are introduced to the melt. Finally, granules are chopped from the melt and fed to a single screw extruder with a die temperature of 210 °C. The extruded filament is cooled by dipping it into a 0.5 m long pool bath after which the filament is wound on a spool and the spool is dried at 50 °C [27].

SEM analysis for fracture, Thermogravimetric analysis for thermal stability and DSC analysis in cycles of 30–200 °C for thermal stability were carried out. SEM analysis photographs indicates a good bonding between PLA and BF. Results showed that the tensile strength of specimens in both CM and FDM was the same. Variations

Table 3 Comparison between various fibers

Reinforcing fiber	Density (g/cm ³)	Linear density (μm)	Fiber diameter (μm)	Temp withstand (°C)	Moisture absorption %	Tensile strength (MPa)	Tensile modulus (GPa)
E-glass	2.45	2400	17	−50 to 450	1.7	2450	80
Carbon	1.8	800	7	−50 to 500	-	4900	230
Basalt	2.6	1200	13–20	−260 to 600	0.02	2850	90

in the strength of various FDM samples were also less which denotes stability of FDM method w.r.t. processing.

The tensile strength of PLA/BF composite is seen to be increased up to 71.9 MPa at 20% weight addition. Whereas, max tensile strength in PLA/CF was observed to be 69 MPa at 10% weight addition. Further addition of CF reduces the tensile strength drastically and the reason is likely the excessive viscosity resulting in poor blending and bonding. As regards to flexural strength and modulus, the max values achieved are 131 MPa and 5.08 GPa at 20% weight BF. CF shows decrement in flexural strength as it is wt. % increases from 5 to 10%, i.e., 94 MPa even lower than PLA. PLA/BF shows better performance as compared to PLA/CF w.r.t. printed specimen as bonding in PLA/BF matrix seems to be better as viscosity of the composite is quite similar to PLA. The results shows that there is an increase in tensile strength and modulus, flexural modulus and impact strength but, a decrease in flexural strength is observed which may be due to larger pores. Table 3 shows comparison between various properties of fibers [28, 29].

5 Adhesion Improvement Using Coupling Agent

Peter G. Pape found that these coupling agents are silicon-based chemicals, which alter the physical and chemical forces at the interface and provide gluing to give much greater adhesion even against heat and moisture. One silicon molecule can contain both organic and inorganic reactivity. This unique nature of silane chemistry to provide such benefits makes it suitable to be used as a coupling agent. Monomeric silicon chemicals are called silane. (If the spacer group is of at least 3 carbon in length then, silane will have similar reactivity as of carbon, or else it will have a reactivity similar to that of silicone.) The coating can prevent debonding at the interface due to moisture and heat. Also, silane can bond well to the inorganic substrate (Glass Fiber). Trialkoxysilane has a higher equilibrium constant toward bonding to inorganic substrate resulting in stronger bonding. The silane should be able to wet the inorganic substrate and stay in a permeable state until it interpenetrates with the polymer. I.e., silane is applied to Glass fiber and then dried before mixing with polymer (integral

blending). Silane is generally applied during mfg. of Glass fiber, but sometimes it can be added to the filler/polymer matrix during compounding stage (but, pre-treatment is preferable to have more control over properties). The silane can be applied in aqueous as well as in vapor state [27].

Jing et al. found that PLA/Glass Fiber shows Poor adhesion and poor mechanical properties. Whereas, PLA/Glass Fiber with silane improves the strength and toughness. PLA/Graphene Oxide provides good crystallization and a higher young's modulus. GFRP properties depend largely on the aspect ratio, content and dispersion of fiber but more importantly on interaction (Silane is also compatible with various polymer matrices like PP, PA, PET, etc.). Graphene Oxide can easily be dispersed into the polymer matrix and can improve the fiber strength by enhancing the interfacial interaction. Glass Fiber can be coated with Graphene oxide with the help of electrostatic assemble strategy. Glass fiber with graphene oxide is obtained by mixing the glass fiber with graphene oxide solution (graphene oxide solution is obtained by mixing graphite oxide with a strong oxidizer like Sulfur and stirring it well for 5 h.) and soaking for 9 h. Then, the glass fiber with graphene oxide is washed to remove any unbound graphene oxide molecules. Twin-screw extruder is used for melt blending of PLA and filler material at 190 °C for 5 min and dumbbell-shaped specimens are injection molded at 120 °C. For recrystallization, the specimens are held at 120 °C for 9 mins. Tensile tests, cryogenically fractured specimens in liquid nitrogen and Dynamic mechanical analysis are the various tests that are performed to evaluate thermomechanical properties. Scanning electron microscopy is done to check if graphene oxide can be successfully coated. The surface finish of graphene oxide coated material is observed to be poorer than that of silane coated material.

Interfacial bonding in PLA and GF is better and recrystallization has little effect on it. Whereas, Interfacial bonding in PLA and GO is good and with recrystallization it improves drastically. It is observed that the length of fibers is longer in GF-S samples resulting in higher bending strength in GF-S samples compared to GF-GO samples. As greater the fiber length fewer chances of crack initiation and propagation due to the bridging effect. Tables 4 and 5 shows the comparison between GF-S and GF-GO with PLA wherein 30 signifies percentage of Glass Fiber addition. GF-S signifies glass fiber with silane coating whereas, GF-GO signifies glass fiber with a graphene oxide coating [30].

These glass-reinforced composites are very susceptible to the effects of ambient humidity. Further, the coefficient of thermal expansion for GF is lower than that of polymer matrix. This results in thermal stresses at the interface. Such stresses

Table 4 Comparison between GF-S and GF-GO with PLA without recrystallization

Specimen (material)	Tensile strength (MPa)	Storage modulus (MPa)
PLA	80	3810
PLA/GF-30	96	7391
PLA/GF-S-30	140	7496
PLA/GF-GO-30	117	8126

Table 5 Comparison between GF-S and GF-GO with PLA with recrystallization of 9 min

Specimen (material)	Elongation at break (%)	Young's modulus (MPa)
PLA	4.4	2593
PLA/GF-30	3.6	5264
PLA/GF-S-30	3.9	5153
PLA/GF-GO-30	2.5	5772

result in reduction of the overall strength of the composite and hence, coupling agents like silane are used. J. G. Matisons conducted a chemical research on Glass fiber with silane and found that Trialkoxysilane improved the water-resistance of the composite. It was generally applied from an aqueous solution, which resulted in the formation of oligomeric silane. Enhancement depends upon the degree of oligomerization which was inversely proportional to the age of silane. So, the properties were more easily controlled if silane was applied just after manufacturing of silane. The Trialkoxysilane formed bonds with both polymer and Filler [20].

Wu et al. observed that silane was not essential for manufacturing of GFRP, but its primary attribute was to improve the wet strength and strength at higher temperatures, Also, its coating reduced the brittleness [31].

6 Conclusion

Composites with synthetic fibers mostly provide better properties than composites with natural fibers. Varying fiber types, fiber lengths, fiber weight percentages and orientations significantly influence various mechanical properties and 3D printability of the composite.

- Basalt Fibers give overall better strength at lower costs as compared to Glass and Carbon fibers, since the Basalt fibers can be added in larger amounts, i.e., up to 45% whereas, CF can only be added up to 15% of wt. fraction. as shown in Fig. 5. However, basalt fiber addition must be restricted for FDM 3D printers to prevent nozzle clogging during printing.
- The findings show that longer fiber length improves tensile strength, Young's modulus, and impact strength which are caused by longer fiber pull-outs. On the other hand, as fiber length increases, flexural strength decreases significantly, which can be clarified by greater pores in the infill interlayer and adhesion failure in composite specimens. Figure 6 shows the same.
- To achieve adequate mechanical properties and 3D printability, KBF fiber length and content should be optimized properly.
- While CF has better mechanical properties than BF as reinforcing fibers, PLA/CF composite samples with the same fiber weight fraction do not perform as well as printed PLA/KBF samples.

Fig. 5 Variation in tensile strength w.r.t. fiber wt% in polymer matrix

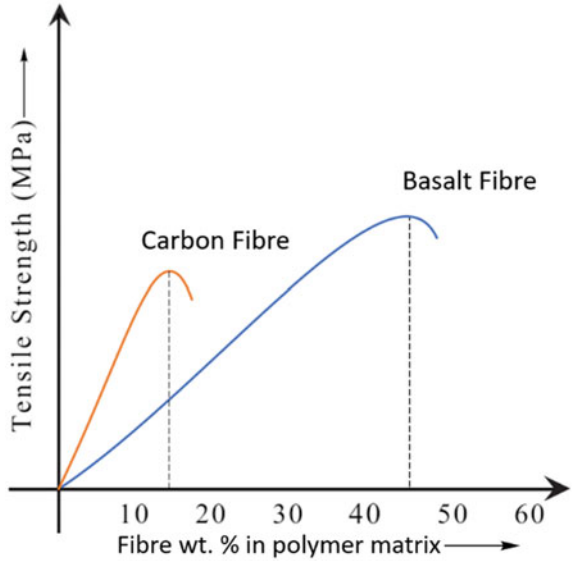
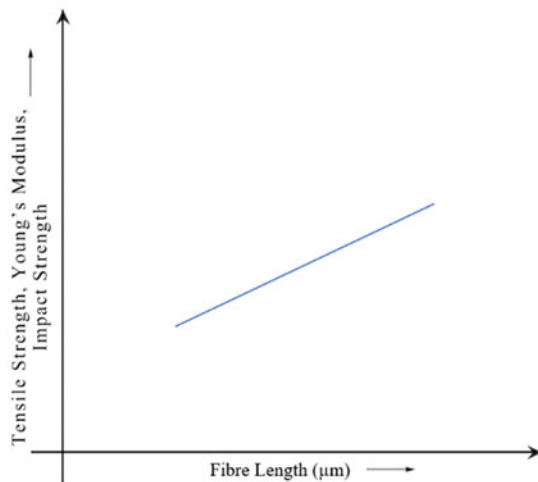


Fig. 6 Variation in various strength characteristics w.r.t. fiber length



- Due to extrusion, FDM provides more oriented fibers than other techniques in relation to printing direction, which increases tensile properties.
- In order to develop green composites, BF can be used as an alternative reinforcement for biodegradable aliphatic polyesters.

Interfacial bonding is an important factor in enhancement of strength characteristics of a composite material. Coupling agent is used to improve the interfacial bonding between polymer matrix and filler material by formation of mechanical and

chemical bonds. Thus, improving mechanical properties to a greater extent. Silane coupling agent is not an essential constituent for formation of a composite but if added, it can protect the bonding at elevated temperature as well as against moisture.

The end point of the curve shows the limit (wt%) upto which fibers can be added in polymer matrix.

References

1. Sekar V, Fouladi MH, Namasivayam SN, Sivanesan S (2019) Additive manufacturing: a novel method for developing an acoustic panel made of natural fiber-reinforced composites with enhanced mechanical and acoustical properties. *J Eng* 2019:1–19
2. Horn T, Harrysson O (2012) Overview of current additive manufacturing technologies and selected applications. *Sci Prog* 95(3):255–282
3. Kumar S, Kruth J (2010) Composites by rapid prototyping technology. *Mater Des* 31:850–856
4. Sodeifiana G, Ghaseminejada S, Yousefid A (2019) Preparation of polypropylene/short glass fiber composite as fused deposition modeling (FDM) filament. *Results Phys* 12(12):205–222
5. Billah K, Lorenzana F, Martinez N, Chacon S, Wicker R, Espalin D (2019) Thermal analysis of thermoplastic materials filled with chopped fiber for large area 3D printing. Paper presented at Solid Freeform Fabrication, Austin, Texas, Aug 2019
6. Cerneels J, Voet A, Ivens J, Kruth J, Leaven K, More T (2013) Additive manufacturing of thermoplastic composites. Paper presented at texcomp-11 conference, Leuven, Belgium, 16–20 Sept 2013
7. Sang L, Han S, Li Z, Yang X, Hou W (2019) Development of short basalt fiber reinforced polylactide composites and their feasible evaluation for 3D printing applications. *Compos B Eng* 164:629–639
8. Wang G, Zhang D, Wan G, Li B, Zhao G (2019) Glass fiber reinforced PLA composite with enhanced mechanical properties, thermal behavior and foaming ability. *Polymer* 181:1–9
9. Lin J, Huang C, Chen C, Liao J, Lou C (2015) Manufacturing and mechanical property evaluations of PLA/carbon fiber/glass fiber composites. *Appl Mech Mater* 749:261–264
10. Kendre R (2014) Alternate materials for glass fibre. *Adv Mater Res* 1077:3–7
11. Bledzki AK, Jaszkiwicz A, Scherzer D (2009) Mechanical properties of PLA composites with man-made cellulose and abaca fibres. *Compos A Appl Sci Manuf* 40(4):404–412
12. Kumar TV, Chandrasekaran M, Santhanam V, Udayakumar N (2017) Characterization of Nylon 6 nano Fiber/E-glass fiber reinforced epoxy composites. *IOP Conf Ser: Mater Sci Eng* 183:1–7
13. Jaszkiwicz A, Bledzki A, Franciszczak A (2013) Improving the mechanical performance of PLA composites with natural, man-made cellulose and glass fibers—a comparison to PP counterparts. *Polimery* 58(6):435–442
14. Varsavas SD, Kaynak C (2018) Effects of glass fiber reinforcement and thermoplastic elastomer blending on the mechanical performance of polylactide. *Compos Commun* 8:24–30
15. Li X, Ni Z, Bai S, Lou B (2018) Preparation and mechanical properties of fiber reinforced PLA for 3D printing materials. *IOP Conf Ser: Mater Sci Eng* 322:1–8
16. Rahimizadeh A, Kalman J, Henri R, Fayazbakhsh R, Lessard L (2019) Recycled glass fiber composites from wind turbine waste for 3D printing feedstock: effects of fiber content and interface on mechanical performance. *Materials* 12(23):1–18
17. Rahimizadeh A, Kalman J, Fayazbakhsh K, Lessard L (2019) Recycling of fiberglass wind turbine blades into reinforced filaments for use in additive manufacturing. *Compos B* 175:1–11
18. Job S (2013) Recycling glass fibre reinforced composites—history and progress. *reinforced plastics. reinforced plastics* 13:19–23
19. Garlotta D (2001) A literature review of Poly(Lactic Acid). *J Polym Environ* 9(2):63–84

20. Matisons JG (2012) *Silicone surface science 2012*. Vol. 4 of advances in silicon science, Springer, Morrisville
21. Summers JW, Faber E, Kinson PL, Rabinovitch EB (1990) Vinyl composites fiberglass reinforced PVC. *J Vinyl Add Tech* 12(2):99–104
22. Bindal A, Singh S, Batra NK, Khanna R (2013) Development of glass/jute fibers reinforced polyester composite. *Indian J Mater Sci* 2013:1–6
23. Mahltig B (2017) *Inorganic and composite fibers*. The textile Institute Book Series, Woodhead Publishing, Mönchengladbach
24. Aslan M, Güler O, Kaya G, Alver U (2018) Effect of fibre content on the mechanical properties of basalt fibre reinforced polylactic acid (PLA) composites. *TEKSTİL ve KONFEKSİYON* 28:66–71
25. Horrocks A (2016) *Handbook of technical textiles*, 2nd edn, vol 2, Woodhead Publication, Bolton
26. Han L, Ma F, Chen S, Pu Y (2019) Effect of short basalt fibers on durability, mechanical properties, and thermal properties of polylactic acid composites. *Polym Renew Resour* 10(1–3):45–59
27. Pape P (2017) Chapter 29: Adhesion promoters. In: Myer K (ed) *Applied plastics engineering handbook*, William Andrew Publishing, Norwich, USA, pp 503–517
28. Militký J (2017) *Handbook of properties of textile and technical fibres*, 2nd edn, vol 18, Woodhead Publishing, Czech Republic
29. Liu S, Yu J, Wu G, Wang P, Liu M, Zhang Y, Zhang J, Yin X, Li F, Zhang M (2019) Effect of silane KH550 on interface of basalt fibers (BFs)/poly (lactic acid) (PLA) composites. *Industria textila* 70(5):408–412
30. Jing M, Che J, Xu S, Liu Z, Fu Q (2018) The effect of surface modification of glass fiber on the performance of poly(lactic acid) composites: graphene oxide versus silane coupling agents. *Appl Surf Sci* 435:1046–1056
31. Wu HF, Dwight DW, Huff NT (1997) Effects of silane coupling agents on the interphase and performance of glass-fiber-reinforced polymer composites. *Compos Sci Technol* 57(8):975–983

Review on Friction-Based Additive Manufacturing Processes: Types, Defects, and Applications



Bhumi K. Patel, Falak P. Patel, and Vishvesh J. Badheka

Abstract Friction stir additive techniques (FSATs) are currently at an evolving stage. The 3D geometry is obtained using the principle of solid-state joining with the help of heat generation because of friction. This method utilizes a layer-by-layer approach and is a promising method for better mechanical properties, good surface finish, and fabricating complex structures. This paper aims to highlight the working concept of FSATs and the research work done in this sector. It also discusses the benefits, limitations, future scope, and potential applications of FSATs with various friction-based additive manufacturing techniques.

Keywords Friction-based AM techniques · Friction stir additive techniques · Additive manufacturing

1 Introduction

Additive manufacturing is a currently developing and in demand manufacturing process. The additive manufacturing technique works on the concept of layer-by-layer fabrication of the 3D component. This technique can help fabricating components of metal, non-metal, and as well as polymers. It is being used in process chains to reduce cost and time requirements [1]. It is a form of manufacturing in which physical three-dimensional components are produced by using various techniques to incorporate material in 2.5 dimensions directly from a CAD design [1]. The products developed by AM techniques have enormous benefits like minimal use of material

B. K. Patel (✉) · F. P. Patel · V. J. Badheka
Department of Mechanical Engineering, SOT, Pandit Deendayal Energy University (PDEU),
Raisan, Gandhinagar, Gujarat 382007, India
e-mail: bhumi.pmc18@sot.pdpu.ac.in

F. P. Patel
e-mail: falak.pmc18@sot.pdpu.ac.in

V. J. Badheka
e-mail: Vishvesh.Badheka@spt.pdpu.ac.in

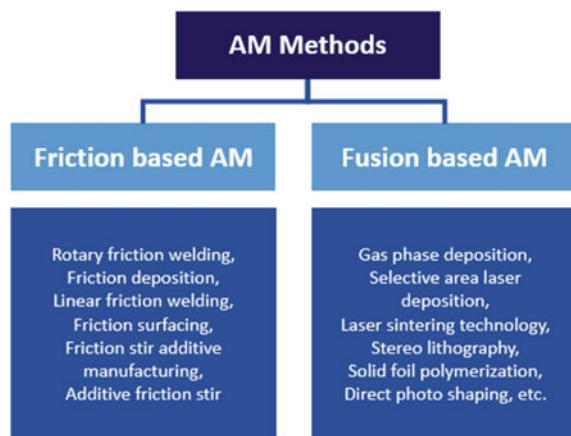
and low heat generation over conventional methods [2]. Better material properties, great dimensional accuracy, improved quality, and good surface finish are achieved by using this method [3]. Nowadays, metal additive manufacturing techniques are the main focus of researchers [4, 5]. As per the current evolution, various MAM technologies are developed like laser-based AM, shape metal deposition, electron beam melting, and friction-based AM. In this paper, detailed explanation on friction-based additive manufacturing method is given. It also gives an overview on the on-going development in this area.

2 Friction-Based Additive Manufacturing Processes

As per current scenario after evolution of Industry 4.0, it has been observed that everyday new challenges come up and solutions for that. Manufacturing industries, on the other hand, need continuous product customization and cost-cutting in order to remain progressive and expand their businesses. AM is a thirty-year-old industrial technology that is still evolving but has proven useful in analyzing designs and manufacturing processes. In additive manufacturing, material addition approach is used rather than subtractive manufacturing. AM can be classified into two different categories, i.e., fusion-based AM, and friction-based AM, which is shown in following Fig. 1. This article majorly focusses on friction stir AM techniques and additive friction stir process.

White, in year 2002, filed a patent of process for combining metal materials using friction joining [6]. Major important aspect of his method was that it was carried out in solid state. Thomas et al. in [7] came up with an application of FSW based processes for additive manufacturing of materials. Airbus, in year 2006, announced additive manufacturing of metal parts using friction stir technique [8].

Fig. 1 Classification of AM [1]



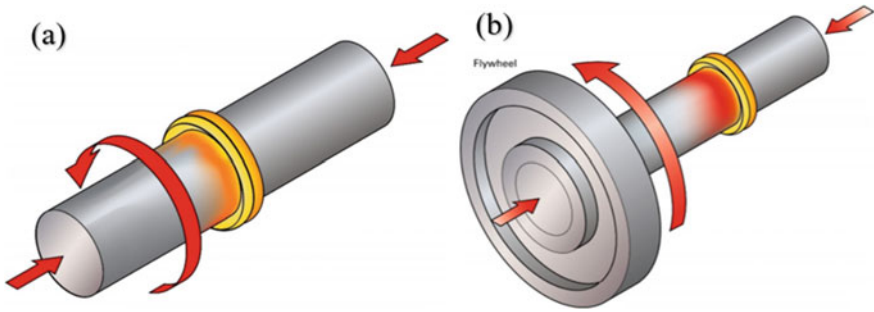


Fig. 2 a Direct drive RFW, b inertia-based RFW [9]

2.1 Classification of Friction-Based Additive Manufacturing Processes

2.1.1 Rotary Friction Welding (RFW)

In rotary friction welding, one part is kept stationary whereas another part is rotating with respect to another while undergoing compressive load. This process is repeated until mating surfaces have attained welding temperature. There are two major categories, i.e., direct drive RF and inertia-based RF. In direct drive RF method, there are two circular rods, and rotating rod is continuously driven by motor, and in inertia-based RF method, speed is controlled by flywheel. RFW is shown following Fig. 2.

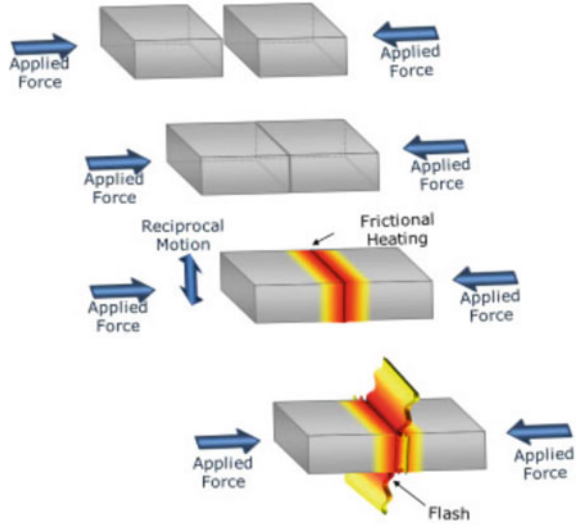
2.1.2 Linear Friction Welding (LFW)

LFW is a solid-state joining process which involves oscillating of one workpiece relative to another while applying a large compressive force. Schematic representation of LFW is shown by following Fig. 3. AM using LFW was initially proposed by the Boeing Company [10]. AM with LFW is quite simple process. In initial stage, two workpieces are joined together according to Fig. 3, and after that, LFW flash is removed by CNC machining. In next stage, we repeat same procedure by jointing third workpiece with previous achieved component, and the process is continued until the final required part is accomplished.

2.1.3 Friction Deposition (FD)

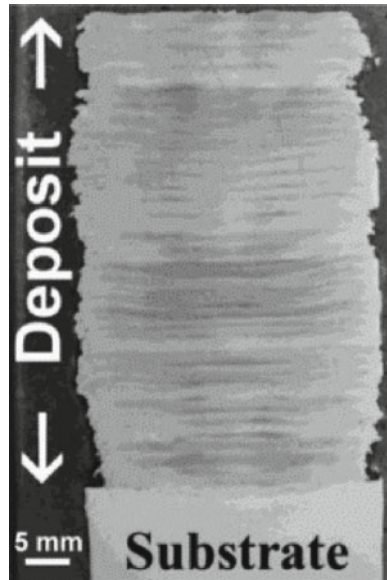
In this technique, one consumable rod attached to spindle is brought in contact with stationary substrate with pre-determined load. Because of rubbing between consumable rod and stationary substrate, frictional heat developed and consumable

Fig. 3 LWF process [11]



rods tend to plastically deform at the end surface. This leads to a layer of deposit on the surface. This can be explained by following Fig. 4. For additive friction deposition, the first step is machined previously achieved substrate by CNC and then obtained desired 3D geometry by subsequently adding one layer on another. Detailed process is described by following Fig. 5.

Fig. 4 FD process [12]



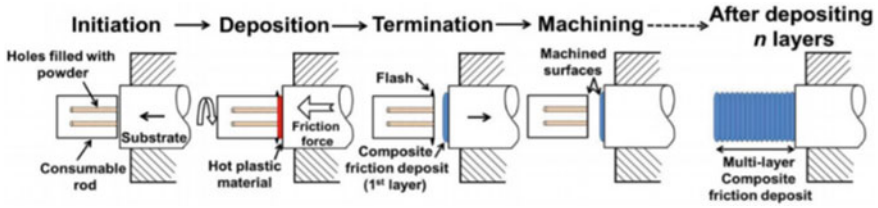
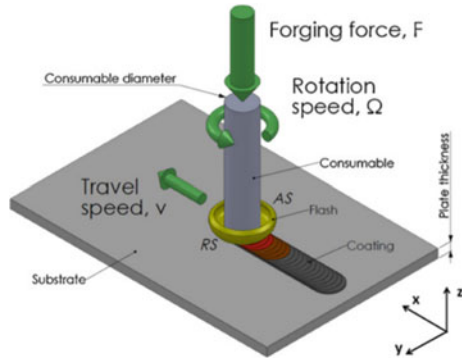


Fig. 5 Steps for FD as additive process [12]

Fig. 6 FS process [13]



2.1.4 Friction Surfacing (FS)

FS works by pressing a rotating mechtrode against a substrate, which is traverse in a predefined under axial pressure. This process is quite similar to friction deposition, but the only difference is the movement of substrate because in friction deposition substrate is kept stationary. FSW process is illustrated in following Fig. 6. As AM process, initial stage of FS to deposit one layer and after that machining of obtained layer takes place. In subsequent stages, initial process is repeated until required fabricated 3D part is achieved. Figure 7 shows detailed step by step procedure for FS as AM process.

2.1.5 Friction Stir Additive Manufacturing (FSAM)

Detailed discussion is further in Sect. 3.

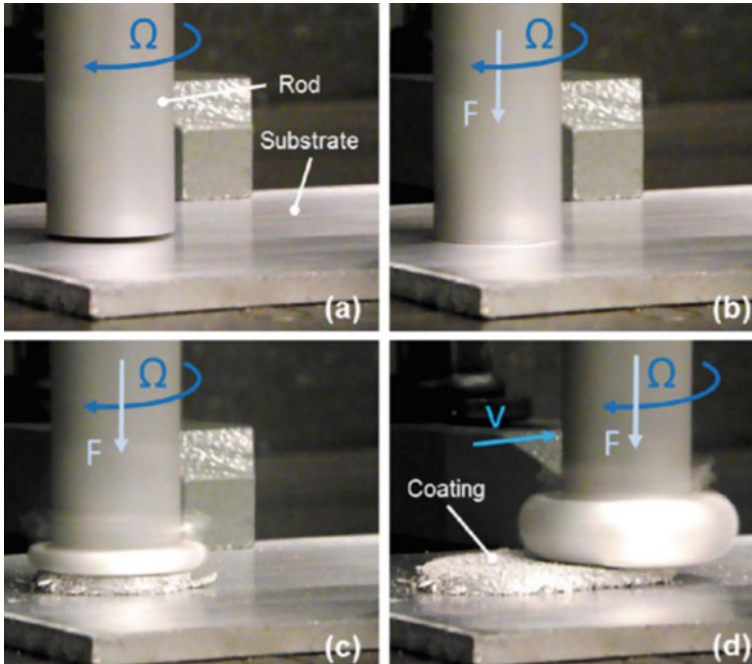


Fig. 7 Steps utilize in FS process [14]

2.1.6 Additive Friction Stir Process (AFS)

Detailed discussion is further in Sect. 4.

In friction-based additive techniques significantly, energy consumption is lower than fusion-based AM methods. In this method, parts are perfectly fused with one another, and we achieved highly efficient fabricated 3D parts.

3 Friction Stir Additive Manufacturing Process

Friction stirring is a method of plastically deforming or extruding a material, until it reaches melting temperature by producing heat through friction. It can be accomplished by combining rotation and translation motion on application of load axially over a non-consumable tool and consumable in the case of friction stir deposition. From this theory, several methods have been evolved as shown in Fig. 8.

TWI (The Welding Institute, United Kingdom) initially originated FSW method in 1991 [16]. This method works on basic principle of heat generation due to friction. If two surfaces are continuously rubbed with each other, than friction takes place between them, and due to this friction, heat generates between two surfaces which will

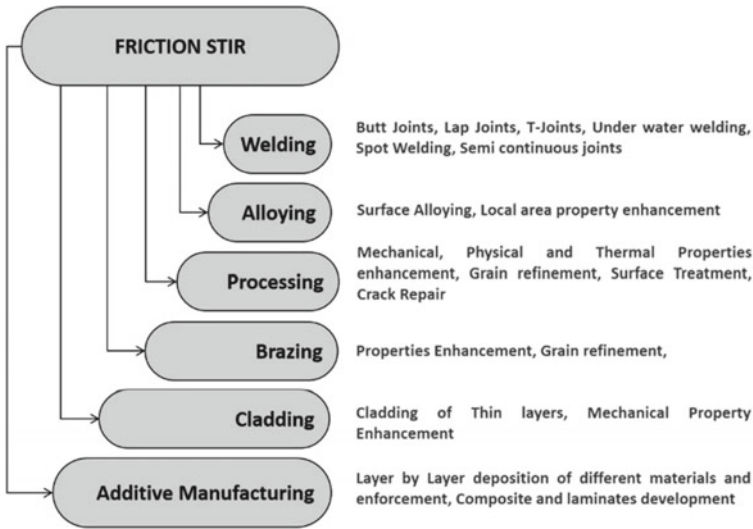
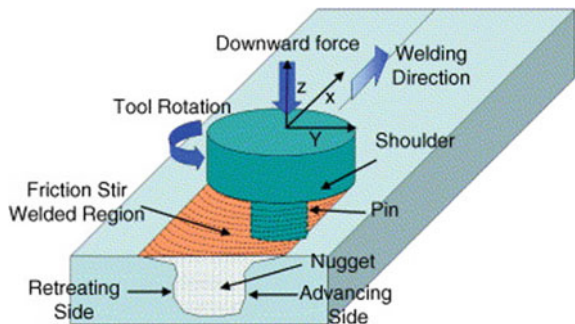


Fig. 8 Employment of friction stir method [15]

result toward softened region near FSW tool. Working of FSW is quite simple, and a rotating tool is used with pin attached to it and shoulder exert force on the surface of substrate while traversing along the joint line (joining line of two metal pieces). Due to rubbing, heat generation takes place, material gets softened, and welding takes place. Butt and lap joints are commonly used joints for FSW. Schematic representation of this process is shown in Fig. 9. Usually, FSW method is applied on aluminum alloys, titanium alloys, copper alloys, mild steel, stainless steel, and magnesium alloys, but considering recent scenario, lot of research was going on related to welding of polymer and as a result FSW can successfully applied in welding of polymers [17].

Usage of friction stir welding as AM method is completely new domain. Basic principle of FSAM is quite similar as FSW. There are many issues like internal porosity [19–21], internal cavities [22], non-homogeneity, anisotropic material behavior [21], inadequate mechanical properties, and structural efficiency [23] faced

Fig. 9 FSW process [18]



during liquid-state-based additive manufacturing methods. To overcome these challenges and obtain efficient output, FSAM is used as an alternative solution for solid-state-based additive manufacturing methods.

3.1 Working of Friction Stir Additive Manufacturing Process

The only variation between FSW and FSAM is that there is only one layer present in the case of FSW, but in FSAM, we join layer-by-layer through digital input and fabricate 3D geometry. Detailed explained schematic arrangement is given in following Fig. 10.

As shown in figure, welding of first layer takes place by stirring operation, and then, we process surface of layer 1 and flattened it. Add another substrate, and due to heat generation, plastic deformation of work material takes place and again flattened substrate. After all of these, continuously repeat all the steps again until we obtained desired material thickness. Material thickness depends on certain parameters, i.e., thickness of individual plates, method of assembling, number of layers, and process parameter restrictions, e.g., dimensions of tool pin [25]. Pin length and tool geometry should be determined accurately and precisely, to control the heat generation due to friction and severe plastic deformation during process [26]. Material flow is also influenced by tool geometry and important process parameters such as tool rotation, traverse speed, and tilt angle [15]. Process steps utilized in FSAM is shown by following Fig. 11.

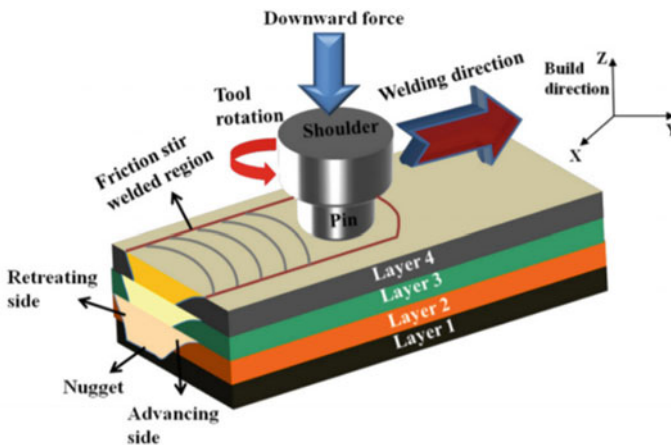


Fig. 10 FSAM process [24]

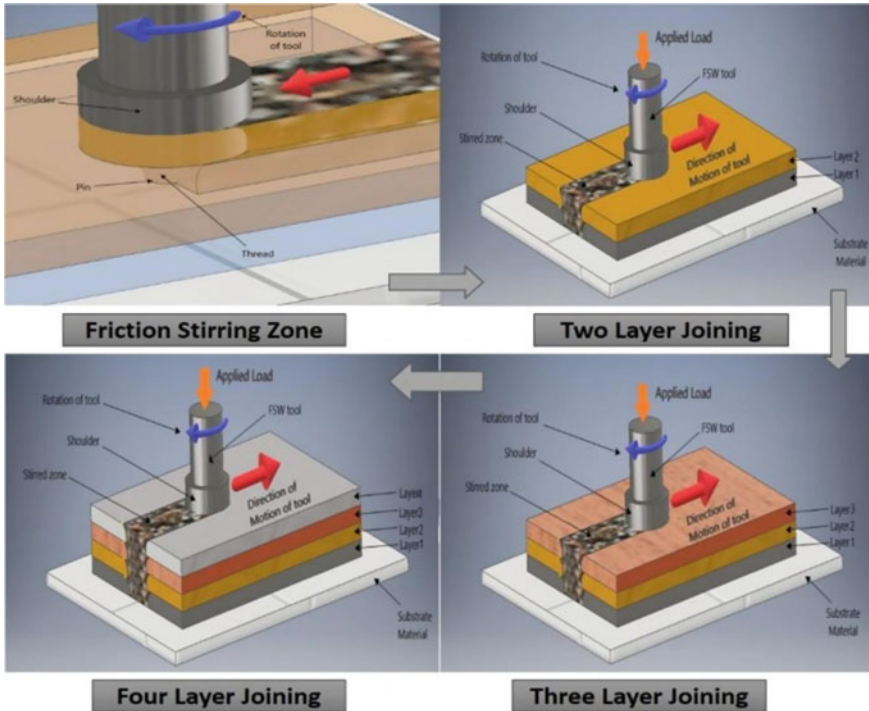


Fig. 11 Steps-wise procedure of FSAM [15]

3.2 Material Flow During Friction Stir Additive Manufacturing

During FSAM, interesting microstructural properties of various layers from bottom to top direction are obtained because of variable thermal gradient of different layers of the manufactured part. At various locations, material flow seems to be different due to distinct and collective effect of tool pin and tool shoulder [1]. From the information obtained from the experiment, it was evident that most of the material was passing from retreating side (RS) which is located at a distance known as extrusion distance from the tool pin close to the top surface and material [27–29]. Also, there is variation in the material flow due to tool pin and tool shoulder. The material flow is also reliant on the geometry of tool and input parameter [30, 31]. In FSAW, different substrate are joined together for example say there are two layers, and for both layers, governing mechanism is different. Material flow for the upper surface of the second layer is directed by tool shoulder and for the lower surface of second layer and upper surface of first layer is directed by tool pin, and so on this is applicable to adjacent layers.

3.3 Defects Associated with Friction Stir Additive Manufacturing

FASM has a number of defects, i.e., formation of hook, cavity, crack, kiss bond, etc. as a result of incorrectly chosen process parameters (Table 1).

4 Additive Friction Stir Technique (AFS)

The essence of AFS is that it is strictly additive in nature not like other friction additive techniques, i.e., extension of additive and subtraction methodologies. Powders, metallic sheets, tubes, etc., are some of the example that can used as initial materials for AFS process. Microstructural properties of fabricated parts are wrought to be uniform [48, 49]. In this method, recrystallization and plastic deformation takes place. As a result of this process, improved toughness and ductility can be obtained. Ductility and toughness of the material improved because of the refinement of grains. Material is subjected to plastic deformation and therefore refines grain sizes [25]. AFS is one of the promising methods that give better properties, homogenous microstructure, refinement of grain size, and pores free structures [50].

4.1 Working of Additive Friction Stir Technique

In FASM process, tool shoulder with tool pin is used, whereas in AFS process, no tool pin is used. Basic principle of AFS process is to deposit material over substrate, and for this, hollow cylindrical tool shoulder is used which consist of filler material, i.e., either in the powder or solid form. When a sheet is properly deposited over the substrate, the tool height is adjusted to accommodate the next layer.

In this process, when tool shoulder rotates constantly due to friction, heat is generated, and it increases temperature and leads to plastic deformation of filler rod. Filler material gets softened and deposited over substrate. When filler material gets softened, bonding at interface with substrate takes place [51]. For fabrication of 3D geometry, repeat these steps until required thickness of part is achieved. This process can be easily explained by following Fig. 12.

5 Comparison Between Friction-Based AM Techniques

See Table 2.

Table 1 Types of defects in FSAM process

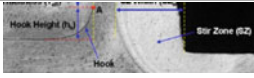
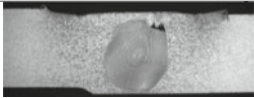
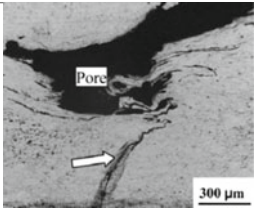
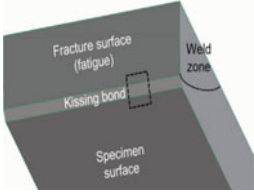
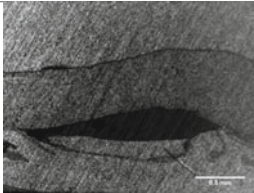
Defect	Description	Cause	
Hook	In the lap joint possessed by two contacting plates, incompletely bonded regions that have trapped materials are observed. A curved region formation due to extreme limits in the unbonded zone is termed as hook defect [32, 33]	Inappropriate selection of tool rotation, traverse speed combinations, insufficient tool tilt angle, tool design, and extreme plunging [1]	 [34]
Void	Void defect is an unoccupied space observed in the direction of FSW [35]	Inadequacy of heat and pressure [36–38]	 [39]
Pores	Small holes (diameter range: 0.1–0.5 mm) [40, 41]	Less penetration and low value of tilt angle [40, 41]	 [42]
Kiss bond	Kiss bond takes place at interfaces in the build stir region [43, 44]	Insufficient pressure, insufficient stirring, inadequacy of heat, improper deposition [43, 44]	 [45]
Tunnel	It is continuous hole which is formed inside, below the upper surface [43]	Improper selection of traverse speed, applied pressure, inadequate tool design, inappropriate rotational speed, low heat input [46, 47]	 [43]

Fig. 12 AFS process [15]

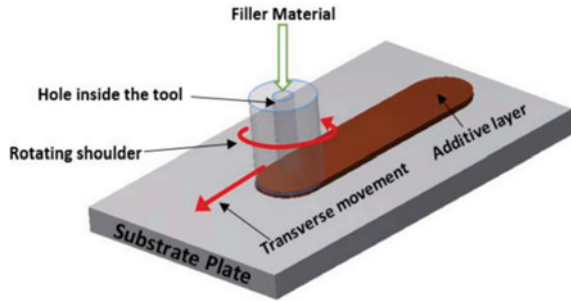


Table 2 Comparison between FATs

Process	Advantage	Disadvantage	Application
RFW [25, 52]	Use to produce large build volume with variety of metal alloy, deposition time is not dependent on part dimension, high-quality welded joint	Only for circular objects, non-homogeneous microstructure, suitable for lesser thickness object (<10 mm)	Two shafts, shaft flange, two tubes, valves, automotive components
LFW [25, 53]	For non-circular objects, for manufacturing complex geometries	Bonding at edges is poor, high investment cost, noisy process	Manufacturing and repairing of aircraft BLISKs, automobile braking blocks, large-sized pipes
FD [25, 54–56]	Provide good tensile strength, no filler material is required, high deposition rate, produces fine grained microstructure	Only for circular objects, unbonded boundaries, machining of each layer for shaping into the desired shape	Development of ferrous and non-ferrous metal deposits, metal–metal composites
FS [25, 57]	Filler material is not required, thickness layer is high	Not recommended for overhangs or downward-facing features, formation of oxide layers on the surface	Coating for high wear and corrosion applications, repair applications
FSAM [25, 58, 59, 24]	Higher production rates, reduced material wastage, good tensile strength, and ductility of material	Non-homogeneous microstructure, higher tool wear	In production of structured components from Al, Mg alloys
AFS [10, 60–63]	Good lateral strength, obtained properties are isotropic in nature	Complex process, dependence on machine variables	Fabrication of high-strength ultrafine-grained magnesium alloys

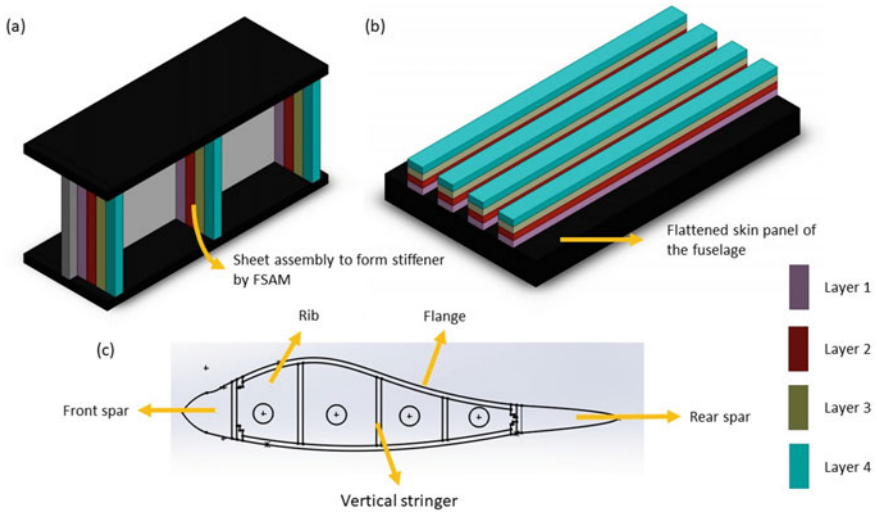


Fig. 13 Stiffener assembly for aerospace industry; **a** I-beam with transverse stiffener, **b** stringers over flattened skin panel of fuselage, **c** air foil C-S that depicts integration in fabricating ribs and stringers in wing spar web [64]

6 Applications of Friction Stir Additive Manufacturing for Fabricating 3D Component

- In aerospace industry, components requiring stiffer and stringer mechanical properties can be manufactured using FSAM. Similar applications of FSAM are found in aviation industry [12] (Fig. 13).
- In fossil and nuclear sectors to overcome failures caused due to creep FSAM, fabrication process is used [65] as shown in Fig. 14.

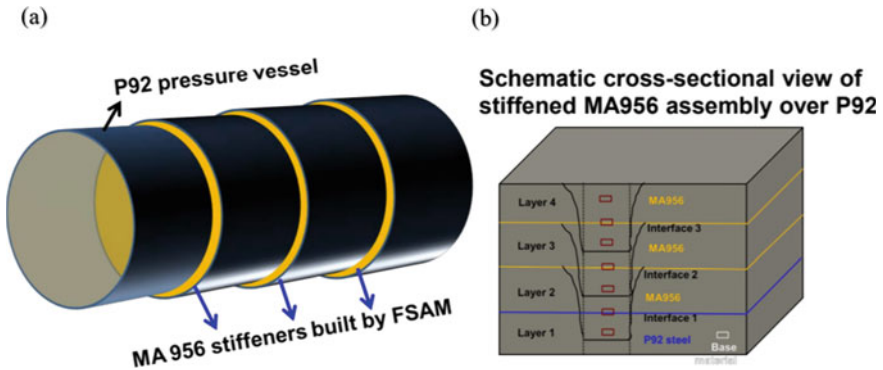


Fig. 14 a MA956 stiffener rings on P92 steel, b cross-sectional view of stiffened MA956 assembly over P92 [65]

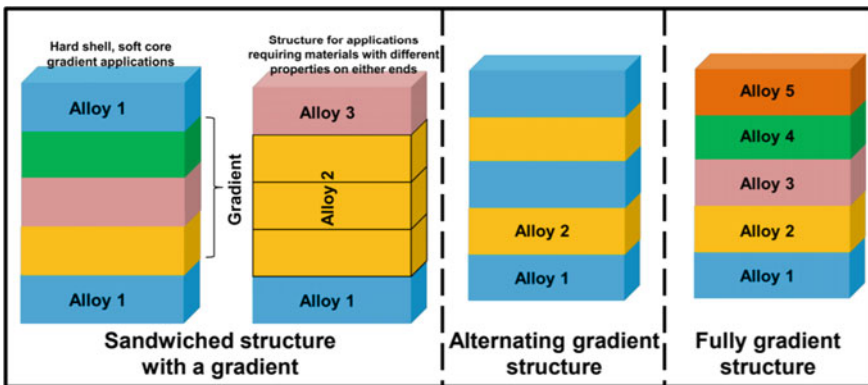


Fig. 15 Possible combinations of alloy gradients [65]

- Fabrication of alternating alloy gradients is possible with the help of FSAM process. Different combinations of alloy gradients are shown in Fig. 15.

7 Limitations and Future Scope

A major concern for the friction-based AM method is that after deposition of every layer machining is required and it is time-consuming. Other major challenges related to FATs are wearing rates of tools, building up residual stress, etc. From many friction-based AM methods, non-homogeneous components are obtained. To overcome these challenges, it is required the development of effective communication techniques, planning various strategies and implementing them, to resolve issues like complexities in material flow, reducing build time.

As far as today's concern, growth in the additive manufacturing sector is increasing exponentially. Friction-based AM techniques have the potential to significantly expand the alloy space, produce functionally graded materials, fabricate components with high structural integrity and reliability, as well as reduce solidification-related defects. It is forecasted that FSAM and AFS will be able to apply in every sector. It is estimated that these techniques will have their applications in the medical field, vehicles, aviation industry, honeycomb structures, controlled grain growth, aerospace industry, coating of shaft journals, etc.

8 Conclusion

FSATs provide better alternative solutions than any conventional method. Friction stir additive manufacturing techniques are a more efficient method that produces 3D components with better mechanical and microstructural properties. FSATs are cost-effective, less time-consuming, less material wastage, and sustainable process. Major machining-related issues are faced in these methods and can be overcome by taking proper measures. Compare to FSAM, AFS is a purely additive method. Although there are many applications for FSATs like in the aerospace industry, producing structural components, etc., yet few areas are unexplored and required proper research.

Acknowledgements The authors gratefully acknowledge Pandit Deendayal Energy University for supporting our work and the Indian Institute of Welding, Baroda Br. for supporting with the registration fee.

References

1. Srivastava M, Rathee S, Maheshwari S, Noor Siddiquee A, Kundra TK (2018) A review on recent progress in solid state friction based metal additive manufacturing: friction stir additive techniques. *Crit Rev Solid State Mater Sci* 44(5):345–377. <https://doi.org/10.1080/10408436.2018.1490250>
2. Anderson IE, White EM, Dehoff R (2018) Feedstock powder processing research needs for additive manufacturing development. *Curr Opin Solid State Mater Sci* 22(1):8–15. <https://doi.org/10.1016/j.cossms.2018.01.002>
3. Lee PH, Chung H, Lee SW, Yoo J, Ko J (2014) Review: dimensional accuracy in additive manufacturing processes. In: Proceedings of the ASME 2014 international manufacturing science and engineering conference collocated with the JSME 2014 international conference on materials and processing and the 42nd North American manufacturing research conference. Volume 1: materials; micro and nano technologies; properties, applications and systems; sustainable manufacturing. Detroit, Michigan, USA, (2014) V001T04A045. ASME. <https://doi.org/10.1115/MSEC2014-4037>
4. Ruan J, Sparks TE, Fan Z, Stroble JK, Panackal A, Liou F (2006) A review of layer based manufacturing processes for metals. In: Proceedings 17th solid freeform fabrication symposium University of Texas, Austin

5. Herzog D, Seyda V, Wycisk E, Emmelmann C (2016) Additive manufacturing of metals. *Acta Mater* 117:371–392. <https://doi.org/10.1016/j.actamat.2016.07.019>
6. White D (2002) Object consolidation employing friction joining, Google Patents
7. Thomas WM, Norris IM, Staines DG, Watts ER (2005) Friction stir welding—process developments and variant techniques. In: *The SME summit Oconomowoc, Milwaukee, USA*
8. Lequeu PH, Muzzolini R, Ehrstrom JC, Bron F, Maziarz R (2006) High performance friction stir welded structures using advanced alloys. In: *Aeromat conference. Seattle, WA (2006)*
9. Rotary friction welding. (n.d.-b) The Welding Institute. Retrieved May 9, 2021, from <https://www.twi-global.com/technical-knowledge/job-knowledge/rotary-friction-welding-148>
10. Rotundo F, Morri A, Ceschini L (2012) Linear friction welding of a 2024 Al alloy: microstructural, tensile and fatigue properties. In: *Light metals 2012, Suarez CE (ed), 2016, Springer International Publishing, Cham, pp 493–496*
11. Linear Friction Welding (n.d.) The Welding Institute. Retrieved May 9, 2021, from <https://www.twi-global.com/technical-knowledge/job-knowledge/linear-friction-welding-146>
12. Karthik G, Ram GJ, Kottada R (2016) Friction deposition of titanium particle reinforced aluminum matrix composites. *Mater Sci Eng, A* 653:71–83. <https://doi.org/10.1016/j.msea.2015.12.005>
13. Gandra J, Miranda R, Vilaça P (2012) Performance analysis of friction surfacing. *J Mater Process Technol* 212(8):1676–1686. <https://doi.org/10.1016/j.jmatprotec.2012.03.013>
14. Gandra J, Krohn H, Miranda R, Vilaça P, Quintino L, dos Santos J (2014) Friction surfacing—a review. *J Mater Process Technol* 214(5):1062–1093. <https://doi.org/10.1016/j.jmatprotec.2013.12.008>
15. Friction stir additive manufacturing—an innovative tool to enhance mechanical and microstructural properties (2020) *Mater Sci Eng B*. Published. <https://doi.org/10.1016/j.mseb.2020.114832>
16. Thomas WM, Nicholas ED, Needham JC, Nurch MG, Temple-Smith P, Dawes C (1991) Friction Stir Butt Welding. G.B., USA International Patent Application No. PCT/GB92/02203 and GB Patent Application No. 9125978.8 and US Patent Application No. 5, 460, 317
17. Sheikh-Ahmad JY, Ali DS, Deveci S, Almaskari F, Jarrar F (2019) Friction stir welding of high density polyethylene—carbon black composite. *J Mater Process Technol* 264:402–413. <https://doi.org/10.1016/j.jmatprotec.2018.09.033>
18. Mishra R, Ma Z (2005) Friction stir welding and processing. *Mater Sci Eng R Rep* 50(1–2):1–78. <https://doi.org/10.1016/j.mser.2005.07.001>
19. Iebba M, Astarita A, Mistretta D, Colonna I, Liberini M, Scherillo F, Pirozzi C, Borrelli R, Franchitti S, Squillace A (2017) Influence of powder characteristics on formation of porosity in additive manufacturing of Ti–6Al–4V components. *J Mater Eng Perform* 26(8):4138–4147. <https://doi.org/10.1007/s11665-017-2796-2>
20. Sun SH, Koizumi Y, Kurosu S, Li YP, Chiba A (2015) Phase and grain size inhomogeneity and their influences on creep behavior of Co–Cr–Mo alloy additive manufactured by electron beam melting. *Acta Mater* 86:305–318. <https://doi.org/10.1016/j.actamat.2014.11.012>
21. du Plessis A, le Roux SG, Booysen G, Els J (2016) Directionality of cavities and porosity formation in powder-bed laser additive manufacturing of metal components investigated using X-Ray tomography. *3D Print Addit Manuf* 3(1):48–55. <https://doi.org/10.1089/3dp.2015.0034>
22. Marya M, Singh V, Marya S, Hascoet JY (2015) Microstructural development and technical challenges in laser additive manufacturing: case study with a 316L industrial part. *Metall and Mater Trans B* 46(4):1654–1665. <https://doi.org/10.1007/s11663-015-0310-5>
23. Yadollahi A, Shamsaei N (2017) Additive manufacturing of fatigue resistant materials: challenges and opportunities. *Int J Fatigue* 98:14–31. <https://doi.org/10.1016/j.ijfatigue.2017.01.001>
24. Palanivel S, Nelaturu P, Glass B, Mishra R (2015) Friction stir additive manufacturing for high structural performance through microstructural control in an Mg based WE43 alloy. *Mater Des* 1980–2015(65):934–952. <https://doi.org/10.1016/j.matdes.2014.09.082>
25. Rathee S, Srivastava M, Maheshwari S, Kundra TK, Siddiquee AN (2018) Friction based additive manufacturing technologies: principles for building in solid state, benefits, limitations, and applications, 1st edn. CRC Press. <https://doi.org/10.1201/9781351190879>

26. Kumar R, Chattopadhyaya S, Dixit AR, Bora B, Zelenak M, Foldyna J, Hloch S, Hlavacek P, Scucka J, Klich J, Sitek L, Vilaca P (2016) Surface integrity analysis of abrasive water jet-cut surfaces of friction stir welded joints. *Int J Adv Manuf Technol* 88(5–8):1687–1701. <https://doi.org/10.1007/s00170-016-8776-0>
27. Nandan R, Roy G, Lienert T, Debroy T (2007) Three-dimensional heat and material flow during friction stir welding of mild steel. *Acta Mater* 55(3):883–895. <https://doi.org/10.1016/j.actamat.2006.09.009>
28. Nandan R, Roy GG, Lienert TJ, Debroy T (2006) Numerical modelling of 3D plastic flow and heat transfer during friction stir welding of stainless steel. *Sci Technol Weld Join* 11(5):526–537. <https://doi.org/10.1179/174329306x107692>
29. Hamilton C, Dymek S, Blicharski M (2008) A model of material flow during friction stir welding. *Mater Charact* 59(9):1206–1214. <https://doi.org/10.1016/j.matchar.2007.10.002>
30. Chen G, Li H, Wang G, Guo Z, Zhang S, Dai Q, Wang X, Zhang G, Shi Q (2018) Effects of pin thread on the in-process material flow behavior during friction stir welding: a computational fluid dynamics study. *Int J Mach Tools Manuf* 124:12–21. <https://doi.org/10.1016/j.ijmachtools.2017.09.002>
31. Dimensional CFD modelling of flow round a threaded friction stir welding tool profile. *J Mater Process Technol* 169(2):320–327. <https://doi.org/10.1016/j.jmatprotec.2005.03.015>
32. Yin Y, Sun N, North T, Hu S (2010) Hook formation and mechanical properties in AZ31 friction stir spot welds. *J Mater Process Technol* 210(14):2062–2070. <https://doi.org/10.1016/j.jmatprotec.2010.07.029>
33. Buffa G, Campanile G, Fratini L, Prisco A (2009) Friction stir welding of lap joints: influence of process parameters on the metallurgical and mechanical properties. *Mater Sci Eng, A* 519(1–2):19–26. <https://doi.org/10.1016/j.msea.2009.04.046>
34. Badarinarayan H, Shi Y, Li X, Okamoto K (2009) Effect of tool geometry on hook formation and static strength of friction stir spot welded aluminum 5754-O sheets. *Int J Mach Tools Manuf* 49(11):814–823. <https://doi.org/10.1016/j.ijmachtools.2009.06.001>
35. Mehta KP, Badheka VJ (2015) A review on dissimilar friction stir welding of copper to aluminum: process, properties, and variants. *Mater Manuf Process* 31(3):233–254. <https://doi.org/10.1080/10426914.2015.1025971>
36. Tutunchilar S, Haghpanahi M, Besharati Givi M, Asadi P, Bahemmat P (2012) Simulation of material flow in friction stir processing of a cast Al–Si alloy. *Mater Des* 40:415–426. <https://doi.org/10.1016/j.matdes.2012.04.001>
37. Chen HB, Yan K, Lin T, Chen SB, Jiang CY, Zhao Y (2006) The investigation of typical welding defects for 5456 aluminum alloy friction stir welds. *Mater Sci Eng, A* 433(1–2):64–69. <https://doi.org/10.1016/j.msea.2006.06.056>
38. Rathee S, Maheshwari S, Noor Siddiquee A (2018) Issues and strategies in composite fabrication via friction stir processing: a review. *Mater Manuf Process* 33(3):239–261
39. Leonard AJ, Lockyer SA (2003) Proceedings 4th international symposium on ‘friction stir welding’, Park City, UT, USA, May 2003, TWI
40. Mehta KP, Badheka VJ (2016) Effects of tool pin design on formation of defects in dissimilar friction stir welding. *Procedia Technol* 23:513–518. <https://doi.org/10.1016/j.protcy.2016.03.057>
41. Trueba L, Heredia G, Rybicki D, Johannes LB (2015) Effect of tool shoulder features on defects and tensile properties of friction stir welded aluminum 6061–T6. *J Mater Process Technol* 219:271–277. <https://doi.org/10.1016/j.jmatprotec.2014.12.027>
42. Zhang H, Lin S, Wu L, Feng J, Ma S (2006) Defects formation procedure and mathematic model for defect free friction stir welding of magnesium alloy. *Mater Des* 27(9):805–809. <https://doi.org/10.1016/j.matdes.2005.01.016>
43. Investigations on tunneling and kissing bond defects in FSW joints for dissimilar aluminum alloys (2015). *J Alloys Compd*. Published. <https://doi.org/10.1016/j.jallcom.2015.06.246>
44. Yuqing M, Liming K, Chunping H, Fencheng L, Qiang L (2015) Formation characteristic, microstructure, and mechanical performances of aluminum-based components by friction stir additive manufacturing. *Int J Adv Manuf Technol* 83(9–12):1637–1647. <https://doi.org/10.1007/s00170-015-7695-9>

45. Kadlec M, Růžek R, Nováková L (2015) Mechanical behaviour of AA 7475 friction stir welds with the kissing bond defect. *Int J Fatigue* 74:7–19. <https://doi.org/10.1016/j.ijfatigue.2014.12.011>
46. Zettler R, Vugrin T, Schmucker M (2010) Effects and defects of friction stir welds. In: Lohwasser D, Chen Z (eds) *Friction stir welding from basics to applications*, Woodhead Publishing Limited, Cambridge, pp 245–265
47. Kim Y, Fujii H, Tsumura T, Komazaki T, Nakata K (2006) Three defect types in friction stir welding of aluminum die casting alloy. *Mater Sci Eng, A* 415(1–2):250–254. <https://doi.org/10.1016/j.msea.2005.09.072>
48. Kandasamy K, Renaghan LE, Calvert JR, Schultz JP (2013) Additive friction stir deposition of WE43 and AZ91 magnesium alloys: microstructural and mechanical characterization. In: *International conference, powder metallurgy & particulate materials 2013, advances in powder metallurgy and particulate materials: Chicago, IL*
49. Calvert JR (2015) Microstructure and mechanical properties of WE43 alloy produced via additive friction stir technology. In: *Materials science and engineering 2015, Virginia Polytechnic Institute and State University, Virginia Tech*
50. Nanci HKK, Jianqing S, Dietrich L, James D (2016) Additive friction stir deposition of Mg alloys using powder filler materials. In: *TMS annual meeting & exhibition*
51. Yu HZ, Jones ME, Brady GW, Griffiths RJ, Garcia D, Rauch HA, Cox CD, Hardwick N (2018) Non-beam-based metal additive manufacturing enabled by additive friction stir deposition. *Scripta Mater* 153:122–130. <https://doi.org/10.1016/j.scriptamat.2018.03.025>
52. Dilip J, Ram GJ, Stucker B (2012) Additive manufacturing with friction welding and friction deposition processes. *Int J Rapid Manuf* 3(1):56. <https://doi.org/10.1504/ijrapidm.2012.046574>
53. Slattery KT, Young KA (2008) *Structural assemblies and preforms therefor formed by friction welding*, 2008, Google Patents
54. John Samuel Dilip J, Kalid Rafi H, Janaki Ram GD (2011) A new additive manufacturing process based on friction deposition. *Trans Indian Inst Met* 64(1–2):27–30. <https://doi.org/10.1007/s12666-011-0005-9>
55. Microstructure evolution in aluminum alloy AA 2014 during multi-layer friction deposition. *Mater Charact* 86:146–151. <https://doi.org/10.1016/j.matchar.2013.10.009>
56. Dilip JJS, Janaki Ram GD (2013) Microstructures and properties of friction freeform fabricated borated stainless steel. *J Mater Eng Perform* 22(10):3034–3042. <https://doi.org/10.1007/s11665-013-0605-0>
57. Dilip JJS, Babu S, Rajan SV, Rafi KH, Ram GJ, Stucker BE (2013) Use of friction surfacing for additive manufacturing. *Mater Manuf Process* 28(2):189–194. <https://doi.org/10.1080/10426914.2012.677912>
58. Kalvala PR, Akram J, Misra M (2016) Friction assisted solid state lap seam welding and additive manufacturing method. *Defence Technol* 12(1):16–24. <https://doi.org/10.1016/j.dt.2015.11.001>
59. Kalvala PR, Akram J, Tshibind AI, Jurovitzki AL, Misra M, Sarma B (2014) Friction spot welding and friction seam welding. 2014. Google Patents
60. Kandasamy K (2016) Solid state joining using additive friction stir processing. 2016. Google Patents
61. Rivera O, Allison P, Jordon J, Rodriguez O, Brewer L, McClelland Z, Whittington W, Francis D, Su J, Martens R, Hardwick N (2017) Microstructures and mechanical behavior of Inconel 625 fabricated by solid-state additive manufacturing. *Mater Sci Eng, A* 694:1–9. <https://doi.org/10.1016/j.msea.2017.03.105>
62. Rodelas J, Lippold J (2013) Characterization of engineered nickel-base alloy surface layers produced by additive friction stir processing. *Metall, Microstruct, Anal* 2(1):1–12. <https://doi.org/10.1007/s13632-012-0056-2>
63. Su J (2013) Additive friction stir deposition of aluminum alloys and functionally graded structures, phase I project SBIR/STTR programs | space technology mission directorate (STMD) NASA report. 2013. US

64. Palanivel S, Sidhar H, Mishra RS (2015) Friction stir additive manufacturing: route to high structural performance. *JOM* 67:616–621. <https://doi.org/10.1007/s11837-014-1271-x>
65. Withers J, Mishra RS (2015) Friction stir additive manufacturing as a potential route to achieve high performing structures. In: Friction stir additive manufacturing as a potential route

Selection of Optimal EDM Process Parameters for Machining Maraging Steel Using Grey-Fuzzy Relational analysis—An Experimental Approach



M. D. Sameer, B. Sai Kartheek Reddy, N. Amrutha, K. Srishma, and K. Samantha

Abstract The Electric Discharge Machine (EDM) is a modern machining technique that uses electrons discharged from the tool to extract material from the workpiece through heat generation. This method is used in the current study to create intricate cavities and contours on the chosen workpiece material. Maraging Steel, an iron-nickel alloy along with trace amounts of cobalt, aluminium, titanium and molybdenum was selected for this research. The parameters to be employed are PULSE-ON time (T_{ON}), discharge current (Amp) and PULSE-OFF time (T_{OFF}). The current research uses a hybrid approach based on grey-fuzzy relational analysis to compare various responses and select the best parameters for achieving the desired target. The best parameter combination that results in the output of a workpiece with a low tool wear rate (TWR) and high material removal rate (MRR) was analyzed. Experiments were developed using the Taguchi L18 orthogonal array architecture of Experiments (DOE).

Keywords Grey-fuzzy relational analysis · EDM · Maraging steel · Optimization

1 Introduction

The key goal of any machining operation is to remove excess material and achieve a high surface finish at the same time achieving the necessary size and shape of the workpiece. Unfortunately, all these surface finish accuracies cannot be fulfilled

M. D. Sameer (✉) · B. Sai Kartheek Reddy · N. Amrutha · K. Srishma · K. Samantha
ME Department, KITSW, Warangal, India
e-mail: mds.me@kitsw.ac.in

N. Amrutha
e-mail: b17me037@kitsw.ac.in

K. Samantha
e-mail: b17me009@kitsw.ac.in

by the conventional machining process due to the wear rate of the tool. Conventional machining processes have several limitations; these can be reduced by unconventional machining processes. Non-conventional machining processes have several advantages. These can produce intricate shapes on different workpiece materials with suitable controlled physical parameters in the process. But the little disadvantage of this method is that all types of materials cannot be machined using unconventional machining. The electric discharge machine works by discharging an electric spark that acts as a cutting tool to create intricate holes or remove material from the workpiece. Dewangan et al. [1] have investigated the optimum settings of the electric discharge machine using a hybrid optimization technique based on the grey-fuzzy technique. The roughness of the wall, the thickness of the white coat and the density of the crack were all considered key factors in this study. An electrode made out of ISI P20 Steel is used as the cutting tool. Prakash et al. [2] have studied the optimization of material by considering suitable parameters to determine and analyze MRR and surface finish. The material used for performing experiments is aluminium-rock dust composite. The methodology followed was Taguchi and Grey Relational Analysis. The ANOVA for material removal rate and feed outcast have the greatest effect. Many researchers have used different optimization techniques for EDM machining. Muthuramalingam et al. [3] analyzed the surface quality of the machining workpiece. Silicon steel is the workpiece material. The Adaptive Network-Based Fuzzy Inference System technique was used in this research (ANFIS). It analyzes the model's precision by comparing experimental and forecast values. There are three process parameters taken into consideration and they are open-circuit voltage, duty cycle and peak current. The electrical process parameters were concluded to have a significant impact on the thickness of the white layer. Kumar et al. [4] investigated input parameters like gap voltage, T_{ON} time and discharge current affecting the output response parameters. This study focuses on tool wear rate, electrode wear rate and relative wear rate. Their findings show that relative wear is proportional to T_{ON} time. The effect of voltage and relative tool wear revealed that relative wear of the tool is inversely proportional to voltage whereas tool wear is directly proportional to voltage. Ubaid et al. [5] conducted experiments on stainless steel and the optimization process followed was the fuzzy approach. They discovered that the T_{ON} time and current were the most influential system parameters in their research. Mausam et al. [6] experimented with GRA (Grey Relational Analysis) so that suitable parameters can be determined. The material considered for the study is carbon nanotube-reinforced fibre nanocomposite. The process parameters considered were T_{ON} time, Peak Current, Gap voltage and Duty Cycle. After conducting the experiments TWR and MRR are calculated and optimized later by GRA. Saha et al. [7] did an investigation to determine the impact of input factors on Ra, MRR and machining time using a wire electric discharge machine. The optimization carried out in this study was a multi-optimization technique and it was based on the techniques called TOPSIS and PCA (Principal Component Analysis). Dayakar et al. [8] analyzed the effect of input factors. The material they used to perform this experiment was Maraging steel. This steel has a very low content of carbon and has high material strength and toughness. They used ANOVA (Analysis Of Variance) and Taguchi Analysis. SR

and MRR were found to be directly proportional to T_{ON} and peak current. Bodukuri et al. [9] study was on the process parameters being optimized on SiCp reinforced Metal Matrix Composite. The tool electrode used was copper material. The technique used was the Taguchi method. Swiercz et al. [10] exercised the desirability function on electric discharge machining of Steel 55NiCrMoV7. Experimental research was mainly based on the process parameters which are discharge current, pulse time and pulse interval. They studied that the desirability function determined the best process parameters. Devi et al. [11] investigated parametric optimization of EDM machining of bamboo leaf-fly ash reinforced aluminium matrix composite using grey relational analysis and concluded that GRA efficiently optimized the process parameters.

The literature available on electrical discharge machining of maraging steel is very limited. The current research aims to observe the effect of input factors on achieving good quality material removal rate and low tool wear rate while machining Maraging steel C300 by EDM using a hybrid methodology termed grey-fuzzy relational analysis.

2 Experimental Procedure

2.1 Machine and Materials Used

The experimentation process was carried out on an EDM machine made by Askar Microns model no: V3525. The dielectric fluid used is EDM30 oil (Fig. 1).

The electrode used is 14 mm in diameter and 70 mm long copper and aluminium materials. Copper is known to be highly conductive, resistant to corrosion elements, has good machinability and is non-magnetic in nature. Table 1 lists the characteristics of the Copper electrode. Aluminium is a lightweight electrode and it has low specific heat and can be shaped or turned easily.

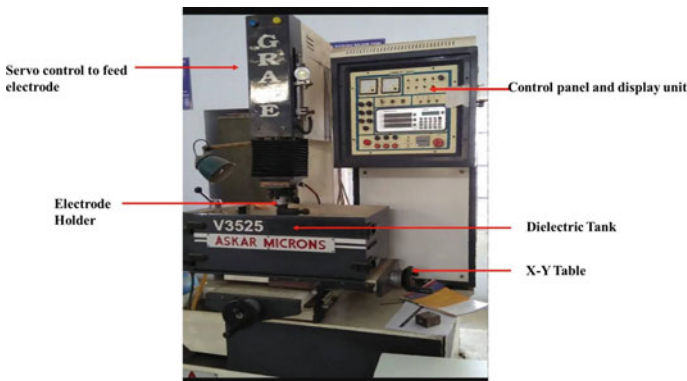


Fig. 1 EDM machined used for performing different experiments

Table 1 Copper and aluminium tool properties

Property	Description	
Specific gravity (g/cm ³)	8.94	2.70
Thermal conductivity (W/mk)	388	237
Melting range (°C)	1065–1083	640–660.37
Specific heat (J/kg K)	385	215

Table 2 Maraging steel properties

Property	Value	Unit
Heat capacity	800	J per kg-kelvin
Density	8.1	g per m ³
Coefficient of thermal expansion	10×10^{-6}	m per m-K
Modulus of elasticity	195×10^3	MPa
Poisson ratio	0.3	–
Thermal conductivity	200	W per cm-K

The material for the workpiece used is Maraging steel. The name ‘Maraging’ has been derived from the strengthening mechanism and that transformation of alloy to Martensite with subsequent age hardening and physical properties are displayed in Table 2.

In the present study, 18 specimens of maraging steel are taken to perform experiments and determine the MRR and TWR. The best specimen is detected to determine which machining conditions and tool electrode constitutes the best set of machining conditions. The size of each specimen is constant and that is $2.5 \times 2.5 \times 0.5$ cm (length \times width \times thickness).

2.2 Design of Experiments

The DOE technique is an experimental method for reducing the number of trials without sacrificing output efficiency. Orthogonal arrays (OA) are a common method of DOE and these parameters used to conduct the studies having levels and machining factors are presented in Table 3.

The Taguchi L18 orthogonal array was used to select a four-column orthogonal array based on the factors and their corresponding levels are presented in Table 4.

Table 3 Machining parameters and their levels

S. No.	EDM parameter	Symbol	Units	Level 1	Level 2	Level 3
1	Tool material	A		Copper (Cu)	Aluminium (Al)	–
2	Discharge current	B	Amp	12	15	18
3	T_{ON} time	C	μs	20	50	100
4	T_{OFF} time	D	μs	10	20	50

Table 4 Taguchi L18 OA

S. No.	Tool material	Discharge current (Amp)	T_{ON} time (μs)	T_{OFF} time (μs)
1	Cu	12	20	10
2	Cu	12	50	20
3	Cu	12	100	50
4	Cu	15	20	20
5	Cu	15	50	50
6	Cu	15	100	10
7	Cu	18	20	50
8	Cu	18	50	10
9	Cu	18	100	20
10	Al	12	20	20
11	Al	12	50	50
12	Al	12	100	10
13	Al	15	20	50
14	Al	15	50	10
15	Al	15	100	20
16	Al	18	20	10
17	Al	18	50	20
18	Al	18	100	50

2.3 Measurement of Output Responses

Table 5 shows the findings of the procedure, the main objective was to determine the best combination of input factors viz., tool material, discharge current (Amp), T_{ON} and T_{OFF} while machining the workpiece, i.e. Maraging Steel so that MRR and TWR are calculated.

Table 5 Observation table

S. No.	Tool material	Discharge current (Amp)	T_{ON} (μs)	T_{OFF} (μs)	MRR (mm^3/min)	TWR (mm^3/min)
1	Cu	12	20	10	15.565	0.8214
2	Cu	12	50	20	15.973	0.7321
3	Cu	12	100	50	17.47	0.8795
4	Cu	15	20	20	24.979	2.6952
5	Cu	15	50	50	25.869	3.2122
6	Cu	15	100	10	23.204	2.9695
7	Cu	18	20	50	29.547	5.9611
8	Cu	18	50	10	28.115	5.8687
9	Cu	18	100	20	31.339	5.734
10	Al	12	20	20	6.534	3.0278
11	Al	12	50	50	10.93	5.0417
12	Al	12	100	10	9.069	4.3657
13	Al	15	20	50	23.534	10.6574
14	Al	15	50	10	17.188	7.0556
15	Al	15	100	20	25.313	12.463
16	Al	18	20	10	32.138	12.8809
17	Al	18	50	20	29.942	11.912
18	Al	18	100	50	33.4	13.7315

3 Optimization Technique

3.1 Grey Relational Analysis

Grey relational analysis (GRA) is a useful tool for multi-objective optimization that relies on several parameters to produce a response.

Step 1 Grey Relational Pre-Processing

The performance parameters are normalized during the pre-processing stages of GRA. The formulae for the normalization process are as follows.

The normalization equation used for higher the better output is:

$$\gamma_i(x) = \frac{\alpha_i(x) - \min \alpha_i(x)}{\max \alpha_i - \min \alpha_i(x)} \tag{1}$$

The normalization equation used for lower the better output is:

$$\gamma_i(x) = \frac{\max \alpha_i(x) - \alpha_i(x)}{\max \alpha_i - \min \alpha_i(x)} \tag{2}$$

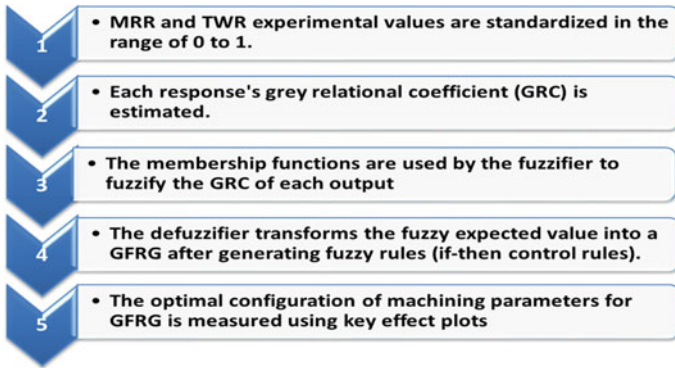


Fig. 2 Sequence of measure of GFRG

where $\gamma_i(x)$ and $\alpha_i(x)$ are the normalized and observed results for the 'ith' experiment with the 'xth' output result, respectively.

Step 2 Grey Relational Coefficient (GRC) calculations

$$\xi_i(A) = \frac{\Delta \min + \nu \Delta \max}{\Delta_i + \nu \Delta \max} \tag{3}$$

In the above equation $\Delta_i = \|\gamma(A) - \gamma_i(A)\|$ = obtained value when $\gamma_i(A)$ is subtracted from $\gamma(A)$, Delta min and delta maximum are largest and lowest values obtained from comparing all the sequences and ν is distinguishing coefficient equal to 0.5 as it defined between $0 \leq \nu \leq 1$.

Step 3 Grey-fuzzy relational grades

The GRA categorizes each outcome into higher, nominal and lowers the better with evaluated outcomes displaying a degree of ambiguity. Using a fuzzy-logic approach, this complexity can be easily investigated.

The measures of the grey-fuzzy relational grades are executed in the subsequent sequence as presented in Fig. 2.

4 Results and Discussion

The experimental data have been standardized for MRR using the 'higher the better' equation and TWR using the 'lower the better' equation, as presented in Table 6.

Grey Relational Coefficients (GRC), Grey-Fuzzy relational grade (GFRG) and their ranking were calculated using the normalized data set in Table 7. Since all consistency attributes were assigned equal weighting, the value of the distinguishing coefficient was set to 0.5.

Table 6 Grey relational coefficient values

Run No.	MRR	TWR
1	0.336	0.993
2	0.351	1.000
3	0.407	0.989
4	0.687	0.849
5	0.720	0.809
6	0.620	0.828
7	0.857	0.598
8	0.803	0.605
9	0.923	0.615
10	0.000	0.823
11	0.164	0.668
12	0.094	0.720
13	0.633	0.236
14	0.397	0.514
15	0.699	0.098
16	0.953	0.065
17	0.871	0.140
18	1.000	0.000

4.1 Grey-Fuzzy Relational Analysis

For generating GFRG values, the Grey-Fuzzy analysis was carried out using the MATLAB R2020a framework tool kit. As presented in Fig. 3, for triangular membership features, two GRC of MRR and TWR are considered, with low, medium and high values.

As observed in Fig. 4, the output vector is further classified into nine subsets. According to “Kumar et al. [12] very very low (VVL), very low (VL), low (L), medium–low (ML), medium (M), medium–high (MH), high (H), very high (VH) and very very high (VVH)”.

A series of nine rules are formed for co-relating grey relational coefficients with grey-fuzzy relational grades to establish inference between them, which is referred to as a fuzzy inference method (FIS) to obtain 18 experiments GFRG values, fuzzy rules [13] are observed in Fig. 5.

Few examples of fuzzy rules in the linguistic form are given below

“According to Jagadish et al. [14] Rule 1: If MRR is low and TWR is low then output (GFRG) is VVL, Rule 2: If MRR is low and TWR is medium then output (GFRG) is VL and so on up to Rule 9: If MRR is high and TWR is high then output (GFRG) is VVH”.

Table 7 Calculated GRC, GFRG and ranking

Exp. No.	Normalized values		GRCs		Grey-fuzzy grades	Rank
	MRR	TWR	MRR	TWR		
1	0.336	0.993	0.4296	0.9864	0.625	6
2	0.351	1.000	0.4353	1.0000	0.625	6
3	0.407	0.989	0.4575	0.9778	0.625	6
4	0.687	0.849	0.6147	0.7680	0.607	11
5	0.720	0.809	0.6408	0.7238	0.620	10
6	0.620	0.828	0.5685	0.7439	0.560	12
7	0.857	0.598	0.7771	0.5542	0.710	4
8	0.803	0.605	0.7177	0.5586	0.659	5
9	0.923	0.615	0.8670	0.5651	0.801	3
10	0.000	0.823	0.3333	0.7390	0.429	17
11	0.164	0.668	0.3741	0.6013	0.438	16
12	0.094	0.720	0.3557	0.6414	0.426	18
13	0.633	0.236	0.5765	0.3957	0.491	15
14	0.397	0.514	0.4531	0.5069	0.50	14
15	0.699	0.098	0.6242	0.3565	0.548	13
16	0.953	0.065	0.9141	0.3485	0.839	2
17	0.871	0.140	0.7953	0.3676	0.622	9
18	1.000	0.000	1.0000	0.3333	0.841	1

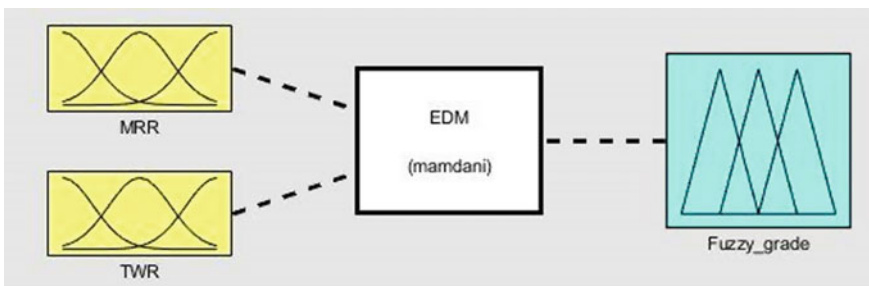


Fig. 3 I/P and O/P membership functions

The GFRG values of 18 trails are observed in Fig. 6. According to Table 7, higher GFRG values mean that the comparability series has a higher similarity to the reference sequence.

The optimal process parameter combination is tool material made of copper, discharge current of 18 Amp, T_{ON} 100 μ s and T_{OFF} 20 μ s as illustrated in Fig. 7 and response table for GFRG is represented in Table 8. The GFRG regression equation is given in Eq. 4.

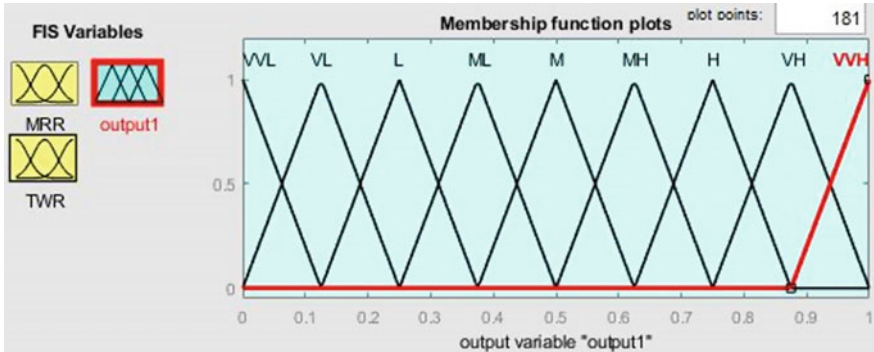


Fig. 4 Output variable membership plots

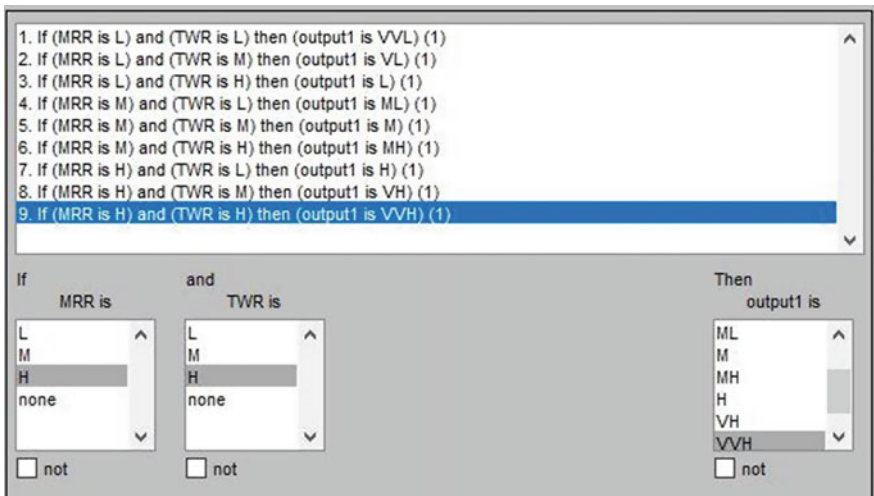


Fig. 5 Fuzzy rules

$$\begin{aligned}
 \text{GFRG} = & 0.496 - 0.0776 \text{ Tool material} \\
 & + 0.109 \text{ Discharge current (Amp)} \\
 & + 0.0083 \text{ Pulse on time} - 0.0024 \text{ Pulse off time} \quad (4)
 \end{aligned}$$

From ANOVA (analysis of variance) for GFRG as illustrated in Table 9 and it can be determined that the most significant factor is discharge current trailed by tool material. A confirmatory experiment was performed and its values are presented in Table 10. It can be observed that machining with optimum process parameter combination would result in improvement in GFRG when compared to initial parameter combination conditions. The predicted GFRG.

(β) can be calculated using Eq. 5.

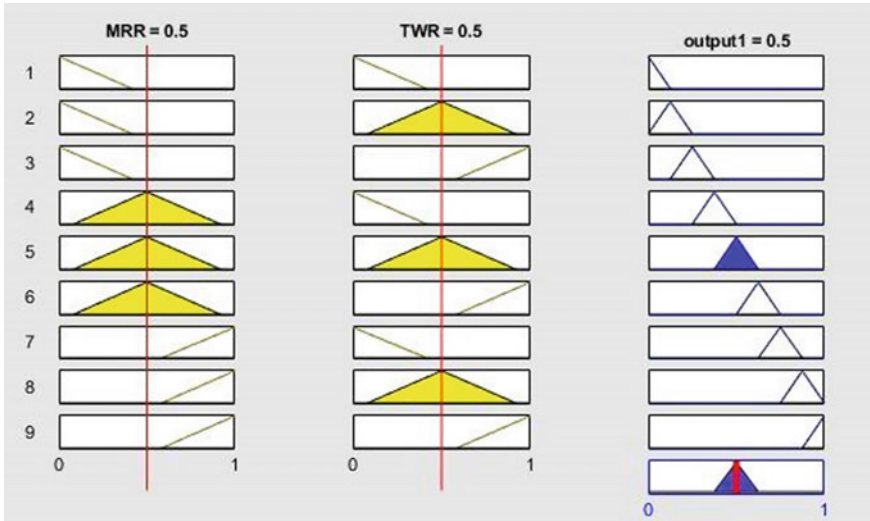


Fig. 6 GFRG values generated using MRR and TWR values of GRCs

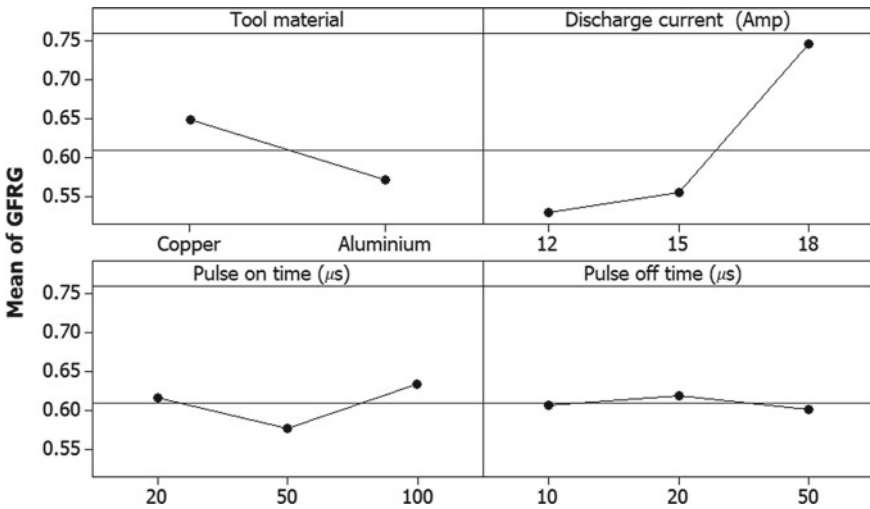


Fig. 7 Response plots for GFRG

$$\beta = Bm + \sum_{i=1}^q (Bi - Bm) \tag{5}$$

On comparing the results obtained from initial parameter combination condition and optimal parameter combination machining condition it can be observed that

Table 8 Response table for GFRG

Level	Tool material	Discharge current (Amp)	T_{ON} time (μ s)	T_{OFF} time (μ s)
1	0.6480	0.5280	0.6168	0.6068
2	0.5704	0.5543	0.5773	0.6188
3	-0.5	0.7453	0.6335	0.6020
Delta	0.0776	0.2173	0.0562	0.0168
Rank	2	1	3	4

Table 9 ANOVA for GFRG

Source	DF	Seq SS	Adj SS	Adj MS	F	P	%Contribution
Tool material	1	0.027067	0.027067	0.027067	3.49	0.091	9.51
Discharge current (Amp)	2	0.168816	0.168816	0.084408	10.87	0.003	59.35
T_{ON} time (μ s)	2	0.009985	0.009985	0.004993	0.64	0.546	3.51
T_{OFF} time (μ s)	2	0.000901	0.000901	0.000451	0.06	0.944	0.34
Residual error	10	0.077637	0.077637	0.007764			27.29
Total	17	0.284407					100

Table 10 Initial and optimal conditions results

Level	Initial condition	Optimal machining condition	
	A1B1C1D1	A1B3C3D2	
		Predicted	Experimental
MRR (mm^3/min)	15.565		31.339
TWR (mm^3/min)	0.8214		5.734
Grey-fuzzy grades	0.625	0.818	0.801
Improvement in grey-fuzzy grades		0.193	0.176

machining with optimum process parameter combination A1B3C3D2 had produced an improvement in Grey-fuzzy grades values in both predicted and experimental with values 0.193 and 0.176 respectively.

5 Conclusions

From the current study, it is concluded by applying hybrid optimization techniques such as Grey-fuzzy relational analysis that the higher MRR and lower TWR can be successfully machined and the following conclusions are made

- The optimal machining condition for high MRR and low TWR was found with tool material copper, discharge current 18 Amp, T_{OFF} 20 μ s and T_{ON} 100 μ s for Maraging steel C300.
- From ANOVA discharge current is the most critical parameter impacting the machining conditions with a 59.35% contribution.
- The improvement in GFRG of predicted and experimental was found to be 0.193 and 0.176 respectively.
- It was found that the EDM process parameters were successfully optimized using the Grey-Fuzzy relational hybrid optimization methodology for machining Maraging steel C300 with good MRR and low TWR and was efficiently executed by interpreting the data.

References

1. Shailesh Dewangan S, Gangopadhyay S, Biswas CK (2015) Multi-response optimization of surface integrity characteristics of EDM process using a grey-fuzzy logic-based hybrid approach. *Eng Sci Technol, An Int J*, pp 361–368
2. Soorya Prakash K, Gopal PM, Karthik S (2020) Multi-objective optimization using Taguchi based grey relational analysis in turning off rock dust reinforced aluminum MMC. *Measurement* 157:1–13
3. Muthuramalingam T, Saravanakumar D, Ganesh Babu L, Phan NH, Pi VN (2019) Experimental investigation of white layer thickness on EDM processed silicon steel using ANFIS approach. Springer
4. Kumar R, Sahani OP, Vashista M (2014) Effect of EDM process parameters on tool wear. *J Basic Appl Eng Res* 1(2):53–56
5. Ubaid AM, Dweiri FT, Aghdeab, Al-Juboor LA (2017) Optimization of EDM process parameters with fuzzy logic for stainless steel 304 (ASTM A240). *J Manuf Sci Eng*, pp 1–24
6. Mausam K, Sharma K, Bharadwaj G, Singh RP (2019) Multi-objective optimization design of die-sinking electric discharge machine (EDM) machining parameter for CNT-reinforced carbon fiber nanocomposite using grey relational analysis. *J Braz Soc Mech Sci Eng*. <https://doi.org/10.1007/s40430-019-1850-4>
7. Saha A, Mondal SC (2018) Statistical analysis and optimization of process parameters in wire cut machining of welded nanostructured hardfacing material. *SILICON* 11:1313–1326. <https://doi.org/10.1007/s12633-018-9924-y>
8. Dayakar K, Krishnam Raju KVM, Rama Bhadri Raju Ch (2019) Prediction and optimization of surface roughness and MRR in wire EDM of maraging steel 350. *Mater Today: Proc* 18(6):2123–2131
9. Bodukuri AK, Chandramouli S, Eswaraiah K, Laxman J (2018) Experimental Investigation and optimization of EDM process parameters on aluminum metal matrix composite. *Mater Today: Proc* 5(11):24731–24740
10. Swiercz R, Swiercz DO, Chmielewski T (2019) Multi-response optimization of electrical discharge machining using the desirability function micromachines 10(1):72. <https://doi.org/10.3390/mi10010072>
11. Devi MB, Sameer MD, Birru AK (2021) EDM machining characteristics of bamboo leaf ash and alumina reinforced aluminum hybrid metal matrix composite using multi-response optimization by grey relational analysis. *Mater Res Express*. <https://doi.org/10.1088/2053-1591/abd824>

12. Das P, Diyaley S, Chakraborty S, Ghadai R (2018) Multi-objective optimization of wire electro discharge machining (WEDM) process parameters using grey-fuzzy approach. *Periodica Polytech Mech Eng*. <https://doi.org/10.3311/PPme.12167>
13. Kumar VG, Bai H, Venkataramaiah P (2017) A fuzzy approach to trim down the struggles in machining of AMMC by optimizing the tool wear and process cost. *Mech, Mater Sci Eng J, Magnolithe*. <https://doi.org/10.2412/mmse.40.42.927>. hal-01966427
14. Jagadish BS, Ray A (2019) Development of fuzzy logic-based decision support system for multi-response parameter optimization of green manufacturing process: a case study. *Soft Comput*. <https://doi.org/10.1007/s00500-018-3656-1>

Shore Hardness Characterization of FDM Printed PLA/Epoxy/MGFs Composite Material Structure



Ammar Mustafa, Bandar Aloyaydi, Subbarayan Sivasankaran, and Fahad A. Al-Mufadi

Abstract In this study, composite material structures consist of PLA lattice, epoxy matrix and milled glass fibres (MGFs) were successfully manufactured by fused deposition modelling (FDM, 3D printing) and solution casting methods. This composite structures were expected to improve the mechanical properties. Pure hollow PLA lattice thermoplastic matrix lattice structure was printed by FDM. Different volume fractions of MGFs with epoxy matrix such as 0, 2.5, 5 and 7.5% were thoroughly stirred mechanically and then poured into a PLA lattice producing composite materials structure. Shore hardness test type D was used to examine the improvement of mechanical strength over the PLA lattice and epoxy/MGFs composite phases. The results have explained that Shore hardness D was increased considerably with the incorporation of MGFs in epoxy matrix in which 7.5 vol.% reinforced MGFs with epoxy matrix sample produced 82.9 Shore D value which was 13.5% higher than unreinforced sample.

Keywords PLA lattice · Milled glass fibres · Epoxy · Composite structure · Shore hardness

A. Mustafa · B. Aloyaydi · S. Sivasankaran (✉) · F. A. Al-Mufadi
Digital Manufacturing Laboratory, Department of Mechanical Engineering, College of Engineering, Qassim University, Buraidah 51452, Saudi Arabia
e-mail: sivasankaran@qec.edu.sa

A. Mustafa
e-mail: ammam_m_a@windowslive.com

B. Aloyaydi
e-mail: aloyaydi@qu.edu.sa

F. A. Al-Mufadi
e-mail: almufadi@qec.edu.sa

1 Introduction

Additive manufacturing technology (AMT), known also as 3D printing, has become in the spot of manufacturers and researchers in the last decades. AMT applies the principle of building parts layer by layer [1, 2] that helps in saving time, cost and material. It is also easier to process more complex part by AMT [3]. AMT can be used in prototyping and producing some functional parts. There are many techniques implied under AMT. The most commonly used technique is fused deposition modelling (FDM) [2, 4, 5]. In FDM, material is injected layer by layer to form the final product. Although, it is easy to produce parts by FDM, thermoplastic parts have lower mechanical properties compared to conventionally produced parts [6, 7]. One solution to such a problem is to inforce the thermoplastics with fibre reinforcement to enhance the mechanical properties [8–10].

Mechanical properties of reinforced 3D printed composite have been investigated through literature. Reddy et al. [11] studied the effect of reinforcing 3D printed PLA with carbon fibres (CFs), and the effect of process parameters on the mechanical properties including tensile stress, flexural stress and hardness. Results showed that the mechanical properties of PLA were enhanced when reinforced by CFs. Also, adjusting the printing parameter can improve the mechanical properties of the materials. Hervan et al. [12] studied the effect of alternating samples' layer thickness and printing orientation on the Shore hardness and friction of FDM printed ABS. Hardness of the samples was influenced by changing the printing orientation, although, there was no significant enhancement by increasing the layer thickness.

In this work, samples consist of 3D printed PLA lattice frame and infilled with epoxy/MGFs were prepared. Shore hardness type D test was applied to identify the hardness of the samples. Since the surface of the samples includes two distinguished regions: PLA lattice area and epoxy/MGFs area, the hardness of each region was tested separately.

2 Materials and Method

2.1 Synthesis of PLA/Epoxy/MGFs Samples

Samples consist of two parts: PLA lattice frame impregnated with epoxy/MGFs mixture. First, PLA lattice frame, with dimensions $52 \times 52 \times 13$ mm (shown in Fig. 1), was designed using Solidworks® CAD software (2015 version). The CAD file was then converted into STL file to be sliced and to set the printing parameters using Cura software. After that, G-Code file was generated by the Cura software to be used by the FDM printer. Lastly, PLA lattice frame was 3D printed using Ender 3 FDM printer, supplied by Creality Inc. Printing parameters are showed in Table 1.

To produce epoxy, two parts (resin and hardener) should be mixed by the volume ratio 1:1. The two part would be mixed and then poured into the PLA lattice frame.

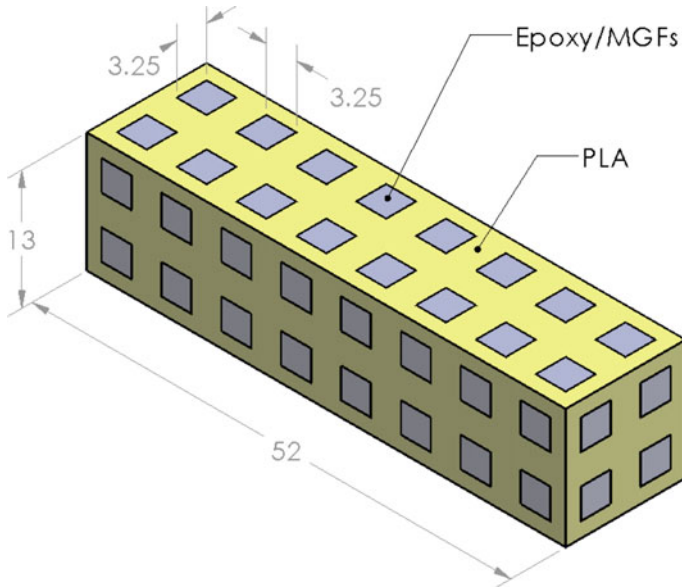


Fig. 1 Illustration of PLA/epoxy/MGFs samples

Table 1 Parameters used to produce samples using FDM printer

Parameter	Selected	Parameter	Selected
Filament diameter	1.75 mm	Layer height	0.2 mm
Platform adhesion type	Brim	Infill pattern	Line
Nozzle diameter	0.4 mm	Extruder temperature	200 °C
Infill density	100%	Printing speed	20 mm/s
Raster angle	0°	Air flow cooling	100%
Build orientation	Flat	Heated bed temperature	N/A

MGFs were added by variations from 0, 0.025, 0.05, 0.075 volume fractions in the total material. Samples were coded as shown in Table 2. MGFs were mixed with part A and stirred for one hour before being mixed with part B. Then, the mixture will be impregnated into the PLA lattice frame and let to cure for 24 h.

Table 2 Coding system for samples

Volume fraction of MGFs	Code
PLA lattice (no resin)	MMS
0	BMS
0.025	TMS-1
0.05	TMS-2
0.075	TMS-3

Table 3 PLA properties as received from supplier

Property	Value	Property	Value
Density	1.24 g/cm ³	Tensile strength	60 MPa
Melting temperature	145–160 °C	Flexural strength	108 MPa
Glass transition temperature	56–64 °C	Young’s modulus	3100 MPa
Poly lactide resin	CAS 9051-89-2	Shore hardness, D	85 Sh D
Purity	98 wt%>	Elongation	9%

2.2 Materials Characterization

PLA lattice frame was 3D printed using PLA filament spool supplied by BQ, Spain. Filament properties are shown in Table 3, as received. Resin used to impregnate the lattice frame was Envirotex Lite epoxy resin supplied by Environmental Technology from USA. MGFs used in preparing samples were supplied by System Three Resins from USA.

2.3 Mechanical Testing

Shore D hardness of the composite samples was tested using ZwickRoell analogue hardness tester, shown in Fig. 2. The test was run according to ASTM 2240 testing standard [13]. For each MGFs-varied volume fraction group, 30 readings, at least, are taken. The surface of each sample was divided into two areas, such as PLA lattice area and epoxy/MGFs area, as shown in Fig. 3.

Fig. 2 ZwickRoell analogue hardness tester



Fig. 3 Areas of the PLA/epoxy/MGFs sample surface

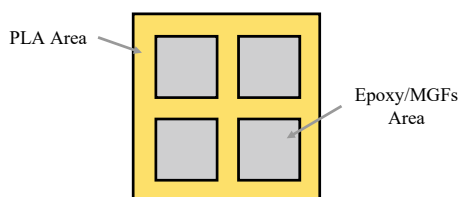


Table 4 Statistical summary of samples hardness results of PLA lattice region

	MMS	BMS	TMS-1	TMS-2	TMS-3
Average	77.33	77.66	78.78	78.74	78.58
SD	3.15	2.62	2.08	2.73	2.71
SE	10.83	11.45	14.38	12.30	11.00

3 Results and Discussion

3.1 Shore D Hardness of the PLA Lattice for Varied MGFs Content

Hardness of the PLA lattice area within the composite samples was tested to show whether the PLA will be affected by varying the MGFs fraction content. Figure 3 shows the results of Shore D hardness test for PLA lattice area. As expected, results indicated that the hardness of PLA varied negligibly within the tested groups, in average. Statistical data are summarized in Table 1, including average, standard deviation and standard error (Table 4).

3.2 Shore D Hardness of Epoxy/MGFs Region for Varied MGFs Content

By testing the Shore D hardness of the epoxy/MGFs area within the composite samples, results are shown in Fig. 4. Hardness of this area increased as the MGFs volume fraction increased. Observations showed that by adding more MGFs to the epoxy resin, the hardness of samples' surface would be enhanced. TMS-3 samples got the maximum Shore D hardness through other groups as 82.07. Table 5 showed the statistical data of the test results summarized in average, standard deviation and standard error (Fig. 5).

4 Conclusions

3D printed composite structure samples consist of PLA/epoxy/MGFs were produced using FDM printed. Hardness of the samples was tested using Shore hardness type D test. Results showed that the PLA lattice frame hardness has change negligible through samples groups. Conversely, the hardness of the epoxy/MGFs region on the samples' surfaces was enhanced by increasing the MGFs content.

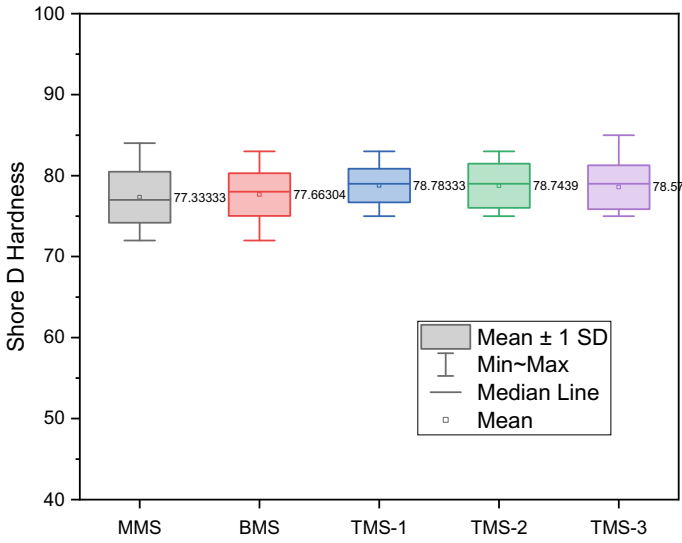


Fig. 4 Shore D hardness of PLA lattice region

Table 5 Statistical summary of samples hardness results of epoxy/MGFs lattice region

	BMS	TMS-1	TMS-2	TMS-3
Average	73.90	77.86	80.22	82.08
SD	3.94	1.156	3.05	2.09
SE	10.35	14.46	12.68	16.09

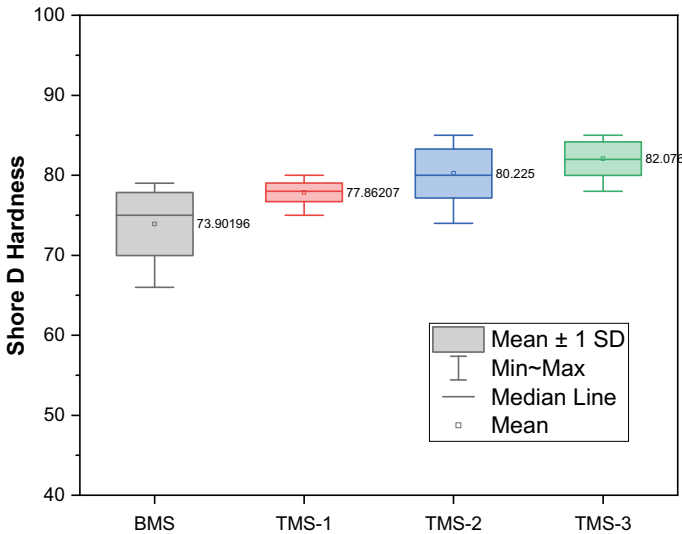


Fig. 5 Shore D hardness of epoxy/MGFs lattice region

References

1. Ngo TD, Kashani A, Imbalzano G, Nguyen KTQ, Hui D (2018) Additive manufacturing (3D printing): a review of materials, methods, applications and challenges. *Compos Part B Eng* 143:172–196. <https://doi.org/10.1016/j.compositesb.2018.02.012>
2. Chacón JM, Caminero MA, García-Plaza E, Núñez PJ (2017) Additive manufacturing of PLA structures using fused deposition modelling: effect of process parameters on mechanical properties and their optimal selection. *Mater Des* 124:143–157. <https://doi.org/10.1016/j.matdes.2017.03.065>
3. Karakurt I, Lin L (2020) 3D printing technologies: techniques, materials, and post-processing. *Curr Opin Chem Eng* 28:134–143. <https://doi.org/10.1016/j.coche.2020.04.001>
4. Dizon JRC, Espera AH, Chen Q, Advincula RC (2018) Mechanical characterization of 3D-printed polymers. *Addit Manuf* 20:44–67. <https://doi.org/10.1016/j.addma.2017.12.002>
5. Daminabo SC, Goel S, Grammatikos SA, Nezhad HY, Thakur VK (2020) Fused deposition modeling-based additive manufacturing (3D printing): techniques for polymer material systems. *Mater Today Chem* 16:100248. <https://doi.org/10.1016/j.mtchem.2020.100248>
6. Wang L, Gramlich WM, Gardner DJ (2017) Improving the impact strength of Poly(lactic acid) (PLA) in fused layer modeling (FLM). *Polymer (Guildf)* 114:242–248. <https://doi.org/10.1016/j.polymer.2017.03.011>
7. Brenken B, Barocio E, Favaloro A, Kunc V, Pipes RB (2018) Fused filament fabrication of fiber-reinforced polymers: a review. *Addit Manuf* 21:1–16. <https://doi.org/10.1016/j.addma.2018.01.002>
8. Chacón JM, Caminero MA, Núñez PJ, García-Plaza E, García-Moreno I, Reverte JM (2019) Additive manufacturing of continuous fibre reinforced thermoplastic composites using fused deposition modelling: effect of process parameters on mechanical properties. *Compos Sci Technol* 181. <https://doi.org/10.1016/j.compscitech.2019.107688>
9. Behalek L, Safka J, Seidl M, Habr J, Bobek J (2018) Fused deposition modelling versus injection moulding: influence of fiber orientation and layer thickness on the mechanical properties. *MM Sci J* 2018:2722–2726. https://doi.org/10.17973/MMSJ.2018_12_2018117
10. Sreenivasulu C, Ramakrishnaiah A, Jawahar JG (2015) Mechanical Properties of Geopolymer Concrete. *Int J Adv Eng Technol* 8:83–91. <https://doi.org/10.2507/30th.iaaam.proceedings.xxx>
11. Durga Prasad Reddy J, Mishra D, Chetty N (2020) Strength and HARDNESS of 3D printed poly lactic acid and carbon fiber poly lactic acid thermoplastics. In: Praveen Kumar A, Dirgantara T, Krishna PV (eds) *Adv. Light. Mater. Struct.* Springer Singapore, Singapore, pp 625–34
12. Hervan SZ, Parlar Z, Temiz V, Altinkaynak A (2019) Friction and hardness characteristics of Fdm-printed plastic materials. In: 21st international research conference, 2019 1505, pp 65–68
13. ASTM (n.d.) Standard test method for rubber property—durometer hardness. ASTM—D2240

Study on Impact Properties of Hybrid Composites Fabricated by VARTM Process for Structural Applications



Prasanth Kumar Kottapalli, Sai Kumar Balla, Himanshu V. Patel, and Harshit K. Dave

Abstract Polymer matrix composites are replacement for plastic, low strength metals in most the areas. The composite world is focused on green composites; that is, both resin and fabric are bio-degradable. The research is going on to find the best possible bio-degradable resin to eliminate the low strength plastic. Natural fibers become the best reinforcement for green composites if perfect bio-degradable resin found. Then, all low-strength plastic material application is replaced with natural fibers. The natural fibers of flax and jute are selected in this study with unsaturated polyester as a resin. Hybrid composite is the combination of two or more fibers in which one type of fiber balances the deficiency of another fiber. This study aims to find the effect of hybridization and stacking sequence on impact properties. The laminates are fabricated in the VARTM process and are prepared with three different (0° , 30° , and 45°) fabric orientations for impact testing. The laminates are prepared with different stacking sequence, and hybridization undergoes impact testing.

Keywords Hybrid composite · Natural fiber · Impact strength · Stacking sequence

1 Introduction

A composite is a material made up of two components called matrix and reinforcement. Matrix is a material that is used to create a bonding with reinforcement. Reinforcement aids in load transfer. Composites are multifunctional materials that can provide better characteristics that cannot be obtained by any discrete material [1]. Composites provide better advantages like high strength, low weight, better corrosion resistance, and economical. Composites have better properties than metals, such as producing less noise and vibration during operation. Natural fiber composites offer a wide range of applications due to their numerous benefits, including easy availability, renewability, biodegradability, low cost, and low density [2]. The applications in aerospace and automotive have increased with natural fibers when they have shifted

P. K. Kottapalli · S. K. Balla (✉) · H. V. Patel · H. K. Dave

Departmental of Mechanical Engineering, S.V. National Institute of Technology, Surat, Gujarat, India

from steel to aluminum and then from aluminum to fibers. The single fiber properties depend on orientation, shape, size, and cell walls thickness [3]. Polymer matrix composites are most widely used because of their mechanical properties comparing to others. Since they exhibit less strength and stiffness, they can be composed with reinforcements to provide better strength and stiffness. The fibers which are used as reinforcements carry loads in a longitudinal direction. Natural fibers have the most applications compared to synthetic fibers even though they cannot compete in mechanical properties with synthetic fibers. Natural fiber quality depends on temperature, growing environment, species, humidity, age of plant, and soil quality [4]. These fibers are used in making door panels, headrests, docks, instrument panels, window frames, armrests, and parcel shelves.

Oleiwi et al. have studied the impact properties of natural fibers reinforced with PMMA by taking two parameters like fibers length and fiber content for denture applications [5]. They have chosen bamboo and siwak as natural fibers that are reinforced with PMMA. They have stated that an increase in fiber length leads to an increase in impact properties and decreases compression properties due to increased void content and clustering of fibers increase in fiber content, on the other contrary, reduces impact properties while increasing compression properties. Yussuf et al. have performed impact testing on two types of natural fibers, i.e., kenaf and rice husk composed with PLA and compared the results [6]. They have concluded that the composite prepared with PLA-kenaf has more impact strength compared to PLA-rice husk. This is because poor adhesion between matrix and reinforcement which causes voids and small cracks that results in less impact strength. Suizu et al. have fabricated a complete green project that was eco-friendly [7]. They have performed mechanical testing on composite fabricated with ramie yarn fibers that was alkali-treated and compared it with untreated fibers. They have stated that treated fibers exhibited impact strength twice comparing to untreated fibers. Due to change in the morphological structure of fibers helped to increase the impact properties. Premnath studied the effect of surface treatment on the mechanical properties of jute and sisal fibers [8]. He had prepared composites with different combinations of laminates with jute and sisal by supplying epoxy resin. Initially, he has treated those fibers with 10% NaOH solution for 24 h. He found that surface treatment of natural fibers is having high effect on impact strength which shows that composite prepared with treated fibers have exhibited 33 J impact strength whereas untreated fiber composite possesses 24 J. Furthermore, he stated that an increase in jute layers increase the energy-absorbing capacity. Sanjay et al. [9] studied the stacking sequence effect on mechanical properties of hybrid composites which are prepared with glass, jute, and kenaf fibers. They have performed experiments by changing the positions of jute and kenaf with glass. They stated that pure glass having high impact strength comparing with the other two fibers. It indicates that hybridization of kenaf and jute with glass improves the impact strength in a considerable way due to interfacial adhesion between matrix and reinforcement. Chaudhary et al. [10] have found that hybridization effects the impact strength. They have prepared composites by hybridizing the fibers jute, hemp, and flax fibers and also individual fibers. They have conducted impact testing on it

and found that hybrid composite having high impact strength compared to individual fiber composite. They have analyzed the failure and found that fiber pull out and debonding are the causes for failure. Athijayamani et al. studied the mechanical properties of Roselle and sisal fibers with polyester [11]. They stated increasing fiber content and fiber length results in decreasing of impact strength. And they reported sisal having a major contribution in decreasing the impact strength than Roselle. This is due to the presence of defects like voids and fiber pullout. Zivkovic et al. observed moisture absorption on impact properties of natural fibers basalt and flax [12]. They are performed impact testing on dry and conditioned composites. They stated that flax fibers are possessing high impact strength comparing with basalt fibers due to ductility increased in a conditioned state. Mueller et al. have investigated the parameters which influence the increase of impact properties [13]. They have concentrated on parameters like temperature, processing conditions, and fiber characteristics. They stated that increasing the temperature between 220 and 240 °C results in high impact strength. Moreover, the fineness of fiber results in good mechanical properties due to having good surface bonding between matrix and reinforcement.

This article describes the impact properties of hybrid composites prepared by jute and flax fibers with unsaturated polyester resin. The hybridization is done by replacing the jute fibers with flax fibers, and stacking sequence is done by taking eight layers of jute and flax in equal amount and placing the fibers in different positions. The hybridized composites are formed by replacing flax with two jute layers each time results in the following formation (J_8 , F_2J_6 , F_4J_4 , F_6J_2 , and F_8) and stacking sequence formed by taking five arrangements results in the following formation $((FJ)_4$, $(FFJJ)_S$, $(JJFF)_S$, (F_4/J_4) , and $(FJJF)_S$).

2 Materials and Experimentation

2.1 Materials

The jute and flax natural fibers having GSM 215 and 210 selected for this study. Jute and flax fibers were supplied from BASU Jutex, Kolkata, India, and Vruksha composites, Tenali, India. The unsaturated polyester resin is used as a matrix with MKEP (methyl ethyl ketone peroxide) as a hardener and the cobalt naphthenate as an accelerator. The mixing ratio of these three is 100:10:1.04 by weight, respectively.

2.2 Composite Fabrication

The composites are prepared by using vacuum-assisted resin transfer molding (VARTM) process. VARTM process is high advantages comparing with traditional manufacturing processes like hand layup. This process is economical and provides a

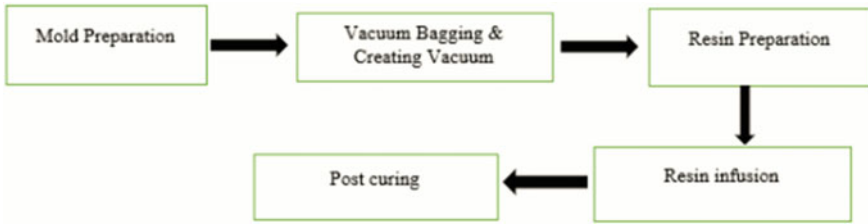


Fig. 1 Steps involved in VARTM setup

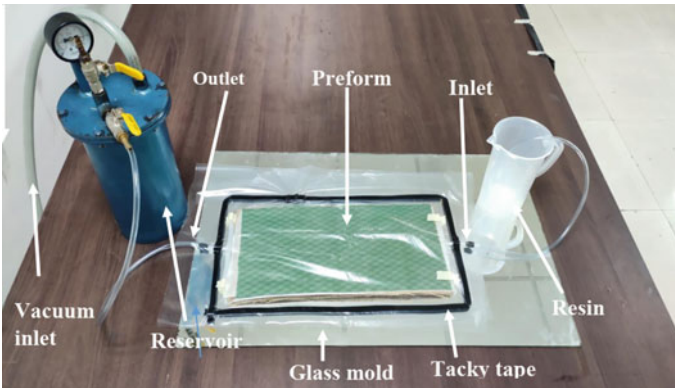


Fig. 2 VARTM setup

better surface finish. It is used to fabricate large components. This process involves five steps in which they are shown in Fig. 1. The jute and flax fabric were cut into layers of the dimension 400 mm × 300 mm, required for the mold. The dry reinforcements were stacked in a way that produced a fiber stacking sequences. After the molding process was completed, resin infusion was done under vacuum within the dry reinforcements. The infusion was required to cure for 12 h under vacuum condition and at room temperature (Fig. 2).

2.3 Specimen Preparation

The laminates are cut into specimens by using abrasive water jet machining. This type of cutting gives accurate dimensions, unlike sawing. In this cutting process, a strong thrust of water and abrasive mix cut the laminates. The AWJM nozzle moved in the specimen contours, which are designed in AutoCAD drafting software. This CAD file contains the movement of the water jet nozzle during machining.

2.4 Impact Testing

Impact testing of hybrid and stacking laminates is carried as per ASTM D256 standard [14]. The specimen length is 63.5 mm, width 12.7 mm, and thickness is varying from 5.1 to 6.2 mm. 2.5 mm deep V-type notch with 45 angles and 0.25 mm radius is cut by AWJM as per required dimensions. The specimens have a tolerance of ± 0.5 mm due to flaring of water thrust in AWJM.

3 Results and Discussions

An impact test is performed to know the ability of a material to resist impact load during the service of the material. The impact test gives how the material responds against impact loads or shock. The Izod test is most commonly used for determining the impact strength of the material. The specimen with or without a notch is kept vertically, and a hammer strikes the specimen. The energy absorbed by the specimen is equal to the energy loss by the hammer, the system calculated the energy only considering the energy loss in the hammer. The hammer angle is released from a 105° angle on the vertically placed specimen. The values of impact energy absorbed by a specimen during testing are shown in Table 1.

The maximum value occurred in F_8 in 30, 45 orientation and F_4J_4 in 0 orientation. The minimum values are less than 23, 27, and 24% with maximum in the orientations 0, 30, 45, respectively. Figure 3a shows that the energy values are decreasing from J_8 to F_4J_4 and increased from F_4J_4 to F_8 in all the 30, 45 orientations. If we see individually of each laminate, the energy values are increasing in ascending order of $0 < 30 < 45$. In Izod testing, the specimen is placed vertically in the fixture. When the impact force is applied perpendicularly to the specimen, the result is less for 0° orientation than for other orientations. The horizontal fibers in the fabric do not affect impact strike, even if the fabric is plain weave; only the vertical fibers absorb the energy. Flax hybridization results in increased absorption energy.

The averaged absorbed energy per unit length of F_4J_4 stacking sequence is shown in Table 2. From Fig. 3b, in each sequence, the absorbed energy increases from 0°

Table 1 Impact energy of hybrid composites

Laminate	Impact Energy(J/M) (0° orientation)	Impact Energy (J/M) (30° orientation)	Impact Energy (J/M) (45° orientation)
J_8	30.0	50.46	48.3
F_2J_6	29.1	43.69	46.0
F_4J_4	37.8	40.4	41.8
F_6J_2	32.3	37.95	47.2
F_8	33.5	52.61	55.1

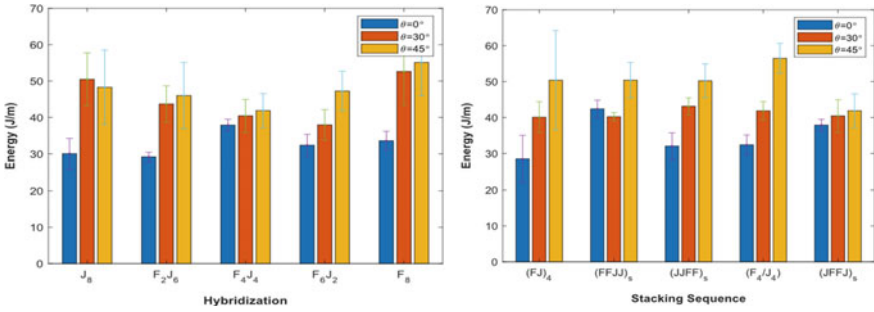


Fig. 3 Impact energy in a hybridization and b F₄J₄ stacking

Table 2 Impact energy for F₄J₄ stacking

Laminate	Impact energy (J/M) (0° orientation)	Impact energy (J/M) (30° orientation)	Impact energy (J/M) (45° orientation)
(FJ) ₄	28.4	40.0	50.3
(FFJJ) _S	42.4	40.2	50.4
(JJFF) _S	32.0	43.1	50.2
(F ₄ /J ₄)	32.3	41.8	56.4
(FJJF) _S	37.8	40.4	41.8

< 30° < 45°, and the reason is the force component is 45° more than the 30° and 0°. The energy values are almost near values in 30° and 45° orientation for most laminates except in (JJFF)_S. The table shows that the stacking order has no effect on the impact energy, but the orientation does. In impact testing, the specimens show brittle failure. The failure is due to a lack of interfacial adhesion between the fibers and the polyester resin. Defects in the laminates, such as fiber pull out and voids, cause the crack to form, resulting in brittle failure.

In this study, the effect of stacking sequence on impact strength is significant. The use of more jute layers instead of flax reduces the energy-absorbing capacity of the composite, lowering the impact energy. Thus, it aids in load transfer in the longitudinal direction. In comparison to jute fibers, individual flax fibers have high impact energy. Flax fibers help increase energy absorption capacity, so stacking sequence laminates with equal amounts of flax and jute fibers have high impact strength when oriented at 0°. The impact properties of the flax fibers are improved when they are placed on the outer layers.

The failure mode of hybrid laminates is illustrated in Fig. 4 below. During impact testing, it is discovered that the laminates are prone to fiber pullout. A brittle failure occurred near the notch, with a crack in the middle of the laminate. As can be seen in the figure, F₄J₄ with 0° orientation has the highest impact energy when compared to other hybrid composites with the same orientation, and the crack started in the center of the notch and propagated in a straight line. However, the same hybrid composite

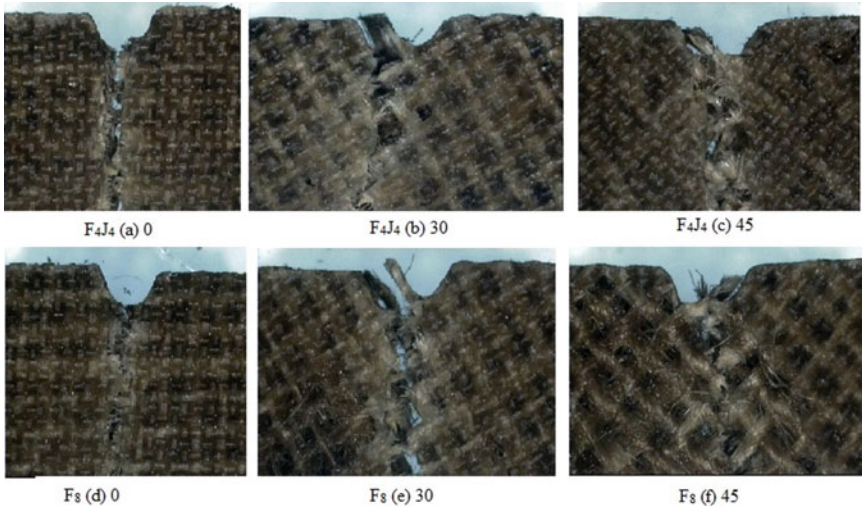


Fig. 4 Failure mode in different laminates

has shown crack near the notch but not at the center in other orientations. Fiber pullout can also be seen in the pictures, along with a zigzag crack. When compared to other laminates, the crack in the F8 laminate occurs at the center of the notch in three orientations, resulting in the best results. F8 laminate has less fiber pullout and debonding, resulting in higher impact energy in 30° and 45° orientations. In all laminates, the failure can be brittle, as shown in the figure.

4 Conclusion

This paper discusses the impact properties of jute and flax fibers reinforced with polyester resin natural fiber hybrid composites. The results revealed that the stacking sequence had a significant effect on the composites. In addition, orientation has a significant impact on impact energy; in all laminates, energy increases in the range of 0°, 30°, and 45°. This is due to the fact that the load is applied perpendicular to the fiber orientation, so the 0° orientation absorbs less energy. The F4J4 stacking has no effect on impact energy, which increases as the amount of flax fiber increases. Using jute instead of flax fibers reduced the impact energy significantly. In comparison to jute fibers, flax fibers are helpful in increasing impact energy. These hybrid composites are primarily used for structural purposes. These composites are used in structural applications in the automotive industry, such as door panels and instrument panels, where maximum passenger safety and crashing properties are required.

Acknowledgements This work was supported by the third phase of Technical Education Quality Improvement Program (TEQIP-III) under micro research project of twinning activity.

References

1. Chandramohan D, Marimuthu K (2011) A review on natural fibers, *Int J Recent Res Appl Stud* 8(2)
2. Sarikayaa E, Çallioglu H, Demirelc H (2019) Production of epoxy composites reinforced by different natural fibers and their mechanical properties. *Compos B* 167:461–466
3. Gholampour A, Ozbakkaloglu T (2020) A review of natural fiber composites: properties, modification and processing techniques, characterization, applications. *J Mater Sci* 55:829–892
4. Sanjay MR, Arpitha GR, Laxmana Naik L, Gopalakrishna K, Yogesha B (2016) Applications of natural fibers and its composites: an overview. *Nat Resour* 7:108–114
5. Oliwei JK, Salih SI, Fadhil HS (2018) Study compression and impact properties of PMMA reinforced by natural fibers used in denture. *Eng Technol J Part A* 36(6):652–655
6. Yussuf AA, Massoumi I, Hassan A (2010) Comparison of polylactic acid/kenaf and polylactic acid/rise husk composites: the influence of the natural fibers on the mechanical, thermal and biodegradability properties. *J Polym Environ* 18:422–429
7. Suizu N, Uno T, Goda K, Ohgi J (2009) Tensile and impact properties of fully green composites reinforced with mercerized ramie fibers. *J Mater Sci* 44:2477–2482
8. Arun Premnath A (2018) Impact of surface treatment on the mechanical properties of sisal and jute reinforced with epoxy resin natural fiber hybrid composites. *J Nat Fibers* 16(5):718–728
9. Sanjay MR, Arpitha GR, Senthamaraikannan P, Kathiresan M, Saibalaji MA, Yogesha B (2018) The hybrid effect of jute/Kenaf/E-Glass woven fabric epoxy composites for medium load applications: impact, inter-laminar Strength, and failure surface characterization. *J Nat Fibers* 16(4):600–612
10. Chaudhary V, Bajpai PK, Maheshwari S (2017) Studies on mechanical and morphological characterization of developed jute/hemp/flax reinforced hybrid composites for structural applications. *J Nat Fibers* 15(1):80–97
11. Athijayamani A, Thiruchitrabalam M, Manikandan V, Pazhanivel B (2010) Mechanical properties of natural fibers reinforced polyester hybrid composites. *Int J Plastic Technol* 14:104–116
12. Zivkovic I, Fragassa C, Pavlovic A, Brugo T (2017) Influence of moisture absorption on the impact properties of flax, basalt and hybrid flax/basalt fiber reinforced green composites. *Compos B* 111:148–164
13. Mueller DH, Krobjilowski A (2004) Improving the impact strength of natural fiber reinforced composites by specifically designed material and process parameters. *Int Nonwovens J* 13(4)
14. ASTM D256-10 (2018) Standard test methods for determining the Izod pendulum impact resistance of plastics, ASTM International, West Conshohocken, PA. www.astm.org

Study on Influence of Process Parameters on Feature Quality and Depth of Features Produced by Heat-Assisted Incremental Forming



Vishal John Mathai, Joseph Babu, Noel Peter, Leo Mathew, and Sobin Siby

Abstract Incremental forming is a cost-effective method of creating parts as it avoids the cost of fabricating a die required for forming operation. Incremental forming using heating assistance is a technique that has been widely reported to be used for forming difficult to form materials. This paper discusses about the influence of process parameters on feature depth and surface quality of high wall angle features on AA6061 sheet materials formed by incremental forming conducted with conductive heating assistance. The paper proposes a simple system that can be used for heat-assisted forming for low melting point materials. Sensitivity analysis has been carried out to understand the parametric-level influence on each of the responses. Results suggest that feature depth or cone depth is mostly influenced by sheet temperature and tool rotational speed. Surface quality, which was measured in terms of R_a and R_z , was found to be mostly influenced by tool rotational speed and feed rate of the tool.

Keywords Incremental forming · Formability · Surface roughness · Sensitivity analysis

V. J. Mathai (✉) · J. Babu · N. Peter · L. Mathew · S. Siby
Department of Mechanical Engineering, Amal Jyothi College of Engineering, Kanjirappally,
Kerala, India

J. Babu
e-mail: josephbabu@me.ajce.in

N. Peter
e-mail: noelpeter@me.ajce.in

L. Mathew
e-mail: leomathew@me.ajce.in

S. Siby
e-mail: sobinsiby@me.ajce.in

1 Introduction

Engineers have been working on to bring out drastic changes in manufacturing sector in order to make the manufacturing of complex shaped objects as simple as possible. To achieve this, new manufacturing process has been introduced. One of the main objectives of an industrialist is to invest less in order to accommodate changes in products being manufactured. Incremental sheet forming is one such a modern manufacturing method, which is highly preferred for customized product development.

In ISF process, the sheet metal is converted into a target shape through a series of miniscule and localized incremental strains. The deformation is induced using an axisymmetric tool with a rounded end. Once the tool is moved by an incremental depth, the tool is made to move along a path that defined the geometry of the target product. The process is repeated after each incremental depth till the target depth and geometry is attained. The operation is carried out on programmable machine systems, like CNC milling or robotic systems, which can execute this task with high level of flexibility. The process has advantages in terms of its flexibility and the capacity to enhance the formability of the materials to certain extent. However, the process will still be constrained by the mechanical properties of the material. Incremental forming with heating assistance is one of the developing methods in this regard. The technique employs heating of the working sheet globally or locally at the time of inducing deformation. Different modes of heating have been proposed by researchers in this regard like heating using a medium like air or liquid, heating with the help of electricity or laser radiation, etc. However, most of the systems tend to be cumbersome and expensive at times. Further, the surface quality of the products developed in such system has also been found to be affected. Another limiting factor is the wall angle of the features that can be successfully formed by incremental forming. Literatures suggest that generation of features wall angles limits in attainment of less feature depth in incremental sheet metal forming.

2 Literature Review

Heat assistance in incremental sheet metal forming is an upcoming area of research for forming hard to form materials like alloys of magnesium. Different modes of heating have been tried by researchers like air heating, conduction heating, electric heating, friction stir heating, halogen heating, laser heating, liquid heating, etc. All these techniques have their own advantages and limitation.

Ji and Park [1] investigated the influence of air heating on formability of AZ 31 B sheets at different temperature levels starting from 20 to 250 °C. They have investigated the influence of temperature on formability and formation of cracks on the formed surface under different temperature conditions. For the formation features with high wall angles, they have proposed the concept of progressive forming as well.

Further, they have also reported that high temperature forming results in to formation of smaller grains, which will result in to increase in formability [2]. Ambrogio et al. [3] investigated the concept of conduction heating during incremental forming of AZ 31B sheets and studied the influence of sheet temperature, tool diameter, and tool depth step on forming load and formability. They have identified that 250 °C is the most appropriate temperature for incremental forming of AZ 31B sheets. Further, they have also inferred that the formation of oxide layers during the heat-assisted forming contribute to the failure of the sheets. Shi [4] investigated influence of temperature, tool diameter, and depth increment on forming limit angle during incremental forming of AZ31B using conduction heating, and it has been reported that small depth and high temperature conditions facilitate attainment of higher forming limit angle, and tool diameter does not have a significant influence on the same. Khazaali and Saniee [5] investigated the influence of process parameter of conduction heating-based incremental forming of AZ31B sheets and reported that temperatures above 160 °C is suitable for incremental forming of such materials. They have reported that when forming above 160 °C, smaller tool diameters are preferable. It has also been reported that sheet temperature has an influence on the hardness of the final product. Ambrogio et al. [6] investigated the concept of joule's heating for heat-assisted incremental forming of AZ31B and Ti-6Al-4 V and reported that surface quality get worse with increase in wall angle, and more energy is needed to be supplied during forming of such features. Sy and Nam [7] investigated the influence of process parameters on accuracy and formability of features formed on AA5055 and AZ31B and reported that spring back errors be reduced with aid of small depth increments. Researchers further reported twisting of features during high temperature forming of deep features. Bao et al. [8] studied the influence of electro pulse assisted incremental forming on formability and microstructure evolution of AZ 31B and reported that higher wall angled features can be obtained using high current intensities. Further, they have also inferred that the use of electro pulse can reduce the dynamic recrystallization temperature of the material and can also restrain the crack growth, thereby improving the formability. Xu et al. [9] compared the potential of frictional stir and electric hot assisted incremental forming of AZ31 B sheets. Based on the comparative study, they have inferred that frictional stir incremental forming has higher processing efficiency. However, electric hot assisted ISF was found to be more suitable for forming features with steep wall angles. Kim et al. [10] discussed the application of halogen lamp heating for incremental forming of AZ31B sheets and reported that depth increment, temperature and wall angle are the most dominant factors that decides successful forming or failure. Hino et al. [11] studied the influence of laser radiation for incremental forming of AZ31B and reported that the localized dynamic heating can reduce stresses that build in the material can be reduced to almost zero and improvement in formability has also been reported. Galdos et al. [12] discussed the concept of liquid heating for incremental forming of magnesium alloys. They have reported that a fully recrystallized micro structure can be obtained with heat-assisted incremental forming. Ulacia et al. [13] investigated the concept of heat-assisted incremental forming and reported that for AZ31B sheets, even though 250 °C sheet temperatures may provide higher elongation, working temperatures

around 200 °C is preferable to reach a compromise between formability and lack of precision in incremental forming.

Review of literature suggests that even though many techniques can be used for carrying out incremental forming of sheet materials, conduction-based heat assistance is relatively cheaper and easier to implement. It has been understood that a wide range of studies have been carried out in the domain incremental forming with heat assistance. However, studies pertaining to influence of process parameters for forming higher wall angled features have been relatively few. This work aims in proposing a simple conduction heating-based fixture system for performing heating assisted incremental sheet metal forming of low melting point metals and to investigate the influence of critical process parameters on formability as well as surface quality characteristics of high wall angled features.

3 Experimental Plan and Procedure

For experimental investigations, AA6061 sheets having thickness of 1 mm have been used. Composition of the workpiece is given in Table 1. The material is commonly used for construction of aircraft structures, automotive parts, aluminum cans for the packaging of food and beverages, etc. EN8 mild steel rods that are turned down to 8 mm diameter were used as tool for conduction of experiments.

All experimentations were carried out on Lakshmi JV 55, three-axis CNC vertical milling machine. For the execution of the project, a separate fixture that can facilitate heating the sheet during the course of the process has been devised. The fixture consists of major parts: clamping block, and insulation-coated bottom block. Insulation block is made of Plaster of Paris (2 cm). At the center of the block, there is a hollow cylinder made of cast iron. For carrying out the incremental forming operation, the cast iron fixture is fixed in the bed of CNC machine. The sheet material is placed in the cast iron fixture in between the Plaster of Paris layer containing coil and top lid. The LM35 sensor is placed in Plaster of Paris layer such that it is in contact with AA6061 sheet. The LM35 sensor is connected with ARDUINO, which is programmed to read, display, and control the temperature. The output of ARDUINO is given to 5 V relay to control the heating coil. Figures 1 and 2, respectively, shows the design of the fixture that have been used during the process and the experimental setup.

Three parameters, viz tool rotational speed, feed rate, and sheet temperature, have been considered for experimental investigation. Experiments were designed using one factor at a time methodology. Parameter levels used for experimentation are given in Table 2. As the target was to investigate the influence of process parameters while forming features with steep features, wall angle of the features were kept constant at 70°. Incremental depth, which has been established as a very significant parameter in terms of surface quality and formability has been kept at a constant level of 0.2 mm. A mixture of graphite powder and white grease have been employed as lubricant during the process.

Table 1 Composition of AA6061

Element	Al	Si	Fe	Cu	Mn	Mg	Cr	Zn	Ti	Others
% by weight	95.85-98.56	0.4-0.8	0.7 (max.)	0.15-0.4	0.15 (max.)	0.8-1.2	0.04-0.35	0.25 (max.)	0.15 (max.)	0.15

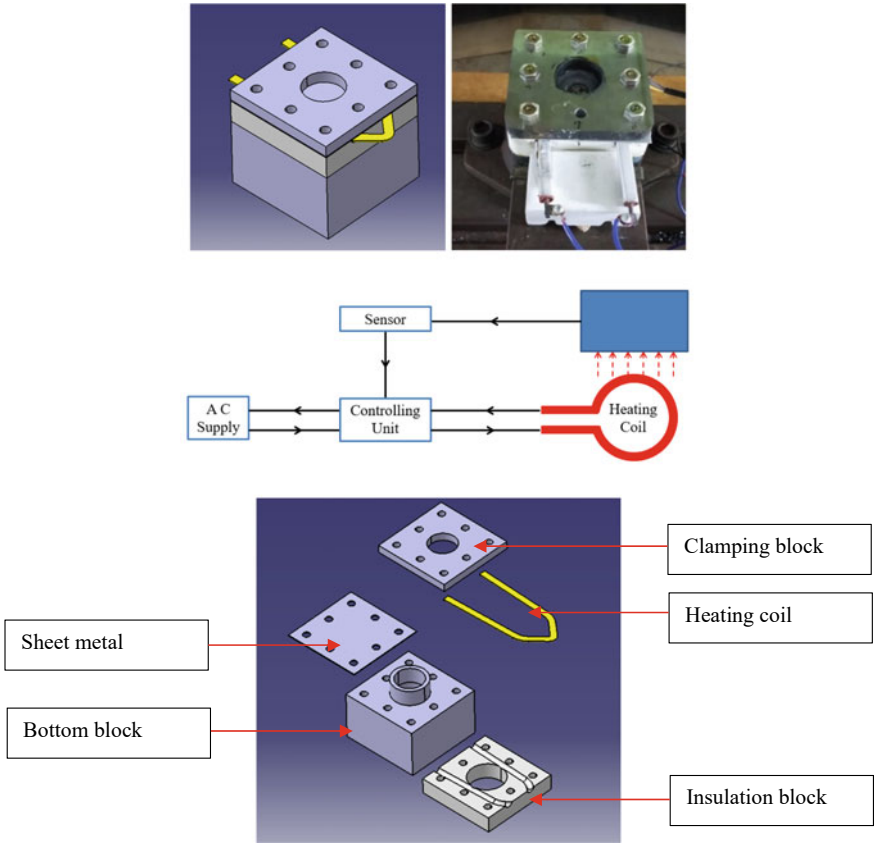


Fig. 1 Fixture assembly and heating system configuration



Fig. 2 Experimental setup

Table 2 Process parameters and levels

Parameters	Unit	Levels
Tool rotational speed	rpm	600, 800, 1000
Feed rate	mm/min	200, 400, 600
Sheet temperature	°C	Room temperature, 80, 120

Responses characteristics considered for present investigations were achievable feature depth and surface quality of the formed features. Achievable feature depth gives an idea about formability that can be attained under a set of conditions. Features were formed until crack initiation. Surface quality has been assessed in terms of two characteristics, viz arithmetic mean roughness (R_a) and average values of five highest-profile peaks and five deepest valleys identified in the evaluation length considered (R_z). Further, local sensitivity analysis has been performed on the obtained data to understand the extent of influence of variation in the process parameters considered on each of the response characteristics considered. Sensitivity index (SI) a value that reflects the aforementioned aspect has been computed using the formula given below.

$$SI = \frac{\left[\frac{OP_{(i+1)} - OP_{(i)}}{OP_{(i)}} \right]}{\left[\frac{IP_{(i+1)} - IP_{(i)}}{IP_{(i)}} \right]} \tag{1}$$

where $IP_{(i)}$ and $IP_{(i+1)}$ are the values of input parameters used at levels i and $i + 1$ and $OP_{(i)}$ and $OP_{(i+1)}$ are the corresponding values of response characteristics obtained when $IP_{(i)}$ and $IP_{(i+1)}$ were employed.

4 Results and Discussions

Surface roughness for each of the specimens were measured using Carl Zeiss make Handysurf portable surface roughness tester. Measurements were taken at four different locations along the feature wall and the values are averaged out for the results. Cone depth has been taken from the CNC machine interface at the time of fracture of the component. Figures 4 and 5 show the graphical representation of results pertaining to cone depth and surface quality characteristics.

It can be seen from Fig. 3 that parameters other than feed rate of the tool facilitates in creation of features with relatively higher depth. This effect is very much evident in the case of variation of sheet metal temperature. The influence of feed rate and tool rotational speed in present study do not show a proper trend for cone depth with the variation of parameter levels. From the graphs, it can be inferred for incremental forming of higher wall angled features with heat assistance on AA6061 sheets, and it is preferable to choose a lower feed rate, higher tool rotational speed, and higher sheet temperature. Similar observations can be drawn from Table 3 as well, which

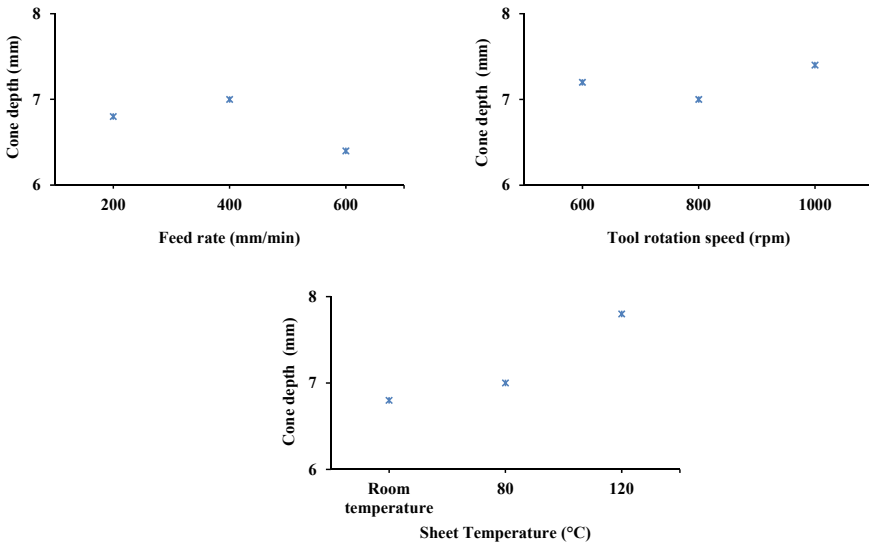


Fig. 3 Effect of process parameters on formed depth

Table 3 Results of local sensitivity analysis

Process parameter	Change in parameter level	Sensitivity index		
		R_a	R_z	CD
Feed rate (mm/min)	200–400	0.45	0.50	0.03
	400–600	0.62	1.25	0.17
Tool rotational speed (rpm)	600–800	1.26	0.13	0.08
	800–1000	1.24	2.50	0.23
Sheet temperature (°C)	30–80	0.31	0.02	0.02
	80–120	0.34	0.17	0.23

shows higher *SI* values for higher range values of tool rotational speed and sheet temperature.

With reference to Fig. 4, which states the influence of process parameters on surface quality characteristics like R_a and R_z , it is worth noting that the variation in values of R_z is more evident when compared to that of R_a when the process parameters are varied. Unlike in the case of response trends observed from cone depth, it is worth noting that feed rate and tool rotational speed have a more pronounced effect on the R_z . It can be inferred from the graphs that a higher value of feed rate, tool rotational speed, and sheet temperature yields in features with relatively better surface quality. Similar results can be seen in Table 3 as well, which shows relatively higher values of *SI* for higher values of tool rotational speed and feed rate.

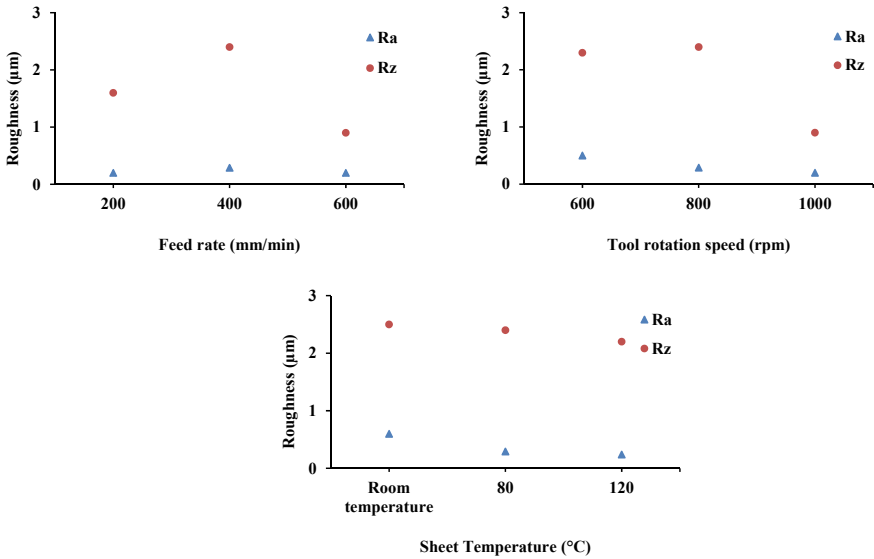


Fig. 4 Effect of process parameters on surface quality characteristics

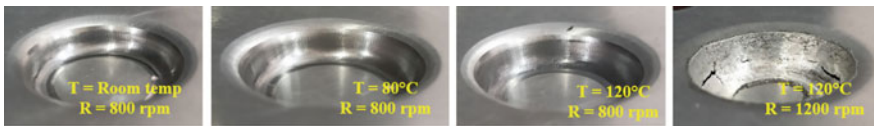


Fig. 5 Photographs of formed features under different temperature and tool rotational speed conditions

However, it is not necessary that employing all parameters at a higher level all together will result in features with good surface quality. Figure 5 shows the photographs of selected features formed under different conditions of sheet temperature and tool rotational speeds. It is worth noting that the surface texture of the features formed at 800 rpm are relatively smooth even at the highest sheet temperature considered.

At the same time, it is worth noticing that with increase in the tool rotational speed the surface quality got deteriorated very much aggressively, with significant signs of scraping of material from the formed surface. This might have even contributed to the premature failure of the sheet material during the course of forming, limiting the attainment of a higher cone depth.

5 Conclusions

Experimental investigations on incremental forming of AA6061 with heat assistance have been carried out. Three process parameters, viz feed rate, tool rotational speed, and sheet temperature, have been considered to assess their influence of attainable cone depth and surface quality characteristics. Sensitivity analysis have been carried out to understand the significances of parameters levels. Preliminary investigations suggest that formability, which is indirectly measured by cone depth achieved till failure is mostly influenced by sheet temperature, and surface quality is mostly influenced by tool rotational speed. However, more elaborate investigations are required to properly understand the combined parameter effects on these characteristics. Further, the surface characteristics in terms of micro hardness, surface elemental analysis, and microstructural changes, which are important in the context of heat-assisted incremental forming, are under investigation.

Acknowledgements The authors are thankful to Department of Science and Technology, New Delhi (SR/FST/COLLEGE-346/2018) for the financial assistance.

References

1. Ji YH, Park JJ (2008) Formability of magnesium AZ31 sheet in the incremental forming at warm temperature. *J Mater Process Technol* 201:354–358
2. Ji YH, Park JJ (2008) Incremental Forming of free surface with magnesium alloy AZ31 sheet at warm temperature. *Trans Nonferrous Met Soc China* 18:165–169
3. Ambrogio G, Filice L, Manco GL (2008) Warm incremental forming of magnesium alloy AZ 31. *CIRP Ann—Manuf Technol* 57:257–260
4. Shi P (2016) A study on the warm incremental forming limit of AZ 31B sheet. In: Paper presented at 3rd international conference on engineering technology and application, pp 761–767
5. Khazaali H, Saniee FF (2017) An Inclusive experimental investigation on the influences of different process parameters in warm incremental forming of AZ 31 Magnesium sheets. *Iran J Sci Technol: Trans Mech Eng*. <https://doi.org/10.1007/s40997-017-0122-0>
6. Ambrogio G, Filice L, Gagliardi F (2012) Formability of light weight alloys by hot incremental forming. *Mater Des* 34:501–508
7. Sy LV, Nam NT (2013) Hot incremental forming of magnesium and aluminium alloy sheets by using direct heating system. *Proc Inst Mech Eng Part B: J Eng Manuf* 227(8):1099–1110
8. Bao W, Chu X, Lin S, Gao J (2015) Experimental investigation on formability and microstructure of AZ31B alloy in electropulse assisted incremental forming. *Mater Des* 87:632–639
9. Xu D, Lu B, Cao T, Chen J, Long H, Cao J (2014) A comparative study on process potentials for friction stir and electric hot assisted incremental sheet forming. *Procedia Eng* 81:2324–2329
10. Kim SW, Lee YS, Kang SH, Lee JH (2007) Incremental forming of Mg alloy sheet at elevated temperatures. *J Mech Sci Technol* 21:1518–1522
11. Hino R, Kawabata K, Yoshida F (2014) Incremental forming with local heating by laser irradiation for magnesium alloy sheet. *Procedia Eng* 81:2330–2335

12. Galdos L, de Argandona ES, Ulacia I, Arruebarrena G (2012) Warm incremental forming of magnesium alloys using hot fluid as heating media. *Key Eng Mater* 504–506:815–820
13. Ulacia I, Galdos L, Esnaola JA, Larranaga J, Arruebarrena G, de Argandona ES, Hurtado I (2014) Warm incremental forming of Mg sheets: From Incremental to Electromagnetic Forming. *Metall and Mater Trans A* 45A:3362–3372

Study the Characterization of Hydroxyapatite and Silver Doped Hydroxyapatite Using Pin-on-Disc



L. B. Mulla, G. G. Mujawar, P. B. Gavali, and Y. N. Dhulugade

Abstract In this present study phase, preparation of hydroxyapatite is done by using sol-gel auto combustion method. For heating the powder at appropriate temperature, we have taken TG-DTA analysis. After calcination at 800 °C, nanoparticles of HA and Ag using same procedure we get nanoparticles of Ag doped HA. For knowing the formed mixture component XRD test is performed by Debye-Scherrer formula, calculation it gives particle size up to 11.39 nm. For biomechanical application ceramic materials are used in dental field hence we check the tribological properties of newly formed Ag doped HA. Pin-on-disc method is used for tribological characterization. For further study, SEM test is done on powder nanoparticle and pin nanoparticles samples. Also, for FTIR analysis is carried out to identify chemical compounds of prepared samples. After taking tribological test SEM images of tested pins are taken. Comparing the properties of HA and Ag doped HA we get the result that, Ag doped HA having better tribological properties than HA.

Keywords Hydroxyapatite · Nanoparticles · Pin-on-disc · Tribology

1 Introduction

Because of its chemical resemblance to human bones, hydroxyapatite (HA) is widely used in medical applications. By combining HA with mechanically strong metals, it

L. B. Mulla (✉) · P. B. Gavali · Y. N. Dhulugade
Sanjay Ghodawat University, Kolhapur, India
e-mail: mulla.lb@sginstitute.in

P. B. Gavali
e-mail: Pankaj.gavali@sanjayghodawatuniversity.ac.in

Y. N. Dhulugade
e-mail: dhulugade.yn@sginstitute.in

G. G. Mujawar
Government Polytechnic, Miraj, India
e-mail: gulnajpatharwat7@gmail.com

can be used in load-bearing applications [1]. Hydroxyapatite (HA) has been widely used in the medical field due to its high biocompatibility. Antibacterial HA, which is prepared by loading silver ions into HA via its good ion exchange capability, reduced the risk of infection in its clinical application. Heat stability is lower in silver-loaded matrix such as zeolite, silica gel, and active charcoal than in Hydroxyapatite [2]. It does not require fluorescence to stimulate the antibacterial effect, which is required for ceramic antibacterial agents containing TiO_2 [3] HA-Ag is widely used in everyday and engineering materials as a replacement for the two types of antibacterial agents mentioned earlier. Human teeth, which are important masticatory organs, are subjected to friction and wear on a daily basis. As a result, anti-wear properties for dental restorative materials are essential. Enamel, dentin, and pulp are the three components that make up a human tooth [4]. Human teeth are the hardest tissue in the body, and they have excellent wear resistance. Human teeth can last a lifetime if properly cared for. Metals, alloys, composites, and ceramics have all been used in dental restorations [5]. When compared to human tooth enamel, these dental restorative materials have different tribological issues in clinical use. Because hydroxyapatite (HA) can form a real bond with the surrounding bone tissue when implanted, it is now used as a biomaterial in a variety of biomedical applications [6]. More research is done for antibacterial character of HA and Ag doped HA but tribological behaviour of Ag doped HA is large field for study. Comparison between the properties of HA and Ag doped HA can show the usefulness of Ag doped HA.

2 Experimental Setup

2.1 Sample Preparation [Pure Hydroxyapatite $\text{Ca}_{10}(\text{PO}_4)_6(\text{OH})_2$]

Simple sol-gel auto combustion method is used for sample preparation, and all chemicals are analytical reagents (Sigma-Aldrich, USA). Calcium nitrate tetrahydrate ($\text{Ca}(\text{NO}_3)_2 \cdot 4\text{H}_2\text{O}$) and di-Ammonium hydrogen orthophosphate $[(\text{NH}_4)_2\text{HPO}_4]$ were used as calcium and phosphorus precursors, respectively, in the preparation of hydroxyapatite [7, 8]. 14.95 g of calcium nitrate tetra hydrate and 5.0195 of di-Ammonium hydrogen orthophosphate was kept in evaporating dish and heated on hot plate till the contents turned in to homogeneous white paste, heating continued till it turned into homogenous white mass. Then this white mass was heat at temperatures of 1000 °C for 2 h. it was observed that calcium nitrate tetra hydrate possesses hygroscopicity, the reactant mixture easily absorbed moisture from air to become a white slurry mixture, which was heated on hot plate and thoroughly dehydrated. The dried mixture possesses the characteristics of combustion and can be ignited to start combustion reaction using muffle furnace.

2.2 *Ag Doped Hydroxyapatite*

In preparation of Silver doped hydroxyapatite, calcium nitrate tetra hydrate $[\text{Ca}(\text{NO}_3)_2 \cdot 4\text{H}_2\text{O}]$ and silver nitrate $[\text{Ag}(\text{NO}_3)]$ were used as precursors of calcium, silver and phosphorus, respectively. For preparation of sample 1 $[\text{Ca}_{9.5}\text{Ag}_{0.5}(\text{PO}_4)_6(\text{OH})_2]$ 14.37 g of calcium nitrate tetra hydrate, 0.543 g. Silver nitrate and 5.078 g di-Ammonium hydrogen orthophosphate were placed in an evaporating dish and heated on a hot plate until the contents formed a homogeneous paste, which was then heated until it became a white mass. The white mass was then heated for four hours at temperatures of 9000 °C. Same procedure carried out for sample 2 $[\text{Ca}_{8.5}\text{Ag}_{1.5}(\text{PO}_4)_6(\text{OH})_2]$ which contain 13.14 g. of calcium nitrate tetra hydrate, 1.1005 g. of Silver nitrate, 5.1326 g. of di-Ammonium hydrogen orthophosphate. And also, for sample 3 $[\text{Ca}_{7.5}\text{Ag}_{2.5}(\text{PO}_4)_6(\text{OH})_2]$ prepared by using 11.85 g. of calcium nitrate tetra hydrate, 2.84 g of Silver nitrate and 5.30 g. of di-Ammonium hydrogen orthophosphate.

2.3 *Pin Preparation*

For pin preparation, hydroxyapatite nanoparticles and Ag Doped hydroxyapatite are utilised. One pin is for hydroxyapatite and the other three are for Ag Doped hydroxyapatite. For pin preparation, hydroxyapatite powder and acrylic repair material (90:10) were employed, and when combined together, they created a semi-solid mass. Semi-solid mass pins with a width of 8 mm and a length of 32 mm were created using this method. The same method was utilised to make Ag doped HA pins.

2.4 *Wear Test*

The wear test was conducted on Tribometer by pin-on-disc method in dry medium. The pin of hydroxyapatite and Ag Doped hydroxyapatite was rotating upon stainless steel disc. In This study of wear and friction characteristics in sliding contact under different load. When pin type of hydroxyapatite and Ag Doped hydroxyapatite comes in contact in with rotating disc at 150rpm, for 10 min, which is hardened to about 50–55 HRC, contact surface of pin were wear. This were measure directly Linear voltage displacement transducer (LVDT) or indirectly by means of weighing the specimen before and after the experiment. Specimen when comes in contact with rotating disc under load 981-5886 N tends to rotate in direction of the disc, because of friction (Fig. 1).

This frictional force can also be directly measure by means of cantilever type load cell (strain gauge). A pin and disc type wear testing machine used for measurement of wear as shown in Fig. 2. The apparatus consist of a disc supported by flange an

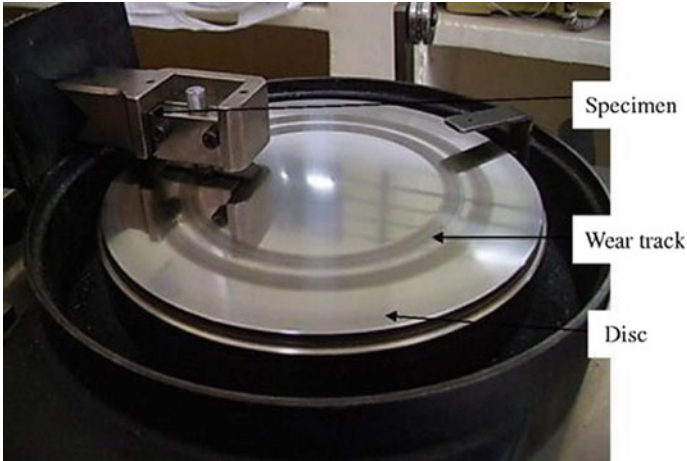


Fig. 1 Front panel of Tribometer including disc and pin

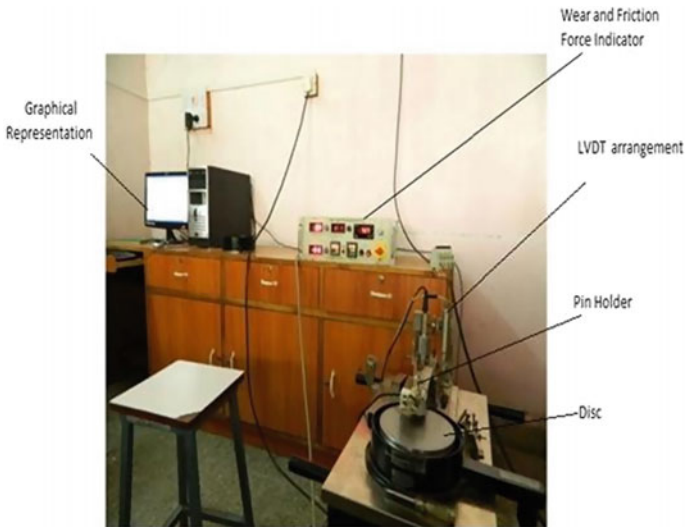


Fig. 2 Pin-on-disc tribometer setup

a motor shaft which is fixed vertically to the base plate, on top of table. A pin of pure hydroxyapatite and another of Ag Doped hydroxyapatite specimen, gripped in holder is fixed at one end of the arm which is balanced at Centre by means of bearing housing, bearing housing is fixed by means of guide to the facilitate up and down adjustment of arm, supported by a screw rod. Arm holding the specimen is fitted the housing by means of bearing, to move arm up and down. Screw rod is fitted to a plate which is sliding on base plate. Loading pan is provided to the specimen by means of

two pulley, mounted on the sliding plate which is fixed with two bars, one of which fixed with scale to measure the radius of disc.

3 Results and Discussion

3.1 XRD Analysis

From the standard JCPDS values we can determine the formation of Hydroxyapatite by observing X-ray diffraction spectrum (XRD). The estimates of crystal size from the XRD peak broadening based on Scherer's formula for the HA powder and Ag doped HA powder taken at the most prominent peaks. From this pick points, we find the crystal size of prepared samples. From XRD analysis it observed that prepared sample contain HA as primary phase and Ago as secondary phase. JCPDS values are useful to identify the structure of prepared samples; this will give the chemical composition of samples. The graphs prepared by XRD analysis shows multiple frequency bands. There are frequency bands regarding to corresponding chemical group observed on the graphs. XRD machine was set at 40 kV and 40 mA at 2θ vary at 10° – 60° with step size of 0.02° . Crystallographic identification of HA and Ag doped HA is found out by comparing with the experimental XRD patterns to standard complied by the JCPDS values. Crystalline size calculated by using Scherer's formula is 34.509 nm for HA, for sample 1 is 43.13 nm, for sample 2 is 21.1227 nm and for sample 3 is 11.3951 nm.

Figure 3 shows the XRD pattern for HA and Ag doped HA. The XRD pattern of pure HA and Ag doped HA powders calcination at 800°C shows the maximum peak at 2θ angle of 31.78° corresponding to HA (211) plane. The deflection intensity of major peak in the calcined powder improved with increase in temperature, indicating an increase in HA phase content, that means both removal of the organic residuals and improve crystal size of HA. From Fig. 1, it is observed that maximum peak at 2θ angle of 33.28° corresponding to Ag (302) plane (Table 1).

The degree of crystallites, current phases of Hydroxyapatite, and crystallite size were all investigated using X-ray analysis. XRD is used to monitor crystal quality, see flaws in a variety of crystalline materials, phase borders, faulty regions, non-crystalline, fractures, surface scratches, stacking faults, dislocations, grain boundaries, point defects, and crystal deformation.

3.2 SEM Analysis

The scanning electron microscope (SEM) generates a variety of signals at the surface of solid objects using a focused beam of high-energy electrons. The signals generated by electron-sample interactions provide information on the sample's exterior

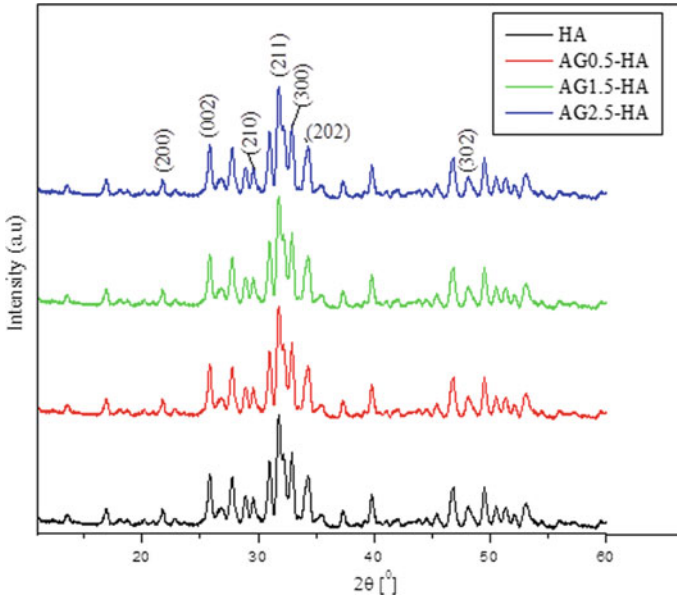


Fig. 3 XRD of Pure HA and AgO doped HA

Table 1 Compositions and their percentage present in prepared samples

Sample	Samples with their component				
		O	P	Ca	Ag
Sample 1	weight	37.38	22.86	35.98	3.78
	Atomic %	58.31	18.42	22.40	0.87
Sample 2	weight	31.60	22.40	35.70	10.30
	Atomic %	53.60	19.63	24.18	2.59
Sample 3	weight	30.84	21.23	31.65	16.28
	Atomic %	54.25	19.29	22.22	4.25
HA	weight	32.85	22.89	44.26	–
	Atomic %	52.69	18.96	28.34	–

morphology (texture), chemical composition, and crystalline structure and orientation of the components that make up the sample, among other things. The SEM can also analyse chosen point locations on the sample, which is particularly useful for assessing chemical compositions, crystalline structure, and crystal orientations qualitatively or semi-quantitatively.

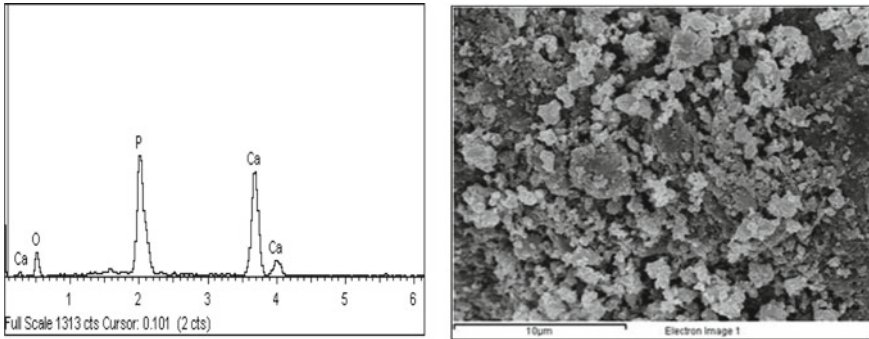


Fig. 4 SEM image of pure HA and the EDS spectrum

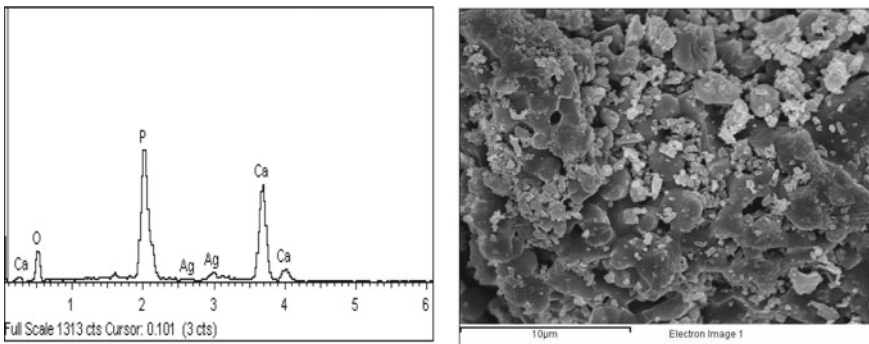


Fig. 5 SEM image of Ag doped HA (sample 1) and the EDS spectrum

3.3 Wear Test Analysis

Pin-on-disc wear testing is a technique for determining the coefficient of friction, frictional force, and wear rate of two materials. A stationary pin articulates against a revolving disc while under a constant applied stress in this tribological test. By observing the graphs formed by testing data it is clear that HA having more strength compare with AgO doped HA.

From above Fig. 6 shows that Wear Rate of silver (AG) at different Loads. The Pure HA (d) shows that at minimum load wear rate is increases and after increases loads as per wear rate is decreases, at 25 °C. The AG doped HA[a] (Ag0.5-HA) shows that the Wear rate is increases with minimum load at constant speed of 150 rpm and constant time of 10 min. The increases the loads with wear rate are deceases at 3.8 KN and wear rate is slowly decreasing as per increasing loads. When the silver composition increases (AG1.5-HA) [b], it shows that wear rate is maximum at 2 KN and loads increases then the wear rate is decreases once and wear rate is constant. When the composition of increases of silver (c), it shows that maximum wear rate

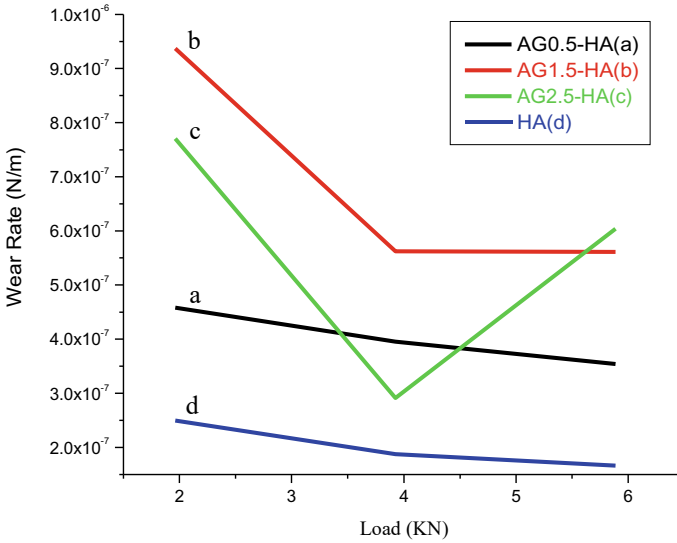


Fig. 6 Wear rate against loads of Pure HA and Ag at different composition

at minimum load and when the load is increase then the wear rate is decreases one stage after this wear rate suddenly increases as per load increases.

The graph of coefficient of friction of pure HA and silver doped HA against different loads as shown in below Fig. 7.

The pure HA indicates that the coefficient of friction is greatest at 2 KN, and that the coefficient of friction diminishes as the load rises. The coefficient of friction is highest at 2 KN in silver doped HA (Ag0.5-HA) and as the load increase then the coefficient of friction is decreases at 4 KN and against the load increases then coefficient of friction is increases at constant speed of disc 150 rpm. The silver doped HA (Ag1.5-HA) shows that coefficient of friction is 1.45 at 2 KN and after the load is increases then the coefficient of friction is continuously decreases.

Silver doped HA (Ag2.5-HA) indicate that coefficient of friction is 0.85 at 2 KN and as the load is increasing the coefficient of friction is decreases. The coefficient of friction is minimum 0.1 at 6 KN.

4 Conclusions

1. From Load against wear rate, it can conclude that lower composition of silver doped HA is having less wear rate as compare to the pure HA.
2. From Time against wear rate, as composition of silver increases wear rate is increased. For lower concentration as time period increases wear rate is going

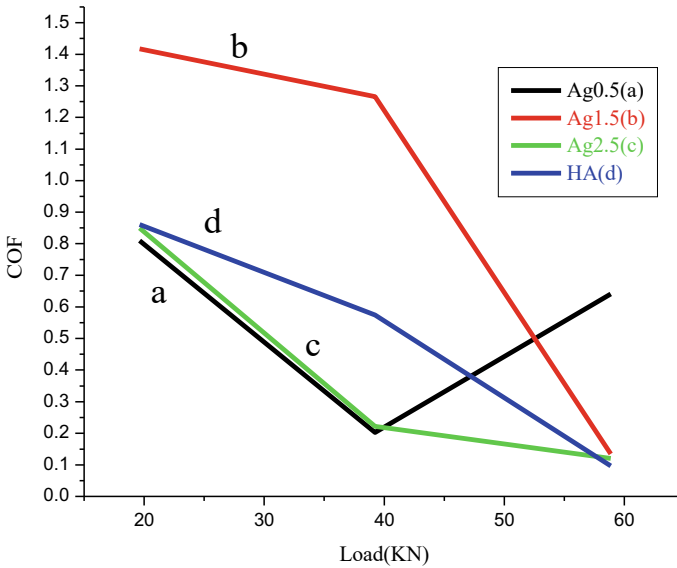


Fig. 7 Coefficient of friction against load of pure HA and silver doped HA at different compositions

to decreases as compare to pure HA, which shows constant increase in wear rate with respect to time period.

- For lower concentration of silver doped HA coefficient of friction is maximum and as the loads increases then the coefficient of friction decreases certain period and suddenly increases. As the silver compositions is increases coefficient of friction is maximum at 2 KN and as the load increase coefficient of friction is continuously decreases. The maximum composition of silver doped HA(Ag2.5-HA) has maximum coefficient of friction at 2 KN and load increases then coefficient of friction smoothly decreases.

References

- Jeong Y, Gnäupel-Herold T, Barlat F, Iadicola M, Creuziger A, Lee M-G (2015) Evaluation of biaxial flow stress based on elasto-viscoplastic self-consistent analysis of X-ray diffraction measurements. *Int J Plast* 66:103–118. ISSN 0749-6419
- Zhao K, Feng Q, Chen G (1999) Antibacterial effects of silver loaded hydroxyapatite, *Tsinghua science and technology*, vol 4(3), pp 1570–1573, September 1999. ISSN 1007-0214, 19/23
- Benea L, Mardare-Danaila E, Celis J-P (2014) Increasing the tribological performances of Ti–6Al–4V alloy by forming a thin nanoporous TiO₂ layer and hydroxyapatite electrodeposition under lubricated conditions. *Tribol Int* 78:168–175. ISSN 0301-679X
- Zheng J, Li Y, Shi MY, Zhang YF, Qian LM, Zhou ZR (2013) Microtribological behaviour of human tooth enamel and artificial hydroxyapatite. *Tribol Int* 63:177–185. ISSN 0301-679X

5. Rmaile A, Carugo D, Capretto L, Zhang X, Wharton JA, Thurner PJ, Aspiras M, Ward M, Stoodley P (2013) Microbial tribology and disruption of dental plaque bacterial biofilms. *Wear* 306(1–2):276–284. ISSN 0043-1648
6. Liu J, Zhu Y, Wang Q, Ge S (2008) Biotribological behavior of ultra high molecular weight polyethylene composites containing bovine bone hydroxyapatite. *J China Univ Mining Technol* 18(4):606–612. ISSN 1006-1266
7. Nakahira A, Nakamura S, Horimoto M (2007) Synthesis of modified hydroxyapatite (HAP) substituted with Fe Ion for DDS application. *IEEE Trans Magn* 43(6):2465–2467. <https://doi.org/10.1109/TMAG.2007.894358>
8. Lu Z, Liu Y, Liu B, Liu M (2013) Micro-tribological properties of hydroxyapatite-based composites in dry sliding. *Mater Des* 46:794–801. ISSN 0261-3069

Synthesis of Bulk Consolidated Ti-46Al-1B (at%) Alloy via Powder Metallurgy Route Using Induction Sintering Technique



Mrigesh N. Verma and Vijay N. Nadakuduru

Abstract The phases present in Ti-46Al-1B (at%) gamma titanium aluminide-based alloy component produced by powder consolidate was analysed. Powder cold compaction were done using a 100-tonne hydraulic press followed by canned induction sintering method and at various temperatures. In canned preform was of mechanically alloyed powder which was canned in a stainless tube for protecting it from environmental contamination. Various characterization and testing were done for analysing the properties of the consolidate formed. It indicated that the compact made was having around 95% density which is not very high but it is moderately high when considered with the cost-effectiveness of the process. The major phase present is found to be TiAl. Also, the mechanical property like hardness is low mainly because of the presence of porosity and with the minor influence of iron contamination in the consolidate. All over it gave an acceptably good preform for further thermomechanical processing which will improve the density and ultimately the properties of the bulk formed.

Keywords Itanium intermetallics · Titanium aluminide · TiAl · Hardness · Induction sintering

1 Introduction

In the present scenario, nickel alloys and stainless steels are highly preferred materials for usage in high-temperature applications like turbine and aeroplane engine parts. The primary advantage of using these materials is the ease of production. But the main disadvantage is the weight or higher density of these materials. In the prime focused usage of these alloys like aerospace and automobile, there is an increase in

M. N. Verma · V. N. Nadakuduru (✉)

Department of metallurgical and materials engineering, Malaviya National Institute of Technology, Jaipur, Rajasthan, India
e-mail: vijay.meta@mnit.ac.in

M. N. Verma

e-mail: 2017rmst9071@mnit.ac.in

© The Author(s), under exclusive license to Springer Nature Singapore Pte Ltd. 2022
H. K. Dave et al. (eds.), *Recent Advances in Manufacturing Processes and Systems*,
Lecture Notes in Mechanical Engineering,
https://doi.org/10.1007/978-981-16-7787-8_76

957

efficiency to a greater extent by weight reduction by the usage of lower density alloys. Intermetallics of titanium and aluminium are a strong candidate for such a replacement. They not only have lower density but have higher strength when corrected with density and also have good thermal stability in comparison with nickel or iron alloys [1]. They also have properties like good corrosion resistance and high melting point which are of prime consideration in some specific applications. However, the manufacturing of these alloys is complicated. In the conventional method of casting, melting needs to be done in vacuum and then also the melt tends to react with crucible material and its remedies are expensive [2–4].

Thus, during the past few decades powder metallurgical route of component production had shown promising results as an alternative and is under constant investigation to improvise the process. In powder metallurgy, a sub-route of prealloyed powder shows some difficulty in powder production due to high melting point and also because hot isostatic pressing or hot extrusion needs to be used for consolidation of powder which is quite expensive. The elemental powder or mechanically alloyed powder route of production shows maximum cost-effectiveness with a success ratio in the component production [5, 6]. These powders further get cold pressed and sintered. Conventional sintering methods like electric or gas furnaces have a major drawback of low heating rate. Thus, it has a longer processing time and subsequently higher power consumption. This results in expensive processing. Other advanced methods like spark plasma sintering [7, 8], hot isostatic pressing [9–11] have their advantages but the initial setup is expensive, and it has a limitation of production quantity to be processed in each batch. Another possible route of consolidation is self-propagating high-temperature synthesis [12–14] or reactive sintering [15–17]. The prime reasons for such processes not widely utilized are because the part produced is porous. Induction sintering is a plausible route that can overcome the limitations of various production techniques [18, 19]. The heating rate is very high and is easily controllable. This helps to reduce the production time, and also, the possibility of unwanted reaction with the environment is lowered. The setup required is also not expensive as it does not require refractor lining for the sintering chamber or so. Thus, when induction sintering is compared with other conventional and advanced sintering processes, it comes out to be relatively faster and economical [19, 20].

There is a very little amount of research done in the field of induction sintering of powder compacts and especially in the field of titanium-based intermetallic alloys. Thus, the present study focuses on elaborating the possibilities of synthesizing bulk consolidated of TiAl-based mechanically alloyed powder having a nominal composition of Ti-46Al-1B (at%) using induction sintering technique and relating the basic properties of bulk consolidate with that of the nearby composition produced by other processing routes.

2 Experimental

Powder of a nominal composition of Ti-46Al-1B (at%) was produced using high-energy planetary ball mill. Wet milling was done for a net time of 12 h at 400 rpm using stainless steel vial and balls. Cold compaction of already mechanically alloyed powder was done using a die with an internal diameter of 16 and 40 mm. Cold compaction was carried out at a load around 200 KN with a holding time of 2 min for 16 mm dia. and around 750 KN for the 40 mm dia. compacts with the same holding time. These compacts were used for further sintering by using a medium-frequency induction sintering machine. The compacts were first canned inside a stainless steel can before sintering. These cans were evacuated by attaching them with a vacuum pump and heating the can to a temperature between 250 and 300 °C for one hour. This is done to remove all present volatile and air from the can. Further sintering was carried out by heating the canned sample by induction heating to a temperature of 1100 °C and maintaining it in a range of ± 20 °C for 60 s while still attached to a vacuum pump. Then it was cooled by normal air cooling, and at this stage, also the vacuum pump was kept attached to prevent oxidation of the compact. Sintered compacts were then removed from the can by EDM cutting, which were then further polished or cut for characterization like SEM, XRD, microhardness, optical microscope imaging and density measurement. Density was measure by the use of Archimedes method and was cross-checked by measuring density by the physical method and also by analysing the optical microscope images.

3 Results

The X-ray diffraction pattern of the powder sample that was collected after 12 h of milling is shown in Fig. 1. Peaks were analysed using PANalytical X'pert Highscore. It was observed that at the present milling, time powder particle size is reduced and because of that, the peaks became broadened which indicates ultrafine grain size. For the consolidation studies of 12 h, milled powder was done as its the stage which confirmed the completion of alloying which is visible in XRD patterns and the grain size of the same (which is in ultrafine range) by bright-field image of the same powder as shown in Fig. 2. Grain size present in particles of the milled powder 12 h of net milling is generated by bright-field imaging mode of TEM. The grain size of around 110 nm to 120 nm is observed after net milling of 12 h which is in the ultrafine range. The 12 h milled powder was further used for the production of green compacts for further processing.

The density of green compacts was measured by the physical dimensional method and found to be approximately around 60% of the theoretical density, green compacts are shown in Fig. 3. The induction-sintered samples after the sintering stage were shown in Figs. 4, 5 and 6. Samples are made using different dies of different diameters but only the sample produced by using a 40 mm diameter die was used for further

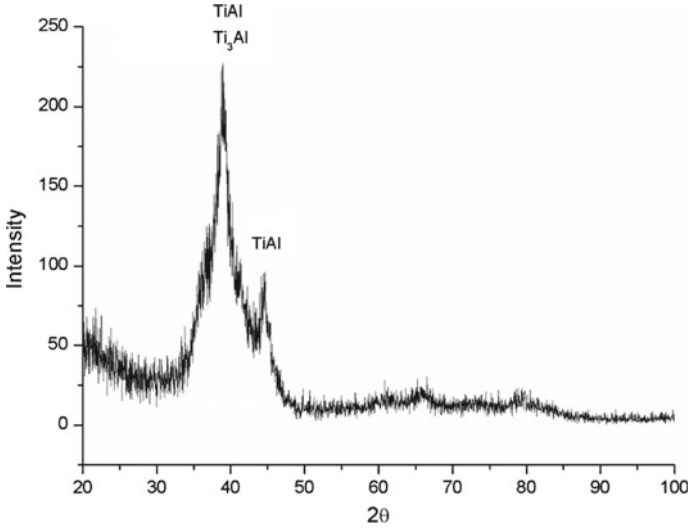
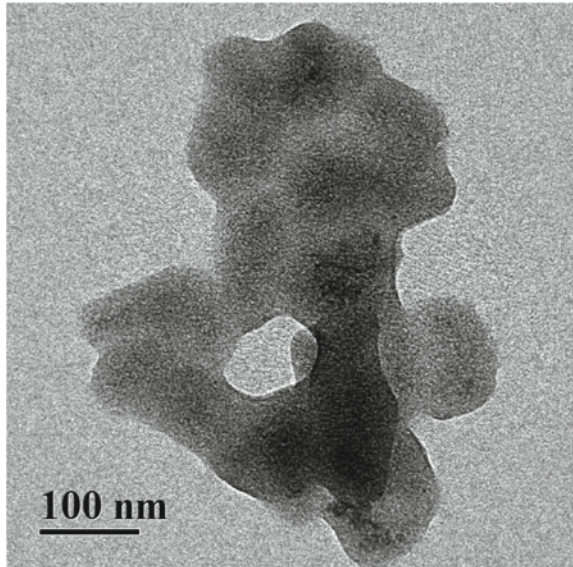


Fig. 1 XRD of 12 h milled powder

Fig. 2 Bright field TEM image of 12 h milled powder



analysis as they provided sufficient bulk for processing required of analysis. The decanned consolidate was further sliced using EDM wire cutting to get a section of specimen out of the bulk, and the section of bulk specimen cut is shown in Fig. 7; the surface was polished for further visual inspection for further characterization and testing. Primary visual inspection has revealed few surface cracks on the curved



Fig. 3 Green compacts (40 mm diameter on left and 16 mm diameter on right)

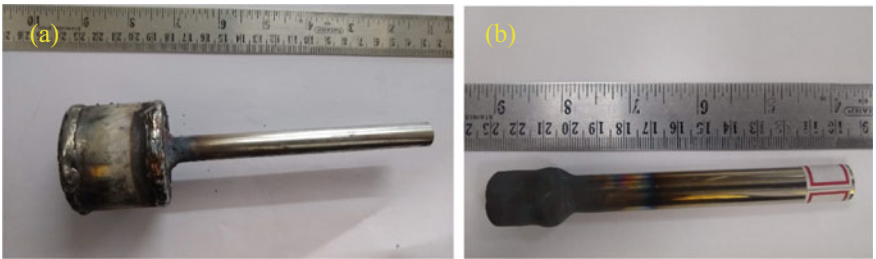


Fig. 4 Canned specimen of a 40 mm diameter and b 16 mm diameter



Fig. 5 Decanned induction sintered consolidate produced using 40 mm diameter die

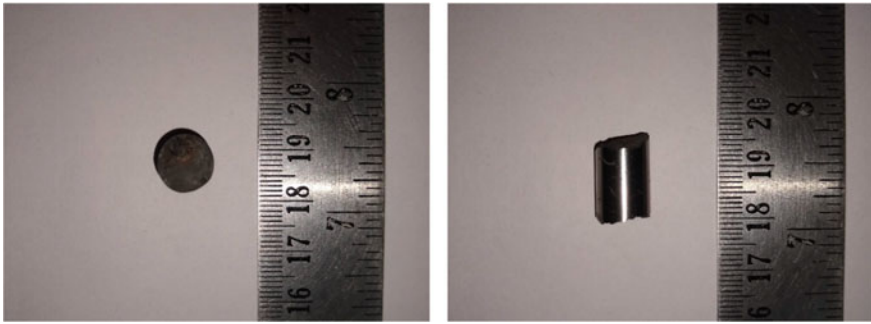


Fig. 6 EDM cut decanned induction sintered consolidate produced using 16 mm diameter die



Fig. 7 EDM cut consolidate sections for further testing

surfaces and a major void at the core at the centre of the sample which is possibly due to the continuous evacuation during the sintering process (Fig. 7).

The relative density of the bulk samples was measured by the Archimedes method and found to be approximately 95%. The hardness of these samples was measured by Vickers microhardness and found to be averaging around 328 HV, the variation of hardness from and the edge of the sample towards the centre is being shown in

Fig. 8, microhardness was observed to be increasing from the periphery towards the centre. Such an increase in the hardness is indicative of the lowering of the porosity in the central region. The hardness of the material is found to be a bit lower than the expected of 365 HV [21]. This decrease in hardness might be because of contamination and porosity present in the bulk. XRD analysis of 40 mm diameter consolidated specimen Figure 9 had shown the presence of TiAl as a major phase in

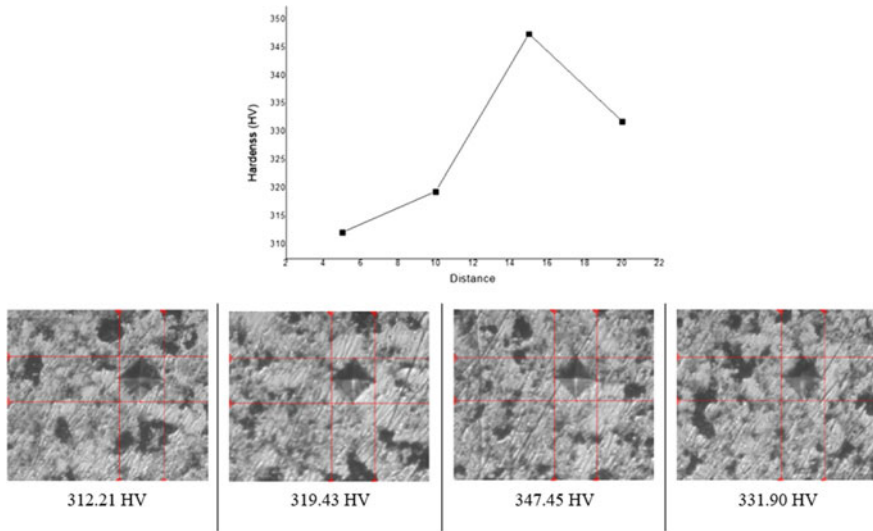


Fig. 8 Microhardness indentation at different locations with hardness value

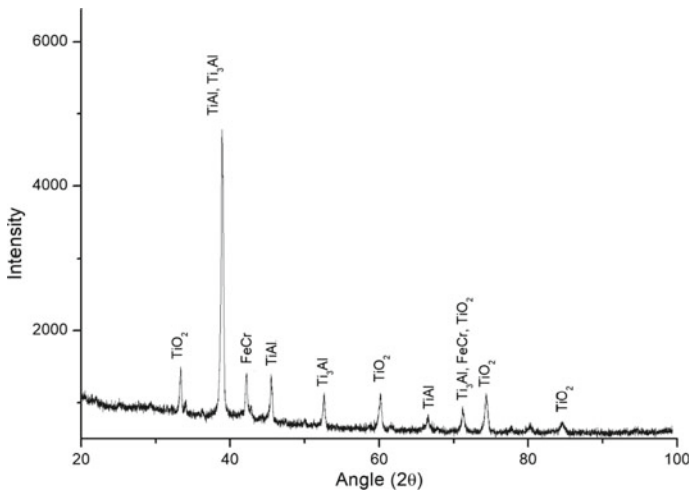


Fig. 9 XRD of 40 mm diameter consolidated sample

the consolidated specimen. There is a minute variation to the natural peak position observed which is primarily because of the presence of impurities that got mixed with the powder during the milling process. These impurities came from the stainless steel vial and ball used during the mechanical alloying of the powder. The same was observed in the EDS results done during SEM imaging. Also from the Scherrer calculation of crystallite size had shown that of around 132 nm, which is in the nanocrystalline range. Thus from the XRD patterns, the grain size is expected to be near ultrafine-grained or nano, which is yet to be confirmed using TEM analysis. The decanned sample was polished to a mirror finish, and images were taken of the sample without etching to observe the porosity present in the sample Fig. 10. This, when analysed, gave a porosity of roughly 7 percentage which is fairly close to what can be said by the density measurement. The same was observed under SEM as shown in Fig. 11a, b, confirming roughly the same amount of porosity. EDS results (Fig. 12) which were done while SEM imaging showed the presence of some amount of iron that was expected to come during the milling process from the wear occurring in vial and balls but majorly it confirms the stoichiometry required for TiAl formation. The iron contamination is minorly present, and thus, it won't be affecting hardness

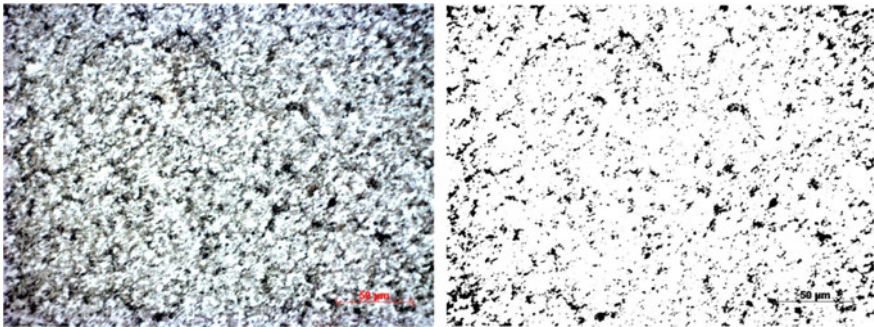


Fig. 10 Micrograph of 40 mm diameter as-sintered sample at 500X (right is the extracted channel image for porosity calculation (~7%))

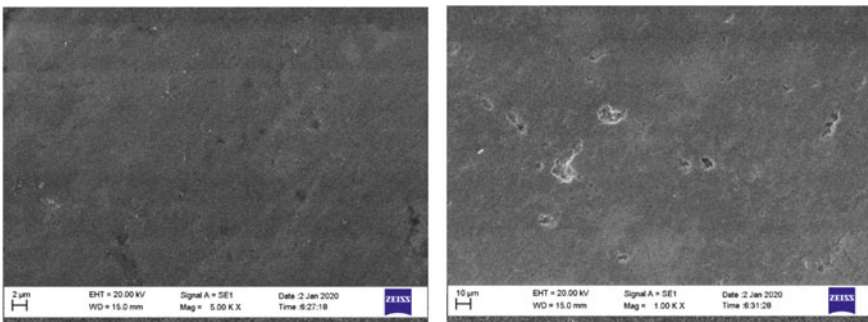


Fig. 11 SEM images a 5000× magnification. b 1000× magnification

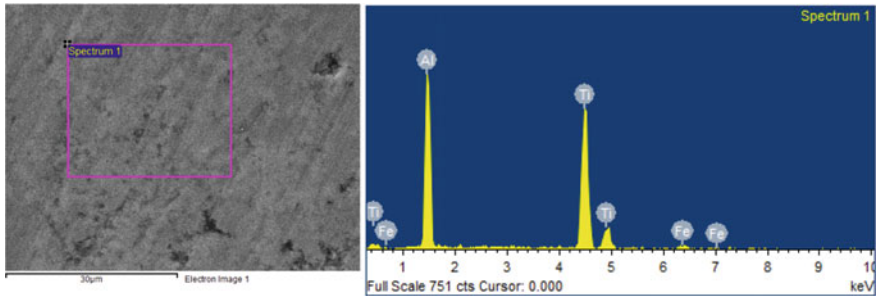


Fig. 12 SEM-EDS analysis of the bulk alloy

value significantly. So it can be concluded that the drop in hardness value is primarily because of the porosity with minor aid by the iron contamination.

4 Discussion

The samples synthesized have shown decent hardness but it is not up to the expectation mark, and this is primarily because of the fractional porosity in the specimens. The porosity in the sample was expected to be due to lack of interparticle bonding during sintering, which is due to the faster heating during the induction sintering process and also less holding time, and also due to lower green density coupled with no molten phase present during sintering to fill up the formed voids. However, the bulk consolidated alloy can be used as a suitable precursor for further processing to improve the quality of the material. From the XRD plot results, it is clear that the TiAl is the major phase present which is the desired and targeted phase in the present study, which was found to be similar to other works [7, 22, 23]; they also reported the presence of Ti₃Al as the minor phase. When we see the overall processing ease and economics the consolidated sample shows TiAl formation at a much easier processing rate concerning time and also the economy, with fewer amount difficulties except the central void which can be eliminated by using some kind of modification in the can design which is already in process for the present study. The density of the consolidated sample has shown a promising result with as induction-sintered consolidate showing approximately 95% density. This level of densification is higher than that feasible from reactive sintering and comparable to the pressureless sintering but is lower than consolidates produced from SPS which ranges from 94% to almost 100% density [22, 24]. The comparison of the density of the finished bulk produced by different processing methods at various processing temperature is shown in Fig. 13 [24–29]. Densification is almost the same as compared to that for as- HIPed bulk alloy which was reported to be around 95% [27, 29]. But when we consider the cost of production and set up the achieved density is quite satisfactory, and also, casting

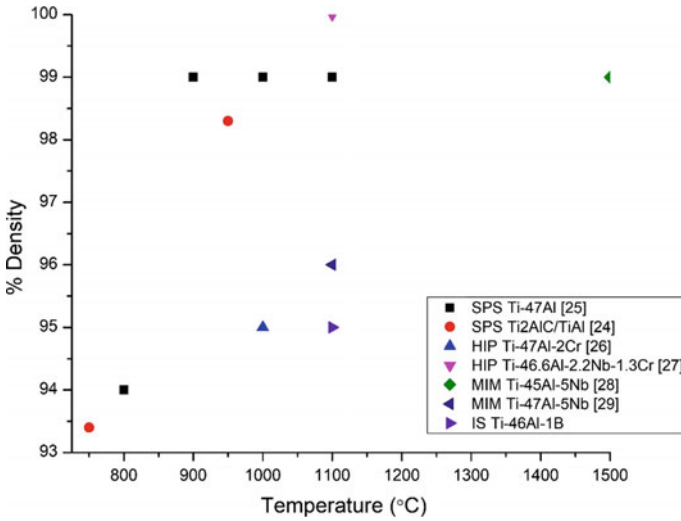


Fig. 13: Density comparison for different processing techniques at different temperature

of titanium aluminide is very tricky and expensive compared to any powder metallurgical route. Considering all present production route has shown the advantages of being relatively economical and simpler and faster production. The quality of the material can be improved by changing the processing parameters of induction sintering and also further processing such as forging.

Further, the number of impurities present in the consolidate can be lowered by using a vial and ball of harder material like tungsten carbide. Figure 14 shows a 20 mm diameter consolidate produced using a powder that was mechanically alloyed using a tungsten carbide ball and vial with the same milling parameters. Also, some canning improvisations are to be tested for the elimination of the central void present in the 40 mm diameter consolidate.



Fig. 14: 20 mm diameter consolidates of same alloy composition powder made using tungsten carbide ball and vial

5 Conclusion

The induction sintering of the green compact of mechanically alloyed powder had shown the good possibility of consolidation via cold compaction followed by induction sintering. There is some amount of porosities present in the sample which are in the acceptable range but there is always room for improvement and which can be improved via thermomechanical processing like forging. The crystallites are of ultrafine crystallite size from the analysis of XRD with TiAl as the major phase present in the bulk.

Acknowledgements The authors are thankful to the Science and Engineering Research Board (SERB), DST, New Delhi, India, for the financial support for the project.

References

1. Su Y, Zhang D, Kong F, Chen Y (2013) Microstructure and mechanical properties of TiAl alloys produced by rapid heating and open die forging of blended elemental powder compacts. *Mater Sci Eng A* 563:46–52
2. Tetsui T, Kobayashi T, Kishimoto A, Harada H (2012) Structural optimization of an yttria crucible for melting TiAl alloy. *Intermetallics* 20:16–23
3. Kothari K, Radhakrishnan R, Wereley NM (2012) Advances in gamma titanium aluminides and their manufacturing techniques. *Prog Aerosp Sci* 55:1–16
4. Thomas M, Raviart JL, Popoff F (2005) Cast and PM processing development in gamma aluminides. *Intermetallics* 13:944–951
5. Long Y, Wang T, Zhang HY, Huang XL (2014) Enhanced ductility in a bimodal ultrafine-grained Ti–6Al–4V alloy fabricated by high energy ball milling and spark plasma sintering. *Mater Sci Eng A* 608:82–89
6. Sun ZM, Hashimoto H (2003) Fabrication of TiAl alloys by MA-PDS process and the mechanical properties. *Intermetallics* 11:825–834
7. Lagos MA, Agote I (2013) SPS synthesis and consolidation of TiAl alloys from elemental powders: microstructure evolution. *Intermetallics* 36:51–56
8. Mizuuchi K, Inoue K, Sugioka M, Itami M, Kawahara M (2004) Microstructure and mechanical properties of Ti-aluminides reinforced Ti matrix composites synthesized by pulsed current hot pressing. *Mater Sci Eng A* 368:260–268
9. Nadakuduru VN, Zhang DL, Cao P, Chiu YL, Gabbitas B (2011) The mechanical behaviour of an ultrafine grained Ti-47Al-2Cr (at%) alloy in tension and compression and at different temperatures. *Mater Sci Eng A* 528:4592–4599
10. Zeng S, Zhao A, Luo L, Jiang H, Zhang L (2017) Development of β -solidifying γ -TiAl alloys sheet. *Mater Lett* 198:31–33
11. Suryanarayana C, Behn R, Klassen T, Bormann R (2013) Mechanical characterization of mechanically alloyed ultrafine-grained Ti5Si3+40vol% γ -TiAl composites. *Mater Sci Eng A* 579:18–25
12. Yeh CL, Su SH (2006) In situ formation of TiAl-TiB₂ composite by SHS. *J Alloys Compd* 407:150–156
13. Yeh CL, Wang HJ, Chen WH (2008) A comparative study on combustion synthesis of Ti-Si compounds. *J Alloys Compd* 450:200–207
14. Taguchi K, Ayada M, Ishihara KN, Shingu PH (1995) Near-net shape processing of TiAl intermetallic compounds via pseudoHIP-SHS route. *Intermetallics* 3:91–98

15. Liu B, Liu Y, Zhang W, Huang JS (2011) Hot deformation behavior of TiAl alloys prepared by blended elemental powders. *Intermetallics* 19:154–159
16. Dilip JJS, Miyajima H, Lassell A, Starr TL, Stucker B (2017) A novel method to fabricate TiAl intermetallic alloy 3D parts using additive manufacturing. *Def Technol* 13:72–76
17. Clemens BH, Kestler H (2000) Processing and applications of intermetallic γ -TiAl-based alloys. 551–570
18. Hermel W, Leitner G, Krumphold R (1980) Review of induction sintering: fundamentals and applications. *Powder Metall* 23:130–135
19. Çavdar U, Atik E, Akgül MB, Karaca H (2014) Thermal analyses for induction sintering of powder metal compacts up to sintering temperature. *Metallfiz i Noveishie Tekhnologii* 36:1247–1258
20. Çavdar U, Atik E (2014) Investigation of conventional-and induction-sintered iron and iron-based powder metal compacts. *Jom* 66:1027–1034
21. Perdrix F, Trichet MF, Bonnetien JL, Cornet M, Bigot J (2001) Influence of nitrogen on the microstructure and mechanical properties of Ti-48Al alloy. *Intermetallics* 9:147–155
22. Chai L, Chen Y, Zhang L, Lin J (2012) Effect of spark plasma sintering temperature on microstructure and mechanical properties of melt-spun TiAl alloys. *Trans Nonferrous Met Soc China* 22:528–533
23. Xiao S, Xu L, Chen Y, Yu H (2012) Microstructure and mechanical properties of TiAl-based alloy prepared by double mechanical milling and spark plasma sintering. *Trans Nonferrous Met Soc China* 22:1086–1091
24. Yang F, Kong FT, Chen YY, Xiao SL (2010) Effect of spark plasma sintering temperature on the microstructure and mechanical properties of a Ti₂AlC/TiAl composite. *J Alloys Compd* 496:462–466
25. Chen YY, Yu HB, Zhang DL, Chai LH (2009) Effect of spark plasma sintering temperature on microstructure and mechanical properties of an ultrafine grained TiAl intermetallic alloy. *Mater Sci Eng A* 525:166–173
26. Adams AG, Rahaman MN, Dutton RE (2008) Microstructure of dense thin sheets of γ -TiAl fabricated by hot isostatic pressing of tape-cast monotapes. *Mater Sci Eng A* 477:137–144
27. Limberg W, Ebel T, Pyczak F, Oehring M, Schimansky FP (2012) Influence of the sintering atmosphere on the tensile properties of MIM-processed Ti 45Al 5Nb 0.2B 0.2C. *Mater Sci Eng A* 552:323–329
28. Gerling R, Schimansky F-P, Wegmann G (2001) Metal injection moulding using intermetallic γ -TiAl alloy powder. *Adv Eng Mater* 3:387–390
29. Nadakuduru VN, Cao P, Zhang DL, Gabbitas B (2007) Ultrafine grained Ti-47Al-2Cr (at%) alloy prepared by high energy mechanical milling and hot isostatic pressing. *Adv Mater Res* 29–30:139–142

The Development of Cemented Carbide with Cobalt Composition Gradient by Powder Metallurgy Method



Rityuj Singh Parihar and Neha Verma

Abstract Functionally graded cemented tungsten carbide (FGCC) is the modern material choice for cutting tool application due to the advantage of superior combination of hardness, toughness, and wear resistance. Cemented carbide is mainly prepared by powder metallurgy method. Although several methods are available from conventional sintering, microwave sintering to state-of-art spark plasma sintering method. But, the development of desired gradient was a challenging task due to migration tendency of cobalt. Thus, the present work was aimed at the preparation of FGCC by spark plasma sintering method and characterization of developed samples for density, microstructure, hardness, and toughness. The obtained results showed that FGCC prepared in spark plasma sintering offer superior density, hardness as well as wear resistance compared to conventional as well as microwave sintering process.

Keywords Cemented carbide · Conventional sintering · Microwave sintering · Spark plasma sintering · Scanning electron microscope · Hardness

1 Introduction

Cemented carbide is a combination of tungsten carbide (WC) and cobalt (Co), wherein Co is matrix and WC works as reinforcement. In general, according to the application, Co content varies from 4 to 30% [1]. The high and low Co content leads to higher toughness and hardness, respectively. As the properties of this material depends upon the Co concentration. Thus, preparation of cemented carbide in the form of functionally graded materials (FGMs) resulted in desirable properties customization [2]. The hybrid material developed with Co composition gradient is

R. S. Parihar (✉) · N. Verma
Department of Mechanical Engineering, Shri Shankaracharya Institute of Professional Management and Technology, Raipur, India
e-mail: r.parihar@ssipmt.com

N. Verma
e-mail: n.verma@ssipmt.com

© The Author(s), under exclusive license to Springer Nature Singapore Pte Ltd. 2022
H. K. Dave et al. (eds.), *Recent Advances in Manufacturing Processes and Systems*,
Lecture Notes in Mechanical Engineering,
https://doi.org/10.1007/978-981-16-7787-8_77

called as functionally graded cemented tungsten carbide (FGCC) [3]. The FGCC can be mainly prepared by powder metallurgy method, wherein the mixture of WC and Co undergoes mixing in ball milling and followed by compaction and finally consolidation of prepared green compact by sintering method [2]. The sintering process can be performed in several ways such as, conventional sintering furnace (tube furnace) under inert atmosphere, and microwave furnace [4, 5].

In conventional sintering process, the green compact is kept inside tube furnace under inert gas atmosphere to avoid oxidation of material. Also, the preferred range of sintering temperature is 1350–1600 °C, according to the Co content [6]. However, the chances of migration of Co in green compact at the time of sintering is very high [7] and density as well as mechanical properties of the prepared material is inferior [8]. Whereas in microwave, sintering heating is performed by electromagnetic waves, wherein due to electromagnetic field, energy is transferred by interaction between molecules of elemental material. This microwave heating resulted in fast sintering and better mechanical properties compare to conventional sintering [9]. Another advantage of microwave sintering is its ability to perform sintering at temperature lower than the usual [10]. Although microwave sintering is capable of fast heating rate but still it is difficult to prepare precise and accurate gradient. Furthermore, in spark plasma sintering (SPS), concept of Joule heating by adopting pulsed electric current is adopted for sample heating and compaction as well as sintering is performed simultaneously [11]. Other advantages of SPS are high heating rate and sintering temperature lower than the usual, short sintering time, and fine grain material [12]. In SPS, high density graphite die is utilized due to its conductive nature. Furthermore, due to the high heating rate and joule heating in controlled atmosphere resulted in high density and good mechanical properties in developed material [13]. Although several works are reported on the development of cemented carbide by microwave sintering and spark plasma sintering [2], but literature on the development of symmetric composition-graded cemented carbide is not yet reported.

Thus, the presented work focused on the development of cemented carbide (WC-10 wt% Co) with symmetric composition gradient by SPS method and characterization of density by Archimedes method, microstructure by scanning electron microscope (SEM), hardness by Vickers hardness test.

2 Materials and Method

WC–Co was chosen as a material composition for development of functionally graded cutting tool material. Wherein, WC was selected as reinforcement, and Co was preferred as a binder or matrix. In symmetric FGCC, the Co composition varied from the core to the surface of the material. In the middle portion, Co content is less, whereas at the surface it was higher. In general, for cutting tool application, Co content varied from 5 to 15 wt%. Thus, in present study, also, the Co content varied from 5 to 10 wt% from surface to core of the material. The selected composition was first ball-milled for proper mixing and particles size reduction in the

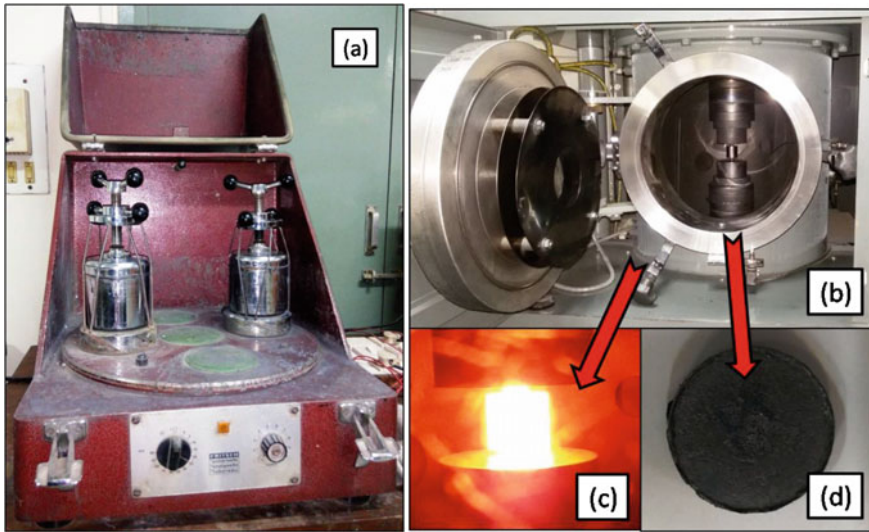


Fig. 1 a Ball milling setup, b Spark plasma sintering (SPS) machine, c Graphite die-punch assembly in heated condition, d Prepared SPSed sample

machine. This process was performed in planetary ball-mill given in Fig. 1a, and the selected parameters were 5:1 powder to ball weight ratio, 250 rpm rotational speed, and milling time of 4 h. Subsequently the milled material mixture deposited in the graphite die-punch assembly as given in Fig. 1c (heated condition). The graphite die-punch assembly was used in the spark plasma sintering (SPS) process given in Fig. 1b. The selected sintering parameters were 100 °C/min heating rate, 10 min sintering time, and 1100, 1150, and 1200 °C sintering temperature. The developed material (as in Fig. 1d) will have 3 layers, wherein composition of middle and surface layers is WC-10 and 5 wt% Co, respectively. The density of developed sample was estimated by Archimedes method, microstructure by scanning electron microscope, hardness by Vickers hardness test, and fracture toughness by indentation method.

3 Results and Discussion

3.1 Density Test on Consolidated Self-Lubricating FGCC

The average particle size before and after ball milling was 6.4 μm and 1.544 μm , respectively. Subsequently, the powdermixture was deposited inside the graphite die. The densification of FGCC in the SPS is performed by particles rearrangement, plastic flow, and liquid/solid-state sintering [8, 14]. The density of the prepared sample depends upon the sintering temperature, for 1100 °C relative density was

close to 99%. Whereas, for 1150 and 1200 °C, it was more than 99%. The highest relative density was obtained at 1200 °C (99.76%). It was observed from the figure that density of sample increases with sintering temperature due to melting of Co and liquid phase sintering. The estimated values are found in complete agreement with Sivaprahasam et al. [1] and Cha et al. [15].

3.2 Microstructure Analysis

In order to perform the microstructure characterization using developed sample using SEM, samples were sectioned using wire electro-discharge machine (WEDM). The sectioned samples were polished using emery papers and followed by polishing using diamond paste and etching by Murakami reagent. The sample was kept under the SEM, and micrograph was taken at three-layers and presented in Fig. 2. It was evident from the figure that microstructure of middle and outer or surface layers were completely different from each other. The outer layers are having more porosity as compare to middle layers due to lower content of Co. Wherein, the dark gray phases are Co, and light gray phases are WC. It was also clear that dark gray content (Co) was more at the middle compared to outer layer [1, 15]. The observed microstructure

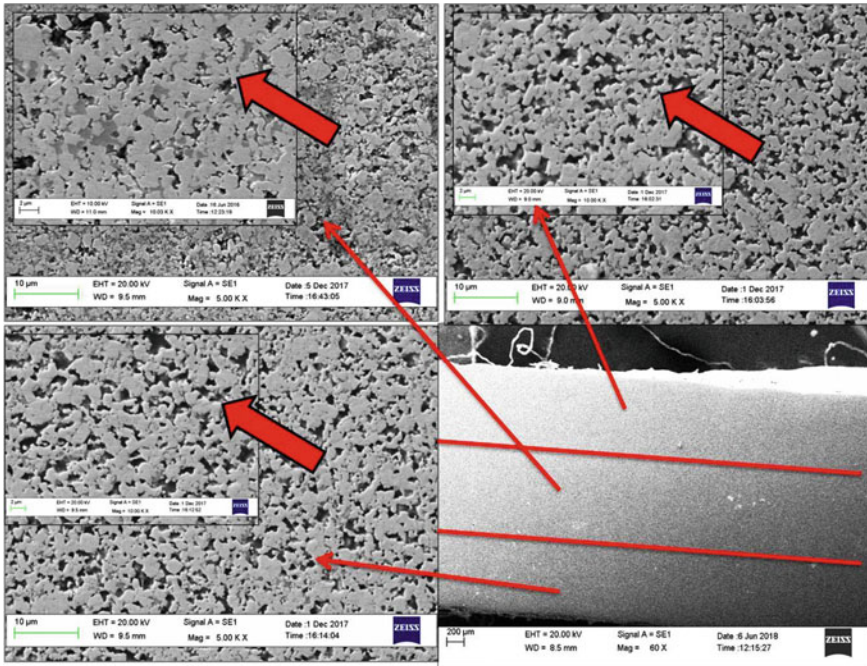


Fig. 2 SEM micrograph of SPS sample

was found identical to the work reported [1, 3, 15]. Apart from the microstructure, EDX scanning was also performed to certain the presence of deposited composition gradient.

3.3 EDX Analysis

The creation of gradient was confirmed by EDX (Electro-dispersive X-ray), and results are presented in Fig. 3. It was clearly seen that the composition gradient deposited in the die-punch assembly was completely consolidated without any migration for sintering temperature of 1100 and 1150 °C. The migration tendency of Co was controlled due to solid-state sintering and high heating rate along with lower holding time. However, at 1200 °C sintering temperature, Co started to homogenize and migrated due to presence of molten phase as well as density difference. This variation in Co composition in fabricated samples also resulted in the variation in mechanical properties.

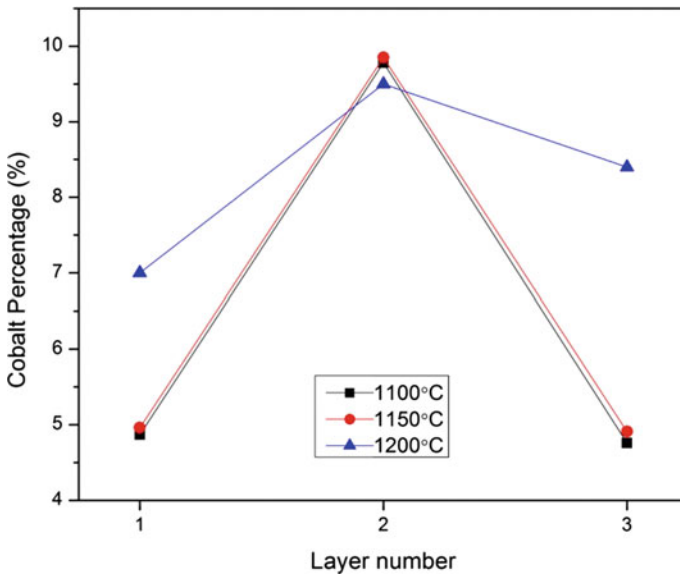


Fig. 3 Variation of Co compositions in the thickness direction

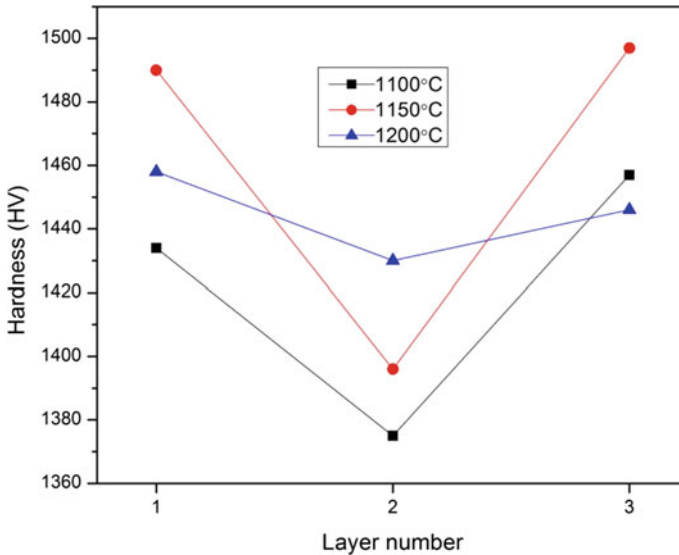


Fig. 4 Variation of hardness in the thickness direction (different layers)

3.4 Mechanical Properties of Self-Lubricating FGCC

3.4.1 Hardness

The hardness of the prepared samples was evaluated by Vickers hardness test using 9.8 N load for 10 min dwell time via diamond indenter. The indentation was taken on three-layers in the thickness direction, and results are presented in Fig. 4. It is evident that in all samples the hardness is highest at the surface and lowest at the middle portion. Additionally, increase in sintering temperature resulted in enhancement in hardness due to high density and the highest value obtained at 1150 °C. Also, it is observed that at 1200 °C variation in hardness is very less due to migration of Co while sintering process. The value of hardness was found in complete agreement with the reported work [1, 15].

3.4.2 Fracture Toughness

The fracture toughness of developed samples was estimated by using indentation method in Vickers hardness tester at 98 N load and presented in Fig. 5. It was observed that variation of Co content also resulted in variation of fracture toughness; thus, it was highest at the middle and lowest at the surface. Additionally, fracture toughness also increased with sintering temperature due to enhancement in density. The values of fracture toughness in prepared samples are found in agreement with the Sivaprahasam et al. [1] and Cha et al. [15].

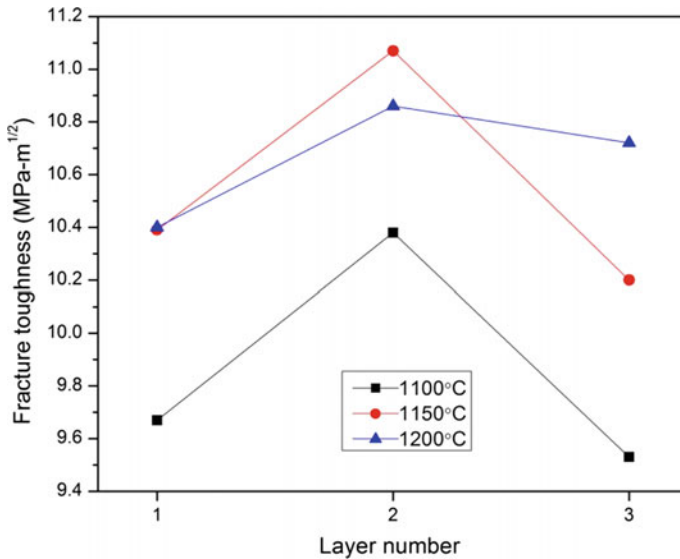


Fig. 5 Variation of fracture toughness in the thickness direction

4 Conclusion

The cemented carbide cutting tool materials were successfully prepared by using spark plasma sintering process. The migration tendency of Co was effectively suppressed by the high heating rate and less holding time while sintering. The presence of Co composition gradient was confirmed by the SEM micrograph and EDX. It was also found that at 1200 °C Co migration started; thus, 1150 °C was an optimum temperature for preparation of cemented carbide with Co composition gradient. In addition to this, prepared sample shows unique characteristics for application as cutting tool materials such as, high hardness and toughness at the surface and middle, respectively.

References

1. Sivaprahasam D, Chandrasekar SB, Sundaresan R (2007) Microstructure and mechanical properties of nanocrystalline WC-12Co consolidated by spark plasma sintering. *Int J Refract Met Hard Mater* 25:144–52. <https://doi.org/10.1016/j.ijrmhm.2006.03.008>
2. Chen J, Zhou L, Deng X, Liu W, Liu J, Ji H et al (2020) Role of Co content on the gradient microstructure evolution and mechanical properties of bilayer functionally graded cemented carbides. *Mater Chem Phys* 248:122910. <https://doi.org/10.1016/j.matchemphys.2020.122910>
3. Zhou H, Wang Z, Wang B (2020) Fabrication of WC-Co/(Ti, W)C graded cemented carbide by spark plasma sintering. *Int J Refract Met Hard Mater* 87:105141. <https://doi.org/10.1016/j.ijrmhm.2019.105141>

4. Rumman R, Chuan LC, Quinton JS, Ghomashchi R (2019) Understanding the potential of microwave sintering on WC-Co. *Int J Refract Met Hard Mater* 81:7–14. <https://doi.org/10.1016/j.ijrmhm.2019.02.007>
5. Tang S, Li P, Liu D, Li P, Niu Q (2019) Cutting performance of a functionally graded cemented carbide tool prepared by microwave heating and nitriding sintering. *High Temp Mater Process* 38:582–589. <https://doi.org/10.1515/htmp-2019-0011>
6. Wang X, Hwang KS, Koopman M, Fang ZZ, Zhang L (2013) Mechanical properties and wear resistance of functionally graded WC-Co. *Int J Refract Met Hard Mater* 36:46–51. <https://doi.org/10.1016/j.ijrmhm.2012.04.011>
7. Konyashin I, Hlawatschek S, Ries B, Mazilkin A (2016) Co drifts between cemented carbides having various WC grain sizes. *Mater Lett* 167:270–273. <https://doi.org/10.1016/j.matlet.2015.12.038>
8. Diouf S, Molinari A (2012) Densification mechanisms in spark plasma sintering: effect of particle size and pressure. *Powder Technol* 221:220–227. <https://doi.org/10.1016/j.powtec.2012.01.005>
9. Bao R, Yi J (2013) Effect of sintering atmosphere on microwave prepared WC-8wt.%Co cemented carbide. *Int J Refract Met Hard Mater* 41:315–321. <https://doi.org/10.1016/j.ijrmhm.2013.05.003>
10. Li J, Cheng J, Chen P, Chen W, Wei C (2018) Fabrication of WC-Co cemented carbides with gradient distribution of WC grain size and Co composition by lamination pressing and microwave sintering. *Ceram Int* 44:11225–11232. <https://doi.org/10.1016/j.ceramint.2018.03.162>
11. Bertolete M, Barbosa PA, de Rossi W, Fredericci C, Machado IF (2020) Mechanical characterisation and machining evaluation of ceramic cutting tools functionally graded with six layers. *Ceram Int* 46:15137–15145. <https://doi.org/10.1016/j.ceramint.2020.03.048>
12. Zhang ZH, Liu ZF, Lu JF, Shen XB, Wang FC, Wang YD (2014) The sintering mechanism in spark plasma sintering—proof of the occurrence of spark discharge. *Scr Mater* 81:56–59. <https://doi.org/10.1016/j.scriptamat.2014.03.011>
13. Ke Z, Zheng Y, Gao L, Zhou W, Zhang J, Zhang G et al (2019) Fabrication of functionally graded WC-Co cemented carbides with plate-like WC grains. *Powder Metall Met Ceram* 58:463–468. <https://doi.org/10.1007/s11106-019-00096-7>
14. Chaim R (2007) Densification mechanisms in spark plasma sintering of nanocrystalline ceramics. *Mater Sci Eng A* 443:25–32. <https://doi.org/10.1016/j.msea.2006.07.092>
15. Cha SI, Hong SH, Kim BK (2003) Spark plasma sintering behavior of nanocrystalline WC-10Co cemented carbide powders. *Mater Sci Eng A* 351:31–38. [https://doi.org/10.1016/S0921-5093\(02\)00605-6](https://doi.org/10.1016/S0921-5093(02)00605-6)

Utilizing Generative Design for Additive Manufacturing



Ioannis Ntintakis, Georgios E. Stavroulakis, Georgios Sfakianakis,
and Nikolaos Fiotodimitrakis

Abstract Over the last years, the significant progress of the Additive Manufacturing techniques gave rise to a great evolution in the designing method of mechanical components. This paper studies the utilization of the generative design in the redesigning of a $\Phi 32$ mm pneumatic cylinder mounting. The following mountings are considered: the Pivot bracket with rigid bearing AB7, the Clevis bracket MP2 base, and the Clevis bracket MP4 base. The main goal of mounts redesign is the weight minimization and the applicability for Fused Filament Fabrication (FFF/FDF) and Wire Laser Metal Deposition (W-LMD) Additive Manufacturing techniques. For FFF/FDM 3d printers the overhang angle is set to 45° and for W-LMD 3d printers the overhang angle is set to 25° . The generative design studies have been executed with the use of Autodesk Fusion 360 software. In order to understand the behavior of the initial models, a Finite Element Analysis has been performed. Then, the Generative Design studies were performed and the resulting structures were evaluated by using Finite Element Analysis again and comparison with the initial results. Due to the reciprocating linear motion of the pneumatic cylinder, two FE Analyses have been executed, one for the outward Stork and one for the return stork movement. From the results, it has been shown that a weight reduction by nearly 60% is feasible without significantly affecting the safety factor. Also, in comparison with initial models, the Von Mises Stress in the generative components did not increase more than 15%, while the increase of the total displacement did not exceed 20%.

Keywords Generative design · Additive manufacturing · FEA · Mechanical design · Weight minimization

I. Ntintakis (✉) · G. Sfakianakis · N. Fiotodimitrakis
Department of Mechanical Engineering, School of Engineer, Hellenic Mediterranean University,
71004 Estauromenos, Heraklion, Greece
e-mail: ntintakis@hmu.gr

G. E. Stavroulakis
Computational Mechanics and Optimization Laboratory, School of Production Engineering and
Management, Technical University of Crete, 73100 Chania, Greece
e-mail: gestavr@dpem.tuc.gr

1 Introduction

When developing a new product, the designers and engineers put a lot of time into the design, the choice of the material, to check the durability and the aesthetic appearance. By adopting the Generative Design (GD) methodology, the designer can now design, in less time, an object with better results and produce optimized products that take into account various constraints, such as the production method, the material, and the cost. The general scheme of a generative system is given by Bohnack et al. (Fig. 1) [1]. Nevertheless, the need for a guiding theoretical framework for generative design is now widely recognized [2, 3], especially the link to topology optimization. The iteration steps are repeated, so that, within each iteration, the GD tests the outcome structure and learning from each step output. The total number of iterations depends on the specified constraints and the final forms are designed in a unique organic shape [4].

GD approach simplifies the work of designers/engineers. The tools offered to reduce the hours required for designing a new product, while the system provides a variety of solutions that, perhaps, the designer could not think of. GD enables

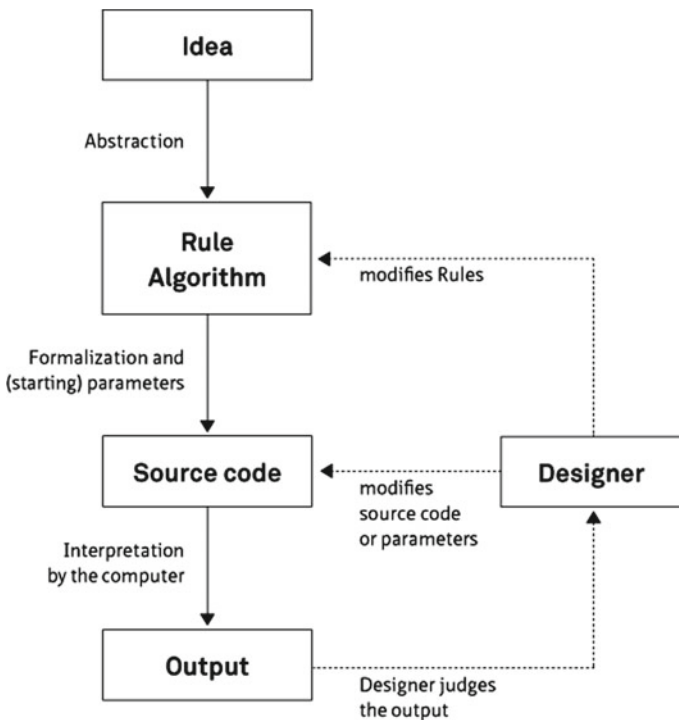


Fig. 1 The overall process of generative system

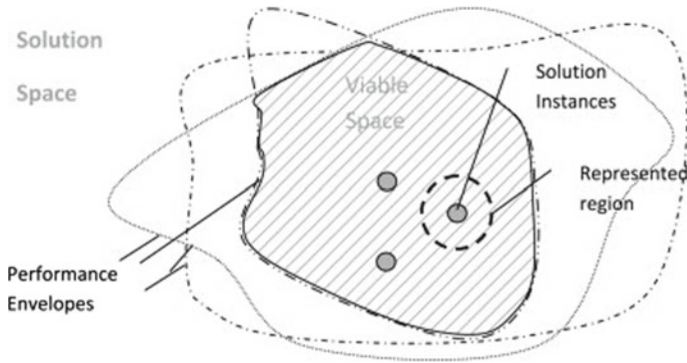


Fig. 2 Potential solution space [5]

engineers-designers to focus on the “WHAT?” of their work instead of the “HOW?” (Fig. 2). The use of GD is closely linked to the use of topology optimization.

More recently, GD has been applied in consumer products and in mechanical synthesis to pursue performance-driven design [5–9]. GD is entering rapidly into the product and parts manufacturing industry. Several GD methods are available like the Generative Design Method (GDM) which is a comprehensive CAD based generative design exploration method designed to work at all stages of the design development process—spanning from conceptual to detailed design [10].

Generative Design (GD) is an iterative design process that will generate a certain number of outputs design solutions that meet certain constraints, and a designer that will fine tune the feasible region by selecting specific output or changing input values, ranges, and distribution. GD mimics nature by using algorithms inspired by the way in which bones grow in animals. Recent research on generative design utilizes topology optimization as a design generator instead of design parameterization and develops the methods to generate numerous designs in parallel with cloud computing. The characteristics of GD are involved in: (a) is a significant tool for concept design stage, (b) appropriate for mass reduction and lightweight structures, (c) creates fully compatible models for Additive Manufacturing, (d) use of Artificial Intelligent algorithms, (e) involves Structure Topology Optimization (TO), (f) the generated models meet certain constraints and boundary conditions, (g) generate potential design solutions, (h) is a human–machine design methodology, (i) minimize the timetable for ready to use products. For the numerical results included in the current GD study, the Autodesk Fusion 360 cloud system has been used.

The potential design solutions of a GD study have to meet the manufacturing constraints of the selected Additive Manufacturing (AM) technique. In many of these techniques, additional support structures are needed. The extended use of support structures leads to increased manufacturing costs and energy waste [11]. Moreover, the design freedom is limited when complex geometries are involved due to an inability to support the stresses inherent within the manufacturing process. In this work, the Fused Filament Fabrication (FFF/FDM) and the Wire Laser Metal

Deposition (W-LMD) techniques are selected. A critical parameter to minimize the support structure volume is the overhang constraint. For FFF/FDM method, an optimal overhang angle is 45° and for W-LMD method it should be up to 25° [12].

1.1 Generative Design and Topology Optimization

Computational mechanics is the scientific area that uses numerical methods to solve engineering problems. Traditionally, the problems of engineering were solved either analytically or experimentally. Computational mechanics is the third way, the development of computers over the last few decades has enabled engineers to approach problems that were impossible to solve in the past either because of the large size or the large amount of computing time required. Computational mechanics complement analytical solutions and significantly reduce the number of required experiments. For the development of new products, it is of great importance to find the best possible topology for given design objectives and constraints at an early stage of the design process. In industrial practice, the product quality and durability have to be improved at relatively low cost. Due to the results of the GD study, the optimum topology and layout design have to be defined. This process is commonly known as Structural Optimization which is a new tool in the area of Computer Aided Engineering and belongs to the broader field of computational mechanics.

Often there is a misunderstanding between Generative Design and Topology Optimization (TO). TO create only one design that has been optimized for structural integrity based on existing criteria and GD creates multiple designs in an evolutionary way. Also, TO is suitable when one has given available space and an overall idea of how the final product should look like and requires the computer to make it as lightweight as possible. On the other hand, GD is mainly used when the whole shape is unknown so that the program will give us a lot of options, taking into consideration things like the desired material and manufacturing method. Certain similarities with repeated usage of topology optimization driven by a nature-inspired optimization technique in [13] can be identified.

In the code used in this study, GD utilizes TO treated by the Level Set Method (LSM) [14], which is widely accepted in the field of shape and topology optimization [15–17]. The potential outcomes design solutions are a combination of TO algorithm and the assigned constraints of different scenarios (e.g., different material, production method restrictions, costs, maximize stiffness, minimize mass) suggest solutions that most satisfy each of them.

1.1.1 The Level Set Method (LSM)

The LSM is a numerical technique for tracking interfaces and shapes. The level set method makes it easy to follow shapes that change topology when a shape splits in two, develops holes, or the reverse of these operations. With LSM level set model

numerical computations can be performed without having to parameterize these objects, which is called the Eulerian approach [14]. The LSM tries to minimize the objective function with the compliance of constraints for the volume of used material. The mathematical formulation of LSM is described as:

$$\begin{aligned} \min_x : c(x) &= U^T K U = \sum_{e=1}^N u_e^T k_e u_e = \sum_{e=1}^N x_e u_e^T k_l u_e \\ V(x) &= V_{\text{req}} \\ K U &= F \\ \text{Subject to : } &\begin{cases} x_e = 0 \\ x_e = 1 \end{cases} \quad \forall_e = 1, \dots, N \end{aligned}$$

where:

$x = (x_1, \dots, x_N)$ is the vector of element densities, with entries of $x_e = 0$ for a void.

element and $x_e = 1$ for a solid element, where e is the element index.

$c(x)$ is the compliance objective function.

F and U are the global force and displacement vectors, respectively.

K is the global stiffness matrix.

u_e and k_e are the element displacement vector and the element stiffness matrix for element e .

k_l is the element stiffness matrix corresponding to a solid element.

N is the total number of elements in the design domain.

$V(x)$ is the total volume of material within all solid elements.

V_{req} is the allowable material used.

1.1.2 Integration of TO and GD with Artificial Intelligent (AI)

The limitations of traditional CAD based design are less with the integration of GD with AL algorithms. This synergy offers great opportunities for designers to move away from the traditional design process and leads to new manufacturing capabilities. It is a great challenge for designers and engineers to develop rigorous and robust models which take into account many aspects of product design as aesthetic, manufacturability, production cost, engineering performance, etc. New design tools describe an initial combination of a generative design and an associative modeling system using XML models [18]. A new approach for GD is the combination with Deep Learning (DL). Relative work presents the need and effectiveness of adopting deep learning for generative design research areas. An AI system based on deep generative design can generate numerous design options which are not only aesthetic but also optimized for engineering performance [19].

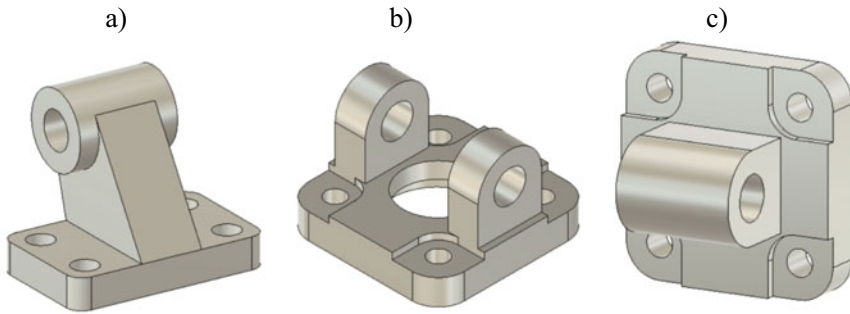


Fig. 3 The initial models of the three mounting components, **a** Pivot bracket with rigid bearing AB7, **b** Clevis bracket MP2, and **c** Clevis bracket MP4

Table 1 FEA results of the initial models

Type of mount	Outward stork		Return stork	
	Max Von Misses stress (MPa)	Max displacement (mm)	Max Von Misses stress (MPa)	Displacement (mm)
Pivot bracket	79.6	0.044	79.5	0.044
Clevis bracket MP2	23.3	0.005	22.5	0.0048
Clevis bracket MP4	25.86	0.047	25.2	0.046

2 Finite Element Analysis

The initial models of standard pneumatic cylinders with detachable mountings are considered conforming to ISO 15552 specification (Fig. 3). In order to evaluate the initial model’s behavior with the generative models, we are going to compare the FEA results between the initials and the generative models. The results from FE Analysis for outward stork and return stork linear motion are presented in Table 1.

3 Generative Design Study

A generative study is a set of data that describes a design problem one wants to solve using generative design. The GD flowcharts start from the input of specific design objectives such as functional, manufacturing, and mechanical requirements. Then follows the definition of boundary conditions, definition of material properties, load cases, and displacement restraints. Once the study is set up a set of designs will be generated that meet these requirements. The purpose of the current study is

to redesign the pneumatic cylinder mounts in order to minimize the weight of the model without significantly affecting the safety factor.

3.1 Define Objectives

Pneumatic cylinders are very common mechanical devices that use the power of compressed gas to produce a force in a reciprocating linear motion. In current study, we execute GD analysis for three pneumatic cylinder mountings in order to minimize their weight (Fig. 3). The mounting components are made of aluminum alloy (Table 2).

Generative design study allows to specify manufacturing constraints that outcomes should satisfy. In current study, the manufacturing constraints are set for FFF/FDM and for W-LMD additive manufacturing techniques. Especially, the overhang angle should be 45° for FFF and 25° for W-LMD, also the minimum wall thickness is set to 1 mm.

After the manufacturing constraints, we define the behavior of each 3d body during the GD study, there are available three different bodies categories for this reason. The first is called preserve geometry, the second is called starting shape and the third is the obstacle geometry. As preserve geometry is defined the model bodies that will keep their initial shape. These bodies should represent the minimum geometry that is needed to be present in the final shape of our design. It should include sections of geometry that are essential for the performance and functionality of the design. A preserve geometry can include: (a) connection to attach a design to other objects, like bolt holes, (b) a part of the design you interact with. Any loads and other constraints are defined on preserve geometry. At least one body of the design space must be defined as preserve geometry. In our study, perverse geometry has defined the holes that support bolts, bearing, and axes. After preserve geometries, we assign the starting shape bodies. As starting shape is defined the design space is predefined by the initial shape of the model. So, the GD study starts with this shape in the initial stage of the design process. The outcome generation is performed based on this shape. The selected starting shape is in contact with the perverse geometry that we previously defined. Finally, we define the obstacle geometry bodies. As obstacle geometry is assigned bodies that we want to avoid in the design. They represent empty spaces where material is not created during the generation of outcomes (Fig. 4).

Table 2 GD material properties

Young's modulus (GPa)	Poisson's ratio	Yield strength (MPa)	Tensile strength (MPa)	Density (g/cm ³)
68,900	0.33	275,000	310,000	2700

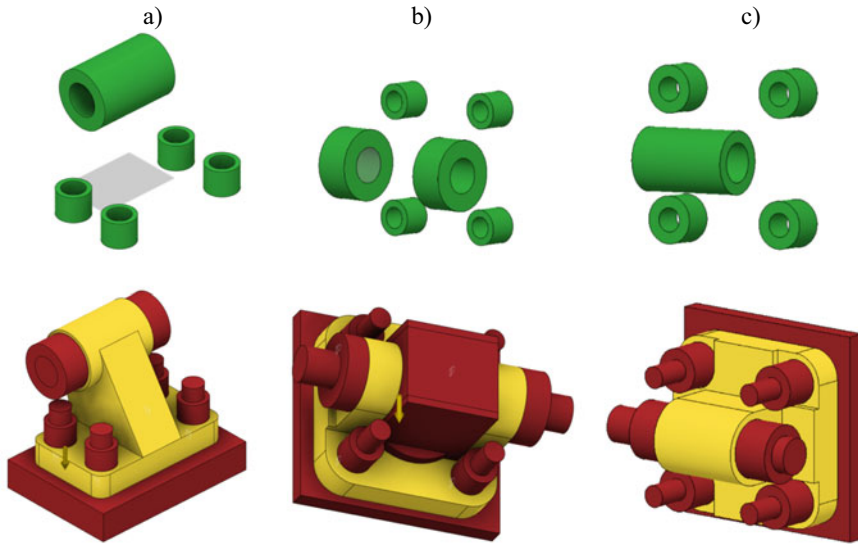


Fig. 4 The assigned perverse geometry displays in green color, the starting geometry displays in yellow color, and the obstacle geometry displays in red color for each model

Structural loads and constraints are applied to the preserve geometry only. Because of the cylinder reciprocating linear motion, we set two different load cases. In the outward stork motion is 804 N and in return stork is 691 N. At the bolt holes, the structural fixed constraints are applied.

4 Results & Discussion

4.1 Generative Models for FFF/FDM 3D Printers

A Generative Design study creates lots of designs in an evolutionary way. According to GD flowchart, the designer judges the outcomes, if the designer does not accept the potential solutions, he or she will change the source code and the parameters study and will run the algorithm again (Fig. 1). From the study results, we obtain a satisfying number of outputs to judge (Fig. 5). During the judge phase, we select the most appropriate solutions for further evaluation (Fig. 6). These design solutions have been selected because they satisfy the main design criteria which is the minimum weight. Also, the selected design solutions are able to be produced with the use of FFF technique. Then after the results of FEA for each generative model (Table 4), we evaluate the generative models and compare them with the initial models.

The main design criterion is to minimize the weight of the three models compared with the initial models, Table 3 presents the weights of the initial and generative

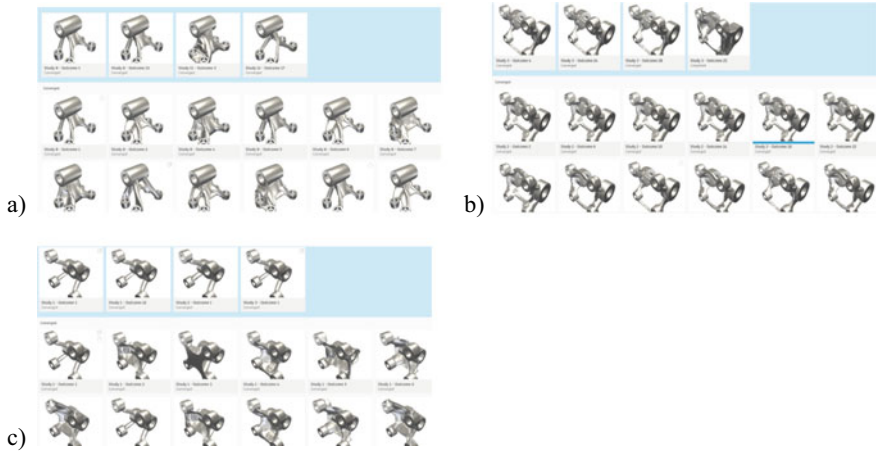


Fig. 5 Potential design solutions outcomes for the components **a** Pivot bracket with rigid bearing AB7, **b** Clevis bracket MP2 and **c** Clevis bracket MP4

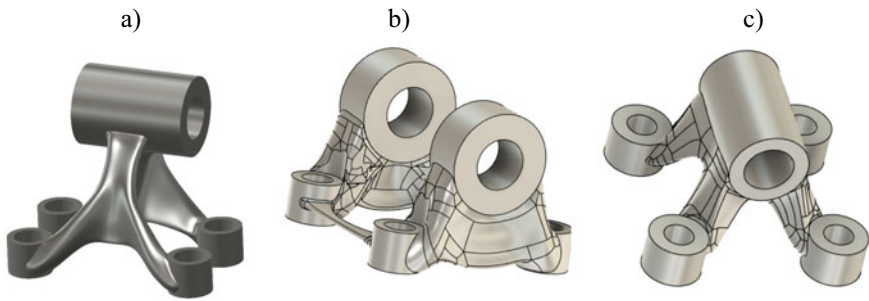


Fig. 6 The selected design solution for each component for further evaluation, **a** Pivot bracket with rigid bearing AB7, **b** Clevis bracket MP2, and **c** Clevis bracket MP4

Table 3 Weight comparison between initial and generative models

Type of mount	Initial model weight (gr)	Generative model weight (gr)	Percentage change (%)
Pivot bracket	69.19	24.58	64.5
Clevis bracket MP2	65.72	25.55	61.1
Clevis bracket MP4	58.43	30.63	61.1

Table 4 FEA results of the generative models

Type of mount	Outward stork		Return stork	
	Max Von Misses stress (MPa)	Max displacement (mm)	Max Von Misses stress (MPa)	Displacement (mm)
Pivot bracket	123.7	0.083	153.8	0.1039
Clevis bracket MP2	85.43	0.0081	85.44	0.0081
Clevis bracket MP4	19.11	0.0025	19.11	0.0025

models.

In generative Pivot bracket model, the Von Misses Stress is 123.7 MPa in outward stork and 153.8 MPa in return stock (Table 4). The increment of Von Misses Stress is higher than the initial model, and there are two reasons which cause this behavior. The first is the significant reduction of model weight which increases the flexibility of the model. The second reason is the assigned fix constraints on the bolts holes where there is the maximum stress. On the rest body, the highest stress value is not up to 30 MPa (Fig. 7). Furthermore, the weight decrease is nearly equal to 60% (Table 3) and the minimum safety factor value is 2.2 on the area of the bolt’s holes, while in the rest areas of the model the safety factor is significantly higher (Fig. 8).

On the generative Clevis bracket MP2 model the Von Misses Stress is 85.43 MPa in outward stork and 85.44 MPa in return stock. The shape of the model changes significantly and has certain similarities to a more organic shape. The total displacement increased also as a result of the higher elastic behavior. On the generative Clevis bracket MP4 model the Von Misses Stress in outward stork and in return stock is 19.11 and the displacement is 0.0025 mm MPa (Table 4). Although the weight of the model has been reduced by 61.1% it is stiffer than the original model.

4.2 *Generative Models for Wire Laser Metal Deposition (W-LMD) 3D Printer*

The results of Sect. 4.1 are referred to as generative models for FFF 3d printers. In this section, the generative models for W-LMD 3d printers are presented. According to manufacturing constraints of the W-LMD additive manufacturing technique, the overhang angle should be up to 25°. This reduction in the maximum overhang angle leads to changes in the structure of the generative models (Fig. 9). The new models are characterized as rigid and robust (Table 5). In comparison with the generative models of Sect. 4.1, the new structures are stiffer near to the areas of the maximum overhang angles.

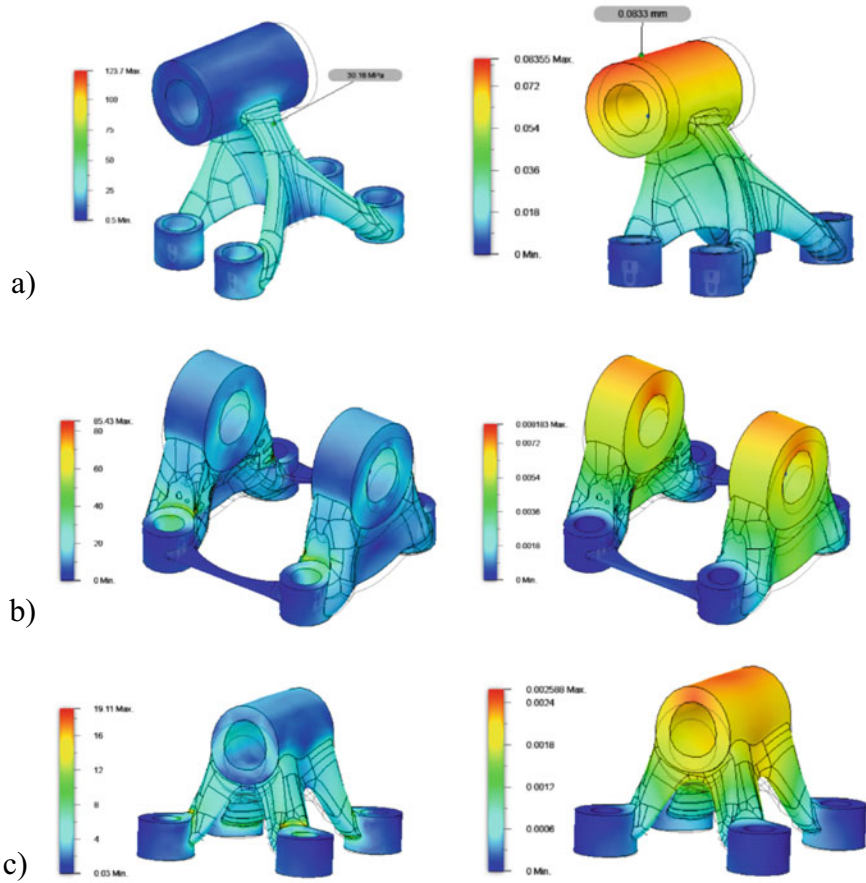


Fig. 7 Results of Von Misses stress and the displacement for generative models, **a** Pivot bracket model becomes more elastic, the Von Misses stress is increased significantly on the bottom edge of the bolt holes, also increased the displacement, **b** in Clevis bracket MP2 stress and displacement increased also, **c** in Clevis bracket MP4 the Von Misses stress and the displacement decreased

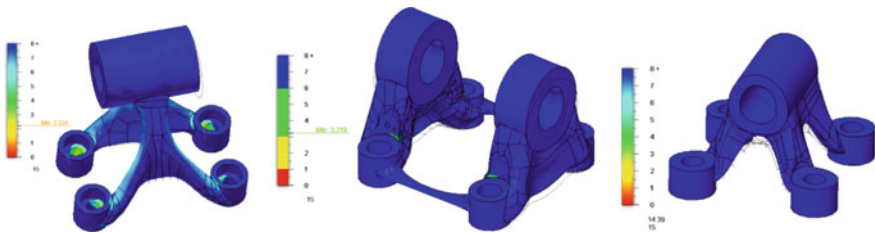


Fig. 8 The minimum safety factor on Pivot bracket model (on the left) is 2.2, on Clevis bracket MP2 is 3.2 and on Clevis bracket, MP4 is 14.39

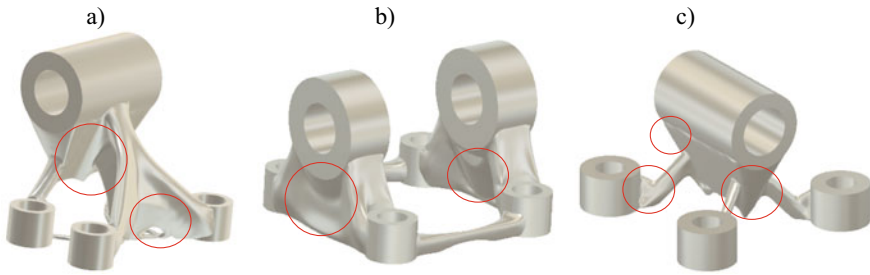


Fig. 9 a Pivot bracket with rigid bearing AB7, b Clevis bracket MP2 and c Clevis bracket MP4. Compared with the generative moles for FFF printers there are significant changes to the structures of the new generative models in the mentioned areas mainly

Table 5 Characteristics of generative models for W-LMD 3d printer

Type of mount	Max Von Misses stress (MPa)	Max displacement (mm)	Mass (gr)	Min factor of safety
Pivot bracket	91.6	0.11	27	3.0
Clevis bracket MP2	101.7	0.01	28	2.7
Clevis bracket MP4	137.5	0.04	22	2.0

5 Conclusion

Even though Generative Design is not a new design methodology, it has become increasingly popular in recent years due to the significant achievements of Additive Manufacturing techniques that enable the production of organic and shape models with high complexity. Generative design study allows to specify manufacturing constraints that outcomes should satisfied. For each option selected, the designer obtains a set of outcomes showing the design problem solving with that manufacturing method in mind. In current study, the manufacturing constraints are different for FFF and W-LMD Additive Manufacturing techniques. A critical parameter to minimize the support structure volume is the overhang angle constraint. For FFF models the overhang angle is set to 45° and for W-LMD set to 25°. Compared to the generative models of FFF and W-LMD there are significant changes in the structures from the different overhang angles. The criterion to redesign the three components is weight reduction. This goal was achieved for all generative models, the weight reduced about 60% without significantly affecting the safety factor.

References

1. Bohnacker H, Laub J, Gross B (2012) *Generative design: visualize, program, and create with processing*. Princeton Architectural Press
2. Caldas L, Duarte J (2004) Implementational issues in generative design systems. In: First international conference on design computing and cognition
3. Chase SC (2005) Generative design tools for novice designers: issues for selection. *Autom Constr* 14(6):689–698
4. McKnight M (2017) Generative design: what it is? How is it being used? Why it's a game changer. *KnE Eng* 2(2):176–181
5. Tsavdaridis KD, Kingman JJ, Toropov VV (2015) Application of structural topology optimisation to perforated steel beams. *Comput Struct* 158:108–123
6. Buonamici F, Carfagni M, Furferi R, Volpe Y, Governi L (2021) Generative design: an explorative study. *Comput Aided Des Appl* 18(1)
7. Ntintakis I, Stavroulakis GE (2020) Progress and recent trends in generative design. In: MATEC web of conferences, vol 318. EDP Sciences, p 01006
8. Ntintakis I, Stavroulakis GE, Plakia N (2020) Topology optimization by the use of 3D printing technology in the product design process. *HighTech Innov J* 1(4):161–171
9. Meriç LH (2021) *Artificial intelligence-aided product design practices*, Ankara
10. Krish S (2011) A practical generative design method. *Comput Aided Des* 43(1):88–100
11. Jiang J, Xu X, Stringer J (2018) Support structures for additive manufacturing: a review. *J Manuf Mater Process* 2(4):64
12. Zapf H, Bendig N, Möller M, Emmelmann C (2017) Design recommendations for laser metal deposition of thin wall structures in Ti–Al6–V4. In: LiM-Lasers in manufacturing conference, München
13. Kaminakis N, Stavroulakis GE (2012) Topology optimization for compliant mechanisms, using evolutionary-hybrid algorithms and application to the design of auxetic materials. *Compos Part B: Eng* 43(6):2655–2668
14. Osher S, Sethian JA (1988) Fronts propagating with curvature-dependent speed: algorithms based on Hamilton-Jacobi formulations. *J Comput Phys* 79(1):12–49
15. Allaire G, Jouve F (2005) A level-set method for vibration and multiple loads structural optimization. *Comput Methods Appl Mech Eng* 194(30–33):3269–3290
16. Allaire G, Jouve F, Toader AM (2004) Structural optimization using sensitivity analysis and a level-set method. *J Comput Phys* 194(1):363–393
17. Wang MY, Wang X, Guo D (2003) A level set method for structural topology optimization. *Comput Methods Appl Mech Eng* 192(1–2):227–246
18. Shea K, Aish R, Gourtovaia M (2005) Towards integrated performance-driven generative design tools. *Autom Constr* 14(2):253–264
19. Oh S, Jung Y, Kim S, Lee I, Kang N (2019) Deep generative design: integration of topology optimization and generative models. *J Mech Des* 141(11)

Vision-Based Object Classification Using Deep Learning for Mixed Palletizing Operation in an Automated Warehouse Environment



Anubhav Dinesh Patel and Abhra Roy Chowdhury

Abstract Present object identification and classification methods in warehouse automation either require a tedious calibration process or run at a speed that is slow for real time application. This research paper proposes a computer vision-based method using a deep convolutional neural learning network to calculate dimensions of 5 distinct objects found in an automated robot warehouse and classify them using images taken from a camera for the purpose of mixed palletizing inside warehouses. It achieved a classification accuracy of 98.94% on the machine parts images dataset created by the authors comprising more than 1450 images by utilizing transfer learning and data augmentation. The employed method ResNet-50 uses a combination of residual learning and deep architecture parsing called residual network architecture. The proposed method for extracting object dimensions has an error rate of 6.492% on average and it runs at 250 frames per second, therefore it is also suitable for applications in automated warehouses.

Keywords Convolutional neural networks · Deep learning · ResNet-50 · Computer vision · Object classification · Warehouse automation · Palletization

1 Introduction

Warehouse automation techniques have the ability to improve efficiency as well as the throughput of logistics operations while also reducing costs. Many big retailers like Walmart, Ocado, and Amazon are working towards it [1]. Automated storage and retrieval systems in warehouses can reduce costs by decreasing manual errors, increasing the speed of operations, and increasing storage density [2–4]. Barcode

A. D. Patel (✉)

Department of Computer Science and Engineering, Indian Institute of Information Technology Kalyani, Kalyani, West Bengal, India

A. R. Chowdhury

Division of Mechanical Sciences, Centre for Product Development and Manufacturing, Indian Institute of Science, Bangalore, India

e-mail: abhra@iisc.ac.in

[5, 6] and RFID [7] tags are typical ways to identify the incoming/outgoing items but both of them suffer from limitations [8]. Barcodes easily get damaged and most barcode scanners require manual operation. RFID tags have limited lifetime and both RFID tags and scanners are costly [8]. In a typical warehouse, incoming items are placed on pallets which are then stored on racks [9]. Manual palletizing is a very labor-intensive task and often needs a large number of workers [4]. It is hard to find enough people to perform such works [10]. Automating palletizing process can be very beneficial. The process of stacking items of different dimensions on a pallet is referred to as mixed palletizing [11]. Mixed palletizing, can benefit modern warehouse which needs to store multiple categories of items. To perform mixed palletization, robot needs to identify dimensions of incoming items and place them according to a precomputed palletizing pattern which is made specifically for each warehouse/production plant [11].

The authors decided to work on the problem of automating palletization operation for transportation of manufacturing components from one location to another when they faced it at the Common Engineer Facility Center (CEFC) Smart Factory facility at Indian Institute of Science (IISc) aimed at demonstrating and offering startups and MSMEs robot automation solutions. This paper presents a vision-based approach for calculating the dimensions of incoming items from an image taken from a 2D camera.

The remainder of the paper is structured in the following way: Related works are presented in Sect. 2. An overview of the method is described in Sect. 3. Sections 4, 5, 6 describe the steps of the method in detail. Section 7 describes the calibration process. Experiments are described in Sect. 8. Section 9 describes the CNN model used for classification and the conclusion is presented in Sect. 10.

2 Related Works

Extracting dimensions of real objects in a given scene is a well-studied problem in robotic vision. These dimensions can be used by the robot for making decisions, localizing manipulators, path planning, collision prevention, and object classification [12]. There is two class of approaches for measuring dimensions: contact and non-contact. For non-contact measurement various methods have been proposed such as [12–16]. The method proposed in [12] utilizes RGB-D images from Microsoft Kinect camera and calculates real world dimensions of an object by using a dynamic resolution matrix. The method produces an accuracy of 90–95% but requires manual segmentation of the object from the image. Fan et al. [15] produce a high accuracy of 98% by using a costly 3D laser camera to create a point cloud data image. The object is then extracted from this point cloud data image by filtering with both Statistical Outlier Removal (SOR) and Voxel Grid Removal (VGR) followed by segmentation with both Random Sample Consensus (RANSAC) and Euclidean clustering. The main drawback of the method is the cost.

Unlike the above methods, [13, 14, 16] all use a 2D image to calculate the dimensions. Kainz et al. [16] calculate the dimensions with an error rate of about 10% but assume that an image of the scene without the object, along with the height of the camera is available. Mane et al. [13] propose a cost-effective method with an average error rate of 2.46% but requires a tedious calibration process which includes drawing equidistant lines on the background. Othman et al. [14] propose a method with an accuracy of 98% but runs at only 4 frames per second. This paper presents a method that uses a single 2D camera with a simple and quick calibration process and runs at a significantly higher speed.

3 Method Overview

This section describes the assumptions made by the authors and briefly describes the steps in the method. The next sections describe each step of the method in detail. The assumptions made were as follows:

1. The camera coordinates are fixed.
2. The background behind the image is composed of a single color and this color is different from the primary color of the object. References [13, 14] makes a similar assumption.

The paper proposes two methods—one for classification of object given an image and other for extracting dimensions of an object present in an image. The proposed dimension extraction method consists of multiple steps. The steps in the method are as follows:

1. Convert the input image into HSV color space (Sect. 4.1).
2. Color Threshold the HSV image for the color range of the background (Sect. 4.2). The color range of the background is calculated during the calibration process (Sect. 7).
3. Apply Gaussian Blur on the image (Sect. 5.1).
4. Perform Adaptive Thresholding on the image (Sect. 5.2).
5. Apply Erosion Morphological Operation (Sect. 5.3).

The proposed object classification method utilizes Convolutional Neural Network and transfers learning.

4 Background Removal

4.1 HSV Color Space

A color space is a mathematical model describing the way to represent color as a tuple of numbers, with an interpretation/description associated with each component

of the tuple. The images were converted into HSV [17] color space from RGB color space since in RGB color space the color and intensity information are mixed which is not suitable for image segmentation [18].

4.2 Color Thresholding

Image segmentation is the process of dividing an image into different regions based on certain criteria. Thresholding is one of the ways to perform image segmentation. Color thresholding divides the image into regions based on color information [19, 20]. Color thresholding is performed in the method to extract the object from the background. During the calibration process, the range of HSV components belonging to the background is determined. A pixel is defined as a part of object if its three HSV components do not all lie within this range (Fig. 1).

$$\forall(x, y) : 0 \leq x \leq W \text{ and } 0 \leq y \leq H$$

$$\text{img}(x, y) = \begin{cases} 0 & \text{if } H_0 \leq h \leq H_1, S_0 \leq s \leq S_1, V_0 \leq v \leq V_1 \\ 1 & \text{otherwise} \end{cases} \quad (1)$$

where

- W width of the image.
- H height of the image.
- h hue of the pixel.
- s saturation of the pixel.
- v value of the pixel.

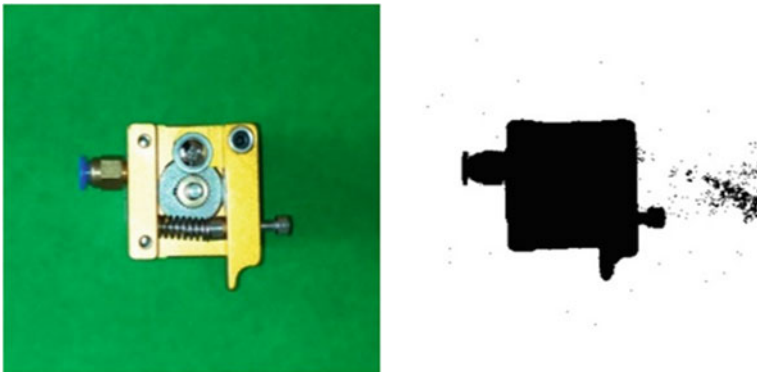


Fig. 1 Result of color thresholding, original image on the left-hand side and the final image on the right

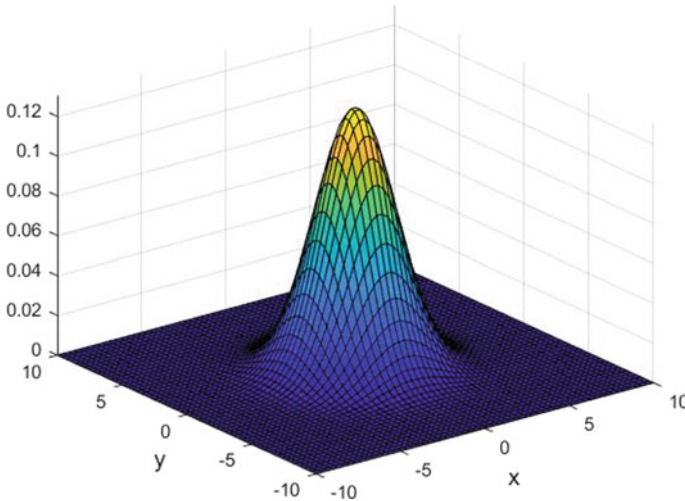


Fig. 2 2D Gaussian function of Eq. (2) with $\sigma = 1.1$

- $[H_0, H_1]$ range of H component of the background.
- $[S_0, S_1]$ range of S component of the background.
- $[V_0, V_1]$ range of V component of the background.

5 Finding Object Boundary

5.1 Gaussian Blur

Gaussian Blurring/Smoothing is a procedure to blur images and remove noise [21]. It involves convoluting an image with a gaussian kernel. Gaussian kernel coefficients are sampled from the 2D Gaussian function. A 5×5 Gaussian kernel with $\sigma = 1.1$ was used in the method (Fig. 2).

$$G(x, y) = \frac{1}{2\pi\sigma^2} e^{-\frac{(x^2+y^2)}{2\pi\sigma^2}} \tag{2}$$

5.2 Adaptive Thresholding

Unlike regular thresholding which uses a global threshold value, adaptive thresholding uses a different threshold value $T(x, y)$ for each pixel in the image [22]. $T(x, y)$ can be calculated in multiple ways. The method utilizes gaussian weighted

mean of 11×11 region around the pixel location (represented by $WA(x, y)$ in equation below) to calculate the thresholding value for each pixel. A constant number $C = 2$ was subtracted from $WA(x, y)$ to obtain $T(x, y)$.

$$T(x, y) = WA(x, y) - C \tag{3}$$

$$img(x, y) = \begin{cases} 1 & \text{if } src(x, y) > T(x, y) \\ 0 & \text{otherwise} \end{cases} \tag{4}$$

5.3 Erosion Morphological Operation

Erosion is a morphological operation in which a kernel M is scanned over the image, the minimum pixel value overlapped by M is computed and the image pixel under the anchor point is replaced with this minimal value [23]. The method utilizes a 3×3 matrix of all ones as M (Fig. 3).

6 Calculating Real Dimensions

For calculating the real dimension of the object, we first perform contour finding followed by multiplying sides with conversion factor.

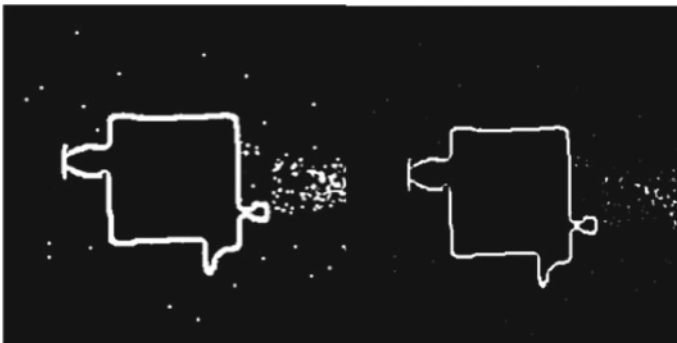


Fig. 3 Result of erosion. Original image on the left and final image on the right

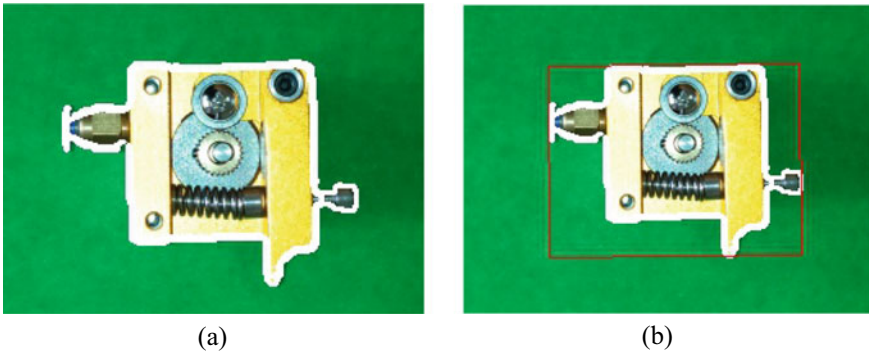


Fig. 4 **a** Contour (represented in white) created by the object boundary. **b** A rotated rectangle of the minimum area enclosing all points on the contour (represented in red)

6.1 Contour Finding

Contours are curves joining all the continuous points (along the boundary), having same color or intensity [24]. Contours provide information about the shape of the object [25]. The algorithm described in [26] was used to find the largest contour. A rotated rectangle of the minimum area enclosing all points on the contour were found. The sides of this rectangle (represented by D_1 and D_2) were calculated (Fig. 4).

6.2 Calculating Real Dimensions

The real dimensions of the object (represented by R_1 and R_2) were calculated by multiplying the sides of the minimum area rectangle (D_1 and D_2) with the Conversion Factor (CF) obtained during the calibration process.

$$R_1 = D_1 * CF \tag{5}$$

$$R_2 = D_2 * CF \tag{6}$$

7 Calibration Process

The calibration process involves determining the range of HSV components of the background and the Conversion Factor (CF)—ratio of distance of two points in the real world to the distance of same two points in the image. For determining

the range of HSV components, an image without any object in it (with only background) was taken and the minimum and maximum value of all 3 components in the entire image was calculated. Let's represent the determined maximum value of hue, saturation value as H_1, S_1 and V_1 respectively. Similarly, let us represent the determined minimum value of hue, saturation, and value as H_0, S_0 and V_0 respectively. H_1, S_1, V_1, H_0, S_0 and V_0 are used in the color thresholding step of the algorithm (Fig. 5).

For calculating the Conversion Factor (CF), an object with known dimensions (larger dimension represented by OD_1 and smaller by OD_2) was taken. Using the algorithm, D_1 and D_2 ($D_1 \geq D_2$), i.e. the length of sides of the rectangular bounding box was calculated. Then the Conversion Factor (CF) was calculated by (Figs. 6 and 7)

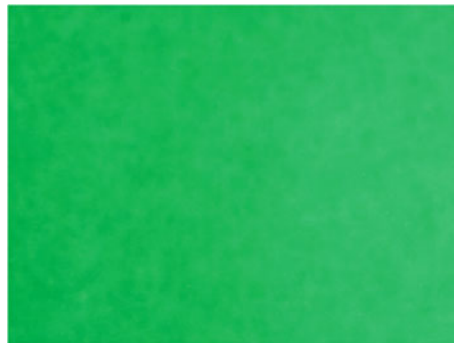


Fig. 5 Image of the background used for calibration

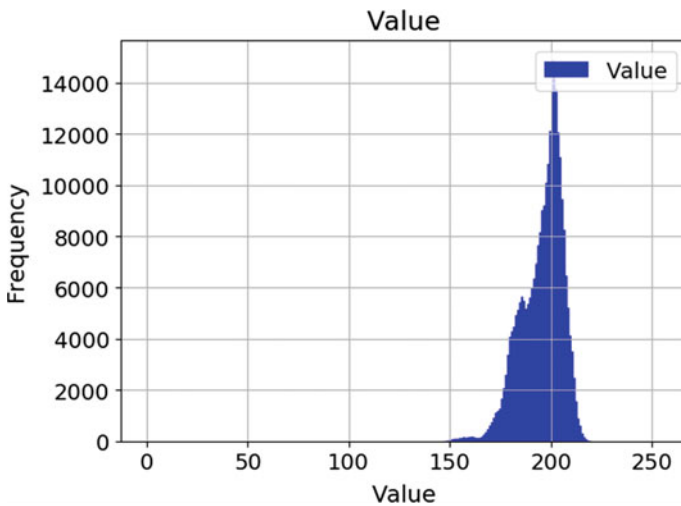


Fig. 6 Histogram of value component of all pixels

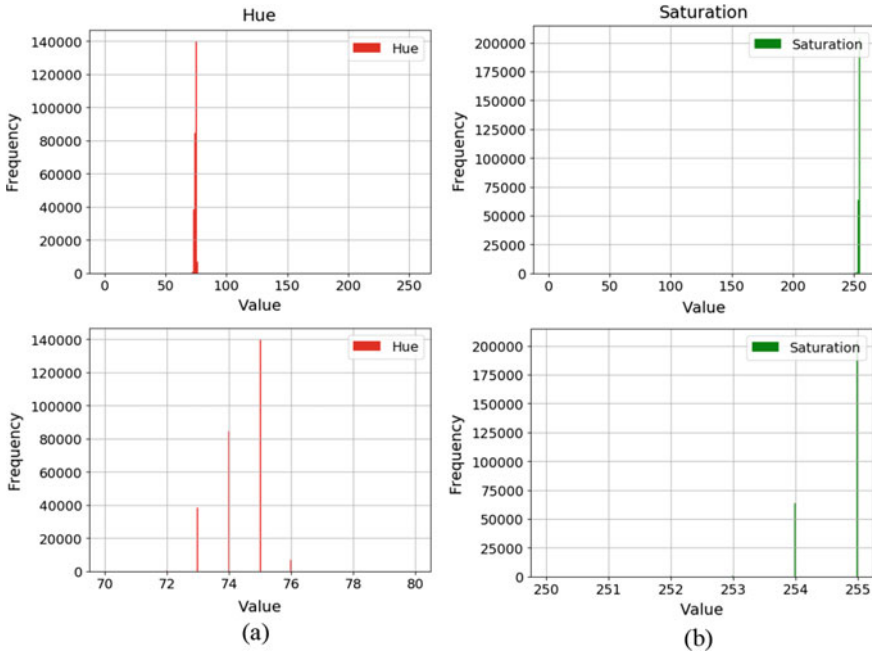


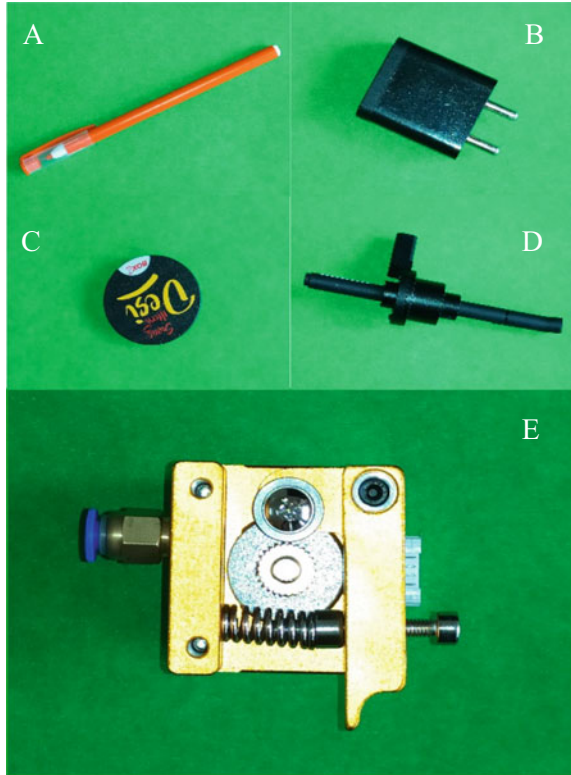
Fig. 7 **a** Histogram of Hue (top) and same histogram zoomed around 70–80 range (bottom). **b** Histogram of Saturation (top) and same histogram zoomed around 250–255 range (bottom)

$$CF = \frac{OD_1}{D_1} \quad \text{or} \quad CF = \frac{OD_2}{D_2} \tag{7}$$

8 Experiments

For evaluating the algorithm, images taken from a 48 megapixels camera (with f/1.8 aperture lens and GM1 sensor) in indoor conditions were used. The camera was placed at a height of forty centimeters and objects were placed beneath it. The algorithm was made to run on an Intel Core i5-8250U CPU with 8 GB of ram. The experiments were performed with 5 different objects found in a robot warehouse environment—pen, mobile charger, mobile pop holder, Dobot [27] Magician’s pen end effector, and Dobot [27] 3D printing kit’s extruder. The equipment present at the CEFC Smart Factory facility of the Indian Institute of Science was used to perform the experiment. See Fig. 8.

Fig. 8 a Pen, b Mobile charger, c Mobile pop holder, d Dobot magician's pen end effector, e Dobot 3D printing Kit's extruder



8.1 Error in Prediction

Setup. Percentage error (PE) is defined as ratio of absolute error in prediction to true dimension, multiplied by 100% (8). Average percentage error (APE) is defined as the mean percentage error on all images (9). For each of the 5 objects, the following procedure was performed—first, the real dimensions of the object were used to calculate the Conversion Factor (CF) then the algorithm was used to predict dimensions on 25 images of each object (total $25 \times 5 = 125$ images). The object wise average percentage error in prediction was noted.

$$PE = \frac{|p - a|}{a} * 100\% \quad (8)$$

$$\text{Average PE(APE)} = \frac{\sum_{i=1}^N PE_i}{N} \quad (9)$$

where p is the predicted dimension, a is the actual dimension, PE_i is the percentage error in prediction for i th image and N is the total number of images (here $N = 125$).

Result. The average percentage error in all 125 images was **6.492%**. Among all the objects, when Pen was used for calculating CF during calibration, the average percentage error in prediction on all 125 images, was minimum at **4.514%**. See Figs. 9 and 10.

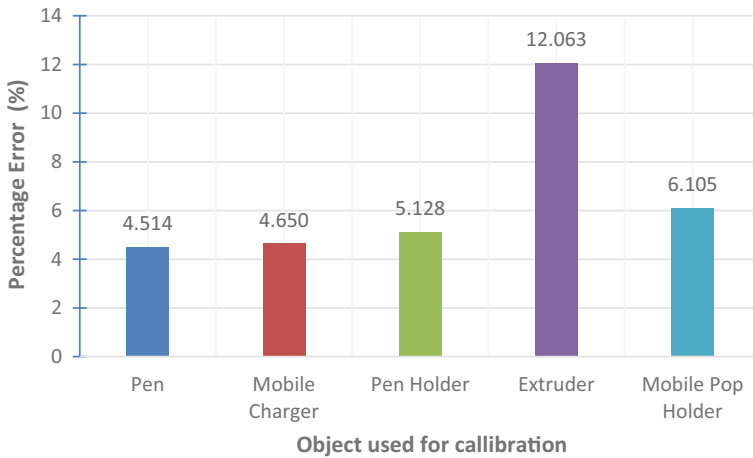


Fig. 9 Average of percentage error in all 125 images when different objects were used for calculating CF

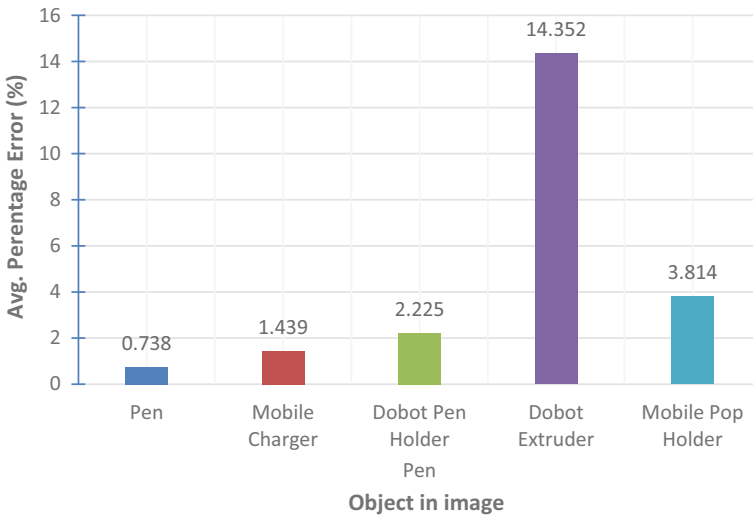


Fig. 10 Percentage error in prediction when the pen was used for calculating the conversion factor

When robot Extruder was used for calculating CF, the average percentage error in all 125 images was at **12.063%**, the maximum. This likely resulted because of the large difference in height of the Extruder (55 mm) and other objects (mean height of other objects were 8.75 mm), which caused the Extruder to appear bigger in the image than it actually was. Therefore, for the best results, the object with height closest to the mean height of all the objects should be chosen for calculating CF (Fig. 11; Table 1).

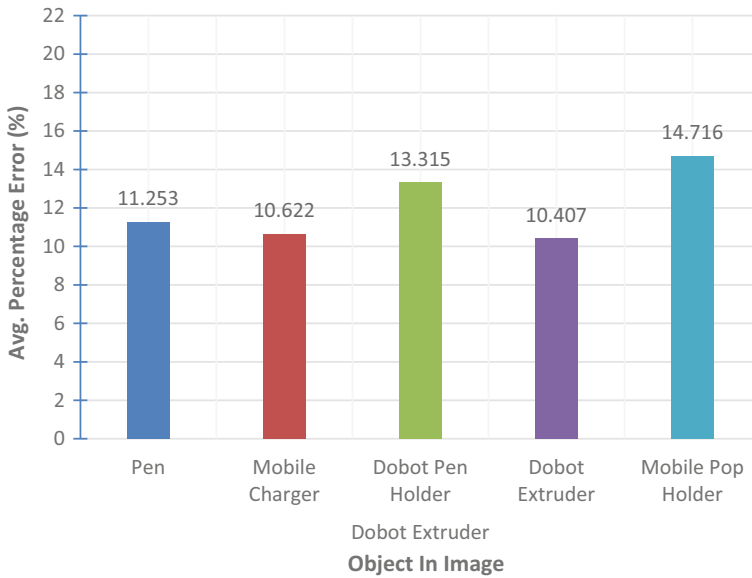


Fig. 11 Percentage error in prediction when the Dobot extruder was used for calculating the conversion factor

Table 1 Object used to calculate CF and the error it yielded in prediction on all objects

Object used to calculate CF	Object in image				
	Pen	Mobile charger	Dobot pen holder	Dobot extruder	Mobile pop holder
Pen	0.738%	1.439%	2.225%	14.352%	3.814%
Mobile charger	0.900%	1.277%	2.904%	13.697%	4.474%
Dobot pen holder	2.417%	3.224%	1.200%	16.590%	2.209%
Dobot extruder	11.253%	10.622%	13.315%	10.407%	14.716%
Mobile pop holder	4.039%	4.780%	1.770%	18.437%	1.499%

8.2 Speed

Setup. Prediction time is defined as the compute time/run time the method takes to make prediction on an image. Average prediction time is defined as the mean prediction time on all images. The speed of the algorithm in frames per second (FPS) is expressed as the inverse of average prediction time (10).

$$FPS = \frac{1}{p} \tag{10}$$

where p is the average prediction time. The algorithm was made to run on 125 images (25 images per object) and for images of each object, the average prediction time was noted (Table 2).

Result. The algorithm roughly took the same time for all the objects, around **4 ms**. The algorithm can be made to run at **250 FPS** (Fig. 12).

Table 2 Time taken by the algorithm for each object

Object	Avg. time taken by the algorithm (milliseconds)
Pen	3.8938
Mobile charger	3.9956
Pen holder	3.8872
Extruder	4.0914
Mobile pop holder	3.8878

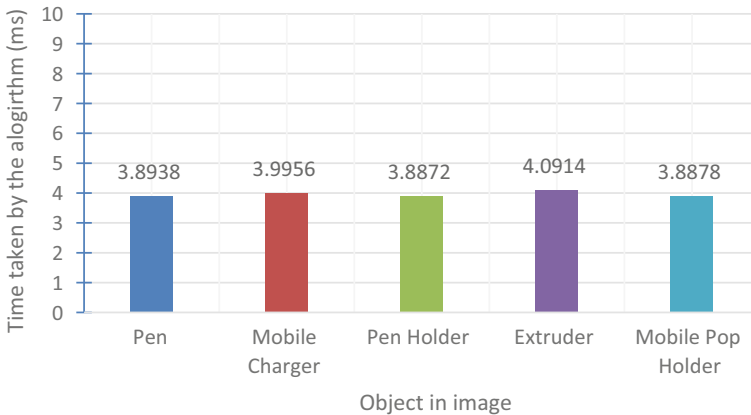


Fig. 12 Prediction time of the algorithm for each classified object during palletization

8.3 Effect of Image Resolution on Error in Prediction

Setup. The algorithm was made to run on 125 images (25 images per object) at 5 different resolutions— 1000×750 , 800×600 , 600×450 , 400×300 and 200×150 . The average percentage error (9) at each resolution was noted down.

Result. The average percentage error decreased with the increase in resolution which can be understood by the fact that an increase in resolution accompanies an increase in the details of the object in the image and allows for creation of a more accurate bounding box (Fig. 13; Table 3).

9 Network Architecture & Training Parameters

As authors' created dataset has 6 classes only but the ImageNet has more than 1000 classes hence the fully connected layers from the end of pre-trained ResNet-50 model

Fig. 13 Average percentage error at different resolutions

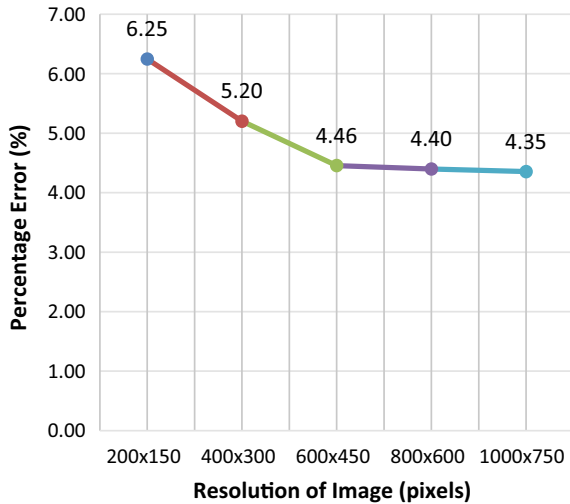


Table 3 Average percentage error at different resolutions

Resolution	Percentage error (%)
200×150	6.25
400×300	5.20
600×450	4.46
800×600	4.40
1000×750	4.35

[28] were removed. In place of those, 4 layers were added—a flattening layer, a fully connected layer comprising of 256 neurons having ReLU activation Eq. 11 [29], followed by a dropout layer [30] with retaining probability set as $p = 0.5$ followed by another fully connected layer of six neurons having softmax activation Eq. 12 [31]. See Fig. 14.

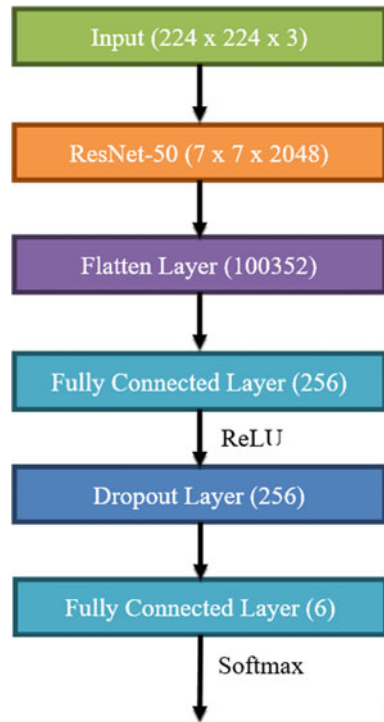
$$\text{Re}(x) = \max(0, x) \tag{11}$$

$$\sigma(\vec{x}) = \frac{e^{x_i}}{\sum_k e^{x_k}} \tag{12}$$

The input images kept to 224×224 sizes. In training, Categorical Cross Entropy (CCE) [32] was utilized as the loss function. Categorical Cross Entropy is depicted in Eq. 13. Stochastic gradient descent was used as the optimizer with a learning rate of 0.0001. The training was done for 30 epochs.

$$\text{CCE} = - \sum_i^C t_i \log(p_i) \tag{13}$$

Fig. 14 The architecture of the CNN model utilized in the proposed method



where, t_i is a binary variable valued 1 if i th category is the correct classification for the image otherwise 0, and p_i is the prediction probability that the image contains object of i th category (Figs. 15, 16 and 17).

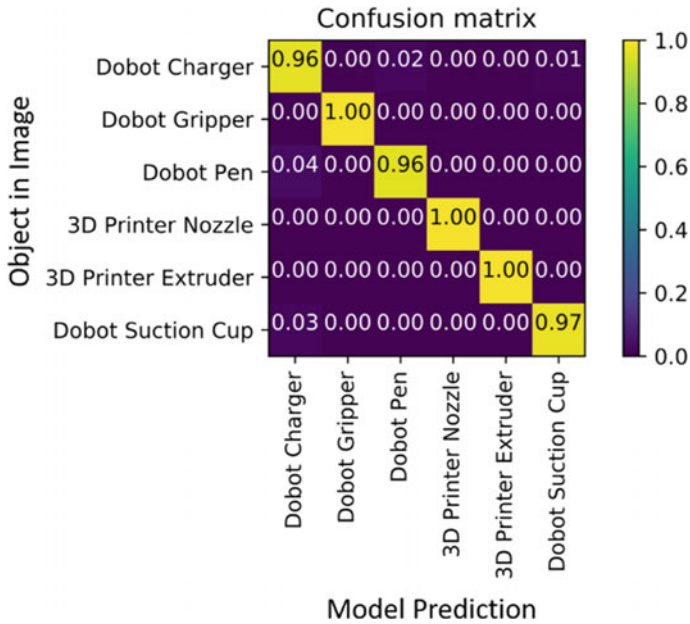


Fig. 15 CNN architecture model prediction

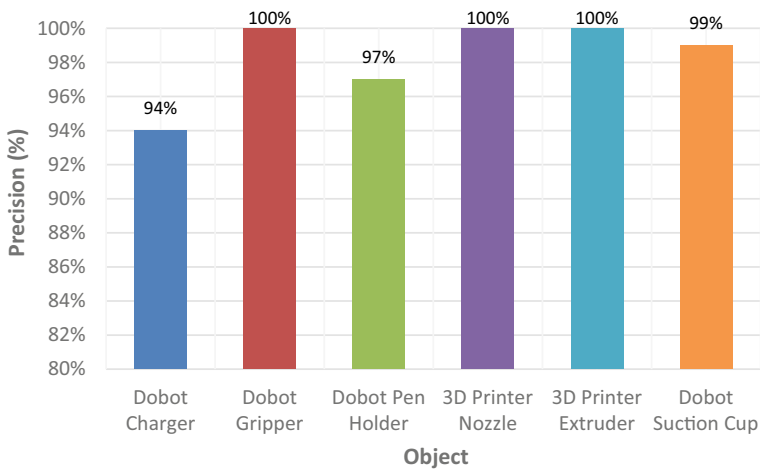


Fig. 16 Precision obtained using the model

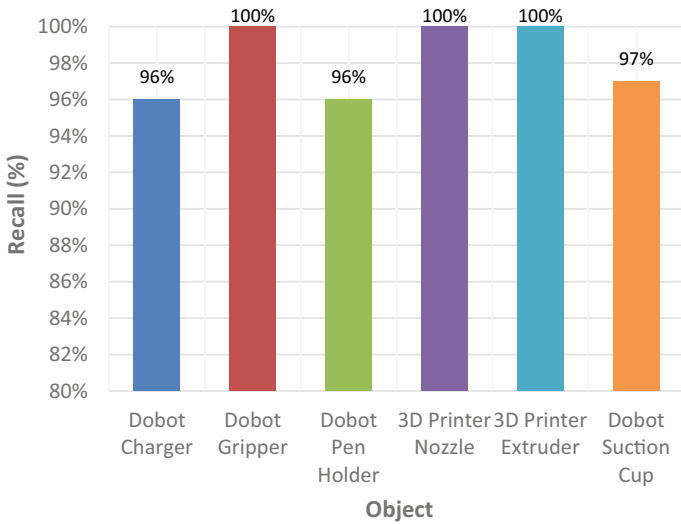


Fig. 17 Recall obtained using the model

For the purpose of evaluation, the test set mentioned in Sect. 7 was used. The tests were performed on a Xeon CPU with Nvidia Tesla Graphics Card and 12 GB of memory. The equipment present at the CEFC Smart Factory facility of the Indian Institute of Science was used to perform the experiment. See Fig. 18.



Fig. 18 The experimental test bed available with collaborative manipulator robot and industrial robot present at the CEFC, IISc Bangalore

9.1 Accuracy

Setup. The Accuracy (Acc) is the percentage of number of correct predictions to the number of total predictions Eq. 14. For determining the accuracy (Acc) of the model, predictions were made for all 472 images present in the test set and then the accuracy (Acc) was computed.

$$\text{Acc} = \frac{\text{correct predictions}}{\text{total predictions}} * 100\% \quad (14)$$

$$\text{Precision} = \frac{\text{TP}}{\text{TP} + \text{FP}} * 100\% \quad (15)$$

$$\text{Recall} = \frac{\text{TP}}{\text{TP} + \text{FN}} * 100\% \quad (16)$$

where TP is the count of true positive results, FP is the count of false positive results, and FN is the count of false negative results.

Result. The prediction obtained using the model had an accuracy of 98.94% on the test set. From the confusion matrix, see Fig. 15, the model seems to confuse between Dobot Pen, Dobot Suction Cup, and Dobot Charger. The precision Eq. 15 and recall Eq. 16 for each class of objects were calculated.

9.2 Prediction Time

Setup. Prediction Time is termed as the time required by the model to make a prediction for an image. The model was utilized to generate predictions on all 472 images present in the test set. Then the mean prediction time was calculated using Eq. (17).

$$\frac{\sum p_i}{N} \quad (17)$$

where, p_i is the time required by the model to make the prediction on the i th image and N is total images present in the test set.

Result. The mean prediction time obtained using the method came out to be 0.230 s per image. Hence, it can run at 4 frames per second (FPS).

10 Discussion and Conclusion

In this paper, a vision-based approach for calculating the dimensions of an object and classifying them using images taken from a two-dimensional camera for the purpose of automatically mixed palletization was presented. The proposed classification method using ResNet50 model achieved an accuracy of 98.94% which is higher than previous works. The results could likely be due to the fact that CNNs like ResNet50 learn to extract features from images and do not depend on handcrafted features. The classification method ran at 4 frames per second (FPS), hence has the potential to be utilized in other applications in warehouses as well. The performance of a classification method highly depends on the features selected. It is difficult to manually find features robust enough to cope with the variations that occur in real life. Previous works utilized either ZFNet model or VGG16 model for feature extraction, both of them are shallower models than the model used in this paper, ResNet50. ResNet50 has demonstrated a higher accuracy than ZFNet and VGG16 models on large scale image classification task [33]. While ResNet50 model does have a slightly higher prediction time than VGG16 but for industrial sorting applications, accurate classification of objects takes precedence over fast prediction times. The algorithm for measuring dimensions had an error of 6.492% on average and ran at 250 frames per second (FPS) which makes it suitable for other real time applications as well. The shortcomings of a few of the current methods namely, tedious calibration process and speed were discussed. Shortcomings of the proposed method namely, the high error percentage (14.716%) when dealing with objects with a very diverse set of heights were also discussed. In the future, work would be done to develop this method further for calculating 3D dimensions using multiple cameras. Dobot Magician [27] would be utilized as a test bed for the method and it would further be used for experimentation. The method will be adapted to solve alignment and sorting of objects.

Funding The funding for this project was provided under Samarth Udyog Project: Funded by CEFC, Department of Heavy Industries, Govt. of India.

References

1. Corbato CH, Bharatheesha M, van Egmond J, Ju J, Wisse M (2018) Integrating different levels of automation: lessons from winning the amazon robotics challenge 2016. *IEEE Trans Industr Inf* 14(11):4916–4926
2. Wang J, Zhang N, He Q (2009) Application of automated warehouse logistics in manufacturing industry. In: 2009 ISECS international colloquium on computing, communication, control, and management, Sanya, pp 217–220
3. Guney MA, Raptis IA (2015) A robotic experimental platform for testing and validating warehouse automation algorithms. In: 2015 IEEE international conference on technologies for practical robot applications (TePRA), Woburn, MA, pp 1–6

4. Krug R et al (2016) the next step in robot commissioning: autonomous picking and palletizing. *IEEE Robot Autom Lett* 1(1):546–553
5. Sriram T, Vishwanatha Rao K, Biswas S, Ahmed B (1996) Applications of barcode technology in automated storage and retrieval systems. In: *Proceedings of the 1996 IEEE IECON, 22nd international conference on industrial electronics, control, and instrumentation, Taipei, Taiwan, vol 1*, pp 641–646
6. Hong-ying S (2009) The application of barcode technology in logistics and warehouse management. In: *2009 first international workshop on education technology and computer science, Wuhan, Hubei*, pp 732–735
7. Wang Q, McIntosh R, Mileham A (2010) A RFID-based automated warehouse design. In: *2010 2nd international conference on computer engineering and technology, Chengdu, 2010*, pp V6–359–V6–363
8. Pihir I, Pihir V, Vidačić S (2011) Improvement of warehouse operations through implementation of mobile barcode systems aimed at advancing sales process. In: *Proceedings of the ITI 2011, 33rd international conference on information technology interfaces, Dubrovnik*, pp 433–438
9. Žunić E, Beširević A, Delalić S, Hodžić K, Hasić H (2018) A generic approach for order picking optimization process in different warehouse layouts. In: *2018 41st international convention on information and communication technology, electronics and microelectronics (MIPRO), Opatija*, pp 1000–1005
10. Zhang B, Skaar SB (2009) Robotic de-palletizing using uncalibrated vision and 3D laser-assisted image analysis. In: *2009 IEEE/RSJ international conference on intelligent robots and systems, St. Louis, MO*, pp 3820–3825
11. Wurll C (2016) Mixed case palletizing with industrial robots. In: *Proceedings of ISR 2016: 47th international symposium on robotics, Munich, Germany*, pp 1–6
12. Anwer A, Baig A, Nawaz R (2015) Calculating real world object dimensions from Kinect RGB-D image using dynamic resolution. In: *2015 12th international Bhurban conference on applied sciences and technology (IBCAST), Islamabad*, pp 198–203
13. Mane SS, Yangandul CG (2016) Calculating the dimensions of an object using a single camera by learning the environment. In: *2016 2nd international conference on applied and theoretical computing and communication technology (iCATccT), Bangalore*, pp 457–460
14. Othman NA, Salur MU, Karakose M, Aydin I (2018) An embedded real-time object detection and measurement of its size. In: *2018 international conference on artificial intelligence and data processing (IDAP), Malatya, Turkey*, pp 1–4
15. Fan X, Zhu A, Huang L (2017) Noncontact measurement of indoor objects with 3D laser camera-based. In: *2017 IEEE international conference on information and automation (ICIA), Macau*, pp 386–391
16. Kainz O, Jakab F, Horečný MW, Cymbalák D (2015) Estimating the object size from static 2D image. In: *2015 international conference and workshop on computing and communication (IEMCON), Vancouver, BC*, pp 1–5
17. Erdoğan K, Yılmaz N (2014) Shifting colors to overcome not realizing objects problem due to color vision deficiency. In: *2014 2nd international conference on advances in computing, electronics and electrical technology—CEET, Kuala Lumpur, Malaysia*
18. Ganesan P, Rajini V, Sathish BS, Shaik KB (2014) HSV color space based segmentation of region of interest in satellite images. In: *2014 international conference on control, instrumentation, communication and computational technologies (ICCICCT), Kanyakumari*, pp 101–105
19. Raof RAA et al (2008) Color thresholding method for image segmentation algorithm of Ziehl-Neelsen sputum slide images. In: *2008 5th international conference on electrical engineering, computing science and automatic control, Mexico City*, pp 212–217
20. Yogarajah P, Condell J, Curran K, Cheddad A, McKeivitt P (2010) A dynamic threshold approach for skin segmentation in color images. In: *2010 IEEE international conference on image processing, Hong Kong*, pp 2225–2228
21. Prabha DS, Kumar JS (2016) Performance analysis of image smoothing methods for low level of distortion. In: *2016 IEEE international conference on advances in computer applications (ICACA), Coimbatore*, pp 372–376

22. Dnyandeo SV, Nipanikar RS (2016) A review of adaptive thresholding techniques for vehicle number plate recognition. *Int J Adv Res Comput Commun Eng* 5(4)
23. Guo H, An J (2010) Image restoration with morphological erosion and exemplar-based texture synthesis. In: 2010 6th international conference on wireless communications networking and mobile computing (WiCOM), Chengdu, pp 1–4
24. Arbeláez P, Maire M, Fowlkes C, Malik J (2011) Contour detection and hierarchical image segmentation. *IEEE Trans Pattern Anal Mach Intell* 33(5):898–916
25. Venkatesh YV, Raja SK, Ramya N (2006) Multiple contour extraction from graylevel images using an artificial neural network. *IEEE Trans Image Process* 15(4):892–899
26. Suzuki S et al (1985) Topological structural analysis of digitized binary images by border following. *Comput Vis Graph Image Process* 30(1):32–46
27. Nagata F et al (2018) Outline font handler for industrial robots. In: 2018 IEEE international conference on mechatronics and automation (ICMA), Changchun, pp 1823–1828
28. He K, Zhang X, Ren S, Sun J (2016) Deep residual learning for image recognition. In: 2016 IEEE conference on computer vision and pattern recognition (CVPR), Las Vegas, NV, pp 770–778
29. Hu Z, Li Y, Yang Z (2018) Improving convolutional neural network using pseudo derivative ReLU. In: 2018 5th international conference on systems and informatics (ICSAD), Nanjing, pp 283–287
30. Ko B, Kim H, Choi H (2017) Controlled dropout: a different dropout for improving training speed on deep neural network. In: 2017 IEEE international conference on systems, man, and cybernetics (SMC), Banff, AB, pp 972–977
31. Wang B, Li T, Huang Y, Luo H, Guo D, Hornng S (2017) Diverse activation functions in deep learning. In: 2017 12th international conference on intelligent systems and knowledge engineering (ISKE), Nanjing, pp 1–6
32. Ghosh A, Kumar H, Sastry PSS (2017) Robust loss functions under label noise for deep neural networks. In: AAAI conference on artificial intelligence, North America, February 2017
33. Russakovsky O, Deng J, Su H, Krause J, Satheesh S, Ma S, Fei-Fei L (2015) Imagenet large scale visual recognition challenge. *Int J Comput Vision* 115(3):211–252

Welding Processes for Additive Manufacturing—Processes, Materials, and Defects



Falak P. Patel, Bhumi K. Patel, and Vishvesh J. Badheka

Abstract Additive manufacturing has changed the whole layout of the manufacturing industry with its layer-by-layer approach. With the help of this technique, the fabrication of complex and intricate parts in the different industries was possible in less time and reduced portfolio cost. Among all the different techniques, the interest in wire arc additive manufacturing (WAAM) is increasing due to its higher deposition rate and cheaper production cost. Significant research is carried out in this area to shift it toward mainstream manufacturing. This paper gives a synopsis of the noteworthy progress made in WAAM and highlights different types along with the mechanical and microstructural properties obtained in the manufactured parts. It also highlights a framework for quality fabrication using WAAM.

Keywords Additive manufacturing · Wire arc additive manufacturing · GTAW · GMAW

1 Introduction

Additive manufacturing (AM) is one of the trending topics in the scientific community because of its ability to manufacture components in layer-by-layer fashion. There are many AM techniques available for the fabrication of metals, non-metals, and polymers. WAAM is one such process used for the fabrication of metal components. Because of the complex nature of this process, it is important to study different parameters like feedstock quality and path planning [1]. Currently, many researches

F. P. Patel (✉) · B. K. Patel · V. J. Badheka
Department of Mechanical Engineering, SOT, Pandit Deendayal Energy University (PDEU),
Raisan, Gandhinagar, Gujarat 382007, India
e-mail: falak.pmc18@sot.pdpu.ac.in

B. K. Patel
e-mail: bhumi.pmc18@sot.pdpu.ac.in

V. J. Badheka
e-mail: Vishvesh.Badheka@spt.pdpu.ac.in

are going on to determine the mechanical and microstructural properties of the parts manufactured using the WAAM process and also to find solution to shift this technique in mainstream manufacturing. A detailed explanation of WAAM process is given in this paper. It also briefly discusses welding discipline in AM techniques.

2 Welding Discipline in Additive Manufacturing

In recent years, additive manufacturing (AM) using direct deposition method (DED) has gained popularity in mainstream fabrication of metal components as it enables the manufacturer to fabricate complex and intricate parts with ease and without much material wastage and in less time when compared to conventional approaches. The combination of AM and welding for metal components is notably new in the manufacturing sector. Associating AM with welding technology has been proven to have profound advantages over conventional manufacturing techniques. These techniques can produce metal components with high strength, non-porous, and high fatigue resistance [2, 3]. But there are some drawbacks to this technique as the parts fabricated undergo significant heating–cooling cycles, so the properties obtained are not homogeneous. Due to the limitation of this technique, commercialization of this combination is not yet possible.

2.1 Types of Welding-Based Additive Manufacturing Techniques

Welding-based additive manufacturing (WAM) process includes techniques like wire arc additive manufacturing (WAAM), laser additive manufacturing (LAM), electron beam additive manufacturing (EBAM), friction stir additive manufacturing (FSW), etc. [2, 3]. Parts fabricated in each and every process have its advantages and disadvantages. Some process may be better suitable for one material than other and yield better mechanical and microstructural properties. For example, gas metal arc welding (GMAW)-based WAAM is better suitable for aluminum and steel but is not suitable for titanium alloys as the titanium causes arc to wander and rough surface is obtained [4]. It is better suitable to manufacture titanium parts using gas tungsten arc welding (GTAW)-based WAAM [5, 6]. Different setups of WAM are shown in Fig. 1. Although this article fully focuses on WAAM.

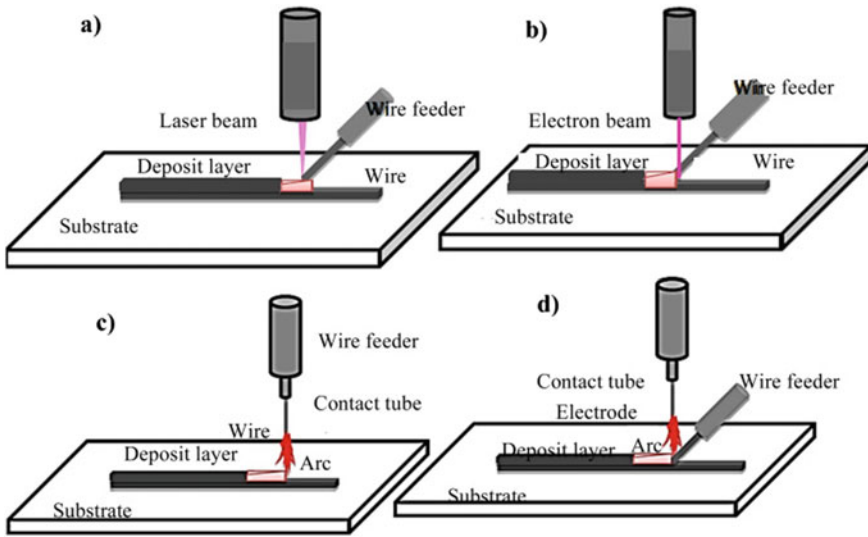


Fig. 1 Welding based AM a LAM, b EBM, c GMAW, d GTAW [2, 3]

3 Wire Arc Additive Manufacturing (WAAM)

The main hurdle of AM techniques was the limitation of the size of the parts. We know that the main principle of welding discipline is metal joining, so to overcome the limitation, techniques with the combination of AM and welding were proposed. In WAAM, an electrical arc is used as heat source and metal wire is used as feed stock, and final part is manufactured by depositing metal in a layer-by-layer fashion. With the help of WAAM part can be manufactured with higher print resolution, low production cost, high surface quality, and in less time compared to other AM processes [3, 7]. This process with its design flexibility and ability to work with nickel and titanium alloys has found its applications in aviation and aerospace industry. This process also has recently found its applications in the production of large-scale engineering structure so with proper research it will eventually find its place in commercial manufacturing [2]. There are lots of studies going on to optimize this process. WAAM process is shown in Fig. 2.

3.1 Classification of Wire Arc Additive Manufacturing

Based upon the type of heat source used, WAAM process can be divided into three types:

- Gas metal arc welding (GMAW)
- Gas tungsten arc welding (GTAW)

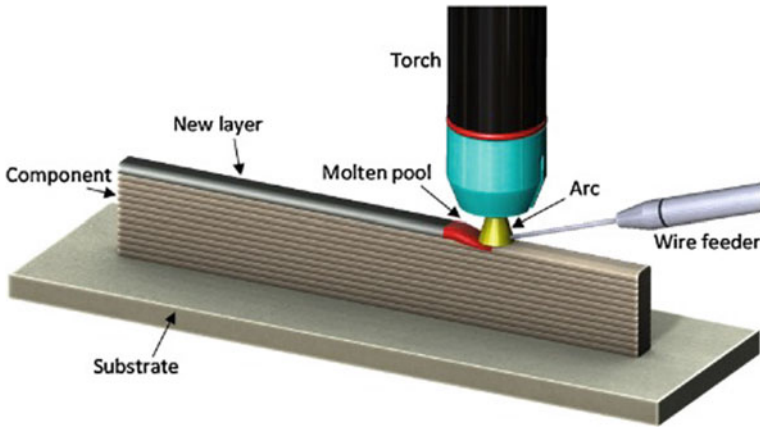


Fig. 2 Wire arc additive manufacturing (WAAM) process [8]

- Plasma arc welding (PAW).

GMAW process uses a consumable electrode. In this process, the electric arc is formed between the consumable electrode and workpiece. While in GTAW and PAW, non-consumable electrodes are used [9]. The wire feed in these processes is varying depending on the orientation of the system. This makes the path planning in GTAW and PAW more complicated than in GMAW [9, 10]. Schematic diagram of all GTAW, GMAW, and PAW is shown in Figs. 3, 4, and 5.

Fig. 3 GTAW [11]

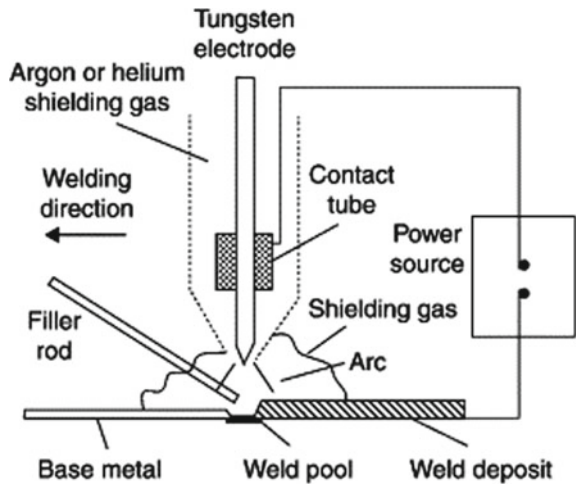


Fig. 4 GMAW [12]

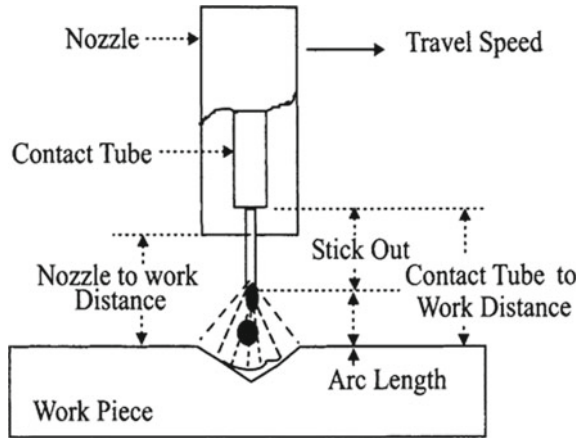
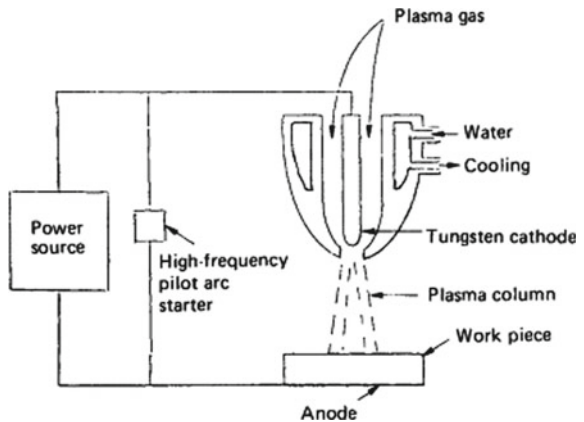


Fig. 5 PAW [13]



3.2 Equipment Setup for Wire Arc Additive Manufacturing

WAAM setups can be mainly bifurcated into two types of system: robot-assisted system or machine tool-based system. Although nowadays for WAAM process robotic arms are used as motion mechanism. On the basis of the shielding gas environment, WAAM setup can be divided into two types. The first design uses a closed chamber to facilitate optimum inert gas shielding environment. The second setup uses existing protecting mechanism to provide shielding gas locally during metal deposition process. This setup can be customized with protective mechanism around a robotic arm. As the first setup uses a closed chamber, the size of the parts manufactured is restricted. But second setup is capable of manufacturing metal structure up to some meters [14]. Both types of setups are shown in Figs. 6 and 7.

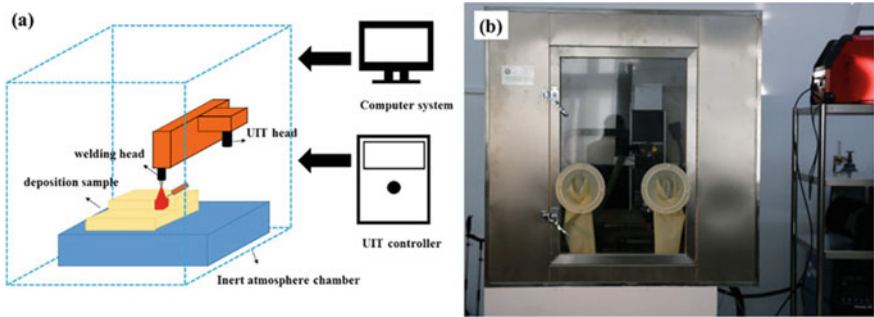


Fig. 6 Closed chambered design system [15]

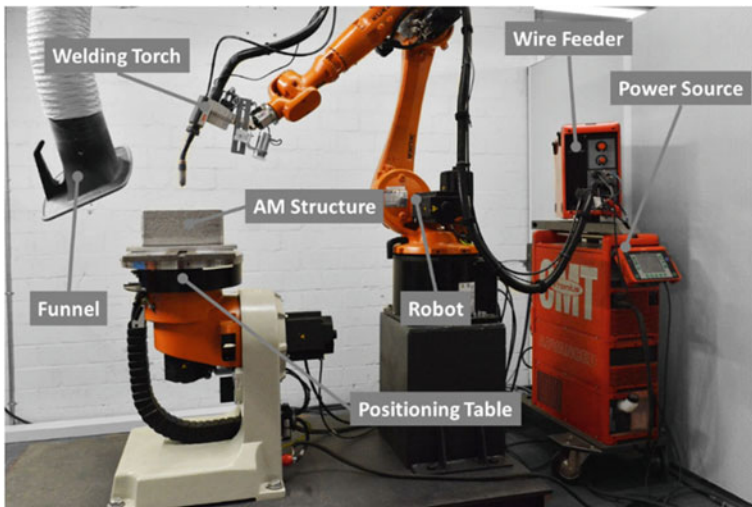


Fig. 7 Robot assisted setup for WAAM [16]

3.3 Step-By-Step Wire Arc Additive Manufacturing Process

Manufacturing of any component using WAAM consists of three main steps: process planning, deposition rate, and post-processing. Figure 8 shows the step-by-step procedure for the fabrication of the part using WAAM.

Frist step is to generate 3D model of the part to be manufactured using CAD software. The next step is to save the 3D model with standard file format (.stl) so that the part can directly be opened in slicing software. Once the part is opened in a slicing software, it converts the 3D model into 2D layers with optimum thickness and plans the path for deposition of material. The path planning and slicing process are done in such manner that least amount of defects are generated in the fabricated part. On the basis of model geometry and material, suitable process parameters are decided.

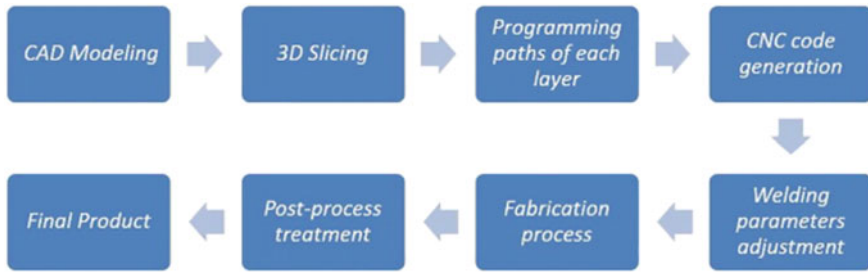


Fig. 8 Step-by-step procedure for WAAM [17]

This step is accompanied by CNC code generator which can be done manually or by computer programming software. After this process, the CNC code and all the parameters are transferred to the WAAM setup and layer deposition process is started. This process continues until the whole part is fabricated. Depending on the properties obtained of the manufactured part, post-processing treatments are chosen to rectify the defects that occurred during fabrication process.

4 Metals Fabricated Using Wire Arc Additive Manufacturing

Mainly in WAAM process, the spooled wires available for welding application are used. The metal wires used in welding are utilized as feedstock in WAAM process. The metal wires of different alloy and combination are already available in the industry. It is crucial to understand all the process parameters, input variables, and effect of these parameters on the metal to fabricate defect-free, resilient, and structurally reliable component [16].

Certain alloys when fabricated using WAAM process have found its application in different fields of the industries. For example, titanium alloys fabricated using WAAM are used in aerospace, marines and in corrosion-resistant and high-temperature-based components. WAAM-based aluminum components are used in automotive and aerospace industries. WAAM-based steel components are used in tooling and automobile industries. Also, nickel alloys fabricated with WAAM process are used in aerospace and for high temperature and corrosion-resistant-based products. Furthermore, the mechanical and microstructural properties of different metals and its alloys are discussed [18–29].

4.1 Titanium Alloys

The fabrication of the components of titanium alloys with the help of conventional method is very costly and time-consuming. So, extensive research is going on to determine the application of WAAM-based titanium components in various industries. Aerospace is one such promising industry where WAAM-based Ti components are used as the components in this industry require high strength-to-weight ratio [14]. Here the fabrication of titanium using WAAM-based process helps in reducing material costing as there is very less wastage of material in these processes.

The microstructural properties of any component depend upon the thermal history during the fabrication process. In WAAM, rapid heating and cooling cycles are involved and because of that non-homogeneous microstructural properties are obtained [30, 31]. For example, when the microstructural properties of Ti6Al4V fabricated using GTAW-based WAAM process were examined, two different types of regions were noticed. In bottom region, alternating bands perpendicular to build region were observed. While in top region needle-like precipitates were found [31]. Furthermore, from different studies it is evident that after post-processing the mechanical and microstructural properties obtained are close to the properties obtained in wrought process [32–38].

4.2 Nickel Alloys

Ability of nickel-based alloys to hold high strength at high temperature makes it one of the most sought-after material researched under AM techniques. Ni-based alloys have found many commercial applications as it is very hard to fabricate using conventional manufacturing methods.

The two of the most studied Ni-alloys under the umbrella of WAAM process are Inconel 718 and Inconel 625 [39]. It was observed in the microstructure of these alloys when fabricated using WAAM process, they form large columnar grains with dendritic boundaries. Moreover, from the studies it is observed that the ultimate tensile strength, yield strength, and ductility of the component are in the same line with the properties obtained in wrought and cast processing [14].

4.3 Aluminum Alloys

Many studies have been successfully carried out for the fabrication of aluminum part using WAAM-based process. From the results of these studies, it is clear that the cost of fabrication of aluminum component is only justifiable when the part has complex geometry and thin-wall structures [40]. The cost of manufacturing simple part using conventional method is very low. This is the main reason that this process is not as

popular for the aluminum components as with the other metals. Also, the challenges like unstable weld pool and porosity are encountered during deposition process [16].

To get refined mechanical and microstructural properties of deposited aluminum, it is necessary that the fabricated part undergo post-processing. Optimum process parameter along with good quality feedstock can help with the porosities in the fabricated part.

4.4 *Stainless Steel*

The fabrication of stainless steel using WAAM-based techniques reflected good mechanical and microstructural properties [41]. The microstructure of steel only contains austenitic phase but when manufactured using WAAM process shows combination of austenite and ferrite in the microstructure [42]. It is also observed that the components had minor inhomogeneity but on proper post-processing can be removed. The mechanical and microstructural properties obtained in this case are very similar to the parts manufactured in conventional machining [43]. Even though there are many advantages, the cost is one of the hurdles in the commercialization of this process for SS.

4.5 *Other Metals*

Many studies are going on to investigate future prospects of WAAM-based methods for the fabrication of bimetallic metals like steel/nickel, steel/bronze, and magnesium alloy [14]. These materials cause major defect when fabricated using WAAM techniques. So, it is very necessary to determine optimum input parameters and proper processing condition for defect-free fabrication of any component.

5 Common Defects in WAAM Fabricated Component

The mechanical properties of component fabricated using WAAM process are mostly similar to the properties of the material fabricated using conventional techniques. But still there are some defects encountered during the fabrication using WAAM-based process. Figure 9 shows relation between different materials and defects produced while fabricated using WAAM process.

5.1 *Porosity*

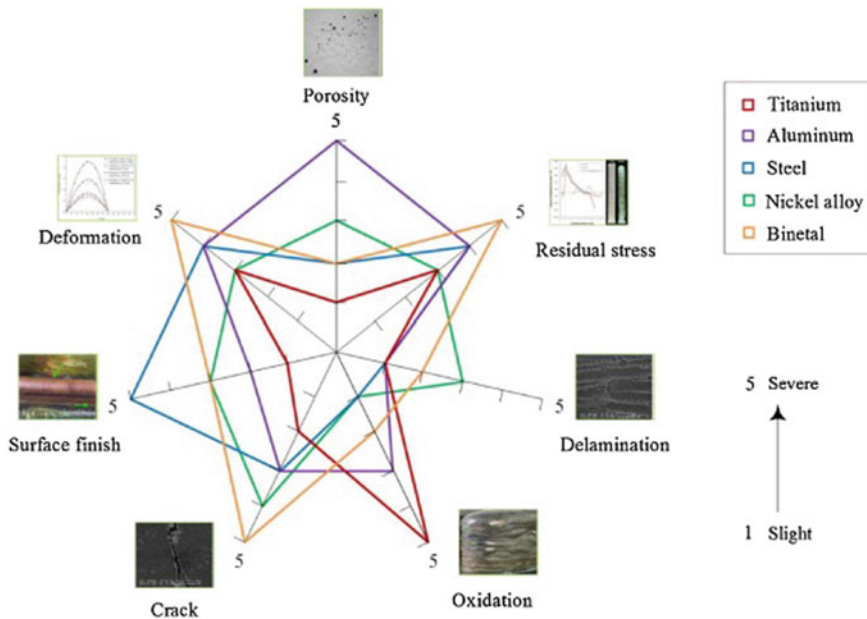


Fig. 9 Defects observed in different metals [14]

The two main reasons for the cause of this process are impure raw material and poor choice of process parameters [18, 44]. The contamination of the raw material with grease, moisture, and dust particles can cause porosity throughout the solidification of the weld pool. Moreover, inappropriate selection of process parameters like deposition rate, shielding gas, and inferior path planning can also generate porosity in the fabricated part. Aluminum is most vulnerable to this type of defect. So in order to evade this defect, it is crucial to clean raw material, particularly Aluminum. All the input parameters should be selected to achieve optimum outcome. The thermal gradient during the process should be supervised and controlled. Also, many post-processing techniques can help in curing porosity in the fabricated part [14, 16].

5.2 Residual Stress and Distortion

When all the external forces are removed from the component, there are still some amount of stresses present in the component. They are called residual stresses. When a part is fabricated using WAAM techniques, it is mostly impossible to steer clear of this defect. Residual stresses are one of the main causes of distortion and delamination in fabricated part. If the magnitude of the residual stress is substantially high, it influences the fatigue behavior and fracture limit of the part [45].

The continuous heating–cooling cycle in the manufacturing process is the main cause of distortion or deformation in the manufactured component. Refining the deposition path can result in major improvement in the quality of fabricated part [46]. Furthermore, it is important to understand the material properties in order to reduce magnitude of the residual stress in any component [16].

5.3 Cracking and Delamination

High thermal gradient during fabrication process is the main cause of cracking in WAAM fabricated part. There are two types of cracks formed in the WAAM fabricated component, i.e., grain boundary crack and solidification crack [44]. As the name suggests the grain, boundary cracks are formed near the grain edge. They are caused due to difference in boundary morphology and due to precipitates formation. While solidification cracks are the resulted when there is blockage in solidifying grain flow. It is also caused in high strain weld pool [47, 48].

Delamination is the separation phenomenon between the adjacent layers. The main cause of this defect is inadequate reheating of the previous solid layer. Pre-treatment processing of feedstock is done in order to avoid prevent this defect. Nickel alloys and bimetal are most vulnerable to this type of defect [16].

6 Scope of Quality Improvement in WAAM Process

It is crucial to have an exhaustive understanding of materials, process control parameters, model setup to fabricate high-quality component. Extensive research is going on to increase the stability of the process and to decrease the amount deposition defect in the fabricated part. The main steps toward this process are process selection, feedstock optimization, and post-process treatment. A detailed framework directing to achieve high-quality fabrication is shown in Fig. 10.

At present, there are many studies going on the variants of WAAM process. The main aim of these variants is to produce parts with better mechanical and microstructural properties without much more need of post-processing techniques. Some of the variants of WAAM are given in Table 1.

7 Applications of WAAM Fabricated Components

The WAAM fabricated parts have specifically found its applications in the industries such as automobile, aerospace, and defense [18, 36, 49]. The ability of the process to topologically optimized component has made it very popular in these industries for fabrication of large, lightweight, and complex engineering structure. It is also used

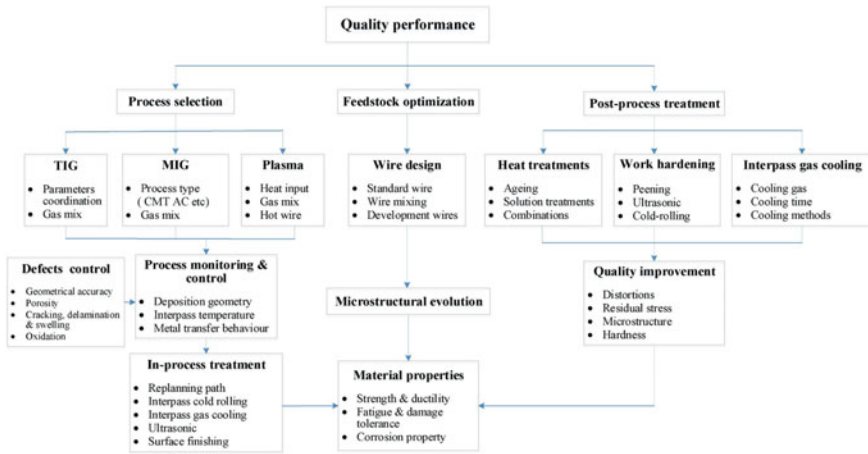


Fig. 10 Overview of WAAM process [14]

to fabricate high costing metals as the material wastage is few and far between in this processes.

At the moment, the focus of aerospace industry is to fabricate titanium and nickel-based structures. This makes WAAM process the most suitable for the fabrication of these components. Norsk Titanium was the first to get the approval from federal aviation administration for additively manufactured titanium component fabricated with WAAM. That part was installed on the Boeing 787 Dreamliner [50].

Nickel- and SS-based alloys are used in nuclear industry. Here the components fabricated must be highly heat and corrosion resistance. The WAAM process can be used here to reduce cost as nickel is costly metal and is hard to process using conventional techniques. WAAM can also replace some less requested portions of nickel parts with stainless steel, allowing the reduction of cost and weight of these components [51].

WAAM process is also used to fabricate large engineering structures. For example, MX3D (shown in Fig. 11) has successfully fabricated metal bridge with a total weight of 4500 kg, 12.5 m in length, and 6.3 m wide using this technique [52].

8 Conclusion

Wire arc additive manufacturing techniques are one of the most suitable for the fabrication of parts in the aerospace and aviation industry as these methods are able to fabricate part in faster, cheaper, and with more design freedom in comparison with conventional methods. Also, this method is applicable to almost all the engineering alloys. But the fabrication of titanium and nickel is more preferred using WAAM as the cost of the process for other alloys is not justifiable for less complicated parts. To

Table 1 Different variants of WAAM [49]

Sr. no	WAAM variant	Advantages	Disadvantages
1	Cold-work-based techniques	<ul style="list-style-type: none"> • This technique can considerably decrease residual stresses and deformation, enhance microstructural regularity and mechanical properties • It reduces porosity and increases the accuracy of final component 	<ul style="list-style-type: none"> • Currently, it has been tried out for simple geometries and methodologies • Heavy machinery is required
2	Interlayer heating or cooling	<ul style="list-style-type: none"> • Concentrated heating/cooling mechanisms have displayed favorable results to reduce the interpass temperature which is responsible for the part-breakdown • Due to that it is possible to attain homogenous properties 	<ul style="list-style-type: none"> • Recent information available in this area is not sufficient to obtain pre-defined microstructural properties. More research is required in this domain
3	Pre-heating of substrate or feedstock	<ul style="list-style-type: none"> • Due to this technique, heat conduction decreases which results in the reduction of heat losses and smaller temperature gradient are obtained • Also, thermal stresses are reduced which leads to less chance of cracking in the part 	<ul style="list-style-type: none"> • Like other variants more research is required in this process to obtain better properties



Fig. 11 MX3D constructed bridge [53]

fabricate the most optimized part, a quality-based framework is also provided in this review. To fabricate a part with enhanced microstructural and mechanical properties, many variants are proposed.

Despite these facts, WAAM is an underdeveloped process and many studies are going on an industrial and academic levels to iron out all the variable parameter to determine the best process parameters to get the most optimized part.

Acknowledgements The authors would like to express gratitude toward Pandit Deendayal Energy University (PDEU) for supporting our study and the Indian Institute of Welding, Baroda Br. for supporting the registration fee.

References

1. Zhang Y, Chen Y, Li P, Male AT (2003) Weld deposition-based rapid prototyping: a preliminary study. *J Mater Process Technol* 135(2–3):347–357. [https://doi.org/10.1016/s0924-0136\(02\)00867-1](https://doi.org/10.1016/s0924-0136(02)00867-1)
2. Karayel E, Bozkurt Y (2020) Additive manufacturing method and different welding applications. *J Market Res* 9(5):11424–11438. <https://doi.org/10.1016/j.jmrt.2020.08.039>
3. Kumar M, Sharma A, Simhambhatla S (2019) Advances in welding technologies for process development. In: *Additive manufacturing with welding*. CRC Press, India
4. Shinn BW, Farson DF, Denney PE (2005) Laser stabilisation of arc cathode spots in titanium welding. *Sci Technol Weld Joining* 10(4):475–481. <https://doi.org/10.1179/174329305x46673>
5. Wang F, Williams S, Colegrove P, Antonysamy AA (2012) Microstructure and mechanical properties of wire and arc additive manufactured Ti–6Al–4V. *Metall and Mater Trans A* 44(2):968–977. <https://doi.org/10.1007/s11661-012-1444-6>
6. Williams SW, Martina F, Addison AC, Ding J, Pardal G, Colegrove P (2016) Wire + arc additive manufacturing. *Mater Sci Technol* 32(7):641–647. <https://doi.org/10.1179/1743284715y.00000073>
7. Lippold JC (2015) *Welding metallurgy and weldability*. Wiley
8. McAndrew AR, Alvarez Rosales M, Colegrove PA, Hönnige JR, Ho A, Fayolle R, Eytayo K, Stan I, Sukrongpang P, Crochemore A, Pinter Z (2018) Interpass rolling of Ti-6Al-4V wire + arc additively manufactured features for microstructural refinement. *Addit Manuf* 21:340–349. <https://doi.org/10.1016/j.addma.2018.03.006>
9. Ding D, Pan Z, Cuiuri D, Li H (2015) Wire-feed additive manufacturing of metal components: technologies, developments and future interests. *Int J Adv Manuf Technol* 81(1–4):465–481. <https://doi.org/10.1007/s00170-015-7077-3>
10. Ding J, Colegrove P, Mehnen J, Ganguly S, Sequeira Almeida P, Wang F, Williams S (2011) Thermo-mechanical analysis of wire and arc additive layer manufacturing process on large multi-layer parts. *Comput Mater Sci*. <https://doi.org/10.1016/j.commatsci.2011.06.023>
11. Álvarez Tejedor T, Singh R, Pilidis P (2013) Maintenance and repair of gas turbine components. *Modern Gas Turbine Syst* 565–634. <https://doi.org/10.1533/9780857096067.3.565>
12. Naidu DS, Ozcelik S, Moore KL (2003) Gas metal arc welding: modeling. Modeling, sensing and control of gas metal arc welding, pp 9–93. <https://doi.org/10.1016/b978-008044066-8/50004-5>
13. Richardson DB, Blanzymski TZ, Gregory EN, Hutchinson AR, Wyatt LM (1994) Manufacturing methods. In: *Mechanical engineer's reference book*, pp 16–1. <https://doi.org/10.1016/b978-0-7506-1195-4.50020-8>
14. Wu B, Pan Z, Ding D, Cuiuri D, Li H, Xu J, Norrish J (2018) A review of the wire arc additive manufacturing of metals: properties, defects and quality improvement. *J Manuf Process* 35:127–139. <https://doi.org/10.1016/j.jmapro.2018.08.001>

15. Köhler M, Fiebig S, Hensel J, Dilger (2019) Wire and arc additive manufacturing of aluminum components. *Metals* 9:608. <https://doi.org/10.3390/met9050608>
16. Singh SR, Khanna P (2021) Wire arc additive manufacturing (WAAM): a new process to shape engineering materials. *Mater Today: Proc* 44:118–128. <https://doi.org/10.1016/j.matpr.2020.08.030>
17. Yang Y, Jin X, Liu C, Xiao M, Lu J, Fan H, Ma S (2018) Residual stress, mechanical properties, and grain morphology of Ti–6Al–4V alloy produced by ultrasonic impact treatment assisted wire and arc additive manufacturing. *Metals* 8(11):934. <https://doi.org/10.3390/met8110934>
18. Busachi A, Erkoyuncu J, Colegrove P, Martina F, Ding J (2015) Designing a WAAM based manufacturing system for defence applications. *Proc CIRP* 37:48–53. <https://doi.org/10.1016/j.procir.2015.08.085>
19. Gu J, Ding J, Williams SW, Gu H, Bai J, Zhai Y, Ma P (2016) The strengthening effect of inter-layer cold working and post-deposition heat treatment on the additively manufactured Al–6.3Cu alloy. *Mater Sci Eng, A* 651:18–26. <https://doi.org/10.1016/j.msea.2015.10.101>
20. Uriondo A, Esperon-Miguez M, Perinpanayagam S (2015) The present and future of additive manufacturing in the aerospace sector: a review of important aspects. *Proc Inst Mech Eng Part G: J Aerospace Eng* 229(11):2132–2147. <https://doi.org/10.1177/0954410014568797>
21. Sing SL, An J, Yeong WY, Wiria FE (2015) Laser and electron-beam powder-bed additive manufacturing of metallic implants: a review on processes, materials and designs. *J Orthop Res* 34(3):369–385. <https://doi.org/10.1002/jor.23075>
22. Murr L, Gaytan S, Ceylan A, Martinez E, Hernandez D, Machado B, Ramirez D, Medina F, Collins S (2010) Characterization of titanium aluminide alloy components fabricated by additive manufacturing using electron beam melting. *Acta Mater* 58(5):1887–1894. <https://doi.org/10.1016/j.actamat.2009.11.032>
23. Guo N, Leu MC (2013) Additive manufacturing: technology, applications and research needs. *Front Mech Eng* 8(3):215–243. <https://doi.org/10.1007/s11465-013-0248-8>
24. Kainer KU (2006) *Metal matrix composites: custom-made materials for automotive and aerospace engineering*. Wiley
25. Kim TB, Yue S, Zhang Z, Jones E, Jones JR, Lee PD (2014) Additive manufactured porous titanium structures: through-process quantification of pore and strut networks. *J Mater Process Technol* 214(11):2706–2715. <https://doi.org/10.1016/j.jmatprotec.2014.05.006>
26. Bastidas DM, Röss J, Bosch J, Martin U (2021) Corrosion mechanisms of high-Mn twinning-induced plasticity (TWIP) steels: a critical review. *Metals* 11(2):287. <https://doi.org/10.3390/met11020287>
27. Aziz-Kerrzo M, Conroy KG, Fenelon AM, Farrell ST, Breslin CB (2001) Electrochemical studies on the stability and corrosion resistance of titanium-based implant materials. *Biomaterials* 22(12):1531–1539. [https://doi.org/10.1016/s0142-9612\(00\)00309-4](https://doi.org/10.1016/s0142-9612(00)00309-4)
28. Lu G, Zangari G (2002) Corrosion resistance of ternary Ni–P based alloys in sulfuric acid solutions. *Electrochim Acta* 47(18):2969–2979. [https://doi.org/10.1016/s0013-4686\(02\)00198-6](https://doi.org/10.1016/s0013-4686(02)00198-6)
29. Bewlay BP, Jackson MR, Subramanian PR, Zhao JC (2003) A review of very-high-temperature Nb-silicide-based composites. *Metall and Mater Trans A* 34(10):2043–2052. <https://doi.org/10.1007/s11661-003-0269-8>
30. Thijs L, Verhaeghe F, Craeghs T, Humbeeck JV, Kruth JP (2010) A study of the microstructural evolution during selective laser melting of Ti–6Al–4V. *Acta Mater* 58(9):3303–3312. <https://doi.org/10.1016/j.actamat.2010.02.004>
31. Baufeld B, van der Biest O (2009) Mechanical properties of Ti–6Al–4V specimens produced by shaped metal deposition. *Sci Technol Adv Mater* 10(1):015008. <https://doi.org/10.1088/1468-6996/10/1/015008>
32. Baufeld B, Brandl E, van der Biest O (2011) Wire based additive layer manufacturing: comparison of microstructure and mechanical properties of Ti–6Al–4V components fabricated by laser-beam deposition and shaped metal deposition. *J Mater Process Technol* 211(6):1146–1158. <https://doi.org/10.1016/j.jmatprotec.2011.01.018>

33. Wang F, Williams S, Rush M (2011) Morphology investigation on direct current pulsed gas tungsten arc welded additive layer manufactured Ti6Al4V alloy. *Int J Adv Manuf Technol* 57(5–8):597–603. <https://doi.org/10.1007/s00170-011-3299-1>
34. Brandl E, Greitemeier D (2012) Microstructure of additive layer manufactured Ti–6Al–4V after exceptional post heat treatments. *Mater Lett* 81:84–87. <https://doi.org/10.1016/j.matlet.2012.04.116>
35. Szost BA, Terzi S, Martina F, Boisselier D, Prytuliak A, Pirling T, Hofmann M, Jarvis DJ (2016) A comparative study of additive manufacturing techniques: residual stress and microstructural analysis of CLAD and WAAM printed Ti–6Al–4V components. *Mater Des* 89:559–567. <https://doi.org/10.1016/j.matdes.2015.09.115>
36. Brandl E, Baufeld B, Leyens C, Gault R (2010) Additive manufactured Ti–6Al–4V using welding wire: comparison of laser and arc beam deposition and evaluation with respect to aerospace material specifications. *Phys Proc* 5:595–606; Wu B et al (2018) *J Manuf Process* 35:127–139, 138
37. Zhang J, Zhang X, Wang X, Ding J, Traoré Y, Paddea S, Williams S (2016) Crack path selection at the interface of wrought and wire+arc additive manufactured Ti–6Al–4V. *Mater Des* 104:365–375. <https://doi.org/10.1016/j.matdes.2016.05.027>
38. Brandl E, Schoberth A, Leyens C (2012) Morphology, microstructure, and hardness of titanium (Ti–6Al–4V) blocks deposited by wire-feed additive layer manufacturing (ALM). *Mater Sci Eng, A* 532:295–307. <https://doi.org/10.1016/j.msea.2011.10.095>
39. Baufeld B (2011) Mechanical properties of INCONEL 718 parts manufactured by shaped metal deposition (SMD). *J Mater Eng Perform* 21(7):1416–1421. <https://doi.org/10.1007/s11665-011-0009-y>
40. Brice C, Shenoy R, Kral M, Buchanan K (2015) Precipitation behavior of aluminum alloy 2139 fabricated using additive manufacturing. *Mater Sci Eng, A* 648:9–14. <https://doi.org/10.1016/j.msea.2015.08.088>
41. Skiba T, Baufeld B, Biest OVD (2009) Microstructure and mechanical properties of stainless steel component manufactured by shaped metal deposition. *ISIJ Int* 49(10):1588–1591. <https://doi.org/10.2355/isijinternational.49.1588>
42. Washko SD, Agger G (1990) Wrought stainless steels. In: *ASM metals handbook*, 10th edn. ASM International Handbook Committee, Ohio, p 841
43. Hosseini AV, Högstrom M, Hurtig K, Valiente Bermejo MA, Stridh LE, Karlsson L (2019) Wire-arc additive manufacturing of a duplex stainless steel: thermal cycle analysis and microstructure characterization. *Weld World* 63(4):975–987. <https://doi.org/10.1007/s40194-019-00735-y>
44. Sames W, Medina F, Peter W, Babu S, Dehoff R (2014) Effect of process control and powder quality on Inconel 718 produced using electron beam melting. In: 8th international symposium on superalloy 718 and derivatives, pp 409–423. <https://doi.org/10.1002/9781119016854.ch32>
45. Sames WJ, List FA, Pannala S, Dehoff RR, Babu SS (2016) The metallurgy and processing science of metal additive manufacturing. *Int Mater Rev* 61(5):315–360. <https://doi.org/10.1080/09506608.2015.1116649>
46. Wang H, Kovacevic R (2000) Variable polarity GTAW in rapid prototyping of aluminum parts. In: *Proceedings of the 11th annual solid freeform fabrication symposium*
47. What is hot cracking (solidification cracking) (2017). TWI Ltd. <http://www.twi-global.com/technical-knowledge/faqs/material-faqs/faq-what-is-hot-cracking-solidification-cracking/>
48. Davis T (2004) The effect of process parameters on laser-deposited Ti–6Al–4V. <https://doi.org/10.18297/etd/319>
49. Rodrigues TA, Duarte V, Miranda R, Santos TG, Oliveira J (2019) Current status and perspectives on wire and arc additive manufacturing (WAAM). *Materials* 12(7):1121. <https://doi.org/10.3390/ma12071121>
50. Scott A Printed titanium parts expected to save millions in boeing dreamliner costs. Available online: <https://www.reuters.com/article/us-norsk-boeing/printed-titanium-parts-expected-to-savemillions-in-boeing-dreamliner-costs-idUSKBN17C264>
51. Abe T, Sasahara H (2016) Dissimilar metal deposition with a stainless steel and nickel-based alloy using wire and arc-based additive manufacturing. *Precis Eng* 45:387–395. <https://doi.org/10.1016/j.precisioneng.2016.03.016>

52. Hirtler M, Jedynek A, Sydow B, Sviridov A, Bambach M (2018) Investigation of microstructure and hardness of a rib geometry produced by metal forming and wire-arc additive manufacturing. In: Proceedings of the 5th international conference on new forming technology (ICNFT 2018), Bremen, Germany, 18–21 Sept 2018, pp 1–6
53. MX3D Bridge (nd). MX3D. <https://mx3d.com/industries/infrastructure/mx3d-bridge>